

Universität Stuttgart

One-Dimensional Topological States of Synthetic Quantum Matter

Von der Fakultät Mathematik und Physik der Universität Stuttgart
zur Erlangung der Würde eines Doktors der Naturwissenschaften
(Dr. rer. nat.) genehmigte Abhandlung.

vorgelegt von

Nicolai Lang

aus Stuttgart

Hauptberichter: Prof. Dr. Hans Peter Büchler

Mitberichterin: Prof. Dr. Maria Daghofer

Tag der mündlichen Prüfung: 18. März 2019

Institut für Theoretische Physik III

Universität Stuttgart

2019

Document Version

1.1 (31.07.2019)

Download a digital copy of this document at

➔ n15.de/phd

Errata and more information on

🔗 www.nicolailang.de

Questions, Comments & Corrections

→ kontakt@nicolailang.de

Cover (Print version only)

Phlox paniculata. Beautiful as physics.

© 2018 Nicolai Lang

Typesetting

This document has been edited with Vim and is composed in

Equity, Concourse, and **Math Time Professional**

with Lua^AT_EX and B^BT_EX.

Abstract

If you are not a scientist with background in physics and/or mathematics, you may want to read the “popular summary.”

Falls Sie kein Wissenschaftler mit fundierten Physik- oder Mathematikkennntnissen sind, bietet es sich an die “Zusammenfassung für Nichtphysiker” zu lesen.

This thesis is based on a collection of papers and addresses several questions on properties and applications of “topological matter,” a concept that drives a particularly active and increasingly complex field of condensed matter physics. If the reader is familiar with this field, there is nothing new I can tell in the few paragraphs of an abstract; if he or she is *not* familiar with the field, an abstract cannot do justice to the complexity of the field anyway. In any case, I recommend reading Sections 1.1 and 1.3 which provide a self-contained and fairly comprehensive review of “topological matter,” its properties and possible applications.

So let me start right away with a structured abstract of the contents:

- In Chapter 1, we review the theoretical foundations of this thesis and locate it within the ever-growing field of condensed matter physics. We start with an introduction to the general concept of topological quantum phases and discuss the role played by symmetries in this context. We address the classification of topological phases with and without interactions between their fermionic or bosonic constituents. Then, we discuss two paradigmatic models—the Su–Schrieffer–Heeger chain and the Majorana chain—as examples of non-interacting topological phases in one dimension. Both models are closely related and used repeatedly in this thesis, either as motivation for or key element of the presented projects. Finally, we review various proposals for applications of topological phases—both quantum and classical—to demonstrate that the concept is more than a theorist’s delight. We briefly comment on experimental results to make contact with the real world.

- In Chapter 2, we study a microscopic model of interacting fermions with topologically protected ground state degeneracy. The model, introduced in Ref. [1], is based on a double-wire setup with local interactions in a number-conserving setting. A compelling property of this model is the exact solvability for its ground states and low-energy excitations. We demonstrate the appearance of topologically protected edge states and derive their braiding properties on a microscopic level. We find the non-abelian statistics of Ising anyons which can be interpreted as Majorana-like edge states. As a result, the model qualifies as a number-conserving relative of Kitaev's paradigmatic Majorana chain.
- In Chapter 3, we show that a linear network of coupled bosonic degrees of freedom, characterized by topological bands, can be employed for the efficient exchange of quantum information. Features of the proposed setup, published in Ref. [2], are that it is robust against quenched disorder, all relevant operations can be performed by global variations of parameters, and the time required for communication between qubits approaches linear scaling with their distance. We show how the proposed concept can be extended to an ensemble of qubits embedded in a two-dimensional network to allow for communication between all of them.
- In Chapter 4, we focus on the application of the one-dimensional Majorana chain as a topological quantum memory and construct a strictly local decoder based on a self-dual cellular automaton. We study numerically and analytically its performance and exploit these results to contrive a scalable decoder with exponentially growing decoherence times in the presence of noise. These results, published in Ref. [3], pave the way for scalable and modular designs of actively corrected one-dimensional topological quantum memories.
- Chapter 5 is a safe haven for all projects that do not deserve their own chapter but are still interesting enough to be discussed somewhere. Some—mostly conceptual—are possible starting points for future projects, some are closely related to projects of the main part, and some are contributions to publications (in particular Ref. [4]) that are not covered in the other chapters.

It is advisable to have a look at “How to Read This Thesis” where the organization of this document is illustrated and explained.

Zusammenfassung für Nichtphysiker

Entsprechend der Promotionsordnung der Universität Stuttgart ist einer englischsprachigen Dissertation eine Zusammenfassung in deutscher Sprache beizufügen. Nun verlangt das Verfassen wissenschaftlicher Texte, deren vorrangiges Ziel ja die Wissensvermittlung ist, in der Regel eine Anpassung an die Leserschaft.

An wen richtet sich also die geforderte Zusammenfassung? An Spezialisten der behandelten Themen sicher nicht; für viele der Fachbegriffe existieren nicht einmal anerkannte deutsche Übersetzungen. Dann vielleicht an Physiker im Allgemeinen? Oder—noch weiter gefasst—Naturwissenschaftler? Auch das scheint mir, speziell im Licht der Internationalisierung praktisch aller naturwissenschaftlicher Disziplinen, nicht überzeugend. Es ist daher unwahrscheinlich, dass ein Leser, der von einer deutschen, *fachlichen* Zusammenfassung profitieren würde, das physikalisch-mathematische Rüstzeug besitzt ihr inhaltlich auch folgen zu können.

Um dieser Zusammenfassung zumindest ein wenig Sinnhaftigkeit zu verleihen, nehme ich mir die Freiheit, diese dediziert Nichtphysikern zu widmen, ja auch Lesern ganz ohne naturwissenschaftlichen Hintergrund.

Populärwissenschaftliche Publikationen—seien es Bücher, Dokumentationen, oder die vorliegende Zusammenfassung einer Dissertation—sind ein zweischneidiges Schwert. Zum einen sind sie essenziell um die Naturwissenschaft in der Breite der Gesellschaft zu verankern, um Menschen an die naturwissenschaftliche Methodik heranzuführen und um allgemein für Grundlagenforschung zu werben. Aber komplexe, hoch spezialisierte Wissenschaft einem Laienpublikum verständlich darzulegen ist, abhängig vom angestrebten Resultat, kompliziert bis unmöglich. Der Grund ist eine praktisch unüberbrückbare Disparität zwischen den Bildern im Kopf des Laien und denen im Kopf des Wissenschaftlers. Die Ursache hierfür ist nicht mangelnde Intelligenz, sondern mangelnde Erfahrung. Und Erfahrung—im Gegensatz zu Wissen—kann man nicht weitergeben. Der Unterschied sind Jahre des Studiums der Physik, Jahre der Gewöhnung an die Seltsamkeiten der Quan-

tenmechanik und die Eigenarten der Relativitätstheorie. Ich kann Ihnen die Bilder in meinem Kopf—mein *Verständnis*—nicht weitergeben. Seien Sie sich also dieser Grenzen bewusst, denn gefährlicher als Unwissen ist Scheinwissen. Seien Sie sich bewusst, dass die Bilder in Ihrem Kopf nur Karikaturen der meinen sind. Überstrapazieren Sie die Aussagekraft von Analogien und Bildern nicht, mögen sie noch so schön sein. Die Quantenmechanik ist *nicht* einfach.

Worum geht es in dieser Dissertation? Fangen wir vorne an: Sie ist angesiedelt im Bereich der *theoretischen Physik*. Während Experimentalphysiker im Labor physikalische Phänomene untersuchen, konstruieren theoretische Physiker abstrakte, mathematische Modelle (mit Bleistift und Papier oder am Computer) um die Beobachtungen der Experimentalphysiker zu erklären. Dieser Ablauf ist aber nicht zwingend: Theoretiker haben eine blühende Fantasie. Nicht selten schlagen sie theoretische Modelle vor, die erst im Anschluss von Experimentatoren im Labor realisiert werden (oder auch nicht; es ist erstaunlich schwer, die Natur dazu zu bringen, das zu tun, was Theoretiker sich ausdenken). Die vorliegende Dissertation ist von dieser Art: Sie befasst sich mit *theoretischen* Modellen die—zumindest auf dem Papier—interessante (und nützliche) Eigenschaften haben. Bis auf eine Ausnahme wurde keines dieser Modelle bisher in Experimenten realisiert. Das klingt nicht sehr ermutigend, ist in der theoretischen Physik aber eher die Regel als die Ausnahme.

Was ist überhaupt ein Modell? In der theoretischen Physik muss man sich unter einem “Modell” einen mathematisch präzise definierten Rahmen vorstellen mit abstrakten Objekten, die ein idealisiertes, physikalisches System beschreiben. In der Regel bedient man sich mathematischer Konzepte wie *Vektoren* und *Funktionen*, um den Zustand eines physikalischen Systems abstrakt darzustellen. Diese werden dann mit Gleichungen in Beziehung zueinander gesetzt, um die zeitliche Entwicklung oder die Reaktion des Systems auf eine Störung vorherzusagen. Ein Modell erlaubt also die mathematische Beschreibung realer Prozesse und Phänomene. Modelle sind das Handwerkszeug jedes theoretischen Physikers.

Um welche Modelle geht es also? Die vorliegende Dissertation ist im Bereich der *kondensierten Materie* angesiedelt. Dabei handelt es sich um ein Fachgebiet der Physik, das sich mit den Eigenschaften und der Beschreibung von Materialien beschäftigt, die vergleichsweise “kalt” und “dicht” sind. Die elementaren Bausteine dieser Materialien sind Atome (oder Ionen, also elektrisch geladene Atome) und Elektronen. Wichtige Teilbereiche dieses Gebiets sind die *Festkörperphysik*, die z. B. kristalline Materialien oder die Halbleiter in Computern untersucht, und die *Physik der Flüssigkeiten*, die sich mit der Dynamik und den Turbulenzen von solchen befasst. Typische Aufgaben der Physik der kondensierten Materie sind zu erklären, wieso Metalle Strom leiten, warum Halbleiter (z. B. Silizium) es nur unter bestimmten Voraussetzungen tun oder weshalb sich Eisen magnetisieren lässt. Ein wichtiger Teilaspekt in diesem Zusammenhang sind *Phasenübergänge*. Phasenübergänge beschreiben die abrupte Veränderung eines Materials, wenn

externe Parameter (z. B. die Temperatur oder der Druck) bestimmte kritische Werte über- oder unterschreiten. Die wohl bekanntesten Phasenübergänge sind das Gefrieren von Wasser bei 0 °C und das Verdampfen bei 100 °C. Obwohl die Bausteine—die Wassermoleküle—in allen drei Phasen dieselben sind, sind Eis, Wasser und Dampf doch völlig unterschiedlich. Solche Unterschiede zu erklären und systematisch zu erfassen ist ein zentrales Anliegen der Physik der kondensierten Materie.

Die letzten 100 Jahre der Physik wurden von zwei einflussreichen Theorien bestimmt: der Relativitätstheorie von ALBERT EINSTEIN und der *Quantenmechanik* (verknüpft mit Namen wie WERNER HEISENBERG, MAX BORN, ERWIN SCHRÖDINGER u.v.m.). Für die Physik der kondensierten Materie ist die Quantenmechanik von überragender Bedeutung, da ihr Ziel die Beschreibung vieler, atomar kleiner Bausteine bei oft sehr niedrigen Temperaturen ist. Die Relativitätstheorie hat auch ihre Auftritte, soll uns hier aber nicht weiter beschäftigen. Bei der Beschreibung von Phasen und ihren Übergängen wurde den Physikern des 20. Jahrhunderts schnell klar, dass die Seltsamkeiten der Quantenmechanik die Eigenschaften von Materie fundamental beeinflussen. Phasen, die nur bei sehr niedrigen Temperaturen auftreten und ausschließlich mit Hilfe der Quantenmechanik beschrieben werden können, nennt man *Quantenphasen*. Das wohl eindrucklichste Beispiel einer solchen ist die *supraleitende Phase* bestimmter Metalle (z. B. von Quecksilber oder Aluminium). Solche Metalle leiten bis zu einer materialspezifischen *kritischen Temperatur* nahe dem absoluten Nullpunkt (-273 °C) den Strom wie gewohnt (d. h. mit einem Widerstand, der zu Verlusten führt). Unterhalb der kritischen Temperatur verschwindet dieser Widerstand vollständig und Strom kann verlustfrei fließen (ein Phänomen, das z. B. bei der Kernspintomografie Anwendung findet). Diese supraleitende Phase unterscheidet sich damit fundamental von der üblichen, metallischen Phase und der Übergang zwischen beiden ist ein weiteres Beispiel für einen Phasenübergang. Die erfolgreiche Beschreibung des widerstandsfreien Ladungstransports in Supraleitern ist eine der großen Errungenschaften der Quantenmechanik und markiert einen Meilenstein in der Physik der kondensierten Materie.

Ein wichtiges Motiv der Physik ist die *Verallgemeinerung*. Physiker versuchen Phänomene anhand von Spezialfällen zu lernen, um sie dann mit allgemeinen Prinzipien zu erklären. Solche Verallgemeinerungen führen oft zu neuen Theorien und können die Denkweise ganzer Generationen von Physikern prägen (man spricht dann von *Paradigmen*). Sowohl das Gefrieren von Wasser als auch der Übergang in den supraleitenden Zustand sind Phasenübergänge. Die nahe liegende Frage eines Physikers wäre dann, ob es allgemeingültige Prinzipien gibt, die auf *alle* Phasenübergängen anwendbar sind. Gibt es ein allgemeines Ordnungsprinzip, das beschreibt, *worin* sich unterschiedliche Phasen unterscheiden? Ein solches Ordnungsprinzip wurde vom sowjetischen Physiker LEV LANDAU (Nobelpreis für Physik 1962) in den 1930er Jahren vorgeschlagen und maßgeblich entwickelt. Die Grundidee ist recht einfach: Unterschiedliche Phasen unterscheiden sich in ihren *Symmetrien*. Eine

Symmetrie eines physikalischen Systems ist eine Transformation, die das System nicht verändert. Eine perfekte Kugel ist z. B. rotations-symmetrisch: Wenn man sie dreht, sieht sie immer gleich aus. Landaus Ordnungsprinzip besagt, dass sich Phasen durch ihre Symmetrien charakterisieren lassen. Am Beispiel von gefrierendem Wasser wird sofort deutlich, was gemeint ist: Während eine Flüssigkeit unter beliebigen Rotationen immer gleich aussieht, ist das bei zu Kristallen gefrorenem Wasser nicht mehr der Fall. In verallgemeinerter Form lässt sich diese Idee auf viele Phasen und Phasenübergänge anwenden— auch auf Supraleiter (dort allerdings mit einer abstrakteren Symmetrie). Landaus Ordnungsprinzip wurde unter dem Namen “spontane Symmetriebrechung” bekannt, weil Phasenübergänge dadurch gekennzeichnet sind, dass bestimmte Symmetrien einer Phase beim Übergang “spontan gebrochen” werden (z. B. bricht der Eiskristall die Rotationssymmetrie flüssigen Wassers “spontan” indem er sich in einer unbestimmten Richtung ausbildet). Die Theorie der spontanen Symmetriebrechung war so erfolgreich, dass Physiker bis in die 1960er Jahre davon überzeugt waren, dass Sie im Grunde alles verstanden hatten was es zu (Quanten-)Phasen und ihren Übergängen zu wissen gibt.

Aber in den frühen 1970er Jahren verdichteten sich die Anzeichen, dass die Sache doch etwas komplizierter sein könnte. Speziell wurden (theoretische) Modelle gefunden, die Phasen mit exakt denselben Symmetrien aufweisen, obwohl diese durch einen Phasenübergang voneinander getrennt sind. Im Jahr 1980 beobachtete dann KLAUS VON KLITZING (Nobelpreis für Physik 1985), dass sich eine spezielle Form der Leitfähigkeit von zweidimensionalen Halbleitern nur in *exakt* bestimmten Schritten ändert, wenn ein starkes Magnetfeld eingeschaltet und variiert wird. Die gemessene Schrittweite ist praktisch unabhängig vom Material (selbst für Proben mit Verunreinigungen) und hängt direkt mit fundamentalen Naturkonstanten zusammen. Dieses Phänomen ist bekannt als *Quanten-Hall-Effekt*¹ und markiert eine Zäsur der modernen Physik. Es ist völlig unverständlich wieso ein Material mit natürlichen Verunreinigungen bei Messungen *perfekte* Werte bestimmter Naturkonstanten liefern sollte. Physikern war eine solche “Robustheit” realer Systeme noch nicht untergekommen. Zu allem Überfluss schienen die beim Quanten-Hall-Effekt realisierten Phasen alle dieselben Symmetrien zu besitzen. Damit war es unbestreitbar, dass Landaus Ordnungsprinzip nicht ausreicht, um alle Quantenphasen beschreiben zu können.

Dank der Arbeiten theoretischer Physiker wurde schnell klar, dass ein in der Physik bis dato selten genutzter Teilbereich der Mathematik von Nöten ist, um diese Phänomene zu verstehen: die *Topologie*. Die Topologie befasst sich (im Gegensatz zur *Geometrie*) mit gegen Verformung robusten Eigenschaften von Körpern. Stellen Sie sich vor, Sie hätten eine Schnur, und Ihr Ziel sei es, sich mit ihrer Hilfe eine Zahl (sagen wir 5) zu merken. Eine mögliche Lösung wäre, die Form der Zahl “5” mit der Schnur nachzulegen; in diesem Fall wäre die Zahl in der *Geometrie* der Schnur codiert. Diese Methode funktioniert zwar, ist aber nicht sonderlich robust: Jede unbedachte Berührung der “5” kann ihre Form—und damit die codierte

¹Die quantisierte Version des klassischen *Hall-Effekts*. Dieser ist benannt nach EDWIN HALL.

Information—zerstören. Eine weitaus cleverere Methode wäre, sich die Schnur fünfmal um den Unterarm zu wickeln und sie dann zu verknoten. So lange die Schnur nicht reißt, wird sich die Zahl der Windungen nicht ändern; selbst wenn sie sich beim Gehen ständig verformt. Die Windungszahl der Schnur ist eine *topologische* Eigenschaft, da sie robust gegen geometrische Deformationen ist. Es sind solche topologischen Windungszahlen, die für die robusten Leitfähigkeiten des Quanten-Hall-Effekts verantwortlich sind (nur winden sich in diesem Fall keine Schnüre, sondern mathematische sehr abstrakte Objekte, die zur quantenmechanischen Beschreibung des Systems dienen). Diese Windungszahlen von Quantenphasen werden als *topologische Indizes* bezeichnet; sie lassen sich üblicherweise nicht direkt messen, haben aber messbare Effekte (wie z. B. die diskreten Leitfähigkeiten). Die Windungszahlen lösen praktischerweise auch das Rätsel um die scheinbar ununterscheidbaren Phasen: Diese haben schlicht unterschiedliche topologische Windungszahlen. Da man die Windungszahlen einem Material nicht direkt ansieht (sie sind in seiner quantenmechanischen Struktur “versteckt”), scheinen diese Phasen gleich zu sein, obwohl sie es nicht sind: Wenn man versucht von einer zur anderen zu kommen, wird man einen Phasenübergang beobachten an dem sich scheinbar nichts ändert; tatsächlich springt dort aber die Windungszahl von einer ganzen Zahl zur nächsten.

Dieses Konzept bildet die Grundlage für einen der derzeit aktivsten Bereiche der Physik und hat unsere Sicht auf *mögliche* Quantenphasen (und die damit einhergehenden Materialien) von Grund auf verändert. Die theoretische und experimentelle Erforschung dieser *topologischen Quantenphasen* ist nicht annähernd abgeschlossen. Sie ist inzwischen so taktgebend für die Physik der kondensierten Materie (und darüber hinaus), dass die theoretischen Vordenker dieser Disziplin—DAVID THOULESS, DUNCAN HALDANE und MICHAEL KOSTERLITZ—im Jahr 2016 mit dem Nobelpreis für Physik ausgezeichnet wurden. Der Übergang von Landaus Ordnungsprinzip der spontanen Symmetriebrechung zum weitaus vielfältigeren Konzept der topologischen Phasen lässt sich am ehesten mit dem Übergang vom Schwarzweiß- zum Farbfernsehen vergleichen: Die Landschaft der Quantenphasen, die noch in der zweiten Hälfte des 20. Jahrhunderts grau-in-grau war, schillert heute in allen Farben des Regenbogens. Um dem Leser eine Einordnung der Größe dieses Forschungsfeldes zu ermöglichen, sei hier darauf hingewiesen, dass alleine im Jahr 2018 über 1300 Veröffentlichungen mit dem Schlüsselwort “topologisch” im Titel gelistet sind; also zwischen 3 und 4 wissenschaftliche Artikel *am Tag*. Allein diese Zahlen sollten dem Leser verdeutlichen, dass das oben gezeichnete Bild die wahre Komplexität des Themas nicht annähernd widerspiegelt.

Die vorliegende Dissertation ist ein Beitrag zum Themenkomplex der topologischen Phasen (und mindestens zwei der mit ihr verknüpften Publikationen zählen zu den 1300). An dieser Stelle bietet sich eine Bemerkung zum Entstehen und Aufbau dieses Dokuments an: Während frühe Doktorarbeiten in der Physik zumeist einen monografischen Charakter hatten, also mit einem einzigen, zusammenhängenden Problem befasst waren, findet heute die *kumulative Dissertation* zunehmend

Verbreitung. Hierbei werden verschiedene, weitgehend unabhängige Projekte vom Doktoranden im Laufe der Promotion bearbeitet (auch in Kollaboration mit anderen) und als eigenständige Artikel veröffentlicht. Die Dissertationsschrift fasst diese schon zuvor veröffentlichten Resultate in einem Dokument zusammen und bettet sie in einen gemeinsamen Themenkomplex ein. Die vorliegende Dissertation ist von dieser Form: Kapitel 1 führt das oben erläuterte Konzept der topologischen Phasen auf einem für Masterstudenten der Physik verständlichen Niveau ein. Die anschließenden Kapitel 2, 3 und 4 bauen auf diesen Grundlagen auf und befassen sich je mit einem spezifischen Projekt. Dabei werden Details, die in den zugehörigen Publikationen aus Platzgründen gestrichen werden mussten, ebenfalls behandelt. In Kapitel 5 werden schließlich kleinere Nebenprojekte vorgestellt, die zum Teil Vorläufer oder Abkömmlinge der drei Hauptprojekte sind.

Lassen Sie mich nun die geleistete Vorarbeit nutzen um Ihnen, zumindest in groben Zügen, einen Überblick über diese Projekte zu geben:

- In Kapitel 2 definiere und analysiere ich ein neues Modell einer topologischen Phase in einer Dimension. (In der Festkörperphysik sind Modelle mit weniger als drei Raumdimensionen keine Seltenheit. Es ist durchaus möglich, eindimensionale “Drähte” künstlicher Quantenmaterialien im Labor zu erzeugen.) Die Bausteine des untersuchten Modells sind stark wechselwirkende *Fermionen* (denken Sie an Elektronen). Seine Eigenschaften werden mit exakten mathematischen Methoden untersucht und mit numerischen Simulationen überprüft. Die topologischen Eigenschaften des Modells manifestieren sich in einer robusten “Entartung des Grundzustandes”: Ein physikalisches System, das durch dieses Modell beschrieben wird, kann bei Temperaturen nahe dem absoluten Nullpunkt verschiedene Zustände einnehmen, die sich nur schwer unterscheiden lassen. Diese Ununterscheidbarkeit kann man ausnutzen um das System zum Manipulieren von *Qubits*, den “Quantenbits” eines hypothetischen Quantencomputers, zu verwenden. Das Modell ist also nicht nur aus akademischer Sicht interessant, sondern verspricht auch die Robustheit topologischer Phasen für die Manipulation von Quanteninformation nutzbar zu machen. (Eine Idee, die nicht auf mich zurückgeht und inzwischen einen eigenen Forschungszweig begründet. Dieser befasst sich mit der theoretischen Beschreibung sogenannter *topologischer Quantencomputer*.)
- In Kapitel 3 benutze ich das Modell einer schon lange bekannten topologischen Phase (wieder in einer Dimension) und übersetze es in einen völlig neuen Kontext. Das ursprüngliche Modell wurde eingeführt, um die Leitfähigkeit eines speziellen Polymers (Polyacetylen) besser verstehen zu können. In diesem Zusammenhang beschreibt es die Bewegung schwach gebundener Elektronen entlang eines Kohlenwasserstoffmoleküls. Nach meiner “Übersetzung” beschreibt es *Photonen* (also Lichtteilchen) in künstlichen Netzwerken aus Resonatoren. Diese Netzwerke “erben” die topologischen Eigenschaften

des ursprünglichen Modells. Ziel ist die Konstruktion eines robusten Mechanismus zum Transport von Quanteninformation (also eine Methode, um ein Qubit zwischen zwei Punkten auf dem Chip eines Quantencomputers zu transportieren ohne es dabei zu zerstören). Die Topologie hilft dabei, indem die zum Transport genutzten Eigenschaften von möglichen Fertigungstoleranzen entkoppelt werden; ähnlich wie die Leitfähigkeit beim Quanten-Hall-Effekt wegen ihres topologischen Ursprungs von der Unordnung im System nichts mitbekommt. Bei diesem Projekt steht also die Anwendung topologischer Phasen für den Transfer von Quanteninformation im Vordergrund.

- In Kapitel 4 untersuche ich eine weitere, eindimensionale topologische Phase aus Fermionen mit dem Ziel, einen skalierbaren *Quantenspeicher* zu konstruieren. Diese Phase ist verwandt mit dem in Kapitel 2 untersuchten Modell, allerdings einfacher theoretisch zu beschreiben. Auch experimentell ist sie leichter zu realisieren. Ihre Einfachheit macht sie zu einer der wenigen topologischen Phasen, die man (hoffentlich) in naher Zukunft in künstlichen, skalierbaren Strukturen aus Halbleitern und Supraleitern implementieren kann. Die topologische Robustheit dieser Phase macht sie zu einem möglichen Baustein eines Quantenspeichers. Der “Random-Access-Memory” (RAM) eines *klassischen* Computers funktioniert nur, weil er ständig auftretende Fehler aktiv korrigiert (daher verschwinden die Daten auch bei einem Stromausfall). Der in Kapitel 4 untersuchte *topologische Quantenspeicher* hat dasselbe Problem: Ohne aktive Fehlerkorrektur “vergisst” er das gespeicherte Qubit. Ziel des Projektes war der Entwurf eines Systems zur Fehlerkorrektur, das den Eigenheiten der topologischen Phase Rechnung trägt und zugleich skalierbar bleibt (je besser der Speicher vor Fehlern schützen soll, desto größer muss er sein; wobei “groß” hier Längen im Bereich von Mikrometern bezeichnet). Um dieses Ziel zu erreichen, wurde das Konzept sogenannter *zellulärer Automaten* aus dem Gebiet der Computerwissenschaften übernommen. Auch dieses Projekt behandelt demnach eine mögliche Anwendung topologischer Phasen in der Quanteninformationstechnologie; in diesem Fall das *Speichern* von Quanteninformation.

Popular Summary

According to the degree regulations of the University of Stuttgart, a thesis in English is to be accompanied by a summary in German. I doubt that there is a single physicist who would profit from a German summary. Therefore, I decided to dedicate it to non-specialists and readers without scientific background. What follows, is a translation of this text.

Publications of popular science—be it books, documentaries, or the summary at hand—cut in both ways. On the one hand, they are essential to bond science and society, to introduce people to the scientific method, and to promote basic research in general. But the communication of complex, highly specialized science to a lay readership is, depending on the desired result, complicated to impossible. There is a virtually unbridgeable disparity between the images cast in the mind of the layman and those in the mind of the scientist. The reason is not a lack of intelligence but a lack of experience. And experience—unlike knowledge—cannot be shared. The difference is years of studying physics, years of getting used to the oddities of quantum mechanics and the peculiarities of relativity. I cannot convey you the pictures in my mind—my *insight*. So be aware of these limits, because more dangerous than ignorance is pseudo-knowledge. Be aware that the pictures I will draw in your mind are just caricatures of mine. Do not trust analogies beyond their domain of validity. Quantum mechanics is *not* easy.

What is this thesis about? Let's begin at the beginning: It contributes to the field of *theoretical physics*. While experimental physicists study physical phenomena in the laboratory, theoretical physicists construct abstract, mathematical models (with pencil and paper or on the computer) to explain the observations made by experimental physicists. But this order is not mandatory: Theoreticians have a wild imagination and often they propose theoretical models that are realized only afterwards in the laboratory (if at all; it is surprisingly difficult to make nature do what theoreticians cook up). The thesis at hand is of this kind: It describes *theoretical* models that—at least on paper—have interesting (and useful) properties.

With one exception, none of these models has yet been realized in experiments. That doesn't sound very encouraging, but this is the rule rather than the exception in theoretical physics.

What is a model anyway? In theoretical physics, a “model” is a mathematically precisely defined framework, with abstract objects describing an idealized, physical system. Mathematical concepts such as *vectors* and *functions* are used to describe the state of the system. These are then related by equations to predict the time evolution or the response of the system to perturbations. In other words, models allow for the mathematical description of real processes and phenomena. Models are the bread-and-butter tools of theoretical physicists.

What are the models studied in this thesis? The thesis at hand belongs to the field of *condensed matter physics*. This discipline is concerned with the properties and the description of materials that are comparatively “cold” and “dense.” The elementary building blocks of these materials are atoms (or ions, i.e., electrically charged atoms) and electrons. Important branches of this field are *solid-state physics* that describes, e.g., crystalline materials and the semiconductors used for computers, and the *physics of fluids* that describes their dynamics and turbulences. Condensed matter physics explains why metals conduct electricity, why semiconductors (e.g. silicon) do so only under certain conditions, and why iron can be magnetized. An important aspect in this context are *phase transitions*. Phase transitions describe abrupt changes of the properties of a material when external parameters (e.g., temperature and pressure) rise above or fall below certain critical values. The best known phase transitions are the freezing of water at 0 °C and its vaporization at 100 °C. Although the building blocks—the water molecules—are the same in all three phases, ice, water and steam are completely different. Explaining and characterizing such differences is a central topic of condensed matter physics.

The last 100 years of physics were dominated by two influential theories: the theory of relativity by ALBERT EINSTEIN and *quantum mechanics* (pioneered by WERNER HEISENBERG, MAX BORN, ERWIN SCHRÖDINGER and others). For condensed matter physics, quantum mechanics is of paramount importance because its goal is the description of many, atomically small particles at very low temperatures. The theory of relativity also plays a role in this context, but we shall not dwell on these issues here. Searching for descriptions of phases and their transitions, the physicists of the 20th century realized that the oddities of quantum mechanics fundamentally influence the properties of matter. Phases that occur at very low temperatures and can only be understood in terms of quantum mechanics are called *quantum phases*. Probably the most impressive example is the *superconducting phase* of certain metals (e.g., mercury and aluminum). Above a material-specific *critical temperature* close to absolute zero (-273 °C), these metals conduct electricity as usual (that is, with a small but non-zero resistance that leads to losses). Below the critical temperature, this resistance disappears completely and current can flow without losses (a phenomenon that is put to use in magnetic resonance scanners). This superconducting phase differs fundamentally from the

common metallic phase, and the transition between the two is another example of a phase transition. The successful description of resistance-free charge transport in superconductors is one of the great achievements of quantum mechanics and marks a milestone of condensed matter physics.

An important motive of physics is *generalization*. Physicists learn phenomena on the basis of special cases, and then try to explain them with general principles. Such generalizations often lead to new theories and can shape the mindset of entire generations of physicists (then called *paradigms*). Both the freezing of water and the transition to the superconducting state are phase transitions. The obvious question to ask is whether there are universal principles that govern all phase transitions. Is there a general ordering principle that describes what distinguishes different phases? Such an ordering principle was proposed and developed by the Soviet physicist LEV LANDAU (Nobel Prize for Physics 1962) in the 1930s. The basic idea is quite simple: Different phases differ in their *symmetries*. A symmetry of a physical system is a transformation that does not change its appearance. For instance, a perfect sphere is rotationally symmetric: When rotated, it always looks the same. Landau's ordering principle states that phases can be characterized by their symmetries. The example of freezing water nicely illustrates the rationale: Liquid water always looks the same under arbitrary rotations. A statement that is no longer true for water that is frozen to crystals. In a generalized form, this idea can be applied to many phases and phase transitions—including superconductors (there, however, with a more abstract symmetry). Landau's ordering principle became known as “spontaneous symmetry breaking” because phase transitions are characterized by the fact that certain symmetries of one phase are “spontaneously broken” at the transition to another phase (for example, ice crystals break the rotation symmetry of liquid water “spontaneously” as they grow along randomly selected directions). The theory of spontaneous symmetry breaking was so successful that until the 1960s, physicists were convinced that they had basically understood everything there is to know about (quantum)phases and their transitions.

But in the early 1970s, there were signs that things could be a bit more complicated. Theoretical models were developed that exhibit phases with exactly the same symmetries while being separated by phase transitions. In 1980, KLAUS VON KLITZING (Nobel Prize for Physics 1985) observed that a special form of the conductivity of two-dimensional semiconductors only changes in precisely defined steps when a strong magnetic field is applied and varied. The measured step size is practically independent of the material (even for samples with impurities) and is directly related to fundamental constants of nature. This phenomenon is known as the *quantum Hall effect*² and marks a milestone of modern physics. It is completely opaque how measurements on a material with natural impurities can yield *perfect* values of certain constants of nature. At that time, physicists had not yet come across such “robustness” in real systems. To make matters worse, the phases

²The quantized version of the classical *Hall effect*, named after EDWIN HALL.

realized in the quantum Hall effect all appeared to have the same symmetries. Thus it was undeniable that Landau's ordering principle cannot account for all quantum phases.

Soon after these discoveries, theoretical physicists pointed out that a discipline of mathematics rarely used in physics is needed to understand these phenomena: *Topology*. Topology (as opposed to *geometry*) deals with deformation-resistant features of objects. Imagine you are given a string and your goal is to use it to remember a number (say 5). One solution would be to mimic the shape of "5" with the string; in this case, the number is encoded in its *geometry*. This approach is viable but not very robust: The shape of the string is easily destroyed by unintentionally touching it (and then the encoded information is lost). A much more sophisticated method would be to wrap the string five times around your forearm and knot it. As long as the string does not break, the number of turns cannot change; even if it is deformed by moving around. The number of turns is therefore a *topological* property as it is robust against geometric deformations. It is such a topological winding number that is responsible for the robust conductivities of the quantum Hall effect (only in this case, the role of strings is played by abstract, mathematical objects that are used for the quantum mechanical description of the system). These winding numbers of quantum phases are called *topological indices*; they can usually not be measured directly, but have measurable effects nonetheless (such as the discrete conductivities). The winding numbers also solve the mystery of seemingly indistinguishable phases: They have simply different winding numbers. Since these numbers are not directly accessible (they are "hidden" in the quantum mechanical structure of a material), these phases seem to be the same, even though they are not. When you try to get from one to the other, a phase transition occurs where seemingly nothing changes; however, there the winding number jumps from one integer to the next.

This concept forms the basis for one of the most active research areas of physics at the time and has radically changed our view on possible quantum phases (and related materials). The theoretical and experimental exploration of these *topological quantum phases* is not nearly complete. By now, the concept has become so influential in condensed matter physics (and beyond) that the theoretical masterminds of this discipline—DAVID THOULESS, DUNCAN HALDANE and MICHAEL KOSTERLITZ—were awarded the Nobel Prize for Physics in 2016. The transition from Landau's principle of spontaneous symmetry breaking to the much more diverse concept of topological quantum phases can be compared to the transition from monochrome to color television: The landscape of quantum phases, which until the second half of the 20th century was gray-in-gray, has now turned into a rainbow-colored painting riddled with mysteries. To gauge the scope of this rather novel field of research, let me point out that in 2018 alone, more than 1300 publications with the keyword "topological" in their title are listed online; that is

roughly 3 to 4 scientific articles *per day*. These figures alone should make it clear to the reader that the picture drawn above cannot reflect the true complexity of this topic.

This doctoral thesis is a contribution to the research field of topological phases (and at least two of the publications it is based on belong to the 1300). Let me briefly comment on the structure of this document: While early doctoral theses in physics often had a monographic character, treating a single problem with a guiding thread throughout the thesis, nowadays, theses that are based on a collection of papers become more and more common. In the course of such a doctorate, several, mostly independent research projects are conducted (often in collaboration with others) and published as independent articles. The doctoral thesis summarizes these previously published results in a single, comprehensive document and integrates them into a common framework. The thesis at hand is of this form: Chapter 1 introduces the concept of topological phases discussed above on a level accessible to students with an undergraduate degree in physics. Each of the following Chapters 2 to 4 builds on these foundations and treats a single project. Calculations that were omitted in the original publications are presented in detail. Finally, in Chapter 5, a few side projects are presented, some of which precursors or descendants of the three main projects.

Let me now use your new knowledge of topological phases for a brief outline of these projects:

- In Chapter 2, I define and study a new model of a topological phase in one spatial dimension. (In solid-state physics, models with less than three dimensions are not uncommon. It is possible to create one-dimensional “wires” of artificial quantum materials in the laboratory.) The building blocks of the investigated model are strongly interacting *fermions* (think of electrons). Its properties are examined with exact mathematical methods and cross-checked with numerical simulations. The topological properties of this model manifest in a robust “ground state degeneracy”: A physical system described by this model at very low temperatures can be in different states that are hard to distinguish. This indistinguishability can be exploited to manipulate *qubits*, the “quantum bits” of a hypothetical quantum computer. Hence, the model is not only interesting from an academic point of view, but demonstrates how to harness the robustness of topological phases for the manipulation of quantum information. (An idea that has been around for a while and already spawned a dedicated branch of research concerned with so called *topological quantum computers*.)
- In Chapter 3, I use the model of a well-known topological phase (again in one dimension) and translate it into a completely different context. The original model was introduced to understand the conductivity of a particular polymer (polyacetylene). In this context, it describes the movement of weakly bound

electrons along a hydrocarbon molecule. After my “translation,” it describes *photons* (i.e., particles of light) in artificial networks of resonators. These networks “inherit” the topological properties of the original model. The goal is to construct a robust mechanism for the transmission of quantum information (i.e., a method for the non-destructive transport of qubits between two sites on the chip of a quantum computer). In the studied approach, topology helps to decouple the properties used for transport from possible manufacturing tolerances; similar to the conductivity of the quantum Hall effect that, due to its topological origin, is oblivious to disorder in the system. In summary, this project demonstrates an application of topological phases for the transfer of quantum information.

- In Chapter 4, I examine another one-dimensional topological phase of fermions with the goal of constructing a scalable *quantum memory*. This phase is related to the model of Chapter 2, but easier to describe theoretically. It is also easier to realize it experimentally. Its simplicity makes it one of the few candidates for topological phases that can (hopefully) be implemented in the near future in artificial, scalable structures of semiconductors and superconductors. The topological robustness of this phase makes it a possible building block for a quantum memory. The random access memory (RAM) of a *classical* computer only works because it corrects errors actively (this is why the data is lost in case of a power failure). The topological quantum memory studied in Chapter 4 faces the same problem: Without active error correction, it “forgets” the stored qubit. The goal of the project was the design of an error correction mechanism that takes the peculiarities of the topological phase into account and, at the same time, remains scalable (the performance of the memory increases with its size; here we are talking about lengths in the range of microns). To achieve this goal, I borrowed the concept of so called *cellular automata* from the field of computer science. In conclusion, this project demonstrates another possible application of topological phases in quantum information technology; in this case, the *storing* of quantum information.

Publications

The following publications accompany this thesis:

→ *Strictly local one-dimensional topological quantum error correction with symmetry-constrained cellular automata*

Nicolai Lang and Hans Peter Büchler

SciPost Phys. 4, 007 (2018)

doi:[10.21468/SciPostPhys.4.1.007](https://doi.org/10.21468/SciPostPhys.4.1.007), arXiv:[1711.08196](https://arxiv.org/abs/1711.08196)

→ *Topological networks for quantum communication between distant qubits*

Nicolai Lang and Hans Peter Büchler

npj Quantum Information 3, 47 (2017)

doi:[10.1038/s41534-017-0047-x](https://doi.org/10.1038/s41534-017-0047-x), arXiv:[1705.06901](https://arxiv.org/abs/1705.06901)

→ *Topological states in a microscopic model of interacting fermions*

Nicolai Lang and Hans Peter Büchler

Phys. Rev. B 92, 041118(R) (2015)

doi:[10.1103/PhysRevB.92.041118](https://doi.org/10.1103/PhysRevB.92.041118), arXiv:[1504.04233](https://arxiv.org/abs/1504.04233)

The following publications are not (or only peripherally) covered:

→ *Experimental realization of a symmetry protected topological phase of interacting bosons with Rydberg atoms*

Sylvain de Léséleuc, Vincent Lienhard, Pascal Scholl, Daniel Barredo, Sebastian Weber, **Nicolai Lang**, Hans Peter Büchler, Thierry Lahaye, and Antoine Browaeys

To appear in Science (2019)

doi:[10.1126/science.aav9105](https://doi.org/10.1126/science.aav9105), arXiv:[1810.13286](https://arxiv.org/abs/1810.13286)

→ *Ising anyonic topological phase of interacting fermions in one dimension*

Kai Guther, **Nicolai Lang** and Hans Peter Büchler

Phys. Rev. B 96, 121109(R) (2017)

doi:[10.1103/PhysRevB.96.121109](https://doi.org/10.1103/PhysRevB.96.121109), arXiv:[1705.01786](https://arxiv.org/abs/1705.01786)

→ *Topological flat bands with Chern number $C = 2$ by dipolar exchange interactions*

David Peter, Norman Y. Yao, **Nicolai Lang**,
Sebastian D. Huber, Mikhail D. Lukin, and Hans Peter Büchler
Phys. Rev. A **91**, 053617 (2015)
doi: [10.1103/PhysRevA.91.053617](https://doi.org/10.1103/PhysRevA.91.053617), arXiv: [1410.5667](https://arxiv.org/abs/1410.5667)

→ *Majorana modes and p -wave superfluids for fermionic atoms in optical lattices*

Adam Bühler, **Nicolai Lang**, Christina V. Kraus,
Gunnar Möller, Sebastian D. Huber, and Hans Peter Büchler
Nature Communications **5**, 4504 (2014)
doi: [10.1038/ncomms5504](https://doi.org/10.1038/ncomms5504), arXiv: [1403.0593](https://arxiv.org/abs/1403.0593)

The following publications date back to my pre-PhD era:

→ *Exploring quantum phases by driven dissipation*

Nicolai Lang and Hans Peter Büchler
Phys. Rev. A **92**, 012128 (2015)
doi: [10.1103/PhysRevA.92.012128](https://doi.org/10.1103/PhysRevA.92.012128), arXiv: [1408.4616](https://arxiv.org/abs/1408.4616)

→ *Minimal instances for toric code ground states*

Nicolai Lang and Hans Peter Büchler
Phys. Rev. A **86**, 022336 (2012)
doi: [10.1103/PhysRevA.86.022336](https://doi.org/10.1103/PhysRevA.86.022336), arXiv: [1206.6994](https://arxiv.org/abs/1206.6994)

My previous theses:

→ *Phase transitions and topological phases by driven dissipation*

Nicolai Lang
Master thesis, University of Stuttgart (2013)
<https://n15.de/msc>

→ *Minimal instance for topological matter*

Nicolai Lang
Bachelor thesis, University of Stuttgart (2011)
<https://n15.de/bsc>

Contents

Abstract	iii
Zusammenfassung für Nichtphysiker	v
Popular Summary	xiii
Publications	xix
Contents	xxi
Acknowledgments	xxv
How to Read This Thesis	xxix
1 Introduction	1
1.1 Phases of Matter	3
1.1.1 Intrinsic Topological Order	7
1.1.2 Symmetry-Protected Topological Order	9
1.2 Examples in One Dimension	19
1.2.1 The Su–Schrieffer–Heeger Chain	19
1.2.2 The Majorana Chain	27
1.3 Applications & Experiments	35
1.3.1 Quantum Systems	37
1.3.2 Classical Systems	41
2 Majorana-Like Edge States & Number Conservation	43
2.1 Introduction	53
2.2 A Chain of Interacting Fermions	54
2.2.1 Definition of the Model	54
2.2.2 Ground States	57
2.3 Ground State Properties	61
2.3.1 Correlations and Edge States	62

2.3.2	Symmetry Protection	67
2.3.3	Entanglement Spectrum and Entropy	72
2.4	Low-Energy Excitations	75
2.4.1	A Class of Exact Eigenstates	75
2.4.2	Scaling of the Spectral Gap	84
2.5	Braiding	92
2.5.1	Construction of Wire Networks	93
2.5.2	Non-Abelian Statistics	97
2.6	Conclusion & Outlook	107
<i>Appendices</i>		111
2.A	Matrix Product State Representation	111
2.B	Estimates on the Spectral Gap	118
2.B.1	Lower Bound for Even Subchain Parity	118
2.B.2	Upper Bound for Odd Total Parity	127
2.B.3	Upper Bound in the Even-Even Sector	143
2.C	Bethe Ansatz Solutions	146
2.C.1	Jordan-Wigner Transformation	146
2.C.2	The Non-Interacting Sectors	150
2.C.3	The Interacting Sector of Two Particles	153
2.C.4	Lifted Excitations on the Double-Chain	180
2.D	Residue of the Majorana Algebra	183
2.D.1	Properties of Majorana Operators	183
2.D.2	Edge Modes in the Number-Conserving Setting	188
3	Quantum Communication Between Qubits	195
3.1	Introduction	203
3.2	Setup	207
3.2.1	Construction of Topological Networks	207
3.2.2	Protocol for State Transfer	213
3.3	Results	215
3.3.1	Optimizing Transfer	217
3.3.2	Symmetry Protection of the Transfer Phase	219
3.3.3	Scaling and Adiabaticity	222
3.3.4	Benchmarking Against Trivial Setups	226
3.3.5	Effects of Disorder and Symmetry Protection	228
3.4	Application & Generalization	230
3.4.1	Controlled-Phase Gate	230
3.4.2	Extension to 2D Networks of Coupled Qubits	233
3.5	Conclusion & Outlook	237

<i>Appendices</i>	241
3.A The Majorana Chain Model	241
3.A.1 Definition and Properties	241
3.A.2 Relation to the SSH Model	245
3.B Symmetry Protection of Generic Networks	247
3.C Influence of Disorder	250
3.D Diagonalization	254
3.D.1 Edge Modes in the Thermodynamic Limit	254
3.D.2 Exact Diagonalization	255
3.D.3 Asymptotic Edge Mode Splitting	258
3.D.4 Analytic Spectrum	260
3.D.5 Scaling at the Critical Point	265
3.D.6 Scaling Away from the Critical Point	266
3.D.7 Universal Scaling	273
3.E Adiabaticity	276
3.F Remarks on Linear Bosonic Networks	286
4 Error Correction with Cellular Automata	289
4.1 Introduction	297
4.2 1D Topological Quantum Codes	301
4.2.1 Majorana Chain	301
4.2.2 Global Majority Voting	306
4.2.3 Constraints by Locality	309
4.3 Cellular Automata	313
4.3.1 Properties of Cellular Automata	313
4.3.2 Density Classification in 1D	316
4.3.3 Boundary Conditions	321
4.4 Decoding with a Self-Dual Density Classifier	324
4.4.1 Numerical Results	324
4.4.2 Rigorous Analytical Results	329
4.5 Error Correction for Continuous Noise	336
4.5.1 Continuous Noise in Strictly One Dimension	336
4.5.2 Evading Noise with a Two-Dimensional Extension	338
4.6 Conclusion & Outlook	346
<i>Appendices</i>	349
4.A Cumulative Binomial Distribution	349
4.B Light Cone Constraint	351
4.B.1 Derivation	351
4.B.2 Scaling Behavior	355
4.C Linear Eroders on Finite Chains	358
4.D Fixed Points	360
4.E Sparse Errors and Correction Time	362
4.F Parameters	374

5	Miscellaneous	377
5.1	SPT Phase with Rydberg Atoms	383
5.1.1	Symmetries of the SSH Model	383
5.1.2	Jordan-Wigner Transformation	391
5.1.3	SPT Phases of One-Dimensional Spin Systems	398
5.1.4	Connection to the Haldane Phase	423
5.2	Coupled Luttinger Liquids	432
5.2.1	Introduction	432
5.2.2	Setup	434
5.2.3	Allowed Operators	437
5.2.4	Renormalization Group Analysis	438
5.2.5	Technical Details	442
5.3	On Apples and Oranges	465
5.3.1	Motivation	465
5.3.2	General Concept & Notation	467
5.3.3	Specialization to Classical Mechanics	473
5.4	Neural Networks for Quantum Error Correction	491
5.4.1	Motivation	491
5.4.2	Artificial Neural Networks	493
5.4.3	Decoding the Majorana Chain	498
5.4.4	Majority Voting in Two Dimensions	502
5.5	Aperiodic Stabilizers	506
5.5.1	Motivation	506
5.5.2	General Setup	508
5.5.3	Wang Stabilizers	511
5.5.4	What to Do Next?	517
5.6	Localization of Symmetries	523
5.6.1	Motivation	523
5.6.2	The Classical Problem	527
5.6.3	Directions to Proceed	534
	List of Figures	537
	Bibliography	540

Acknowledgments

The knowledge and experience I acquired in the last few years—not only in physics but in many other fields as well—are invaluable. In a sense, it is only in the course of a doctorate that the many pieces gathered during one’s undergraduate studies start to fall into place to form a coherent picture of interrelated theories, concepts and models. It is this new perspective on our description of nature that I value the most—not the rather specific results documented in this thesis. This journey has been accompanied and supported by many people, both intellectually and personally:

First and foremost I would like to thank Hans Peter Büchler for his guidance and support. Thank you for providing counsel when needed and constructive criticism where appropriate. Thank you for running an institute with clear responsibilities and a fair attribution of work, where all opinions are heard and hierarchy doesn’t beat reason. Most importantly, thank you for the freedom to follow my interests and develop my own ideas—even when they were not in your focus of research.

Many thanks go also to Maria Daghofer for instantly accepting to review my thesis, and to Tilman Pfau for presiding the examining board. Furthermore, I would like to thank Sebastian Huber for his hospitality and stimulating discussions; his demonstration of the role played by topology in classical mechanics was enlightening.

During my studies, I was lucky to share an office with two bright minds: first with David Peter and later with Jan Kumlin. To both I owe uncounted hours of stimulating discussions, constructive criticism and suggestions that broadened my horizons. Adopting Vim as text editor—without which editing *this* thesis would not have been possible³—is just one example. Thank you for sharing your opinions on a broad range of topics (especially if they weren’t in line with mine)! With Adam Bühler and Sebastian Weber I spent hours discussing “topological stuff” and proof-reading manuscripts (let alone ranting about the skills of today’s students⁴); thank you for these interesting collaborations and your pivotal contributions!

³More often than not it is the *tools* that determine what we can achieve.

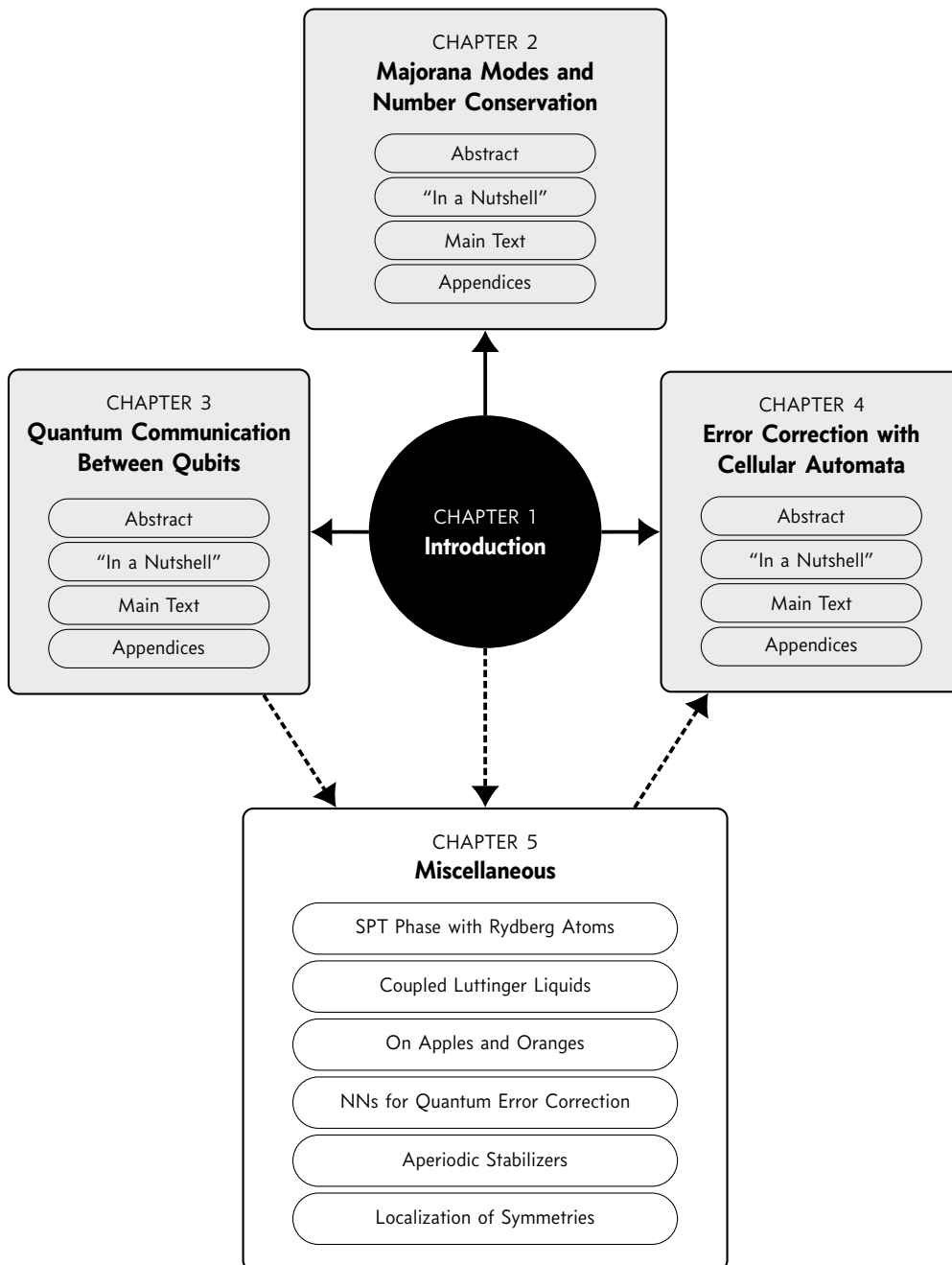
⁴Everything was better in the old days.

Particular thanks go to my colleagues Przemysław Bienias, Stephan Humeniuk, Daniel Huerga, Tobias Ilg, and Kevin Kleinbeck for diverting conversations and, quite generally, being part of a social environment that I enjoyed very much. I also enjoyed being asked questions as it is the most efficient method to segregate superficial knowledge from true insight. The most nasty ones are typically asked by students—and I had the opportunity to give advice to and receive input from quite a few: Kai Guthier, Martin Tschöpe, Tizian Wenzel, Yuan Miao, Luka Jibuti, Anna Wackerow and Felix Roser. Thank you for asking questions until I ran out of answers and answering several questions on my mental to-do list!

As far as I am concerned, academia could be based on two pillars: research and teaching. However, there is a footing beneath where bureaucracy resides. I would like to express my gratitude to Ildiko Poljak and, above all, Oliver Nagel for providing an interface to this opaque and sometimes nerve-stretching world. Thank you for keeping the institute running!

This thesis, and the scientific results that come with it, are, first and foremost, a product of my devotion to science. Devotion, however, is a time-consuming luxury that one cannot take for granted. I was in the fortunate situation that I could—thanks to the unconditional support by my family. Thank you so much!

Nicolai Lang
Stuttgart, January 2019



Solid arrows indicate necessary requirements. Dashed arrows denote loose dependencies.

How to Read This Thesis

The doctoral thesis at hand is the product of a series of papers, which reflects in its structure (see flowchart to the left). It is organized in five chapters that, with few exceptions, can be read independently: Chapter 1 provides a brief introduction to the key concepts and sets the stage for the other four; it is the only one without novel results. The following three Chapters 2, 3 and 4 are based on a single publication each and together form the main part of this thesis. They draw inspiration from the models introduced in Chapter 1 while being only loosely interrelated.

To reconcile the author's inclination to pedantic documentation with the — reasonable — demand for readability, these three chapters share a common structure: They start with a brief abstract that conveys the main message of the chapter. It follows a synopsis of less than ten pages titled “In a Nutshell” and highlighted by shaded pages. In contrast to the abstract, the synopsis is more detailed, yet still non-technical to be comprehensible by a non-specialist reader with background in general physics. Reading the shaded pages is sufficient to grasp the gist of this thesis. The synopsis is followed by the main text of the chapter, typically an extended version of the publication it is based on. Technical calculations and discussions that would fray the golden thread of the main part can be found in the appendices.

The last chapter, Chapter 5, departs from this structure as it does not correspond to a single publication but covers various topics, some of which related to the three main chapters, some potential starting points for future projects.

Generic Abbreviations

<i>cf.</i>	confer (“compare”)
<i>d.o.f.</i>	degree(s) of freedom
<i>e.g.</i>	exempli gratia (“for example”)
<i>etc.</i>	et cetera (“and so forth”)
<i>et al.</i>	et alii (“and others”)
<i>i.e.</i>	id est (“that is”)
<i>viz.</i>	videlicet (“namely”)
<i>vs.</i>	versus (“against”)
<i>w.l.o.g.</i>	without loss of generality
<i>w.r.t.</i>	with respect to
✱	<i>Reference to the appendix</i>
↪	<i>Caption continued on next page</i>

Special Abbreviations

AFHM	AntiFerromagnetic Heisenberg Model
AKLT	Affleck-Kennedy-Lieb-Tasaki
ALPS	Algorithms and Libraries for Physics Simulations
ANN	Artificial Neural Network
BCS	Bardeen-Cooper-Schrieffer
BF	<i>A topological quantum field theory</i>
BdG	Bogoliubov-de Gennes
CA	Cellular Automaton
CDW	Charge Density Wave
CMOS	Complementary Metal-Oxide-Semiconductor
CNN	Convolutional Neural Network
CP	Controlled-Phase
CPU	Central Processing Unit
CUDA	<i>Software interface for graphics processing units by Nvidia</i>
DMRG	Density Matrix Renormalization Group
ED	Exact Diagonalization
EOM	Equation Of Motion

ES	Entanglement Spectrum
ET	Explanation Tree
FQHE	Fractional Quantum Hall Effect
GKL	Gács-Kurdyumov-Levin
HOTI	Higher-Order Topological Insulator
HgTe	Mercury Telluride
LDPC	Low-Density Parity-Check
LHS	Left-Hand Side
LL	Luttinger Liquid
MBC	Mirrored Boundary Conditions
MCQC	Majorana Chain Quantum Code
ML	Machine Learning
MMWB	Minimum–Maximum-Weight Basis
MPS	Matrix Product States
MWB	Minimum-Weight Basis
MWPM	Minimum Weight Perfect Matching
NN	Nearest-Neighbor
NNN	Next–Nearest-Neighbor
OBC	Open Boundary Conditions
PBC	Periodic Boundary Conditions
PH	Particle-Hole
PsBC	Parity-split Binomial Coefficient
QED	Quantum ElectroDynamics
RAM	Random Access Memory
RG	Renormalization Group
RHS	Right-Hand Side
ReLU	Rectified Linear Unit
SET	Symmetry-Enriched Topological
SLL	Sliding Luttinger Liquid
SPT	Symmetry-Protected Topological
SSH	Su–Schrieffer–Heeger
TI	Topological Insulator
TKNN	Thouless-Kohmoto-Nightingale-Nijs
TLV	Two-Line Voting
TNS	Tensor Network States
TQC	Topological Quantum Computation

TQFT	Topological Quantum Field Theory
TRB	Time-Reversal Breaking
TRI	Time-Reversal Invariant
UMTC	Unitary Modular Tensor Category

Mathematical Symbols

A	Unitary symmetry class of the tenfold way
AI	Orthogonal symmetry class of the tenfold way
AIII	Chiral unitary symmetry class of the tenfold way
BDI	Chiral orthogonal symmetry class of the tenfold way
D	One of the BdG symmetry classes of the tenfold way
AND	Logical AND gate
MAJ3	Logical majority gate on three bits
NAND	Logical NAND (“not AND”) gate
OR	Logical OR gate
XOR	Logical XOR (“exclusive OR”) gate
NP	“Nondeterministic Polynomial time” (Complexity class)
P	“Polynomial time” (Complexity class)
\mathbb{R}	real numbers
$\mathbb{R}^+ / \mathbb{R}_0^+$	positive / non-negative real numbers
\mathbb{Z}	integers
$\mathbb{N} / \mathbb{N}_0$	positive / non-negative integers
\mathbb{F}_2	finite field of order two
\mathbb{Z}_n	cyclic group of order n
$U(n)$	Lie group of $n \times n$ unitary matrices
$O(n)$	Lie group of $n \times n$ orthogonal matrices
$SU(n)$	Lie group of $n \times n$ unitary matrices with determinant 1

1

Introduction

*“There was so much to grok,
so little to grok from.”*

— ROBERT A. HEINLEIN
in Stranger in a Strange Land

Here we review the theoretical foundations of this thesis and locate it within the ever-growing field of condensed matter physics. In Section 1.1 we introduce the general concept of *topological quantum phases* and discuss the role played by symmetries in this context. We address the classification of topological phases with and without interactions between their fermionic or bosonic constituents. In Section 1.2 we discuss two paradigmatic models—the *Su-Schrieffer-Heeger chain* and the *Majorana chain*—as examples of non-interacting topological phases in one spatial dimension. Both models are closely related and used repeatedly in this thesis, either as motivation for or key element of the presented projects. In Section 1.3 we review various proposals for applications of topological phases—both quantum and classical—to demonstrate that the concept is more than a theorist’s delight. We briefly comment on experimental results to make contact with the real world.

This page is intentionally left blank.

1.1 Phases of Matter

Energy can be thought of as a “fifth” dimension (extending our 3 + 1-dimensional spacetime) in that it defines the relevant constituents and their interactions that govern the physics on a specific energy scale. For instance, the Planck energy $\sim 10^{19}$ GeV defines the realm of “quantum gravity” (whatever this is) with possibly “stringy” constituents. Down the energy axis, we pass the standard model of high-energy physics with quarks and leptons as constituents interacting through the exchange of strong, weak and electromagnetic gauge bosons. At even lower energies, we enter the realm of nuclear physics with neutrons and protons that interact via the nuclear force (a residual of the strong force).

Here we are interested in (conventional⁵) *condensed matter physics* that seeks for descriptions of states of matter on the energy scale of ~ 1 eV and below (far away from the ~ 1 MeV of nuclear physics). Thus the constituents (or *particles*) are negatively charged electrons and positively charged nuclei among which interactions are mediated by the electromagnetic field. The term “condensed” refers to systems that are governed by *interactions* (as in liquids or solids) rather than kinetic energy (as in gases or plasmas). Typically, this requires temperatures of the order of (or below) the interaction energies that determine the dynamics of the constituents.

The objective of condensed matter physics is the quantitative and qualitative description of systems that comprise many (possibly strongly interacting) particles. That this quest turns out to be highly non-trivial and theoretically demanding is not a consequence of the (rather sparse) set of constituents, but of the vast possibilities to combine them into qualitatively distinct, more or less correlated structures. The latter are referred to as *phases* and form the centerpiece of condensed matter physics. A system with fixed particle content can be in different phases, depending on the temperature and the parameters that control the interactions between the particles. For instance, atoms on a lattice that interact via their magnetic dipole moments can be in a *ferromagnetic phase* at low temperatures (where all dipoles point into the same direction) and in a *paramagnetic phase* at high temperatures (where the orientation of dipoles is scrambled by thermal fluctuations). These two states of matter are *qualitatively* different (for instance, the ferromagnetic phase displays a macroscopic magnetization whereas the paramagnet does not). Interestingly, this qualitative change in the macroscopic properties of a system can be triggered by small and continuous changes in the temperature (or the parameters of the system). This suggests that the properties of phases and the transitions between them are *emergent phenomena* that can only be explained by the collective behavior of many, strongly correlated particles.

⁵Some concepts of condensed matter physics are so fundamental that their validity extends to other energy scales. For instance, the theory of *Fermi liquids*—typically used to describe electrons in a metal—can also be applied to protons and neutrons in atomic nuclei.

INTRODUCTION

Formally, phases are defined through the transitions between them: Two systems are in the same phase if they can be parametrically connected without a phase transition (which are typically indicated by non-analytic thermodynamic potentials and/or diverging response coefficients and correlation lengths). This definition qualifies phases as *equivalence classes* of which particular systems can be representatives; furthermore, it formalizes the term “system X is *in* phase Y” as “the state of system X is a representative of the class of states Y.” If a system crosses the border between two equivalence classes, it undergoes a phase transition. Note that the converse is not necessarily true: Crossing a phase transition does not imply a change of phases (despite the term’s naïve interpretation) because critical lines in parameter space can terminate at critical points; for example, liquid and gas “phases” of fluids are actually the *same* phase (they share the same symmetries, see below) despite their separation by a first-order transition at low temperatures.

Now that the notion of phases and phase transitions has been formalized, a natural next step is the characterization of these equivalence classes or phases. Indeed, a major goal of condensed matter physics is the construction of “labeling schemes” such that two representatives belong to the same class if and only if their labels are identical. The most successful “labeling scheme” as been introduced by Lev Landau [5–7] and is nowadays known as the paradigm of *spontaneous symmetry breaking*. According to Landau, the “labels” that characterize phases (and hence are shared by all its representatives) are the symmetry group G_S of the system and the symmetry group G_E under which the equilibrium state is invariant. In the “disordered” phase, the state inherits all symmetries from the Hamiltonian that describes the system: $G_E = G_S$. In the example of atoms that try to align their magnetic moments, this corresponds to the high-temperature paramagnetic phase where both Hamiltonian and state are invariant under rotations: $G_E = O(3) = G_S$. If a system is driven across a phase transition into another phase (e.g., by lowering the temperature), the symmetry of the Hamiltonian remains unchanged, $G'_S = G_S$, but the state breaks some (or all) of these symmetries *spontaneously*: $G'_E \subset G'_S$. Thus the “labels” of the phases of a system with fixed symmetry group G_S are given by subgroups $G_E^{(1)}, G_E^{(2)}, \dots \subset G_S$ under which representative states are invariant. Then, transitions between different phases are signaled by a change of symmetry $G_E^{(1)} \rightarrow G_E^{(2)}$ in the equilibrium state of the system. Phases that do not inherit the full symmetry group of the system, $G_E \neq G_S$, are referred to as *ordered* or *symmetry-broken* phases. In our example, the ferromagnetic phase (where all moments point into the same direction) breaks the full rotation symmetry $G_S = O(3)$ of the Hamiltonian down to $G_E = O(2)$. This happens spontaneously⁶ in that the direction of the moments is not determined by the description of the system (recall that $G_S = O(3)$ implies that the Hamiltonian has no preferred direction).

⁶Strictly speaking, spontaneous symmetry breaking is only possible in the thermodynamic limit, i.e., in infinite systems. The same is true for non-analyticities and divergences at phase transitions.

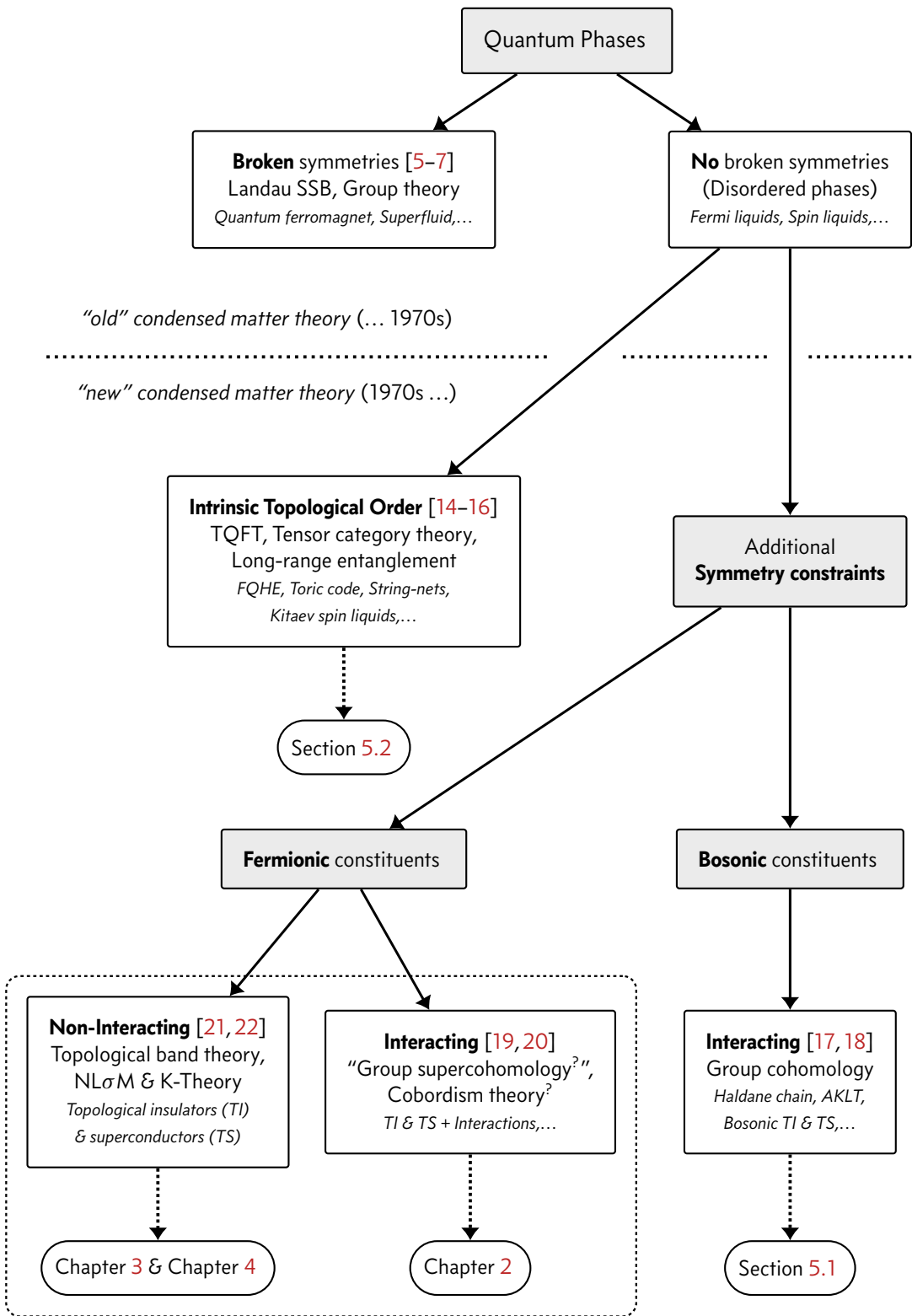
The concept of symmetry breaking is tightly related to the notion of an *order parameter* that indicates the phase transition. In Landau theory [5, 6] (of which the phenomenological Ginzburg-Landau theory is a special case [7]), order parameters are local quantities that vanish in the disordered phase and (continuously) develop a non-zero expectation value in the symmetry-broken phase. Order parameters transform non-trivially under the action of the symmetries that are spontaneously broken and thereby provide a “label” for the distinct equilibrium states that are mixed by the symmetry transformations. In the Heisenberg model, the order parameter is the local magnetization of the spins; it vanishes in the paramagnetic phase and points into a spontaneously chosen direction in the ferromagnetic phase.

That there is more to (continuous) phase transitions than spontaneous symmetry breaking and local order parameters became clear in the early 1970s when Kosterlitz and Thouless studied two-dimensional models with continuous symmetries [8]; in particular the XY model [9] (which describes ferromagnetically coupled, classical spins on a lattice that rotate in the plane). This model features a continuous $O(2)$ symmetry that cannot be broken at finite temperature due to the presence of a gapless Goldstone mode—a consequence of the Mermin–Wagner–Hohenberg theorem [10–12]. Nevertheless, the two-dimensional XY model exhibits a phase transition at finite temperature with (weak) singularities that separates a disordered high-temperature phase (with exponentially decaying correlations) from another disordered phase with correlations that decay algebraically (so called “quasi long-range order”). The theoretical description of this transition by mean field arguments and renormalization group techniques earned John Kosterlitz and David Thouless (together with Duncan Haldane, see below) the 2016 Nobel Prize in Physics.

So far we only skimmed the microscopic mechanism that is responsible for phase transitions. In classical physics, transitions between symmetric and symmetry-broken phases are driven by *thermal* fluctuations (recall the example of a ferromagnet where thermal fluctuations above a critical temperature destroy the alignment of magnetic moments). However, at very low temperatures, quantum mechanics provides another mechanism that allows for phase transitions: *quantum* fluctuations that arise from non-commuting terms in the Hamiltonian. Since the strength of such fluctuations is completely controlled by the relative strength of these terms, such phase transitions can occur even at zero temperature, i.e., in the absence of thermal fluctuations. These phases—and the transitions between them—are referred to as *quantum phases* and *quantum phase transitions* [13].

Here we are interested in quantum phases that do not break the symmetries of the Hamiltonian and cannot be identified by local order parameters; i.e., quantum phases that are “disordered” according to Landau’s paradigm of symmetry breaking. Examples are *quantum spin liquids* [23–26] (where quantum fluctuations due to frustration can preclude long-range order), *fractional quantum Hall fluids* [27–29] (where strong electron-electron interactions can destabilize the formation of Wigner crystals), and *Fermi liquids* [30] (which are adiabatically connected to a Fermi gas). In this scenario—and in the light of the results by Kosterlitz and Thouless—a

INTRODUCTION



natural question to ask is whether Landau’s symmetry-based “labeling scheme” is exhaustive for quantum phases. In other words: Are there systems with several “disordered” phases at zero temperature that nevertheless are separated by a phase transition? If so, what are the “labels” that characterize these phases? Just as quantum fluctuations provide a new mechanism for phase transitions, there might be genuine “quantum ingredients” that allow us to distinguish phases even if their symmetry is the same.

1.1.1 Intrinsic Topological Order

The new ingredient is *entanglement*. The pattern of entanglement in the many-body ground state wave functions of gapped quantum systems constitutes a new “label” that is not accessible by symmetries, local order parameters or correlations [31, 32]. Nonetheless it allows for the characterization of quantum phases in the absence of symmetry breaking [16]: There are global features of entanglement patterns that cannot be removed by smooth variations of local Hamiltonians as long as the system remains gapped (which can be read as the absence of continuous phase transitions, see Ref. [16] and references therein). These features give rise to distinct equivalence classes of *long-range entanglement*, where the equivalence relation is given by the transformation of one ground state into the other by means of gapped, local Hamiltonians, or, equivalently, local⁷ quantum circuits of constant depth⁸ [16]. Thus ground states that are equivalent (belong to the same phase) share a common pattern of long-range entanglement and differ only by *local* unitary deformations. The equivalence class that contains states that can be transformed into a product state (e.g., a simple paramagnet $|+\rangle_1 \otimes |+\rangle_2 \otimes \dots$) is referred to as *trivial phase*, whereas the other classes are identified with different types of *intrinsic topological order* (the “intrinsic” is often omitted). The latter is a genuine quantum property and has no counterpart in classical physics.

The concept of topological order marks a paradigm shift in condensed matter physics and was spearheaded by the discovery of the *fractional quantum Hall effect* in 1982 by Daniel Tsui and Horst Störmer [27]. In the wake of this discovery (for which Tsui, Störmer and Robert Laughlin were awarded the 1998 Nobel Prize in Physics), the study of topologically ordered phases became a prominent field of research that demonstrated the incompleteness of Landau theory and brought an

⁷Here, “local” characterizes operators with non-trivial action on a finite number of nearby degrees of freedom. The important point is that this “radius of action” does not grow with the system size.

⁸The term “long-range entanglement” is not used consistently in the literature. Here we use Xiao-Gang Wen’s definition [16] that relies on local unitary deformations of states. Another convention, introduced by Alexei Kitaev, attributes “long-range entanglement” to states for which the *topological entanglement entropy* does not vanish [31]. Kitaev’s definition relates more directly to fractional statistics (see below), while Wen’s definition gives rise to an equivalence relation that is more suitable to classify phases. An example where the two definitions differ are *integer* quantum Hall states: they are short-range entangled by Kitaev’s definition [33] but long-range entangled according to Wen [34].

INTRODUCTION

unforeseen variety of quantum phases to light. As it turns out, fractional quantum Hall liquids are paradigmatic for the concept of topological order in that they exhibit many features that are associated with non-trivial patterns of long-range entanglement:

- They cannot be characterized by a local order parameter and all correlations decay exponentially.
- The ground state degeneracy on closed manifolds depends on their topology (whether it is a sphere, a torus, etc.) and is robust in the presence of arbitrary perturbations that do not close the gap [35].
- There are exponentially localized excitations (*quasiparticles*) that carry fractionalized charges [36].
- These excitations obey neither fermionic nor bosonic statistics—they are *anyons* and obey *fractional* or *anyonic statistics* [37, 38].
- On manifolds with boundaries, there are robust, gapless edge states that allow for scattering-free transport [39].
- The low-energy effective description is given by a *topological quantum field theory (TQFT)* (see Ref. [40] and references therein), i.e., a quantum field theory defined by an action that is a topological invariant⁹ [14].

Several—but not all (detailed below)—of these features are theoretically predicted for other topologically ordered phases as well; e.g., Kitaev spin liquids [24], quantum double models like the *toric code* [45], and Levin-Wen string-net condensates [46]. In particular, the existence of anyonic excitations, the robust ground state degeneracy on non-trivial manifolds, and the description in terms of topological quantum field theories are mutually dependent features that give rise to one of the most exciting crossovers of condensed matter physics and quantum information theory: *topological quantum computation* [45, 47, 48] and *topological quantum memories* [49, 50]. The former exploits the peculiar braiding properties of anyonic excitations to apply fault-tolerant unitary gates to qubits that are encoded in delocalized degrees of freedom of topologically ordered states, while the latter leverages the robust degeneracy on topologically non-trivial surfaces to encode qubits that are then naturally protected from decoherence.

We conclude with a few remarks: First, long-range entanglement is necessary but not sufficient for the anyonic statistics of intrinsic excitations. For instance, integer quantum Hall states are long-range entangled but do not host excitations

⁹This is the case for actions that do not depend on the metric so that the field theory is oblivious to smooth deformations of the system and, consequently, features only global degrees of freedom. Examples are *Chern-Simons theories* [41] that describe fractional quantum Hall states [40, 42] and *BF theories* [43] that describe conventional superconductors [44].

with fractional statistics [34] (an example of so called *invertible topological order* [51]). Second, gapless edge states are not tied to topological order either. The toric code [45, 52] is a prime example of topological order that hosts anyonic excitations without gapless edge states. Third, topological order is not restricted to two-dimensional systems (as the fractional quantum Hall states might suggest) but can be realized in arbitrary dimensions¹⁰ with higher-dimensional (e.g., string-like) excitations¹¹. And finally, the mathematical machinery needed to capture and classify the characteristic features of topologically ordered phases is *category theory* [55, 56]. For instance, the description of fusion, braiding, and rotation of anyons in two-dimensional topologically ordered phases requires categories with additional structures known as *ribbon fusion categories* and *unitary modular tensor categories* [48, 57]. Compared to group theory (the mathematical framework of spontaneous symmetry breaking) this abstract and rather special field of mathematics is less well understood and its application to condensed matter physics is an active area of research [58].

Although topological order is not the main focus of this thesis, we touch on the subject in Section 5.2 where we study an unconventional construction of fractional quantum Hall states, in Chapter 2 where we analyze the non-abelian braiding statistics of endpoints in networks of one-dimensional quantum wires, and in Section 5.5 where we discuss certain aspects of topological quantum memories.

1.1.2 Symmetry-Protected Topological Order

So far, we can label quantum phases by the symmetries they break and their pattern of long-range entanglement. The latter allows us to distinguish phases that do not break any symmetry of the Hamiltonian—phases that have traditionally been viewed as disordered under Landau’s paradigm of spontaneous symmetry breaking. The concept of topological order demonstrates that quantum states can exhibit “hidden” types of order that cannot be probed by local order parameters. Ground states with different “hidden” orders are nonetheless separated by quantum phase transitions, which makes the concept of topological order just as relevant as the concept of symmetry breaking.

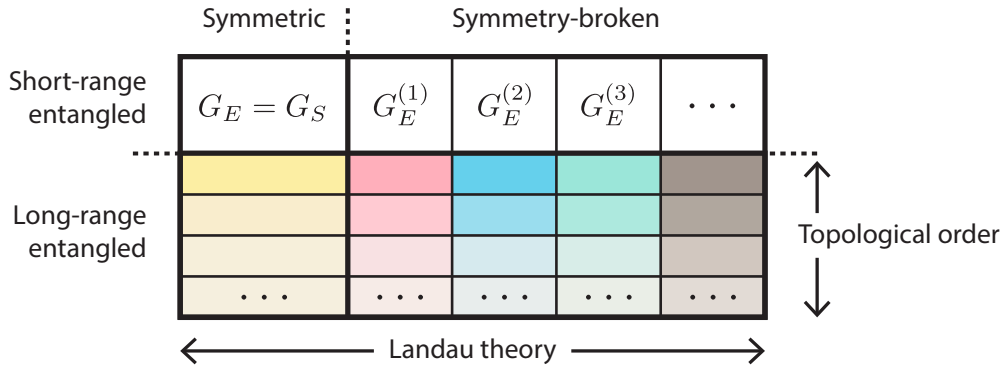
Before we add another ingredient to obtain an even more fine-grained characterization of quantum phases, we stress that the two concepts we discussed so far are by no means exclusive [16]: It is conceivable that a symmetry-broken “phase” splits further into distinct phases that share a common symmetry but differ in their

¹⁰Except for one-dimensional spin systems [17].

¹¹Contrary to many expositions in the literature, conventional *s*-wave superconductors in three dimensions are topologically ordered if the electromagnetic gauge field is dynamical [53] (which it undeniably is in the real world). Then, fractional statistics is associated with the braiding of point-like quasiparticles and string-like vortex loops [44]. Thus the conventional wisdom that fractional quantum Hall states are the first topologically ordered states of matter that have been found in nature is, strictly speaking, not correct [54].

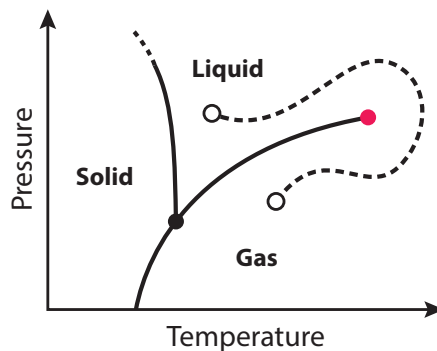
INTRODUCTION

patterns of long-range entanglement. For instance, *chiral spin liquids* [59, 60] spontaneously break time-reversal and parity symmetry (and develop a corresponding local order parameter); however, they are also topologically ordered which manifests, for example, in ground state degeneracies on compact manifolds [61]. Hence the new “labeling scheme” for quantum phases can be illustrated as follows:



Let us now split this landscape even further. To this end, assume that we have two gapped Hamiltonians H_i ($i = a, b$) with corresponding ground states $|\Omega_a\rangle$ and $|\Omega_b\rangle$. According to the sketchy definition given at the beginning of Subsection 1.1.1, they belong to the same phase if there is a family of *gapped* and *local* Hamiltonians $\hat{H}(\alpha)$ that depends continuously on $\alpha \in [0, 1]$ such that $H_a = \hat{H}(0)$ and $H_b = \hat{H}(1)$. The two constraints (gapped and local) ensure that the macroscopic properties of the ground states only change gradually along the path (which precludes the traversal of phase boundaries).

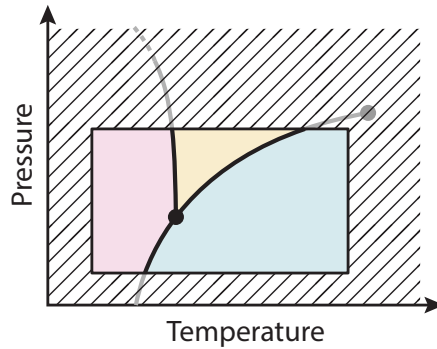
Now let us forget quantum mechanics for a second and return to thermodynamic phases, say, the phases of water. Schematically the phase diagram looks as follows:



As mentioned earlier, gas (or vapor) and liquid are actually the same phase since there are continuous paths through the supercritical regime that connect these states without hitting a phase transition (dashed path). So why do we refer to gas and liquid as different phases in everyday life? The reason is that the temperature $T_{\text{cr}} \approx 370^\circ\text{C}$ and pressure $P_{\text{cr}} \approx 22\text{ MPa}$ of the critical point (red dot, where the

PHASES OF MATTER

first-order transition terminates) are far away from the values we usually experience. Thus the *relevant* phase diagram for most physical processes on earth looks rather like this:



This is just a “masked” version of the complete phase diagram. But under the additional constraint of physically realistic temperatures and pressures, there is no longer a path that connects the two phases without crossing a phase transition. In this restricted parameter space, gas and liquid are indeed *different* phases that are completely separated by a phase transition.

The bottom line of this detour is that continuous paths connecting two states of matter might not be relevant (or accessible) in a specific context due to constraints imposed by the setting. Such constraints do not necessarily take the form of quantitative restrictions of parameters. In quantum mechanics, for instance, systems often feature characteristic *symmetries* that govern the dynamics and are not violated by typical perturbations of the idealized model. For example, closed systems often come with a natural $U(1)$ symmetry in the form of particle number conservation. Such symmetries can restrict the allowed paths that connect different states and thereby induce an effective separation of phases into different “patches” that cannot be connected without crossing a phase transition *or* violating the symmetry.

Another perspective is the following: Assume we find a system that supports gapless edge modes on its boundaries. As it happens, there is a continuous path of Hamiltonians (with a gapped bulk) that connects this peculiar state to a trivial product state where the edge modes are gone. According to the definition of topological order, both states belong to the same phase and are thereby assigned the label “trivial.” Apparently the “labeling scheme” of topological order is too coarse as it misses the existence of edge states (which clearly are an interesting feature and may even be useful for applications). It does so because this feature (the edge states) does not rely on long-range entanglement and can be removed from the system without a phase transition in the bulk. The question that comes to mind is whether there is an appropriate “mask” for the phase diagram that excludes this path and splits the “trivial” phase into two patches—separated by a phase transition—such that all states in one patch exhibit gapless edge modes while the states in the other patch do not. Such a restricted phase diagram would be useful as it conveys information on the perturbations that can be added to the system without

gapping out the edge modes. As it turns out, the “mask” we are looking for exists and is again defined by certain symmetries that the Hamiltonian(s) must satisfy. From this perspective, symmetries are *means to an end* and perturbations that violate the symmetries must be avoided (e.g., by energy penalties).

The last two paragraphs motivate the use of *protecting* symmetries as another ingredient for the classification of quantum phases. In contrast to Landau theory, we are not interested in ground states that break them but in Hamiltonians that *preserve* them. To formalize this, we modify the equivalence relation from above:

Assume that we have two gapped Hamiltonians H_i ($i = a, b$) with common symmetry group G , represented by unitary operators U_g for $g \in G$. Denote the corresponding ground states as $|\Omega_i\rangle$ and assume that there is no spontaneous symmetry breaking, i.e., $U_g|\Omega_i\rangle = |\Omega_i\rangle$ for all $g \in G$. Then, the states $|\Omega_i\rangle$ belong to the same phase if there is a family of *gapped, local and symmetric*¹² Hamiltonians $\hat{H}(\alpha)$ that depends continuously on $\alpha \in [0, 1]$ such that $H_a = \hat{H}(0)$ and $H_b = \hat{H}(1)$.

This equivalence relation is applicable to both short-range and long-range entangled states. Since the new definition is more restrictive than the old one, states with the same pattern of long-range entanglement can fall into different phases under the new definition. The structure of these new phases depends obviously on the choice of the symmetry group G_P (P for “protecting”). If we focus on systems without spontaneous symmetry breaking ($G_E = G_S$), there are two classes of phases to be considered:

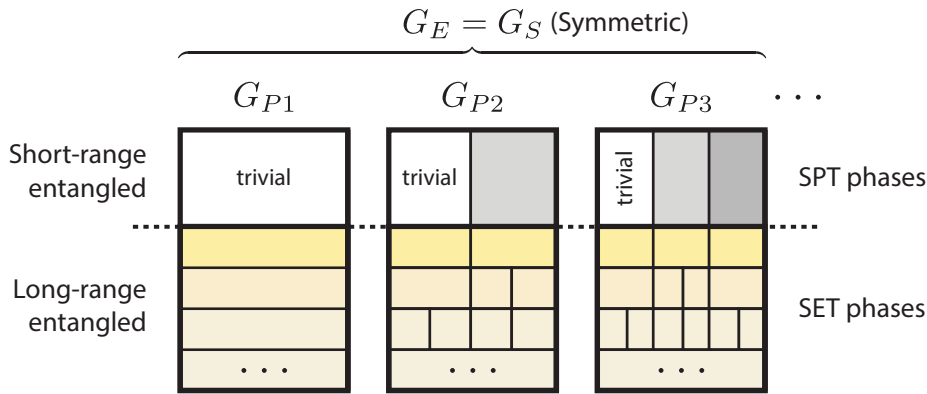
- States that can be connected to a product state are “trivial” both in symmetry breaking terms and in the context of topological order. However, depending on the protecting symmetry G_P , this equivalence class can *split* into “patches” of short-range entangled states, separated by phase transitions, that can only be connected to the trivial product state if the protecting symmetry G_P is violated along the path $\hat{H}(0) \rightarrow \hat{H}(1)$ (or if a phase transition occurs, of course). These “patches” are referred to as *symmetry-protected topological*¹³ (*SPT*) *phases* [34]. The most prominent example is the famous Haldane phase of the one-dimensional spin-1 Heisenberg antiferromagnet [62, 63] which is protected by (optionally) spin-rotation, time-reversal or inversion symmetry [64, 65].
- Similarly, states with long-range entanglement that can be smoothly connected might get separated by an additional protecting symmetry. The resulting “patches” of long-range entangled states are called *symmetry-enriched topological* (*SET*) *phases* [34]. The term “enriched” refers to the fact that symmetries can endow anyonic excitations (which are tied to topologically ordered phases)

¹²That is, $[\hat{H}(\alpha), U_g] = 0$ for all $\alpha \in [0, 1]$ and $g \in G$.

¹³The term “topological” is somewhat misleading as these states are *not* topologically ordered. Thus “SPT” is sometimes read as “symmetry-protected *trivial*” instead.

with *fractional charges*¹⁴. For example, the fractional charges of quasiparticles in fractional quantum Hall liquids [36] and the quantized Hall conductance of these systems [27] are symmetry-protected by charge conservation $G_P = U(1)$ [66, 67].

We conclude that with symmetries as “masks,” the new, more fine-grained landscape of quantum phases can be sketched as follows:



Note that it is also conceivable that there are *no* new SPT or SET phases defined by imposing a protecting symmetry (illustrated by G_{P1} above).

Given this rather abstract concept of symmetry-protected quantum phases, it is natural to ask for a “labeling scheme,” i.e., a mathematical framework that, given a protecting symmetry G_P and a spatial dimension D , assigns “labels” to all ground states of gapped Hamiltonians that do not break G_P , such that two states carry the same “label” if and only if they belong to the same G_P -protected phase. In other words: We are looking for a replacement of *group theory* (which underlies spontaneous symmetry breaking).

In the following, we focus on SPT phases to avoid the intricacies of topological order and fractionalized excitations¹⁵. Even though we thereby discard a plethora of interesting states of matter (such as fractional quantum Hall liquids), the ensuing picture is stunningly complex. The quest for the classification of SPT phases gave rise to (at least¹⁶) three major directions of research that attracted lots of attention in recent years:

¹⁴Formally, the anyons transform under *projective* representations of the global symmetry group; a phenomenon known as *symmetry fractionalization*. See Subsection 5.1.3 for an application of projective representations in the context of SPT phases.

¹⁵We are a bit sloppy here: The classification schemes discussed below capture also some phases that are actually long-range entangled according to Wen’s definition (see Footnote 8); examples are the 1D Majorana chain and the 2D integer quantum Hall states [34]. The important point is that we exclude phases with anyonic bulk excitations.

¹⁶See Ref. [68] for a review on the various approaches to classify quantum phases in the presence of symmetries.

- The classification that has been studied most intensively (and is by now well understood) covers *non-interacting fermion Hamiltonians* and the quantum phases that are realized as their many-body ground states (constructed by filling all single-particle eigenstates with negative energy).

The first and most prominent phases that fall under these restrictions are the integer quantum Hall states [69] which can be understood in terms of non-interacting fermions. Different quantum Hall states are characterized by their quantized Hall conductance which, in turn, can be related to a *topological invariant* $\nu \in \mathbb{Z}$ known as TKNN *invariant*¹⁷ [70]. ν is the first example of a “label” that discriminates quantum phases that cannot be characterized by the symmetries they break. A few years later, Haldane introduced the prototype of a *Chern insulator* and showed that the magnetic field is not crucial for a quantized Hall conductance [71], a phenomenon called *quantum anomalous Hall effect*. Since the Haldane model breaks time-reversal symmetry (just as quantum Hall systems do), it seemed reasonable that this is a necessary ingredient for the emergence of topological states of matter. However, in 2005 Kane and Mele came up with a time-reversal symmetric model that cannot be deformed into a trivial insulating state without closing the gap or breaking time-reversal symmetry [72]. The Kane-Mele model realizes the *quantum spin Hall effect* and became the prototype for a class of quantum states nowadays known as *topological insulators (TI)*¹⁸. It is associated with a new topological invariant $\bar{\nu} \in \mathbb{Z}_2$ which separates the trivial ($\bar{\nu} = 0$) from the topological phase ($\bar{\nu} = 1$) [73]. Shortly afterwards it was predicted [74] and experimentally demonstrated [75] that the quantum spin Hall effect can be realized in HgTe quantum wells. In the same year, generalizations for topological insulators in three dimensions were proposed [76, 77], followed by experimental observations one year later [78]. Another diverse class of quadratic Hamiltonians—so called *Bogoliubov-de Gennes (BdG)* Hamiltonians—describes conventional *superconductors* on the mean field level (with fermion parity symmetry and broken U(1) symmetry). Due to mathematical similarities in the description of band insulators and BCS superconductors, it comes as no surprise that many of the topological features found for insulators have superconducting counterparts. Indeed, in 2000 Read and Green introduced a time-reversal breaking *p*-wave superconductor with chiral edge modes [79] (in analogy to integer quantum Hall states), and the discovery of the Kane-Mele model was followed by the construction of superconductors (and superfluids) with counterpropagating edge modes protected by time-reversal symmetry [80, 81]. These edge modes are rather

¹⁷Mathematically an example of a (first) *Chern number*.

¹⁸The term “topological insulator” is not used consistently in the literature: Sometimes it refers specifically to the Kane-Mele model, sometimes it is used as a label for the class of gapped free fermion theories with time-reversal symmetry and particle number conservation, and sometimes it refers to arbitrary band insulators with topologically protected edge modes (including, e.g., Chern insulators).

special: they are *Majorana modes*, a characteristic feature of superconductors due to their intrinsic particle-hole symmetry. Majorana modes can also appear at the boundaries of one-dimensional superconductors [82] (Subsection 1.2.2) and in vortices [83].

All these models can be described by non-interacting fermion Hamiltonians and are covered by the *classification of topological insulators and superconductors*¹⁹. There are two ingredients that make this classification possible: First, the restriction to non-interacting fermions allows for the description of the many-body ground states in terms of *single-particle* eigenstates. And second, the protecting symmetries are restricted to the *generic symmetries*²⁰ \mathcal{T} (time-reversal symmetry), \mathcal{C} (particle-hole symmetry), and $\mathcal{S} = \mathcal{T} \cdot \mathcal{C}$ (chiral- or sublattice symmetry). It can be shown that there are only ten possibilities for a quadratic Hamiltonian to transform under these symmetries. Translated to the single-particle Hamiltonian, these define ten classes of random matrices that are characterized by certain reality conditions, a scheme known as *Altland-Zirnbauer classification* or “tenfold way” [90] which can be traced back to Wigner and Dyson [91–93]. Each of these ten classes corresponds to a specific “mask” on the parameter space of non-interacting fermion Hamiltonians which may or may not give rise to new phases. These phases can be labeled with integers known as *topological invariants*, which often can be evaluated explicitly in translationally invariant systems by an integration over the Brillouin zone [70, 73, 94] (the most prominent example being the TKNN invariant). The topological invariants and their allowed values depend on the symmetry class and the spatial dimension and define the SPT phases that can be distinguished under these circumstances [22, 95]. Various methods can be used to derive this classification scheme in arbitrary dimensions: Most notably, the description of Anderson localization [96] in terms of nonlinear σ models (NL σ M) [21, 95, 97] and the mathematical framework of *K-Theory* [22]. A central result of both approaches is that in every dimension D , *five* of the ten symmetry classes support non-trivial²¹ topological phases and, quite surprisingly, the labeling scheme is periodic in D : the allowed topological indices in D and $D + 8$ dimensions are the same (a feature known

¹⁹Here, the term “topological insulator” is used in the widest sense, i.e., it refers to arbitrary band insulators with non-trivial topological indices and robust edge modes; see Footnote 18.

²⁰These symmetries are the only ones that a disordered fermion system without any *unitary* symmetry on the single-particle level can possess; this is what makes them “generic.” Unlike “conventional” symmetries, they are realized as antiunitary symmetries or unitary/antiunitary “pseudo-symmetries” on the single-particle Hamiltonian (“pseudo-symmetries” *anticommute* with the Hamiltonian). See Ref. [84] for a mathematical treatment and Ref. [85] for a pedagogical exposition. We stress that one can extend the classification by considering additional unitary symmetries. This has been done for spatial symmetries (reflections etc.) and results suggest that it complicates the classification considerably [86–89].

²¹Non-trivial topological phases have a non-zero topological invariant.

in K-Theory as *Bott periodicity* [22]). This motivates the term “periodic table of topological insulators and superconductors” [22]; here we will refer to it simply as the *tenfold way*²².

Finally, let us point out that the phase of a system is a property of the *bulk*; it does not depend on the presence or absence of *boundaries* because phases are, strictly speaking, only well-defined in the thermodynamic limit where boundaries clearly are irrelevant. However, a unifying property of the topological insulators and superconductors presented above is the existence of gapless edge modes that are exceptionally robust to disorder. Thus, while boundaries do not affect the bulk, the bulk clearly affects the boundaries. As it turns out, the existence of gapless edge modes is a mathematical consequence of the topologically non-trivial bulk²³, a relation known as *bulk-boundary correspondence*²⁴ [98, 99] (see also Ref. [100] and references therein). It essentially states that whenever two media with different topological indices touch, there are necessarily gapless modes localized at the boundary²⁵. Thereby the robustness of these edge modes derives from the robustness of the topological invariants that describe the bulk.

For a pedagogical introduction to the tenfold way we refer the reader to Refs. [85, 101], for comprehensive and historical reviews on topological insulators and superconductors see Refs. [102, 103]. Finally, we note that recently a generalization to so called “higher-order topological insulators (HOTI)” has been proposed [104, 105]; in contrast to “conventional topological insulators,” these states feature no conducting surfaces but gapless modes bound to *hinges* or *corners*. Recent experimental results established bismuth as a HOTI with symmetry-protected conducting hinge modes [106].

In this thesis, we make use of the tenfold way repeatedly in Chapter 3 and Chapter 4 where we employ one-dimensional models that can be classified in this scheme. In Section 1.2 we introduce and discuss these models.

- We saw that non-interacting fermion Hamiltonians give rise to a variety of interesting SPT phases and, at the same time, describe many real-world materials reasonably well (as explained by Fermi liquid theory). This, however, is not always true and a more generic classification that includes interactions is desirable. From the perspective of the tenfold way, this means that restrictions are loosened such that additional (interacting) paths can be used

²²Strictly speaking, the “tenfold way” refers only to the Altland-Zirnbauer classification of random matrices—without any association to topological invariants or SPT phases. As we are primarily interested in the latter (and “tenfold way” is short and catchy), we use it to refer to the periodic table of topological insulators and superconductors instead.

²³This relation allows for the characterization and classification of topological phases by means of their boundary physics, an approach taken by the $NL\sigma M$ -based classification scheme [21, 95, 97].

²⁴Sometimes called *bulk-edge* correspondence.

²⁵This explains the appearance of robust edge modes at the boundaries of topological insulators and superconductors because the surrounding “vacuum” always has a topological index equal to zero.

to connect gapped Hamiltonians. Thus it is conceivable that distinct phases in the tenfold way can be connected by paths through interacting regions of parameter space. This is similar to our classical example above: Removing the “mask” from the phase diagram of water makes liquid and vapor belong to the same fluid phase.

Indeed, it can be demonstrated explicitly that certain one-dimensional topological superconductors—which are classified by a \mathbb{Z} topological index²⁶ in the tenfold way—are classified by a \mathbb{Z}_8 topological index when interactions are allowed [107]: Removing the “mask” from parameter space connects an infinite number (\mathbb{Z}) of disconnected patches such that only 8 separate regions survive (\mathbb{Z}_8); similar results can be shown in two dimensions [108].

Contriving a general classification of interacting, symmetry-protected topological phases is a highly non-trivial endeavor for several reasons: First, whereas the tenfold way classifies quantum phases by classifying single-particle Hamiltonians instead, such a simplification is not possible for interacting theories. Second, the tenfold way only covers three generic symmetries; a complete classification, however, should be applicable to more general symmetries as well. And third, there might be SPT phases that are intrinsically interacting, i.e., phases that lack non-interacting representatives (actually, there *are* such phases [109]).

While the classification in one and two dimensions has been intensively studied [109–113], proposals for a complete classification in three dimensions are still scarce [114, 115]. The most prominent mathematical toolset employed for these classifications is “*group supercohomology*”²⁷ [19], while another proposal makes use of *cobordism groups* [20] (an approach that extends to interacting bosonic phases as well). Thus, at the time of writing, the classification of interacting fermions is very much “work in progress”—even more than for bosons (see below). We refer the reader to Ref. [115] and references therein for a recent review with focus on classification schemes and to Ref. [116] for a more model-centered perspective.

In this thesis, we study a symmetry-protected topological phase of interacting fermions in Chapter 2, although we do not relate it to a classification scheme due to subtleties to be discussed.

- Topological phases that are protected by symmetries (with or without long-range entanglement) can also arise from *bosonic* constituents. However, there is a fundamental difference between bosons and fermions: The many-body ground states of non-interacting (i.e., quadratic) *fermionic* Hamiltonians

²⁶Topological indices label distinct phases: Ground states with different indices cannot be smoothly connected without closing the gap or violating the symmetry; see Section 1.2 for examples.

²⁷A generalization of the mathematical concept of *group cohomology* (which can be used for the classification of bosonic SPT phases, see Subsection 5.1.3 for an application).

give rise to quantum phases that inherit their features from a significant part of the single-particle spectrum due to the Pauli exclusion principle (by filling the bands with negative energy). In particular, filled bands with a topological character (e.g., non-vanishing Chern number) imprint these properties on the many-body ground state wave function [117, 118], with measurable consequences, e.g., for transport [70, 73]. The same single-particle Hamiltonians can also be used to describe bosons (on the single-particle level, statistics is meaningless). But the *many-body* ground states of these non-interacting theories are simply Bose-Einstein condensates (where all bosons condense into a single lowest-energy mode). These states do not probe entire bands but only single modes and therefore cannot inherit any of their topological features (if present).

The upshot is that there are no non-interacting topological quantum phases of bosons and there is no bosonic counterpart of the tenfold way²⁸. Thus any classification of bosonic SPT (or SET) phases necessarily involves interactions—which makes it mathematically much more challenging, see Ref. [34] and references therein. At the time of writing, the most comprehensive classification scheme makes use of suitable “fixed point” representations of many-body ground state wave functions and employs algebraic properties of their transformation under the symmetry operations to characterize quantum phases [17, 18, 64, 112, 119, 120]. Formally, the scheme is built on *group cohomology theory* and quantum phases are labeled by elements of certain cohomology groups that encode algebraic properties of the protecting symmetries; however, recent results suggest that in 3D there are SPT phases that are not captured by this classification [121–123]. In the wake of these findings, it has been proposed that *cobordism groups* may provide a unifying toolset for an exhaustive classification of SPT order in any dimension [124, 125]. Thus, just as for interacting fermions, the classification of bosonic SPT phases is subject to ongoing research and a conclusive picture—comparable to the tenfold way for free fermions—has yet to be drawn.

In this thesis, the cohomology-based classification of one-dimensional SPT phases of interacting spins (alternatively: hard-core bosons) plays a role in Chapter 5, more precisely in Section 5.1 where we discuss and apply the framework in an experimentally relevant setting.

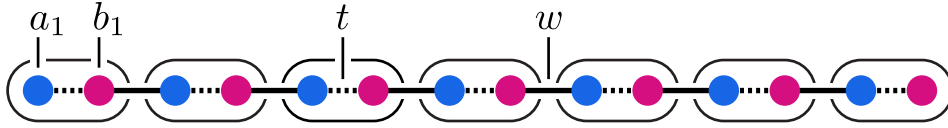
²⁸This does not mean that there is no use for the fermionic tenfold way in bosonic settings. The crucial point is that only *single-particle excitations* can be affected (see Chapter 3 for an example and Section 1.3 for proposed applications) but not the features of *quantum phases* (which are characterized by many-body ground states).

1.2 Examples in One Dimension

1.2.1 The Su–Schrieffer–Heeger Chain

The *Su–Schrieffer–Heeger (SSH) chain* is a model of non-interacting, spinless fermions in one dimension that has been introduced by Su, Schrieffer and Heeger in 1979 to describe soliton formation in polyacetylene [126]. The model has become the example of choice to illustrate topological invariants and the emergence of robust edge modes [127]. It is classified by the tenfold way and hence the prime example of a non-interacting, fermionic, symmetry-protected topological phase.

The model is defined on a one-dimensional lattice of spinless fermion modes a_i and b_i , $1 \leq i \leq L$, that are grouped into L unit cells:



The Hamiltonian that defines the SSH chain is given by simple fermion hopping with alternating amplitudes t and w :

$$H_{\text{SSH}} = t \sum_{i=1}^L (a_i^\dagger b_i + b_i^\dagger a_i) + w \sum_{i=1}^{L'} (b_i^\dagger a_{i+1} + a_{i+1}^\dagger b_i), \quad 1.1$$

where $L' = L - 1$ for open (OBC) and $L' = L$ for periodic boundary conditions (PBC). Let us focus on PBC where we can use translational invariance to (partially) diagonalize the Hamiltonian by a Fourier transform. In the Fourier basis \tilde{a}_k and \tilde{b}_k the Hamiltonian (1.1) reads

$$H_{\text{SSH}} = \sum_{k \in \text{BZ}} \begin{bmatrix} \tilde{a}_k^\dagger & \tilde{b}_k^\dagger \end{bmatrix} \cdot \underbrace{\begin{bmatrix} 0 & t + w e^{-ik} \\ t + w e^{ik} & 0 \end{bmatrix}}_{h(k)} \cdot \begin{bmatrix} \tilde{a}_k \\ \tilde{b}_k \end{bmatrix} \quad 1.2$$

with the Bloch Hamiltonian $h(k)$; as traceless and Hermitian 2×2 -matrix, it can be expanded in Pauli matrices:

$$h(k) = (t + w \cos k) \sigma^x + w \sin k \sigma^y = \mathbf{d}(k) \cdot \boldsymbol{\sigma} \quad 1.3$$

with the three-dimensional vector

$$\mathbf{d}(k) = \begin{bmatrix} t + w \cos k \\ w \sin k \\ 0 \end{bmatrix}. \quad 1.4$$

INTRODUCTION

The eigenvalues of $H(k)$ are simply

$$E_{\pm}(k) = \pm|\mathbf{d}(k)| = \pm\sqrt{t^2 + w^2 + 2tw \cos k} \quad 1.5$$

and collectively constitute the single-particle spectrum of H_{SSH} . The band gap is easily evaluated and reads $\Delta E = 2||t| - |w||$: the system is a gapped band insulator for all $t, w \in \mathbb{R}$ except for $|t| = |w|$ where the gap closes. Let us focus on the case where $t, w \geq 0$ (the other three cases can be shown to be equivalent via a canonical transformation of the fermion modes). Then the two regimes $t < w$ and $t > w$ both constitute gapped phases with many-body ground states given by a completely filled lower band. Connecting these two phases via H_{SSH} is not possible without crossing the critical, gapless point at $t = w$ where $\Delta E = 0$. This (continuous) phase transition suggests that the two regimes for $t < w$ and $t > w$ are actually *different* phases. If so, there should be some qualitative feature that is stable but different in the two parameter regimes and changes abruptly at $t = w$. Let us try whether Landau’s paradigm of spontaneous symmetry breaking tells us anything useful: According to Landau—if different—the two phases should transform differently under the symmetries of the Hamiltonian. But this cannot be the case because in both regimes the ground state is unique. So Landau tells us that the two regimes actually belong to the *same* disordered phase. What is the conclusion within the scope of the new concepts introduced in Subsections 1.1.1 and 1.1.2? Let us first show that the “coarser” notion without symmetry-protection (the one that defines intrinsic topological order) comes to the same conclusion as Landau. We will then argue that this definition is too blunt to characterize the SSH chain properly and demonstrate that the more “fine-grained” concept of symmetry-protected topological phases is the appropriate framework.

Recall the definition of quantum phases according to which two ground states belong to the same phase if and only if there is a continuous family of gapped, local Hamiltonians that interpolates between them. We already saw that the paths $\hat{H}_{\text{SSH}}(t, w) \equiv H_{\text{SSH}}$ parametrized by w and t fail miserably because they must cross a gapless point at $w = t$. But the definition is very permissive: It allows for arbitrary modifications of the Hamiltonian as long as it remains local and gapped. Thus we are free to choose $\hat{H}(t, w, \mu) \equiv \hat{H}_{\text{SSH}}(t, w) + \mu H'$ to connect the gapped Hamiltonians $H_{\text{SSH}}(t < w) = \hat{H}(t < w, 0)$ and $H_{\text{SSH}}(t > w) = \hat{H}(t > w, 0)$; our goal is to *circumvent* the gap closing by switching on another local Hamiltonian H' ($\mu > 0$), cross the point $w = t$ (where the gap no longer closes due to H'), and then switch H' off again ($\mu = 0$). The correct choice for H' follows from the spectrum (1.5) and the vector (1.4). Indeed, with a staggered chemical potential

$$H' = \sum_{i=1}^L (a_i^\dagger a_i - b_i^\dagger b_i) \quad 1.6$$

the Bloch Hamiltonian of $\hat{H}(t, w, \mu)$ leads to

$$\mathbf{d}(k) = \begin{bmatrix} t + w \cos k \\ w \sin k \\ \mu \end{bmatrix} \quad 1.7$$

so that the modified spectrum

$$\pm E_{\pm}(k) = |\mathbf{d}(k)| = \sqrt{\mu^2 + t^2 + w^2 + 2tw \cos k} \geq |\mu| \quad 1.8$$

becomes gapped for arbitrary t and w (in particular $t = w$) if $\mu > 0$. We conclude that the two gapped phases of the SSH chain are actually the *same* phase if we use the definition that underlies the concept of intrinsic topological order.

Note that the spectrum (1.5) becomes flat for $t \cdot w = 0$ and the many-body ground state of H_{SSH} for $t > 0$ and $w = 0$ is a simple product state at half-filling with one delocalized fermion per unit cell; we label this state as “trivial.” For $t = 0$ and $w > 0$ the bands are again flat and the many-body ground state can be read off the Hamiltonian (1.1): now the fermions are delocalized between two modes of *adjacent* unit cells. The family of Hamiltonians $\hat{H}(t, w, \mu)$ connects these two representatives adiabatically, i.e., without crossing a phase transition. Thus, according to this concept of phases, the state with $t = 0$ and $w > 0$ is just as “trivial” as the one with $t > 0$ and $w = 0$.

However, in Subsection 1.1.2 we argued that this classification scheme can be too coarse—it might fail to capture the characteristic features of the system. We provided arguments why a more fine-grained classification of phases is desirable. Let us revisit these arguments for the SSH chain:

→ Symmetries are of paramount importance in quantum mechanics. Often the symmetries of a system can be divided into *accidental* and *natural* symmetries. Natural symmetries are robust symmetries of the Hamiltonian that survive typical perturbations of the system. By contrast, accidental symmetries require fine-tuning and are therefore less robust.

Obvious symmetries of H_{SSH} are ...

- *particle number conservation*, i.e., the U(1) symmetry generated by the particle number operator $N = \sum_i (a_i^\dagger a_i + b_i^\dagger b_i)$ and represented by the unitary operators $\mathcal{R}_\phi = e^{i\phi N}$ for $\phi \in [0, 2\pi)$.
- *time-reversal symmetry* $\mathbb{Z}_2^T = \{\mathbb{1}, \mathcal{T}\}$, here represented by the *antiunitary* operator $\mathcal{T} = \mathcal{K}$ (\mathcal{K} denotes complex conjugation) that leaves the (spinless!) fermions invariant: $\mathcal{T} x_i \mathcal{T}^{-1} = x_i$ with $x \in \{a, b\}$.
- *translation symmetry* \mathbb{Z}_L , represented by unitary operators \mathcal{D}_n that act as $\mathcal{D}_n x_i \mathcal{D}_n^{-1} = x_{i+n \bmod L}$.
- *particle-hole symmetry* $\mathbb{Z}_2^C = \{\mathbb{1}, \mathcal{C}\}$, here represented by the unitary operator $\mathcal{C} = \prod_i (a_i^\dagger - a_i)(b_i^\dagger + b_i)$ with the action $\mathcal{C} a_i \mathcal{C}^{-1} = a_i^\dagger$ and $\mathcal{C} b_i \mathcal{C}^{-1} = -b_i^\dagger$.

INTRODUCTION

It is easy to check that all four operators commute with the many-body Hamiltonian (1.1): $[H_{\text{SSH}}, \mathcal{X}] = 0$ for $\mathcal{X} \in \{\mathcal{R}_\phi, \mathcal{D}_n, \mathcal{T}, \mathcal{C}\}$. The total symmetry group G_S of the system of course includes arbitrary products of these operators. As we will see, one is particularly important for the SSH chain:

$$\mathcal{S} = \mathcal{T} \circ \mathcal{C} = \prod_i (a_i^\dagger - a_i)(b_i^\dagger + b_i) \circ \mathcal{K}. \quad 1.9$$

The invariance $[H_{\text{SSH}}, \mathcal{S}] = 0$ is called *sublattice symmetry* (see the remarks in Subsection 5.1.1 for a motivation of the name; for now, regard it as a label). The classification of non-interacting fermion Hamiltonians—the tenfold way—is based on the presence or absence of the three symmetries $\{\mathcal{T}, \mathcal{C}, \mathcal{S}\}$. One can show [85] that always $\mathcal{S}^2 = \mathbb{1}$ but for \mathcal{T} and \mathcal{C} one finds

$$\mathcal{T}^2 = \mathbb{1} \quad \text{or} \quad \mathcal{T}^2 = \mathcal{P} \quad 1.10a$$

$$\text{and} \quad \mathcal{C}^2 = \mathbb{1} \quad \text{or} \quad \mathcal{C}^2 = \mathcal{P}, \quad 1.10b$$

where $\mathcal{P} = (-1)^N$ is the fermion parity operator. For a specific Hamiltonian, the absence or presence of the three symmetries $\{\mathcal{T}, \mathcal{C}, \mathcal{S}\}$, in combination with (1.10), gives rise to the 10 symmetry classes of the *tenfold way*²⁹. Note that the *representations* of these symmetries depend on the system, i.e., a sublattice symmetry may not be represented by Eq. (1.9) in other systems.

The 10 symmetry classes are given labels that are motivated by mathematics³⁰. It is easy to check that the representations $\{\mathcal{T}, \mathcal{C}, \mathcal{S}\}$ that are symmetries of H_{SSH} satisfy $\mathcal{T}^2 = \mathbb{1} = \mathcal{C}^2$; therefore the SSH chain belongs to a symmetry class with the label **BDI**. Now we could have a look at the classification tables of the tenfold way [85] to check if (or which) topological phases can be protected in one-dimensional systems that belong to this symmetry class (the answer would be that there is a \mathbb{Z} topological index, i.e., there are infinitely many topological phases labeled by an integer $\nu \in \mathbb{Z}$).

While the SSH chain *can* be placed in **BDI**, it is not its natural symmetry class. Recall that we started this discussion with the distinction of *natural* and *accidental* symmetries. It is reasonable that we should only take natural symmetries into account for the symmetry protection of topological phases as

²⁹A given Hamiltonian may or may not commute with the time-reversal symmetry of the system. If it does, the time-reversal operator squares either to $\mathbb{1}$ or \mathcal{P} . This yields three possibilities, usually labeled by $T = 0, +1, -1$ where $T = 0$ denotes the absence of time-reversal symmetry and $T = +1(-1)$ denotes the presence of a time-reversal symmetry with $\mathcal{T}^2 = \mathbb{1}(\mathcal{P})$. Similarly, particle-hole symmetry gives rise to three possibilities: $C = 0, +1, -1$. This yields $3 \times 3 = 9$ symmetry classes. The sublattice symmetry $\mathcal{S} = \mathcal{T} \circ \mathcal{C}$ is not independent: its presence ($S = 1$) is implicit whenever $C \neq 0$ and $T \neq 0$. But for $T = 0 = C$ there are *two* cases: \mathcal{S} may ($S = 1$) or may not ($S = 0$) be a symmetry since $\mathcal{T} \circ \mathcal{C}$ has still the chance to commute with the Hamiltonian even if \mathcal{T} and \mathcal{C} do not commute with it separately. In total, there are $3 \times 3 + 1 = 10$ symmetry classes—which explains the name “tenfold way.” See Ref. [85] for more details.

³⁰By Élie Cartan’s classification of *symmetric spaces*.

these are the more robust ones (this is a physical argument, not a mathematical one). So which of the SSH chain symmetries $\{\mathcal{R}_\phi, \mathcal{D}_n, \mathcal{T}, \mathcal{C}, \mathcal{S}\}$ are natural and which are accidental? The answer depends on what we deem “natural perturbations” of H_{SSH} and thereby on the physical system that it describes. A reasonable approach is to classify perturbations that only alter the parameters of H_{SSH} (but not its form) as “natural.” In this sense, the “generic” Hamiltonian of the SSH chain reads

$$\tilde{H}_{\text{SSH}} = \sum_{i=1}^L (t_i a_i^\dagger b_i + t_i^* b_i^\dagger a_i) + \sum_{i=1}^L (w_i b_i^\dagger a_{i+1} + w_i^* a_{i+1}^\dagger b_i), \quad 1.11$$

where $t_i, w_i \in \mathbb{C}$ are now site-dependent and possibly complex hopping amplitudes. It is clear that translations \mathcal{D}_n are no longer a symmetry of this Hamiltonian; the same is true for time-reversal \mathcal{T} and the particle-hole transformation \mathcal{C} . However, particle number conservation \mathcal{R}_ϕ and, most importantly, the sublattice symmetry \mathcal{S} still commute with \tilde{H}_{SSH} . We conclude that only $\{\mathcal{R}_\phi, \mathcal{S}\}$ should be counted as natural symmetries of the SSH chain: a real system that implements the SSH-physics is likely to possess the robust symmetries $\{\mathcal{R}_\phi, \mathcal{S}\}$; by contrast, $\{\mathcal{D}_n, \mathcal{T}, \mathcal{C}\}$ are, at best, accidental symmetries that require fine-tuning of the couplings.

If we return to the tenfold way (which only involves the generic symmetries $\{\mathcal{T}, \mathcal{C}, \mathcal{S}\}$), only the sublattice symmetry \mathcal{S} remains as robust candidate for symmetry protection. The symmetry class of Hamiltonians that only³¹ exhibit a sublattice symmetry is labeled **AIII** and features also a \mathbb{Z} topological index in one dimension [85]. We conclude that the proper symmetry class of the SSH chain is **AIII** and conjecture that the two regimes $w > t$ and $w < t$, separated by the critical point $w = t$, are actually *different* topological phases (labeled by different topological indices) *if* the sublattice symmetry is not broken. In a physical setting where \mathcal{S} is a natural symmetry, all continuous paths that connect the two regimes would then necessarily cross the phase transition at $w = t$; in this situation, it makes sense to consider the regimes $w > t$ and $w < t$ as *different* phases—despite the existence of (inaccessible) paths that circumvent the phase transition. This argument parallels our classical example: it makes sense to consider liquid water and vapor as different phases if we do not have the means to connect them via the supercritical regime. However, there is a crucial difference: liquid and vapor can be distinguished by the local density. There is no such thing for the two phases of the SSH chain. They differ by a *global* property that is hidden in the band structure; this property is quantified by a topological index that also serves as a “label” for the two phases.

³¹Of course additional, accidental symmetries are allowed. The SSH chain with its additional time-reversal and particle-hole symmetries is an example.

INTRODUCTION

To understand the definition of this topological index and its relation to the sublattice symmetry, we have to understand the restriction that \mathcal{S} imposes on the Bloch Hamiltonian $h(k)$. Note that particle number conservation $[H_{\text{SSH}}, \mathcal{R}_\phi] = 0$ does not impose any restrictions on $h(k)$, see Eq. (1.2). By contrast, the condition $\mathcal{S} H_{\text{SSH}} \mathcal{S}^{-1} \stackrel{!}{=} H_{\text{SSH}}$ is equivalent to

$$\sigma^z h(k) \sigma^z \stackrel{!}{=} -h(k) \quad \text{for all } k \in \text{BZ} \quad 1.12$$

which, in turn, can be rewritten as

$$\sigma^z \sigma^\alpha d_\alpha(k) \sigma^z \stackrel{!}{=} -\sigma^\alpha d_\alpha(k) \quad \Leftrightarrow \quad d_z(k) \stackrel{!}{=} 0 \quad \text{for all } k \in \text{BZ}. \quad 1.13$$

Here, σ^α denotes Pauli matrices and we use the Einstein sum convention. It is evident that our modification with the staggered chemical potential H' *violates* this condition with $d_z(k) = \mu$, recall Eq. (1.7). The path $\hat{H}(t, w, \mu)$ that connects the two regimes is therefore forbidden if the sublattice symmetry \mathcal{S} is required. This is consistent with the conjecture that the two regimes constitute different phases, but it does not disprove the existence of other paths. This is where the topological index enters the stage:

Recall that the band gap at momentum k is given by the length of the vector $\mathbf{d}(k) \in \mathbb{R}^3$: $\Delta E(k) = 2|\mathbf{d}(k)|$. Hence we can normalize this vector for all $k \in \text{BZ}$,

$$\hat{\mathbf{d}}(k) \equiv \frac{\mathbf{d}(k)}{|\mathbf{d}(k)|}, \quad 1.14$$

whenever the Hamiltonian is gapped. In the thermodynamic limit ($L \rightarrow \infty$), the Brillouin zone is a continuous interval $\text{BZ} = (-\pi, \pi]$ with the topology of a circle S^1 . Then, the normalized vector $\hat{\mathbf{d}}(k) : S^1 \rightarrow S^2$ defines a continuous map from the circle S^1 to the sphere S^2 . Pictorially, $\hat{\mathbf{d}}(k)$ “draws” a circle on the sphere; it is intuitively clear that two such circles $\hat{\mathbf{d}}_1(k)$ and $\hat{\mathbf{d}}_2(k)$ can always be continuously deformed into each other. In mathematical terms, this is equivalent to the triviality of the *first homotopy group* of the sphere: $\pi_1(S^2) = 0$. Physically, this means that the corresponding Hamiltonians $H_1 = H[\mathbf{d}_1]$ and $H_2 = H[\mathbf{d}_2]$ can be continuously connected without closing the gap. We illustrated this with the staggered chemical potential above. But if we require the sublattice symmetry, the condition (1.13) confines $\mathbf{d}(k)$ to the x - y -plane and $\hat{\mathbf{d}}(k) : S^1 \rightarrow S^1$ now maps the circle of the Brillouin zone to a *great circle* of S^2 . It is a well-known (and quite intuitive) fact of topology that there are different equivalence classes of such continuous maps $\hat{\mathbf{d}}(k)$ that cannot be continuously deformed into each other. The label that distinguishes these *homotopy classes* is the number of times that the domain-circle S^1 “winds around” the image-circle S^1 , a fact that leads to the non-trivial first homotopy group of the circle: $\pi_1(S^1) = \mathbb{Z}$. This *winding number* ν can be calculated by a simple integration over the domain of the

map, in our case the Brillouin zone:

$$\nu = \nu[\hat{\mathbf{d}}] = \frac{1}{2\pi} \int_{\text{BZ}} \left[\hat{\mathbf{d}}(k) \times \partial_k \hat{\mathbf{d}}(k) \right] \cdot \mathbf{e}_z dk, \quad 1.15$$

where \mathbf{e}_z is the unit vector in z -direction and “ \times ” denotes the cross product in \mathbb{R}^3 . It can be shown that ν is always integer if $\hat{\mathbf{d}}(k)$ sticks to the x - y -plane, i.e., if the Hamiltonian does not violate the sublattice symmetry³². ν is the *topological index* that labels quantum phases in the symmetry class **AIII** in one dimension; that it takes values in \mathbb{Z} is in accordance with the tenfold way for one-dimensional systems [22, 95].

Using (1.4) one can check that for the SSH chain

$$\nu = \begin{cases} 0 & \text{for } t > w \\ 1 & \text{for } t < w. \end{cases} \quad 1.16$$

This proves our conjecture: The phase with $t > w$ is characterized by $\nu = 0$ and is called *trivial phase*. The phase with $t < w$ is characterized by $\nu = 1$ and constitutes the *topological phase* of the SSH chain. If we remain in the domain of the tenfold way (where interactions are forbidden) and do not break the sublattice symmetry \mathcal{S} , these two phases cannot be connected without crossing a phase transition because ν takes different integer values on these phases and depends continuously on the Hamiltonian via (1.15). The value of ν can only jump if it is ill-defined; this happens exactly when the gap of the system closes because then the normalization $\mathbf{d}(k) \rightarrow \hat{\mathbf{d}}(k)$ is not defined.

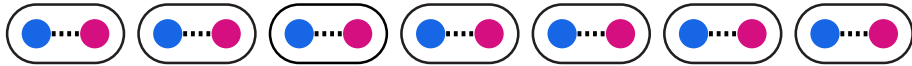
Finally, note that the tenfold way guarantees the *existence* of the topological index $\nu \in \mathbb{Z}$ if the sublattice symmetry is present. The classification does not make any claim about the actual *realization* of topologically non-trivial phases (with $\nu \neq 0$) in a specific system. The SSH chain is an interesting model because there happens to be a phase with $\nu = 1$. But the tenfold way and Eq. (1.15) also allow for $\nu > 1$; these phases cannot be realized with the SSH chain Hamiltonian (1.1).

- So far we considered only periodic boundary conditions. This allowed us a treatment of H_{SSH} in momentum space and eventually led to the definition of the topological index ν . This index explains mathematically why we cannot hope to connect the two SSH phases without crossing a phase transition or breaking the sublattice symmetry. But the index is not an observable (at least not in a straightforward sense)—it is a topological feature of the band structure. Is there any *observable* difference between the two phases?

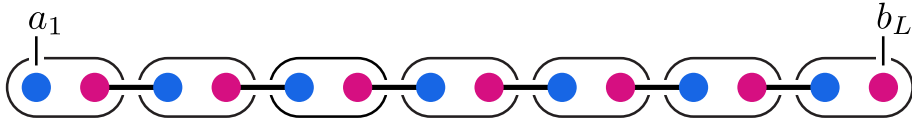
³²If it *does* violate the symmetry, ν can take real values that continuously interpolate between these integers.

INTRODUCTION

The answer is positive and this brings us to our second argument why distinguishing symmetry-protected topological phases is useful for the characterization of quantum systems. The most striking difference between the two phases can be observed if the system is cut open, i.e., for $L' = L - 1$ in Hamiltonian (1.1). In Subsection 1.1.2 we discussed the *bulk-boundary correspondence* which predicts gapless edge modes whenever a topologically non-trivial bulk ($\nu \neq 0$) has an interface with the vacuum ($\nu = 0$). If this is true, then our previous findings suggest gapless edge modes at the endpoints of an open SSH chain for $t < w$ and their absence for $t > w$. That this is indeed the case, is particularly evident at the special points where the bands are flat. In the trivial phase, at $t > 0$ and $w = 0$, the Hamiltonian can be illustrated as follows (edges denote non-zero fermion hopping amplitudes):



There is nothing interesting happening at the endpoints: clearly there are no zero-energy modes because all fermion modes are dimerized into pairs and form (anti)symmetric on-site eigenmodes with positive and negative eigenenergies. However, in the topological phase, at $t = 0$ and $w > 0$, the pattern of dimers is shifted by half a lattice site; this leads to *one* missing dimer due to the open boundary conditions:



Consequently, the outermost modes $a_l \equiv a_1$ and $b_r \equiv b_L$ drop from the Hamiltonian and therefore define fermionic zero-energy eigenmodes located at the boundaries. The many-body ground state $|n_l, n_r\rangle$ of this chain is then four-fold degenerate and can be labeled by the edge mode occupation numbers $n_l = a_l^\dagger a_l$ and $n_r = b_r^\dagger b_r$.

The existence of these states is not tied to the special points with flat bands but rather a generic feature of the entire topological phase with $t < w$, i.e., where the on-site hopping t is weaker than the inter-site hopping w . This non-trivial fact is dictated by the bulk-boundary correspondence and the $\nu = 1$ topological index for $t < w$. Recall that for the definition of ν we had to consider the thermodynamic limit $L \rightarrow \infty$ to make the Brillouin zone a true circle; only then the winding number of *continuous* maps $\hat{d}(k)$ can be properly defined. Thus the bulk-boundary correspondence implies the existence of *exact* zero-energy edge modes only for $L \rightarrow \infty$. In finite systems, the degeneracy of the four states will generally be lifted by corrections that vanish

exponentially with the system size L (only at the special points depicted above it is exact even for finite L). The exponentially small splitting can be understood with perturbative arguments: Starting from $t = 0$ and $w > 0$, one can treat a weak on-site hopping $0 < t \ll w$ as a perturbation of the perfectly dimerized system. The degeneracy of the four ground states is then lifted by tunneling of fermions between the edge modes a_1 and b_L ; but these are processes of order $\mathcal{O}(L)$ and therefore suppressed by $(t/w)^L$. Solving the SSH chain with $0 < t < w$ and open boundaries *exactly* is challenging (see ✱ Subsection 3.D.2). However, approximate expressions for the edge modes read as follows:

$$\tilde{a}_l = \mathcal{N} \sum_{i=1}^L \left(-\frac{t}{w} \right)^{i-1} a_i, \quad 1.17a$$

$$\tilde{b}_r = \mathcal{N} \sum_{i=1}^L \left(-\frac{t}{w} \right)^{i-1} b_{L-i+1}. \quad 1.17b$$

Here, \mathcal{N} is an appropriate normalization. It is straightforward to show that these fermionic modes are zero-energy eigenmodes of H_{SSH} up to corrections that vanish with $(t/w)^L$. Note that these edge modes are no longer perfectly localized but decay exponentially into the bulk; the perfect localization on the edge is a special feature of systems with $t = 0$.

To conclude this subsection, let us point out that the existence and degeneracy of edge modes does *not* depend on translation invariance—even though the definition of the topological index in terms of band vectors $\hat{\mathbf{d}}(k)$ suggests otherwise. In fact, it is a central (and non-trivial) result of the tenfold way [22, 95] that these topological features are robust even in the presence of disorder as long as it (i) does not close the gap and (ii) respects the sublattice symmetry.

In Chapter 3, we translate the SSH Hamiltonian into a setting of coupled bosonic modes and show how its edge states can be used for controllable transfer of quantum information. In Section 5.1, we study an interacting SSH chain filled with hard-core bosons and discuss its classification in terms of group cohomology.

1.2.2 The Majorana Chain

The *Majorana chain* is another model of non-interacting, spinless fermions in one dimension that has been introduced by Kitaev³³ in 2001 to demonstrate the appearance of unpaired Majorana modes at the endpoints of superconducting quantum wires [82]. It is the simplest topological *superconductor* and therefore a prime example for the interplay of topology and superconductivity [128].

³³Hence it is also known as “Kitaev chain.”

INTRODUCTION

The Majorana chain is defined on a one-dimensional lattice of L spinless fermion modes a_i and the quadratic Hamiltonian is of the Bogoliubov-de Gennes (BdG) form [82]

$$H_{\text{MC}} = - \sum_{i=1}^{L'} \left(w c_i^\dagger c_{i+1} - \Delta c_i c_{i+1} + \text{h.c.} \right) - \sum_{i=1}^L \mu \left(c_i^\dagger c_i - \frac{1}{2} \right), \quad 1.18$$

where w is the tunneling amplitude, Δ the superconducting order parameter, and μ denotes the chemical potential. As before, we set $L' = L - 1$ for open and $L' = L$ for periodic boundary conditions. In contrast to the SSH chain, H_{MC} violates the $U(1)$ symmetry due to the mean field pairing terms with $\Delta = e^{i\theta} |\Delta| \in \mathbb{C}$. A canonical transformation of the fermions $\hat{c}_i \equiv e^{i\theta/2} c_i$ can absorb the complex phase of Δ so that w.l.o.g. $\Delta \rightarrow |\Delta|$ can be taken as real and positive (we relabel $\hat{c}_i \rightarrow c_i$ in the following). For periodic boundary conditions, the Hamiltonian (1.18) becomes block-diagonal if expressed in terms of Fourier modes \tilde{c}_k :

$$H_{\text{MC}} = \frac{1}{2} \sum_{k \in \text{BZ}} \begin{bmatrix} \tilde{c}_k^\dagger & \tilde{c}_{-k} \end{bmatrix} \cdot \underbrace{\begin{bmatrix} -(2w \cos k + \mu) & -2|\Delta| \sin k \\ 2|\Delta| \sin k & (2w \cos k + \mu) \end{bmatrix}}_{h(k)} \cdot \begin{bmatrix} \tilde{c}_k \\ \tilde{c}_{-k}^\dagger \end{bmatrix}. \quad 1.19$$

The Bloch Hamiltonian $h(k)$ can again be expanded in Pauli matrices,

$$h(k) = -(2w \cos k + \mu) \sigma^z + 2|\Delta| \sin k \sigma^y = \mathbf{d}(k) \cdot \boldsymbol{\sigma} \quad 1.20$$

with the vector

$$\mathbf{d}(k) = \begin{bmatrix} 0 \\ 2|\Delta| \sin k \\ -(2w \cos k + \mu) \end{bmatrix}. \quad 1.21$$

The single-particle spectrum of H_{MC} is then given by³⁴

$$E(k) = |\mathbf{d}(k)| = \sqrt{(2w \cos k + \mu)^2 + 4|\Delta|^2 \sin^2 k} \quad 1.22$$

and we conclude that for $|\Delta| \neq 0$ the single-particle gap can vanish either at $k = 0$ or at $k = \pi$; this leads to $|\pm 2w + \mu| = 0$ and we find a gapless system for $2|w| = |\mu|$. Let $w, \mu \geq 0$ in the following. Then, the Majorana chain exhibits two gapped phases for $2w > \mu$ and $2w < \mu$, separated by a phase transition at $2w = \mu$. Moreover, if one sets $|\Delta| = w > 0$ and $\mu = 0$ or $|\Delta| = 0 = w$ and $\mu > 0$, the spectrum (1.22) becomes flat. All this sounds very familiar and suggests a relation to the SSH chain.

³⁴Note that the calculations are a bit more involved than for the SSH chain because the spinors of a BdG Hamiltonian live in an extended ‘‘Nambu-space’’ with an intrinsic particle-hole symmetry. This leads to an artificial doubling of the spectrum and is responsible for the factor $\frac{1}{2}$ in Eq. (1.19). The single-particle spectrum of H_{MC} then corresponds to the *positive* eigenvalues of the Bloch Hamiltonian, see Ref. [129] for detailed calculations.

EXAMPLES IN ONE DIMENSION

To make this relation explicit, we define *Majorana operators*

$$\gamma_{2i-1} \equiv c_i + c_i^\dagger \quad \text{and} \quad \gamma_{2i} \equiv i(c_i^\dagger - c_i) \quad 1.23$$

for $i = 1, \dots, L$. One checks easily that $\gamma_n^\dagger = \gamma_n$ and $\gamma_n^2 = \mathbb{1}$. They obey (up to normalization) fermionic anticommutation relations³⁵:

$$\{\gamma_n, \gamma_m\} = 2\delta_{n,m} \quad \text{for} \quad n, m = 1, \dots, 2L. \quad 1.24$$

According to (1.23), each “complex” fermion c_i can be decomposed into two real Majorana fermions: its “real part” γ_{2i-1} and its “imaginary part” γ_{2i} . Then

$$c_i = \frac{1}{2}(\gamma_{2i-1} + i\gamma_{2i}) \quad \text{and} \quad c_i^\dagger = \frac{1}{2}(\gamma_{2i-1} - i\gamma_{2i}) \quad 1.25$$

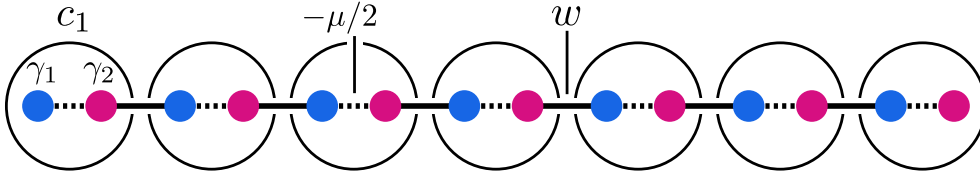
can be used to express H_{MC} in terms of Majorana fermions. We find

$$\begin{aligned} H_{\text{MC}} &= \frac{i}{2} \sum_{i=1}^{L'} [(|\Delta| + w) \gamma_{2i} \gamma_{2i+1} + (|\Delta| - w) \gamma_{2i-1} \gamma_{2i+2}] \\ &\quad - \frac{i}{2} \sum_{i=1}^L \mu \gamma_{2i-1} \gamma_{2i} \end{aligned} \quad 1.26$$

where the i is necessary for the Hermiticity of the Majorana pairs. The connection to the SSH chain becomes manifest for $|\Delta| = w$,

$$H_{\text{MC}} = -\frac{\mu}{2} \sum_{i=1}^L (i\gamma_{2i-1}\gamma_{2i}) + w \sum_{i=1}^{L'} (i\gamma_{2i}\gamma_{2i+1}) \quad 1.27$$

with the identification $-\mu/2 \leftrightarrow t$ and $w \leftrightarrow w$. And indeed, the critical point $|t| = |w|$ of the SSH chain translates into the critical point $2|w| = |\mu|$ of the Majorana chain. In this case, we can illustrate the couplings between Majorana modes as follows:



This parallels the figure of the SSH chain. Its physical interpretation is completely different, though: Here, each colored disc corresponds to “half” a fermion (a Majorana mode) and the black circles denote *single* fermion modes. A Majorana chain of length L has therefore L fermionic degrees of freedom, an SSH chain of the same length has $2L$.

³⁵These Majorana fermions are—as the term suggests—*fermionic* quasiparticles of superconductors [34]. They are not anyons.

INTRODUCTION

The vector $\mathbf{d}(k)$ in Eq. (1.21) can again be used to define a topological index via a winding number. One finds $\nu = 0$ in the phase with $2w < \mu$ and $\nu = 1$ for $2w > \mu$. The latter is therefore the topological phase of the Majorana chain. The crucial symmetry needed for this classification is the *intrinsic* particle-hole symmetry of Bogoliubov-de Gennes Hamiltonians. This symmetry does not impose restrictions on the many-body Hamiltonian H_{MC} but is a consequence of its description in an extended mode space of Nambu spinors $\Psi = [c_1, c_1^\dagger, \dots]^T$. The components of this spinor are not independent degrees of freedom but related via the fermion algebra. This leads to non-trivial constraints on the Bloch Hamiltonian that take the form of a particle-hole symmetry. This symmetry is qualitatively different from the particle-hole symmetry of the SSH chain as it cannot be broken as long as the system remains in the BdG class. This symmetry places the Majorana chain in class **D** of the tenfold way and defines a \mathbb{Z}_2 topological index in one dimension [85]. In addition, the Majorana chain is symmetric with respect to a (physical) time-reversal symmetry \mathcal{T} . In combination with the intrinsic particle-hole symmetry, this defines a (physical) sublattice symmetry that places the Majorana chain also in the class **BDI** with the same \mathbb{Z} topological index that applies to the SSH chain. Since the time-reversal symmetry *can* be broken, this classification is not as robust as the \mathbb{Z}_2 classification that only relies on the particle-hole symmetry³⁶. Here we shall not focus on the topological band structure and its associated topological indices but on the peculiar structure of the degenerate many-body ground states for open boundary conditions (the existence of which is—as for the SSH chain—dictated by the bulk-boundary correspondence and the non-zero topological index for $2w > \mu$).

The features we are interested in are most evident in the case of flat bands, i.e., for $w = |\Delta| > 0$ and $\mu = 0$ or $w = |\Delta| = 0$ and $\mu > 0$; these two points are also convenient to demonstrate the fundamentally different physics of Majorana and SSH chain (despite their mathematical similarities).

→ Let us start with the case $w = |\Delta| = 0$ and $\mu > 0$. The Hamiltonian reads

$$H_{\text{MC}} = -\frac{\mu}{2} \sum_{i=1}^L (i \gamma_{2i-1} \gamma_{2i}) = -\sum_{i=1}^L \mu \left(c_i^\dagger c_i - \frac{1}{2} \right). \quad 1.28$$

The ground state is even more trivial than its SSH counterpart: for $\mu > 0$, it is the Fock state where all microscopic fermion modes c_i are filled. For open boundary conditions there is no degeneracy and the ground state is unique (consistent with $\nu = 0$).

³⁶The difference between the \mathbb{Z}_2 classification of **D** and the \mathbb{Z} classification of **BDI** is not important for a single Majorana chain but becomes crucial for bundles of parallel Majorana chains: If time-reversal symmetry is not broken, these systems realize topological phases with $\nu > 1$.

EXAMPLES IN ONE DIMENSION

→ For $w = |\Delta| > 0$ and $\mu = 0$ the dimerization is such that the Majorana modes of *different* (physical) fermions form pairs:

$$H_{\text{MC}} = w \sum_{i=1}^{L'} (i \gamma_{2i} \gamma_{2i+1}) = w \sum_{i=1}^{L-1} (i \gamma_{2i} \gamma_{2i+1}). \quad 1.29$$

As a consequence of the shifted pairing, the edge Majorana modes $\gamma_l \equiv \gamma_1$ and $\gamma_r \equiv \gamma_{2L}$ do not appear in (1.29). This is completely analogous to the SSH chain. But there the edge modes were *fermions*—now they are “half” fermions. To appreciate the implications of this curiosity, we define new fermion modes as

$$\mathbf{c}_i \equiv \frac{1}{2}(\gamma_{2i} + i \gamma_{2i+1}) \quad \text{and} \quad \mathbf{c}_i^\dagger = \frac{1}{2}(\gamma_{2i} - i \gamma_{2i+1}) \quad 1.30$$

for $i = 1, \dots, L-1$. It is easy to check that the \mathbf{c}_i indeed form a fermion algebra: $\{\mathbf{c}_i, \mathbf{c}_j^\dagger\} = \delta_{ij}$. In these modes, the Hamiltonian (1.29) reads

$$H_{\text{MC}} = 2w \sum_{i=1}^{L-1} \left(\mathbf{c}_i^\dagger \mathbf{c}_i - \frac{1}{2} \right). \quad 1.31$$

Compared to the trivial case, Eq. (1.28), there seems to be one fermion mode missing. This missing mode is formed by the two Majorana modes that do not appear in the Hamiltonian:

$$\mathbf{e} \equiv \frac{1}{2}(\gamma_{2L} + i \gamma_1) \quad \text{and} \quad \mathbf{e}^\dagger = \frac{1}{2}(\gamma_{2L} - i \gamma_1). \quad 1.32$$

We call it “ \mathbf{e} ” for “edge.” The ground state of (1.31) is characterized by empty \mathbf{c}_i -modes (for $w > 0$), but the occupation of the \mathbf{e} -mode is not fixed since $[H_{\text{MC}}, \mathbf{e}] = 0$. The ground state $|\Omega_n\rangle$ can therefore be labeled by the edge occupation $n = \mathbf{e}^\dagger \mathbf{e}$ and is *two-fold* degenerate. This is in stark contrast to the SSH chain which had a *four-fold* degeneracy due to its fermionic edge modes; the Majorana chain features only a single fermionic mode that is *delocalized* between the two endpoints of the chain. This curiosity has profound implications:

Let us construct the two many-body ground states of (1.31) from the physical vacuum $|\mathbf{0}\rangle$ with $c_i |\mathbf{0}\rangle = 0$ for all $i = 1, \dots, L$. To this end, we define

$$|\Omega\rangle_L \equiv \prod_{i=1}^{L-1} \mathbf{c}_i |\mathbf{0}\rangle. \quad 1.33$$

If this state is normalizable (i.e., if $|\Omega\rangle_L \neq 0$), it is one of the ground states of H_{MC} (up to normalization). At this point, it is unclear how $|\Omega\rangle_L$ relates to $|\Omega_0\rangle$ and $|\Omega_1\rangle$. Let $\mathcal{P} = (-1)^N$ denote the fermion parity operator

INTRODUCTION

with $N = \sum_i c_i^\dagger c_i$. Then it follows that $\mathcal{P}|\Omega\rangle_L = (-1)^{L-1}|\Omega\rangle_L$ is a parity eigenstate. We claim that $|\Omega\rangle_L$ is (proportional to) the *equal-weight superposition*

$$|\alpha\rangle \equiv \sum_{\substack{\mathbf{n} \in \mathbb{Z}_2^L \text{ with} \\ (-1)^{|\mathbf{n}|} = \alpha}} |\mathbf{n}\rangle \equiv \sum_{\mathbf{n}(\alpha)} |\mathbf{n}\rangle \quad 1.34$$

of all fermion Fock states

$$|\mathbf{n}\rangle \equiv (c_1^\dagger)^{n_1} (c_2^\dagger)^{n_2} \dots (c_L^\dagger)^{n_L} |\mathbf{0}\rangle \quad 1.35$$

if one sets $\alpha = (-1)^{L-1}$. Here, $|\mathbf{n}| \equiv \sum_i n_i$ denotes the total number of fermions in the configuration $\mathbf{n} \in \mathbb{Z}_2^L$. The parity is therefore the defining property of this state and there is no other microscopic structure that characterizes it.

Proof. To prove this statement, we note that the quasiparticles \mathbf{c}_i can be written in terms of the original fermions c_i as

$$\mathbf{c}_i = \frac{i}{2} \left(c_i^\dagger - c_i + c_{i+1} + c_{i+1}^\dagger \right) \quad 1.36$$

and the edge mode reads

$$\mathbf{e} = \frac{i}{2} \left(c_L^\dagger - c_L + c_1 + c_1^\dagger \right). \quad 1.37$$

The proof is by induction: Let $L = 2$. Then indeed

$$|\Omega\rangle_2 = \mathbf{c}_1 |0, 0\rangle \propto |1, 0\rangle + |0, 1\rangle = |\alpha = -1\rangle \quad 1.38$$

and our claim is true for $L = 2$. Let us introduce the shorthand notation

$$|\mathbf{n}\rangle = |\mathbf{n}', n_{L-k+1}, \dots, n_{L-1}, n_L\rangle \quad 1.39$$

where we write only the last k components of \mathbf{n} explicitly. Now assume that our claim holds for some $L \geq 2$. Then we have for $L' = L + 1$ with $\alpha' = (-1)^{L'-1} = -(-1)^{L-1} = -\alpha$

$$|\Omega\rangle_{L+1} = \prod_{i=1}^L \mathbf{c}_i |\mathbf{0}\rangle = \mathbf{c}_L \prod_{i=1}^{L-1} \mathbf{c}_i |\mathbf{0}', 0\rangle \propto \mathbf{c}_L \sum_{\mathbf{n}'(\alpha)} |\mathbf{n}', 0\rangle, \quad 1.40$$

where we used the induction hypothesis for the last step. Write the occupation of the mode c_L explicitly and split the sum as follows:

$$\sum_{\mathbf{n}'(\alpha)} |\mathbf{n}', 0\rangle = \sum_{\mathbf{n}''(\alpha)} |\mathbf{n}'', 0, 0\rangle + \sum_{\mathbf{n}''(-\alpha)} |\mathbf{n}'', 1, 0\rangle. \quad 1.41$$

EXAMPLES IN ONE DIMENSION

Now we can use Eq. (1.36) to show

$$\begin{aligned}
 |\Omega\rangle_{L+1} \propto & \sum_{\mathbf{n}''(\alpha)} (c_L^\dagger + c_{L+1}^\dagger) |\mathbf{n}'', 0, 0\rangle \\
 & + \sum_{\mathbf{n}''(-\alpha)} (-c_L + c_{L+1}^\dagger) |\mathbf{n}'', 1, 0\rangle.
 \end{aligned} \tag{1.42}$$

Recall that $c_L^\dagger |\mathbf{n}'', 0, 0\rangle = \alpha |\mathbf{n}'', 1, 0\rangle$ but $c_L |\mathbf{n}'', 1, 0\rangle = (-\alpha) |\mathbf{n}'', 0, 0\rangle$ as there is one fermion less to commute with; therefore

$$\begin{aligned}
 |\Omega\rangle_{L+1} \propto & \sum_{\mathbf{n}''(\alpha)} [\alpha |\mathbf{n}'', 1, 0\rangle + \alpha |\mathbf{n}'', 0, 1\rangle] \\
 & + \sum_{\mathbf{n}''(-\alpha)} [\alpha |\mathbf{n}'', 0, 0\rangle + \alpha |\mathbf{n}'', 1, 1\rangle]
 \end{aligned} \tag{1.43}$$

which can be combined to ($\alpha' = -\alpha$ and $L' = L + 1$)

$$|\Omega\rangle_{L'} \propto \sum_{\mathbf{n}(\alpha')} |\mathbf{n}\rangle. \tag{1.44}$$

This concludes the proof. ■

Using similar arguments and keeping the fermion ordering (1.35) in mind, one can show that the edge mode \mathbf{e} acts on $|\Omega\rangle_L$ as follows:

$$\mathbf{e} |\Omega\rangle_L \propto \begin{cases} 0 & \text{for } L \text{ even} \\ |\alpha = -1\rangle & \text{for } L \text{ odd} \end{cases} \tag{1.45}$$

and similarly

$$\mathbf{e}^\dagger |\Omega\rangle_L \propto \begin{cases} |\alpha = +1\rangle & \text{for } L \text{ even} \\ 0 & \text{for } L \text{ odd}. \end{cases} \tag{1.46}$$

The gist of these results is that, independent of L , the many-body ground state $|\Omega_0\rangle$ of the Majorana chain with *empty* edge mode is the equal-weight superposition of all fermion configurations with *odd* parity: $|\Omega_0\rangle = |\alpha = -1\rangle$. Conversely, the ground state $|\Omega_1\rangle$ with occupied edge mode is given by the equal-weight superposition with *even* parity: $|\Omega_0\rangle = |\alpha = +1\rangle$. Thus the two degenerate ground states differ only in the total fermion parity. *Locally*, they are completely featureless and look the same; only a *global* parity measurement with \mathcal{P} or $\mathbf{e}^\dagger \mathbf{e}$ can distinguish them. This is the many-body manifestation of the topologically protected degeneracy for open boundary conditions.

It is instructive to compare these results with the SSH chain. Recall that the degeneracy of the edge modes in the topological phase is dictated by the bulk-boundary correspondence which, in turn, requires specific protecting symmetries

INTRODUCTION

to be robust. This implies that local perturbations cannot gap out the edge modes unless they break the protecting symmetry. Consider the two degenerate ground states $|0, 0\rangle$ and $|1, 0\rangle$ of the SSH chain; they differ by the occupation of the left edge mode a_1 (and also by their global parity). If we perturb the Hamiltonian H_{SSH} with the local chemical potential $n_l = a_1^\dagger a_1$, their degeneracy is immediately lifted since the *local* observable n_l can distinguish the two states. This is completely consistent with our previous findings because n_l *violates* the sublattice symmetry \mathcal{S} . By contrast, to lift the degeneracy of $|\Omega_0\rangle$ and $|\Omega_1\rangle$ in the Majorana chain, H_{MC} must be perturbed by $n = \mathbf{e}^\dagger \mathbf{e}$. This operator does not violate the protecting particle-hole symmetry³⁷; instead, it is highly *non-local* and therefore not an admissible perturbation of the Hamiltonian in the first place.

These arguments suggest that the two-fold degeneracy of the Majorana chain is qualitatively different from the four-fold degeneracy of the SSH chain. Indeed, the degeneracy of the former is robust to *any* local perturbation whereas the latter requires the protecting sublattice symmetry (which can be broken by physical terms). Therefore the SSH chain is indeed a symmetry-protected topological phase—but the non-trivial phase of the Majorana chain is actually *topologically ordered* in that it requires no symmetry protection at all [22, 34].

Here we discussed only the topological degeneracy of the Majorana chain. We omitted several interesting features regarding the *braiding* of its edge modes [130]. We briefly comment on these features in Subsection 1.3.1 where the Majorana chain appears as primitive for topological quantum computing. Details on the relation of Majorana fermions and non-abelian braiding can be found in \clubsuit Subsection 2.D.1.

Concluding Remark — The statement that the Majorana chain does not require any symmetry is subtle. To see this, one can check that the Majorana edge modes $\gamma_l = \gamma_1$ and $\gamma_r = \gamma_{2L}$ act on the ground states as follows:

$$\gamma_l |\alpha\rangle = |-\alpha\rangle \quad \text{and} \quad \gamma_r |\alpha\rangle = i\alpha |-\alpha\rangle. \quad 1.47$$

Since these operators are Hermitian and can be constructed from local fermion modes, we could add them to the Hamiltonian as a perturbation, e.g., $\tilde{H}_{\text{MC}} = H_{\text{MC}} + \gamma_l$. This perturbation lifts the degeneracy such that the ground state of \tilde{H}_{MC} is unique, namely $|+1\rangle - |-1\rangle$. This is not surprising as γ_l *violates* the fermion parity symmetry $\mathbb{Z}_2^f = \{\mathbb{1}, \mathcal{P}\}$. So the Majorana chain *is* protected by a symmetry after all: fermion parity. In the literature, however, this symmetry is often not counted as a real symmetry but as an implicit feature of fermionic Hamiltonians (for instance, quadratic Hamiltonians automatically commute with \mathcal{P}). This makes sense for the following reason:

³⁷As mentioned above, this symmetry is intrinsic to the BdG Hamiltonian and cannot be violated on the operator level.

Assume that the Hermitian (and unitary) operators γ_l and γ_r are admissible observables of the theory. Make the length L of the chain large and assume that Alice can measure $\gamma_l = c_1 + c_1^\dagger$ on the left endpoint while Bob can apply the unitary gate $\gamma_r = i(c_L^\dagger - c_L)$ on the right endpoint. Define the basis $|x\rangle \equiv | +1\rangle + (-1)^x | -1\rangle$ and let the system be initialized in the symmetric state $|x = 0\rangle$ so that Alice measures $+1$ with certainty. Now Bob can send Alice a classical bit $x \in \mathbb{Z}_2$ of information by flipping or not flipping this state with γ_r :

$$(\gamma_r)^x |0\rangle \propto \begin{cases} |0\rangle & \text{for } x = 0 \\ |1\rangle & \text{for } x = 1. \end{cases} \quad 1.48$$

This clearly violates causality since the bit x can be transmitted instantaneously over arbitrary distances L ; this is really a “spooky action at a distance” and should not be possible with *local* measurements and operations. Therefore γ_l and γ_r are actually *non-local* operators, despite their local appearance in terms of fermion modes! The reason is that fermions are intrinsically non-local objects due to their statistics, and this non-locality becomes relevant for operators that violate fermion parity. The upshot is that the parity symmetry required for the Majorana chain (or any other fermion Hamiltonian) is a logical consequence of *locality*—and not an additional symmetry constraint.

One application of the Majorana chain—as topological quantum memory—is discussed in Chapter 4. In Chapter 2, we study a one-dimensional system of interacting fermions and argue that it plays the role of a particle number conserving relative of the mean field Majorana chain. In Chapter 3, we use the Majorana chain as blueprint for the construction of bosonic networks geared towards transfer of quantum information.

1.3 Applications & Experiments

In Section 1.1, we already mentioned a few experimental breakthroughs that established some of the paradigmatic models in the field of topological quantum matter as valid descriptions of real world materials. From the perspective of “pure” condensed matter physics the pivotal question is: *Which quantum phases are conceivable?* This is what the classification schemes attempt to answer.

However, the overarching theme of this thesis is the application of topological matter for the purpose of quantum information processing. We do not extend the classification but use it as a tool to identify systems of interest. Thus we ask the more mundane question: *What can we do with these states of matter?* After all, possible applications have been the predominant driving force of the field in recent years.

These applications fall into two categories, depending on whether they depend on quantum phenomena or can be described by purely classical means. That *classical* applications exist at all may be surprising at first sight (given the fact that all our discussions so far were concerned with *quantum* phases). The explanation is subtle but important: There are (at least) two distinct notions of “topology” that play a role in the classification of quantum phases:

- 1 *Topologically ordered* states of matter are long-range entangled quantum phases with a low-energy physics that is described by topological quantum field theories (i.e., quantum field theories with topological terms in their action—this is where *topology* enters the stage). These systems exhibit typically anyonic bulk excitations and stable ground state degeneracies on closed manifolds with handles (but not necessarily gapless edge modes on manifolds with boundaries). Examples are fractional quantum Hall states and some quantum spin liquids. Since these states are characterized by their long-range entanglement (which is a necessary ingredient for both the existence of anyons and topological ground state degeneracies), topological order is a phenomenon that is *inherently quantum*—with no classical counterpart.
- 2 The topological insulators and superconductors classified by the tenfold way are *not* topologically ordered but symmetry-protected topological phases³⁸. They are labeled by topological invariants (this is where *topology* comes into play) that are defined by single-particle Hamiltonians; thus it is the topology of *band structures* (in the mathematical sense of fiber bundles [101]) that makes them “topological.” This is very different from the entanglement-based notion of topology in that band structures are *not* tied to quantum systems. In fact, many classical systems (such as metamaterials) can be described by these mathematical objects as well and are thereby affected by their topological properties. This explains how classical applications come about but gives rise to another subtlety: In *quantum* systems, the Pauli exclusion principle allows for the construction of many-body ground states from band structures by filling them with non-interacting fermions. These many-body ground states define *quantum phases* in the thermodynamic limit which—for topological bands—are referred to as “topological phases.” In *classical* systems, however, band structures typically describe the *dynamics* of coupled degrees of freedom in terms of eigenmodes, and not (thermal) phases that one might call “topological.”

In the following, we provide a brief survey of proposed and—in some cases—even realized applications of topological states of matter both in quantum and classical systems. Note that this survey is by no means exhaustive.

³⁸Up to some subtleties, see Footnote 15.

1.3.1 Quantum Systems

→ The most prominent, most cited, but also most elusive application of topological states of matter is known as *topological quantum computation (TQC)* [45, 131, 132], see Ref. [47] for a review of this mathematically sophisticated concept. Despite its mathematical depth, the rationale of TQC is easy to understand: Topologically ordered phases host localized bulk excitations, called *anyons*, that obey neither bosonic nor fermionic statistics (this is true up to some subtleties, see Footnotes 8 and 15). Anyons come in two flavors: *abelian* and *non-abelian*. Exchanging abelian anyons results in a global phase that depends only on the topology of their world lines but not their geometric shape—a feature that makes these phases exceptionally robust. Phases, however, are not enough for a full-fledged quantum computer where unitary gates must be applied to a degenerate state space of logical qubits. Here non-abelian anyons excel due to a peculiar feature: Imagine a state with a well-defined pattern of anyons. If (and only if) the anyons are *non-abelian*, there are *multiple* orthogonal quantum states that give rise to this pattern. It is the superpositions of these states that realize the logical qubits of a topological quantum computer. Measurements on these states can be performed by bringing two anyons together (called *fusion*) and observing the anyon they form as a compound³⁹. Unitary gates can be applied by winding anyons in intricate patterns around each other, terminating with the initial pattern (called *braiding*). Since, for non-abelian anyons, this pattern corresponds to a degenerate subspace, braiding can give rise to unitary operations on the latter. Just as the phases for abelian anyons, these unitaries are completely determined by the world line topology⁴⁰ of the braiding procedure. They realize the unitary gate sequences of a topological quantum computer in an inherently robust and decoherence-free manner.

Given the fact that decoherence is the nemesis of quantum information processing, the prospect of topological quantum computation ignited a hunt for materials with topological order and non-abelian anyons. Luckily, the first family of candidates had already been observed in the laboratory when TQC was invented: fractional quantum Hall states [27–29]. Whereas the first state discovered at filling fraction $\nu = 1/3$ is presumably described by a so called *Laughlin wave function* with abelian excitations [36], the state with filling fraction $\nu = 5/2$ observed a few years later [29] is believed to be described by a *Moore-Read wave function* which supports non-abelian *Ising anyons* [38]. Although the unitaries that can be implemented by braiding Ising anyons are not sufficient for universal quantum computation, there are specific proposals to use the $\nu = 5/2$ state as substrate for TQC [133, 134].

³⁹It can happen that two anyons annihilate; formally this is described as a “trivial anyon” or the *vacuum*.

⁴⁰How word lines “tangle” in the $2 + 1$ -dimensional spacetime of the system.

Even more interesting is the experimentally observed state at filling fraction $\nu = 12/5$ [135] which might realize a non-abelian *Read-Rezayi state* [136]. In contrast to Ising anyons, this state facilitates a universal set of unitary gates by braiding. While the existence of these fractional quantum Hall states is undeniable, the theoretically predicted non-abelian braiding statistics of their excitations is experimentally hard to verify. At the time of writing, the fractional charge of quasiparticles at filling $\nu = 1/3$ has been experimentally verified [137–139], and similar result were later obtained for the $\nu = 5/2$ state [140–142]. While these results are consistent with theoretical predictions, the smoking gun—non-abelian statistics—requires sophisticated interference experiments [143, 144].

The non-abelian Ising anyons of the $\nu = 5/2$ Moore-Read state are also predicted for rather different systems, namely chiral $p_x + ip_y$ *superconductors* where Majorana zero modes are bound to vortices [79, 83]; by now, there are various theoretical proposals to realize this physics on different platforms, e.g. Refs. [145–148]. Later it has been argued that very similar physics can be realized on the surface of three-dimensional topological insulators [149] and in even simpler semiconductor heterostructures [150, 151]. Recent experimental evidence indeed supports the presence of Majorana bound states in vortices of certain superconductors [152–154].

An alternative, experimentally more accessible way to non-abelian Ising anyons has been paved by Kitaev who pointed out that unpaired Majorana zero modes can appear at the endpoints of one-dimensional p -wave superconductors [82] (Subsection 1.2.2). Although “braiding” of point-like particles is only well-defined in *two* spatial dimensions in a strict sense (because only in $3 = 2 + 1$ spacetime dimensions one-dimensional world lines can be non-trivially knotted), the non-abelian braiding statistics of Ising anyons⁴¹ can be recovered in *networks* of one-dimensional quantum wires [130], a scheme that may be simplified even further in Floquet settings [157, 158]. The anticipated observation of Majorana bound states at the endpoints of quantum wires has been driving experimental solid-state physics in recent years, ever since it has been realized that spin-orbit coupling in semiconductor quantum wires that are proximity-coupled to conventional s -wave superconductors might do the trick [159, 160]. Shortly after, first experimental evidence of Majorana bound states has been reported [161], strengthened by subsequent experiments, see Ref. [162] and references therein.

⁴¹In a strict sense, the endpoints give rise to a *projective* representation of Ising anyons, i.e., they are Ising anyons “up to phases.” The reason is that Majorana zero modes bound to the endpoints of quantum wires are *not* intrinsic excitations of the system (like anyons in fractional quantum Hall states) but extrinsic deformations of the Hamiltonian (they are *defects*). This is also the case for vortices in $p_x + ip_y$ superconductors when the gauge field is static. In both cases, only the “non-abelian part” of Ising anyons can be recovered; the collected abelian phase (which is fixed for Ising anyons due to algebraic constraints [24]) is non-universal and depends on the braiding procedure [155, 156].

So far, only systems with fermionic constituents played a role. This is not necessary, though: In 2005, Kitaev introduced a spin- $\frac{1}{2}$ model on the honeycomb lattice with strong frustration due to anisotropic spin-spin interactions that prevent magnetic ordering [24]. Its ground states are examples of *spin liquids* and accessible analytically by a formal mapping to free fermions. The Kitaev honeycomb model features two phases: one is gapped and hosts abelian anyons akin to the toric code (see below), the other is gapless but becomes gapped in a magnetic field where it hosts non-abelian Ising anyons. This phase is sometimes referred to as *Kitaev spin liquid* and the search for “Kitaev materials” that realize this state of matter picked up pace after a mechanism had been found that might give rise to the required anisotropic spin-spin interactions in certain crystalline compounds with a planar honeycomb structure [163,164] (these compounds belong to the diverse family of *iridates*). At the time of writing, no Kitaev spin liquid states have been identified in experiments although evidence for anisotropic interactions has been reported [165] (see Ref. [166] for a review on iridates). Recently, other materials have been identified that are conjectured to be in (or close to) a Kitaev spin liquid phase with experimental results that are predicted by the Kitaev honeycomb model [167,168]. We refer the reader to Refs. [26,169,170] for broad reviews on the diverse field of spin liquids and to Ref. [171] for a dedicated review on Kitaev materials.

In Chapter 2, we study the properties of a one-dimensional symmetry-protected topological phase of interacting fermions and demonstrate that braiding implements unitary gates on the ground states.

- Scalable quantum computation does not only require tools for manipulating qubits but also for storing them reliably in the presence of noise. The idea behind *topological quantum memories* is to leverage the robust degeneracy of topologically ordered media on manifolds with handles (or tailored boundaries) to encode qubits. These qubits are naturally protected from decoherence because topological degeneracies cannot be lifted by local perturbations. Topological quantum memories are conceptually simpler than topological quantum *computers* since abelian phases suffice for the former but not for the latter. The most prominent model of this kind is Kitaev’s *toric code*⁴² [45], but alternatives are also explored [172,173]. The toric code can be realized by placing qubits/spins on the edges of a two-dimensional square lattice with toroidal geometry (i.e., periodic boundary conditions) and encodes two protected qubits non-locally. A similar but technically more accessible approach uses planar patches of the square lattice with appropriately chosen boundaries (then referred to as *surface code*). For comprehensive reviews on topological quantum memories see Refs. [50,174].

⁴²Here, “code” is a fancy name for a linear subspace of the Hilbert space to which the condensed matter physicist would refer as “ground state space.”

Surface codes are one of the most promising candidates for feasible quantum memories due to their high error threshold and the comparatively simple, local operations needed to perform error correction (essentially four-qubit parity measurements). This explains why the preparation and control of surface code states has been a driving force of experimental efforts in recent years: First minimal instances were realized with photons [175, 176], quickly followed by solid-state platforms with superconducting circuits [177–181]; see Ref. [182] for a review of this promising and rapidly evolving field. Encouraged by these experimental achievements, various scalable implementations of surface codes (and its relatives) in solid-state systems have been contrived, e.g. [183–187]. Note that the toolkits provided by ultracold atoms [188, 189] and trapped ions [190] open alternative routes to reach these goals.

In Chapter 4, we study a strategy to store quantum information reliably in the ground state space of a one-dimensional topological superconductor.

- There are three pivotal tasks that must be solved before we can construct scalable quantum computers: the reliable *transformation*, *storage*, and *transport* of quantum information. For the first two we already discussed possible approaches that leverage the peculiar features of topological quantum matter. What about transport?

An outstanding feature of many two-dimensional topological phases is the existence of stable, gapless boundary modes that are immune to scattering from impurities (either due to the *breaking* of time-reversal symmetry, as in quantum Hall states, or *protection* by time-reversal symmetry, as in topological insulators). It has been proposed to employ these scattering-free channels for the coherent transfer of quantized excitations (and thereby quantum information) in chiral spin liquids [191] and bosonic counterparts of quantum Hall systems [192]. However, the implementation of these concepts is experimentally challenging; useful tools are provided by platforms with ultracold atoms [193] and topological photonics [194, 195] (see below). In experiments, chiral edge states in synthetic matter have been reported for bosonic and fermionic ultracold atoms using artificial gauge fields [196, 197], and an implementation of the Haldane model with ultracold fermions [198] demonstrates that quantum phases with topological bands and chiral edge modes can be engineered in systems that allow for exceptional control of their constituents.

In Chapter 3, we study the capabilities of a one-dimensional network of bosonic modes (derived from a one-dimensional topological insulator) to transfer quantum information.

1.3.2 Classical Systems

- Mechanical metamaterials are artificially designed structures of mechanical degrees of freedom (e.g. oscillators) that are coupled such that their macroscopic, collective degrees of freedom display interesting and/or useful properties. They are described by Newton’s equations of motion, a system of ordinary differential equations where the connectivity of the elementary degrees of freedom is naturally encoded in a matrix [199]. This matrix provides the connection to topological band theory and allows for classical analogs of quantum mechanical models that are described by *single-particle Hamiltonians*.

The field was pioneered by Kane and Lubensky who studied mechanical constructs called *isostatic lattices* [200]. Some of these systems exhibit curiously robust zero-frequency modes at boundaries (“floppy modes”). Indeed, it can be shown that this robustness is a consequence of topologically non-trivial bands and the bulk-boundary correspondence [200]. By now, topological “floppy modes” have been applied in several ways, e.g., for Origami folding [201]. While zero-frequency “floppy modes” can influence the low-energy response of a mechanical system, topologically protected, chiral edge modes with non-zero frequency allow for robust and scattering-free excitations—a useful feature for information and/or energy transmission. This has been demonstrated experimentally by mechanical analogs of the time-reversal *breaking* Chern insulator [202] (realized as a gyroscopic phononic crystal [203]) and the time-reversal *protected* quantum spin Hall insulator [204]. Both setups allow for scattering-free transport along their edges, a feature that suggests technological applications [205]. Recently, even higher-order topological insulators with protected *corner modes* have been implemented with mechanical metamaterials [206]. For a pedagogical review of the emerging field of “topological mechanics” see Ref. [199]. Finally, we note that the related field of “topological acoustics” [207] follows the same rationale to transmit sound waves through robust, scattering-free channels; see, e.g., Ref. [208] for the experimental demonstration of an “acoustic Chern insulator.”

- Topological mechanics and acoustics are facets of a more general principle: Any theory that exhibits wave-like excitations can, in principle, be affected by non-trivial band topology and its associated phenomena—and *classical electrodynamics* is no exception. This particular incarnation of topological band theory is known as “topological photonics” [195] and was kick-started by Haldane and Raghu [209, 210] who proposed a classical analog of the Chern insulator for photonic crystals. Similar to topological mechanics—and contrary to the “quantum applications” in Subsection 1.3.1—experimental results followed soon after: Using magneto-optical photonic crystals, Wang *et al.* demonstrated the appearance of time-reversal breaking, chiral edge modes

for microwaves [211], results that were transferred to the optical regime by Rechtsman *et al.* without magnetic fields in a Floquet setting [212]. At the same time, symmetry-protected analogs of topological insulators were presented in a silicon-based lattice of photonic resonators [213]. See Ref. [195] for a review of platforms used for the implementation of topological photonic circuits.

It is worthwhile to note that the scope of topological photonics extends beyond microwaves into the radio-frequency regime where circuits composed of lumped elements (inductors, capacitors, etc.) can be tailored to exhibit symmetry-protected edge modes [214]. The ensuing concept of “topoelectrical circuits” [215] is one of the cheapest and most accessible routes to explore topological phenomena with table-top experiments, an approach that seems particularly suited for lab courses [216]. Finally, we note that higher-order topological insulators have already been experimentally realized both in the microwave regime [217] and with “topoelectrical circuits” [218].

- Topological photonics provides us with scattering-free waveguides on the boundary of topological metamaterials. Adding gain and loss into the mix, one arrives at the intriguing concept of “topological insulator lasers” [219] where the chiral edge mode serves as a cavity for efficient single-mode lasing. And indeed, lasing in the topological edge modes of arrays of coupled resonators has already been observed experimentally [220, 221].
- Last but not least, we stress that the link between robust boundary physics and topologically non-trivial bulk properties is neither restricted to artificial nor to *small* systems: Recently it has been realized that the fluid dynamics on the surface of rotating spheres exhibits robust, chiral modes that are trapped at the equator and protected by non-zero Chern numbers⁴³ [222]. These modes have long been known to influence Earth’s atmospheric and oceanic flow systems. Thanks to findings in an entirely different field of science—condensed matter physics—we now have a mathematically satisfying and elegant explanation for their existence.

⁴³A consequence of the Coriolis force which breaks time-reversal symmetry and vanishes at the equator, effectively creating a boundary that separates the two hemispheres.

2

Majorana-Like Edge States in a Number-Conserving Theory

*“The prosaic fact of the universe’s existence alone
defeats both the pragmatist and the romantic.”*

— STEPHEN KING
in The Dark Tower: The Gunslinger

In this chapter, we study a microscopic model of interacting fermions with topologically protected ground state degeneracy. The model, introduced in Ref. [1], is based on a double-wire setup with local interactions in a number-conserving setting. A compelling property of this model is the exact solvability for its ground states and low-energy excitations. We demonstrate the appearance of topologically protected edge states and derive their braiding properties on a microscopic level. We find the non-abelian statistics of Ising anyons which can be interpreted as Majorana-like edge states. As a result, the model qualifies as a number-conserving relative of Kitaev’s paradigmatic Majorana chain.

This page is intentionally left blank.

The very purpose of a personal computer is to manipulate data. And the fact that there *are* personal computers already tells us that this cannot be too hard. Indeed, manipulating classical information (*bits*) is rather straightforward with electronic circuitry once controllable “switches” can be integrated in vast amounts. In classical computers, they are realized as *transistors* that are lithographically etched into a silicon slab; two of them are enough to implement basic logic gates (AND, OR, NAND, ...), and there are more than a billion of them in modern processors. Apparently the underlying physical mechanisms scale well, and this makes the manipulation of *classical* information cheap (from both economical and technological perspective).

Manipulating *quantum* information is not. The controlled manipulation of quantum bits (*qubits*) poses a formidable technological challenge since “manipulation” always entails the coupling of the information carrier (e.g., a single atom) to a typically much larger system that performs the operation (e.g., a laser). But nature makes no distinction between a “useful” system that controls a qubit and the rest of the world (viz. the environment). Uncontrolled environmental couplings are the nemesis of scalable quantum information processing as they accompany operations on qubits quite naturally. The study of concepts that decouple the environment without detrimental effects on controllability is therefore a major topic of research. The most promising solution is referred to as *topological quantum computation (TQC)*—so far, an entirely theoretical proposal with only few proof-of-principle experiments that focus on partial aspects of the concept.

The roots of TQC go deep, all the way down to *category theory*, a mathematical discipline of great beauty, sometimes affectionately referred to as *general abstract nonsense*. Fortunately, category theory is not needed to grasp the essence of TQC: The idea is to encode quantum information into degenerate states of two-dimensional physical systems (e.g., spins on a lattice) that are *topologically ordered*. This means that the degeneracy is robust against local perturbations and the stored qubits are completely delocalized. But delocalized qubits decouple from the environment because the latter acts *locally* on the system. This solves the problem of “unwanted” operations on the qubit, that is, *decoherence*.

What about controlled manipulations? Here another property of topologically ordered systems comes to the rescue: The delocalization of qubits is accompanied by a pattern of long-range entanglement that can endow localized excitations with a permutation statistics⁴⁴ that is neither fermionic nor bosonic—they are *anyons*. Some have the peculiar property that a given configuration of well-separated anyons corresponds to more than one quantum state (such anyons are called *non-abelian*). This defines the required degenerate subspace in which quantum information can be encoded reliably. The key to TQC is that unitary operations on this subspace can be realized by winding anyons around each other, a dynamical process that returns to the initial anyon configuration; this is called *braiding*. These unitaries

⁴⁴To be more precise, in two dimensions particles are *braided*, not *permuted*. In three and more dimensions, this is the same because the world lines of particles cannot be tangled in a spacetime of four dimensions and more.

are “discrete” in that they depend only on the *topology* of the anyon world lines (how they are “tangled” in spacetime) but not on their *geometry* (their shape). Since uncorrelated noise can only nudge anyons locally, it might deform the *shape* of their trajectories but not their *topology* (as long as the anyons remain far apart when braided). This scheme facilitates the controlled manipulation of qubits without making them susceptible to environmental noise. It is one of the most elegant concepts for scalable quantum computation—but also the most demanding in terms of technological requirements, most of which are far beyond current capabilities.

Thus, whether or not a topological quantum computer truly can be built is unclear. All the more important is the exploration of systems that might host topological phases and allow for braiding of anyons. One-dimensional p -wave superconductors have been identified as a promising framework that features all the needed key mechanisms if generalized appropriately. The *Majorana chain*, discussed in Subsection 1.2.2, is the prime example which, if extended to networks, allows for the braiding of particles known as *Ising anyons*⁴⁵ (which are non-abelian). Here, “particles” refers to the endpoints of one-dimensional chains that carry “half” a fermion each (a *Majorana mode*). Braiding them generates robust unitaries on qubits encoded in the degenerate ground state space of the network. Although these unitaries do not cover all transformations needed for *universal* quantum computation, they still are useful building blocks for fault-tolerant quantum operations.

The popularity of the Majorana chain (and its derivatives) is partly rooted in its analytical accessibility: as quadratic theory of *non-interacting* fermions, all its physical quantities can be computed efficiently and the topological features are not obfuscated by the clutter of many-body physics. This simplicity, however, is consequence of a mean field approximation, the validity of which is not guaranteed for closed systems with a well-defined number of particles (a property met in cold atom settings).

In this chapter, we introduce and study a *number-conserving* model that features many of the peculiar properties of a topological phase. Most notably, we will show that its chain endpoints behave like Ising anyons—a property that makes it a number-conserving cousin of the Majorana chain and potentially useful for topological quantum computation.

Our model is defined on an open *double-chain* of spinless fermions a_i (upper subchain) and b_i (lower subchain) of length L , Figure 2.1 (a). The Hamiltonian

$$H = H^a + H^b + H^{ab} \tag{2.1}$$

combines *intra-chain* contributions H^x ($x = a, b$) with *inter-chain* couplings H^{ab} , Figure 2.1 (b). The intra-chain Hamiltonian takes the form

$$H^x = \sum_{i=1}^{L-1} A_i^x (\mathbb{1} + A_i^x) \tag{2.2}$$

⁴⁵This statement is only true “up to phases,” see Footnote 41.

IN A NUTSHELL

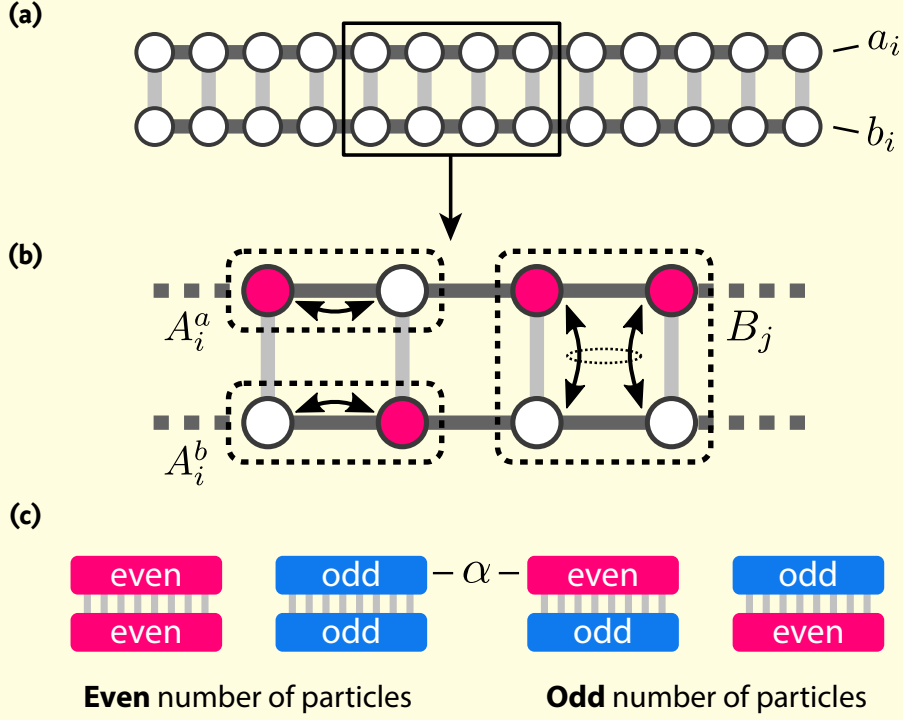


FIGURE 2.1 • Setup & ground states. (a) We consider a double-chain of length L with open boundary conditions and spinless fermions a_i and b_i living on the sites. (b) The number-conserving Hamiltonian is given by intra-chain terms A_i^x ($x = a, b$) that describe single-particle hopping as well as density-density interactions, and the inter-chain couplings B_j that encode correlated pair hopping together with four-fermion density-density interactions. (c) For a fixed number of particles, there are two degenerate zero-energy ground states, characterized by their (upper) subchain parity α .

with the single-particle hopping terms

$$A_i^a = a_i a_{i+1}^\dagger + a_{i+1} a_i^\dagger \quad \text{and} \quad A_i^b = b_i b_{i+1}^\dagger + b_{i+1} b_i^\dagger. \quad 2.3$$

H^x combines single-particle hopping with a nearest-neighbor attraction on each chain separately. The inter-chain interaction H^{ab} takes a similar form,

$$H^{ab} = \sum_{i=1}^{L-1} B_i (\mathbb{1} + B_i), \quad 2.4$$

with the pair hopping between the two chains

$$B_i = a_i^\dagger a_{i+1}^\dagger b_i b_{i+1} + b_i^\dagger b_{i+1}^\dagger a_i a_{i+1}. \quad 2.5$$

H^{ab} describes correlated *pair* hopping and four-fermion density-density interactions between the chains. The Hamiltonian H conserves the total number of particles N such that the filling $\rho = N/2L$ is the only free parameter of the model. It

also features two additional symmetries: The *subchain parity* P_x for $x = a, b$, and *time-reversal symmetry* T . The former follows since H^{ab} exchanges only fermion *pairs* between the chain while the latter is a consequence of the real-valued hopping amplitudes and the absence of spin. Since $P_a P_b = (-1)^N$ relates the two subchain parities to the total number of fermions, one can chose $\alpha \equiv P_a$ and N to label subspaces \mathcal{H}_α^N of the Hilbert space that are not coupled by H .

We can make use of this restriction and the form of H^x and H^{ab} to derive the (unique) ground state $|N, \alpha\rangle$ in each sector \mathcal{H}_α^N *exactly*. This is possible because the interactions in terms like $B_i(\mathbb{1} + B_i)$ make H a positive semi-definite⁴⁶ operator. The ground states $|N, \alpha\rangle$ are zero-energy eigenstates of H and their structure is amazingly simple: Given $0 \leq N \leq 2L$ and $\alpha = \pm 1$, add up all states that describe fermion configurations on the double-chain with N fermions in total and subchain parity $P_a = \alpha$; up to normalization, this is $|N, \alpha\rangle$. Note that for a fixed particle number N , $\mathcal{H}_{+1}^N \oplus \mathcal{H}_{-1}^N$ is the Hilbert space of accessible states. This includes the degenerate zero-energy subspace of states $|\Psi\rangle = \psi_+|N, +1\rangle + \psi_-|N, -1\rangle$ which can be used to store a qubit reliably (under which conditions this is true will be discussed in detail), see Figure 2.1 (c).

Due to the structural simplicity of the states $|N, \alpha\rangle$, the evaluation of correlators and overlaps reduces to combinatorial expressions that can be computed efficiently. For instance, fermion pair correlations become constant and do not vanish in the limit $L \rightarrow \infty$ for fixed filling $0 < \rho < 1$,

$$|\langle x_i^\dagger x_{i+1}^\dagger y_j y_{j+1} \rangle| \rightarrow \rho^2 (1 - \rho)^2 \quad \text{for } i \neq j; x, y \in \{a, b\}; \quad 2.6$$

this indicates a condensate of p -wave pairs with true long-range order.

The intra-chain single-particle correlations $\langle a_i^\dagger a_j \rangle$ (the Green's function) can also be computed straightforwardly. They decay exponentially in the bulk,

$$\langle a_i^\dagger a_j \rangle = e^{-\gamma(\rho)|i-j|} \quad \text{for } 1 \ll i, j \ll L, \quad 2.7$$

where γ is some function of the filling with $\gamma(0.5) = \infty$. Interestingly, there is a revival at the endpoints of the chain independent of their distance,

$$|\langle a_1^\dagger a_L \rangle| \rightarrow \rho(1 - \rho) > 0, \quad 2.8$$

that heralds exponentially localized *edge states* with perfect localization at half-filling $\rho = 0.5$, Figure 2.2 (a). Less formally: There is something special about the endpoints of the chains.

Their importance is confirmed if we focus on overlaps $\langle N, -\alpha | \mathcal{O}_j^\phi | N, \alpha \rangle$ instead of correlations. Here, $\mathcal{O}_j^\phi = e^{i\phi} a_j^\dagger b_j + e^{-i\phi} b_j^\dagger a_j$ describes single-particle hopping *between* the chains; it violates subchain parity (and time-reversal symmetry if ϕ is not a multiple of π). One can think of \mathcal{O}_j^ϕ either as perturbations of H or as intended couplings that realize the “fusion” of two chain endpoints. In any case,

⁴⁶I.e., all its eigenvalues are non-negative.

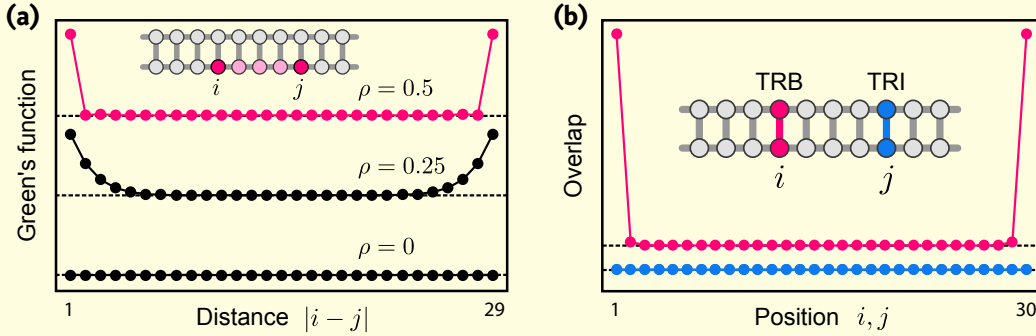


FIGURE 2.2 • Ground state properties. (a) Intra-chain single-particle correlation $\langle a_i^\dagger a_j \rangle$ (Green's function) as a function of the distance $|i - j|$ on a chain of length $L = 30$ (here for $i = 1$ and j running). The revival for $|i - j| \sim L$ indicates exponentially localized edge states. The correlation length depends on the filling ρ . (b) Overlap of the ground states $|N, \pm 1\rangle$ for time-reversal invariant (TRI) and time-reversal breaking (TRB) single-particle hopping $\mathcal{O}_{i,j}^\phi$ ($\phi = 0, \frac{\pi}{2}$) in dependence of the position i, j at half-filling $\rho = 0.5$. Note that time-reversal invariant single-particle hopping does not create overlaps between the ground states, and time-reversal *breaking* hopping does so only close to the endpoints.

a finite overlap $\langle N, -\alpha | \mathcal{O}_j^\phi | N, \alpha \rangle \neq 0$ would lift the two-fold degeneracy of the ground state space. Let us focus on the time-reversal invariant/breaking (TRI/TRB) couplings for $\phi = 0$ and $\phi = \frac{\pi}{2}$, respectively; one finds

$$\text{TRI} : \quad \langle N, -\alpha | \mathcal{O}_\delta^0 | N, \alpha \rangle \rightarrow 0 \quad 2.9a$$

$$\text{TRB} : \quad \langle N, -\alpha | \mathcal{O}_\delta^{\frac{\pi}{2}} | N, \alpha \rangle \rightarrow e^{-\mu(\rho)\delta} \quad 2.9b$$

for the distance $\delta \ll L$ from the endpoints of the double-chain, Figure 2.2 (b). Surprisingly, single-particle hopping between the chains does *not* create overlaps if the coupling is time-reversal invariant; and even when this symmetry is broken, only hopping close to the endpoints can lift the degeneracy of two ground states.

The bottom line is that a qubit $|\Psi\rangle$ that is encoded in the degenerate ground state space of $|N, \pm 1\rangle$ can be protected from decoherence either by subchain-parity or time-reversal symmetry. This qualifies our model H as a so called *symmetry-protected topological phase (SPT)*, a less versatile (but more accessible) relative of the topologically ordered phases described above.

The states of a SPT can often be identified by their entanglement structure. A quantity that has proven particularly useful in this context is the *entanglement spectrum*, the spectrum of an artificial Hamiltonian that encodes information on the entanglement between a (macroscopic) subsystem and its complement. We find a two-fold degeneracy of this spectrum for $|N, \alpha\rangle$, a well-known manifestation of topologically protected ground state manifolds. Interestingly, the *amount* of

entanglement (measured by the *entanglement entropy*) that is shared between a subsystem of size S and its complement grows logarithmically with S . For quantum chains, this heralds a *gapless* spectrum of the Hamiltonian.

Indeed, the single-chain Hamiltonians H^x ($x = a, b$) with open boundaries can be mapped to the ferromagnetic, isotropic *Heisenberg model* via Jordan-Wigner transformation⁴⁷. We exploit this mapping and construct the analog of single-magnon states for the double-chain Hamiltonian, denoted $|k; N, \alpha\rangle$ and labeled by wavenumbers $k = m\frac{\pi}{L}$ with $0 \leq m < L$. These are exact eigenstates of H in the sector \mathcal{H}_α^N with the quadratic spectrum $E_k = 4 \sin^2(k/2)$. As anticipated from the growth of the entanglement entropy, the energy gap between ground state and first excited state vanishes for $L \rightarrow \infty$. That H is in a *gapless phase* is a consequence of particle number conservation and sets it apart from the mean field Majorana chain (which is gapped).

So far, we discussed the double-chain Hamiltonian, its ground states, and some of its excited states. The robust ground state degeneracy qualifies the model as (symmetry-protected) topological phase, and the single-particle correlators (and overlaps) certify the presence of edge states.

The stage is set—what about braiding? The anyons we would like to braid can be identified with the endpoints of chains because these are the only locations where single-particle hopping induces unitaries on the ground state space (recall the overlaps!). In order to braid two endpoints, we go beyond the single double-chain setup and consider a *wire network* of four open subchains with parities α_i , coupled by a common “bath” chain as depicted in Figure 2.3 (a) and described by a Hamiltonian H_0 . To braid two of the four endpoints, we need only interactions between the four open chains. Thus, the total subchain parity $\alpha = \alpha_1\alpha_2\alpha_3\alpha_4$ is conserved and can be fixed (here $\alpha = -1$); this reduces the number of relevant ground states to 8, Figure 2.3 (b). The braiding is described completely within this 8-dimensional ground state space of H_0 , and implemented by a Hamiltonian $H_{\text{int}}(t)$ that encodes the smooth sequence of single-particle hopping depicted in Figure 2.3 (c). $H_{\text{int}}(t)$ hybridizes edge states such that the 8-fold degeneracy is lifted and only 4 ground states remain degenerate during the braiding protocol. We are then interested in the unitary realized by braiding on this 4-dimensional subspace (which encodes two qubits).

To this end, we start with one of the four initial zero-energy states of $H_{\text{int}}(t = 0)$ which we denote by $|00\rangle$; it is characterized by $\alpha_1 = -1 = \alpha_2$ and $\alpha_3\alpha_4 = -1$, see Figure 2.3 (d). If we apply the cyclic time evolution that describes the braiding, $|00\rangle$ is mapped to the orthogonal state

$$|11\rangle = \mathcal{T} \exp \left[-i \int_0^8 dt H_{\text{int}}(t) \right] |00\rangle = U_{\text{B}} |00\rangle \quad 2.10$$

⁴⁷A mathematically exact transformation that maps fermions to spins and vice versa.

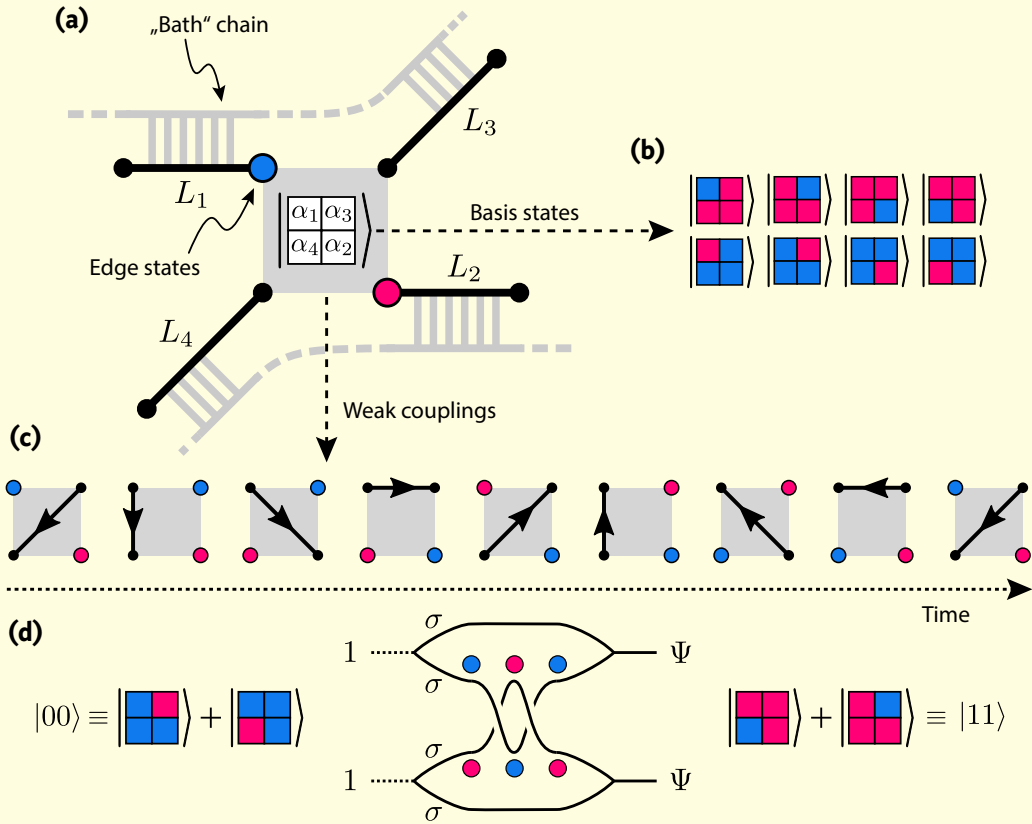


FIGURE 2.3 • Braiding. (a) Wire network of four open chains $L_i, i = 1, \dots, 4$, (black) with controllable weak single-particle couplings between the inner four endpoints (gray square). The partner chains (gray) are not involved in the braiding and take the role of a “bath.” (b) The dynamics takes place in the 8-dimensional Hilbert space spanned by zero-energy ground states with fixed total parity $\alpha = \alpha_1\alpha_2\alpha_3\alpha_4 = -1$. The colors label the subchain parities α_i of the four black chains. (c) A black arrow indicates single-particle hopping between the endpoints of chains. Braiding is achieved by the composition of two exchanges, each subdivided into 4 steps that are interpolated smoothly via $H_{\text{int}}(t)$. (d) The braiding unitarily rotates the state $|00\rangle$ into the orthogonal state $|11\rangle$. This can be interpreted as the braiding of two “Majoranas” σ , each of which belongs to a pair created from the vacuum 1; afterwards, the pairs fuse to fermions Ψ .

characterized by $\alpha_1 = +1 = \alpha_2$ and $\alpha_3\alpha_4 = -1$. (\mathcal{T} denotes the time-ordering operator.) The unitary U_B represents the braiding of two anyons on the four-fold degenerate ground state space of $H_{\text{int}}(0)$; its effect is to invert the parities of the open subchains 1 and 2.

What are the implications for the “particles” attached to the endpoints? To understand this, one has to associate the parity α_i of a subchain to the result one obtains when its two endpoints are *fused*, i.e., combined to a new “particle”; in practice, this is achieved by single-particle hopping between the two endpoints. This establishes periodic boundary conditions—and we show that there are two possible outcomes: For odd subchain parity, the energy density at the relevant edge

remains zero, whereas for even subchain parity, it is finite. In condensed matter physics, a localized finite energy density is nothing but a “particle”; here we call it a *fermion* Ψ . If we denote the particles attached to the endpoints as σ (and write 1 for the “trivial” particle that indicates the absence of both Ψ and σ), we can write formally

$$\sigma \otimes \sigma = 1 \oplus \Psi, \tag{2.11}$$

i.e., combining (\otimes) two endpoints (σ) yields either zero energy (1) or (\oplus) non-zero energy (Ψ). Equation (2.11) is the *fusion rule* that characterizes *Ising anyons*, a particular class of non-abelian anyons that also describe the edge modes of the Majorana chain (where σ labels the Majorana modes). In this parlance, the braiding described above reads as follows [see Figure 2.3 (d)]: We start with two pairs of “Majoranas” σ that fuse to the “vacuum” 1 (because $\alpha_1 = -1 = \alpha_2$ in $|00\rangle$). By braiding two “Majoranas” of different pairs, the pairs fuse to fermions Ψ afterwards (because $\alpha_1 = +1 = \alpha_2$ in $|11\rangle$). This is a characteristic feature of Ising anyons and substantiates the role of our model as number-conserving cousin of the Majorana chain.

2.1 Introduction

Topologically protected ground state degeneracies in many-body quantum systems, and the closely related (non-abelian) anyonic statistics of excitations and defects, are of special interest from a theoretical point of view [37, 223], and have been recognized as promising concepts for scalable, fault-tolerant quantum computation [45, 47]. Intensely studied and well understood are topological states with Majorana zero-energy edge modes that appear within mean field descriptions of topological superconductors [224]. Due to their description in terms of matrix ensembles, these free fermion theories have been classified exhaustively [22, 97], and the properties of the Majorana zero modes at boundaries [82] and in vortices [83] have been characterized. By contrast, interacting and gapless phases are intrinsically harder to explore and therefore less well understood [17, 110, 119, 225]: To which extent existence and non-abelian properties of edge states carry over to interacting theories is an interesting question lacking conclusive answers [226].

Our understanding of topological phases is driven by exactly solvable microscopic models; archetypal for the existence of topologically protected Majorana edge modes is the one-dimensional Majorana chain [82]. It has inspired a variety of proposals for its experimental realization in condensed matter systems [159, 160, 224, 227], and signatures consistent with Majorana modes have been experimentally observed [152, 161, 228, 229]. However, such models require large particle reservoirs to justify their mean field description, whereas very little is known about the fate of Majorana zero-energy edge modes in intrinsically interacting and particle conserving settings—a particularly important scenario for realizations with ultracold atoms in optical lattices. Previous attempts for number-conserving theories featuring Majorana-like edge states relied either on bosonization [230–234] or on numerical methods (DMRG) [235], while the only exactly solvable models require unphysical long-range interactions [236].

In this chapter, we introduce and study a microscopic, number-conserving theory with local interactions that features non-abelian edge states at the boundaries. The theory allows for an exact derivation of its many-body ground state as well as its low-energy excitations, and thereby provides a viable playground for analyzing its characteristic properties. We show that the ground state is characterized by a condensate of p -wave pairs with a robust, topological degeneracy. The Green’s function exhibits a revival at the edges, revealing the presence of edge states. Remarkably, the model can be generalized to arbitrary wire networks, which allow us to derive the non-abelian braiding statistics of the edge states on a microscopic level.

The presentation of these results is structured as follows:

We start with the definition of the model in Subsection 2.2.1 and proceed with the derivation of its exact ground states in Subsection 2.2.2 where we find a two-fold degeneracy for a fixed particle number. In Subsection 2.3.1, we exploit the simple structure of these ground states to calculate their correlations; in particular, the

Green’s function reveals localized states at the boundaries. In Subsection 2.3.2, we proceed with symmetry considerations and show that local perturbations cannot lift the ground state degeneracy in the bulk but only at the edges and only if time-reversal symmetry is broken. This classifies the ground state manifold as a *symmetry-protected topological phase*. We substantiate this claim in Subsection 2.3.3 by an analysis of the entanglement spectrum which features a robust two-fold degeneracy. In this context, a logarithmic growth of the entanglement entropy hints at a gapless spectrum due to the presence of a Goldstone mode. This is underpinned in Subsection 2.4.1 where we derive a submanifold of exact eigenstates with a quadratic excitation spectrum. In Subsection 2.4.2, we complete this picture with a discussion of the gap scaling for open and closed boundary conditions. In the last part, we first generalize the model to more complicated networks of coupled wires in Subsection 2.5.1. In particular, we show that the ground states of these networks are still analytically accessible. In Subsection 2.5.2, we use a particular arrangement of wires—and our knowledge of their ground states—to simulate the braiding of edge states on a microscopic level. As a main result, we find the non-abelian statistics of Ising anyons which qualifies the edge states as number-conserving analogues of mean field Majorana modes. We conclude in Section 2.6 where we also point to related results that supplement the findings of this chapter.

Additional results are presented in the appendices where we describe the ground states as matrix product states (§ Section 2.A), derive rigorous bounds on the spectral gap (§ Section 2.B), calculate exact eigenstates with Bethe ansatz methods (§ Section 2.C), and discuss possible remnants of the Majorana (Clifford) algebra (§ Section 2.D).

2.2 A Chain of Interacting Fermions

We start in Subsection 2.2.1 with the definition of the fermionic Hamiltonian the properties of which are subject of this chapter. Subsequently, in Subsection 2.2.2, we derive and describe its exact zero-energy ground states. The simplicity of these ground states is a characteristic feature of the introduced Hamiltonian and allows for the efficient analysis of its quantum phase.

2.2.1 Definition of the Model

We consider a double-chain (“two-leg ladder”) of spinless fermions with L lattice sites and open boundary conditions. The fermionic annihilation operators at site i are described by a_i (upper chain) and b_i (lower chain), see Figure 2.4 (a) for a schematic illustration.

The many-body Hamiltonian

$$H = H^a + H^b + H^{ab} \quad 2.12$$

describing the interacting fermion theory combines *intra*-chain contributions H^x ($x = a, b$) with *inter*-chain couplings H^{ab} . The intra-chain Hamiltonian takes the form

$$H^x = \sum_{i=1}^{L-1} A_i^x (\mathbb{1} + A_i^x) \quad 2.13$$

with the single-particle hopping terms

$$A_i^a = a_i a_{i+1}^\dagger + a_{i+1} a_i^\dagger \quad \text{and} \quad A_i^b = b_i b_{i+1}^\dagger + b_{i+1} b_i^\dagger. \quad 2.14$$

Thus, the terms of the sum (2.13) combine single-particle hopping with a nearest-neighbor attraction $n_i^x + n_{i+1}^x - 2n_i^x n_{i+1}^x$ on each chain separately. The inter-chain interaction H^{ab} takes a similar form,

$$H^{ab} = \sum_{i=1}^{L-1} B_i (\mathbb{1} + B_i), \quad 2.15$$

with the pair hopping between the two chains

$$B_i = a_i^\dagger a_{i+1}^\dagger b_i b_{i+1} + b_i^\dagger b_{i+1}^\dagger a_i a_{i+1}. \quad 2.16$$

The terms in (2.15) then expand to a correlated pair hopping and additional four-fermion density-density interactions between the chains.

Let us briefly comment on reasons to consider Hamiltonian (2.12) in the first place: Recall that we are looking for a *number-conserving* analogue of the *parity-conserving* Majorana chain. As we showed in Subsection 1.2.2, the two many-body zero-energy ground states of the Majorana chain differ only in their total fermion parity. The fact that a global quantity like parity is inaccessible to local observables renders their degeneracy topological. But fixing the total particle number fixes also the total parity. Hence we resort to a *double-wire* setup where the total particle number does not fix the parities of each *subchain*. A reasonable Hamiltonian has to conserve this *subchain parity*. Generically, this leads to a Hamiltonian with single-particle hopping within the chains and a correlated pair hopping between them; this is realized by the linear terms A_i^x and B_i in (2.12). The quadratic terms $(A_i^x)^2$ and B_i^2 do not violate the subchain symmetry and turn (2.12) into the parent Hamiltonian of ground states with exceptionally simple structure, in analogy to the “sweet spot” of the Majorana chain (see Subsection 2.2.2 below).

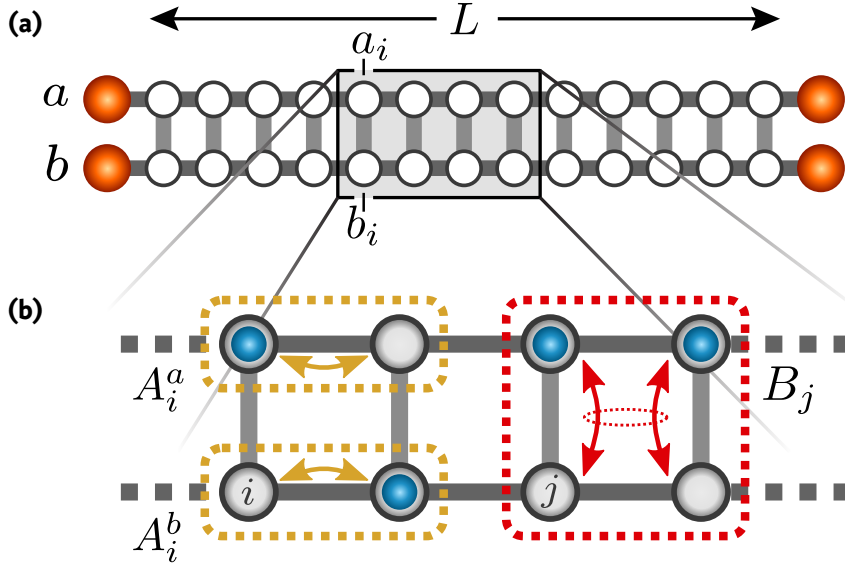


FIGURE 2.4 • Setup. (a) We consider a double-chain (“two-leg ladder”) of length L with open boundary conditions and spinless fermions a_i and b_i living on the sites; the upper/lower chains are labeled by a/b , respectively. (b) The number-conserving Hamiltonian is given by intra-chain terms A_i^x ($x = a, b$) that describe single-particle hopping as well as density-density interactions, and the inter-chain couplings B_j that encode correlated pair hopping together with four-fermion density-density interactions.

Since the Hamiltonian H conserves the total number of particles N , this defines the only free parameter of the theory and is conveniently expressed as the density $\rho = N/2L$. Besides the global $U(1)$ symmetry, H features two⁴⁸ additional, relevant symmetries:

- 1 The already mentioned *subchain parity*

$$P_x \equiv (-1)^{\sum_i x_i^\dagger x_i} \quad \text{for } x = a, b, \quad 2.17$$

- 2 and *time-reversal* symmetry $T \equiv \mathcal{K}$, represented by complex conjugation \mathcal{K} and $T x_i^{(\dagger)} T^{-1} \equiv x_i^{(\dagger)}$ for $x = a, b$.

Time-reversal symmetry is also present in the mean field Majorana chain and, if preserved, protects Majorana edge modes that transform identically under T from gapping out⁴⁹. The subchain symmetry P_x , however, differs quite a bit from the *total* parity P conserved by the Majorana chain in that the former is an intrinsic symmetry of the Hamiltonian which can be broken by additional terms

⁴⁸There is a third one which we do not consider here, namely the “chain exchange symmetry” $a_i \leftrightarrow b_i$. We refer the reader to Ref. [237] for more information.

⁴⁹This is a manifestation of the \mathbb{Z} topological index in symmetry class **BDI** of the tenfold way [97].

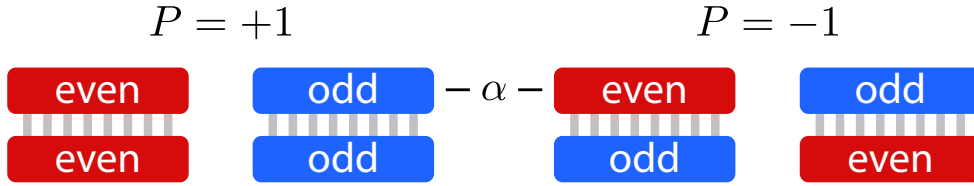


FIGURE 2.5 • Ground states—Degeneracy. For every filling N with total parity $P = (-1)^N$, there are *two* degenerate zero-energy ground states for open boundary conditions, characterized by their (upper) subchain parity $\alpha = P_a$.

without modifying the structure of the theory (single-particle hopping between the chains does the job). By contrast, a quadratic fermionic theory that describes a closed system always conserves the total fermion parity. In reality, though, there is always an environment that interferes; for the Majorana chain, tunneling of single quasiparticles from a (superconducting) environment can violate the parity symmetry (this is known as *quasiparticle poisoning* [238, 239]). But this cannot be described without enlarging the system (i.e., the Hilbert space) to encompass the environment. By contrast, subchain parity can be violated within the double-wire setup alone.

2.2.2 Ground States

A characteristic feature of Hamiltonian (2.12) is that its ground states can be derived exactly. To do this, the observation that H is the sum of local projectors and therefore a *positive semi-definite* operator⁵⁰ is crucial (for brevity, we omit the “semi-definite” in the following). We can then exploit that any zero-energy ground state must be annihilated by all local terms in (2.13) and (2.15) separately. That is, *if* we find a state with zero energy which is annihilated by all local terms, we can be sure that it is a ground state. This yields a viable method to construct them from scratch—provided zero-energy ground states exist.

For a ladder with *open* boundary conditions, one finds exactly two degenerate zero-energy ground states for each filling $0 < N < 2L$ denoted as $|N, \alpha\rangle$ and characterized by the upper subchain parity $\alpha \equiv P_a \in \{+1, -1\}$, see Figure 2.5. Before we discuss their derivation below, let us first comment on their structure:

⁵⁰To show that H is positive (semi-definite), recall that the sum of positive operators is again positive. So we can prove the positivity of H^x and H^{ab} separately which, in turn, boils down to the positivity of their summands. The eigenvalues of A_i^x and B_i are easily calculated as 0 and ± 1 . Thus the eigenvalues of $A_i^x(\mathbb{1} + A_i^x)$ and $B_i(\mathbb{1} + B_i)$ are 0 and 2, which qualifies them as positive operators (and explains why we choose this form, and not just A_i^x and B_i as in Ref. [235]).

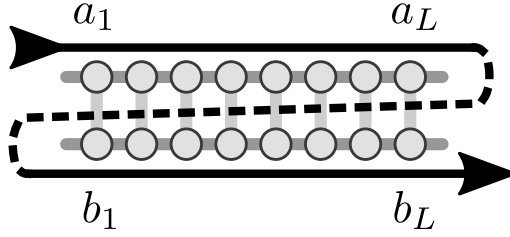


FIGURE 2.6 • Ground states—Fermion gauge. The shown fermion ordering defines a particular basis of the Fock space. The chosen gauge is needed for the simple description of the ground states in terms of these basis states.

For an appropriate choice of the fermion ordering⁵¹ (see Figure 2.6), each ground state is given by the equal-weight superposition of distributing N particles on the two chains, constrained by the fixed subchain parity α .

To cast this in a formal description, we first introduce the fermion number states $|\mathbf{n}\rangle_x$ with $x = a, b$ and $\mathbf{n} \in \{0, 1\}^L$, i.e.,

$$|\mathbf{n}\rangle_a = (a_1^\dagger)^{n_1} \dots (a_i^\dagger)^{n_i} \dots (a_L^\dagger)^{n_L} |0\rangle_a \quad 2.18$$

for the upper chain with the number of fermions $|\mathbf{n}| = \sum_{i=1}^L n_i$. Then, the equal-weight superposition of states on each chain with a fixed number of particles n can be written as

$$|n\rangle_x \equiv \sum_{|\mathbf{n}|=n} |\mathbf{n}\rangle_x; \quad 2.19$$

note that this state is not normalized. Finally, the *equal-weight superposition* with fixed particle number N and subchain parity α is given as

$$|N, \alpha\rangle \equiv \mathcal{N}_{L,N,\alpha}^{-1/2} \sum_{n, (-1)^n = \alpha} |n\rangle_a |N - n\rangle_b \quad 2.20$$

where $\mathcal{N}_{L,N,\alpha}^{-1/2}$ is the normalizing factor that counts the number of superimposed fermion configurations (see Section 2.3 for an explicit expression).

By contrast, for a ladder with *closed* boundary conditions the situation is more subtle: For *even* total particle number $N = 2K$, there is a unique zero-energy ground state $|2K, -1\rangle$ in the odd-odd ($\alpha = -1$) subchain-parity sector, whereas in the odd- N sectors all states are lifted to finite energy. This is summarized in Figure 2.12 where we discuss the low-energy scaling of H , see Subsection 2.4.2.

At this point, it seems advisable to compare the ground states $|N, \alpha\rangle$ with those of a *single* (mean field) Majorana chain which, in analogy, features two zero-energy ground states $|P = \pm 1\rangle$ for open boundary conditions (see Subsection 1.2.2 and Ref. [82]): For vanishing chemical potential (i.e., perfectly localized edge modes),

⁵¹The ordering of fermions determines a particular number basis of the Fock space but has no *physical* meaning; it can therefore be seen as a gauge condition fixing a purely mathematical freedom.

the ground states of the Majorana chain are given by the equal-weight superposition of particle number states with fixed *global* parity $P = \pm 1$ but undetermined particle number N ; a manifestation of the superconducting condensate where pairs of quasiparticles can fuse to the vacuum. By contrast, here the chains act as mutual particle reservoirs and the ground state degeneracy arises due to two admissible subchain parity configurations within each fixed particle number sector (Figure 2.5).

We now prove that $|N, \alpha\rangle$ are the only zero-energy ground states of H . The reader may skip this derivation on first reading and proceed with Section 2.3.

Construction of the Ground States

It is straightforward to show that the two states $|N, \alpha = \pm 1\rangle$ in each filling sector N are annihilated by H , and therefore belong to the ground state space (recall that H is a positive operator). Here we want to show more, namely their *uniqueness*, by constructing all zero-energy eigenstates from scratch. To this end, consider the binary vectors $(\mathbf{n}, \mathbf{m}) \in \{0, 1\}^{2L}$ describing the fermion configurations on the ladder. The Fock space \mathcal{H} is spanned by the number states $|\mathbf{n}, \mathbf{m}\rangle \equiv |\mathbf{n}\rangle_a |\mathbf{m}\rangle_b \in \mathcal{H}$, where we choose the fermion ordering (gauge) according to Figure 2.6; this defines a representation of the fermion algebra $\{a_i, a_i^\dagger, b_i, b_i^\dagger \mid 1 \leq i \leq L\}$ on \mathcal{H} .

It is easy to show that the action of this representation allows us to write

$$A_i^x (\mathbb{1} + A_i^x) |\mathbf{n}, \mathbf{m}\rangle = |\mathbf{n}, \mathbf{m}\rangle - |\varepsilon_i^x(\mathbf{n}, \mathbf{m})\rangle \quad 2.21$$

and

$$B_i (\mathbb{1} + B_i) |\mathbf{n}, \mathbf{m}\rangle = |\mathbf{n}, \mathbf{m}\rangle - |\tau_i(\mathbf{n}, \mathbf{m})\rangle \quad 2.22$$

(this is where the ordering of Figure 2.6 becomes important). Here we used the single-bit swap-operators

$$\varepsilon_i^a((\dots, n_i, n_{i+1}, \dots), \mathbf{m}) \equiv ((\dots, n_{i+1}, n_i, \dots), \mathbf{m}) \quad 2.23a$$

$$\varepsilon_i^b(\mathbf{n}, (\dots, m_i, m_{i+1}, \dots)) \equiv (\mathbf{n}, (\dots, m_{i+1}, m_i, \dots)) \quad 2.23b$$

for arbitrary (\mathbf{n}, \mathbf{m}) and the bit-pair swap-operators

$$\begin{aligned} & \tau_i((\dots, n_i, n_{i+1}, \dots), (\dots, m_i, m_{i+1}, \dots)) \\ & \equiv ((\dots, m_i, m_{i+1}, \dots), (\dots, n_i, n_{i+1}, \dots)) \end{aligned} \quad 2.24$$

if and only if $n_i = n_{i+1}$ and $m_i = m_{i+1}$ with $\tau_i = \text{Id}$ otherwise.

It is convenient to introduce the partition $\bigcup_N B_N = \{0, 1\}^{2L}$ of binary vectors with the decomposition $B_N = B_N^+ \cup B_N^-$, where B_N^α is the set of vectors (\mathbf{n}, \mathbf{m}) with filling $\sum_i (n_i + m_i) = N$ and subparity $\prod_i (-1)^{n_i} = \alpha$. It is now easy to see that

- 1 $\varepsilon_i^x, \tau_i : B_N^\alpha \rightarrow B_N^\alpha$ are bijections for $x = a, b$ and $1 \leq i \leq L - 1$ (note that $\varepsilon_i^x \varepsilon_i^x = \text{Id} = \tau_i \tau_i$), and

- 2** for any pair $(\mathbf{n}, \mathbf{m}), (\mathbf{n}', \mathbf{m}') \in B_N^\alpha$ there is a finite sequence σ of ε_i^x, τ_i such that $(\mathbf{n}, \mathbf{m}) = \sigma(\mathbf{n}', \mathbf{m}')$. That is, the connected components of $\{0, 1\}^{2L}$ under the described family of bit-operations

$$\Pi \equiv \{\pi\} = \{\varepsilon_i^a, \varepsilon_i^b, \tau_i \mid 1 \leq i \leq L-1\} \quad 2.25$$

are exactly the B_N^α for $N = 0, \dots, 2L$ and $\alpha = \pm 1$.

We proceed with a generic state $|\Psi\rangle \in \mathcal{H}$,

$$|\Psi\rangle = \sum_{(\mathbf{n}, \mathbf{m})} \Psi(\mathbf{n}, \mathbf{m}) |\mathbf{n}, \mathbf{m}\rangle \quad 2.26$$

and evaluate its energy expectation value

$$\langle \Psi | H | \Psi \rangle = \sum_{i,x} \langle \Psi | A_i^x (\mathbb{1} + A_i^x) | \Psi \rangle + \sum_i \langle \Psi | B_i (\mathbb{1} + B_i) | \Psi \rangle \quad 2.27$$

which reads

$$\langle \Psi | H | \Psi \rangle = \sum_{\pi \in \Pi} \sum_{\substack{(\mathbf{n}, \mathbf{m}) \\ (\mathbf{n}', \mathbf{m}')}} \Psi^*(\mathbf{n}', \mathbf{m}') \Psi(\mathbf{n}, \mathbf{m}) \times \langle \mathbf{n}', \mathbf{m}' | [|\mathbf{n}, \mathbf{m}\rangle - |\pi(\mathbf{n}, \mathbf{m})\rangle] \rangle \quad 2.28a$$

$$= \sum_{\pi \in \Pi} \sum_{(\mathbf{n}, \mathbf{m})} [\Psi^*(\mathbf{n}, \mathbf{m}) \Psi(\mathbf{n}, \mathbf{m}) - \Psi^* \pi(\mathbf{n}, \mathbf{m}) \Psi(\mathbf{n}, \mathbf{m})] . \quad 2.28b$$

Doubling the sum, substituting $\pi(\mathbf{n}, \mathbf{m}) \rightarrow (\mathbf{n}, \mathbf{m})$, and using the bijectivity $\pi\{0, 1\}^{2L} = \{0, 1\}^{2L}$, yields

$$\begin{aligned} \langle \Psi | H | \Psi \rangle &= \frac{1}{2} \sum_{\pi \in \Pi} \sum_{(\mathbf{n}, \mathbf{m})} [\Psi^*(\mathbf{n}, \mathbf{m}) \Psi(\mathbf{n}, \mathbf{m}) - \Psi^* \pi(\mathbf{n}, \mathbf{m}) \Psi(\mathbf{n}, \mathbf{m})] \\ &\quad + \frac{1}{2} \sum_{\pi \in \Pi} \sum_{(\mathbf{n}, \mathbf{m})} [\Psi^* \pi(\mathbf{n}, \mathbf{m}) \Psi \pi(\mathbf{n}, \mathbf{m}) - \Psi^*(\mathbf{n}, \mathbf{m}) \Psi \pi(\mathbf{n}, \mathbf{m})] \\ &= \frac{1}{2} \sum_{\pi \in \Pi} \sum_{(\mathbf{n}, \mathbf{m})} |\Psi(\mathbf{n}, \mathbf{m}) - \Psi \pi(\mathbf{n}, \mathbf{m})|^2 . \end{aligned} \quad 2.29$$

Splitting the second sum into the connected components B_N^α gives the final result

$$\langle \Psi | H | \Psi \rangle = \frac{1}{2} \sum_{N,\alpha} \sum_{\pi \in \Pi} \sum_{(\mathbf{n}, \mathbf{m}) \in B_N^\alpha} |\Psi(\mathbf{n}, \mathbf{m}) - \Psi \pi(\mathbf{n}, \mathbf{m})|^2 . \quad 2.30$$

Since $|\Psi\rangle$ is a zero-energy eigenstate if and only if⁵² $\langle \Psi | H | \Psi \rangle = 0$, and the B_N^α are the connected components under the repeated action of Π , we conclude that for any normalizable zero-energy state, it is necessary and sufficient that the amplitudes

⁵²The implication $H|\Psi\rangle = 0 \Rightarrow \langle \Psi | H | \Psi \rangle = 0$ is trivial. The other direction follows from the positivity of H : Consider the spectral decomposition $H = \sum_\lambda \lambda |\lambda\rangle \langle \lambda|$ with eigenvalues $\lambda \geq 0$. Then $0 = \langle \Psi | H | \Psi \rangle = \sum_\lambda \lambda |\langle \lambda | \Psi \rangle|^2$ implies that $\lambda |\langle \lambda | \Psi \rangle|^2 = 0$ for all eigenvectors $|\lambda\rangle$, i.e., $|\Psi\rangle$ is a linear combination of eigenvectors with eigenvalue $\lambda = 0$ and therefore $H|\Psi\rangle = 0$.

are constant within each sector B_N^α ,

$$H|\Psi\rangle = 0 \Leftrightarrow \Psi(\mathbf{n}, \mathbf{m}) = \Psi_N^\alpha \in \mathbb{C}, \quad \forall(\mathbf{n}, \mathbf{m}) \in B_N^\alpha. \quad 2.31$$

These are exactly the equal-weight superpositions $|N, \alpha\rangle$ of fixed particle number N and subchain parity α defined in Eq. (2.20).

We stress that these statements are modified for *closed* boundary conditions within the even-even and odd-even/even-odd subchain-parity sectors where some of the summands in Eq. (2.30) read $|\Psi(\mathbf{n}, \mathbf{m}) + \Psi_\pi(\mathbf{n}, \mathbf{m})|^2$ due to the fermionic statistics. From this it follows immediately that no normalizable state with zero eigenenergy can exist, though the ground state energy may vanish in the thermodynamic limit (see Subsection 2.4.2).

2.3 Ground State Properties

In this section, we harness the simple structure of the zero-energy ground states $|N, \alpha\rangle$ to explore their properties in detail. In Subsection 2.3.1, we calculate important correlators and use the Green's function to uncover non-local correlations between the edges. Possible perturbations of the Hamiltonian H are studied in Subsection 2.3.2: We show that the ground state degeneracy can only be lifted if time-reversal symmetry is broken close to the boundaries of the chain. Finally, in Subsection 2.3.3, we discuss the entanglement spectrum of the ground states and find a logarithmic growth of the entanglement entropy.

These results follow from combinatorial considerations dictated by the structure of the ground states. In this context, quantities termed *parity-split binomial coefficients* appear frequently and allow for terse expressions. Thus we preface the following discussion with some preliminary notes:

Mathematical Preliminaries

As we will show below, the evaluation of arbitrary expectation values and correlators of the zero-energy ground states $|N, \alpha\rangle$ is particularly efficient because the evaluation of matrix elements reduces to counting fermion configurations on $g - 1$ subsystems⁵³ of size L_1, \dots, L_{g-1} with parity constraints $\alpha_1, \dots, \alpha_{g-1} \in \{\pm 1\}$.

⁵³The g th subsystem is the “rest” or the “environment,” the parity α_g of which is determined by the total number of particles N and the parities of the other $g - 1$ subsystems.

DEFINITION 2.1: Parity-split binomial coefficients (PsBC)

Therefore we introduce the parity-split binomial coefficients (PsBC)

$$\binom{L_1, \dots, L_g}{\alpha_1, \dots, \alpha_{g-1}}_N \equiv \sum_{n_1, \dots, n_{g-1}}^N \binom{L_g}{N - \sum_{i=1}^{g-1} n_i} \prod_{i=1}^{g-1} \delta_{n_i}^{\alpha_i} \binom{L_i}{n_i} \quad 2.32$$

with $\delta_{n_i}^{\alpha_i} \equiv [1 + \alpha_i(-1)^{n_i}] / 2$. Here, $\sum_{i=1}^g L_i = L$ is the total number of sites, $0 \leq N \leq L$ the number of particles to be distributed, and $\alpha_i = \pm 1$ fixes the parity of the i th segment.

The PsBC counts the number of possibilities to distribute N identical particles on L sites, partitioned into g segments of length L_i ($i = 1, \dots, g$), so that the parity of each segment is α_i . Note that for $g = 1$ there are no parity constraints and the PsBC is the usual binomial coefficient $\binom{L}{N}$. The PsBCs can be evaluated efficiently on a computer, though we are not aware of closed forms for arbitrary splittings g .

However, the simplest non-trivial PsBC (which describes the splitting of the double-chain in upper and lower wires of equal length L) allows for a closed form, namely

$$\binom{L, L}{\alpha}_N = \frac{1}{2} \binom{2L}{N} + \frac{\alpha}{2} \frac{1 + (-1)^N}{2} (-1)^{N/2} \binom{L}{N/2}. \quad 2.33$$

Thus the leading order is $\frac{1}{2} \binom{2L}{N}$. This is exact for *odd* N , as one would expect due to the exchange symmetry mapping between even-odd ($\alpha = +1$) and odd-even ($\alpha = -1$) subparities. For *even* fillings N , however, there are corrections of order $\binom{L}{N/2}$ due to the inequivalence of even-even and odd-odd subparities⁵⁴.

As a final remark, we give the alternative form of a generic $g = 2$ PsBC

$$\binom{L_1, L_2}{\alpha}_N = \frac{1}{2} \binom{L_1 + L_2}{N} + \frac{\alpha}{2} \sum_{n=0}^N (-1)^n \binom{L_1}{n} \binom{L_2}{N-n}, \quad 2.34$$

which separates the leading contribution from the α -dependent corrections. We make use of this result below.

2.3.1 Correlations and Edge States

We start exploiting the concise description of the ground states to derive simple expressions for density correlations, superfluid order parameter and the Green's function (single-particle correlation). Due to the simple structure of the ground

⁵⁴This inequivalence is most pronounced for small N , e.g., for $N = 2$ one has L^2 possible patterns in the odd-odd sector but only $2L(L-1)/2 = L^2 - L$ in the even-even sector.

states, all correlation functions and expectation values of $|N, \alpha\rangle$ can be rewritten in terms of finite combinations of PsBCs. Let us explain this rationale using the example of the normalizing factor $\mathcal{N}_{L,N,\alpha}$ introduced in Eq. (2.20). It can be computed as follows:

$$\mathcal{N}_{L,N,\alpha} \stackrel{\text{def}}{=} \sum_{(\mathbf{n}, \mathbf{m}) \in B_N^\alpha} \sum_{(\mathbf{n}', \mathbf{m}') \in B_N^\alpha} \underbrace{\langle \mathbf{n}, \mathbf{m} | \mathbf{n}', \mathbf{m}' \rangle}_{\delta_{\mathbf{n}, \mathbf{n}'} \delta_{\mathbf{m}, \mathbf{m}'}} \quad 2.35a$$

$$= |B_N^\alpha| \quad 2.35b$$

$$= \left| \left\{ \begin{array}{l} \text{Configurations } (\mathbf{n}, \mathbf{m}) \in \mathbb{Z}_2^L \times \mathbb{Z}_2^L \\ \text{with } \sum_i (n_i + m_i) = N \text{ particles} \\ \text{and parity constraint } \prod_i (-1)^{n_i} = \alpha \end{array} \right\} \right| \quad 2.35c$$

$$\stackrel{\text{def}}{=} \binom{L, L}{\alpha}_N. \quad 2.35d$$

The normalization of the two ground states $|N, \alpha\rangle$ is therefore given by Eq. (2.33). To keep our discussion of the following results free from technicalities, we postpone similar counting arguments to the end of this subsection.

As a first result, we find that the inter- and intra-chain density-density correlation function factorizes,

$$\langle n_i^x n_j^y \rangle = \langle x_i^\dagger x_i y_j^\dagger y_j \rangle \rightarrow \rho^2 \quad \text{for } i \neq j; x, y \in \{a, b\}, \quad 2.36$$

in the thermodynamic limit $L, N \rightarrow \infty$ with fixed particle density $\rho = N/2L$. Furthermore, the pair correlations become constant and non-zero

$$|\langle x_i^\dagger x_{i+1}^\dagger y_j y_{j+1} \rangle| \rightarrow \rho^2 (1 - \rho)^2 \quad \text{for } i \neq j; x, y \in \{a, b\}, \quad 2.37$$

which indicates a condensate of p -wave pairs with true long-range order. Note that the results for both correlators do *not* depend on the subchain parity α of the ground states. As we show below, this is true up to exponential corrections vanishing with $L \rightarrow \infty$. For particularly symmetric setups (e.g., $x \neq y$ and N odd) these corrections even vanish identically.

The intra-chain Green's function (indicating single-particle off-diagonal long-range order [240]) can also be expressed in terms of PsBCs ($j > i + 1$),

$$\langle a_i^\dagger a_j \rangle = \mathcal{N}_{L,N,\alpha}^{-1} [\Lambda_{+1,-\alpha} - \Lambda_{-1,\alpha}], \quad 2.38$$

where $\Lambda_{\alpha_1, \alpha_2} \equiv \binom{j-i-1, L-j+i-1, L}{\alpha_1, \alpha_2}_{N-1}$; see below for the derivation. In the thermodynamic limit, one finds exponentially decaying correlations in the bulk (see Figure 2.7),

$$\langle x_i^\dagger x_j \rangle = e^{-\nu(\rho)|i-j|} \quad \text{for } 1 \ll i, j \ll L; x \in \{a, b\} \quad 2.39$$

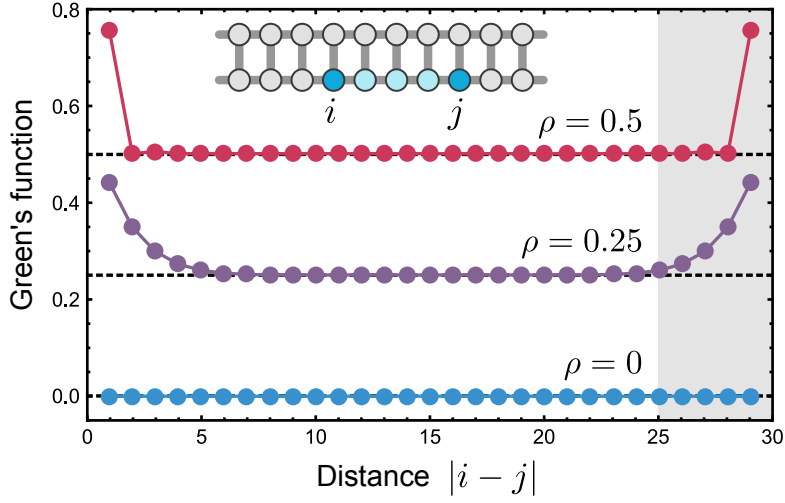


FIGURE 2.7 • Ground state properties—Edge states. Intra-chain single-particle correlation $\langle a_i^\dagger a_j \rangle$ (Green's function) as a function of the distance $|i - j|$ for three densities $\rho = 0.5, 0.25, 0.0$ and a chain of length $L = 30$. The revival for $|i - j| \sim L$ indicates exponentially localized edge states (gray region).

where γ is some function of the density with $0 < \gamma(\rho) \leq \infty$ and $\gamma(1/2) = \infty$. Most importantly, the boundary terms read

$$|\langle a_1^\dagger a_L \rangle| \rightarrow \rho(1 - \rho) > 0 \quad 2.40$$

in the thermodynamic limit, indicating the existence of exponentially localized edge states with perfect localization at half-filling $\rho = 1/2$, Figure 2.7.

Derivation of the Correlators

Let us now discuss how the density-density correlations, the superfluid pair correlations, and the intra-chain Green's function can be expressed and evaluated in terms of PsBCs. The reader may skip these derivations on first reading and proceed with Subsection 2.3.2.

We start with the density-density correlations for which simple counting of fermion configurations in $|N, \alpha\rangle$ that are not annihilated by $n_i^x n_j^y$ yields

$$\langle x_i^\dagger x_i y_j^\dagger y_j \rangle = \begin{cases} \binom{L-1, L-1}{-\alpha}_{N-2} \binom{L, L}{\alpha}_N^{-1} & \text{for } x \neq y, \\ \binom{L-2, L}{\alpha}_{N-2} \binom{L, L}{\alpha}_N^{-1} & \text{for } x = y. \end{cases} \quad 2.41$$

Indeed, this follows from counting all fermion configurations in $|N, \alpha\rangle$ with occupied modes x_i and y_j , thereby reducing the number of fermions to be distributed to $N - 2$ and the number of available modes accordingly. The additional PsBC in each

row follows from the normalization $\mathcal{N}_{L,N,\alpha}^{-1}$. Note that for the inter-chain correlator, one fixes a single fermion on each chain, reducing the number of free modes to $L - 1$ per chain (and inverting the parity of the configurations to $-\alpha$ due to the excluded fermion). The intra-chain correlator, by contrast, fixes *two* fermions in one of the two chains, reducing its length to $L - 2$ without changing the parity (removing *two* fermions does not change the parity).

Along the same lines, counting configurations with occupied modes y_j and y_{j+1} and vacant modes x_i and x_{i+1} yields similar expressions for the superfluid pair correlations,

$$|\langle x_i^\dagger x_{i+1}^\dagger y_j y_{j+1} \rangle| = \begin{cases} \binom{L-2, L-2}{\alpha}_{N-2} \binom{L, L}{\alpha}_N^{-1} & \text{for } x \neq y, \\ \binom{L-4, L}{\alpha}_{N-2} \binom{L, L}{\alpha}_N^{-1} & \text{for } x = y. \end{cases} \quad 2.42$$

In the light of Eq. (2.41) and Eq. (2.42), it seems advisable to consider the general expression

$$\binom{L-l_1, L-l_2}{\alpha}_{N-m} \binom{L, L}{\beta}_N^{-1} \quad 2.43$$

in more detail.

Using the alternative form (2.34) and setting $N = 2L\rho$, one can derive the expression

$$\begin{aligned} & \binom{L-l_1, L-l_2}{\alpha}_{2L\rho-m} \binom{L, L}{\beta}_{2L\rho}^{-1} \\ &= \binom{2L-l_1-l_2}{2L\rho-m} \binom{2L}{2L\rho}^{-1} + \alpha \mathcal{O}(e^{-\lambda L}) + \beta \mathcal{O}(e^{-\mu L}) \end{aligned} \quad 2.44$$

which shows that any distinction due to the subparities α, β is suppressed exponentially. Straightforward simplifications for $L \rightarrow \infty$ lead to the final result

$$\begin{aligned} & \binom{L-l_1, L-l_2}{\alpha}_{2L\rho-m} \binom{L, L}{\beta}_{2L\rho}^{-1} \\ & \sim \rho^m (1-\rho)^{l_1+l_2-m} + \alpha \mathcal{O}(e^{-\lambda L}) + \beta \mathcal{O}(e^{-\mu L}). \end{aligned} \quad 2.45$$

The correlators from above follow now as special cases,

$$\langle x_i^\dagger x_i y_j^\dagger y_j \rangle = \rho^2 \quad 2.46a$$

$$\text{and } |\langle x_i^\dagger x_{i+1}^\dagger y_j y_{j+1} \rangle| = \rho^2 (1-\rho)^2, \quad 2.46b$$

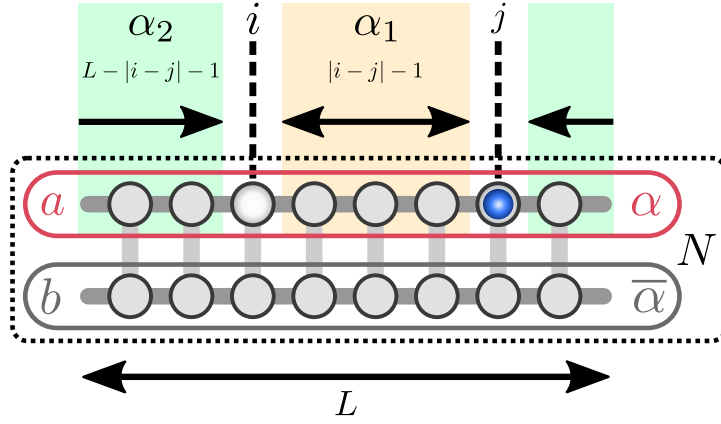


FIGURE 2.8 • Green’s function—Derivation. Partition for the derivation of the intra-chain Green’s function $\langle a_i^\dagger a_j \rangle$ of the zero-energy ground states $|N, \alpha\rangle$, used for counting states of fixed subsector parities α_1 and α_2 . The single-particle hopping from mode a_j to the (vacant) mode a_i measures the parity α_1 of the subsector between them (yellow).

up to exponential corrections depending on the subchain parity α of the ground state $|N, \alpha\rangle$. We stress that for both correlators, the pattern of fermions between⁵⁵ modes x_i and y_j can safely be ignored because either there is no hopping at all (as for $x_i^\dagger x_i y_j^\dagger y_j$), or hopping is restricted to that of bosonic *pairs* (as for $x_i^\dagger x_{i+1}^\dagger y_j y_{j+1}$). In either case, the fermionic parity of the modes between x_i and y_j drops out.

In the remainder of this subsection, we focus on the intra-chain Green’s function. Here, the derivation is more subtle since the parity of the single-chain segment separating the two support regions of the operators must be taken into account. For $j > i$ one finds

$$\langle a_i^\dagger a_j \rangle = \binom{L, L}{\alpha}_N^{-1} [\Lambda_{+1, -\alpha} - \Lambda_{-1, \alpha}] \quad 2.47$$

where

$$\Lambda_{\alpha_1, \alpha_2} = \binom{j - i - 1, L - j + i - 1, L}{\alpha_1, \alpha_2}_{N-1} \quad 2.48$$

is a PsBC with $g = 3$ segments. This follows from simple counting arguments and the convenient partition depicted in Figure 2.8:

$a_i^\dagger a_j$ chooses all states of the equal-weight superposition in $|N, \alpha\rangle$ with vacant mode a_i and occupied mode a_j . These states are not annihilated and contribute ± 1 to the result as there is exactly one dual state in $\langle N, \alpha|$ for each number state in $a_i^\dagger a_j |N, \alpha\rangle$. The sign of the contribution depends on the parity of the segment between mode a_i and a_j due to the fermion ordering from left to right along the chains (Figure 2.6). We therefore have to count all configurations of the $N - 1$ unaffected fermions (one is fixed by the hopping) on $g = 3$ segments:

⁵⁵“Between” is meant with respect to the fermion ordering in Figure 2.6.

- 1 The *first segment* has length $|i - j| - 1$ and parity α_1 and is bounded by the modes a_i and a_j .
- 2 The *second segment* comprises the rest of the upper chain of length $L - |i - j| - 1$ (excluding the modes a_i and a_j) with parity α_2 .
- 3 The *third segment* is the complete lower chain of length L with fixed parity $\bar{\alpha} = \alpha(-1)^N$.

The total parity of the first two segments is fixed to $\alpha_1\alpha_2 = -\alpha$ because a single fermion is excluded and used for the hopping. Therefore we find exactly $\Lambda_{+1,-\alpha}$ configurations which contribute $+1$ (i.e., the parity of the segment between a_i and a_j is $+1$) and $\Lambda_{-1,\alpha}$ configurations which contribute -1 . Divided by the total number of configurations in $|N, \alpha\rangle$, this yields the result in (2.47).

A numerical evaluation of this expression is given in Figure 2.7 and reveals the single-particle off-diagonal long-range order close to the boundaries of the ladder—a consequence of the fixed subchain parity. Note that the vanishing of the Green's function in the bulk for $1 \ll i \ll j \ll L$ is facilitated by the subtraction of $\Lambda_{+1,-\alpha}$ and $\Lambda_{-1,\alpha}$ in (2.47) where both terms are (almost) identical.

2.3.2 Symmetry Protection

The degeneracy of the (mean field) Majorana chain is robust in the presence of disorder that preserves the quadratic form of the Hamiltonian and is weak compared to the spectral gap. In our number-conserving setting, the topological protection of the ground state degeneracy is most conveniently characterized in terms of their *local indistinguishability* [226, 241]: Let \mathcal{O} denote an arbitrary local (Hermitian) operator and write $|\alpha\rangle = |N, \alpha\rangle$. Then, the expectation values $\langle \alpha | \mathcal{O} | \alpha \rangle$ and $\langle -\alpha | \mathcal{O} | -\alpha \rangle$ are identical up to an exponentially small correction—as follows from the above analysis of the correlation functions:

$$|\langle \alpha | \mathcal{O} | \alpha \rangle - \langle -\alpha | \mathcal{O} | -\alpha \rangle| \sim e^{-\lambda_1(\rho)L}. \quad 2.49$$

This is also evident because a *local* operator \mathcal{O} cannot discriminate between two states that differ only by a *global* property (the subchain parity α). The local indistinguishability of $|\pm 1\rangle$ renders superpositions

$$|\Psi\rangle = \Psi_+|+1\rangle + \Psi_-|-1\rangle \quad 2.50$$

resilient against *dephasing* due to local perturbations of the Hamiltonian; a necessary condition to realize a topologically protected qubit in the ground state space of H .

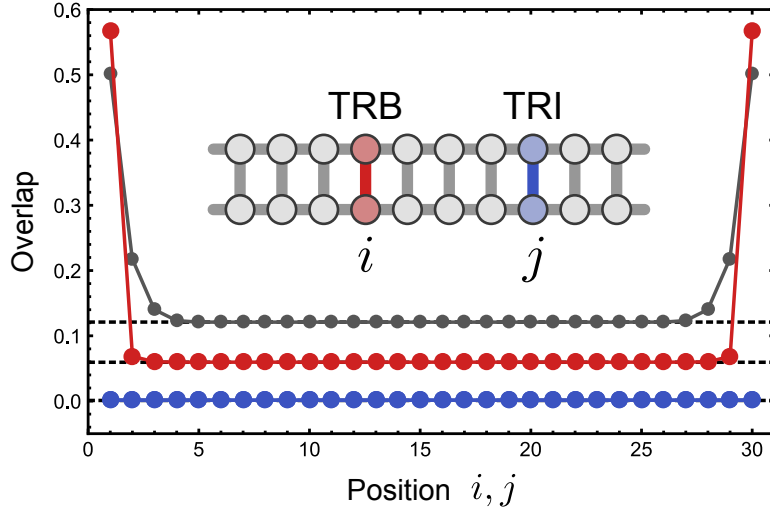


FIGURE 2.9 • Ground state properties—Symmetry protection. Overlap of the ground states $|\pm 1\rangle = |N, \pm 1\rangle$ for time-reversal invariant (TRI) and time-reversal breaking (TRB) perturbations $\mathcal{O}_j \propto h_j^\pm$ of H , in dependence of the position i, j of the subchain parity violating single-particle hopping (blue: $\rho = 0.5$ TRI, red: $\rho = 0.5$ TRB, gray: $\rho = 0.25$ TRB). Note that time-reversal invariant single-particle hopping does not create overlaps between the ground states.

However, it is not sufficient because operators that violate the subchain parity P_x can give rise to *depolarizing* perturbations of $|\Psi\rangle$. Thus, the overlap $\langle -\alpha | \mathcal{O} | \alpha \rangle$ must vanish,

$$|\langle -\alpha | \mathcal{O} | \alpha \rangle| \sim e^{-\lambda_2(\rho)L}, \quad 2.51$$

up to exponential corrections. Only if the states $|\pm 1\rangle$ are locally indistinguishable *and* cannot be mapped into each other by local operations, the ground state manifold $\text{span}\{|\pm 1\rangle\}$ is topologically degenerate and $|\Psi\rangle$ is protected from both dephasing and depolarization.

The evaluation of $\langle -\alpha | \mathcal{O} | \alpha \rangle$ is somewhat subtle. We illustrate this for the simplest case of a single-particle inter-chain hopping (the statements can be generalized to more complex P_x -violating terms, though). Consider a site-dependent perturbation $\mathcal{O} = \mathcal{O}_j$ which is given as

$$\mathcal{O}_j = e^{i\phi_j} a_j^\dagger b_j + e^{-i\phi_j} b_j^\dagger a_j \quad 2.52$$

with complex hopping phase $\phi_j \in [0, 2\pi)$. If we split this perturbation into time-reversal invariant (TRI) and time-reversal breaking (TRB) contributions,

$$\mathcal{O}_j = \underbrace{\cos(\phi_j) (a_j^\dagger b_j + b_j^\dagger a_j)}_{\equiv h_j^+ \text{ (TRI)}} + i \underbrace{\sin(\phi_j) (a_j^\dagger b_j - b_j^\dagger a_j)}_{\equiv h_j^- \text{ (TRB)}}, \quad 2.53$$

one finds by evaluating the corresponding PsBCs (see below)

$$\text{TRI} : \langle -\alpha | h_\delta^+ | \alpha \rangle \rightarrow 0 \quad 2.54a$$

$$\text{TRB} : \langle -\alpha | h_\delta^- | \alpha \rangle \rightarrow e^{-\mu(\rho)\delta} \quad 2.54b$$

for the distance $\delta \ll L$ from the edges of the ladder, when $L \rightarrow \infty$ and ρ is fixed. These site-dependent overlaps are illustrated in Figure 2.9. Surprisingly, single-particle hopping between the chains does *not* lead to a lifting of the ground state degeneracy in leading order, if the coupling is time-reversal invariant, Eq. (2.54a). And even when the symmetry is broken, only hopping close to the edges creates relevant overlaps between the two ground states, Eq. (2.54b).

The upshot is that the topological ground state degeneracy for the double-wire setup can be protected *either* by time-reversal symmetry T or subchain parity P_x , and is only spoiled if both symmetries are broken at the same time. That the degeneracy can be lifted by symmetry-breaking perturbations at the boundary is not surprising as the two edge states on the upper and lower wire are not spatially separated⁵⁶. We will show in Subsection 2.5.1 that the Hamiltonian (2.12) can be generalized to wire networks where the edge states *are* spatially separated. Then it follows immediately that their topological degeneracy is protected against any local operator \mathcal{O} conserving the total number of particles.

Derivation of the Overlaps

Here we conclude the previous discussion with a derivation of the overlaps due to subchain parity violating single-particle hopping between the chains. The reader may skip this derivation on first reading and proceed with Subsection 2.3.3.

We are interested in $\langle -\alpha | h_j^\pm | \alpha \rangle$ as defined in (2.53). This reduces to the computation of the inter-chain single-particle correlators

$$\langle -\alpha | a_i^\dagger b_j | \alpha \rangle \quad \text{and} \quad \langle -\alpha | b_j^\dagger a_i | \alpha \rangle, \quad 2.55$$

where we consider independent sites i and j to demonstrate the generality of the following approach:

Splitting the double-chain into $g = 4$ segments, as sketched in Figure 2.10, allows for an evaluation similar to the intra-chain Green's function. Indeed, counting fermion configurations with one of the sites i, j empty and the other occupied, sorting them according to their subsegment parities α_i ($i = 1, 2, 3$) yields the

⁵⁶This situation is similar to that of two parallel Majorana chains, each in the topological phase with winding number $\nu = +1$. Then, a time-reversal breaking coupling between the adjacent edge modes lifts their degeneracy. In the non-interacting case, this is a manifestation of the difference between symmetry class **BDI** with a \mathbb{Z} topological index and unbroken time-reversal symmetry, and class **D** with a \mathbb{Z}_2 invariant and broken time-reversal symmetry [22, 97].

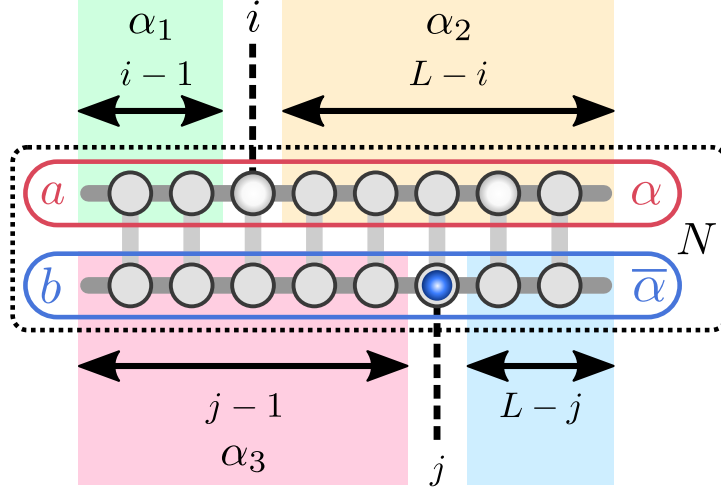


FIGURE 2.10 • Symmetry protection—Derivation. The partition used for the derivation of the inter-chain single-particle overlap $\langle N, -\alpha | a_i^\dagger b_j | N, \alpha \rangle$. The single-particle hopping between site j and the (vacant) site i measures the combined parity $\alpha_2 \alpha_3$ of two segments (yellow and red) due to the fermion gauge in Figure 2.6. The results can be expressed in terms of PsBCs and are described in the text.

expression

$$\begin{aligned} \langle -\alpha | a_i^\dagger b_j | \alpha \rangle &= \binom{L, L}{\alpha}_N^{-1/2} \binom{L, L}{-\alpha}_N^{-1/2} \\ &\times [\Lambda_{\alpha, +1, +1} + \Lambda_{-\alpha, -1, -1} - \Lambda_{\alpha, +1, -1} - \Lambda_{-\alpha, -1, +1}] \end{aligned} \quad 2.56$$

with the $g = 4$ split PsBCs

$$\Lambda_{\alpha_1, \alpha_2, \alpha_3} = \binom{i-1, L-i, j-1, L-j}{\alpha_1, \alpha_2, \alpha_3}_{N-1}. \quad 2.57$$

The special case $i = j$ allows us to write

$$\begin{aligned} \langle -\alpha | h_j^\pm | \alpha \rangle &\propto [\Lambda_{\alpha, +1, +1} + \Lambda_{-\alpha, -1, -1} - \Lambda_{\alpha, +1, -1} - \Lambda_{-\alpha, -1, +1}] \\ &\pm [\Lambda_{\alpha, -1, -1} + \Lambda_{-\alpha, +1, +1} - \Lambda_{-\alpha, +1, -1} - \Lambda_{\alpha, -1, +1}] \end{aligned} \quad 2.58$$

for the overlaps due to time-reversal invariant/breaking perturbations h_j^\pm .

Doing the math yields for the *time-reversal invariant* perturbation

$$\langle -\alpha | h_j^+ | \alpha \rangle \propto \sum_{n_1, n_2, n_3=0}^{N-1} \binom{L-j}{N-1-n_1-n_2-n_3} \times \binom{j-1}{n_1} \binom{L-j}{n_2} \binom{j-1}{n_3} (-1)^{n_2+n_3} \quad 2.59a$$

$$= \frac{1 - (-1)^N}{2} (-1)^{\frac{N-1}{2}} \binom{L-1}{\frac{N-1}{2}}. \quad 2.59b$$

Incorporating the normalizing factors, we get as final result

$$\langle -\alpha | h_j^+ | \alpha \rangle = [1 - (-1)^N] (-1)^{\frac{N-1}{2}} \binom{L-1}{\frac{N-1}{2}} \binom{2L}{N}^{-1} \quad 2.60a$$

$$\sim [1 - (-1)^N] (-1)^{\frac{N-1}{2}} \mathcal{O}(e^{-\lambda(\rho)L}) \quad 2.60b$$

for $N = 2\rho L$ and $L \rightarrow \infty$; here we used Eq. (2.33) for the normalizing factors. As result, we find that the overlap of the two ground states $|\pm 1\rangle$ due to subchain parity violating but time-reversal invariant perturbations h_j^\pm vanishes—identically for even fillings, and up to exponential corrections for odd fillings.

Finally, an analogous calculation for the *time-reversal breaking* hopping yields

$$\langle -\alpha | h_j^- | \alpha \rangle \propto \alpha \sum_{n_1, n_2, n_3=0}^{N-1} \binom{L-j}{N-1-n_1-n_2-n_3} \times \binom{j-1}{n_1} \binom{L-j}{n_2} \binom{j-1}{n_3} (-1)^{n_1+n_3} \quad 2.61a$$

$$= \alpha \sum_{n=0}^{N-1} (-1)^n \binom{2j-2}{n} \binom{2L-2j}{N-1-n} \quad 2.61b$$

which then gives rise to the lengthy expression

$$\langle -\alpha | h_j^- | \alpha \rangle = 2\alpha \left[\binom{2L}{N}^2 - \frac{1 + (-1)^N}{2} \binom{L}{\frac{N}{2}}^2 \right]^{-1/2} \times \sum_{n=0}^{N-1} (-1)^n \binom{2j-2}{n} \binom{2L-2j}{N-1-n}. \quad 2.62$$

In contrast to (2.59b), here the dependence on site j does *not* drop out.

A numerical evaluation of (2.62) is given in Figure 2.9. For fixed density ρ and large L , one finds exponentially decaying overlaps in the bulk (the localization length depends on ρ and vanishes at half-filling) but finite values for j close to the

edges, i.e., for $j \approx 1, L$. This is derived easily in the odd filling sector where for $j = 1, L$ the term in (2.62) simplifies to

$$|\langle -\alpha | h_{1,L}^- | \alpha \rangle| = 2 \binom{2L-2}{N-1} \binom{2L}{N}^{-1} \quad 2.63a$$

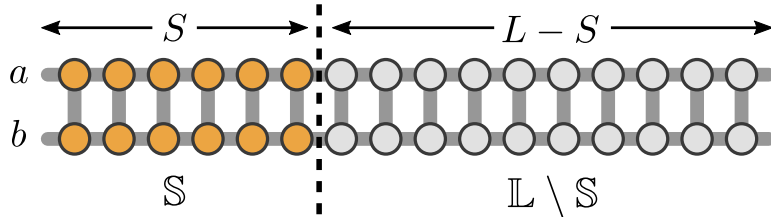
$$\sim 2\rho(1-\rho) \quad \text{for } L \rightarrow \infty, \quad 2.63b$$

which reaches its maximum $\frac{1}{2}$ at half-filling $\rho = \frac{1}{2}$ where the edge states and their overlaps are perfectly localized on the boundary sites $j = 1, L$.

Note that $|\langle -\alpha | h_{1,L}^- | \alpha \rangle| < 1$ tells us that the two ground states *cannot* be mapped into each other by a unitary located at one of the boundary sites. This is in stark contrast to the mean field Majorana chain where such a mapping is realized by the Majorana operators γ_1 and γ_{2L} on the edges (the *edge modes*); see Subsection 1.2.2 and ✨ Section 2.D for more details.

2.3.3 Entanglement Spectrum and Entropy

Besides their local indistinguishability, another well-known signature of topological states is a stable degeneracy of their *entanglement spectrum* (ES) [111, 242, 243]. The latter encodes information on the entanglement structure of a state (here, the ground states $|N, \alpha\rangle$) with respect to a bipartition ($\mathbb{S}|\bar{\mathbb{S}}$) of the total system \mathbb{L} into a subsystem \mathbb{S} and the “rest” $\bar{\mathbb{S}} = \mathbb{L} \setminus \mathbb{S}$. In our case, we split the ladder into two pieces of size S and $L - S$, respectively:



Let $|n, \alpha\rangle_{\mathbb{X}}$ be the (normalized) equal-weight superposition on the system \mathbb{X} for $\mathbb{X} \in \{\mathbb{S}, \mathbb{L} \setminus \mathbb{S}, \mathbb{L}\}$; the states are clearly orthonormal, $\langle n, \alpha | m, \beta \rangle_{\mathbb{X}} = \delta_{n,m} \delta_{\alpha,\beta}$. It is then easy to see that the state of the complete chain $|N, \alpha\rangle = |N, \alpha\rangle_{\mathbb{L}}$ can be decomposed as follows:

$$|N, \alpha\rangle_{\mathbb{L}} = \sum_n \sum_{\beta=\pm 1} \lambda_{n,\beta} |n, \beta\rangle_{\mathbb{S}} |N-n, \alpha\beta\rangle_{\mathbb{L} \setminus \mathbb{S}}. \quad 2.64$$

This is called the *Schmidt decomposition* of $|N, \alpha\rangle$ with *Schmidt coefficients*

$$\lambda_{n,\beta} = \sqrt{\frac{\mathcal{N}_{S,n,\beta} \times \mathcal{N}_{L-S,N-n,\alpha\beta}}{\mathcal{N}_{L,N,\alpha}}}, \quad 2.65$$

GROUND STATE PROPERTIES

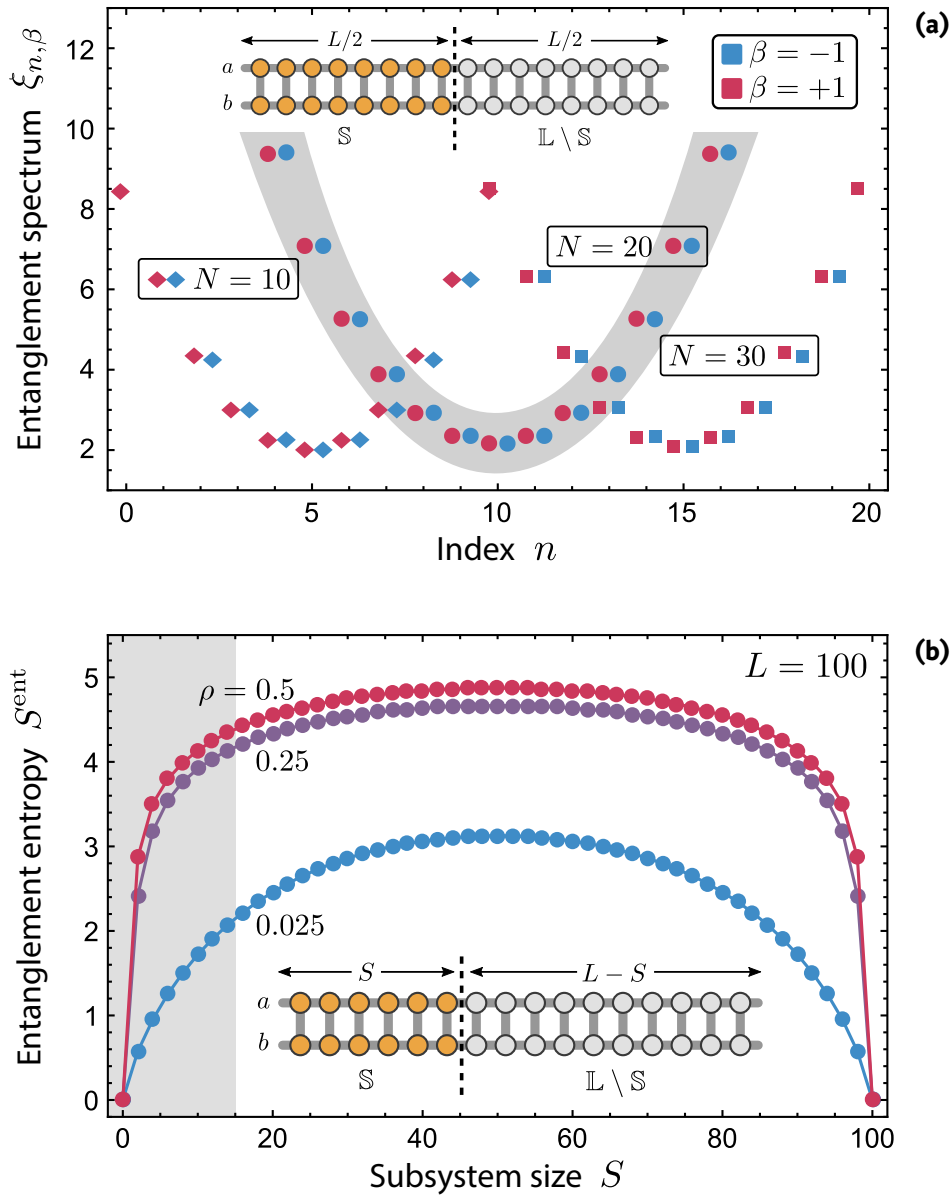


FIGURE 2.11 • Ground state entanglement. (a) The two branches ($\beta = \pm 1$: red/blue) of the entanglement spectrum $\{\xi_{n,\beta}\}$ for a chain of length $L = 20$ and subsystem size $S = 10$ with fillings $N = 10, 20, 30$ (diamonds, circles, squares). The values for half-filling are highlighted gray and the two branches $\beta = \pm 1$ are shifted by ∓ 0.25 in n -direction for reasons of clarity. Physically, the index n describes the subsystem filling and β the subsystem subchain parity. Note the two-fold degeneracy of the entanglement spectrum. (b) The entanglement entropy $S^{\text{ent}} = S^{\text{ent}}[S]$ as a function of the subsystem size S for various densities ρ . It obeys an area law $S^{\text{ent}} \sim \ln S + \text{const}$ with logarithmic corrections for $S \ll L$ (gray region). Note that generic (e.g., random) states typically exhibit a volume law $S^{\text{ent}} \sim S + \text{const}$ instead—as naively expected for an extensive quantity like entropy.

which follows because the states $|\bullet, \bullet\rangle_{\mathbb{X}}$ on the right-hand side of Eq. (2.64) must be “un-normalized” to make the sum *equal-weight* (before the total sum is “re-normalized” again). Then, the entanglement spectrum $\{\xi_{n,\beta}\}$ is defined as [242]

$$e^{-\xi_{n,\beta}/2} = \lambda_{n,\beta} \quad \Leftrightarrow \quad \xi_{n,\beta} = \ln \lambda_{n,\beta}^{-2} \quad 2.66$$

and can be written in terms of PsBCs [recall Eq. (2.35)]

$$\xi_{n,\beta} = -\ln \left[\binom{L-S, L-S}{\alpha\beta}_{N-n} \binom{S, S}{\beta}_n / \binom{L, L}{\alpha}_N \right] \quad 2.67$$

where $\max\{0, N - 2L + 2S\} \leq n \leq \min\{N, 2S\}$ and $\beta = \pm 1$. Note that the PsBCs all describe partitions into $g = 2$ segments of equal length and can therefore be evaluated with Eq. (2.33).

The $\beta = \pm 1$ -branches of the spectra for a half-split ($S = L/2$) system of length $L = 20$ are plotted in Figure 2.11 (a) for different fillings N . They reveal a two-fold degeneracy of the entanglement spectrum due to the subsystem subchain parity β , consistent with the topological degeneracy of the ground states. Note that the minimum of the parabolic spectrum $\xi_{n,\beta}$ corresponds to the largest Schmidt coefficients $\lambda_{n,\beta}$, Eq. (2.66). E.g, for a chain at half-filling with $L = 20$ and $N = 20$, the Schmidt coefficients identify $|n = 10, \pm 1\rangle_{\mathbb{S}} |10, \pm \alpha\rangle_{\mathbb{L} \setminus \mathbb{S}}$ as the states of highest weight (which makes sense because these comprise many possible fermion configurations, as compared to, say, $|n = 20, +1\rangle_{\mathbb{S}} |0, +1\rangle_{\mathbb{L} \setminus \mathbb{S}}$ which describes a single fermion configuration only).

The structured information of the entanglement spectrum can be distilled into a single quantity dubbed *entanglement entropy* $S^{\text{ent}}[\mathbb{S}]$. It is conventionally defined as

$$S^{\text{ent}}[\mathbb{S}] \equiv -\text{Tr} [\rho_{\mathbb{S}} \ln \rho_{\mathbb{S}}] , \quad 2.68$$

with the reduced density matrix $\rho_{\mathbb{S}} = \text{Tr}_{\mathbb{L} \setminus \mathbb{S}} [\rho]$ and $\rho = |N, \alpha\rangle\langle N, \alpha|$. $S^{\text{ent}}[\mathbb{S}]$ quantifies the amount of entanglement shared between the subsystem \mathbb{S} and the rest of the system (in particular, it vanishes for unentangled product states), and its scaling with the subsystem size S yields insight into the low-energy physics of the theory. $S^{\text{ent}}[\mathbb{S}]$ derives directly from the entanglement spectrum via

$$S^{\text{ent}}[\mathbb{S}] = \sum_{n,\beta} e^{-\xi_{n,\beta}} \xi_{n,\beta} . \quad 2.69$$

Figure 2.11 (b) shows the (filling dependent) variation of entanglement between a subsystem \mathbb{S} and its environmental system $\mathbb{L} \setminus \mathbb{S}$ as function of the subsystem size S : The entanglement entropy obeys an *area law* with logarithmic corrections, $S^{\text{ent}}[\mathbb{S}] \sim \ln S + \text{const}$, as expected for a critical (gapless) one-dimensional system [244]. That is, in contrast to the gapped Majorana chain (where $S^{\text{ent}} = \text{const}$ is independent of S), here we face a low-energy theory of gapless Goldstone modes due to particle number conservation. With this in mind, we have a closer look at the low-energy excitations of H in Section 2.4.

2.4 Low-Energy Excitations

Here we focus on the low-energy physics of the double-wire setup. In Subsection 2.4.1, we construct a class of exact eigenstates with arbitrary filling and subchain parity; their quadratic spectrum proves the gaplessness of the complete spectrum. In Subsection 2.4.2, we discuss the scaling of the gap in the thermodynamic limit for open and closed boundary conditions in the two subchain-parity sectors. To this end, we combine rigorous estimates on the gap with numerical results from density matrix renormalization group simulations.

2.4.1 A Class of Exact Eigenstates

So far, the only exact eigenstates of the interacting many-body Hamiltonian $H = H^a + H^b + H^{ab}$ in (2.12) are the zero-energy ground states $|N, \alpha\rangle$ (for open boundary conditions). In the following, we present a submanifold of *excited* eigenstates with quadratic spectrum, the derivation of which is presented below. The crucial observation that grants access to more than just the ground states is the following:

The single-chain Hamiltonians H^x ($x = a, b$) for a ladder with open boundaries can be mapped to the ferromagnetic, isotropic Heisenberg model via Jordan-Wigner transformation. The complete spectrum of H^x is therefore accessible via the Bethe ansatz [245], see also § Section 2.C. Exploiting this mapping, it is possible to construct the analog of single-magnon states for the full Hamiltonian H (see below). These exact low-energy eigenstates for the open *double-chain* take the (unnormalized) form

$$|k; N, \alpha\rangle = P_1^a(k) \oplus P_1^b(k) |N, \alpha\rangle \quad 2.70$$

with momentum $k = m\frac{\pi}{L}$, $0 \leq m < L$, and the operator

$$P_1^x(k) = \sum_{j=1}^L \cos\left[\frac{k}{2}(2j-1)\right] (-1)^{x_j^\dagger x_j}. \quad 2.71$$

In particular, $|0; N, \alpha\rangle \propto |N, \alpha\rangle$ is a zero-energy ground state. The eigenenergies are given by a quadratic excitation spectrum

$$E_k = 4 \sin^2\left(\frac{k}{2}\right), \quad 2.72$$

and the gap between ground and lowest excited states vanishes in the thermodynamic limit: $\lim_{L \rightarrow \infty} E_{k_1} = 0$ for $k_1 = \frac{\pi}{L}$. The eigenstates (2.70) correspond to the *Goldstone mode* of the single-chain Hamiltonians due to the broken $SU(2)$

symmetry (see below) in sectors with fixed particle number⁵⁷. Their presence is in excellent agreement with the appearance of a true condensate and vanishing compressibility⁵⁸. An equivalent behavior is well known for non-interacting bosons and the ferromagnetic Heisenberg model in one-dimension. We conclude that the exactly solvable Hamiltonian H describes a *critical* system (on the brink of phase separation, see Ref. [248]).

Derivation of the Eigenstates

The derivation of the results (2.70), (2.71) and (2.72) is presented in four steps: First, we show that a Jordan-Wigner transformation maps the fermionic theory with open boundaries to a local spin- $\frac{1}{2}$ model of two interacting Heisenberg chains. Second, we focus on the spin-equivalent of H^x and derive its single-magnon excitations. In a third step, we show how the global SU(2) symmetry of the Heisenberg model allows us to “lift” these excited states into sectors of arbitrary filling N . The final step combines these results to construct a chain-symmetric analogue of these states on the double-chain; we prove that these are eigenstates of H , despite the chain coupling H^{ab} . The reader may skip this derivation on first reading and proceed with Subsection 2.4.2.

Jordan-Wigner Transformation

The Jordan-Wigner transformation defines a representation ρ of the fermion algebra generated by $\{a_i, b_i, a_i^\dagger, b_i^\dagger \mid i = 1, \dots, L\}$ on the Hilbert space $\mathcal{H} = \bigotimes_i^{2L} \mathbb{C}_i^2$ in terms of the spin- $\frac{1}{2}$ representations of $2L$ spins σ_i^α and $\hat{\sigma}_i^\alpha$ for $\alpha = x, y, z$ and $i = 1, \dots, L$. Here the spins σ_i ($\hat{\sigma}_i$) correspond to the fermions on the upper (lower) chain a (b). The Jordan-Wigner transformation is then given by

$$\rho(a_i) = \left[\prod_{k=1}^{i-1} \sigma_k^z \right] \sigma_i^+ \quad 2.73a$$

$$\rho(b_i) = \left[\prod_{k=1}^L \sigma_k^z \right] \times \left[\prod_{k=1}^{i-1} \hat{\sigma}_k^z \right] \hat{\sigma}_i^+ \quad 2.73b$$

where $\sigma_j^\pm = \frac{1}{2}(\sigma_j^x \pm i\sigma_j^y)$. The mapping for the lower-chain fermions b_i takes the fermion ordering in Figure 2.6 into account.

⁵⁷Although for fixed particle number (=magnetization) *two* generators of SU(2) are broken, there is only *one* Goldstone mode due to the non-relativistic, *quadratic* dispersion $E_k \propto \sin^2(k/2)$ [246, 247].

⁵⁸Recall that for any fixed number of particles there are zero-energy ground states.

The transformation (2.73) implies

$$\rho(n_i^a) = \frac{1}{2}(\mathbb{1} - \sigma_i^z) \quad 2.74a$$

$$\rho(a_i^\dagger a_{i+1} + a_{i+1}^\dagger a_i) = \frac{1}{2}(\sigma_i^x \sigma_{i+1}^x + \sigma_i^y \sigma_{i+1}^y). \quad 2.74b$$

An application of these transformations on the single-chain Hamiltonian H^a yields

$$\rho(H^a) = -\sum_{i=1}^{L-1} \left[\sigma_i^- \sigma_{i+1}^+ + \sigma_i^+ \sigma_{i+1}^- - \frac{1}{2}(1 - \sigma_i^z \sigma_{i+1}^z) \right] \quad 2.75a$$

$$= -2 \sum_{i=1}^{L-1} \mathbf{S}_i \mathbf{S}_{i+1} + \frac{L-1}{2}, \quad 2.75b$$

which is just the ferromagnetic, isotropic Heisenberg model for an open chain of L spins $\mathbf{S}_i = \frac{1}{2}\boldsymbol{\sigma}_i$ (with shifted energy). For H^b , we have the same expression with $\sigma \mapsto \hat{\sigma}$ for spins on the lower chain. We stress that this mapping becomes invalid⁵⁹ for *periodic* boundaries in the even-subchain-parity sector $\alpha = +1$ due to the sign for fermions traveling around the chain, see \clubsuit Section 2.C.

The inter-chain interaction H^{ab} translates into the intimidating Hamiltonian

$$\rho(H^{ab}) = -\sum_{i=1}^{L-1} \left\{ \begin{array}{c} \sigma_i^- \sigma_{i+1}^- \hat{\sigma}_i^+ \hat{\sigma}_{i+1}^+ + \sigma_i^+ \sigma_{i+1}^+ \hat{\sigma}_i^- \hat{\sigma}_{i+1}^- \\ -\frac{1 - \sigma_i^z}{2} \frac{1 - \sigma_{i+1}^z}{2} \frac{1 + \hat{\sigma}_i^z}{2} \frac{1 + \hat{\sigma}_{i+1}^z}{2} \\ -\frac{1 - \hat{\sigma}_i^z}{2} \frac{1 - \hat{\sigma}_{i+1}^z}{2} \frac{1 + \sigma_i^z}{2} \frac{1 + \sigma_{i+1}^z}{2} \end{array} \right\} \quad 2.76$$

coupling both chains with four-spin interactions. Fortunately, we only need it in the last step and can ignore it for the time being.

Before we proceed, let us note that $\rho(n_i^a) = \frac{1}{2}(\mathbb{1} - \sigma_i^z)$ implies

$$\rho(N^a) = \sum_{i=1}^L \rho(n_i^a) = \frac{L}{2} - \frac{1}{2} \sum_{i=1}^L \sigma_i^z = \frac{L}{2} - S^z, \quad 2.77$$

so that the fermion filling $N^a = \sum_i n_i^a$ of chain a and the total magnetization S^z can be identified (similarly for N^b and \hat{S}^z). In the following, we omit the explicit application of ρ and use spin and fermion representation interchangeably.

⁵⁹Here we focus completely on open boundaries. For *closed* boundaries, the results presented in the following apply only to double-chains with even filling N and odd subchain parity α . Only then, the mapping to the Heisenberg Hamiltonian remains valid on *both* chains. See also Subsection 2.4.2 for the low-energy properties of chains with periodic boundaries.

Single-Particle Excitations

The isotropic Heisenberg model (2.75) is well known to be solvable by the Bethe ansatz [245]. So let us focus on the single-chain Hamiltonian H^x for now (w.l.o.g. $x = a$). The isotropic Heisenberg Hamiltonian features a global $SU(2)$ spin-rotation symmetry. In particular, $[H^a, S^z] = 0$, such that the total magnetization is conserved (this corresponds to the number conservation of the fermionic model). Therefore, H^a can be diagonalized in sectors \mathcal{H}_{N^a} of $\mathcal{H} = \bigoplus_{N^a} \mathcal{H}_{N^a}$ with well-defined magnetization/filling. The simplest, non-trivial sector \mathcal{H}_1 is spanned by the L “single-particle” states

$$|n\rangle = |\uparrow, \dots, \downarrow, \dots, \uparrow\rangle \stackrel{\rho}{\leftrightarrow} a_n^\dagger |0\rangle \quad 2.78$$

of a single flipped spin at site n . A generic state $|\Psi\rangle \in \mathcal{H}_1$ reads

$$|\Psi\rangle = \sum_{n=1}^L \psi(n) |n\rangle, \quad 2.79$$

and we are looking for eigenstates with eigenvalue E ,

$$H^a |\Psi\rangle = E |\Psi\rangle. \quad 2.80$$

Plugging (2.79) and (2.75) in (2.80) yields

$$H^a |\Psi\rangle = \sum_{i=1}^{L-1} \sum_{n=1}^L \psi(n) H_i^a |n\rangle \quad 2.81a$$

$$= \sum_{i=1}^{L-1} \sum_{n=1}^L \psi(n) \left\{ \begin{array}{l} \delta_{i,n} |n\rangle + \delta_{i,n-1} |n\rangle \\ -\delta_{i,n} |n+1\rangle - \delta_{i,n-1} |n-1\rangle \end{array} \right\} \quad 2.81b$$

$$= \sum_{i=1}^{L-1} \left\{ \begin{array}{l} \psi(i) |i\rangle + \psi(i+1) |i+1\rangle \\ -\psi(i) |i+1\rangle - \psi(i+1) |i\rangle \end{array} \right\} \quad 2.81c$$

$$= [\psi(1) - \psi(2)] |1\rangle + [\psi(L) - \psi(L-1)] |L\rangle \\ + \sum_{n=2}^{L-1} [2\psi(n) - \psi(n+1) - \psi(n-1)] |n\rangle \quad 2.81d$$

$$\stackrel{!}{=} E \sum_{n=1}^L \psi(n) |n\rangle, \quad 2.81e$$

where we rearranged the sum in the fourth row to separate the edge terms from the bulk terms (only the latter remain for *periodic* boundary conditions). Thus, for $|\Psi\rangle$ to be an eigenstate, the following three equations must be satisfied ($2 \leq n \leq L-1$):

$$E\psi(n) = 2\psi(n) - \psi(n-1) - \psi(n+1), \quad 2.82a$$

$$E\psi(1) = \psi(1) - \psi(2), \quad 2.82b$$

$$E\psi(L) = \psi(L) - \psi(L-1). \quad 2.82c$$

Eq. (2.82a) can easily be solved with the ansatz $\psi(n) = A e^{ikn}$ if

$$E = 2 - e^{-ik} - e^{ik} = 2[1 - \cos(k)] = 4 \sin^2\left(\frac{k}{2}\right) \equiv E_k, \quad 2.83$$

which already determines the functional form of the spectrum (so far, $k \in \mathbb{R}$ is unrestricted). To satisfy the boundary conditions (2.82b) and (2.82c), we make the ansatz

$$\Psi(n) = e^{ik(n-\frac{1}{2})} + e^{-ik(n-\frac{1}{2})}. \quad 2.84$$

Here we use $E_k = E_{-k}$ so that (2.82a) is still satisfied. A straightforward calculation shows that (2.82b) is automatically satisfied and does not constrain k . Plugging (2.84) into (2.82c) yields

$$E = 2 - \frac{\left(e^{-i\frac{k}{2}} + e^{i\frac{k}{2}}\right) e^{-ik} + \left(e^{-i\frac{k}{2}} + e^{i\frac{k}{2}}\right) e^{-2ikL} e^{ik}}{e^{-i\frac{k}{2}} + e^{-2ikL} e^{i\frac{k}{2}}} \quad 2.85a$$

$$\stackrel{!}{=} 2 - \left(e^{-ik} + e^{ik}\right) = E_k, \quad 2.85b$$

which simplifies to E_k if and only if $e^{-2ikL} = 1$, viz. $k = \frac{\pi}{L}\mathbb{Z}$. This determines the L eigenvalues E_k with $k = m\frac{\pi}{L}$ for $0 \leq m < L$, and we conclude that the (unnormalized) single-particle eigenstates of $\{\rho(H^a), H^a\}$ are given by

$$|k; 1\rangle \equiv \sum_{n=1}^L \underbrace{\cos\left[\frac{k}{2}(2n-1)\right]}_{\equiv \psi_k(n)} \{|n\rangle, a_n^\dagger|0\rangle\} \quad 2.86$$

with momentum $k = m\frac{\pi}{L}$ ($0 \leq m < L$). In the context of the Heisenberg model, $|k; 1\rangle$ describes *single-magnon excitations* of the spin chain.

The above procedure works similarly in the other sectors with $N^a > 1$ where, however, the analogue of Eq. (2.82) becomes much more complicated. Solutions are given by the Bethe ansatz [245], which we apply in \clubsuit Section 2.C to the $N = 2$ -particle sector of the double-chain.

Lifting Excitations on a Single-Chain

Given the single-magnon excitations in the $N = 1$ -sector⁶⁰, we show next how they can be “lifted” into sectors of arbitrary magnetization/filling $N > 1$. To illustrate the generality of the following approach, we start with a generic N -magnon eigenstate and return to the special case $N = 1$ later. For H^x , the general eigenvectors for fixed magnetization/particle number N can be written as

$$|\{\lambda_i\}; N\rangle = \sum_{n_1 < \dots < n_N} \psi_{\{\lambda_i\}}(n_1, \dots, n_N) |n_1, \dots, n_N\rangle \quad 2.87$$

with Bethe quantum numbers λ_i , $i = 1, \dots, N$, and eigenenergy $E(\{\lambda_i\})$ (this includes both *scattering* and *bound* states). Here, $|n_1, \dots, n_N\rangle$ denotes the product state with N flipped spins $|\downarrow\rangle$ at sites $n_1 < n_2 < \dots < n_N$. As H^x is just the isotropic Heisenberg Hamiltonian, there is a global $U(2) = [U(1) \times SU(2)]/\mathbb{Z}_2$ symmetry⁶¹ which can be utilized to construct eigenstates in sectors with arbitrary magnetization/filling by “lifting” eigenstates from lower ones.

To this end, assume that we found an exact eigenstate $|\{\lambda_i\}; N^*\rangle$ by solving the Bethe equations ($0 \leq N^* \leq L$ arbitrary). We introduce the Hadamard gate

$$\tilde{H} = \frac{1}{\sqrt{2}} \begin{bmatrix} 1 & 1 \\ 1 & -1 \end{bmatrix} \quad 2.88$$

and the phase gate

$$R_\varphi = \begin{bmatrix} e^{-i\varphi/2} & 0 \\ 0 & e^{i\varphi/2} \end{bmatrix}, \quad 2.89$$

both of which clearly belong to the fundamental representation of $U(2)$ on \mathbb{C}^2 . Obviously

$$R_\varphi \tilde{H} |\uparrow, \downarrow\rangle = \frac{1}{\sqrt{2}} \left[e^{-i\varphi/2} |\uparrow\rangle \pm e^{i\varphi/2} |\downarrow\rangle \right]. \quad 2.90$$

Let now $\hat{H} \equiv \bigotimes_{i=1}^L \tilde{H}^i$ and $\hat{R}_\varphi \equiv \bigotimes_{i=1}^L R_\varphi^i$ act globally on the chain. Then $\hat{R}_\varphi \hat{H} \in U(2)$ (now realized on $\bigotimes_{i=1}^L \mathbb{C}_i^2$ as product representation) and

$$\left[\hat{R}_\varphi \hat{H}, H^x \right] = 0 \quad 2.91$$

characterizes a symmetry of the Hamiltonian H^x . Therefore

$$|\{\lambda_i\}; N^*\rangle_\varphi \equiv \hat{R}_\varphi \hat{H} |\{\lambda_i\}; N^*\rangle \quad 2.92$$

is still an eigenvector of H^x with the same eigenvalue for any φ .

⁶⁰To tidy up our notation, we omit the superscript and write $N = N^a$.

⁶¹This is easy to see: Each term in H^x has the isotropic Heisenberg form $\sigma_i \sigma_{i+1} = \sigma_i^\alpha \otimes \sigma_{i+1}^\alpha$. A global unitary $U = u \otimes \dots \otimes u \in U(2)$ acts on each spin as $u \sigma_i^\alpha u^\dagger = u^{\alpha\beta} \sigma_i^\beta$ where $u^{\alpha\beta}$ is an orthogonal matrix. Then, it follows $U H^x U^\dagger = H^x$ because for each term $u \sigma_i^\alpha u^\dagger \otimes u \sigma_{i+1}^\alpha u^\dagger = (u^{\alpha\beta} u^{\alpha\gamma}) \sigma_i^\beta \otimes \sigma_{i+1}^\gamma = \sigma_i^\beta \otimes \sigma_{i+1}^\beta = \sigma_i \sigma_{i+1}$.

LOW-ENERGY EXCITATIONS

Let us have a closer look at the generic product state $|n_1, \dots, n_{N^*}\rangle$ with N^* flipped spins:

$$\begin{aligned} \hat{R}_\varphi \hat{H} |n_1, \dots, n_{N^*}\rangle &= \frac{1}{2^{L/2}} \bigotimes_{n \in \{n_1, \dots, n_{N^*}\}} \left[e^{-i\varphi/2} |\uparrow\rangle_n - e^{i\varphi/2} |\downarrow\rangle_n \right] \\ &\quad \otimes \bigotimes_{n \notin \{n_1, \dots, n_{N^*}\}} \left[e^{-i\varphi/2} |\uparrow\rangle_n + e^{i\varphi/2} |\downarrow\rangle_n \right] \end{aligned} \quad 2.93$$

which can be written as

$$\begin{aligned} &\hat{R}_\varphi \hat{H} |n_1, \dots, n_{N^*}\rangle \\ &= \frac{1}{2^{L/2}} \prod_{n \in \{n_1, \dots, n_{N^*}\}} \sigma_n^z \bigotimes_m \left[e^{-i\varphi/2} |\uparrow\rangle_m + e^{i\varphi/2} |\downarrow\rangle_m \right]. \end{aligned} \quad 2.94$$

Expanding the tensor product yields a sum over all possible combinations of up- and down-spins, namely

$$\hat{R}_\varphi \hat{H} |n_1, \dots, n_{N^*}\rangle = \frac{1}{2^{L/2}} \prod_{n \in \{n_1, \dots, n_{N^*}\}} \sigma_n^z \sum_{\mathbf{m} \in \{0,1\}^L} e^{i\frac{\varphi}{2}(2|\mathbf{m}|-L)} |\mathbf{m}\rangle, \quad 2.95$$

where $0 \equiv \uparrow$ and $1 \equiv \downarrow$. Now multiply by $e^{i\frac{\varphi}{2}(L-2N)}$ with $0 \leq N \leq L$ arbitrary. That is,

$$\begin{aligned} &e^{i\frac{\varphi}{2}(L-2N)} \hat{R}_\varphi \hat{H} |n_1, \dots, n_{N^*}\rangle \\ &= \frac{1}{2^{L/2}} \prod_{n \in \{n_1, \dots, n_{N^*}\}} \sigma_n^z \sum_{\mathbf{m} \in \{0,1\}^L} e^{i\varphi(|\mathbf{m}|-N)} |\mathbf{m}\rangle. \end{aligned} \quad 2.96$$

We can easily project this state onto the N -particle subspace via integration over φ :

$$\begin{aligned} &\int_0^{2\pi} \frac{d\varphi}{2\pi} e^{i\frac{\varphi}{2}(L-2N)} \hat{R}_\varphi \hat{H} |n_1, \dots, n_{N^*}\rangle \\ &= \frac{1}{2^{L/2}} \prod_{n \in \{n_1, \dots, n_{N^*}\}} \sigma_n^z \sum_{\mathbf{m} \in \{0,1\}^L} \int_0^{2\pi} \frac{d\varphi}{2\pi} e^{i\varphi(|\mathbf{m}|-N)} |\mathbf{m}\rangle \end{aligned} \quad 2.97a$$

$$= \frac{1}{2^{L/2}} \prod_{n \in \{n_1, \dots, n_{N^*}\}} \sigma_n^z \sum_{\mathbf{m} \in \{0,1\}^L} \delta_{|\mathbf{m}|, N} |\mathbf{m}\rangle \quad 2.97b$$

$$= \frac{1}{2^{L/2}} \prod_{n \in \{n_1, \dots, n_{N^*}\}} \sigma_n^z |N\rangle. \quad 2.97c$$

Here, $|N\rangle$ denotes the (unnormalized) equal-weight superposition of states with N flipped spins.

We employ our findings to map the given N^* -particle eigenstate of H^x to another eigenstate in the N -particle sector, i.e.,

$$\begin{aligned} & \int_0^{2\pi} \frac{d\varphi}{2\pi} e^{i\frac{\varphi}{2}(L-2N)} \hat{R}_\varphi \hat{H} |\{\lambda_i\}; N^*\rangle \\ &= \frac{1}{2^{L/2}} \sum_{n_1 < \dots < n_{N^*}} \psi_{\{\lambda_i\}}(n_1, \dots, n_{N^*}) \prod_{n \in \{n_1, \dots, n_{N^*}\}} \sigma_n^z |N\rangle. \end{aligned} \quad 2.98$$

We conclude that

$$\begin{aligned} & |\{\lambda_i\}; N^*\rangle_N \equiv \\ & \mathcal{N} \underbrace{\left[\sum_{n_1 < \dots < n_{N^*}} \psi_{\{\lambda_i\}}(n_1, \dots, n_{N^*}) \prod_{n \in \{n_1, \dots, n_{N^*}\}} \sigma_n^z \right]}_{\equiv P_{N^*}(\{\lambda_i\})} |N\rangle \end{aligned} \quad 2.99$$

describes an N^* -magnon excitation in the N -particle sector with eigenenergy $E = E(\{\lambda_i\})$; \mathcal{N} denotes an appropriately chosen normalizing factor. The operator

$$P_{N^*}(\{\lambda_i\}) = \sum_{n_1 < \dots < n_{N^*}} \psi_{\{\lambda_i\}}(n_1, \dots, n_{N^*}) \prod_{n \in \{n_1, \dots, n_{N^*}\}} \sigma_n^z \quad 2.100$$

encodes the structure of the excited state (given by $\psi_{\{\lambda_i\}}$) into a phase pattern on the equal-weight superposition $|N\rangle$. Notably, the energy $E(\{\lambda_i\})$ is independent of N (but not of N^* !) and therefore

$$|\Psi; \{\lambda_i\}\rangle \equiv \sum_N \Psi_N |\{\lambda_i\}; N^*\rangle_N \quad 2.101$$

is still an eigenstate of H^x for arbitrary $\Psi_N \in \mathbb{C}$.

Lifting Excitations on the Double-Chain

Let us now return to the full Hamiltonian $H = H^a + H^b + H^{ab}$ that describes two coupled Heisenberg chains after Jordan-Wigner transformation. We find the following result:

LEMMA 2.1: Lifted excitations on the double-chain

Let $|\{\lambda_i\}; N^*\rangle$ be an N^* -magnon eigenstate of the single-chain Hamiltonian H^x with eigenenergy $E = E(\{\lambda_i\})$. Then, Eq. (2.100) determines operators $P_{N^*}^x(\{\lambda_i\})$ acting on the chains $x = a, b$. Define the (unnormalized) double-chain state

$$|\{\lambda_i\}; N^*\rangle_{N,\alpha}^\oplus \equiv \left[P_{N^*}^a \oplus P_{N^*}^b \right] (\{\lambda_i\}) \sum_{M: (-1)^M = \alpha} |M\rangle_a |N - M\rangle_b \quad 2.102$$

for fixed but arbitrary total magnetization/filling N and arbitrary subchain parity α . For single-magnon excitations ($N^* = 1$) this is an eigenstate of the full Hamiltonian H with energy E . In Eq. (2.102), \oplus denotes the Kronecker sum $A \oplus B = A \otimes \mathbb{1} + \mathbb{1} \otimes B$.

The proof is rather technical and its details are presented in $\star\star$ Subsection 2.C.4. Here we provide only a sketch to convey the central ideas:

Proof. We first consider the single-chain components and show that

$$\left[H^a \oplus H^b \right] |\{\lambda_i\}; N^*\rangle_{N,\alpha}^\oplus = E(\{\lambda_i\}) |\{\lambda_i\}; N^*\rangle_{N,\alpha}^\oplus, \quad 2.103$$

where the H^x ($x = a, b$) have to be considered single-chain Hamiltonians⁶². We would like to show

$$\left[P_{N^*}^a \oplus P_{N^*}^b, H^{ab} \right] = 0, \quad 2.104$$

so that the proposed symmetric states (2.102) are not affected by the chain coupling at all. However, this is *not* true in general but only for single-magnon excitations with $N^* = 1$ and $0 \leq N \leq 2L$ arbitrary. In this case, we find

$$H |\{\lambda_i\}; N^*\rangle_{N,\alpha}^\oplus = E(\{\lambda_i\}) |\{\lambda_i\}; N^*\rangle_{N,\alpha}^\oplus, \quad 2.105$$

which concludes the proof. \blacksquare

In conclusion, combining the solvability of H in the single-particle sector with the $SU(2)$ symmetry of the single-chain Hamiltonians H^x for open boundary conditions, yields the submanifold of excited states

$$|\{\lambda_i\}; N^*\rangle_{N,\alpha}^\oplus \xrightarrow{N^*=1, \lambda_1 \propto k} |k; N, \alpha\rangle \quad 2.106a$$

$$\text{with } P_{N^*}^x(\{\lambda_i\}) \xrightarrow{\psi_{i\lambda_i}, \{n_i\} = \psi_k(n)} P_1^x(k) \quad 2.106b$$

⁶²The original H^a in Eq. (2.12) corresponds to $H^a \otimes \mathbb{1}$ in the current notation.

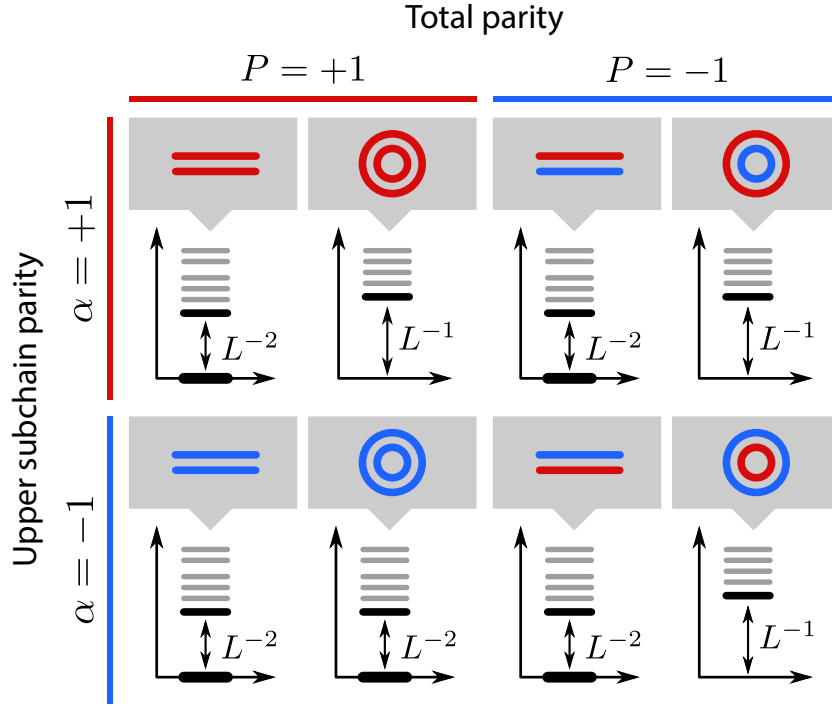


FIGURE 2.12 • Ground states & Gap scaling. Structure of the spectrum in the low-energy sector of symmetry subspaces \mathcal{H}_α^P classified by the total parity $P = (-1)^N$ and the subchain parity α . Both open (OBC) and periodic (PBC) boundary conditions are shown, zero-energy states are drawn bold and parities ± 1 of subchains are colored red/blue. For OBC, there are zero-energy ground states in all parity sectors and the gap closes with L^{-2} . For PBC, only the sector \mathcal{H}_{-1}^{+1} with odd subchain parity on both chains harbors zero-energy states, which are *unique* ground states in sectors $\mathcal{H}_{+1}^N \oplus \mathcal{H}_{-1}^N$ with even particle number N . All other sectors do not contain zero-energy states and their lowest-energy eigenstates approach zero-energy with L^{-1} .

and quadratic spectrum $E(\{\lambda_i\}) \rightarrow E_k = 4 \sin^2(k/2)$ in sectors with arbitrary (non-trivial) filling $2 \leq N \leq 2L - 2$. Note that the Jordan-Wigner transformation (2.73) implies $\sigma_i^z = (-1)^{a_i^\dagger a_i}$ such that (2.100) in combination with (2.86) yields the result (2.71).

2.4.2 Scaling of the Spectral Gap

Here we study the ground state structure and the scaling of the gap to the first excited state in more detail. We do this for both open (OBC) and periodic (PBC) boundary conditions to highlight their differences; the results of this comparison are illustrated in Figure 2.12. Note that in the previous sections, we focused exclusively on chains with *open* boundaries due to their topological ground state

degeneracy (with potential applications to quantum information processing, see also the discussion of braiding in Section 2.5). We start with this case to summarize our findings so far, and then explore periodic chains below.

Open Boundary Conditions

We showed in Subsection 2.2.2 that for OBC there is a unique zero-energy eigenstate $|N, \alpha\rangle \in \mathcal{H}_\alpha^N$ for arbitrary filling N and subchain parity α . That is, all four parity sectors \mathcal{H}_α^P of the double-chain Fock space \mathcal{H} — characterized by the subchain parity $\alpha = (-1)^{N^\alpha} = \pm 1$ and the total parity $P = (-1)^N = \pm 1$ — host zero-energy eigenstates of H :

$$\mathcal{H} = \bigoplus_{N, \alpha = \pm 1} \mathcal{H}_\alpha^N = \underbrace{\mathcal{H}_+^+ \oplus \mathcal{H}_-^+ \oplus \mathcal{H}_+^- \oplus \mathcal{H}_-^-}_{\text{Zero-energy ground states}}. \quad 2.107$$

For fixed N , this implies a two-fold degeneracy of the ground state manifold (which we identified as topological). For given N and α , we can ask about the eigenenergy E_1 of the first excited state of H restricted to the sector \mathcal{H}_α^N of states with the same filling and subchain parity⁶³. Via

$$\mathcal{H}_\alpha^P = \bigoplus_{N : (-1)^N = P} \mathcal{H}_\alpha^N, \quad 2.108$$

this conveys information about the scaling of the energy gap $\Delta E_0(L) = |E_0 - E_1| = |E_1|$ within the four parity sectors \mathcal{H}_α^P .

As explained in Subsection 2.4.1, one can derive the single-particle excitations in each sector \mathcal{H}_α^N rigorously. The single-particle excitation with lowest energy has momentum $k_1 = \frac{\pi}{L}$ and energy

$$E_1(L) = 4 \sin^2\left(\frac{\pi}{2L}\right) \sim \frac{\pi^2}{L^2} \quad 2.109$$

which yields an upper bound for the energy gap:

$$\Delta E_0(L) \lesssim \frac{\pi^2}{L^2}. \quad 2.110$$

Note that we did *not* disprove the existence of eigenstates with lower energy (e.g., bound states). This is, in general, a highly non-trivial task. For instance, it has been shown rigorously that the gap above the ground state of the ferromagnetic, isotropic Heisenberg model is given by $1 - \cos(\pi/L) = 2 \sin^2(\pi/2L)$ [249], which indeed agrees with the single-particle excitations for $k_1 = \frac{\pi}{L}$ given above⁶⁴. From a

⁶³Recall that N , P and α are symmetries of the double-chain Hamiltonian H ; therefore a restriction to the subspaces \mathcal{H}_α^N or \mathcal{H}_α^P makes sense.

⁶⁴The additional factor of 2 follows from the definition of H in terms of spinless fermions.

rigorous point of view, this statement can only be transferred to $H^a + H^b$ which describes two non-interacting isotropic Heisenberg chains. However, we conjecture that the additional interaction H^{ab} cannot decrease the first excited energy given by the k_1 -magnons (due to the positivity of H^{ab} , this would certainly be true for *weak* perturbations εH^{ab} , $\varepsilon \ll 1$).

To substantiate this claim, we performed density matrix renormalization group (DMRG) simulations with the ALPS framework [250, 251]. More precisely, we computed the lowest three⁶⁵ eigenenergies E_0 , E'_0 and E_1 for half-filling up to chains of length $L = 108$. The results in Figure 2.13 (a) show that the energy gap $\Delta E_0 = |E_0 - E_1|$ reproduces the analytical result (2.109) to very high accuracy. This suggests that the single-magnon excitations (2.70) are indeed responsible for the scaling (and closing) of the gap.

In conclusion, there is ample evidence that for OBC the gap above the zero-energy ground states $|N, \alpha\rangle$ closes as

$$\Delta E_0(L) \sim \frac{\pi^2}{L^2} \quad 2.111$$

in all sectors $\mathcal{H}_\alpha^{N,P}$, see Figure 2.12.

Periodic Boundary Conditions

We proceed with the case of periodic boundary conditions. The Hamiltonian is given by (2.12) where in (2.13) and (2.15) an additional term for $i = L$ is added (with index arithmetic modulo L). As already mentioned in Subsection 2.4.1 and Subsection 2.2.2, now there is a difference between the odd-odd⁶⁶ sector [$P = (-1)^N = +1$ and $\alpha = -1$] with an exact zero-energy state, and the even-even and even-odd/odd-even sectors without such states. In particular, there is no longer a two-fold degenerate zero-energy ground state space within sectors $\mathcal{H}_{+1}^N \oplus \mathcal{H}_{-1}^N$ of fixed particle number. This is analogous to the (mean field) Majorana chain where the degeneracy of the ground state manifold vanishes together with the edge modes for periodic chains.

In our case, the existence/absence of zero-energy ground states follows from the procedure in Subsection 2.2.2 with the modifications

$$A_i^a(\mathbb{1} + A_i^a)|\mathbf{n}, \mathbf{m}\rangle = |\mathbf{n}, \mathbf{m}\rangle - (-\alpha)^{\delta_{i,L}} |\varepsilon_i^a(\mathbf{n}, \mathbf{m})\rangle \quad 2.112a$$

$$A_i^b(\mathbb{1} + A_i^b)|\mathbf{n}, \mathbf{m}\rangle = |\mathbf{n}, \mathbf{m}\rangle - (-\bar{\alpha})^{\delta_{i,L}} |\varepsilon_i^b(\mathbf{n}, \mathbf{m})\rangle \quad 2.112b$$

for $n_i \neq n_{i+1}$ in (2.112a) and $m_i \neq m_{i+1}$ in (2.112b) (all other terms vanish).

⁶⁵For the simulations, we exploited the conserved particle number N to restrict the Hilbert space to $\mathcal{H}^N = \mathcal{H}_+^N \oplus \mathcal{H}_-^N$ without fixing the subchain parity α . Therefore the lowest two eigenstates are the zero-energy states $|N, \pm 1\rangle$ (we verified that $E_0 \approx 0 \approx E'_0$).

⁶⁶We refer to the sectors \mathcal{H}_α^P by their two subchain parities α and $\bar{\alpha} = (-1)^N \alpha$. E.g., the odd-odd sector has an even number of particles ($P = +1$) with an odd upper subchain parity ($\alpha = -1$).

LOW-ENERGY EXCITATIONS

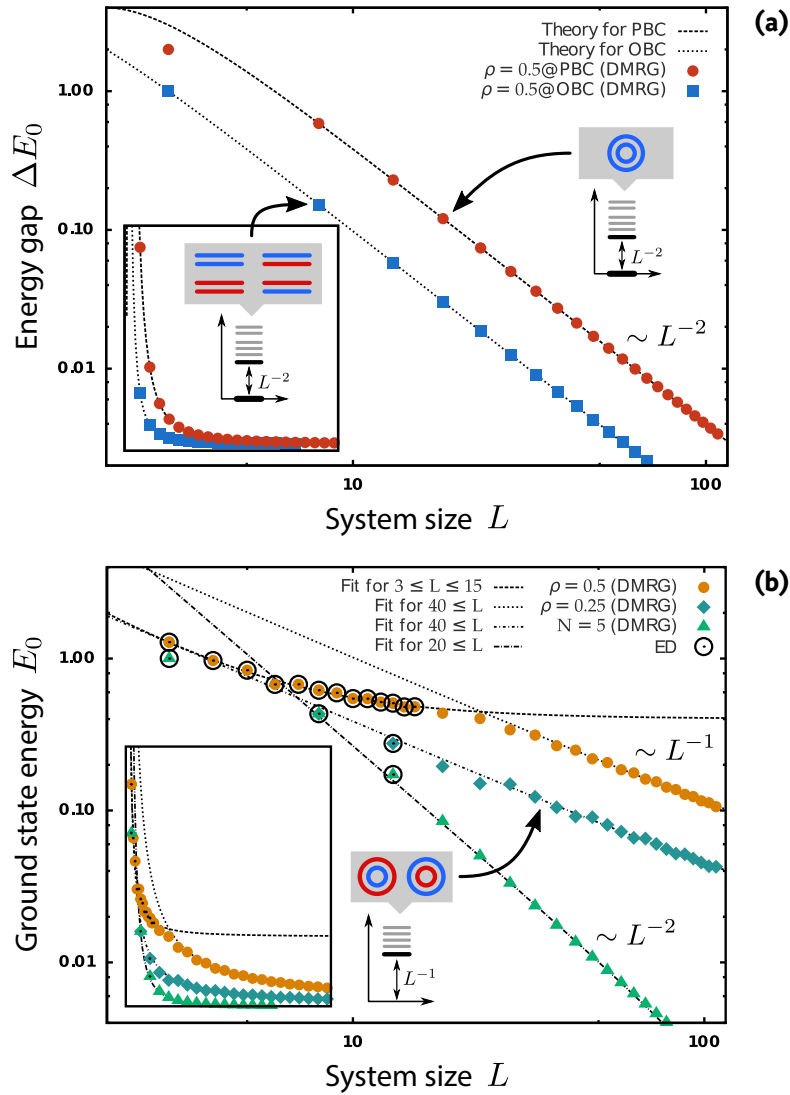


FIGURE 2.13 • DMRG results. (a) Log-log plot of the energy gap $\Delta E_0 = \Delta E_0(L)$ for double-chains with open and closed boundaries in the even particle number sector ($P = +1$) within the odd-odd subsector ($\alpha = -1$) for $\rho = 0.5$. The comparison with the analytical result (2.109) for single-magnon excitations with momentum $k_1 = \frac{\pi}{L}$ (OBC) and $k_1 = \frac{2\pi}{L}$ (PBC) reveals perfect agreement. The insets show the same data in linear scale. Note that for OBC the results are also valid in the other subchain-parity sectors. **(b)** Log-log plot of the ground state energy $E_0 = E_0(L)$ for a double-chain with periodic boundaries in the odd particle number sector ($P = -1$) for fixed density $\rho = 0.5, 0.25$ and fixed particle number $N = 5$. The ground state energy vanishes asymptotically with L^{-1} for fixed density, and with L^{-2} for fixed particle number. Note that exact diagonalization (ED) up to $L = 15$ suggests a single-particle gap—which is invalidated by DMRG up to $L = 108$. The fits are guides to the eye and not based on theoretical results. All simulations were performed with the ALPS libraries [250,251].

Similarly, for $n_i = n_{i+1} \neq m_i = m_{i+1}$ we have

$$B_i(\mathbb{1} + B_i)|\mathbf{n}, \mathbf{m}\rangle = |\mathbf{n}, \mathbf{m}\rangle - (\alpha\bar{\alpha})^{\delta_{i,L}} |\tau_i(\mathbf{n}, \mathbf{m})\rangle, \quad 2.113$$

where $\alpha\bar{\alpha} = P = (-1)^N$ and the representations (2.112) and (2.113) are valid on subspaces with well-defined subchain parity, i.e., $\mathcal{H}_\alpha^{N,P}$. The parity-dependent signs are a consequence of the fermion ordering in Figure 2.6 and the Jordan-Wigner string in (2.73).

If we follow the procedure in Subsection 2.2.2, the energy expectation value of an arbitrary state $|\Psi\rangle = \sum_i \Psi_i |i\rangle \in \mathcal{H}$ takes the abstract form

$$\langle \Psi | H | \Psi \rangle \propto \sum_{(ij) \in G} |\Psi_i - \alpha_{ij} \Psi_j|^2, \quad 2.114$$

where $i \equiv (\mathbf{n}, \mathbf{m})$ labels fermion configurations and the graph G encodes the couplings $i \leftrightarrow j = \pi(i)$ ($\pi \in \Pi$) realized by H and described by (2.112) and (2.113). The sign $\alpha_{ij} = \pm 1$ associated to its edges is determined by the additional sign of the second terms in (2.112) and (2.113). For OBC, we had $\alpha_{ij} = +1$ for all edges in G because the parity-dependence drops out; this led to the zero-energy ground states in Subsection 2.2.2. For PBC, and depending on the parity sector \mathcal{H}_α^P , there are edges with $\alpha_{ij} = -1$; this is true for all parity sectors except \mathcal{H}_-^+ , i.e., for $\alpha = -1 = \bar{\alpha}$. We can conclude immediately that the latter still allows for zero-energy ground states given as equal-weight superposition⁶⁷ of all fermion configurations within a sector of fixed particle number N and subchain parity α . These sectors are identified with the connected components of G since both N and α are symmetries of H .

In all other parity sectors, there are some edges with $\alpha_{ij} = -1$ scattered among the vast majority of edges with positive sign. The crucial observation is the following: There are always *cycles* C in G that include a single⁶⁸ edge $(i^* j^*)$ with negative sign. This implies

$$\langle \Psi | H | \Psi \rangle \geq \sum_{(ij) \in C} |\Psi_i - \alpha_{ij} \Psi_j|^2 \quad 2.115a$$

$$= |\Psi_{i^*} + \Psi_{j^*}|^2 + \sum_{(i^* j^*) \neq (ij) \in C} |\Psi_i - \Psi_j|^2. \quad 2.115b$$

But this expression cannot vanish for any normalized state $|\Psi\rangle$ due to frustration. We conclude that the sectors \mathcal{H}_+^+ and \mathcal{H}_\pm^- (the ones with at least one subchain of positive parity) cannot harbor zero-energy ground states of H (Figure 2.12). The existence of suitable cycles C follows from the fact that the propagation of a single fermion between two sites on a periodic chain always allows for *two* topologically distinct paths: one traverses the edge between site 1 and L and the other does

⁶⁷This zeros all terms in (2.114) irrespective of the coupling graph G .

⁶⁸More precisely: An *odd* number of edges with negative sign is sufficient.

not. The combination of both paths describes a cycle on the graph of fermion configurations G with a negative weighted edge. More details on this approach can be found in \clubsuit Subsection 2.B.1.

With these results in mind, we can ask the question if and how the spectrum approaches zero-energy in the thermodynamic limit. In the odd-odd sector, we focus on the gap between zero-energy ground state and first excited state. In the other sectors, we are interested in the scaling of the lowest (non-zero) eigenenergy.

Odd-odd sector — Consider the odd-odd sector first, i.e., $P = +1$ and $\alpha = -1$. There the fermionic statistics has no effect and the zero-energy ground state is the same as for open boundaries. Performing a Jordan-Wigner transformation yields the ferromagnetic, isotropic Heisenberg model for each subchain with (untwisted) periodic boundaries. Due to the survival of the global $SU(2)$ symmetry, all statements about the ground state and the single-particle excitations carry over from our discussion in Subsection 2.4.1; in particular the gap scaling, now with

$$\Delta E_0(L) \sim \frac{(2\pi)^2}{L^2} \quad 2.116$$

as the magnon with lowest energy has momentum $k_1 = \frac{2\pi}{L}$ (cf. $k_1 = \frac{\pi}{L}$ for OBC). These statements can again be verified to high accuracy with DMRG simulations, see Figure 2.13 (a). In the end, PBC and OBC are quite similar in the odd-odd sector \mathcal{H}_-^+ .

We proceed with the remaining three sectors where at least one subchain has even parity (Figure 2.12). In contrast to all previous cases (OBC and PBC alike), here we have neither access to exact ground nor excited states, which complicates the analysis considerably. In the following, we only present the results and sketch the central ideas; for details see \clubsuit Section 2.B.

Even-even sector — We start with the even-even sector, i.e., $P = +1$ and $\alpha = +1$. Here one can rigorously derive the following bounds on the lowest eigenenergy $E_0 > 0$:

$$\frac{C_2}{L^3} \leq E_0(L) \leq \frac{C_1}{L}. \quad 2.117$$

The upper bound follows with the ansatz wave function ($0 \leq K \leq L$)

$$|G_0\rangle \equiv \exp \left[i \frac{\pi}{L} \sum_{s=1}^L s (a_s^\dagger a_s + b_s^\dagger b_s) \right] |2K, +1\rangle \quad 2.118$$

which imprints a single-particle phase field onto the equal-weight superposition to satisfy the twisted boundary conditions with vanishing energy in the thermodynamic limit. It can be shown by straightforward calculation (\clubsuit Subsection 2.B.3) that

$$\langle G_0 | H | G_0 \rangle = 2 \cdot 4\rho(1 - \rho) \cdot L \cdot \sin^2 \left(\frac{\pi}{2L} \right) \quad 2.119a$$

$$\sim \frac{2\rho(1 - \rho)\pi^2}{L} \quad 2.119b$$

with density $\rho = N/2L = K/L$. The energy is due to intra-chain interactions H^x alone; the inter-chain contributions H^{ab} vanish. Since $\langle G_0 | H | G_0 \rangle \geq E_0$, this provides a vanishing upper bound on the lowest eigenenergy.

The derivation of the lower bound (which establishes the algebraic decay) is much more subtle as it makes statements about *all* possible states, in contrast to the upper bound which follows from a specific ansatz wave function. The idea is to start from Eq. (2.114) for a generic state in the even-even sector,

$$\langle \Psi | H | \Psi \rangle \propto \sum_{(ij) \in G} |\Psi_i - \alpha_{ij} \Psi_j|^2. \quad 2.120$$

Then, one constructs a set \mathcal{L} of cycles C in G so that (i) the length of each cycle is at most $\sqrt{A_1}$, (ii) every configuration i is visited by at least $A_2 > 0$ cycles, (iii) every cycle contains one edge ($i^* j^*$) with negative sign, and (iv) every edge in G is covered by at most A_3 cycles in \mathcal{L} . Physically, these cycles can be interpreted as virtual tunneling of a single fermion around one leg of the ladder. Restricting the sum (2.120) to edges covered by cycles in \mathcal{L} yields

$$\langle \Psi | H | \Psi \rangle \geq \frac{1}{A_3} \sum_{C \in \mathcal{L}} \sum_{(ij) \in C} |\Psi_i - \alpha_{ij} \Psi_j|^2. \quad 2.121$$

An application of Hölder's inequality followed by the triangle inequality yields

$$\langle \Psi | H | \Psi \rangle \geq \frac{1}{A_1 A_3} \sum_{C \in \mathcal{L}} \sum_{i \in C} |\Psi_i|^2. \quad 2.122$$

Here, $i \in C$ denotes configurations i visited by cycle C . For this step, the single edge with negative sign is crucial. If one finally uses that each configuration is visited by at least A_2 cycles and that $|\Psi\rangle$ is normalized, i.e., $\sum_{i \in G} |\Psi_i|^2 = 1$, we end up with the $|\Psi\rangle$ -independent lower bound

$$\langle \Psi | H | \Psi \rangle \geq \frac{A_2}{A_1 A_3} \sum_{i \in G} |\Psi_i|^2 = \frac{A_2}{A_1 A_3}. \quad 2.123$$

Due to our construction of \mathcal{L} —which is basically a collection of cycles in G that describe the propagation of a single fermion once around the chain—we find

$$\langle \Psi | H | \Psi \rangle \geq \frac{1}{L^2 N} \sim \frac{1}{L^3} \quad 2.124$$

for constant density $\rho = N/2L$. This establishes the algebraic lower bound. See \clubsuit Subsection 2.B.1 for all the gory details of the derivation and the construction of \mathcal{L} .

However, numerical results based on DMRG (not shown) and analytical results for the Heisenberg model with twisted boundary conditions [252–254] support the stronger statement (which saturates the *upper* bound due to the ansatz wave function)

$$E_0(L) \propto \frac{1}{L}, \quad 2.125$$

as indicated in Figure 2.12. It is therefore reasonable to assume that our construction of \mathcal{L} can be optimized to make the lower bound strict.

Odd-even/even-odd sectors — Finally, we consider the odd-even/even-odd sectors, i.e., $P = -1$ and $\alpha = \pm 1$. The previous sketch providing the *lower* bound $\propto L^{-3}$ relies on the existence of chains with even filling (required for the $\alpha_{ij} = -1$ edges on the cycles). However, in \clubsuit Subsection 2.B.1 we exploit that the inter-chain coupling H^{ab} is not needed for the construction of \mathcal{L} (which gives rise to the lower bound). This simplification is no longer valid in the odd-even/even-odd sectors where H^{ab} becomes an indispensable ingredient for the disappearance of zero-energy ground states. Nevertheless, it seems reasonable that a more general (and more complicated) construction of \mathcal{L} is still applicable and restricts the decay of the ground state energy to be at most algebraic (this is supported by DMRG simulations, see below).

The former ansatz wave function (2.118) yields a finite energy expectation value since only *one* of the two chains requires a single-particle phase to compensate the even filling. The naïve ansatz

$$|\tilde{G}_0\rangle = \exp\left[i\frac{\pi}{L}\sum_{s=1}^L s a_s^\dagger a_s\right] |2K+1, +1\rangle \quad 2.126$$

(here for $\alpha = +1$) with a single-particle phase on the upper chain fails with an extensively growing energy⁶⁹ due to the “phase-locking” induced by the inter-chain Hamiltonian H^{ab} .

⁶⁹Let $U_L^a \equiv \exp\left[i\frac{\pi}{L}\sum_{s=1}^L s a_s^\dagger a_s\right]$; then it is easy to show that $[H^{ab}, U_L^a] \neq 0$ due to the asymmetric phase pattern between upper and lower chain. A straightforward calculation yields

$$\langle \tilde{G}_0 | H^{ab} | \tilde{G}_0 \rangle = 4\rho^2(1-\rho)^2 \sum_{s=1}^L \sin^2\left[\frac{\pi}{2L}(2s+1)\right] \xrightarrow{L \rightarrow \infty} 2\rho^2(1-\rho)^2 L; \quad 2.127$$

an extensive energy expectation value. Note that this is even worse than for the unmodified states $|2K+1, +1\rangle$ for which $\langle 2K+1, +1 | H | 2K+1, +1 \rangle = \text{const} > 0$ for $L \rightarrow \infty$.

In this picture of single-particle phases⁷⁰ one might come to the conclusion that the ground state energy is finite: $\lim_{L \rightarrow \infty} E_0(L) > 0$. This would establish a *single-particle gap*, i.e., a finite difference of ground state energies between even and odd filling sectors. This conclusion is even supported by exact diagonalization (ED) for $\rho = 0.5$ up to $L = 15$ where the ground state energy seems to approach a finite value, Figure 2.13 (b). However, DMRG up to $L = 108$ proves this conclusion wrong and suggests clearly

$$E_0(L) \propto \frac{1}{L} \quad 2.128$$

for arbitrary density ρ , Figure 2.12.

In \clubsuit Subsection 2.B.2, we tackle this problem analytically with an improved ansatz wave function $|G_0\rangle$ that yields the asymptotic upper bound (for $L \geq L_\varepsilon$ large enough)

$$\langle G_0 | H | G_0 \rangle \leq \frac{1}{L^{1-\varepsilon}} \quad \text{for arbitrary } \varepsilon > 0, \quad 2.129$$

close to the numerically observed result. The wave function $|G_0\rangle$ leverages the vanishing compressibility of H to imprint smooth *density* fluctuations on the equal-weight superposition. This “unlocks” the phases on upper and lower chain in depleted regions and thereby avoids energy contributions from H^{ab} . The derivation of Eq. (2.129) in \clubsuit Subsection 2.B.2 is rigorous up to mild assumptions borrowed from statistical mechanics.

The non-existence of a single-particle gap, suggested by (2.128) and (2.129), is presumably owed to the “double criticality” of the very peculiar point described by H in that it is not only a gapless phase but also on the brink of phase separation; see Ref. [248] for more details.

2.5 Braiding

It is common knowledge that the edge modes of mean field Majorana chains can be probed for their non-abelian statistics in wire networks [130]. In this section, we demonstrate the same for the number-conserving setting of double-wires. In particular, we introduce a generalization of the double-chain Hamiltonian in Subsection 2.5.1 to contrive wire networks that host an arbitrary number of Majorana-like edge states. Most importantly, the description of the ground state manifold in terms of equal-weight superpositions carries over and grants access to all relevant quantities. In Subsection 2.5.2 we exploit this to simulate the full time evolution of a braiding protocol in the ground state space. Our findings demonstrate that the many-body edge states obey the non-abelian statistics of Ising anyons⁷¹.

⁷⁰This picture is distantly related to the bosonized version of the fermionic double-chain, described by bosonic phase and density fields $\varphi_i(x)$ and $\theta_i(x)$ in the continuum limit [248, 255, 256].

⁷¹Up to non-universal phases, see Footnote 41.

2.5.1 Construction of Wire Networks

The braiding procedure described in the next Subsection 2.5.2 calls for a more complicated setup than the “simple” two-leg ladder introduced in Subsection 2.2.1 and described by H . Here we lay the groundwork for this application. We will see that a broad class of Hamiltonians, defined on “wire networks,” can be described in analogy to the two-leg ladder, with degenerate zero-energy ground states given as equal-weight superpositions. In consequence, the powerful evaluation scheme of correlators and observables in terms of PsBCs is available.

Examples of possible network topologies accessible by these techniques are shown in Figure 2.14. In (a) two wires attached to a common periodic “bath” chain give rise to a two-dimensional ground state degeneracy, characterized by the parities α_i ($i = 1, 2$) of the two open subchains⁷². In (b) a more complex patch from a stacked wire setup is shown; the boundaries of open subchains carry edge states. The more intricate setup in (c) will be used in the following to illustrate the construction of a generic network Hamiltonian as descendant of the two-leg version considered so far.

In fact, for any network of g open and g' closed (single) chains, sectionally connected as double-wires, one can write down a generalized version of the Hamiltonian H so that in any filling sector N , there are exactly 2^{g-1} ($g \geq 1$) zero-energy ground states $|N; \alpha_1, \dots, \alpha_{g-1}\rangle$ given as equal-weight superpositions of fermion configurations with the i th subchain parity fixed at $\alpha_i = \pm 1$. In the special case of $g = 1$, the ground state $|N\rangle$ for each filling N is uniquely determined. The subchain parity of *closed* single-chains is fixed at $\alpha = -1$ to make the ground state energy vanish identically (see Subsection 2.4.2); that is, only *open* chains contribute to the ground state degeneracy.

For instance, consider the $g = 2$ (and $g' = 1$) wire network in Figure 2.14 (a) where the upper “bath” chain is closed and therefore has fixed parity $\alpha_0 = -1$. Then the two open chain parities α_1 and α_2 are constrained by the total parity via $\alpha_1\alpha_2 = -(-1)^N$. Thus the ground state space is two-fold degenerate for fixed filling N , illustrated by the two possible subchain-parity sectors for even N . Although the degeneracy is the same as for the straight ladder setup used before, here the edge states are spatially separated and stable even in the presence of time-reversal breaking perturbations, see Subsection 2.3.2.

To write down a local Hamiltonian featuring the properties sketched above, we start with an arbitrary wire network \mathcal{L} of fermionic sites [for instance, the setup depicted in Figure 2.14 (c)]. Formally, $\mathcal{L} = (\mathbb{V}, \mathcal{C}, \mathcal{P})$ is defined on a (so far unordered) set \mathbb{V} of vertices s (fermionic sites) as a collection \mathcal{C} of unoriented chains C (open or closed) and a collection \mathcal{P} of *pairing sections* P that describe the attachment of two chains C_1 and C_2 to form a two-leg ladder on a finite segment.

⁷²Recall (Subsection 2.4.2) that the *periodic* “bath” chain features zero-energy eigenstates only with odd subchain parity.

MAJORANA-LIKE EDGE STATES & NUMBER CONSERVATION

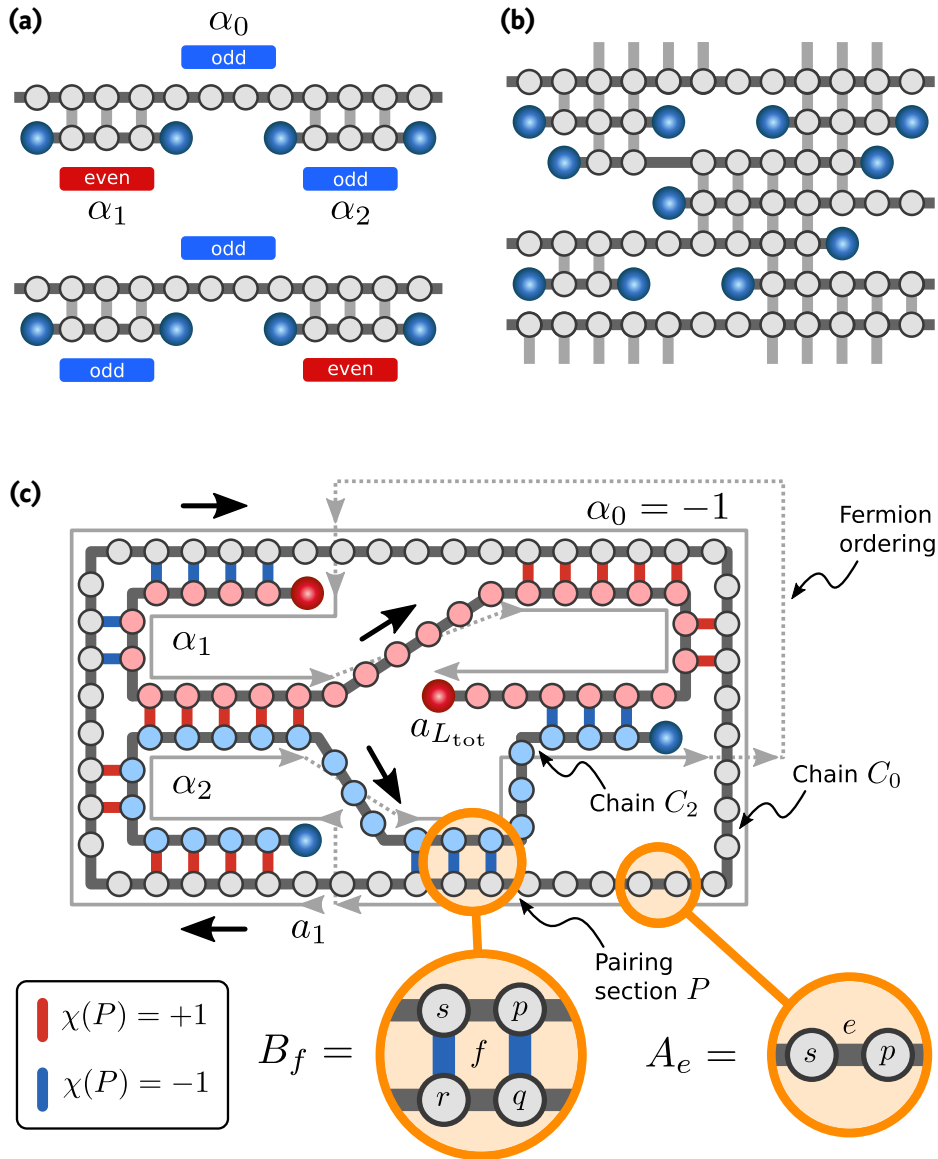


FIGURE 2.14 • Wire networks. (a) Simple wire network with two open chains connected by a common periodic “bath” chain with fixed subchain parity $\alpha_0 = -1$. For fixed particle number, the zero-energy ground states are characterized by the subchain parities α_1 and α_2 . (b) Patch of a more complex network of stacked chains. The degeneracy grows with the number of open chain ends (blue spheres). (c) Example of a more intricate wire setup with a periodic “bath” chain (gray sites) fixed at $\alpha_0 = -1$ and two open chains (red and blue sites) with unrestricted subchain parities α_1 and α_2 . There are two exact zero-energy ground states in each particle number sector characterized by $-\alpha_1\alpha_2 = (-1)^N$. This system accompanies the introduction of a generic network Hamiltonian in the text.

Note that a single-chain C can be oriented in two different ways without changing the neighborhood of sites. Let us choose an orientation for each chain (which is arbitrary, completely unphysical, and therefore a gauge choice). In Figure 2.14 (c), a possible choice is indicated by the black arrows for all three chains. The only relevant manifestation of this orientation is defined on pairing sections $P \in \mathcal{P}$ as a binary function $\chi : \mathcal{P} \rightarrow \{-1, +1\}$ via $\chi(P) = +1$ (-1) if the orientations of the two bonded chains are parallel (antiparallel). In the following, wire networks \mathcal{L} are always thought of being augmented by an orientation function χ .

After these formal preliminaries, we can write down the Hamiltonian that governs the physics on the wire network \mathcal{L} as follows:

$$H[\mathcal{L}] \equiv \sum_{C \in \mathcal{C}} H'[C] + \sum_{P \in \mathcal{P}} H''[P] \quad 2.130$$

where H' describes the intra-chain physics,

$$H'[C] \equiv \sum_{e \in C} A_e (\mathbb{1} + A_e) \quad 2.131$$

with the single-particle hopping $A_e = a_s a_p^\dagger + a_p a_s^\dagger$ on edge $e = (s, p)$ [cf. Eq. (2.14)], and H'' is responsible for the inter-chain interactions,

$$H''[P] \equiv \sum_{f \in P} B_f (\chi(P) + B_f) \quad 2.132$$

with the pair hopping between the two chains $B_f = a_s^\dagger a_p^\dagger a_r a_q + a_r^\dagger a_q^\dagger a_s a_p$ [cf. Eq. (2.16)]. Here, $f = (s, p; q, r)$ defines a “face” on the pairing section P with corners s, p on the “upper” and q, r on the “lower” chain, Figure 2.14 (c). Note that the choice of chain orientations χ affects only the definition of H'' . This follows from the invariance of A_e with respect to orientation inversion on a single-chain ($s \leftrightarrow p$) as compared to the sign $B_f \leftrightarrow -B_f$ induced by orientation inversion on one of the two chains of a pairing section (e.g., $s \leftrightarrow p$).

We point out that on the level of the fermion algebra $\{a_s\}_{s \in \mathbb{V}}$, the gauge transformation $a_s \mapsto i a_s$ for $s \in C$ inverts all signs of $\chi(P)$ for pairing sections P including chain C . In this sense, the orientations of chains can be inverted by the $U(1)$ -rotation of the fermions on these chains. This explains why the choice of orientations has no physical significance as the resulting Hamiltonians are related by gauge transformations. But beware: Whereas the choice of orientations is arbitrary, the *relative orientations* χ are implicitly given by this choice *and the topology of the wire network*. In other words, there are different gauge equivalence classes of Hamiltonians for a given wire network \mathcal{L} , and only the representatives $H[\mathcal{L}]$ defined in (2.130) give rise to degenerate zero-energy ground states (which singles out a particular gauge equivalence class).

For instance, there are network topologies where it is *not* possible to gauge all relative orientations to $\chi(P) = +1$ (which would be the naïve generalization of our original two-leg ladder to networks). One such example is given in Figure 2.14 (c) where the colors of inter-chain pair interactions encode the sign of $\chi(P)$ with respect to the orientations given by the black arrows. Note that there is no choice of orientations so that all pairing sections feature parallel orientations.

It remains to be shown that the ground state space of $H[\mathcal{L}]$ is spanned by zero-energy states given by equal-weight superpositions and characterized by the parities of the open subchains in \mathcal{L} . To this end, a representation of the fermion algebra on the Hilbert space is required. This is achieved by defining a number state basis $\{|\mathbf{n}\rangle\}$ of the Fock space based on a total ordering of the fermion modes. A convenient choice for the construction of the ground states is to order fermions along single-chains and parallel to the previously chosen orientations. The order of the single-chains relative to each other is not important as long as only parity-symmetric operations between the chains are concerned (which is certainly true for $H[\mathcal{L}]$). Note that the order of chains becomes important for the evaluation of subchain parity violating observables/correlators, such as inter-chain Green's functions and single-particle hopping. A possible ordering is drawn in Figure 2.14 (c) with gray arrows.

The construction of the ground states follows the same procedure as for the double-chain in Subsection 2.2.2, generalized to multiple connected chains. The single-particle hopping within the chains can be described on the previously defined Fock basis as

$$A_e(\mathbb{1} + A_e)|\mathbf{n}\rangle = |\mathbf{n}\rangle - |\varepsilon_e(\mathbf{n})\rangle \quad 2.133$$

with

$$\varepsilon_e(\dots, n_i, n_{i+1}, \dots) \equiv (\dots, n_{i+1}, n_i, \dots) \quad 2.134$$

for $e = (i, i + 1)$; we no longer split the fermion configuration into two subchain configurations \mathbf{n} and \mathbf{m} but consider the global configurations $\mathbf{n} \in \{0, 1\}^{L_{\text{tot}}}$ with the total (single-) chain length $L_{\text{tot}} = \sum_{i=1}^{g+g'} L_i$ of all $g + g'$ chains. For the double-chain, it is $g = 2, g' = 0$ and $L_{\text{tot}} = L + L = 2L$. Henceforth we assume that closed chains are occupied by an odd number of fermions so that the additional sign in (2.112) does not appear in (2.133).

For the inter-chain pair interaction one finds

$$B_f(\chi(P) + B_f)|\mathbf{n}\rangle = |\mathbf{n}\rangle - |\tau_f(\mathbf{n})\rangle \quad 2.135$$

with

$$\begin{aligned} \tau_f(\dots, n_i, n_{i+1}, \dots, n_j, n_{j+1}, \dots) \\ \equiv (\dots, n_j, n_{j+1}, \dots, n_i, n_{i+1}, \dots) \end{aligned} \quad 2.136$$

if $n_i = n_{i+1}$ and $n_j = n_{j+1}$, and $\tau_f = \text{Id}$ otherwise; here, $f = (i, i + 1; j + 1, j)$ is the face of a pairing section. Equation (2.135) demonstrates that the sign $\chi(P)$ in H'' compensates for the signs due to fermion pair hopping—these are different

for hopping between chains of parallel and antiparallel order (the latter implies an exchange of the pair fermions). The effect of $H[\mathcal{L}]$ (depending on the chain orientations through χ) on the basis $|\mathbf{n}\rangle$ (depending on the chain orientations via the chosen fermion ordering) is therefore *invariant* under the choice of chain orientations and takes the same form as for the double-chain [Eq. (2.22)].

In particular, the energy expectation still has the generic form

$$\langle \Psi | H[\mathcal{L}] | \Psi \rangle \propto \sum_{(\mathbf{n}, \mathbf{n}') \in G} |\Psi(\mathbf{n}) - \Psi(\mathbf{n}')|^2, \quad 2.137$$

where $(\mathbf{n}, \mathbf{n}') \in G$ if it is possible to transform the fermion configurations $\mathbf{n} \leftrightarrow \mathbf{n}'$ into each other by an elementary process⁷³ of $H[\mathcal{L}]$. Note that (2.137) is only valid because of the restriction to sectors with odd subchain parity for closed chains.

The zero-energy ground states of the positive semi-definite Hamiltonian $H[\mathcal{L}]$ are therefore given by states with constant weights on all connected components of G , that is, by equal-weight superpositions of all fermion configurations with fixed total particle number N and subchain parities $\alpha_i = \pm 1$ for $i = 1, \dots, g - 1$. This gives rise to the claimed 2^{g-1} -fold degeneracy of the ground state space in each filling sector N , spanned by the exact zero-energy ground states $|N; \alpha_1, \dots, \alpha_{g-1}\rangle$. It is now evident that arbitrary correlators/observables can be expressed in terms of PsBCs. However, their splitting degree is typically much larger than in Section 2.3 for the double-chain.

2.5.2 Non-Abelian Statistics

In the previous Subsection 2.5.1, we introduced the generalization $H[\mathcal{L}]$ for networks \mathcal{L} of sectionally paired chains; it was shown that their ground state degeneracy for fixed particle number is given by 2^{g-1} if the network hosts g open chains. Put another way, the ground state degeneracy scales as $2^{E/2-1}$ with $E \geq 2$ the number of open subchain ends. This is in agreement with the interpretation of the localized edge states as interacting equivalent of Majorana zero modes, that is, *Majorana-like edge states*.

This brings up the question whether the braiding statistics of these edge states coincides with the anyonic Ising statistics of Majorana zero modes [24, 130]. To derive the full braiding statistics, we have to contrive a network \mathcal{L} and a time-dependent Hamiltonian $H(t) = H[\mathcal{L}](t)$ that drives the adiabatic braiding (i.e., double-exchange) of two edge states.

In contrast to the *gapped* phase of the Majorana chain, here the energy ΔE_0 between the subspace of zero-energy ground states and the first excited states vanishes algebraically, $\Delta E_0 \propto L^{-2}$, see Figure 2.12 in Subsection 2.4.2. This is not in accordance with the conventional notion of topological phases where the low-energy physics is described by topological quantum field theories that endow

⁷³That is, single-particle hopping within a chain or pair hopping between chains in a pairing section.

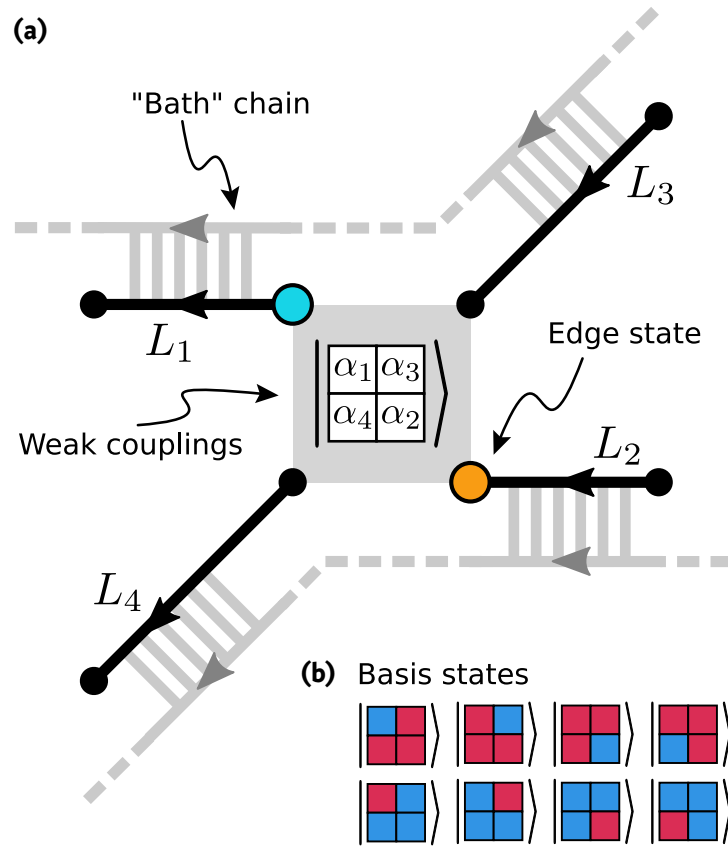


FIGURE 2.15 • Braiding—Setup. (a) Setup of four open chains $L_i, i = 1, \dots, 4$, (black) with controllable weak single-particle couplings between the inner four endpoints (gray square). The partner chains (gray) are not involved in the braiding and can be disregarded for the evaluation of the time evolution. (b) The dynamics takes place in the 8-dimensional Hilbert space spanned by the zero-energy ground states with fixed total parity $\alpha = \alpha_1\alpha_2\alpha_3\alpha_4 = -1$. The colors label the subchain parities α_i of the four black chains.

localized quasiparticles with anyonic statistics. Most importantly, the braiding of excitations requires adiabaticity to be well-defined⁷⁴. In *gapped* systems, there is a size-independent timescale on which quasiparticles can be braided; a property useful for applications such as topological quantum computation.

However, gapless theories (such as ours) often feature many of the characteristic properties of gapped topological phases (e.g., robust ground state degeneracies that depend on the spatial topology of the system). This motivates the broader notion of *quasi-topological phases* [226]. In particular, braiding must be slow enough to adiabatically decouple the ground state space from the excited sectors. This limits the strength of the couplings used for braiding to values much smaller than the gap

⁷⁴Braiding “too fast” excites a cloud of particle-antiparticle pairs that scramble any (non-abelian) geometric phase of particles moving through that cloud.

ΔE_0 ; equivalently, the time needed for the braiding protocol grows for networks of linear size L with L^2 to guarantee adiabaticity. For applications, this may be a problematic restriction—for the theoretical analysis, however, it is not.

In order to braid two localized edge states, we consider the wire network of four open subchains coupled by a common “bath” chain depicted in Figure 2.15 (a) and described by H_0 . Only the highlighted chains L_i ($i = 1, \dots, 4$) take part in the braiding evolution. Thus the grayed out subchain can be neglected henceforth and considered as a “bath,” the effect of which is fully incorporated into the exactly known zero-energy ground states. The latter are labeled by the total filling N and the subchain parities $\alpha_1, \dots, \alpha_4$ of the open chains, spanning a $2^4 = 16$ -dimensional ground state space in each particle number sector (the subchain parity of the “bath” chain is implicitly determined by the filling). As we consider only interactions between the four subchains, the total subchain parity $\alpha = \alpha_1\alpha_2\alpha_3\alpha_4$ is conserved and can be fixed (here we set $\alpha = -1$); this reduces the number of relevant ground states to 8, pictorially given in Figure 2.15 (b). Everything that follows takes place in this 8-dimensional low-energy Hilbert space \mathcal{H}_0 .

The braiding of two edge states is described by a Hamiltonian $H_{\text{int}}(t)$ and achieved by adiabatically turning off the coupling between two edges and simultaneously turning on the coupling between the next two edges (without closing the gap in \mathcal{H}_0); the full sequence of couplings for the winding of two edge states around each other is shown below Figure 2.16 (a), where arrows indicate single-particle couplings analogous to $A_i(1 + A_i)$. At all times t , $H_{\text{int}}(t)$ hybridizes edge states such that the 8-fold degeneracy of H_0 on \mathcal{H}_0 is lifted on the scale of $H_{\text{int}}(t)$ and only 4 degenerate ground states remain. The time dependence of this low-energy spectrum is plotted in Figure 2.16 (a). Details on the construction of $H_{\text{int}}(t)$ are presented below.

We study the braiding with a full numerical time evolution of the complete Hamiltonian

$$H(t) = H_0 + \frac{\varepsilon}{L^2} H_{\text{int}}(t) \quad 2.138$$

restricted to the low-energy subspace \mathcal{H}_0 . Here, $\varepsilon \ll 1$ guarantees the (quasi-)adiabatic evolution and $0 \leq t \leq 8$ derives from the 8 substeps needed for a double-exchange. Let

$$\left| \begin{array}{c} \alpha_1 \alpha_3 \\ \alpha_4 \alpha_2 \end{array} \right\rangle \equiv |N; \alpha_1, \alpha_2, \alpha_3, \alpha_4\rangle \quad 2.139$$

label the basis of \mathcal{H}_0 (Figure 2.15). We start with the initial (unnormalized) zero-energy state of $H_{\text{int}}(t = 0)$

$$|00; 0\rangle \equiv \left| \begin{array}{c} -+ \\ -- \end{array} \right\rangle + \left| \begin{array}{c} -- \\ +- \end{array} \right\rangle \equiv \left| \begin{array}{c} - \\ - \end{array} \right\rangle \times \left(\left| \begin{array}{c} + \\ - \end{array} \right\rangle + \left| \begin{array}{c} - \\ + \end{array} \right\rangle \right), \quad 2.140$$

with $\alpha_1 = -1 = \alpha_2$ and $\alpha_3\alpha_4 = -1$. Here, the notation with “ \times ” is purely formal and does not denote a tensor product; due to the fixed particle number, the state does *not* factorize.

MAJORANA-LIKE EDGE STATES & NUMBER CONSERVATION

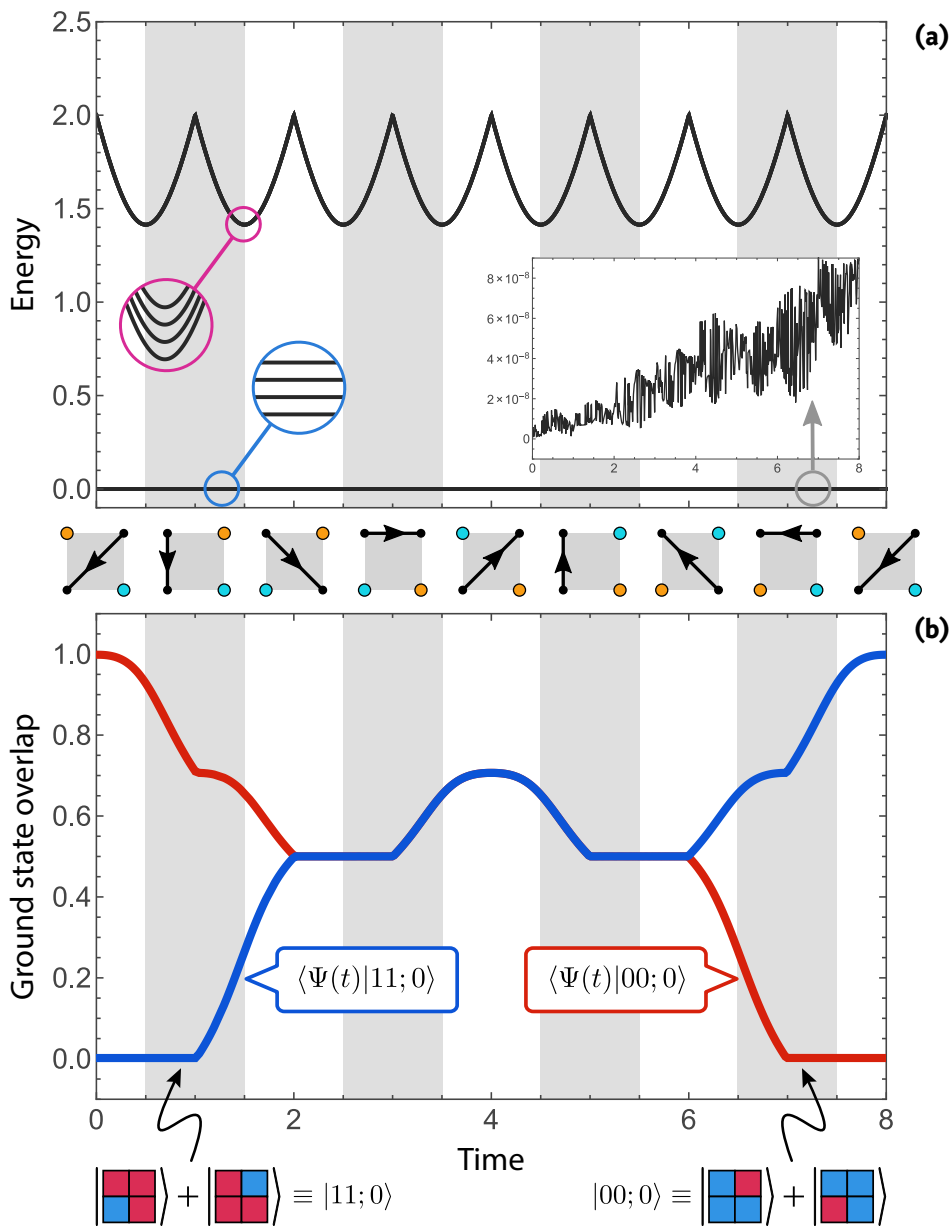


FIGURE 2.16 • Braiding—Results. (a) Spectrum of the weak-coupling Hamiltonian $H_{\text{int}}(t)$ in the 8-dimensional ground state space of H_0 during the braiding procedure depicted below the plot. A black arrow indicates single-particle hopping connecting the endpoints of chains. Due to the hybridization of edge states, 4 of the 8 states in the low-energy subspace are lifted to finite energies (purple). For the 4 ground states (blue), the deviation from zero-energy (for perfect adiabaticity) due to the finite time evolution is negligible ($\sim 10^{-8}$), as shown in the inset. (b) Time evolution for the initial zero-energy state $|00; 0\rangle$. Shown are the (moduli of the) overlaps with $|00; 0\rangle$ and $|11; 0\rangle$, defined pictorially below the plot. Note that the Hamiltonian returns to its initial configuration, whereas the state does not.

If we apply the cyclic⁷⁵ time evolution of $H_{\text{int}}(t)$, $|00; 0\rangle$ is mapped to the orthogonal final state

$$|11; 0\rangle \equiv \begin{pmatrix} ++ \\ -+ \end{pmatrix} + \begin{pmatrix} +- \\ ++ \end{pmatrix} \equiv \begin{pmatrix} + \\ + \end{pmatrix} \times \left(\begin{pmatrix} - \\ + \end{pmatrix} + \begin{pmatrix} - \\ + \end{pmatrix} \right) \quad 2.141a$$

$$= \underbrace{\mathcal{T} \exp \left[-i \int_0^8 dt H_{\text{int}}(t) \right]}_{\equiv U(t=8)} |00; 0\rangle, \quad 2.141b$$

characterized by $\alpha_1 = +1 = \alpha_2$ and $\alpha_3\alpha_4 = -1$. Here, \mathcal{T} denotes the time-ordering operator. The numerical results are shown in Figure 2.16 (b). We stress that the unitary time evolution in (2.141b) is the manifestation of a non-abelian Berry phase collected along the cyclic path $H_{\text{int}}(0) \rightarrow H_{\text{int}}(8) = H_{\text{int}}(0)$ in the space of Hamiltonians.

Interpretation of the Results

What does the result in Eq. (2.141b) tell us about the braiding statistics of the edge states? Before we can answer this question, a few comments on the braiding of edge states are in order:

The abstract framework that captures the concept of anyonic statistics is agnostic of the physical system that realizes the braiding. It is formulated in terms of *category theory* [55, 56] and makes use of a class of highly structured categories termed *unitary modular tensor categories (UMTC)* [48], see Ref. [57] and [128] for an introduction. The original motivation to study these objects in physics stems from their usefulness in describing topological quantum field theories (TQFT) [14], but the conceptual foundation of UMTCs is more general and applicable to a diverse class of physical systems: UMTCs encode the content and structure of systems that host localized entities (called *particles* or *anyons*) that can be combined (or *fused*) to new entities, enriched with a compatible notion of moving these entities around each other (called *braiding*). While the “fusion-part” is independent of the spatial dimension, the “braiding-part” restricts the latter to 2 because only there the braid group does not trivialize to the symmetric group of permutations.

As our world is three-dimensional, anyonic particles described by UMTCs play no role in conventional high-energy physics, but enter the stage through condensed matter physics where the study of two-dimensional systems is quite common both in theory and experiment (e.g., graphene and quantum Hall fluids). In this context, the most natural identification is that of localized excitations (quasiparticles) as anyons of a UMTC, the movement (and braiding) of which is described by a

⁷⁵It is $H_{\text{int}}(t) = H_{\text{int}}(t \bmod 4)$.

low-energy modification of the Hamiltonian that describes the ground state⁷⁶. If such quasiparticles feature anyonic (that is, neither bosonic nor fermionic) statistics, this indicates long-range entanglement in the ground state that gives rise to non-trivial braid group representations on the Hilbert space. Such systems are *intrinsic topological phases* and their low-energy physics is described by a TQFT; the most prominent example being the *toric code* [45].

The braiding of edge states is conceptually different (both for the number-conserving theory and the Majorana chain) in that the localized “particles” are not intrinsic, localized excitations of a static Hamiltonian but point-like *defects* that are moved by high-energy deformations of the Hamiltonian. In non-interacting theories, these defects can host localized modes described by Majorana fermions, the algebra of which allows for the construction of non-trivial Braid group representations, see \clubsuit Subsection 2.D.1. The localized *edge modes* can be identified as abstract “particles” of a UMTC that can be braided and fused by deformation of the Hamiltonian [130]. This is what we achieved above by adding H_{int} to the network Hamiltonian H_0 . In contrast to the Majorana chain, there is no exact Clifford algebra of Majorana modes associated to the edges of the chains (see \clubsuit Subsection 2.D.2) as H_0 is an interacting theory where the very notion of *modes* no longer applies. We can only talk about many-body quantum states of the whole system (the states in \mathcal{H}_0) with the peculiar property that unitaries on \mathcal{H}_0 are generated by couplings between the endpoints of chains (recall Subsection 2.3.2). This qualifies the endpoints as special entities of the theory and renders their braiding and fusion meaningful in the sense of UMTCs. So what did we find above by braiding two of these abstract “particles”?

According to the coupling sequence illustrated in Figure 2.16 (and described below), the non-trivial holonomy [257] $U_{s_1 s_2} \equiv U(4)$ on the four-fold degenerate ground state space describes the exchange ($U_{s_1 s_2}$) and braiding ($U_{s_1 s_2}^2$) of the two localized edge states associated with the endpoints s_1 and s_2 . The ground state space at $t = 0 \pmod{4}$ is characterized by a coupling of chains L_3 and L_4 and therefore spanned by the four states $|\alpha_1, \alpha_2\rangle|\alpha_3\alpha_4\rangle_+$ with $\alpha_1\alpha_2\alpha_3\alpha_4 = -1$ defined as

$$|\alpha_1, \alpha_2\rangle|\alpha_3\alpha_4\rangle_+ \equiv \begin{vmatrix} \alpha_1 & \alpha_3 \\ \alpha_4 & \alpha_2 \end{vmatrix} + \begin{vmatrix} \alpha_1 & -\alpha_3 \\ -\alpha_4 & \alpha_2 \end{vmatrix} \quad 2.142a$$

$$\equiv \begin{vmatrix} \alpha_1 \\ \alpha_2 \end{vmatrix} \times \left(\begin{vmatrix} \alpha_3 \\ \alpha_4 \end{vmatrix} + \begin{vmatrix} -\alpha_3 \\ -\alpha_4 \end{vmatrix} \right) \quad 2.142b$$

up to normalizations, recall (2.140) and (2.141). Again, the notation “ $|\alpha_1, \alpha_2\rangle|\alpha_3\alpha_4\rangle_+$ ” is purely formal and emphasizes the different roles of the subparities—it does *not* denote a tensor product.

⁷⁶Formally, the concept of localized particles in condensed matter physics is based on the notion of *superselection sectors*: States that can be mapped to each other by *local* operations belong to the same superselection sector and describe the same configuration of quasiparticles.

Repeating the analysis for the other ground states, the action of the braiding $U_{s_1 s_2}^2$ is found to be diagonal in the $\alpha_3 \alpha_4$ blocks and reads

$$U_{s_1 s_2}^2 |\alpha_1, \alpha_2\rangle |\alpha_3 \alpha_4\rangle_+ = |-\alpha_1, -\alpha_2\rangle |\alpha_3 \alpha_4\rangle_+, \quad 2.143$$

up to global phases.

In order to understand this result more thoroughly, it is instructive to cast these expressions into the language of the quadratic Majorana chain, keeping in mind that due to the interactions there are neither fermion nor Majorana modes describing the ground states. Remember that the delocalized, fermionic edge mode of the Majorana chain is empty (occupied) if the total chain parity is odd (even), Subsection 1.2.2. From this perspective, we may call the edge state of a subchain in our interacting model empty (occupied) if its subchain parity is odd (even). Formally, the occupation n_1 of the “fermion mode” defined by the pair of “Majorana modes” at p_1 and s_1 [Figure 2.18 (a)] translates into the subchain parity α_1 via $\alpha_1 = -(-1)^{n_1}$; and the same for L_2 . This defines the new naming scheme

$$|n_1, n_2\rangle |n_{34}\rangle_+ \equiv |\alpha_1, \alpha_2\rangle |\alpha_3 \alpha_4\rangle_+ \quad 2.144$$

with $n_{1,2} = 0, 1$ and $\alpha_3 \alpha_4 = -(-1)^{n_{34}}$. Note that it also motivates the labels used for the states in (2.140) and (2.141) with the compact notation $|n_1 n_2; n_{34}\rangle = |n_1, n_2\rangle |n_{34}\rangle_+$. Then, the action of braiding the “Majoranas” s_1 and s_2 reads

$$U_{s_1 s_2}^2 |0, 0\rangle |0\rangle_+ = |1, 1\rangle |0\rangle_+. \quad 2.145$$

In the quadratic mean field theory of the Majorana chain, this would be interpreted as the creation of a fermion pair $1 \rightarrow \Psi \otimes \Psi$ out of the superconducting condensate by braiding two Majorana modes; this is illustrated in Figure 2.17 and a hallmark of non-abelian Ising anyons [24]; see Ref. [148] for an application of this signature in the context of topological p -wave superfluids, realized with fermionic atoms in optical lattices.

The fusion rule

$$\sigma \otimes \sigma = 1 \oplus \Psi \quad 2.146$$

that renders Ising anyons σ (associated to endpoints s_i and p_i) non-abelian, can be read as the two possible outcomes for the subchain parity α_i of chain L_i : the fusion channel is 1 (Ψ) for $\alpha_i = -1$ ($+1$). The “fusion” can be realized by a single-particle coupling between s_i and p_i . But this is just a fancy name for periodic boundary conditions: We saw in Subsection 2.4.2 that this coupling results in zero-energy (=fusion to the vacuum 1) only for $\alpha_i = -1$, whereas $\alpha_i = +1$ results in a state with finite energy (=fusion to a fermion Ψ). This is in complete analogy to the mean field Majorana chain—except for the missing fermionic edge mode $\gamma_1 + i\gamma_{2L}$, the occupation of which determines the fusion outcome in the non-interacting case, Subsection 1.2.2.

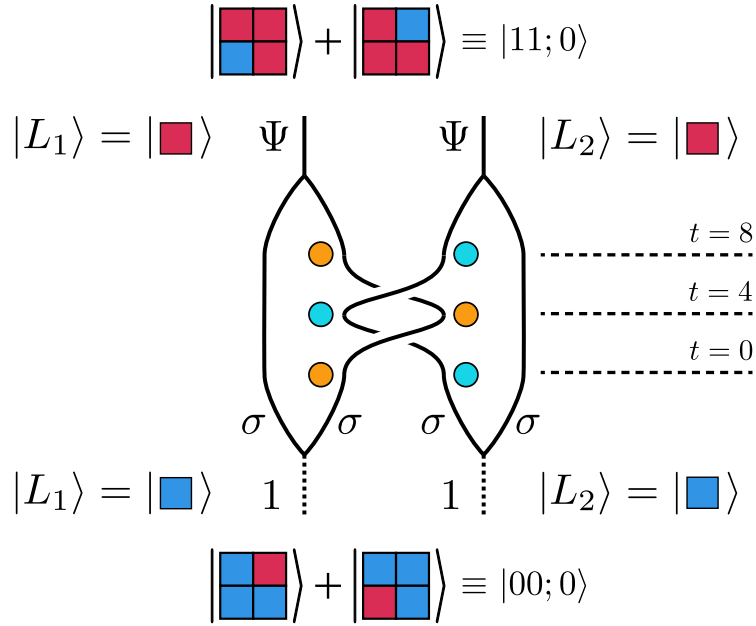


FIGURE 2.17 • Braiding—Theory. Schematic illustration of the process simulated in Figure 2.16. The system is initialized in the state $|00; 0\rangle$ and subsequently transformed into the orthogonal state $|11; 0\rangle$ by the double-exchange/braiding unitary $U_{s_1 s_2}^2$. This can be interpreted as the braiding of two “Majoranas” σ , each of which belongs to a pair initialized in the vacuum fusion channel, $1 \rightarrow \sigma \otimes \sigma$ (bottom). After the braiding, the pairs fuse to fermions, $\sigma \otimes \sigma \rightarrow \Psi$ (top). Note that the complete system is still in the vacuum superselection sector since $\Psi \otimes \Psi = 1$. Details are discussed in the text.

Pairing the Majorana modes of two *different* Majorana chains into a fermion mode, one finds that the symmetric/antisymmetric linear combination of the two ground states that are compatible with a fixed total parity corresponds to an empty/occupied mode. Translated into our case, this means that the occupation m of the “fermion mode” created from “Majorana modes” at s_1 and s_2 is given by

$$|m\rangle|m', n_{34}\rangle \equiv [|\alpha_1, \alpha_2\rangle + (-1)^m |-\alpha_1, -\alpha_2\rangle] |\alpha_3 \alpha_4\rangle_+ \quad 2.147$$

which, of course, is just a basis transformation in the four-dimensional ground state space of $H_{\text{int}}(0)$. Here, $\alpha_1 \alpha_2 = -(-1)^{m'}$ describes the occupation m' of the “fermion mode” defined by the outer “Majoranas” p_1 and p_2 , Figure 2.18 (a). In this basis, the action of the braiding is particularly simple, namely diagonal

$$U_{s_1 s_2}^2 |m\rangle|m', n_{34}\rangle = (-1)^m |m\rangle|m', n_{34}\rangle, \quad 2.148$$

up to a phase independent of m . This is exactly the relative phase one would expect from rotating a fermion mode with occupation m by 2π : It accounts

for the *topological spin*⁷⁷ θ of both the vacuum 1 ($\theta_1 = 1$) and the fermion Ψ ($\theta_\Psi = -1$) [128]. Note that this result is also in accordance with the *spin-statistics theorem*, a relation that appears naturally in anyon models [57].

We conclude that a non-abelian representation of the braid group is acting on the ground state space of wire networks that identifies their endpoints as Ising anyons, the same anyon model (UMTC) that describes Majorana edge modes in non-interacting theories. This justifies the term *Majorana-like edge states* for the ground states of our model.

Construction of H_{int}

The reader may skip this construction on first reading and proceed with Section 2.6. The Hamiltonian $H_{\text{int}}(t)$ in (2.138) couples the four chains L_i , $i = 1, \dots, 4$, via single-particle hopping as follows:

$$\tilde{H}_{\text{int}}(t) = \begin{cases} (1 - \tau) H_{\text{int}}^{34} + \tau H_{\text{int}}^{14} & \text{for } 0 \leq t < 1 \quad \text{and } \tau = t - 0, \\ (1 - \tau) H_{\text{int}}^{14} + \tau H_{\text{int}}^{12} & \text{for } 1 \leq t < 2 \quad \text{and } \tau = t - 1, \\ (1 - \tau) H_{\text{int}}^{12} + \tau H_{\text{int}}^{13} & \text{for } 2 \leq t < 3 \quad \text{and } \tau = t - 2, \\ (1 - \tau) H_{\text{int}}^{13} + \tau H_{\text{int}}^{14} & \text{for } 3 \leq t < 4 \quad \text{and } \tau = t - 3. \end{cases} \quad 2.149$$

Then we set $H_{\text{int}}(t) \equiv \tilde{H}_{\text{int}}(t \bmod 4)$ to allow for a double-exchange (that is, full braiding) of the two edge states associated with the inner endpoints s_1 and s_2 of chains L_1 and L_2 for $0 \leq t \leq 8$.

The coupling Hamiltonians are defined analogous to the intra-chain coupling $A_i(\mathbb{1} + A_i)$, namely

$$H_{\text{int}}^{34} = a_{s_3} a_{s_4}^\dagger + a_{s_4} a_{s_3}^\dagger + n_{s_3}(\mathbb{1} - n_{s_4}) + n_{s_4}(\mathbb{1} - n_{s_3}), \quad 2.150a$$

$$H_{\text{int}}^{14} = i a_{s_1} a_{s_4}^\dagger - i a_{s_4} a_{s_1}^\dagger + n_{s_1}(\mathbb{1} - n_{s_4}) + n_{s_4}(\mathbb{1} - n_{s_1}), \quad 2.150b$$

$$H_{\text{int}}^{12} = a_{s_1} a_{s_2}^\dagger + a_{s_2} a_{s_1}^\dagger + n_{s_1}(\mathbb{1} - n_{s_2}) + n_{s_2}(\mathbb{1} - n_{s_1}), \quad 2.150c$$

$$H_{\text{int}}^{13} = a_{s_1} a_{s_3}^\dagger + a_{s_3} a_{s_1}^\dagger + n_{s_1}(\mathbb{1} - n_{s_3}) + n_{s_3}(\mathbb{1} - n_{s_1}), \quad 2.150d$$

where s_i denotes the terminating fermion site on chain L_i , see Figure 2.18. Note that the single-particle hopping in H_{int}^{14} breaks time-reversal symmetry; this is necessary to create a finite overlap between ground states for couplings between chains with reversed fermion ordering [shown in Figure 2.18 (a)].

⁷⁷The topological spin is a (possibly fractional) phase θ_x that occurs when an anyon x is rotated by 2π around its axis. For anyon models in condensed matter physics, it is a consequence of the finite extent of quasiparticles. This implies that the “world lines” of anyons are not actual *lines* but *ribbons*; explaining the occurrence of *ribbon fusion categories* in this context [48, 57].

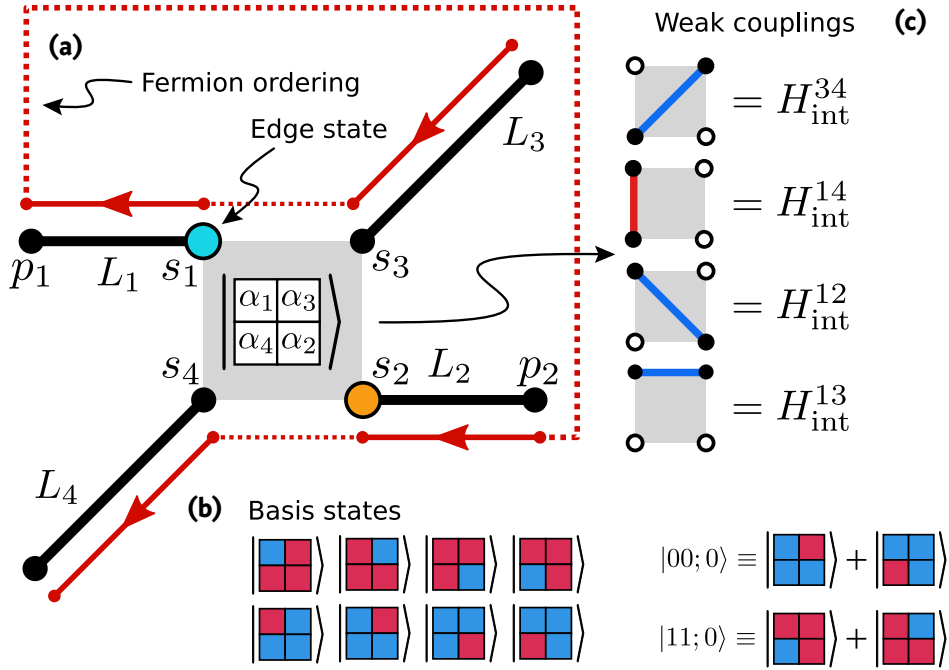


FIGURE 2.18 • Braiding—Derivation. (a) Braiding setup with four chains $L_i, i = 1, \dots, 4$. The “bath” chain is omitted as it is not relevant for the low-energy physics. The chosen fermion ordering that defines the Fock basis is drawn red. The α_i denote the subchain parities constrained by $\alpha_1\alpha_2\alpha_3\alpha_4 = -1$. The endpoints of chains are labeled by s_i and p_i . (b) The 8 basis states that span the ground state space of H_0 . The linear combinations $|00;0\rangle$ and $|11;0\rangle$ are mapped to each other by the braiding holonomy. (c) The weak single-particle couplings used for the construction of $H_{\text{int}}(t)$ that drives the braiding. Blue (red) edges denote time-reversal invariant (breaking) single-particle hopping.

In the ground state basis (2.139), the matrix elements of the coupling Hamiltonians (2.150) read as follows (here exemplarily for H_{int}^{34})

$$\begin{aligned} \langle \beta_1\beta_3 | H_{\text{int}}^{34} | \alpha_1\alpha_3 \rangle &= & 2.151 \\ \langle \beta_4\beta_2 | & \\ & \left[\delta_{\alpha,\beta} \mathcal{N}_\alpha^{-1} + \delta_{\alpha_1,\beta_1} \delta_{\alpha_2,\beta_2} \delta_{\alpha_3,-\beta_3} \delta_{\alpha_4,-\beta_4} \mathcal{N}_\alpha^{-1/2} \mathcal{N}_\beta^{-1/2} (-\alpha_1\alpha_2) \right] \\ & \times \left[\binom{L_1, L_2, L_3 - 1, L_4 - 1, L_0}{\alpha_1, \alpha_2, \alpha_3, -\alpha_4}_{N-1} + \binom{L_1, L_2, L_3 - 1, L_4 - 1, L_0}{\alpha_1, \alpha_2, -\alpha_3, \alpha_4}_{N-1} \right] \end{aligned}$$

with the shorthand notation $\delta_{\alpha,\beta} \equiv \prod_{i=1}^4 \delta_{\alpha_i,\beta_i}$, the length of the “bath” chain L_0 , and the normalization

$$\mathcal{N}_\alpha = \binom{L_1, L_2, L_3, L_4, L_0}{\alpha_1, \alpha_2, \alpha_3, \alpha_4}_N. \quad 2.152$$

Using that

$$\begin{aligned} & \left(\begin{array}{c} L_1, L_2, L_3, L_4, L_0 \\ \alpha_1, \alpha_2, \alpha_3, \alpha_4 \end{array} \right)_N^{-1} \left(\begin{array}{c} L_1, L_2, L_3 - 1, L_4 - 1, L_0 \\ \beta_1, \beta_2, \beta_3, \beta_4 \end{array} \right)_{N-1} \\ & \longrightarrow \rho(1 - \rho) \quad \text{for} \quad L_i, N \rightarrow \infty \end{aligned} \quad 2.153$$

up to exponentially small α - and β -dependent terms, yields the expressions

$$\left\langle \begin{array}{c} \beta_1 \beta_3 \\ \beta_4 \beta_2 \end{array} \middle| H_{\text{int}}^{34} \begin{array}{c} \alpha_1 \alpha_3 \\ \alpha_4 \alpha_2 \end{array} \right\rangle \sim \delta_{\alpha, \beta} \cdot 1 + \delta_{\alpha_1, \beta_1} \delta_{\alpha_2, \beta_2} \delta_{\alpha_3, -\beta_3} \delta_{\alpha_4, -\beta_4} \cdot (-\alpha_1 \alpha_2) \quad 2.154a$$

$$\left\langle \begin{array}{c} \beta_1 \beta_3 \\ \beta_4 \beta_2 \end{array} \middle| H_{\text{int}}^{14} \begin{array}{c} \alpha_1 \alpha_3 \\ \alpha_4 \alpha_2 \end{array} \right\rangle \sim \delta_{\alpha, \beta} \cdot 1 + \delta_{\alpha_1, -\beta_1} \delta_{\alpha_2, \beta_2} \delta_{\alpha_3, \beta_3} \delta_{\alpha_4, -\beta_4} \cdot (-i \alpha_1 \alpha_2) \quad 2.154b$$

$$\left\langle \begin{array}{c} \beta_1 \beta_3 \\ \beta_4 \beta_2 \end{array} \middle| H_{\text{int}}^{12} \begin{array}{c} \alpha_1 \alpha_3 \\ \alpha_4 \alpha_2 \end{array} \right\rangle \sim \delta_{\alpha, \beta} \cdot 1 + \delta_{\alpha_1, -\beta_1} \delta_{\alpha_2, -\beta_2} \delta_{\alpha_3, \beta_3} \delta_{\alpha_4, \beta_4} \cdot (+\alpha_1 \alpha_2) \quad 2.154c$$

$$\left\langle \begin{array}{c} \beta_1 \beta_3 \\ \beta_4 \beta_2 \end{array} \middle| H_{\text{int}}^{13} \begin{array}{c} \alpha_1 \alpha_3 \\ \alpha_4 \alpha_2 \end{array} \right\rangle \sim \delta_{\alpha, \beta} \cdot 1 + \delta_{\alpha_1, -\beta_1} \delta_{\alpha_2, \beta_2} \delta_{\alpha_3, -\beta_3} \delta_{\alpha_4, \beta_4} \cdot (-1). \quad 2.154d$$

We omit the global factor of $2\rho(1 - \rho)$ as it is independent of the parities α_i up to exponentially small corrections. The matrix elements (2.154) define the representation of $H_{\text{int}}(t)$ on \mathcal{H}_0 and can be used to integrate the time evolution (2.141b) numerically. To this end, we make use of the approach described in Subsection 3.3.1 of Chapter 3 for the evaluation of the time-ordered exponential.

2.6 Conclusion & Outlook

This chapter was dedicated to the fate of topologically protected Majorana modes when the particle number is conserved. To that end, we introduced a theory of interacting spinless fermions, hopping on a double-chain with open boundaries, that preserves both the total particle number and the fermion parity on subchains. The interactions were chosen such that the local terms of the Hamiltonian are positive semi-definite operators. As a consequence, we were able to construct its many-body ground states from scratch: they are given by equal-weight superpositions of all fermion configurations with fixed total particle number and well-defined subchain parity. In particular, there are *two* degenerate zero-energy ground states in each particle number sector, characterized by their subchain parity.

The evaluation of correlators simplified to purely combinatorial expressions, which paved the way to many physical quantities of interest: The ground states host a condensate of p -wave pairs with true long-range order (as indicated by non-vanishing pair correlations). Most notably, the single-particle correlations decay exponentially in the bulk but feature a revival at the boundaries of the chain; a signature of many-body edge states. Correspondingly, overlaps of degenerate ground states can only be established by single-particle hopping between endpoints of subchains if time-reversal symmetry is broken. This qualifies the ground state

degeneracy as topological, protected by either subchain parity or time-reversal symmetry. The topological degeneracy also leaves its mark on the entanglement spectrum of each ground state which we found to be two-fold degenerate. In this context—and in contrast to the Majorana chain—we noticed a logarithmic growth of the entanglement entropy; we read this as evidence for the vanishing gap of the theory.

Fortunately, not only the ground states, but also a class of excited states is accessible by analytical means. This allowed us to prove and characterize the closing of the gap above the zero-energy ground states: We found a quadratic spectrum of Goldstone modes, in line with the single-magnon excitations of the ferromagnetic, isotropic Heisenberg chain. As for the Majorana chain, we argued that for *periodic* boundaries the two-fold degeneracy is lost as zero-energy ground states are restricted to sectors of odd subchain parity.

Finally, we made an attempt to tighten the relation between Majorana chain and the number-conserving double-chain. To this end, we generalized the double-chain setup to networks of single wires, sectionally interacting via parity-conserving pair hopping. We pointed out that the characteristic ground state structure survives this procedure and contrived a setup with 8-fold degeneracy to implement a rudimentary braiding protocol. Realizing the latter with weak couplings allowed for the numerical evaluation of the full time evolution in the low-energy subspace. We found non-abelian unitary representations acting on the ground state manifold which characterize the edge states as Ising anyons.

In conclusion, many of the intriguing features of the mean field theory can be found in number-conserving settings as well. Most importantly, robust ground state degeneracies and non-abelian statistics of edge states are realized in systems with well-defined particle number. Nevertheless, there are notable differences: First, particle number conservation entails a gapless spectrum which interferes with the concept of braiding, and, second, symmetry protection becomes crucial as degenerate ground states belong to the *same* parity superselection sector. Note that these are not “disadvantages” of the number-conserving theory but consequences of its honesty: On a fundamental level, the number of fermions *is* conserved and only the presence of a large superconducting reservoir renders the quadratic mean field approximation valid.

Open Questions and Related Results

There are some closely related results that complement the findings of this chapter:

- More details on the symmetries of the double-chain setup—in particular the “chain exchange symmetry” that we did not discuss here—can be found in Ref. [237].

CONCLUSION & OUTLOOK

- An alternative parent Hamiltonian of the equal-weight superpositions $|N, \alpha\rangle$ was introduced in Ref. [258], inspired by dissipative schemes for the preparation of topological phases [259]. Several of the ground state properties that we discussed in this chapter have been verified in Ref. [258].
- The system is at a critical point and certain perturbations to the Hamiltonian will drive the system into a phase-separated state (e.g., increasing the attractive interactions), while we expect resilience of the topological properties against other perturbations (e.g., increasing the hopping). But when the relative strength of hopping and interactions is varied (for the intra- or inter-chain couplings), the positivity of the Hamiltonian is lost and the derivation of exact expressions for the ground states fails. Thus one has to resort to numerical and field-theoretic methods, similar to previous approaches [230–234]. In Ref. [248], extensive DMRG simulations and a bosonized description of the low-energy physics are used to explore the *vicinity* of the critical point that we studied in this chapter (for more details, see also [260]). Main results are that the zero-energy ground states $|N, \alpha\rangle$ are representatives of an *extended* topological phase embedded in a rich phase diagram, and that the critical point indeed lives on the verge of phase separation. Moreover, the equivalence with a topological phase that has been studied previously in Ref. [235] by means of DMRG is established.

Despite these additions to the overall picture, there are still some white spots that deserve further study:

- To set the stage for braiding, we generalized the double-wire setup in Subsection 2.5.1 to wire networks. We discussed the construction of Hamiltonians that remain positive semi-definite and thereby retain the simple structure of their ground states. However, we omitted the construction of low-energy excited states. A detailed (numerical?) analysis of the low-energy physics and the effects of inter-chain single-particle hopping might be a promising field for future work. In particular, the efficient application of MPS⁷⁸-based DMRG to such graph-like structures of linked, one-dimensional systems would be interesting.
- In Subsection 2.4.1, we presented the construction of a class of exact eigenstates that is clearly not exhaustive. In ✨ Section 2.C, we invoke the Bethe ansatz to derive the complete spectrum in the interacting sector of $N = 2$ particles. It is not clear whether this ansatz succeeds for arbitrary $N > 2$ (that is, whether the double-chain Hamiltonian H is integrable), and if so, whether it is *feasible* (i.e., whether physical properties can be extracted efficiently⁷⁹).

⁷⁸Matrix product states, a special case of tensor network states, see ✨ Section 2.A.

⁷⁹The applicability of the Bethe ansatz does not necessarily imply the efficient solvability of the Bethe equations.

- In Subsection 2.4.2, we discussed the scaling of the gap for periodic boundary conditions. Whereas the closing of the gap in the odd-odd sector with zero-energy ground state follows from the known class of exact eigenstates, the scaling of the lowest eigenenergy in the other sectors is much harder to derive. In Subsection 2.4.2, we presented an ansatz wave function for the even-even sector with provably vanishing energy in the thermodynamic limit. For the even-odd/odd-even sectors, we also claimed that there is an ansatz wave function that establishes a vanishing gap. The proof, presented in ✱ Subsection 2.B.2, is rigorous up to a (reasonable) assumption from statistical mechanics. How can this assumption be proven and/or circumvented? Are there more elegant routes to rigorous upper bounds on the lowest eigenenergy?
- The braiding in Subsection 2.5.2 established the notion of “Majorana-like” edge states based on their non-abelian statistics. What about their algebraic properties? Is there a (potentially approximate) realization of Majorana operators and their Clifford algebra in sectors of fixed particle number? In ✱ Subsection 2.D.2 we propose operators that are exponentially localized on the edges; these operators map degenerate zero-energy states into each other, just like the Majorana operators of the mean field theory. It would be interesting to unveil their algebraic structure and draw possible connections to “true” Majorana operators.

APPENDICES FOR CHAPTER 2

2.A Matrix Product State Representation

Matrix product states (MPS) are the one-dimensional special case of more general tensor network states (TNS) [261]. The latter parametrize many-body quantum states by means of tensor contractions. In one dimension, tensor networks simplify to chain-like graphs such that contractions become matrix products; the quantum state is then encoded by the matrix entries. As long as the amount of entanglement between a subsystem of the chain and its complement grows at most logarithmically with the subsystem size, the dimension of the matrices (the *bond dimension* D) grows only polynomially with the system size. This implies that “weakly entangled” states can be described by a polynomial number of parameters—quite unusual in an exponentially large Hilbert space. Therefore, MPS representations are a powerful and versatile tool for the description and numerical exploration of one-dimensional strongly correlated quantum systems [262, 263].

Here we derive the MPS representation of the exact zero-energy ground states $|N, \alpha\rangle$. As their parent Hamiltonian H is gapless (and the entanglement entropy grows logarithmically, Subsection 2.3.3), we find a polynomially growing bond dimension D . In the following, we proceed along the lines of Ref. [261].

We consider ground states of the form ($0 \leq N \leq 2L$ and $\alpha = \pm 1$)

$$|N, \alpha\rangle \propto \sum_{M, (-1)^M = \alpha} |M\rangle_a |N - M\rangle_b, \quad 2.155$$

i.e., equal-weight superpositions of fixed total particle number N and (upper) subchain parity α . Here $|M\rangle_x$ denotes the unnormalized equal-weight superposition

of M particles ($|\downarrow\rangle = |1\rangle$ in spin representation)

$$|M\rangle_x = \sum_{\mathbf{m} \in \{0,1\}^L, |\mathbf{m}|=M} |\mathbf{m}\rangle_x \quad 2.156$$

for chain $x \in \{a, b\}$ of length L . Recall that states of this form are zero-energy ground states for all N and α for *open boundary conditions*. With *closed boundary conditions*, this is true only if N is even and $\alpha = -1$, that is, whenever both subchains have odd parity, see Subsection 2.4.2 and $\star\star$ Section 2.B.

We aim at a representation of these ground states as MPS, namely

$$|N, \alpha\rangle = \sum_{\mathbf{n}, \mathbf{m} \in \{0,1\}^L} \text{Tr} \left[A_{n_1, m_1}^{[1]} \cdots A_{n_L, m_L}^{[L]} \right] |\mathbf{n}\rangle_a |\mathbf{m}\rangle_b \quad 2.157$$

with matrices $A_{n_i, m_i}^{[i]} \in \mathbb{C}^{D_i \times D_{i+1}}$ and bond dimensions D_i ($D_{L+1} = D_1$). In general, $D_i = D_i(L)$ grows with the system size L . If this growth is only polynomial, expectation values of (local) observables may be evaluated efficiently in terms of the matrices $A_{n_i, m_i}^{[i]}$. To determine the latter, we expand the equal-weight superpositions successively in terms of their Schmidt decomposition [264].

First, we observe that fixing the subchain parity is particularly simple in the MPS formalism; indeed,

$$\text{Tr} \left[\frac{1}{2} (\sigma^z)^{\frac{1-\alpha}{2}} \cdot (\sigma^z)^{n_1} \cdots (\sigma^z)^{n_L} \right] = \begin{cases} 1 & \text{for } (-1)^{|\mathbf{n}|} = \alpha, \\ 0 & \text{otherwise,} \end{cases} \quad 2.158$$

is a matrix product of fixed bond dimension $D = 2$. If we define $C_{n_i}^{[i]} \equiv (\sigma^z)^{n_i}$ for $1 \leq i < L$ and $C_{n_L}^{[L]} \equiv \frac{1}{2} (\sigma^z)^{\frac{1-\alpha}{2}} (\sigma^z)^{n_L}$, we can drop the subchain parity condition and henceforth focus on the equal-weight superposition with fixed particle number only,

$$|N\rangle = \sum_{|\mathbf{n}|+|\mathbf{m}|=N} |\mathbf{n}\rangle_a |\mathbf{m}\rangle_b \quad 2.159a$$

$$\stackrel{!}{=} \sum_{\mathbf{n}, \mathbf{m} \in \{0,1\}^L} \text{Tr} \left[B_{n_1, m_1}^{[1]} \cdots B_{n_L, m_L}^{[L]} \right] |\mathbf{n}, \mathbf{m}\rangle. \quad 2.159b$$

Then we have $A_{n_i, m_i}^{[i]} = B_{n_i, m_i}^{[i]} \otimes C_{n_i}^{[i]}$ as the sought-after MPS description of $|N, \alpha\rangle$.

We start by splitting off the first pair of sites (indices n_1 and m_1) from the bulk by Schmidt decomposition

$$|N\rangle = \sum_{\beta_1=0}^{d_1-1} \lambda_{\beta_1}^{[1]} |\tau_{\beta_1}^{[1]}\rangle \otimes |\tau_{\beta_1}^{[2\dots L]}\rangle \quad 2.160$$

MATRIX PRODUCT STATE REPRESENTATION

where $\lambda_{\beta_1}^{[1]}$ denotes the first Schmidt coefficients and $|\tau_{\beta_1}^{[1]}\rangle, |\tau_{\beta_1}^{[2\dots L]}\rangle$ are the orthonormal Schmidt vectors. The indices β_1 run from 0 to $d_1 - 1$ where $d_1 \leq 4$ denotes the Schmidt rank. Note that we dropped the normalization of $|N\rangle$ for the sake of simplicity as it only rescales the Schmidt coefficients.

Here we find $d_1 = 3$ (because the first two modes a_1 and b_1 can contain at most $d_1 - 1 = 2$ particles) and

$$|\tau_{\beta_1}^{[1]}\rangle = |\beta_1\rangle_2, \quad |\tau_{\beta_1}^{[2\dots L]}\rangle = |N - \beta_1\rangle_{2(L-1)} \quad 2.161$$

where $|M\rangle_K$ denotes the *normalized* equal-weight superposition of K (single!) sites with M particles. The Schmidt coefficients are then given by the inverse normalizing factors, namely

$$\lambda_{\beta_1}^{[1]} = \binom{2}{\beta_1}^{1/2} \binom{2L-2}{N-\beta_1}^{1/2}. \quad 2.162$$

Next, we expand the left Schmidt vector in the local standard basis $|\mathbf{i}_1 = (n_1, m_1)\rangle$, which yields

$$|N\rangle = \sum_{\beta_1=0}^{d_1-1} \sum_{\mathbf{i}_1 \in \{0,1\}^2} \Gamma_{\beta_1}^{[1]\mathbf{i}_1} \lambda_{\beta_1}^{[1]} |\mathbf{i}_1\rangle \otimes |\tau_{\beta_1}^{[2\dots L]}\rangle \quad 2.163$$

with the coefficients

$$\Gamma_{\beta_1}^{[1]\mathbf{i}_1} = \delta_{|\mathbf{i}_1|, \beta_1} \binom{2}{\beta_1}^{-1/2}. \quad 2.164$$

The right Schmidt vector $|\tau_{\beta_1}^{[2\dots L]}\rangle$ can be written as

$$|\tau_{\beta_1}^{[2\dots L]}\rangle = \sum_{\mathbf{i}_2 \in \{0,1\}^2} |\mathbf{i}_2\rangle \otimes |\omega_{\beta_1 \mathbf{i}_2}^{[3\dots L]}\rangle \quad 2.165$$

with the unnormalized state

$$|\omega_{\beta_1 \mathbf{i}_2}^{[3\dots L]}\rangle = \binom{2L-2}{N-\beta_1}^{-1/2} \sum_{\substack{\mathbf{n}, \mathbf{m} \in \{0,1\}^{L-2} \\ |\mathbf{n}| + |\mathbf{m}| = N - \beta_1 - |\mathbf{i}_2|}} |\mathbf{n}', \mathbf{m}'\rangle. \quad 2.166$$

This state can be easily expressed in terms of the right Schmidt vectors $|\tau_{\beta_2}^{[3\dots L]}\rangle$ for the partition $(1, 2|3, \dots, L)$, namely

$$|\omega_{\beta_1 \mathbf{i}_2}^{[3\dots L]}\rangle = \sum_{\beta_2=0}^{d_2-1=4} \Gamma_{\beta_1 \beta_2}^{[2]\mathbf{i}_2} \lambda_{\beta_2}^{[2]} |\tau_{\beta_2}^{[3\dots L]}\rangle \quad 2.167$$

where $|\tau_{\beta_2}^{[3\dots L]}\rangle = |N - \beta_2\rangle_{2(L-2)}$ is the (normalized) equal-weight superposition and the Schmidt coefficients are given as

$$\lambda_{\beta_2}^{[2]} = \binom{4}{\beta_2}^{1/2} \binom{2L-4}{N-\beta_2}^{1/2} \quad 2.168$$

with the basis coefficients

$$\Gamma_{\beta_1\beta_2}^{[2]i_2} = \delta_{\beta_1+|i_2|,\beta_2} \binom{4}{\beta_2}^{-1/2} \binom{2L-2}{N-\beta_1}^{-1/2}. \quad 2.169$$

Plugging (2.167) in (2.165) and the latter in (2.163) yields

$$|N\rangle = \sum_{i_1, i_2 \in \{0,1\}^2} \sum_{\beta_1=0}^{d_1-1} \sum_{\beta_2=0}^{d_2-1} \left(\Gamma_{\beta_1}^{[1]i_1} \lambda_{\beta_1}^{[1]} \Gamma_{\beta_1\beta_2}^{[2]i_2} \lambda_{\beta_2}^{[2]} \right) |i_1\rangle \otimes |i_2\rangle \otimes |\tau_{\beta_2}^{[3\dots L]}\rangle. \quad 2.170$$

We can iterate this expansion once more, i.e., expand the right Schmidt vector

$$|\tau_{\beta_2}^{[3\dots L]}\rangle = \sum_{i_3 \in \{0,1\}^2} |i_3\rangle \otimes |\omega_{\beta_2 i_3}^{[4\dots L]}\rangle \quad 2.171$$

with

$$|\omega_{\beta_2 i_3}^{[4\dots L]}\rangle = \sum_{\beta_3=0}^{d_3-1=6} \Gamma_{\beta_2\beta_3}^{[3]i_3} \lambda_{\beta_3}^{[3]} |\tau_{\beta_3}^{[4\dots L]}\rangle \quad 2.172$$

and derive the coefficients

$$\lambda_{\beta_3}^{[3]} = \binom{6}{\beta_3}^{1/2} \binom{2L-6}{N-\beta_3}^{1/2} \quad 2.173a$$

$$\text{and } \Gamma_{\beta_2\beta_3}^{[3]i_3} = \delta_{\beta_2+|i_3|,\beta_3} \binom{6}{\beta_3}^{-1/2} \binom{2L-4}{N-\beta_2}^{-1/2}. \quad 2.173b$$

The last Schmidt vector is special as there is no further Schmidt decomposition pending:

$$|\tau_{\beta_{L-1}}^{[L]}\rangle = \sum_{i_L \in \{0,1\}^2} \Gamma_{\beta_{L-1}}^{[L]i_L} |i_L\rangle. \quad 2.174$$

This yields the last coefficient,

$$\Gamma_{\beta_{L-1}}^{[L]i_L} = \delta_{\beta_{L-1}+|i_L|,N} \binom{2}{N-\beta_{L-1}}^{-1/2}. \quad 2.175$$

Thus, iteration over the whole chain yields the MPS expansion

$$|N\rangle = \sum_{\mathbf{i}_1, \dots, \mathbf{i}_L} \sum_{d_1, \dots, d_{L-1}=0}^{d_1, \dots, d_{L-1}-1} \left(\Gamma_{\beta_1}^{[1]i_1} \lambda_{\beta_1}^{[1]} \Gamma_{\beta_1 \beta_2}^{[2]i_2} \lambda_{\beta_2}^{[2]} \dots \lambda_{\beta_{L-1}}^{[L-1]} \Gamma_{\beta_{L-1}}^{[L]i_L} \right) \times |\mathbf{i}_1\rangle |\mathbf{i}_2\rangle \dots |\mathbf{i}_L\rangle \quad 2.176a$$

$$\stackrel{!}{=} \sum_{\mathbf{i}_1, \dots, \mathbf{i}_L} \text{Tr} \left[B_{\mathbf{i}_1}^{[1]} B_{\mathbf{i}_2}^{[2]} \dots B_{\mathbf{i}_L}^{[L]} \right] |\mathbf{i}_1\rangle |\mathbf{i}_2\rangle \dots |\mathbf{i}_L\rangle \quad 2.176b$$

with the tensors

$$\left(B_{\mathbf{i}_k}^{[k]} \right)_{\beta_{k-1}, \beta_k} \equiv \Gamma_{\beta_{k-1} \beta_k}^{[k]i_k} \lambda_{\beta_k}^{[k]} \quad 2.177a$$

$$= \delta_{\beta_{k-1} + |\mathbf{i}_k|, \beta_k} \binom{2L - 2(k-1)}{N - \beta_{k-1}}^{-1/2} \binom{2L - 2k}{N - \beta_k}^{1/2} \quad 2.177b$$

for $1 < k < L$ and

$$\left(B_{\mathbf{i}_1}^{[1]} \right)_{\beta_1} = \Gamma_{\beta_1}^{[1]i_1} \lambda_{\beta_1}^{[1]} = \delta_{|\mathbf{i}_1|, \beta_1} \binom{2L - 2}{N - \beta_1}^{1/2} \quad 2.178a$$

$$\left(B_{\mathbf{i}_L}^{[L]} \right)_{\beta_{L-1}} = \Gamma_{\beta_{L-1}}^{[L]i_L} = \delta_{\beta_{L-1} + |\mathbf{i}_L|, N} \binom{2}{N - \beta_{L-1}}^{-1/2} \quad 2.178b$$

on the boundary.

This is certainly a valid MPS in canonical form; however, the gauge freedom allows us to redistribute the binomial coefficients between adjacent tensors. One immediately realizes that “shifting” the factors

$$\binom{2L - 2k}{N - \beta_k}^{1/2} \quad 2.179$$

one tensor to the right cancels all of them; we are left with the much simpler expressions

$$\left(B_{\mathbf{i}_1}^{[1]} \right)_{\beta_1} = \delta_{|\mathbf{i}_1|, \beta_1}, \quad 2.180a$$

$$\left(B_{\mathbf{i}_k}^{[k]} \right)_{\beta_{k-1}, \beta_k} = \delta_{\beta_{k-1} + |\mathbf{i}_k|, \beta_k}, \quad 2.180b$$

$$\left(B_{\mathbf{i}_L}^{[L]} \right)_{\beta_{L-1}} = \delta_{\beta_{L-1} + |\mathbf{i}_L|, N}, \quad 2.180c$$

for $1 < k < L$. If we define $\beta_0 \equiv 0$ and $\beta_L \equiv N$, we can even write

$$\left(B_{\mathbf{i}_k}^{[k]} \right)_{\beta_{k-1}, \beta_k} = \delta_{\beta_{k-1} + |\mathbf{i}_k|, \beta_k} \quad \text{for } 1 \leq k \leq L. \quad 2.181$$

We observe the following:

→ It is obvious that the described MPS is an *equal-weight* superposition of number states as there is a single non-vanishing component of the traced tensor for each pattern $(\mathbf{i}_1, \dots, \mathbf{i}_L)$ with $0 \leq |\mathbf{i}_k| \leq 2$.

→ For $\text{Tr}[B_{\mathbf{i}_1}^{[1]} B_{\mathbf{i}_2}^{[2]} \dots B_{\mathbf{i}_L}^{[L]}]$ not to vanish, the virtual bond indices must satisfy

$$0 \leq \beta_1 \leq 2 \quad 2.182a$$

$$\text{and } \beta_{k-1} \leq \beta_k \leq \beta_{k-1} + 2 \quad 2.182b$$

$$\text{and } N - 2 \leq \beta_{L-1} \leq N; \quad 2.182c$$

especially

$$0 \leq \beta_1 \leq \beta_2 \leq \dots \leq \beta_{L-1} \leq N \leq 2L. \quad 2.183$$

Thus we can choose a *uniform* bond dimension $D_k \equiv D = N + 1$ for $1 < k \leq L$ (and $D_1 = 1 = D_{L+1}$) which is bounded from above by $2L$. Note that $D \leq \text{Poly}(L)$ was to be expected for a critical one-dimensional system such as H [262].

We point out that this simple tensor network ensures by its local constraints $\delta_{\beta_{k-1}+|\mathbf{i}_k|, \beta_k}$ that the virtual index sequence $\{\beta_k\}$ counts the number of particles, i.e.,

$$\beta_k = \sum_{l=1}^k |\mathbf{i}_l| = \sum_{l=1}^k (n_l + m_l) \quad 2.184$$

and therefore $\beta_L = N$.

To fix both particle number N and subchain parity α , we conjunct the conditions by tensoring the according tensor networks, Figure 2.19:

$$A_{n_i, m_i}^{[i]} \equiv B_{n_i, m_i}^{[i]} \otimes C_{n_i}^{[i]}. \quad 2.185$$

Recall that $C_{n_i}^{[i]} = (\sigma^z)^{n_i}$ for $1 \leq i < L$, so

$$\left(C_{n_i}^{[i]}\right)_{\bar{\beta}_{i-1}, \bar{\beta}_i} = \delta_{\bar{\beta}_{i-1}, \bar{\beta}_i} (-1)^{n_i \delta_{\bar{\beta}_i, 2}} \quad \text{for } \bar{\beta}_{i-1}, \bar{\beta}_i \in \{1, 2\} \quad 2.186$$

in coordinate representation. The last tensor is special as it fixes the subchain-parity sector:

$$\left(C_{n_L}^{[L]}\right)_{\bar{\beta}_{L-1}, \bar{\beta}_L} = \frac{1}{2} \delta_{\bar{\beta}_{L-1}, \bar{\beta}_L} (-1)^{[(1-\alpha)/2 + n_L] \delta_{\bar{\beta}_L, 2}}. \quad 2.187$$

MATRIX PRODUCT STATE REPRESENTATION

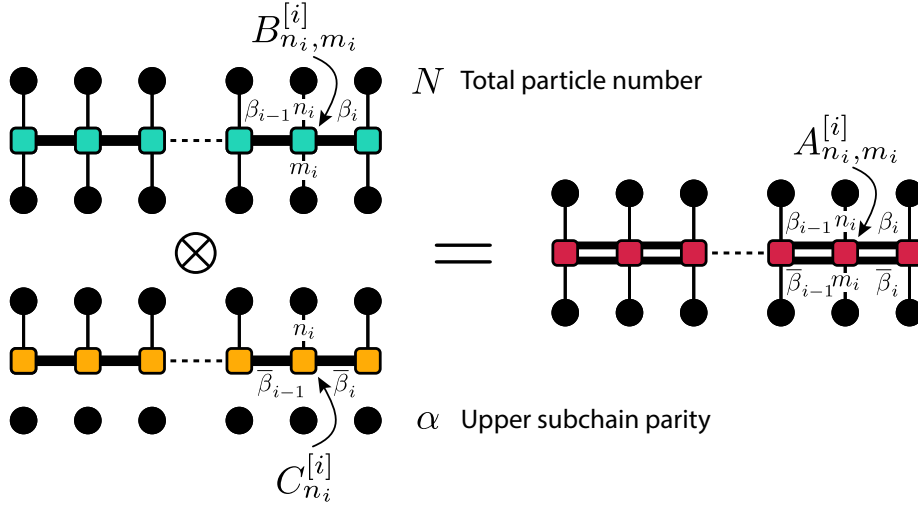


FIGURE 2.19 • Matrix product state representation. We show a schematic representation of the two MPS constructions described in the text. Physical bonds n_i, m_i are drawn by thin vertical lines, whereas the virtual bonds $\beta_i, \bar{\beta}_i$ are given by thick horizontal lines. Black circles denote physical sites (spins or fermion modes), colored squares the tensors A (red), B (green), and C (yellow). The total particle number N is fixed by B , the upper subchain parity α by C . The conjunction of both conditions is realized by their tensor product A .

Within this representation, one can easily check

$$\text{Tr} [C_{n_1}^{[1]} \dots C_{n_L}^{[L]}] = \sum_{\bar{\beta}_0, \dots, \bar{\beta}_L} \delta_{\bar{\beta}_0, \bar{\beta}_1} (-1)^{n_1 \delta_{\bar{\beta}_1, 2}} \dots \frac{1}{2} \delta_{\bar{\beta}_{L-1}, \bar{\beta}_L} \times (-1)^{[(1-\alpha)/2 + n_L] \delta_{\bar{\beta}_L, 2}} \underbrace{\delta_{\bar{\beta}_0, \bar{\beta}_L}}_{\text{Trace}} \quad 2.188a$$

$$= \frac{1}{2} \sum_{\bar{\beta}_0=1,2} (-1)^{\delta_{\bar{\beta}_0, 2} [\sum_{i=1}^L n_i + (1-\alpha)/2]} \quad 2.188b$$

$$= \frac{1}{2} [1 + \alpha P_a(\mathbf{n})] = \delta_{\alpha, P_a(\mathbf{n})} \quad 2.188c$$

with the upper subchain parity $P_a(\mathbf{n})$.

For the tensor product, we introduce the pair indices $\beta_i \equiv (\beta_i, \bar{\beta}_i)$ with $0 \leq \beta_i \leq N \leq 2L$ and $\bar{\beta}_i = 1, 2$. Thus, the final tensors' $A_{n_i, m_i}^{[i]}$ virtual bond dimension is bounded by $4L$. We find

$$\left(A_{n_i, m_i}^{[i]} \right)_{\beta_{i-1}, \beta_i} = \left(B_{n_i, m_i}^{[i]} \right)_{\beta_{i-1}, \beta_i} \cdot \left(C_{n_i}^{[i]} \right)_{\bar{\beta}_{i-1}, \bar{\beta}_i} \quad 2.189a$$

$$= \delta_{\beta_{i-1} + n_i + m_i, \beta_i} \cdot \delta_{\bar{\beta}_{i-1}, \bar{\beta}_i} (-1)^{n_i \delta_{\bar{\beta}_i, 2}} \quad 2.189b$$

for $1 \leq i < L$; the last tensor reads

$$\begin{aligned} \left(A_{n_L, m_L}^{[L]}(N, \alpha) \right)_{\beta_{L-1}, \beta_L} &= \frac{1}{2} \delta_{\beta_{L-1} + n_L + m_L, N} \cdot \delta_{\bar{\beta}_{L-1}, \bar{\beta}_L} \\ &\times (-1)^{[(1-\alpha)/2 + n_L] \delta_{\bar{\beta}_L, 2}}, \end{aligned} \quad 2.190$$

which allows us to fix the particle number $0 \leq N \leq 2L$ and the subchain parity $\alpha = \pm 1$. We conclude that for an open chain, the ground states can be expressed exactly by an MPS with linearly growing bond dimension $D \sim 4L$,

$$|N, \alpha\rangle = \sum_{\mathbf{n}, \mathbf{m} \in \{0,1\}^L} \text{Tr} \left[A_{n_1, m_1}^{[1]} \dots A_{n_L, m_L}^{[L]}(N, \alpha) \right] |\mathbf{n}, \mathbf{m}\rangle \quad 2.191$$

with the tensors given by (2.189b) and (2.190) (up to normalization).

2.B Estimates on the Spectral Gap

Here we provide details on the derivation of the upper/lower bounds on the spectral gap that we discussed in Subsection 2.4.2: In \clubsuit Subsection 2.B.1 we show how to construct a rigorous *lower* bound on the ground state energy in the even-even sector (for periodic double-chains). In \clubsuit Subsection 2.B.2 we discuss the construction of an *upper* bound in sectors of odd total parity; the result suggests the vanishing of the single-particle gap in the thermodynamic limit. We conclude in \clubsuit Subsection 2.B.3 with the derivation of an *upper* bound in the even-even sector.

2.B.1 Lower Bound for Even Subchain Parity

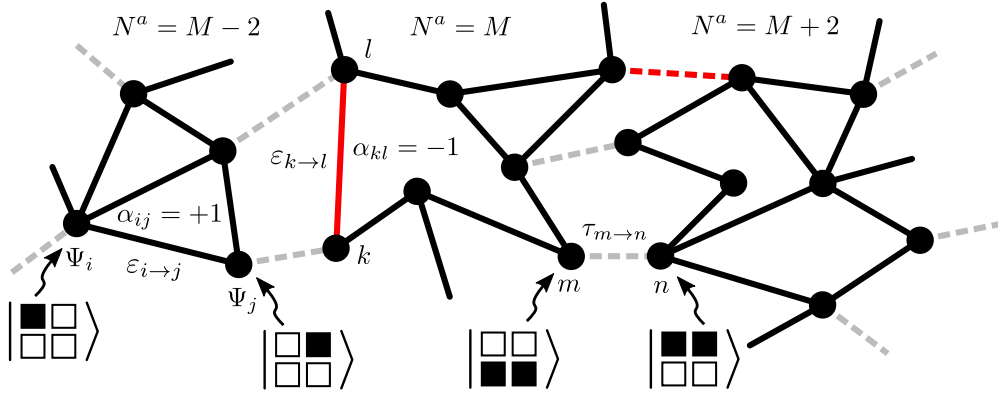
Let H denote the double-chain Hamiltonian with *periodic boundary conditions* (introduced in Subsection 2.4.2). In the following, we assume that at least one subchain has *even* parity. We already know that there are no zero-energy ground states with such parities; here we are interested in a *lower* bound on the smallest eigenenergy in these sectors to prove its algebraic decay in the thermodynamic limit. The construction of lower bounds is subtle as it makes statements about *all* possible states—in contrast to upper bounds which follow from specific ansatz wave functions [recall Eq. (2.118) and see \clubsuit Subsection 2.B.2 and \clubsuit Subsection 2.B.3 below].

The basic line of thought is to consider the energy expectation value of H for a generic state $|\Psi\rangle$ [recall Eq. (2.114)],

$$\langle \Psi | H | \Psi \rangle \propto \sum_{(ij) \in G} |\Psi_i - \alpha_{ij} \Psi_j|^2, \quad 2.192$$

where $\alpha_{ij} = \pm 1$ due to the fermionic statistics and i, j are indices labeling fermion configurations (\mathbf{n}, \mathbf{m}) on both chains. We stress that the only assumption necessary for the following results is the structure of (2.192) which, for instance, is also satisfied by the *single-chain* Hamiltonians H^x on a chain of fixed particle number (we will exploit this below).

G can be thought of as a graph that encodes possible local transformations $\Psi_i \mapsto \Psi_j$ by the Hamiltonian H , pictorially:



Each edge is assigned a sign $\alpha_e = \alpha_{ij} = \pm 1$; negative edges are highlighted red. On the double-chain H , there are two different types of local transformations: intra-chain single-particle hopping denoted by ε and solid lines, and inter-chain pair hopping denoted by τ and dashed lines [recall their definition in Eq. (2.23) and (2.24) and the generalization for periodic chains in Eq. (2.112) and (2.113)]. The latter connect components of G with different upper-chain particle number N^a in ± 2 -intervals. Note that both ε - and τ -hopping can occur with negative edge weight α_e on double-chains with periodic boundary conditions. The local structure of G is illustrated in Figure 2.20 in more detail.

Assume that C is a cycle (closed loop) in G . Then we can estimate

$$\langle \Psi | H | \Psi \rangle \geq \sum_{(ij) \in C} |\Psi_i - \alpha_{ij} \Psi_j|^2 \quad 2.193$$

as C is just a subset of edges in G . Using Hölder's inequality, one can find the lower bound

$$\sum_{(ij) \in C} |\Psi_i - \alpha_{ij} \Psi_j|^2 \geq \frac{1}{|C|} \left[\sum_{(ij) \in C} |\Psi_i - \alpha_{ij} \Psi_j| \right]^2, \quad 2.194$$

where $|C|$ is the length of C .

MAJORANA-LIKE EDGE STATES & NUMBER CONSERVATION

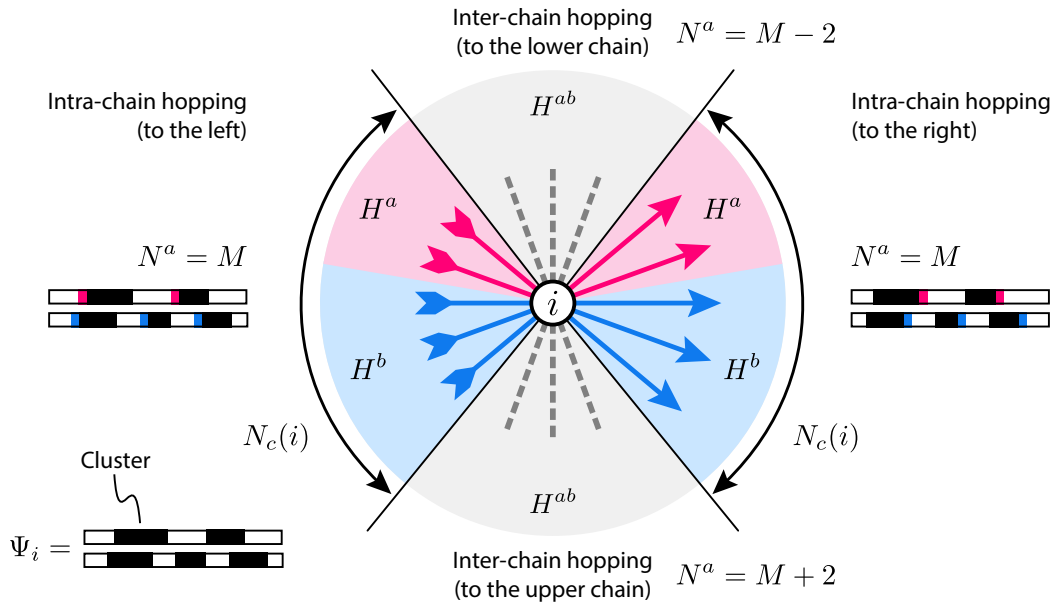
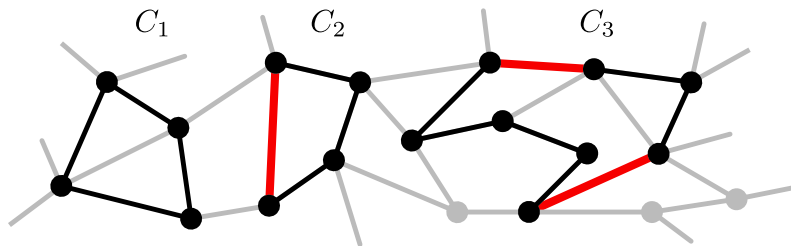


FIGURE 2.20 • Local structure of G . Within each N^a -sector, the upper- (red) and lower-chain (blue) single-particle hopping connects the vertices of G . For each hopping to the right (outgoing edges), there is a corresponding hopping to the left (incoming edges) as each cluster has two boundaries. The total number of intra-chain edges is then $2N_c(i)$ where $N_c(i)$ denotes the numbers of clusters in configuration Ψ_i . Pair hopping between the subchains is indicated by dashed gray edges which connect to different N^a -sectors in G .

If one applies the (inverse) triangle inequality to the sum (under the square), and chooses the signs of the terms $|\Psi_i - \alpha_{ij} \Psi_j|$ appropriately, it is easy to see that the lower bound

$$\frac{1}{|C|} \left[\sum_{(ij) \in C} |\Psi_i - \alpha_{ij} \Psi_j| \right]^2 \geq \frac{1}{|C|} |\Psi_{i^*}|^2 \quad 2.195$$

follows for an arbitrary vertex $i^* \in C$ whenever the number of negative edges on C is *odd*, as for C_2 in the figure below:



This follows because the sum after the (inverse) triangle inequality is a telescoping series with non-vanishing boundary term. For cycles with an *even* number of negative edges (C_1 and C_3 above), the same procedure leads only to *differences* of vertex fields Ψ_i on C as lower bounds (which vanish identically for equal-weight superpositions).

Let \mathcal{C}^- denote the set of all cycles in G with an odd number of negative edges. As the previous estimate holds for arbitrary $i^* \in C \in \mathcal{C}^-$, it also holds for the mean of vertex weights $|\Psi_i|^2$ over the whole cycle C :

$$\frac{1}{|C|} \left[\sum_{(ij) \in C} |\Psi_i - \alpha_{ij} \Psi_j| \right]^2 \geq \frac{1}{|C|^2} \sum_{i \in C} |\Psi_i|^2. \quad 2.196$$

Let us assume there is a subset $\mathcal{L} \subseteq \mathcal{C}^-$ of cycles C with length $|C| \leq \sqrt{A_1}$ in $G = G_{L,N}$ such that every admissible configuration i for filling N and system size L is visited by at least $A_2 > 0$ cycles in \mathcal{L} and every edge in G is used by at most A_3 cycles in \mathcal{L} ($A_{1,2,3}$ are positive, possibly N - and/or L -dependent constants). Physically, these cycles will be interpreted as virtual tunneling of a single fermion around the periodic (double-)chain; we construct them explicitly below. But first, let us apply the previous estimates to the cycles in \mathcal{L} :

Since every edge in G is used by at most A_3 cycles in \mathcal{L} , we have

$$\langle \Psi | H | \Psi \rangle \geq \frac{1}{A_3} \sum_{C \in \mathcal{L}} \sum_{(ij) \in C} |\Psi_i - \alpha_{ij} \Psi_j|^2. \quad 2.197$$

Using the estimates (2.194) and (2.196) for a single “odd” cycle $C \in \mathcal{C}^-$ yields

$$\langle \Psi | H | \Psi \rangle \geq \frac{1}{A_1 A_3} \sum_{C \in \mathcal{L}} \sum_{i \in C} |\Psi_i|^2, \quad 2.198$$

where we used the bounded length $|C| \leq \sqrt{A_1}$ of cycles in \mathcal{L} . Due to the fact that every configuration i is visited by at least A_2 cycles in \mathcal{L} , it follows immediately

RESULT 2.1: Lower bound on the ground state energy

$$\langle \Psi | H | \Psi \rangle \geq \frac{A_2}{A_1 A_3} \sum_{i \in G} |\Psi_i|^2 = \frac{A_2}{A_1 A_3}. \quad 2.199$$

Here we used the normalization condition for the vertex field Ψ_i (the coefficients of the wave function $|\Psi\rangle$). Note that this last step is crucial for a non-trivial (that is, non-zero) lower bound. Eq. (2.199) depends on the set of cycles \mathcal{L} which, in turn, depends on the coupling graph G . Since \mathcal{L} is merely restricted but not uniquely determined by G , it is the choice of \mathcal{L} that decides on the strictness of this lower bound.

Construction of \mathcal{L}

Let us construct a family of cycles $\mathcal{L} \subseteq \mathcal{C}^-$ and evaluate their parameters $A_{1,2,3}$ to find and explicit lower bound on the ground state energy. To do so, we need some preliminary simplifications.

Consider a double-chain with periodic boundary conditions, length L and non-trivial total filling $0 < N < 2L$ within a subchain-parity sector with at least one subchain of even parity (i.e., there is no zero-energy ground state). In addition, recall that due to the positivity of all local terms in the Hamiltonian, it is

$$\langle \Psi | H | \Psi \rangle = \langle \Psi | H^a + H^b + H^{ab} | \Psi \rangle \quad 2.200a$$

$$\geq \langle \Psi | H^a | \Psi \rangle + \langle \Psi | H^b | \Psi \rangle, \quad 2.200b$$

which leaves us effectively with two decoupled chains of filling N^a and $N^b = N - N^a$. Since H^x trivially commutes with N^x , we can restrict $|\Psi\rangle$ to the subspace \mathcal{H}_{N^a, N^b} with fixed upper- and lower-chain filling for $0 \leq N^a \leq \min\{N, L\}$ and $N^b = N - N^a$.

There are two cases to be considered separately:

- **N even:** In the even-even subsector, there is always a non-empty subchain with even filling; this follows from the Hilbert space decomposition

$$\mathcal{H}_{\alpha=+1}^N = \mathcal{H}_{0,N} \oplus \mathcal{H}_{2,N-2} \oplus \cdots \oplus \mathcal{H}_{N-2,2} \oplus \mathcal{H}_{N,0}. \quad 2.201$$

Thus in all possible subsectors \mathcal{H}_{N^a, N^b} either H^a or H^b (or both) can yield a non-trivial lower bound for the energy due to the intra-chain interactions alone (for $0 < N < L$). Note that at half-filling ($N = L$) the subspaces $\mathcal{H}_{0,L}$ and $\mathcal{H}_{L,0}$ both host zero-energy states of $H^a + H^b$ (which complicates the analysis, see next case).

- **N odd:** In the even-odd/odd-even subsectors, there is always a subsector with empty “even”-parity and non-empty odd-parity subchain (for $N \leq L$), namely

$$\mathcal{H}_{\alpha=+1}^N = \mathcal{H}_{0,N} \oplus \mathcal{H}_{2,N-2} \oplus \cdots \oplus \mathcal{H}_{N-3,3} \oplus \mathcal{H}_{N-1,1} \quad 2.202a$$

$$\mathcal{H}_{\alpha=-1}^N = \mathcal{H}_{1,N-1} \oplus \mathcal{H}_{3,N-3} \oplus \cdots \oplus \mathcal{H}_{N-2,2} \oplus \mathcal{H}_{N,0}. \quad 2.202b$$

This is a problem as the decomposition shows that there is a zero-energy ground state for the Hamiltonian $H^a + H^b$ within the highlighted subsectors (similar to the case of half-filling for even N). This precludes the intended reduction (2.200b) to a problem of decoupled single-chains.

In summary, for *even* filling $0 < N < L$, the absence of a zero-energy ground state and possible lower bounds on the ground state energy are already implied by the *intra-chain* interactions H^x alone. However, for *odd* filling (or even half-filling), the *inter-chain* coupling H^{ab} is necessary to establish similar results, and the lower

bound (2.200b) must be replaced by (2.200a). This complicates the construction of \mathcal{L} since both intra- and inter-chain hopping must be taken into account. Lest technicalities get out of hand, we limit the following discussion to the simpler case of even N ($0 < N < L$) and leave the other cases for future studies.

For $|\Psi\rangle \in \mathcal{H}_{\alpha=+1}^N$, we are interested in the lower bound

$$\langle \Psi | H | \Psi \rangle \geq \langle \Psi | H^a | \Psi \rangle + \langle \Psi | H^b | \Psi \rangle \quad 2.203a$$

$$= \sum_{k=0}^{N/2} |c_{2k}|^2 \left[\langle \Psi_{2k} | H^a | \Psi_{2k} \rangle + \langle \Psi_{2k} | H^b | \Psi_{2k} \rangle \right] \quad 2.203b$$

$$\geq \sum_{k=0}^{N/2} |c_{2k}|^2 \max \left\{ \langle \Psi_{2k} | H^a | \Psi_{2k} \rangle, \langle \Psi_{2k} | H^b | \Psi_{2k} \rangle \right\}, \quad 2.203c$$

where $|\Psi\rangle = \sum_k c_{2k} |\Psi_{2k}\rangle$ with $|\Psi_n\rangle \in \mathcal{H}_{n, N-n}$ and $\sum_k |c_{2k}|^2 = 1$, recall Eq. (2.201). Equation (2.203c) allows us to replace the construction of \mathcal{L} for $\langle \Psi | H | \Psi \rangle$ by a simpler construction for $\langle \Psi_{2k} | H^x | \Psi_{2k} \rangle$. Note that the result (2.199) is still valid since the single-chain Hamiltonians feature all properties needed for its derivation [in particular, $\langle \Psi_{2k} | H^x | \Psi_{2k} \rangle$ has the form (2.192)]. The simplification is due to the new graph G which now only describes configurations of $2k$ (or $N - 2k$) fermions on a *single* chain.

Hence we consider a single, periodic chain of length L filled with N^x fermions where $N^x (= 2k$ or $N - 2k)$ is even and $0 < N^x < L$. We seek for a procedure to define an appropriate family of cycles \mathcal{L} constructively. To this end, we adopt the notion of a *finite transition system* $\mathcal{T} = (S, \rightarrow)$ describing the transitions “ \rightarrow ” between a finite set of states S . If a system maps state $s \in S$ to $s' \in S$, we write $s \rightarrow s'$. A closed chain of states under “ \rightarrow ,” such as

$$s_0 \rightarrow s_1 \rightarrow s_2 \rightarrow \cdots \rightarrow s_m \rightarrow s_0, \quad 2.204$$

is called a *cycle*. The set of all cycles is denoted $\mathcal{C}(\mathcal{T})$.

- 1 In our case, a state $s = (\mathbf{n}, \mathbf{e}, \mathbf{h})$ is given by (1) a configuration of N^x fermions $\mathbf{n} \in \{0, 1\}^L$ with $|\mathbf{n}| = N^x$, (2) a configuration of either one or two “virtual charges” $\mathbf{e} \in \{0, 1\}^L$ with $|\mathbf{e}| \in \{1, 2\}$, and (3) a configuration of at most one “virtual hole” $\mathbf{h} \in \{0, 1\}^L$ with $|\mathbf{h}| \in \{0, 1\}$.

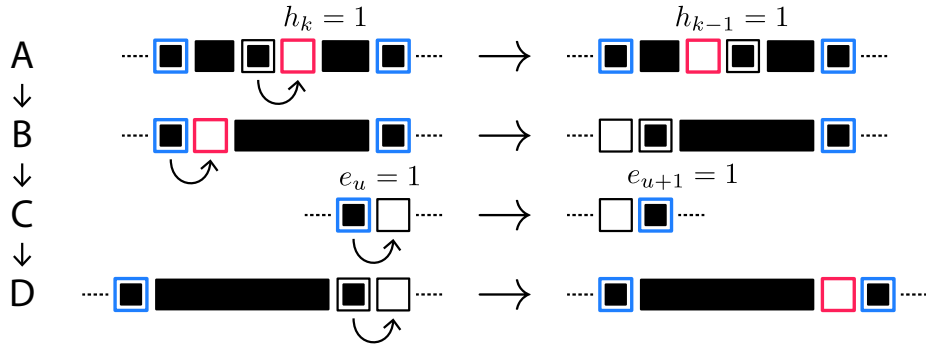
The complete set S of admissible states is then defined as follows: For any given configuration \mathbf{n} , one may place either a *single* charge $e_u = 1$ on any occupied site u (where $n_u = 1$), or *two* charges on occupied sites with a *single* hole in-between; the latter is then assigned a virtual hole $h_k = 1$.

This construction can be illustrated pictorially:



The blue (red) boxes indicate virtual charges (holes), the black fields label occupied sites in n (single sites as boxes, clusters as continuous rectangles), the dotted lines denote arbitrary configurations of the environment without virtual charges/holes.

- 2 To complete the definition of \mathcal{T} , we have to provide the transition function “ \rightarrow ” that acts on these states. This is done best by picture:



The rules should be read in a if...else if...else if... fashion from top to bottom:

One starts with A and checks whether the current state s matches the left-hand side. If so, the transformation is applied and the loop starts over again acting on the result. If a rule does not match, the algorithm proceeds to the next row, and so forth. The given transitions encode the general rules “holes before charges,” “holes move to the left,” and “charges move to the right.” Whenever a hole hits a charge, the pair annihilates. When a charge hits a cluster, a hole-charge pair is created on the opposite boundary so that the emitted hole eventually annihilates the original charge. Note that this defines a unique transition from every admissible state in S to another admissible state in S .

In a nutshell: The transition rule “ \rightarrow ” realizes the propagation of a fermion to the right along the chain.

It is important that this transition is *injective* and *total* in that every state $s \in S$ is assigned a unique successor $s' \in S$ and there is only one such state that maps to s' . Hence the finiteness of S implies that it decomposes into

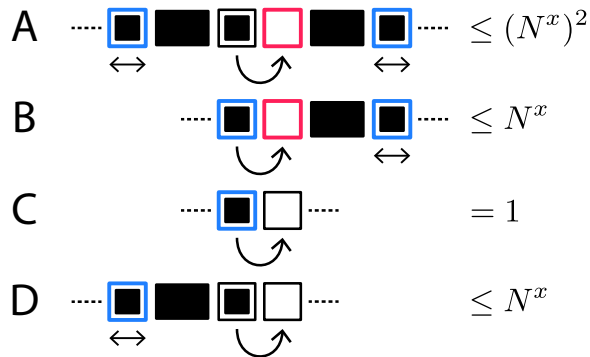
closed cycles of states. This is just another way to put that " \rightarrow " : $S \rightarrow S$ is a bijection⁸⁰ on a discrete set, i.e., a permutation; and it is well-known that every permutation has a cycle representation.

Given the transition system $\mathcal{T} = (S, \rightarrow)$, we find the following:

- There is a surjective map $\iota : S \rightarrow V(G)$ mapping states to vertices in G (configurations of fermions) via $\iota(s = (\mathbf{n}, \mathbf{e}, \mathbf{h})) \equiv \mathbf{n} = i$. Due to the definition of admissible states S , it follows that the preimage $\iota^{-1}(i)$ of an arbitrary fermion configuration i has *at least* N^x elements (one can place N^x single charges and possibly additional charge-hole-charge complexes).
- This induces a map $\iota : \mathcal{C}(\mathcal{T}) \rightarrow \mathcal{C}(G)$ of transition cycles in S to cycles in the coupling graph G because the abstract transitions in \mathcal{T} are realized by the single-fermion hopping of H^x . It is easy to see that all these image cycles include exactly one edge with $\alpha_{ij} = -1$ [recall that the transition system describes the propagation of a single fermion around the periodic chain, and combine this with Eq. (2.112)]. Thus we have

$$\iota : \mathcal{C}(\mathcal{T}) \rightarrow \mathcal{C}^- . \tag{2.205}$$

- The length of all cycles in $\iota(\mathcal{C}(\mathcal{T}))$ is L by construction.
- Every configuration $\mathbf{n} = i$ is traversed by at least N^x distinct cycles. (One can label each of the N^x fermions with a virtual charge; these N^x states in S generate distinct orbits in $\mathcal{C}(\mathcal{T})$.)
- A given transition $i = \mathbf{n} \rightarrow \mathbf{n}' = j$ of fermion configurations (an edge in G) can have up to $1 + N^x + N^x + (N^x)^2 \sim (N^x)^2$ preimages as transitions in S . This follows from the maximum number of preimages s with $\iota(s) = i$ that lead to the hopping of the same fermion under " \rightarrow ":



⁸⁰Injectivity of endomorphisms on finite domains is equivalent to bijectivity.

This is important as it tells us that edges in G may occur up to $\sim (N^x)^2$ times in the set of cycles $\iota(\mathcal{C}(\mathcal{T}))$. (Eventually we are interested in the limit $N^x \rightarrow \infty$ so that we can drop the linear corrections.)

DEFINITION 2.2: Family of odd cycles on a single chain

With this in mind, we define the set of odd cycles on G as

$$\mathcal{L} \equiv \iota(\mathcal{C}(\mathcal{T})) \quad 2.206$$

where $\sqrt{A_1} \sim L$ (the length of the cycles is L), $A_2 \sim N^x$ (each configuration is visited by at least N^x cycles), and $A_3 \sim (N^x)^2$ (each transition is used by at most $(N^x)^2$ cycles).

With this definition of \mathcal{L} , we can use (2.199) to derive an algebraic lower bound for the ground state energy of H^x on a single chain,

$$\langle \Psi_{2k} | H^a | \Psi_{2k} \rangle \stackrel{k \neq 0}{\geq} \frac{A_2}{A_1 A_3} \sim \frac{2k}{L^2 (2k)^2} = \frac{1}{L^2 (2k)} \quad 2.207a$$

$$\langle \Psi_{2k} | H^b | \Psi_{2k} \rangle \stackrel{k \neq \frac{N}{2}}{\geq} \frac{A_2}{A_1 A_3} \sim \frac{N - 2k}{L^2 (N - 2k)^2} = \frac{1}{L^2 (N - 2k)}. \quad 2.207b$$

In particular,

$$\langle \Psi_{2k} | H^x | \Psi_{2k} \rangle \geq \frac{1}{L^2 N} \quad 2.208$$

for $k \neq 0$ ($k \neq \frac{N}{2}$) and $x = a$ ($x = b$). With this, (2.203c) yields

$$\langle \Psi | H | \Psi \rangle \geq \sum_{k=0}^{N/2} |c_{2k}|^2 \max \left\{ \langle \Psi_{2k} | H^a | \Psi_{2k} \rangle, \langle \Psi_{2k} | H^b | \Psi_{2k} \rangle \right\} \quad 2.209a$$

$$\geq \sum_{k=0}^{N/2} |c_{2k}|^2 \frac{1}{L^2 N} = \frac{1}{L^2 N}. \quad 2.209b$$

For fixed density with $N = 2\rho L$, we have the algebraic lower bound

$$\langle \Psi | H | \Psi \rangle \gtrsim \frac{1}{L^3}. \quad 2.210$$

Since numerical results (not shown) suggest that the actual decay is *slower* for fixed density (namely L^{-1}), it is an interesting question whether the construction of \mathcal{L} can be optimized to make the lower bound strict. The stronger statement $E_0(L) = \langle \Psi_0 | H | \Psi_0 \rangle \propto L^{-1}$ for the ground state $|\Psi_0\rangle$ is also supported by analytical results for the Heisenberg model with twisted boundary conditions [252–254].

If the total filling N is *odd* (or even at half-filling), the restriction to a single chain is no longer possible; the requirements on \mathcal{L} remain the same, though. To construct cycles of fermion configurations of length $\sim L$ with an odd number of negative edges, one has to combine pair hopping between and single-particle hopping along the subchains [recall that pair hopping can also give rise to negative edges, Eq. (2.113)]. Note that the DMRG results shown in Figure 2.13 (b) also reveal a slower L^{-1} -decay. Thus it seems reasonable that a similar approach as above can be used to construct an appropriate family of odd cycles. However, the generating transition system is expected to be more complicated so that we leave its construction as an open problem for future studies or the amusement of the inclined reader.

2.B.2 Upper Bound for Odd Total Parity

Here we study the mechanism that is responsible for the vanishing of the single-particle gap in that it explains the existence of states with arbitrary low energy in sectors of odd total parity. Since this mechanism equally applies to other subchain-parity sectors and open boundary conditions, it sheds light on the peculiar low-energy physics of our model as a result of criticality and vanishing compressibility.

The Hamiltonian for periodic boundaries reads

$$H = H^a + H^b + H^{ab} \quad 2.211$$

with intra-chain interactions

$$H^x = \sum_{i=1}^L \left[\begin{array}{l} -x_{i+1}^\dagger x_i - x_i^\dagger x_{i+1} \\ +n_i^x (\mathbb{1} - n_{i+1}^x) + n_{i+1}^x (\mathbb{1} - n_i^x) \end{array} \right] \quad 2.212$$

for $x = a, b$, and inter-chain couplings

$$H^{ab} = \sum_{i=1}^L \left[\begin{array}{l} -a_i^\dagger a_{i+1}^\dagger b_{i+1} b_i - b_i^\dagger b_{i+1}^\dagger a_{i+1} a_i \\ +n_i^a n_{i+1}^a (\mathbb{1} - n_i^b) (\mathbb{1} - n_{i+1}^b) \\ +n_i^b n_{i+1}^b (\mathbb{1} - n_i^a) (\mathbb{1} - n_{i+1}^a) \end{array} \right]. \quad 2.213$$

We seek for a sequence of states $|G_{N,\alpha}\rangle$ so that for fixed filling $\rho = N/2L$

$$\langle G_{N,\alpha} | H | G_{N,\alpha} \rangle \rightarrow 0 \quad \text{for} \quad L, N \rightarrow \infty \quad 2.214$$

in sectors of odd total particle number N (where we already know that no exact zero-energy ground states exists). We assume that our ansatz wave functions are of the form $|G_{N,\alpha}\rangle \propto \mathcal{P} |N,\alpha\rangle$ where the operator \mathcal{P} is a function of $n_i^a + n_i^b$; it therefore commutes with each term of the inter-chain Hamiltonian H^{ab} and conserves both N and α .

To evaluate the energy expectation value, it is convenient to split the Hamiltonian into its OBC part H_o containing terms from site 1 to $L - 1$, and the boundary part H_∂ including the single term that couples sites L and 1:

$$H = H_o + H_\partial. \quad 2.215$$

Then, the energy expectation value can be written as

$$\begin{aligned} \langle G_{N,\alpha} | H | G_{N,\alpha} \rangle &= \sum_{x=a,b} \frac{\langle N, \alpha | \mathcal{P}^\dagger H_o^x \mathcal{P} | N, \alpha \rangle}{\langle N, \alpha | \mathcal{P}^\dagger \mathcal{P} | N, \alpha \rangle} \\ &\quad + B^{a,b}(N, \alpha) + B^{ab}(N, \alpha) \end{aligned} \quad 2.216$$

with the boundary contributions

$$B^{a,b}(N, \alpha) \equiv \sum_{x=a,b} \frac{\langle N, \alpha | \mathcal{P}^\dagger H_\partial^x \mathcal{P} | N, \alpha \rangle}{\langle N, \alpha | \mathcal{P}^\dagger \mathcal{P} | N, \alpha \rangle} \quad 2.217a$$

$$B^{ab}(N, \alpha) \equiv \frac{\langle N, \alpha | \mathcal{P}^\dagger H_\partial^{ab} \mathcal{P} | N, \alpha \rangle}{\langle N, \alpha | \mathcal{P}^\dagger \mathcal{P} | N, \alpha \rangle}. \quad 2.217b$$

Note that one of the two intra-chain boundary terms vanishes identically, depending on the subchain-parity sector α . To arrive at the above result, we used that $[\mathcal{P}, H_o^{ab}] = 0$ and $H_o^{ab} | N, \alpha \rangle = 0$.

We stress that due to the chosen parity sector (N odd which allows for even-odd/odd-even subchain parities), there are two non-vanishing boundary terms that we have to deal with:

$$H_\partial^x | N, \alpha \rangle \neq 0 \quad \text{and} \quad H_\partial^{ab} | N, \alpha \rangle \neq 0, \quad 2.218$$

where $x = a, b$ depends on α .

Since both bulk energy and boundary contributions are non-negative (due to the semi-positivity of all local terms), we have to make sure that they vanish separately in the thermodynamic limit $L \rightarrow \infty$ for $\rho = \text{const}$.

Bulk Energy

Let us postpone the problem of boundary energies for a moment and focus on the bulk energy

$$E(N, \alpha) \equiv \frac{\langle N, \alpha | \mathcal{P}^\dagger (H_o^a \oplus H_o^b) \mathcal{P} | N, \alpha \rangle}{\langle N, \alpha | \mathcal{P}^\dagger \mathcal{P} | N, \alpha \rangle}. \quad 2.219$$

Recall [Eq. (2.20)] that the OBC zero-energy ground states can be written as

$$|N, \alpha\rangle = \mathcal{N}_{L,N,\alpha}^{-1/2} \sum_{n, (-1)^n = \alpha} |n\rangle_a |N-n\rangle_b \quad 2.220$$

with unnormalized equal-weight superpositions $|n\rangle_x$ for subchain x with filling n and the property that $H_\circ^x |n\rangle_x = 0$.

We make the observation that due to the symmetry between the $\alpha = \pm 1$ -sectors for odd total filling N , the normalizing factors are equal, $\mathcal{N}_{L,N,+1} = \mathcal{N}_{L,N,-1}$, and we get as symmetric superposition

$$|N\rangle \equiv \frac{1}{\sqrt{2}} (|N, +1\rangle + |N, -1\rangle) = \binom{2L}{N}^{-1/2} \sum_{|\mathbf{n}|=N} |\mathbf{n}\rangle_{ab}; \quad 2.221$$

viz. the equal-weight superposition on the double-chain with fixed particle number N without subchain parity constraint. Due to orthogonality, it follows that

$$E(N) \equiv \frac{\langle N | \mathcal{P}^\dagger (H_\circ^a \oplus H_\circ^b) \mathcal{P} | N \rangle}{\langle N | \mathcal{P}^\dagger \mathcal{P} | N \rangle} = \frac{1}{2} [E(N, +1) + E(N, -1)] \quad 2.222$$

and we can show that $E(N, \alpha)$ vanishes for both $\alpha = \pm 1$ by proving that $E(N)$ vanishes for $L \rightarrow \infty$. Using this trick, we also freed ourselves from the annoying subsector parity constraint $P_a = \alpha$ for the following discussion. Note that we used the fact that $\langle N, \alpha | \mathcal{P}^\dagger \mathcal{P} | N, \alpha \rangle$ cannot depend on α because \mathcal{P} (by assumption) only depends on the symmetric occupation numbers $n_i^a + n_i^b$; this explains the prefactor $\frac{1}{2}$.

DEFINITION 2.3: Ansatz wave function

Let us now introduce our ansatz for \mathcal{P} , namely

$$\mathcal{P} = \mathcal{P}_{\beta, \theta} \equiv \exp \left[-\beta \sum_{i=1}^L \theta \left(\frac{i}{L} \right) (n_i^a + n_i^b) \right] \quad 2.223$$

with non-negative inverse temperature $\beta \geq 0$ and the smooth potential $\theta \in C^\infty([0, 1], [0, 1])$, w.l.o.g. normalized so that $\max_x \theta(x) = 1$ and scaling is controlled by β .

The naming scheme, inspired by statistical mechanics, is purely formal and will become clear below. $\mathcal{P}_{\beta, \theta}$ obviously satisfies all requirements used so far in the derivations.

First, a glance at the normalizing factor

$$\langle N | \mathcal{P}^\dagger \mathcal{P} | N \rangle = \sum_{|\mathbf{n}|=N} e^{-2\beta \sum_{i=1}^L \theta \left(\frac{i}{L} \right) (n_i^a + n_i^b)} = Z(\beta, N) \quad 2.224$$

reveals that this is nothing else than the (thermal) canonical partition function $Z(\beta, N)$ of a non-interacting lattice gas with two-fold degenerate sites in the potential landscape θ with (inverse) temperature β . Here and henceforth, we ignore the normalizing factor of $|N\rangle$ as it cancels in $E(N)$ anyway.

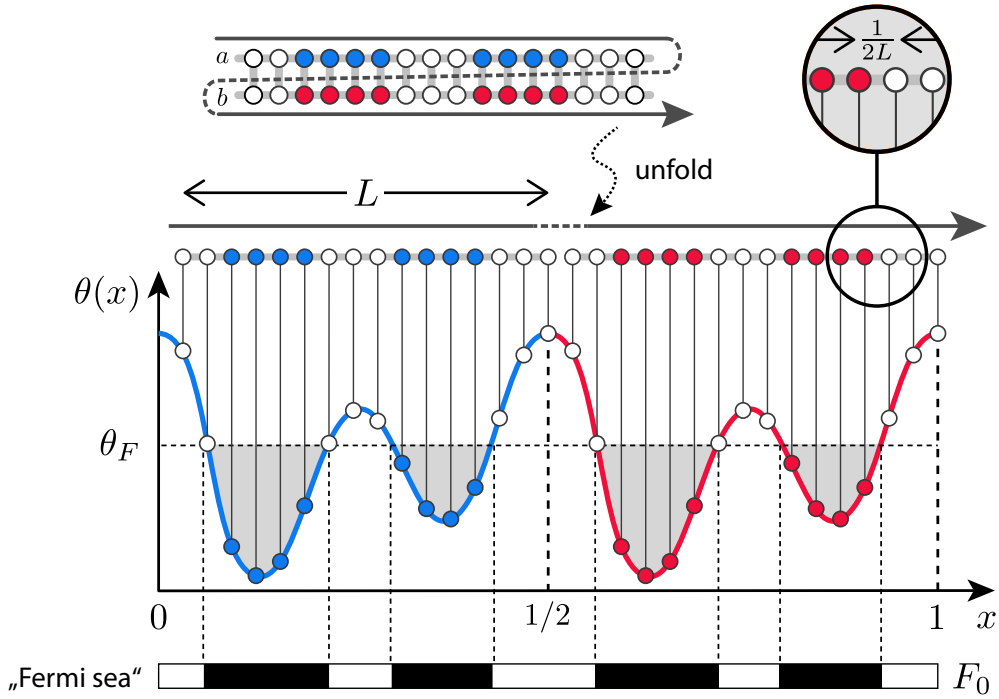


FIGURE 2.21 • Schematic potential. Example of a smooth potential $\theta(x)$ to illustrate the unfolding of the double-chain. The shown particle distribution corresponds to zero temperature or $\beta \rightarrow \infty$ and is characterized by a filled “Fermi sea” F_0 with “Fermi energy” θ_F . The potential is discretized with lattice spacing $1/2L$. The $\frac{1}{2}$ -periodicity ensures vanishing energy contributions of inter-chain interactions H_{\circ}^{ab} in that the symmetry of upper and lower subchain remains unbroken.

Importantly, due to the missing interactions (not counting the on-site hard-core repulsion as defining property of a lattice gas) one can equivalently think of an extended potential θ^* on $[0, 1]$ derived from two squeezed copies of θ with $2L$ sites and without local degeneracies⁸¹, Figure 2.21. In the following, we use this picture and relabel the sites such that \mathcal{P} reads

$$\mathcal{P}_{\beta, \theta} = \exp \left[-\beta \sum_{i=1}^{2L} \theta \left(\frac{i}{2L} \right) n_i \right], \quad 2.225$$

where we renamed θ^* to θ since we still allow for arbitrary potentials θ (in particular, the “doubled” ones).

The numerator of Eq. (2.222) translates similarly

$$\langle N | \mathcal{P}^\dagger (H_{\circ}^a \oplus H_{\circ}^b) \mathcal{P} | N \rangle = \langle N | \mathcal{P}^\dagger H_{\circ} \mathcal{P} | N \rangle \quad 2.226$$

⁸¹We unfold the double-chain to a single-chain of length $2L$.

where

$$H_o = \sum_{1 \leq i < L < i < 2L} \left[\begin{array}{l} -c_{i+1}^\dagger c_i - c_i^\dagger c_{i+1} \\ +n_i(\mathbb{1} - n_{i+1}) + n_{i+1}(\mathbb{1} - n_i) \end{array} \right] \quad 2.227$$

with fermions c_i^\dagger on sites $1 \leq i \leq 2L$. Note that the sum skips the two boundary terms H_o^a and H_o^b due to the linearized index scheme. The excluded indices $i = L, 2L$ describe inter-chain cross tunneling (not present in the original theory).

Given this simplification⁸² of the double-chain, we proceed with the evaluation of (2.222) with the shortcut $\sum'_i = \sum_{1 \leq i < L < i < 2L}$:

$$\langle N | \mathcal{P}^\dagger H_o \mathcal{P} | N \rangle = \sum_{|\mathbf{n}|, |\mathbf{m}|=N} \sum'_i \langle \mathbf{m} | \mathcal{P}^\dagger H_{o,i} \mathcal{P} | \mathbf{n} \rangle \quad 2.228a$$

$$\begin{aligned} &= - \sum_{|\mathbf{n}|, |\mathbf{m}|=N} \sum'_i \langle \mathbf{m} | \mathcal{P}^\dagger [c_{i+1}^\dagger c_i + c_i^\dagger c_{i+1}] \mathcal{P} | \mathbf{n} \rangle \quad 2.228b \\ &\quad + \sum_{|\mathbf{n}|, |\mathbf{m}|=N} \sum'_i \langle \mathbf{m} | \mathcal{P}^\dagger \left[\begin{array}{l} n_i(\mathbb{1} - n_{i+1}) \\ +n_{i+1}(\mathbb{1} - n_i) \end{array} \right] \mathcal{P} | \mathbf{n} \rangle. \end{aligned}$$

The second (density-density) term immediately yields

$$\sum'_i \sum_{|\mathbf{n}|=N} [n_i(1 - n_{i+1}) + n_{i+1}(1 - n_i)] e^{-2\beta \sum_{j=1}^{2L} \theta(\frac{j}{2L}) n_j}, \quad 2.229$$

whereas the first one has to be treated a bit more carefully:

$$- \sum'_i \sum_{|\mathbf{n}|=N} \left[\begin{array}{l} n_i(1 - n_{i+1}) e^{\beta[\theta(i/2L) - \theta(i+1/2L)]} \\ +n_{i+1}(1 - n_i) e^{\beta[\theta(i+1/2L) - \theta(i/2L)]} \end{array} \right] e^{-2\beta \sum_{j=1}^{2L} \theta(\frac{j}{2L}) n_j}. \quad 2.230$$

The additional exponentials account for the changed weights due to the hopping sandwiched between \mathcal{P} and \mathcal{P}^\dagger .

We can now put together Eq. (2.222): The division of these terms by the partition function $Z(\beta, N)$ results in “thermal” density-density correlators evaluated in the canonical ensemble with fixed particle number,

$$\begin{aligned} E(N) &= \sum'_i \left[\begin{array}{l} 1 - e^{\beta[\theta(i/2L) - \theta(i+1/2L)]} \\ + \left[1 - e^{\beta[\theta(i+1/2L) - \theta(i/2L)]} \right] \end{array} \right] \langle n_i(1 - n_{i+1}) \rangle \quad 2.231 \\ &\quad + \left[1 - e^{\beta[\theta(i+1/2L) - \theta(i/2L)]} \right] \langle n_{i+1}(1 - n_i) \rangle. \end{aligned}$$

In the following, we write $E(N) = E(\beta, N)$ to highlight the β -dependence of E . As we are interested in the thermodynamic limit $L \rightarrow \infty$, it is reasonable to expand the square brackets in orders of L^{-1} :

$$\theta(i/2L) - \theta(i + 1/2L) = -\frac{\theta'(i/2L)}{2L} + \mathcal{O}(1/L^2). \quad 2.232$$

⁸²The unfolding is only useful because of the missing subchain parity constraints—which are rather unnatural in this picture.

Thus

$$\left[1 - e^{\beta[\theta(i/2L) - \theta(i+1/2L)]}\right] = \frac{\beta}{2L} \theta'(i/2L) + \mathcal{O}(\beta^2/L^2), \quad 2.233a$$

$$\left[1 - e^{\beta[\theta(i+1/2L) - \theta(i/2L)]}\right] = -\frac{\beta}{2L} \theta'(i/2L) + \mathcal{O}(\beta^2/L^2), \quad 2.233b$$

which yields

$$E(\beta, N) = \sum_i' \left[\frac{\beta}{2L} \theta'(i/2L) \langle n_i - n_{i+1} \rangle + \mathcal{O}(\beta^2/L^2) \right]. \quad 2.234$$

Here, the Landau symbols $\mathcal{O}(\bullet)$ are defined for the limit $L, \beta \rightarrow \infty$ whenever $\beta/L \rightarrow 0$. Note that these conditions are important in that they allow us to incorporate the term $\beta \mathcal{O}(1/L^2)$ in $\mathcal{O}(\beta^2/L^2)$ (which is not correct in the limit $\beta \rightarrow 0$).

To evaluate the last expression, we have to control the density gradient $\langle n_i - n_{i+1} \rangle$ to some extent. One finds

$$\langle n_i - n_{i+1} \rangle = Z^{-1}(\beta, N) \sum_{|\mathbf{n}|=N} (n_i - n_{i+1}) e^{-2\beta \sum_{j=1}^{2L} \theta(\frac{j}{2L}) n_j} \quad 2.235a$$

$$= Z^{-1}(\beta, N) \sum_{\substack{|\mathbf{n}|=N \\ n_i=1, n_{i+1}=0}} \left\{ 1 - e^{2\beta[\theta(i/2L) - \theta(i+1/2L)]} \right\} \times e^{-2\beta \sum_{j=1}^{2L} \theta(\frac{j}{2L}) n_j} \quad 2.235b$$

$$= \left\{ 1 - e^{2\beta[\theta(i/2L) - \theta(i+1/2L)]} \right\} \frac{Z_i^*(\beta, N)}{Z(\beta, N)} \quad 2.235c$$

$$= \left\{ \frac{\beta}{L} \theta'(i/2L) + \mathcal{O}(\beta^2/L^2) \right\} \frac{Z_i^*}{Z}, \quad 2.235d$$

where $Z_i^*(\beta, N)$ is the restricted partition sum in (2.235b) and we point out that $0 \leq Z_i^*/Z \leq 1$ for all i . Combining this result with Eq. (2.234) yields

$$E(\beta, N) = \sum_i' \left[\frac{\beta}{2L} \theta'(i/2L) \left\{ \frac{\beta}{L} \theta'(i/2L) + \mathcal{O}(\beta^2/L^2) \right\} \frac{Z_i^*}{Z} + \mathcal{O}(\beta^2/L^2) \right] \quad 2.236a$$

$$\leq \frac{\beta^2}{L} \sum_i' \frac{1}{2L} |\theta'(i/2L)|^2 + \beta \mathcal{O}(\beta^2/L^2) + \mathcal{O}(\beta^2/L), \quad 2.236b$$

where we lost an order of L^{-1} in the rightmost term due to the sum over $2L - 2$ sites⁸³; the upper bound follows from $0 \leq Z_i^*/Z \leq 1$.

⁸³We stress that the functions formally written as their Landau classes $\mathcal{O}(\bullet)$ are not independent of i in general! Here, however, this is indeed the case since they originate from the derivative (2.232) of the *uniformly* differentiable function θ (recall that θ is smooth and θ' continuous on the compact interval $[0, 1]$).

RESULT 2.2: Bulk energy

For large L , the result can be rewritten⁸⁴ as

$$E(\beta, N) \leq \frac{\beta^2}{L} \int_0^1 dx |\theta'(x)|^2 + \mathcal{O}(\beta^2/L) = \mathcal{O}(\beta^2/L), \quad 2.237$$

using the definition of the Riemann integral (which exists for $\theta \in C^\infty([0, 1], [0, 1])$).

Let us discuss the results so far (see also Figure 2.22):

- $E(\beta, N)$ is only the bulk contribution to the total energy expectation value. We still have to deal with the two boundary terms. But if we consider a system with OBC, then Result 2.2 describes the energy of the state $\mathcal{P}_{\beta, \theta}|N, \alpha\rangle$ completely. We conclude that for arbitrary inverse temperature β and potential θ , the considered family of many-body wave functions belongs to the low-energy sector of the Hamiltonian H and their energy vanishes (at least) with L^{-1} . Note that this result tells us nothing new about the *ground states* as we already know that there *are* zero-energy ground states for OBC.
- In the *high-temperature limit* $\beta \rightarrow 0$, the result tells us that $E(\beta, N) \rightarrow 0$ for any finite L . This is easily understood if we consider the form of the ansatz wave function:

$$\begin{aligned} \mathcal{P}_{\beta, N}|N, \alpha\rangle &= \exp \left[-\beta \sum_{i=1}^L \theta \left(\frac{i}{L} \right) (n_i^a + n_i^b) \right] |N, \alpha\rangle \\ &\xrightarrow{\beta \rightarrow 0} |N, \alpha\rangle \end{aligned} \quad 2.238$$

So the infinite-temperature fixed point (which is independent of the potential θ) corresponds to the original equal-weight zero-energy ground states.

- To gain intuition about the *low-temperature limit* $\beta \rightarrow \infty$, we have to realize that the states $\mathcal{P}_{\beta, N}|N, \alpha\rangle$ encode the Gibbs ensemble of N hard-core particles in the potential θ (discretized on $2L$ lattice sites) with an additional subchain parity constraint (which we can get rid of as demonstrated above). For low temperatures, the particles fill the potential up to some “Fermi energy” θ_F and form a clustered or *phase-separated* state, Figure 2.22. The cluster structure is determined by the density ρ and the potential θ . It is easy to show (using the OBC double-chain Hamiltonian H) that any chain-symmetrically phase-separated state has non-vanishing energy. This manifests in the diverging upper bound $\mathcal{O}(\beta^2/L)$ for $\beta \rightarrow \infty$.

⁸⁴Use $\beta\mathcal{O}(\beta^2/L^2) \subseteq \beta\mathcal{O}(\beta/L) = \mathcal{O}(\beta^2/L)$ to collect all remainders in $\mathcal{O}(\beta^2/L)$.

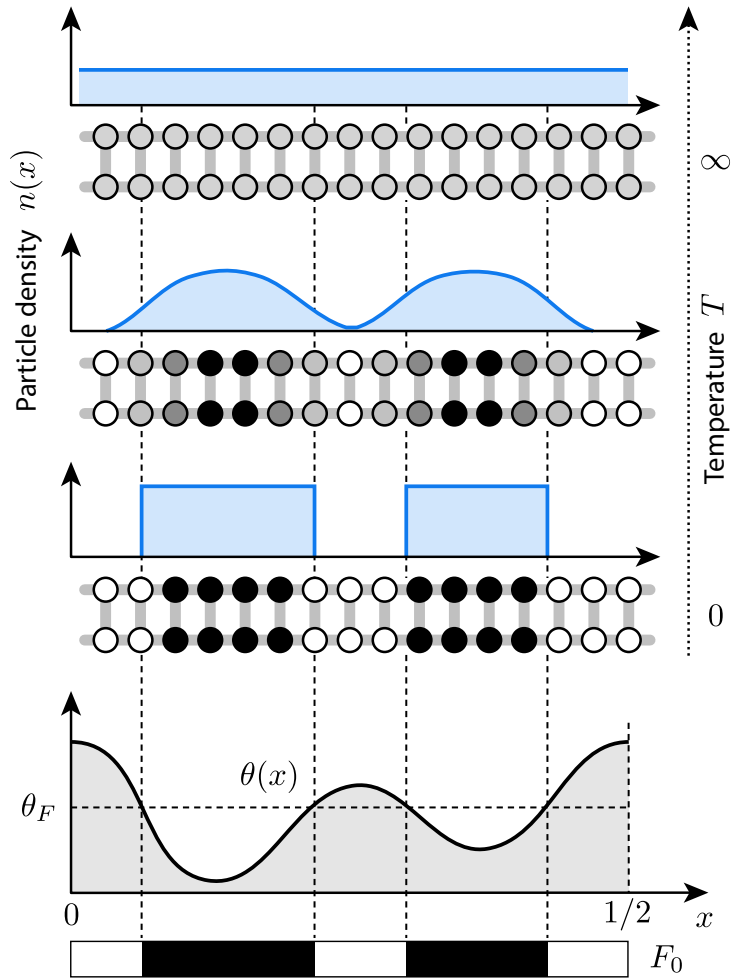


FIGURE 2.22 • Temperature dependence of the local density. Exemplary particle density distribution $n(x)$ of the ansatz wave function $\mathcal{P}_{\beta,\theta}|N, \alpha\rangle$ for the shown potential $\theta(x)$ and three temperatures $\beta = T^{-1}$ ranging from $T = 0$ to $T = \infty$. For zero temperature, the state is phase-separated and acquires a finite energy in all cases; the particles form a “Fermi sea” F_0 with “Fermi energy” θ_F . For $T \rightarrow \infty$, the states approach the equal-weight superpositions $|N, \alpha\rangle$, i.e., the zero-energy ground states.

The bottom line is the following: We showed that for OBC, there is a low-energy sector without any phase-modulation [like Eq. (2.118)], spanned by chain-symmetric, “smoothly” ($\beta < \infty$) density-modulated states that are conveniently described as Gibbs ensembles of particles in a given potential. It stands to reason that this is a consequence of the vanishing compressibility at the critical point.

Boundary Energy

We now turn towards the ominous boundary terms. What makes them “ominous” is a single, inverted relative sign between hopping and density-density interactions that is responsible for a positive energy in sectors of odd particle number.

Intra-chain boundary — We start with the finite intra-chain boundary term, i.e., the term of the even-parity chain (here again for the symmetric superposition to get rid of the subchain parity constraint). It reads:

$$B^a(\beta, N) \equiv \frac{1}{2} \left(\underbrace{B^a(N, +1)}_{\geq 0; \rightarrow \neq 0} + \underbrace{B^a(N, -1)}_{\geq 0; \rightarrow 0} \right) = \frac{\langle N | \mathcal{P}^\dagger H_\partial^a \mathcal{P} | N \rangle}{\langle N | \mathcal{P}^\dagger \mathcal{P} | N \rangle} \quad 2.239a$$

$$= \left[\langle n_L(1 - n_1) \rangle + \langle P_a n_L(1 - n_1) \rangle e^{\beta[\theta(L/2L) - \theta(1/2L)]} \right] + \left[\langle n_1(1 - n_L) \rangle + \langle P_a n_1(1 - n_L) \rangle e^{\beta[\theta(1/2L) - \theta(L/2L)]} \right]. \quad 2.239b$$

Here, $P_a = (-1)^{N^a}$ denotes the a -chain parity⁸⁵. This follows from the subchain-parity-dependence of single-particle hopping across the (gauge dependent) boundary $1 \leftrightarrow L$, recall the gauge string in Figure 2.6. As we are only interested in the vanishing of $B^a(\beta, N)$, and the first terms in the square brackets must vanish anyway, we make use of the (admittedly blunt) estimate

$$|\langle P_a n_L(1 - n_1) \rangle| \leq \langle n_L(1 - n_1) \rangle \quad 2.240$$

to get rid of the subchain parity P_a ,

$$B^a(\beta, N) \leq \left[1 + e^{\beta[\theta(L/2L) - \theta(1/2L)]} \right] \langle n_L(1 - n_1) \rangle + \left[1 + e^{\beta[\theta(1/2L) - \theta(L/2L)]} \right] \langle n_1(1 - n_L) \rangle. \quad 2.241$$

Now recall that we can think of θ as the same potential squeezed twice on the interval $[0, 1]$ to ensure that the potentials in upper and lower chain are equal for each site i (this is implicit in the form of \mathcal{P} and required to make the inter-chain interactions vanish). Formally, this means $\theta(x) = \theta(x + \frac{1}{2})$ for $0 \leq x < \frac{1}{2}$, Figure 2.21. If we require that θ is smooth on $[0, 1]$, this implies that θ is $\frac{1}{2}$ -periodic and smooth at $\theta(0) = \theta(\frac{1}{2})$. Therefore

$$\theta(L/2L) - \theta(1/2L) = -\frac{\theta'(0)}{2L} + \mathcal{O}(1/L^2), \quad 2.242$$

⁸⁵Note that we need P_a as an operator only because $|N\rangle$ includes both subchain parities. If we computed $\langle N, \alpha | \mathcal{P}^\dagger H_\partial^a \mathcal{P} | N, \alpha \rangle$ instead, we had $P_a = +1$.

and we find with the same arguments as before

$$\left[1 + e^{\beta[\theta(L/2L) - \theta(1/2L)]}\right] = 2 - \frac{\beta}{2L} \theta'(0) + \mathcal{O}(\beta^2/L^2) \quad 2.243a$$

$$\left[1 + e^{\beta[\theta(1/2L) - \theta(L/2L)]}\right] = 2 + \frac{\beta}{2L} \theta'(0) + \mathcal{O}(\beta^2/L^2), \quad 2.243b$$

where the 0th order no longer drops out. Thus there is an additional term in the boundary contribution:

$$B^a(\beta, N) \leq \frac{\beta}{2L} \theta'(0) \langle n_1 - n_L \rangle + \mathcal{O}(\beta^2/L^2) \quad 2.244$$

$$+ 2\langle n_1 + n_L - 2n_1n_L \rangle.$$

If we use $\langle n_1 - n_L \rangle = \mathcal{O}(1)$ and $\beta/2L = \mathcal{O}(\beta^2/L)$ for $L, \beta \rightarrow \infty$ and $\beta/L \rightarrow 0$, this reads

$$B^a(\beta, N) \leq 2\langle n_1 + n_L - 2n_1n_L \rangle + \mathcal{O}(\beta^2/L). \quad 2.245$$

The last term accounts for the density gradient contribution, as known from the bulk energy, and vanishes accordingly (thus we may ignore it)—whereas the first term is new and a direct consequence of the even–subchain–parity components in $|N\rangle$. This contribution is absent for $|N, -1\rangle$ (instead of $|N\rangle$); then, the other boundary term $B^b(\beta, N)$ takes the form of (2.245).

It is easy to see that for $\beta = 0$, where $\mathcal{P}_{0,N}|N, \alpha\rangle = |N, \alpha\rangle$, the first term equals $4\rho(1 - \rho)$; it makes the energy of the equal-weight superpositions positive except for the limiting cases of empty or completely filled systems. To get rid of this contribution, we have two choices:

- 1 The ansatz wave function only incorporates configurations where $n_1 = n_L$, so that single-particle hopping is prohibited.
- 2 The ansatz wave function is empty in the vicinity of the “boundary” sites 1 and L , i.e., $n_1 = 0 = n_L$.

The first choice is more general as it still allows particles at the boundary—but only with perfect correlations. We are going for the second one as it is perfectly compatible with our ansatz wave functions $\mathcal{P}_{\beta,N}|N, \alpha\rangle$ in that the local particle density can be conveniently controlled via the potential θ .

To this end, we point out that

$$\langle n_1 + n_L - 2n_1n_L \rangle \leq \langle n_1 \rangle + \langle n_L \rangle, \quad 2.246$$

so all we have to achieve is $\langle n_i \rangle \rightarrow 0$ for $L \rightarrow \infty$ and fixed density $0 < \rho < 1$ with $i = 1, L$. In conclusion, the total intra-chain boundary energy can be estimated as

$$B^{a,b}(\beta, N) = B^a(\beta, N) + B^b(\beta, N) \quad 2.247a$$

$$\leq 2\langle n_1 + n_L + n_{L+1} + n_{2L} \rangle + \mathcal{O}(\beta^2/L). \quad 2.247b$$

Inter-chain boundary — Analogous reasoning leads to the conclusion that the inter-chain boundary contribution $B^{ab}(N, \alpha)$ vanishes together with the local particle density at the double-chain boundary $\langle n_1 + n_L + n_{L+1} + n_{2L} \rangle$. We define

$$B^{ab}(\beta, N) \equiv \frac{1}{2} (B^{ab}(N, +1) + B^{ab}(N, -1)) = \frac{\langle N | \mathcal{P}^\dagger H_\theta^{ab} \mathcal{P} | N \rangle}{\langle N | \mathcal{P}^\dagger \mathcal{P} | N \rangle}. \quad 2.248$$

If we now use that $[H_\theta^{ab}, \mathcal{P}] = 0$ and $(-1)^N = -1$ by assumption, the evaluation of (2.248) yields the simple result

$$B^{ab}(\beta, N) = 2\langle n_1 n_L (1 - n_{L+1})(1 - n_{2L}) \rangle + 2\langle n_{L+1} n_{2L} (1 - n_1)(1 - n_L) \rangle. \quad 2.249$$

Therefore we can upper bound the inter-chain boundary energy by

$$B^{ab}(\beta, N) \leq \langle n_1 + n_L + n_{L+1} + n_{2L} \rangle, \quad 2.250$$

the same condition as for the intra-chain boundary energy (2.247b). Here we used the simple estimate $\langle XY \rangle \leq \frac{1}{2}(\langle X \rangle + \langle Y \rangle)$ for binary random variables X and Y .

As a final remark, we stress that $[H_\theta^{ab}, \mathcal{P}] = 0$ makes all inter-chain bulk contributions vanish such that there is no bulk energy associated to pair hopping (as explained previously). Due to the “chain exchange symmetry” of \mathcal{P} , the imprinted density gradient only increases the intra-chain energy density.

Local Density of a Lattice Gas

To make the energy of $\mathcal{P}_{\beta, \theta} | N, \alpha \rangle$ go to zero on a periodic double-chain with odd total filling, the boundary density $\langle n_i \rangle$ must vanish for $L \rightarrow \infty$ and fixed $0 < \rho < 1$; if possible as fast as $\mathcal{O}(\beta^2/L)$ for the upper bound to be as tight as possible. We have to choose β and θ appropriately to achieve this. The idea is the following:

- 1 For $L \rightarrow \infty$ and fixed ρ , $\langle n_1 \rangle$ describes the local particle density of a lattice gas at inverse temperature β at position $x = 0$ (actually $x_1 = 1/2L$). The same is true for $\langle n_L \rangle$ which probes the density at $x_L = L/2L = 1/2$.
- 2 The shape of $\theta \in C^\infty([0, 1], [0, 1])$ (the “energy landscape”) and the density $0 < \rho < 1$ determine the lowest-energy configuration $\mathbf{n}_0 \in \{0, 1\}^{2L}$ of $H(\mathbf{n}) = \sum_{i=1}^{2L} \theta(i/2L) n_i$ with $|\mathbf{n}_0| = N = 2L\rho$. \mathbf{n}_0 takes the form of a filled “Fermi sea” $F_0 \equiv \{i \mid (\mathbf{n}_0)_i = 1\}$ due to the hard-core constraint of the particles, Figure 2.21.

In the thermodynamic limit, F_0 can be considered a continuous subset of $[0, 1]$ so that

$$\langle n(x) \rangle \xrightarrow{\beta \rightarrow \infty} \begin{cases} 0 & \text{for } x \notin F_0, \\ 1 & \text{for } x \in F_0, \end{cases} \quad 2.251$$

and

$$\int_0^1 dx n(x) = \rho = \text{const}. \quad 2.252$$

- 3** Intuition tells us that the particle density *outside* the Fermi sea is exponentially suppressed with β , i.e., for x separated from F_0 , one expects for large L the Fermi-Dirac distribution

$$\langle n(x) \rangle = \frac{1}{1 + e^{\beta(\theta(x) - \theta_F)}} \sim e^{-\beta(\theta(x) - \theta_F)}, \quad 2.253$$

for $\beta \rightarrow \infty$ with the ‘‘Fermi energy’’ $\theta_F \equiv \max_{x \in F_0} \theta(x)$. Some remarks on Eq. (2.253) follow below.

- 4** We conclude that if $\theta(x)$ is chosen so that the region around $x = 0$ (equivalently, $x = 1/2$) lies outside the Fermi sea F_0 , the boundary densities $\langle n(0) \rangle = \langle n(1/2) \rangle$ can be *exponentially* suppressed with β . At the same time, the upper bound of the bulk energy grows only *polynomially* with β , namely with β^2/L (Result 2.2).

As β is a free parameter of the ansatz $\mathcal{P}_{\beta, \theta}$, we are free to choose

$$\beta = \beta(L) \equiv \Delta \theta^{-1} \log L \quad 2.254a$$

$$\Rightarrow |G\rangle = |G(L, \rho, \alpha)\rangle \equiv \mathcal{P}_{\beta(L), \theta} |2L\rho, \alpha\rangle \quad 2.254b$$

with the energy gap $\Delta \theta \equiv \theta(0) - \theta_F$.

Then, the energy of $|G\rangle$ can be bounded from above for L large enough:

$$\langle G|H|G\rangle \leq \underbrace{C_1 \frac{\log^2 L}{L}}_{\text{Bulk}} + \underbrace{C_2 \frac{1}{L}}_{\text{Boundary}} \quad \text{with } C_1, C_2 > 0. \quad 2.255$$

Here we combined the results (2.216), (2.237), (2.247b), (2.250) and (2.253) with the logarithmically diverging inverse temperature (2.254a).

- 5** As a last step, we point out that for all $\varepsilon > 0$ there exists an $L_\varepsilon > 0$ such that for all $L \geq L_\varepsilon$

$$\frac{\log^2 L}{L} \leq \frac{L^\varepsilon}{L} = \frac{1}{L^{1-\varepsilon}}, \quad 2.256$$

so that

RESULT 2.3: Upper bound on the lowest eigenenergy

$$\langle G|H|G\rangle \leq \frac{C}{L^{1-\varepsilon}} \quad \text{for all } \varepsilon > 0 \quad \text{and } L \geq L_\varepsilon \quad 2.257$$

with constant $C > 0$.

This is as close to the observed scaling L^{-1} as we get [recall the DMRG results in Figure 2.13 (b)].

Fermi-Dirac distribution — As promised, we conclude our discussion with some remarks on the Fermi-Dirac distribution. Recall that Eq. (2.253) is crucial for the line of argument that establishes the upper bound (2.257).

The derivation of

$$\langle n(x) \rangle = \frac{1}{1 + e^{\beta(\theta(x) - \theta_F)}} \quad 2.258$$

is straightforward for the *grand*-canonical ensemble with the (classical) Hamiltonian $H(\mathbf{n}) = \sum_{s=1}^L \theta(s/L)n_s$. There we have

$$Z(\beta, \mu) = \sum_{\mathbf{n} \in \{0,1\}^L} \exp \left[-\beta \sum_{s=1}^L \theta(x_s)n_s + \beta \mu \sum_{s=1}^L n_s \right] \quad 2.259a$$

$$= \prod_{s=1}^L \sum_{n_s=0,1} e^{-\beta(\theta(x_s) - \mu)n_s} \quad 2.259b$$

with $x_s \equiv s/L$. Consequently

$$\langle n(y) \rangle = -\frac{1}{\beta} \frac{\partial \ln Z(\beta, \mu)}{\partial \theta(y)} \quad 2.260a$$

$$= -\frac{1}{\beta} \frac{\partial}{\partial \theta(y)} \ln \left[1 + e^{-\beta(\theta(y) - \mu)} \right] = \frac{1}{1 + e^{\beta(\theta(y) - \mu)}} \quad 2.260b$$

and we are done. Note that the chemical potential μ takes the place of the Fermi energy θ_F since the particle number fluctuates.

In the *canonical* ensemble this becomes much more complicated to derive rigorously⁸⁶. For finite systems, there is no chemical potential in the canonical ensemble but a N -dependent quantity $\mu(\beta, N)$ that takes its place and depends non-trivially on both temperature and particle number:

$$\langle n(y_r) \rangle = Z(\beta, N)^{-1} \sum_{|\mathbf{n}|=N} n_r e^{-\beta H(\mathbf{n})} = \frac{1}{1 + \frac{\sum_{n_r=0} e^{-\beta H(\mathbf{n})}}{\sum_{n_r=1} e^{-\beta H(\mathbf{n})}}}, \quad 2.261$$

where the sums are all constrained by the particle number N . If we introduce the primed system as given by θ but with site r removed (thus of size $L - 1$), we can write

$$\langle n(y_r) \rangle = \frac{1}{1 + e^{\beta\theta(y_r)} \frac{Z'(\beta, N)}{Z'(\beta, N-1)}}, \quad 2.262$$

where we extracted the prefactor $e^{\beta\theta(y_r)}$ from the sum in the denominator ($n_r = 1$).

⁸⁶This is so because the form (2.258) is valid only in the thermodynamic limit where canonical and grand-canonical ensemble become equivalent.

If we define the chemical potential of the primed system as free energy difference for adding a single particle,

$$\mu'(\beta, N) \equiv A'(\beta, N) - A'(\beta, N - 1) \quad 2.263a$$

$$= -\frac{1}{\beta} \log Z'(\beta, N) + \frac{1}{\beta} \log Z'(\beta, N - 1), \quad 2.263b$$

this yields the expression

$$\langle n(y_r) \rangle = \frac{1}{1 + e^{\beta(\theta(y_r) - \mu'(\beta, N))}}. \quad 2.264$$

Here we concealed all our problems in the unknown expression $\mu'(\beta, N)$.

Due to the equivalence of ensembles, it is expected that for fixed filling ρ first

$$\lim_{L \rightarrow \infty} \mu'(\beta, \rho L) = \mu(\beta, \rho) < \infty, \quad 2.265$$

and second

$$\lim_{\beta \rightarrow \infty} \mu(\beta, \rho) = \theta_F(\rho), \quad 2.266$$

where $\theta_F(\rho) \equiv \lim_{L \rightarrow \infty} \theta_F(N = \rho L, L)$ is the Fermi energy in the thermodynamic limit (which depends on the potential θ and the density ρ). The function $\theta_F = \theta_F(N, L)$ for finite L is well-defined by filling N particles in the discretized potential $\theta(x_s)$, illustrated in Figure 2.21 and Figure 2.22 as “Fermi sea” F_0 .

For a rigorous justification of Result 2.3, a likewise rigorous treatment of the limits (2.265) and (2.266) is required. We leave this as a challenge for the future.

Low-Energy Physics with Phase Slips

The preceding discussion was based on double-chains with PBC in the odd- N sectors. We found that by choosing a potential $\theta(x)$ with maximum at the critical sites 1 and L , the ground state energy approaches zero in the thermodynamic limit. Thus the even-odd/odd-even sectors are gapless for PBC and there is no single-particle gap—in accordance with numerical results.

We can, however, apply these findings to systems with OBC and exact zero-energy ground states as well. To this end, consider the generic single-particle phase field

DEFINITION 2.4: Single-particle phase field

$$\Pi_{\phi_a, \phi_b} \equiv \exp \left\{ i \sum_{s=1}^L \left[\phi_a \binom{s}{L} n_s^a + \phi_b \binom{s}{L} n_s^b \right] \right\} \quad 2.267$$

which imprints the single-particle phases $\phi_a, \phi_b : [0, 1] \rightarrow [0, 2\pi)$ on the upper and lower chain, respectively:

$$|\phi_a, \phi_b; N, \alpha\rangle \equiv \Pi_{\phi_a, \phi_b} |N, \alpha\rangle. \quad 2.268$$

In contrast to our previously considered family of *density-modulated* wave functions,

$$|\beta, \theta; N, \alpha\rangle \equiv \frac{1}{\sqrt{Z}} \mathcal{P}_{\beta, \theta} |N, \alpha\rangle, \quad 2.269$$

the new *phase-modulated* family is automatically normalized as Π_{ϕ_a, ϕ_b} is unitary.

In the following, we use the combined density- and phase-modulated wave functions

$$|\theta, \phi\rangle = |\beta, \theta, \phi_a, \phi_b; N, \alpha\rangle \equiv \frac{1}{\sqrt{Z}} \mathcal{P}_{\beta, \theta} \Pi_{\phi_a, \phi_b} |N, \alpha\rangle \quad 2.270$$

to shed light on the low-energy bulk physics. Note that the order of Π and \mathcal{P} does not matter as both depend on n_i^x only.

A first observation is that there is a non-trivial phase transformation, $\phi = (\phi_a, \phi_b) = (\pi, 0)$, which imprints a constant phase of π on one (here, the upper) chain and none on the other. This phase does not affect the inter-chain interaction H^{ab} as the latter is subchain-parity-symmetric. Therefore $[H, \Pi_{\pi, 0}] = 0$, irrespective of the boundary conditions.

Let us now try to construct low-energy states that mix both phase and density modulation:

- 1 We consider the phase field $\phi_{x_1, x_2}^a(x) \equiv (\varphi_{x_1, x_2}(x), 0)$, where $\varphi_{x_1, x_2}(x) \equiv \pi \cdot \mathbb{1}_{[x_1, x_2]}(x)$. The field ϕ_{x_1, x_2}^a imprints a phase of π between positions x_1 and x_2 on the upper chain, Figure 2.23.

The state $|\theta = 0, \phi_{x_1, x_2}^a\rangle$ has finite energy since both the intra-chain terms H^a of chain a at sites $x_{1,2}$ and the corresponding inter-chain coupling terms H^{ab} yield finite energy expectation values. In between x_1 and x_2 there is no contribution due to the uniformity of the phase and the fixed relative phase of π between the chains.

- 2 Since the reason for the finite energy density at x_1 and x_2 is the same as for PBC with odd total filling at the boundary (that is, a single-particle “phase slip” of π), it can be avoided by the same means: Choose a potential $\theta_{x_1, x_2}(x)$ with smooth peaks at x_1 and x_2 so that for given ρ both points are well-separated from and above the “Fermi surface” F_0 . The inverse temperature is again $\beta(L) \propto \log L$ so that the system is “cooled down” in the thermodynamic limit.

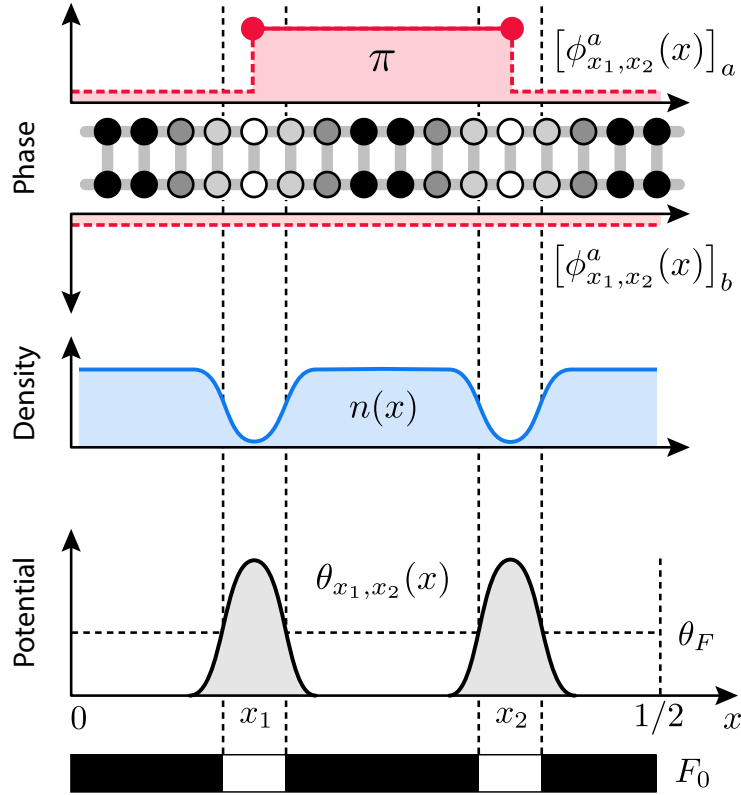


FIGURE 2.23 • Low-energy phase slip. Asymmetric low-energy phase slip in a double-chain with open boundary conditions. The maxima of an appropriately chosen potential $\theta_{x_1,x_2}(x)$ are used to suppress the particle density $n(x)$ smoothly at the two separate locations x_1 and x_2 on the double-chain. The imprinted single-particle phase $\phi_{x_1,x_2}^a(x)$ realizes a phase slip of π that is pinned to the density minima without energy penalty. The intra-chain energy of the density gradient vanishes in the thermodynamic limit.

- 3** The result of this construction is illustrated in Figure 2.23: The bulk energy from the density gradient vanishes for $L \rightarrow \infty$ while the slowly decreasing temperature $T \rightarrow 0$ depletes the positions x_1 and x_2 where the phase slips might cause energetic trouble. We end up with a family of low-energy states

$$|x_1, x_2\rangle \equiv |\theta_{x_1,x_2}, \phi_{x_1,x_2}\rangle \quad 2.271$$

that describe the propagation of a π -phase slip through the system. The importance of this result is underpinned by the observation

$$|1, L\rangle = \prod_{\phi_{1,L}^a} |N, \alpha\rangle = e^{i\pi \sum_s n_s^a} |N, \alpha\rangle = \alpha |N, \alpha\rangle, \quad 2.272$$

i.e., “pulling” a π -phase slip through the whole upper chain yields access to the non-local subchain parity α .

For a concluding remark, we return to the original problem: Periodic boundary conditions with odd total parity. Clearly, the Hamiltonian H is translationally invariant whereas the constructed states $|G\rangle = |\theta_0, \phi = 0\rangle$ with vanishing energy in the thermodynamic limit and depleted sites 1 and L are *not*. (Here, θ_y is characterized by a single, smooth peak at y so that y is above the Fermi level for given ρ .)

As a matter of fact, whether we deplete the chain smoothly at $y = 0$ or any other position $0 \leq y \leq 1$ should not make any difference—due to the translational invariance of H any such state must belong to the low-energy sector. To understand why this intuitive statement is indeed true, define the following family of states

$$|y\rangle \equiv |\theta_y, \phi_{0,y}^a\rangle, \quad 2.273$$

characterized by a density dip at y and a π -phase slip between 0 and y . By construction, there is no energy to be paid at the phase slip boundary y as it is depleted by θ_y (for $L \rightarrow \infty$). If we derive this state from $|N, +1\rangle$ with N odd subject to the PBC Hamiltonian H , then, due to the fermion gauge and the positive upper-chain parity, there is a *statistics-induced* phase difference of π between sites 1 and L [recall (2.112) and (2.113)]. In $|y\rangle$, this difference is increased to a phase jump of 2π by the artificially introduced phase slip of π at $y = 0$. So in this subchain-parity sector ($\alpha = +1$), we no longer pay energy at the origin but *would* pay energy at y instead if we had not called for a density dip at this very position.

In a nutshell: By introducing π -phase slips, one can shift the “boundary” to arbitrary positions on the PBC double-chain. Thus the “boundary” is not physically distinct but emerges due to (partially) fixing the fermion gauge. Introducing the upper-chain phase slip $\Pi_{\phi_{0,y}^a}$ then corresponds to a gauge transformation.

2.B.3 Upper Bound in the Even-Even Sector

Here we show that the energy of the phase-modulated state

$$|G_0\rangle = \exp \left[\underbrace{i \frac{\pi}{L} \sum_{s=1}^L s (a_s^\dagger a_s + b_s^\dagger b_s)}_{\equiv U_L^{ab}} \right] |2K, +1\rangle \quad 2.274$$

reads

$$\langle G_0 | H | G_0 \rangle = 2 \cdot 4\rho(1 - \rho) \cdot L \cdot \sin^2 \left(\frac{\pi}{2L} \right) \quad 2.275$$

and vanishes with L^{-1} for $L \rightarrow \infty$. The motivation for $|G_0\rangle$ is to imprint a chain-symmetric single-particle phase on the equal-weight superposition to compensate for the twisted boundary conditions (2.112) in the thermodynamic limit.

Obviously $[H^{ab}, U_L^{ab}] = 0$ so that

$$\begin{aligned} \langle G_0 | H | G_0 \rangle &= \langle 2K, +1 | U_L^{ab\dagger} (H^a + H^b + H^{ab}) U_L^{ab} | 2K, +1 \rangle \\ &= 2 \underbrace{\langle 2K, +1 | U_L^{a\dagger} H^a U_L^a | 2K, +1 \rangle}_{= \langle G_0 | H^a | G_0 \rangle}. \end{aligned} \quad 2.276$$

Here we used that $H^{ab} | 2K, +1 \rangle = 0$ —even for periodic boundary conditions, recall Eq. (2.113) for $\alpha\bar{\alpha} = +1$. Furthermore, we defined

$$U_L^a = \exp \left[i \frac{\pi}{L} \sum_{s=1}^L s a_s^\dagger a_s \right] \quad 2.277$$

and used that upper and lower chain are completely symmetric in the even-even sector. Thus it is sufficient to evaluate the expectation value for one of the two subchains:

$$\langle G_0 | H^a | G_0 \rangle = \mathcal{N}_{L,2K,+1}^{-1} \sum_{\substack{n,m; \\ (-1)^{n,m}=+1}} \langle n | U_L^{a\dagger} H^a U_L^a | m \rangle_a \underbrace{\langle 2K-n | 2K-m \rangle_b}_{\binom{L}{2K-n} \delta_{n,m}}. \quad 2.278$$

We find

$$\begin{aligned} &\langle n | U_L^{a\dagger} H^a U_L^a | n \rangle_a \\ &= \sum_{s=1}^L \langle n | e^{-i \frac{\pi}{L} [s n_s^a + (s+1) n_{s+1}^a]} H_s^a e^{i \frac{\pi}{L} [s n_s^a + (s+1) n_{s+1}^a]} | n \rangle_a \end{aligned} \quad 2.279$$

with

$$H_s^a = -a_{s+1}^\dagger a_s - a_s^\dagger a_{s+1} + n_s^a (\mathbb{1} - n_{s+1}^a) + n_{s+1}^a (\mathbb{1} - n_s^a). \quad 2.280$$

It is easy to see that

$$\begin{aligned} &e^{-i \frac{\pi}{L} [s n_s^a + (s+1) n_{s+1}^a]} H_s^a e^{i \frac{\pi}{L} [s n_s^a + (s+1) n_{s+1}^a]} \\ &= \left\{ \begin{array}{l} -e^{-i \frac{\pi}{L}} a_{s+1}^\dagger a_s - e^{i \frac{\pi}{L}} a_s^\dagger a_{s+1} \\ + n_s^a (\mathbb{1} - n_{s+1}^a) + n_{s+1}^a (\mathbb{1} - n_s^a) \end{array} \right\} \end{aligned} \quad 2.281$$

for $1 \leq s < L$, and for $s = L$

$$\begin{aligned} &e^{-i \frac{\pi}{L} [L n_L^a + n_1^a]} H_L^a e^{i \frac{\pi}{L} [L n_L^a + n_1^a]} \\ &= \left\{ \begin{array}{l} -e^{i \frac{\pi}{L} (L-1)} a_1^\dagger a_L - e^{-i \frac{\pi}{L} (L-1)} a_L^\dagger a_1 \\ + n_L^a (\mathbb{1} - n_1^a) + n_1^a (\mathbb{1} - n_L^a) \end{array} \right\}. \end{aligned} \quad 2.282$$

If we apply the equal-weight superpositions $|n\rangle_a$ on both sides, we find

$$\begin{aligned} & \langle n | e^{-i\frac{\pi}{L}[sn_s^a + (s+1)n_{s+1}^a]} H_s^a e^{i\frac{\pi}{L}[sn_s^a + (s+1)n_{s+1}^a]} | n \rangle \\ &= \left\{ -e^{-i\frac{\pi}{L}} - e^{i\frac{\pi}{L}} + 1 + 1 \right\} \times \binom{L-2}{n-1} \end{aligned} \quad 2.283a$$

$$= 2 \left[1 - \cos\left(\frac{\pi}{L}\right) \right] \times \binom{L-2}{n-1} \quad 2.283b$$

$$= 4 \sin^2\left(\frac{\pi}{2L}\right) \times \binom{L-2}{n-1} \quad 2.283c$$

in *both* cases, i.e., for $1 \leq s \leq L$. This is only true because n is *even* so that the hopping $a_1^\dagger a_L$ across the chain yields an additional minus sign that cancels the factors $e^{\pm i\frac{\pi}{L}L} = -1$ in Eq. (2.282) (recall the fermion ordering in Figure 2.6).

As the last expression does not depend on s , it is

$$\langle n | U_L^{a\dagger} H^a U_L^a | n \rangle_a = 4L \sin^2\left(\frac{\pi}{2L}\right) \times \binom{L-2}{n-1}, \quad 2.284$$

and finally

$$\begin{aligned} \langle G_0 | H^a | G_0 \rangle &= 4L \sin^2\left(\frac{\pi}{2L}\right) \\ &\times \mathcal{N}_{L,2K,+1}^{-1} \sum_{n; (-1)^n = +1} \binom{L}{2K-n} \binom{L-2}{n-1}. \end{aligned} \quad 2.285$$

If we write

$$\sum_{n \text{ even}} \binom{L}{2K-n} \binom{L-2}{n-1} = \sum_{m \text{ odd}} \binom{L}{(2K-1)-m} \binom{L-2}{m}, \quad 2.286$$

the last terms can be cast into PsBCs:

$$\mathcal{N}_{L,2K,+1}^{-1} \sum_{n; (-1)^n = +1} \binom{L}{2K-n} \binom{L-2}{n-1} = \binom{L, L}{+1}_{2K}^{-1} \binom{L-2, L}{-1}_{2K-1}. \quad 2.287$$

Then we can use relation (2.45) for the asymptotic expression

$$\binom{L, L}{+1}_{2K}^{-1} \binom{L-2, L}{-1}_{2K-1} \sim \rho(1-\rho) \quad 2.288$$

at fixed density ρ for $L \rightarrow \infty$. This yields the final result

$$\langle G_0 | H | G_0 \rangle = 2 \cdot 4\rho(1-\rho) \cdot L \cdot \sin^2\left(\frac{\pi}{2L}\right). \quad 2.289$$

For $L \rightarrow \infty$, we get the algebraic decay

$$\langle G_0 | H | G_0 \rangle \sim \frac{2\rho(1-\rho)\pi^2}{L}. \quad 2.290$$

The energy of $|G_0\rangle$ vanishes due to the smoothly varying single-particle phase that cancels the sign of fermions that propagate across the chain. Since the phase field is the same for both subchains, the inter-chain interaction H^{ab} is not affected by this modification and only intra-chain contributions prevent $|G_0\rangle$ from being a zero-energy ground state in finite systems.

2.C Bethe Ansatz Solutions

In this section, we employ Bethe ansatz wave functions [245] to solve our model completely in the $N \leq 2$ -particle sectors (for periodic boundary conditions). The most complex (and most interesting) sector is the even-subchain-parity sector for filling $N = 2$, which is the simplest *interacting* many-particle sector. There we find three fundamentally distinct classes of excitations: one describes two-fermion *bound states*; the other two are *scattering states* with either finite or vanishing fermion pairing, respectively.

We start in \clubsuit Subsection 2.C.1 with a careful translation of our fermionic theory into a spin model via Jordan-Wigner transformation; in particular, we show how translational invariance can be restored by an appropriate choice of the fermion gauge. In \clubsuit Subsection 2.C.2 we revisit the non-interacting single-particle sector for the sake of completeness—and to prepare for \clubsuit Subsection 2.C.3 where we study the interacting two-particle sector in detail. We conclude in \clubsuit Subsection 2.C.4 with a detailed proof of Lemma 2.1.

2.C.1 Jordan-Wigner Transformation

We start with the general form of our model in Jordan-Wigner representation with periodic boundary conditions. First, remember that the Hamiltonian reads

$$H = \sum_{i=1}^L \left(H_i^a + H_i^b + H_i^{ab} \right) \quad 2.291$$

where the indices are integers modulo L . Each subchain $x = a, b$ is governed by intra-chain interactions

$$H_i^x = x_i x_{i+1}^\dagger + x_{i+1} x_i^\dagger + n_i^x (\mathbb{1} - n_{i+1}^x) + n_{i+1}^x (\mathbb{1} - n_i^x). \quad 2.292$$

In addition, both subchains are coupled via pair hopping:

$$\begin{aligned}
 H_i^{ab} &= a_i^\dagger a_{i+1}^\dagger b_i b_{i+1} + b_i^\dagger b_{i+1}^\dagger a_i a_{i+1} \\
 &\quad + n_i^a n_{i+1}^a (\mathbb{1} - n_i^b) (\mathbb{1} - n_{i+1}^b) \\
 &\quad + n_i^b n_{i+1}^b (\mathbb{1} - n_i^a) (\mathbb{1} - n_{i+1}^a).
 \end{aligned} \tag{2.293}$$

Let us introduce the following pictorial representation of projectors acting on the spin- $\frac{1}{2}$ Hilbert space $\mathcal{H}_L = \bigotimes_{i=1}^L (\mathbb{C}_i^a)^2 \otimes (\mathbb{C}_i^b)^2$:

$$\left| \begin{array}{|c|c|} \hline \blacksquare & \blacksquare \\ \hline \end{array} \right\rangle \left\langle \begin{array}{|c|c|} \hline \blacksquare & \blacksquare \\ \hline \end{array} \right|_i \equiv \mathbb{1}_1^a \dots |\downarrow\rangle \langle \downarrow|_i^a \otimes |\uparrow\rangle \langle \uparrow|_{i+1}^a \dots \mathbb{1}_L^a \otimes \mathbb{1}_1^b \dots \mathbb{1}_L^b \tag{2.294a}$$

$$\left| \begin{array}{|c|c|} \hline \square & \blacksquare \\ \hline \end{array} \right\rangle \left\langle \begin{array}{|c|c|} \hline \square & \blacksquare \\ \hline \end{array} \right|_i \equiv \mathbb{1}_1^a \dots \mathbb{1}_L^a \otimes \mathbb{1}_1^b \dots |\uparrow\rangle \langle \uparrow|_i^b \otimes |\downarrow\rangle \langle \downarrow|_{i+1}^b \dots \mathbb{1}_L^b, \tag{2.294b}$$

and similarly for other configurations of sites i and $i + 1$ on the upper and lower chain. In particular, we write

$$\left| \begin{array}{|c|c|} \hline \blacksquare & \blacksquare \\ \hline \end{array} \right\rangle \left\langle \begin{array}{|c|c|} \hline \blacksquare & \blacksquare \\ \hline \end{array} \right|_i \equiv \mathbb{1}_1^a \dots |\downarrow\rangle \langle \downarrow|_i^a \otimes |\downarrow\rangle \langle \downarrow|_{i+1}^a \dots \mathbb{1}_L^a \otimes \mathbb{1}_1^b \dots |\uparrow\rangle \langle \uparrow|_i^b \otimes |\uparrow\rangle \langle \uparrow|_{i+1}^b \dots \mathbb{1}_L^b \tag{2.295a}$$

$$\left| \begin{array}{|c|c|} \hline \blacksquare & \blacksquare \\ \hline \end{array} \right\rangle \left\langle \begin{array}{|c|c|} \hline \blacksquare & \blacksquare \\ \hline \end{array} \right|_i \equiv \mathbb{1}_1^a \dots |\uparrow\rangle \langle \uparrow|_i^a \otimes |\uparrow\rangle \langle \uparrow|_{i+1}^a \dots \mathbb{1}_L^a \otimes \mathbb{1}_1^b \dots |\downarrow\rangle \langle \downarrow|_i^b \otimes |\downarrow\rangle \langle \downarrow|_{i+1}^b \dots \mathbb{1}_L^b. \tag{2.295b}$$

If we recall the chosen fermion gauge (the numbering of fermion sites in Figure 2.6), it is easy to see that the Jordan-Wigner representations of the intra-chain Hamiltonians read

$$\begin{aligned}
 H_i^a &= -(-\alpha)^{\delta_{i,L}} \left[\left| \begin{array}{|c|c|} \hline \square & \blacksquare \\ \hline \end{array} \right\rangle \left\langle \begin{array}{|c|c|} \hline \square & \blacksquare \\ \hline \end{array} \right|_i + \left| \begin{array}{|c|c|} \hline \blacksquare & \blacksquare \\ \hline \end{array} \right\rangle \left\langle \begin{array}{|c|c|} \hline \blacksquare & \blacksquare \\ \hline \end{array} \right|_i \right] \\
 &\quad + \left[\left| \begin{array}{|c|c|} \hline \blacksquare & \square \\ \hline \end{array} \right\rangle \left\langle \begin{array}{|c|c|} \hline \blacksquare & \square \\ \hline \end{array} \right|_i + \left| \begin{array}{|c|c|} \hline \square & \square \\ \hline \end{array} \right\rangle \left\langle \begin{array}{|c|c|} \hline \square & \square \\ \hline \end{array} \right|_i \right]
 \end{aligned} \tag{2.296}$$

and

$$\begin{aligned}
 H_i^b &= -(-\bar{\alpha})^{\delta_{i,L}} \left[\left| \begin{array}{|c|c|} \hline \square & \blacksquare \\ \hline \end{array} \right\rangle \left\langle \begin{array}{|c|c|} \hline \square & \blacksquare \\ \hline \end{array} \right|_i + \left| \begin{array}{|c|c|} \hline \blacksquare & \blacksquare \\ \hline \end{array} \right\rangle \left\langle \begin{array}{|c|c|} \hline \blacksquare & \blacksquare \\ \hline \end{array} \right|_i \right] \\
 &\quad + \left[\left| \begin{array}{|c|c|} \hline \blacksquare & \square \\ \hline \end{array} \right\rangle \left\langle \begin{array}{|c|c|} \hline \blacksquare & \square \\ \hline \end{array} \right|_i + \left| \begin{array}{|c|c|} \hline \square & \square \\ \hline \end{array} \right\rangle \left\langle \begin{array}{|c|c|} \hline \square & \square \\ \hline \end{array} \right|_i \right],
 \end{aligned} \tag{2.297}$$

where α ($\bar{\alpha}$) denotes the subchain parities for chain a (b). The subchain-parity-dependent signs are associated with the hopping between sites 1 and L which corresponds to an exchange of the hopping fermion with all other fermions of a subchain. An equivalent representation is given in Eq. (2.112) of Subsection 2.4.2.

An analogous reasoning leads to the representation of the inter-chain interaction

$$\begin{aligned}
 H_i^{ab} = & -(\alpha\bar{\alpha})^{\delta_{i,L}} \left[\left| \begin{array}{|c|c|} \hline \blacksquare & \blacksquare \\ \hline \blacksquare & \blacksquare \\ \hline \end{array} \right\rangle \left\langle \begin{array}{|c|c|} \hline \blacksquare & \blacksquare \\ \hline \blacksquare & \blacksquare \\ \hline \end{array} \right|_i + \left| \begin{array}{|c|c|} \hline \blacksquare & \blacksquare \\ \hline \blacksquare & \blacksquare \\ \hline \end{array} \right\rangle \left\langle \begin{array}{|c|c|} \hline \blacksquare & \blacksquare \\ \hline \blacksquare & \blacksquare \\ \hline \end{array} \right|_i \right] \\
 & + \left[\left| \begin{array}{|c|c|} \hline \blacksquare & \blacksquare \\ \hline \blacksquare & \blacksquare \\ \hline \end{array} \right\rangle \left\langle \begin{array}{|c|c|} \hline \blacksquare & \blacksquare \\ \hline \blacksquare & \blacksquare \\ \hline \end{array} \right|_i + \left| \begin{array}{|c|c|} \hline \blacksquare & \blacksquare \\ \hline \blacksquare & \blacksquare \\ \hline \end{array} \right\rangle \left\langle \begin{array}{|c|c|} \hline \blacksquare & \blacksquare \\ \hline \blacksquare & \blacksquare \\ \hline \end{array} \right|_i \right],
 \end{aligned} \tag{2.298}$$

where $\alpha\bar{\alpha} = (-1)^N$ with filling N . Again, an equivalent representation is given in Eq. (2.113) of Subsection 2.4.2.

Depending on the subchain parities α and $\bar{\alpha}$, the Hamiltonian (2.291) is in general *not* translationally invariant in this representation. This leads to technical difficulties in the context of the Bethe ansatz—which makes use of plane wave solutions (with additional scattering phases) and thereby relies on translational invariance.

Restoring Translational Invariance

We therefore are encouraged to find a translationally invariant representation of the Hamiltonian. Since the original *fermion* Hamiltonian is translationally invariant by construction, the observed breaking of translational invariance must be limited to the gauge level. Thus, for a given subchain-parity sector $(\alpha, \bar{\alpha})$, we can hope for an appropriately chosen fermion gauge that restores translational invariance of the representation.

A general U(1) gauge transformation of the fermion algebra is given by

$$\tilde{x}_j \equiv e^{-i\xi_j^x} x_j \quad \text{for } x = a, b \quad \text{and } j = 1, \dots, L \tag{2.299}$$

for arbitrary functions $\xi^x : \{1, \dots, L\} \rightarrow [0, 2\pi)$. This unitary transformation clearly preserves the fermion algebra, $\{\tilde{x}_i, \tilde{x}_j^\dagger\} = \delta_{ij}$, and induces a transformation on the Fock basis via

$$|\mathbf{n}, \mathbf{m}\rangle = (a_1^\dagger)^{n_1} \dots (a_L^\dagger)^{n_L} (b_1^\dagger)^{m_1} \dots (b_L^\dagger)^{m_L} |0\rangle \tag{2.300a}$$

$$= e^{-i\sum_j (\xi_j^a n_j + \xi_j^b m_j)} (\tilde{a}_1^\dagger)^{n_1} \dots (\tilde{a}_L^\dagger)^{n_L} (\tilde{b}_1^\dagger)^{m_1} \dots (\tilde{b}_L^\dagger)^{m_L} |0\rangle \tag{2.300b}$$

$$\equiv e^{-i\sum_j (\xi_j^a n_j + \xi_j^b m_j)} |\mathbf{n}, \mathbf{m}\rangle^\sim \tag{2.300c}$$

with the fermion number operators $n_j^x = x_j^\dagger x_j = \tilde{x}_j^\dagger \tilde{x}_j$. If we define the unitary $T_\xi \equiv e^{i\sum_j (\xi_j^a n_j + \xi_j^b m_j)}$, the gauge transformation simply reads

$$|\mathbf{n}, \mathbf{m}\rangle^\sim = T_\xi |\mathbf{n}, \mathbf{m}\rangle \quad \text{and} \quad \tilde{x}_j = T_\xi x_j T_\xi^\dagger. \tag{2.301}$$

We can express the fermionic Hamiltonian in this U(1)-rotated Fock basis and subsequently apply the Jordan-Wigner transformation⁸⁷. Then its local components read

$$H_i^a = -(\alpha)^{\delta_{i,L}} \left\{ \begin{array}{l} e^{i(\xi_i^a - \xi_{i+1}^a)} \left| \begin{array}{|c|} \hline \blacksquare \\ \hline \end{array} \right\rangle \left\langle \begin{array}{|c|} \hline \blacksquare \\ \hline \end{array} \right|_i \widetilde{\phantom{\left\langle \begin{array}{|c|} \hline \blacksquare \\ \hline \end{array} \right|_i}} \\ + e^{-i(\xi_i^a - \xi_{i+1}^a)} \left| \begin{array}{|c|} \hline \blacksquare \\ \hline \end{array} \right\rangle \left\langle \begin{array}{|c|} \hline \square \\ \hline \end{array} \right|_i \widetilde{\phantom{\left\langle \begin{array}{|c|} \hline \square \\ \hline \end{array} \right|_i}} \end{array} \right\} + \dots, \quad 2.302a$$

$$H_i^b = -(\bar{\alpha})^{\delta_{i,L}} \left\{ \begin{array}{l} e^{i(\xi_i^b - \xi_{i+1}^b)} \left| \begin{array}{|c|} \hline \square \\ \hline \end{array} \right\rangle \left\langle \begin{array}{|c|} \hline \square \\ \hline \end{array} \right|_i \widetilde{\phantom{\left\langle \begin{array}{|c|} \hline \square \\ \hline \end{array} \right|_i}} \\ + e^{-i(\xi_i^b - \xi_{i+1}^b)} \left| \begin{array}{|c|} \hline \square \\ \hline \end{array} \right\rangle \left\langle \begin{array}{|c|} \hline \blacksquare \\ \hline \end{array} \right|_i \widetilde{\phantom{\left\langle \begin{array}{|c|} \hline \blacksquare \\ \hline \end{array} \right|_i}} \end{array} \right\} + \dots, \quad 2.302b$$

and

$$H_i^{ab} = -(\alpha\bar{\alpha})^{\delta_{i,L}} \left\{ \begin{array}{l} e^{-i(\xi_i^a + \xi_{i+1}^a - \xi_i^b - \xi_{i+1}^b)} \left| \begin{array}{|c|c|} \hline \blacksquare & \blacksquare \\ \hline \end{array} \right\rangle \left\langle \begin{array}{|c|c|} \hline \blacksquare & \blacksquare \\ \hline \end{array} \right|_i \widetilde{\phantom{\left\langle \begin{array}{|c|c|} \hline \blacksquare & \blacksquare \\ \hline \end{array} \right|_i}} \\ + e^{i(\xi_i^a + \xi_{i+1}^a - \xi_i^b - \xi_{i+1}^b)} \left| \begin{array}{|c|c|} \hline \blacksquare & \square \\ \hline \end{array} \right\rangle \left\langle \begin{array}{|c|c|} \hline \square & \blacksquare \\ \hline \end{array} \right|_i \widetilde{\phantom{\left\langle \begin{array}{|c|c|} \hline \square & \blacksquare \\ \hline \end{array} \right|_i}} \end{array} \right\} + \dots, \quad 2.303$$

where we suppressed the invariant density terms. Note that the indices i are numbers modulo L , i.e., $\xi_{L+1}^x \equiv \xi_1^x$ (this is a definition and not a constraint on ξ^x).

Given $(\alpha, \bar{\alpha})$, we seek for a gauge transformation ξ^x so that the coefficients become translationally invariant, i.e., independent of i . Here we are particularly interested in the $N = 2$ -particle sector; thus we restrict our discussion to the symmetric sectors with $\alpha = \bar{\alpha}$:

If $\alpha = -1 = \bar{\alpha}$, the Hamiltonian is already translationally invariant and we can set $\xi_j^x \equiv 0$ for all $j = 1, \dots, L$ and $x = a, b$. By contrast, for $\alpha = +1 = \bar{\alpha}$ the naïve Jordan-Wigner representation is not translationally invariant due to the sign between sites 1 and L . To restore translational invariance, we set $\xi_j^x \equiv j \frac{\pi}{L}$ for all $j = 1, \dots, L$ and $x = a, b$.

Indeed,

$$(-\alpha)^{\delta_{j,L}} e^{-i(\xi_j^a - \xi_{j+1}^a)} = (-\bar{\alpha})^{\delta_{j,L}} e^{-i(\xi_j^b - \xi_{j+1}^b)} \quad 2.304a$$

$$= \begin{cases} e^{i \frac{\pi}{L}} & j \neq L, \\ (-1) \cdot e^{-i(\xi_L^x - \xi_1^x)} = e^{i \frac{\pi}{L}} & j = L, \end{cases} \quad 2.304b$$

and

$$(\alpha\bar{\alpha})^{\delta_{j,L}} e^{-i(\xi_j^a + \xi_{j+1}^a - \xi_j^b - \xi_{j+1}^b)} = 1. \quad 2.305$$

Loosely speaking, we “distribute” the phase jump of π for a fermion going once around a subchain uniformly on all hopping amplitudes along the chain.

With these preliminaries, we are now in the position to apply the Bethe ansatz: Due to the restored translational invariance, we can expect the eigenvalue equations to become particularly simple in momentum space, and the eigenstates to be related to plane waves with well-defined momenta.

⁸⁷Of course this can be done in one step with a modified Jordan-Wigner transformation that takes the phases ξ_i^x into account. After all, this is about unitary equivalent representations of the same physical model.

2.C.2 The Non-Interacting Sectors

For the sake of completeness (and to prepare for \clubsuit Subsection 2.C.3), we start with the simplest sectors of the Hilbert space, namely both single-particle subsectors ($N = 1$) and the odd-odd subsector with two particles ($N = 2$). As there are no relevant interactions in these subsectors, the theory is trivially solvable by plane waves.

The Free Sectors for $N = 1$

In the single-particle sector $N = 1$ there are two subchain-parity subsectors, indexed by $(\alpha, \bar{\alpha}) = (+1, -1)$ and $(-1, +1)$, depending on the location of the single fermion. As both cases are symmetric, we consider w.l.o.g. the case where the fermion is in chain a (upper chain) such that we can diagonalize the Hamiltonian on the L -dimensional Hilbert space \mathcal{H}_α^N with $N = 1$ and $\alpha = -1$. Note that the following calculation is almost identical to the one in Subsection 2.4.1—except for the periodic boundary conditions (only the allowed momenta are different).

If we introduce

$$|n\rangle \equiv |\uparrow_1 \dots \downarrow_n \dots \uparrow_L\rangle^a \otimes |\uparrow_1 \dots \uparrow_L\rangle^b \leftrightarrow a_n^\dagger |0\rangle \quad 2.306$$

with one “fermion” at site n on the upper chain⁸⁸, a generic state reads

$$|\Psi\rangle = \sum_n a(n) |n\rangle, \quad a(n) \in \mathbb{C}. \quad 2.307$$

To solve $H|\Psi\rangle = E|\Psi\rangle$, we apply $H = \sum_i (H_i^a + H_i^b + H_i^{ab})$ on $|\Psi\rangle$ and exploit that only the terms H_i^a contribute. Since $\alpha = -1$, the resulting Hamiltonian is

⁸⁸Note that in the single-particle sector, there is no difference between Fock states and the spin- $\frac{1}{2}$ states of the Jordan-Wigner representation.

already translationally invariant and one derives easily

$$H|\Psi\rangle = \sum_{i=1}^L \sum_{n=1}^L a(n) H_i^a |n\rangle \quad 2.308a$$

$$= \sum_{i=1}^L \sum_{n=1}^L a(n) \left\{ \begin{array}{l} \delta_{i,n}|n\rangle + \delta_{i,n-1}|n\rangle \\ -\delta_{i,n}|n+1\rangle - \delta_{i,n-1}|n-1\rangle \end{array} \right\} \quad 2.308b$$

$$= \sum_{n=1}^L a(n) [2|n\rangle - |n+1\rangle - |n-1\rangle] \quad 2.308c$$

$$= \sum_{n=1}^L [2a(n) - a(n-1) - a(n+1)] |n\rangle \quad 2.308d$$

$$\stackrel{!}{=} E \sum_{n=1}^L a(n) |n\rangle, \quad 2.308e$$

where we performed an index shift in the second-last row and used the boundary condition $a(n+L) = a(n)$.

This yields the equation

$$2a(n) - a(n-1) - a(n+1) = E a(n) \quad 2.309$$

which is immediately solved by the plane wave ansatz $a(n) = A e^{ikn}$ with momenta $k \in \mathbb{R}$ if and only if

$$E = 2 \left[1 - \frac{e^{ik} + e^{-ik}}{2} \right] = 4 \sin^2 \left(\frac{k}{2} \right) \equiv E(k). \quad 2.310$$

So far k is arbitrary. However, above we required the L -periodicity of $a(n)$ which restricts the wavenumber to discrete values:

$$e^{ik(n+L)} \stackrel{!}{=} e^{ikn} \Leftrightarrow kL \in 2\pi\mathbb{Z} \Leftrightarrow k \in \frac{2\pi}{L}\mathbb{Z}. \quad 2.311$$

Restricting k further to the first Brillouin zone, $0 \leq k < 2\pi$, yields the orthogonal eigenstates

$$|k\rangle \equiv |k; N=1, \alpha=-1\rangle = \frac{1}{\sqrt{L}} \sum_{n=1}^L e^{ikn} |n\rangle \quad 2.312$$

with $k \in \frac{2\pi}{L}\{0, 1, \dots, L-1\}$. For $k=0$, we recover the already known ground state $|0; N=1, \alpha=-1\rangle = |N, \alpha\rangle$ with energy $E(0) = 0$, namely the equal-weight superposition of all single-fermion states. The eigenstates $|k\rangle$ are commonly termed *single-magnon states* for the Heisenberg chain [265, 266].

The Free Sector for $N = 2$

In the subsector \mathcal{H}_α^N with $N = 2$ and $\alpha = -1$, there is one fermion in each subchain and—due to the subchain-parity conservation of the Hamiltonian—we expect them to propagate freely. To derive the spectrum rigorously, define the Jordan-Wigner representation of $a_n^\dagger b_m^\dagger |0\rangle$,

$$|n, m\rangle \equiv |\uparrow_1 \dots \downarrow_n \dots \uparrow_L\rangle^a \otimes |\uparrow_1 \dots \downarrow_m \dots \uparrow_L\rangle^b, \quad 2.313$$

with one “fermion” on site n in the upper and another one on site m in the lower chain. A generic state reads then

$$|\Psi\rangle = \sum_{n,m} c(n, m) |n, m\rangle, \quad c(n, m) \in \mathbb{C}. \quad 2.314$$

Application of the Hamiltonian yields

$$H|\Psi\rangle = \sum_{i=1}^L \sum_{n,m=1}^L c(n, m) [H_i^a |n, m\rangle + H_i^b |n, m\rangle] \quad 2.315a$$

$$= \sum_{n,m=1}^L c(n, m) \left\{ \begin{array}{l} 2|n, m\rangle - |n+1, m\rangle - |n-1, m\rangle \\ +2|n, m\rangle - |n, m+1\rangle - |n, m-1\rangle \end{array} \right\} \quad 2.315b$$

$$= \sum_{n,m=1}^L \left\{ \begin{array}{l} 4c(n, m) - c(n-1, m) - c(n+1, m) \\ -c(n, m-1) - c(n, m+1) \end{array} \right\} |n, m\rangle \quad 2.315c$$

$$\stackrel{!}{=} E \sum_{n,m=1}^L c(n, m) |n, m\rangle, \quad 2.315d$$

where the inter-chain part H^{ab} vanishes and the intra-chain terms are translationally invariant due to $\alpha = \bar{\alpha} = -1$.

Once again, periodicity translates into boundary conditions for the wave function:

$$c(n+L, m) = c(n, m) = c(n, m+L). \quad 2.316$$

The eigenvalue equation reads

$$\left\{ \begin{array}{l} 4c(n, m) - c(n-1, m) - c(n+1, m) \\ -c(n, m-1) - c(n, m+1) \end{array} \right\} = E c(n, m) \quad 2.317$$

and is solved by $c(n, m) = C e^{ik_a n + ik_b m}$ for $k_a, k_b \in \mathbb{R}$ with a dispersion

$$E = 4 \sin^2 \left(\frac{k_a}{2} \right) + 4 \sin^2 \left(\frac{k_b}{2} \right) \equiv E(k_a, k_b) \quad 2.318$$

that is just the sum of the energies of two magnons with wavenumbers k_a and k_b , respectively. The periodicity (2.316) leads to discrete wavenumbers $k_a, k_b \in \frac{2\pi}{L}\mathbb{Z}$ and the eigenbasis is given by

$$|k_a, k_b; N = 2, \alpha = -1\rangle = \frac{1}{L} \sum_{n,m=1}^L e^{ik_a n + ik_b m} |n, m\rangle \quad 2.319$$

with $k_a, k_b \in \frac{2\pi}{L}\{0, 1, \dots, L-1\}$; the zero-energy ground state is again the equal-weight superposition of two fermions with fixed subchain parity,

$$|0, 0; N = 2, \alpha = -1\rangle = |N, \alpha\rangle. \quad 2.320$$

Finally, note that (2.319) is nothing but the tensor product of two free magnon states,

$$\frac{1}{L} \sum_{n,m=1}^L e^{ik_a n + ik_b m} |n, m\rangle = \frac{1}{\sqrt{L}} \sum_{n=1}^L e^{ik_a n} |n\rangle^a \otimes \frac{1}{\sqrt{L}} \sum_{m=1}^L e^{ik_b m} |m\rangle^b, \quad 2.321$$

as the system equals the sum of two non-interacting chains each within its single-particle sector.

2.C.3 The Interacting Sector of Two Particles

The simplest sector where genuine fermion-fermion scattering takes place is the even-subchain-parity subsector in the two-particle sector, that is, $\mathcal{H}_{\alpha=1}^{N=2}$. The latter is $L(L-1)/2 + L(L-1)/2 = L(L-1)$ -dimensional and its generic states have the form

$$|\Psi\rangle = \sum_{1 \leq n < m \leq L} \left[a(n, m) \left| \begin{matrix} n, m \\ 0 \end{matrix} \right\rangle^{\sim} + b(n, m) \left| \begin{matrix} 0 \\ n, m \end{matrix} \right\rangle^{\sim} \right], \quad 2.322$$

where we introduced the states ($n < m$)

$$\left| \begin{matrix} n, m \\ 0 \end{matrix} \right\rangle^{\sim} \equiv |\uparrow_1 \dots \downarrow_n \dots \downarrow_m \dots \uparrow_L\rangle^a \otimes |\uparrow_1 \dots \uparrow_L\rangle^b \quad 2.323a$$

$$\left| \begin{matrix} 0 \\ n, m \end{matrix} \right\rangle^{\sim} \equiv |\uparrow_1 \dots \uparrow_L\rangle^a \otimes |\uparrow_1 \dots \downarrow_n \dots \downarrow_m \dots \uparrow_L\rangle^b \quad 2.323b$$

that correspond to $\tilde{a}_n^\dagger \tilde{a}_m^\dagger |0\rangle$ and $\tilde{b}_n^\dagger \tilde{b}_m^\dagger |0\rangle$, respectively.

Recall that, since $\alpha = 1 = \bar{\alpha}$, we need to re-gauge the fermions $x \rightarrow \tilde{x}$ to obtain a translationally invariant Hamiltonian in Jordan-Wigner representation. Then, the Hamiltonian takes the form

$$H = \sum_{j=1}^L \left\{ \begin{array}{l} |\square\square\rangle\langle\square\square|_j + |\square\square\rangle\langle\square\square|_j \\ -e^{-i\frac{\pi}{L}} |\square\square\rangle\langle\square\square|_j - e^{i\frac{\pi}{L}} |\square\square\rangle\langle\square\square|_j \\ + |\square\square\rangle\langle\square\square|_j + |\square\square\rangle\langle\square\square|_j \\ -e^{-i\frac{\pi}{L}} |\square\square\rangle\langle\square\square|_j - e^{i\frac{\pi}{L}} |\square\square\rangle\langle\square\square|_j \\ + |\square\square\rangle\langle\square\square|_j + |\square\square\rangle\langle\square\square|_j \\ - |\square\square\rangle\langle\square\square|_j - |\square\square\rangle\langle\square\square|_j \end{array} \right\} \quad 2.324$$

with complex hopping amplitudes that are reminiscent of the fermionic statistics of the original model⁸⁹.

Derivation of the Bethe Equation

Expanding the eigenvalue equation in terms of the amplitudes $a(n, m)$ and $b(n, m)$ is here more involved since the inter-chain interaction H_i^{ab} does not vanish anymore:

$$H|\Psi\rangle = \sum_{j=1}^L \sum_{1 \leq n < m \leq L} \left\{ \begin{array}{l} a(n, m) (H_j^a + H_j^{ab}) \left| \begin{array}{c} n, m \\ 0 \end{array} \right\rangle \\ + b(n, m) (H_j^b + H_j^{ab}) \left| \begin{array}{c} 0 \\ n, m \end{array} \right\rangle \end{array} \right\} \quad 2.325a$$

$$\stackrel{!}{=} E \sum_{1 \leq n < m \leq L} \left[a(n, m) \left| \begin{array}{c} n, m \\ 0 \end{array} \right\rangle + b(n, m) \left| \begin{array}{c} 0 \\ n, m \end{array} \right\rangle \right]. \quad 2.325b$$

A closer look at this equation yields a simple procedure to write down the eigenvalue equations for $a(n, m)$ and $b(n, m)$ without any cumbersome calculations: Start, for example, with the coefficient $Ea(n, m)$ on the right-hand side. Then we have to find all possible *original* states (and their coefficients) on the left-hand side which can be mapped by either H_i^a or H_i^{ab} onto this very state. We can write down their coefficients on the right-hand side of the equation $Ea(n, m) = \dots$ immediately if we consider two cases separately:

⁸⁹From this perspective, the statistics of fermions arises due to the Aharonov-Bohm phase and a magnetic flux in an equivalent bosonic theory. This relation between statistics and gauge fields is ubiquitous in condensed matter physics, exemplified by Chern-Simons gauge theories that describe the anyonic excitations of fractional quantum Hall fluids [40, 42].

- 1** *The two particles are **not** adjacent, i.e., $n < m - 1$ and $n \neq 1 \vee m \neq L$.*

Such configurations can only emerge from particles in the same chain (since inter-chain pair hopping requires adjacent particles). Each particle could have jumped from the left or right adjacent site to its current position. Hence we find four contributions from shifted coefficients and, in addition, four coefficients from particles that did not move at all:

$$E a(n, m) = \left\{ \begin{array}{l} 4a(n, m) - e^{i\frac{\pi}{L}}a(n+1, m) - e^{-i\frac{\pi}{L}}a(n-1, m) \\ - e^{i\frac{\pi}{L}}a(n, m+1) - e^{-i\frac{\pi}{L}}a(n, m-1) \end{array} \right\}, \quad 2.326a$$

$$E b(n, m) = \left\{ \begin{array}{l} 4b(n, m) - e^{i\frac{\pi}{L}}b(n+1, m) - e^{-i\frac{\pi}{L}}b(n-1, m) \\ - e^{i\frac{\pi}{L}}b(n, m+1) - e^{-i\frac{\pi}{L}}b(n, m-1) \end{array} \right\}. \quad 2.326b$$

We stress that each jump involves a complex phase $e^{\pm i\frac{\pi}{L}}$. Furthermore, notice that in this case both subchains decouple due to the gap between the particles. These equations hold for all $1 \leq n < m \leq L$ under the additional constraints given above. This involves so far undefined expressions of the form $a(0, m)$ and $a(n, L+1)$ (see below).

- 2** *The two particles are adjacent, i.e., $n = m - 1$ or $n = 1 \wedge m = L$.*

We discuss the two subcases separately:

- a** *Let $n = m - 1$.*

In this case there are only *two* possible single-particle jumps: the left particle could have jumped to the right or the right to the left. In addition, the pair hopping contributes a coefficient from the other chain which couples the upper- and lower-chain coefficients:

$$E a(n, m) = \left\{ \begin{array}{l} 3a(n, m) - e^{i\frac{\pi}{L}}a(n, m+1) \\ - e^{-i\frac{\pi}{L}}a(n-1, m) - b(n, m) \end{array} \right\}, \quad 2.327a$$

$$E b(n, m) = \left\{ \begin{array}{l} 3b(n, m) - e^{i\frac{\pi}{L}}b(n, m+1) \\ - e^{-i\frac{\pi}{L}}b(n-1, m) - a(n, m) \end{array} \right\}. \quad 2.327b$$

These equations hold for all $n = 1, 2, \dots, L-1$ and $m = n+1$.

- b** *Let $n = 1 \wedge m = L$.*

As above, there are two possible single-particle jumps: the left particle could have jumped to the left or the right to the right. In addition, the pair hopping contributes a coefficient from the other chain:

$$E a(1, L) = \left\{ \begin{array}{l} 3a(1, L) - e^{i\frac{\pi}{L}}a(1+1, L) \\ - e^{-i\frac{\pi}{L}}a(1, L-1) - b(1, L) \end{array} \right\}, \quad 2.328a$$

$$E b(1, L) = \left\{ \begin{array}{l} 3b(1, L) - e^{i\frac{\pi}{L}}b(1+1, L) \\ - e^{-i\frac{\pi}{L}}b(1, L-1) - a(1, L) \end{array} \right\}. \quad 2.328b$$

This special case is due to the shortcomings of our notation and of no physical significance (recall that the system is translationally invariant, see below).

To make sense of the above equations in the cases $n = 1$ or $m = L$, we require the “twisted” boundary conditions

$$\begin{aligned} a(n, L + 1) &= a(1, n) \\ \text{and } a(1 - 1, m) &= a(m, L) \quad \text{for all } 1 < n < m < L, \end{aligned} \quad 2.329$$

which is a consequence of the fixed ordering $1 \leq n < m \leq L$ in the sum (the same holds for b).

In order to solve all three classes of equations, we make the ansatz

$$a(n, m) = A e^{ip_1 n + ip_2 m} + A' e^{ip_1 m + ip_2 n} \quad 2.330a$$

$$b(n, m) = B e^{ip_1 n + ip_2 m} + B' e^{ip_1 m + ip_2 n} \quad 2.330b$$

where $p_1, p_2 \in \mathbb{C}$ are so far arbitrary (in general, complex) momenta and the coefficients $A, A', B, B' \in \mathbb{C}$ are undetermined as well. We can solve the equations (2.326) for separated particles for arbitrary $A, A', B, B' \in \mathbb{C}$, $p_1, p_2 \in \mathbb{C}$, and $n, m \in \mathbb{N}$ if the energy is of the form

$$\begin{aligned} E(p_1, p_2) &= \\ 2 \left[1 - \frac{e^{i(p_1 + \frac{\pi}{L})} + e^{-i(p_1 + \frac{\pi}{L})}}{2} \right] &+ 2 \left[1 - \frac{e^{i(p_2 + \frac{\pi}{L})} + e^{-i(p_2 + \frac{\pi}{L})}}{2} \right], \end{aligned} \quad 2.331$$

which can be easily checked by inserting the ansatz wave function into (2.326). This can be rewritten as

$$E(p_1, p_2) = 4 \sin^2 \frac{p_1 + \pi/L}{2} + 4 \sin^2 \frac{p_2 + \pi/L}{2}, \quad 2.332$$

which is the already known (shifted) spectrum of two magnons. Notice that the allowed momenta p_1 and p_2 are not yet fixed—thus we cannot determine the discrete spectrum at this stage.

If we insert this expression for $E = E(p_1, p_2)$ and the ansätze for a and b (2.330) in Eq. (2.327), we find the two expressions

$$(A + A') \left[1 + e^{i(q_1 + q_2)} \right] = (A + B) e^{iq_2} + (A' + B') e^{iq_1} \quad 2.333a$$

$$(B + B') \left[1 + e^{i(q_1 + q_2)} \right] = (A + B) e^{iq_2} + (A' + B') e^{iq_1}, \quad 2.333b$$

where we introduced the shifted momenta $q_i \equiv p_i + \frac{\pi}{L}$ for $i = 1, 2$.

BETHE ANSATZ SOLUTIONS

For $q_1 + q_2 \notin (2\mathbb{Z} + 1)\pi$, this is equivalent to

$$(A + A') \left[1 + e^{i(q_1+q_2)} \right] = (A + B)e^{iq_2} + (A' + B')e^{iq_1} \quad 2.334a$$

$$\text{and } A + A' = B + B'. \quad 2.334b$$

Before we consider the special case (2.328), let us first derive the constraints due to the twisted boundary conditions (2.329). To this end, we introduce the *scattering phases*

$$e^{i\theta_a} \equiv \frac{A}{A'}, \quad e^{i\theta_b} \equiv \frac{B}{B'} \quad \text{and} \quad e^{i\theta_{ab}} \equiv \sqrt{\frac{AA'}{BB'}}, \quad 2.335$$

which can be in general complex numbers, $\theta_a, \theta_b, \theta_{ab} \in \mathbb{C}$.

This allows us to rewrite the ansatz wave function as

$$a(n, m) = e^{ip_1n+ip_2m+i(\theta_a+\theta_{ab})/2} + e^{ip_1m+ip_2n-i(\theta_a-\theta_{ab})/2} \quad 2.336a$$

$$b(n, m) = e^{ip_1n+ip_2m+i(\theta_b-\theta_{ab})/2} + e^{ip_1m+ip_2n-i(\theta_b+\theta_{ab})/2} \quad 2.336b$$

(up to a global normalizing factor). If we insert this in (2.329), we find

$$\begin{aligned} & e^{ip_1n+ip_2(L+1)+i\theta_x} + e^{ip_1(L+1)+ip_2n} \\ &= e^{ip_1+ip_2n+i\theta_x} + e^{ip_1n+ip_2} \end{aligned} \quad 2.337$$

for $x = a, b$ and all $1 < n < L - 1$. By comparison, this implies

$$e^{ip_1L} = e^{i\theta_x} \quad \text{and} \quad e^{ip_2L} = e^{-i\theta_x}, \quad 2.338$$

which can be recast in the form

$$p_1 = \frac{2\pi}{L}\lambda_1^x + \frac{\theta_x}{L} \quad 2.339a$$

$$\text{and } p_2 = \frac{2\pi}{L}\lambda_2^x - \frac{\theta_x}{L} \quad \text{for } \lambda_1^x, \lambda_2^x \in \mathbb{Z} \quad 2.339b$$

where λ_1^x and λ_2^x are called *Bethe quantum numbers*. Since the left-hand side of the equations does not depend on x , we have the relations

$$2\pi(\lambda_1^a - \lambda_1^b) = \theta_b - \theta_a \quad 2.340a$$

$$\text{and } 2\pi(\lambda_2^a - \lambda_2^b) = \theta_a - \theta_b. \quad 2.340b$$

Due to the definition of θ_x , it is sufficient to restrict the real part $\text{Re } \theta_x$ to $[0, 2\pi)$. In combination with the equations above, this results in a unique scattering phase $\theta \equiv \theta_a \pmod{2\pi} = \theta_b \pmod{2\pi}$ and, consequently, unique Bethe quantum numbers $\lambda_i \equiv \lambda_i^a = \lambda_i^b$ for $i = 1, 2$.

This leads to the quantized momenta

$$p_1 = \frac{2\pi}{L}\lambda_1 + \frac{\theta}{L} \quad \text{and} \quad p_2 = \frac{2\pi}{L}\lambda_2 - \frac{\theta}{L} \quad 2.341$$

for $0 \leq \lambda_1, \lambda_2 < L$, where we restricted the Bethe quantum numbers so that all physically distinct momenta with $\text{Re } p_i \in [0, 2\pi)$ can be uniquely defined [recall the ansatz (2.336)].

We can rewrite the condition (2.334b) in terms of the scattering phases (2.335),

$$e^{i\theta_{ab}} \cos \frac{\theta_a}{2} = \cos \frac{\theta_b}{2}, \quad 2.342$$

which yields $e^{i\theta_{ab}} = 1$ for $\theta = \theta_a = \theta_b \neq \pi$, i.e., $\theta_{ab} = 0$ for $\text{Re } \theta_{ab} \in [0, 2\pi)$. This, however, holds *not* for the special case $\theta = \pi$ (which will be discussed in detail below).

The general solutions now have the form (up to a normalizing factor)

$$\begin{aligned} |\Psi_{\lambda_1, \lambda_2, \theta}\rangle = & \sum_{1 \leq n < m \leq L} \left[e^{i(p_1 n + p_2 m + \theta/2)} + e^{i(p_1 m + p_2 n - \theta/2)} \right] \\ & \times \left[\left| \begin{array}{c} 0 \\ n, m \end{array} \right\rangle^{\sim} + e^{i\theta_{ab}} \left| \begin{array}{c} n, m \\ 0 \end{array} \right\rangle^{\sim} \right], \end{aligned} \quad 2.343$$

where $p_{1,2}$ depend on the Bethe quantum numbers $\lambda_{1,2}$ and the scattering phase θ via (2.341). Note that we still do not know which momenta (or scattering phases) are allowed! So far we only derived that $\theta_{ab} = 0$ whenever $\theta \neq \pi$.

Let us now turn towards the remaining eigenvalue equations. Namely Eq. (2.334a) and the special cases (2.328). The combination of (2.334b) and $\theta_a = \theta_b \Rightarrow A/A' = B/B'$ yields

$$A = B \quad \text{and} \quad A' = B' \quad \text{for} \quad A + A' \neq 0 \Leftrightarrow \theta \neq \pi \quad 2.344$$

(which corresponds to $\theta_{ab} = 0$). Therefore we find from Eq. (2.334a) in this case

$$(A + A') \left[1 + e^{i(q_1 + q_2)} \right] = 2A e^{iq_2} + 2A' e^{iq_1} \quad 2.345a$$

$$\Leftrightarrow (1 + e^{i\theta}) \left[1 + e^{i(q_1 + q_2)} \right] = 2e^{i\theta} e^{iq_2} + 2e^{iq_1} \quad 2.345b$$

which is equivalent to the

RESULT 2.4: Bethe equation

$$e^{i\theta} = - \frac{e^{i(q_1 + q_2)} + 1 - 2e^{iq_1}}{e^{i(q_1 + q_2)} + 1 - 2e^{iq_2}} \quad 2.346$$

with $q_1 = L^{-1}(2\pi\lambda_1 + \pi + \theta)$ and $q_2 = L^{-1}(2\pi\lambda_2 + \pi - \theta)$ and Bethe quantum numbers $0 \leq \lambda_1, \lambda_2 < L$ (for $\theta \neq \pi$).

For the special case $\theta = \pi$, it is $A = -A'$ and $B = -B'$ which renders Eq. (2.334b) trivial. In this case, Eq. (2.334a) reduces to

$$0 = (e^{iq_2} - e^{iq_1}) \cdot (A + B) \quad 2.347a$$

$$\Leftrightarrow e^{iq_2} = e^{iq_1} \vee (A = -B \Leftrightarrow \theta_{ab} = \pi), \quad 2.347b$$

where $e^{iq_2} = e^{iq_1}$ with $\theta = \pi$ translates to

$$\frac{2\pi}{L}\lambda_1 + \frac{\pi}{L} = \frac{2\pi}{L}\lambda_2 - \frac{\pi}{L} \quad \Leftrightarrow \quad \lambda_1 + 1 = \lambda_2. \quad 2.348$$

We conclude the evaluation of the eigenvalue equations with the special case (2.328). Inserting (2.330) and (2.332) yields the two equations

$$\left(B' \frac{A}{A'} + B \frac{A'}{A}\right) [1 + e^{i(q_1+q_2)}] = \frac{A}{A'}(A' + B')e^{iq_2} + \frac{A'}{A}(A + B)e^{iq_1} \quad 2.349a$$

$$\left(A' \frac{B}{B'} + A \frac{B'}{B}\right) [1 + e^{i(q_1+q_2)}] = \frac{B}{B'}(B' + A')e^{iq_2} + \frac{B'}{B}(B + A)e^{iq_1} \quad 2.349b$$

where we used the fact that $-e^{iq_1L} = e^{ip_1L} = e^{i\theta} = A/A'$ and $-e^{iq_2L} = e^{ip_2L} = e^{-i\theta} = A'/A$. If we recall that $A/A' = B/B'$ (this holds regardless whether $\theta = \pi$ or not), this simplifies to

$$(B + B') [1 + e^{i(q_1+q_2)}] = (A + B)e^{iq_2} + (A' + B')e^{iq_1} \quad 2.350a$$

$$(A + A') [1 + e^{i(q_1+q_2)}] = (A + B)e^{iq_2} + (A' + B')e^{iq_1} \quad 2.350b$$

which is equivalent the combination of Eq. (2.334a) and (2.334b). So there are no additional constraints and we already covered this special case with our previous discussion (which makes sense as the system is translational invariant and this special case is a product of our labeling scheme without physical significance).

Solutions

In the following, we discuss all solutions of the eigenvalue equations systematically to prove that they constitute a complete set of eigenvectors in the Hilbert space sector $\mathcal{H}_{\alpha=1}^{N=2}$.

Solutions of Class A

Here we consider the solutions for $\theta \neq \pi$. It is then convenient to restrict the scattering phase to $\text{Re } \theta \in (-\pi, \pi)$ rather than $[0, 2\pi) \setminus \{\pi\}$. This class of solutions turns out to be both the most complex and most interesting one.

So far we know that for $\theta \neq \pi$ and $q_1 + q_2 = p_1 + p_2 + \frac{2\pi}{L} = \frac{2\pi}{L}(\lambda_1 + \lambda_2 + 1) \notin (2\mathbb{Z} + 1)\pi$ we have $A + A' = B + B'$ and $A/A' = B/B'$ which combines to $A = B$ and $A' = B'$. This is equivalent to $\theta_{ab} = 0$ and $a(n, m) = b(n, m)$ and

hence a general eigenstate of this class reads

$$|\Psi\rangle = \sum_{1 \leq n < m \leq L} \underbrace{\left[e^{i(q_1 n + q_2 m + \theta/2)} + e^{i(q_1 m + q_2 n - \theta/2)} \right]}_{\psi(n,m)} \times \left[\left| \begin{array}{c} 0 \\ n, m \end{array} \right\rangle + \left| \begin{array}{c} n, m \\ 0 \end{array} \right\rangle \right] \quad 2.351$$

where we re-gauged the basis $|\bullet\rangle \sim e^{i\frac{\theta}{L}(n+m)}|\bullet\rangle$ to allow for the replacement $p_i \rightarrow q_i$. We discuss the special case $q_1 + q_2 \in (2\mathbb{Z} + 1)\pi$ below as Subclass A2-II.

The momenta are given by

$$q_1 = \frac{2\pi}{L} \left(\lambda_1 + \frac{1}{2} \right) + \frac{\theta}{L}$$

and $q_2 = \frac{2\pi}{L} \left(\lambda_2 + \frac{1}{2} \right) - \frac{\theta}{L}$ for $0 \leq \lambda_1, \lambda_2 < L$ 2.352

and the scattering phase must satisfy the Bethe equation

$$e^{i\theta} \cdot \left[e^{i(q_1 + q_2)} + 1 - 2 e^{iq_2} \right] = - \left[e^{i(q_1 + q_2)} + 1 - 2 e^{iq_1} \right]. \quad 2.353$$

If we use the relations for the momenta, this gives for each combination of Bethe quantum numbers $0 \leq \lambda_1, \lambda_2 < L$ an implicit equation for $\theta \in \mathbb{C}$,

$$e^{i\theta} \cdot \left[e^{\frac{2\pi i}{L}(\lambda_1 + \lambda_2 + 1)} + 1 - 2 e^{\frac{2\pi i}{L}(\lambda_2 + \frac{1}{2}) - i\frac{\theta}{L}} \right] = - \left[e^{\frac{2\pi i}{L}(\lambda_1 + \lambda_2 + 1)} + 1 - 2 e^{\frac{2\pi i}{L}(\lambda_1 + \frac{1}{2}) + i\frac{\theta}{L}} \right]. \quad 2.354$$

Before we start our hunt for solutions, we point out that for a given solution $(\lambda_1, \lambda_2, \theta_{\lambda_1, \lambda_2})$ with Bethe quantum numbers $\lambda_1 < \lambda_2$, the related pair $(\lambda_2, \lambda_1, -\theta_{\lambda_1, \lambda_2})$ also solves Eq. (2.354). This transformation swaps the momenta, $q_1 \leftrightarrow q_2$, and in combination with $\theta \leftrightarrow -\theta$ leaves the eigenstate (2.351) invariant. Therefore we restrict without loss of generality the Bethe quantum numbers to the lower triangle:

$$0 \leq \lambda_1 \leq \lambda_2 < L. \quad 2.355$$

In the following, we discuss two subclasses of solutions (A1 and A2) in detail. Figure 2.24 parallels this discussion for a chain of length $L = 32$: In Figure 2.24 (a) we illustrate the two subclasses, in (b) we show the corresponding eigenenergies, and in (c) we plot the localization of the bound states of subclass A2 (see below).

Subclass A1 — We start with the simplest class of solutions of Eq. (2.354), namely the ones for which $\lambda_1 + 1 < \lambda_2$. If we go back to Eq. (2.346), a straightforward calculation yields the equivalent form

$$2 \cot \frac{\theta}{2} = \cot \frac{q_1}{2} - \cot \frac{q_2}{2}. \quad 2.356$$

BETHE ANSATZ SOLUTIONS

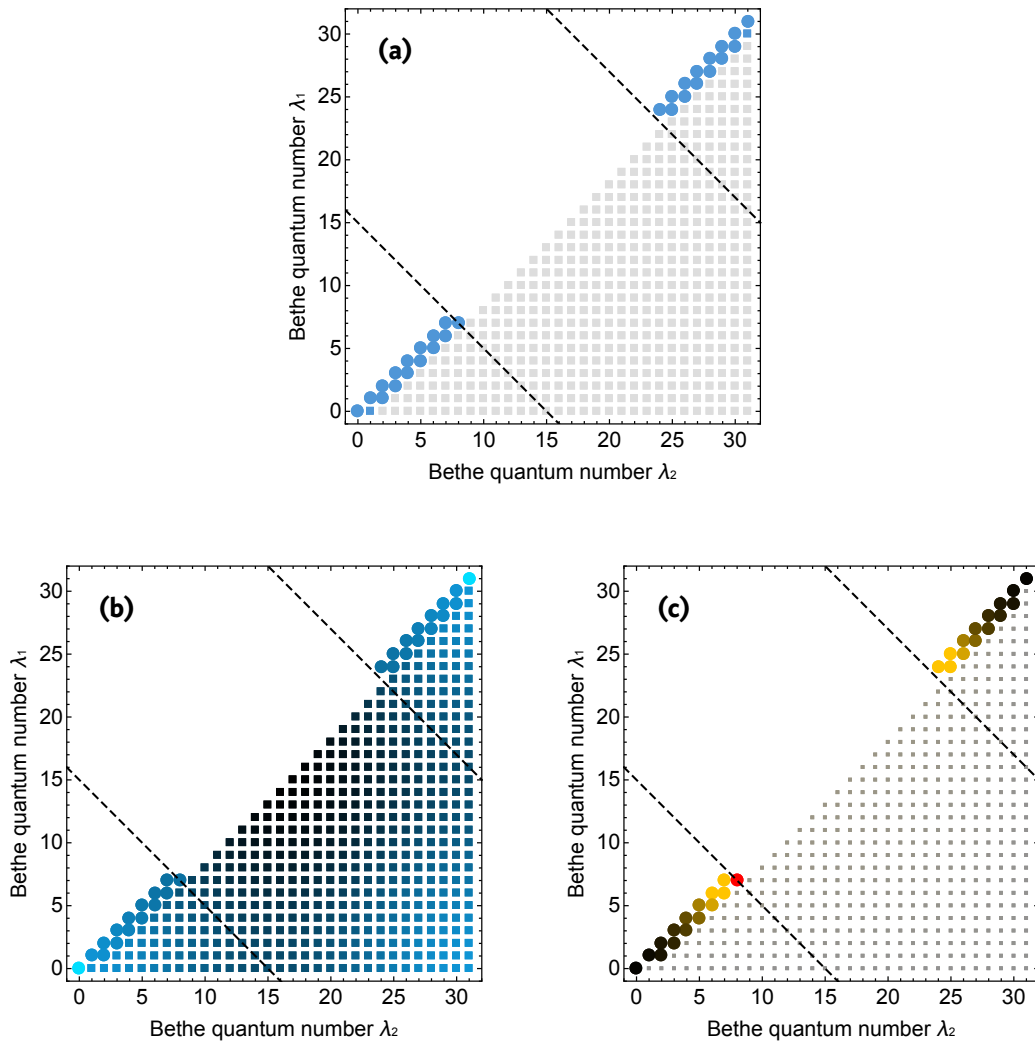


FIGURE 2.24 • Characterization of class-A Bethe wave functions. The lower right triangle shows the class-A Bethe wave functions with Bethe quantum numbers $0 \leq \lambda_1 \leq \lambda_2 < L$ for a system of length $L = 32$. Squares (bullets) denote scattering states (bound states). The dashed lines indicate quantum numbers that satisfy Eq. (2.368) and allow for limiting solutions of class A2-II. **(a)** highlights the two subclasses A1 (gray) and A2 (blue) introduced and discussed in the text. **(b)** illustrates the *eigenenergies* color-coded from low (blue) to high (black) values. The two degenerate ground states with finite energy are highlighted (cyan). See also Figure 2.28. **(c)** encodes the *localization* ($\propto |\text{Im } \theta|$) of the bound states from loosely bound (black) to tightly bound (yellow). The perfectly paired state discussed separately in the text (A2-II) is highlighted red and located at $\lambda_1 = 7, \lambda_2 = 8$ such that $\lambda_1 + \lambda_2 + 1 = 16 = 32/2$, i.e., it coincides with the lower dashed line.

MAJORANA-LIKE EDGE STATES & NUMBER CONSERVATION

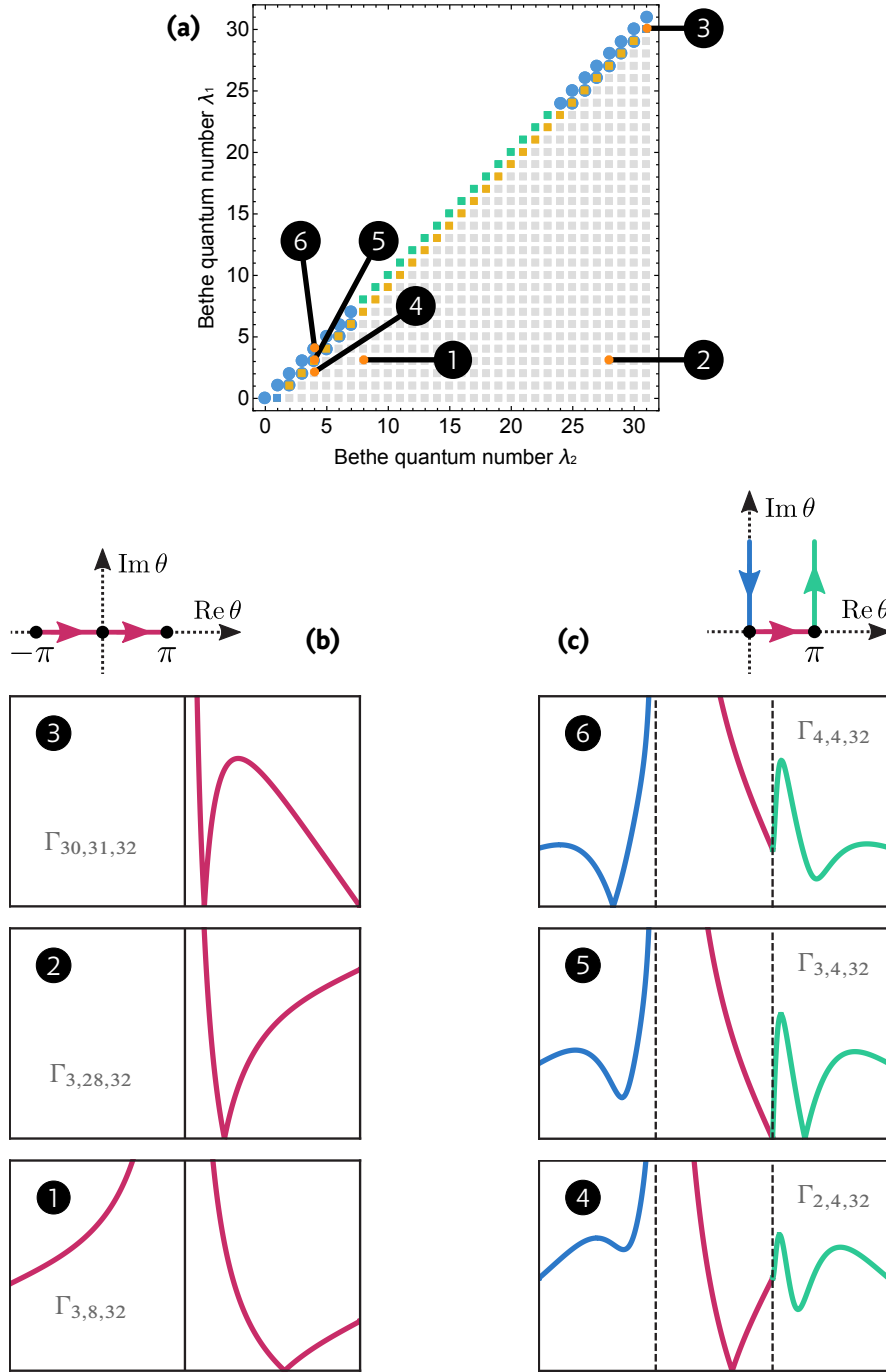


FIGURE 2.25 • Detailed analysis of type-A solutions for $\theta \neq \pi$. The detailed analysis of the complex solutions of Eq. (2.357) yields several subclasses of qualitatively distinct solutions. (a) shows the lower triangle of Bethe quantum numbers $0 \leq \lambda_1 \leq \lambda_2 < L$ for a system of length $L = 32$. Squares denote real solutions $\theta \in \mathbb{R}$ (scattering states) and bullets indicate solutions with finite imaginary part $\text{Im } \theta > 0$ (bound states); note that there is always a linearly dependent complex conjugate solution. ↷

BETHE ANSATZ SOLUTIONS

↷ Grey markers denote the class-A1 solutions for which $\lambda_1 + 1 < \lambda_2$. The class-A2 solutions are colored according to their characteristic features: Blue markers denote valid, finite solutions for which $-\pi < \text{Re } \theta \leq \pi$ and $\theta \neq \pi$; they define subclass A2-I. The green quantum numbers do not yield finite solutions. The limiting solution of class A2-II is not shown. Finally, the orange markers represent additional real solutions with $\theta = \pi$. These do not correspond to normalizable eigenvectors and can be neglected. Note that all class-A2 solutions are bound states except the two at $(\lambda_1, \lambda_2) = (0, 1)$ and $(30, 31)$. **(b)** To illustrate the solutions of Eq. (2.357), we plot the function (2.358). The plots (1)-(3) indicate real solutions for $\theta \in (-\pi, \pi)$ by roots of $\Gamma_{\lambda_1, \lambda_2, L}(\theta)$. The closer the quantum numbers are to the region of class A2, the closer θ is to π . The special class A2 solution $(30, 31)$ corresponds to the root in (3) which is close to the origin (and not the one at $\theta = \pi$). **(c)** illustrates the transition from class A1 to class A2-I solutions. Whereas for $\lambda_1 + 1 < \lambda_2$ there is a single real solution, see (4), there emerge additional complex solutions for $\lambda_1 + 1 = \lambda_2$ with $\text{Re } \theta = \pi$. For $\lambda_1 = \lambda_2$ the real solutions are replaced by imaginary ones with $\text{Re } \theta = 0$.

Then we have to find solutions θ for

RESULT 2.5: Bethe equation (alternative form)

$$2 \cot \frac{\theta}{2} = \cot \left[\frac{\pi}{L} \left(\lambda_1 + \frac{1}{2} \right) + \frac{\theta}{2L} \right] - \cot \left[\frac{\pi}{L} \left(\lambda_2 + \frac{1}{2} \right) - \frac{\theta}{2L} \right] \quad 2.357$$

with the restriction $\lambda_1 + 1 < \lambda_2$.

There is, to the best of my knowledge, no general analytic solution to this equation. Therefore we rely on numerical methods to count them and infer their general structure:

One finds a single, real solution $\theta \in (-\pi, \pi)$ for every pair (λ_1, λ_2) in the triangle with $\lambda_1 + 1 < \lambda_2$. This is illustrated in Figure 2.25 (a) and (b) where we plot the function

$$\Gamma_{\lambda_1, \lambda_2, L}(\theta) = 2 \cot \frac{\theta}{2} - \cot \left[\frac{\theta}{2L} + \frac{\pi}{L} \left(\lambda_1 + \frac{1}{2} \right) \right] - \cot \left[\frac{\theta}{2L} - \frac{\pi}{L} \left(\lambda_2 + \frac{1}{2} \right) \right] \quad 2.358$$

for the highlighted Bethe quantum numbers and $L = 32$ along the shown path for real θ . Roots of $\Gamma_{\lambda_1, \lambda_2, L}$ correspond to valid eigenvectors which are, due to the reality of θ , *scattering states*. We conclude that there are $(L - 1)(L - 2)/2$ linearly independent eigenvectors of class A1. A typical wave function is shown in Figure 2.26 (a): the non-vanishing amplitude for separated fermions qualifies it as scattering state.

MAJORANA-LIKE EDGE STATES & NUMBER CONSERVATION

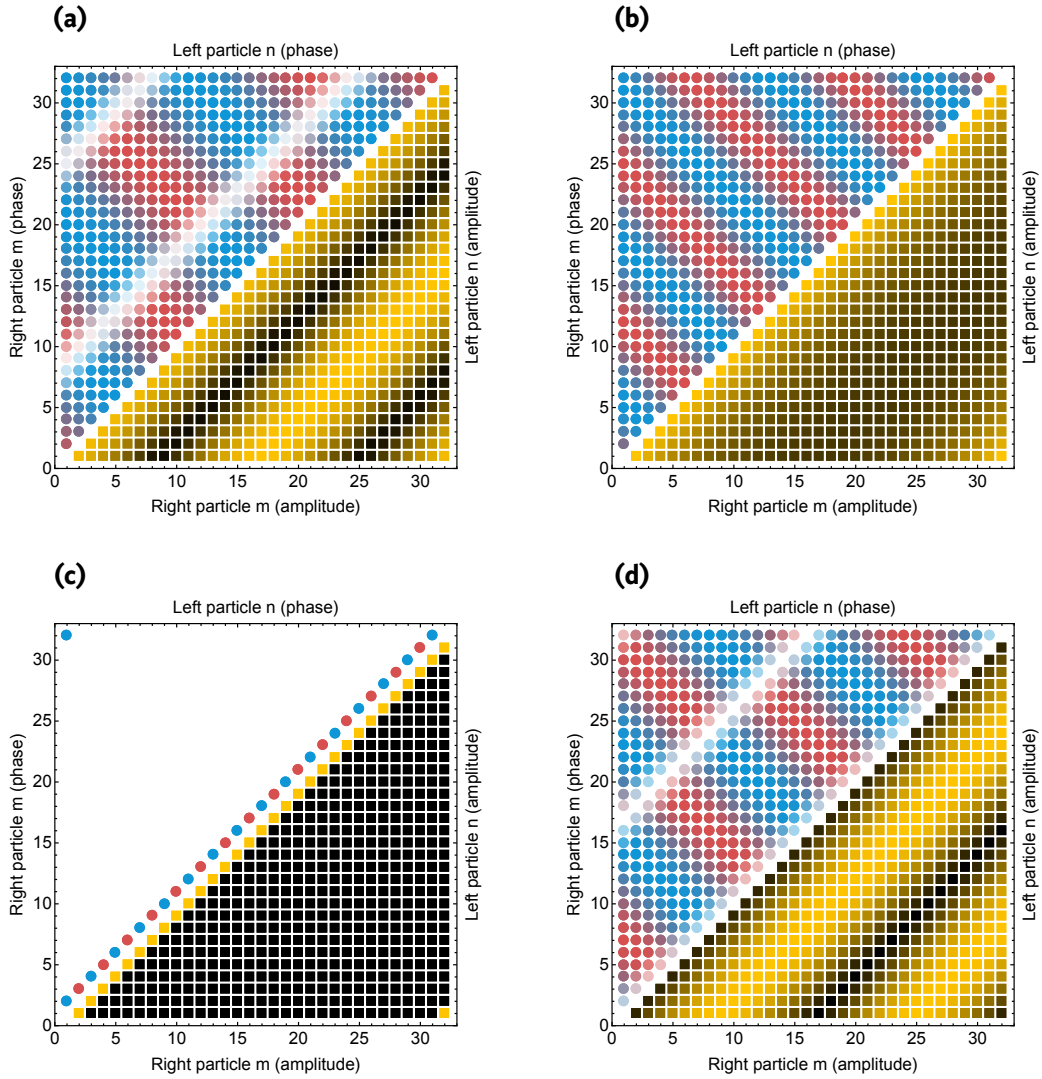


FIGURE 2.26 • Typical two-particle wave functions. In each panel, the lower right (upper left) triangle shows the amplitude $|a(n, m)|$ (phase $\arg a(n, m)$) of the wave function $a(n, m)$ in dependence of the left (right) particle position n (m) on the adjacent axes; the system length is $L = 32$. **(a)** Scattering state of class A1 with Bethe quantum numbers $\lambda_1 = 0$ and $\lambda_2 = 2$. Notice the oscillating amplitude for varying inter-particle distance $m - n$, characteristic for a scattering state. The shown state features a finite probability to find the two electrons close to each other. **(b)** Bound state of class A2-I with Bethe quantum numbers $\lambda_1 = 2 = \lambda_2$. The finite value in the lower right corner is due to periodic boundary conditions. **(c)** Limiting bound state of class A2-II with $q_1 + q_2 = \pi$ and $\theta_I = \infty$. The two electrons are perfectly paired and the relative sign alternates with the position of the pairs. **(d)** Scattering state of class B with Bethe quantum numbers $\lambda_1 = 0$ and $\lambda_2 = 3$ ($\mu_1 = 1, \mu_2 = 3$). The amplitude again oscillates with $m - n$ but here features a vanishing probability to find the two electrons close to each other.

Subclass A2-I — We proceed with the more interesting states for which $\lambda_1 + 1 = \lambda_2$ or $\lambda_1 = \lambda_2$. Subclass A2-I is defined by the latter restriction of Bethe quantum numbers with the additional condition that $|\theta| < \infty$ is finite and $\theta \neq \pi$.

Indeed, for $\lambda_1 + 1 = \lambda_2$ one finds $q_2 - q_1 = \frac{2}{L}(\pi - \theta)$ which yields $q_1 = q_2$ for $\theta = \pi$. In combination with $\cot \frac{\theta}{2} = \cot \frac{\pi}{2} = 0$, it seems that $\theta = \pi$ is always a solution on the first minor diagonal $\lambda_1 + 1 = \lambda_2$. However, these correspond to wave functions of the form

$$\begin{aligned} & \left[e^{i(q_1 n + q_2 m + \pi/2)} + e^{i(q_1 m + q_2 n - \pi/2)} \right] \\ \propto & \left[e^{i(q_1 n + q_2 m)} - e^{i(q_1 m + q_2 n)} \right] = 0, \end{aligned} \quad 2.359$$

(where we used $q_1 = q_2$) which are no eigenstates so that we can ignore them. These solutions are marked by orange squares in Figure 2.25 (a).

Further (numerical) inspection of the Bethe equation (2.357) yields the following results (see Figure 2.25 for illustrations):

- On the *diagonal* $\lambda_1 = \lambda_2$ there are two complex conjugate solutions with vanishing real part $\theta_R = 0$ for each pair (λ_1, λ_2) whenever $\lambda_i \lesssim 1/4 L \vee \lambda_i \gtrsim 3/4 L$, see Figure 2.25 (c). The \sim accounts for the fact that L may not be divisible by four; furthermore, there is an even-odd effect (see below). The imaginary part $|\theta_I| > 0$ grows for $\lambda_i \nearrow 1/4 L$ and $\lambda_i \searrow 3/4 L$ and remains small but finite for $\lambda_i \rightarrow 0$ and $\lambda_i \rightarrow L - 1$. These imaginary scattering phases characterize *bound states*, indicated by blue bullets in Figure 2.25 (a); a typical wave function is shown in Figure 2.26 (b).
- On the *minor diagonal* $\lambda_1 + 1 = \lambda_2$ there are (in addition to $\theta = \pi$ as discussed above) also pairs of complex conjugate solutions $\theta = \theta_R + i\theta_I$ for $0 < \lambda_1 \lesssim 1/4 L \vee 3/4 L \lesssim \lambda_1 < L - 2$, see Figure 2.25 (c). In this interval one finds $\theta_R = \pi$ fixed and $|\theta_I|$ growing for $\lambda_i \nearrow 1/4 L$ and $\lambda_i \searrow 3/4 L$ (as above). Between these two subintervals there are no solutions but the trivial ones ($\theta = \pi$). Special cases are found in the corners of the triangle, namely for $\lambda_1 = 0, \lambda_2 = 1$ and $\lambda_1 = L - 2, \lambda_2 = L - 1$ with a single scattering solution $\theta = \theta_R < \pi$ for each of the two pairs (λ_1, λ_2) . These are marked by blue squares in Figure 2.25 (a) and one is shown in detail in Figure 2.25 (b).
- As mentioned above, for each complex solution θ the complex conjugate θ^* is a solution of (2.357) as well. Such pairs (θ, θ^*) correspond to linearly *dependent* eigenvectors and therefore it is sufficient to consider the solutions for which $\text{Im } \theta \geq 0$. To see this, expand the coefficients $a(n, m) = b(n, m)$

in terms of $\theta = \theta_R + i\theta_I$ and q_1, q_2 :

$$\begin{aligned}
 & \exp \left\{ \frac{2\pi i}{L} \left(\lambda_1 + \frac{1}{2} \right) n + \frac{2\pi i}{L} \left(\lambda_2 + \frac{1}{2} \right) m \right\} \\
 & \cdot \exp \{ +i\theta_R f(n, m) \} \cdot \exp \{ -\theta_I f(n, m) \} \\
 & + \exp \left\{ \frac{2\pi i}{L} \left(\lambda_1 + \frac{1}{2} \right) m + \frac{2\pi i}{L} \left(\lambda_2 + \frac{1}{2} \right) n \right\} \\
 & \cdot \exp \{ -i\theta_R f(n, m) \} \cdot \exp \{ +\theta_I f(n, m) \}
 \end{aligned} \tag{2.360}$$

with

$$f(n, m) \equiv \frac{1}{2} + \frac{1}{L}(n - m). \tag{2.361}$$

Complex solutions can be found only for $\lambda_1 = \lambda_2$ and $\lambda_1 + 1 = \lambda_2$. In the former case, we argued that the solutions are purely imaginary: $\theta_R = 0$. The coefficients then read

$$\begin{aligned}
 & \exp \left\{ \frac{2\pi i}{L} \left(\lambda_1 + \frac{1}{2} \right) n + \frac{2\pi i}{L} \left(\lambda_2 + \frac{1}{2} \right) m \right\} \\
 & \times [\exp \{ -\theta_I f(n, m) \} + \exp \{ \theta_I f(n, m) \}]
 \end{aligned} \tag{2.362}$$

and are obviously invariant under the transformation $\theta_I \leftrightarrow -\theta_I$, i.e., complex conjugation of θ . In the latter case, $\lambda_1 + 1 = \lambda_2$, we found $\theta_R = \pi$. This yields, after rearranging the coefficients,

$$\begin{aligned}
 & \exp \left\{ \frac{2\pi i}{L} (\lambda_1 + 1) n + \frac{2\pi i}{L} \lambda_2 m \right\} \\
 & \times i [\exp \{ -\theta_I f(n, m) \} - \exp \{ \theta_I f(n, m) \}],
 \end{aligned} \tag{2.363}$$

which is again invariant under complex conjugation of θ (here up to a global minus sign). We conclude that the pairs of complex conjugate solutions (θ, θ^*) correspond to a common eigenvector.

These results allow for an efficient numerical calculation of all class-A solutions (except one special case labeled A2-II, see below). To this end, one first solves for roots of (2.358) with the additional constraint $-\pi < \text{Re } \theta \leq \pi$ and subsequently throws away all solutions with $\theta = \pi$ and $\text{Im } \theta < 0$.

As already mentioned, counting the class-A2-I solutions reveals an even-odd effect: Recall that we are looking for $L(L - 1)$ eigenstates to diagonalize the Hamiltonian in the sector $\mathcal{H}_{\alpha=1}^{N=2}$. As we will see below, half of them, $L(L - 1)/2$, belong to the yet undefined class B. Thus we must come up with the same number in class A. Class A1 gave $(L - 2)(L - 1)/2$ linearly independent solutions, all of which were scattering states. Thus L pairs (λ_1, λ_2) with $\lambda_1 + 1 = \lambda_2$ or $\lambda_1 = \lambda_2$ cannot yield solutions (at least not linearly independent ones). The candidates to drop are certainly the green and orange squares in Figure 2.25 (a) which do not yield normalizable solutions. But if one counts the number of these pairs, an even-odd

BETHE ANSATZ SOLUTIONS

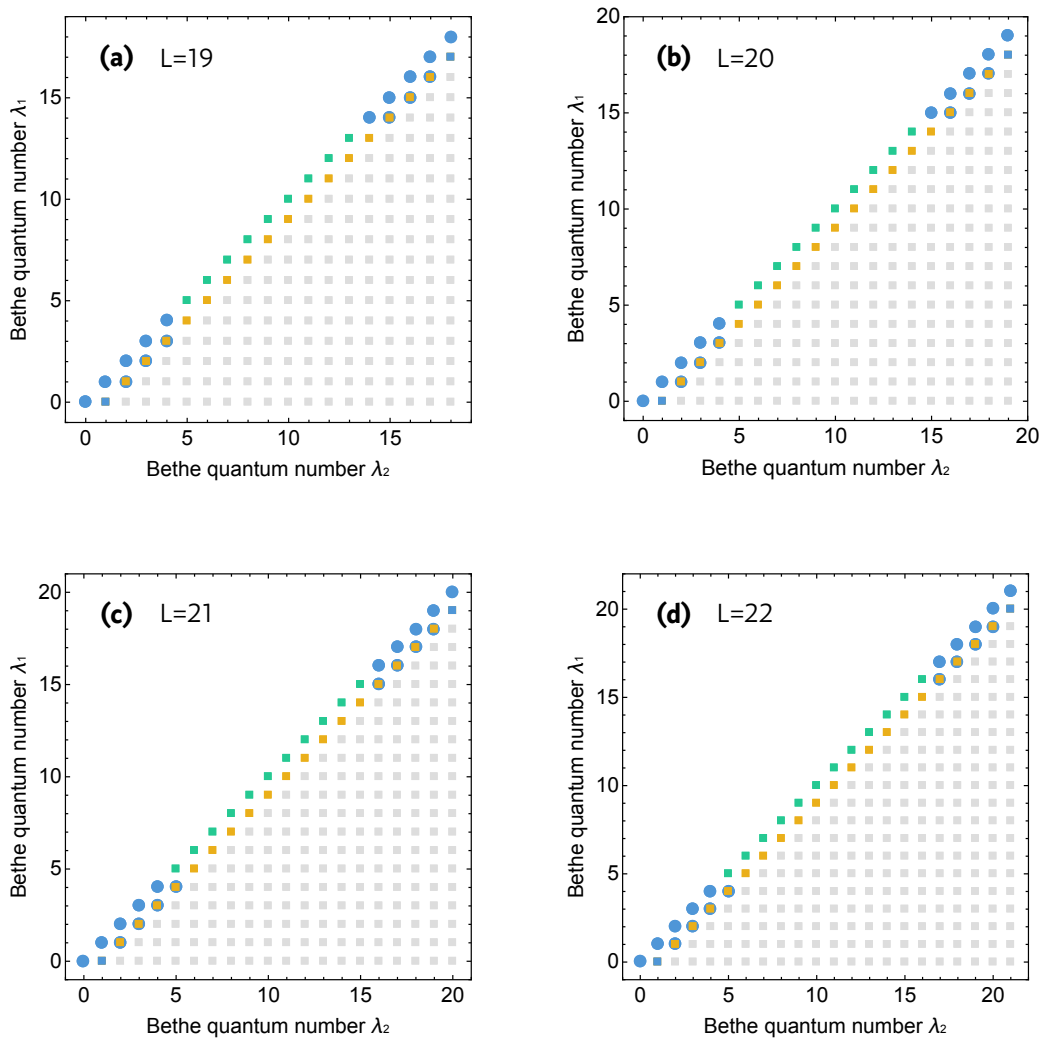


FIGURE 2.27 • Even-Odd effect for class-A2 solutions. The lower triangle $0 \leq \lambda_1 \leq \lambda_2 < L$ comprises $L(L+1)/2$ pairs (λ_1, λ_2) . Due to the number of class-B solutions, there must be $L(L-1)/2$ solutions of class A in total. Therefore one has to *exclude* L pairs in the lower triangle which yield *no* eigenstates. As the orange ($\theta = \pi$) and green squares (no finite solution) do not yield valid solutions, they should sum up to L . **(a)** For $L = 19$ there are 19 pairs which do not yield a solution. Thus the special class A2-II is empty. **(b)** For $L = 20$ there are 21 pairs which do not yield a solution. Thus one solution is missing and can be found as limiting case in class A2-II (which is not shown here). **(c)** For $L = 21$ there are again 21 pairs which do not yield a solution and class A2-II is empty. **(d)** For $L = 22$ there are 23 pairs which do not yield a solution and there is an additional solution in class A2-II. We conclude that the limiting solution in class A2-II occurs for chains of *even* length. Note that the global structure of the shown plots features a $\Delta L = 4$ -periodicity.

effect becomes apparent (see Figure 2.27): For chains of *odd* length L , their number equals L and one finds that there are $L - 1$ class-A2-I solutions which sum up with the class-A1 solutions to the desired total of $L(L - 1)/2$ eigenstates in class A. So we are done.

But for chains of *even* length L , there happen to be $L + 1$ such pairs which do not yield valid solutions. That is, we are missing an eigenstate which does not show up in numerical root finding algorithms.

Subclass A2-II — This missing eigenstate cannot be found numerically as it is characterized by the limit $\text{Im } \theta = \theta_I \rightarrow \infty$. This is the defining property of class A2-II and describes perfectly paired bound states, see Figure 2.26 (c) for an example on a chain of $L = 32$.

The argument goes as follows: We already found all valid solutions within the given bounds numerically. Thus we cannot expect the missing solution to be detectable by numerics and we are left with the assumption that it might correspond to a scattering phase θ “at infinity.” To this end, we write $\theta = \theta_R + i\theta_I$ with real and imaginary parts $\theta_R, \theta_I \in \mathbb{R}$. Additionally, let $A + A' = B + B'$ and therefore $A = B$ and $A' = B'$. Note that this is so far an arbitrary constraint⁹⁰. Then solutions must satisfy the Bethe equation (2.346), namely

$$e^{i\theta} \left[e^{i(q_1+q_2)} + 1 - 2e^{iq_2} \right] = - \left[e^{i(q_1+q_2)} + 1 - 2e^{iq_1} \right] \quad 2.364$$

with

$$q_1 = \frac{2\pi}{L} \left(\lambda_1 + \frac{1}{2} \right) + \frac{\theta_R + i\theta_I}{L} \quad 2.365a$$

$$\text{and } q_2 = \frac{2\pi}{L} \left(\lambda_2 + \frac{1}{2} \right) - \frac{\theta_R + i\theta_I}{L} \quad 2.365b$$

for $0 \leq \lambda_1, \lambda_2 < L$. Clearly, the limit $\theta_R \rightarrow \pm\infty$ is not well-defined for both sides of equation (2.364). However, the limit to complex infinity, $\theta_I \rightarrow \pm\infty$, exists and one easily verifies that for $L \geq 2$ equation (2.364) reduces to

$$0 = e^{i(q_1+q_2)} + 1 \quad \Leftrightarrow \quad q_1 + q_2 \in (2\mathbb{Z} + 1)\pi. \quad 2.366$$

For $q_1, q_2 \in [0, 2\pi)$ this is equivalent to

$$\frac{2\pi}{L}(\lambda_1 + \lambda_2 + 1) = \pi \quad \text{or} \quad \frac{2\pi}{L}(\lambda_1 + \lambda_2 + 1) = 3\pi. \quad 2.367$$

We conclude that Bethe quantum numbers for which a limiting solution can exist must satisfy

$$\lambda_1 + \lambda_2 = \frac{1}{2}L - 1 \quad \text{or} \quad \lambda_1 + \lambda_2 = \frac{3}{2}L - 1. \quad 2.368$$

⁹⁰This constraint follows rigorously for $q_1 + q_2 \notin (2\mathbb{Z} + 1)\pi$ which, as we will see in a moment, is not the case for A2-II. Nevertheless we are allowed to *impose* this constraint to simplify calculations—as long as we find a valid solution in the end.

This defines two straight lines in the lower triangle orthogonal to the diagonal that cross the latter at $\sim 1/4 L$ and $\sim 3/4 L$ (see Figure 2.24). From (2.368) it follows that L must be *even* for (integer) Bethe quantum numbers to satisfy these conditions. This is consistent with our previous findings that there must be an additional solution for even L .

Let us assume that L is even and Eq. (2.368) is satisfied. This leaves still undetermined the values of the Bethe quantum numbers (λ_1, λ_2) and the real scattering phase θ_R . We will show in the following that the limiting *eigenstate* nevertheless is unique and accounts exactly for the missing eigenbasis vector.

Under these restrictions, and before taking the limit $\theta_I \rightarrow \pm\infty$, a general eigenstate reads

$$|\Psi\rangle = \mathcal{N} \sum_{1 \leq n < m \leq L} \left[e^{i(q_1 n + q_2 m + \theta/2)} + e^{i(q_1 m + q_2 n - \theta/2)} \right] \times \left[\begin{array}{c} 0 \\ |n, m\rangle \\ n, m \end{array} \right] + \left[\begin{array}{c} |n, m\rangle \\ 0 \end{array} \right], \quad 2.369$$

where we explicitly introduced the normalizing factor $\mathcal{N} = \mathcal{N}(\lambda_1, \lambda_2, \theta)$. If we insert the expressions for q_1, q_2 and θ , the coefficients read

$$\begin{aligned} & \exp i \left\{ \begin{array}{l} \left[\frac{2\pi}{L} \left(\lambda_1 + \frac{1}{2} \right) + \frac{\theta_R + i\theta_I}{L} \right] n \\ + \left[\frac{2\pi}{L} \left(\lambda_2 + \frac{1}{2} \right) - \frac{\theta_R + i\theta_I}{L} \right] m + \frac{1}{2}(\theta_R + i\theta_I) \end{array} \right\} \\ & + \exp i \left\{ \begin{array}{l} \left[\frac{2\pi}{L} \left(\lambda_1 + \frac{1}{2} \right) + \frac{\theta_R + i\theta_I}{L} \right] m \\ + \left[\frac{2\pi}{L} \left(\lambda_2 + \frac{1}{2} \right) - \frac{\theta_R + i\theta_I}{L} \right] n - \frac{1}{2}(\theta_R + i\theta_I) \end{array} \right\} \end{aligned} \quad 2.370$$

which can be regrouped to

$$\begin{aligned} & \exp \left\{ \frac{2\pi i}{L} \left(\lambda_1 + \frac{1}{2} \right) n + \frac{2\pi i}{L} \left(\lambda_2 + \frac{1}{2} \right) m \right\} \\ & \cdot \exp \{ +i\theta_R f(n, m) \} \cdot \exp \{ -\theta_I f(n, m) \} \\ & + \exp \left\{ \frac{2\pi i}{L} \left(\lambda_1 + \frac{1}{2} \right) m + \frac{2\pi i}{L} \left(\lambda_2 + \frac{1}{2} \right) n \right\} \\ & \cdot \exp \{ -i\theta_R f(n, m) \} \cdot \exp \{ +\theta_I f(n, m) \} \end{aligned} \quad 2.371$$

with

$$f(n, m) \equiv \frac{1}{2} + \frac{1}{L}(n - m). \quad 2.372$$

The question is which coefficients remain finite in the limit $\theta_I \rightarrow +\infty$ ($\theta_I \rightarrow -\infty$ yields the same result). Note that the normalizing factor \mathcal{N} must vanish for $\theta_I \rightarrow +\infty$ in such a way that the *fastest growing* coefficients of the form above yield

finite results⁹¹. Hence we have to focus on the modulus and sign of f in dependence of n and m (recall that $n < m$). Clearly, for $m - n = L/2$ we have $f(n, m) = 0$ which describes the pairs of fermions that are farthest apart. For $m - n < L/2$ we have $f(n, m) > 0$ and for $m - n > L/2$ we find $f(n, m) < 0$. In the first (second) case, the second (first) summand of (2.371) dominates for $\theta_I \rightarrow \infty$. Due to the normalizing factor \mathcal{N} , only the *fastest* growing terms survive. They are characterized by the largest absolute value of $f(n, m)$ (which occurs for adjacent particles), i.e.,

$$m = n + 1 \quad \Rightarrow \quad f(n, m) = \frac{1}{2} - \frac{1}{L} > 0 \quad 2.373a$$

$$\text{or } n = 1 \wedge m = L \quad \Rightarrow \quad f(n, m) = \frac{1}{L} - \frac{1}{2} < 0. \quad 2.373b$$

Thus for $\theta_I \rightarrow +\infty$ the only surviving components are states which describe adjacent pairs of particles. Of course this is consistent with the interpretation of θ_I as inverse binding length.

If we define

$$|n, m|\pm\rangle \equiv \left| \begin{array}{c} 0 \\ n, m \end{array} \right\rangle \pm \left| \begin{array}{c} n, m \\ 0 \end{array} \right\rangle, \quad 2.374$$

the limiting eigenstates read (up to a normalizing factor)

$$\begin{aligned} |\Psi^\infty\rangle &= \sum_{n=1}^{L-1} e^{\frac{2\pi i}{L}(\lambda_1 + \frac{1}{2})(n+1) + \frac{2\pi i}{L}(\lambda_2 + \frac{1}{2})n} \cdot e^{-i\theta_R(\frac{1}{2} - \frac{1}{L})} |n, n+1|+\rangle \\ &+ e^{\frac{2\pi i}{L}(\lambda_1 + \frac{1}{2}) + \frac{2\pi i}{L}(\lambda_2 + \frac{1}{2})L} \cdot e^{+i\theta_R(\frac{1}{L} - \frac{1}{2})} |1, L|+\rangle. \end{aligned} \quad 2.375$$

At this point it is evident that the so far undetermined real scattering phase θ_R drops out as an irrelevant global phase factor; we can write

$$\begin{aligned} |\Psi^\infty\rangle &= \sum_{n=1}^{L-1} e^{\frac{2\pi i}{L}(\lambda_1 + \frac{1}{2})(n+1) + \frac{2\pi i}{L}(\lambda_2 + \frac{1}{2})n} |n, n+1|+\rangle \\ &+ e^{\frac{2\pi i}{L}(\lambda_1 + \frac{1}{2}) + \frac{2\pi i}{L}(\lambda_2 + \frac{1}{2})L} |1, L|+\rangle. \end{aligned} \quad 2.376$$

Recall that the Bethe quantum numbers satisfy $\frac{2\pi}{L}(\lambda_1 + \lambda_2 + 1) \in (2\mathbb{Z} + 1)\pi$. This yields

$$|\Psi^\infty\rangle = e^{\frac{2\pi i}{L}(\lambda_2 + \frac{1}{2})L} |1, L|+\rangle + \sum_{n=1}^{L-1} (-1)^n |n, n+1|+\rangle \quad 2.377$$

where we dropped the global phase $e^{\frac{2\pi i}{L}(\lambda_1 + \frac{1}{2})}$. By simplification of the first term, λ_2 drops out as well and we finally arrive at the unique limiting eigenstate

$$|\Psi^\infty\rangle = \sum_{n=1}^{L-1} (-1)^n |n, n+1|+\rangle - |1, L|+\rangle \quad 2.378$$

⁹¹If it vanishes faster, the eigenstate vanishes completely; if it vanishes slower, the eigenstate is not normalizable since at least one of its coefficients diverges.

which describes perfectly paired fermions with staggered phases.

The careful reader will probably wonder whether the minus in front of $|1, L|+\rangle$ is correct as it breaks the translational invariance of the state and (seemingly) distinguishes the pair sitting on the splice of the chain. This, however, is a consequence of the chosen gauge and reminiscent of the fermionic statistics of the original model. Be aware that this state is written in the original basis where the Hamiltonian itself features a minus for jumps across this bond [recall (2.296) and (2.297)]. One can re-gauge the basis via $|n, m|+\rangle = e^{-\frac{i\pi}{L}(n+m)}|n, m|+\rangle^{\sim}$ to make the state translationally invariant,

$$|\Psi^\infty\rangle = \sum_{n=1}^{L-1} \left(-e^{-\frac{2\pi i}{L}}\right)^n e^{-\frac{i\pi}{L}} |n, n+1|+\rangle^{\sim} + e^{-\frac{i\pi}{L}} |1, L|+\rangle^{\sim}, \quad 2.379$$

so that it can be written more compactly as

$$|\Psi^\infty\rangle = \sum_{n=1}^L \left(-e^{-\frac{2\pi i}{L}}\right)^n |n, n+1|+\rangle^{\sim} \quad 2.380$$

[cf. (2.302a) and (2.302b)]; here, n is an index modulo L , $|L, 1|+\rangle^{\sim} \equiv |1, L|+\rangle^{\sim}$, and L is even.

To conclude this paragraph, we determine the eigenenergy E^∞ of $|\Psi^\infty\rangle$. Recall that we found for the spectrum

$$E(q_1, q_2) = 4 - [e^{iq_1} + e^{-iq_1} + e^{iq_2} + e^{-iq_2}] \quad 2.381$$

which yields for $q_1 + q_2 \in (2\mathbb{Z} + 1)\pi$ immediately $E = 4$ —*and this is wrong!* Remember that we derived the expression for E from Eq. (2.326) by inserting the ansatz for $a(n, m)$ and *dividing* by $a(n, m)$. This equation, however, holds only for $n + 1 < m$, that is, for separated particles. But these coefficients vanish altogether in the perfectly paired state $|\Psi^\infty\rangle$ and we *cannot* derive the expression for E via (2.326) as these equations are trivially satisfied. Instead we have to employ the equations (2.327),

$$\begin{aligned} E a(n, m) &= 3a(n, m) - e^{i\frac{\pi}{L}} a(n, m+1) \\ &\quad - e^{-i\frac{\pi}{L}} a(n-1, m) - b(n, m), \end{aligned} \quad 2.382$$

as they hold for the non-vanishing nearest-neighbor coefficients $a(n, m = n+1)$. From the state (2.380) we read off

$$a(n, n+1) = b(n, n+1) = \left(-e^{-\frac{2\pi i}{L}}\right)^n \quad 2.383a$$

$$\text{and } a(n, m) = b(n, m) = 0 \quad \text{otherwise} \quad 2.383b$$

which immediately yields $E^\infty = 2$. This result is indeed verified by exact diagonalization. We point out that the eigenstate $|\Psi^\infty\rangle$ (whenever it exists) features the highest energy of all bound states (see Figure 2.28).

Before we continue with the last class of eigenstates, let us summarize the eigenstates that we found so far:

RESULT 2.6: Class-A eigenstates

For Bethe quantum numbers $0 \leq \lambda_1 \leq \lambda_2 < L$, the family of class-A eigenstates

$$|\lambda_1, \lambda_2\rangle_A = \sum_{n < m} \left[e^{i(q_1 n + q_2 m + \theta/2)} + e^{i(q_1 m + q_2 n - \theta/2)} \right] |n, m|+\rangle \quad 2.384$$

with momenta

$$q_1 = \frac{2\pi}{L} \left(\lambda_1 + \frac{1}{2} \right) + \frac{\theta}{L}, \quad q_2 = \frac{2\pi}{L} \left(\lambda_2 + \frac{1}{2} \right) - \frac{\theta}{L} \quad 2.385$$

and scattering phase $\theta = \theta(\lambda_1, \lambda_2) \in \mathbb{C}$ that satisfies the Bethe equation

$$2 \cot \frac{\theta}{2} = \cot \frac{q_1}{2} - \cot \frac{q_2}{2} \quad (\theta \neq \pi) \quad 2.386$$

make up for half the dimensions of the total subsector $\mathcal{H}_{\alpha=1}^{N=2}$ whenever L is odd; their eigenenergy is $E(q_1, q_2) = 4 \sum_{i=1,2} \sin^2 \frac{q_i}{2}$. For even L , there is an additional, perfectly paired eigenstate

$$|\infty\rangle_A = \sum_{n=1}^{L-1} (-1)^n |n, n+1|+\rangle - |1, L|+\rangle \quad 2.387$$

with eigenenergy $E^\infty = 2$.

Solutions of Class B

Here we consider the solutions for the special case $\theta = \pi$. We already showed that all eigenvalue equations reduce to

$$0 = (e^{iq_2} - e^{iq_1}) \cdot (A + B) \quad 2.388$$

which can be solved by $A + B = 0 \Leftrightarrow A = -B$. The other possibility, $e^{iq_1} = e^{iq_2} \Leftrightarrow \lambda_1 + 1 = \lambda_2$ does not yield normalizable solutions, recall (2.347) and (2.359).

So let $A = -B$ and keep in mind that $\lambda_1 + 1 \neq \lambda_2$ to obtain normalizable eigenvectors. In combination with $-1 = e^{i\pi} = A/A' = B/B'$, this leads to $A' = -B'$ and therefore the eigenfunctions

$$|\Psi\rangle = \sum_{n < m} \left[e^{i(q_1 n + q_2 m)} - e^{i(q_1 m + q_2 n)} \right] \left[\left| \begin{matrix} n, m \\ 0 \end{matrix} \right\rangle - \left| \begin{matrix} 0 \\ n, m \end{matrix} \right\rangle \right] \quad 2.389$$

BETHE ANSATZ SOLUTIONS

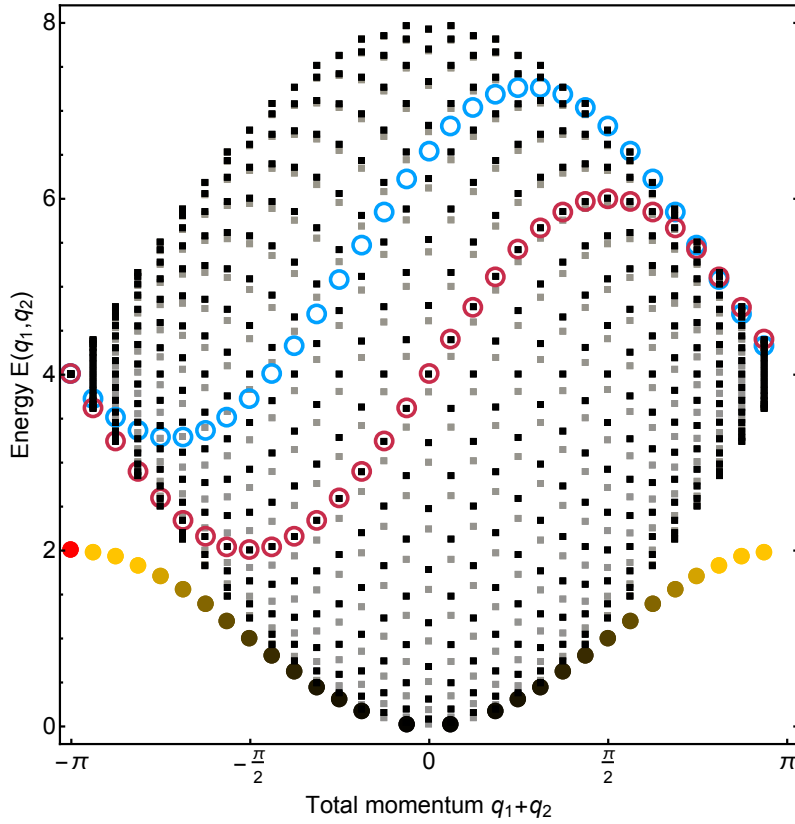


FIGURE 2.28 • Spectrum of the even-subchain-parity two-particle sector. The plot shows the eigenenergies in dependence of the total momentum $q_1 + q_2 = \frac{2\pi}{L}(\lambda_1 + \lambda_2 + 1) = \frac{2\pi}{L}(\mu_1 + \mu_2)$ (modulo 2π) for an $L = 32$ -chain with periodic boundaries. There are three distinct classes of states: (1) The symmetric scattering states of class A1 (gray squares), (2) the antisymmetric scattering states of class B (black squares), and (3) the symmetric bound states of class A2 (bullets). The color-grading from black to yellow for the bound states encodes their localization $\propto |\text{Im } \theta|$ (black: loosely bound, yellow: tightly bound). For comparison, we show an exemplary branch of the *free* ($\theta = 0$) two-magnon spectrum $E(q_1, q_2)$ with $\lambda_1 = 20$, $\lambda_2 = 0, \dots, 31$ (blue circles) which does *not* fit the spectrum. The red circles describe an exemplary branch of the *interacting* two-magnon spectrum with scattering angle $\theta = \pi$ and $\lambda_1 = 23$, $\lambda_2 = 0, \dots, 31$; this describes the class-B scattering states (black squares). The limiting eigenstate $|\infty\rangle_A$ of class A2-II is marked red. Note that the three apparent holes in the bound state branch close to zero momentum correspond to the three scattering states (gray squares) at $(\lambda_1 = 0, \lambda_2 = 1)$, $(L-2, L-1)$, and $(0, L-1)$. The former two belong to class A2 while the latter belongs to class A1 and has momentum $q_1 + q_2 = \frac{2\pi}{L}(0 + L - 1 + 1) = 2\pi = 0$, recall Figure 2.24 (b).

where we again re-gauged the Fock basis $|\bullet\rangle^\sim = e^{\frac{i\pi}{L}(n+m)}|\bullet\rangle$ to shift the momenta $p_i \rightarrow q_i$. The allowed momenta read

$$q_1 = \frac{2\pi}{L} (\lambda_1 + 1) \quad 2.390a$$

$$\text{and } q_2 = \frac{2\pi}{L} \lambda_2 \quad \text{for } 0 \leq \lambda_1, \lambda_2 < L \quad 2.390b$$

and the eigenenergies are given by

$$E(\lambda_1, \lambda_2) = 4 \sin^2 \left[\frac{\pi}{L} (\lambda_1 + 1) \right] + 4 \sin^2 \left[\frac{\pi}{L} \lambda_2 \right]. \quad 2.391$$

So far we restricted the Bethe quantum numbers to $0 \leq \lambda_1, \lambda_2 < L$ which certainly includes all possible linearly *independent* eigenvectors of this class. However, there are also linearly *dependent* solutions in this family—and we should get rid of them. To this end, define the shifted Bethe quantum numbers

$$\mu_1 \equiv \lambda_1 + 1 \quad \text{and} \quad \mu_2 \equiv \lambda_2 \quad 2.392$$

which again can be restricted to $0 \leq \mu_1, \mu_2 < L$ (we can shift the range of each Bethe quantum number separately by any integer as long as the interval is of length L). There are two crucial points: First, for $\mu_1 = \mu_2$ the eigenstate (2.389) vanishes; thus we exclude the diagonal of the square $0 \leq \mu_1, \mu_2 < L$. And second, given a pair $\mu_1 < \mu_2$, the substitution $\mu_1 \leftrightarrow \mu_2$ corresponds to the substitution $q_1 \leftrightarrow q_2$ of momenta which leads to $|\Psi\rangle \leftrightarrow -|\Psi\rangle$ and therefore does not yield a new eigenvector. Hence we can restrict the Bethe quantum numbers to the lower triangle $0 \leq \mu_1 < \mu_2 < L$ which comprises $L(L-1)/2$ linearly independent eigenstates. We conclude:

RESULT 2.7: Class-B eigenstates

For Bethe quantum numbers $0 \leq \mu_1 < \mu_2 < L$, the family of class-B eigenstates

$$|\mu_1, \mu_2\rangle_B = \sum_{n < m} \left[e^{i(q_1 n + q_2 m)} - e^{i(q_1 m + q_2 n)} \right] |n, m|-\rangle \quad 2.393$$

with momenta

$$q_1 = \frac{2\pi}{L} \mu_1, \quad q_2 = \frac{2\pi}{L} \mu_2 \quad 2.394$$

and eigenenergy $E(q_1, q_2) = 4 \sum_{i=1,2} \sin^2 \frac{q_i}{2}$ make up for half the dimensions of the total subsector $\mathcal{H}_{\alpha=1}^{N=2}$.

A typical wave function of class B is shown in Figure 2.26 (d) for $L = 32$. As a final remark, we point out that the exclusion of the diagonal $\mu_1 = \mu_2$ prevents the eigenenergy $E(q_1, q_2)$ from vanishing. This is consistent with our expectation that there is no zero-energy ground state anymore. In the thermodynamic limit, where $2\pi\mu_i/L \rightarrow 0$, the ground state energy vanishes nevertheless.

The combination of the $L(L-1)/2$ symmetric ($|n, m|+\rangle$) class-A solutions with the $L(L-1)/2$ antisymmetric ($|n, m|-\rangle$) class-B solutions yields the eigenbasis of H in the $L(L-1)$ -dimensional two-particle Hilbert space $\mathcal{H}_{\alpha=1}^{N=2}$. The complete spectrum for $L = 32$ is shown in Figure 2.28 where eigenvectors are labeled by their total momentum $q_1 + q_2 = \frac{2\pi}{L}(\lambda_1 + \lambda_2 + 1) = \frac{2\pi}{L}(\mu_1 + \mu_2)$ (modulo 2π).

We cross-checked the validity of these results by exact diagonalization of chains with lengths $L = 2, 3, \dots, 6$: both eigenenergies and eigenstates were identical up to machine precision.

Variable Inter-Chain Coupling

So far we considered the model at a critical point where the ratio of the inter-chain coupling H^{ab} and the intra-chain couplings H^a and H^b is equal to $\gamma = 1$. However, for the applicability of the Bethe ansatz, this should not be crucial. Here we consider the more general case where

$$H_\gamma = \sum_{i=1}^L \left[H_i^a + H_i^b + \gamma H_i^{ab} \right] \quad 2.395$$

with $\gamma \in \mathbb{R}$ an arbitrary (positive or negative) coupling strength. We will show how the Bethe equation generalizes accordingly (the evaluation of which we postpone to the future). Along the way, we show how the separation into symmetric and antisymmetric eigenstates appears quite naturally.

In the following, we drop the \sim for the gauge-transformed Fock states to clean up the notation. The Hamiltonian reads then after Jordan-Wigner transformation

$$H_\gamma = \sum_{j=1}^L \left\{ \begin{array}{l} \left(\begin{array}{l} \left[\begin{array}{|c|} \hline \blacksquare \\ \hline \end{array} \right] \left\langle \begin{array}{|c|} \hline \blacksquare \\ \hline \end{array} \right|_j + \left[\begin{array}{|c|} \hline \blacksquare \\ \hline \end{array} \right] \left\langle \begin{array}{|c|} \hline \blacksquare \\ \hline \end{array} \right|_j \\ -e^{-i\frac{\pi}{L}} \left[\begin{array}{|c|} \hline \blacksquare \\ \hline \end{array} \right] \left\langle \begin{array}{|c|} \hline \blacksquare \\ \hline \end{array} \right|_j - e^{i\frac{\pi}{L}} \left[\begin{array}{|c|} \hline \blacksquare \\ \hline \end{array} \right] \left\langle \begin{array}{|c|} \hline \blacksquare \\ \hline \end{array} \right|_j \\ + \left[\begin{array}{|c|} \hline \blacksquare \\ \hline \end{array} \right] \left\langle \begin{array}{|c|} \hline \blacksquare \\ \hline \end{array} \right|_j + \left[\begin{array}{|c|} \hline \blacksquare \\ \hline \end{array} \right] \left\langle \begin{array}{|c|} \hline \blacksquare \\ \hline \end{array} \right|_j \\ -e^{-i\frac{\pi}{L}} \left[\begin{array}{|c|} \hline \blacksquare \\ \hline \end{array} \right] \left\langle \begin{array}{|c|} \hline \blacksquare \\ \hline \end{array} \right|_j - e^{i\frac{\pi}{L}} \left[\begin{array}{|c|} \hline \blacksquare \\ \hline \end{array} \right] \left\langle \begin{array}{|c|} \hline \blacksquare \\ \hline \end{array} \right|_j \end{array} \right\} \quad 2.396$$

$$+ \gamma \sum_{j=1}^L \left\{ \left[\begin{array}{|c|c|} \hline \blacksquare & \blacksquare \\ \hline \end{array} \right] \left\langle \begin{array}{|c|c|} \hline \blacksquare & \blacksquare \\ \hline \end{array} \right|_j + \left[\begin{array}{|c|c|} \hline \blacksquare & \blacksquare \\ \hline \end{array} \right] \left\langle \begin{array}{|c|c|} \hline \blacksquare & \blacksquare \\ \hline \end{array} \right|_j - \left[\begin{array}{|c|c|} \hline \blacksquare & \blacksquare \\ \hline \end{array} \right] \left\langle \begin{array}{|c|c|} \hline \blacksquare & \blacksquare \\ \hline \end{array} \right|_j - \left[\begin{array}{|c|c|} \hline \blacksquare & \blacksquare \\ \hline \end{array} \right] \left\langle \begin{array}{|c|c|} \hline \blacksquare & \blacksquare \\ \hline \end{array} \right|_j \right\}$$

in the two-particle even-subchain-parity sector $\mathcal{H}_{\alpha=1}^{N=2}$.

With the (slightly altered) definitions

$$|n, m|\pm\rangle \equiv \frac{1}{\sqrt{2}} \left[\begin{array}{c} |n, m\rangle \\ |0\rangle \end{array} \pm \begin{array}{c} |0\rangle \\ |n, m\rangle \end{array} \right] \quad 2.397$$

and the fact that $\mathcal{H}_{\alpha=1}^{N=2} \cong \mathcal{L} \otimes \mathbb{C}^2$ —where the first factor $\mathcal{L} = \text{span}\{|n, m\rangle \mid 1 \leq n < m \leq L\}$ describes a *single* chain occupied by two particles and the last factor encodes the subchain—it is convenient to consider the isomorphism

$$|n, m|\pm\rangle \cong |n, m\rangle \otimes |\pm\rangle \equiv |n, m|\pm\rangle \quad 2.398$$

where $|\pm\rangle$ denotes the usual eigenbasis of σ^x and $|n, m\rangle$ describes a state of L spins with flipped spins at sites n and m . With the transformation

$$\begin{array}{c} |n, m\rangle \\ |0\rangle \end{array} \cong \frac{1}{\sqrt{2}} [|n, m\rangle|+\rangle + |n, m\rangle|-\rangle] \quad 2.399a$$

$$\begin{array}{c} |0\rangle \\ |n, m\rangle \end{array} \cong \frac{1}{\sqrt{2}} [|n, m\rangle|+\rangle - |n, m\rangle|-\rangle] \quad 2.399b$$

we can rewrite the Hamiltonian in the isomorphic Hilbert space $\mathcal{L} \otimes \mathbb{C}^2$:

$$\begin{aligned} H_\gamma \cong & \sum_{j=1}^L \left\{ \begin{array}{c} |\blacksquare\blacksquare\rangle \langle\blacksquare\blacksquare|_j + |\square\blacksquare\rangle \langle\square\blacksquare|_j \\ -e^{-i\frac{\pi}{L}} |\square\blacksquare\rangle \langle\blacksquare\blacksquare|_j - e^{i\frac{\pi}{L}} |\blacksquare\blacksquare\rangle \langle\square\blacksquare|_j \end{array} \right\} \otimes |+\rangle\langle+| \\ & + \sum_{j=1}^L \left\{ \begin{array}{c} |\blacksquare\blacksquare\rangle \langle\blacksquare\blacksquare|_j + |\square\blacksquare\rangle \langle\square\blacksquare|_j \\ -e^{-i\frac{\pi}{L}} |\square\blacksquare\rangle \langle\blacksquare\blacksquare|_j - e^{i\frac{\pi}{L}} |\blacksquare\blacksquare\rangle \langle\square\blacksquare|_j \\ +2\gamma |\blacksquare\blacksquare\rangle \langle\blacksquare\blacksquare|_j \end{array} \right\} \otimes |-\rangle\langle-|. \end{aligned} \quad 2.400$$

This reveals the decoupling of the $|\pm\rangle$ subspaces according to $\mathcal{H}_{\alpha=1}^{N=2} = \mathcal{H}^+ \oplus \mathcal{H}^-$ where $\mathcal{H}^\pm \cong \mathcal{L}$. Note that the Hamiltonian that acts on the symmetric $|+\rangle$ -sector coincides with its antisymmetric counterpart for $\gamma = 0$ (i.e., for decoupled chains). Therefore the complete spectrum can be derived as

$$\text{Double-Chain}(\gamma) = \text{Single-Chain}(0) \oplus \text{Single-Chain}(\gamma) \quad 2.401$$

which allows us to restrict the following analysis to the reduced Hamiltonian

$$H_\gamma^{\mathcal{L}} = \sum_{j=1}^L \left\{ \begin{array}{c} |\blacksquare\blacksquare\rangle \langle\blacksquare\blacksquare|_j + |\square\blacksquare\rangle \langle\square\blacksquare|_j \\ -e^{-i\frac{\pi}{L}} |\square\blacksquare\rangle \langle\blacksquare\blacksquare|_j - e^{i\frac{\pi}{L}} |\blacksquare\blacksquare\rangle \langle\square\blacksquare|_j \\ +2\gamma |\blacksquare\blacksquare\rangle \langle\blacksquare\blacksquare|_j \end{array} \right\} \quad 2.402$$

that acts on the $L(L-1)/2$ -dimensional Hilbert space \mathcal{L} . With this definition, we can write formally $H_\gamma = H_0^{\mathcal{L}} \oplus H_\gamma^{\mathcal{L}}$.

Bethe Ansatz Solution for $H_\gamma^{\mathcal{L}}$

It is straightforward generalize our previous Bethe ansatz to solve the reduced single-chain Hamiltonian $H_\gamma^{\mathcal{L}}$. The generic wave function in the single-chain Hilbert space \mathcal{L} with two particles (flipped spins) reads

$$|\Psi\rangle = \sum_{1 \leq n < m \leq L} a(n, m) |n, m\rangle, \quad 2.403$$

where again we drop the \sim . Solving the eigenvalue equation $H_\gamma^{\mathcal{L}}|\Psi\rangle = E|\Psi\rangle$ is equivalent to the following equations for the wave function $a(n, m)$:

- 1** *The two particles are **not** adjacent, i.e., $n < m - 1$ and $n \neq 1 \vee m \neq L$.*

For such configurations, the pairing term $2\gamma \langle \blacksquare \blacksquare \rangle \langle \blacksquare \blacksquare \rangle_j$ drops out. Since there are four possible single-particle jumps, the relation reads

$$E a(n, m) = 4a(n, m) - e^{i\frac{\pi}{L}} a(n+1, m) - e^{-i\frac{\pi}{L}} a(n-1, m) - e^{i\frac{\pi}{L}} a(n, m+1) - e^{-i\frac{\pi}{L}} a(n, m-1), \quad 2.404$$

which is the same as in the previous treatment, recall Eq. (2.326).

- 2** *The two particles are adjacent, i.e., $n = m - 1$ or $n = 1 \wedge m = L$.*

We discuss the two subcases separately:

- a** *Let $n = m - 1$.*

In this case there are only *two* possible single-particle jumps and the pairing contributes an additional coefficient $a(n, m)$. This yields

$$E a(n, m) = (2 + 2\gamma)a(n, m) - e^{i\frac{\pi}{L}} a(n, m+1) - e^{-i\frac{\pi}{L}} a(n-1, m) \quad 2.405$$

which holds for all $n = 1, 2, \dots, L-1$ and $m = n+1$.

- b** *Let $n = 1 \wedge m = L$.*

In this case there are two possible “reversed” single-particle jumps such that

$$E a(1, L) = (2 + 2\gamma)a(1, L) - e^{i\frac{\pi}{L}} a(1+1, L) - e^{-i\frac{\pi}{L}} a(1, L-1). \quad 2.406$$

Again, this special case is a consequence of our index scheme and periodic boundary conditions; it is of no particular physical significance.

As before, we require the coefficients to satisfy the twisted boundary conditions

$$a(n, L + 1) = a(1, n) \quad 2.407a$$

$$\text{and } a(1 - 1, m) = a(m, L) \quad \text{for all } 1 < n < m < L \quad 2.407b$$

to conform with the periodic boundary conditions and the ordering $n < m$ in the summation. With the plane wave ansatz

$$a(n, m) = e^{i(p_1 n + p_2 m + \theta/2)} + e^{i(p_1 m + p_2 n - \theta/2)} \quad 2.408$$

and the scattering phase $\theta \in \mathbb{C}$, a completely analogous calculation yields the known form of the energy

$$E(q_1, q_2) = 4 \sin^2 \frac{q_1}{2} + 4 \sin^2 \frac{q_2}{2} \quad 2.409$$

and the constraints on allowed momenta $q_i = p_i + \pi/L$

$$q_1 = \frac{2\pi}{L} \left(\lambda_1 + \frac{1}{2} \right) + \frac{\theta}{L} \quad 2.410a$$

$$\text{and } q_2 = \frac{2\pi}{L} \left(\lambda_2 + \frac{1}{2} \right) - \frac{\theta}{L} \quad \text{for } 0 \leq \lambda_1, \lambda_2 < L. \quad 2.410b$$

The crucial difference, as compared to our previous discussion, stems from condition (2.405) which yields after straightforward calculations

RESULT 2.8: Bethe equation (generalized form)

$$e^{i\theta} = - \frac{e^{i(q_1 + q_2)} + 1 - 2(1 - \gamma) e^{iq_1}}{e^{i(q_1 + q_2)} + 1 - 2(1 - \gamma) e^{iq_2}} \quad 2.411$$

for $\gamma \in \mathbb{R}$. The special relation (2.406) at the boundary is equivalent to (2.411) due to the imposed boundary conditions (2.407)⁹².

We point out that for $\gamma = 0$, equation (2.411) reduces to the original Bethe equation (2.346) which described for $\theta \neq \pi$ the class-A solutions (recall that for $\theta = \pi$ the condition $e^{iq_1} = e^{iq_2}$ does not yield normalizable solutions). However, for $\gamma = 1$ it follows immediately $\theta = \pi$ which corresponds to the class-B solutions. Since $H_1 = H_0^{\mathcal{L}} \oplus H_1^{\mathcal{L}}$, this implies that the eigenstates occupy two subspaces of equal dimension, characterized by symmetric and antisymmetric states, respectively.

Interestingly, for $\gamma \neq 1$ the relation $H_\gamma = H_0^{\mathcal{L}} \oplus H_\gamma^{\mathcal{L}}$ implies that the spectrum in the *symmetric* sector \mathcal{H}^+ remains the same (i.e., the class-A wave functions are still eigenstates), whereas the sector of antisymmetric states (the class-B wave functions) can be affected by the inter-chain coupling. In particular, there can

⁹²More precisely: Eq. (2.405) and (2.406) lead to (2.411) and the constraint $p_2 - p_1 = \frac{2\pi}{L}k - \frac{2\theta}{L}$ for $k \in \mathbb{Z}$ arbitrary. The latter is satisfied by the “twisted” boundary conditions (2.407).

BETHE ANSATZ SOLUTIONS

be additional bound states in the antisymmetric sector for $\gamma \neq 1$ (we postpone a thorough analysis to the future). Note that the symmetric class-A solutions completely decouple from the *inter*-chain interactions such that the occurrence of bound states in this sector must be attributed to the *intra*-chain interactions alone. The partition of the spectrum into (anti)symmetric eigenstates is a consequence of the “chain exchange symmetry” of the Hamiltonian (see Ref. [237]).

2.C.4 Lifted Excitations on the Double-Chain

In Subsection 2.4.1 we discussed single-particle excitations on a single chain with open boundary conditions. We then showed that these *single-magnon excitations* can be “lifted” to sectors of arbitrary filling N if one exploits the global $U(2)$ symmetry of the single-chain Hamiltonians H^x , $x = a, b$. Here we provide the technical details of the proof for Lemma 2.1 which states that this procedure also yields valid eigenstates

$$|\{\lambda_i\}; N^*\rangle_{N,\alpha}^\oplus \equiv \left[P_{N^*}^a \oplus P_{N^*}^b \right] (\{\lambda_i\}) \sum_{M:(-1)^M=\alpha} |M\rangle_a |N-M\rangle_b \quad 2.412$$

of the *double-chain* Hamiltonian $H = H^a + H^b + H^{ab}$ despite the inter-chain interaction H^{ab} if $N^* = 1$. Here,

$$P_{N^*}(\{\lambda_i\}) = \sum_{n_1 < \dots < n_{N^*}} \psi_{\{\lambda_i\}}(n_1, \dots, n_{N^*}) \prod_{n \in \{n_1, \dots, n_{N^*}\}} \sigma_n^z \quad 2.413$$

encodes the structure of the excited state (given by $\psi_{\{\lambda_i\}}$) into a phase pattern on the equal-weight superposition $|M\rangle$. N^* denotes the number of excitations (*magnons*) and $\lambda_1, \dots, \lambda_{N^*}$ are the Bethe quantum numbers that label the excited state.

Proof. First, consider the single-chain components, namely

$$\left[H^a \oplus H^b \right] |\{\lambda_i\}; N^*\rangle_{N,\alpha}^\oplus \quad 2.414a$$

$$= \left\{ \begin{array}{l} H^a P_{N^*}^a \oplus H^b P_{N^*}^b \\ + H^a \otimes P_{N^*}^b + P_{N^*}^a \otimes H^b \end{array} \right\} \sum_{M:(-1)^M=\alpha} |M\rangle_a |N-M\rangle_b \quad 2.414b$$

$$= \left[H^a P_{N^*}^a \oplus H^b P_{N^*}^b \right] \sum_{M:(-1)^M=\alpha} |M\rangle_a |N-M\rangle_b \quad 2.414c$$

$$= \left\{ \begin{array}{l} \sum_{M:(-1)^M=\alpha} H^a P_{N^*}^a |M\rangle_a \otimes |N-M\rangle_b \\ + \sum_{M:(-1)^M=\alpha} |M\rangle_a \otimes H^b P_{N^*}^b |N-M\rangle_b \end{array} \right\} \quad 2.414d$$

$$= \left\{ \begin{array}{l} E \sum_{M:(-1)^M=\alpha} P_{N^*}^a |M\rangle_a \otimes |N-M\rangle_b \\ + E \sum_{M:(-1)^M=\alpha} |M\rangle_a \otimes P_{N^*}^b |N-M\rangle_b \end{array} \right\} \quad 2.414e$$

$$= E(\{\lambda_i\}) |\{\lambda_i\}; N^*\rangle_{N,\alpha}^\oplus, \quad 2.414f$$

where \oplus denotes the Kronecker sum $A \oplus B = A \otimes \mathbb{1} + \mathbb{1} \otimes B$ and the H^x have to be read as *single chain* Hamiltonians. In the third line we used that $H^x |M\rangle = 0$ for $x = a, b$ and arbitrary M .

Next, we show that $[P_{N^*}^a \oplus P_{N^*}^b, H^{ab}] = 0$ for $N^* = 1$ so that the proposed symmetric states (2.412) are not affected by the chain coupling. To this end, let us write

$$P_{N^*}^a \oplus P_{N^*}^b = \sum_{\{n_i\}} \psi(\{n_i\}) \left(\prod_{n \in \{n_i\}} \sigma_n^z + \prod_{n \in \{n_i\}} \hat{\sigma}_n^z \right) \quad 2.415$$

to simplify expressions. We are interested in

$$\left[P_{N^*}^a \oplus P_{N^*}^b, H^{ab} \right] = \sum_i \sum_{\{n_j\}} \psi(\{n_j\}) \left[\prod_{n \in \{n_j\}} \sigma_n^z + \prod_{n \in \{n_j\}} \hat{\sigma}_n^z, H_i^{ab} \right] \quad 2.416$$

with [recall (2.298)]

$$H_i^{ab} = \left\{ \begin{array}{l} -(\sigma_i^- \sigma_{i+1}^- \hat{\sigma}_i^+ \hat{\sigma}_{i+1}^+ + \sigma_i^+ \sigma_{i+1}^+ \hat{\sigma}_i^- \hat{\sigma}_{i+1}^-) \\ + \frac{1 - \sigma_i^z}{2} \frac{1 - \sigma_{i+1}^z}{2} \frac{1 + \hat{\sigma}_i^z}{2} \frac{1 + \hat{\sigma}_{i+1}^z}{2} \\ + \frac{1 - \hat{\sigma}_i^z}{2} \frac{1 - \hat{\sigma}_{i+1}^z}{2} \frac{1 + \sigma_i^z}{2} \frac{1 + \sigma_{i+1}^z}{2} \end{array} \right\}. \quad 2.417$$

Summands of (2.416) clearly vanish for all i such that $i \wedge i + 1 \notin \{n_1, \dots, n_{N^*}\}$. Let $i \in \{n_1, \dots, n_{N^*}\}$. It is easy to see that summands where $i = n_j$ for some $1 \leq j \leq N^*$ and $n_{j+1} = n_j + 1$ also vanish since products of adjacent pairs $\sigma_{n_j}^z \sigma_{n_j+1}^z$ commute with all components of H_{n_j} . Therefore we restrict our further inquiries on summands where *either* i or $i + 1$ are in $\{n_1, \dots, n_{N^*}\}$ (but not both); w.l.o.g. let $i \in \{n_j\}$ (since H_i^{ab} is symmetric with respect to $i \leftrightarrow i + 1$).

First, note that $[\sigma_i^z, \sigma_i^\pm] = \pm 2\sigma_i^\pm$ and therefore

$$\begin{aligned} & [\sigma_i^z, \sigma_i^- \sigma_{i+1}^- \hat{\sigma}_i^+ \hat{\sigma}_{i+1}^+ + \sigma_i^+ \sigma_{i+1}^+ \hat{\sigma}_i^- \hat{\sigma}_{i+1}^-] \\ &= -2 \sigma_i^- \sigma_{i+1}^- \hat{\sigma}_i^+ \hat{\sigma}_{i+1}^+ + 2 \sigma_i^+ \sigma_{i+1}^+ \hat{\sigma}_i^- \hat{\sigma}_{i+1}^- \end{aligned} \quad 2.418a$$

$$\begin{aligned} & [\hat{\sigma}_i^z, \sigma_i^- \sigma_{i+1}^- \hat{\sigma}_i^+ \hat{\sigma}_{i+1}^+ + \sigma_i^+ \sigma_{i+1}^+ \hat{\sigma}_i^- \hat{\sigma}_{i+1}^-] \\ &= +2 \sigma_i^- \sigma_{i+1}^- \hat{\sigma}_i^+ \hat{\sigma}_{i+1}^+ - 2 \sigma_i^+ \sigma_{i+1}^+ \hat{\sigma}_i^- \hat{\sigma}_{i+1}^-. \end{aligned} \quad 2.418b$$

With this, it follows

$$\begin{aligned} & \left[\prod_{n \in \{n_j\}} \sigma_n^z + \prod_{n \in \{n_j\}} \hat{\sigma}_n^z, H_i^{ab} \right] \\ &= - \left[\prod_{n \in \{n_j\}} \sigma_n^z + \prod_{n \in \{n_j\}} \hat{\sigma}_n^z, \sigma_i^- \sigma_{i+1}^- \hat{\sigma}_i^+ \hat{\sigma}_{i+1}^+ + \sigma_i^+ \sigma_{i+1}^+ \hat{\sigma}_i^- \hat{\sigma}_{i+1}^- \right] \end{aligned} \quad 2.419a$$

$$= \left\{ \begin{aligned} & - \left(\prod_{i \neq n \in \{n_j\}} \sigma_n^z \right) \cdot \left[\sigma_i^z, \sigma_i^- \sigma_{i+1}^- \hat{\sigma}_i^+ \hat{\sigma}_{i+1}^+ + \sigma_i^+ \sigma_{i+1}^+ \hat{\sigma}_i^- \hat{\sigma}_{i+1}^- \right] \\ & - \left(\prod_{i \neq n \in \{n_j\}} \hat{\sigma}_n^z \right) \cdot \left[\hat{\sigma}_i^z, \sigma_i^- \sigma_{i+1}^- \hat{\sigma}_i^+ \hat{\sigma}_{i+1}^+ + \sigma_i^+ \sigma_{i+1}^+ \hat{\sigma}_i^- \hat{\sigma}_{i+1}^- \right] \end{aligned} \right\} \quad 2.419b$$

$$= 2 \left(\prod_{i \neq n \in \{n_j\}} \sigma_n^z - \prod_{i \neq n \in \{n_j\}} \hat{\sigma}_n^z \right) (\sigma_i^- \sigma_{i+1}^- \hat{\sigma}_i^+ \hat{\sigma}_{i+1}^+ - \sigma_i^+ \sigma_{i+1}^+ \hat{\sigma}_i^- \hat{\sigma}_{i+1}^-) \quad 2.419c$$

which is a *non-vanishing* expression in general. Therefore

$$\begin{aligned} & H |\{\lambda_i\}; N^*\rangle_{N,\alpha}^\oplus \\ &= (H^a \oplus H^b + H^{ab}) |\{\lambda_i\}; N^*\rangle_{N,\alpha}^\oplus \end{aligned} \quad 2.420a$$

$$= E(\{\lambda_i\}) |\{\lambda_i\}; N^*\rangle_{N,\alpha}^\oplus \quad 2.420b$$

$$+ \left[H^{ab}, P_{N^*}^a \oplus P_{N^*}^b \right] \sum_{M: (-1)^M = \alpha} |M\rangle_a |N - M\rangle_b \quad 2.420c$$

$$+ \left[P_{N^*}^a \oplus P_{N^*}^b \right] H^{ab} \sum_{M: (-1)^M = \alpha} |M\rangle_a |N - M\rangle_b \quad 2.420d$$

which simplifies to

$$\begin{aligned} & E(\{\lambda_i\}) |\{\lambda_i\}; N^*\rangle_{N,\alpha}^\oplus \\ &+ \left[H^{ab}, P_{N^*}^a \oplus P_{N^*}^b \right] \sum_{M: (-1)^M = \alpha} |M\rangle_a |N - M\rangle_b. \end{aligned} \quad 2.421$$

There are two obvious cases for which the second term vanishes: (1) for $N^* = 1$ and $0 \leq N \leq 2L$ arbitrary and (2) for $N^* = 2$ and $N = 2$. In the first case, $\prod_{i \neq n \in \{n_j\}} \sigma_n^z = \mathbb{1} = \prod_{i \neq n \in \{n_j\}} \hat{\sigma}_n^z$ such that Eq. (2.419c) vanishes identically. In the second case there are only two particles in $\sum_{M: (-1)^M = \alpha} |M\rangle_a |N - M\rangle_b$ such that either the first or the second factor in Eq. (2.419c) annihilate this state. In any case, we find that

$$H |\{\lambda_i\}; N^*\rangle_{N,\alpha}^\oplus = E(\{\lambda_i\}) |\{\lambda_i\}; N^*\rangle_{N,\alpha}^\oplus \quad 2.422$$

which concludes the proof. ■

2.D Residue of the Majorana Algebra

In this section, we focus on the algebraic properties of the zero-energy subspace of wire networks (as introduced in Subsection 2.5.1). We start in \clubsuit Subsection 2.D.1 with a brief exposition of the Majorana algebra, its relation to non-abelian braid group representations, and the action of Majorana edge modes on the zero-energy ground states. In \clubsuit Subsection 2.D.2, we introduce exponentially localized edge operators for the number-conserving setting that map the degenerate ground states into each other. We study their properties and discuss their relation to the Majorana algebra.

2.D.1 Properties of Majorana Operators

We start this subsection with a brief exposition of the Majorana algebra, the braid group, and the representation of the latter by the former. Afterwards, we revisit the action of the Majorana edge modes on the zero-energy ground states and define a subalgebra to bridge the gap between mean field theory and its number-conserving analogue.

Braid Group Representations from the Majorana Algebra

Here we derive two possible braid group representations realized by the Majorana algebra: an abelian and a non-abelian one. The latter describes the braiding statistics of Ising anyons⁹³, found in the low-energy sector of models that carry Majorana modes either in vortices [83] or at the end of one-dimensional chains [82].

We start with a $2N$ -generator Majorana algebra M_{2N} (isomorphic to a N -fermion Dirac algebra), the generators of which are denoted $\gamma_1, \dots, \gamma_{2N}$ and fulfill the relations of a (complex) Clifford algebra:

$$\gamma_i \gamma_j + \gamma_j \gamma_i = \{\gamma_i, \gamma_j\} = 2\delta_{ij} \mathbb{1}. \quad 2.423$$

In particular, $\gamma_i^2 = \mathbb{1}$ which makes M_{2N} finite-dimensional. Together with the defining hermiticity condition $\gamma_i^\dagger = \gamma_i$, M_{2N} becomes an operator algebra acting on a Hilbert space \mathcal{H} ; henceforth we take $\mathcal{H} = \mathcal{H}_N^-$ to be the Fock space of N fermions on which M_{2N} acts in the usual way (Subsection 1.2.2).

Next, we identify each generator γ_i with a “strand” i of the braid group B_{2N} , which is presented as

$$B_{2N} = \left\langle \sigma_1, \dots, \sigma_{2N-1} \left| \begin{array}{l} \sigma_i \sigma_{i+1} \sigma_i = \sigma_{i+1} \sigma_i \sigma_{i+1} \quad \text{and} \\ \sigma_i \sigma_j = \sigma_j \sigma_i \quad \text{for } |i - j| > 1 \end{array} \right. \right\rangle. \quad 2.424$$

⁹³Up to non-universal phases, see Footnote 41.

Since the generator σ_i describes the exchange of the i th with the $i + 1$ th strand, we introduce the more descriptive labeling $\sigma_{i,i+1} \equiv \sigma_i$. The interpretation of Majorana generators γ_i as strands originates from the physical picture of spatially localized zero-energy modes associated to these operators. Thus they may be subject to unitary evolutions that represent the braiding of these localized modes.

To find a representation $\rho : B_{2N} \rightarrow M_{2N}$, we have to define ρ on the generators $\sigma_{i,i+1}$ and ensure that the defining relations of B_{2N} are satisfied in M_{2N} . In the following, we restrict admissible representations by demanding *locality*, that is, $\rho(\sigma_{i,i+1})$ maps to the subalgebra generated by the corresponding strands γ_i and γ_{i+1} . Furthermore, we require translational invariance, i.e., the coefficients of ρ do not depend on the site i . This leads to the general form

$$\rho(\sigma_{i,i+1}) = a \mathbb{1} + b \gamma_i + c \gamma_{i+1} + d \gamma_i \gamma_{i+1} \quad 2.425$$

with yet undetermined coefficients $a, b, c, d \in \mathbb{C}$.

It is straightforward to see that $\rho(\sigma_i)\rho(\sigma_j) = \rho(\sigma_j)\rho(\sigma_i)$ for non-adjacent sites i and j ($|i - j| > 1$) requires all terms with an *odd* number of Majoranas to vanish as they anticommute with each other. Hence we are left with

$$\rho(\sigma_{i,i+1}) = a \mathbb{1} + d \gamma_i \gamma_{i+1} \quad 2.426$$

which, plugged into the braiding relation,

$$\begin{aligned} & \rho(\sigma_{i,i+1})\rho(\sigma_{i+1,i+2})\rho(\sigma_{i,i+1}) \\ & \stackrel{!}{=} \rho(\sigma_{i+1,i+2})\rho(\sigma_{i,i+1})\rho(\sigma_{i+1,i+2}), \end{aligned} \quad 2.427$$

yields

$$\begin{aligned} & (a \mathbb{1} + d \gamma_i \gamma_{i+1})(a \mathbb{1} + d \gamma_{i+1} \gamma_{i+2})(a \mathbb{1} + d \gamma_i \gamma_{i+1}) \\ & = (a^3 - ad^2) + 2a^2d \gamma_i \gamma_{i+1} + (a^2d + d^3) \gamma_{i+1} \gamma_{i+2} \end{aligned} \quad 2.428$$

on the left-hand side and

$$\begin{aligned} & (a \mathbb{1} + d \gamma_{i+1} \gamma_{i+2})(a \mathbb{1} + d \gamma_i \gamma_{i+1})(a \mathbb{1} + d \gamma_{i+1} \gamma_{i+2}) \\ & = (a^3 - ad^2) + 2a^2d \gamma_{i+1} \gamma_{i+2} + (a^2d + d^3) \gamma_i \gamma_{i+1} \end{aligned} \quad 2.429$$

on the right-hand side. We conclude that the form $a \mathbb{1} + d \gamma_i \gamma_{i+1}$ satisfies the braiding relations if and only if

$$2a^2d = a^2d + d^3 \quad \Leftrightarrow \quad a^2d = d^3. \quad 2.430$$

There are two possible solutions: For $d = 0$, there is no restriction on a and we find the abelian representation

$$\rho_{\text{abelian}}(\sigma_{i,i+1}) = a \mathbb{1}. \quad 2.431$$

For $d \neq 0$, we have $a = \pm d$ and therefore the two non-abelian representations

$$\rho_{\text{non-abelian}}(\sigma_{i,i+1}) = a (\mathbb{1} \pm \gamma_i \gamma_{i+1}). \quad 2.432$$

We can sharpen this result by demanding unitarity of the representation; this is motivated by physics where the braid group representation is generated by the unitary time evolution on a Hilbert space. So assume

$$\rho(\sigma_{i,i+1})\rho(\sigma_{i,i+1})^\dagger = \mathbb{1} \quad \Leftrightarrow \quad \rho(\sigma_{i,i+1}^{-1}) = \rho(\sigma_{i,i+1})^\dagger, \quad 2.433$$

which leads to

$$\begin{aligned} & (a \mathbb{1} + d \gamma_i \gamma_{i+1})(a^* \mathbb{1} - d^* \gamma_i \gamma_{i+1}) \\ &= |a|^2 \mathbb{1} - (ad^* - a^*d)\gamma_i \gamma_{i+1} + |d|^2 \mathbb{1} \stackrel{!}{=} \mathbb{1}. \end{aligned} \quad 2.434$$

Unitarity is therefore equivalent to

$$|a|^2 + |d|^2 = 1 \quad \text{and} \quad ad^* = da^*, \quad 2.435$$

which leads in the abelian case to the final result

$$\rho_{\text{abelian}}(\sigma_{i,i+1}) = e^{i\varphi} \mathbb{1} \quad 2.436$$

and in the non-abelian case to

$$\rho_{\text{non-abelian}}(\sigma_{i,i+1}) = \frac{e^{i\varphi}}{\sqrt{2}} (\mathbb{1} \pm \gamma_i \gamma_{i+1}). \quad 2.437$$

Using $(\gamma_i \gamma_{i+1})^{2n} = (-1)^n$, we can rewrite this in terms of anti-Hermitian generators:

$$\frac{1}{\sqrt{2}} (\mathbb{1} \pm \gamma_i \gamma_{i+1}) = \mathbb{1} \cos \frac{\pi}{4} \pm \gamma_i \gamma_{i+1} \sin \frac{\pi}{4} \quad 2.438a$$

$$= \sum_{n=0}^{\infty} \frac{(\gamma_i \gamma_{i+1} \cdot \pi/4)^{2n}}{(2n)!} \pm \sum_{n=0}^{\infty} \frac{(\gamma_i \gamma_{i+1} \cdot \pi/4)^{2n+1}}{(2n+1)!} \quad 2.438b$$

$$= \exp \left[\pm \frac{\pi}{4} \gamma_i \gamma_{i+1} \right]. \quad 2.438c$$

RESULT 2.9: Non-abelian braid group representation

Thus we find the non-abelian braid group representation(s)

$$\rho_{\text{non-abelian}}(\sigma_{i,i+1}) = \exp \left[i\varphi \pm \frac{\pi}{4} \gamma_i \gamma_{i+1} \right] \quad 2.439$$

in terms of Majorana modes γ_i and γ_j with arbitrary phase $\varphi \in \mathbb{R}$. It is common to set $\varphi = 0$ since φ has no effect on the non-abelian structure of the representation⁹⁴. The two sign choices (\pm) exchange the representations for $\sigma_{i,i+1}$ and its inverse $\sigma_{i,i+1}^{-1}$.

For a broader view on the relation between Majorana fermions and braid group representations, we refer the reader to Ref. [267].

⁹⁴This phase is fixed to $\varphi = \pi/8$ for “true” (i.e., non-projective) Ising anyons [24, 156].

It is instructive to interpret the representation ρ as acting on M_{2N} via conjugation [48]:

$$\rho(\sigma_{i,i+1})(\gamma_k) \equiv \rho(\sigma_{i,i+1})\gamma_k\rho(\sigma_{i,i+1})^\dagger. \quad 2.440$$

This leads to the transformation rules

$$\gamma_k \mapsto \gamma_k \quad \text{for } k \neq i, i+1 \quad 2.441a$$

$$\gamma_i \mapsto -\gamma_{i+1} \quad 2.441b$$

$$\gamma_{i+1} \mapsto \gamma_i \quad 2.441c$$

which is in line with the interpretation of γ_i, γ_j as “strands” that are swapped by $\rho(\sigma_{i,i+1})$. Note that

$$U_{i,i+1} \equiv \rho(\sigma_{i,i+1})\rho(\sigma_{i,i+1}) = \rho(\sigma_{i,i+1}^2) \neq \mathbb{1} \quad 2.442$$

describes a double-exchange, i.e., *braiding* of one mode around another one. This sets the braid group B_{2N} apart from the symmetric group S_{2N} (where permuting twice yields the identity) and facilitates non-trivial state transformations by braiding. In particular, for fermion modes

$$a = \frac{1}{2}(\gamma_1 + i\gamma_2) \quad \text{and} \quad b = \frac{1}{2}(\gamma_3 + i\gamma_4) \quad 2.443$$

we have

$$U_{2,3} a U_{2,3}^\dagger = a^\dagger \quad \text{and} \quad U_{2,3} b U_{2,3}^\dagger = -b^\dagger, \quad 2.444$$

such that two empty modes a, b are populated by a pair of fermions by braiding appropriate Majorana modes. This immediately suggests connections to superconductivity: Only a condensate of fermion pairs (viz. *Cooper pairs*) can provide the two particles that are “created” by braiding. In Subsection 2.5.2 we discussed the number-conserving analog of $U_{2,3}$ and found a parity flip of both involved subchains; this parallels the change in parity of the modes a and b in (2.444).

As a final remark, we point out that braiding two Majorana modes that make up a common fermion mode yields

$$U_{1,2} a U_{1,2}^\dagger = -a = \theta_\Psi a. \quad 2.445$$

This can be understood if we realize that in the Ising anyon model, a fermion $\Psi \sim a$ is an *extended* object composed of two Majoranas $\sigma \sim \gamma$. Braiding these two constituents around each other then describes a 2π -rotation of the fermion around its axis. This gives rise to the *topological spin* $\theta_\Psi = -1$ of the fermion Ψ —in accordance with the known relation between fermionic statistics and half-integer spin⁹⁵.

⁹⁵Although our fermions a and b are spinless (or spin-polarized), the half-integer nature of their spin is intrinsic to the Ising anyon model (UMTC). Note that the fermions are confined in two dimensions where the spin algebra is *abelian* (it has a single generator) with one-dimensional irreducible representations. Such “2D-fermions” are spin-polarized “by default” and their spin manifests as a minus sign when rotated by 2π in-plane.

Action on the Ground States

To motivate the discussion in \clubsuit Subsection 2.D.2, we recall (Subsection 1.2.2) that at the “sweet spot” of the Majorana chain, the two degenerate zero-energy many-body ground states for open boundary conditions are given by the equal-weight superpositions of fixed (total) parity $P = (-1)^N$,

$$|+\rangle = \sum_{\mathbf{n}: |\mathbf{n}| \text{ even}} |\mathbf{n}\rangle \quad \text{and} \quad |-\rangle = \sum_{\mathbf{n}: |\mathbf{n}| \text{ odd}} |\mathbf{n}\rangle. \quad 2.446$$

With the edge mode Majorana operators

$$\gamma_L \equiv a_1 + a_1^\dagger \quad \text{and} \quad \gamma_R \equiv -i(a_L - a_L^\dagger) \quad 2.447$$

one can easily switch between the two ground states with unit overlap:

$$|+\rangle = \gamma_L |-\rangle \quad \text{and} \quad |-\rangle = i\gamma_R |+\rangle. \quad 2.448$$

It is a crucial point that this mapping is only possible at the edges (sites 1 and L). Majorana operators located in the bulk still change the parity but create no overlap with the other ground state; this is a smoking gun for edge states.

Despite its algebraic possibility, this is not a physically admissible operation as it changes the total parity P : It cannot occur as the time evolution of a Hamiltonian that respects a parity superselection rule (and thus can only include *even* products of Majorana operators). The problem can be solved in a system of *two* separate open chains which can be brought together so that their endpoints are close to each other. Then, for a fixed total parity $P = +1$, it is reasonable to drive local transitions such as

$$|+\rangle_1 |+\rangle_2 \propto \gamma_L^{(1)} \gamma_L^{(2)} |-\rangle_1 |-\rangle_2 \quad 2.449$$

where the relative phase now depends on the chosen gauge (fermion order). The product of two Majorana operators $\gamma_L^{(1)} \gamma_L^{(2)}$ is “physical” as it conserves the total parity (but not the total particle number⁹⁶).

The fact that only even products of Majorana operators can occur in any physically legitimate scenario motivates the definition of the *even* Majorana subalgebra:

$$M_{2N}^+ \equiv \langle \gamma_i \gamma_j \mid i, j \in \{1, \dots, 2N\} \rangle \leq M_{2N}. \quad 2.450$$

Note that a set of *independent* generators is given by any spanning tree of the complete graph on $2N$ vertices, for example $\{\gamma_1 \gamma_i \mid 1 < i \leq 2N\}$, and therefore $2N - 1$ generators are sufficient. Compared to the $2N$ generators of M_{2N} , only a single generator is missing (which corresponds to a “basepoint”). If we define

$$\chi_{lm} \equiv i\gamma_l \gamma_m \in M_{2N}^+, \quad 2.451$$

⁹⁶This is not necessary, as can be seen from the mean field description of superconductivity.

it is easy to confirm that

$$\chi_{lm}^\dagger = \chi_{lm} \quad 2.452a$$

$$\chi_{lm}^2 = \mathbb{1} \quad 2.452b$$

$$\chi_{lm} = -\chi_{ml} \quad 2.452c$$

$$[\chi_{lm}, \chi_{no}] = 0 \quad \text{for } \{l, m\} \cap \{n, o\} = \emptyset \quad 2.452d$$

and additionally

$$\chi_{lm}\chi_{mn} = i\chi_{ln}. \quad 2.453$$

It is clear that any quadratic (and therefore parity-conserving) fermionic Hamiltonian can be written as

$$H = \sum_e h_e \chi_e \quad 2.454$$

with $h_e \in \mathbb{R}$ and edges $e = (lm)$. Thus all the relevant physics is actually described by M_{2N}^+ and we can forget about the substructure of χ_e in terms of Majorana operators and the rest of M_{2N} .

For instance, the elementary adiabatic deformation used for braiding reads⁹⁷

$$H_{ijk}(\tau) = (1 - \tau) \chi_{ij} + \tau \chi_{jk} \quad (0 \leq \tau \leq 1), \quad 2.455$$

and the non-abelian braid group representation becomes

$$\rho(\sigma_j) = e^{\mp i \frac{\pi}{4} \chi_j} = \frac{1}{\sqrt{2}} (\mathbb{1} \mp i \chi_j) \quad 2.456$$

if we define $\chi_i \equiv \chi_{i,i+1}$.

Note that $\chi_{lm}^2 = \mathbb{1}$ and $\chi_{lm}^\dagger = \chi_{lm}$ leads to eigenvalues ± 1 . Their physical interpretation becomes clear if we recall the fermionic origin:

$$\chi_{lm} = i\gamma_l\gamma_m = (a - a^\dagger)(a + a^\dagger) = 1 - 2a^\dagger a = (-1)^{a^\dagger a}, \quad 2.457$$

where we defined the fermion mode as $a = (\gamma_m + i\gamma_l)/2$. So the eigenvalue of χ_{lm} is the *parity* of the fermion mode that results from the fusion of the Majorana modes at sites l and m .

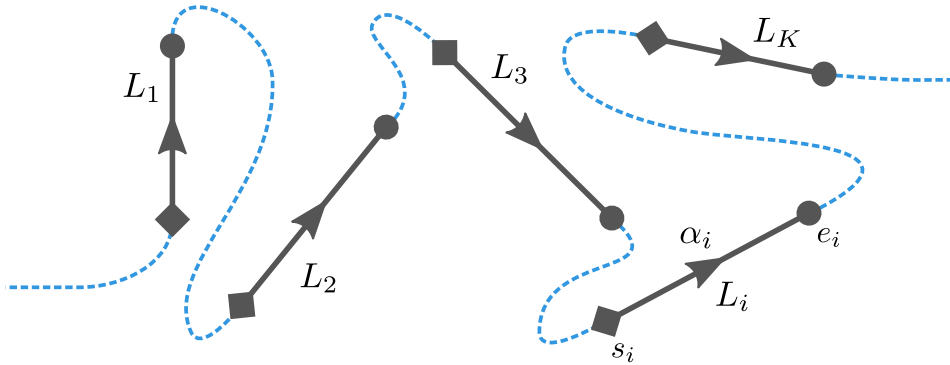
2.D.2 Edge Modes in the Number-Conserving Setting

In this subsection, we introduce a class of number-conserving operators as replacement for the even products of Majorana operators in M_{2N}^+ . We discuss some of their properties, especially the possibility to map ground states of wire networks into each other—a feature that supports their role as number-conserving “edge modes.”

⁹⁷This Hamiltonian starts off with a localized Majorana zero mode γ_k and ends up with a zero mode at γ_i . The spectrum remains gapped with an exact zero-energy mode throughout the evolution. Thus it describes the adiabatic transfer of a Majorana mode from k to i via j .

Number-Conserving Edge Operators

Let us consider a system of K single (open) chains L_i that are all connected by parity-conserving couplings to a common (open) bath chain, so that the complete system is characterized by the total filling N and the subchain parities $\alpha_i = \pm 1$ for $i = 1, \dots, K$. If we choose a gauge along the chains, this still leaves open the direction and relative order of the chains. A possible setup looks like this:



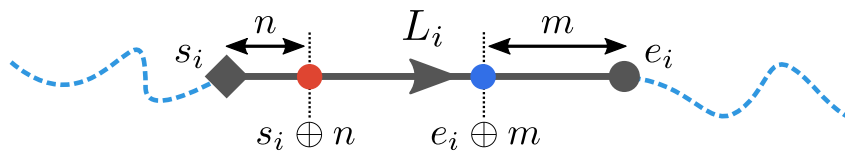
We omit the bath chain for the sake of simplicity. The chosen gauge is drawn as dashed blue line. The direction of the gauge string determines the orientation of the chain segments as indicated by the arrows; the relative order of the chains is induced by the gauge string as well. Due to the global ordering (including the invisible bath chain, of course), there is a common index μ for all fermion sites running from 1 to $\sum_i L_i + L_{\text{bath}}$, the total number of sites; μ runs along the gauge string. We can assign a Hamiltonian H_0 to this system so that the zero-energy ground state space \mathcal{H}_0 is 2^K degenerate and the ground states are given by equal-weight superpositions $|\alpha_1, \dots, \alpha_K\rangle$ (we omit the filling N in the labeling of the states), recall Subsection 2.5.1.

For what follows, it is convenient to introduce distinct labels for the sites at the chain endpoints. As depicted above, s_i (e_i) denotes the index of the first (last) site of chain i ; again, “first” and “last” is defined relative to the orientation of the chain. If we introduce the handy notation

$$s_i \oplus n \equiv s_i + n \quad 2.458a$$

$$e_i \oplus n \equiv e_i - n \quad 2.458b$$

for a shift $0 \leq n < L_i$ (and the *-modifier: $e_i^* \equiv s_i$ and $s_i^* \equiv e_i$, see below), this allows us to parametrize the chain relative to its edges:



Let in the following $x, y \in \{s, e\}$ label generic boundary sites of chains. Then we can define for $1 \leq \delta < \min\{L_l, L_m\}$ and two chains l and m the projector

$$\eta_\delta(x_l, y_m) \equiv \prod_{i=0}^{\delta-1} [n_{x_l \oplus i} \cdot n_{y_m \oplus i} + (\mathbb{1} - n_{x_l \oplus i}) \cdot (\mathbb{1} - n_{y_m \oplus i})] \quad 2.459$$

with the fermionic number operators $n_\mu = a_\mu^\dagger a_\mu$; for $\delta = 0$, let $\eta_0(x_l, y_m) \equiv \mathbb{1}$.

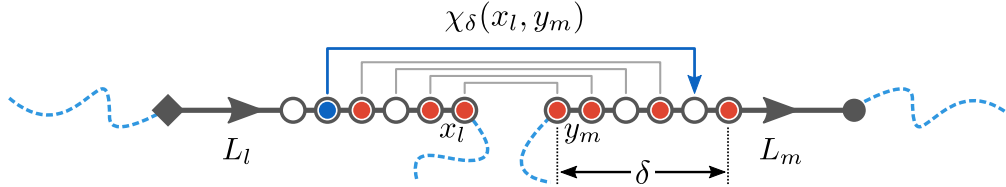
DEFINITION 2.5: Number-conserving edge operators

With these preliminaries, we can define the edge operators

$$\chi_\delta(x_l, y_m) \equiv \sum_{k=0}^{\delta-1} \eta_k(x_l, y_m) \times \begin{cases} (-1)^{\delta_{x,e}} \times (a_{x_l \oplus k}^\dagger a_{y_m \oplus k} + a_{y_m \oplus k}^\dagger a_{x_l \oplus k}) & \text{for } x \neq y \\ i \times (a_{x_l \oplus k}^\dagger a_{y_m \oplus k} - a_{y_m \oplus k}^\dagger a_{x_l \oplus k}) & \text{for } x = y \end{cases} \quad 2.460$$

that are Hermitian and number-conserving as they tunnel single fermions between the boundaries x_l and y_m of chains l and m .

Their action is best explained with an illustration in the number basis:



The δ summands in $\chi_\delta(x_l, x_m)$, indexed by k , are given by a projector $\eta_k(x_l, y_m)$ that compares the first k sites on chains l and m (counting from the boundary sites x and y) and projects onto states that are *symmetrically occupied*, as depicted above for the first 4 sites on either chain. This prevents single-particle hopping between chains from site $x_l \oplus i$ to $y_m \oplus i$ (and vice versa) for $0 \leq i < k$. The projection is combined with a Hermitian single-particle hopping between the sites $x_l \oplus k$ and $y_m \oplus k$ (the $k + 1$ th sites counted from the edges). For the number state depicted above, the $k = 4$ summand in $\chi_\delta(x_l, y_m)$ acts non-trivially by tunneling the blue fermion from chain l to chain m ; all other summands vanish. It is clear by construction that $\chi_\delta(x_l, y_m)$ flips the subchain parities $\alpha_{l,m} \rightarrow -\alpha_{l,m}$ and thereby fulfills a necessary condition for an operator that acts as a non-trivial automorphism on the ground state space \mathcal{H}_0 of the wire network.

Two questions arise immediately: First, is \mathcal{H}_0 invariant under the action of χ_δ (possibly in some approximate sense), and second, what are the algebraic properties of χ_δ when restricted to \mathcal{H}_0 ? We will not give conclusive answers here but sketch

possible directions for future studies. However, we conjecture that the χ_δ give rise to an *approximate* (in δ) representation of M_{2K}^+ on \mathcal{H}_0 , i.e., they play the role of *pairs* of Majorana edge modes in the number-conserving setting.

Some Properties of χ_δ

To reveal the similarities of $\chi_\delta(x_l, y_m)$ and χ_{lm} , we have a look at the square

$$[\chi_\delta(x_l, y_m)]^2 = \pm \sum_{k=0}^{\delta-1} \eta_k^2(x_l, y_m) \left(a_{x_l \oplus k}^\dagger a_{y_m \oplus k} \pm a_{y_m \oplus k}^\dagger a_{x_l \oplus k} \right)^2, \quad 2.461$$

where we used the orthogonality of different terms to obtain the diagonal form of the sum. It can be simplified to

$$[\chi_\delta(x_l, y_m)]^2 = \sum_{k=0}^{\delta-1} \eta_k(x_l, y_m) \times \begin{bmatrix} n_{x_l \oplus k} (\mathbb{1} - n_{y_m \oplus k}) \\ + n_{y_m \oplus k} (\mathbb{1} - n_{x_l \oplus k}) \end{bmatrix} \quad 2.462a$$

$$\equiv \sum_{k=0}^{\delta-1} \xi_k(x_l, y_m), \quad 2.462b$$

a sum of projectors $\xi_k(x_l, y_m)$ onto number states characterized by *symmetric* configurations for sites $1 \leq i \leq k$ and an *asymmetric* occupation of the $k + 1$ th pair of modes. It is easy to see that they are orthogonal for different indices $k = a, b$, i.e.,

$$\xi_a(x_l, y_m) \xi_b(x_l, y_m) = \delta_{a,b} \xi_a(x_l, y_m). \quad 2.463$$

Equation (2.462b) suggests the decomposition

$$\chi_\delta^2 = \mathbb{1} + R_\delta, \quad 2.464$$

where the residual operator R_δ is expected to vanish⁹⁸ rapidly with growing δ as more and more orthogonal projectors contribute to the square.

We do not provide a proof of Eq. (2.464) but the following intuition: The basis $|\alpha_1, \dots, \alpha_K\rangle$ of \mathcal{H}_0 is given by equal-weight superpositions of all fermion configurations under conditions on particle number and subchain parity that are clearly not altered by χ_δ^2 . We can now ask about the probability that a random (admissible) configuration is *annihilated* by the sum of orthogonal projectors in (2.462b) (these are states that contribute to the operator norm $\|R_\delta\|$). Such states feature a completely symmetric occupation pattern on chains l and m starting from their edges x_l and y_m inwards for (at least) δ sites. For a given density $0 < \rho < 1$, this probability vanishes exponentially with δ . Since $|\alpha_1, \dots, \alpha_K\rangle$ are

⁹⁸We have to specify what we mean by “vanish”: As we are interested in the action on ground states, all statements about χ_δ must hold only within \mathcal{H}_0 . Therefore “vanish” here means that the operator norm $\|R_\delta\|_0$ on \mathcal{H}_0 vanishes.

equal-weight superpositions, this translates into an exponentially vanishing loss of norm due to the application of χ_δ^2 ; thus we have $\|R_\delta\|_0 = \mathcal{O}(e^{-\delta})$. Note that this is *not* true on the total Hilbert space \mathcal{H} which includes states with a completely symmetric configuration on both chains. These are annihilated by χ_δ for all δ since no symmetric single-particle hopping is possible; thus $\|R_\delta\| \geq 1$ on \mathcal{H} .

A similar counting argument can be applied to χ_δ itself. Again, up to losses that are exponentially suppressed in δ , $\chi_\delta(x_l, y_m)$ maps (α_l, α_m) -configurations to $(-\alpha_l, -\alpha_m)$ -configurations via single-particle hopping. Most importantly, due to the *symmetric* occupations between the boundaries and the site to/from which the fermion hops, the collected sign is the same for all k -terms in (2.460). In particular, an equal-weight superposition $|\alpha_l, \alpha_m\rangle$ is mapped to another equal-weight superposition $|\alpha_l, \alpha_m\rangle$ up to losses in norm of the order $\mathcal{O}(e^{-\delta})$.

Due to their (obvious) Hermiticity, we conclude that the operators $\chi_\delta(x_l, y_m)$ are “unitary up to exponential corrections” on \mathcal{H}_0 and exponentially localized on the boundaries:

$$\chi_\delta^2 = \mathbb{1} + \mathcal{O}(e^{-\delta}) \quad \Rightarrow \quad \chi_\delta^\dagger = \chi_\delta^{-1} + \mathcal{O}(e^{-\delta}). \quad 2.465$$

This and the fact that $\chi_\delta(x_l, y_m)|\alpha_l, \alpha_m\rangle$ has definite subchain parities $-\alpha_l$ and $-\alpha_m$ (and the only subspace with these parities in \mathcal{H}_0 is generated by $|\alpha_l, \alpha_m\rangle$) leads us to the following conjecture:

CONJECTURE 2.1: Unitary (quasi-)automorphism on \mathcal{H}_0

$\chi_\delta(x_l, y_m)$ acts as unitary automorphism on \mathcal{H}_0 up to exponential corrections. Its action is given on the subchain parity basis $|\alpha_1, \dots, \alpha_K\rangle = |\alpha_l, \alpha_m\rangle$ as

$$\chi_\delta(x_l, y_m)|\alpha_l, \alpha_m\rangle = c |-\alpha_l, -\alpha_m\rangle + \mathcal{O}(e^{-\delta}). \quad 2.466$$

Here, $c \in \mathbb{C}$ is a phase, $|c| = 1$.

From now on, we neglect the exponential corrections (and the cutoff subscript δ) in all equations. To derive the algebra generated by the $\chi(x_l, y_m)$ on \mathcal{H}_0 , the precise form of the phase c and its dependence on the quantum numbers α_i is required. To this end, we need additional notation. Recall that the gauge string defines an order on the chains, and let $\alpha_i \equiv P_i$ denote the parity (operator) on the i th chain. Then we define ($l < m$)

$$\pi(x_l, y_m) \equiv (\alpha_l)^{\delta_{x,s}} \cdot \left(\prod_{l < i < m} \alpha_i \right) \cdot (\alpha_m)^{\delta_{y,e}} \quad 2.467$$

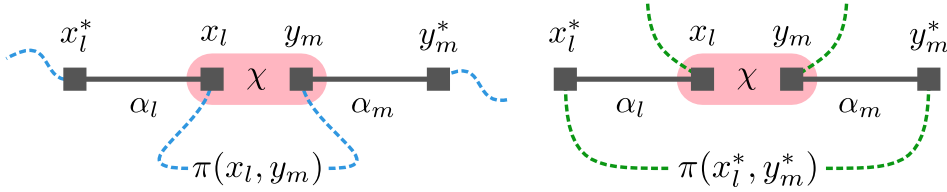
as the subsystem parity of chains between l and m . To indicate the evaluation of π on a given parity configuration $\alpha = (\alpha_1, \dots, \alpha_K)$, we write $\pi_\alpha(x_l, y_m)$.

A careful evaluation of signs collected during the hopping from one boundary x_l to another y_m reveals that in order to yield finite overlaps in the thermodynamic limit, time-reversal invariant couplings are necessary whenever the orientations of the two chains are parallel ($x \neq y$), and conversely, time-reversal breaking couplings must be applied between chains of antiparallel orientation⁹⁹ ($x = y$); this explains our choice in the definition (2.460) of $\chi(x_l, y_m)$. Note that the global sign $(-1)^{\delta_{x,e}}$ for $x \neq y$ is only necessary to make $\chi(x_l, y_m)$ antisymmetric,

$$\chi(x_l, y_m) = -\chi(y_m, x_l), \quad 2.468$$

irrespective of x and y ; compare with the mean field versions in Eq. (2.452).

Let us start with the first case of parallel orientations coupled via time-reversal invariant hopping. There are two distinct gauge string topologies for such orientations, pictorially:



As all statements that follow are invariant under an inversion of orientation (up to a global sign), we omit arrows on the chains and consequently label boundary sites neutrally as $x, y \in \{s, e\}$; due to the chosen topology it is implicit that $x \neq y$. Remember that an arbitrary collection of chains (not shown above) may lie “between” the coupled boundary sites. Those are not affected by the hopping process, but their parity has to be taken into account nevertheless (due to the chosen gauge). This parity is encoded in π , as suggested by the figure above.

For the two cases depicted above, one finds the action ($\bar{\alpha} \equiv -\alpha$)

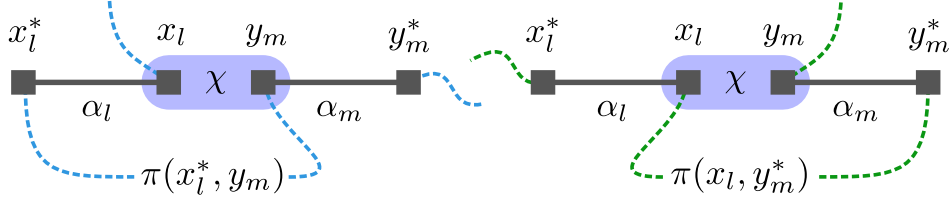
$$\chi(x_l, y_m) |\alpha_l, \alpha_m\rangle = (-1)^{\delta_{x,e}} \pi_{\alpha}(x_l, y_m) |\bar{\alpha}_l, \bar{\alpha}_m\rangle \quad 2.469a$$

$$\begin{aligned} \chi(x_l, y_m) |\alpha_l, \alpha_m\rangle &= (-1)^{\delta_{x,e}} (-\alpha_l \alpha_m) \pi_{\alpha}(x_l^*, y_m^*) |\bar{\alpha}_l, \bar{\alpha}_m\rangle \\ &= (-1)^{\delta_{x,s}} \pi_{\alpha}(x_l, y_m) |\bar{\alpha}_l, \bar{\alpha}_m\rangle. \end{aligned} \quad 2.469b$$

The crucial difference between the two cases is whether the particle traverses its own chain or not. If so (shown in the right-hand panel above), an additional minus sign occurs because the particle has to be subtracted from the effective parity of its chain.

⁹⁹This is in line with the well-known fact that time-reversal symmetry must be broken to gap out two Majorana chains of parallel orientation (topological index $1 + 1 = 2$); this breaks the \mathbb{Z} topological index of symmetry class **BDI** down to the \mathbb{Z}_2 index of class **D**. For chains of antiparallel orientation (topological index $1 + (-1) = 0$), no time-reversal symmetry must be broken as this corresponds to a Majorana chain with periodic boundaries.

Similarly, there are two distinct configurations for antiparallel orientations where time-reversal breaking hopping is the appropriate choice to couple states:



Carefully counting fermion parities yields the action

$$\begin{aligned}\chi(x_l, y_m)|\alpha_l, \alpha_m\rangle &= i(+\alpha_l) \pi_{\alpha}(x_l^*, y_m) |\bar{\alpha}_l, \bar{\alpha}_m\rangle \\ &= i \pi_{\alpha}(x_l, y_m) |\bar{\alpha}_l, \bar{\alpha}_m\rangle\end{aligned}\quad 2.470a$$

$$\begin{aligned}\chi(x_l, y_m)|\alpha_l, \alpha_m\rangle &= i(-\alpha_m) \pi_{\alpha}(x_l, y_m^*) |\bar{\alpha}_l, \bar{\alpha}_m\rangle \\ &= -i \pi_{\alpha}(x_l, y_m) |\bar{\alpha}_l, \bar{\alpha}_m\rangle,\end{aligned}\quad 2.470b$$

where again both cases differ in a minus sign only and $x = y$ follows implicitly from the gauge string topology.

Using (2.469) and (2.470), the matrix algebra of

$$\{\chi(x_l, y_m) \mid l, m \in \{1, \dots, K\}; x, y \in \{e, s\}\} \quad \text{on } \mathcal{H}_0 \quad 2.471$$

can be derived in principle. We leave this calculation to the motivated reader but conjecture that they realize an approximation of the even Majorana subalgebra M_{2K}^+ . Furthermore, it would be interesting to elucidate how $\chi(x_l, y_m)$ relates to the concept of *weak zero modes* that has been introduced in the context of interacting parafermion chains [268, 269].

3

Topological Networks for Quantum Communication Between Distant Qubits

*“Reality is that which,
when you stop believing in it,
doesn’t go away.”*

— PHILIP K. DICK

Efficient communication between qubits relies on robust networks which allow for fast and coherent transfer of quantum information. It seems natural to harvest the remarkable properties of systems characterized by topological invariants to perform this task. In this chapter, we show that a linear network of coupled bosonic degrees of freedom, characterized by topological bands, can be employed for the efficient exchange of quantum information. Features of the proposed setup, published in Ref. [2], are that it is robust against quenched disorder, all relevant operations can be performed by global variations of parameters, and the time required for communication between qubits approaches linear scaling with their distance. We show how the proposed concept can be extended to an ensemble of qubits embedded in a two-dimensional network to allow for communication between all of them.

This page is intentionally left blank.

In modern computers, the central processing unit (CPU) applies instructions to a massive amount of data every fraction of a second. These instructions are so fast that the speed of information processing is often not limited by the operations themselves but the time needed to transfer data from, to and between random access memory (RAM) and the various temporary memories (caches) of the CPU. While this “data management” is a formidable task of modern chip design, the physical mechanism for information transfer is not that elaborate: Lithographically fabricated “wires” allow for the transmission of voltage pulses—encoding the bits—at (almost) the speed of light. This is how most of the data is shuffled around in *classical* computers, and there are no fundamental difficulties that bar the way.

Unfortunately, *quantum* computers are picky in almost every respect. Not even the transmission of a *qubit* from one register to another (on the same chip!) is as easy as it sounds. This is because qubits are fragile and any interaction with an uncontrolled environment degrades their coherence. But just as the performance and scalability of classical information processing rests on efficient methods for information transfer, the *coherent* transfer of quantum information is crucial for the construction of scalable *quantum* processors. In this chapter, we discuss a scheme—realized in topological materials—as promising quantum analogue for the “wires” of classical CPUs: Our main mission is to transfer a qubit, stored in a two-level system C, coherently to another two-level system T which is too far away for direct coupling.

To complete this mission, we borrow findings from condensed matter physics. More precisely, we focus on *symmetry-protected topological phases* in one dimension, such as the famous Su–Schrieffer–Heeger (SSH) model

$$\hat{H}_{\text{SSH}} = \sum_{i=1}^L w_i c_i^\dagger c_{\bar{i}} + \sum_{i=1}^{L-1} t_i c_{\bar{i}}^\dagger c_{i+1} + \text{h.c.}, \quad 3.1$$

which describes an open chain of $2L$ fermions (two per site: $c_i^{(+)}$ and $c_{\bar{i}}^{(+)}$) with alternating hopping amplitudes w_i and t_i ; see Subsection 1.2.1 for a review. We are going to use this *fermionic* model as a blueprint to construct a *bosonic* network (think of coupled cavities) that inherits its most intriguing feature: For uniform couplings $w_i \equiv \bar{w} = 0$ and $t_i \equiv \bar{t} > 0$, the leftmost and rightmost modes c_1 and $c_{\bar{L}}$ do not show up in \hat{H}_{SSH} and become degenerate zero-energy modes located at the boundaries of the chain. For $0 < \bar{w} < \bar{t}$, these *edge modes* are still localized at the edges but leak further into the bulk when \bar{w} approaches \bar{t} . In finite chains, this leads to hybridization of the two edge modes with an energy splitting ΔE_{edge} . The edge modes vanish for $\bar{w} = \bar{t}$ where the chain undergoes a *topological phase transition* into a trivial phase for $\bar{w} > \bar{t}$ where no edge modes are present.

A network of *bosonic* modes with the same properties might be the solution for our posed task: We connect the qubits C and T by a “SSH-like” chain of bosonic modes of appropriate length \tilde{L} deep in the topological phase ($\bar{w} = 0$) so that the edge modes (call them \tilde{b}_C and \tilde{b}_T) are tightly localized at the ends of the chain. The

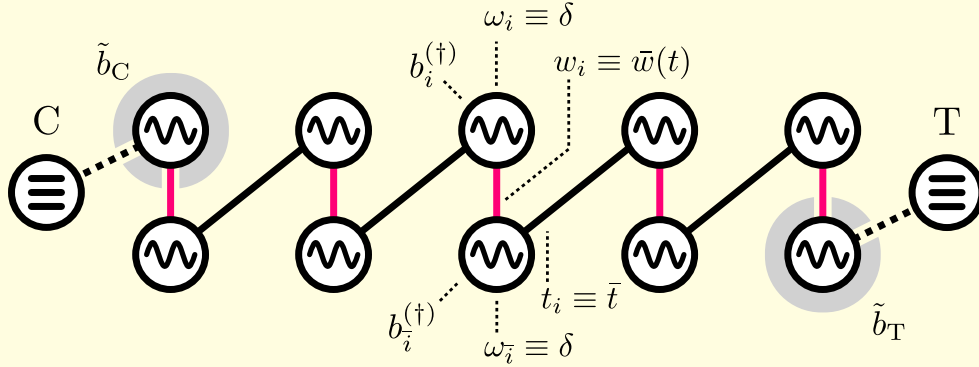


FIGURE 3.1 • Setup. Linear bosonic network \hat{H}_{bSSH} for topological state transfer. The model consists of locally coupled bosonic modes b_i and $b_{\bar{i}}$ with qubits C and T coupled (dashed edges) to the edge modes \tilde{b}_C and \tilde{b}_T (gray discs). The only (globally) tunable parameter is the on-site coupling $\bar{w}(t)$ (red edges). Inter-site couplings \bar{t} (black edges) and mode frequencies δ are uniform and static. The network derives from the fermionic SSH chain.

state of the two-level system C can then be mapped into its adjacent edge mode \tilde{b}_C as bosonic excitation. If the mode coupling $\bar{w} = \bar{w}(t)$ is slowly switched on, both edge modes hybridize and allow for a Rabi pulse that transfers an excitation from one edge to the other. Turning \bar{w} off again relocalizes the edge modes and with them potential excitations. Finally, a transferred excitation can be mapped back from the edge mode \tilde{b}_T to the two-level system T, which completes the transfer.

To translate the fermionic Hamiltonian into a bosonic one (without spoiling the topological features), it is instructive to write

$$\hat{H}_{\text{SSH}} = \Phi^\dagger H_{\text{SSH}} \Phi \quad 3.2$$

with the pseudo-spinor $\Phi = (c_1, c_{\bar{1}}, \dots, c_L, c_{\bar{L}})^T$. Here, H_{SSH} is a Hermitian $(2L \times 2L)$ -matrix encoding the non-interacting many-body Hamiltonian \hat{H}_{SSH} . But the *matrix* H_{SSH} does not know anything about the fermionic nature of \hat{H}_{SSH} (nor anything about quantum mechanics, for that matter). The edge modes of \hat{H}_{SSH} , however, are *single-particle features* and therefore already encoded in H_{SSH} . If we add a constant energy shift, $H_{\text{bSSH}} \equiv H_{\text{SSH}} + \delta \mathbb{1}$, this clearly does not change the eigenstates (most importantly: the edge states) and makes H_{bSSH} positive for $\delta > 0$ large enough.

Now we can simply define the bosonic Hamiltonian¹⁰⁰

$$\hat{H}_{\text{bSSH}} \equiv \Xi^\dagger H_{\text{bSSH}} \Xi \quad 3.3$$

¹⁰⁰The positivity of H_{bSSH} is necessary for the existence of a stable ground state of \hat{H}_{bSSH} in the bosonic Fock space. For the fermionic theory \hat{H}_{SSH} , this was not necessary due to the Pauli exclusion principle.

with $\Xi = (b_1, b_{\bar{1}}, \dots, b_L, b_{\bar{L}})^T$ and the $2L$ bosons b_i and $b_{\bar{i}}$ replacing the fermions c_i and $c_{\bar{i}}$. The bosonic network described by \hat{H}_{bSSH} is illustrated in Figure 3.1, together with the conceived coupling of the qubits C and T with their respective edge modes \tilde{b}_C and \tilde{b}_T . Note that the shift δ is identified with the (uniform) mode frequencies ω_i and $\omega_{\bar{i}}$.

A considerable part of this chapter is dedicated to an assessment of the performance of this scheme for a particular choice of the ‘‘transfer protocol,’’ namely the time dependence of the uniform on-site coupling

$$\bar{w}(t) = \bar{w}_{\max} \mathcal{F}(t), \quad 3.4$$

where $\mathcal{F}(t) = \sin^2(\pi t/\tau)$ for $0 \leq t \leq \tau$. Here, $\bar{w}_{\max} < \bar{t}$ and τ are parameters specifying the protocol. Our choice of the pulse *shape* accounts for the intuition that a *smooth* time evolution is necessary, lest undesired scattering into bulk modes obstructs the transfer. Indeed, we find that for appropriately chosen \bar{w}_{\max} and τ , near to perfect transfer is possible, see Figure 3.2 (a) for an example.

To quantify these results, we write $|1, \mathbf{0}, 0\rangle \equiv |1\rangle_1 \otimes |0, \dots, 0\rangle_{\text{Bulk}} \otimes |0\rangle_{\bar{L}} = \tilde{b}_C^\dagger |0\rangle$ for an excitation in the edge mode \tilde{b}_C (and similar for \tilde{b}_T), and introduce the three figures of merit \mathcal{O} , φ , and \mathcal{E} as

$$\langle 0, \mathbf{0}, 1 | U_{\bar{w}_{\max}}(\tau) | 1, \mathbf{0}, 0 \rangle \equiv \sqrt{\mathcal{O}} e^{i\varphi} \quad 3.5$$

and

$$\mathcal{E} \equiv \mathcal{O} + |\langle 1, \mathbf{0}, 0 | U_{\bar{w}_{\max}}(\tau) | 1, \mathbf{0}, 0 \rangle|^2, \quad 3.6$$

where $U_{\bar{w}_{\max}}(\tau)$ describes the unitary time evolution by $\hat{H}_{\text{bSSH}}(t)$. \mathcal{O} and φ measure the transfer fidelity and phase, whereas \mathcal{E} quantifies the adiabatic decoupling of the two edge modes from the bulk modes.

The time τ needed for this decoupling, indicated by $\mathcal{E} \approx 1$, is determined by the gap between edge and bulk modes ΔE_{bulk} , see Figure 3.2 (b). An additional (lower) bound on τ follows from the requirement of high transfer fidelity (indicated by $\mathcal{O} \approx 1$), namely $\tau \sim \Delta E_{\text{edge}}^{-1}$ for the hybridization energy ΔE_{edge} . A central message of this chapter is that a scaling $\Delta E_{\text{edge}} \sim L^{-1}$ and $\Delta E_{\text{bulk}} \sim L^{-1}$ is achievable if the critical coupling is approached as $\bar{w}_{\max} = \bar{t} - \text{const}/L$. Using analytic upper bounds on the non-adiabatic losses, we show that this allows for transfer times $\tau \sim L^{1+\frac{1}{2}}$ close to the ideal (linear) scaling $\tau \sim L$. It is even possible to approach linear transfer times for optimized pulse shapes.

Another major part of this chapter deals with the effects of *quenched disorder* on the performance of the transfer protocol. In this context, the *symmetry protection* of the original SSH chain becomes important, where combinations of the three ‘‘generic’’ symmetries T (time-reversal), C (particle-hole), and S (sublattice) are known to be responsible for the robustness of the edge modes. For the derived *bosonic* network, this boils down to the uniformity of the mode frequencies

$$\forall_{i,\bar{i}} : \omega_i = \delta = \omega_{\bar{i}}, \quad 3.7$$

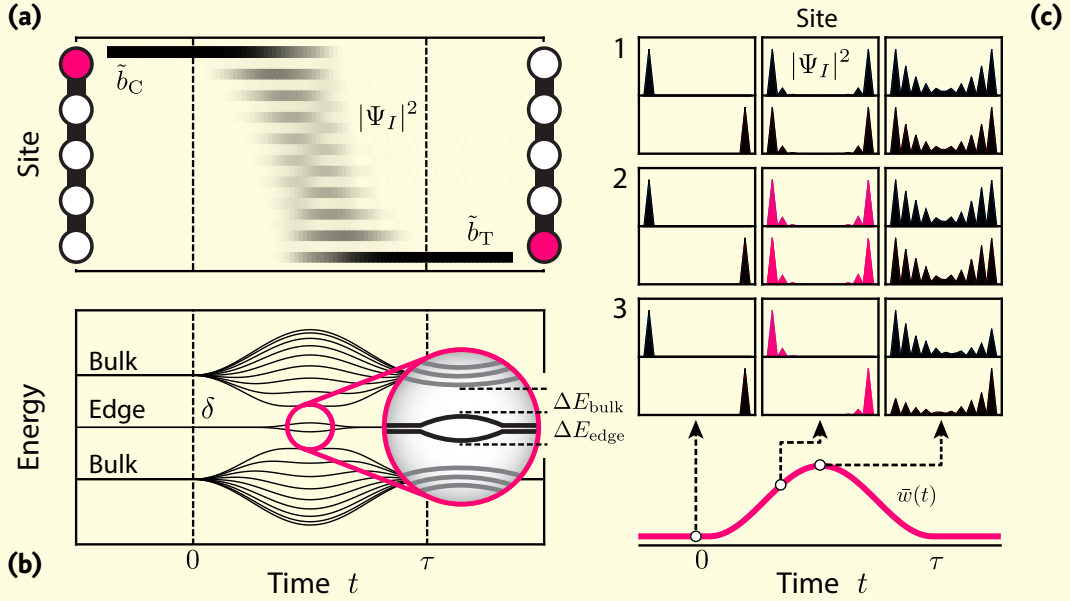


FIGURE 3.2 • Results. (a) shows the squared amplitude $|\Psi_I|^2$ of a single-particle wave function evolved by $\hat{H}_{\text{bSSH}}(t)$ for an excitation that is initially localized in the edge mode \tilde{b}_C and transferred to the edge mode \tilde{b}_T . The protocol parameter \bar{w}_{max} and the timescale τ are tuned to optimize the transfer fidelity and the adiabatic decoupling. (b) parallels the time evolution in (a) with the single-particle spectrum of $\hat{H}_{\text{bSSH}}(t)$. The spectrum is symmetric to the mode frequency δ due to particle-hole symmetry. The inset highlights the splitting ΔE_{edge} of the edge modes and their separation ΔE_{bulk} from the bulk modes. (c) shows the spatial amplitudes $|\Psi_I|$ of both edge modes at three times during the protocol $\bar{w}(t)$ for (1) no disorder, (2) particle-hole symmetric disorder, and (3) particle-hole breaking disorder. Note the *delocalization* of the edge modes for particle-hole symmetric disorder in (2) and their *localization* for particle-hole breaking disorder in (3) (red panels).

together with the reality of the couplings w_i and t_i (the values of which may be subject to site-dependent disorder!). Most importantly, we show that for disorder that respects the particle-hole symmetry C , the transfer phase φ is fixed at $\pm \frac{\pi}{2}$ and the fidelity \mathcal{O} is only marginally affected. We argue that the edge modes do *not* localize for particle-hole symmetric disorder, which explains their hybridization and the robust state transfer despite disordered couplings, see Figure 3.2 (c). To gauge these results, we compare the SSH-based scheme to a simple, “non-topological” tunneling setup and highlight the benefits of the topological approach.

In the last part of this chapter, we discuss a possible application of the topological transfer scheme: The implementation of a controlled-phase (CP) gate on the two remote qubits C and T described by

$$\mathcal{U}_{\text{CP}} = \Pi_{\text{T}} \circ T_{\text{C} \leftrightarrow \text{T}} \circ \Pi_{\text{C}}^2 \circ T_{\text{C} \leftrightarrow \text{T}} \circ \Pi_{\text{T}}. \quad 3.8$$

Here, $T_{C \leftrightarrow T}$ denotes the topological state transfer and Π_C/Π_T are local π -pulses that describe the mapping between the physical qubits C/T and their adjacent edge modes \tilde{b}_C/\tilde{b}_T . We demonstrate numerically that this sequence of unitaries indeed realizes a controlled-phase gate $\mathcal{U}_{CP}|x\rangle_C|y\rangle_T = (-1)^{xy}|x\rangle_C|y\rangle_T$ with $x, y \in \{0, 1\}$ for the conditional phase $\phi = \pi$.

Finally, we discuss possible generalizations of the one-dimensional setup in two dimensions that allow for the controlled communication between arbitrary pairs of $N > 2$ qubits. In this context, we highlight the role of the various symmetries and conclude with possible directions for future studies.

This page is intentionally left blank.

3.1 Introduction

Systems characterized by topological invariants are well known to exhibit unique properties—such as robust edge modes, stable ground state degeneracies, and anyonic excitations—with potential applications in quantum information processing and engineering [47]. Ever since the first experimental observation of the integer quantum Hall effect [69, 270, 271], many other condensed matter systems have been identified and experimentally characterized, such as fractional quantum Hall fluids [27–29] and topological insulators and superconductors [21, 22, 75, 78, 95, 97, 102, 103, 272]. The latter belong to a particularly well-understood family of topological systems described by non-interacting fermions, where topological invariants can be defined on classes of random matrices [90–93]. This concept can be straightforwardly generalized to bosonic setups as well as classical systems [202, 204, 213], where the topological features still give rise to intriguing properties such as localized and chiral edge modes. Here we are interested in such systems: We demonstrate that their topological properties can be harvested for robust and efficient transfer of quantum information.

Several different platforms for the realization of topological systems of artificial matter with *bosonic* degrees of freedom (d.o.f.) are currently explored: The construction of topological band structures and the observation of edge states has been achieved with photonic circuits in the optical [212, 213, 273] and the radio-frequency [214] regime, as well as with classical coupled harmonic oscillators [202, 204, 205], and with cold atomic gases [196–198, 274–277]. These experimental advances have been prepared and are supported by many theoretical proposals, e.g. [194, 195, 200, 203, 209, 278–283]. Several of the above platforms are suitable to carry a single quantized excitation with low losses and almost vanishing dissipation along protected edge channels, which opens the opportunity to harvest topological phenomena for guiding and transmitting quantum information reliably. First approaches in this direction have been proposed [191, 192] and primarily focus on the transmission of excitations along protected edge modes on the boundary of a two-dimensional, topologically non-trivial medium.

In this chapter, we show that a linear network of coupled bosonic d.o.f. — characterized by topological bands — can be employed for the efficient transfer of quantum information over mesoscopic distances (e.g., on a chip). We demonstrate that this setup outperforms its topologically trivial counterparts and exemplify its application with the implementation of a robust quantum phase gate. The concept under study is based on (quasi) one-dimensional setups, characterized by a \mathbb{Z} topological invariant [94], and derived from Kitaev’s paradigmatic Majorana chain [82] and the Su–Schrieffer–Heeger (SSH) model [126]. The basic mechanism for topological state transfer is simple: We employ symmetry-protected, localized edge modes, the extend and overlap of which can be tuned via global coupling parameters, to facilitate controllable communication between them. Prominent

features of this approach are that all relevant operations can be performed by *global* tuning of parameters, its robustness with respect to the pulse shapes used for the transfer protocol, and that the time needed for transfer scales favorably (that is, *almost* linearly) with the separation of the qubits. Its outstanding performance is paid by quite complex preparation schemes as the coupling parameters have to respect certain symmetries needed to define the topological invariants [204, 205, 213, 214]. Finally, we demonstrate that this concept can be extended to an ensemble of qubits embedded in a two-dimensional network of local bosonic d.o.f. to establish communication between all of them.

To present these results consistently and in a self-contained fashion, this chapter subdivides into three main parts: In Section 3.2, the topological setup is introduced (Subsection 3.2.1) and the applied protocol for state transfer is explained (Subsection 3.2.2). Subsequently, in Section 3.3 the performance of the topological transfer mechanism is studied in detail (Subsection 3.3.1) and its scalability is analyzed analytically (Subsection 3.3.3). The topological approach is compared with “non-topological” competitors in Subsection 3.3.4; effects of disorder and the required symmetry protection are discussed in Subsection 3.3.5. Finally, in Section 3.4 we employ topological state transfer for the mediation of a controlled-phase gate between a single pair of distant qubits (Subsection 3.4.1). We extend this to an arbitrary number of spatially distributed qubits and briefly sketch a generalization to quasi-two-dimensional setups (Subsection 3.4.2). We conclude in Section 3.5 and point the reader to some open ends that deserve further study. In the remainder of this section, we outline the idea of topological state transfer in one dimension and sketch possible applications thereof.

Basic Setup

We consider mesoscopically¹⁰¹ separated qubits that are coupled by a linear quantum network of bosonic modes, see Figure 3.3 (a) for an example. The quantum network itself is constructed from bosonic d.o.f. with only local couplings between them, and generically described by the Hamiltonian

$$\hat{H}_N = \sum_{i,j} b_i^\dagger H_{ij} b_j . \quad 3.9$$

Here, b_i^\dagger (b_i) are bosonic creation (annihilation) operators accounting for the mode at site i with H_{ij} the coupling amplitudes. The network is designed such (see Subsection 3.2.1 below) that at the end p of each branch, a localized bosonic edge mode \tilde{b}_p emerges with a controllable coupling between this mode and a local qubit. The conceptually simplest setup is an optical network coupled to a single atom with the level structure shown in Figure 3.3 (b). There, the coupling Hamiltonian for

¹⁰¹Imagine two atoms confined in distinct microtraps on a single chip and connected by a network of optical cavities.

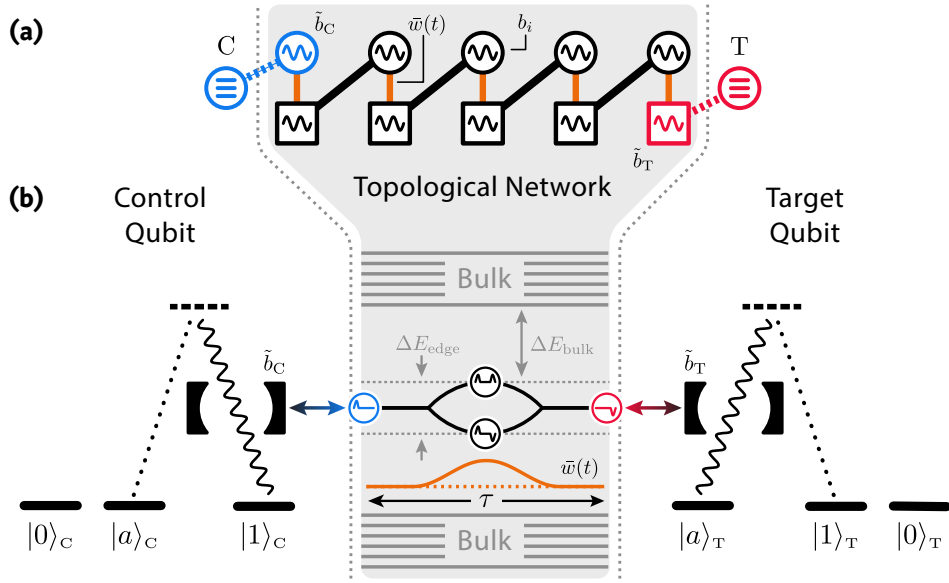


FIGURE 3.3 • Basic setup. (a) One-dimensional chain of bosonic modes b_i with globally tunable, time-dependent on-site couplings $\bar{w}(t)$ (orange); derived from the SSH chain. It features a topological band structure with localized edge modes \tilde{b}_T and \tilde{b}_C (perfectly localized for $\bar{w} = 0$) which can be coupled to local qubits T and C. (b) The local qubits are realized as three-level systems with logical states $|0\rangle_p$, $|1\rangle_p$ and the auxiliary state $|a\rangle_p$. The state $|a\rangle_C$ ($|1\rangle_T$) can decay into $|1\rangle_C$ ($|a\rangle_T$) via an off-resonant transition and thereby emits an excitation into the localized edge mode \tilde{b}_C (\tilde{b}_T). Tunneling excitations between the two edges is facilitated by temporarily tuning the chain close to the phase transition via $\bar{w}(t)$ and adiabatically decoupling bulk from edge modes. The latter requires the protocol timescale τ to be large compared to the (inverse) gap between edge and bulk modes $\Delta E_{\text{bulk}}^{-1}$ ($\hbar = 1$). By contrast, a lower bound on the time required for a transfer is given by the (inverse) edge mode splitting $\Delta E_{\text{edge}}^{-1}$.

the target qubit T, located at one end of a one-dimensional network, takes the form (within the rotating wave approximation)

$$\hat{H}_T(t) = g_T(t) \left[\tilde{b}_T^\dagger |a\rangle\langle 1|_T + \tilde{b}_T |1\rangle\langle a|_T \right]. \quad 3.10$$

The coupling $g_T(t)$ is controlled by external laser fields and allows for the application of π -pulses between the qubit state $|1\rangle_T$ and the edge mode \tilde{b}_T , i.e., the emission of a photon into the edge mode \tilde{b}_T from state $|1\rangle_T$ is accompanied by a transition into the auxiliary state $|a\rangle_T$; in the following, we denote such a π -pulse at edge $p \in \{T, C\}$ by the unitary operation Π_p . Note that the Hamiltonian $\hat{H}_C(t)$ for the control qubit C is similar, with the role of $|1\rangle_C$ and $|a\rangle_C$ exchanged.

Several fundamental tasks of quantum information processing between the qubits T and C reduce to the transfer of edge excitations within the linear network; we denote the corresponding unitary operation that describes the transfer of excitations between edge modes b_p and b_q as $T_{p \leftrightarrow q}$.

As an example, the protocol for a controlled-phase (CP) gate between a control qubit C and a target qubit T reads

$$\mathcal{U}_{\text{CP}} = \Pi_{\text{T}} \circ T_{\text{C} \leftrightarrow \text{T}} \circ \Pi_{\text{C}}^2 \circ T_{\text{C} \leftrightarrow \text{T}} \circ \Pi_{\text{T}} \quad 3.11$$

where the 2π -pulse Π_{C}^2 imprints a phase of -1 if and only if the control qubit is in state $|1\rangle_{\text{C}}$. Another example, the transport of a control qubit c to a target position τ , is simply described by the protocol

$$\mathcal{U}_{\text{SWAP}} = \mathcal{A}_{\text{C}} \circ \Pi_{\text{T}} \circ \Pi_{\text{C}} \circ T_{\text{C} \leftrightarrow \text{T}} \circ \Pi_{\text{C}} \circ \Pi_{\text{T}} \circ \mathcal{A}_{\text{C}}. \quad 3.12$$

Here, \mathcal{A}_p denotes the exchange of the two states $|1\rangle_p$ and $|a\rangle_p$. Note that this operation even performs the full exchange of the two qubits due to the linearity of the network; a detailed discussion of these operations can be found in Subsection 3.4.1.

Motivated by these observations, we are in the following interested in the efficient transfer ($T_{\text{C} \leftrightarrow \text{T}}$) of edge excitations within the linear network. The basic idea is most conveniently illustrated for two qubits coupled by a one-dimensional network, as illustrated in Figure 3.3 (a): If the coupling structure of the network gives rise to topological bands with a gapped dispersion relation, the bulk-boundary correspondence entails the existence of degenerate and localized edge modes within the bulk gap. As the existence of edge modes is topologically protected, it is robust against disorder. In a *finite* system, the degeneracy of the topological edge states is only lifted exponentially in the edge separation. However, globally tuning the quantum network closer to the topological phase transition into the trivial phase increases overlap and finite-size splitting of the edge states, which eventually allows for a π -pulse $T_{\text{C} \leftrightarrow \text{T}}$ between the two edges. This simple idea is the core of topological state transfer in one dimension and the subject of this chapter; compared to topologically trivial systems, it features several neat properties regarding the speed of state transfer and its robustness against disorder. Because the coupling of edge modes is controlled by the phase of the network (more precisely: how close it is to criticality), individual addressing of parts is not required.

To conclude this introduction, we stress that the envisioned scheme is generic and various experimental platforms lend themselves for its implementation. In addition to the discussed optical network [213], alternative setups are coupled optical cavities and circuit QED systems [284, 285] as well as trapped polar molecules or Rydberg atoms with a coupling mediated by dipolar exchange interactions [283], while the local qubits can be artificial atoms [286], nitrogen-vacancy centers in diamond [287], or trapped ions [288].

3.2 Setup

In this section, we introduce the subject of scrutiny: A linear network of bosonic modes with localized edge modes, the controlled hybridization of which allows for state transfer between them. The procedure to construct the network is described in Subsection 3.2.1, augmented by three alternative setups for comparison (one topological, two trivial). In Subsection 3.2.2, we introduce a protocol that can be applied to the previously defined network(s) to initiate the transfer of excitations between the edge modes. This sets the stage for the results presented in the subsequent Section 3.3.

3.2.1 Construction of Topological Networks

Let us start with the derivation of a quantum network \hat{H}_N that exhibits topologically protected edge modes in a one-dimensional chain with two edges, as illustrated in Figure 3.3 (a); a generalization to two-dimensional networks is discussed briefly in Subsection 3.4.2.

One of the most prominent (and most studied) models of symmetry-protected topological phases in one dimension is the *Majorana chain*, originally formulated for spinless fermions with a mean field p -wave pairing term [82]. This model is closely related to the *Su-Schrieffer-Heeger (SSH) model* [126] in the single-particle picture. It turns out that both models are useful blueprints for the task at hand (i.e., topological state transfer), but the necessary steps to translate these models into a bosonic quantum network language are more conveniently performed for the SSH model; an analogous discussion for the Majorana chain and its relation to the SSH chain is presented in Section 3.A.

The SSH model on a chain with L sites and open boundaries is defined by the Hamiltonian (Subsection 1.2.1)

$$\hat{H}_{\text{SSH}} = \sum_{i=1}^L w_i c_i^\dagger c_{\bar{i}} + \sum_{i=1}^{L-1} t_i c_{\bar{i}}^\dagger c_{i+1} + \text{h.c.} \quad 3.13$$

with the two fermion operators c_i and $c_{\bar{i}}$ on each site. Note that the indices i label the “upper” fermionic modes whereas bar-ed indices \bar{i} denote the “lower” ones, see Figure 3.4 (a); in the following, we use upper-case indices I if we refer to both indifferently. In (3.13), w_i and t_i are the hopping amplitudes. For a uniform system with $w_i \equiv \bar{w}$ and $t_i = \bar{t}$, one finds a gapless spectrum for $\bar{w} = \bar{t}$, separating a topological phase for $\bar{w} < \bar{t}$ from the trivial phase for $\bar{w} > \bar{t}$. The former features topologically protected edge modes which are fermionic in nature¹⁰². The

¹⁰²This is in contrast to the Majorana chain where *pairs* of edge modes carry a *single* fermionic d.o.f.

QUANTUM COMMUNICATION BETWEEN QUBITS

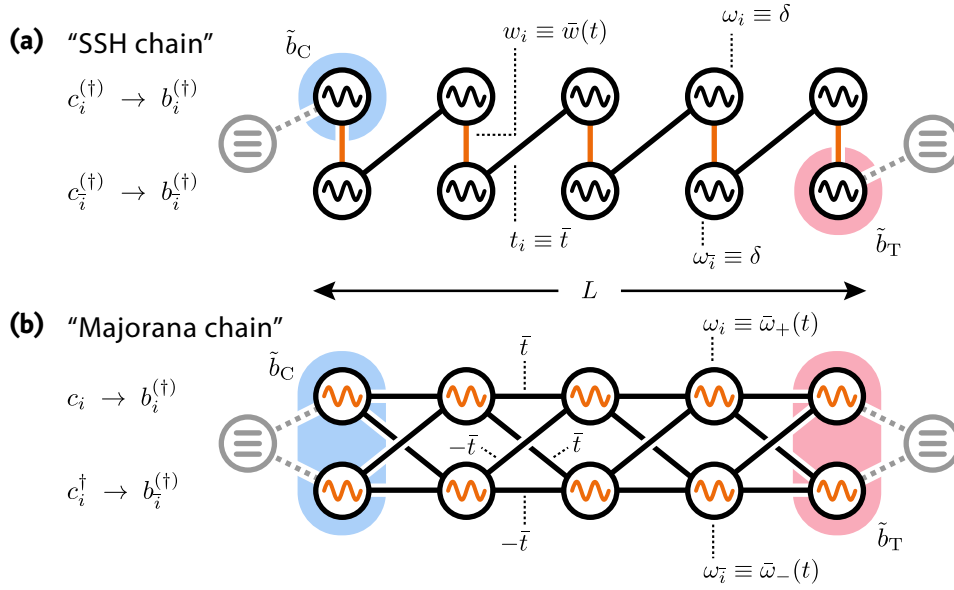


FIGURE 3.4 • Setups. Possible setups for state transfer via global control parameters. The left panel depicts networks with topological bands. The models in the right panel are used for comparison and feature only trivial bands. Each model consists of locally coupled bosonic modes with qubits coupled to the edge modes \tilde{b}_C and \tilde{b}_T . **(a)** The SSH chain inspired setup described by $\hat{H}_{\text{bSSH}}(t)$; globally tunable are only the on-site couplings $\bar{w}(t)$. **(b)** Network inspired by the Majorana chain (unitarily equivalent to the SSH setup) and described by $\hat{H}_{\text{bMC}}(t)$; the uniform eigenfrequency differences $\delta\bar{\omega}(t) \equiv \bar{\omega}_-(t) - \bar{\omega}_+(t)$ are tunable. For details we refer the reader to \clubsuit Section 3.A. \curvearrowright

second-quantized Hamiltonian (3.13) can be encoded by a matrix H_{SSH} via

$$\hat{H}_{\text{SSH}} = \Phi^\dagger H_{\text{SSH}} \Phi \quad 3.14$$

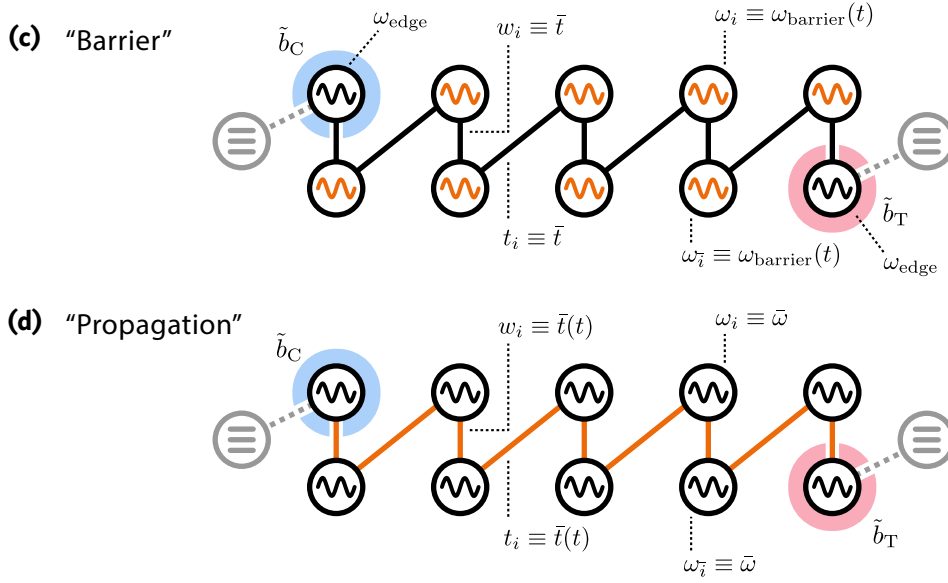
with the pseudo-spinor $\Phi = (c_1, c_{\bar{1}}, \dots, c_L, c_{\bar{L}})^T$. The matrix H_{SSH} takes a simple off-diagonal form

$$H_{\text{SSH}} = \begin{bmatrix} 0 & w_1 & 0 & 0 \\ w_1 & 0 & t_1 & 0 \\ 0 & t_1 & \ddots & \ddots \\ 0 & 0 & \ddots & \ddots \end{bmatrix}, \quad 3.15$$

the diagonalization of which is numerically straightforward but analytically challenging, see \clubsuit Section 3.D.

For real hopping amplitudes w_i and t_i (which we will assume henceforth), the Hamiltonian exhibits time-reversal symmetry $T = \mathcal{K}$ where \mathcal{K} denotes complex conjugation. Furthermore, time-reversal T in combination with the sublattice

SETUP



↪ (c) Model with two artificial edge modes separated by a simple tunneling barrier of tunable eigenfrequencies $\omega_{\text{barrier}}(t)$; described by the Hamiltonian $\hat{H}_{\text{bb}}(t)$. (d) The simplest model, based on free propagation of excitations and described by $\hat{H}_{\text{bp}}(t)$; all couplings $\bar{t}(t)$ are tuned simultaneously. A comparison of the two non-topological models with the topological SSH setup is presented in Subsection 3.3.4.

symmetry $S = U_C^{\text{SSH}}$, represented by the unitary

$$U_C^{\text{SSH}} = \underbrace{\mathbb{1}_{L \times L}}_{L \text{ sites}} \otimes \underbrace{\begin{bmatrix} 1 & 0 \\ 0 & -1 \end{bmatrix}}_{2 \text{ modes per site}}, \quad 3.16$$

yields the particle-hole (PH) symmetry $C = \mathcal{K}U_C^{\text{SSH}}$ with $C^2 = +1$ and the transformation

$$CH_{\text{SSH}}C^{-1} = U_C^{\text{SSH}}H_{\text{SSH}}^*(U_C^{\text{SSH}})^\dagger = -H_{\text{SSH}}. \quad 3.17$$

Hence, the SSH chain is in symmetry class **BDI** of the Altland-Zirnbauer classification¹⁰³ [90–93]. In one dimension, this allows for the definition of a \mathbb{Z} topological invariant [21, 22, 95, 97], which is responsible for the emergence of the disorder-resilient edge modes bound to the open ends of the chain in the topological phase.

¹⁰³The Altland-Zirnbauer classification [90] extends Dyson’s classification [93] of random matrices by four additional ensembles. Each of its 10 ensembles of random matrices—distinguished by the presence/absence of time-reversal (T), sublattice (S), and particle-hole (C) symmetry—allows for the definition of different topological invariants in different spatial dimensions. This leads to the “tenfold way” [97], a complete classification of topological insulators/superconductors of non-interacting fermions with the generic symmetries T, S , and C .

Let us now use the SSH model as a blueprint to construct a network of coupled bosonic modes that inherits the topological features on the single-particle level. Since the latter are properties of the *matrix* H_{SSH} (which is unaware of the fermionic nature of \hat{H}_{SSH}), the implementation of an analogue system with bosonic d.o.f. is straightforward: We replace the fermionic operators by bosonic ones, i.e.,

$$c_i^{(\dagger)} \rightarrow b_i^{(\dagger)} \quad 3.18a$$

$$c_{\bar{i}}^{(\dagger)} \rightarrow b_{\bar{i}}^{(\dagger)}, \quad 3.18b$$

see Figure 3.4 (a). The bosonic Hamiltonian takes the form

$$\hat{H}_{\text{bSSH}} \equiv \Xi^\dagger [H_{\text{SSH}} + \delta \mathbf{1}] \Xi = \Xi^\dagger H_{\text{bSSH}} \Xi \quad 3.19$$

with $\Xi = (b_1, b_{\bar{1}}, \dots, b_L, b_{\bar{L}})^T$ and $H_{\text{bSSH}} \equiv H_{\text{SSH}} + \delta \mathbf{1}$. The constant positive energy shift $\delta > 0$ is required to enforce positivity on the matrix H_{bSSH} and accounts for the energy ω_I of each bosonic mode b_I . Due to its construction, the bosonic Hamiltonian \hat{H}_{bSSH} features the same single-particle band structure as the original fermionic chain and inherits its topological properties. Thus it gives rise to the same edge modes. Note that these are statements about *single*-particle physics where the statistics of particles is not relevant.

To satisfy the PH symmetry C (necessary for the definition of a discrete topological invariant), one must respect the sublattice symmetry S . Using Eq. (3.16) and (3.17), this is equivalent to the simple constraints

$$\omega_i = \delta = \omega_{\bar{i}} \quad 3.20$$

for all sites i and \bar{i} , i.e., all bosonic modes must have the same energy. Note that there are no constraints on the couplings w_i and t_i except for their reality (this is not a requirement of the sublattice symmetry S but of time-reversal T , and thereby indirectly of the PH symmetry C ; see also \clubsuit Section 3.B). To sum it up, the linear bosonic network described by Hamiltonian (3.19) features stably degenerate¹⁰⁴ topological edge modes for couplings $\bar{w} < \bar{t}$, as long as condition (3.20) is satisfied.

Alternative Setups

Let us mention three additional setups, all of which feature localized edge modes for specific choices of parameters and allow for a controlled transfer of excitations between them. Their network topology is illustrated in the remainder of Figure 3.4. We comment briefly on their operating principles:

¹⁰⁴Up to a small splitting for $\bar{w} > 0$ due to hybridization; this splitting is exponentially suppressed with the chain length L .

SETUP

→ At the beginning of this section, we mentioned that the Majorana chain, a fermionic p -wave superconductor, can also be used to construct a bosonic network with topological edge modes. Here we briefly sketch the procedure to obtain the network shown in Figure 3.4 (b). For details we refer the reader to \clubsuit Section 3.A.

The Majorana chain Hamiltonian [82] for spinless fermions $c_i^{(\dagger)}$ on an open chain of length L reads (Subsection 1.2.2)

$$\hat{H}_{\text{MC}} = \sum_{i=1}^{L-1} \left(w_i c_i^\dagger c_{i+1} - \Delta_i c_i c_{i+1} + \text{h.c.} \right) + \sum_{i=1}^L \mu_i \left(c_i^\dagger c_i - \frac{1}{2} \right), \quad 3.21$$

where w_i is the tunneling amplitude, Δ_i the superconducting gap, and μ_i denotes the chemical potential. For uniform parameters $\mu_i \equiv \bar{\mu}$ and $w_i \equiv \bar{w} = \bar{\Delta} \equiv \Delta_i$, one finds two gapped phases for $|\bar{\mu}| \leq 2|\bar{w}|$ connected by a topological phase transition at $|\bar{\mu}| = 2|\bar{w}|$. The topological phase ($|\bar{\mu}| < 2|\bar{w}|$) exhibits two degenerate edge modes that give rise to a two-fold ground state degeneracy.

In contrast to the SSH chain (3.13), the Majorana chain (3.21) describes a superconductor with pairing terms. To encode \hat{H}_{MC} into a matrix, one has to introduce the $2L$ -dimensional Nambu spinors

$$\Psi = \left(c_1^\dagger, c_1, \dots, c_L^\dagger, c_L \right)^T \quad 3.22$$

with an artificial mode doubling¹⁰⁵ to account for the pairing of fermions. Then one can write

$$\hat{H}_{\text{MC}} = \frac{1}{2} \Psi^\dagger H_{\text{MC}} \Psi. \quad 3.23$$

with the symmetric matrix

$$H_{\text{MC}} = \begin{bmatrix} -\mu_1 & 0 & -w_1 & -\Delta_1 & & \\ 0 & +\mu_1 & \Delta_1 & w_1 & & \\ -w_1 & \Delta_1 & \ddots & \ddots & \ddots & \\ -\Delta_1 & w_1 & \ddots & \ddots & \ddots & \end{bmatrix}. \quad 3.24$$

¹⁰⁵Note that there are only L fermionic modes involved. By contrast, the SSH chain Hamiltonian \hat{H}_{SSH} operates on $2L$ fermionic modes.

The derivation of the bosonic network follows a similar procedure as before. However, each fermionic site of the original Majorana chain is replaced by *two* bosonic modes:

$$c_i \rightarrow b_i^{(\dagger)} \quad 3.25a$$

$$c_i^\dagger \rightarrow b_{\bar{i}}^{(\dagger)} \quad 3.25b$$

Compare this with the substitution (3.18) for the SSH setup. By this construction, the Majorana chain translates into a linear chain of length L with *two* quantum harmonic oscillators per site. The bosonic Hamiltonian takes the form

$$\hat{H}_{\text{bMC}} \equiv \Xi^\dagger [H_{\text{MC}} + \delta \mathbb{1}] \Xi = \Xi^\dagger H_{\text{bMC}} \Xi \quad 3.26$$

with the same $2L$ -dimensional bosonic mode vectors Ξ as for the SSH setup. If one relabels the parameters in H_{bMC} to a naming scheme appropriate for bosonic networks¹⁰⁶, one finds that the role of the chemical potential $2\mu_i$ is now played by the difference $\delta\omega_i = \omega_{\bar{i}} - \omega_i$ of the local mode frequencies at each site, while the hopping amplitudes $t_{i,i+1}$ and $t_{\bar{i},\bar{i}+1}$ connecting adjacent modes of the same sublattice are identified with the fermion tunneling rate w_i ; the amplitudes $t_{i,\bar{i}+1}$ and $t_{\bar{i},i+1}$ stem from the superconducting order parameter Δ_i .

For robust edge modes, the Majorana chain requires also time-reversal $T = \mathcal{K}$ and particle-hole symmetry¹⁰⁷ $C = \mathcal{K}U_C^{\text{MC}}$; the latter being represented by another unitary U_C^{MC} . Translating the particle-hole symmetry $CH_{\text{MC}}C^{-1} = -H_{\text{MC}}$ to the bosonic setting yields the constraints

$$\omega_i + \omega_{\bar{i}} = 2\delta \quad 3.27a$$

$$t_{i,\bar{i}+1} = -t_{\bar{i},i+1} \quad 3.27b$$

$$t_{i,i+1} = -t_{\bar{i},\bar{i}+1}. \quad 3.27c$$

Again, all of them can be fulfilled by pairwise, *local* fine-tuning of the modes and their couplings to nearest neighbors.

To complete the picture, we point out that the bosonic realization of the Majorana chain H_{bMC} is unitarily equivalent to that of the SSH chain H_{bSSH} ; this is shown in \clubsuit Subsection 3.A.2. Despite their unitary equivalence, in terms of elementary building blocks the two networks impose *different* symmetry constraints on the coupling Hamiltonians, cf. (3.20) and (3.27). Depending on the experimental framework, it may be advantageous *in practice* to implement one or the other of the unitary equivalent models. From a

¹⁰⁶That is, ω_I for mode frequencies and $t_{I,J}$ for couplings between modes I and J .

¹⁰⁷Note that the particle-hole symmetry of the Majorana chain is intrinsic to any (fermionic) Bogoliubov-de Gennes Hamiltonian due to the mode doubling in Nambu space. Here, however, it translates to a non-trivial *real* symmetry of the new bosonic theory.

theoretical stance, there is no difference in performance to be expected if their symmetries are kept intact, which explains our focus on the conceptually simpler SSH model in the following.

- Given the setup of bosonic modes used for the topological transfer with either the SSH or the Majorana setup (note that these differ only in their couplings and tunable parameters but not their layout of modes), one can contrive various “non-topological” schemes that also feature localized edge modes and are potential candidates for state transfer. The most trivial one, depicted in Figure 3.4 (d), simply tunes all couplings of a linear chain uniformly. If all couplings are switched off, all modes are independent; in particular, the left- and rightmost modes decouple and serve as trivial “edge modes.” Since switching on all couplings uniformly leads to a free propagation of an excitation that was initially stored in one of the edge modes, we call this the “Propagation setup” and denote its network Hamiltonian by \hat{H}_{bp} . Its time-dependent parameters are the uniform couplings $\bar{t}(t)$. See Subsection 3.3.4 for a comparison with the SSH model.
- A more sophisticated (non-topological) wiring of the given modes is shown in Figure 3.4 (c). All modes are connected by static couplings \bar{t} . Edge modes are created by raising the eigenfrequencies ω_{barrier} of all modes except for the left- and rightmost one. If $\omega_{\text{barrier}} \gg \omega_{\text{edge}}$, the tunneling between the two artificial edge modes is exponentially suppressed due to the energy barrier of oscillators in between. Lowering the barrier then allows for the controlled coupling of the edge modes. We call this the “Barrier setup” and denote its Hamiltonian by \hat{H}_{bb} . Here, the time-dependent parameters are the frequencies $\omega_{\text{barrier}}(t)$ of the barrier modes. See Subsection 3.3.4 for a comparison with the SSH model.

3.2.2 Protocol for State Transfer

Now that the setups and their parameters are given, we discuss the protocol for state transfer exemplarily for the SSH setup. One of its key features is that it requires only global (translational invariant), time-dependent tuning of the on-site hopping amplitudes $w_i = \bar{w}$; in particular, single-site addressability and control is not required. The goal is to coherently transfer a single quantized excitation from one of the localized edge modes to the other by means of an adiabatic variation of the couplings \bar{w} in \hat{H}_{bSSH} .

The crucial property to exploit for state transfer is that for *finite* systems and in the topological phase (for $0 < \bar{w} < \bar{t}$), there is a finite overlap between the edge modes due to their exponential extension into the bulk¹⁰⁸. While deep in the

¹⁰⁸In the context of the Majorana chain, edge mode hybridization can be a serious issue as it dephases the delocalized topological qubit; for our purpose, and in the bosonic setting, it is a central *feature*.

topological phase ($\bar{w} \approx 0$) this overlap is exponentially suppressed in the edge mode separation L , it can be strongly enhanced by tuning \bar{w} closer to \bar{t} from below, allowing for tunneling between the macroscopically separated edge modes. In order to prevent scattering into bulk modes, edge and bulk physics have to be adiabatically decoupled. This can be achieved by tuning \bar{w} smoothly (and slowly, see Subsection 3.3.3) towards the topological phase transition and return to the “sweet spot” $\bar{w} = 0$ afterwards to relocalize (and thereby decouple) the edge modes.

To put this scheme into action, we introduce a time-dependent hopping rate

$$\bar{w}(t) = \bar{w}_{\max} \mathcal{F}(t) \quad 3.28$$

giving rise to the time-dependent network Hamiltonian $\hat{H}_{\text{bSSH}}(t)$ with perfectly localized edge modes at $t = 0$ and $t = \tau$. For simplicity, we choose for the adiabatic process the smooth pulse shape

$$\mathcal{F}(t) = \sin^2\left(\frac{\pi t}{\tau}\right) \quad \text{for } 0 \leq t \leq \tau. \quad 3.29$$

Here, τ denotes the characteristic timescale of the pulse. The exact pulse shape *does* have influence on the performance of the protocol, and setup-specific optimizations may yield quantitatively better results than (3.29), see Subsection 3.3.3 and ✱ Section 3.E. The adjustable protocol parameters for the SSH setup are therefore the pulse time τ and the peak coupling strength \bar{w}_{\max} .

A similar protocol (using the same pulse \mathcal{F} but a different parameter) can be contrived for the alternative Majorana chain setup, see ✱ Subsection 3.A.1. The protocols used for the non-topological setups are again based on the pulse \mathcal{F} and explained briefly in Subsection 3.3.4 where we compare their performance to the topological SSH setup.

Figures of Merit

The stage is now set. In the next Section 3.3, we study the properties of this protocol (and setup) for state transfer. As a first step, we would like to quantify the transfer efficiency and its dependence on the parameters τ and \bar{w}_{\max} by numerically evaluating the full unitary time evolution of the protocol. To this end, we define three figures of merit:

We start with an excitation in the left edge mode \tilde{b}_C ,

$$|\Psi_0\rangle = |1\rangle_1 \otimes |0, \dots, 0\rangle_{\text{bulk}} \otimes |0\rangle_{\bar{L}} \equiv |1, \mathbf{0}, 0\rangle, \quad 3.30$$

and are interested in the transfer to the right edge mode \tilde{b}_T , i.e., the state $|0, \mathbf{0}, 1\rangle$. This transfer is characterized by the overlap

$$\langle 0, \mathbf{0}, 1 | U_{\bar{w}_{\max}}(\tau) | 1, \mathbf{0}, 0 \rangle \equiv \sqrt{\mathcal{O}} e^{i\varphi}, \quad 3.31$$

where $\mathcal{O} \geq 0$ denotes the *transfer fidelity* (or just *transfer*), while φ is the *relative phase* (or *transfer phase*) accumulated during the adiabatic process.

$$U_{\bar{w}_{\max}}(t) \equiv \mathcal{T} \exp \left[-i \int_0^t ds \hat{H}_{\text{bSSH}}(s) \right] \quad 3.32$$

is the time-ordered (\mathcal{T}) unitary time evolution operator at time t which depends parametrically on \bar{w}_{\max} . \mathcal{O} and φ quantify the transfer; to quantify the degree of adiabaticity, we introduce another characteristic quantity that describes the total *edge mode population* (or *edge weight*),

$$\mathcal{E} = \mathcal{O} + |\langle 1, \mathbf{0}, 0 | U_{\bar{w}_{\max}}(\tau) | 1, \mathbf{0}, 0 \rangle|^2. \quad 3.33$$

Deviations of \mathcal{E} from 1 indicate undesired losses into bulk modes. Note that $0 \leq \mathcal{O} \leq \mathcal{E} \leq 1$ and we aim at parameter settings for which $\mathcal{O} = \mathcal{E} = 1$, i.e., an excitation deposited in one edge mode is completely transferred to the other one without exciting bulk modes. The three figures of merit $\{\mathcal{E}, \mathcal{O}, \varphi\}$ also apply to the three alternative setups, then with \hat{H}_{bMC} , \hat{H}_{bB} , and \hat{H}_{bP} in Eq. (3.32), respectively.

3.3 Results

In this section we study the SSH setup in detail, using both numerical and analytical tools. We start in Subsection 3.3.1 with a numerical evaluation of the figures of merit in dependence of the protocol parameters. As an unexpected but potentially useful feature, we find that the transfer phase is fixed—independent of the achieved transfer fidelity; this effect is studied in Subsection 3.3.2 using a minimal model. In Subsection 3.3.3 we use rigorous upper bounds on non-adiabatic losses to quantify the undesired scattering into bulk modes. This allows us to derive the necessary scaling of the transfer time in dependence of the edge mode separation. We also comment on optimizations of the pulse shape to speed up the protocol. In Subsection 3.3.4 we discuss numerical results for the performance of the non-topological competitors, namely the barrier and propagation setups. We compare them with the topological SSH setup and discuss the advantages of the latter. Finally, in Subsection 3.3.5 we study the effects of disorder in the networks for both the SSH setup and the barrier setup. We demonstrate that the topological setup outperforms the trivial setup clearly for particle-hole symmetric disorder.

QUANTUM COMMUNICATION BETWEEN QUBITS

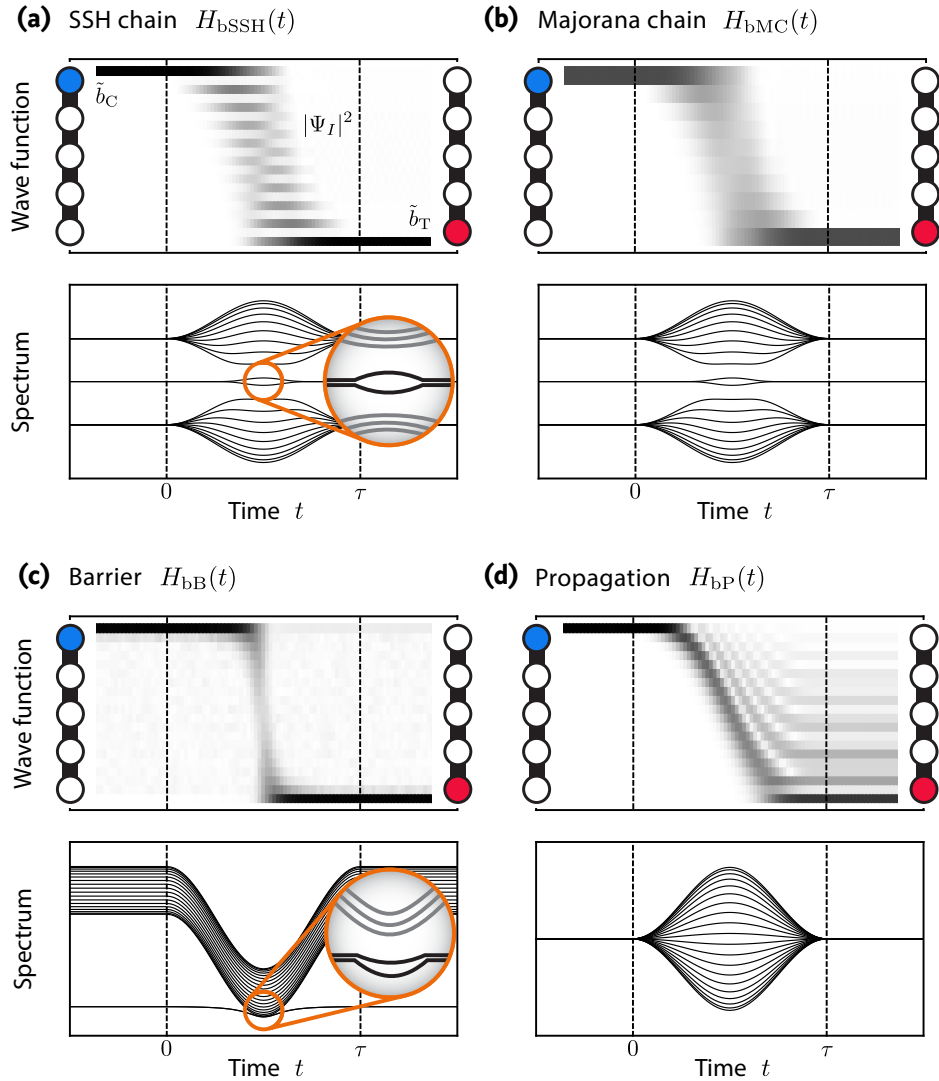


FIGURE 3.5 • State transfer (qualitative results). For the four setups depicted in Figure 3.4 and the corresponding protocols described in the text, we show the full time evolution of a single excitation that is initially localized in the left edge mode \tilde{b}_C and transferred to the right edge mode \tilde{b}_T . The protocol parameters \bar{w}_{\max} (a), $\delta\bar{\omega}_{\max}$ (b), $\omega_{\text{barrier}}^{\min}$ (c), \bar{t}_{\max} (d) and the time scale τ are tuned to optimize transfer \mathcal{O} and edge weight \mathcal{E} . In each panel, the upper row shows the squared amplitude of the single-particle wave function under the time evolution prescribed by $\hat{H}_\bullet(t)$. The lower row parallels the time evolution by the single-particle spectrum of $\hat{H}_\bullet(t)$, i.e., the spectrum of $H_\bullet(t)$. In the course of this chapter, we focus on the topological setup derived from the SSH chain (a) and compare it with the trivial setup of a simple tunneling barrier (c). The Majorana chain setup in (b) is described in \clubsuit Section 3.A in detail. The evaluation of the trivial setups in (c) and (d) is presented in Subsection 3.3.4.

3.3.1 Optimizing Transfer

We evaluate the propagator (3.32) numerically in the $2L$ -dimensional single-particle Hilbert space by expanding the time-ordered matrix exponential [289, 290]:

$$U_{\bar{w}_{\max}}(t) = \mathcal{T} \exp \left[-i \int_0^t ds H_{\text{bSSH}}(s) \right] \\ \stackrel{\text{def}}{=} \lim_{m \rightarrow \infty} \prod_{k=0}^m \exp \left[-i \frac{t}{m} H_{\text{bSSH}} \left(\frac{kt}{m} \right) \right] \quad 3.34a$$

$$\approx \prod_{k=0}^M \exp \left[-i \frac{t}{M} H_{\text{bSSH}} \left(\frac{kt}{M} \right) \right] \equiv \tilde{U}_{\bar{w}_{\max}}(t). \quad 3.34b$$

Note that the products here are *ordered*, with the factor for $k = 0$ to the right. For large but finite M , this yields practically useful approximations $\tilde{U}_{\bar{w}_{\max}}(t)$ for the time evolution operator. For all numerical results that follow, we increased the number of slices M until the time evolution became stable. Once $\tilde{U}_{\bar{w}_{\max}}(t)$ is known, arbitrary overlaps (as used, e.g., for the definition of $\{\mathcal{E}, \mathcal{O}, \varphi\}$) can be computed straightforwardly.

We start with qualitative results for the transfer with the SSH setup, shown in Figure 3.5 (a) for an optimized set of parameters τ and \bar{w}_{\max} . To this end, we plot the time evolution of the excitation density for an excitation that starts initially in the left edge mode \tilde{b}_c . From visual inspection, we find perfect transfer and decoupling of edge and bulk modes. We also plot the time-dependent single-particle spectrum of $\hat{H}_{\text{bSSH}}(t)$, which is mirror-symmetric with respect to zero energy (we set $\delta = 0$ for simplicity) due to particle-hole symmetry. The edge mode hybridization—responsible for the transfer—is clearly visible in the spectrum as temporary splitting of the otherwise degenerate edge mode eigenenergies. For the sake of completeness, we present the analogous results for the Majorana chain setup in Figure 3.5 (b). Due to its unitary equivalence (\clubsuit Subsection 3.A.2), its spectrum is identical to (a). The results for the non-topological setups are discussed below in Subsection 3.3.4.

The overall performance is quantified by \mathcal{O} , φ and \mathcal{E} , and depends on how close the protocol parameter \bar{w}_{\max} is to the critical value \bar{t} , the size of the system L , and the global timescale τ ; see Figure 3.6 (a) and (b) for a chain of length $L = 5$ where we plot $\{\mathcal{E}, \mathcal{O}, \varphi\}$ as function of τ and $\Delta\bar{w}_{\min} \equiv \bar{t} - \bar{w}_{\max}$. The edge weight \mathcal{E} (gray background tiles) equals 1 almost everywhere, except for very fast protocols and tiny bulk-edge gaps. We observe quite generally that for a smooth pulse shape like \mathcal{F} , the adiabatic bulk-edge decoupling is rather generically established in the topological setup. In Figure 3.6, the size of *colored* squares denotes the transfer \mathcal{O} , while the color accounts for the value of the phase φ accumulated during the transfer (measured in the rotating frame of the localized edge modes). We find several disjoint branches with $\mathcal{O} \approx 1$ corresponding to an increasing number of

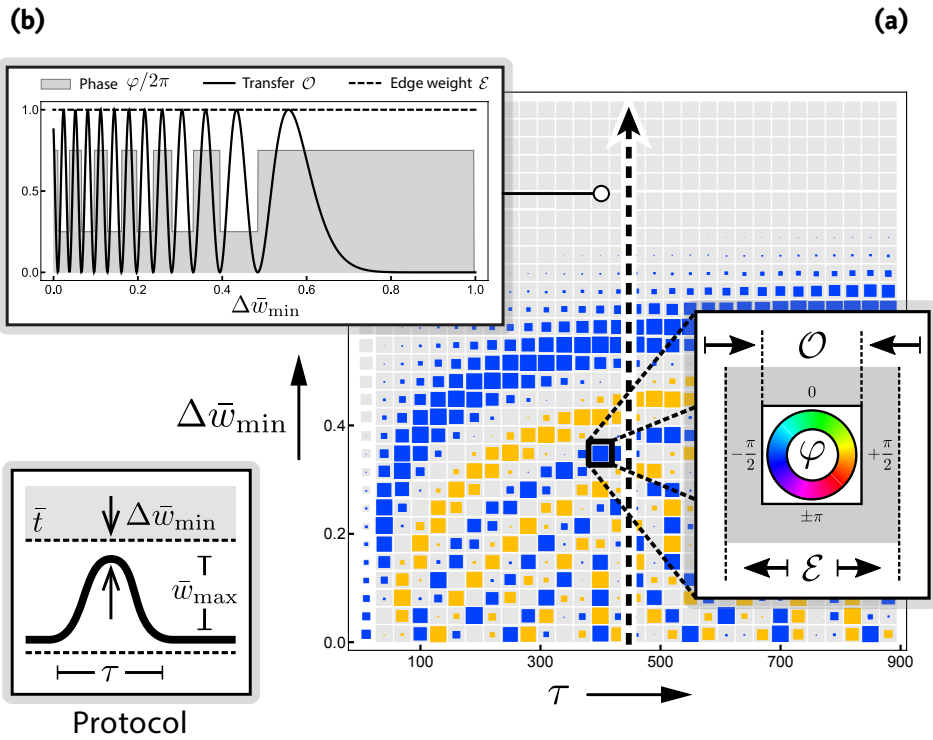
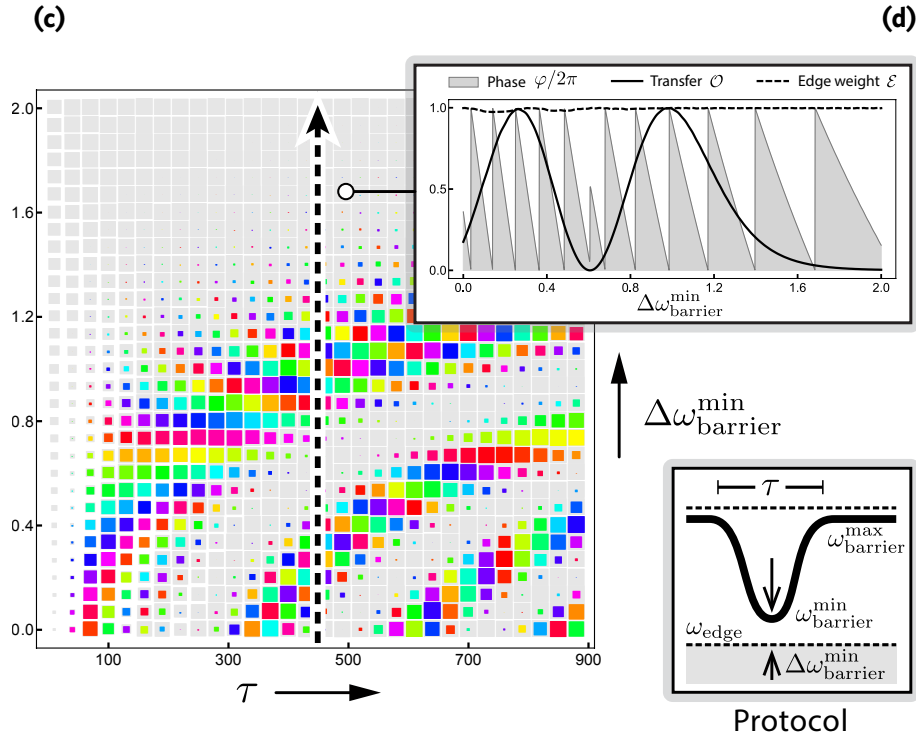


FIGURE 3.6 • State transfer (quantitative results). In (a) and (c) we plot the figures of merit for transfers driven by $\hat{H}_{\text{bSSH}}(t)$ and $\hat{H}_{\text{bB}}(t)$ in dependence of the protocol timescale τ and the distance from criticality, namely $\Delta \bar{w}_{\min} = \bar{t} - \bar{w}_{\max}$ for \hat{H}_{bSSH} and $\Delta \omega_{\text{barrier}}^{\min} = \omega_{\text{barrier}}^{\min} - \omega_{\text{edge}}$ for \hat{H}_{bB} . The diameter of the gray background squares encodes the edge weight \mathcal{E} ; a thinning of the gray background tiling therefore indicates a loss of adiabaticity. In the shown parameter regimes, however, the edge weight is almost everywhere close to unity as there is barely any loss to bulk excitations (except for regions of fast protocols close to criticality). \curvearrowright

round trips of the excitation; see Figure 3.6 (b). The outermost branch allows for the fastest and most robust transfer, and is therefore the desired parameter regime to perform quantum operations. However, the most striking property of this setup is a fixed phase φ accumulated during a transfer, i.e., $\varphi = \pm \frac{\pi}{2}$. The sign depends on the number of round trips and on the parity of the chain length L , see \clubsuit Section 3.C, \clubsuit Subsection 3.D.1 and particularly Subsection 3.3.2 below. This remarkable feature is a peculiarity of the PH symmetric topological setup and in general violated for other setups (see comparison in Subsection 3.3.4). In Subsection 3.3.2 below, we demonstrate that for the limiting case of a length- $L = 1$ chain, PH symmetry is responsible for fixing the transfer phase at $\pm \frac{\pi}{2}$.

As a concluding remark, note that there may be residual couplings $\bar{w}_{\text{res}} \ll \bar{w}_{\max}$ that cannot be switched off for $t < 0$ and $t > \tau$ such that the qubits cannot be completely decoupled before and after the pulse—with possibly detrimental effects on the overall quantum protocol. However, weak residual couplings \bar{w}_{res} (weak

RESULTS



↷ The diameter (color) of the colored squares encodes the transfer \mathcal{O} (phase φ) after the protocol reached its final state (φ is measured in the rotating frame of the localized edge modes). (a) shows results for a topological SSH setup of size $L = 5$. (c) shows the corresponding data for a trivial tunneling barrier setup of the same size. In (b) and (d) we plot \mathcal{O} , φ , and \mathcal{E} along the dashed slices in (a) and (c), respectively. Note that the phase is fixed for the topological setup: $\varphi = \pm \frac{\pi}{2}$. The results for the trivial setup in (c) and (d) are discussed in Subsection 3.3.4.

compared to \bar{t}) can be tolerable on the relevant timescales as they are exponentially suppressed with the qubit distance L in the topological phase, whereas *controlled* coupling is always possible for $\bar{w}_{\text{max}} \rightarrow \bar{t}$.

3.3.2 Symmetry Protection of the Transfer Phase

To understand why the particle-hole symmetry is responsible for the fixed transfer phase $\varphi = \pm \frac{\pi}{2}$, it is instructive to consider as a minimal model a chain of length $L = 1$, i.e., the local coupling of two adjacent modes b_l and b_r described by the time-reversal invariant Rabi Hamiltonian

$$\tilde{H}_{\text{Rabi}} = \begin{bmatrix} 0 & A \\ A & \omega \end{bmatrix} = A (|l\rangle\langle r| + |r\rangle\langle l|) + \omega |r\rangle\langle r| \quad 3.35$$

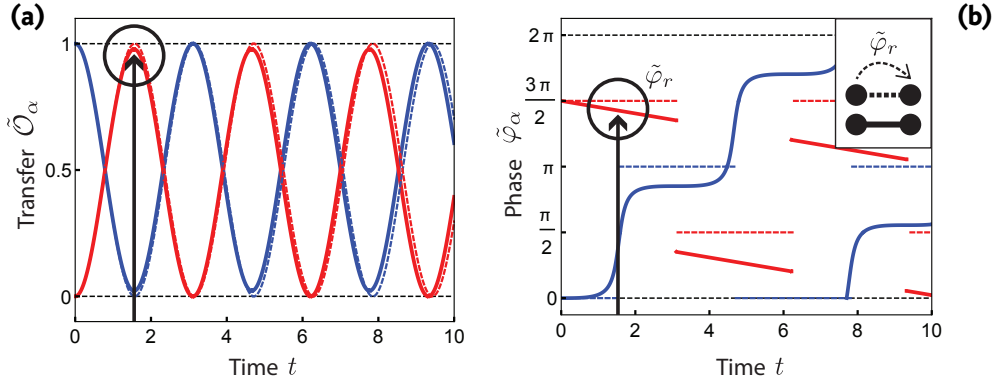


FIGURE 3.7 • Time evolution of a minimal model. (a) Population transfer $\tilde{\mathcal{O}}_l = |\langle l | \tilde{U}_{\text{Rabi}}(t) | l \rangle|^2$ (blue) and $\tilde{\mathcal{O}}_r = |\langle r | \tilde{U}_{\text{Rabi}}(t) | l \rangle|^2$ (red) of a simple Rabi model without detuning $\omega = 0$ (dashed) and with detuning $\omega = 0.3$ (solid), starting in the “left” mode $|l\rangle$ for coupling $A = 1$ as a function of time t . The first optimal transfer is slightly reduced and shifted in time for the PH breaking system with $\omega \neq 0$ (see circle). (b) The corresponding phases $\tilde{\varphi}_l$ (blue) and $\tilde{\varphi}_r$ (red) of the overlaps. Note that for PH symmetric setups, $\tilde{\varphi}_r = \frac{3}{2}\pi$ is fixed for the time of first optimal transfer (dashed line in circle). When PH symmetry is broken (here $\omega > 0$), the dynamical phase $e^{-i\frac{\omega}{2}t}$ induces a t - and ω -dependent phase shift, $\tilde{\varphi}_r = \frac{3}{2}\pi + \delta\tilde{\varphi}_r(\omega, t)$ (solid line in circle). The inset indicates that these results hold for both tunable (dashed) and fixed (solid) links of a network (see Figure 3.8).

where $A \in \{\bar{w}, \bar{t}\} \in \mathbb{R}$ and the local mode frequency (“detuning”) $\omega \neq 0$ breaks the PH symmetry U_C^{SSH} explicitly. The time evolution of (3.35) reads

$$\tilde{U}_{\text{Rabi}}(t) = \mathcal{T} \exp[-it\tilde{H}_{\text{Rabi}}] = \begin{bmatrix} \tilde{U}_{ll} & \tilde{U}_{lr} \\ \tilde{U}_{rl} & \tilde{U}_{rr} \end{bmatrix} \quad 3.36$$

with matrix elements¹⁰⁹

$$\tilde{U}_{ll} = \langle l | \tilde{U}_{\text{Rabi}}(t) | l \rangle = e^{-i\frac{\omega}{2}t} \left[\cos\left(\frac{\Omega}{2}t\right) + \frac{i\omega}{\Omega} \sin\left(\frac{\Omega}{2}t\right) \right] \equiv \sqrt{\tilde{\mathcal{O}}_l} e^{i\tilde{\varphi}_l} \quad 3.37a$$

$$\tilde{U}_{rl} = \langle r | \tilde{U}_{\text{Rabi}}(t) | l \rangle = e^{-i\frac{\omega}{2}t} \left[-\frac{2iA}{\Omega} \sin\left(\frac{\Omega}{2}t\right) \right] \equiv \sqrt{\tilde{\mathcal{O}}_r} e^{i\tilde{\varphi}_r} \quad 3.37b$$

and Rabi frequency $\Omega = \sqrt{4A^2 + \omega^2}$. The overlaps $\tilde{\mathcal{O}}_\alpha$ and phases $\tilde{\varphi}_\alpha$ for $\alpha = l$ (blue) and $\alpha = r$ (red) are plotted in Figure 3.7 for a PH symmetric (dashed) and PH breaking (solid) system. For a PH symmetric setup ($\omega = 0$), the phases are discrete, $\tilde{\varphi}_l = \pm\pi$ and $\tilde{\varphi}_r = \pm\frac{\pi}{2}$, and robust against (weak) variations of the coupling strength A . Note that for an excitation initially in b_l , $\tilde{\varphi}_r = \varphi$ denotes the transfer phase.

¹⁰⁹It is $\tilde{U}_{lr} = \tilde{U}_{rl}$ and \tilde{U}_{rr} equals \tilde{U}_{ll} up to the sign in the sum.

RESULTS

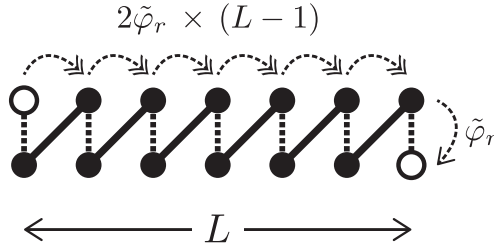


FIGURE 3.8 • Accumulation of transfer phases. Macroscopic transfers from one edge mode to the other can be thought of as concatenated single transfers, accumulating a total of $2L - 1$ transfer phases $\tilde{\varphi}_r$. If all $\tilde{\varphi}_r$ are kept fixed by PH symmetry, the total transfer phase $\varphi = L\pi + \frac{\pi}{2}$ is also fixed and only shifts in steps of π with L .

We conclude that PH symmetry entails perfect Rabi oscillations,

$$U_C^{\text{SSH}} \tilde{H}_{\text{Rabi}}^* (U_C^{\text{SSH}})^\dagger = -\tilde{H}_{\text{Rabi}}$$

$$\Rightarrow \tilde{U}_{\text{Rabi}}(t) = \begin{bmatrix} \cos(At) & -i \sin(At) \\ -i \sin(At) & \cos(At) \end{bmatrix}. \quad 3.38$$

By contrast, PH symmetry breaking ($\omega \neq 0$) renders $\tilde{\varphi}_{r,l}$ time- and ω -dependent due to the dynamical phase $e^{-i\frac{\omega}{2}t}$ and, in addition, varies the relative phase $\tilde{\varphi}_r - \tilde{\varphi}_l$ between both edge modes with ω and t , see Eq. (3.37a).

To make the transition to non-trivial chains of length $L > 1$, it is illustrative to think of the *macroscopic* transfer from the left to the right edge mode as a sequence of elementary transfers between adjacent bosonic modes b_I , see Figure 3.8. The accumulated phase for *PH symmetric* chains is then (modulo 2π)

$$\varphi = 2\tilde{\varphi}_r(L-1) + \tilde{\varphi}_r = (2L-1)\tilde{\varphi}_r = \frac{3}{2}(2L-1)\pi = L\pi + \frac{\pi}{2} \quad 3.39$$

which matches the numerical results of Subsection 3.3.1 and the findings of \clubsuit Subsection 3.D.1 [see Eq. (3.99)]. Breaking PH symmetry invalidates the conclusion of Eq. (3.39) because $\tilde{\varphi}_r \in [0, 2\pi)$ becomes unrestricted.

Remark

The detuning ω used above breaks the sublattice symmetry S and thereby the PH symmetry $C = TS$. However, there is another possibility to break C , namely by a violation of the time-reversal symmetry T . In this case, the hopping amplitudes $A \in \mathbb{C}$ become complex. But any non-trivial phase of A is added to the overall transfer phase φ , so that the latter again becomes variable (now depending on the unspecified phases of couplings $A \in \{\bar{w}, \bar{t}\}$ and not the unspecified mode frequencies $\omega \in \{\omega_i, \omega_{\bar{i}}\}$). We conclude that breaking the PH symmetry *always*

entails a random transfer phase φ . Conversely, if the PH symmetry is preserved, the transfer phase becomes discrete. We demonstrated this in Subsection 3.3.1 for the case when additionally time-reversal symmetry is present (class **BDI**). But PH symmetry can survive the breaking of time-reversal symmetry T if this is countered by an appropriate breaking of the sublattice symmetry S so that the product $C = TS$ is still a symmetry. This characterizes class **D** and we argue in Subsection 3.4.2 that even in this case (where purely imaginary hopping amplitudes are admissible) the transfer phase φ is discrete.

3.3.3 Scaling and Adiabaticity

An important aspect for quantum information processing is the scalability of the setup with growing separation L between the qubits. We identify the two relevant timescales of the transfer protocol: The inverse edge mode splitting $\Delta E_{\text{edge}}^{-1}$ determines the time for a state transfer between the two edge states, and second, the inverse of the bulk-edge separation $\Delta E_{\text{bulk}}^{-1}$ gives a lower bound on the protocol timescale due to the required adiabatic bulk-edge decoupling, recall Figure 3.3.

Scaling of Characteristic Energies

We start by considering the scaling of these energies when the topological phase transition $\bar{w} = \bar{t}$ is approached from the topological phase $\bar{w} < \bar{t}$. To this end, we derive an analytic expression for the characteristic polynomial $\det(H_{\text{bSSH}} - \lambda \mathbb{1})$. Its roots determine the spectrum $\{\lambda_i\}$ of H_{bSSH} via the equation

$$\frac{1 + \xi_{\bar{w}}(\lambda) - \eta_{\bar{w}}(\lambda)}{1 + \xi_{\bar{w}}(\lambda) + \eta_{\bar{w}}(\lambda)} = \left[\frac{1 - \xi_{\bar{w}}(\lambda) - \eta_{\bar{w}}(\lambda)}{1 - \xi_{\bar{w}}(\lambda) + \eta_{\bar{w}}(\lambda)} \right]^L \quad 3.40$$

with $\xi_{\bar{w}}(\lambda) = \lambda^2 - \bar{w}^2$ and

$$\eta_{\bar{w}}(\lambda) = \sqrt{[1 - (\lambda^2 - \bar{w}^2)]^2 - 4\bar{w}^2}. \quad 3.41$$

Here we set $\bar{t} = 1$ so that energies like λ and \bar{w} are measured in \bar{t} . We refer the reader to \clubsuit Subsections 3.D.2 and 3.D.7 for details of the derivation¹¹⁰.

Here, we are interested in the L -scaling of the two lowest positive eigenenergies λ_0 and λ_1 , which determine $\Delta E_{\text{edge}} = 2\lambda_0$ and $\Delta E_{\text{bulk}} = |\lambda_1 - \lambda_0|$. To this end, we define *rescaled* quantities (labeled by primes):

$$\lambda' \equiv L\lambda \quad \text{and} \quad \Delta \bar{w}' \equiv L\Delta \bar{w} = L(1 - \bar{w}) \quad 3.42$$

for $\bar{t} = 1$.

¹¹⁰Note that the diagonalization of H_{bSSH} (and for that matter, H_{SSH} and H_{MC}) is complicated by the *open* boundary conditions. For *periodic* boundaries, diagonalization is straightforward by a discrete Fourier transform.

RESULTS

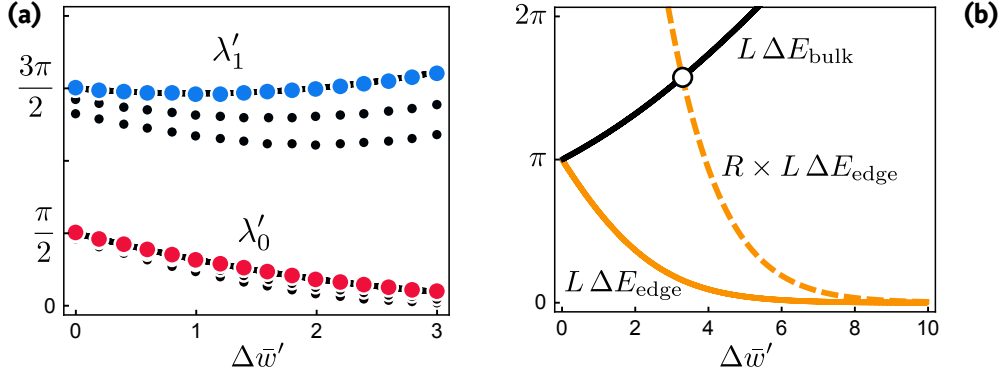


FIGURE 3.9 • Universal scaling. (a) Rescaled lowest eigenvalues $\lambda'_i = L\lambda_i$ ($i = 0, 1$) of H_{bSSH} as function of the rescaled coupling $\Delta\bar{w}' = L(1 - \bar{w})$. Solid lines denote solutions of equation (3.43), exact for $L \rightarrow \infty$; bullets denote finite-size results for $L = 5, 10$ (black) and $L = 200$ (red/blue). (b) Energy scales $L \Delta E_{\text{edge}} = 2\lambda'_0$ (solid yellow) and $L \Delta E_{\text{bulk}} = |\lambda'_1 - \lambda'_0|$ (solid black) for $L \rightarrow \infty$, calculated from the results in (a). Fixing the ratio $R = \Delta E_{\text{bulk}}/\Delta E_{\text{edge}}$ (here $R = 10$) determines $\Delta\bar{w}'$ via the intersection marked with a circle (here $\Delta\bar{w}' \approx 3.3$).

Rewriting Eq. (3.40) in terms of the primed quantities λ' and $\Delta\bar{w}'$, and taking the limit $L \rightarrow \infty$ on both sides, yields the transcendental equation

$$\frac{\Delta\bar{w}' - \sqrt{\Delta\bar{w}'^2 - \lambda'^2}}{\Delta\bar{w}' + \sqrt{\Delta\bar{w}'^2 - \lambda'^2}} = e^{-2\sqrt{\Delta\bar{w}'^2 - \lambda'^2}}. \quad 3.43$$

The lowest two positive solutions λ'_0 and λ'_1 of (3.43) determine the *asymptotics* of the relevant energies ΔE_{edge} and ΔE_{bulk} , namely

$$\Delta E_{\text{edge}} \sim \frac{2\lambda'_0}{L} \quad \text{and} \quad \Delta E_{\text{bulk}} \sim \frac{|\lambda'_1 - \lambda'_0|}{L} \quad \text{for} \quad \Delta\bar{w} = \frac{\Delta\bar{w}'}{L}, \quad 3.44$$

see Figure 3.9 (a) for a comparison with numerical finite-size results. Notably, both energies scale as L^{-1} if the critical point $\Delta\bar{w} = 0$ is approached with L^{-1} for $L \rightarrow \infty$; in particular, their ratio $R = \Delta E_{\text{bulk}}/\Delta E_{\text{edge}}$ saturates for large L . The gist of this calculation is that to keep a fixed ratio R of the two energy scales, it is necessary to approach the critical point as $\Delta\bar{w} = \bar{t} - \bar{w} \sim 1/L$. E.g., for $R = 10$ and $\bar{t} = 1$ one finds $1 - \bar{w} \approx 3.3/L$, see Figure 3.9 (b).

This result demonstrates that if one requires an adiabatic protocol $\bar{w}(t)$ with a fixed minimum ratio $R^{\text{min}} = \Delta E_{\text{bulk}}^{\text{min}}/\Delta E_{\text{edge}}^{\text{max}}$ at the minimum distance $\Delta\bar{w}_{\text{min}} = \bar{t} - \bar{w}_{\text{max}}$ from the critical coupling, then the time τ for the protocol scales as $\tau \sim \Delta E_{\text{edge}}^{-1} \sim L$ if the protocol parameter scales as $\Delta\bar{w}_{\text{min}} \sim L^{-1}$; see Figure 3.10 (a) and (b) for simulations. This corresponds to the optimal scaling achievable since the Lieb-Robinson bound predicts a finite propagation speed for information in systems with local interactions [291].

Adiabatic Bulk-Edge Decoupling

However, we still need to adiabatically decouple bulk from edge modes since losses to the bulk cannot be refocused in edge modes via global tuning of parameters. A common (and conservative) estimate for adiabaticity then reads

$$\tau \gtrsim (\Delta E_{\text{bulk}}^{\min})^{-2} \sim L^2 \quad 3.45$$

due to the vanishing of the bulk-edge separation with L^{-1} when $\Delta \bar{w}_{\min} \sim L^{-1}$. This condition is far from the (optimal) linear scaling that followed for the edge mode splitting above. We demonstrate in the following that a much better scaling is achievable by a rigorous estimate on the non-adiabatic losses.

To this end, we parametrize the time with $s = t/\tau$, $s \in [0, 1]$, and make the ansatz¹¹¹

$$\bar{w}(s) = \bar{w}_{\max} \cdot \mathcal{P}(s) = \left(1 - \frac{\Delta \bar{w}'_{\min}}{L}\right) \cdot \mathcal{P}(s) \quad 3.46$$

for the time dependency of the on-site coupling strength. Here, the generic pulse $\mathcal{P} : [0, 1] \rightarrow [0, 1]$ and its first derivative \mathcal{P}' vanish for $s \in \{0, 1\}$, and we fix $\mathcal{P}(1/2) = 1$. The single-particle Hamiltonian of the SSH setup can be written in the form

$$H_{\text{bSSH}}(s) = H_{\text{top}} + \bar{w}(s) H_{\text{triv}} \quad 3.47$$

where H_{top} (H_{triv}) describes the topological (trivial) dimerization of the chain with all couplings set to 1. In \S Section 3.E, we argue (based on results derived in \S Section 3.D) that the bulk-edge separation of Hamiltonian (3.47) can be lower-bounded by $\Delta \bar{w}$,

$$|\lambda_1 - \lambda_0| = \Delta E_{\text{bulk}} \geq \Delta \bar{w} = 1 - \bar{w}. \quad 3.48$$

Given these preliminary facts, we employ results of Ref. [292] where a rigorous upper bound

$$1 - \mathcal{E} \leq C^2 \quad 3.49$$

on the non-adiabatic losses $1 - \mathcal{E}$ is derived.

The upper bound C depends on the time of the evolution τ and the (generic) time-dependent Hamiltonian $H(s)$ via

$$C = \frac{2}{\tau} \left[\frac{\|H'(0)\|}{g^2(0)} + \frac{\|H'(1)\|}{g^2(1)} \right] + \frac{2}{\tau} \int_0^1 ds \left(\frac{\|H''(s)\|}{g^2(s)} + 7\sqrt{2} \frac{\|H'(s)\|^2}{g^3(s)} \right) \quad 3.50$$

where $\|\bullet\|$ is the operator norm, H' (H'') denotes the first (second) derivative with respect to s , and $g(s)$ is (half) the gap separating a submanifold of the spectrum from the rest. In the present case, it is $H(s) = H_{\text{bSSH}}(s)$, the submanifold of interest is given by the two edge modes, and the “rest” encompasses the bulk modes; therefore $2g(s) = |\lambda_1(s) - \lambda_0(s)| = \Delta E_{\text{bulk}}(s)$.

¹¹¹By a slight abuse of notation, we write $\bar{w}(s) = \bar{w}(t)$ for $s = t/\tau$, i.e., we label functions of real and dimensionless time with the same symbol as their argument specifies them unambiguously.

RESULTS

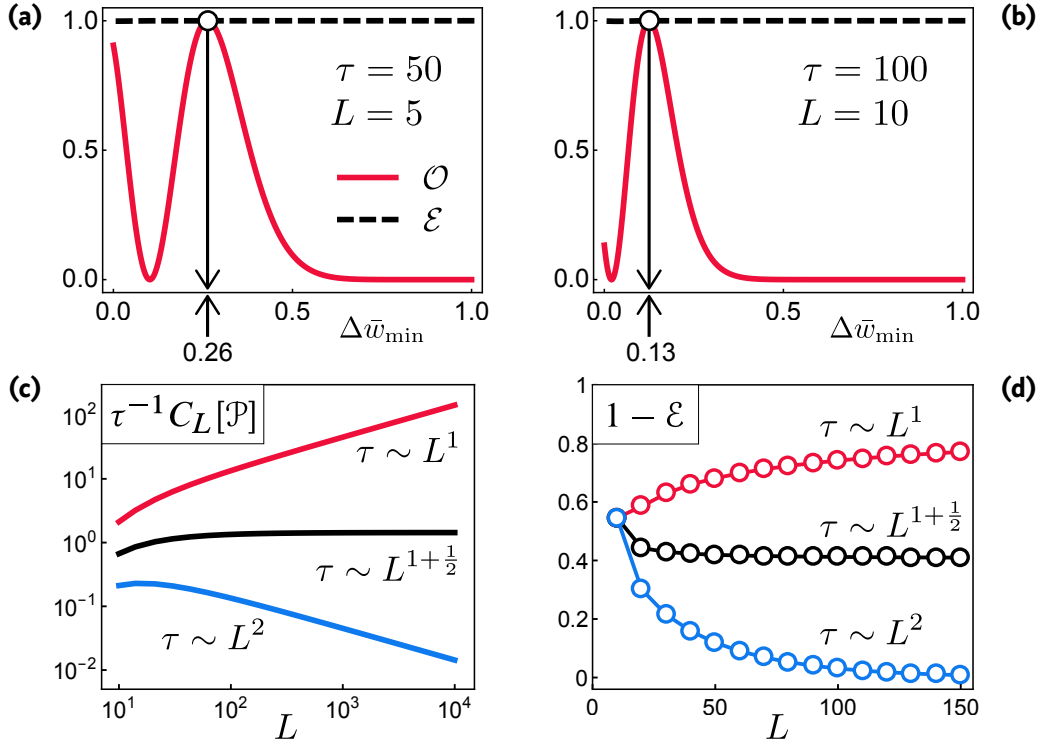


FIGURE 3.10 • Scaling of the transfer time (numerics). **(a)** Simulations of transfer fidelity \mathcal{O} (solid red) and edge weight \mathcal{E} (dashed black) for system size $L = 5$, protocol timescale $\tau = 50$ and pulse $\bar{w}(t) = (1 - \Delta\bar{w}_{\min}) \cdot \mathcal{F}(t)$ as function of $\Delta\bar{w}_{\min}$. Optimal transfer for fixed L and τ is found numerically for $\Delta\bar{w}_{\min} \approx 0.26$ with bulk loss $1 - \mathcal{E} \approx 1 \cdot 10^{-4}$. **(b)** The same for doubled size $L = 10$ and timescale $\tau = 100$. Now, optimal transfer is achieved for $\Delta\bar{w}_{\min} \approx 0.26/2 = 0.13$ with bulk loss $1 - \mathcal{E} \approx 2 \cdot 10^{-5}$. **(c)** Rigorous upper bounds $\tau^{-1}C_L[\mathcal{P}]$ for $\mathcal{P}(s) = \mathcal{F}(s) = \sin^2(\pi s)$ and $\tau = \tau_0 \cdot L^{1+\alpha}$ with $\alpha = 0, \frac{1}{2}, 1$ and $\tau_0 = 100$, $\Delta\bar{w}'_{\min} = 3.3$. A scaling $\tau \sim L^{1+\frac{1}{2}}$ yields constant bulk losses for $L \rightarrow \infty$. **(d)** Simulations of the bulk losses $0 \leq 1 - \mathcal{E} \leq 1$ for the parameters in (c) without tuning for optimal transfer. We find that the scaling follows the analytic upper bounds. Note that the loss was chosen large ($\sim 50\%$ for $L = 10$) for illustrative purposes and can be controlled via τ_0 (here $\tau_0 = 1, 0.3, 0.1$ for $\alpha = 0, \frac{1}{2}, 1$).

Merging Eq. (3.50) with the structure of our Hamiltonian (3.47), its time dependence (3.46), and the bulk-edge separation (3.48), yields the upper bound on the non-adiabatic bulk losses

$$1 - \mathcal{E} \leq \left(\frac{C_L[\mathcal{P}]}{\tau} \right)^2, \quad (3.51)$$

where

$$C_L[\mathcal{P}] \equiv \int_0^1 ds \frac{C_1 |\mathcal{J}''|}{(\varepsilon_L + \mathcal{J})^2} + \int_0^1 ds \frac{C_2 |\mathcal{J}'|^2}{(\varepsilon_L + \mathcal{J})^3} \quad (3.52)$$

with $\mathcal{J} \equiv 1 - \mathcal{P}$, $C_{1,2}$ numerical constants, and $\varepsilon_L = \Delta \bar{w}'_{\min}/(L - \Delta \bar{w}'_{\min})$. Note that $\mathcal{J}(1/2) = 0$ and $\varepsilon_L \sim L^{-1}$ such that $C_L[\mathcal{P}]$ *diverges* for $L \rightarrow \infty$ in general. In order to bound the bulk losses in Eq. (3.51), the scaling of τ has to match the scaling of $C_L[\mathcal{P}]$ for $L \rightarrow \infty$. A more detailed derivation of (3.52) and the following results is presented in \clubsuit Section 3.E.

For the pulse $\mathcal{P}(s) = \mathcal{F}(s) = \sin^2(\pi s)$ used in this chapter, we find $C_L[\mathcal{F}] \sim L^{1+\frac{1}{2}}$ so that a scaling of $\tau \sim L^{1+\frac{1}{2}}$ is necessary for adiabatic bulk-edge decoupling in the limit of long chains, see Figure 3.10 (c). This beats the quadratic scaling expected from the minimal gap $\Delta E_{\text{bulk}}^{\min}$. Unfortunately, the optimal scaling $\tau \sim L$ allowed by the Lieb-Robinson bound *cannot* be reached by the unoptimized¹¹² pulse \mathcal{F} . Note that *prima facie* this result applies to an *upper bound* of the bulk losses and not the bulk losses themselves—the true losses could still be bounded with only linear scaling $\tau \sim L$. However, numerical simulations for various scalings of τ reveal that they indeed follow the prescribed scaling of the rigorous upper bounds, see Figure 3.10 (d).

One can do better, though: In \clubsuit Section 3.E we prove that there is a sequence of polynomial pulses \mathcal{P}_n , characterized by

$$\left. \frac{d^m}{ds^m} \right|_{s=1/2} [1 - \mathcal{P}_n(s)] = 0 \quad \text{for all } m < n, \quad 3.53$$

such that $C_L[\mathcal{P}_n] \sim L^{1+\frac{1}{n}}$ for $n \geq 2$ even integers. Thus the scaling can be drastically improved by pulse optimization so that linear scaling can be approached to an arbitrary degree. However, the coefficients in $C_L[\mathcal{P}_n]$ grow with n such that there is a payoff between scaling and offset. In practice, one may even benefit from pulses with poor scaling (like \mathcal{F}) if only chains of a specific length are relevant. The problem of topological state transfer then becomes a playground for *quantum optimal control* [293, 294], a field of active research which we will not dwell on here.

3.3.4 Benchmarking Against Trivial Setups

To unveil the characteristic features of the topological setup, we contrast it with two similar but topologically trivial networks; recall Figure 3.4 (c) and (d) and their description in Subsection 3.2.1.

Arguably the simplest approach to transfer excitations between a distinct pair of modes is based on a chain of initially decoupled modes at fixed frequency $\omega_I \equiv \bar{\omega}$ and a uniform tuning of all couplings

$$w_i(t) = t_i(t) = \bar{t}(t) \equiv \bar{t}_{\max} \mathcal{F}(t) \quad \text{for all } i. \quad 3.54$$

¹¹²We chose the pulse $\mathcal{F}(s) = \sin^2(\pi s)$ because it performs reasonably well and is easy to implement numerically; no rigorous optimization procedure was used.

This scheme employs free bulk propagation of the initially localized edge modes and is described by $\hat{H}_{\text{bp}}(t)$ [Figure 3.4 (d)]. As demonstrated in Figure 3.5 (d), this approach *fails* to relocalize and capture the excitation at the opposite edge due to the dispersive propagation via bulk modes; to succeed, such a protocol would require either fine-tuning of the pulse shape via optimal control and/or local addressability of all couplings within the network. In this light, $\hat{H}_{\text{bp}}(t)$ is *not* competitive against the topological setup and we exclude it from our discussions henceforth.

A more sophisticated approach mimics the presence of localized edge modes by a large tunnel barrier: The two modes at the edge have fixed frequency $\omega_1 = \omega_{\bar{L}} = \omega_{\text{edge}} = \text{const}$, and are separated from each other by a “potential barrier” of modes with tunable frequencies $\omega_{\text{barrier}}(t)$ and fixed couplings $\bar{t} = \bar{w}$ in between. We introduced this Hamiltonian previously as $\hat{H}_{\text{bb}}(t)$ and sketched the corresponding network in Figure 3.4 (c). In analogy to the topological setup, this network exhibits exponentially localized edge modes. Again, transfer is achieved by lowering the excitation gap to the bulk modes, which allows for tunneling between the edges. The protocol of this scheme reads

$$\omega_{\text{barrier}}(t) = \omega_{\text{barrier}}^{\text{max}} + (\omega_{\text{barrier}}^{\text{min}} - \omega_{\text{barrier}}^{\text{max}}) \cdot \mathcal{F}(t) \quad 3.55$$

where $\omega_{\text{barrier}}^{\text{max}} \gg \omega_{\text{edge}}$ will be kept fixed and $\omega_{\text{barrier}}^{\text{min}} > \omega_{\text{edge}}$ is a tunable protocol parameter (in addition to the pulse length τ); this defines $\hat{H}_{\text{bb}}(t)$.

As shown in Figure 3.5 (c), this tunneling approach still allows for almost perfect transfer, given optimal parameters and long times. However, the *qualitative* comparison in Figure 3.6 (c) shows that the trivial tunneling approach requires longer timescales for the protocol to succeed, and is more sensitive to bulk losses [compare the gray tiles measuring \mathcal{E} in (a) and (b) for $\tau \lesssim 100$]. In general, the adiabatic decoupling is much harder to achieve with $\hat{H}_{\text{bb}}(t)$ than with $\hat{H}_{\text{bSSH}}(t)$, as the plots of \mathcal{E} along the dashed cuts in Figure 3.6 (b) and (d) reveal.

The most striking difference, however, is the *phase* accumulated during the transfer: for the trivial setup, it is highly sensitive to both parameters $\omega_{\text{barrier}}^{\text{min}}$ and τ . This is expected for a generic adiabatic protocol and is in stark contrast to the topological setup (recall Subsection 3.3.1). The reason for this qualitative difference is rooted in the PH symmetry of the SSH setup (as discussed in Subsection 3.3.2) which gives rise to the symmetric band structure depicted in Figure 3.5 (a), as opposed to the asymmetric band structure of the barrier setup in Figure 3.5 (c). In consequence, we find that even for the *ideal*, topologically trivial setup, adiabatic protocols are handicapped as the sensitivity of the transfer phase increases for longer chains: a transfer preserving quantum coherence requires fine-tuning of the shape of the control pulse. This effect becomes even more drastic in the presence of disorder (see Subsection 3.3.5 and ✨ Section 3.C).

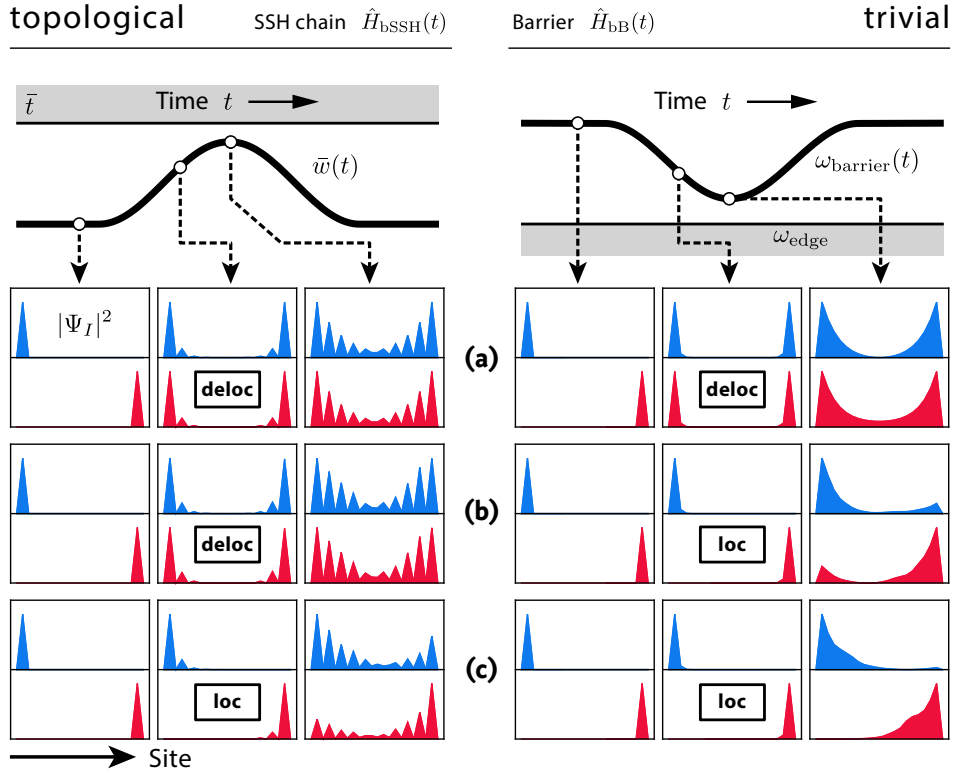


FIGURE 3.11 • Edge mode localization. We show the spatial amplitudes $|\Psi_I|$ of the two edge modes (blue & red) at three different times during the protocols of the SSH setup $\hat{H}_{\text{SSH}}(t)$ (left) and the barrier setup $\hat{H}_{\text{bB}}(t)$ (right) for **(a)** no disorder, **(b)** PH symmetric disorder, and **(c)** PH breaking disorder. Note the (de-)localization of the edge modes for PH symmetric disorder in (b). For the disordered setups, a random but typical realization of the network was selected.

3.3.5 Effects of Disorder and Symmetry Protection

The unique features of the topological setup stand out even more in the presence of disorder and/or imperfections in the preparation of the network. Here we focus on *quenched* disorder on the timescales of the transfer. To this end, disorder on modes and couplings is described as Gaussian noise with dimensionless standard deviation p detuning the parameters in the Hamiltonian from site to site, e.g., for the on-site hopping we have

$$\langle\langle w_i \rangle\rangle = \bar{w} \quad \text{and} \quad \langle\langle w_i^2 - \bar{w}^2 \rangle\rangle = p^2 \bar{w}^2 \quad 3.56$$

with $\langle\langle \bullet \rangle\rangle$ the disorder average and typically $p \ll 1$. In the following, two classes of disorder will be of interest:

- *PH symmetric* disorder affects only mode couplings (w_i and t_i), but assumes perfectly uniform mode frequencies ($\omega_I \equiv \delta$); recall condition (3.20).

RESULTS

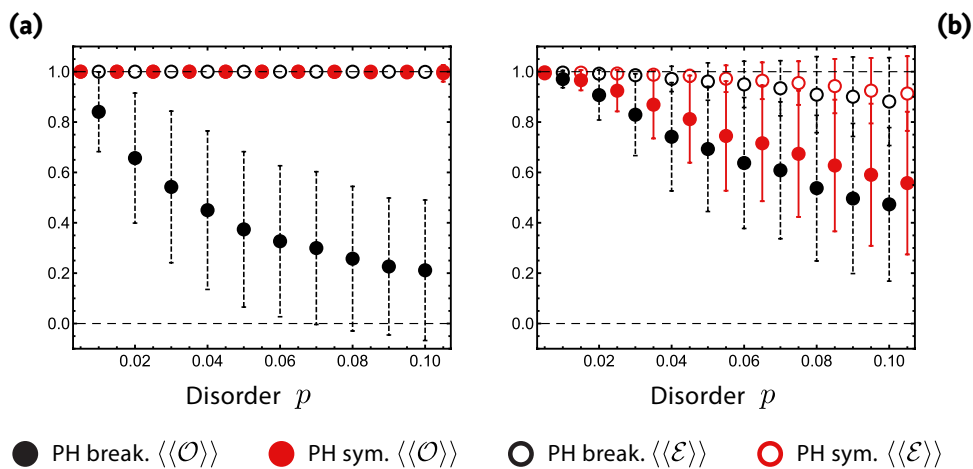


FIGURE 3.12 • Effects of disorder (numerics). We show the average transfer $\langle\langle\mathcal{O}\rangle\rangle$ (bullets) and edge weight $\langle\langle\mathcal{E}\rangle\rangle$ (circles) for PH breaking (black) and symmetric (red) disorder in the **(a)** topological and **(b)** trivial setup, respectively. The averages are computed from $N = 1000$ realizations for a chain of length $L = 5$ with an adjustment of τ for every single disorder realization to optimize transfer. The error bars denote one standard deviation of the sample. Note that the markers for $\langle\langle\mathcal{O}\rangle\rangle$ and $\langle\langle\mathcal{E}\rangle\rangle$ coincide for PH symmetric disorder in (a).

→ By contrast, *PHbreaking* disorder affects both mode couplings and frequencies, that is, ω_I becomes randomly distributed just like w_i and t_i . For simplicity, we use the same dimensionless standard deviation p for both mode couplings and frequencies.

For the topological *trivial* setup described by $\hat{H}_{\text{bb}}(t)$, both types of disorder give rise to Anderson localization [96] of the “artificial” edge modes, see Figure 3.11 (a-c). But the transfer protocol relies on the hybridization of the edge modes, which is thwarted by Anderson localization. As a consequence, disorder leads to a significant reduction of transfer fidelity and increased bulk losses, Figure 3.12 (b). In addition, the phase φ accumulated during the transfer strongly varies for each disorder realization; more details on this aspect are given in \clubsuit Section 3.C.

By contrast, for the topological SSH setup $\hat{H}_{\text{SSH}}(t)$, *PH symmetric* disorder respects the protecting symmetry (3.20). Then, Anderson localization of the edge modes is forbidden by a topological obstruction [21, 95, 97] and the required overlap between the two edge modes can be established, see Figure 3.11 (b). As a consequence, the transfer can still be performed perfectly with a fixed phase. Whereas transfer phase $\varphi = \pm \frac{\pi}{2}$ and edge weight $\mathcal{E} \approx 1$ are unaffected by (weak) PH symmetric disorder, optimizing the transfer fidelity $\mathcal{O} \approx 1$ makes it necessary that for each disorder realization the transfer time τ of the protocol is adjusted. In an experimental setup this corresponds, for example, to imperfections in sample preparation which can be overcome by calibrating the transfer protocol beforehand.

Finally, and similar to the trivial setup above, *PH breaking* disorder results in Anderson localization of the edge modes [Figure 3.11 (c)] and thereby a significant reduction of transfer fidelity, see Figure 3.12 (a). It is remarkable, however, that despite the breaking of PH symmetry, the adiabatic bulk-edge decoupling is still much better than for the trivial setup [certified by $\mathcal{E} \approx 1$ in Figure 3.12 (a)].

3.4 Application & Generalization

After the introduction of the SSH-based topological state transfer in Section 3.2 and the study of its features in Section 3.3, here we will contrive a minimal setup for the application of a controlled-phase gate on two remote qubits, see Subsection 3.4.1. Furthermore, we comment on the possibility to couple more than two qubits in a two-dimensional grid of dimerized modes, see Subsection 3.4.2.

3.4.1 Controlled-Phase Gate

As an application, we demonstrate how the proposed topological state transfer—protected by PH symmetry—can be employed for a controlled-phase (CP) gate between two remote qubits that are coupled to the local edge modes of the SSH network.

The protocol for a CP gate between a target qubit T and a control qubit C is based on a well-known scheme that makes use of auxiliary levels [295]. We focus on the setup shown in Figure 3.3 of Section 3.1: Each qubit T/C is coupled to its dedicated edge mode $\tilde{b}_{T/C}$ of the SSH setup (a) and realized by a three-level system (b) with auxiliary level $|a\rangle_{T/C}$. The coupling Hamiltonian between the qubits and their adjacent edge modes is given by Eq. (3.10), namely

$$\hat{H}_T(t) = g_T(t) \left[\tilde{b}_T^\dagger |a\rangle\langle 1|_T + \tilde{b}_T |1\rangle\langle a|_T \right] \quad 3.57a$$

$$\hat{H}_C(t) = g_C(t) \left[\tilde{b}_C^\dagger |1\rangle\langle a|_C + \tilde{b}_C |a\rangle\langle 1|_C \right]. \quad 3.57b$$

Note that the qubit operators in \hat{H}_C and \hat{H}_T differ, qualifying T as the target and C as the control qubit¹¹³. Together with the network Hamiltonian $\hat{H}_{\text{bSSH}}(t)$ that governs the mode couplings, this describes the setup completely. Then, the full protocol for the CP gate follows the procedure in Eq. (3.11), that is,

$$\mathcal{U}_{\text{CP}} = \Pi_T \circ T_{C \leftrightarrow T} \circ \Pi_C^2 \circ T_{C \leftrightarrow T} \circ \Pi_T. \quad 3.58$$

¹¹³This is actually an artifact of our implementation since the abstract CP gate is symmetric under qubit exchange, see Eq. (3.67).

APPLICATION & GENERALIZATION

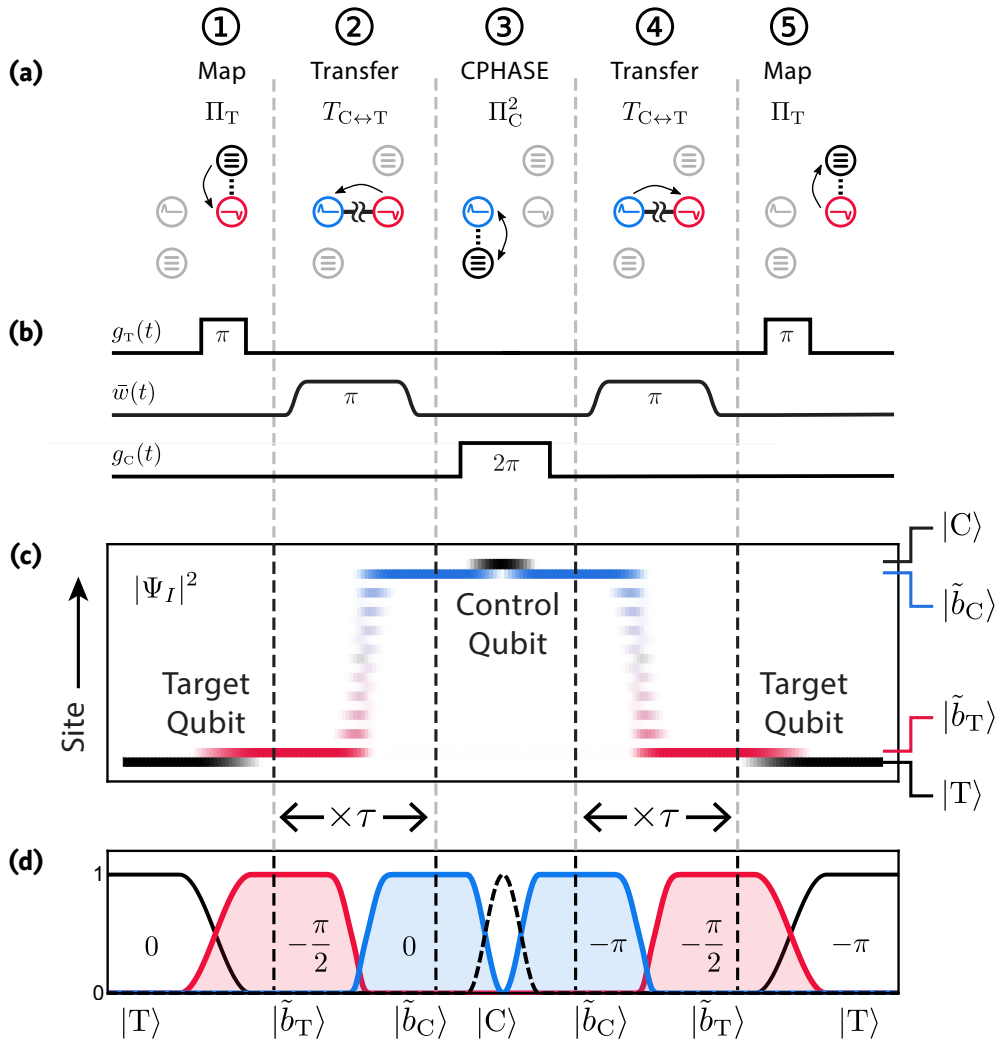


FIGURE 3.13 • CP gate—Pulse sequence & Results. (a) Schematic illustration of the five steps needed to perform the CP gate \mathcal{U}_{CP} (3.58) on two remote qubits, see setup in Figure 3.3. (b) The complete pulse sequence consisting of two π -pulses Π_T to map the target qubit to and from edge mode \tilde{b}_T , a 2π -pulse Π_C^2 to perform the actual CP gate, and two state transfer pulses $T_{C\leftrightarrow T}$. (c) Numerical single-particle evolution for the two-qubit basis state $|1\rangle_C|1\rangle_T$ for a chain of length $L = 10$. The density plot encodes the squared single-particle amplitude where the upper and lower two rows correspond to the states $|C\rangle/|\tilde{b}_C\rangle$ and $|\tilde{b}_T\rangle/|T\rangle$, respectively; see the description in the text. (d) Square of the absolute value of the overlaps with $|T\rangle$ (solid black), $|\tilde{b}_T\rangle$ (solid red), $|\tilde{b}_C\rangle$ (solid blue), and $|C\rangle$ (dashed black). The relative phases with respect to the target qubit are shown as insets. Note that the scales for the Rabi pulses and the topological state transfer differ by a factor of τ .

To extend our motivation in Section 3.1, here we provide *explicit* implementations of the unitaries in (3.58). In particular,

$$T_{C \leftrightarrow T} = \mathcal{T} \exp \left[-i \int_0^\tau dt \hat{H}_{\text{bSSH}}(t) \right] \quad 3.59$$

describes the topological state transfer with appropriate choices for \bar{w}_{max} and τ . This is the crucial part as it utilizes our findings of this chapter. The π -pulses Π_C and Π_T are described by

$$\Pi_\alpha = \mathcal{T} \exp \left[-i \int_0^{T_\alpha} dt \hat{H}_\alpha(t) \right] \quad 3.60$$

for $\alpha \in \{T, C\}$ and $\int_0^{T_\alpha} g_\alpha(t) dt = \frac{\pi}{2}$. The protocol (3.58), realized by (3.59) and (3.60), is described below; see Figure 3.13 for an illustration of the pulse sequence and numerical results. For the sake of simplicity, we introduce the following notation used in the text and the description of Figure 3.13:

$$|x\rangle_C |y\rangle_T \equiv \overbrace{|x\rangle_C |y\rangle_T}^{\text{Qubits}} \otimes \overbrace{|0, \mathbf{0}, 0\rangle}^{\text{Network}}, \quad 3.61a$$

$$|\tilde{b}_C\rangle \equiv |1\rangle_C |a\rangle_T \otimes |1, \mathbf{0}, 0\rangle, \quad 3.61b$$

$$|\tilde{b}_T\rangle \equiv |1\rangle_C |a\rangle_T \otimes |0, \mathbf{0}, 1\rangle, \quad 3.61c$$

$$|T\rangle \equiv |1\rangle_C |1\rangle_T \otimes |0, \mathbf{0}, 0\rangle, \quad 3.61d$$

$$|C\rangle \equiv |a\rangle_C |a\rangle_T \otimes |0, \mathbf{0}, 0\rangle. \quad 3.61e$$

Here, $|1, \mathbf{0}, 0\rangle \equiv \tilde{b}_C^\dagger |\mathbf{0}\rangle$ and $|0, \mathbf{0}, 1\rangle \equiv \tilde{b}_T^\dagger |\mathbf{0}\rangle$ denotes states of the network occupied by a single excitation in an edge mode. $x, y \in \{0, 1\}$ encode the states of the qubits.

We begin our discussion with the observation that the full sequence \mathcal{U}_{CP} leaves the states $|0\rangle_C |0\rangle_T$ and $|1\rangle_C |0\rangle_T$ invariant because there are no excitations in the network [here the difference of Eq. (3.57a) and Eq. (3.57b) is crucial]. On the other hand, for $|0\rangle_C |1\rangle_T$ and $|1\rangle_C |1\rangle_T$ the first π -pulse Π_T on the target qubit maps the state $|1\rangle_T$ to a bosonic excitation in the right edge mode \tilde{b}_T with the phase $-\frac{\pi}{2}$:

$$|x\rangle_C |1\rangle_T \otimes |0, \mathbf{0}, 0\rangle \xrightarrow{\Pi_T} -i |x\rangle_C |a\rangle_T \otimes |0, \mathbf{0}, 1\rangle. \quad 3.62$$

It is important that this operation is performed slowly compared to the energy gap to bulk excitations in the SSH chain: Then, energy conservation allows one to only address the coupling to the edge states and suppress admixture of bulk excitations¹¹⁴.

The subsequent transfer of the excitation to the left edge mode,

$$|x\rangle_C |a\rangle_T \otimes |0, \mathbf{0}, 1\rangle \xrightarrow{T_{C \leftrightarrow T}} i(-1)^L |x\rangle_C |a\rangle_T \otimes |1, \mathbf{0}, 0\rangle, \quad 3.63$$

¹¹⁴This is why we introduce $g_\alpha(t)$ and do not just apply a *static* Hamiltonian for time T_α . However, in the simplified setting presented here, we omit residual couplings to bulk modes and there is no restriction on $g_\alpha(t)$ except $\int_0^{T_\alpha} g_\alpha(t) dt = \frac{\pi}{2}$.

implies an additional phase $\frac{\pi}{2} + L\pi$. The full Rabi cycle Π_C^2 provides a phase π if and only if the control qubit is in state $|1\rangle_C$ (recall that the logical qubit states $|0\rangle_{T/C}$ decouple completely from the dynamics):

$$|x\rangle_C|a\rangle_T \otimes |1, \mathbf{0}, 0\rangle \xrightarrow{\Pi_C^2} (-1)^x |x\rangle_C|a\rangle_T \otimes |1, \mathbf{0}, 0\rangle \quad 3.64$$

for $x \in \{0, 1\}$. The subsequent transfer back $T_{C \leftrightarrow T}$ and the π -pulse Π_T provide additional phases $\frac{\pi}{2} + L\pi$,

$$|x\rangle_C|a\rangle_T \otimes |1, \mathbf{0}, 0\rangle \xrightarrow{T_{C \leftrightarrow T}} i(-1)^L |x\rangle_C|a\rangle_T \otimes |0, \mathbf{0}, 1\rangle, \quad 3.65$$

and $-\frac{\pi}{2}$,

$$|x\rangle_C|a\rangle_T \otimes |0, \mathbf{0}, 1\rangle \xrightarrow{\Pi_T} -i |x\rangle_C|1\rangle_T \otimes |0, \mathbf{0}, 0\rangle. \quad 3.66$$

Therefore, the full protocol implements the mapping $|1\rangle_C|1\rangle_T \rightarrow -|1\rangle_C|1\rangle_T$ while all orthogonal states remain invariant. Given quantum coherence during the protocol, this realizes a controlled-phase gate with phase π :

$$\mathcal{U}_{CP}|x\rangle_C|y\rangle_T = (-1)^{xy} |x\rangle_C|y\rangle_T. \quad 3.67$$

A full numerical time evolution for the state $|1\rangle_C|1\rangle_T$ is shown in Figure 3.13 (c) and (d), confirming the above argumentation.

Finally, we point out that the linearity of the network¹¹⁵ implies that the transfer takes place for each excitation of edge modes independently. I.e., if $|n_C, n_T\rangle$ denotes the state with n_C excitations in the left edge mode \tilde{b}_C and n_T excitations in the right edge mode \tilde{b}_T , the transfer operation $T_{C \leftrightarrow T}$ implements the mapping $|n_C, n_T\rangle \rightarrow (\pm i)^{n_C + n_T} |n_T, n_C\rangle$ (for even/odd L). This observation immediately implies that the unitary operation $\mathcal{U}_{\text{SWAP}}$ in Eq. (3.12) of Section 3.1 swaps the qubits.

3.4.2 Extension to 2D Networks of Coupled Qubits

An important aspect of the one-dimensional SSH setup considered so far is its symmetry class **BDI**¹¹⁶ which gives rise to a \mathbb{Z} topological invariant. This allows us to extend the scheme to two-dimensional setups by placing several SSH chains parallel to each other and adding symmetry-conserving couplings between them, see Figure 3.14 (a) for a possible realization on a honeycomb lattice. As long as these couplings are real and respect the sublattice symmetry, the setup is still topologically protected and each chain endpoint carries an edge mode (in this case, the topological invariant counts the pairs of such edge modes).

¹¹⁵The bosonic excitations in our network do not interact.

¹¹⁶With time-reversal symmetry $T^2 = +\mathbb{1}$ due to the real hopping amplitudes w_i/t_i , the sublattice symmetry S due to the bipartite network, and consequently the PH symmetry $C = TS$ with $C^2 = +\mathbb{1}$.

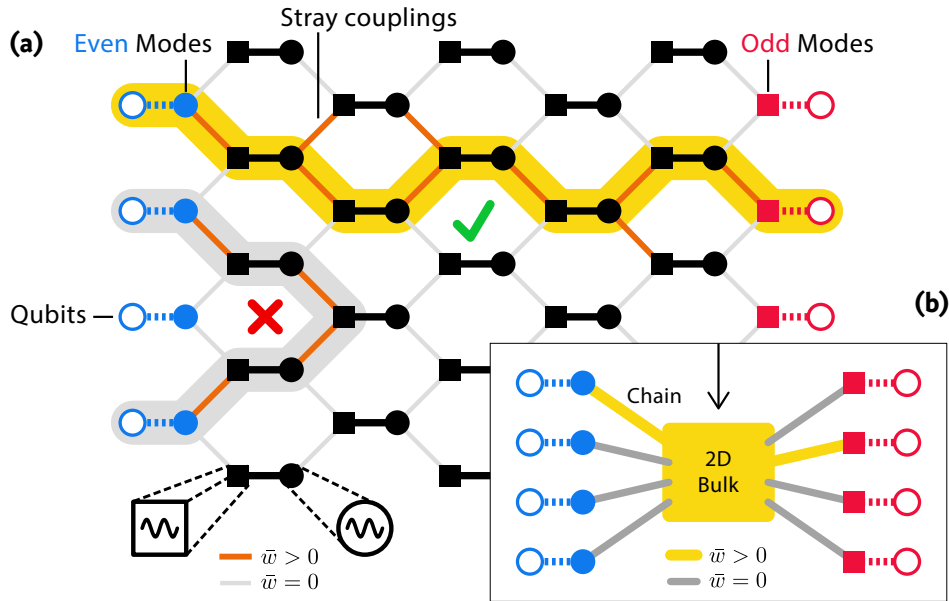


FIGURE 3.14 • Coupling many qubits. (a) Possible 2D generalization of the network on a dimerized honeycomb lattice. Scattering-free transport is guaranteed by topological protection which requires a sublattice symmetry. The latter is realized by directly coupling only “even” (filled circles) with “odd” modes (filled squares). Direct state transfer between qubits (empty circles) of different/same parities is possible/impossible, illustrated by the bold yellow/gray path. Weak stray couplings in the bulk (shown for the upper path) are not detrimental to the transfer fidelity. (b) Instead of locating the edge modes (filled colored circles and squares) with their qubits at the boundary, emanating SSH chains can be used to separate the qubits from each other and the 2D bulk. There is no need to trace out a specific path as in (a), only a weak addressability of the individual chains is sufficient so that the couplings of the bulk can be tuned globally.

Due to the representation of the sublattice symmetry

$$U_C^{\text{SSH}} = \mathbb{1}_{L \times L} \otimes \begin{bmatrix} 1 & 0 \\ 0 & -1 \end{bmatrix}, \quad 3.68$$

there are two types (or *parities*) of modes—“even” and “odd” ones—depending on whether they transform with +1 or −1 under $S = U_C^{\text{SSH}}$. In \clubsuit Section 3.B we prove that edge mode pairs of *different* parities can be hybridized if paths of symmetry-conserving couplings $\bar{w} > 0$ connect them. This allows for efficient state transfer between arbitrary pairs of edge modes (of different parity) by tuning the couplings along a path that resembles the one-dimensional SSH setup; this is illustrated in Figure 3.14 (a). Because of the bulk gap (due to the complete dimerization), this procedure is very robust and couplings that deviate from the desired path (“stray couplings”) have no detrimental effect on the state transfer, as long as they are weak, respect the symmetries, and do not couple to other edge

modes. The last requirement can be guaranteed by a modification of the setup so that qubits and edge modes are relocated at the end of one-dimensional chains that emanate from the 2D bulk, see Figure 3.14 (b). Remarkably, this setup allows for an enhancement of the edge mode overlap by tuning the couplings of the 2D bulk *globally* instead of tracing out a particular path that connects the qubits. In this setup, the minimal experimental requirement is the individual addressability of each branch that connects an edge mode to the 2D bulk. Since the edge modes can now be separated from each other, this constraint is very weak, and in general already satisfied by the requirement of local gate operations on the qubit.

There is a hitch: Coupling edge modes of the *same* parity is obstructed by the sublattice symmetry, as indicated by the lower path in Figure 3.14 (a). The reason is that *any* network Hamiltonian \tilde{H} that satisfies the sublattice symmetry $S\tilde{H}S^{-1} = -\tilde{H}$ has (at least) $|n^+ - n^-|$ exact zero-energy modes, where n^\pm denotes the number of even (+) and odd (-) modes; this is proven in \clubsuit Section 3.B. If two modes of the *same* parity are coupled, the relevant part of the network consists of dimerized pairs of opposite parity and two “excess” modes of the same parity (the edge modes). Therefore $|n^+ - n^-| = 2$ guarantees the existence of two zero modes at any time [even if the two modes are coupled as in Figure 3.14 (a)]; this precludes the hybridization of the edge modes and makes state transfer impossible.

However, the implementation of an exchange of qubits via $\mathcal{U}_{\text{SWAP}}$ [recall Eq. (3.12)] facilitates the application of, e.g., the controlled-phase gate \mathcal{U}_{CP} between *any* pair of qubits: If the two qubits couple to edge modes of *different* parities, one can directly perform the CP gate between them. Conversely, if the qubits couple to edge modes of the *same* parity, one first performs an exchange $\mathcal{U}_{\text{SWAP}}$ with an arbitrary qubit of the opposite parity, applies the CP gate, and maps the qubit back by another exchange.

To conclude this part, let us briefly comment on the symmetries and their ramifications for general linear networks of bosonic modes (including the one-dimensional SSH setup as a special case): In this section (and throughout this chapter, actually) we worked with networks compliant with the strict symmetry requirements of **BDI**: Real couplings lead to time-reversal symmetry T and the bipartite coupling structure to the sublattice symmetry S . Combined these yield the PH symmetry $C = TS$. Since $T^2 = +1 = C^2$, we end up in the symmetry class **BDI** with \mathbb{Z} topological invariant in one dimension. This setting features an arbitrary number of protected edge modes and a fixed transfer phase $\pm\frac{\pi}{2}$, which renders it suitable for quantum state transfer and allows for extensions in two dimensions. Let us start from this setting and break the symmetries systematically:

- 1 Breaking the *sublattice symmetry* S with real couplings connecting modes of the same parity/sublattice, automatically breaks PH symmetry $C = TS$, but leaves time-reversal symmetry T intact. We end up with a network in class **AI**

which does not feature non-trivial topological phases in one dimension and therefore no protected, zero-dimensional edge modes. Such setups are clearly useless for state transfer.

- 2 Breaking *time-reversal symmetry* T — by adding random phases to couplings — automatically breaks PH symmetry $C = TS$, but leaves the sublattice symmetry S intact. We are left with a network in class **AIII** which features a \mathbb{Z} topological index in one dimension such that there are still protected edge modes, and even the extension to multiple adjacent edge modes in two dimensions is possible. However, the unrestricted coupling phases entail random transfer phases, which renders the network unsuited for *quantum*¹¹⁷ state transfer.
- 3 Breaking *PH symmetry* $C = TS$ implies the breaking of either time-reversal T or sublattice symmetry S (or both). If only one of them is broken and the other is preserved, this is already covered by the previous two cases. If *both* are broken, the network does not feature any symmetries and belongs to class **A** without a topological invariant in one dimension. Again, this is useless for state transfer due to the lack of localized edge modes.
- 4 Breaking *time-reversal symmetry* T and *sublattice symmetry* S simultaneously is compatible with a preservation of the PH symmetry $C = TS$ if both T and S are broken such that their product is conserved. This can be achieved if couplings between modes of the same (different) parities are purely imaginary (real); in particular, random phases are not allowed. This describes a network in class **D** which features a \mathbb{Z}_2 topological index. For the networks considered here, this is a rather unnatural (or artificial) setting as there are rigid but non-uniform phase constraints on the couplings; it nevertheless allows for a single pair of protected edge modes and features (perhaps surprisingly) a fixed transfer phase¹¹⁸.

More details on general networks and the symmetry constraints are presented in **✂** Section 3.B.

¹¹⁷This setting can still be useful for the controlled transfer of classical, incoherent information and/or energy.

¹¹⁸This statement is suggested by simulations and the fact that random coupling phases are forbidden in this scenario.

3.5 Conclusion & Outlook

Can the peculiar features of symmetry-protected topological phases in one dimension be harvested for the efficient transfer of quantum information? This chapter answered this question in the affirmative.

We started off by setting the scene: Qubits coupled to localized modes of a (yet to be determined) linear bosonic network should interact by tuning *globally* the parameters of the network, sidestepping the need for single-site addressability. To achieve this, we chose the fermionic Su–Schrieffer–Heeger (SSH) chain as a template to derive a bosonic network featuring topological bands that come with disorder-resilient, localized edge modes in one dimension. We discussed the required constraints on the mode frequencies and couplings that were inherited from the SSH chain, namely time-reversal and particle-hole symmetry. The protocol to transfer an excitation from one edge mode to the other is simple: Starting from deep within the topological phase (where the edge modes are decoupled perfectly), the relevant parameter \bar{w} is tuned slowly to a value \bar{w}_{\max} close the topological phase transition. Thereby the edge modes temporarily extend into the bulk and hybridize, which allows for controlled state transfer between them. We identified non-adiabatic losses to bulk modes as potentially harmful and introduced figures of merit to quantify the performance of the protocol.

In a first step, we presented numerical results for these figures of merit in dependence of the transfer time τ and the parameter \bar{w}_{\max} : For appropriately chosen τ and \bar{w}_{\max} , non-adiabatic losses are negligible and the transfer is close to perfect. Strikingly, the accumulated *transfer phase* is fixed at $\pm\frac{\pi}{2}$; a useful property for quantum state transfer. A minimal model revealed the relation between particle-hole symmetry and the fixed phase: Breaking the former results in arbitrary transfer phases. We then switched focus to the crucial question of scalability and identified the energy splitting of the edge modes ΔE_{edge} and their separation from the bulk spectrum ΔE_{bulk} as decisive for the transfer time τ . In particular, we proved by analytical means that a scaling of $\Delta E_{\text{edge}} \sim L^{-1}$ is achievable if the protocol parameter \bar{w}_{\max} approaches the critical value. Since $\Delta E_{\text{edge}}^{-1}$ provides a lower bound on the transfer time, we found that an (optimal) linear scaling of τ is possible in principle. However, the vanishing of the bulk-edge separation $\Delta E_{\text{bulk}} \sim L^{-1}$ gives rise to suboptimal lower bounds on τ by sufficient conditions for adiabaticity. We showed that $\tau \sim L^{1+\frac{1}{2}}$ follows for our particular protocol and sketched possible optimizations of the pulse shape to approach linear scaling. Subsequently, we compared the performance of the topological setup with a “non-topological,” trivial setup which realizes artificial edge modes with a separating “barrier” of high-energy modes. We found that both the topological and the trivial setup allow for controlled transfer of excitations. As disadvantages of the trivial setup, we identified higher losses to bulk modes and, most importantly, a transfer phase that depends on the microscopic parameters of the network. We concluded that the topological setup

outperforms its trivial competitor clearly. This superiority became even more drastic in the presence of quenched disorder: If the latter preserves particle-hole symmetry, the transfer fidelity of the topological setup remains close to optimal if the protocol is calibrated accordingly. By contrast, the trivial setup suffers from dramatic losses due to Anderson localization of its artificial edge modes.

In the last chapter, we discussed as a possible application the implementation of a controlled-phase gate on two remote qubits. To this end, we coupled the two qubits (described by two logical states and an additional auxiliary state) to the edge modes of the topological network. The topological state transfer then allows for robust qubit shuttling to apply the two-qubit gate on the spatially separated qubits. Finally, we commented on possible generalizations to couple more than two qubits in a (quasi) 2D geometry of dimerized pairs of modes on a honeycomb lattice. We also highlighted the role of symmetries in this generic setting and pointed to possible alternative setups.

In summary, we have shown that the unique properties of (quasi) one-dimensional topological systems can be harvested for efficient quantum communication between qubits. These benefits come with the price of higher complexity in realization and preparation as the network parameters have to respect protecting symmetries. Nevertheless, the introduced scheme adds to the toolbox for manipulating quantum information reliably and may be of use in the context of (classical) metamaterials.

Open Questions

There are a few interesting questions that deserve further study:

- Throughout this chapter, we focused on the single-excitation subspace of the bosonic networks: Since its dimension scales linearly in the network size L , time evolutions can be computed quite efficiently. In reality, it may be hard to cool the network into the ground state with zero excitations and/or dissipative couplings during the protocol may inject excitations into the network at random sites. To study the (presumably detrimental) effects on state transfer numerically, time evolutions in the much larger N -particle sectors of the Hilbert space must be computed and evaluated. While the time evolution itself is straightforwardly described by evolving the bosonic modes $b_l^{(\dagger)}$ in time (the network is populated by non-interacting bosons after all), the *evaluation* of correlators can be prohibitively complex for large excitation numbers N due to combinatorial intricacies known from boson sampling [296–299], see ✨ Section 3.F.
- During our discussion of the scaling of the transfer time needed for adiabatic decoupling in Subsection 3.3.3, we concluded that optimizing the pulse shape may be of interest not only to achieve better scaling for $L \rightarrow \infty$ (which is

certainly interesting from a theoretical point of view, but is of less relevance for specific implementations), but also to optimize the adiabatic bulk-edge decoupling and speed of the transfer for a given chain length L . This requires methods from quantum optimal control theory [293, 294] which studies the design of Hamiltonian time evolutions for the efficient preparation of prescribed quantum states. It would be interesting to compare our intuitively chosen pulse $\mathcal{F}(t)$ to more sophisticated time dependencies of $\bar{w}(t)$.

- In our concluding discussion of the role played by the symmetries in Subsection 3.4.2 (see also ✱ Section 3.B), it became clear that the conditions for quantum state transfer—topologically protected, localized edge modes and a fixed transfer phase—are not only satisfied by the “most symmetric” class **BDI** (considered throughout this chapter), but also in the Bogoliubov-de Gennes class **D**. The latter poses rather artificial conditions on the allowed couplings, which renders the implementation of the network more demanding. However, the \mathbb{Z}_2 topological invariant is potentially useful in 2D setups: Whereas a setup like Figure 3.14 (a) is not suitable in this case (adjacent edge modes of the same parity can accidentally hybridize by imaginary stray couplings), a setup like Figure 3.14 (b) is *not* susceptible to this problem due to the edge mode separation. Such a setting might even outperform the sublattice symmetric one presented in Subsection 3.4.2 because *all* qubits can communicate directly: Edge modes of *different* parities hybridize via *real* couplings, whereas edge modes of the *same* parity hybridize via *imaginary* couplings. Note that this scheme requires a rather evolved control over the coupling phases.
- In Subsection 3.3.4 (and Subsection 3.3.5) we compared the topological state transfer with the SSH setup to the “non-topological” state transfer with trivial setups. The purpose of this discussion was to highlight the features of the topological setup, or, simply put, to tell the reader why the topological setup is *better* than the trivial one. In science, contriving solutions to problems that are—often in some very nebulous sense—*better* than other solutions, is a very common *modus operandi* to pave the way for publication. In science, experience tells us that few things are for free. In the present case, we pay with symmetry (time-reversal and sublattice) to keep Anderson localization in check. On this reading, the topological network is *better* than the trivial one because the former converts the symmetries into something useful (scattering-free transport) while the latter does not. But this comparison is only meaningful because both setups use the same building blocks (bosonic modes and their couplings). This motivates the question how solutions to a given task (here: quantum state transfer) can be compared *quantitatively* in a formal framework, including a notion of *value* or *cost* for each building block. In Section 5.3 we let our thoughts ramble and sketch a possible framework to

QUANTUM COMMUNICATION BETWEEN QUBITS

tackle the problem of quantifying the costs of solutions for a given task. It would be intriguing to work this out more properly and apply it to the task of state transfer quantitatively.

APPENDICES FOR CHAPTER 3

3.A The Majorana Chain Model

Here we introduce an alternative solution to the state transfer problem, derived from the famous Majorana chain Hamiltonian. In [§ Subsection 3.A.1](#) we demonstrate parallel to our discussion of the SSH setup, how the bosonic network Hamiltonian and the protecting symmetries can be obtained from the fermionic parent theory. In [§ Subsection 3.A.2](#) we show that the Majorana and SSH chain setups are related by a unitary transformation on the mode space. This explains our focus on the SSH setup in the main text.

3.A.1 Definition and Properties

The original Majorana chain Hamiltonian [\[82\]](#) for spinless fermions on an open chain of length L reads (Subsection [1.2.2](#))

$$\hat{H}_{\text{MC}} = \sum_{i=1}^{L-1} \left(w_i c_i^\dagger c_{i+1} - \Delta_i c_i c_{i+1} + \text{h.c.} \right) + \sum_{i=1}^L \mu_i \left(c_i^\dagger c_i - \frac{1}{2} \right), \quad 3.69$$

where c_i^\dagger (c_i) denote *fermionic* creation (annihilation) operators, w_i is the tunneling amplitude, Δ_i the superconducting gap (which can always be gauged real), and μ_i denotes the chemical potential, all of which can be, in principle, site-dependent. For uniform parameters $\mu_i \equiv \bar{\mu}$ and $w_i \equiv \bar{w} = \bar{\Delta} \equiv \Delta_i$, one finds two gapped phases for $|\bar{\mu}| \lesssim 2|\bar{w}|$ connected by a gapless spectrum at $|\bar{\mu}| = 2|\bar{w}|$ indicating a phase transition. The latter is of topological nature as the symmetries of both phases are the same. For the topological phase, $|\bar{\mu}| < 2|\bar{w}|$, one finds two degenerate edge modes that give rise to a two-fold ground state degeneracy; hence the modes are identified as Majorana bound states. In the trivial phase, $|\bar{\mu}| > 2|\bar{w}|$, the ground state is unique and no localized edge modes are present.

In the $2L$ -dimensional space of Nambu spinors

$$\Psi = \left(c_1^\dagger, c_1, \dots, c_L^\dagger, c_L \right)^T \quad 3.70$$

the Hamiltonian can be encoded by a Hermitian matrix H_{MC} via

$$\hat{H}_{\text{MC}} = \frac{1}{2} \Psi^\dagger H_{\text{MC}} \Psi . \quad 3.71$$

This matrix features an *intrinsic* (antilinear) particle-hole (PH) symmetry $CH_{\text{MC}}C^{-1} = -H_{\text{MC}}$ with $C = \mathcal{K}U_C^{\text{MC}}$ and $C^2 = +\mathbb{1}$. Here, \mathcal{K} denotes complex conjugation and the unitary U_C^{MC} takes the form

$$U_C^{\text{MC}} = \mathbb{1}_{L \times L} \otimes \begin{bmatrix} 0 & 1 \\ 1 & 0 \end{bmatrix}, \quad 3.72$$

i.e., the PH symmetry acts as $c_i^\dagger \leftrightarrow c_i$ on Nambu space. Hence the Majorana chain is in symmetry class **D** of the Altland-Zirnbauer classification [90–93]. In one dimension, this allows for the definition of a \mathbb{Z}_2 topological invariant ν [21, 22, 95, 97] which is responsible for the emergence of the disorder-resilient edge modes bound to the open ends of the chain whenever $\nu \neq 0 \pmod{2} \Leftrightarrow |\bar{\mu}| < 2|\bar{w}|$, i.e., in the topological phase. If all tunneling amplitudes w_i and superconducting pairings Δ_i are real, the Hamiltonian features additionally the time-reversal symmetry $T = \mathcal{K}$ with $T^2 = +\mathbb{1}$. Then, the model can be considered as an element of the symmetry class **BDI** with a \mathbb{Z} topological index [21, 22, 95, 97].

The implementation of an analogue system with bosonic d.o.f. follows a straightforward procedure: First, each fermionic site in the original Majorana chain is replaced by *two* bosonic modes. The two bosonic modes at site i are denoted by the bosonic operators $b_i^{(\dagger)}$ and $b_{\bar{i}}^{(\dagger)}$,

$$c_i \rightarrow b_i^{(\dagger)} \quad \text{and} \quad c_i^\dagger \rightarrow b_{\bar{i}}^{(\dagger)}. \quad 3.73$$

Note that the original indices $i = 1, \dots, L$ label now the “upper” sites whereas bar-ed indices $\bar{i} = \bar{1}, \dots, \bar{L}$ denote the “lower” sites, see Figure 3.15. By this construction, the Majorana chain translates to a linear chain of length L with *two* quantum harmonic oscillators per site. The bosonic Hamiltonian takes the form

$$\hat{H}_{\text{bMC}} \equiv \Xi^\dagger [H_{\text{MC}} + \delta \mathbb{1}] \Xi \equiv \Xi^\dagger H_{\text{bMC}} \Xi \quad 3.74$$

with

$$\Xi = \left(b_1, b_{\bar{1}}, \dots, b_i, b_{\bar{i}}, \dots, b_L, b_{\bar{L}} \right)^T \quad 3.75$$

and $H_{\text{bMC}} = H_{\text{MC}} + \delta \mathbb{1}$ the matrix appearing in Eq. (3.74). The constant positive energy shift $\delta > 0$ is required to enforce positivity on the matrix H_{bMC} ; its value can be chosen arbitrarily (as long as $H_{\text{bMC}} > 0$) and does not change the topological properties (e.g., the existence of edge modes).

To make the new interpretation in terms of bosonic modes explicit, we substitute the parameters in H_{bMC} , inherited from the Majorana chain (3.69), as follows:

$$\begin{aligned}
 H_{\text{bMC}} &= \begin{bmatrix} \delta - \mu_1 & 0 & -w_1 & -\Delta_1 \\ 0 & \delta + \mu_1 & \Delta_1 & w_1 \\ -w_1 & \Delta_1 & \ddots & \ddots \\ -\Delta_1 & w_1 & \ddots & \ddots \end{bmatrix} \\
 &\rightarrow \begin{bmatrix} \omega_1 & 0 & t_{1,2} & t_{1,\bar{2}} \\ 0 & \omega_{\bar{1}} & t_{\bar{1},2} & t_{\bar{1},\bar{2}} \\ t_{1,2} & t_{\bar{1},2} & \ddots & \ddots \\ t_{1,\bar{2}} & t_{\bar{1},\bar{2}} & \ddots & \ddots \end{bmatrix} = H_{\text{bMC}}. \tag{3.76}
 \end{aligned}$$

The diagonal elements of H_{bMC} describe the eigenfrequencies ω_I ($I = i, \bar{i}$) of the local modes b_I , whereas the off-diagonal elements capture the real hopping amplitudes $t_{I,J}$ connecting modes b_I and b_J . E.g., $\omega_{\bar{1}}$ denotes the eigenfrequency of the lower mode $b_{\bar{1}}$ and $t_{1,\bar{2}}$ the coupling between the upper mode b_1 and the lower mode $b_{\bar{2}}$, see Figure 3.15.

Using the identifications in Eq. (3.76), one finds that the role of the chemical potential $2\mu_i$ is now played by the difference $\delta\omega_i = \omega_{\bar{i}} - \omega_i$ of the local mode frequencies at each site, while the horizontal hopping amplitudes $t_{i,i+1}$ and $t_{\bar{i},\bar{i}+1}$ are identified with the fermion tunneling rate w_i , and the diagonal amplitudes $t_{i,\bar{i}+1}$ and $t_{\bar{i},i+1}$ stem from the superconducting order parameter Δ_j .

The bosonic Hamiltonian \hat{H}_{bMC} features the same single-particle band structure as the original Majorana chain, and exhibits the same topological properties and topological quantum numbers. Therefore it gives rise to the same edge modes. Note that these are statements about *single*-particle physics where statistics is not relevant. Furthermore, it is crucial to stress a conceptual difference between the fermionic Hamiltonian \hat{H}_{MC} and its bosonic descendant \hat{H}_{bMC} : The former is described by L fermionic modes and only in Nambu space an artificial mode doubling occurs, giving rise to the intrinsic particle-hole symmetry C . The bosonic setup is truly described by $2L$ *independent* bosonic modes, as the mode doubling at each lattice site is required for the implementation. This has immediate consequences for the interpretation of the topology-protecting PH symmetry: The latter—inherent to any (fermionic) Bogoliubov-de Gennes Hamiltonian in Nambu space—is converted to a non-trivial *real* symmetry of the new bosonic theory. Either the identifications in equation (3.76), or the symmetry relation $CH_{\text{bMC}}C^{-1} = -H_{\text{bMC}} + 2\delta \mathbb{1}$, give rise to

QUANTUM COMMUNICATION BETWEEN QUBITS

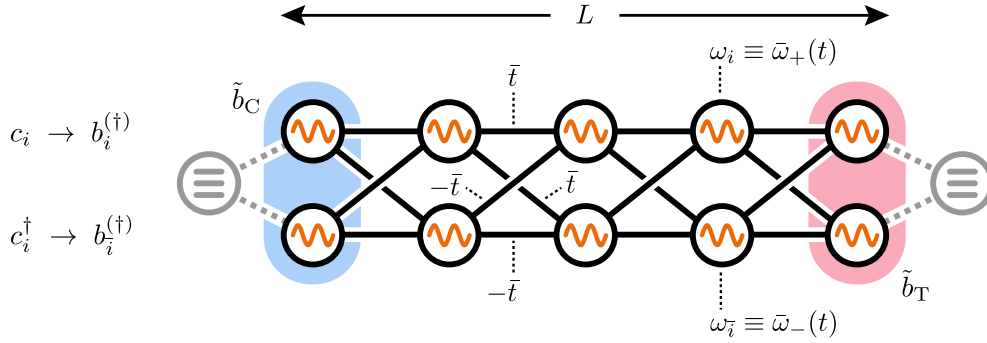


FIGURE 3.15 • The Majorana chain model. The model consists of locally coupled bosonic modes with qubits (gray) coupled to the edge modes \tilde{b}_C and \tilde{b}_T which, in contrast to the SSH setup, are not localized on a single physical mode (blue and red pairs). The linear network is described by the time-dependent Hamiltonian $\hat{H}_{\text{bMC}}(t)$; the uniform eigenfrequency differences $\delta\bar{\omega}(t) \equiv \bar{\omega}_-(t) - \bar{\omega}_+(t)$ are tunable. In contrast to the SSH setup, no tunable couplings are required. Details are given in the text.

the *local* constraints

$$\omega_i + \omega_{\bar{i}} = 2\delta \quad 3.77a$$

$$t_{i,i+1} = -t_{\bar{i},\bar{i}+1} \quad 3.77b$$

$$t_{i,i+1} = -t_{\bar{i},\bar{i}+1} \cdot \quad 3.77c$$

Note that the value of δ merely determines the global energy scale whereas its site-*independence* is crucial for PH symmetry. All these constraints can be fulfilled by pairwise, *local* fine-tuning of the modes and their couplings to nearest neighbors.

For the purpose of state transfer, we choose uniform frequencies $\bar{\omega}_- \equiv \omega_i$ and $\bar{\omega}_+ \equiv \omega_{\bar{i}}$, the difference of which is (globally) tunable: $\delta\bar{\omega}(t) = \bar{\omega}_-(t) - \bar{\omega}_+(t)$. In contrast to the SSH setup discussed in the main text, here the mode couplings are fixed at $t_{i,i+1} \equiv \bar{t} \equiv t_{\bar{i},\bar{i}+1}$ and $t_{\bar{i},\bar{i}+1} \equiv -\bar{t} \equiv t_{i,i+1}$. Note that the spatial uniformity assumed for couplings and mode frequencies is not essential (due to the topological protection) as long as the local symmetries (3.77) are respected. For $\delta\bar{\omega} = 0$, one finds the flat-band “sweet spot” of perfectly localized (and degenerate) edge modes $\tilde{b}_C \propto b_1 + b_{\bar{1}}$ and $\tilde{b}_T \propto b_L - b_{\bar{L}}$. At the critical point $\delta\bar{\omega}_{\text{crit}} = 4\bar{t}$, the spectrum becomes gapless and the topological phase transition occurs. For $\delta\bar{\omega} > \delta\bar{\omega}_{\text{crit}}$ the chain becomes gapped again but features no edge modes anymore. Therefore the protocol for state transfer reads

$$\delta\bar{\omega}(t) = \delta\bar{\omega}_{\text{max}} \cdot \mathcal{F}(t) \quad 3.78$$

with the protocol parameter $\delta\bar{\omega}_{\text{max}} < \delta\bar{\omega}_{\text{crit}}$ and the smooth pulse

$$\mathcal{F}(t) = \sin^2\left(\frac{\pi t}{\tau}\right) \quad \text{for } 0 \leq t \leq \tau, \quad 3.79$$

as already defined in (3.29) of the main text. Together with the previously given fixed values of mode couplings, this defines the time-dependent network Hamiltonian $\hat{H}_{\text{bMC}}(t)$ with perfectly localized edge modes at $t = 0$ and $t = \tau$.

Due to the unitary equivalence of \hat{H}_{bMC} and \hat{H}_{bSSH} (see \clubsuit Subsection 3.A.2 below), their characteristics regarding state transfer are the same. This explains why we focused solely on the SSH setup in the main text. However, their practical requirements differ as \hat{H}_{bMC} (\hat{H}_{bSSH}) relies on tunable (fixed) mode frequencies and fixed (tunable) mode couplings. Their local symmetry constraints [compare Eq. (3.77) and Eq. (3.20)] are also different and may (or may not) be suited for specific implementations.

3.A.2 Relation to the SSH Model

The single-particle theories for the Majorana chain \hat{H}_{MC} (described in Subsection 3.A.1 above) and the SSH setup \hat{H}_{SSH} (described in Subsection 3.2.1 of the main text),

$$H_{\text{MC}} = \begin{bmatrix} -\mu_1 & 0 & -w_1 & -\Delta_1 \\ 0 & +\mu_1 & \Delta_1 & w_1 \\ -w_1 & \Delta_1 & \ddots & \ddots \\ -\Delta_1 & w_1 & \ddots & \ddots \end{bmatrix} \quad 3.80$$

and

$$H_{\text{SSH}} = \begin{bmatrix} 0 & w_1 & 0 & 0 \\ w_1 & 0 & t_1 & 0 \\ 0 & t_1 & \ddots & \ddots \\ 0 & 0 & \ddots & \ddots \end{bmatrix}, \quad 3.81$$

can be related by the unitary transformation $M_L = \mathbb{1}_{L \times L} \otimes M_1$, where

$$M_1 = \frac{1}{\sqrt{2}} \begin{bmatrix} 1 & 1 \\ -1 & 1 \end{bmatrix}, \quad 3.82$$

via

$$M_L H_{\text{MC}} M_L^\dagger = \begin{bmatrix} 0 & \mu_1 & 0 & w_1 - \Delta_1 \\ \mu_1 & 0 & w_1 + \Delta_1 & 0 \\ 0 & w_1 + \Delta_1 & \ddots & \ddots \\ w_1 - \Delta_1 & 0 & \ddots & \ddots \end{bmatrix}. \quad 3.83$$

For the special case $\Delta_i = w_i$, one has $H_{\text{SSH}} = M_L H_{\text{MC}} M_L^\dagger$ with the identifications $\mu_j \leftrightarrow w_j$ and $2\Delta_j \leftrightarrow t_j$. In this case, the *bosonic* many-body theories \hat{H}_{bSSH} and \hat{H}_{bMC} are unitarily equivalent—which is why we focus on the conceptually simpler \hat{H}_{bSSH} in this chapter. By contrast, this unitary equivalence holds only for the single-particle spectrum of the *fermionic* versions \hat{H}_{SSH} and \hat{H}_{MC} but not for the many-body theories since the former acts on $2L$ and the latter on L fermionic modes.

Remark

As a final remark, we note that in the context of the fermionic Majorana chain, another unitary transformation is commonly used, namely

$$M'_1 = \frac{1}{\sqrt{2}} \begin{bmatrix} 1 & 1 \\ -i & i \end{bmatrix} = \begin{bmatrix} 1 & 0 \\ 0 & i \end{bmatrix} \cdot M_1 \quad 3.84$$

which transforms the fermion algebra $\{c_i, c_j^\dagger\} = \delta_{ij}$ via

$$\gamma_{2j-1} = \frac{c_j + c_j^\dagger}{\sqrt{2}} \quad \text{and} \quad \gamma_{2j} = i \frac{c_j - c_j^\dagger}{\sqrt{2}} \quad 3.85$$

into the eponymous Majorana algebra $\{\gamma_i, \gamma_j\} = \delta_{ij}$ with self-adjoint (Majorana) fermions $\gamma_j^\dagger = \gamma_j$. Then ($\Delta_i = w_i$)

$$M'_L H_{\text{MC}} M_L'^\dagger = \begin{bmatrix} 0 & -i \mu_1 & 0 & 0 \\ i \mu_1 & 0 & i 2\Delta_1 & 0 \\ 0 & -i 2\Delta_1 & \ddots & \ddots \\ 0 & 0 & \ddots & \ddots \end{bmatrix} \quad 3.86$$

encodes the Majorana chain in terms of “Majorana dimers” $\gamma_j \gamma_{j+1}$ which parallels the SSH chain.

3.B Symmetry Protection of Generic Networks

In Subsection 3.4.2, we argued that the envisioned networks, such as the one shown in Figure 3.14 (a), require two types (*parities*) of edge modes (dubbed “even” and “odd”) and that direct transfer is only possible between pairs of different parities. Here we show the reason for this constraint for a generic class of networks that allows for topologically protected, localized (zero-dimensional) edge modes.

To this end, we consider systems/protocols of the form

$$\tilde{H}(t) = \bar{t} \tilde{H}_0 + \bar{w}(t) \tilde{H}_1 \quad 3.87$$

with $\bar{w}(t) = \bar{w}_{\max} \cdot \mathcal{P}(t)$ where the generic pulse $\mathcal{P}(t)$ is only required to obey $\mathcal{P}(0) = 0 = \mathcal{P}(\tau)$. The parameter \bar{w}_{\max} is unconstrained for the following discussion. Here, \tilde{H}_0 encodes an arbitrary, completely dimerized setup of $2N$ (bulk) modes where the tunneling amplitudes are required to be of order $\mathcal{O}(1)$ to account for a bulk gap of order $\mathcal{O}(\bar{t})$; apart from this, they may be disordered and/or complex-valued. Now add M *additional* modes which remain uncoupled by \tilde{H}_0 (these are the localized zero-energy edge modes). The Hamiltonian \tilde{H}_1 can now couple all $2N + M$ modes, again with possibly disordered/complex amplitudes of order $\mathcal{O}(1)$.

The only generic symmetry we demand is the sublattice symmetry $U_S \tilde{H} U_S^\dagger = -\tilde{H}$ with representation

$$U_S = \mathbb{1}_{N \times N} \otimes \begin{bmatrix} 1 & 0 \\ 0 & -1 \end{bmatrix} \oplus \text{diag}(s_1, \dots, s_M), \quad 3.88$$

because time-reversal $T = \mathcal{K}$ is broken due to the (possibly) complex couplings. The transformations $s_i = \pm 1$ of the M edge modes are determined by their coupling to the bulk via \tilde{H}_1 . This places $\tilde{H}(t)$ in symmetry class **AIII** of the Altland-Zirnbauer classification [90–93] and allows for a \mathbb{Z} topological index [21, 22, 95, 97] in one dimension.

The representation (3.88) partitions the $2N + M$ modes into two classes: The modes multiplied by $+1$ (-1) when acted upon by U_S will be called “even” (“odd”). The sublattice symmetry suggests the illustrative interpretation of \tilde{H} as adjacency matrix of a graph with modes as vertices and (complex) weighted edges, see Figure 3.16. Then, $U_S \tilde{H} U_S^\dagger = -\tilde{H}$ is equivalent to the statement that this coupling graph has to be *bipartite*, i.e., only edges between the two classes of “even” and “odd” vertices are allowed.

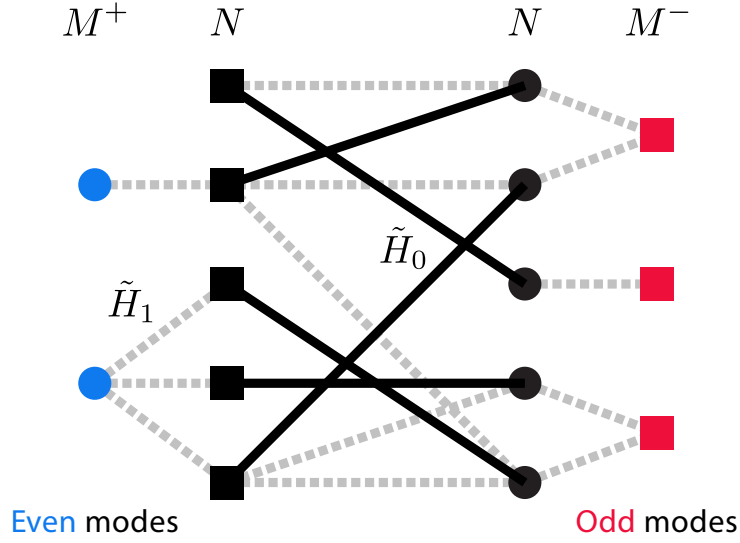


FIGURE 3.16 • Generic network. The Hamiltonian $\tilde{H}(t)$ defines a coupling graph with modes as vertices and (complex) weighted edges. The sublattice symmetry corresponds to the bipartiteness of this graph, grouping its vertices into “even” (circles) and “odd” (squares) with only edges between the classes. The couplings of \tilde{H}_0 (\tilde{H}_1) are indicated as solid black (dashed gray) edges. The $M = M^+ + M^-$ zero-energy edge states do not belong to the dimerized bulk of \tilde{H}_0 and are shown as colored vertices.

If we sort the mode basis/vertices into these classes, the single-particle Hamiltonian/adjacency matrix has the generic form

$$\tilde{H} = \begin{bmatrix} 0 & A \\ A^\dagger & 0 \end{bmatrix} \quad 3.89$$

with complex $(n^+ \times n^-)$ -matrix A where $n^\pm \in \mathbb{N}$. Then it follows that \tilde{H} has *at least* $|n^+ - n^-|$ exact zero eigenvalues. Indeed, squaring \tilde{H} yields

$$\tilde{H}^2 = \begin{bmatrix} AA^\dagger & 0 \\ 0 & A^\dagger A \end{bmatrix}. \quad 3.90$$

Let $n^- \geq n^+$ without loss of generality. Then, the $(n^+ \times n^+)$ -matrix AA^\dagger has $\text{rank}(AA^\dagger) \leq n^+$ (which is a trivial bound since $n^- \geq n^+$). However, the $(n^- \times n^-)$ -matrix $A^\dagger A$ yields the non-trivial bound $\text{rank}(A^\dagger A) \leq n^+ \leq n^-$ due to its composite structure. Therefore $\text{rank}(\tilde{H}^2) \leq 2n^+$ and for the corank we find $\text{corank}(\tilde{H}^2) \geq n^+ + n^- - 2n^+ = |n^- - n^+|$ which concludes the proof.

Coming back to our setup of $2N$ dimerized bulk modes coupled with M edge modes via \tilde{H}_1 , we realize that $n^\pm = N + M^\pm$ with $M = M^+ + M^-$, where the sublattice symmetric couplings \tilde{H}_1 determine the class of each edge mode

(i.e., $s_i = \pm 1$) and thereby M^\pm . Then we just showed that $\tilde{H}(t)$ has (at least)

$$|n^+ - n^-| = |M^+ - M^-| \quad 3.91$$

exact zero-energy modes at any time. We discuss three special cases:

- If \tilde{H}_1 connects two edge modes of *opposite* parity, we have $|M^+ - M^-| = |1 - 1| = 0$ exact zero modes. These modes will generically gap out during $0 < t < \tau$ and allow for state transfer between them. The considered SSH chain setup is a minimal example of this case.
- If \tilde{H}_1 connects two edge modes of the *same* parity, we have $|M^+ - M^-| = |2 - 0| = 2$ exact zero modes. Assuming adiabatically decoupled bulk modes, initial edge excitations are bound to this two-dimensional zero-energy subspace for all times. The only possible unitary acting on this subspace stems from the non-abelian Berry connection $\mathcal{A}_{kl}^{\bar{w}} = i \langle \Psi_k(\bar{w}) | \partial_{\bar{w}} | \Psi_l(\bar{w}) \rangle$ with $\Psi_l(\bar{w})$ the two zero-energy states ($l = 1, 2$) for coupling \bar{w} . The geometric unitary is then given by (the exponential of) the integral of the Berry connection along the path traced by $\bar{w}(t)$ in parameter space. In our case, the latter is simply connected and one-dimensional so that all loop integrals vanish identically, i.e., there is no holonomic transformation of edge modes possible. We conclude that, despite their delocalization for $0 < t < \tau$, all excitations end up in their initial edge mode and there is no transfer.
- If \tilde{H}_1 connects three edge modes, two “even” and one “odd,” we have $|M^+ - M^-| = |2 - 1| = 1$ exact zero mode. For $0 < t < \tau$, the three-dimensional edge manifold gaps out and allows for transfer between the two “even” modes via the “odd” mode. We point out that this allows for a “transistor-like” setup where two modes talk to each other only if a third “gate”-mode is coupled to the system.

It is important to note that the presence/absence of time-reversal symmetry has *no effect* on the existence of protected edge modes as both symmetry classes **BDI** and **AIII** allow for \mathbb{Z} topological invariants in one dimension. The locked transfer phase $\varphi = \pm \frac{\pi}{2}$, however, requires time-reversal symmetry because disordered coupling phases obviously randomize φ in the absence of additional symmetries (such as the PH symmetry of class **D**, recall Subsection 3.4.2).

As a final remark, note that one could alternatively require \tilde{H} to be PH symmetric, i.e., $U_S \tilde{H}^* U_S^\dagger = -\tilde{H}$, instead of imposing the sublattice symmetry $U_S \tilde{H} U_S^\dagger = -\tilde{H}$. Then, its generic form were

$$\tilde{H}_{\text{PH}} = \begin{bmatrix} iA_+ & B \\ B^T & iA_- \end{bmatrix} \quad 3.92$$

with the antisymmetric real matrices A_\pm and the arbitrary real matrix B , cf. Eq. (3.89). Then, couplings between modes of different (the same) parities must be real (imaginary). We stress two important differences:

- 1 With broken time-reversal symmetry, \tilde{H}_{PH} belongs to the symmetry class **D**, which only allows for \mathbb{Z}_2 topological invariants in one dimension. Thus there is at most *one* pair of protected, localized edge modes, and setups with *adjacent* qubits [recall Figure 3.14 (a)] are no longer stable.
- 2 The coupling structure (3.89) is much more natural than the PH symmetric version (3.92): In the first case, one has only to guarantee that no modes of the same parity couple while arbitrary couplings between modes of different parities are allowed. By contrast, the PH symmetry allows for couplings between arbitrary modes which, however, must satisfy non-uniform reality conditions.

Note that the three symmetry classes **BDI**, **D**, and **AIII** exhaust all possibilities to construct topologically protected edge modes in one-dimensional systems with representations of PH and time-reversal that square to unity, i.e., $C^2 = +\mathbb{1}$ and $T^2 = +\mathbb{1}$.

3.C Influence of Disorder

In this section, we focus on the effects of disorder on the transfer. We present additional numerical results for particle-hole (PH) symmetric/breaking disorder, and discuss its effect on the transfer phase.

In Figure 3.11 of the main text we show the spatial amplitudes of the edge modes for the topological and the trivial setup for (a) clean setups, (b) PH symmetric disorder, and (c) PH breaking disorder. Depending on $\bar{w}(t)$, the delocalization of eigenmodes varies between perfectly localized and delocalized. The edge modes reveal a striking difference for PH symmetric disorder: While *any* kind of disorder localizes the “artificial” edge modes of the trivial setup, there is no localization in the topological setup for PH symmetric disorder. This is a distinctive feature of topologically protected edge states in general: Anderson localization is forbidden for the latter as long as the protective symmetries are kept intact (here the PH symmetry). Due to this feature, the topological setups (SSH and Majorana) are outperforming the trivial barrier setup as tunneling between the edges directly relies on their overlap close to criticality.

To substantiate this claim, we sampled both setups for PH symmetric and breaking disorder and computed their average figures of merit $\langle\langle\mathcal{O}\rangle\rangle$ and $\langle\langle\mathcal{E}\rangle\rangle$, see Subsection 3.2.2 and Subsection 3.3.5 for the definition. The results for fixed protocols are shown in Figure 3.17 (a) as a function of the disorder strength p . *Fixed* means that for a given system size L and timescale τ , the protocol parameter is tuned such that—in the clean system—the transfer is maximized. This procedure captures effects of slow, uncorrelated drift in the constituent’s parameters on the

the right-hand edge mode; in the trivial setup, the transfer drops considerably even for weak disorder. Moreover, there is no qualitative difference between PH breaking and symmetric disorder for the trivial setup.

However, the fundamental difference between the topological and the trivial setup becomes apparent if we allow for the protocol to adapt to each disorder realizations by tuning the timescale τ in order to maximize the transfer fidelity. The results are shown in Figure 3.17 (b) [reproduced from Figure 3.12 in the main text for convenience] and reveal a fundamental difference between topological and trivial setup: The already modest losses of transfer for PH symmetric disorder can be canceled completely by adapting the pulse length τ . This is not possible for PH breaking disorder where the edge mode localization suppresses tunneling exponentially. Again, the trivial setup does not reveal qualitative differences between PH symmetric and breaking disorder with only minor improvements from the protocol adaption.

To discuss the last figure of merit, the relative transfer phase φ , it is illustrative to plot a sample (without protocol adaption) for fixed disorder strength p in a 2D scatter plot (Figure 3.18) where points encode pairs (φ_r, φ_l) with $\varphi_r = \varphi$ the phase of the right-hand edge mode and φ_l its left-hand counterpart [cf. Eq. (3.31)],

$$\langle 1, \mathbf{0}, 0 | U_\tau(\bar{w}_{\max}) | 1, \mathbf{0}, 0 \rangle = \sqrt{\mathcal{E} - \mathcal{O}} e^{i\varphi_l}. \quad 3.93$$

As expected, the trivial setup shows random, uncorrelated phases even for weak disorder, irrespective of whether the PH symmetry is preserved or not. For PH breaking disorder, the topological setup cannot sustain locked phases either, as shown in the lower left panel of Figure 3.18 for very weak disorder $p = 0.005$. However, even for strong PH symmetric disorder ($p = 0.1$ in the upper left panel of Figure 3.18) the phases are locked for the SSH-based transfer at four discrete points: Most of the population is located at $(\varphi_r, \varphi_l) = (-\frac{\pi}{2}, 0)$ and $(-\frac{\pi}{2}, \pi)$; the number of samples that accumulates at $(\frac{\pi}{2}, \pi)$ and $(\frac{\pi}{2}, 0)$ is considerably lower, see the exemplary ratios in Figure 3.18. Note that both φ_r and φ_l are ill-defined whenever their corresponding overlap vanishes; however, due to numerics and the disorder, in practice this never happens.

It is easily checked that a single transfer accumulates a phase of $-\frac{\pi}{2}$ if the length L of the chain is odd and $+\frac{\pi}{2}$ if it is even (see also Subsection 3.3.2 and \clubsuit Subsection 3.D.1 below); in the following, we discuss the results for the odd- L ($L = 5$) setup used for Figure 3.17 and Figure 3.18: As a consequence of the still perfect bulk-edge decoupling in the presence of disorder, we can express its effect by simply shifting the protocol parameter $\bar{w}_{\max} + \delta\bar{w}_{\max}$ of the clean system by a realization-dependent value $\delta\bar{w}_{\max}$. If a single, clean, and perfectly tuned transfer leaves φ_l undefined due to the vanishing left-hand population, sampling in the vicinity of this parameter yields $\varphi_l = 0$ and π with about the same probability whereas $\varphi_r = -\frac{\pi}{2}$ is fixed and stable due to the plateau of $\mathcal{O} \approx 1$. This explains the two dominant phase combinations in Figure 3.18. The rarely sampled combination $(\frac{\pi}{2}, \pi)$ is due to samples with strong disorder where a complete Rabi cycle returns

INFLUENCE OF DISORDER

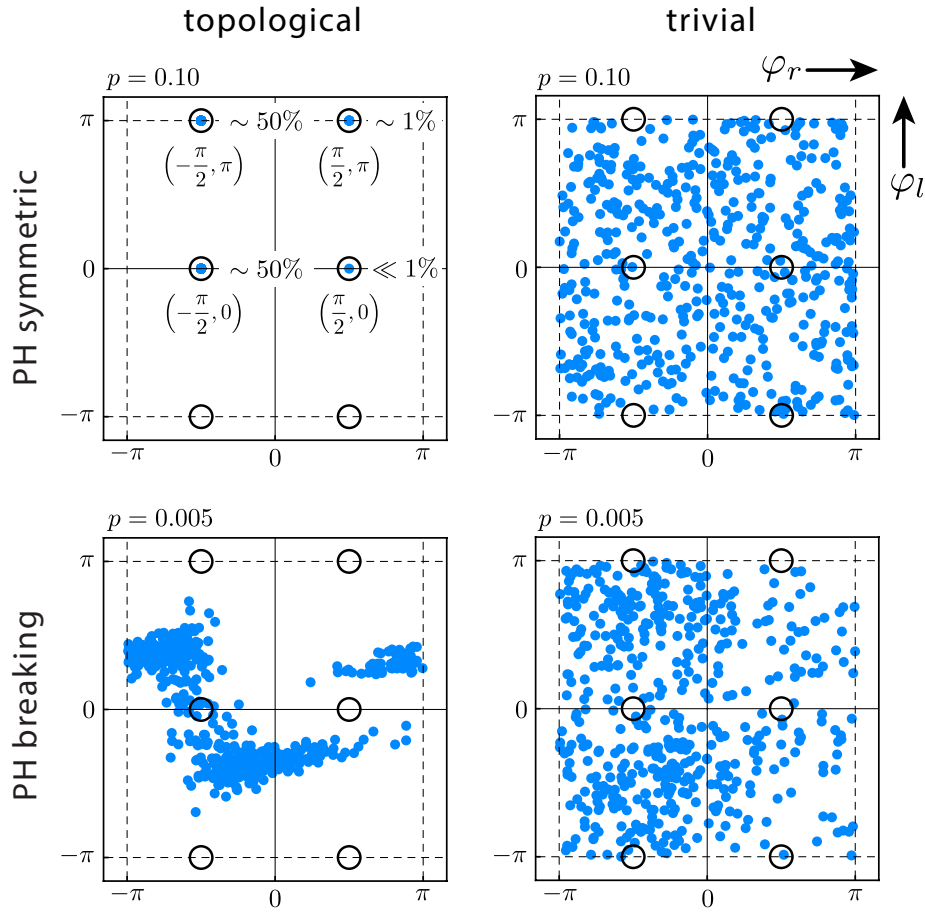


FIGURE 3.18 • Effects of disorder—Phases. Samples for $N = 500$ disorder realizations of the right-hand edge mode phase $\varphi_r = \varphi$ and its left-hand counterpart φ_l for PH symmetric (upper row) and breaking (lower row) disorder for the topological setup (left column) and the trivial setup (right column). The phases are measured in the rotating frame of the left-hand edge mode at $t = 0$. Note that the disorder rate was chosen large ($p = 0.10$) for PH symmetric and small ($p = 0.005$) for PH breaking disorder for illustrative purposes. Details are given in the text.

the population to the left edge mode such that φ_r jumps by π . In *extremely* rare cases, an additional half cycle transfers the population back to the right edge mode which leads to the last phase combination $(\frac{\pi}{2}, 0)$. For chains of even length, all statements remain true but for the sign flip $\varphi_r \rightarrow -\varphi_r$.

In conclusion, detrimental effects of disorder on the transfer phase φ are negligible for the topological setup—if the PH symmetry is preserved—due to the rareness of double transfers for weak disorder and the irrelevance of the left-hand phase for a reasonably well tuned complete transfer to the right-hand edge mode.

3.D Diagonalization

In this section, we tackle the diagonalization of H_{bSSH} analytically and use the results to derive scaling properties of the relevant energies for state transfer. In \clubsuit Subsection 3.D.1, we start with a simple effective description of the edge modes for long chains. In \clubsuit Subsection 3.D.2, we derive the spectrum of H_{bSSH} as solutions of a non-trivial equation which constitutes the foundation for all subsequent subsections. In \clubsuit Subsection 3.D.3, we study the asymptotic splitting of the edge modes for $L \rightarrow \infty$. In \clubsuit Subsection 3.D.4, we massage the equation of \clubsuit Subsection 3.D.2 into a transcendental form that allows us to unveil the emergence of edge modes at the topological phase transition. In \clubsuit Subsection 3.D.5, we discuss the asymptotics of both edge mode splitting and bulk gap at the critical point; in \clubsuit Subsection 3.D.6 we extend this discussion to couplings away from criticality. Finally, \clubsuit Subsection 3.D.7 presents the derivation of the universal scaling of eigenenergies for $L \rightarrow \infty$.

3.D.1 Edge Modes in the Thermodynamic Limit

In order to derive the exact edge modes for $L \rightarrow \infty$, it is convenient to recast the Hamiltonian \hat{H}_{bSSH} in the single-particle subspace spanned by $|I\rangle \equiv b_I^\dagger|0\rangle$. Let $w_i \equiv \bar{w}$ and set the remaining couplings $t_i \equiv \bar{t}$ to 1. If we shift the edge mode energies to zero (by setting the local mode frequencies $\omega_I \equiv 0$), the single-particle Hamiltonian reads

$$H_{\text{bSSH}} = \bar{w} \sum_{i=1}^L |i\rangle\langle\bar{i}| + \sum_{i=1}^{L-1} |\bar{i}\rangle\langle i+1| + \text{h.c.} . \quad 3.94$$

Looking sharply at this Hamiltonian (and possibly some numerical results \odot) suggests the following form of the left and right edge modes:

$$|\xi_l\rangle = \mathcal{N} \sum_{i=1}^L (-\bar{w})^{i-1} |i\rangle \quad 3.95a$$

$$|\xi_r\rangle = \mathcal{N} \sum_{i=1}^L (-\bar{w})^{i-1} |\overline{L-i+1}\rangle \quad 3.95b$$

Here, $\mathcal{N} = \sqrt{(1-\bar{w}^2)/(1-\bar{w}^{2L})}$ is the normalizing factor. These states are motivated by the observation that (1) the mode weight decays exponentially with the distance from the corresponding edge, (2) the local modes contribute with an alternating sign, and (3) only every other local mode carries relevant weight.

DIAGONALIZATION

All we have to do is to show that $|\xi_{l,r}\rangle$ become degenerate zero-energy eigenstates of H_{bSSH} for $L \rightarrow \infty$. This follows by straightforward calculations,

$$H_{\text{bSSH}}|\xi_l\rangle = \bar{w} \mathcal{N} \sum_{i=1}^L (-\bar{w})^{i-1} |\bar{i}\rangle + \mathcal{N} \sum_{i=1}^{L-1} (-\bar{w})^i |\bar{i}\rangle \quad 3.96a$$

$$= -\mathcal{N} \sum_{i=1}^{L-1} (-\bar{w})^i |\bar{i}\rangle + \mathcal{N} \sum_{i=1}^{L-1} (-\bar{w})^i |\bar{i}\rangle + \bar{w} \mathcal{N} (-\bar{w})^{L-1} |\bar{L}\rangle \quad 3.96b$$

$$= -(-\bar{w})^L \sqrt{\frac{1-\bar{w}^2}{1-\bar{w}^{2L}}} |\bar{L}\rangle \xrightarrow{L \rightarrow \infty} 0, \quad 3.96c$$

in the topological phase for $0 \leq \bar{w} < 1$. The same holds for the right edge mode $|\xi_r\rangle$. Obviously $\langle \xi_l | \xi_r \rangle = 0$ for all L , but as long as $L < \infty$, H_{bSSH} couples both states with an overlap exponentially small in L ,

$$\langle \xi_r | H_{\text{bSSH}} | \xi_l \rangle = -(-\bar{w})^L \frac{1-\bar{w}^2}{1-\bar{w}^{2L}} \quad 3.97a$$

$$\langle \xi_\alpha | H_{\text{bSSH}} | \xi_\alpha \rangle = 0 \quad \text{for } \alpha \in \{r, l\}, \quad 3.97b$$

so that in the $\{|\xi_l\rangle, |\xi_r\rangle\}$ -subspace the Hamiltonian takes the form

$$\tilde{H}_{\text{bSSH}} = -(-\bar{w})^L \frac{1-\bar{w}^2}{1-\bar{w}^{2L}} \begin{bmatrix} 0 & 1 \\ 1 & 0 \end{bmatrix} \quad 3.98$$

and the degeneracy is lifted by $\Delta E_{\text{edge}} \sim \bar{w}^L (1-\bar{w}^2)/(1-\bar{w}^{2L})$ in this naïve approximation. In the following subsections, we derive a much more rigorous result for the edge mode splitting in finite systems.

As a final remark, we point out that Eq. (3.98) explains the observed even-odd effect of the relative transfer phases (recall \S Section 3.C and Subsection 3.3.2): For even chain length L , the couplings in \tilde{H}_{bSSH} are negative, which gives rise to a dynamical phase of $+\frac{\pi}{2}$ after a complete Rabi cycle,

$$\tilde{U} = \mathcal{T} \exp \left[-i \int_0^\tau dt \mathcal{F}(t) \tilde{H}_{\text{bSSH}} \right] = (-1)^L \begin{bmatrix} 0 & i \\ i & 0 \end{bmatrix} \quad 3.99$$

for $\bar{w}^L (1-\bar{w}^2)/(1-\bar{w}^{2L}) \int_0^\tau dt \mathcal{F}(t) = \frac{\pi}{2}$. Compare this result with Eq. (3.39) in Subsection 3.3.2.

3.D.2 Exact Diagonalization

REMARK 3.1:

To streamline mathematical expressions, we set $\delta = 0$ ($\Leftrightarrow \omega_I \equiv 0$) and $\bar{t} = 1$, and rename \bar{w} to t in \S Subsection 3.D.2, \S Subsection 3.D.3 and \S Subsection 3.D.4 (there is no time t involved until \S Section 3.E).

Here we derive a closed expression for the characteristic polynomial of H_{bSSH} . The characteristic polynomial $P[H_{\text{bSSH}}](\lambda) = \det(H_{\text{bSSH}} + \lambda \mathbb{1})$ can be calculated recursively by Laplace expansion¹¹⁹. To this end, we introduce the class of “even” $2L \times 2L$ matrices

$$H_L^+ \equiv \begin{bmatrix} \lambda & t & & & & \\ t & \lambda & 1 & & & \\ & \ddots & \ddots & \ddots & & \\ & & & 1 & \lambda & t \\ & & & & t & \lambda \end{bmatrix} \quad 3.100$$

describing an SSH chain of length L , and its “odd” $(2L - 1) \times (2L - 1)$ descendant

$$H_L^- \equiv \begin{bmatrix} \lambda & 1 & & & & \\ 1 & \lambda & t & & & \\ & \ddots & \ddots & \ddots & & \\ & & & 1 & \lambda & t \\ & & & & t & \lambda \end{bmatrix} \quad 3.101$$

which describes the bosonic SSH network of length L where the left mode b_1 has been deleted¹²⁰.

The Laplace expansion yields the recursion

$$\det H_L^+ = \lambda \det H_L^- - t^2 \det H_{L-1}^+ \quad 3.102a$$

$$\det H_L^- = \lambda \det H_{L-1}^+ - \det H_{L-1}^- . \quad 3.102b$$

If we insert the second equation into the first, we find

$$\det H_L^+ = (\lambda^2 - t^2) \det H_{L-1}^+ - \lambda \det H_{L-1}^- \quad 3.103a$$

$$\det H_L^- = \lambda \det H_{L-1}^+ - \det H_{L-1}^- \quad 3.103b$$

which is the recursive definition of two coupled polynomial sequences that can be compactly written in vectorial form as

$$\begin{bmatrix} \det H_L^+ \\ \det H_L^- \end{bmatrix} = \begin{bmatrix} \lambda^2 - t^2 & -\lambda \\ \lambda & -1 \end{bmatrix} \begin{bmatrix} \det H_{L-1}^+ \\ \det H_{L-1}^- \end{bmatrix} . \quad 3.104$$

To find an explicit expression for $\det H_L^+$ and $\det H_L^-$, we diagonalize the matrix with the transformation

$$\begin{bmatrix} \chi_L^+ \\ \chi_L^- \end{bmatrix} \equiv \begin{bmatrix} -\frac{\lambda}{\eta_t(\lambda)} & \frac{1}{2} \left(1 + \frac{1+\lambda^2-t^2}{\eta_t(\lambda)} \right) \\ +\frac{\lambda}{\eta_t(\lambda)} & \frac{1}{2} \left(1 - \frac{1+\lambda^2-t^2}{\eta_t(\lambda)} \right) \end{bmatrix} \begin{bmatrix} \det H_L^+ \\ \det H_L^- \end{bmatrix} , \quad 3.105$$

¹¹⁹Recall that we have open boundary conditions and cannot simply diagonalize by Fourier transform.

¹²⁰Note that in our bosonic setup this is even *physically* realizable, though not necessary for the following discussion; this is in contrast to the fermionic parent theory.

DIAGONALIZATION

defining new sequences χ_L^+ and χ_L^- , where

$$\eta_t(\lambda) \equiv \sqrt{[1 - (\lambda^2 - t^2)]^2 - 4t^2}. \quad 3.106$$

This yields the decoupled recursion

$$\begin{bmatrix} \chi_L^+ \\ \chi_L^- \end{bmatrix} = \begin{bmatrix} P^+ & 0 \\ 0 & P^- \end{bmatrix} \begin{bmatrix} \chi_{L-1}^+ \\ \chi_{L-1}^- \end{bmatrix}, \quad 3.107$$

with eigenvalues $P^\pm = -\frac{1}{2}[1 - (\lambda^2 - t^2) \pm \eta_t(\lambda)]$, the solutions of which read

$$\chi_L^\pm = (P^\pm)^{L-1} \chi_1^\pm. \quad 3.108$$

To determine the initial values χ_1^\pm , we calculate

$$\det H_1^+ = \det \begin{bmatrix} \lambda & t \\ t & \lambda \end{bmatrix} = \lambda^2 - t^2 \quad 3.109a$$

$$\det H_1^- = \det [\lambda] = \lambda, \quad 3.109b$$

and apply the transformation (3.105). This yields

$$\chi_1^\pm = \mp \frac{\lambda}{\eta_t(\lambda)} (\lambda^2 - t^2) + \frac{\lambda}{2} \left(1 \pm \frac{1 + \lambda^2 - t^2}{\eta_t(\lambda)} \right). \quad 3.110$$

Finally, the inverse transformation

$$\begin{bmatrix} \det H_L^+ \\ \det H_L^- \end{bmatrix} = \begin{bmatrix} \frac{1 + \lambda^2 - t^2 - \eta_t(\lambda)}{2\lambda} & \frac{1 + \lambda^2 - t^2 + \eta_t(\lambda)}{2\lambda} \\ 1 & 1 \end{bmatrix} \begin{bmatrix} \chi_L^+ \\ \chi_L^- \end{bmatrix} \quad 3.111$$

yields the closed expression

$$P[H_{\text{bSSH}}] = \det H_L^+ = \frac{1 + \lambda^2 - t^2 - \eta_t(\lambda)}{2\lambda} \cdot \chi_L^+ + \frac{1 + \lambda^2 - t^2 + \eta_t(\lambda)}{2\lambda} \cdot \chi_L^- \quad 3.112$$

which can be massaged into the form

$$P[H_{\text{bSSH}}] = \frac{1 + \lambda^2 - t^2 - \eta_t(\lambda)}{\eta_t(\lambda)} [1 - (\lambda^2 - t^2) + \eta_t(\lambda)]^L - \frac{1 + \lambda^2 - t^2 + \eta_t(\lambda)}{\eta_t(\lambda)} [1 - (\lambda^2 - t^2) - \eta_t(\lambda)]^L. \quad 3.113$$

Note that this indeed is a polynomial in λ , despite the square root in $\eta_t(\lambda)$ (see $\clubsuit\clubsuit$ Subsection 3.D.3 below). We conclude with the following result:

RESULT 3.1: Spectrum of $H_{\text{bSSH}}, H_{\text{SSH}}, H_{\text{bMC}}, H_{\text{MC}}$

The single-particle spectrum of the SSH (and Majorana) chain with open boundary conditions and chain length L is determined by the roots of Eq. (3.113), i.e., the solutions of

$$\frac{1 + (\lambda^2 - t^2) - \eta_t(\lambda)}{1 + (\lambda^2 - t^2) + \eta_t(\lambda)} = \left[\frac{1 - (\lambda^2 - t^2) - \eta_t(\lambda)}{1 - (\lambda^2 - t^2) + \eta_t(\lambda)} \right]^L. \quad 3.114$$

3.D.3 Asymptotic Edge Mode Splitting

Here we derive an asymptotic expression for the edge mode splitting ΔE_{edge} as a function of the coupling strength t in the topological phase, i.e., for $0 \leq t < 1$. An application of the binomial theorem allows us to rewrite the characteristic polynomial of H_{bSSH} in Eq. (3.113) as the sum

$$\begin{aligned} P[H_{\text{bSSH}}] &= \sum_{n=0}^{\lfloor L/2 \rfloor} \left(\frac{1 + (\lambda^2 - t^2)}{1 - (\lambda^2 - t^2)} \cdot \frac{L - 2n}{2n + 1} - 1 \right) \\ &\quad \times \binom{L}{2n} [1 - (\lambda^2 - t^2)]^{L-2n} \\ &\quad \times \left\{ [1 - (\lambda^2 - t^2)]^2 - 4t^2 \right\}^n, \end{aligned} \quad 3.115$$

so that the polynomial nature of $P[H_{\text{bSSH}}]$ in λ is now evident¹²¹. Finding the roots of this polynomial, or, equivalently, solving Eq. (3.114), is a non-trivial task as it can be recast as a transcendental equation (see \clubsuit Subsection 3.D.4).

As we are interested in the edge mode energies which are, at least for L large and/or t not too close to unity, nearly zero-energy eigenstates, we might assume that these nearly vanishing roots are determined by quadratic terms of $P[H_{\text{bSSH}}]$ up to minor corrections due to a polynomial of degree four. Collecting summands in Eq. (3.115) of degree zero and two, and evaluating the sums yields

$$P[H_{\text{bSSH}}] = -2^{L-1} (t^2 + t^{2L}) + 2^{L-1} \frac{t^2 + Lt^{2L} - 1 - L}{t^2 - 1} \cdot \lambda^2 + \mathcal{O}(\lambda^4). \quad 3.116$$

Alternatively, this follows by Taylor expanding Eq. (3.113) up to second order at $\lambda = 0$. Solving $P[H_{\text{bSSH}}] = 0$ in this approximation yields the solutions

$$\lambda_{\pm} = \pm \frac{t^L(t^2 - 1)}{\sqrt{1 - (1 + L)t^{2L} + Lt^{2+2L}}} \quad 3.117$$

¹²¹Note that $L - 2n = 0$ for $n = L/2$.

DIAGONALIZATION

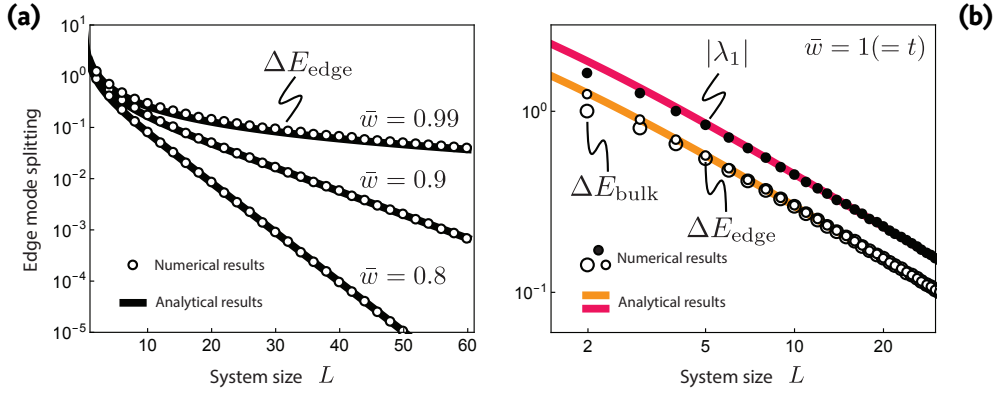


FIGURE 3.19 • Asymptotic vs. numerical results. (a) Comparison of numerical results (circles) for the edge mode splitting ΔE_{edge} and the analytically derived asymptotically exact expression (black bold lines) Eq. (3.118a) in the topological phase for $\bar{w}(=t) = 0.8, 0.9, 0.99$. Close to the phase transition (large edge mode splitting), small deviations between (exact) numerical and (approximate) analytical results are visible. Note that the observed deviations from the expected exponential decay for small systems ($L \sim 5$) are captured well by our analytic expression. (b) Numerical values for ΔE_{edge} (small circles), ΔE_{bulk} (large circles) and the asymptotic expressions derived in \S Subsection 3.D.5 (both yellow) at the phase transition $\bar{w}(=t) = 1 = \bar{t}$. Note that the spectrum becomes linear for $L \rightarrow \infty$ close to the band crossing and therefore $\Delta E_{\text{edge}} = \Delta E_{\text{bulk}}$ for the asymptotic expressions. In addition, we plot numerical values for $|\lambda_1|$ (black bullets) and compare it with the asymptotic expression (red). For $L \gtrsim 10$ finite-size effects are negligible. Compare the (critical) algebraic decay with the (gapped) exponential decay in (a).

so that the edge mode splitting can be approximated as

$$\Delta E_{\text{edge}} = \lambda_+ - \lambda_- = \frac{2t^L(1-t^2)}{\sqrt{1-(1+L)t^{2L} + Lt^{2+2L}}} \quad 3.118a$$

$$\sim 2(1-t^2)e^{-L/\xi} \quad 3.118b$$

with $\xi = -1/\log t$. As expected, for $L \rightarrow \infty$ and/or $t \rightarrow 0$, the edge mode splitting vanishes exponentially in L : $\Delta E_{\text{edge}} \sim t^L$. Equation (3.118) also tells us that the gap closes again for $t \rightarrow 1$ where the topological phase transition occurs¹²². Interestingly, Eq. (3.118a) also predicts deviations of the exponential decay for small systems that are not too close to the topological transition. These can indeed be verified by numerically diagonalizing H_{bSSH} , as shown in Figure 3.19 (a).

¹²²In this case the exponential decay is replaced by an algebraic one.

3.D.4 Analytic Spectrum

Here we derive transcendental equations from Eq. (3.114) that implicitly determine the exact spectrum of $H_{(b)SSH}$ and $H_{(b)MC}$ (for open boundary conditions). We use them below to find asymptotically exact expressions for the scaling of ΔE_{edge} and ΔE_{bulk} close to and at the phase transition. It will become graphically transparent how the edge modes emerge or vanish for t crossing the critical value 1.

The discriminating quantity appearing in Eq. (3.114) is

$$\eta_t(\lambda) = \sqrt{[1 - (\lambda^2 - t^2)]^2 - 4t^2}. \quad 3.119$$

There are two qualitatively different ranges for λ : The one for which η_t is purely imaginary and the one for which it is real. η_t is purely imaginary if ($t \geq 0$)

$$[1 - (\lambda^2 - t^2)]^2 - 4t^2 \leq 0 \quad \Leftrightarrow \quad |1 + t^2 - \lambda^2| \leq 2t. \quad 3.120$$

In the first case, we have $1 + t^2 - \lambda^2 \geq 0 \Leftrightarrow |\lambda| \leq \sqrt{1 + t^2}$ and

$$1 + t^2 - \lambda^2 \leq 2t \quad \Leftrightarrow \quad |\lambda| \geq \sqrt{(1 - t)^2} = |1 - t|, \quad 3.121$$

and in the second case we have $1 + t^2 - \lambda^2 < 0 \Leftrightarrow |\lambda| > \sqrt{1 + t^2}$ and

$$-1 - t^2 + \lambda^2 \leq 2t \quad \Leftrightarrow \quad |\lambda| \leq \sqrt{(1 + t)^2} = |1 + t|. \quad 3.122$$

Combining both results yields

$$|1 - t| \leq |\lambda| \leq |1 + t| \quad 3.123$$

with $\eta_t \equiv iy$ and $y \equiv \sqrt{4t^2 - [1 - (\lambda^2 - t^2)]^2} \in \mathbb{R}$.

In the complementary region,

$$|\lambda| < |1 - t| \quad \text{or} \quad |\lambda| > |1 + t|, \quad 3.124$$

we have $\eta_t \in \mathbb{R}$. Let us have a look at Eq. (3.114) for the two cases separately:

→ For $|1 - t| \leq |\lambda| \leq |1 + t|$, Eq. (3.114) takes the form

$$\frac{x_1 - iy}{x_1 + iy} = \left[\frac{x_2 - iy}{x_2 + iy} \right]^L \quad \Leftrightarrow \quad \frac{z_1^*}{z_1} = \left[\frac{z_2^*}{z_2} \right]^L \quad 3.125$$

where we introduced $x_1 \equiv 1 - t^2 + \lambda^2$ and $x_2 \equiv 1 + t^2 - \lambda^2$. With $z_k \equiv x_k + iy \equiv |z_k|e^{i\varphi_k}$, this reads

$$e^{-2i\varphi_1} = e^{-2Li\varphi_2} \quad \Leftrightarrow \quad \varphi_1 = L\varphi_2 + \pi\mathbb{Z}. \quad 3.126$$

If we define the angular arctangent function $\text{atan}(y/x)$ as

$$\arg(x + iy) = \text{atan}(y/x) \equiv \begin{cases} \arctan\left(\frac{y}{x}\right) & \text{for } x > 0, \\ \arctan\left(\frac{y}{x}\right) + \pi & \text{for } x < 0, \end{cases} \quad 3.127$$

DIAGONALIZATION

Eq. (3.114) becomes

$$\begin{aligned} A(\lambda) &\equiv \operatorname{atan} \left[\frac{\sqrt{4t^2 - [1 - (\lambda^2 - t^2)]^2}}{1 - t^2 + \lambda^2} \right] \\ &\stackrel{!}{=} L \operatorname{atan} \left[\frac{\sqrt{4t^2 - [1 - (\lambda^2 - t^2)]^2}}{1 + t^2 - \lambda^2} \right] + \pi \mathbb{Z} \equiv \mathbb{B}(\lambda) \end{aligned} \quad 3.128$$

which is valid for $|1 - t| \leq |\lambda| \leq |1 + t|$ and implicitly determines (almost, see below) the complete spectrum of H_{bSSH} .

→ For $|\lambda| < |1 - t|$ or $|\lambda| > |1 + t|$, both sides of Eq. (3.114) are real which motivates the definition

$$R_k \equiv \frac{x_k - \eta_t}{x_k + \eta_t} \quad 3.129$$

so that Eq. (3.114) takes the simple form

$$R_1 = R_2^L. \quad 3.130$$

The solvability of this equation (for some L) is determined by the modulus of R_k :

$$|R_k| \leq 1 \quad \Leftrightarrow \quad |x_k - \eta_t| \leq |x_k + \eta_t| \quad \Leftrightarrow \quad x_k \geq 0 \quad 3.131$$

Here we used that $\eta_t \geq 0$ for all allowed λ . This boils down to the conditions

$$|R_1| \leq 1 \quad \Leftrightarrow \quad 1 - t^2 + \lambda^2 \geq 0 \quad \Leftrightarrow \quad \lambda^2 \geq t^2 - 1 \quad 3.132a$$

$$|R_2| \leq 1 \quad \Leftrightarrow \quad 1 + t^2 - \lambda^2 \geq 0 \quad \Leftrightarrow \quad |\lambda| \leq \sqrt{1 + t^2}. \quad 3.132b$$

These ranges must be combined with the allowed intervals for λ .

First, let $|\lambda| > |1 + t|$. Clearly $|1 + t| \geq \sqrt{1 + t^2}$, so we have $|\lambda| > \sqrt{1 + t^2}$ and therefore $|R_2| > 1$. Furthermore $\lambda^2 > (1 + t)^2 \geq t^2 - 1$ and we find $|R_1| < 1$. Combined, this reads for $|\lambda| > |1 + t|$:

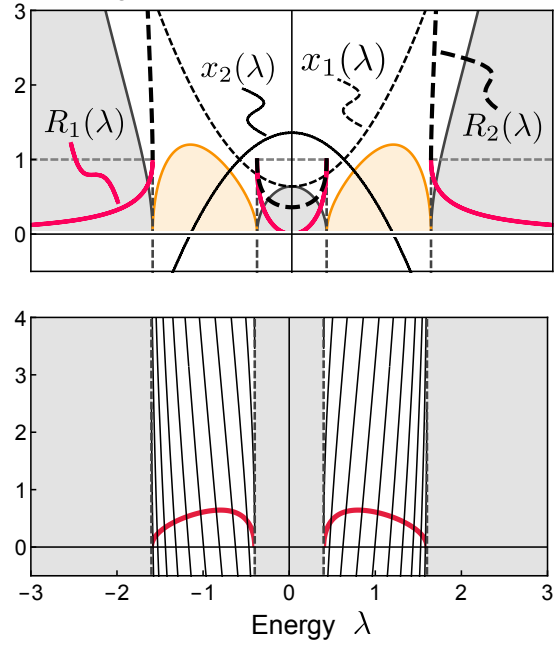
$$|R_1| < 1 < |R_2| \leq |R_2|^L \quad \Rightarrow \quad \forall L : R_1 \neq R_2^L \quad 3.133$$

We conclude that there are *no* additional solutions for $|\lambda| > |1 + t|$, independent of t .

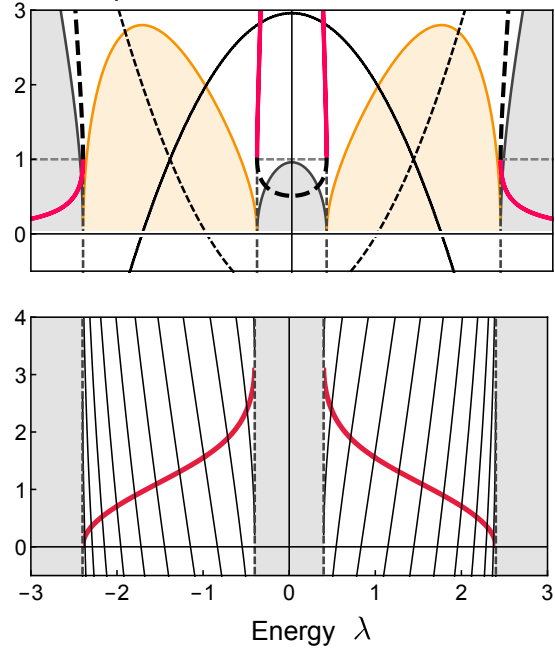
Second, let $|\lambda| < |1 - t|$. This is more interesting: Clearly $\sqrt{1 + t^2} \geq |1 - t|$, so we have $|\lambda| < |1 - t| \leq \sqrt{1 + t^2}$ which leads to $|R_2| < 1$. Now comes the crucial step: In the *trivial phase* we have $t > 1$ which allows us to estimate $(1 - t)^2 = t^2 - 1 + 2(1 - t) \leq t^2 - 1$ and thereby $\lambda^2 < t^2 - 1$ which yields $|R_1| > 1$. Following the same argument as above, it follows that there are no additional solutions in the range $|\lambda| < |1 - t|$. Then all solutions are determined by Eq. (3.128) and we identify the intervals $|1 - t| \leq |\lambda| \leq |1 + t|$ with the PH symmetric energy bands gapped by $2|1 - t|$. As we just proved, there exist no states in this gap.

QUANTUM COMMUNICATION BETWEEN QUBITS

(a) Topological phase



(c) Trivial phase



DIAGONALIZATION

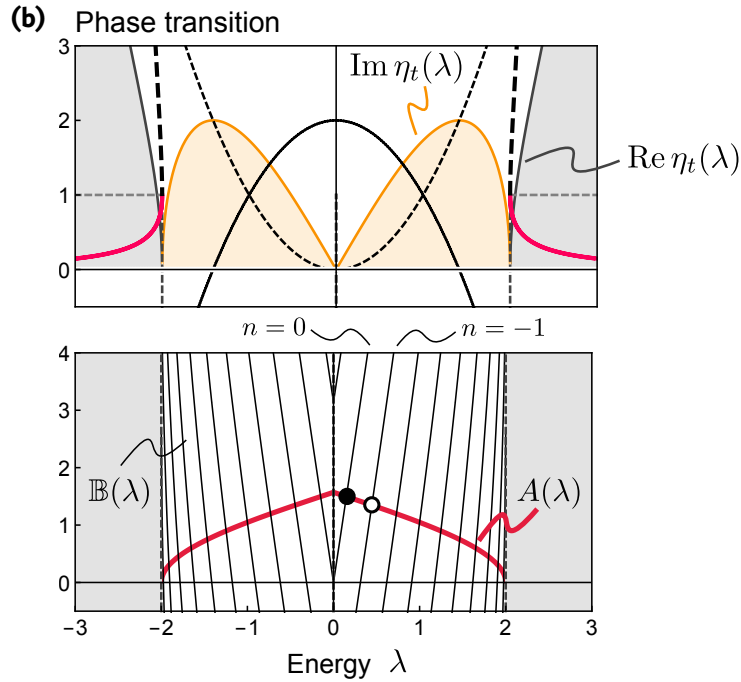


FIGURE 3.20 • Analytic spectrum—Bulk modes. Illustration of the analytic quantities defined in the text (** Subsection 3.D.4) for couplings **(a)** $t = 0.6$ (topological phase), **(b)** $t = 1.0$ (phase transition), and **(c)** $t = 1.4$ (trivial phase). In the upper row, the quantities $\text{Im } \eta_t(\lambda)$, $\text{Re } \eta_t(\lambda)$, $x_1(\lambda)$, $x_2(\lambda)$, $R_1(\lambda)$, and $R_2(\lambda)$ are plotted. Note that $R_2 > 1$ and $R_1 < 1$ above and below the bands ($|\lambda| > |1 + t|$) whereas (a) $R_1 < 1$ and $R_2 < 1$ in the band gap ($|\lambda| < |1 - t|$) in the topological phase for $t < 1$ but (c) $R_1 > 1$ and $R_2 < 1$ in the trivial phase for $t > 1$. In the lower row the quantities $A(\lambda)$ and $\mathbb{B}(\lambda)$ are shown. Each intersection of $A(\lambda)$ with one of the branches of $\mathbb{B}(\lambda)$ corresponds to an eigenenergy of a bulk mode.

In the *topological phase* for $t < 1$, it follows trivially $\lambda^2 \geq 0 > t^2 - 1$ and therefore $|R_1| < 1$. Note that the statement $|R_2| < 1$ remains valid since it does not depend on t . This opens the possibility for non-trivial solutions of Eq. (3.130). It is easy to see that at the lower band edge, $|\lambda| = |1 - t|$, one has $\eta_t(\lambda) = 0$, hence $R_1 = 1 = R_2$. Furthermore $R_1(\lambda = 0) \propto 1 - t^2 - (1 - t^2) = 0$ but $R_2(\lambda = 0) \propto 1 + t^2 - (1 - t^2) \neq 0$. Together with $R_1, R_2 \geq 0$, this guarantees at least one pair $\pm\lambda_0$ of additional solutions for L large enough since $\lim_{L \rightarrow \infty} R_2^L(\lambda) = 0$ for $|\lambda| < |1 - t|$. These solutions, of course, are taken from Eq. (3.128) to make up for the fixed dimension of the Hilbert space. Monotonicity arguments show that there is indeed just a *single* pair of additional solutions $\pm\lambda_0$ for $t < 1$ —these are the edge states. Their energy is determined by the equation

$$\begin{aligned} X(\lambda) &\equiv [1 + \lambda^2 - t^2 - \eta_t(\lambda)][1 - \lambda^2 + t^2 + \eta_t(\lambda)]^L \\ &\stackrel{!}{=} [1 + \lambda^2 - t^2 + \eta_t(\lambda)][1 - \lambda^2 + t^2 - \eta_t(\lambda)]^L \equiv Y(\lambda) \end{aligned} \quad 3.134$$

QUANTUM COMMUNICATION BETWEEN QUBITS

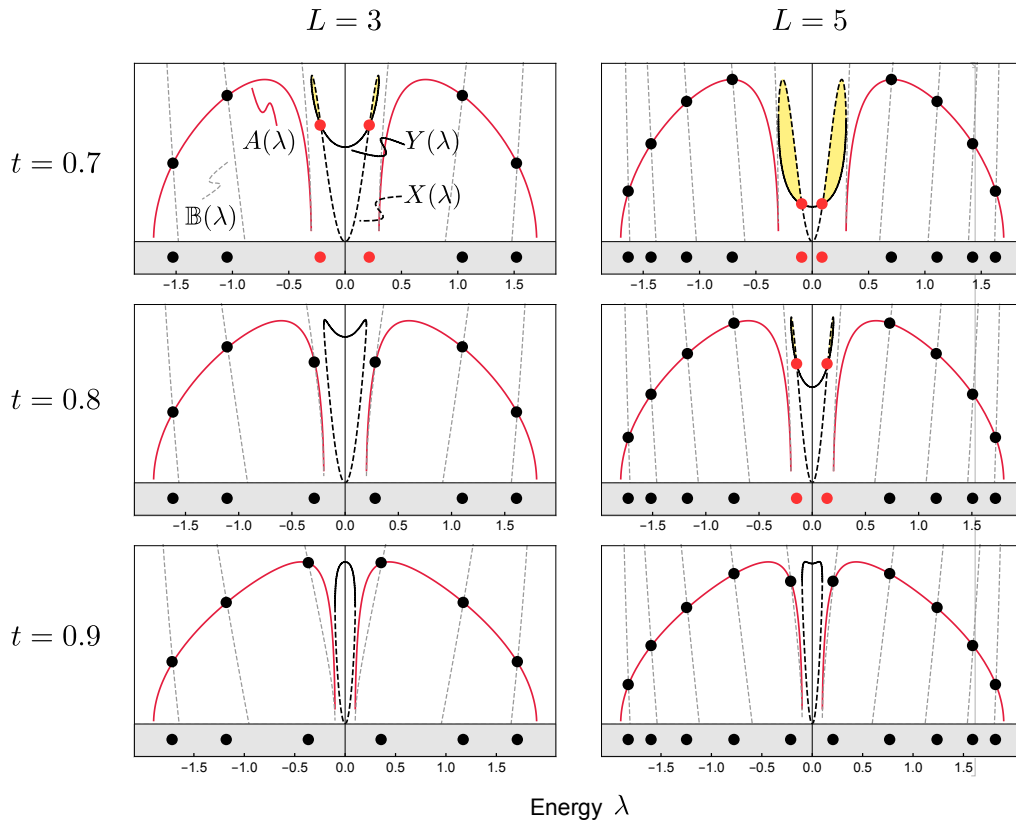


FIGURE 3.21 • Analytic spectrum—Edge modes. We plot $A(\lambda)$, $\mathbb{B}(\lambda)$, $X(\lambda)$, and $Y(\lambda)$ for three topological couplings $t = 0.7, 0.8, 0.9$ and two chain lengths $L = 3, 5$. Intersections of $A(\lambda)$ and $\mathbb{B}(\lambda)$ (black bullets) represent bulk eigenmodes. Intersections of $X(\lambda)$ and $Y(\lambda)$ (red bullets) correspond to edge modes. All intersections are projected onto the energy axis to illustrate the spectrum. Note that at $t = 0.8$ there are only bulk modes for the $L = 3$ setup while the $L = 5$ setup already “relabels” two of the bulk modes as edge modes.

which is solvable for $|\lambda| < |1 - t|$ with $0 \leq t < 1$ by the above arguments for L large enough.

Interestingly, the critical coupling t^* for which the edge mode solutions appear depends on the chain length L and one finds $t^*(L) < t_{\text{crit}} = 1$ with $\lim_{L \rightarrow \infty} t^*(L) = t_{\text{crit}}$, see Figure 3.21.

We illustrate the relevant quantities of this discussion in Figure 3.20 for three parameters t below, at, and above the critical value. In Figure 3.21 we show the size-dependent emergence of the edge mode solutions in the topological phase for three different couplings and two system sizes.

3.D.5 Scaling at the Critical Point

REMARK 3.2:

To simplify calculations, we set $\delta = 0$ ($\Leftrightarrow \omega_I \equiv 0$) and $\bar{t} = 1$ as before. However, we revert the notation from the technical previous parts, $t \rightarrow \bar{w}$, in \clubsuit Subsection 3.D.5, \clubsuit Subsection 3.D.6 and \clubsuit Subsection 3.D.7.

Let $\Delta\bar{w} = \bar{t} - \bar{w}$. Here we consider a chain at criticality, $\Delta\bar{w} = 0$, and set $\bar{t} = 1$. Then Eq. (3.128) reads

$$\operatorname{atan} \left[\frac{\sqrt{4 - [2 - \lambda^2]^2}}{\lambda^2} \right] \stackrel{!}{=} L \operatorname{atan} \left[\frac{\sqrt{4 - [2 - \lambda^2]^2}}{2 - \lambda^2} \right] + n\pi, \quad n \in \mathbb{Z} \quad 3.135$$

which is valid for all $0 < |\lambda| < 2$ since $|\bar{w} - 1| = 0$ and $|1 + \bar{w}| = 2$. Inspection shows [see Figure 3.20 (b)] that the solutions $\pm\lambda_0$ of minimum absolute value (the ones which eventually become edge states for $\Delta\bar{w} > 0$) can be found for $n = 0$, whereas the next pair of eigenvalues $\pm\lambda_1$ (evolving into the lower band edge for $\Delta\bar{w} > 0$) is specified by $n = -1$; there are only solutions for $-L < n \leq 0$.

To evaluate $\Delta E_{\text{edge}} \equiv 2|\lambda_0|$ and $\Delta E_{\text{bulk}} \equiv |\lambda_1 - \lambda_0|$, we have to solve Eq. (3.135) for $n = 0, -1$. As we already know that the gap closes, we can expect $\lambda_0, \lambda_1 \rightarrow 0$ for $L \rightarrow \infty$. Thus we may expand Eq. (3.135) into linear order of λ to find asymptotically exact expressions for both eigenenergies:

$$\frac{\pi}{2} - \frac{\lambda}{2} + \mathcal{O}(\lambda^3) = L\lambda + \mathcal{O}(\lambda^3) + n\pi \quad \text{for} \quad n \in \mathbb{Z}. \quad 3.136$$

Thus we have

$$\lambda_0 \sim \frac{\pi}{2L + 1} \sim \frac{\pi}{2L} \quad 3.137a$$

$$\lambda_1 \sim \frac{3\pi}{2L + 1} \sim \frac{3\pi}{2L} \quad 3.137b$$

asymptotically for $L \rightarrow \infty$.

RESULT 3.2:

We find for the timescales

$$\Delta E_{\text{edge}}^{-1} \sim \frac{2L + 1}{2\pi} \sim \frac{L}{\pi} \quad \text{and} \quad \Delta E_{\text{bulk}}^{-1} \sim \frac{2L + 1}{2\pi} \sim \frac{L}{\pi}. \quad 3.138$$

We compare these expressions with numerical results in Figure 3.19 (b). There we find that “ $L \rightarrow \infty$ ” can roughly be read as $L \gtrsim 10$ in practice.

3.D.6 Scaling Away from the Critical Point

Here we consider the case $|\Delta\bar{w}| > 0$. Recall that the lower band edge is $|\Delta\bar{w}|$ which motivates the new energy variable $\delta = \lambda - |\Delta\bar{w}|$ to measure the distance of bulk modes ($\lambda > |\Delta\bar{w}|$) from the lower band edge.

If we define the LHS argument

$$\alpha_L \equiv \frac{\sqrt{\delta(\delta + 2|\Delta\bar{w}|)[4(1 - \Delta\bar{w}) - \delta(\delta + 2|\Delta\bar{w}|)]}}{2\Delta\bar{w} + \delta(\delta + 2|\Delta\bar{w}|)} \quad 3.139$$

and the RHS argument

$$\alpha_R \equiv \frac{\sqrt{\delta(\delta + 2|\Delta\bar{w}|)[4(1 - \Delta\bar{w}) - \delta(\delta + 2|\Delta\bar{w}|)]}}{2(1 - \Delta\bar{w}) - \delta(\delta + 2|\Delta\bar{w}|)}, \quad 3.140$$

Eq. (3.128) takes the form

$$\text{atan } \alpha_L = L \text{atan } \alpha_R + \pi\mathbb{Z}. \quad 3.141$$

There is a singularity for $\Delta\bar{w} \rightarrow \pm 0$ and $\delta \rightarrow 0$ in the sense that the left-hand side is discontinuous

$$\lim_{\delta \rightarrow 0} \text{atan } \alpha_L = \begin{cases} 0 & \text{for } \Delta\bar{w} > 0 \quad (\text{topological}), \\ \frac{\pi}{2} & \text{for } \Delta\bar{w} = 0 \quad (\text{critical}), \\ \pi & \text{for } \Delta\bar{w} < 0 \quad (\text{trivial}), \end{cases} \quad 3.142$$

induced by the true singularity of the argument

$$\begin{aligned} & \lim_{\delta \rightarrow 0} \frac{\sqrt{\delta(\delta + 2|\Delta\bar{w}|)[4(1 - \Delta\bar{w}) - \delta(\delta + 2|\Delta\bar{w}|)]}}{2\Delta\bar{w} + \delta(\delta + 2|\Delta\bar{w}|)} \\ &= \begin{cases} +0 & \text{for } \Delta\bar{w} > 0 \quad (\text{topological}), \\ \infty & \text{for } \Delta\bar{w} = 0 \quad (\text{critical}), \\ -0 & \text{for } \Delta\bar{w} < 0 \quad (\text{trivial}). \end{cases} \end{aligned} \quad 3.143$$

By contrast, the right-hand side is non-singular,

$$\lim_{\delta \rightarrow 0} \text{atan } \alpha_R = 0 \quad \text{for all } \Delta\bar{w}. \quad 3.144$$

Here we used the definition in Eq. (3.127). See Figure 3.20 [$A(\lambda)$, red curves in the lower panels] for an illustration of these statements. This behavior is responsible for both the emergence of edge modes for $\Delta\bar{w} > 0$ and the replacement of the asymptotic $1/L$ decay of the bulk modes at $\Delta\bar{w} = 0$ by an $1/L^2$ decay towards the lower band edge $|\Delta\bar{w}|$ for $\Delta\bar{w} \neq 0$.

DIAGONALIZATION

The discontinuity of the LHS in Eq. (3.128) forbids a consistent expansion for $\delta \rightarrow 0$ and $\Delta\bar{w} \rightarrow 0$ at the same time. Therefore we consider two cases to simplify Eq. (3.141) separately:

- 1 $\alpha_L \ll 1, \alpha_R \ll 1$, which allows us to solve $\alpha_L (+\pi) = \alpha_R + \pi\mathbb{Z}$ instead of Eq. (3.141).
- 2 $\alpha_L \gg 1, \alpha_R \ll 1$, which allows us to solve $\frac{\pi}{2} = \alpha_R + \pi\mathbb{Z}$ instead of Eq. (3.141).

In addition, we always assume that $\delta \ll 1$ and $|\Delta\bar{w}| \ll 1$, i.e., we consider bulk modes close to the lower band edge and close to criticality. For the simplified equations, we used that the arctangent function can be linearized if we take into account definition (3.127) as

$$\text{atan}(y/x) \approx y/x (+\pi) \quad \text{for} \quad x > 0 \ (x < 0). \quad 3.145$$

First Regime: $\alpha_L \ll 1$

We start with the first case, $\alpha_L \ll 1, \alpha_R \ll 1$, which allows to simplify Eq. (3.141) as

$$\alpha_L (+\pi) = \alpha_R + \pi\mathbb{Z} \quad 3.146$$

where the optional $+\pi$ follows in the trivial phase for $\Delta\bar{w} < 0$. We are interested in the bulk modes with lowest energy, i.e., closest to the lower band edge. This yields the two equations (upper: $\Delta\bar{w} > 0$; lower: $\Delta\bar{w} < 0$)

$$\begin{aligned} & \frac{\sqrt{\delta(\delta + 2|\Delta\bar{w}|)[4(1 - \Delta\bar{w}) - \delta(\delta + 2|\Delta\bar{w}|)]}}{2\Delta\bar{w} + \delta(\delta + 2|\Delta\bar{w}|)} + \begin{cases} 0 \\ \pi \end{cases} \\ & = L \frac{\sqrt{\delta(\delta + 2|\Delta\bar{w}|)[4(1 - \Delta\bar{w}) - \delta(\delta + 2|\Delta\bar{w}|)]}}{2(1 - \Delta\bar{w}) - \delta(\delta + 2|\Delta\bar{w}|)} + \begin{cases} -\pi \\ 0 \end{cases} \end{aligned} \quad 3.147$$

which are valid for $\delta \ll \min\{C_{\alpha_L=1}^\delta(\Delta\bar{w}), C_{\alpha_R=1}^\delta(\Delta\bar{w})\}$ with yet to be determined functions $C_{\alpha_L=1}^\delta$ and $C_{\alpha_R=1}^\delta$ that determine the range of validity for the linearization of the LHS and RHS arctangent functions. Note that the scaling of the bulk modes is the same for $\Delta\bar{w} \gtrless 0$. For the choice of the correct value of $\pi\mathbb{Z}$ in Eq. (3.146), see Figure 3.20.

We have to solve the equation

$$\begin{aligned} & \frac{\pi}{\sqrt{\delta(\delta + 2|\Delta\bar{w}|)[4(1 - \Delta\bar{w}) - \delta(\delta + 2|\Delta\bar{w}|)]}} \\ & = \frac{L}{2(1 - \Delta\bar{w}) - \delta(\delta + 2|\Delta\bar{w}|)} - \frac{1}{2\Delta\bar{w} + \delta(\delta + 2|\Delta\bar{w}|)} \end{aligned} \quad 3.148$$

which reduces to

$$\pi \sqrt{1 - \Delta\bar{w}} \Delta\bar{w} = \sqrt{\delta} \cdot \sqrt{2|\Delta\bar{w}|} (L\Delta\bar{w} + \Delta\bar{w} - 1) \quad 3.149$$

in lowest order of δ . Note that this expansion requires the additional condition $\delta \ll 1$ so that our total range of validity reads now

$$\delta \ll \min\{1, C_{\alpha_L=1}^\delta(\Delta\bar{w}), C_{\alpha_R=1}^\delta(\Delta\bar{w})\}. \quad 3.150$$

Solving for δ yields

$$\delta_{\text{bulk}}^{L \rightarrow \infty} \equiv \frac{\pi^2}{2} \frac{(1 - \Delta\bar{w})|\Delta\bar{w}|}{(L\Delta\bar{w} + \Delta\bar{w} - 1)^2} \quad 3.151a$$

$$\stackrel{L \rightarrow \infty}{\sim} \frac{\pi^2(1 - \Delta\bar{w})}{2|\Delta\bar{w}|} \frac{1}{L^2} \equiv \tilde{\delta}_{\text{bulk}}^{L \rightarrow \infty} \quad 3.151b$$

valid for $0 < |\Delta\bar{w}| < 1$.

RESULT 3.3:

To sum it up, in the gapped phases ($|\Delta\bar{w}| \neq 0$), the bulk modes closest to the band edge have the asymptotic energy

$$\begin{aligned} E_{\text{bulk}}^{L \rightarrow \infty} &= |\Delta\bar{w}| + \delta_{\text{bulk}}^{L \rightarrow \infty} \\ &= |\Delta\bar{w}| \left[1 + \frac{\pi^2/2}{\frac{\Delta\bar{w}^2}{1-\Delta\bar{w}}L^2 - 2\Delta\bar{w}L + (1 - \Delta\bar{w})} \right] \end{aligned} \quad 3.152a$$

$$\sim |\Delta\bar{w}| + \frac{\pi^2(1 - \Delta\bar{w})}{2|\Delta\bar{w}|} \frac{1}{L^2} \quad (L \rightarrow \infty). \quad 3.152b$$

Note that due to the exponential decay of the edge mode energy ΔE_{edge} , one has $E_{\text{bulk}}^{L \rightarrow \infty} = |\lambda_1| \approx |\lambda_1 - \lambda_0| = \Delta E_{\text{bulk}}$ in the topological phase.

We are left with the determination of $C_{\alpha_{R/L}=1}^\delta(\Delta\bar{w})$, i.e., the range of δ for which these relations are valid. We define $C_{\alpha_{R/L}=1}^\delta(\Delta\bar{w})$ as the smallest positive solutions for δ where α_R and α_L are equal to one:

→ The condition $\alpha_L \stackrel{!}{=} 1$ reduces to

$$\begin{aligned} &\delta(\delta + 2|\Delta\bar{w}|)[4(1 - \Delta\bar{w}) - \delta(\delta + 2|\Delta\bar{w}|)] \\ &= [2\Delta\bar{w} + \delta(\delta + 2|\Delta\bar{w}|)]^2 \end{aligned} \quad 3.153$$

which yields the smallest positive solution

$$\begin{aligned} &C_{\alpha_L=1}^\delta(\Delta\bar{w}) \\ &= \left[(\Delta\bar{w} - 1)^2 - \sqrt{2\Delta\bar{w}^2 - 4\Delta\bar{w} + 1} \right]^{1/2} - |\Delta\bar{w}| \end{aligned} \quad 3.154a$$

$$\sim (\sqrt{2} - 1) \Delta\bar{w} \quad 3.154b$$

$$\approx 0.4 \Delta\bar{w} \quad 3.154c$$

DIAGONALIZATION

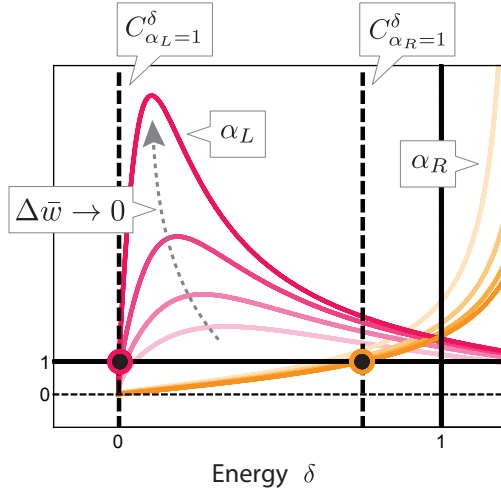


FIGURE 3.22 • Scaling away from the critical point—Lower band edge. We plot the left-hand (right-hand) arguments α_L (α_R) defined in Eq. (3.139) and Eq. (3.140) as functions of the energy $\delta = \lambda - |\Delta\bar{w}|$ for couplings $\Delta\bar{w} \rightarrow 0$ in the topological phase close to the phase transition ($0 < \Delta\bar{w} \ll 1$). Note that α_L diverges close to the lower band edge $|\Delta\bar{w}|$ ($\delta = 0$) for $\Delta\bar{w} \rightarrow 0$ whereas α_R remains finite. $C_{\alpha_{R/L}=1}^\delta$ denote values of δ for which $\alpha_{R/L}$ are of order $\mathcal{O}(1)$; see text for details.

where the linear terms follow for $0 < \Delta\bar{w} \ll 1$, i.e., close to the topological phase transition but within the topological phase. If we take into account the behavior of α_L for $\delta \rightarrow 0$, see Figure 3.22, we conclude that for $0 \leq \delta < C_{\alpha_L=1}^\delta(\Delta\bar{w})$ it is $\alpha_L \ll 1$ and the linearization of the LHS arctangent is valid. Contrary, for $C_{\alpha_L=1}^\delta(\Delta\bar{w}) < \delta \ll 1$ we conclude that $\alpha_L \gg 1$ for $\Delta\bar{w} \ll 1$.

→ The condition $\alpha_R \stackrel{!}{=} 1$ reduces to

$$\begin{aligned} & \delta(\delta + 2|\Delta\bar{w}|)[4(1 - \Delta\bar{w}) - \delta(\delta + 2|\Delta\bar{w}|)] \\ & = [2(\Delta\bar{w} - 2) + \delta(\delta + 2|\Delta\bar{w}|)]^2 \end{aligned} \quad 3.155$$

which yields the smallest positive solution

$$C_{\alpha_R=1}^\delta(\Delta\bar{w}) = \left[\Delta\bar{w}^2 + (2 - \sqrt{2})(1 - \Delta\bar{w}) \right]^{1/2} - |\Delta\bar{w}| \quad 3.156a$$

$$\sim \sqrt{2 - \sqrt{2}} - \left(1 + \frac{1}{2}\sqrt{2 - \sqrt{2}} \right) \Delta\bar{w} \quad 3.156b$$

$$\approx 0.8 - 1.4 \Delta\bar{w} \quad 3.156c$$

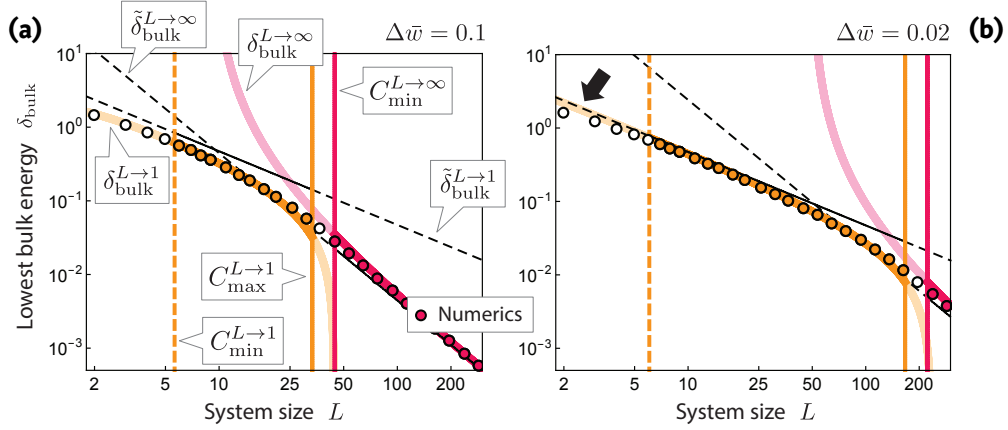


FIGURE 3.23 • Scaling away from the critical point—System size. (a) Lowest bulk energy $\delta_{\text{bulk}} = \lambda_1 - |\Delta\bar{w}|$ in the topological phase for $\Delta\bar{w} = 0.1$ vs. chain length L . We compare numerical results (circles) with the asymptotic analytical ones (solid lines) derived in the text. The latter are valid in their respective L -intervals (vertical lines). In the left (yellow) interval, the $1/L$ decay dominates whereas in the right (red) interval the faster $1/L^2$ decay takes over. (b) The same for $\Delta\bar{w} = 0.02$, closer to the critical point. Note how the $1/L$ decay dominates for a larger L -range. Marked by the arrow, finite-size deviations from the approximate expression $\delta_{\text{bulk}}^{L \rightarrow 1}$ become visible; as expected for $L \lesssim C_{\text{min}}^{L \rightarrow 1}$.

where the linear terms again follow for $0 < \Delta\bar{w} \ll 1$. If we take into account the smooth behavior of α_R for $\delta \rightarrow 0$, see Figure 3.22, we conclude that for $0 \leq \delta \ll C_{\alpha_R=1}^\delta(\Delta\bar{w})$ it is $\alpha_R \ll 1$ and the linearization of the RHS arctangent is valid.

To be self-consistent, we have to plug in our solution (3.151a) into the upper bounds on δ , namely Eq. (3.154c) and Eq. (3.156c), and the additional constraint $\delta \ll 1$,

$$\frac{\pi^2}{2} \frac{(1 - \Delta\bar{w})|\Delta\bar{w}|}{(L\Delta\bar{w} + \Delta\bar{w} - 1)^2} \ll \min \{0.4 \Delta\bar{w}, 0.8 - 1.4 \Delta\bar{w}, 1\} = 0.4 \Delta\bar{w} \quad 3.157$$

for $\Delta\bar{w} \rightarrow +0$. We see that the decisive bound is given by the constraint $\alpha_L \ll 1$ for small $\Delta\bar{w}$. Solving [recall Eq. (3.154)]

$$\frac{\pi^2}{2} \frac{(1 - \Delta\bar{w})\Delta\bar{w}}{(L\Delta\bar{w} + \Delta\bar{w} - 1)^2} = (\sqrt{2} - 1) \Delta\bar{w} \quad 3.158$$

leads to the condition on the system size

$$L \gg \frac{\pi \sqrt{\frac{1}{2} + \frac{1}{\sqrt{2}}} + 1}{\Delta \bar{w}} - \frac{1}{8} \sqrt{\frac{1}{2} + \frac{1}{\sqrt{2}}} \pi \Delta \bar{w} - \frac{1}{4} \sqrt{2\sqrt{2} + 2\pi} - 1 \quad 3.159a$$

$$\sim \frac{\pi \sqrt{\frac{1}{2} + \frac{1}{\sqrt{2}}} + 1}{\Delta \bar{w}} \sim \frac{4.5}{\Delta \bar{w}} \equiv C_{\min}^{L \rightarrow \infty}(\Delta \bar{w}) \quad 3.159b$$

valid for $\Delta \bar{w} \rightarrow +0$. See the red data in Figure 3.23 (a) and (b) for an illustration of this range. We immediately see that the quadratic decay of bulk modes towards the band edge is a unique feature of the gapped phases (trivial and topological¹²³) that sets in for larger system sizes the closer the system is to criticality. At $\Delta \bar{w} = 0$, there is no quadratic decay anymore and we end up with the $1/L$ decay already derived in $\ast\ast$ Subsection 3.D.5.

The scaling derived here is asymptotically correct ($L \rightarrow \infty$) for small deviations from criticality, $0 < \Delta \bar{w} \ll 1$. As we are anyway interested in chains driven close to $\Delta \bar{w} \approx 0$ from within the topological phase, the latter is not restrictive. However, it would be interesting to know the scaling that dominates for *small* chains, $L \sim 1$.

Second Regime: $\alpha_L \gg 1$

To this end, we assume that $C_{\alpha_L=1}^{\delta}(\Delta \bar{w}) < \delta \ll \min\{1, C_{\alpha_R=1}^{\delta}(\Delta \bar{w})\}$ and again $0 < \Delta \bar{w} \ll 1$. This implies that $\alpha_L \gg 1$ and $\alpha_R \ll 1$. This allows us to approximate Eq. (3.141) with $\frac{\pi}{2} = \alpha_R - \pi$ for the lowest bulk modes. Additionally, we use $\delta \ll 1$ to expand the RHS in second order of δ , and finally, we expand in linear order of $\Delta \bar{w}$.

This yields the quadratic equation

$$9\Delta \bar{w} L \delta^2 + 4L(2 + \Delta \bar{w}) \delta + 4(2L\Delta \bar{w} - 3\pi) = 0 \quad 3.160$$

with relevant (positive) solution

$$\delta_{\text{bulk}}^{L \rightarrow 1} = \frac{1}{9\Delta \bar{w}} \left[-4 - 2\Delta \bar{w} + 2\sqrt{4 - 17\Delta \bar{w}^2 + \Delta \bar{w} \left(4 + \frac{27\pi}{L} \right)} \right] \quad 3.161a$$

$$\sim \frac{3\pi}{2L} - \Delta \bar{w} \left(1 + \frac{3\pi}{4L} + \frac{81\pi^2}{32L^2} \right) \quad \text{for } \Delta \bar{w} \ll 1 \quad 3.161b$$

$$\sim \frac{3\pi}{2L} \equiv \tilde{\delta}_{\text{bulk}}^{L \rightarrow 1} \quad \text{for } \Delta \bar{w} = 0. \quad 3.161c$$

¹²³Here we showed this only for the *topological* phase as we assumed $\Delta \bar{w} > 0$ to simplify calculations.

To be consistent, we expand the solution (3.161a) once more into linear order of $\Delta\bar{w}$ and find for $0 < \Delta\bar{w} \ll 1$ the

RESULT 3.4:

$$E_{\text{bulk}}^{L \rightarrow 1} = |\Delta\bar{w}| + \delta_{\text{bulk}}^{L \rightarrow 1} = \frac{3\pi}{2L} - \Delta\bar{w} \left(\frac{3\pi}{4L} + \frac{81\pi^2}{32L^2} \right). \quad 3.162$$

Compare this with the result (3.137b) for λ_1 in the limit $\Delta\bar{w} \rightarrow 0$. Note that this limit works because we “defused” the singularity by setting the LHS to $\frac{\pi}{2}$. The yellow data in Figure 3.23 (a) and (b) illustrates this approximation and its relation to the asymptotic expression derived above.

Self-consistency demands that

$$0.4 \Delta\bar{w} < \frac{3\pi}{2L} - \Delta\bar{w} \left(1 + \frac{3\pi}{4L} + \frac{81\pi^2}{32L^2} \right) \quad 3.163a$$

$$\ll \min \{0.8 - 1.4 \Delta\bar{w}, 1\} \quad 3.163b$$

$$= 0.8 - 1.4 \Delta\bar{w} \quad 3.163c$$

where we used Eq. (3.156c) and Eq. (3.154c). The left-hand inequality can be solved via the solution of [recall Eq. (3.154)]

$$\frac{3\pi}{2L} - \Delta\bar{w} \left(1 + \frac{3\pi}{4L} + \frac{81\pi^2}{32L^2} \right) = (\sqrt{2} - 1) \Delta\bar{w} \quad 3.164$$

which reads

$$L < \frac{27}{16} \pi \Delta\bar{w} + \frac{3\pi}{2\sqrt{2}\Delta\bar{w}} - \frac{3\pi}{4\sqrt{2}} \quad 3.165a$$

$$\sim \frac{3\pi}{2\sqrt{2}\Delta\bar{w}} \sim \frac{3.3}{\Delta\bar{w}} \equiv C_{\text{max}}^{L \rightarrow 1}(\Delta\bar{w}). \quad 3.165b$$

The right-hand inequality can be solved via the solution of [recall Eq. (3.156)]

$$\frac{3\pi}{2L} - \Delta\bar{w} \left(1 + \frac{3\pi}{4L} + \frac{81\pi^2}{32L^2} \right) = \sqrt{2 - \sqrt{2}} - \left(1 + \frac{1}{2} \sqrt{2 - \sqrt{2}} \right) \Delta\bar{w} \quad 3.166$$

which reads

$$L \gg \frac{3\pi}{4\sqrt{2 - \sqrt{2}}} \left[\sqrt{\frac{9\sqrt{2 - \sqrt{2}}\Delta\bar{w} + \Delta\bar{w} - 2}{\Delta\bar{w} - 2}} + 1 \right] \quad 3.167a$$

$$\sim \frac{3\pi}{2\sqrt{2 - \sqrt{2}}} - \frac{27\pi\Delta\bar{w}}{16} \sim 6.2 - 5.3 \Delta\bar{w} \equiv C_{\text{min}}^{L \rightarrow 1}(\Delta\bar{w}). \quad 3.167b$$

In Figure 3.23 (a) and (b) we illustrate the interval bounded from below by Eq. (3.167b) and from above by Eq. (3.165b). Note that the upper bound diverges for $\Delta\bar{w} \rightarrow 0$ as the $1/L$ decay towards $|\Delta\bar{w}|$ takes over from the $1/L^2$ decay. In the limit $\Delta\bar{w} \rightarrow 0$, we find the already known result

$$\lim_{\Delta\bar{w} \rightarrow 0} E_{\text{bulk}}^{L \rightarrow 1} = \tilde{\delta}_{\text{bulk}}^{L \rightarrow 1} = \frac{3\pi}{2L} \quad 3.168$$

with a validity range of $6 \lesssim L$. Indeed, for small chains of length $L \lesssim 6$ one finds finite-size deviations from the exact $1/L$ decay, indicated by the arrow in Figure 3.23 (b); this is not even captured by our more sophisticated expression in Eq. (3.162).

3.D.7 Universal Scaling

Here we derive the universal scaling of the eigenenergies in the thermodynamic limit exactly. Recall that for the purpose of state transfer (see Subsection 3.3.3), we have to tune the system closer to the critical point ($\Delta\bar{w} \rightarrow 0$) for $L \rightarrow \infty$ to allow for optimal scaling of the transfer time ($\tau \sim L$) which requires $\Delta E_{\text{edge}} \sim 1/L$ for the edge mode splitting. In the following, we make these statements rigorous.

To this end, we introduce the rescaled variables $\lambda' \equiv L\lambda$ for energies and $\Delta\bar{w}' \equiv L\Delta\bar{w}$ for couplings; we are interested in the $\Delta\bar{w}'$ -dependence of $\Delta E'_{\text{bulk}} = |\lambda'_1 - \lambda'_0|$ and $\Delta E'_{\text{edge}} = 2\lambda'_0$ in the thermodynamic limit $L \rightarrow \infty$. We start by rewriting Eq. (3.114) in terms of the new variables,

$$\frac{x'_1 - \eta'_t}{x'_1 + \eta'_t} = \left[\frac{x'_2 - \eta'_t}{x'_2 + \eta'_t} \right]^L \quad 3.169$$

where

$$x'_{1/2} = 1 \pm \frac{1}{L^2} [\lambda'^2 - (L - \Delta\bar{w}')^2] \quad 3.170$$

and

$$\eta'_t = \frac{1}{L^2} \sqrt{[\Delta\bar{w}'^2 - \lambda'^2][(\Delta\bar{w}' - 2L)^2 - \lambda'^2]}. \quad 3.171$$

We did not introduce the relative energies $\delta' = \lambda' - |\Delta\bar{w}'|$ (cf. \clubsuit Subsection 3.D.6) because we are also interested in the edge mode which lives in the band gap. We can now take the limit $L \rightarrow \infty$ of both sides in Eq. (3.169) to find the transcendental equation

RESULT 3.5:

$$\frac{\Delta\bar{w}' - \sqrt{\Delta\bar{w}'^2 - \lambda'^2}}{\Delta\bar{w}' + \sqrt{\Delta\bar{w}'^2 - \lambda'^2}} = e^{-2\sqrt{\Delta\bar{w}'^2 - \lambda'^2}}. \quad 3.172$$

Here we used that $\lim_{L \rightarrow \infty} L x'_1 = 2\Delta\bar{w}'$ and

$$\lim_{L \rightarrow \infty} L \eta'_t = 2\sqrt{\Delta\bar{w}'^2 - \lambda'^2} \quad 3.173$$

which leads to

$$\lim_{L \rightarrow \infty} \frac{x'_1 - \eta'_t}{x'_1 + \eta'_t} = \frac{\Delta\bar{w}' - \sqrt{\Delta\bar{w}'^2 - \lambda'^2}}{\Delta\bar{w}' + \sqrt{\Delta\bar{w}'^2 - \lambda'^2}}. \quad 3.174$$

For the right-hand side of Eq. (3.169) we used the well-known relation $\lim_{L \rightarrow \infty} (1 + x/L)^L = \exp(x)$ to derive

$$\lim_{L \rightarrow \infty} \left[\frac{x'_2 \pm \eta'_t}{2} \right]^L = e^{\pm\sqrt{\Delta\bar{w}'^2 - \lambda'^2} - \Delta\bar{w}'} \quad 3.175$$

and therefore

$$\lim_{L \rightarrow \infty} \left[\frac{x'_2 - \eta'_t}{x'_2 + \eta'_t} \right]^L = e^{-2\sqrt{\Delta\bar{w}'^2 - \lambda'^2}}. \quad 3.176$$

As already mentioned in \clubsuit Subsection 3.D.4, there are two types of solutions for Eq. (3.172): For $|\lambda'| < |\Delta\bar{w}'|$, the above equation defines solutions within the gap (which is bounded by $|\Delta\bar{w}'|$) in the thermodynamic limit and is well-defined in the field of real numbers; this implies the exponential decay of the edge mode splitting. By contrast, for $|\lambda'| > |\Delta\bar{w}'|$ (in-band), the equation becomes complex-valued

$$\frac{\Delta\bar{w}' - i\sqrt{\lambda'^2 - \Delta\bar{w}'^2}}{\Delta\bar{w}' + i\sqrt{\lambda'^2 - \Delta\bar{w}'^2}} = e^{-2i\sqrt{\lambda'^2 - \Delta\bar{w}'^2}} \quad 3.177$$

which can be recast as the transcendental equation over \mathbb{R}

RESULT 3.6:

$$\operatorname{atan} \left[\frac{\sqrt{\lambda'^2 - \Delta\bar{w}'^2}}{\Delta\bar{w}'} \right] = \sqrt{\lambda'^2 - \Delta\bar{w}'^2} + \pi\mathbb{Z} \quad 3.178$$

encoding an algebraic decay of bulk modes towards the band edge $|\Delta\bar{w}'|$.

Inspection shows that the transmutation of “complex” bulk solutions to “real” edge solutions occurs at $\Delta\bar{w}' = 1$, see Figure 3.24 (a). Formally, the energy $\lambda'_{0,e}$ of the edge mode is determined by

$$\frac{\Delta\bar{w}' - \sqrt{\Delta\bar{w}'^2 - \lambda'^2_{0,e}}}{\Delta\bar{w}' + \sqrt{\Delta\bar{w}'^2 - \lambda'^2_{0,e}}} = e^{-2\sqrt{\Delta\bar{w}'^2 - \lambda'^2_{0,e}}} \quad \text{for } \Delta\bar{w}' > 1 \quad 3.179$$

and

$$\operatorname{atan} \left[\frac{\sqrt{\lambda'^2_{0,b} - \Delta\bar{w}'^2}}{\Delta\bar{w}'} \right] = \sqrt{\lambda'^2_{0,b} - \Delta\bar{w}'^2} \quad \text{for } 0 \leq \Delta\bar{w}' \leq 1. \quad 3.180$$

DIAGONALIZATION

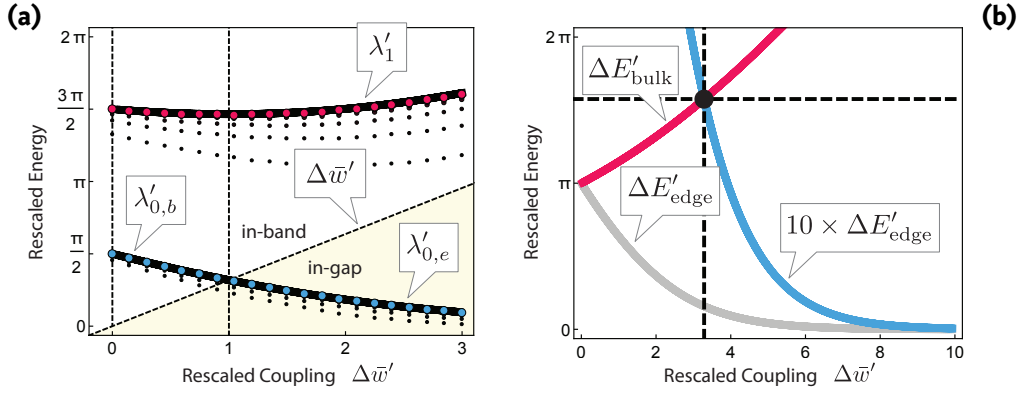


FIGURE 3.24 • Universal scaling. (a) Numerical (bullets) and analytical (lines) data for the rescaled lowest (edge mode) energy $\lambda'_0 = L\lambda_0$ and the lowest band (bulk mode) energy $\lambda'_1 = L\lambda_1$ as a function of the rescaled coupling $\Delta\bar{w}' = L\Delta\bar{w}$. Bold colored bullets mark numerical data for a quasi-infinite system of length $L = 200$ whereas finite-size effects are evident for smaller systems (small black bullets) starting at $L = 5$. Note that the solutions for λ'_0 split into the two types $\lambda'_{0,b}$ for $\lambda'_0 > \Delta\bar{w}'$ (in-band) and $\lambda'_{0,e}$ for $\lambda'_0 < \Delta\bar{w}'$ (in-gap). (b) Analytical results for the rescaled bulk-edge separation $\Delta E'_{\text{bulk}} = |\lambda'_1 - \lambda'_0|$ and the rescaled edge mode splitting $\Delta E'_{\text{edge}} = 2\lambda'_0$. Additionally, we show the scaled edge mode energy $10 \times \Delta E'_{\text{edge}}$; the intersection of the latter with $\Delta E'_{\text{bulk}}$ determines parameters of fixed bulk-edge energy ratio. We find $\Delta\bar{w}' \approx 3.3$ and $\Delta E'_{\text{bulk}} \approx 5.0$ (black bullet). Note that $\Delta E'_{\text{bulk}} = \pi = \Delta E'_{\text{edge}}$ for $\Delta\bar{w}' = 0$, i.e., at the critical point where the spectrum becomes linear.

By contrast, the energy of the lowest bulk mode is determined by

$$\text{atan} \left[\frac{\sqrt{\lambda_1'^2 - \Delta\bar{w}'^2}}{\Delta\bar{w}'} \right] = \sqrt{\lambda_1'^2 - \Delta\bar{w}'^2} - \pi \quad \text{for all } \Delta\bar{w}' \geq 0. \quad 3.181$$

These results are illustrated in Figure 3.24 (a) and compared to finite-size numerical results.

The bottom line of this analysis is that we can fix the ratio R of the two relevant energy scales for a transfer, namely ΔE_{edge} and ΔE_{bulk} if we approach the topological phase transition from within the topological phase as $\Delta\bar{w} = \Delta\bar{w}'/L$ for $L \rightarrow \infty$:

$$\Delta E_{\text{bulk}} = R \Delta E_{\text{edge}}$$

$$\Leftrightarrow \lambda'_1 - \lambda'_0 = \Delta E'_{\text{bulk}} = R \Delta E'_{\text{edge}} = 2R \lambda'_0 \quad 3.182a$$

$$\Leftrightarrow \lambda'_1 = (2R + 1) \lambda'_0. \quad 3.182b$$

In conjunction with Eq. (3.172), this constraint implicitly determines $\Delta\bar{w}'$. E.g., for $R = 10$ we find

$$\Delta\bar{w}' \approx 3.3 \quad 3.183a$$

$$\lambda'_1 = 21 \lambda'_0 \approx 5.2 \quad 3.183b$$

$$\Delta E'_{\text{bulk}} = 20 \lambda'_0 \approx 5.0 \quad 3.183c$$

$$\Delta E'_{\text{edge}} = 2 \lambda'_0 \approx 0.5 \quad 3.183d$$

which is illustrated in Figure 3.24 (b). Therefore we have

$$\Delta\bar{w} \sim \frac{3.3}{L} \quad \text{and} \quad \tau \gtrsim 2.0 \cdot L = \Delta E_{\text{edge}}^{-1} \quad 3.184$$

for the given energy ratio $R = 10$. Note that the condition $\tau \gtrsim \Delta E_{\text{edge}}^{-1}$ is merely *necessary* to facilitate at least one Rabi cycle between the edges; in particular, it allows for optimal scaling $\tau \sim L$. However, adiabatically decoupling bulk modes from the edge subspace is determined by ΔE_{bulk} which vanishes also with L^{-1} . This motivates the analysis of \clubsuit Section 3.E below.

3.E Adiabaticity

REMARK 3.3:

To streamline mathematical expressions, we replace the calligraphic symbols \mathcal{P} and \mathcal{F} used for pulses in Subsection 3.3.3 by lower-case letters p and f .

Here we use rigorous bounds on non-adiabatic losses [292] in conjunction with the previously (\clubsuit Subsection 3.D.7) derived scaling of the edge mode splitting and bulk gap to study the adiabatic bulk-edge decoupling quantitatively. In the following, we write the SSH chain Hamiltonian in the form

$$H(s) = H_0 + \bar{w}(s) H_1 \quad 3.185$$

where H_0 (H_1) describes the topological (trivial) dimerization of the chain (all couplings set to 1), $0 \leq \bar{w}(s) \leq 1$ encodes the coupling, and $s = a + (b - a)t/\tau$ is a dimensionless time with $s \in [a, b]$, whereas $t \in [0, \tau]$. Let $g = \Delta E_{\text{bulk}}/2$ be half the gap separating bulk from edge modes. With our previous results [see also Figure 3.25 (a)], we can estimate

$$2g(\bar{w}) = \Delta E_{\text{bulk}} \geq \Delta\bar{w} = 1 - \bar{w} \quad 3.186$$

which becomes asymptotically an equality for $L \rightarrow \infty$.

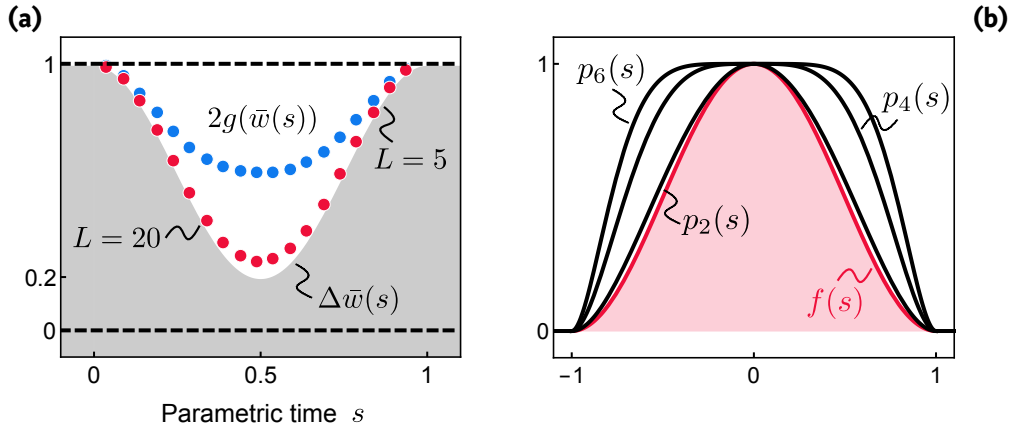


FIGURE 3.25 • Adiabatic bulk-edge decoupling—Pulses. (a) Finite-size bulk gap $\Delta E_{\text{bulk}} = 2g(\bar{w}(s))$ for $\bar{w}(s) = 0.8 \cdot \sin^2(\pi s)$ as a function of the parametric time $s \in [0, 1]$ for two systems of size $L = 5$ (blue bullets) and $L = 20$ (red bullets). For comparison, the exact bulk gap $\Delta\bar{w}(s) = 1 - \bar{w}(s)$ in the thermodynamic limit ($L \rightarrow \infty$) is drawn as shaded region. Clearly $2g(\bar{w}(s)) \geq \Delta\bar{w}(s)$ for systems of finite size; this lower bound on g is used in the text for the estimation of the bulk losses. (b) The three polynomial pulses (black lines) $p_n(s)$ for $n = 2, 4, 6$ as derived in the text, see Eq. (3.215). For comparison, we show the shifted and rescaled pulse $f(s) = \sin^2\left[\frac{\pi}{2}(x-1)\right]$ (red) which was used in the main text (e.g, Subsection 3.3.3). All four pulses are compactly supported on $I = [-1, 1]$ and continuously differentiable on \mathbb{R} .

In [292], the following rigorous upper bound on the non-adiabatic losses was derived:

$$1 - \mathcal{E} = \langle \Psi_0 | U_\tau^\dagger Q_0 U_\tau | \Psi_0 \rangle \leq C^2 \quad 3.187$$

with

$$C = \frac{2}{\tau} \left[\frac{\|\dot{H}(a)\|}{g^2(a)} + \frac{\|\dot{H}(b)\|}{g^2(b)} \right] + \frac{2}{\tau} \int_a^b ds \left(\frac{\|\ddot{H}(s)\|}{g^2(s)} + 7\sqrt{2} \frac{\|\dot{H}(s)\|^2}{g^3(s)} \right) \quad 3.188$$

where $Q_0 = \mathbb{1} - |1, \mathbf{0}, 0\rangle\langle 1, \mathbf{0}, 0| - |0, \mathbf{0}, 1\rangle\langle 0, \mathbf{0}, 1|$ is the projector onto the bulk sector at the beginning ($s = a$) and at the end ($s = b$) and $\|\bullet\|$ is the operator norm. We have $\|H_0\| = 1 = \|H_1\|$ ¹²⁴ and will consider pulses $\bar{w}(s) \in C^k(\mathbb{R}, [0, 1])$ ¹²⁵ with $k \geq 1$ which are compactly supported on an interval $I = [a, b]$ so that¹²⁶

$$C = \frac{2}{\tau} \int_a^b ds \left(\frac{|\ddot{\bar{w}}(s)|}{g^2(s)} + 7\sqrt{2} \frac{|\dot{\bar{w}}(s)|^2}{g^3(s)} \right). \quad 3.189$$

¹²⁴Both describe decoupled dimers with maximum absolute eigenvalue 1.

¹²⁵Mappings from \mathbb{R} to $[0, 1]$ the k th derivative of which is continuous.

¹²⁶ $\dot{\bar{w}}$ and $\ddot{\bar{w}}$ denote derivatives with respect to s (to avoid confusion with $\Delta\bar{w}'$ and similar rescaled quantities).

Eq. (3.186) allows us to estimate

$$C \leq \frac{2}{\tau} \int_a^b ds \left[2^2 \frac{|\ddot{\bar{w}}(s)|}{(1 - \bar{w}(s))^2} + 7\sqrt{2} 2^3 \frac{|\dot{\bar{w}}(s)|^2}{(1 - \bar{w}(s))^3} \right]. \quad 3.190$$

To allow for a complete state transfer, we showed in \clubsuit Subsection 3.D.7 that the critical coupling has to be approached as $\bar{w}_{\max} \sim 1 - \Delta\bar{w}'_{\min}/L$, where $\bar{w}_{\max} = \max_{s \in I} \bar{w}(s)$, in combination with an (at least) linearly growing protocol timescale $\tau \gtrsim L$. Therefore we assume the form

$$\bar{w}(s) = (1 - \Delta\bar{w}'_{\min}/L) \cdot p(s) \quad 3.191$$

for $L > \Delta\bar{w}'_{\min}$ with $p(a) = 0 = p(b)$, $p(c) = 1$, and p monotonically increasing (decreasing) on $[a, c]$ ($[c, b]$), where $c = (a + b)/2$. For the following analysis, it is more convenient to introduce $\bar{p}(s) = 1 - p(s)$ which vanishes during the pulse: $\bar{p}(c) = 0$.

RESULT 3.7: Upper bound on bulk losses

Then we have¹²⁷

$$C \leq \frac{C_1}{\tau} \underbrace{\int_a^b ds \frac{|\bar{p}''(s)|}{(\varepsilon_L + \bar{p}(s))^2}}_{\equiv \chi_1} + \frac{C_2}{\tau} \underbrace{\int_a^b ds \frac{|\bar{p}'(s)|^2}{(\varepsilon_L + \bar{p}(s))^3}}_{\equiv \chi_2} \equiv \frac{C_L[\bar{p}]}{\tau} \quad 3.192$$

with

$$C_1 = \frac{2^3}{1 - \Delta\bar{w}'_{\min}/L} \sim \text{const}, \quad C_2 = \frac{7\sqrt{2} 2^4}{1 - \Delta\bar{w}'_{\min}/L} \sim \text{const} \quad 3.193$$

and

$$\varepsilon_L = \frac{\Delta\bar{w}'_{\min}}{L - \Delta\bar{w}'_{\min}} \sim \frac{1}{L}. \quad 3.194$$

For $L \rightarrow \infty$, $C_L[\bar{p}]$ will diverge due to the vanishing of $\bar{p}(s)$ at $s = c$ and $\lim_{L \rightarrow \infty} \varepsilon_L = 0$. To keep the bulk losses $1 - \mathcal{E}$ constant for $L \rightarrow \infty$, we have to scale the protocol timescale as $\tau \sim L^{1+\alpha_{\bar{p}}}$ with $\alpha_{\bar{p}} \geq 0$ such that the asymptotic order of $C_L[\bar{p}]$ is matched and $\lim_{L \rightarrow \infty} C_L[\bar{p}]/L^{1+\alpha_{\bar{p}}} = \text{const}$.

We stress that an often used criterion requires $\tau \gtrsim 1/g_{\min}^2 \sim L^2$ for adiabaticity (since $g_{\min} \approx \varepsilon_L \sim 1/L$), i.e., $\alpha_{\bar{p}} = 1$. By contrast, the Lieb-Robinson bound [291] (and $\Delta E_{\text{edge}} \sim 1/L$) in principle allows for linear scaling, i.e., $\alpha_{\bar{p}} = 0$.

¹²⁷For generic functions p, f, \dots , we switch back to the conventional notation for derivatives: p', p'', \dots

Scaling for Specific Pulses

In the following, we apply Result 3.7 to specific pulses: First, we demonstrate that the pulse $\bar{p}(s) = \cos^2(\pi s) = 1 - \sin^2(\pi s)$, introduced in Subsection 3.2.2, yields a scaling of $\alpha_{\bar{p}} = \frac{1}{2}$ and thereby already surpasses the naïve estimates for adiabaticity. Finally, we discuss a sequence of pulses $\bar{p}_n(s)$ for which provably $\alpha_{\bar{p}_n} = \frac{1}{n}$, so that the optimal scaling $\alpha_{\bar{p}} = 0$ can be approached systematically. The question whether there is an optimal pulse $p(s)$ with $\alpha_{\bar{p}} = 0$ remains unanswered. We compare all estimates (which are, after all, only *sufficient* conditions for adiabaticity) with numerical simulations of the bulk losses and find that the actual scaling saturates the upper bounds (up to L -independent prefactors).

- 1 We start with $\bar{p}(s) = \bar{f}(s) = \cos^2(\pi s) = 1 - \sin^2(\pi s)$ for $s \in [0, 1]$, as used in Subsection 3.2.2 and Subsection 3.3.3. We have to evaluate

$$C_L[\bar{f}] = \int_0^1 ds \left[C_1 \frac{2\pi^2 |\cos(2\pi s)|}{(\varepsilon_L + \cos^2(\pi s))^2} + C_2 \frac{\pi^2 \sin^2(2\pi s)}{(\varepsilon_L + \cos^2(\pi s))^3} \right] \quad 3.195$$

where we set $\Delta \bar{w}'_{\min} = 3.3$ for demonstrative purposes (recall Subsection 3.D.7). We evaluate the integrals numerically and plot $C_L[\bar{f}]/\tau$ as a function of L for $\tau = \tau_0 \cdot L^{1+\alpha}$ with $\alpha = 0, \frac{1}{2}, 1$ in Figure 3.26 (a). To compare the scaling of the rigorous upper bounds on the bulk losses with the real system, we simulate the time evolution for $f(s) = \sin^2(\pi s)$ with $\tau = \tau_0 \cdot L^{1+\alpha}$ ($\alpha = 0, \frac{1}{2}, 1$) and $\bar{w}_{\max} = 1 - 3.3/L$ and calculate the bulk loss $1 - \mathcal{E}$ at $t = \tau$. Note that we do *not* tune \bar{w}_{\max} or τ in any way to optimize the *transfer* \mathcal{O} as we are only interested in the adiabatic decoupling of bulk and edge at this point. The numerical losses are shown in Figure 3.26 (b): Up to finite-size effects and L -independent prefactors, the rigorous upper bounds capture the scaling of the actual system correctly. In particular, the result $\alpha_{\bar{f}} = \frac{1}{2}$ is verified. The latter surpasses the conservative estimate $\tau \gtrsim 1/g_{\min}^2 \sim L^2$ but does not reach optimal (linear) scaling $\alpha_{\bar{f}} = 0$.

- 2 Let us now follow a more systematic approach and consider pulses of the form

$$\bar{p}_n(s) = s^n \cdot q(s) \quad \text{for } s \in I = [-1, 1], \quad n \geq 2 \text{ even} \quad 3.196$$

with $s^{-n} \geq q(s) > 0$ on I and $q(\pm 1) = 1$. We impose the continuity conditions

$$\begin{aligned} \bar{p}'_n(\pm 1) &= \pm n q(\pm 1) + q'(\pm 1) = 0 \\ \Rightarrow \quad q'(\pm 1) &= \mp n \end{aligned} \quad 3.197$$

so that the boundary terms in Eq. (3.188) vanish and $\bar{p}_n(s)$ becomes a C^1 -function if set to 1 outside I (which corresponds to the stable situation of statically decoupled edge modes). One could smoothen the function further

by requiring

$$\begin{aligned} \bar{p}_n''(\pm 1) &= n(n-1)q(\pm 1) \pm 2nq'(\pm 1) + q''(\pm 1) = 0 \\ \Rightarrow q''(\pm 1) &= n(n+1) \sim n^2 \end{aligned} \quad 3.198$$

so that $\bar{p}_n \in C^2$ if extended with 1 to \mathbb{R} . This, however, will not change the gist of the statements that follow. The upshot of these considerations is that getting rid of higher derivatives at the critical time $s = 0$ (when the gap is of order $1/L$) has to be balanced by growing derivatives of $q(s)$ at the boundaries of I to smoothen the transition into the stationary, decoupled state before and after the pulse.

Note that for the m th derivative one has

$$\bar{p}_n^{(m)} = \sum_{k=0}^m \binom{m}{k} \frac{n!}{(n-k)!} s^{n-k} q^{(m-k)}(s) \quad 3.199$$

so that $\bar{p}_n^{(m)}(0) = 0$ for $m < n$. The motivation is that flattening the pulse close to the critical region at $s = 0$ (where $g \approx g_{\min} \sim 1/L$) may be beneficial for the scaling of τ with L .

In particular,

$$\bar{p}(s) = s^n q(s) \quad 3.200a$$

$$\bar{p}'(s) = n s^{n-1} q(s) + s^n q'(s) \quad 3.200b$$

$$\bar{p}''(s) = n(n-1) s^{n-2} q(s) + 2n s^{n-1} q'(s) + s^n q''(s). \quad 3.200c$$

In Eq. (3.192), this yields

$$\begin{aligned} \chi_1 \leq n(n-1) \underbrace{\int_I ds \frac{|s^{n-2} q(s)|}{(\varepsilon_L + s^n q(s))^2}}_{\chi_{1,1}} + 2n \underbrace{\int_I ds \frac{|s^{n-1} q'(s)|}{(\varepsilon_L + s^n q(s))^2}}_{\chi_{1,2}} \\ + \underbrace{\int_I ds \frac{|s^n q''(s)|}{(\varepsilon_L + s^n q(s))^2}}_{\chi_{1,3}} \end{aligned} \quad 3.201$$

and

$$\begin{aligned} \chi_2 \leq n^2 \underbrace{\int_I ds \frac{|s^{2n-2} q^2(s)|}{(\varepsilon_L + s^n q(s))^3}}_{\chi_{2,1}} + 2n \underbrace{\int_I ds \frac{|s^{2n-1} q(s) q'(s)|}{(\varepsilon_L + s^n q(s))^3}}_{\chi_{2,2}} \\ + \underbrace{\int_I ds \frac{|s^{2n} (q'(s))^2|}{(\varepsilon_L + s^n q(s))^3}}_{\chi_{3,3}} \end{aligned} \quad 3.202$$

where we made use of the triangle inequality.

If we introduce the minimum $0 < q \equiv \min_{s \in I} |q(s)|$ and the maximum $Q \equiv \max_{s \in I} |q(s)|$ (similarly for derivatives: Q' and Q''), the integrals can be estimated straightforwardly:

→ The first term of χ_1 reads

$$\chi_{1,1} = \int_{-1}^1 ds \frac{|s^{n-2}q(s)|}{(\varepsilon_L + s^n q(s))^2} \quad 3.203a$$

$$\leq \int_{-1}^1 ds \frac{s^{n-2}Q}{(\varepsilon_L + s^n q)^2} = \frac{2}{\varepsilon_L^2} \int_0^1 ds \frac{s^{n-2}Q}{(1 + s^n q/\varepsilon_L)^2} \quad 3.203b$$

$$= 2Q \frac{\varepsilon_L^{-2+1/n+1-2/n}}{q^{1/n+1-2/n}} \int_0^{(q/\varepsilon_L)^{1/n}} du \frac{u^{n-2}}{(1+u^n)^2} \quad 3.203c$$

$$\leq 2Q \varepsilon_L^{-1-1/n} q^{1/n-1} \int_0^\infty du \frac{u^{n-2}}{(1+u^n)^2} \quad 3.203d$$

$$= 2Q \varepsilon_L^{-1-1/n} q^{1/n-1} \frac{\pi}{n^2 \sin \frac{\pi}{n}} \quad 3.203e$$

$$= \frac{1}{\varepsilon_L} \left[\frac{q}{\varepsilon_L} \right]^{1/n} \frac{2\pi}{n^2 \sin \frac{\pi}{n}} \frac{Q}{q} \quad 3.203f$$

where we used that $s^n \geq 0$ for even n . In the second row we substituted $u = (q/\varepsilon_L)^{1/n} s$. Note that the last estimate becomes an equality for $L \rightarrow \infty$ since $\varepsilon_L \rightarrow 0$.

→ The second term reads

$$\chi_{1,2} = \int_{-1}^1 ds \frac{|s^{n-1}q'(s)|}{(\varepsilon_L + s^n q(s))^2} \quad 3.204a$$

$$\leq \int_{-1}^1 ds \frac{|s|^{n-1}Q'}{(\varepsilon_L + s^n q)^2} = \frac{2}{\varepsilon_L^2} \int_0^1 ds \frac{s^{n-1}Q'}{(1 + s^n q/\varepsilon_L)^2} \quad 3.204b$$

$$= 2Q' \frac{\varepsilon_L^{-2+1/n+1-1/n}}{q^{1/n+1-1/n}} \int_0^{(q/\varepsilon_L)^{1/n}} du \frac{u^{n-1}}{(1+u^n)^2} \quad 3.204c$$

$$\leq 2Q' \varepsilon_L^{-1} q^{-1} \int_0^\infty du \frac{u^{n-1}}{(1+u^n)^2} \quad 3.204d$$

$$= 2Q' \varepsilon_L^{-1} q^{-1} \frac{1}{n} = \frac{1}{\varepsilon_L} \frac{2}{n} \frac{Q'}{q}. \quad 3.204e$$

→ The third term reads

$$\chi_{1,3} = \int_{-1}^1 ds \frac{|s^n q''(s)|}{(\varepsilon_L + s^n q(s))^2} \quad 3.205a$$

$$\leq \int_{-1}^1 ds \frac{s^n Q''}{(\varepsilon_L + s^n q)^2} = \frac{2}{\varepsilon_L^2} \int_0^1 ds \frac{s^n Q''}{(1 + s^n q/\varepsilon_L)^2} \quad 3.205b$$

$$= 2Q'' \frac{\varepsilon_L^{-2+1/n+1}}{q^{1/n+1}} \int_0^{(q/\varepsilon_L)^{\frac{1}{n}}} du \frac{u^n}{(1 + u^n)^2} \quad 3.205c$$

$$\leq 2Q'' \varepsilon_L^{-1+1/n} q^{-1-1/n} \int_0^\infty du \frac{u^n}{(1 + u^n)^2} \quad 3.205d$$

$$= 2Q'' \varepsilon_L^{-1+1/n} q^{-1-1/n} \frac{\pi}{n^2 \sin \frac{\pi}{n}} \quad 3.205e$$

$$= \frac{1}{\varepsilon_L} \left[\frac{\varepsilon_L}{q} \right]^{\frac{1}{n}} \frac{2\pi}{n^2 \sin \frac{\pi}{n}} \frac{Q''}{q}. \quad 3.205f$$

→ The first term of χ_2 reads

$$\chi_{2,1} = \int_{-1}^1 ds \frac{|s^{2n-2} q^2(s)|}{(\varepsilon_L + s^n q(s))^3} \quad 3.206a$$

$$\leq \int_{-1}^1 ds \frac{s^{2n-2} Q^2}{(\varepsilon_L + s^n q)^3} = \frac{2}{\varepsilon_L^3} \int_0^1 ds \frac{s^{2n-2} Q^2}{(1 + s^n q/\varepsilon_L)^3} \quad 3.206b$$

$$= 2Q^2 \frac{\varepsilon_L^{-3+1/n+2-2/n}}{q^{1/n+2-2/n}} \int_0^{(q/\varepsilon_L)^{\frac{1}{n}}} du \frac{u^{2n-2}}{(1 + u^n)^3} \quad 3.206c$$

$$\leq 2Q^2 \varepsilon_L^{-1-1/n} q^{-2+1/n} \int_0^\infty du \frac{u^{2n-2}}{(1 + u^n)^3} \quad 3.206d$$

$$= 2Q^2 \varepsilon_L^{-1-1/n} q^{-2+1/n} \frac{\pi(n-1)}{2n^3 \sin \frac{\pi}{n}} \quad 3.206e$$

$$= \frac{1}{\varepsilon_L} \left[\frac{q}{\varepsilon_L} \right]^{\frac{1}{n}} \frac{\pi(n-1)}{n^3 \sin \frac{\pi}{n}} \left[\frac{Q}{q} \right]^2. \quad 3.206f$$

→ The second term reads

$$\chi_{2,2} = \int_{-1}^1 ds \frac{|s^{2n-1} q(s) q'(s)|}{(\varepsilon_L + s^n q(s))^3} \quad 3.207a$$

$$\leq \int_{-1}^1 ds \frac{|s|^{2n-1} Q Q'}{(\varepsilon_L + s^n q)^3} = \frac{2}{\varepsilon_L^3} \int_0^1 ds \frac{s^{2n-1} Q Q'}{(1 + s^n q/\varepsilon_L)^3} \quad 3.207b$$

$$= 2Q Q' \frac{\varepsilon_L^{-3+1/n+2-1/n}}{q^{1/n+2-1/n}} \int_0^{(q/\varepsilon_L)^{\frac{1}{n}}} du \frac{u^{2n-1}}{(1 + u^n)^3} \quad 3.207c$$

$$\leq 2Q Q' \varepsilon_L^{-1} q^{-2} \int_0^\infty du \frac{u^{2n-1}}{(1 + u^n)^3} \quad 3.207d$$

$$= 2Q Q' \varepsilon_L^{-1} q^{-2} \frac{1}{2n} = \frac{1}{\varepsilon_L} \frac{1}{n} \frac{Q Q'}{q^2}. \quad 3.207e$$

ADIABATICITY

→ The third term reads

$$\chi_{2,3} = \int_{-1}^1 ds \frac{|s^{2n} (q'(s))^2|}{(\varepsilon_L + s^n q(s))^3} \quad 3.208a$$

$$\leq \int_{-1}^1 ds \frac{s^{2n} Q'^2}{(\varepsilon_L + s^n q)^3} = \frac{2}{\varepsilon_L^3} \int_0^1 ds \frac{s^{2n} Q'^2}{(1 + s^n q/\varepsilon_L)^3} \quad 3.208b$$

$$= 2Q'^2 \frac{\varepsilon_L^{-3+1/n+2}}{q^{1/n+2}} \int_0^{(q/\varepsilon_L)^{1/n}} du \frac{u^{2n}}{(1 + u^n)^3} \quad 3.208c$$

$$\leq 2Q'^2 \varepsilon_L^{-1+1/n} q^{-2-1/n} \int_0^\infty du \frac{u^{2n}}{(1 + u^n)^3} \quad 3.208d$$

$$= 2Q'^2 \varepsilon_L^{-1+1/n} q^{-2-1/n} \frac{\pi(n+1)}{2n^3 \sin \frac{\pi}{n}} \quad 3.208e$$

$$= \frac{1}{\varepsilon_L} \left[\frac{\varepsilon_L}{q} \right]^{\frac{1}{n}} \frac{\pi(n+1)}{n^3 \sin \frac{\pi}{n}} \left[\frac{Q'}{q} \right]^2. \quad 3.208f$$

Combining these results in Eq. (3.201) and (3.202) with Eq. (3.192) yields the final upper bound for bulk losses

$$\begin{aligned} C_L[\bar{p}_n] \varepsilon_L &\leq \left[\frac{q}{\varepsilon_L} \right]^{\frac{1}{n}} \frac{2\pi C_1 n(n-1)}{n^2 \sin \frac{\pi}{n}} \frac{Q}{q} \\ &\quad + \frac{2C_1 2n}{n} \frac{Q'}{q} \\ &\quad + \left[\frac{\varepsilon_L}{q} \right]^{\frac{1}{n}} \frac{2\pi C_1}{n^2 \sin \frac{\pi}{n}} \frac{Q''}{q} \end{aligned} \quad 3.209a$$

$$\begin{aligned} &\quad + \left[\frac{q}{\varepsilon_L} \right]^{\frac{1}{n}} \frac{\pi(n-1) C_2 n^2}{n^3 \sin \frac{\pi}{n}} \left[\frac{Q}{q} \right]^2 \\ &\quad + \frac{C_2 2n}{n} \frac{Q Q'}{q^2} \\ &\quad + \left[\frac{\varepsilon_L}{q} \right]^{\frac{1}{n}} \frac{\pi(n+1) C_2}{n^3 \sin \frac{\pi}{n}} \left[\frac{Q'}{q} \right]^2 \\ &\stackrel{L \rightarrow \infty}{\leq} \left[\frac{q}{\varepsilon_L} \right]^{\frac{1}{n}} \frac{3\pi(n-1)}{n \sin \frac{\pi}{n}} \left[2C_1 \frac{Q}{q} + C_2 \left(\frac{Q}{q} \right)^2 \right] \end{aligned} \quad 3.209b$$

where the last line describes the dominant term for $L \rightarrow \infty$.

RESULT 3.8: Upper bound for polynomial pulses

In conclusion, we have

$$\sqrt{1 - \varepsilon} \stackrel{L \rightarrow \infty}{\leq} \frac{1}{\tau \varepsilon_L^{1+\frac{1}{n}}} \underbrace{\frac{3\pi(n-1) q^{\frac{1}{n}}}{n \sin \frac{\pi}{n}} \left[2C_1 \frac{Q}{q} + C_2 \left(\frac{Q}{q} \right)^2 \right]}_{\equiv C_n[q]}. \quad 3.210$$

With $\varepsilon_L \sim \frac{1}{L}$ it follows that $\tau \sim L^{1+\frac{1}{n}}$ is sufficient to keep the bulk losses constant for $L \rightarrow \infty$ if a pulse of the form \bar{p}_n is used instead of $\bar{f}(s) = \cos^2(\pi s)$.

There are a few comments in order:

- 1 If we expand $\bar{f}(s) = \cos^2(\pi s)$ around its minimum at $s = \frac{1}{2}$,

$$\cos^2(\pi s) = \left(s - \frac{1}{2}\right)^2 \cdot \underbrace{\left[\pi^2 - \frac{\pi^4}{3} \left(s - \frac{1}{2}\right)^2 + \dots\right]}_{>0 \text{ for } s \in [0,1]}, \quad 3.211$$

we immediately conclude that $\alpha_{\bar{f}} = \frac{1}{2}$ since $\bar{f}(s)$ is of the form $\bar{p}_2(s)$ for appropriately chosen $q(s)$ (and shifted/rescaled s).

- 2 It is important to stress that the coefficient

$$C_n[q] = \frac{3\pi (n-1) q^{\frac{1}{n}}}{n \sin \frac{\pi}{n}} \left[2C_1 \frac{Q}{q} + C_2 \left(\frac{Q}{q}\right)^2 \right] \quad 3.212$$

is independent of L but *does* depend on the pulse shape via n and Q/q : First, for $n \rightarrow \infty$, we have

$$\frac{\pi (n-1)}{n \sin \frac{\pi}{n}} \rightarrow n. \quad 3.213$$

The better scaling comes at the price of larger upper bounds, i.e., longer timescales τ to begin with. Second, Q tends to diverge with $n \rightarrow \infty$ as well. We already showed that continuous differentiability at the beginning and end of the pulse implies (at least) $|q'(\pm 1)| = n$ and therefore $Q' \geq n$, and $|q''(\pm 1)| \sim n^2 \Rightarrow Q'' \geq n^2$ if $\bar{p}_n \in C^2$ is required. Note that this blows up the coefficients of the sub-leading terms in Eq. (3.209a).

The interplay of $C_n[q]$ and the $L^{1+\frac{1}{n}}$ -scaling can lead to the situation depicted in Figure 3.26 (c) where it is beneficial for small L to choose n smaller despite the inferior L -scaling, simply because the prefactors can be prohibitively large when L is not yet large enough.

- 3 Constructing possible $q(s)$ for given n so that $p_n(s) = 1 - \bar{p}_n(s)$ is compactly supported on $[-1, 1]$ and k times continuously differentiable on \mathbb{R} is easily accomplished with the polynomial ansatz

$$1 - p_n(s) = \sum_{j=n}^D \rho_j s^j \quad 3.214$$

for large enough $D \geq n$.

ADIABATICITY

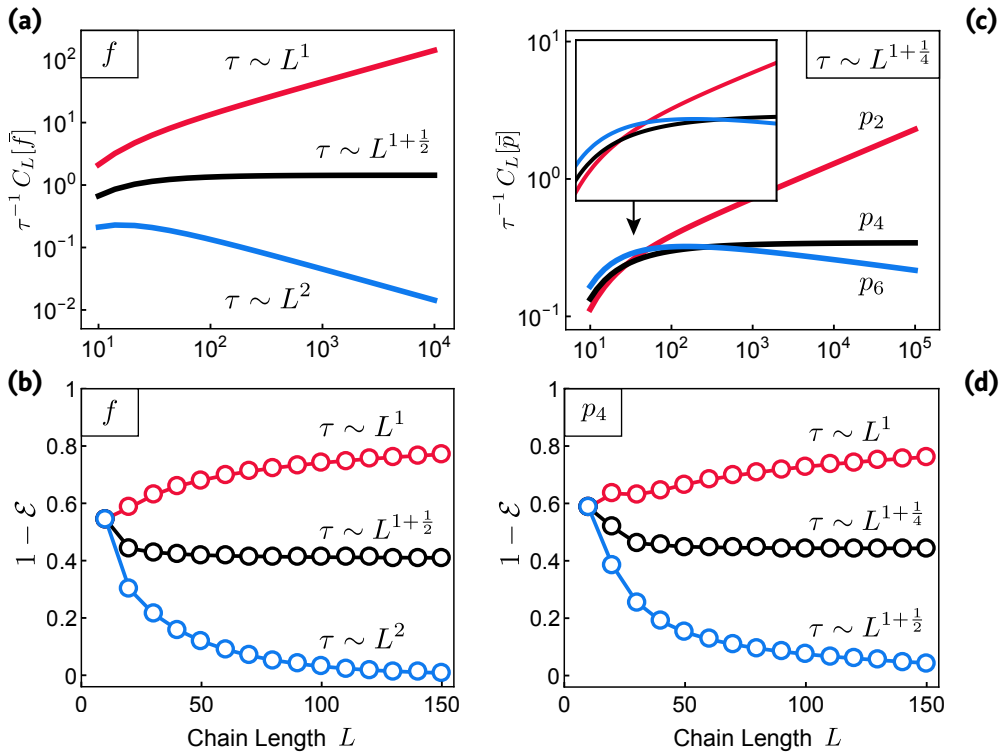


FIGURE 3.26 • Adiabatic bulk-edge decoupling—Numerics. (a) Numerical evaluations of the upper bounds $C_L[\bar{f}]/\tau$ for $f(s) = \sin^2(\pi s)$ with $\tau = \tau_0 \cdot L^{1+\alpha}$ for $\alpha = 0, \frac{1}{2}, 1$ ($\tau_0 = 10^3$). Obviously $\tau \sim L^{1+\frac{1}{2}}$ leads to a finite upper bound C for $L \rightarrow \infty$, i.e., $\alpha_{\bar{f}} = \frac{1}{2}$. (b) Numerical simulations of the bulk losses $1 - \mathcal{E}$ with $f(s) = \sin^2(\pi s)$, $\bar{w}_{\max} = 1 - 3.3/L$ and $\tau = \tau_0 \cdot L^{1+\alpha}$ for $\alpha = 0, \frac{1}{2}, 1$ (τ_0 is normalized so that $\tau = 10$ for $L = 10$). Note that for $\tau \sim L$ the bulk losses increase with L whereas for $\tau \sim L^{1+\frac{1}{2}}$ they converge towards a constant value which can be made arbitrarily small by increasing the prefactor τ_0 . (c) Numerical evaluations of the upper bounds $C_L[\bar{p}]/\tau$ for polynomials $p_n(s)$ with $n = 2, 4, 6$ as plotted in Figure 3.25 (b). $\tau = \tau_0 \cdot L^{1+\frac{1}{4}}$ ($\tau_0 = 500$) is fixed for all three such that $C_L[\bar{p}_4]/\tau$ converges to a finite value. The inset illustrates the dependence of the prefactors $C_n[q]$ on the pulse shape (that is, n): With n , the prefactors grow such that the upper bounds intersect when plotted over L . Thus it may be beneficial to choose pulse shapes with poor scaling in L for small systems. (d) Numerical simulations of $1 - \mathcal{E}$ with the polynomial pulse $p_4(s)$, $\bar{w}_{\max} = 1 - 3.3/L$ and $\tau = \tau_0 \cdot L^{1+\alpha}$ for $\alpha = 0, \frac{1}{4}, \frac{1}{2}$. For $\tau \sim L$ the bulk losses increase with L , whereas for $\tau \sim L^{1+\frac{1}{4}}$ they converge to a finite, non-trivial value; for $\tau \sim L^{1+\frac{1}{2}}$ the losses vanish with $L \rightarrow \infty$. Compare these results with (b).

Solving for $\{\rho_j\}$ yields possible solutions ($k = 1$, i.e., $p_n \in C^1$)

$$p_2(s) = 1 - x^2(2 - 1x^2) \quad 3.215a$$

$$p_4(s) = 1 - x^4(3 - 2x^2) \quad 3.215b$$

$$p_6(s) = 1 - x^6(4 - 3x^2) \quad 3.215c$$

\vdots

which are plotted in Figure 3.25 (b) and compared with $f(s) = \sin^2(\pi s)$. In Figure 3.26 (d) we show numerical results for the bulk loss $1 - \mathcal{E}$ for the polynomial pulse $p_4(s)$.

3.F Remarks on Linear Bosonic Networks

This is a brief excursion and discussion of known results on the complexity of linear bosonic networks with multiple excitations. Although we focus on the single-excitation sector throughout this chapter (which allows for the efficient simulation and evaluation of arbitrary quantities), it seems natural to watch for possible complications if $N > 1$ excitations occupy our networks at the same time.

Recall that the (trivial and topological) networks introduced in Subsection 3.2.1 and \clubsuit Subsection 3.A.1 are all described by quadratic theories of L bosonic modes:

$$\hat{H} = \sum_{i,j} b_i^\dagger H_{ij} b_j. \quad 3.216$$

Here, $H = (H_{ij}) \in \mathbb{R}^{L \times L}$ is a positive and symmetric matrix. The second-quantized Hamiltonian requires positivity as any negative eigenvalue precludes the existence of a finite-energy ground state. The reality of all couplings H_{ij} is not required *per se*; complex hopping amplitudes are conceivable. For the sake of simplicity, we assume the couplings to be real in the following (this applies also to the particular networks studied in this chapter).

Here we want to comment on the solvability of linear bosonic networks if more than one excitation is present. To this end, we introduce the vector notation

$$\hat{H} = \mathbf{b}^\dagger H \mathbf{b}. \quad 3.217$$

As there is no pairing of bosonic creation- and annihilation operators, any unitary S that diagonalizes H defines a canonical transformation

$$SHS^\dagger = \text{diag}(\{\varepsilon_i\}), \quad \mathbf{a} \equiv S\mathbf{b} \quad \Rightarrow \quad \hat{H} = \sum_i \varepsilon_i a_i^\dagger a_i \quad 3.218$$

with eigenmodes a_i and positive eigenenergies $\varepsilon_i > 0$. In this sense, any linear quantum oscillator network (3.216) is exactly solvable. However, “solvability” is a subtle statement as the following discussion demonstrates:

For *fermionic* quadratic theories it is usually taken for granted that “solving” the theory by diagonalizing the corresponding (single-particle) Hamiltonian matrix H allows for the efficient¹²⁸ evaluation of N -particle propagators

$$\langle m_1, \dots, m_L | U_T | n_1, \dots, n_L \rangle \quad 3.219$$

where m_i, n_i denotes the occupation of mode $1 \leq i \leq L$, $\sum_i m_i = \sum_i n_i = N$ is the total particle number, and $U_T = \exp(-i \hat{H} T)$ is the time evolution operator ($\hbar = 1$). Experimentally, this describes the probability (amplitude) to find $\{m_i\}$ fermions in the elementary modes $\{b_i\}$ at time $t = T$ if one inserts $\{n_i\}$ fermions at time $t = 0$.

Asking the same question for one of our networks of L coupled quantum oscillators (where one is interested in the probability of $\{n_i\}$ initial excitations evolving into another configuration $\{m_i\}$) leads directly into the realm of *boson sampling* [296–299]: Despite the “solvability” of the theory, the evaluation of arbitrary propagators proves computationally hard in the number N of excitations. This can be seen as follows:

In the Heisenberg picture, the time evolution of eigenmodes is

$$a_j(t) = U_t^\dagger a_j U_t = e^{-i\varepsilon_j t} a_j. \quad 3.220$$

For the local (physical) oscillators b_i this reads

$$b_i(t) = S_{ij}^\dagger a_j(t) = S_{ij}^\dagger e^{-i\varepsilon_j t} a_j = S_{ij}^\dagger e^{-i\varepsilon_j t} S_{jk} b_k \equiv \Lambda_{ik}^\dagger(t) b_k \quad 3.221$$

where $\Lambda^\dagger(t)\Lambda(t) = \mathbb{1}$ describes the unitary time evolution of the elementary modes b_i . Consequently, the time evolution of a Fock state is given by

$$U_t |n_1, \dots, n_L\rangle = \frac{b_1(t)^{\dagger n_1}}{\sqrt{n_1!}} \dots \frac{b_L(t)^{\dagger n_L}}{\sqrt{n_L!}} |0\rangle \quad 3.222a$$

$$= \prod_{i=1}^L \frac{1}{\sqrt{n_i!}} \left[\sum_{k_i} \Lambda_{k_i, i}(t) b_{k_i}^\dagger \right]^{n_i} |0\rangle. \quad 3.222b$$

It is a well-known fact [297] that evaluating an overlap with another Fock state $\langle m_1, \dots, m_L |$ can be massaged into the form

$$\langle \{m_i\} | U_t | \{n_i\} \rangle = \left(\prod_i n_i! \right)^{-\frac{1}{2}} \left(\prod_i m_i! \right)^{-\frac{1}{2}} \text{per}(\Lambda(t)[\Omega' | \Omega]) \quad 3.223$$

¹²⁸Here, *efficient* means polynomial in the system’s extensive parameters such as mode number L and particle number N .

where

$$\text{per}(M) \equiv \sum_{\sigma \in S_N} \prod_{i=1}^N M_{i,\sigma(i)} \quad 3.224$$

is called the *permanent* of the $(N \times N)$ -matrix M and can be thought of as *determinant* without the signum of the permutation σ (bosons!). The matrix $\Lambda(t)[\Omega'|\Omega]$ is a specific $(N \times N)$ -matrix (N is the number of bosons) depending on both $\{n_i\}$ and $\{m_i\}$ which can be constructed efficiently from the $(L \times L)$ -matrix $\Lambda(t)$ (L is the number of modes), see Ref. [297] for details.

The crucial observation is that the evaluation of the permanent of a generic matrix is #P-complete and the best known algorithm scales exponentially in N [296]. It is generally assumed that there exists no efficient algorithm to evaluate this function [298]—as such would imply P=NP which, in turn, is thought to be highly unlikely. Note that the additional signum in the definition of the *determinant*

$$\det(M) \equiv \sum_{\sigma \in S_N} \prod_{i=1}^N \text{sign}(\sigma) M_{i,\sigma(i)} \quad 3.225$$

makes all the difference: The determinant *can* be evaluated in polynomial time by Gaussian elimination.

It is important to stress that the hardness for evaluating N -boson propagators does stem from their statistics alone. The “solvability” of the theory allows for an efficient calculation of $\Lambda(t)$ independent of the particle number N . Only trying to use this matrix to compute N -boson propagators turns out to be exponentially hard. The bottom line is that when physicists talk of “solvable” systems, this does not necessarily imply that all quantities of interest are accessible. For our networks of interest, this means that an evaluation of their dynamics for large numbers of excitations N is computationally expensive, despite their quadratic description.

4

Topological Quantum Error Correction with Symmetry Constrained Cellular Automata

*“These are men who are trying to work out how
the world fits together, not by magic, not by religion,
but just by inserting their brains in whatever crack
they can find and trying to lever it apart.”*

— TERRY PRATCHETT
in Pyramids

Active quantum error correction on topological codes is one of the most promising routes to long-term qubit storage. In view of future applications, the scalability of the used decoding algorithms in physical implementations is crucial. In this chapter, we focus once again on the one-dimensional Majorana chain and construct a strictly local decoder based on a self-dual cellular automaton. We study numerically and analytically its performance and exploit these results to contrive a scalable decoder with exponentially growing decoherence times in the presence of noise. These results, published in Ref. [3], pave the way for scalable and modular designs of actively corrected one-dimensional topological quantum memories.

This page is intentionally left blank.

Storing data on a personal computer is nothing special. We do it all the time and expect the zeros and ones on the platter of our hard drive to remain unaltered over time. Our expectations are met because the data is imprinted on a ferromagnetic coating that retains its magnetization almost indefinitely at room temperature. Physically speaking, we exploit that ferromagnets below their Curie temperature are in a symmetry-broken phase and therefore non-ergodic, i.e., they remember their initial state on all relevant timescales. From a more abstract point of view, each of our precious bits is copied to billions of atomic magnetic moments pointing all in the same direction due to their ferromagnetic interaction. This physically realized “repetition code” makes storing classical bits easy.

If we want to build a *quantum* computer, storing *qubits* for long times becomes a major obstacle. This is so, because the coherence of qubits is easily lost due to inevitable interactions with our classical world. What gets things completely into a mess is that we cannot just *copy* qubits to build a “quantum hard drive.” This follows immediately from the linearity of quantum mechanics and is therefore hard to sweep under the rug. Fortunately, there are more sophisticated methods to protect qubits from decoherence by storing them in cleverly designed corners of the Hilbert space. Such “quantum (error correction) codes” (which is just a fancy name for a linear subspace with some useful properties) allow for the detection and correction of errors without perturbing the stored qubit. The price one has to pay is that many *physical* qubits are necessary to distill a single *logical* qubit that can be protected from environmental perturbations. The need for an abundance of controllable, physical qubits is still a major hurdle that has to be overcome one way or the other before robust logical qubits can be realized in laboratories.

In this chapter, we boldly assume that the “how to control an arbitrary number of qubits”-problem has been solved by means that already loom on the horizon at the time of writing. Instead, we are interested in possible issues that may arise if one implements a quantum code and its error correction algorithm *in hardware* (e.g., on a chip). To this end, we focus on a simple scalable quantum code and ask the question of how the classical computations required for error correction can be implemented efficiently, taking alleged subtleties such as finite communication speed and the size of logic gates into account.

Our quantum code of choice is given by the two-fold degenerate ground state space of the Majorana chain (Subsection 1.2.2) and is aptly referred to as *Majorana chain quantum code (MCQC)* henceforth. Its elementary building blocks are fermions described by c_j and c_j^\dagger . These can be (formally) split into two Majorana modes each, $\gamma_{2j} \equiv i(c_j^\dagger - c_j)$ and $\gamma_{2j-1} \equiv c_j^\dagger + c_j$, see Figure 4.1 (a). Then, the operators $S_j \equiv -i\gamma_{2j}\gamma_{2j+1}$, pairing two modes of adjacent sites, are easily seen to commute, $[S_i, S_j] = 0$, and obey $S_j^\dagger = S_j$ and $S_j^2 = \mathbb{1}$. This makes the ground state manifold \mathcal{C} of the Hamiltonian

$$H_{\text{MC}} = - \sum_{j=1}^{L-1} S_j \tag{4.1}$$

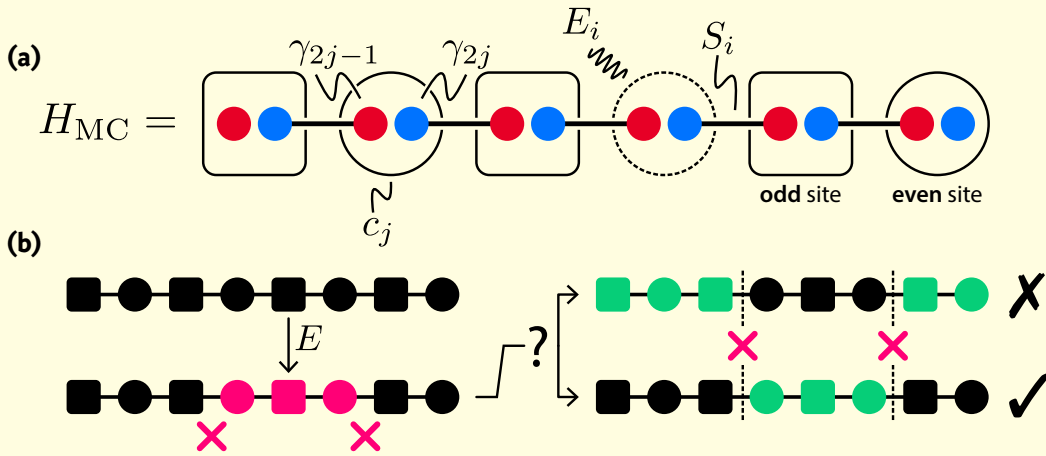


FIGURE 4.1 • The Majorana chain quantum code. (a) The Majorana chain quantum code is defined as two-fold degenerate ground state manifold of a chain of fermions c_j . Each fermion is composed of two Majorana modes γ_{2j-1} and γ_{2j} . The Hamiltonian fixes the parity of inter-site modes defined by connected pairs of Majorana modes S_i . Errors E_i act on fermionic sites (dashed circle) and anticommute with the adjacent terms of the Hamiltonian. Odd/even fermionic sites are labeled by squares/circles (to be used later). (b) A clean system is affected by a cluster of three errors (red cells). Measuring the stabilizers S_i yields the syndromes (red crosses) that indicate boundaries of error strings. There are two possible corrective operations (green cells) which are compatible with the syndrome. Here, the shorter one is the correct choice; interpreted as a classical repetition code, this corresponds to majority voting.

on an open chain of L fermions particularly simple as it is characterized by states that are S -invariant, i.e., $\mathcal{C} \equiv \{ |\Psi\rangle \mid \forall_j : S_j |\Psi\rangle = |\Psi\rangle \}$. This linear subspace is easily shown to be two-dimensional and is identified with the codespace of the MCQC. Errors on the MCQC are described by $E_j \equiv -i \gamma_{2j-1} \gamma_{2j}$ (shifted pedants of S_j). Indeed, E_i anticommutes with S_j if and only if $j = i$ or $j = i - 1$ (otherwise they commute) so that a state $|\Psi\rangle \in \mathcal{C}$ is thrown out of the codespace: $E_i |\Psi\rangle \notin \mathcal{C}$. To extract information on an error pattern $E_{i_1} E_{i_2} \dots$ we can only measure observables that leave \mathcal{C} invariant lest we perturb the stored qubit. These are exactly the S_j -operators with eigenvalues ± 1 . Measuring all S_j then yields a binary *syndrome pattern* of ± 1 where -1 indicates the *boundary* of an error string $E_i E_{i+1} \dots$; this is illustrated in Figure 4.1 (b). Decoding the MCQC means to cancel all errors so that the state returns unaltered to the codespace. Because of $E_i^2 = 1$, we only have to apply the error pattern $E_{i_1} E_{i_2} \dots$ a second time (now deliberately) and we are done. A complication arises due to the fact that for a given syndrome pattern (indicating edges of error strings), there are *two* complementary error configurations that match¹²⁹, see Figure 4.1 (b). Only if we choose the correct pattern, the qubit is restored to its original state. What to do?

¹²⁹On the boundaries of the open chain, syndromes cannot be measured and endpoints of error strings remain covert.

If we assume that errors are scarce (say, only 10% of the physical qubits suffer from an error E_i on average), then the error pattern with *fewer* errors is more probable [the lower one in Figure 4.1 (b)]. Note that we can compute the number of required errors for both choices based on the syndrome data alone. In most cases, this will be the correct choice but in some cases we might fail (this is unavoidable). The above prescription of selecting the pattern with fewer errors is also used for *classical* repetition codes where a bit is copied L times. If a small fraction (say 10%) of the copies is flipped, we can recover the original bit by selecting the *majority* of the disturbed L bits. Again, in most cases this procedure is successful. It is known as *majority voting* and this is just what we did to decode the MCQC: Flipping the *minority* of bits (= applying the pattern with *fewest* errors) reestablishes the *majority* as consensus among all.

Majority voting is a very powerful decoding scheme in that its failure rate vanishes if more and more copies are used ($L \rightarrow \infty$) as long as the error probability on each copy (or fermionic site, in the case of the MCQC) is below 50%¹³⁰. Implementing majority voting *in hardware* for $L \gg 1$ sites is tricky because it is an inherently global function. To see this, consider the bit pattern

$$010101010101010101X \tag{4.2}$$

with the task to set each bit to the majority of all. Since $X \in \{0, 1\}$ tips the scales, the target value of the first bit depends on the current value X of the last. If the register (4.2) is realized on a chip, information has to flow from one end to the other to apply the majority vote in all cases exactly. This takes time and restricts the rate at which the majority vote can be applied to counter errors in a noisy environment. This becomes particularly restrictive if (4.2) describes the error pattern on an extended Majorana chain because the distance between the endpoints of the chain is crucial for its resilience against noise (the further apart, the better).

The objective of this chapter is to find and study an *approximation* of majority voting that applies local corrections to the MCQC based on *nearby* syndrome measurements only. The locality of such a decoder renders it scalable by construction and averts possible timing issues since long-range communication is not required. To achieve this goal, we employ the concept of (binary) cellular automata¹³¹: Cells, each hosting a bit, are placed on a regular lattice (here a one-dimensional chain of L cells) and evolved in time by local rules that are applied periodically and for all cells at the same time. “Local rules” here refers to a deterministic prescription of how to set the bit of cell i in dependence of the bits of neighboring cells up to distance R (where R is a fixed integer specific for a particular automaton). Cellular automata are a well-developed framework of “physical computation” where the already mentioned spatio-temporal constraints of real systems are intrinsic, while still being abstract enough to allow for concise mathematical statements.

¹³⁰Note that for 50% error probability, the majority of L bits is scrambled for all L .

¹³¹A quite famous cellular automaton (in two dimensions) is *Conway’s Game of Life*.

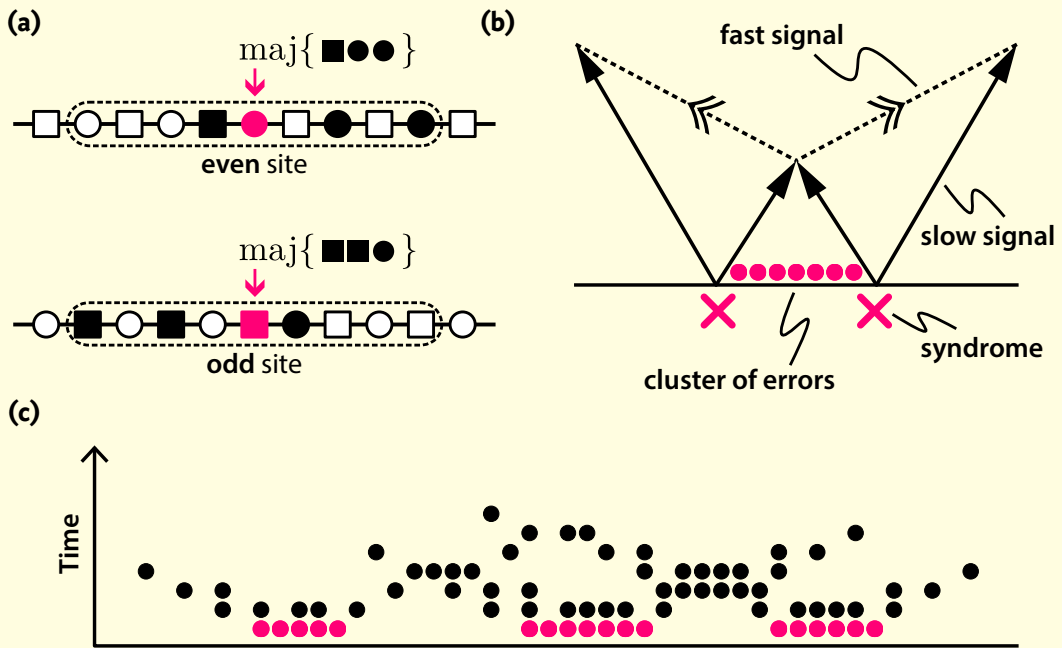


FIGURE 4.2 • The Two-Line Voting automaton. (a) Definition of the two local rules for TLV-updates. There are different rules for even and odd sites (mirror images of each other). Periodically and synchronously, all sites are set to the majority of three of their neighbors (black cells). (b) These rules realize the core mechanism of TLV: Syndromes (boundaries of error clusters) spawn symmetric slow signals to scout for nearby partners to pair with. Two colliding slow signals are converted into counterpropagating fast signals that eat away errors and capture the other two slow signals propagating away from the cluster. (c) Exemplary time evolution of TLV on an ensemble of three nearby error clusters. Note that the signals of different clusters interact whereas the complex of three clusters is still eroded successfully in just 6 time steps.

A cellular automaton that decodes the MCQC has to fulfill two requirements: First, it should perform majority voting (or an approximation thereof), and second, it is only allowed to use syndrome information to achieve this task (that is, the rules “see” only endpoints of error strings and not the errors themselves). The first task is known as *density classification* and has been studied heavily in the past. The second requirement is equivalent to a symmetry of the local rules called *self-duality*¹³². In “cellular automaton jargon,” we are looking for a *self-dual density classifier*.

Possible automata are scarce; however, the so called *Two-Line Voting (TLV)* automaton fulfills both requirements: If $x_i \in \{0, 1\}$ denotes the current state of cell i and x'_i its next state, the local update is defined as

$$x'_i \equiv \begin{cases} \text{maj}[x_{i-1}, x_{i+2}, x_{i+4}] & \text{for } i \text{ even,} \\ \text{maj}[x_{i+1}, x_{i-2}, x_{i-4}] & \text{for } i \text{ odd,} \end{cases} \quad 4.3$$

¹³²Self-dual rules yield the inverted ($0 \leftrightarrow 1$) result when applied to an inverted input.

where $\text{maj}[x_1, x_2, x_3]$ denotes the majority of the three bits $x_{1,2,3}$; this is illustrated in Figure 4.2 (a). In our case, $x_i = 1$ encodes a state of the MCQC with the error E_i applied. *Prima facie*, the rules (4.3) seem to use the error pattern itself instead of the measured syndromes. We show in this chapter that this is not so: Exploiting its self-duality, (4.3) can be rewritten in a form that only uses syndromes as inputs and returns correction operations as outputs. Therefore, TLV is a legitimate aspirant for replacing the global majority vote as MCQC decoder. A large part of this chapter is dedicated to study its performance both numerically and analytically.

Despite the rather enigmatic form of (4.3), the mechanism that allows TLV to remove sparse clusters of errors—when only their boundaries are known—is quite simple [see Figure 4.2 (b)]: The rules spawn “slow signals” (particular binary patterns of cell states) at boundaries of error strings. These signals travel symmetrically in both directions to scout for other slow signals that indicate, hopefully, the other boundary of the same error string. When two slow signals meet, they are converted into “fast signals” (another binary pattern) that travels back to capture the other “unsuccessful” slow signal heading away from the error cluster. Along the way, it cleans the error cluster by flipping the bits accordingly. A spacetime diagram of the actual evolution of an initial error pattern consisting of three separate clusters is shown in Figure 4.2 (c). There, the three clusters are too close and their signals interact; nevertheless, the complex consisting of the three clusters is cleaned successfully after only 6 time steps.

The fact that only 6 time steps are necessary to remove a rather large complex of errors hints already at an advantage of *local* decoders (such as TLV) over *global* ones (such as exact majority voting): They can decode MCQCs of linear size L in *sublinear* time—which is impossible for global decoders because collecting data from distributed sites requires $\mathcal{O}(L)$ time steps due to the finite speed of information transfer. One of the main results presented in this chapter is a mathematically rigorous quantification of this claim for the specific case of TLV. More precisely, we show that if TLV runs for at most

$$t_{\max} \sim L^\kappa \tag{4.4}$$

time steps on an initially error-afflicted MCQC of length L , where $0 < \kappa < 1$ is arbitrary, the probability Pr for the MCQC to be *not* completely error-free vanishes exponentially fast for longer chains, i.e.,

$$\text{Pr}(\text{Errors survive } t_{\max}(L) \text{ steps}) \rightarrow 0 \quad \text{for } L \rightarrow \infty, \tag{4.5}$$

as long as the error probability on each site is below some critical value. This is underpinned and in accordance with numerical results we obtained from simulated evolutions sampled over many random error patterns. The bottom line is that for low enough error rates the global nature of exact majority voting is not required and can be replaced by the local decoding strategy implemented by TLV. This is good news because the scalability of the latter comes for free with its description as a cellular automaton.

There is, however, a pitfall that demands for a more sophisticated setup when errors on the quantum chain occur during the evolution of TLV; that is, when TLV is not used to decode a *static* pattern of errors but to fight a *continuously* accumulating stream of errors. In the last part of this chapter, we demonstrate that the evolution of TLV is profoundly altered when errors appear randomly during runtime and, as a consequence, that an accumulation of errors cannot be fought efficiently. This is bad news because this is what reality is like: There is a never-ending stream of errors from the environment trying to decohere the qubit stored in the MCQC.

Fortunately, we can come up with a setup that combines D copies of TLV, without requiring long-range communication between its parts, so that errors do no longer accumulate but are dealt with in a time-sliced fashion by parallel instances of TLV. The price to pay is additional (classical) hardware, quantified by the number of instances D . As this number is directly linked to the required decoding time for a single instance, we find that

$$D \sim L^\kappa \tag{4.6}$$

is enough to extend the coherence time of the stored qubit exponentially for $L \rightarrow \infty$. This result tells us that for realistic error rates, shallow circuits along the quantum chain are sufficient to stabilize the MCQC for long times.

In conclusion, the application of the cellular automaton TLV as a decoder for the Majorana chain quantum code may be a viable alternative to simple majority voting, featuring better scalability and a simpler implementation. The results presented in this chapter may be useful for future designs of quantum memories as building blocks of applied quantum computers.

4.1 Introduction

Storing quantum information in a noisy, classical environment is essential for scalable quantum computation and communication [300]. Kick-started by Shor's 9-qubit code [301], quantum error correction comes to the rescue: Logical qubits are stored in virtual subsystems [302] that decouple from typical environmental perturbations and allow for error detection and correction [174, 303].

Quantum error correction codes come in two flavors:

- The conventional ones (e.g., Shor's code) have no physical interpretation and are treated as abstract entities, isolated from the underlying computational architecture (much like *classical* error correction codes).
- *Topological* quantum codes, by contrast, are tied to the real world in that they are realized as ground state manifolds of local Hamiltonians and thereby inherit the geometry of their environment.

For the latter class, prominent examples are the Majorana chain (a p -wave superconductor) in one [82, 173] and the toric code in two spatial dimensions [24, 49], both of which have seen experimental progress in the last years, see e.g. [178, 304–306] and references therein. Here we are interested in such topological codes in one dimension and introduce a method to stabilize them using only strictly local resources.

Topological codes allow, in principle, for two modes of operation:

- Taking their realization as ground states seriously entails the intriguing concept of *self-correction* where errors appear as excitations that are energetically suppressed by the parent Hamiltonian [307–309].
- By contrast, *active* error correction adopts the algorithmic scheme of conventional codes, i.e., an external decoder is fed with measured syndromes and computes compatible corrections.

The fragility of low-dimensional topological order to thermal excitations [310–312], and the so far unsettled quest for realizable self-correcting codes [50], makes *active* error correction on topological codes one of the most promising routes to long-term qubit coherence [313–315].

As realizable quantum architectures loom on the horizon [316], convenient abstractions face the intricacies of reality: Can active error correction be implemented efficiently? How can it be scaled up when it is cast into hardware? Since space and time constraints can rule out implementations of otherwise promising algorithms, it is a crucial question whether and how topological quantum codes can be stabilized by manifestly local decoders. For the toric code, this has been tackled with a completely local but hierarchical decoder in [317] (inspired by [318]), with

translationally invariant cellular automata [319, 320], with a modular setup of simple units connected by noisy links in [321], and with optimized versions of minimum weight perfect matching [322–325]. Prolonging the lifetime of certain stabilizer codes by local unitary operations (instead of full-fledged error correction) may be a viable alternative [326]. However, rigorous results on the performance of decoders with strict space and time constraints are scarce.

Here, we focus on the simplest case of a one-dimensional topological quantum code, defined by the ground state space of the Majorana chain [82], and remodel a known (classical) cellular automaton [327, 328] to contrive a convenient, strictly local quantum decoder. We prove that both the probability for successful decoding and the time required to do so scales favorably with the chain length, surpassing conventional *global* decoding schemes. For realistic error rates, this allows for the stabilization of logical qubits in the presence of continuous (uncorrelated) noise using shallow, translationally invariant circuits with local wiring only. This may be useful for scalable and modular on-chip realizations of actively corrected topological quantum memories based on one-dimensional p -wave superconductors.

In the following, we provide a detailed outline of the methods and approaches used to derive these results:

Outline

In Subsection 4.2.1 we start with a description of the quantum code defined by the degenerate ground state space of the Majorana chain, where dephasing is topologically suppressed and depolarizing errors are forbidden by fermionic parity superselection (which can be violated in real setups due to quasiparticle poisoning [238, 239]). This paradigmatic model exemplifies topological quantum error correction and relates to the familiar toric code via Jordan-Wigner transformation in the degenerate case of a $L \times 1$ square lattice with open boundaries. The syndromes of the Majorana chain quantum code (MCQC) are fermionic quasiparticles flanking strings of parity-conserving errors. Maximum-likelihood decoding therefore requires pairing quasiparticles with minimum-length error strings; this scheme is known as *minimum weight perfect matching* (MWPM) [329] for the toric code and reduces in one dimension to simple *majority voting*, the decoding scheme used for classical repetition codes. In Subsection 4.2.2, we review the known result that applying majority voting at a fixed rate to the MCQC leads to an exponentially growing lifetime of the encoded logical qubit with the chain length L . This is true for continuous, uncorrelated (Bernoulli) noise on the physical qubits with arbitrary on-site error probability p_0^X —except for the singular, completely mixing channel with $p_0^X = \frac{1}{2}$; there is no non-trivial error threshold, in contrast to “true” two-dimensional MWPM for the toric code [322, 330]. However, global majority voting violates locality as it requires *space* for each logic gate and *time* for communication between them. This raises the question whether this extraordinary robustness of majority voting survives in realistic setups. In Subsection 4.2.3 we argue that

low-level decoders of quantum memories must be realized *in hardware* and close to the coherent subsystem (here the Majorana chain) to allow for modularity and scalability, both in the number of chains and their length. Then, collecting the syndromes of an extended chain in a central processing unit, and distributing corrections afterwards requires *time*—which scales with the system size L . We demonstrate that this important feature of global majority voting precludes its application at a fixed rate for $L \rightarrow \infty$, and thereby spoils the favorable scaling of decay times.

This line of thought motivates our search for a manifestly *local* decoder of the MCQC, taking finite communication speed and spatial extent seriously. Then, locality implies that restrictions on the time granted for decoding translate into restrictions on the syndromes that can influence a local correction. We derive a generic upper bound on the success probability for decoding the MCQC with local decoders and discuss implications for the scaling of the decoding time with the chain length.

After setting the scene (and sketching what we *can* expect and what we *cannot*), we aim for a feasible local decoder of the MCQC. To this end, Subsection 4.3.1 introduces the concept of *cellular automata* (CA) as well-developed prime example for physically realistic local computation. The natural invariance of local CA rules in space narrows down the choice of local decoders but allows for implementations that can be scaled up easily. While CAs naturally operate on classical bits, the physical qubits of the MCQC are not accessible—only the syndromes can be measured without perturbing the state (we call this the “quantum handicap”). We argue that only CAs featuring a particular symmetry (called *self-duality*) can be employed as MCQC decoders.

To decode the MCQC by means of a CA, implementing a *global* majority vote by *local* rules seems a good approach. This task is known as *density classification problem* [331, 332] and has been shown to be unsolvable for binary CAs in any dimension [333]. In Subsection 4.3.2 we review some of the results on *approximate* density classifiers which could provide viable replacements for perfect majority voting if error rates are small (i.e., away from $p_0^x = \frac{1}{2}$). We present two binary CAs that are known to perform well on density classification, one of which (called TLV) is self-dual; it can be rewritten in a form that complies with the “quantum handicap”: It naturally takes syndromes as input and produces correction operations as output. Before we can explore the performance of TLV as MCQC decoder, the question of boundary conditions has to be addressed. It is common to place CAs on finite chains with *periodic* boundaries. In Subsection 4.3.3 we point out that this is not compatible with *locality* of classical computations on the one hand and the necessity of a *stretched* quantum chain on the other. Hence a modification of TLV at the boundaries is required (denoted by $\overline{\text{TLV}}$). We demonstrate that for MCQC decoding, *mirrored* boundary conditions are the way to go: The CA operates in a cavity-like geometry to pair quasiparticles with partners in the edge modes of the MCQC.

In Subsection 4.4.1 we start our analysis of $\overline{\text{TLV}}$ with a numerical evaluation of its decoding capabilities. Sampling uncorrelated Bernoulli random configurations with on-site error probability p_0^X and subsequent evolution with $\overline{\text{TLV}}$ allows us to gauge the possible downsides of performing only *approximate* majority voting. Despite the existence of periodic cycles that cannot be decoded, numerics suggests that for $p_0^X < \frac{1}{2}$ only an exponentially (in L) small fraction of error patterns fails to be corrected successfully. Moreover, the typical time needed to rotate an error-afflicted instance of the MCQC back into the codespace grows sublinearly with the chain length L (in contrast to *global* majority voting). To substantiate these claims, we apply the concept of *sparse errors* to the particular case of $\overline{\text{TLV}}$. In Subsection 4.4.2 we derive a central statement of this chapter: The probability to decode a length- L MCQC successfully with $\overline{\text{TLV}}$ after $t \propto L^\kappa$ time steps (with $\kappa > 0$ arbitrary) tends to 1 exponentially fast for $L \rightarrow \infty$ and small but finite error probabilities $p_0^X \ll \frac{1}{2}$. This provides us with a much simpler and faster decoder than global majority voting (the decoding time of which scales linearly with L), and especially implies that for these error probabilities the “expensive” global nature of majority voting is not required for efficient decoding.

In the remainder, we shift our focus from the *decoding* of static error patterns to the *protection* of the MCQC in the presence of continuous (Bernoulli) noise. In Subsection 4.5.1 we realize this scenario by applying the local rules of $\overline{\text{TLV}}$ and on-site errors with probability p_0^X alternately. We demonstrate numerically that $\overline{\text{TLV}}$ *cannot* cope with such perturbations of its evolution in that the lifetime of the logical qubit grows only subexponentially with the chain length. In the light of known results on the behavior of one-dimensional CAs, this is unfortunate but not surprising: Simple, one-dimensional CAs subject to noise are expected to be ergodic; this is known as the *positive rates conjecture* [334]—it is well-established that this conjecture is incorrect, but the only known counterexample is extraordinary complex [318, 335, 336], and we cannot expect that our setup is a simpler one.

If one abandons strictly one-dimensional decoders (with circuit complexity $\sim L$), there is a rather generic solution to this problem: Any given decoder can be employed to counter continuous noise by repetitive applications with a fixed rate. If the time required to decode a fixed error pattern grows with the code size L , so does the number of required instances running in parallel to prevent errors from accumulating. Thus the additional hardware overhead due to continuous noise correlates with the decoding time for fixed error patterns. In Subsection 4.5.2 we follow this idea and stack copies of $\overline{\text{TLV}}$ in the second dimension perpendicular to the quantum chain. The *depth* of this classical circuit quantifies the hardware overhead required for the retention of the logical qubit in the presence of noise; as it directly relates to the decoding time of $\overline{\text{TLV}}$, it grows sublinearly with the chain length, so that shallow circuits suffice for reasonably low error rates. Indeed, the complexity of these circuits scales with $L^{1+\kappa}$ for $0 < \kappa < 1$, in contrast to the typical L^2 -scaling of global majority voting.

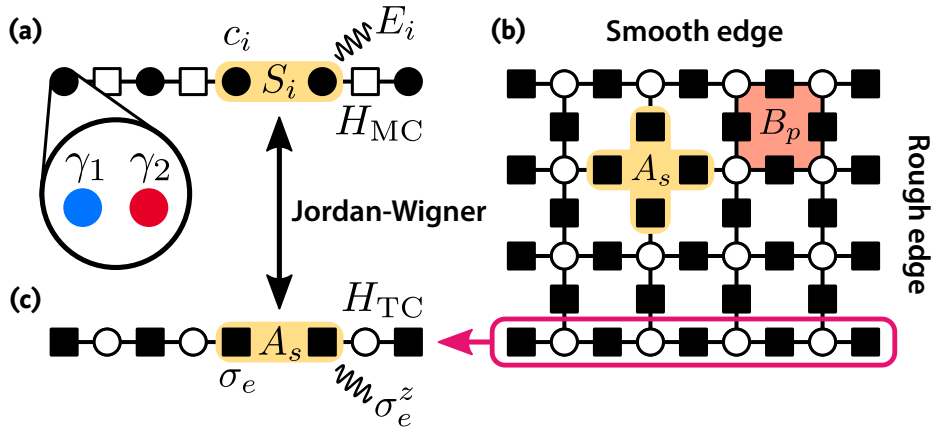


FIGURE 4.3 • Topological quantum memories. (a) The Majorana chain with fermions c_i on sites, composed of Majorana fermions γ_j , parity-symmetric errors E_i and syndrome measurements S_i . (b) The toric code on a planar square lattice with rough and smooth edges. Stabilizers A_s (B_p) act on spins on edges adjacent to sites s (faces p). (c) The degenerate $L \times 1$ toric code is the Jordan-Wigner transform of the Majorana chain. Thus it features the same error syndromes and correction schemes, namely *majority voting*.

4.2 1D Topological Quantum Codes

We start this section with a description of the Majorana chain and thereby review the realization of a topological quantum code as degenerate ground state space of a local Hamiltonian. In particular, we revisit the procedure of quantum error correction using syndrome measurements and demonstrate that it reduces to global majority voting in this particular case. This decoding scheme features an exponentially growing lifetime of the encoded logical qubit with the chain length L . However, global majority voting violates locality as it relies on the evaluation of a function of spatially distributed syndrome measurements. But the time required for collecting the syndromes of an extended chain in a central processing unit (and distributing corrections afterwards) scales with the system size L . We conclude by demonstrating that taking into account this processing time eliminates the exponential scaling of the qubit lifetime. This sets the stage for the construction and study of a strictly local, inherently scalable replacement for global majority voting.

4.2.1 Majorana Chain

The simplest example of a topological quantum error correction code in one dimension is given by the degenerate ground state manifold of the paradigmatic Majorana chain [82], see Figure 4.3 (a); see also Subsection 1.2.2 for an introduction.

The Hamiltonian for an open chain of L spinless fermions c_i reads

$$H_{\text{MC}} = \sum_{i=1}^{L-1} \left(w_i c_i^\dagger c_{i+1} + \Delta_i c_i c_{i+1} + \text{h.c.} \right) + \sum_{i=1}^L \mu_i \left(c_i^\dagger c_i - \frac{1}{2} \right) \quad 4.7$$

where c_i, c_i^\dagger denote fermionic annihilation and creation operators, w_i is the tunneling amplitude, Δ_i the superconducting gap parameter, and μ_i denotes the chemical potential. At the ‘‘sweet spot,’’ $\mu_i = 0$ and $w_i = -\Delta_i = 1$, the Hamiltonian takes the form

$$H_{\text{MC}} = i \sum_{j=1}^{L-1} \gamma_{2j} \gamma_{2j+1} = - \sum_{j=1}^{L-1} S_j \quad 4.8$$

with Majorana fermions $\gamma_{2j} \equiv i(c_j^\dagger - c_j)$ and $\gamma_{2j-1} \equiv c_j^\dagger + c_j$, $\gamma_j^\dagger = \gamma_j$ and $\{\gamma_i, \gamma_j\} = 2\delta_{ij}$. The operators $S_j = -i\gamma_{2j}\gamma_{2j+1} = (-1)^{\tilde{c}_j^\dagger \tilde{c}_j}$ measure the parity of the localized quasiparticle modes \tilde{c}_j^\dagger above the superconducting condensate and play the role of a stabilizer known from quantum information theory [173, 264]: $[S_i, S_j] = 0$, $S_j^\dagger = S_j$, and $S_j^2 = \mathbb{1}$. Let $\mathcal{S} = \langle \{S_1, \dots, S_{L-1}\} \rangle$ be the (Abelian) stabilizer group. The codespace $\mathcal{C} \equiv \{ |\Psi\rangle \in \mathcal{H} \mid \mathcal{S} |\Psi\rangle = |\Psi\rangle \}$ is the \mathcal{S} -invariant subspace and encodes a single logical qubit, $\dim \mathcal{C} = 2$; this space is equivalent to the degenerate ground state space of Eq. (4.8). This observation can be understood as follows: Since the edge Majorana modes $\gamma_L \equiv \gamma_1$ and $\gamma_R \equiv \gamma_{2L}$ are missing in Hamiltonian (4.8), one finds that $\Sigma^z = S_{\text{edges}} \equiv -i\gamma_L\gamma_R$ acts on the ground state space \mathcal{C} since $[\Sigma^z, S_j] = 0$. Furthermore, it allows for the definition of a convenient basis of the codespace, namely

$$\Sigma^z |\pm 1\rangle = \pm |\pm 1\rangle. \quad 4.9$$

Flipping the encoded qubit is possible via the edge modes $\Sigma^x \equiv \gamma_L$ and $\Sigma^y \equiv \gamma_R$, e.g.,

$$\Sigma^x |\pm 1\rangle = |\mp 1\rangle \quad 4.10$$

without violating any stabilizer constraint, $[\Sigma^{x,y}, S_j] = 0$. The operators Σ^α characterize the logical qubit completely as they realize the Pauli algebra $[\Sigma^\alpha, \Sigma^\beta] = 2i\varepsilon_{\alpha\beta\gamma}\Sigma^\gamma$ on \mathcal{C} .

Crucial for realizing a quantum memory is its resilience against depolarizing and dephasing noise. The Majorana chain fights these types differently: Depolarizing (bit-flip) noise cannot be suppressed by the Hamiltonian since the logical operators Σ^x and Σ^y are perfectly local in any embedding of the open chain and energetically not penalized by the Hamiltonian in Eq. (4.8). However, in terms of the fermions it is $\Sigma^x = c_1^\dagger + c_1$ and $\Sigma^y = i(c_L^\dagger - c_L)$ —operators which break the fermionic parity symmetry of the superconducting Hamiltonian. In superconducting systems, fermionic parity is considered a natural symmetry that can be enforced to high precision because fermions are created by breaking cooper pairs (though it *can* be

violated by quasiparticle poisoning [238, 239]). In that sense, the fermionic nature of the physical realization is exploited to suppress depolarizing errors. Strictly speaking, this is just symmetry protection.

By contrast, dephasing noise operates as $\Sigma^z \propto \gamma_L \gamma_R$ on the chain which is a non-local operator that cannot be induced directly by a noisy environment respecting locality. Indeed, the generic form of environmental noise that is both local and parity-symmetric has the form $E_j = -i \gamma_{2j-1} \gamma_{2j}$ (note that pairs shifted by a single site act trivially on the codespace). Since $\{E_i, S_j\} = 0$ if and only if $j = i$ or $j = i - 1$ (otherwise $[E_i, S_j] = 0$), a single error E_i is flanked by a pair of syndromes or *charges* with $S_i = -1 = S_{i-1}$. From the condensed matter point of view, this accounts for breaking a cooper pair and lifting the localized quasiparticles above the superconducting gap. Subsequent errors can move and/or create additional quasiparticle pairs that can, as time goes on, traverse the macroscopic chain in a noise-driven, diffusive process. Once a pair of charges traverses the whole chain, it is described by

$$\prod_{j=1}^L E_j = -i \gamma_L \left[\prod_{i=1}^{L-1} S_i \right] \gamma_R = \Sigma^z, \quad 4.11$$

where we used $S_i = \mathbb{1}$ on the codespace. Thus dephasing noise on the logical qubit is only possible if quasiparticles travel freely through the system. Unfortunately, save for the energy gap which penalizes the *creation* of charges, there is no cost for *moving* them. This deconfinement renders the Hamiltonian theory unstable at finite temperatures¹³³.

To protect the logical qubit from dephasing, active error correction must be employed. Assume the system is initialized in state $|\Psi\rangle \in \mathcal{C}$ and subsequently has been affected by the error $E(\mathbf{x}) = \prod_j E_j^{x_j}$, encoded by the binary vector $\mathbf{x} = (x_1, \dots, x_L) \in \mathbb{F}_2^L$. Because $E_i^2 = \mathbb{1}$, applying the same error twice cancels the latter and removes all syndromes,

$$E(\mathbf{x})E(\mathbf{x})|\Psi\rangle = E(\mathbf{x} \oplus \mathbf{x})|\Psi\rangle = E(\mathbf{0})|\Psi\rangle = |\Psi\rangle, \quad 4.12$$

rotating the system's state back into the codespace \mathcal{C} . Here, \oplus denotes the (element-wise) modulo-2 addition. To infer \mathbf{x} , the local stabilizers $\{S_1, \dots, S_{L-1}\}$ are measured periodically to yield a binary syndrome pattern $\mathbf{s} = (s_{1+\frac{1}{2}}, \dots, s_{L-1+\frac{1}{2}}) \in \mathbb{F}_2^{L-1}$ (with $S_j = (-1)^{s_{j+\frac{1}{2}}}$) that indicates the boundaries of $E(\mathbf{x})$. (Recall that only projective measurements that leave \mathcal{C} invariant do not destroy the logical qubit—these are exactly the stabilizer generators.) In terms of binary vectors, this reads

$$\mathbf{s} = \partial \mathbf{x} \quad \text{with} \quad (\partial \mathbf{x})_{i+\frac{1}{2}} \equiv x_i \oplus x_{i+1}. \quad 4.13$$

¹³³This is related to the fact that there is no phase transition for the one-dimensional classical Ising model.

The index shift by $\frac{1}{2}$ for syndromes is purely formal to distinguish them from error patterns x_i . Inferring \mathbf{x} from s is complicated by the fact that $\partial \mathbf{x} = s = \partial \mathbf{x}^c$, where $(\mathbf{x}^c)_i = x_i \oplus 1$ is the element-wise binary complement. The decoding problem is therefore not unique as complementary error strings share the same syndrome. If \mathbf{x}^c is chosen to specify the correction, one has

$$E(\mathbf{x}^c)E(\mathbf{x})|\Psi\rangle = E(\mathbf{x}^c \oplus \mathbf{x})|\Psi\rangle = E(\mathbf{1})|\Psi\rangle = \Sigma^z|\Psi\rangle \quad 4.14$$

and thereby (unknowingly) applies a quantum gate on the stored qubit; this follows from Eq. (4.11). Thus it is of paramount importance to choose the correct error pattern. The optimal decoding strategy depends on the error channel that gave rise to $E(\mathbf{x})$.

Here we will always assume \mathbf{x} to be a sequence of uncorrelated Bernoulli random variables x_i with parameter $0 \leq p_0^x \leq \frac{1}{2}$ so that $\Pr(x_i = 1) = p_0^x$ for all $i = 1, \dots, L$. Then, the provably best decoder Δ is (global) *majority voting*,

$$\Delta(s) \equiv \mathbf{y} \quad \text{with} \quad \partial \mathbf{y} = s \quad \text{and} \quad |\mathbf{y}| < |\mathbf{y}^c| \quad 4.15$$

which realizes maximum-likelihood decoding for repetition codes, i.e., \mathbf{y} is preferred over \mathbf{y}^c because the former requires less errors ($x_i = 1$) and this makes it more probable with respect to a Bernoulli distribution with $p_0^x < \frac{1}{2}$. In the context of quantum codes (in particular the toric code), the prescription (4.15) is also called *minimum weight perfect matching*, which is equivalent to majority voting in one dimension (see below). Here, the weight $|\mathbf{x}|$ is the number of non-zero components $x_i = 1$ and we require L to be odd to avoid ties ($|\mathbf{x}| = |\mathbf{x}^c|$).

Note that Δ indeed performs majority voting on \mathbf{x} in the sense that

$$\mathbf{x} \oplus \Delta(\partial \mathbf{x}) = \begin{cases} \mathbf{x} \oplus \mathbf{x} = \mathbf{0} & \text{if } |\mathbf{x}| \leq \frac{L-1}{2} \\ \mathbf{x} \oplus \mathbf{x}^c = \mathbf{1} & \text{if } |\mathbf{x}| \geq \frac{L+1}{2} \end{cases} \quad 4.16a$$

$$= \text{maj}[x_1, \dots, x_L] . \quad 4.16b$$

Here the majority function on L binary inputs x_i is defined as

$$\text{maj}[x_1, \dots, x_L] \equiv \left\lfloor \frac{1}{2} + \frac{1}{L} \left(\sum_{i=1}^L x_i - \frac{1}{2} \right) \right\rfloor \quad 4.17$$

(ties evaluate to 0 with this definition) and the bold version $\text{maj}[\bullet]$ indicates a vectorized result with each entry given by $\text{maj}[\bullet]$; $\lfloor x \rfloor$ denotes the greatest integer less than or equal to x . We conclude that the “quantum handicap” of having only access to the syndrome s for decoding the topological code does not change the decoding strategy as compared to a *classical* repetition code.

Indeed, for a correctable binary error pattern \mathbf{x} ($|\mathbf{x}| < |\mathbf{x}^c| \Leftrightarrow \text{maj}[\mathbf{x}] = \mathbf{0}$), the classical repetition code word $\Psi \in \{\mathbf{0}, \mathbf{1}\}$, and the quantum code word $|\Psi\rangle \in \mathcal{C}$, we have for the *classical* code

$$\Psi \xrightarrow{E} \mathbf{x} \oplus \Psi = \Psi' \quad 4.18a$$

$$\xrightarrow{C} \Delta(\partial\Psi') \oplus \Psi' \quad 4.18b$$

$$= \Delta(\partial\mathbf{x}) \oplus \mathbf{x} \oplus \Psi \quad 4.18c$$

$$= \text{maj}[\mathbf{x}] \oplus \Psi \quad 4.18d$$

$$= \Psi \quad 4.18e$$

and the *quantum* analogue

$$|\Psi\rangle \xrightarrow{E} E(\mathbf{x})|\Psi\rangle \quad 4.19a$$

$$\xrightarrow{C} E(\Delta(\partial\mathbf{x})) E(\mathbf{x})|\Psi\rangle \quad 4.19b$$

$$= E(\Delta(\partial\mathbf{x}) \oplus \mathbf{x})|\Psi\rangle \quad 4.19c$$

$$= E(\text{maj}[\mathbf{x}])|\Psi\rangle \quad 4.19d$$

$$= |\Psi\rangle, \quad 4.19e$$

where E (C) denotes the application of errors (corrections).

To make connection with another well-known topological quantum code, let us, just for a second, peek into the second dimension: There, the simplest model is given by the toric code [24, 45, 49] which features a four-fold degenerate ground state manifold (the codespace) and is defined by the Hamiltonian

$$H_{\text{TC}} = - \sum_{\text{Sites } s} A_s - \sum_{\text{Faces } p} B_p \quad 4.20$$

with stabilizer operators

$$A_s = \prod_{e \in s} \sigma_e^x \quad \text{and} \quad B_p = \prod_{e \in p} \sigma_e^z \quad 4.21$$

living on an $L_x \times L_y$ square lattice with periodic boundary conditions and spin- $\frac{1}{2}$ representations σ_e (physical qubits) on the edges. While the toroidal geometry of Hamiltonian (4.20) is crucial for its four-fold ground state degeneracy, it also renders the model experimentally challenging (even more than it already is due to its four-spin interactions). However, if the above Hamiltonian is adapted to a *planar* square lattice with appropriately chosen (“rough” and “smooth”) open boundaries [52], the experimental implementation becomes more attractive while the ground state manifold is still two-fold degenerate and constitutes a topological quantum memory with the two Abelian anyonic excitations $A_s = -1$ and $B_p = -1$, see Figure 4.3 (b).

Reducing this code to the degenerate, one-dimensional case $L_x = L$ and $L_y = 1$, yields a one-dimensional spin system which maps directly to the Majorana chain under the Jordan-Wigner transformation

$$\gamma_{2j} \leftrightarrow \left[\prod_{i=1}^{j-1} \sigma_i^z \right] \sigma_j^y \quad 4.22a$$

$$\gamma_{2j-1} \leftrightarrow \left[\prod_{i=1}^{j-1} \sigma_i^z \right] \sigma_j^x \quad 4.22b$$

[Figure 4.3 (c)] with the identifications

$$S_j \leftrightarrow \sigma_j^x \sigma_{j+1}^x (= A_s) \quad 4.23a$$

$$E_j \leftrightarrow \sigma_j^z. \quad 4.23b$$

Note that in one dimension there are no faces and the B_p stabilizers are absent. Then, Hamiltonian (4.20) describes the 1D Ising model and local errors $E_j = \sigma_j^z$ correspond to spin-flips in the σ^x -basis; syndromes $S_j = \sigma_j^x \sigma_{j+1}^x = -1$ can be associated with domain walls.

The physical distinction between Majorana chain and 1D toric code/Ising chain becomes evident if one realizes that error strings $E(\mathbf{x})$ can be directly measured by $\sigma_j^x = \pm 1$ in the 1D toric code/Ising chain (and not only their endpoints by $S_j = \pm 1$). The analogous operator for the Majorana chain error strings violates the fermionic parity and is thereby suppressed. Similarly, while $\Sigma^x = \gamma_L$ is forbidden in the fermionic setting of the Majorana chain due to parity superselection, there is no natural symmetry in the spin chain preventing $\Sigma^x = \sigma_1^x$ from depolarizing the logical qubit. This is why it is legit to call the Majorana chain a 1D topological *quantum* memory whereas the mathematically equivalent 1D toric code/Ising chain only protects a *classical* bit by realizing a repetition code.

Nevertheless, from the algorithmic point of view, both theories carry the same syndromes and therefore can be corrected with the same algorithms. In particular, MWPM on the toric code degenerates into majority voting on the Majorana chain. Note that for the degenerate toric code, this active error correction procedure has already been demonstrated experimentally with transmon qubits [178, 305].

4.2.2 Global Majority Voting

We proceed with a brief analysis of global majority voting. As we argued above, we can ignore the “quantum handicap“ that restricts our knowledge to the endpoints of error strings (the syndromes) and instead work with the actual error patterns.

Assume a classical bit x , initialized as $x = 0$, is flipped by a (unbiased) Bernoulli process with probability $0 \leq p_0^x \leq \frac{1}{2}$ per time step δt . If we think of the state $x = 0$ as the “clean“ one while $x = 1$ indicates a site that is error-afflicted, the probability

to find $x = 1$ after t time steps is given by

$$p^x(t) = \frac{1}{2} \left[1 - (1 - 2p_0^x)^t \right] \quad 4.24$$

which renormalizes to the completely mixed state $p^x(t) \rightarrow \frac{1}{2}$ exponentially fast whenever $0 < p_0^x < 1$. If we copy the bit L times, (x_1, \dots, x_L) , and encode a logical bit X via a simple repetition code,

$$X = 0 \quad \rightarrow \quad \mathbf{x} = (0, 0, \dots, 0), \quad 4.25$$

then, for uncorrelated Bernoulli error processes on the physical bits x_i , the best decoder is given by the global majority vote

$$X = \text{maj}[x_1, \dots, x_L]. \quad 4.26$$

An erroneous logical bit $X = 1$ occurs whenever the majority is altered by the local errors. Formally, the probability to find $X = 1$ after t time steps of accumulating errors is given by (L odd)

$$P_{L,p_0^x}^x(t) = \sum_{k=\frac{L+1}{2}}^L \binom{L}{k} [p^x(t)]^k [1 - p^x(t)]^{L-k} \quad 4.27a$$

$$= \frac{L+1}{2} \binom{L}{\frac{L+1}{2}} \int_0^{p^x(t)} [x - x^2]^{\frac{L-1}{2}} dx \quad 4.27b$$

where in the last line we used the regularized incomplete beta function to express the cumulative Binomial distribution in a closed form [337] (see [§ Section 4.A](#) for details). We illustrate $P_{L,p_0^x}^x(t) = 1 - P_{L,p_0^x}^x(t)$ as a function of t in Figure 4.4 (a) for different system sizes L and fixed continuous noise p_0^x . Note that the decay time grows very slowly with the system size L .

After a *single* time step, we have the logical failure probability $P_{L,p_0^x}^x \equiv P_{L,p_0^x}^x(t = 1)$. Assume that after each time step δt the errors that occurred during δt are immediately countered by majority voting, i.e., following Eq. (4.18) for classical and Eq. (4.19) for quantum codes. The probability of the logical (qu)bit to be in its original state after t time steps is then

$$\tilde{P}_{L,p_0^x}^x(t) = \frac{1}{2} \left[1 + (1 - 2P_{L,p_0^x}^x)^t \right] \quad 4.28$$

which yields the timescale T_{L,p_0^x} for the logical information loss

$$T_{L,p_0^x} = \left[\log \frac{1}{1 - 2P_{L,p_0^x}^x} \right]^{-1} \xrightarrow{L \rightarrow \infty} \frac{1}{P_{L,p_0^x}^x} \quad 4.29$$

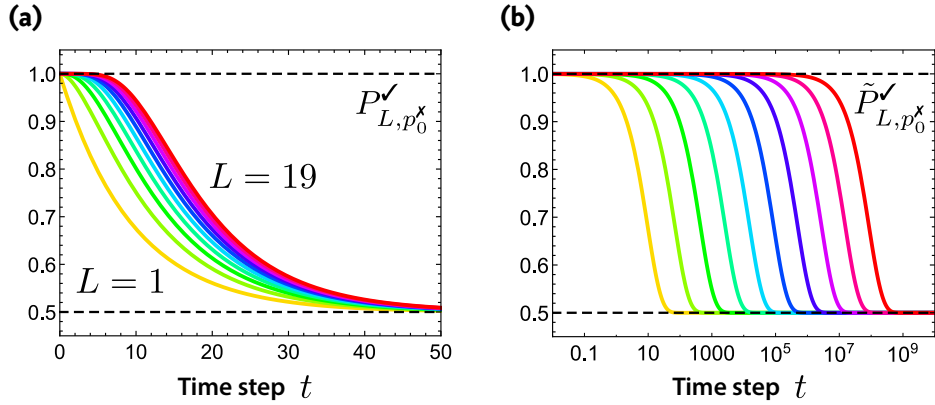


FIGURE 4.4 • Global majority voting. (a) The probability $P_{L,p_0}^{\checkmark}(t)$ of correctly decoding an ensemble of L bits by global majority voting under continuous noise $p_0^{\checkmark} = 0.05$ as a function of time t for different system sizes $L = 1, \dots, 19$ without any stabilizing correction performed. (b) The same $[P_{L,p_0}^{\checkmark}(t)]$ for a stabilized system with global majority voting and active correction after each time step. Mind the logarithmic t -axis.

if $\lim_{L \rightarrow \infty} P_{L,p_0}^{\checkmark} = 0$. Moreover, it is straightforward to show that it diverges exponentially with the system size for any non-trivial (and non-critical) microscopic error probability $0 < p_0^{\checkmark} < \frac{1}{2}$. Indeed, we can use Eq. (4.27b) to derive the upper bound

$$P_{L,p_0}^{\checkmark} \leq \frac{L+1}{2} \binom{L}{\frac{L+1}{2}} p_0^{\checkmark} q^{L-1} \sim \sqrt{L} e^{L \log(2q)} \quad 4.30$$

with $q = \sqrt{p_0^{\checkmark}(1-p_0^{\checkmark})} < \frac{1}{2}$ for $p_0^{\checkmark} < \frac{1}{2}$; in the last step, we used the asymptotic approximation $\binom{L}{\frac{L+1}{2}} \sim \sqrt{\frac{2}{\pi}} \frac{2^L}{\sqrt{L}}$ for $L \rightarrow \infty$. It follows the exponentially diverging decay time of the code

$$T_{L,p_0}^{\checkmark} \gtrsim \frac{e^{L \log \frac{1}{2q}}}{\sqrt{L}}. \quad 4.31$$

This is illustrated in Figure 4.4 (b) by plotting $\tilde{P}_{L,p_0}^{\checkmark}(t)$ over time for different system sizes and fixed continuous error rate. Eq. (4.31) is a quantitative manifestation of the perfect decoding properties of global majority voting on a repetition code. Note that the only error rate for which decoding fails in the thermodynamic limit is the singular point $p_0^{\checkmark} = \frac{1}{2}$ for which $2q = 1 \Rightarrow \log \frac{1}{2q} = 0$.

4.2.3 Constraints by Locality

Eq. (4.31) tells us that global majority voting is a very powerful decoding scheme for the 1D quantum code realized by the Majorana chain: its critical error rate $p_c^x = \frac{1}{2}$ is optimal. In physics, nothing is for free. This begs the question what it is that we are paying with by employing the global majority decoder Δ (or, equivalently, the function $\text{maj}[\dots]$). One particularly expensive feature of $\text{maj}[x_1, \dots, x_L]$ is its global nature: It depends non-trivially on all L inputs while their number grows with the system size [see Eq. (4.17)]. Indeed, one needs to take into account *at least* $\frac{L+1}{2}$ of the inputs to be sure about the majority; for generic inputs even more. This makes the evaluation of $\text{maj}[\dots]$ a relevant factor that has to be taken into account when the scaling of the quantum code with L is addressed.

A generic global function, depending on $\sim L$ spatially distributed inputs (syndromes) requires *at least* $\sim c^{-1}L$ time steps to gather its input data (for a 1D geometry). Here c denotes the speed of classical information propagation in the auxiliary systems framing the quantum chain. This is illustrated by the light cone in Figure 4.5 (a). In addition, the evaluation itself (shaded region) also requires *at least* $\mathcal{O}(L)$ time steps because every input has to be read at least once, see e.g., Eq. (4.17). Depending on the decoder, the latter may be improved by parallelization (which, in turn, is paid for by additional hardware overhead), whereas the former argument remains valid as it is based on physical constraints alone.

An immediate consequence for the global majority decoder Δ is sketched in the left panel of Figure 4.5 (b): The time between syndrome measurement (blue square) and correction (red disk) scales with the system size L . Depending on the relevant velocity c (which should be henceforth thought of as comprising both information propagation and computations) and chain length L , this upper bounds the rate at which Δ can be applied to fight continuous noise on the quantum code.

This has important consequences: The probability that Δ flips the logical (qu)bit after accumulating errors for $t = c^{-1}L$ time steps is given by Eq. (4.27b),

$$\hat{P}_{L,p_0^x}^x \equiv P_{L,p_0^x}^x(t = c^{-1}L) \xrightarrow{L \rightarrow \infty} \frac{1}{2} \quad 4.32$$

where the limit holds for all $0 < p_0^x \leq \frac{1}{2}$, see ****** Section 4.A for the derivation. This is in contrast to

$$P_{L,p_0^x}^x = P_{L,p_0^x}^x(t = 1) \xrightarrow{L \rightarrow \infty} 0 \quad 4.33$$

which led to the exponential growth of T_{L,p_0^x} if the correction rate is *independent* of the system size, see Eq. (4.30). We conclude that the exponential growth of T_{L,p_0^x} (which depends on the exponential vanishing of the logical error probability $P_{L,p_0^x}^x$) is lost if we take into account the time needed to evaluate the global majority vote.

A possibility to keep both a size-independent correction rate and the global majority vote decoder Δ is illustrated in the right panel of Figure 4.5 (b): Multiple copies of Δ running in parallel can keep up with continuous noise if after each time

ERROR CORRECTION WITH CELLULAR AUTOMATA

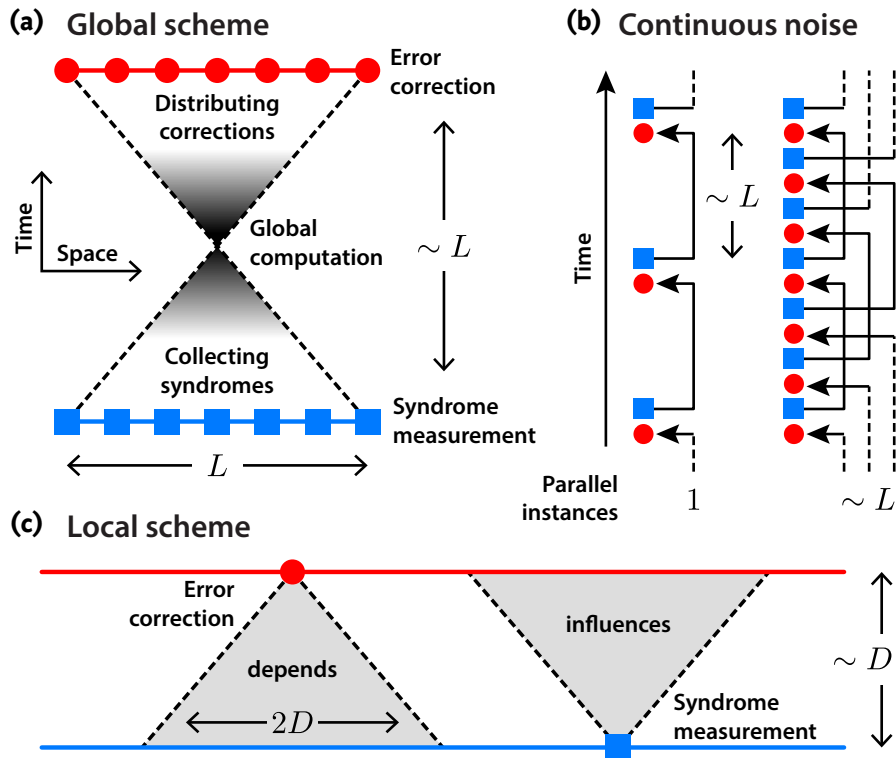


FIGURE 4.5 • Locality constraints. (a) A global correction scheme on a quantum code of linear size L requires the syndrome data to be merged, processed, and afterwards the results to be distributed again. The finite communication speed makes the time between syndrome measurements (blue squares) and error corrections (red circles) scale with L in the best case. (b) With constrained hardware overhead, only one instance of the syndrome processing runs at once, giving rise to intervals without correction growing with $\sim L$. Repeating syndrome measurements and corrections with a period independent of L requires $\sim L$ instances running in parallel, thus increasing the hardware overhead dramatically. (c) Local schemes can be used to keep hardware overhead in check by reducing the computation time needed to sublinear (or even logarithmic) scaling if $D \sim L^\kappa$ with $\kappa < 1$. This restricts the syndromes that a local correction operation depends on to a subsystem inside the past light cone of diameter $2D$, and allows syndromes to influence only corrections in their future light cone.

step δt a new instance of Δ is fed with the syndrome $\partial(\mathbf{x}_{t-1} \oplus \mathbf{x}_t) = \partial\mathbf{x}_{t-1} \oplus \partial\mathbf{x}_t$ that encodes only errors accumulated during δt . Note that intertwining corrections and errors is acceptable as both commute. The obvious downside of this approach is its hardware overhead: The number of parallel instances required (the “depth” of the decoder) scales with the time needed for a single instance to finish, that is, with L .

If we retrace our line of thought, it is obvious that the *global* nature of Δ is responsible for the L -scaling of the depth in the presence of continuous noise. This motivates the question whether the global decoder Δ can be replaced by a *local*

version Δ^D which requires only syndrome data within a radius D of each site to compute the correction at this very site; the corresponding spacetime diagram is shown in Figure 4.5 (c). The benefits of such a local decoder would be less hardware overhead, simpler implementation, and thus better scaling properties. It cannot implement $\text{maj}[\dots]$ perfectly and one has to expect decoding errors in some cases (where Δ would have succeeded). However, if these cases are rare for low error rates $p_0^x < p_c^x$ with finite critical rate $0 < p_c^x \leq \frac{1}{2}$, and the relaxation time T_{L,p_0^x} still scales exponentially with L , this would be perfectly acceptable. It is such a “ D -local” decoder that we describe and analyze in the following:

DEFINITION 4.1: D -local decoders

Given a decoder $\Delta : \mathbb{F}_2^{L-1} \rightarrow \mathbb{F}_2^L$ for the Majorana chain of length L that maps a syndrome pattern $\partial \mathbf{x} \in \mathbb{F}_2^{L-1}$ to the correction string $\Delta(\partial \mathbf{x}) \in \mathbb{F}_2^L$. Let

$$\pi_i^D \mathbf{x} = (x_{\max\{i-D,1\}}, \dots, x_i, \dots, x_{\min\{i+D,L\}}) \quad 4.34$$

denote the neighborhood of site i with radius D .

The decoder Δ is called D -local (write Δ^D) if

$$\Delta_i^D(\partial \mathbf{x}) = f_i(\partial \pi_i^D \mathbf{x}) \quad 4.35$$

for some family of functions $\{f_i\}$: Its correction at site i only depends on (syndromes of) error patterns within distance D of i .

Since D -local decoders finish after $\sim D$ time steps (if the f_i can be evaluated efficiently), the required depth [cf. Figure 4.5 (c)] also scales with D .

In the remainder of this subsection, and before we zoom in on our particular decoder, we discuss a constraint that follows for the class of D -local decoders Δ^D quite generally. Namely the (weak) upper bound for the probability $P_{\text{dec}}^\checkmark$ of successfully decoding Bernoulli samples with a D -local decoder

$$P_{\text{dec}}^\checkmark \leq \left[1 + \left(\frac{p_0^x}{1 - p_0^x} \right)^{2D+1} \right]^{-\frac{1}{2D+1}}. \quad 4.36$$

Note that this result is generic in the sense that it holds for all decoders of the MCQC where the correction of site i depends only on nearby syndromes in the neighborhood $\pi_i^D \mathbf{x}$, irrespective of their local functions $\{f_i\}$. We call Eq. (4.36) the *light cone constraint*; its proof can be found in \clubsuit Subsection 4.B.1.

Here we discuss some scaling limits of Eq. (4.36) and their implications for potential decoders replacing Δ . We assume $D = D(L)$ to be a function of the linear size L of the code (the length of the quantum chain). We stress that the interpretation of the radius D can be either a spatial depth of a feedforward physical circuit or a time-like depth in a spacetime diagram of a truly one-dimensional

physical automaton. In the first case, scaling D with L means growing the system into the second dimension; in the second case, it accounts for a longer runtime of the decoder. Note that the class of decoders with at least $D \sim L$ comprises exactly the global ones (e.g., Δ). We discuss two important cases:

- 1 $D = \text{const.}$ This describes a truly one-dimensional feedforward circuit of finite depth D . We find in the thermodynamic limit

$$\lim_{L \rightarrow \infty} P_{\text{dec}}^{\checkmark} \leq \begin{cases} 0 & \text{for } 0 < p_0^{\checkmark} \leq \frac{1}{2}, \\ 1 & \text{for } p_0^{\checkmark} = 0, \end{cases} \quad 4.37$$

i.e., there is no successful decoding possible for any finite microscopic error rate $p_0^{\checkmark} > 0$.

- 2 $2D + 1 \sim L^\kappa$ ($\kappa > 0$). This describes a truly two-dimensional feedforward circuit, possibly slowly growing in the second dimension if $\kappa \approx 0$. We find in the thermodynamic limit

$$\lim_{L \rightarrow \infty} P_{\text{dec}}^{\checkmark} \leq \begin{cases} 1 & \text{for } 0 \leq p_0^{\checkmark} < \frac{1}{2}, \\ 0 & \text{for } p_0^{\checkmark} = \frac{1}{2} \text{ and } \kappa < 1, \\ \frac{1}{2} & \text{for } p_0^{\checkmark} = \frac{1}{2} \text{ and } \kappa = 1, \\ 1 & \text{for } p_0^{\checkmark} = \frac{1}{2} \text{ and } \kappa > 1, \end{cases} \quad 4.38$$

i.e., except for the critical point $p_0^{\checkmark} = \frac{1}{2}$, there is no constraint on $P_{\text{dec}}^{\checkmark}$. At the critical point, the upper bounds depend on whether the second dimension scales slower or faster than the length of the chain. For faster scaling depth, there is no constraint, whereas for slower scaling depth, non-trivial upper bounds arise. Note that actually $P_{\text{dec}}^{\checkmark} \leq \frac{1}{2}$ follows for $p_0^{\checkmark} = \frac{1}{2}$ for *all* decoders (not only D -local ones) since a completely mixing Bernoulli process destroys all encoded information. $P_{\text{dec}}^{\checkmark} < \frac{1}{2}$ arises whenever the decoder fails to get rid of all syndromes (this is in contrast to the global decoder Δ which always succeeds in removing all syndromes). $P_{\text{dec}}^{\checkmark} = \frac{1}{2}$ *can* be realized if the decoder succeeds in removing all syndromes but still fails to recover the original state in 50% of the cases. A detailed derivation of these results is presented in ✱ Subsection 4.B.2.

In conclusion, decoding the Majorana chain in a single step with a constant- D decoder is impossible in the thermodynamic limit. However, while $D \sim L^\kappa$ with $\kappa \geq 1$ describes only global decoders (in particular, the global majority vote Δ), there is also no restriction on $P_{\text{dec}}^{\checkmark}$ for the larger class of *local* decoders with $0 < \kappa < 1$. This leaves the possibility open for local decoders with less hardware overhead than Δ .

One of the main results presented in this chapter is a *lower* bound on $P_{\text{dec}}^{\checkmark}$ for a class of local decoders which allows to scale D at will. In particular, we find that Eq. (4.36) is saturated in the thermodynamic limit for $D \sim L^\kappa$ with arbitrary $\kappa > 0$ below a critical error rate $p_c^x > 0$.

4.3 Cellular Automata

In this section, we introduce a strictly local decoder for the MCQC. Our approach is based on cellular automata, thus we start with a description of this framework and the relevant properties. In particular, we demonstrate that for the MCQC—where only the syndromes can be measured—we have to resort to CAs that are characterized by *self-duality*, a symmetry of the local evolution rules. The natural choice is then to focus on such CAs which additionally approximate global majority voting. This task is known as *density classification* and we present two CAs that are known to perform well as density classifiers, one of which (called TLV) exhibits self-duality. Since the quantum code is embedded on a finite chain with open boundaries, it is essential to modify TLV at the edges; this new CA is denoted as $\overline{\text{TLV}}$. We argue that it acts as a self-dual density classifier on finite chains, and thereby qualifies as a promising local replacement for global majority voting on the MCQC.

4.3.1 Properties of Cellular Automata

To describe our local decoder, we make use of the well-known framework of one-dimensional, binary cellular automata [338, 339]; discrete dynamical systems defined on a 1D lattice \mathcal{L} of binary cells $i \in \mathcal{L}$ with indices in $\mathcal{L} = \mathbb{Z}$ (infinite), \mathbb{N} (semi-infinite), or $\{1, \dots, L\}$ (finite). A *state* $\mathbf{x} \in \mathbb{F}_2^{\mathcal{L}}$ is formally a map $\mathbf{x} : \mathcal{L} \rightarrow \mathbb{F}_2$ assigning a state x_i to each cell $i \in \mathcal{L}$. Equivalently, $\mathbf{x} \subseteq \mathcal{L}$ may be read as the subset of lattice indices $i \in \mathcal{L}$ where $x_i = 1$. A cellular automaton $\Gamma_{\mathcal{L}} : \mathbb{F}_2^{\mathcal{L}} \rightarrow \mathbb{F}_2^{\mathcal{L}}$ of radius $R \in \mathbb{N}$ is defined by a collection of binary functions $\gamma_i : \mathbb{F}_2^{2R+1} \rightarrow \mathbb{F}_2$ that determines a discrete time evolution on $\mathbb{F}_2^{\mathcal{L}}$ via

$$x'_i = \Gamma_i(\mathbf{x}) \equiv \gamma_i(\pi_i^R \mathbf{x}). \quad 4.39$$

We write $\mathbf{x}' = \Gamma_{\mathcal{L}}(\mathbf{x})$ for short. If $\gamma_i = \gamma$ for all $i \in \mathcal{L}$, $\Gamma_{\mathcal{L}}$ is called *translationally invariant*. For $R > 0$, translational invariant CAs can be defined on infinite chains $\mathcal{L} = \mathbb{Z}$ and finite chains $\mathcal{L} = \{1, \dots, L\}$ with periodic boundary conditions, as opposed to semi-infinite chains $\mathcal{L} = \mathbb{N}$ and finite chains with open boundaries where modifications at the boundaries are necessary (see below). We write $\mathbf{x}(t) = \Gamma_{\mathcal{L}}^t(\mathbf{x}(0))$ for the state $\mathbf{x}(t)$ that is produced by t consecutive applications of $\Gamma_{\mathcal{L}}$ on the initial state $\mathbf{x}(0)$. A state \mathbf{x}^* with $\mathbf{x}^* = \Gamma_{\mathcal{L}}(\mathbf{x}^*)$ is called *fixed point* of $\Gamma_{\mathcal{L}}$. More generally, a finite subset of states $C \subseteq \mathbb{F}_2^{\mathcal{L}}$ which is invariant, $\Gamma_{\mathcal{L}}(C) = C$,

and does not contain a proper invariant subset is called a *cycle* (a fixed point is a cycle with one element). On finite chains $\mathcal{L} = \{1, \dots, L\}$, the CA always ends up in a cycle after a finite relaxation time due to the finiteness of the state space $\mathbb{F}_2^{\mathcal{L}}$. For a given cycle C , the maximal set of states $A_C \subseteq \mathbb{F}_2^{\mathcal{L}}$ with $\lim_{t \rightarrow \infty} \Gamma_{\mathcal{L}}^t(A_C) = C$ is called *attractor* of C . We will be interested in CAs with the uniform fixed points $\mathbf{x}^* = \mathbf{0}$ and $\mathbf{1}$ (characterized by the absence of syndromes) and their corresponding attractors $A_{\mathbf{0}}$ and $A_{\mathbf{1}}$.

The dynamics of a CA can be strongly influenced and restricted by symmetries of the transition rules $\Gamma_{\mathcal{L}}$. In the following, we are particularly interested in the special class of *self-dual* CAs:

DEFINITION 4.2: Self-duality

A binary cellular automaton $\Gamma_{\mathcal{L}} : \mathbb{F}_2^{\mathcal{L}} \rightarrow \mathbb{F}_2^{\mathcal{L}}$ described by $x'_i = \Gamma_i(\mathbf{x})$ is called self-dual if $(\Gamma_i(\mathbf{x}))^c = \Gamma_i(\mathbf{x}^c)$ for all $i \in \mathcal{L}$ with the binary complement $x_i^c \equiv x_i \oplus 1$.

Self-duality is therefore a *symmetry* satisfied only by particular CA rules $\Gamma_{\mathcal{L}}$. For example, local rules based on majority votes of adjacent cells are automatically self-dual because the binary majority function is¹³⁴,

$$\text{maj}[x_1^c, \dots] = (\text{maj}[x_1, \dots])^c, \tag{4.40}$$

whereas logical dis- and conjunctions violate the symmetry, e.g.,

$$x_1^c \wedge x_2^c = (x_1 \vee x_2)^c \neq (x_1 \wedge x_2)^c. \tag{4.41}$$

The importance of self-dual CAs in the context of quantum error correcting the Majorana chain stems from the following observation:

LEMMA 4.1: State-state and syndrome-delta representation

Let $\Gamma_{\mathcal{L}}$ be a self-dual, binary cellular automaton $\Gamma_{\mathcal{L}} : \mathbb{F}_2^{\mathcal{L}} \rightarrow \mathbb{F}_2^{\mathcal{L}}$ acting on a one-dimensional chain \mathcal{L} (infinite, semi-infinite, open or periodic boundaries); let $s = \partial \mathbf{x}$ denote the syndromes. Then there are two equivalent representations of $\Gamma_{\mathcal{L}}$:

→ The state-state representation is given by the conventional transformation rule

$$\mathbf{x} \mapsto \mathbf{x}' = \Gamma_{\mathcal{L}}(\mathbf{x}) \tag{4.42}$$

which transforms the current state \mathbf{x} into the new state \mathbf{x}' . It operates on the states of cells $\mathbb{F}_2^{\mathcal{L}}$ on the lattice \mathcal{L} .

¹³⁴This is true if ties are excluded, i.e., for an odd number of inputs.

→ The syndrome-delta representation is given by the two-step process

$$\mathbf{s} \mapsto \mathbf{\Delta} = \partial\Gamma_{\mathcal{L}}(\mathbf{s}) \quad 4.43a$$

$$(\mathbf{\Delta}, \mathbf{s}) \mapsto \mathbf{s}' = \partial\mathbf{\Delta} \oplus \mathbf{s} \quad 4.43b$$

and transforms the current syndrome \mathbf{s} into the new syndrome \mathbf{s}' via the intermediate result (delta) $\mathbf{\Delta}$. It operates on states of syndromes $\mathbb{F}_2^{\partial\mathcal{L}}$ on the dual lattice $\partial\mathcal{L}$. The derived rule $\partial\Gamma_{\mathcal{L}}$ is defined for $i \in \mathcal{L}$ as

$$\partial\Gamma_i(\mathbf{s}) \equiv \Gamma_i(\{x_k = \bigoplus_{\sigma \in \overline{ki}} s_\sigma\}) \quad 4.44$$

where for two sites $k, i \in \mathcal{L}$, $\overline{ki} = \overline{ik}$ denotes the set of sites in $\partial\mathcal{L}$ (edges in \mathcal{L}) between i and k ¹³⁵.

The following (rather technical) proof can be skipped on first reading if the existence of the syndrome-delta representation is intuitively understood and/or accepted as a fact.

Proof. We show that there is a one-to-one correspondence between the two descriptions by constructing them explicitly. To this end, consider an arbitrary self-dual binary function $f : \mathbb{F}_2^{\mathcal{L}} \rightarrow \mathbb{F}_2$. First, note that self-duality is equivalent to the property

$$f(\{y \oplus x_i\}) = y \oplus f(\{x_i\}) \quad 4.45$$

for $y \in \mathbb{F}_2$ since $x_i^c = 1 \oplus x_i$. If we use that

$$x_i \oplus x_k = x_i \oplus (x_{i+1} \oplus x_{i+1}) \oplus \cdots \oplus (x_{k-1} \oplus x_{k-1}) \oplus x_k \quad 4.46a$$

$$= (x_i \oplus x_{i+1}) \oplus (x_{i+1} \oplus \cdots \oplus x_{k-1}) \oplus (x_{k-1} \oplus x_k) \quad 4.46b$$

$$= s_{i+\frac{1}{2}} \oplus \cdots \oplus s_{k-\frac{1}{2}} = \bigoplus_{\sigma \in \overline{ik}} s_\sigma \quad 4.46c$$

and therefore

$$x_i = x_k \oplus \bigoplus_{\sigma \in \overline{ik}} s_\sigma \quad 4.47$$

for any $k \in \mathcal{L}$ and $\mathbf{s} = \partial\mathbf{x}$, it follows (for fixed but arbitrary k)

$$f(\{x_i\}) = f(\{x_k \oplus \bigoplus_{\sigma \in \overline{ik}} s_\sigma\}) \quad 4.48a$$

$$= x_k \oplus f(\{\bigoplus_{\sigma \in \overline{ik}} s_\sigma\}) \quad 4.48b$$

$$\equiv x_k \oplus \tilde{f}|_k(\{s_\sigma\}) \quad 4.48c$$

$$= x_k \oplus \tilde{f}|_k(\partial\mathbf{x}). \quad 4.48d$$

For a self-dual CA in state-state representation, this reads

$$x'_i = \Gamma_i(\{x_j\}) = x_k \oplus \tilde{\Gamma}_i|_k(\mathbf{s}) \quad 4.49$$

¹³⁵For periodic boundary conditions, this is well-defined due to $\bigoplus_{\sigma \in \partial\mathcal{L}} s_\sigma = 0$.

for arbitrary $k \in \mathcal{L}$. If we set $k = i$, this becomes

$$x'_i \oplus x_i = \Gamma_i(\{x_j\}) \oplus x_i = \tilde{\Gamma}_i|_i(s). \quad 4.50$$

If we define the state change as $\mathbf{\Delta} \equiv \mathbf{x}' \oplus \mathbf{x}$ and $\partial\Gamma_i(s) \equiv \tilde{\Gamma}_i|_i(s)$, we arrive at

$$\Delta_i = \partial\Gamma_i(s) = \Gamma_i(\{x_k = \bigoplus_{\sigma \in \bar{k}i} s_\sigma\}). \quad 4.51$$

On the other hand, it is

$$s'_{i+\frac{1}{2}} = x'_i \oplus x'_{i+1} = (x_i \oplus \Delta_i) \oplus (x_{i+1} \oplus \Delta_{i+1}) \quad 4.52a$$

$$= (\Delta_i \oplus \Delta_{i+1}) \oplus (x_i \oplus x_{i+1}) = (\partial\mathbf{\Delta})_{i+\frac{1}{2}} \oplus s_{i+\frac{1}{2}} \quad 4.52b$$

so that

$$s' = \partial\mathbf{\Delta} \oplus s \quad \text{with} \quad \mathbf{\Delta} = \partial\Gamma_{\mathcal{L}}(s) \quad 4.53$$

indeed describes the evolution of the syndrome $s = \partial\mathbf{x}$ given by the action of $\Gamma_{\mathcal{L}}$ on the states \mathbf{x} . Thus we provided a procedure to derive a syndrome-delta representation from a given state-state representation. Conversely, it is enough to realize that the knowledge of $\mathbf{\Delta} = \partial\Gamma_{\mathcal{L}}(\partial\mathbf{x})$ allows for the computation of \mathbf{x}' via $\mathbf{x}' = \mathbf{x} \oplus \mathbf{\Delta}$, i.e.,

$$\mathbf{x}' = \Gamma_{\mathcal{L}}(\mathbf{x}) = \mathbf{x} \oplus \partial\Gamma_{\mathcal{L}}(\partial\mathbf{x}). \quad 4.54$$

This concludes the proof. ■

It should be clear that it is exactly the syndrome-delta representation of a self-dual CA that makes it suited for decoding the Majorana chain and comply with the ‘‘quantum handicap’’: It operates on the measured syndromes s via the correction operations $\mathbf{\Delta}$ that can be applied directly to the quantum chain.

4.3.2 Density Classification in 1D

We seek to apply a simple, one-dimensional binary CA as local decoder for the MCQC. If we upper bound the allowed runtime of a radius- R CA $\Gamma_{\mathcal{L}}$ with T time steps, the map $\Gamma_{\mathcal{L}}^T$ is $D = RT$ -local per construction (since information spreads over R sites per time step under CA evolution). Then the depth scaling discussed previously becomes a matter of required runtime for a specific CA.

As we know that (global) majority voting is a perfect decoder for the Majorana chain, it is natural to ask whether one can implement the function $\text{maj}[x_1, \dots, x_L]$ by a hypothetical CA $\text{MAJ}_{\mathcal{L}}$ such that

$$\lim_{t \rightarrow \infty} \text{MAJ}_{\mathcal{L}}^t(\mathbf{x}) = \mathbf{0}(\mathbf{1}) \quad \text{if} \quad \text{maj}[\mathbf{x}] = 0(1); \quad 4.55$$

this is known as the *density classification problem* [331, 332]. Unfortunately, it can be rigorously shown that perfect majority voting cannot be achieved with binary CAs in any dimension [333]. This, however, is not a deal breaker for majority-based

error correction (both classical and quantum) as long as the erroneously classified instances are rare with respect to the noise channel in question. Motivated by applications for classical error correction, there evolved a vivid field concerned with the construction of *approximate* density classifiers (e.g., [327, 340–343]) and extensions capable of performing density classification exactly (e.g., [344–347]), see [332] for a review.

This is how we address the problem of finding a local decoder for the MCQC: Lemma 4.1 allows us to filter the literature of one-dimensional binary CAs for *self-dual density classifiers*; rewritten in syndrome-delta representation, these could be directly applied as potential Majorana chain decoders.

The first, most famous and well-studied (approximate) density classifier is dubbed “soldiers rule” and has been introduced by Gács, Kurdyumov, and Levin (GKL) [340, 348]. On $\mathcal{L} = \mathbb{Z}$, it is defined by the transition rule

$$x'_i = \text{GKL}_i(\mathbf{x}) \equiv \begin{cases} \text{maj}[x_i, x_{i-1}, x_{i-3}] & \text{if } x_i = 0, \\ \text{maj}[x_i, x_{i+1}, x_{i+3}] & \text{if } x_i = 1, \end{cases} \quad 4.56$$

with radius $R = 3$ [see Figure 4.6 (a)]. Unfortunately, it is easy to check that it violates self-duality,

$$(\text{GKL}_{\mathcal{L}}(\mathbf{x}))^c \neq \text{GKL}_{\mathcal{L}}(\mathbf{x}^c) \quad 4.57$$

due to the dependence of the evaluated sites in the local majority vote on the state of site i . This can also be seen from the exemplary time evolution of a three-cluster configuration under GKL shown in Figure 4.7 (a): The emerging patterns are different for the left and right boundaries of clusters. This cannot be interpreted in terms of syndromes because on this level both boundaries are indistinguishable and hence must give rise to the same pattern.

Note that most elementary CAs (one-dimensional binary CAs with radius $R = 1$) violate self-duality as well, and the few that do not are unsuited for (approximate) density classification [349]. Most generalizations capable of exact density classification are not self-dual either [344, 345, 350] and/or reformulate the task such that a solution is no longer applicable as Majorana chain decoder [344, 350].

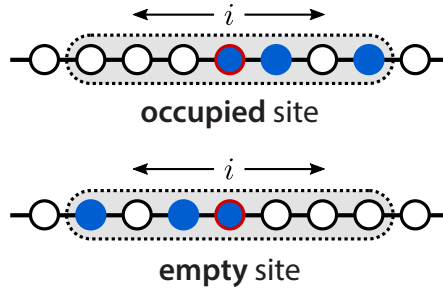
There are stochastic generalizations of density classifiers, some of which *are* self-dual [341, 342] and some of which are not [343]. However, we prefer *deterministic* CAs due to their simpler realization in terms of elementary logic gates. We therefore resort to the less known “two-line voting” automaton (TLV) introduced by Toom [327]. Originally, it is defined on the extended state space $(\mathbb{F}_2 \times \mathbb{F}_2)^{\mathcal{L}}$ describing two parallel binary chains (“two lines”) and defined by the transition rule

$$\text{TLV}_{i,\alpha}(\mathbf{x}) \equiv \begin{cases} \text{maj}[x_i^{-1}, x_{i-1}^{+1}, x_{i-2}^{+1}] & \text{for } \alpha = +1, \\ \text{maj}[x_i^{+1}, x_{i+1}^{-1}, x_{i+2}^{-1}] & \text{for } \alpha = -1, \end{cases} \quad 4.58$$

depicted in Figure 4.6 (b). In x_i^α , the index $i = 1, \dots, L$ denotes the position along the chains while $\alpha = \pm 1$ selects the subchain (up or down).

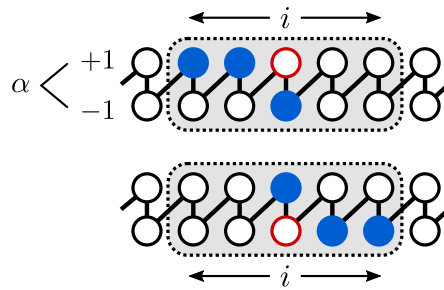
ERROR CORRECTION WITH CELLULAR AUTOMATA

(a) GKL



(b) TLV (two-line)

$$\circ = \text{maj}\{\bullet \bullet \bullet\}$$



(c) TLV (stretched)

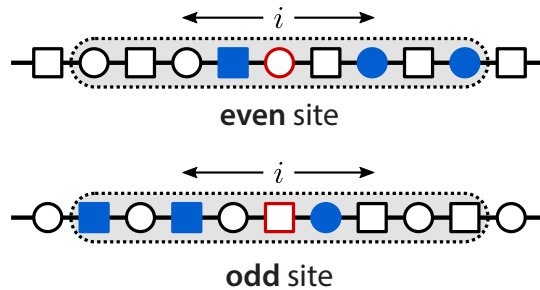
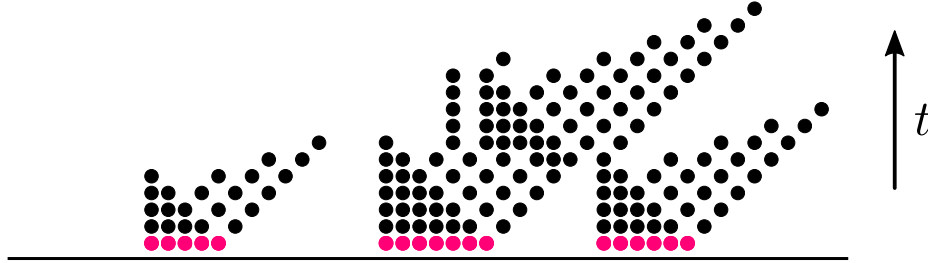


FIGURE 4.6 • Two classical density classifiers. (a) The famous Gács-Kurdyumov-Levin (GKL) CA features $R = 3$ rules with a state-dependent choice for local majority voting. (b) The two-line voting (TLV) CA can be considered a symmetrized version of GKL that gets rid of the state-dependent majority vote by adding an additional bit per site. (c) In our case, the stretched version of TLV is more intuitive: Instead of adding new states, one adds new sites with different transition rules for even and odd positions.

(a) Example: GKL



(b) Example: TLV (stretched)

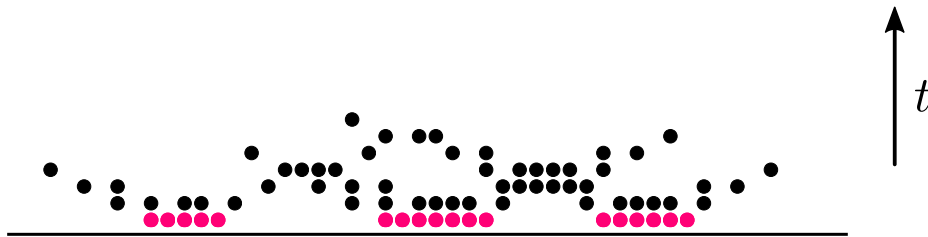


FIGURE 4.7 • Exemplary time evolution. (a) Example evolution of a three-cluster state (red) under GKL transitions (time runs upwards). (b) Decoding of the same initial state under TLV transitions. Note the different messaging behavior of GKL (asymmetric) and TLV (symmetric).

The payoff of this more complicated geometry is the sought-after self-duality which is easily checked to hold,

$$(\text{TLV}_{\mathcal{L}}(\mathbf{x}))^c = \text{TLV}_{\mathcal{L}}(\mathbf{x}^c), \quad 4.59$$

due to the new *independence* of the evaluated sites in the local majority vote on the state of site i (as compared to GKL).

For our purpose, it is more convenient to rewrite TLV in its “stretched” form [Figure 4.6 (c)] with state space $\mathbb{F}_2^{\mathcal{L}}$ and state-state representation

$$x'_i = \text{TLV}_i(\mathbf{x}) \equiv \begin{cases} \text{maj}[x_{i-1}, x_{i+2}, x_{i+4}] & \text{for } i \text{ even,} \\ \text{maj}[x_{i+1}, x_{i-2}, x_{i-4}] & \text{for } i \text{ odd,} \end{cases} \quad 4.60$$

for even and odd sites i . Figure 4.7 (b) depicts the evolution of the same three-cluster configuration as in (a). In contrast to GKL, left and right boundaries spawn symmetric patterns that eventually annihilate (initially, the majority of cells was white).

Despite the rather abstract rules (4.60), the spatio-temporal visualization reveals the simple functional principle of TLV [see Figure 4.7 (b) and also Figure 4.17 (a) below]: Domain walls emit “slow signals” of the form $\dots 010101 \dots$ *symmetrically* in both directions, seeking for nearby domain walls to pair with. When two counterpropagating slow signals meet, they transmute into “fast signals” that head back and delete the 01-markers along the way. Since the velocity of the fast signal is twice that of the other slow signal traveling into the same direction, the latter is overtaken by the returning fast signal eventually. As a result, TLV fills the gaps between the pairs of domain walls which are closest; if errors are sparse, this implies convergence to the uniform state $\text{maj}[\mathbf{x}(0)]$.

We can now apply Lemma 4.1 to construct the syndrome-delta representation. Namely,

$$\begin{aligned} \Delta_i &= \partial \text{TLV}_i(\mathbf{s}) \\ &= \text{maj} \left[s_{i \mp \frac{1}{2}}, s_{i \pm \frac{1}{2}} \oplus s_{i \pm \frac{3}{2}}, s_{i \pm \frac{1}{2}} \oplus s_{i \pm \frac{3}{2}} \oplus s_{i \pm \frac{5}{2}} \oplus s_{i \pm \frac{7}{2}} \right] \end{aligned} \quad 4.61$$

and $s'_{i+\frac{1}{2}} = s_{i+\frac{1}{2}} \oplus (\Delta_i \oplus \Delta_{i+1})$; here the upper (lower) signs correspond to i even (odd).

This describes the action of TLV completely in the quantum mechanically more suitable language of syndromes \mathbf{s} (obtained by measurements) and deltas $\mathbf{\Delta}$ (applicable by local operations). Due to the equivalence of both representations, we can (and will) still use the “common” state-state representation (4.60) to discuss the properties of TLV. The implementation, however, requires Eq. (4.61) as a concession to the “quantum handicap.”

Eroder Property

Both GKL and TLV can be shown to share a property which is known to be responsible for their superior performance as approximate density classifier [328]. Clearly, the uniform (syndrome-free) configurations $\mathbf{0}$ and $\mathbf{1}$ are fixed points (a necessary condition for density classifiers). What distinguishes them from most other CAs with these fixed points is the structure of the attractors $A_{\mathbf{0}}$ and $A_{\mathbf{1}}$, i.e., the perturbed states which are drawn towards the uniform fixed points: Every *finite* perturbation of diameter l on an infinite uniform background of zeros or ones is eroded after a time $t_{\text{dec}} \leq m l$ where $m \in \mathbb{R}^+$ is a CA-specific constant. Therefore GKL and TLV are called *linear eroders*—a crucial property for their use as approximate density classifiers (see below) and responsible for their stability close to the uniform fixed points. The time evolutions in Figure 4.7 (a) and (b) are examples for the erosion of finite perturbations of ones (red/black) on a background of zeros (white).

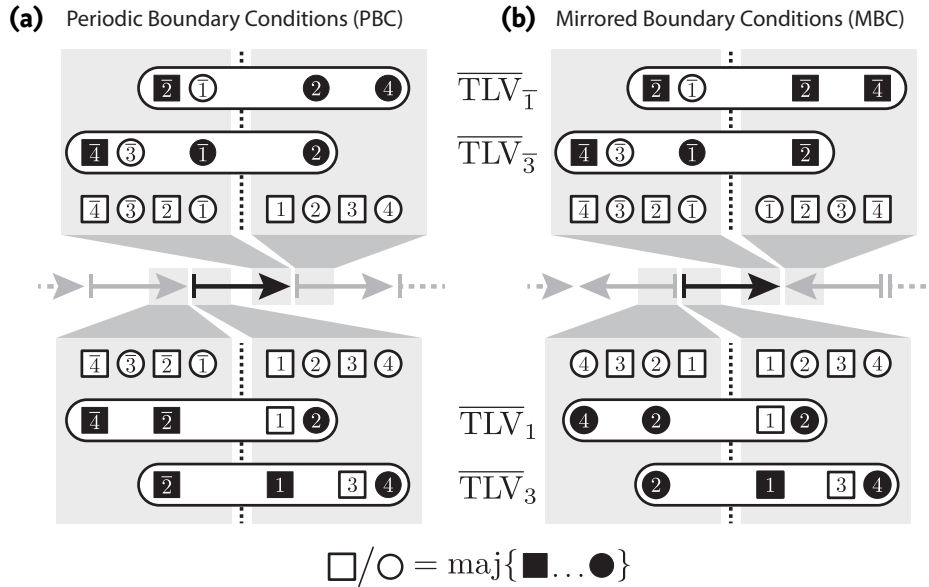


FIGURE 4.8 • Boundary conditions—Definition. (a) Periodic boundary conditions (PBC). A finite system of length L (black arrow) is copied and chained without inverting the direction. Four local rules traverse the boundary and are modified accordingly. (b) Mirrored boundary conditions (MBC). Here every other copy is reversed, giving rise to a finite system bounded by two mirrors with modified rules $\overline{\text{TLV}}_x$.

4.3.3 Boundary Conditions

Often CAs are studied in the limit of infinite system size with state space $\mathbb{F}_2^{\mathbb{Z}}$. However, we employ the CA for physical means which requires finite systems. Finiteness, in turn, entails a choice of boundary conditions and complicates the analysis due to finite-size effects. Periodic boundary conditions (PBC) are common as they mimic the infinite case as closely as possible [see Figure 4.8 (a)]: Translational invariant CAs on \mathbb{Z} remain translational invariant on a finite system with PBC and no modification of the rules is necessary.

Again, due to physical constraints we cannot use periodic boundaries: It is crucial that the quantum subsystem is an *open* chain with spatially separated endpoints (edge modes). Thus we are forced to modify TLV close to the endpoints to comply with open boundary conditions. Modifying the rather complicated rules of TLV can go amiss easily. It is therefore helpful to specify our goal: Since the edges of the quantum chain carry edge modes, they can host endpoints of error strings which do not show up in the syndrome, see Eq. (4.11); physically, this corresponds to a quasiparticle in the delocalized edge mode. It is therefore crucial that solitary quasiparticles close to the edges are transferred into the corresponding

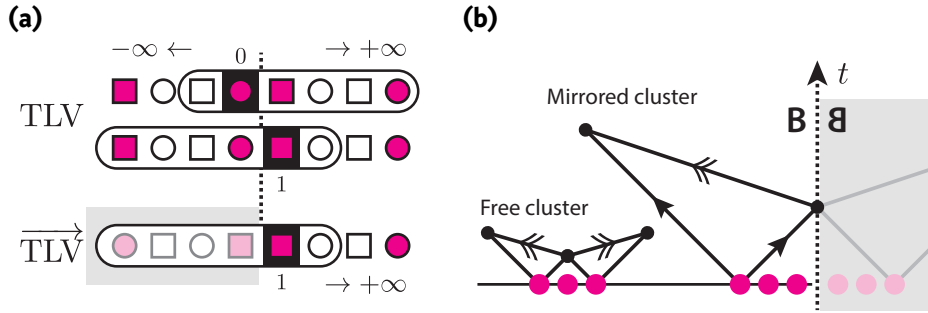


FIGURE 4.9 • Boundary conditions—Effects. (a) An unmodified TLV operating on an infinite chain and restricted to bond-inversion symmetric states (magenta/white sites for $x_i = 1/0$) is equivalent to a modified $\overrightarrow{\text{TLV}}$ operating on a semi-infinite chain with MBC on the edge. This is a consequence of the bond-inversion symmetry of the unmodified TLV rules. (b) A finite cluster of errors can be effectively doubled in size if it is close to the mirror. Consequently, correction times close to the mirror can be longer than for a free cluster of the same size.

edge mode. Thus we have to modify TLV so that syndromes are attracted by the edges (which do not emit signals themselves), while preserving self-duality and the eroder property (in a modified sense, see below and \S Section 4.C).

A neat trick to come up with the correct modifications is to put the finite chain in a “cavity,” between two imaginary mirrors placed left (right) of the first (last) site, see Figure 4.8 (b). Rules which traverse the edges use the mirrored cells to compute their local update. Formally this is achieved by redefining these rules to use the corresponding “real” cells of the system (note that this is a *local* modification for a stretched open chain, in contrast to periodic boundaries); we call this *mirrored boundary conditions* (MBC). If we denote the finite-size version of TLV on $\mathcal{L} = \{1, \dots, L\}$ with mirrored boundary conditions as $\overrightarrow{\text{TLV}}$, the modified rules on the left edge read

$$\overrightarrow{\text{TLV}}_1(\mathbf{x}) = \text{maj}[x_2, x_2, x_4] \quad 4.62a$$

$$\overrightarrow{\text{TLV}}_3(\mathbf{x}) = \text{maj}[x_4, x_1, x_2] \quad 4.62b$$

and on the right edge (L even)

$$\overrightarrow{\text{TLV}}_{\bar{1}}(\mathbf{x}) = \text{maj}[x_{\bar{2}}, x_{\bar{2}}, x_{\bar{4}}] \quad 4.63a$$

$$\overrightarrow{\text{TLV}}_{\bar{3}}(\mathbf{x}) = \text{maj}[x_{\bar{4}}, x_{\bar{1}}, x_{\bar{2}}], \quad 4.63b$$

where we used the shorthand notation $\bar{k} \equiv L + 1 - k$ to index cells from the end of the chain (e.g., $\bar{1} = L$), see Figure 4.8 (b). For all other sites it is $\overrightarrow{\text{TLV}}_i = \text{TLV}_i$.

Clearly, $\mathbf{0}$ and $\mathbf{1}$ are still fixed points of $\overrightarrow{\text{TLV}}$ (there are no static signal sources introduced) and self-duality is also preserved. By construction, a slow signal emitted from a solitary syndrome close to the edge will meet its mirror image at the edge which sends it back as a fast signal to capture the other slow signal heading into the

bulk and thereby initiates pairing towards the edge, see Figure 4.9 (b). Note that this mechanism affects the time needed to erode a contiguous cluster of errors: Adjacent (or close) to the mirror, the number of errors is “doubled” artificially; correction time and affected territory double accordingly. In Figure 4.9 (b) we illustrate this effect by comparing the same cluster far away and close to the edge.

An important observation allows for the analysis of systems with mirrored boundary conditions in terms of the unmodified rules (on the infinite chain $\mathcal{L} = \mathbb{Z}$): Let $\mathbf{x} \in \mathbb{F}_2^{\mathbb{Z}}$ be an arbitrary state and define the bond-centered inversion \mathfrak{S}_s as

$$(\mathfrak{S}_s \mathbf{x})_i \equiv x_{2s-i+1}. \quad 4.64$$

$\mathfrak{S}_s \mathbf{x}$ describes the configuration that is obtained by inversion of \mathbf{x} at the bond $(s, s + 1)$. We define the set of invariant configurations,

$$\mathcal{K}_s \equiv \{ \mathbf{x} \in \mathbb{F}_2^{\mathbb{Z}} \mid \mathfrak{S}_s \mathbf{x} = \mathbf{x} \} \quad 4.65$$

and argue that \mathfrak{S}_s is a symmetry of TLV for any $s \in \mathbb{Z}$, namely

$$\text{TLV}_{\mathcal{L}}(\mathfrak{S}_s \mathbf{x}) = \mathfrak{S}_s \text{TLV}_{\mathcal{L}}(\mathbf{x}). \quad 4.66$$

Indeed, this follows from the fact that TLV_i is related to TLV_{i+1} by a bond-centered inversion at $(i, i + 1)$; this is true for both even and odd sites i , see Figure 4.6 (c). It follows that $\mathcal{K}_s \subset \mathbb{F}_2^{\mathbb{Z}}$ is invariant under the evolution of TLV which hence can be restricted to \mathcal{K}_s . Note that this is a special feature of TLV, in contrast to GKL, for instance. Without loss of generality, we set $s = 0$ in the following, i.e., $(\mathfrak{S}_0 \mathbf{x})_i = x_{1-i}$. Then we can describe a semi-infinite chain on $\mathcal{L} = \mathbb{N}$ with a single mirrored boundary (we write $\overrightarrow{\text{TLV}}$) by the unmodified rules of TLV operating on the infinite chain $\mathcal{L} = \mathbb{Z}$ if we restrict the state space to \mathcal{K}_0 . Indeed,

$$\overrightarrow{\text{TLV}}_1(\mathbf{x}) = \text{maj}[x_2, x_2, x_4] = \text{maj}[x_2, x_{-1}, x_{-3}] = \text{TLV}_1(\mathbf{x}) \quad 4.67a$$

$$\overrightarrow{\text{TLV}}_3(\mathbf{x}) = \text{maj}[x_4, x_1, x_2] = \text{maj}[x_4, x_1, x_{-1}] = \text{TLV}_3(\mathbf{x}) \quad 4.67b$$

where we used $x_4 = x_{-3}$ and $x_2 = x_{-1}$ for $\mathbf{x} \in \mathcal{K}_0$; see Figure 4.9 (a) for an example. This allows us to trade the rule modifications of $\overrightarrow{\text{TLV}}$ for a restriction on the state space of TLV which, in turn, simplifies the analysis of the *finite* version $\overline{\text{TLV}}$ (see below). As an immediate consequence, it follows that the semi-infinite $\overrightarrow{\text{TLV}}$ is an eroder because TLV is one¹³⁶.

While the previously introduced definition of eroders carries over to semi-infinite chains, it cannot be applied to *finite* systems because there is no longer a qualitative difference between perturbation and background (both of which are necessarily finite). A possible finite-size modification reads as follows: A cellular automaton on a finite chain $\mathcal{L} = \{1, \dots, L\}$ is a finite-size linear eroder if there exist real constants $0 < a < 1$ and $m \in \mathbb{R}^+$ such that for any size $L < \infty$ and any

¹³⁶Note that mirrored finite perturbations remain finite.

finite perturbation of $\mathbf{0}$ ($\mathbf{1}$) with diameter $l \leq aL$, the unperturbed state $\mathbf{0}$ ($\mathbf{1}$) is recovered at $t_{\text{dec}} \leq ml$. It is easy to check that $\overrightarrow{\text{TLV}}$ is an eroder in this sense if one uses that $\overrightarrow{\text{TLV}}$ is an eroder in the original sense (see \clubsuit Section 4.C). Alternatively, note that the majority function is *monotonic*, i.e., changing an input bit from 0 to 1 *cannot* change the output bit from 1 to 0. Therefore the evolution of a generic, non-contiguous, finite cluster of errors under $\text{TLV}/\overrightarrow{\text{TLV}}/\overline{\text{TLV}}$ can be constructed from the evolution of a contiguous cluster of the same size by erasing errors in the spacetime diagram, and it is sufficient to consider contiguous intervals of errors to check for the eroder property (which is straightforward to verify).

4.4 Decoding with a Self-Dual Density Classifier

In the previous section, we introduced $\overline{\text{TLV}}$ and argued that it is a self-dual, finite-size linear eroder. These properties make $\overline{\text{TLV}}$ a promising candidate for decoding errors $E(x)$ that are small compared to L and/or *sparse* enough. In the following, we assess the decoding performance of $\overline{\text{TLV}}$ by numerical and analytical means. We show that error patterns for which the erosion (viz. decoding) fails are rare for reasonably small error rates, and that the time t_{dec} required for decoding scales sublinearly with the chain length—one of the main benefits of locality.

4.4.1 Numerical Results

We start with a qualitative discussion of possible evolutions under $\overline{\text{TLV}}$: Apart from the two stable uniform fixed points $\mathbf{0}$ and $\mathbf{1}$, there are four additional (unstable) fixed points for TLV [327] two of which cannot be realized by $\overline{\text{TLV}}$ on finite chains with MBC (see \clubsuit Section 4.D). This leads to the four possible fixed points depicted in Figure 4.10 (a) and (b). Note that their realization on finite chains with MBC (vertical lines) is only possible if their realization on $\mathcal{L} = \mathbb{Z}$ is consistent with the boundary conditions given by the mirrors. Whereas the uniform fixed points survive, independent of the bond where the mirror is placed [Figure 4.10 (a)], the two additional fixed points can only be realized if the leftmost (rightmost) site is denoted by an even (odd) index [Figure 4.10 (b)]. Henceforth, we will take the first index to be odd (i.e., $i = 1$) and the last to be even (i.e., L), which eliminates these two additional fixed points. Note that this choice coincides with the default labeling of sites $\mathcal{L} = \{1, \dots, L\}$. We stress that the elimination of the two additional fixed points (which are not syndrome-free) is not crucial for the performance of the decoder: First, both are characterized by a density of set bits $\rho = 0.5$ which is

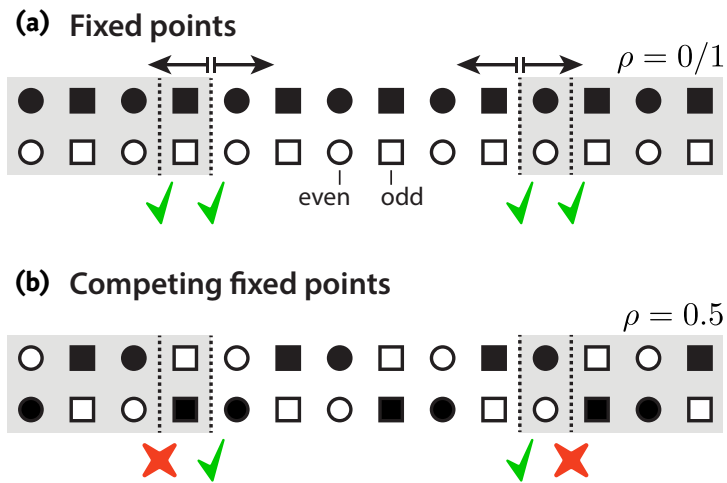


FIGURE 4.10 • Properties of $\overline{\text{TLV}}$ —Fixed points. (a) The uniform fixed points of $\overline{\text{TLV}}$ with minimum/maximum filling $\rho = 0/1$ correspond to the syndrome-free states of the quantum code. The eroder property makes them stable in that (small enough) perturbations are erased and do not proliferate. (b) Two of four additional fixed points of TLV are inherited by $\overline{\text{TLV}}$ if the leftmost/rightmost site are labeled by even/odd indices (check marks). Those are characterized by a critical filling $\rho = 0.5$.

far from the relevant error densities realistic for small p_0^X . Second, simulations suggest that their attractors are trivial, i.e., contain only the fixed points themselves (* Section 4.D).

However, there are competing cycles of various lengths and with non-trivial attractors; three examples are shown in Figure 4.11. The longer a cycle and the larger its attractor, the more probable it is with respect to Bernoulli noise. This explains why the largest cycle in Figure 4.11 is by far the most common in simulations. Note that it also illustrates the MBC nicely by “bouncing” a cluster of errors hence and forth between the two mirrors. Again, these cycles are characterized by densities ρ close to criticality, which renders them rare for $p_0^X \ll \frac{1}{2}$. In Figure 4.12 we sketch the attractor landscape of the total state space ordered by the density ρ : Close to the extreme densities $\rho = 0/1$ every configuration is drawn towards the corresponding uniform fixed point due to the eroder property. This is where $\overline{\text{TLV}}$ implements effectively majority voting by local rules and therefore becomes a viable replacement for the global decoder Δ . Only close to criticality $\rho \approx 0.5$, $\overline{\text{TLV}}$ fails to decode a (still small) fraction of error patterns by evolving them into cycles instead of cleaning them according to a global majority vote. This underpins our previous statement that the impossibility of realizing global majority voting perfectly is not too much of an issue if it fails in regions of the state space which are exponentially suppressed by Bernoulli noise for physically realistic error rates.

ERROR CORRECTION WITH CELLULAR AUTOMATA

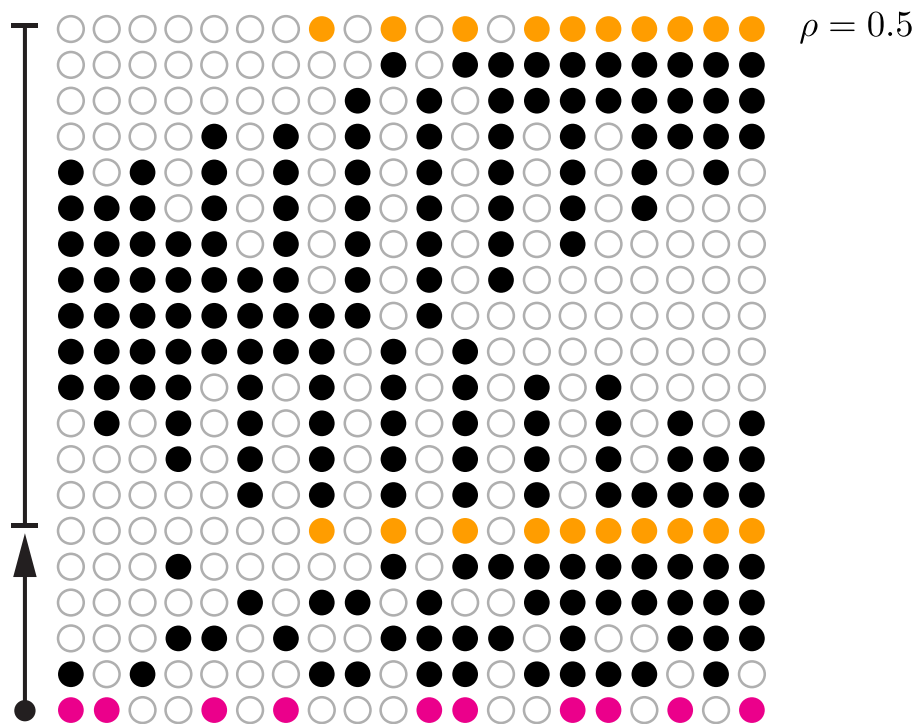
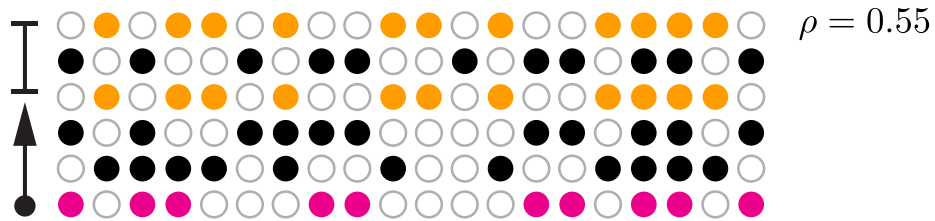
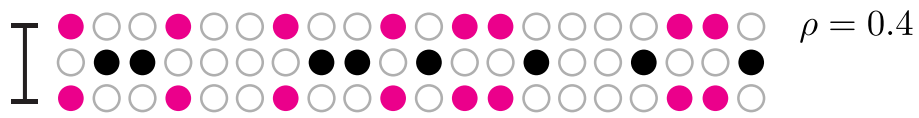


FIGURE 4.11 • Properties of \overline{TLV} —Cycles. Three examples of random initial configurations (magenta) which relaxed into cycles of various lengths. The first recurring configurations are highlighted with the same color to separate the cycle from the relaxation path. We find only cycles close to criticality with $\rho \approx 0.5$.

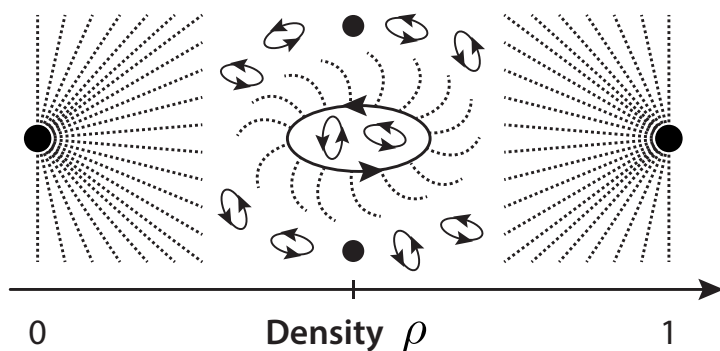


FIGURE 4.12 • Properties of $\overline{\text{TLV}}$ —Attractor landscape. Sketch of the state space with dashed attractor paths, based on the results in Figure 4.10 and Figure 4.11. The two uniform fixed points are attractors of all states away from criticality; this motivates the application of $\overline{\text{TLV}}$ as decoder for the MCQC.

In the remainder of this subsection, we will quantify these statements by sampling error patterns from a Bernoulli distribution with fixed rate p_0^x and evolving them with $\overline{\text{TLV}}$ until we can decide whether it reached a fixed point or entered a cycle. We interpret the empty state $\mathbf{0}$ as error-free and define the probability of successful decoding as

$$P_{\text{dec}}^{\checkmark} \equiv \Pr \left(\left\{ \mathbf{x} \in \mathbb{F}_2^{\mathcal{L}} \mid \lim_{t \rightarrow \infty} \overline{\text{TLV}}_{\mathcal{L}}^t(\mathbf{x}) = \mathbf{0} \right\} \right). \quad 4.68$$

We stress that in addition to $\lim_{t \rightarrow \infty} \overline{\text{TLV}}_{\mathcal{L}}^t(\mathbf{x}) = \mathbf{1}$, and in contrast to the global decoder Δ , $\overline{\text{TLV}}$ can also fail by evolving into cycles which are not syndrome-free. *Both* cases make up for the failed decodings of $\overline{\text{TLV}}$ and are measured by the probability $P_{\text{dec}}^x = 1 - P_{\text{dec}}^{\checkmark}$. As a consequence, $P_{\text{dec}}^x > \frac{1}{2}$ is possible for $\overline{\text{TLV}}$ even for $p_0^x \leq \frac{1}{2}$.

In Figure 4.13 (a) we plot estimates for P_{dec}^x as function of the system size for various error rates $0 < p_0^x \leq 0.5$. Except for the critical value $p_0^x = 0.5$, the probability of unsuccessful decoding vanishes exponentially with the chain length L , confirming our hope that $\overline{\text{TLV}}$ is a viable replacement for Δ . Note that this result already tells us that the measure of all attractors of cycles vanishes quickly for $L \rightarrow \infty$. Indeed, in Figure 4.13 (b) we plot the probability of an error pattern to belong to the attractor of a non-trivial cycle, again as function of L for the same error rates as in (a): For $p_0^x < 0.5$ and $L \gtrsim 50$, there seems to be an exponential decay which is in accordance with the results in (a). Whether at criticality $p_0^x = 0.5$ the probability vanishes or saturates at a small but non-zero value cannot be inferred from (b). Interestingly, the results so far not only support the hope that $\overline{\text{TLV}}$ can replace Δ for $p_0^x \leq p_c^x$ with a non-trivial critical rate $0 < p_c^x < \frac{1}{2}$, but even suggest that $p_c^x = \frac{1}{2}$ is still optimal (at least $0.4 \lesssim p_c^x$).

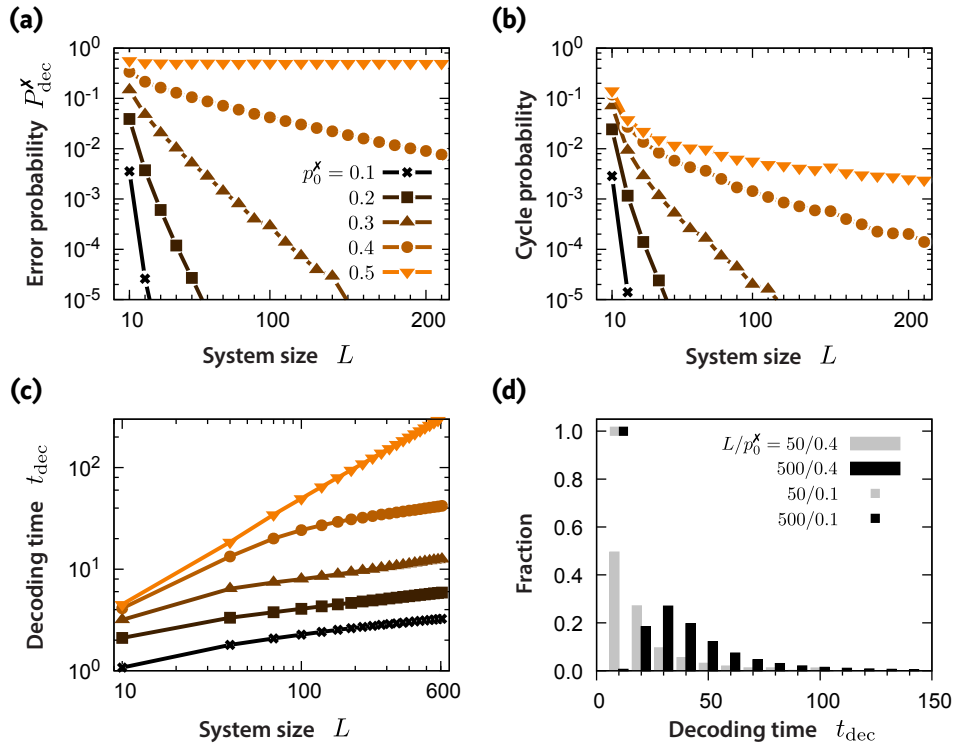


FIGURE 4.13 • Properties of $\overline{\text{TLV}}$ —Numerics. (a) Numerical results for the probability of erroneous decoding $P_{\text{dec}}^x = 1 - P_{\text{dec}}^{\checkmark}$ vs. chain length L for different microscopic error probabilities p_0^x . P_{dec}^x vanishes exponentially in the thermodynamic limit for any $p_0^x < 0.5$. (b) Away from criticality (presumably for $p_0^x < 0.5$) the probability to relax into a cycle vanishes exponentially. For realistic error rates ($p_0^x \leq 0.1$), cycles cannot be observed in reasonable sample sizes. (c) Averaged time needed to reach a uniform fixed point (t_{dec}) as a function of the system size L for various error rates p_0^x . The growth is remarkably slow but unbounded for $p_0^x > 0$. Whether t_{dec} grows algebraically or only logarithmically for small $p_0^x > 0$ cannot be inferred from these results. (d) Distributions of the decoding times t_{dec} for two error rates $p_0^x = 0.1/0.4$ and system sizes $L = 50/500$. For $p_0^x = 0.1$, there is barely any difference between $L = 50$ and $L = 500$ visible (squares). We sampled 10^6 random initial states for each data point in (a-d).

Now that we know that the decoding probability of $\overline{\text{TLV}}$ approaches 1 exponentially with $L \rightarrow \infty$ comes a crucial question we shunned so far: How many steps t_{dec} does $\overline{\text{TLV}}$ need, on average, to evolve an error pattern x into the error-free state $\mathbf{0}$? If the decoding time scaled linear, $t_{\text{dec}} \sim L$, there would be barely any benefit from replacing the global decoder Δ by the local one. Fortunately, Figure 4.13 (c) reveals that the average decoding time grows linearly *only* at criticality whereas the growth for $p_0^x < 0.5$ is much slower. E.g., for $L = 600$ and $p_0^x = 0.1$ on average only $t_{\text{dec}} \approx 3$ steps are necessary to eliminate all errors correctly. We stress that due to the almost vanishing slope in (c) it is not possible to decide whether $t_{\text{dec}} \propto L^\kappa$ for $0 < \kappa \ll 1$ or $t_{\text{dec}} \sim \log L$, even though the very fact that t_{dec} grows so slowly hints at a logarithmic scaling. To describe the required decoding times in

detail, we show the complete probability distribution in Figure 4.13 (d) for two sizes $L = 50/500$ and error rates $p_0^X = 0.1/0.4$ in bins of $\Delta t_{\text{dec}} = 10$. Most strikingly, for the lower error rate ($p_0^X = 0.1$) there is no difference between $L = 50$ and a chain of the tenfold length; again a manifestation of the extremely slow growth of t_{dec} for reasonable error rates.

4.4.2 Rigorous Analytical Results

In this subsection, we prove a central statement of this chapter: The probability for $\overline{\text{TLV}}$ on a chain of length L with MBC to be in a non-empty state $\mathbf{x}(t) \neq \mathbf{0}$ after $t \propto L^\kappa$ time steps vanishes exponentially with L for arbitrary $\kappa > 0$ if the initial state $\mathbf{x}(0)$ is a Bernoulli random configuration with single-site error probability $p_0^X < p_c^X$ for some critical value $0 < p_c^X \leq \frac{1}{2}$. In Section 4.5 we will use this result to construct a completely local decoder for the Majorana chain with length L and depth $\propto L^\kappa$ that stabilizes a logical qubit for times that grow exponentially with L . Furthermore, it confirms the numerical results of Subsection 4.4.1: Neither competing fixed points nor cycles threaten the performance of $\overline{\text{TLV}}$ as long as p_0^X is small enough. To prove the claimed result, we follow the lines of [351] with modifications to account for the finiteness of $\overline{\text{TLV}}$ and the mirrored boundaries. In the following, we present three crucial steps but provide only brief sketches of their proofs; the details are presented in \clubsuit Section 4.E.

Before we can state our first result, we have to introduce the pivotal concepts of *independence* and *sparseness* [318, 335, 336, 351, 352]. Let $\mathbf{x} \subseteq \mathbb{Z}$ be an arbitrary subset (error pattern). A finite subset $I \subseteq \mathbf{x}$ is called *cluster* of diameter $\|I\| = \max\{|x - y| \mid x, y \in I\}$. If we fix an integer $k > 0$ (the *sparseness parameter*, to be chosen later), the *territory* $T_k(I)$ is defined as the interval of integers with distance at most $k\|I\|$ from I . Two clusters I_1 and I_2 are called *independent* if at least one does not intersect the territory of the other, i.e., $I_2 \cap T_k(I_1) = \emptyset$ or $I_1 \cap T_k(I_2) = \emptyset$ (or both); since $I \subset T_k(I)$, this implies $I_1 \cap I_2 = \emptyset$. This concept is illustrated in the lower part of Figure 4.14. If, in addition, there exists a partition of \mathbf{x} into a family $\mathcal{J} = \{I_a\}$ of pairwise independent clusters I_a , $\mathbf{x} = \bigcup_a I_a$, then \mathbf{x} is called *sparse*.

We need some additional terminology: First, $\mathcal{J}_{\leq l}$ denotes the family of clusters $I \in \mathcal{J}$ with diameter $\|I\| \leq l$ and $\mathbf{x} \setminus \mathcal{J}_{\leq l} \equiv \mathbf{x} \setminus \bigcup_{I \in \mathcal{J}_{\leq l}} I$ is the subset of sites for given \mathbf{x} that remains after cleaning all independent clusters of diameter at most l . Second, a (*infinite*) *mirrored* Bernoulli random configuration $\mathbf{x} \subseteq \mathbb{Z}$ is defined by the single-site probability $\Pr(x_i = 1) = p_0^X$ for sites $i > 0$ and the mirror constraint $x_i = x_{1-i}$ [recall Eq. (4.65)].

We can now state our variation of the main result of Ref. [351]:

PROPOSITION 4.1: Cluster decomposition on infinite chains

Consider infinite mirrored Bernoulli random configurations \mathbf{x} with single-site probability p_0^x . Let $k \in \mathbb{N}$ be a given sparseness parameter.

Then, for each instance \mathbf{x} , there exists a constructive family \mathcal{I}^x of pairwise independent clusters¹³⁷ such that the probability of a site $i \in \mathbb{Z}$ to be in \mathbf{x} and remain uncovered by independent clusters of diameter l or less (write $\mathcal{I}_{\leq l}^x$) is bounded from above by

$$\Pr(i \in \mathbf{x} \setminus \mathcal{I}_{\leq l}^x) \leq \alpha^{l^\beta} \tag{4.69}$$

for $\beta = \ln(2)/\ln(4k + 3)$ (and therefore $0 < \beta < 1$) and $\alpha = (2k)(4k + 3)\sqrt{p_0^x}$. If we define the critical value

$$\tilde{p}_c^x \equiv [(2k)(4k + 3)]^{-2}, \tag{4.70}$$

for $p_0^x < \tilde{p}_c^x$ it is $\alpha < 1$ and Eq. (4.69) becomes an exponentially decaying upper bound.

The proof can be divided roughly into three steps: First, the family \mathcal{I}^x is constructed recursively in the cluster diameter l for a given instance \mathbf{x} . In a second step it is shown that this prescription always yields a family of pairwise independent clusters. In the crucial third step, an upper bound on the probability for a site $i \in \mathbf{x}$ to be *not* covered by a cluster in \mathcal{I}^x of diameter l or less is derived. To do this, one constructs so called *explanation trees*, hypothetical error patterns that explain why a given site i could survive the construction of \mathcal{I}^x without being covered by clusters up to diameter l . The probability for its survival is then estimated by finding an upper bound on the number of possible explanation trees and calculating their probability with respect to a mirrored Bernoulli distribution. One finds that the number of explanation trees *grows* exponentially (with cluster diameter l) while the probability for a single explanation tree to be realized by a Bernoulli process *vanishes* exponentially. The latter factor dominates for $p_0^x < \tilde{p}_c^x$ so that the probability for the existence of at least one explanation tree vanishes exponentially for increasing l ; this leads to Eq. (4.69).

The rationale behind TLV (or any other linear eroder) is the following: For an error to survive the erosion process, there must be other errors nearby that protect it; and these, in turn, require further errors in *their* neighborhood to survive and so forth. Such a structure of errors that protect each other from being eroded constitutes an explanation tree which prevents a global error pattern from decaying into independent clusters. Explanation trees are *dense* in a very specific sense—and this denseness renders their existence improbable for low error rates. By contrast, *sparse* error patterns are those without explanation trees that span the whole system.

¹³⁷It is not necessarily $\mathbf{x} = \bigcup_{I \in \mathcal{I}^x} I$, i.e., \mathbf{x} does not have to be sparse.

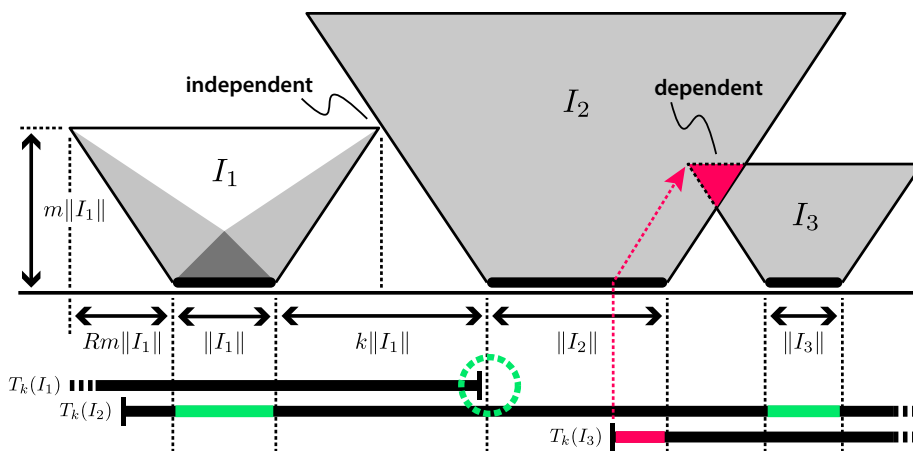


FIGURE 4.14 • Independent clusters. A pattern of three clusters I_i ($i = 1, 2, 3$) with $\|I_3\| < \|I_1\| < \|I_2\|$. The erosion process of TLV is sketched for I_1 whereas for I_2 and I_3 only the causal patches that cover the erosion are shaded gray (time runs upwards). For a linear eroder, the erasure of an independent cluster requires at most $m\|I_i\|$ time steps, the height of the shown trapezoids. During this time, signals can travel at most $Rm\|I_i\|$ sites from the boundary of a cluster I_i . Clusters that are *independent* with sparseness parameter $k = 2Rm$ do not interact; this is true for I_1 and I_2 since $I_2 \cap T_k(I_1) = \emptyset$ (dashed circle). Note that $I_{1,3} \cap T_k(I_2) \neq \emptyset$ (green intervals) has no effect on their (in-)dependence because $\|I_2\| \geq \|I_1\|, \|I_3\|$. By contrast, since $I_2 \cap T_k(I_3) \neq \emptyset$ (red interval), the causal trapezoids of I_2 and I_3 intersect (red triangle). Thus, I_2 and I_3 are *dependent* and may not be erased separately.

They are initial states of linear eroders such that the causal regions of correlated sites in the spacetime diagram do not percolate through the system, but instead separate into many local patches which are eroded independently. The initial seeds of these patches are the independent clusters from above: Linear eroders clean a single cluster I after at most $m\|I\|$ time steps, and can therefore influence only sites with maximum distance $Rm\|I\|$ from I . Then, a collection of pairwise independent clusters is eroded *independently* if the sparseness parameter is set to $k = 2Rm$, see Figure 4.14. It is this causal locality on sparse sets which results in the sublinear scaling of decoding times for TLV [recall Figure 4.13 (c)].

Eventually we want to use Proposition 4.1 to derive an upper bound for the probability of errors to survive the first t steps of $\overline{\text{TLV}}$ on a *finite* chain with mirrored boundaries. To this end, we first need an intermediate step:

LEMMA 4.2: Cleaning of semi-infinite chains

Consider a semi-infinite chain on $\mathcal{L} = \mathbb{N}$ governed by $\overrightarrow{\text{TLV}}_{\mathcal{X}}$ with initial configurations $\mathbf{x}(0) \subseteq \mathcal{L}$ drawn from a Bernoulli distribution with parameter $p_0^{\mathbf{x}}$. Let $\mathcal{J} \subset \mathcal{L}$ be an arbitrary finite interval on the chain.

Then the probability of $\mathbf{x}(t) = \overrightarrow{\text{TLV}}_x^t(\mathbf{x}(0))$ to be non-empty on \mathcal{J} is bounded from above by

$$\Pr(\mathbf{x}(t) \cap \mathcal{J} \neq \emptyset) \leq (2tR + |\mathcal{J}|) \exp\left(-\gamma \lfloor t/m \rfloor^\beta\right) \quad 4.71$$

with $\gamma = -\log(\alpha)$ ($\gamma > 0$ for $p_0^x < \tilde{p}_c^x$), and $0 < \beta < 1$ as in Proposition 4.1. Here the sparseness parameter is given by $k = 2Rm = 8$ where $m = 1$ and $R = 4$ are the eroder parameter and the radius of TLV, respectively. $\lfloor x \rfloor$ denotes the greatest integer less than or equal to x .

The proof exploits that $\overrightarrow{\text{TLV}}$ is equivalent to TLV for symmetric states in \mathcal{K}_0 . Then Proposition 4.1 provides us with a family \mathcal{J}^x that fails to cover errors in \mathbf{x} with a probability that vanishes exponentially with increasing cluster diameter l . If an error $x_i = 1$ belongs to an independent cluster of diameter l , the linear eroder property of TLV ensures that it is eroded after at most ml time steps. It is important to realize that this does *not* imply $x_i = 0$ for all later times as signals from distant, larger clusters may enter the territory of smaller ones (e.g., I_1 and I_2 in Figure 4.14). With R the radius of local rules, the neighborhood $U_{tR}(\mathcal{J})$ includes all sites that potentially influence sites in \mathcal{J} after t time steps, i.e., sites with distance at most tR from \mathcal{J} . Therefore one has to demand that *all* sites in the growing neighborhood $U_{tR}(\mathcal{J})$ belong to clusters of maximum diameter l in \mathcal{J}^x to guarantee that \mathcal{J} is clean after $t = ml$ time steps. Subadditivity of probability measures then leads to the upper bound of Lemma 4.2 where $(2tR + |\mathcal{J}|)$ is the size of $U_{tR}(\mathcal{J})$.

With Lemma 4.2, we are now prepared to tackle the case of *finite* chains:

LEMMA 4.3: Cleaning of finite chains

Consider a finite chain of length L on $\mathcal{L} = \{1, \dots, L\}$ governed by $\overrightarrow{\text{TLV}}$ with mirrored boundaries and initial configurations $\mathbf{x}(0) \subseteq \mathcal{L}$ drawn from a Bernoulli distribution with parameter p_0^x .

Then the probability of $\mathbf{x}(t) = \overrightarrow{\text{TLV}}_x^t(\mathbf{x}(0))$ to be non-empty is bounded from above by

$$\Pr(\mathbf{x}(t) \neq \emptyset) \leq (4R \{t\} + L) \exp\left(-\gamma \lfloor \{t\}/m \rfloor^\beta\right) \quad 4.72$$

with $\{t\} \equiv \min\{t, t_L^*\}$ and $t_L^* = \lfloor L/2R \rfloor$. The parameters are the same as in Proposition 4.1 and Lemma 4.2.

Whereas the *infinite* TLV and the *semi-infinite* $\overrightarrow{\text{TLV}}$ are qualitatively similar due to the discussed equivalence on \mathcal{K}_0 , there are fundamental differences to the *finite* $\overrightarrow{\text{TLV}}$. This can be understood intuitively as follows: $\overrightarrow{\text{TLV}}$ equals TLV with pairwise correlations between mirrored sites. These pairwise correlations lead to the square in the expression for \tilde{p}_c^x (recall Proposition 4.1). By contrast, $\overrightarrow{\text{TLV}}$

introduces an *infinite* number of perfectly correlated partners for each of the L sites due to the cavity geometry¹³⁸. To avoid these complications, we use a trick: For times $t \leq t_L^* = \lfloor L/2R \rfloor$, there is no site with *both* boundaries (mirrors) in its past light cone (the site(s) closest to the center of the chain can get “aware” of the cavity geometry earliest at $t_L^* + 1$). Therefore locally the *finite* system $\overline{\text{TLV}}$ behaves exactly as the semi-infinite system $\overline{\text{TLV}}$ for $t \leq t_L^*$ and the results of Lemma 4.2 apply. For $t > t_L^*$ we can exploit the finiteness of \mathcal{L} : Recall that in the context of Lemma 4.2 we stressed that an empty interval does not necessarily remain empty on a (semi-)infinite chain because signals from outside the interval may interfere at later times. Now \mathcal{L} is finite and the argument no longer holds: if $\mathbf{x}(t) = \emptyset$ at some time t , it follows $\mathbf{x}(t') = \emptyset$ for all later times $t' > t$. Thus the probability of $\mathbf{x}(t) \neq \emptyset$ is monotonically decreasing in t . This leads to the replacement $t \rightarrow \{t\} = \min\{t, t_L^*\}$ in Lemma 4.3.

Note that the lower-bounded decay of the probability in Lemma 4.3 is to be expected for finite systems: Due to the finite state space, there is an upper bound for t (depending on L) such that the system either (1) relaxed to the clean state, (2) to a non-clean fixed point, or (3) entered a non-trivial cycle. In the first case, it is clean forever, whereas in the latter two cases, it can never become clean. Therefore the probability to be not clean cannot decrease arbitrarily and must be bounded from below for fixed L and $t \rightarrow \infty$. However, if we are interested in the limit $L \rightarrow \infty$, we can ask how long one has to wait for $\overline{\text{TLV}}$ to clean the system almost surely.

This leads to our main result:

COROLLARY 4.1: Scaling of cleaning times

Consider a finite chain of length L on $\mathcal{L} = \{1, \dots, L\}$ governed by $\overline{\text{TLV}}$ with mirrored boundaries and initial configurations $\mathbf{x}(0) \subseteq \mathcal{L}$ drawn from a Bernoulli distribution with parameter p_0^x .

For $\kappa \in \mathbb{R}$ with $0 < \kappa < 1$, the probability of $\mathbf{x}(t) = \overline{\text{TLV}}_x^t(\mathbf{x}(0))$ to be non-empty after

$$t_{\max}(L) \equiv \lfloor L^\kappa \rfloor \quad 4.73$$

time steps is bounded from above by

$$\Pr(\mathbf{x}(t_{\max}) \neq \emptyset) \leq (4R + 1)L \exp\left(-\gamma \lfloor L^\kappa / m \rfloor^\beta\right) \quad 4.74$$

for $L \geq L_R$ with $0 < L_R < \infty$ a R -dependent constant. For $p_0^x < \tilde{p}_c^x$ it follows that

$$\Pr(\mathbf{x}(t_{\max}(L)) \neq \emptyset) \rightarrow 0 \quad \text{for } L \rightarrow \infty \quad 4.75$$

exponentially fast. The parameters are the same as in Proposition 4.1 and Lemma 4.2.

¹³⁸Imagine standing in front of a single mirror vs. standing between two opposing mirrors.

To prove this, we use the result of Lemma 4.3 with $t_{\max}(L) < t_L^*$ for $L \geq L_R$ large enough, thus $\{t_{\max}(L)\} = \min\{t_{\max}(L), t_L^*\} = t_{\max}(L)$. With $\lfloor L^k \rfloor \leq L$ and $\lfloor \lfloor L^k \rfloor / m \rfloor = \lfloor L^k / m \rfloor$ (for $m \in \mathbb{N}$), Eq. (4.74) follows immediately.

The important message of Corollary 4.1 is that the probability

$$\overline{P}_{\text{dec}}^{\checkmark} \equiv \Pr \left(\left\{ \mathbf{x} \in \mathbb{F}_2^{\mathcal{L}} \mid \overline{\text{TLV}}_{\mathcal{L}}^{t_{\max}(L)}(\mathbf{x}) = \mathbf{0} \right\} \right) \quad 4.76$$

of successfully decoding a Bernoulli random configuration *with time constraint* $t_{\max}(L)$ [cf. Eq. (4.68)] approaches 1 rapidly for longer chains even if the allocated decoding time $t_{\max}(L)$ increases sublinearly—as long as $p_0^{\checkmark} < \tilde{p}_c^{\checkmark}$. We stress that there is no statement about $p_0^{\checkmark} \geq \tilde{p}_c^{\checkmark}$; Corollary 4.1 only asserts that there is a finite range for p_0^{\checkmark} where decoding with $\overline{\text{TLV}}$ is possible and that the required decoding time t_{dec} scales favorably with L on average.

To conclude this subsection, we present numerical results for $\overline{P}_{\text{dec}}^{\checkmark}$ as a function of the microscopic error probability $0.3 \leq p_0^{\checkmark} \leq 0.5$ and for different chain lengths $L = 16, \dots, 784$ in Figure 4.15. As constraints we use (a) $t_{\max} = \infty$, (b) $t_{\max} = L$, (c) $t_{\max} = L^{0.5}$, and (d) $t_{\max} = \text{const} = 20$. Instances that are not empty after $t_{\max}(L)$ time steps count as failed decodings, even if they are cleaned eventually (for $t \rightarrow \infty$). In addition, forbidden regions due to the light cone constraint (4.36) with $D = R t_{\max}(L)$ (with $R = 4$) are shaded for $L = 16$ (orange) and $L = 784$ (black). Note that for $t_{\max} = \infty$ it is $\overline{P}_{\text{dec}}^{\checkmark} = P_{\text{dec}}^{\checkmark}$, compare Eq. (4.68) and Eq. (4.76).

All numerical results satisfy the rigorous bounds of the light cone constraint which manifests as a weak upper bound for p_0^{\checkmark} close to criticality. Note the difference between (a), (b), and (c) where the light cone constraint does not rule out successful decoding for any non-critical p_0^{\checkmark} and $L \rightarrow \infty$, and (d) where it does. The rigorous results from above complete this picture by providing *lower* bounds that imply $\lim_{L \rightarrow \infty} \overline{P}_{\text{dec}}^{\checkmark} = 1$ for $p_0^{\checkmark} < \tilde{p}_c^{\checkmark}$. However, we do not know the true error threshold p_c^{\checkmark} except that it is larger than $\tilde{p}_c^{\checkmark} \approx 3.2 \times 10^{-6}$ for $\overline{\text{TLV}}$ and therefore finite (see ~~§~~ Section 4.F). Figure 4.15 (a) and (b) suggest that $p_c^{\checkmark} = \frac{1}{2}$ for (super-)linear t_{\max} which matches the performance of global majority voting (but also requires at least the same runtime scaling). By contrast, Figure 4.15 (c) is compatible with a non-optimal $0 < p_c^{\checkmark} < \frac{1}{2}$, even though we believe that still $p_c^{\checkmark} = \frac{1}{2}$ due to a (slow) tendency of the crossing point towards $\frac{1}{2}$ for $L \rightarrow \infty$. Finally, Figure 4.15 (d) confirms that $p_c^{\checkmark} = 0$ for a fixed-depth decoder, in compliance with both Lemma 4.3 and the light cone constraint.

DECODING WITH A SELF-DUAL DENSITY CLASSIFIER

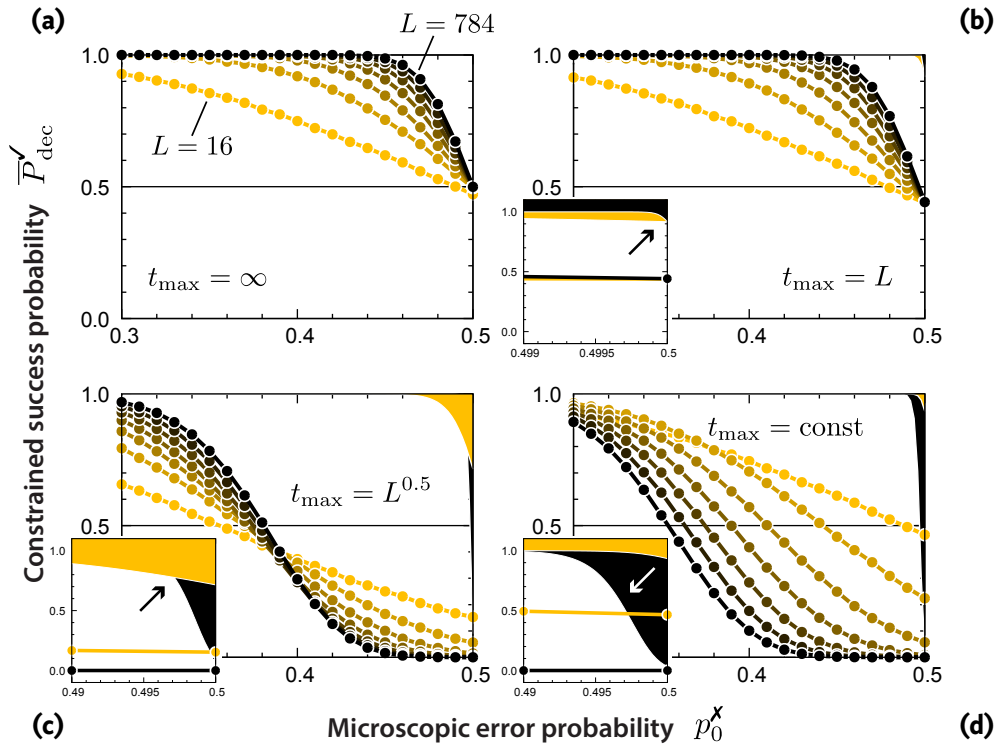


FIGURE 4.15 • Constrained TLV-decoding. The four plots show the probability $\overline{P}_{\text{dec}}^v$ of successfully decoding an initial Bernoulli random configuration with microscopic error probability p_0^x using TLV on chains of length $L = 16, \dots, 784$. Evolutions that take longer than $t_{\text{max}}(L)$ steps are regarded as failed decodings. Upper bounds from the light cone constraint are shaded orange (black) for $L = 16$ ($L = 784$) and compared with the respective numerical results in the insets close to $p_0^x = 0.5$. We sampled over 10^6 realizations for each data point. **(a)** Unrestricted: $t_{\text{max}} = \infty$. The minimum $\overline{P}_{\text{dec}}^v = 0.5$ is reached only for $p_0^x = 0.5$ for $L \rightarrow \infty$. **(b)** Linear: $t_{\text{max}} = L$. The minimum of $\overline{P}_{\text{dec}}^v$ dips slightly below 0.5 for the critical system $p_0^x = 0.5$. Presumably there is still perfect performance for $p_0^x < 0.5$ and $L \rightarrow \infty$. **(c)** Sublinear: $t_{\text{max}} = L^{0.5}$. The results suggest $\lim_{L \rightarrow \infty} \overline{P}_{\text{dec}}^v = 1$ for $0 \leq p_0^x < p_c^x$. Whether $p_c^x < \frac{1}{2}$ cannot be inferred from numerics (note that the light cone constraint allows for $p_c^x = \frac{1}{2}$). **(d)** Constant: $t_{\text{max}} = \text{const}(= 20)$. As dictated by the light cone constraint, there is no decoding possible for $p_0^x > 0$ and consequently $\lim_{L \rightarrow \infty} \overline{P}_{\text{dec}}^v = 0$.

4.5 Error Correction for Continuous Noise

So far, we focused on the *decoding* of initial error patterns $\mathbf{x}(0)$, the probability of success $P_{\text{dec}}^{\checkmark}$ (respectively $\overline{P}_{\text{dec}}^{\checkmark}$) and the time needed to clean the system t_{dec} . The ultimate goal, however, is the preservation of the logical qubit in the presence of *continuous noise*: While we assume error-free processing of classical information, decoherence of the quantum chain is a constant source of errors, characterized by the microscopic error rate p_0^{\times} per time step δt . In this section, we first demonstrate numerically that $\overline{\text{TLV}}$ *cannot* cope with such perturbations of its evolution in that the lifetime of the logical qubit grows only subexponentially with the chain length. In the second part, we resolve this problem by extending the $\overline{\text{TLV}}$ -decoder into the second dimension, and show that its depth grows weakly (sublinearly) with the chain length. We conclude that shallow circuits suffice for reasonably low error rates.

4.5.1 Continuous Noise in Strictly One Dimension

As a first step, we evaluate the performance of $\overline{\text{TLV}}$ as follows: Starting from an error-free chain, $\mathbf{x}(0) = \mathbf{0}$, we apply errors $\mathbf{x}'(t+1) = \mathbf{e}(t+1) \oplus \mathbf{x}(t)$ and $\overline{\text{TLV}}$ -steps $\mathbf{x}(t+1) = \overline{\text{TLV}}_{\mathcal{X}}(\mathbf{x}'(t+1))$ in turns. Here $\mathbf{e}(t+1) \in \mathbb{F}_2^{\mathcal{L}}$ is drawn from a Bernoulli distribution with parameter p_0^{\times} and describes the accumulated errors on the quantum chain between time t and $t+1$. To quantify the ability of $\overline{\text{TLV}}$ to prevent errors from accumulating, we introduce the time to the first majority flip T_{ff} , i.e., $\text{maj}[\mathbf{x}(T_{\text{ff}})] = 1$ and $\text{maj}[\mathbf{x}(t)] = 0$ for $t < T_{\text{ff}}$. Sampling over many error histories $\{\mathbf{e}(t)\}$ yields the average $\langle T_{\text{ff}} \rangle$ characterizing the timescale over which the logical qubits survives (decay time).

Numerical results are shown in Figure 4.16. In (a) $\langle T_{\text{ff}} \rangle$ is plotted versus $1/p_0^{\times}$ for different lengths L , revealing an substantial growth of the decay time for $p_0^{\times} \rightarrow 0$. By contrast, the dependence of $\langle T_{\text{ff}} \rangle$ on L seems to be much less pronounced. This is confirmed in (b) where $\langle T_{\text{ff}} \rangle$ is plotted as function of the system size L for two error rates $p_0^{\times} = 0.050$ and 0.125 : The growth with L is clearly subexponential, although the absolute scale of $\langle T_{\text{ff}} \rangle$ strongly depends on the error rate. To assess the gain in decay time by using $\overline{\text{TLV}}$, we compare it with global majority voting (Δ ; complete correction after each time step) and no correction at all (\times ; accumulating errors without corrective actions). As shown in Figure 4.16 (b), global majority voting exhibits perfectly exponential growth of $\langle T_{\text{ff}} \rangle$ and outperforms $\overline{\text{TLV}}$ clearly. The comparison of a system without corrective actions and $\overline{\text{TLV}}$ reveals that the latter does *not* improve on the scaling but only increases the absolute values of $\langle T_{\text{ff}} \rangle$ and their susceptibility to variations in p_0^{\times} . In conclusion, continuous noise thwarts

ERROR CORRECTION FOR CONTINUOUS NOISE

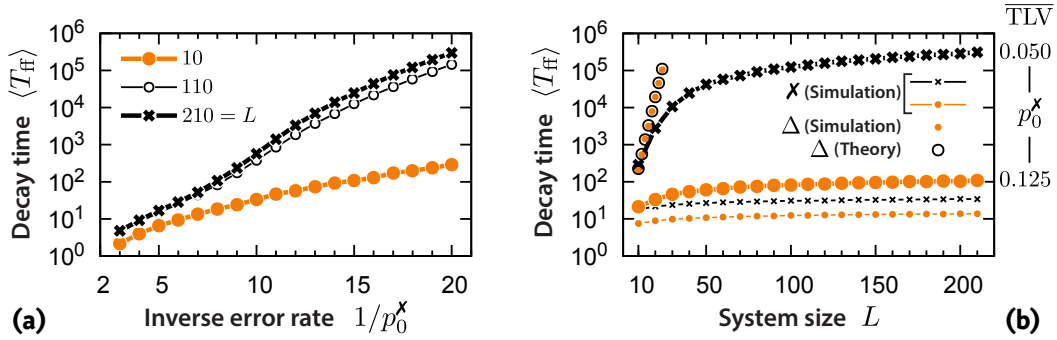


FIGURE 4.16 • Noise-induced deconfinement—Numerics. (a) Average time to the first majority flip $\langle T_{\text{ff}} \rangle$ vs. the inverse microscopic error rate $1/p_0^X$ for different system sizes $L = 10, \dots, 210$ for $\overline{\text{TLV}}$. The dependence on $1/p_0^X$ is approximately exponential. (b) The same data vs. the system size L for different error rates $p_0^X = 0.050$ and 0.125 (joined bold crosses and bullets for $\overline{\text{TLV}}$). The numerics clearly suggests that there is *no* exponential growth of $\langle T_{\text{ff}} \rangle$ for $L \rightarrow \infty$, i.e., the storage time of the encoded qubit grows considerably slower than for *global* majority voting (Δ) with constant correction rate; for comparison, we show simulations and theory for Δ with $p_0^X = 0.125$ (disjoined bullets and circles). With no correction (X), $\langle T_{\text{ff}} \rangle$ becomes almost constant (joined small crosses and bullets for $p_0^X = 0.050$ and 0.125 , respectively). For statistics, we sampled 10^3 evolutions per data point to measure T_{ff} ; the standard error of the shown sample mean is $\sim 3\%$ such that the error bars are not visible.

the benefits one expects from making the quantum chain longer. This is in contrast to the previous sections where we considered the *decoding* of static error patterns and found an exponentially suppressed failure rate P_{dec}^X for increasing chain length.

The susceptibility of $\overline{\text{TLV}}$ to continuous noise can be most easily understood by example: Figure 4.17 (a) depicts the spacetime diagram encoding the evolution of an initial cluster of errors under $\overline{\text{TLV}}$ *without* continuous noise; as this is the decoding procedure discussed above, $\overline{\text{TLV}}$ erodes the cluster reliably. Since $\overline{\text{TLV}}$ effectively operates on the syndrome space, it is instructive to think of the evolution as attraction and subsequent annihilation of \mathbb{Z}_2 -charges (the syndromes, red bullets). If continuous noise is switched on [Figure 4.17 (b)], the attractive interaction is screened by a bath of noise-induced charge-anticharge pairs and the cluster’s endpoints are governed by an undirected, diffusive process. From a renormalization group perspective, there is a confinement-deconfinement transition at $p_0^X = 0$ which prevents the erosion of large clusters of errors, supporting their proliferation throughout the system. The susceptibility of simple one-dimensional CAs to continuous noise is a well-known phenomenon, see e.g. Ref. [328] for TLV and GKL. Indeed, due to the lack of counterexamples, it was conjectured that *all* one-dimensional CAs subject to noise are ergodic, that is, forget about their initial state eventually; this is known as the *positive rates conjecture* [334]. Peter Gács proved it wrong by providing an extraordinary complex counterexample that relies on self-simulation [318, 335, 336]. To the author’s knowledge, there is no simpler

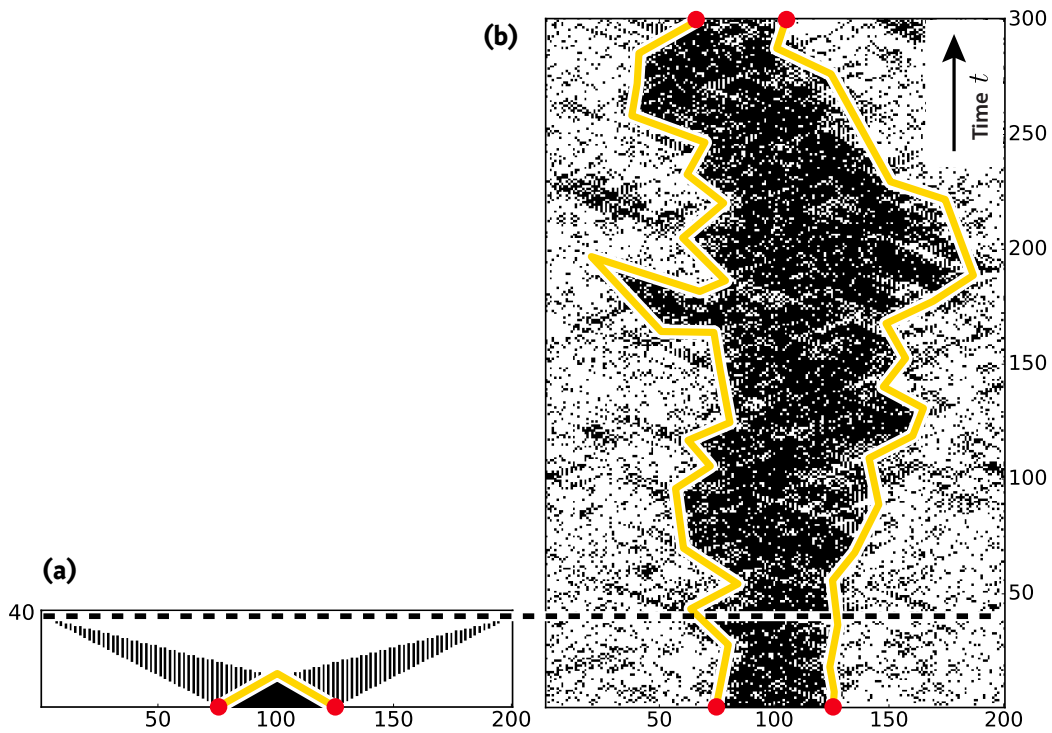


FIGURE 4.17 • Noise-induced deconfinement—Example. (a) Spacetime diagram of a large cluster without continuous noise ($p_0^X = 0$) and $\overline{\text{TLV}}$ -evolution. (b) Evolution of the same initial state with continuous noise $p_0^X = 0.1$ and the same scale as in (a). Note that the messaging between left and right boundary of the cluster is jammed by the noise within the cluster, leading to an effective deconfinement of the charges at the cluster boundaries.

counterexample known till this day, and it is widely believed that any non-ergodic CA in 1D must, in some form or another, implement the core mechanisms of Gács' automaton. It is therefore highly unlikely that a simple CA (such as $\overline{\text{TLV}}$) can retain information about its initial state for $t \rightarrow \infty$ if continuous noise is switched on. This is exactly what our numerical results suggest: The timescale T_{ff} after which $\overline{\text{TLV}}$ forgets about the initial majority does *not* diverge exponentially in the thermodynamic limit—an indicator for ergodicity.

4.5.2 Evading Noise with a Two-Dimensional Extension

To protect the evolution of $\overline{\text{TLV}}$ in the face of continuous noise, we pay with (classical) hardware by unrolling the time evolution into the (spatial) second dimension, perpendicular to the quantum chain. Then, our previous discussions and results on the *time* required for decoding translate directly into statements about the scaling of the *depth* of this “overhead dimension.”

Setup

We start with a description of the envisioned setup in Figure 4.18. Note that the details of its implementation, described in the next few paragraphs, serve as a *proof of principle* only and may be subject to optimizations depending on the physical setup chosen for its realization.

We start with the quantum chain which is placed on top of a 2D substrate that hosts a classical two-layer circuit parallel and attached to the chain. The circuit has the topology of a cylinder glued to the quantum chain, see Figure 4.18 (a); we illustrate both layers by slicing the cylinder along the chain and unfolding the circuit into the plane. The logical wiring of the circuit is sketched in Figure 4.18 (b), Figure 4.19, and Figure 4.20 on various levels of detail. Its width equals the length of the chain L whereas the depth D_L (folded up $D_L/2$) is arbitrary (up to a fixed overhead), see (b) and below. All syndrome measurements are performed periodically—once per time step—and fed into the syndrome register in the top layer of the circuit [Substep 1 in (b), red]. Subsequently each (binary) cell of the two-dimensional classical system is updated synchronously according to specific rules that take as inputs values of spatially adjacent cells [Substep 2 in (b), black]. Finally, set bits in the final correction register on the lower layer (again adjacent to the chain) are used to determine the unitary error correction, the application of which completes a single time step [Substep 3 in (b), red]. Note that due to the spatially local computations, the time needed for a single time step is constant and does neither scale with L nor with D_L .

The rules defining the classical automaton (applied in Substep 2) can be divided roughly into two functional classes [see Figure 4.18 (b) Substep 2]. The first is independent of the depth D_L and located close to the chain. It consists of the syndrome register (upper layer), syndrome memory (upper layer), and the final correction register (lower layer) and computes the syndrome of errors that accumulated since the last syndrome measurement, taking into account the correction operations at the end of the last step. Formally,

$$\mathbf{x}(t+1) = \mathbf{e}(t+1) \oplus \mathbf{c}(t) \oplus \mathbf{x}(t) \quad 4.77a$$

$$\Rightarrow \partial \mathbf{e}(t+1) = \partial \mathbf{x}(t+1) \oplus \partial \mathbf{x}(t) \oplus \partial \mathbf{c}(t) \quad 4.77b$$

$$= \mathbf{s}(t+1) \oplus \mathbf{s}(t) \oplus \partial \mathbf{c}(t) \quad 4.77c$$

with

$$\partial c_{i+\frac{1}{2}}(t) = c_i(t) \oplus c_{i+1}(t), \quad 4.78$$

where $\mathbf{s}(t+1)$ denotes the newly measured syndrome (in the syndrome register), $\mathbf{s}(t)$ is the *previously* measured syndrome (in the syndrome memory), and $\mathbf{c}(t)$ encodes the previously applied correction (in the final correction register); the (inaccessible) error configuration is $\mathbf{x}(t)$ and $\mathbf{e}(t+1)$ denotes the accumulated errors during $[t, t+1]$. Eventually, the syndrome memory is overwritten with the values of the syndrome register.

ERROR CORRECTION WITH CELLULAR AUTOMATA

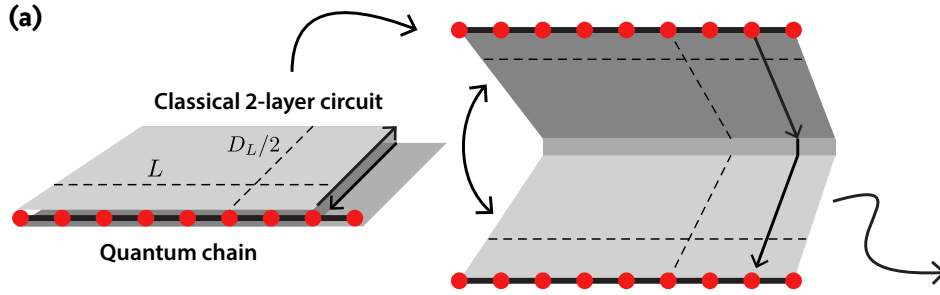
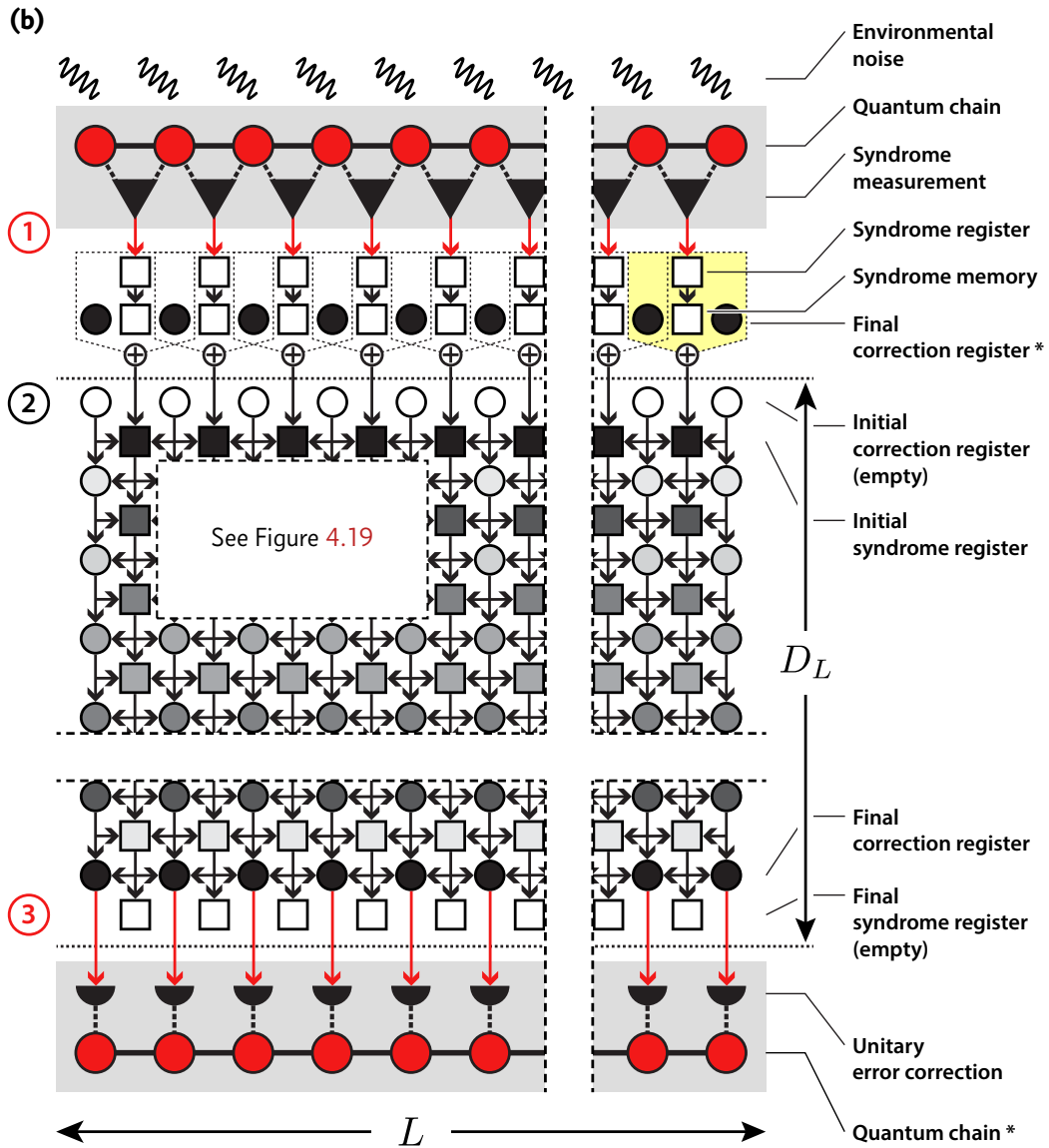


FIGURE 4.18 • 2D-evolved $\overline{\text{TLV}}$ —Setup. (a) The quantum chain is placed on top and framed by a 2D substrate that allows for the implementation of classical two-layer circuitry (e.g., by photo lithography) that connects to projective gates (measurements) and unitary gates along the chain. The classical circuits are used to process measurement results and control unitary gates in an integrated, scalable fashion. For illustrative purposes, the two layers are drawn unfolded with a copy of the quantum chain at top and bottom. The length of the chain is L and the depth of the (unfolded) circuit is denoted by D_L , the scaling of which is discussed in the text. (b) Detailed setup to fight continuous noise on the quantum chain. Information propagates in a feedforward manner from top (syndrome measurements) to bottom (correction operations). At the beginning of each time step, the syndrome pattern from projective measurements is fed into the syndrome register (Substep 1, red arrows). Subsequently, the content of all horizontal registers is evolved to the next row (Substep 2, black arrows). Finally, the results in the final correction register are applied to the quantum chain (Substep 3, red arrows). The initial syndrome register is fed by the parity of syndrome memory, syndrome register and the syndrome of the last applied correction in the final correction register (indicated by the yellow box). The shading of classical bits (squares and circles) from black to white (or vice versa) illustrates the typical operation of the circuit: The syndrome register starts off in a non-empty state at the top whereas the cumulative correction register is initialized with all bits zero. Propagation to the bottom transforms the correction register into the non-trivial result of the decoding procedure while depleting the syndrome register. The latter reaches an empty state at the bottom (with high probability, see text). The elements marked by (*) are drawn twice for illustrative purposes and exist only once in hardware [see (a)].

The result (4.77c) describes *only errors* that occurred in the previous time interval $[t, t + 1]$ and ignores both older errors (which are already taken into account) and previous corrections (which are not to be “corrected”). (4.77c) is fed into the first row (initial syndrome register) of the second sector, a translationally invariant 2D circuit (except for the boundaries) with freely adjustable depth D_L . Its purpose is to simulate $\overline{\text{TLV}}$ in the syndrome-delta representation in a feedforward manner, from top to bottom in Figure 4.18 (b), where $\Delta = \partial \overline{\text{TLV}}_{\mathcal{X}}(s)$ is accumulated modulo 2 in the correction registers (circles) and $s' = \partial \Delta \oplus s$ is written into the syndrome register of the next row. $\partial \overline{\text{TLV}}_{\mathcal{X}}$ is given by Eq. (4.61) and the MBC modifications in (4.62) and (4.63)—and can be implemented as illustrated in Figure 4.19.

ERROR CORRECTION FOR CONTINUOUS NOISE



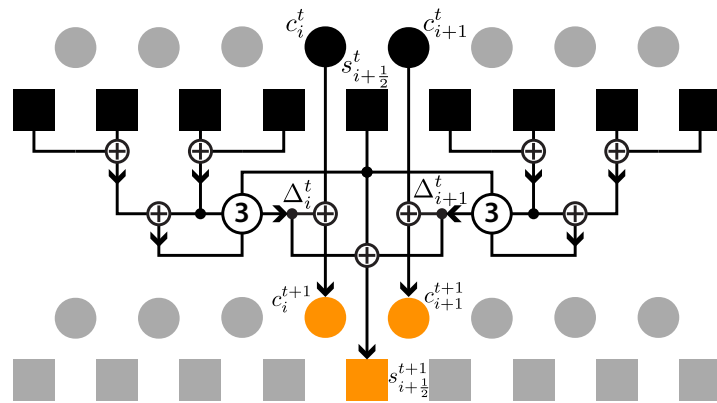


FIGURE 4.19 • 2D-evolved $\overline{\text{TLV}}$ —Details. Detailed logical flow in the scalable bulk that defines the new state of the next row in dependence of the state of the last row. The shown operations implement the evolution of $\overline{\text{TLV}}$ in syndrome-delta representation directly on the syndrome registers (squares) while accumulating all applied operations on the qubits in the correction registers (circles). Note that actual qubit rotations are only applied once at the bottom, defined by the state of the final correction register (see Figure 4.18). For the sake of compactness, we write $c_i^t = c_i(t)$ etc. as compared to the text.

Notably, there are only two types of logic gates required, both of which can be easily reduced to elementary gates. The XOR-gates (\oplus) are equivalent to $X \oplus Y = (X \vee Y) \wedge \neg(X \wedge Y)$ while the majority gates on three bits (MAJ3) can be rewritten as

$$\text{maj}[X, Y, Z] = (X \wedge Y) \vee (X \wedge Z) \vee (Y \wedge Z), \quad 4.79$$

see Figure 4.20. The XOR-gate can be realized in established CMOS technology with only 3 transistors [353, 354], while the MAJ3-gate requires about 14 transistors. However, going beyond CMOS may be beneficial [355], depending on the environment preferred by the coherent subsystem (the quantum chain): Whereas the MAJ3-gate is rather complex in CMOS technology, it becomes an elementary logic gate in the framework of quantum-dot cellular automata [356].

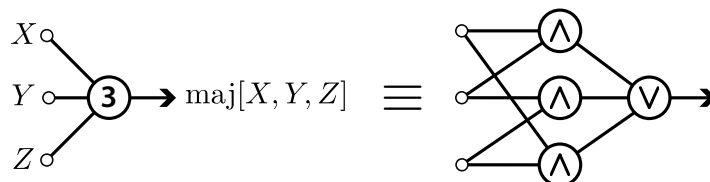


FIGURE 4.20 • Majority gate. Besides the ubiquitous XOR-gates, the only additional gate required is the majority gate with three inputs (MAJ3-gate) which can be easily translated into a network of elementary AND- and OR-gates.

Evaluation

The second sector evolves $\overline{\text{TLV}}$ on $\partial e(t+1)$ *in space* and thereby circumvents the noise-induced deconfinement because subsequent errors $e(t+2) \dots$ are tackled by a completely decoupled evolution of $\overline{\text{TLV}}$. If $\overline{\text{TLV}}$ decodes the syndrome $\partial e(t+1)$ successfully in

$$t_{\text{dec}} \leq t_{\text{max}}(L) = D_L \quad 4.80$$

time steps, the final syndrome register is empty at $t^* = t + 1 + D_L$ and the final correction register contains $c(t^*) = e(t+1)$ which is applied to the quantum chain in Substep 3 to cancel the errors $E(e(t+1))$. We point out that the occurrence of errors e and the application of corresponding corrections c are separated by D_L time steps, the depth of the circuit, which reflects the finite speed of information transfer in a spatially extended decoder [recall Figure 4.5 (c)]. Since errors and correction operations commute, this is not an issue.

We demonstrate the evolution of the complete circuit for a single (minority) cluster of errors without continuous noise in Figure 4.21 on a chain of length $L = 10$ with depth $D_L = 5$. Note how the syndrome memory prevents the automaton from issuing multiple instances of the same computation (Frames 4-6), and how the final correction register prevents the “correction of the correction” in Frame 9. Most importantly, the classical subsystem only uses syndrome information and is *not* aware of the actual error pattern (which we plot as blacked out qubits for convenience only).

Our setup fails to protect the qubit if, at some point in time, an error pattern accumulates during a single time step which cannot be successfully corrected by $\overline{\text{TLV}}$ within D_L time steps. This may be because it is eroded to $\mathbf{1}$ instead of $\mathbf{0}$ or there are syndromes left after D_L time steps so that residual errors survive. The last case splits into two subcases: First, $\overline{\text{TLV}}$ might have succeeded and reached $\mathbf{0}$ after $t_{\text{dec}} > D_L$ time steps, or, second, the initial configuration was in the attractor of a cycle such that no correction was possible anyway (even for $t \rightarrow \infty$).

The time that quantifies the performance of our setup is then the *time-to-first-failure* T_{tff} (“decay time”), i.e., the time after which the first uncorrectable (in the above sense) error pattern appears. Its expectation value is given by

$$\langle T_{\text{tff}} \rangle = \sum_{T=1}^{\infty} T \overline{P}_{\text{dec}}^{\times} (1 - \overline{P}_{\text{dec}}^{\times})^{T-1} = \frac{1}{\overline{P}_{\text{dec}}^{\times}} \quad 4.81$$

where $\overline{P}_{\text{dec}}^{\times} = 1 - \overline{P}_{\text{dec}}^{\checkmark}$ denotes the restricted failure probability of $\overline{\text{TLV}}$ with $t_{\text{max}}(L) = D_L$, as discussed previously [recall Eq. (4.76)]. Eq. (4.81) follows because each time step corresponds to a Bernoulli sample independent of the previous error patterns, a consequence of the spatial evolution of $\overline{\text{TLV}}$ in our 2D circuit.

ERROR CORRECTION WITH CELLULAR AUTOMATA

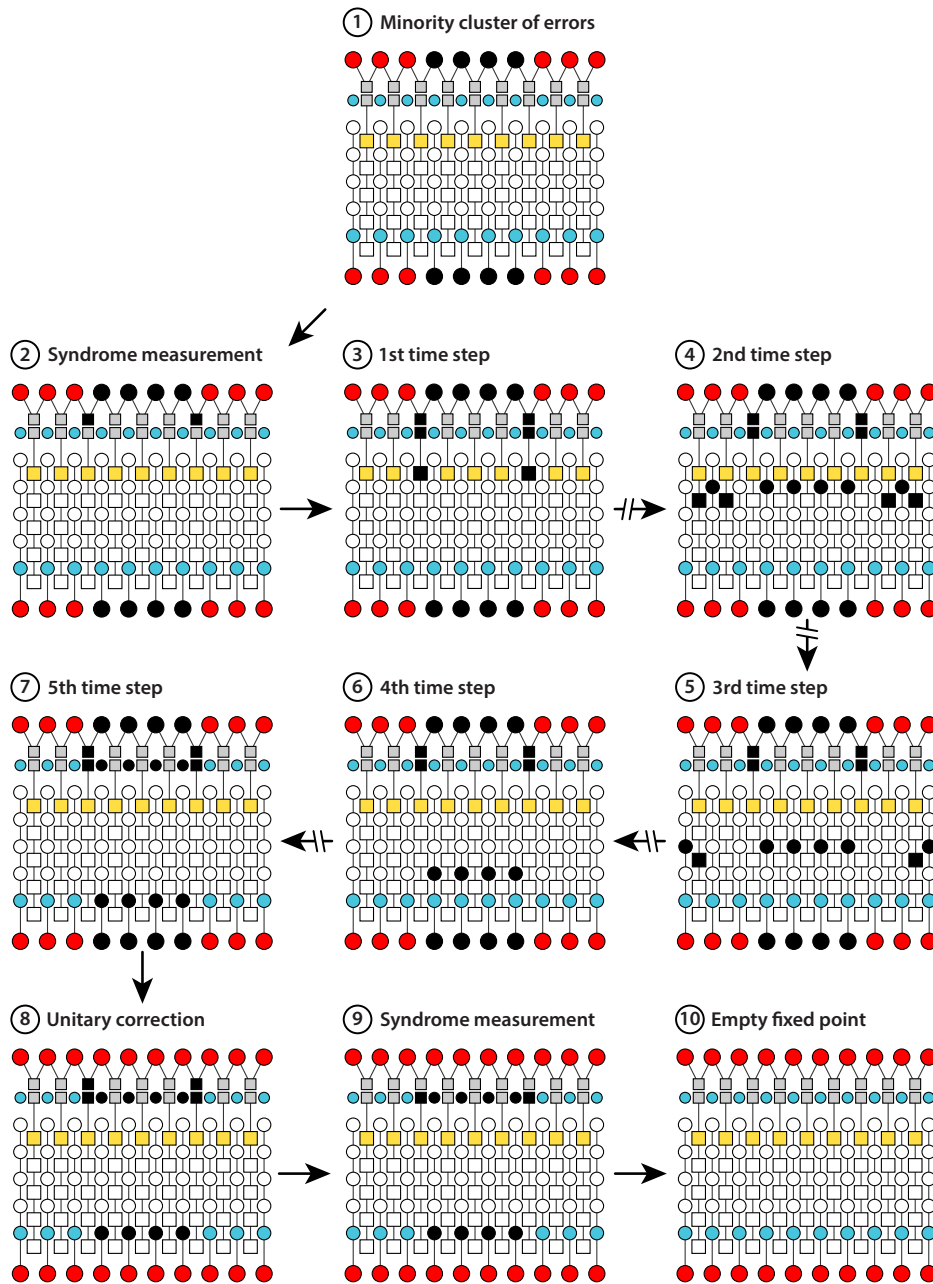


FIGURE 4.21 • Exemplary evolution of 2D-evolved $\overline{\text{TLV}}$. Exemplary evolution of a depth $D_L = 5$ 2D-evolved $\overline{\text{TLV}}$ -automaton of length $L = 10$ without continuous noise, starting from a contiguous minority cluster of errors in the center. (See Figure 4.18 (b) for a description of the setup.) The initial syndrome register and the final correction register are highlighted yellow and green, respectively. A copy of the final correction register is reproduced between syndrome register and syndrome memory (gray) to emphasize that the initialization of the initial syndrome register depends on all of them. Shown are 6 time steps in total, each consisting of three substeps: syndrome measurement, a single step of the 2D CA, and a unitary correction. \curvearrowright

ERROR CORRECTION FOR CONTINUOUS NOISE

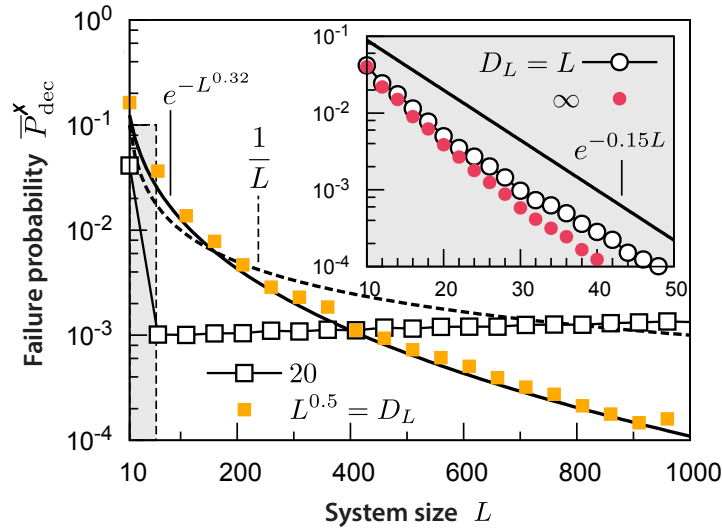


FIGURE 4.22 • Failure probability for 2D-evolved $\overline{\text{TLV}}$. Failure probability $\overline{P}_{\text{dec}}^x$ of decoding error configurations with a 2D-evolved $\overline{\text{TLV}}$ -decoder of depth D_L as a function of the system size L for microscopic error rate $p_0^x = 0.2$. Note that failed decodings include both syndrome-free states with corrupted logical qubit and states with residual syndromes. We sampled $5 \cdot 10^6$ instances per data point. The gray rectangle (dashed boundary) is shown as inset. The solid and dashed lines show the analytic functions $e^{-L^{0.32}}$, $1/L$, and $e^{-0.15L}$ as a guide to the eye; these are neither fits nor analytical results. We compare setups with constant depth $D_L = \text{const} = 20$ (empty squares) and sublinear depth $D_L = L^{0.5}$ (filled squares). Note that the curves intersect for $L = 400$ because $\sqrt{400} = 20$. The inset depicts the much faster decreasing cases of unbounded depth $D_L = \infty$ (filled circles) and linear depth $D_L = L$ (empty circles). There is no qualitative difference between the two for the shown parameters.

In Figure 4.22 we show simulations of $\overline{P}_{\text{dec}}^x$ as function of L for fixed error rate $p_0^x = 0.2$ and four different depth scalings D_L (see also Figure 4.15). Decreasing failure probabilities $\overline{P}_{\text{dec}}^x$ translate via Eq. (4.81) into growing decay times $\langle T_{\text{ff}} \rangle$: A constant-depth $D_L = 20$ decoder does not benefit from longer quantum chains whereas both “infinite depth” and linear depth decoder perform similarly and yield exponentially increasing decay times T_{ff} . Decoders with slowly growing algebraic depths, such as the shown $D_L = L^{0.5}$, still exhibit exponential growth of T_{ff} , although weaker than that of global decoders with $D_L \gtrsim L$.

↷ We omit trivial substeps (measurements and corrections), indicated by broken arrows. The first time step comprises frames 1-3 where the correction step is omitted at the end. Time steps 2-4 are shown in frames 4-6 where both measurements and corrections are omitted. The 5th time step starts in frame 7 and ends with the first (and last) non-trivial correction in frame 8. The 6th and final time step starts with a non-trivial syndrome measurement in frame 9 and resets the CA to the empty fixed point in frame 10. Details are given in the text.

4.6 Conclusion & Outlook

Motivated by the requirement for scalable and modular decoders for topological quantum memories, we set out to construct a strictly local decoder for the one-dimensional Majorana chain quantum code. As the latter constitutes the quantum analogue of the classical repetition code, it can be efficiently decoded and stabilized by global majority voting *if* spatio-temporal constraints are ignored. Taking into account the time needed for classical syndrome processing and communication suggests the implementation of decoders as cellular automata. We argued that the decoding problem at hand translates into the problem of one-dimensional density classification with the additional symmetry constraint of self-duality; this led us to the *two-line voting* automaton TLV as promising local decoder. We equipped the latter with mirrored boundaries (called $\overline{\text{TLV}}$) to comply with the requirement of open boundaries on the level of the quantum chain.

Both numerics and rigorous analytical results showed that $\overline{\text{TLV}}$ succeeds in decoding Bernoulli random patterns with exponentially vanishing failure rate as $L \rightarrow \infty$. Whereas the rigorous results are restricted to small but finite microscopic error probabilities $p_0^X < \tilde{p}_c^X \approx 3.2 \times 10^{-6}$, numerics suggest that $p_0^X < \frac{1}{2}$ may be enough for successful decoding. In addition, the time needed for decoding scales sublinearly for $p_0^X < \frac{1}{2}$. In particular, we proved that the failure rate for decoding a code of length L in at most $t \propto L^\kappa$ time steps ($\kappa > 0$ arbitrary) vanishes exponentially with $L \rightarrow \infty$ for small but finite $p_0^X < \tilde{p}_c^X$. In a nutshell: for low error rates, *global* majority voting is not required.

In the final section we investigated the performance of $\overline{\text{TLV}}$ in the presence of continuous noise. In accordance with the expected ergodicity of simple, one-dimensional cellular automata, we argued that $\overline{\text{TLV}}$ *cannot* fight continuous noise because long-range communication is cut off by locally created charge-anticharge pairs. As a consequence, we had to evolve $\overline{\text{TLV}}$ into the second dimension to prevent errors from accumulating during the syndrome processing. Thereby the superior (i.e., sublinear) scaling of decoding times for $\overline{\text{TLV}}$ —as opposed to the linear scaling of global majority voting—was turned into a modest scaling of classical hardware overhead: For reasonably low error rates, simple, shallow circuits, lacking the capability of global communication, can replace the hardware-expensive global majority voting. These results add to the quest of scalable and modular realizations of actively corrected topological quantum memories.

Open Questions

In the light of these results, there are a few open ends that deserve further scrutiny:

- One of our main results was that, for realistic error rates $p_0^X \ll \frac{1}{2}$, there is no need to implement the capabilities for *global* majority voting since the *local* rules of $\overline{\text{TLV}}$ perform well enough. It would be interesting to gauge the benefits of $\overline{\text{TLV}}$, as compared to global majority voting, *quantitatively*. To this end, an implementation of a scalable global majority decoder, in terms of the same building blocks (i.e., logic gates) as used for our implementation of $\overline{\text{TLV}}$, is required. Then, a cost-benefit analysis (number of gates vs. decay time) would allow for a thorough assessment of both approaches¹³⁹.
- A qubit stored in the ground state space of the Majorana chain is protected by topology *and* fermionic parity symmetry (if the chain couples to an environment). By contrast, two-dimensional topological quantum codes (such as the toric code) feature intrinsic topological order and do not require any symmetry to protect the logical qubit from decoherence. It is therefore an interesting question to which extent the techniques and results presented here can be applied to the decoding and stabilization of two-dimensional topological quantum codes. For the toric code, this is presumably a highly non-trivial task because true minimum weight perfect matching is inherently more complex than simple majority voting. Furthermore, it is not clear whether and how the core mechanism of TLV can be generalized to two dimensions where point-like messages can miss each other easily¹⁴⁰.

¹³⁹A similar question arose in Chapter 3 which motivated a formal framework for describing tasks and quantifying solutions thereof (introduced in Section 5.3).

¹⁴⁰The transition from one to two dimensions is often accompanied by fundamental changes in physics. For instance, the classical Ising model gains a phase transition and interacting fermions gain a quasiparticle description in terms of Fermi liquid theory.

APPENDICES FOR CHAPTER 4

4.A Cumulative Binomial Distribution

Here we prove some of the statements about global majority voting used in Subsection 4.2.2 and Subsection 4.2.3 of the main text. To this end, we start with the probability for more than half of L (odd) binary sites x_i to be error-afflicted (i.e., in state $x_i = 1$) after t rounds of additive, uncorrelated Bernoulli noise:

$$P_{L,p_0}^{\mathbf{x}}(t) = \sum_{k=\frac{L+1}{2}}^L \binom{L}{k} [p^{\mathbf{x}}(t)]^k [1 - p^{\mathbf{x}}(t)]^{L-k} \quad 4.82$$

where

$$p^{\mathbf{x}}(t) = \frac{1}{2} \left[1 - (1 - 2p_0^{\mathbf{x}})^t \right] \quad 4.83$$

is the renormalized single-site probability for $X(t) = X_1 \oplus \dots \oplus X_t$ with X_i Bernoulli random variables with parameter $p_0^{\mathbf{x}}$, i.e.,

$$\Pr(X(t) = 1) = \sum_{k \text{ odd}} \binom{t}{k} (p_0^{\mathbf{x}})^k (1 - p_0^{\mathbf{x}})^{t-k} \quad 4.84a$$

$$= \frac{1}{2} \left[1 - (1 - 2p_0^{\mathbf{x}})^t \right]. \quad 4.84b$$

Eq. (4.82) is a special case of the cumulative binomial distribution function which is known to be expressible in a closed form by the incomplete beta function,

$$B(x; a, b) = \int_0^x y^{a-1} (1-y)^{b-1} dy \quad 4.85$$

via [337]

$$P_{L,p_0}^{\mathbf{x}}(t) = I_{p^{\mathbf{x}}(t)} \left(\frac{L+1}{2}, L - \frac{L+1}{2} + 1 \right) \quad 4.86$$

where $I_x(a, b) = B(x; a, b)/B(1; a, b)$ is called *regularized* incomplete beta function. With $a, b \in \mathbb{N}$ we can use

$$B(1; a, b) = \frac{\Gamma(a)\Gamma(b)}{\Gamma(a+b)} = \frac{(a-1)!(b-1)!}{(a+b-1)!} \quad 4.87$$

to evaluate

$$B\left(1; \frac{L+1}{2}, L - \frac{L+1}{2} + 1\right) = \left[\frac{L+1}{2} \binom{L}{\frac{L+1}{2}}\right]^{-1}. \quad 4.88$$

Then Eq. (4.86) reads

$$P_{L, p_0}^x(t) = \frac{L+1}{2} \binom{L}{\frac{L+1}{2}} \int_0^{p^x(t)} [x - x^2]^{\frac{L-1}{2}} dx \quad 4.89$$

which is a useful form to derive estimates and limits of Eq. (4.82).

In particular, we can now derive the limit for $0 < p_0^x \leq \frac{1}{2}$ and $0 < c < \infty$

$$\lim_{L \rightarrow \infty} P_{L, p_0}^x(t = c^{-1}L) = \frac{1}{2} \quad 4.90$$

if we use the asymptotic expression (Stirling's approximation)

$$\binom{L}{\frac{L+1}{2}} \sim \sqrt{\frac{2}{\pi}} \frac{2^L}{\sqrt{L}} \quad \text{for } L \rightarrow \infty. \quad 4.91$$

Indeed, with $t = \frac{L}{c}$

$$P_{L, p_0}^x(t) = \frac{L+1}{2} \binom{L}{\frac{L+1}{2}} \int_0^{p^x(t)} [x - x^2]^{\frac{L-1}{2}} dx \quad 4.92a$$

$$\sim \frac{\sqrt{L}}{\sqrt{2\pi}} \int_0^{p^x(t)} [2(2x) - (2x)^2]^{\frac{L-1}{2}} d(2x) \quad 4.92b$$

$$\stackrel{y=2x}{=} \frac{\sqrt{L}}{\sqrt{2\pi}} \int_0^{2p^x(t)} [2y - y^2]^{\frac{L-1}{2}} dy \quad 4.92c$$

$$\stackrel{u=y-1}{=} \frac{\sqrt{L}}{\sqrt{2\pi}} \int_{-1}^{2p^x(t)-1} [1 - u^2]^{\frac{L-1}{2}} du \quad 4.92d$$

$$\sim \frac{1}{\sqrt{\pi}} \int_{-\sqrt{\frac{L-1}{2}}}^{-\sqrt{\frac{L-1}{2}}(1-2p_0^x)^{\frac{1}{c}}} \left[1 - \frac{x^2}{\frac{L-1}{2}}\right]^{\frac{L-1}{2}} dx \quad 4.92e$$

where we used the substitution $x = \sqrt{\frac{L-1}{2}} u$ in the last row. If we use that ($0 < p_0^\star \leq \frac{1}{2}$)

$$\lim_{L \rightarrow \infty} \int_{-\sqrt{\frac{L-1}{2}}(1-2p_0^\star)^{\frac{L}{c}}}^0 \left[1 - \frac{x^2}{\frac{L-1}{2}} \right]^{\frac{L-1}{2}} dx = 0 \quad 4.93$$

and

$$\lim_{n \rightarrow \infty} \int_{-n}^0 \left(1 - \frac{x^2}{n^2} \right)^{n^2} dx = \lim_{n \rightarrow \infty} n \int_0^1 (1 - y^2)^{n^2} dy \quad 4.94a$$

$$= \frac{\sqrt{\pi}}{2} \lim_{n \rightarrow \infty} \frac{n \Gamma(1 + n^2)}{\Gamma(\frac{3}{2} + n^2)} \quad 4.94b$$

$$= \frac{\sqrt{\pi}}{2}, \quad 4.94c$$

we find for $0 < p_0^\star \leq \frac{1}{2}$ and $0 < c < \infty$ the final result

$$\lim_{L \rightarrow \infty} P_{L, p_0^\star}^\star(c^{-1}L) = \frac{1}{2} = \frac{1}{\sqrt{\pi}} \int_{-\infty}^0 e^{-x^2} dx. \quad 4.95$$

Note that $\lim_{L \rightarrow \infty} P_{L, p_0^\star}^\star(c^{-1}L) > 0$ only because $p^\star(t)$ renormalizes to $\frac{1}{2}$ exponentially fast with t , such that the upper bound of the integral converges to zero. Similarly, for $\lim_{L \rightarrow \infty} P_{L, p_0^\star}^\star(t = 1)$ one easily re-derives the exponential decay to zero (modified by \sqrt{L} from the integral bounds).

4.B Light Cone Constraint

In Subsection 4.2.3 we introduced the light cone constraint Eq. (4.36) and discussed its scaling properties. Below, in \clubsuit Subsection 4.B.1, we present its derivation in detail; in \clubsuit Subsection 4.B.2 the limits for various relations between depth D and size L are discussed.

4.B.1 Derivation

Here we prove the following upper bound for the decoding probability $P_{\text{dec}}^\checkmark$ of a D -local physical decoder of linear size L :

$$P_{\text{dec}}^\checkmark \leq \left[1 + \left(\frac{p_0^\star}{1 - p_0^\star} \right)^{2D+1} \right]^{-\frac{L}{2D+1}}. \quad 4.96$$

The microscopic error probability per qubit and time step is p_0^x . Let the error pattern be described by the vector \mathbf{x} of length L with syndrome $s = \partial\mathbf{x}$. A given D -local decoder Δ^D then calculates a correction $\Delta^D(s)$ such that $\Delta^D(s) \oplus \mathbf{x}$ describes the new error state after the correction has been applied. For an arbitrary but fixed site $1 \leq i \leq L$ we define two sets :

$$\mathcal{X}_i^\vee \equiv \{ \mathbf{x} \mid \Delta_i^D(s) \oplus x_i = 0 \} , \quad 4.97a$$

$$\mathcal{X}_i^\times \equiv \{ \mathbf{x} \mid \Delta_i^D(s) \oplus x_i = 1 \} . \quad 4.97b$$

\mathcal{X}_i^\vee and \mathcal{X}_i^\times describe the sets of all error patterns that Δ^D (un)successfully corrects at site i , respectively. We define the local complement operator C_i^D such that for $\mathbf{x}' = C_i^D \mathbf{x}$

$$x'_j = \begin{cases} x_j & \text{for } |j - i| > D , \\ x_j \oplus 1 & \text{for } |j - i| \leq D , \end{cases} \quad 4.98$$

i.e., it inverts the error pattern in a region of radius D around site i . Clearly $C_i^D \circ C_i^D = \mathbb{1}$, such that C_i^D defines a bijection on the total error state space $\mathcal{X} = \mathcal{X}_i^\vee \dot{\cup} \mathcal{X}_i^\times = \mathbb{F}_2^L$. Let $\pi_i^D : \mathcal{X} \rightarrow \mathbb{F}_2^{2D+1}$ be the projector that slices the range on which C_i^D acts non-trivially from a state \mathbf{x} . We have $\partial\mathbf{x} \neq \partial C_i^D \mathbf{x}$ due to the boundaries of the partial complement. However,

$$\partial\pi_i^D \mathbf{x} = \partial\pi_i^D C_i^D \mathbf{x} \quad 4.99$$

since the syndrome does not change inside the range of the local complement. We can now define the two sets

$$\bar{\mathcal{X}}_i^\vee \equiv C_i^D \mathcal{X}_i^\vee = \{ C_i^D \mathbf{x} \mid \mathbf{x} \in \mathcal{X}_i^\vee \} , \quad 4.100a$$

$$\bar{\mathcal{X}}_i^\times \equiv C_i^D \mathcal{X}_i^\times = \{ C_i^D \mathbf{x} \mid \mathbf{x} \in \mathcal{X}_i^\times \} . \quad 4.100b$$

Since C_i^D is a bijection, we still have $\mathcal{X} = \bar{\mathcal{X}}_i^\vee \dot{\cup} \bar{\mathcal{X}}_i^\times$.

Now comes a crucial step: Because Δ^D is D -local, its action on site i only depends on the syndromes within $\pi_i^D \mathbf{x}$, i.e., $\partial\pi_i^D \mathbf{x}$. Therefore we find that if $\mathbf{x} \in \mathcal{X}_i^\vee$ is successfully corrected at site i , then Δ^D fails to correct $C_i^D \mathbf{x}$ because its action on site i is the same. In a nutshell,

$$\mathbf{x} \in \mathcal{X}_i^\vee \Leftrightarrow C_i^D \mathbf{x} \in \mathcal{X}_i^\times . \quad 4.101$$

Thus we have $\bar{\bar{\mathcal{X}}}_i^\vee = \overline{\mathcal{X}_i^\vee} = \mathcal{X}_i^\times$ and $\bar{\bar{\mathcal{X}}}_i^\times = \overline{\mathcal{X}_i^\times} = \mathcal{X}_i^\vee$ where $\bar{\bullet}$ denotes the complement in \mathcal{X} .

For a Bernoulli process, the probability of the error pattern \mathbf{x} is

$$\Pr_{p_0^x}(\mathbf{x}) = (p_0^x)^{|\mathbf{x}|} (1 - p_0^x)^{L - |\mathbf{x}|} \quad 4.102$$

width $|\mathbf{x}| = \sum_i x_i$ the total number of errors. For the local complement, we have

$$\Pr_{p_0^\mathbf{x}}(C_i^D \mathbf{x}) = (p_0^\mathbf{x})^{|C_i^D \mathbf{x}|} (1 - p_0^\mathbf{x})^{L - |C_i^D \mathbf{x}|} \quad 4.103a$$

$$= \left(\frac{p_0^\mathbf{x}}{1 - p_0^\mathbf{x}} \right)^{|C_i^D \mathbf{x}| - |\mathbf{x}|} \Pr_{p_0^\mathbf{x}}(\mathbf{x}) \quad 4.103b$$

where

$$|C_i^D \mathbf{x}| - |\mathbf{x}| = (2D + 1) - 2|\pi_i^D \mathbf{x}| \quad 4.104$$

is the change of errors in the light cone due to the local complement. Thus

$$\Pr_{p_0^\mathbf{x}}(C_i^D \mathbf{x}) = \left(\frac{p_0^\mathbf{x}}{1 - p_0^\mathbf{x}} \right)^{(2D+1) - 2|\pi_i^D \mathbf{x}|} \Pr_{p_0^\mathbf{x}}(\mathbf{x}) . \quad 4.105$$

We start from the trivial relation

$$\sum_{\mathbf{x} \in \mathcal{X}_i^\vee} \Pr_{p_0^\mathbf{x}}(\mathbf{x}) + \sum_{\mathbf{x} \in \mathcal{X}_i^\times} \Pr_{p_0^\mathbf{x}}(\mathbf{x}) = 1 \quad 4.106$$

and rewrite the first term

$$\sum_{\mathbf{x} \in \mathcal{X}_i^\vee} \Pr_{p_0^\mathbf{x}}(\mathbf{x}) = \sum_{\mathbf{x} \in \mathcal{X}_i^\vee} \Pr_{p_0^\mathbf{x}}(C_i^D \mathbf{x}) \quad 4.107a$$

$$= \sum_{\mathbf{x} \in \mathcal{X}_i^\times} \left(\frac{p_0^\mathbf{x}}{1 - p_0^\mathbf{x}} \right)^{(2D+1) - 2|\pi_i^D \mathbf{x}|} \Pr_{p_0^\mathbf{x}}(\mathbf{x}) \quad 4.107b$$

which yields

$$\sum_{\mathbf{x} \in \mathcal{X}_i^\times} \left[1 + \left(\frac{p_0^\mathbf{x}}{1 - p_0^\mathbf{x}} \right)^{(2D+1) - 2|\pi_i^D \mathbf{x}|} \right] \Pr_{p_0^\mathbf{x}}(\mathbf{x}) = 1 . \quad 4.108$$

So far, all statements are exact and valid for $0 \leq p_0^\mathbf{x} \leq 1$. Now we assume $0 \leq p_0^\mathbf{x} \leq \frac{1}{2}$ and estimate

$$\left(\frac{p_0^\mathbf{x}}{1 - p_0^\mathbf{x}} \right)^{(2D+1) - 2|\pi_i^D \mathbf{x}|} \leq \left(\frac{1 - p_0^\mathbf{x}}{p_0^\mathbf{x}} \right)^{2D+1} \quad 4.109$$

where we used that $|\pi_i^D \mathbf{x}| \leq 2D + 1$ and $p_0^\mathbf{x}/(1 - p_0^\mathbf{x}) \leq 1$ for $p_0^\mathbf{x} \leq \frac{1}{2}$. We have

$$1 \leq \left[1 + \left(\frac{1 - p_0^\mathbf{x}}{p_0^\mathbf{x}} \right)^{2D+1} \right] \cdot \sum_{\mathbf{x} \in \mathcal{X}_i^\times} \Pr_{p_0^\mathbf{x}}(\mathbf{x}) \quad 4.110$$

and therefore the lower bound on the error probability

$$\left[1 + \left(\frac{1 - p_0^x}{p_0^x} \right)^{2D+1} \right]^{-1} \leq \sum_{\mathbf{x} \in \mathcal{X}_i^x} \Pr_{p_0^x}(\mathbf{x}) . \quad 4.111$$

Note that this is the probability that an error at site i survives a single correction procedure with Δ^D . This lower bound can be easily recast as an upper bound on the probability of successful correction,

$$\sum_{\mathbf{x} \in \mathcal{X}_i^y} \Pr_{p_0^x}(\mathbf{x}) = 1 - \sum_{\mathbf{x} \in \mathcal{X}_i^x} \Pr_{p_0^x}(\mathbf{x}) \leq \left[1 + \left(\frac{p_0^x}{1 - p_0^x} \right)^{2D+1} \right]^{-1} . \quad 4.112$$

The last step is to use this result for an upper bound on the *global* correction probability

$$P_{\text{dec}}^y = \sum_{\mathbf{x} \in \cap_i \mathcal{X}_i^y} \Pr_{p_0^x}(\mathbf{x}) \quad 4.113a$$

$$= \sum_{\mathbf{x} \in \mathcal{X}} \Pr_{p_0^x}(\mathbf{x}) \prod_i \mathbb{1}_{\mathcal{X}_i^y}(\mathbf{x}) \quad 4.113b$$

$$= \left\langle \prod_i \mathbb{1}_{\mathcal{X}_i^y} \right\rangle \neq \prod_i \langle \mathbb{1}_{\mathcal{X}_i^y} \rangle \quad 4.113c$$

where $\mathbb{1}_{\mathcal{X}_i^y}$ denotes the indicator function of \mathcal{X}_i^y . The last inequality follows from the fact that $\mathbb{1}_{\mathcal{X}_i^y}$ and $\mathbb{1}_{\mathcal{X}_j^y}$ may be correlated random variables for $|i - j| < 2D + 1$, i.e., if their past light cones overlap and they depend on common syndrome measurements. This motivates the second estimate

$$\left\langle \prod_i \mathbb{1}_{\mathcal{X}_i^y} \right\rangle \leq \left\langle \prod_{k=1}^{L/(2D+1)} \mathbb{1}_{\mathcal{X}_{k(2D+1)}^y} \right\rangle \quad 4.114$$

where we assume for simplicity that L is a multiple of $2D + 1$. We can separate the system into subsystems \mathbf{x}_k of length $2D + 1$ such that $\mathbb{1}_{\mathcal{X}_{k(2D+1)}^y}(\mathbf{x}) = \mathbb{1}_{\mathcal{X}_{k(2D+1)}^y}(\mathbf{x}_k)$ (slight abuse of notation) with $\mathbf{x}_k = \pi_{k(2D+1)}^D \mathbf{x}$. Here we use the fact that the correctability of site $k(2D + 1)$ only depends on a causal region of radius D . The last step is to realize that $\Pr_{p_0^x}(\mathbf{x})$ is a product measure due to the uncorrelated Bernoulli process,

$$\Pr_{p_0^x}(\mathbf{x}) = \prod_k \Pr_{p_0^x}(\mathbf{x}_k) , \quad 4.115$$

so that

$$\left\langle \prod_{k=0}^{L/(2D+1)} \mathbb{1}_{\mathcal{X}_{k(2D+1)}^\vee} \right\rangle = \prod_{k=1}^{L/(2D+1)} \left\langle \mathbb{1}_{\mathcal{X}_{k(2D+1)}^\vee} \right\rangle \quad 4.116$$

factorizes. Using translational invariance and our result Eq. (4.112), it follows the final result

RESULT 4.1: Light cone constraint

$$P_{dec}^\vee \leq \left\langle \mathbb{1}_{\mathcal{X}_i^\vee} \right\rangle^{\frac{L}{2D+1}} \leq \left[1 + \left(\frac{p_0^\vee}{1 - p_0^\vee} \right)^{2D+1} \right]^{-\frac{L}{2D+1}}. \quad 4.117$$

Note that this result is generic and we used only that the decoder (1) has only access to the syndrome $\partial \mathbf{x}$ which is invariant under complementation of error patterns and (2) the correction of site i only depends on nearby syndromes in the neighborhood $\pi_i^D \mathbf{x}$.

4.B.2 Scaling Behavior

Here we derive some scaling limits of Eq. (4.117). To this end, we assume $D = D(L)$ to be a function of the linear size L of the code. There are three major cases:

→ $D = \text{const.}$ This describes a truly one-dimensional feedforward circuit of finite depth D . We find in the thermodynamic limit

$$\begin{aligned} \lim_{L \rightarrow \infty} P_{dec}^\vee &\leq \lim_{L \rightarrow \infty} \left[1 + \left(\frac{p_0^\vee}{1 - p_0^\vee} \right)^{2D+1} \right]^{-\frac{L}{2D+1}} \\ &= \begin{cases} 0 & \text{for } 0 < p_0^\vee \leq \frac{1}{2}, \\ 1 & \text{for } p_0^\vee = 0, \end{cases} \end{aligned} \quad 4.118$$

i.e., there is no successful decoding possible for any finite microscopic error rate $p_0^\vee > 0$.

→ $2D + 1 \sim L^\kappa$ ($\kappa > 0$). This describes a truly two-dimensional feedforward circuit, possibly slowly growing in the second dimension if $\kappa \approx 0$. We find in the thermodynamic limit

$$\begin{aligned} \lim_{L \rightarrow \infty} P_{\text{dec}}^\vee &\leq \lim_{L \rightarrow \infty} \left[1 + \left(\frac{p_0^\times}{1 - p_0^\times} \right)^{L^\kappa} \right]^{-L^{1-\kappa}} \\ &= \begin{cases} 1 & \text{for } 0 \leq p_0^\times < \frac{1}{2}, \\ 0 & \text{for } p_0^\times = \frac{1}{2} \text{ and } \kappa < 1, \\ \frac{1}{2} & \text{for } p_0^\times = \frac{1}{2} \text{ and } \kappa = 1, \\ 1 & \text{for } p_0^\times = \frac{1}{2} \text{ and } \kappa > 1, \end{cases} \end{aligned} \quad 4.119$$

i.e., except for the critical point $p_0^\times = \frac{1}{2}$, there is no constraint on P_{dec}^\vee coming from Eq. (4.117). At the critical point, the upper bounds depend on whether the second dimension scales slower or faster than the length of the chain. For faster scaling depth, there is no constraint, whereas for slower scaling depth, non-trivial upper bounds arise. Note that $P_{\text{dec}}^\vee \leq \frac{1}{2}$ follows for $p_0^\times = \frac{1}{2}$ since a completely mixing Bernoulli process destroys all encoded information about the majority. $P_{\text{dec}}^\vee < \frac{1}{2}$ arises whenever the decoder fails to get rid of all syndromes. $P_{\text{dec}}^\vee = \frac{1}{2}$ can be realized if the decoder succeeds in removing all syndromes but still fails to recover the original state in 50% of the cases.

To prove the result for $0 \leq p_0^\times < \frac{1}{2}$, we write $p_0^\times/(1 - p_0^\times) = q$ with $0 \leq q < 1$. First, note that

$$\lim_{L \rightarrow \infty} [1 + q^{L^\kappa}]^{-L^{1-\kappa}} \leq \lim_{L \rightarrow \infty} 1^{-L^{1-\kappa}} = 1 \quad 4.120$$

because of $q \geq 0$.

Furthermore it is $-L^\kappa \log q \geq \log L$ for $q < 1$, $\kappa > 0$ and L large enough. This allows us to estimate

$$[1 + q^{L^\kappa}]^L = \left[1 + \left(\frac{1}{e} \right)^{-L^\kappa \log q} \right]^L \quad 4.121a$$

$$\leq \left[1 + \left(\frac{1}{e} \right)^{\log L} \right]^L = \left[1 + \frac{1}{L} \right]^L \quad 4.121b$$

$$\leq C \quad 4.121c$$

for some constant $C > 0$ and where we used that $1/e < 1$ and $\lim_{L \rightarrow \infty} (1 + 1/L)^L = e$. With this result, we can find a lower bound as follows:

$$\lim_{L \rightarrow \infty} [1 + q^{L^\kappa}]^{-L^{1-\kappa}} \geq \lim_{L \rightarrow \infty} \frac{1}{C \frac{1}{L^\kappa}} = 1 \quad 4.122$$

LIGHT CONE CONSTRAINT

for $\kappa > 0$. In conclusion, we have shown $\lim_{L \rightarrow \infty} [1 + q^{L^\kappa}]^{-L^{1-\kappa}} = 1$ for $q < 1$ and $\kappa > 0$.

→ $2D + 1 \sim \log L^\kappa$ ($\kappa > 0$). This describes still a two-dimensional feedforward circuit, but with an exponentially smaller second dimension. In a certain sense, it interpolates between the one- and two-dimensional cases above.

Indeed,

$$\begin{aligned} \lim_{L \rightarrow \infty} P_{\text{dec}}^\vee &\leq \lim_{L \rightarrow \infty} \left[1 + \left(\frac{p_0^\times}{1 - p_0^\times} \right)^{\kappa \log L} \right]^{-\frac{L}{\kappa \log L}} \\ &= \begin{cases} 1 & \text{for } p_0^\times \leq p_c^\times, \\ 0 & \text{for } p_0^\times > p_c^\times, \end{cases} \end{aligned} \quad 4.123$$

where the critical microscopic error rate is

$$p_c^\times = \frac{1}{1 + e^{1/\kappa}}. \quad 4.124$$

To show this, we write

$$[1 + q^{\kappa \log L}]^L = \left[1 + \frac{1}{L^{-\kappa \log q}} \right]^L = \left[1 + \frac{1}{L^\eta} \right]^L \quad 4.125$$

with $q = p_0^\times / (1 - p_0^\times)$ and $\eta = -\kappa \log q$. Using $\lim_{x \rightarrow 0} \log(1 + x)/x = \lim_{x \rightarrow 0} 1/(1 + x) = 1$, we find

$$\lim_{L \rightarrow \infty} \log(1 + L^{-\eta}) / L^{-\eta} = 1 \quad 4.126$$

for $\eta > 0$. Hence

$$\begin{aligned} &\lim_{L \rightarrow \infty} [1 + q^{\kappa \log L}]^{-\frac{L}{\kappa \log L}} \\ &= \lim_{L \rightarrow \infty} \exp \left[-\frac{L^{1-\eta}}{\kappa \log L} \cdot \log(1 + L^{-\eta}) / L^{-\eta} \right] \end{aligned} \quad 4.127a$$

$$= \begin{cases} 0 & \text{for } \eta < 1, \\ 1 & \text{for } \eta \geq 1. \end{cases} \quad 4.127b$$

The critical value $\eta_c = 1$ corresponds to $-\kappa \log q_c = 1 \Leftrightarrow q_c = e^{-1/\kappa}$ and therefore $p_c^\times = 1/(1 + e^{1/\kappa})$.

Whereas constant depth allows for no correction if $p_0^\times > 0$ and algebraically growing D , in principle, imposes no restriction at all (except for $p_0^\times = \frac{1}{2}$ of course), a logarithmically growing depth could still be sufficient for low enough error rates $p_0^\times \leq p_c^\times < \frac{1}{2}$.

4.C Linear Eroders on Finite Chains

Regarding the eroder property of a *finite* chain, we have to relax the definition to account for the finiteness of the system as there is no qualitative difference between perturbation and background (both of which are finite). A possible modification reads as follows:

DEFINITION 4.3: Finite-size linear eroders

A cellular automaton on a finite chain $\mathcal{L} = \{1, \dots, L\}$ (with arbitrary boundary conditions) is a finite-size linear eroder if there exist real constants $0 < a < 1$ and $m \in \mathbb{R}^+$ such that for any size $L < \infty$ and any finite perturbation of $\mathbf{0}$ ($\mathbf{1}$) with diameter $l \leq aL$, the unperturbed state $\mathbf{0}$ ($\mathbf{1}$) is recovered at $t_{dec} \leq ml$.

Here we focus on $\overline{\text{TLV}}$. Clearly, a contiguous cluster of errors touching the mirror is eventually eroded by the modified TLV rules if it is small enough (so that no signal reaches the opposite boundary before dissolving). Since the majority function is monotonic (changing an input bit $0 \rightarrow 1$ never changes the output bit from $1 \rightarrow 0$), the evolution of $\overline{\text{TLV}}$ from a non-contiguous, finite cluster of errors can be constructed from the evolution of a contiguous cluster of the same size (its convex hull) by erasing errors in the spacetime diagram. This implies that $\overline{\text{TLV}}$ is an eroder in the above sense.

We can make this statement more rigorous (see Figure 4.23): It is straightforward to verify that a finite cluster I of diameter $\|I\| = l$ (without loss of generality contiguous, due to monotonicity) is eroded by TLV in a spacetime rectangle of dimensions $[(2Rm + 1)l] \times (ml)$ for appropriately chosen $m \in \mathbb{R}^+$ (for TLV it is $m = 1$ and $R = 4$, see \clubsuit Section 4.F). This holds also for $\overline{\text{TLV}}$ if I is separated from the edges by more than $\delta(l) \equiv Rml$ sites since $(2Rm + 1)l = l + 2\delta(l)$ guarantees that the cluster is eroded before the boundaries can have any effect, see Figure 4.23 (1). Necessary for this situation is

$$(2Rm + 1)l \leq L \Leftrightarrow l \leq \frac{L}{2Rm + 1}. \tag{4.128}$$

If, on the other hand, I is *closer* than $\delta(l)$ to one of the edges, we can no longer guarantee that it can be eroded in the neighborhood given by $\delta(l)$ due to possible interactions with its mirror image. We define a padded interval $I' \supseteq I$ of length $l \leq l' < l + \delta(l) = (Rm + 1)l$ that closes the gap between I and the critical edge. Now we know that this interval is eroded in a spacetime box of dimensions $[(2Rm + 1)2l'] \times (m2l')$ due to the mirror. In the “real” chain, this accounts for an interval of length $l' + \delta(2l') = (2Rm + 1)l'$ adjacent to the corresponding edge. If the latter does *not* make contact with the opposite edge, the original cluster I is

LINEAR ERODERS ON FINITE CHAINS

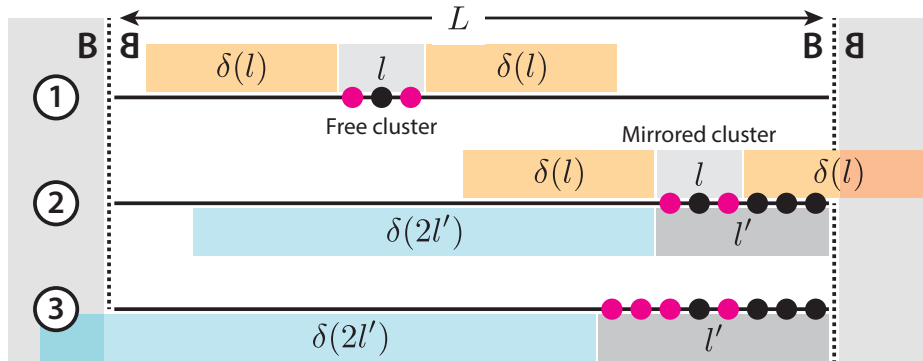


FIGURE 4.23 • Eroders on finite chains. Eroder property for a finite system with mirrored boundary conditions. Errors in the cluster I are marked red. Without loss of generality, I can be made contiguous by padding holes with additional errors (black). An explanation is given in the text of \clubsuit Section 4.C.

guaranteed to be eroded, see Figure 4.23 (2). We have the sufficient condition

$$(2Rm + 1)l' \leq L \Leftrightarrow l' \leq \frac{L}{2Rm + 1}. \quad 4.129$$

If we require instead

$$l + \delta(l) \leq \frac{L}{2Rm + 1} \Leftrightarrow l \leq \frac{L}{(2Rm + 1)(Rm + 1)}, \quad 4.130$$

this implies Eq. (4.129) for all critical lengths $l' < l + \delta(l)$ and Eq. (4.128) trivially. We conclude that with $a \equiv (2Rm + 1)^{-1}(Rm + 1)^{-1}$ any cluster of diameter $l \leq aL$ is eroded in finite time (linear in l). For $\overline{\text{TLV}}$ we find¹⁴¹ $a = 1/45 \approx 0.02$.

Note that if the interval $l' + \delta(2l')$ is larger than the system [Figure 4.23 (3)], it is possible that the cluster relaxes into non-uniform fixed points or non-trivial cycles. This is a consequence of the two mirrors which allow for the periodic reflection of messages in this “CA cavity.”

¹⁴¹This is an extremely conservative lower bound; $\overline{\text{TLV}}$ allows for much larger values of a as simulations suggest.

4.D Fixed Points

In addition to the two uniform fixed points (which are stable due to the eroder property), TLV-based automata can feature up to 4 unstable fixed points, depending on the boundary conditions imposed. As shown rigorously in [Section 4.E](#), these are no threat to the decoding capabilities because their occurrence in a Bernoulli random process is exponentially suppressed. For the sake of completeness, we discuss them in the following:

- *Infinite chain.* The original TLV features six fixed points [[327](#)]: The two uniform (stable) ones and, in addition, the four periodic (unstable) configurations shown in [Figure 4.24 \(b\)](#).
- *Semi-infinite chain with mirrored boundary.* A modified $\overrightarrow{\text{TLV}}$ with a single mirrored boundary features 2 of the 4 unstable fixed points of the infinite chain. Note that the first two patterns in [Figure 4.24 \(b\)](#) are not bond-inversion symmetric and therefore cannot be interpreted as a valid configuration on the semi-infinite chain. However, the latter two are bond-inversion symmetric if the mirror is placed such that the first cell is even. By contrast, if the cell next to the mirror is odd [[lower two patterns in Figure 4.24 \(c\)](#)], there are no additional fixed points.
- *Finite chain with periodic boundaries.* If TLV is placed on a closed ring of length $L \in 2\mathbb{N}$, potential fixed points can be used to construct periodic ones on the infinite chain. Since there are only the four depicted in [Figure 4.24 \(b\)](#), we have to check which of those remains invariant under periodic boundary conditions. As illustrated in [Figure 4.24 \(d\)](#), if L is a multiple of 4, all four fixed points in (b) can be transferred to the finite chain with PBCs. However, if $L \notin 4\mathbb{N}$, the two 4-periodic patterns are no longer invariant and only the two 2-periodic patterns survive (compare the yellow patterns on the left with the colored patterns on the right).
- *Finite chain and mirrored boundaries.* If TLV is placed on a chain of length $L \in 2\mathbb{N}$ with mirrored boundaries, we can infer from the semi-infinite case in [Figure 4.24 \(c\)](#) that only if the first (left) cell is even and the last (right) cell is odd, two additional fixed points survive. Otherwise the uniform configurations are the only ones, [Figure 4.24 \(e\)](#). This is the modification $\overrightarrow{\text{TLV}}$ we use throughout this chapter.

FIXED POINTS

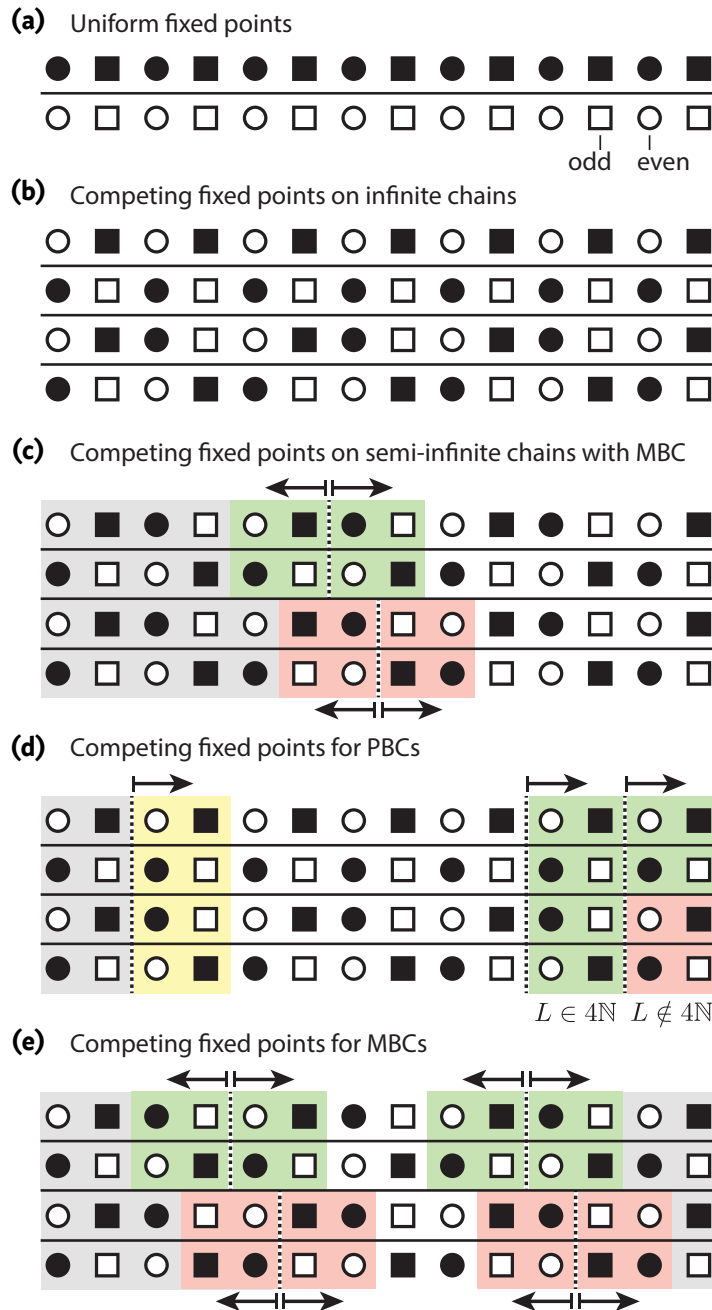


FIGURE 4.24 • Fixed points. (a) The uniform fixed points are always present and the only stable ones (due to the eroder property). Competing (unstable) fixed points are possible but depend on the boundary conditions: (b) Infinite chain (4 additional fixed points). (c) Semi-infinite chain with mirrored boundary condition (2 additional fixed points if the first cell is even, none otherwise). (d) Periodic boundary conditions (4 additional fixed points if L is a multiple of 4, 2 otherwise). (e) Mirrored boundary conditions (2 additional fixed points if the first cell is even and the last is odd, none otherwise).

None of the additional fixed points are relevant for the correction of Bernoulli random patterns because the probability of their occurrence is exponentially suppressed with L . This follows directly from the fact that there are no non-trivial preimages of these fixed points, i.e., their attractors are trivial: The only way to end up in one of them is that the noise gives rise to its pattern by chance. We checked this for finite chains of $\overline{\text{TLV}}$ by solving the corresponding systems of Boolean equations to determine all fixed points and their preimages.

4.E Sparse Errors and Correction Time

Here we prove a central statement of this chapter: The probability for a chain of length L , ruled by $\overline{\text{TLV}}$ with MBC to be in a non-empty state $\mathbf{x}(t) \neq \mathbf{0}$ after $t \propto L^\kappa$ time steps vanishes exponentially with L for arbitrary $\kappa > 0$ if the initial state is a Bernoulli random configuration with single-site error probability $p_0^\mathbf{x} < p_c^\mathbf{x}$ for some critical value $0 < p_c^\mathbf{x} \leq \frac{1}{2}$.

For convenience, we reproduce the definitions from Subsection 4.4.2: Let $\mathbf{x} \subseteq \mathbb{Z}$ be an arbitrary subset (error pattern). A finite subset $I \subseteq \mathbf{x}$ is called *cluster* of diameter $\|I\| = \max\{|x - y| \mid x, y \in I\}$. If we fix an integer $k > 0$ (the *sparseness parameter*, to be chosen later), the *territory* $T_k(I)$ is defined as the interval of integers with distance at most $k\|I\|$ from I . Two clusters I_1 and I_2 are called *independent* if at least one does not intersect the territory of the other, i.e., $I_2 \cap T_k(I_1) = \emptyset$ or $I_1 \cap T_k(I_2) = \emptyset$ (or both); since $I \subset T_k(I)$, this implies $I_1 \cap I_2 = \emptyset$. If there exists a partition of \mathbf{x} into a family $\mathcal{I} = \{I_a\}$ of pairwise independent clusters I_a , $\mathbf{x} = \bigcup_a I_a$, then \mathbf{x} is called *sparse*. A cluster $I \subseteq \mathbf{x}$ with $T_k(I) \cap \mathbf{x} = I$ is called *independent in \mathbf{x}* and we write $I \sqsubseteq \mathbf{x}$.

To state our first result, we need some additional terminology: First, $\mathcal{I}_{\leq l}$ denotes the family of clusters $I \in \mathcal{I}$ with diameter $\|I\| \leq l$ and $\mathbf{x} \setminus \mathcal{I}_{\leq l} \equiv \mathbf{x} \setminus \bigcup_{I \in \mathcal{I}_{\leq l}} I$ is the subset of sites for given \mathbf{x} that remains after cleaning all clusters of diameter at most l . Second, a (*infinite*) *mirrored* Bernoulli random configuration $\mathbf{x} \subseteq \mathbb{Z}$ is defined by the single-site probability $\Pr(x_i = 1) = p_0^\mathbf{x}$ for sites $i > 0$ and the mirror constraint $x_i = x_{1-i}$.

We can now state our main result (an adaptation of Theorem 4 in Ref. [351] for mirrored Bernoulli random configurations) which is also given in Subsection 4.4.2:

PROPOSITION 4.1: Cluster decomposition on infinite chains

Consider infinite mirrored Bernoulli random configurations \mathbf{x} with single-site probability $p_0^\mathbf{x}$. Let $k \in \mathbb{N}$ be a given sparseness parameter.

Then, for each instance \mathbf{x} , there exists a constructive family $\mathcal{I}^{\mathbf{x}}$ of pairwise independent clusters¹⁴² such that the probability of a site $i \in \mathbb{Z}$ to be in \mathbf{x} and remain uncovered by independent clusters of diameter l or less (write $\mathcal{I}_{\leq l}^{\mathbf{x}}$) is bounded from above by

$$\Pr(i \in \mathbf{x} \setminus \mathcal{I}_{\leq l}^{\mathbf{x}}) \leq \alpha^{l^\beta} \quad 4.131$$

for $\beta = \ln(2)/\ln(4k+3)$ (and therefore $0 < \beta < 1$) and $\alpha = (2k)(4k+3)\sqrt{p_0^{\mathbf{x}}}$. If we define the critical value

$$\tilde{p}_c^{\mathbf{x}} \equiv [(2k)(4k+3)]^{-2}, \quad 4.132$$

for $p_0^{\mathbf{x}} < \tilde{p}_c^{\mathbf{x}}$ it is $\alpha < 1$ and Eq. (4.131) becomes an exponentially decaying upper bound.

Proof. Let $\mathbf{x} \subseteq \mathbb{Z}$ be an arbitrary mirrored configuration. Fix the sparseness parameter $k \in \mathbb{N}$. We proceed stepwise:

- 1 *Construction of $\mathcal{I}^{\mathbf{x}}$.* Ignoring the inversion symmetry of \mathbf{x} , we construct the family of clusters $\mathcal{I}^{\mathbf{x}}$ recursively: Set $\mathcal{I}_0^{\mathbf{x}} \equiv \emptyset$ and $\mathcal{I}_{<l}^{\mathbf{x}} \equiv \bigcup_{0 \leq k < l} \mathcal{I}_k^{\mathbf{x}}$. Define $\mathcal{I}_l^{\mathbf{x}}$ ($l > 0$) as the family of all independent clusters $I \subseteq (\mathbf{x} \setminus \mathcal{I}_{<l}^{\mathbf{x}})$ of diameter $\|I\| = l$; i.e., I consists of errors in \mathbf{x} that do not belong to already defined smaller clusters and I is independent in \mathbf{x} after deleting all these smaller clusters. The construction of $\mathcal{I}_l^{\mathbf{x}}$ is well-defined because two different clusters I_1 and I_2 of diameter l cannot intersect due to $T_k(I_a) \cap (\mathbf{x} \setminus \mathcal{I}_{<l}^{\mathbf{x}}) = I_a$, $a = 1, 2$ (note that a cluster I_a can be thought of as an interval of length l with “holes” away from the edges). Then we define $\mathcal{I}^{\mathbf{x}} \equiv \bigcup_l \mathcal{I}_l^{\mathbf{x}}$.
- 2 *Independence of $\mathcal{I}^{\mathbf{x}}$.* We show that distinct clusters in $\mathcal{I}^{\mathbf{x}}$ are pairwise independent by construction.

Since being independent is an *asymmetric* relation between two clusters of unequal diameter (if $\|I_1\| \geq \|I_2\|$, then $I_2 \cap T_k(I_1) = \emptyset \Rightarrow I_1 \cap T_k(I_2) = \emptyset$ and it is enough to check for $I_1 \cap T_k(I_2) = \emptyset$), it is sufficient to check that (1) all equal-sized clusters in $\mathcal{I}_l^{\mathbf{x}}$ are pairwise independent and (2) they do not intersect the territories of the smaller clusters in $\mathcal{I}_{<l}^{\mathbf{x}}$.

- (1) follows immediately from the well-defined construction of $\mathcal{I}_l^{\mathbf{x}}$ (see previous paragraph).
- (2) follows because $I \in \mathcal{I}_l^{\mathbf{x}}$ belongs to $\mathbf{x} \setminus \mathcal{I}_{<l'}^{\mathbf{x}}$ for all $l' < l$ and hence $I' \cap I = \emptyset$ for all $I' \in \mathcal{I}_{<l'}^{\mathbf{x}}$. Since I' was chosen independent from all other elements in $\mathbf{x} \setminus \mathcal{I}_{<l'}^{\mathbf{x}}$, it follows that $T_k(I') \cap I = \emptyset$, i.e., I' and I are independent.

¹⁴²It is not necessarily $\mathbf{x} = \bigcup_{I \in \mathcal{I}^{\mathbf{x}}} I$, i.e., \mathbf{x} does not have to be sparse.

- 3** *Completeness of \mathcal{J}^x .* Here we show that the constructed \mathcal{J}^x is complete in the sense that

$$i \in \mathbf{x} \setminus \mathcal{J}_{\leq l}^x \Rightarrow \forall I \sqsubseteq (\mathbf{x} \setminus \mathcal{J}_{< l}^x), \|I\| \leq l : i \notin I \quad 4.133$$

which we will use in step 4 below.

Eq. (4.133) is a bit subtle because only

$$i \in \mathbf{x} \setminus \mathcal{J}_{\leq l}^x \Rightarrow \forall I \sqsubseteq (\mathbf{x} \setminus \mathcal{J}_{< l}^x), \|I\| = l : i \notin I \quad 4.134$$

follows trivially from the construction of \mathcal{J}_l^x (see step 1 above). To prove Eq. (4.133), we show that $\forall I \sqsubseteq (\mathbf{x} \setminus \mathcal{J}_{< l}^x) : \|I\| \geq l$, i.e., our construction never recreates clusters of smaller diameter¹⁴³:

Assume $\exists I^* \sqsubseteq (\mathbf{x} \setminus \mathcal{J}_{< l}^x) : \|I^*\| = l^* < l$. It must have been $T_k(I^*) \cap (\mathbf{x} \setminus \mathcal{J}_{< l^*}^x) \supset I^*$ because otherwise our prescription demands $I^* \in \mathcal{J}_{l^*}^x$ and we had $I^* \cap (\mathbf{x} \setminus \mathcal{J}_{< l}^x) = \emptyset$. Since $T_k(I^*) \cap (\mathbf{x} \setminus \mathcal{J}_{< l}^x) = I^*$ by assumption, there must have been a cluster $\tilde{I} \in \mathcal{J}_{\tilde{l}}^x$ with $l^* \leq \tilde{l} < l$ and $T_k(I^*) \cap \tilde{I} \neq \emptyset$. But because $\|\tilde{I}\| \geq \|I^*\|$, this implies $T_k(\tilde{I}) \cap I^* \neq \emptyset$. Since $I^* \not\subseteq \tilde{I}$ and $I^* \subseteq \mathbf{x} \setminus \mathcal{J}_{< \tilde{l}}^x$, this contradicts the independence of \tilde{I} in $\mathbf{x} \setminus \mathcal{J}_{< \tilde{l}}^x$ and we are done.

- 4** *Explanation trees.* Clearly $(\mathbf{x} \setminus \mathcal{J}_{\leq l}^x) \subseteq (\mathbf{x} \setminus \mathcal{J}_{< l}^x)$, i.e., fewer and fewer errors in \mathbf{x} survive with increasing l because on each level additional clusters are deleted from \mathbf{x} . This monotonicity holds also for all monotonic sequences $(l_n) \in \mathbb{N}^{\mathbb{N}}$ with $l_n > l_{n-1}$ for all $n \in \mathbb{N}$: $(\mathbf{x} \setminus \mathcal{J}_{\leq l_n}^x) \subseteq (\mathbf{x} \setminus \mathcal{J}_{\leq l_{n-1}}^x)$. In the end, we aim to upper bound the probability of an arbitrary site $i \in \mathbb{Z}$ to belong to $\mathbf{x} \setminus \mathcal{J}_{\leq l}^x$. We first prove this for $\mathbf{x} \setminus \mathcal{J}_{\leq l_n}^x$ instead, where (l_n) will be specified below, and generalize our result (with some tradeoff) to $l_n = n$ in the next (and last) step 5.

For the sake of simplicity, let l_n be an odd integer for $n \geq 1$ and define $l_0 \equiv 0$ in the following. To bound the probability for $i \in \mathbf{x} \setminus \mathcal{J}_{\leq l_n}^x$ from above, we start with a trivially true, *sufficient* condition: For an arbitrary configuration \mathbf{y} with $i \in \mathbf{y}$, we have ($n \geq 1$)

$$\begin{aligned} \forall j \in \mathbf{y} : |i - j| \leq \frac{l_n}{2} \vee |i - j| > \left(k + \frac{1}{2}\right) l_n \\ \Rightarrow \exists I^* \sqsubseteq \mathbf{y}, \|I^*\| \leq l_n : i \in I^* \end{aligned} \quad 4.135$$

(I^* includes all $j \in \mathbf{y}$ with $|i - j| \leq \frac{l_n}{2}$; the strict “ $>$ ” becomes important only for *even* l_n).

¹⁴³In principle, this could happen because we are successively deleting clusters.

The (equivalent) contraposition reads

$$\begin{aligned} & \forall I \subseteq y, \|I\| \leq l_n : i \notin I \\ \Rightarrow & \exists j^* \in y : \frac{l_n}{2} < |i - j^*| \leq \left(k + \frac{1}{2}\right) l_n. \end{aligned} \quad 4.136$$

If we now set $y = \mathbf{x} \setminus \mathcal{J}_{\leq l_{n-1}}^{\mathbf{x}} = \mathbf{x} \setminus \mathcal{J}_{\leq l_n}^{\mathbf{x}}$ and use Eq. (4.133) with $l = l_n$ (this is the crucial step that exploits the structure of $\mathcal{J}^{\mathbf{x}}$), we end up with the sequence of implications

$$\begin{aligned} & i \in \mathbf{x} \setminus \mathcal{J}_{\leq l_n}^{\mathbf{x}} \\ \Rightarrow & \forall I \subseteq (\mathbf{x} \setminus \mathcal{J}_{\leq l_n}^{\mathbf{x}}), \|I\| \leq l_n : i \notin I \end{aligned} \quad 4.137a$$

$$\Rightarrow \exists j^* \in \mathbf{x} \setminus \mathcal{J}_{\leq l_{n-1}}^{\mathbf{x}} : \frac{l_n}{2} < |i - j^*| \leq \left(k + \frac{1}{2}\right) l_n \quad 4.137b$$

$$\Rightarrow \exists j^* \in \mathbf{x} \setminus \mathcal{J}_{\leq l_{n-1}}^{\mathbf{x}} : \frac{l_n}{2} < |i - j^*| \leq \left(k + \frac{1}{2}\right) l_n \quad 4.137c$$

where we used $\mathbf{x} \setminus \mathcal{J}_{\leq l_{n-1}}^{\mathbf{x}} \subseteq \mathbf{x} \setminus \mathcal{J}_{\leq l_{n-1}}^{\mathbf{x}}$ (since $l_{n-1} \leq l_n - 1$) in the last line; this is illustrated in Figure 4.25 (a). In combination with $i \in \mathbf{x} \setminus \mathcal{J}_{\leq l_n}^{\mathbf{x}} \Rightarrow i \in \mathbf{x} \setminus \mathcal{J}_{\leq l_{n-1}}^{\mathbf{x}}$, Eq. (4.137c) gives rise to a binary tree of depth n (with sites as vertices) that explains the existence of $i \in \mathbf{x} \setminus \mathcal{J}_{\leq l_n}^{\mathbf{x}}$ at its root if the sites at all its leafs belong to $\mathbf{x} \setminus \mathcal{J}_{\leq 0}^{\mathbf{x}} = \mathbf{x}$; it is aptly called *explanation tree* (ET) [352]. An example is shown in Figure 4.25 (b).

By counting possible ETs and calculating their probability of being realized based on the (mirrored) Bernoulli distribution on their leafs, it is possible to upper bound the probability for $i \in \mathbf{x} \setminus \mathcal{J}_{\leq l_n}^{\mathbf{x}}$ because the existence of at least one realized explanation tree is a *necessary* condition. Counting explanation trees and computing their probability (by counting their leafs) is complicated by the fact that for arbitrary $l_n > l_{n-1} > l_{n-2} > \dots > l_0$ the allowed ranges for j^* on different levels n intersect. Therefore the number of leafs is not fixed and only bounded from above by 2^n (reducing the number of leafs can be achieved by “reusing” a site to explain more than one other site). This complicates the derivation of the probability for the existence of a realized explanation tree considerably. If, by contrast, (l_n) is chosen so that different subtrees cannot intersect, the number of leafs for any ET is fixed at 2^n . This can be guaranteed if on each level $1 \leq m \leq n$ the distance between any site i and its explanatory site j^* is larger than the maximum width of the subtrees emanating from each of them. Formally,

$$\frac{l_m}{2} \geq 2 \left(k + \frac{1}{2}\right) \sum_{k=1}^{m-1} l_k \quad 4.138$$

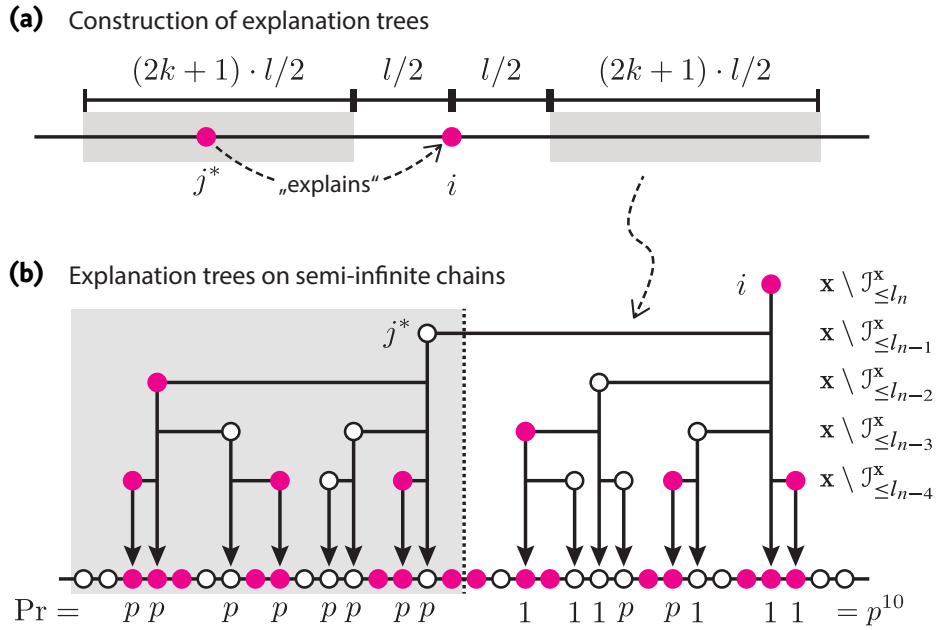


FIGURE 4.25 • Explanation trees. (a) Illustration of the implication in Eq. (4.137b): An element $i \in \mathbf{x} \setminus \mathcal{J}_{\leq l}^{\mathbf{x}}$ requires the existence of another element $j^* \in \mathbf{x} \setminus \mathcal{J}_{\leq l-1}^{\mathbf{x}}$ in a specific range given by k and \bar{l} . (b) Explanation tree on the semi-infinite chain with mirrored boundary condition. Cells in state 0 (1) are marked white (red). The probability to realize the shown explanation tree by a mirrored Bernoulli process with rate $p = p_0^{\mathbf{x}}$ is labeled by Pr . Note that the shown error pattern (red) *fails* to realize this explanation tree (arrows) since some explanatory sites are empty. Details are given in step 4 of the proof of Proposition 4.1 in \S Section 4.E.

where a factor of 2 is necessary because *two* subtrees (one at i and one at j^*) grow independently. Equating both sides yields the tightest solution via the recursion

$$l_{m+1} = 4 \left(k + \frac{1}{2} \right) \sum_{k=1}^m l_k \tag{4.139a}$$

$$= 4 \left(k + \frac{1}{2} \right) l_m + l_m = (4k + 3)l_m \tag{4.139b}$$

which is solved by

$$l_m = (4k + 3)^{m-1} \tag{4.140}$$

with $l_1 = 1$.

Let N_n denote the number of possible ETs of depth n (i.e., the number of ETs that can explain $i \in \mathbf{x} \setminus \mathcal{J}_{\leq l_n}^{\mathbf{x}}$, all of which are *realized* in the completely filled state $\mathbf{x} = \mathbf{1}$). It holds recursively that $N_m \leq 2kl_m N_{m-1}^2$ for all $1 \leq m \leq n^{144}$.

¹⁴⁴For non-overlapping trees, this is an equality.

One factor, N_{m-1} , counts the possible subtrees attached to i while another factor, $2kl_m N_{m-1}$, counts the possible positions for the new root j^* [$2kl_m$, recall Eq. (4.137c)] and the possible subtrees attached to this root (N_{m-1}). Clearly

$$\log N_m \leq a(m-1) + b + 2 \log N_{m-1} \quad 4.141$$

with $a = \log(4k+3) > 0$ and $b = \log(2k) > 0$ for our specific choice of l_m in Eq. (4.140). An upper bound on $\log N_m$ can be found by solving the corresponding *equality* which corresponds to the affine recursion of two sequences

$$\begin{bmatrix} g_m \\ f_m \end{bmatrix} = \begin{bmatrix} 2 & a \\ 0 & 1 \end{bmatrix} \cdot \begin{bmatrix} g_{m-1} \\ f_{m-1} \end{bmatrix} + \begin{bmatrix} b \\ 1 \end{bmatrix} \quad 4.142$$

with $g_m = \log N_m$ and $f_m = m$ and initial conditions $g_0 = 0 = f_0$ ($N_0 = 1$). Diagonalization of the matrix yields

$$\begin{bmatrix} \chi_m \\ \varphi_m \end{bmatrix} = \begin{bmatrix} 2 & 0 \\ 0 & 1 \end{bmatrix} \cdot \begin{bmatrix} \chi_{m-1} \\ \varphi_{m-1} \end{bmatrix} + \begin{bmatrix} a+b \\ \sqrt{1+a^2} \end{bmatrix} \quad 4.143$$

with $\chi_m = af_m + g_m$ and $\varphi_m = \sqrt{1+a^2}f_m$. Now we can use that recursions of the form $X_n = AX_{n-1} + B$ are generically solved by

$$X_n = X_0 A^n + B \frac{1-A^n}{1-A} \quad \text{for } A \neq 1 \quad 4.144$$

and $X_n = X_0 + Bn$ for $A = 1$. With the initial conditions, we find immediately $\varphi_m = \sqrt{1+a^2}m$ and $\chi_m = (2^m - 1)(a+b)$. Transforming χ_m and φ_m back into g_m and f_m yields the result $f_m = m$ and

$$g_m = (2^m - 1)(a+b) - am \quad 4.145$$

which is the solution of the recursive *equality* in Eq. (4.141). It is automatically an upper bound, thus

$$N_m \leq \exp[(2^m - 1)(a+b) - am] \leq \exp[2^m(a+b)] \quad 4.146$$

and we find $N_m \leq [(2k)(4k+3)]^{2^m}$ with $e^{a+b} = (2k)(4k+3)$.

Now comes the only step where we use the mirror symmetry of the Bernoulli configuration \mathbf{x} : The probability for all 2^n leafs of a particular ET to be occupied is $(p_0^x)^{2^n}$ for sites that are *independent* Bernoulli random variables. The mirror symmetry, however, introduces perfect correlations between pairs of sites. Since all leafs are distinct sites (on \mathbb{Z}) there are at least $2^n/2$ independent Bernoulli random variables associated to an ET (the worst case being a completely mirror-symmetric explanation tree). Therefore the probability for an arbitrary ET to be realized is bounded from above by $\sqrt{p_0^x}^{2^n}$

(as compared to $(p_0^x)^{2^n}$ in systems without mirror symmetry). This reflects the fact that mirrors “enlarge” error clusters artificially by their mirror images. This is illustrated in Figure 4.25 (b).

In conclusion, we find an upper bound

$$\Pr(i \in \mathbf{x} \setminus \mathcal{J}_{\leq l_n}^{\mathbf{x}}) \leq N_n \sqrt{p_0^x}^{2^n} \leq \left[(2k)(4k+3) \sqrt{p_0^x} \right]^{2^n} \quad 4.147$$

for an arbitrary site $i \in \mathbb{Z}$ to be in \mathbf{x} but uncovered by clusters up to diameter l_n of the constructive family $\mathcal{J}^{\mathbf{x}}$. This follows from the subadditivity of probability measures and the statement that $i \in \mathbf{x} \setminus \mathcal{J}_{\leq l_n}^{\mathbf{x}}$ if there is *at least* one of N_n possible ETs realized by \mathbf{x} .

If we define $(2k)(4k+3)\sqrt{\tilde{p}_c^x} = 1 \Leftrightarrow \tilde{p}_c^x \equiv [(2k)(4k+3)]^{-2}$, it follows with $\alpha \equiv (2k)(4k+3)\sqrt{p_0^x}$

$$\Pr(i \in \mathbf{x} \setminus \mathcal{J}_{\leq l_n}^{\mathbf{x}}) \leq \alpha^{2^n}. \quad 4.148$$

For on-site probabilities $p_0^x < \tilde{p}_c^x \Leftrightarrow \alpha < 1$, this leads to a *double-exponential* decay of the probability to remain uncovered on level l_n .

- 5** *Upper bound.* Above we showed that $\Pr(i \in \mathbf{x} \setminus \mathcal{J}_{\leq l_n}^{\mathbf{x}}) \leq \alpha^{2^n}$ with $l_n = (4k+3)^{n-1}$. The double-exponential decay of the probability with n and the exponential growth of the level l_n suggest that there is an exponentially decaying upper bound with l^{145} .

Indeed, if we use the monotonicity

$$\Pr(i \in \mathbf{x} \setminus \mathcal{J}_{\leq l}^{\mathbf{x}}) \leq \Pr(i \in \mathbf{x} \setminus \mathcal{J}_{\leq l-1}^{\mathbf{x}}), \quad 4.149$$

it follows that

$$\Pr(i \in \mathbf{x} \setminus \mathcal{J}_{\leq l}^{\mathbf{x}}) \leq \alpha^{l^\beta} \quad 4.150$$

if we require $\alpha^{l^\beta} \stackrel{!}{=} \alpha^{2^{n-1}}$ for $\beta > 0$, because for $l \in [l_{n-1}, l_n]$ we know that

$$\Pr(i \in \mathbf{x} \setminus \mathcal{J}_{\leq l}^{\mathbf{x}}) \leq \alpha^{2^{n-1}} \quad \text{and} \quad \alpha^{2^{n-1}} \leq \alpha^{l^\beta} \quad 4.151$$

per construction (because $\alpha < 1$).

This determines β via $(4k+3)^{\beta(n-1)} \stackrel{!}{=} 2^{n-1}$, i.e.,

$$\beta = \frac{\ln(2)}{\ln(4k+3)} < 1. \quad 4.152$$

This concludes the proof. ■

¹⁴⁵Recall that our choice of l_n was technically motivated: it is easier to count the leafs of ETs if their branches do not intersect.

Note that for $p_0^x > \tilde{p}_c^x$ the upper bounds become trivial which still allows for an exponential decay of $\Pr(i \in \mathbf{x} \setminus \mathcal{I}_{\leq l}^x)$. Therefore we conclude that there is a critical value p_c^x with $0 < \tilde{p}_c^x \leq p_c^x$ such that $\Pr(i \in \mathbf{x} \setminus \mathcal{I}_{\leq l}^x)$ vanishes exponentially for $l \rightarrow \infty$ if $p_0^x < p_c^x$. Simulations suggest that $p_c^x = \frac{1}{2}$ so that $\tilde{p}_c^x \ll 1$ is a rather weak lower bound on the true critical value, see \clubsuit Section 4.F.

Eventually we want to employ Proposition 4.1 to derive an upper bound for the probability of errors to survive the first t steps of $\overrightarrow{\text{TLV}}$ on a *finite* chain with mirrored boundaries. To this end, we first need a consequence of Proposition 4.1:

LEMMA 4.2: Cleaning of semi-infinite chains

Consider a semi-infinite chain on $\mathcal{L} = \mathbb{N}$ governed by $\overrightarrow{\text{TLV}}_{\mathcal{L}}$ with initial configurations $\mathbf{x}(0) \subseteq \mathcal{L}$ drawn from a Bernoulli distribution with parameter p_0^x . Let $\mathcal{J} \subset \mathcal{L}$ be an arbitrary finite interval on the chain.

Then the probability of $\mathbf{x}(t) = \overrightarrow{\text{TLV}}_{\mathcal{L}}^t(\mathbf{x}(0))$ to be non-empty on \mathcal{J} is bounded from above by

$$\Pr(\mathbf{x}(t) \cap \mathcal{J} \neq \emptyset) \leq (2tR + |\mathcal{J}|) \exp\left(-\gamma \lfloor t/m \rfloor^\beta\right) \tag{4.153}$$

with $\gamma = -\log(\alpha)$ ($\gamma > 0$ for $p_0^x < \tilde{p}_c^x$), and $0 < \beta < 1$ as in Proposition 4.1. Here the sparseness parameter is given by $k = 2Rm = 8$ where $m = 1$ and $R = 4$ are the eroder parameter and the radius of $\overrightarrow{\text{TLV}}$, respectively.

Proof. Because $\overrightarrow{\text{TLV}}$ is an eroder, there is a constant m such that any cluster of errors I on a background of zeros is erased for $t \geq m\|I\|$. During this process, signals emitted beyond the boundaries of I can at most travel $Rm\|I\|$ sites where R is the radius of the local rules (or the propagation speed of information). If we set $k = 2Rm$ as sparseness parameter, an error cluster $I \subseteq \mathbf{x}(0)$ that is independent in $\mathbf{x}(0)$, is safely erased after at most $m\|I\|$ time steps without interfering with its environment. This follows because signals from I and $\mathbf{x}(0) \setminus I$ can meet only after traversing the void territory $T_k(I) \setminus I$ which takes at least $k\|I\|/(2R) = m\|I\|$ time steps—but the last trace of I is erased after $m\|I\|$ time steps. Therefore the evolution of $\mathbf{x}(t)$ for $t \geq m\|I\|$ is completely independent of the configuration within the boundaries of I (this motivates the notion of *independent* clusters). See Figure 4.14 in Subsection 4.4.2 for an illustration.

If $\mathbf{x}(0)$ is a mirrored Bernoulli random configuration with parameter $p_0^x < \tilde{p}_c^x$ with k set as above, we know from Proposition 4.1 that the probability of any site $i \in \mathbb{N}$ to be uncovered by clusters in $\mathcal{I}^{\mathbf{x}(0)}$ of diameter at most l is bounded from above by

$$\Pr(i \in \mathbf{x}(0) \setminus \mathcal{I}_{\leq l}^{\mathbf{x}(0)}) \leq \alpha^{l^\beta} \tag{4.154}$$

with $0 < \alpha, \beta < 1$. By subadditivity, an analogous bound holds for any finite subset $J \subset \mathbb{N}$,

$$\Pr \left(J \cap \left(\mathbf{x}(0) \setminus \mathcal{J}_{\leq l}^{\mathbf{x}(0)} \right) \neq \emptyset \right) \leq |J| \alpha^{l^\beta}. \quad 4.155$$

Let $U_r(\mathcal{J})$ be the interval of all sites within distance $r \geq 0$ from \mathcal{J} and set $J = U_{tR}(\mathcal{J})$ for time $t \geq 0$. Then

$$\Pr \left(U_{tR}(\mathcal{J}) \cap \left(\mathbf{x}(0) \setminus \mathcal{J}_{\leq l}^{\mathbf{x}(0)} \right) \neq \emptyset \right) \leq (2tR + |\mathcal{J}|) \alpha^{l^\beta}. \quad 4.156$$

This holds for all $l \in \mathbb{N}$, especially for $l = \lfloor t/m \rfloor$ ($\lfloor \bullet \rfloor$ is the floor function):

$$\Pr \left(U_{tR}(\mathcal{J}) \cap \left(\mathbf{x}(0) \setminus \mathcal{J}_{\leq \lfloor t/m \rfloor}^{\mathbf{x}(0)} \right) \neq \emptyset \right) \leq (2tR + |\mathcal{J}|) \alpha^{\lfloor t/m \rfloor^\beta} \quad 4.157$$

If we exploit that no signal from outside $U_{tR}(\mathcal{J})$ can reach \mathcal{J} up to time t and that all errors that belong to independent clusters of diameter $l \leq \lfloor t/m \rfloor \leq t/m$ are erased at time t , we can conclude that

$$\begin{aligned} U_{tR}(\mathcal{J}) \cap \left(\mathbf{x}(0) \setminus \mathcal{J}_{\leq \lfloor t/m \rfloor}^{\mathbf{x}(0)} \right) &= \emptyset \\ \Rightarrow \mathbf{x}(t) \cap \mathcal{J} &= \emptyset \end{aligned} \quad 4.158$$

and consequently

$$\Pr(\mathbf{x}(t) \cap \mathcal{J} \neq \emptyset) \leq \Pr \left(U_{tR}(\mathcal{J}) \cap \left(\mathbf{x}(0) \setminus \mathcal{J}_{\leq \lfloor t/m \rfloor}^{\mathbf{x}(0)} \right) \neq \emptyset \right). \quad 4.159$$

Therefore we find

$$\Pr(\mathbf{x}(t) \cap \mathcal{J} \neq \emptyset) \leq (2tR + |\mathcal{J}|) \alpha^{\lfloor t/m \rfloor^\beta}. \quad 4.160$$

If we define $\gamma = -\log(\alpha)$ (with $\gamma > 0$ for $p_0^x < \tilde{p}_c^x$), it follows

$$\Pr(\mathbf{x}(t) \cap \mathcal{J} \neq \emptyset) \leq (2tR + |\mathcal{J}|) \exp \left(-\gamma \lfloor t/m \rfloor^\beta \right) \quad 4.161$$

and we are done. ■

With Lemma 4.2, we are ready to tackle the case of *finite* chains:

LEMMA 4.3: Cleaning of finite chains

Consider a finite chain of length L on $\mathcal{L} = \{1, \dots, L\}$ governed by $\overline{\text{TLV}}$ with mirrored boundaries and initial configurations $\mathbf{x}(0) \subseteq \mathcal{L}$ drawn from a Bernoulli distribution with parameter p_0^* .

Then the probability of $\mathbf{x}(t) = \overline{\text{TLV}}_x^t(\mathbf{x}(0))$ to be non-empty is bounded from above by

$$\Pr(\mathbf{x}(t) \neq \emptyset) \leq (4R \lfloor t \rfloor + L) \exp\left(-\gamma \lfloor t \rfloor / m\right)^\beta \quad 4.162$$

with $\lfloor t \rfloor \equiv \min\{t, t_L^*\}$ and $t_L^* = \lfloor L/2R \rfloor$. The parameters are the same as in Proposition 4.1 and Lemma 4.2.

Proof. Let $\mathbf{x}_0 = \mathbf{x}(0) \subseteq \mathbb{Z} \cap [1, L]$ be an arbitrary configuration of length L and $\mathbf{y}_0 = \mathbf{y}(0) \subset \mathbb{Z} \cap [L+1, \infty)$ another arbitrary, half-infinite configuration. Denote by $\mathbf{x}_0 \mathbf{y}_0 = \mathbf{x}_0 \cup \mathbf{y}_0$ the extension of the finite chain \mathbf{x}_0 by \mathbf{y}_0 to a half-infinite chain. If we write $\bar{\mathbf{x}}(t) = \overline{\text{TLV}}_{[1, L]}^t(\mathbf{x}_0)$ and $\vec{\mathbf{x}}(t) \mathbf{y}(t) = \overline{\text{TLV}}_{\mathbb{N}}^t(\mathbf{x}_0 \mathbf{y}_0)$, it is clear that (L even)

$$\bar{x}_i(t) = \vec{x}_i(t) \quad \text{for } 1 \leq i \leq \frac{L}{2}, \quad 0 \leq t \leq t_L^* \quad 4.163$$

with $t_L^* = \lfloor L/2R \rfloor$ due to the finite speed R of information transfer. To put it in a nutshell: the leftmost half of a finite chain evolves exactly like the corresponding section of a half-infinite chain adjacent to the mirrored boundary for $t \leq t_L^*$. This is obvious because these sites cannot be influenced by the existence/non-existence of the rightmost boundary as long as it does not enter their past light cone (which happens at $t \sim L/2R$ or later). If we combine this with the fact that, for Bernoulli distributed initial states, \mathbf{x}_0 and \mathbf{y}_0 are uncorrelated, it follows immediately that all results on $\overline{\text{TLV}}$ hold also for $\overline{\text{TLV}}$ as long as only times $t \leq t_L^*$ and sites in $[1, L/2]$ are concerned.

In particular, Lemma 4.2 tells us that

$$\Pr(\bar{\mathbf{x}}(t) \cap [1, L/2] \neq \emptyset) \leq (2tR + L/2) \exp\left(-\gamma \lfloor t/m \rfloor^\beta\right) \quad 4.164$$

for $t \leq t_L^*$. On account of the reflection symmetry of TLV , all statements hold also for the rightmost half $[L/2 + 1, L]$ with a mirrored boundary to the right (then with a reflected, half-infinite set of rules $\overleftarrow{\text{TLV}}$). Therefore subadditivity yields

$$\Pr(\bar{\mathbf{x}}(t) \neq \emptyset) \leq (4tR + L) \exp\left(-\gamma \lfloor t/m \rfloor^\beta\right) \quad 4.165$$

for $t \leq t_L^*$.

Here comes the crucial step: Since the chain is *finite* and $\bar{x} = \emptyset$ is a fixed point of $\overline{\text{TLV}}$, it is $\bar{x}(t_L^*) = \emptyset \Rightarrow \bar{x}(t) = \emptyset$ for all $t \geq t_L^*$. It follows that

$$\Pr(\bar{x}(t) \neq \emptyset) \leq \Pr(\bar{x}(t_L^*) \neq \emptyset) \quad 4.166$$

for $t \geq t_L^*$. This leads to

$$\Pr(\bar{x}(t) \neq \emptyset) \leq (4R \{t\} + L) \exp\left(-\gamma \lfloor \{t\}/m \rfloor^\beta\right) \quad 4.167$$

with $\{t\} \equiv \min\{t, t_L^*\}$ for all $t \geq 0$. ■

Note that the lower-bounded decay of the probability is to be expected for a *finite* system: Due to the finite state space, there is an upper bound for t (depending on L) such that the system either (1) relaxed to the clean state, (2) to a non-clean fixed point, or (3) entered a non-trivial cycle. In the first case, it is clean forever, whereas in the latter two cases, it can never become clean. Therefore the probability to be not clean cannot decrease arbitrarily and must be bounded from below for fixed L and $t \rightarrow \infty$.

However, if we are interested in the thermodynamic limit, $L \rightarrow \infty$, we can ask how long one has to wait for $\overline{\text{TLV}}$ to clean the system almost surely. This leads us to our main result:

COROLLARY 4.1: Scaling of cleaning times

Consider a finite chain of length L on $\mathcal{L} = \{1, \dots, L\}$ governed by $\overline{\text{TLV}}$ with mirrored boundaries and initial configurations $\mathbf{x}(0) \subseteq \mathcal{L}$ drawn from a Bernoulli distribution with parameter p_0^* .

For $\kappa \in \mathbb{R}$ with $0 < \kappa < 1$, the probability of $\mathbf{x}(t) = \overline{\text{TLV}}_{\mathcal{L}}^t(\mathbf{x}(0))$ to be non-empty after

$$t_{\max}(L) \equiv \lfloor L^\kappa \rfloor \quad 4.168$$

time steps is bounded from above by

$$\Pr(\mathbf{x}(t_{\max}) \neq \emptyset) \leq (4R + 1) L \exp\left(-\gamma \lfloor L^\kappa/m \rfloor^\beta\right) \quad 4.169$$

for $L \geq L_R$ with $0 < L_R < \infty$ a R -dependent constant. For $p_0^* < \tilde{p}_c^*$ it follows that

$$\Pr(\mathbf{x}(t_{\max}(L)) \neq \emptyset) \rightarrow 0 \quad \text{for } L \rightarrow \infty \quad 4.170$$

exponentially fast. The parameters are the same as in Proposition 4.1 and Lemma 4.2.

Proof. Use the result of Lemma 4.3 with $t = t_{\max}(L) < t_L^*$ for $L > L_R$ where L_R is a finite R -dependent constant. Then

$$\{t_{\max}(L)\} = \min\{t_{\max}(L), t_L^*\} = t_{\max}(L) \quad 4.171$$

and we have

$$\Pr(\mathbf{x}(t_{\max}) \neq \emptyset) \leq (4R t_{\max} + L) \exp\left(-\gamma \lfloor t_{\max}/m \rfloor^\beta\right). \quad 4.172$$

If we use that $\lfloor \lfloor L^\kappa \rfloor / m \rfloor = \lfloor L^\kappa / m \rfloor$ (for $m \in \mathbb{N}$), this yields the final result

$$\begin{aligned} & \Pr(\mathbf{x}(t_{\max}) \neq \emptyset) \\ & \leq (4R \lfloor L^\kappa \rfloor + L) \exp\left(-\gamma \lfloor L^\kappa / m \rfloor^\beta\right) \end{aligned} \quad 4.173a$$

$$\leq (4R + 1) L \exp\left(-\gamma \lfloor L^\kappa / m \rfloor^\beta\right) \quad 4.173b$$

which vanishes for $L \rightarrow \infty$ for $\kappa, \beta > 0$ and $\gamma > 0$, i.e., if $p_0^\kappa < \tilde{p}_c^\kappa$. \blacksquare

Remarks

Note that one could get rid of the remaining floor function via

$$\lfloor L^\kappa / m \rfloor \geq L^\kappa / m - 1 \geq (1 - \varepsilon) L^\kappa / m \quad 4.174$$

where the last lower bound requires

$$\varepsilon L^\kappa / m \geq 1 \quad 4.175$$

which holds for all $\varepsilon > 0$ if $L > L_\varepsilon$ is large enough. Then, for $L > \max\{L_R, L_\varepsilon\}$, one finds

$$\Pr(\mathbf{x}(t_{\max}) \neq \emptyset) \leq (4R + 1) L \exp\left(-\gamma [(1 - \varepsilon)/m]^\beta L^{\kappa\beta}\right) \quad 4.176$$

which clearly vanishes exponentially fast for $L \rightarrow \infty$ if $0 < \varepsilon < 1$ and $\gamma, \kappa, \beta > 0$.

As a concluding remark, we note that the growth of t_{\max} with L can be much slower, namely (poly-)logarithmic,

$$t_{\max}(L) = \lfloor (\ln L)^\kappa \rfloor \quad 4.177$$

for large enough $\kappa > 0$. Indeed, the probability still vanishes for $L \rightarrow \infty$ (but now subexponentially),

$$\Pr(\mathbf{x}(t_{\max}) \neq \emptyset) \lesssim L \exp\left[-\tilde{\gamma} (\ln L)^{\kappa\beta}\right] \quad 4.178a$$

$$= L^{1-\tilde{\gamma}/\ln(L)^{1-\kappa\beta}} \longrightarrow 0 \quad \text{for } L \rightarrow \infty \quad 4.178b$$

if $\kappa\beta > 1 \Leftrightarrow \kappa > \beta^{-1} = \ln(4k + 3)/\ln(2)$ and for some $\tilde{\gamma} > 0$.

4.F Parameters

TLV is a linear eroder, i.e., clusters on a background of zeros/ones with diameter l are erased after at most ml time steps, where $m \in \mathbb{R}^+$ is a rule-specific constant:

$$t_{\text{dec}} \leq m \|I\| \tag{4.179}$$

for arbitrary (independent) clusters I . To determine m , it is easiest to simulate the evolution of uniform clusters of ones on a background of zeros for increasing diameter l . The monotonicity of TLV (holes in the initial cluster entail holes in the spacetime diagram) makes the inferred upper bound valid for arbitrary clusters.

In Figure 4.26 we show results for $0 \leq l \leq 25$. The exact results feature a 4-periodic structure which is related to the rules of radius $R = 4$. The most stringent upper bound reads

$$t_{\text{dec}} \leq \frac{3}{4} \cdot l + 1 \tag{4.180}$$

which does not exactly fit our needs of linearity (due to the affine offset, it can be recast into a purely linear upper bound for large enough l with slightly increased prefactor $\frac{3}{4} + \varepsilon$). For the sake of simplicity, we choose

$$t_{\text{dec}} \leq 1 \cdot l, \tag{4.181}$$

such that the eroder parameter becomes $m = 1$. Figure 4.26 confirms that this upper bound on t_{dec} is valid for all $l \geq 0$.

With Lemma 4.2, Proposition 4.1 and the radius $R = 4$ we find the (non-optimal) sparseness parameter $k = 2Rm = 8$, and the lower bound on p_c^x evaluates to

$$\tilde{p}_c^x = \frac{1}{[(2k)(4k + 3)]^2} \approx 3.2 \times 10^{-6}. \tag{4.182}$$

Note that this result does not convey any information on the true critical value p_c^x (below which successful decoding is possible) but that it is larger than the above value and therefore non-zero. In fact, simulations suggest that $p_c^x = \frac{1}{2}$ and \tilde{p}_c^x is only a weak lower bound¹⁴⁶.

¹⁴⁶This explains why there is no much sense in optimizing m slightly from $m = 1$ to $m = \frac{3}{4} + \varepsilon$.

PARAMETERS

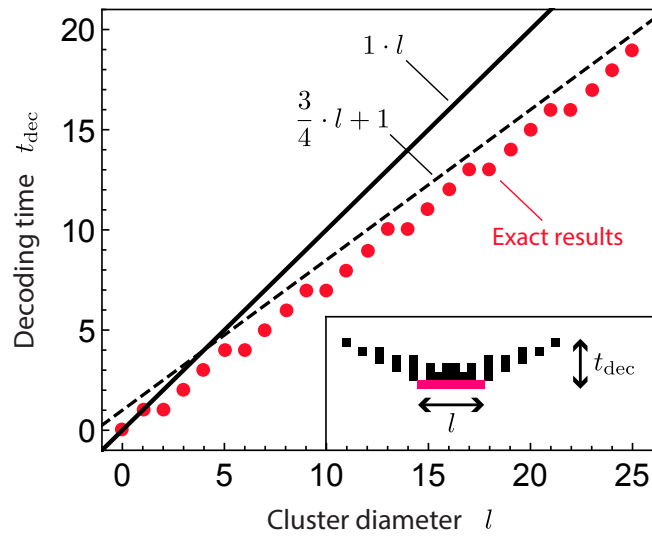


FIGURE 4.26 • Eroder parameter. Time t_{dec} needed by TLV to erase a uniform cluster of diameter l completely. The red bullets mark exact results from simulations, featuring a 4-periodic structure that derives from the rules of radius $R = 4$. The most stringent upper bound is given by $t_{\text{dec}} \leq \frac{3}{4} \cdot l + 1$ (dashed line) but we use $t_{\text{dec}} \leq 1 \cdot l$ (solid line) for the sake of simplicity (i.e., $m = 1$). These bounds are also valid for non-uniform clusters due to the monotonicity of TLV.

5

Miscellaneous

*“No-one knows the reason for all this,
but it is probably quantum.”*

— TERRY PRATCHETT
in Pyramids

This chapter is a safe haven for all projects that do not deserve their own chapter but are still interesting enough to be discussed somewhere. Some—mostly conceptual—are possible starting points for future projects, some are closely related to projects of the main part, and some are contributions to publications that were not covered so far.

This page is intentionally left blank.

There is no common theme to the projects covered in this chapter:

- In Section 5.1 we present an extended and pedagogically inclined discussion of the theoretical foundations of Ref. [4] about the “*Experimental realization of a symmetry protected topological phase of interacting bosons with Rydberg atoms.*”

We start from the fermionic Su–Schrieffer–Heeger (SSH) chain (known from Chapter 3) and then shift to its bosonic counterpart, i.e., a dimerized chain of interacting hard-core bosons (in the experiment realized as Rydberg excitations). We discuss the bosonic counterpart of the sublattice symmetry—which protects the topological phase of the fermionic model—and demonstrate that the former allows for perturbations that are forbidden for fermions (a counterintuitive feature that has been verified experimentally). We then review the general classification of interacting, symmetry-protected topological (SPT) phases in one dimension. An application to the bosonic SSH chain demonstrates that the experimentally realized ground state belongs to an SPT phase protected by particle number conservation and the bosonic counterpart of the sublattice symmetry. In the last part of this section, we explore the environment of the bosonic SSH chain in “theory space.” In particular, we discuss its relation to the famous Haldane phase of the spin-1 antiferromagnetic Heisenberg chain.

- In Section 5.2 we study a proposal by Kane *et al.* [357] for the construction of fractional quantum Hall states from coupled quantum wires of interacting fermions or bosons (which form a *Luttinger liquid*). The idea is to place a two-dimensional array of parallel quantum wires in a perpendicular magnetic field and add interactions between close-by wires to describe the strongly correlated quantum phases of fractional quantum Hall fluids in an anisotropic limit. In this limit, Luttinger liquid theory and the renormalization group provide powerful tools to gain insights that are hard to come by in the natural but isotropic setting of the fractional quantum Hall effect.

Here we focus on the *bosonic* fractional quantum Hall state with half-filled lowest Landau level (that is, a *Laughlin state*). We calculate the inter-wire density-density interactions needed to render a particular “Laughlin interaction” between the wires relevant. Here, “relevant” refers to the property of a perturbation to dominate the long-wavelength physics of a theory (“to flow to strong coupling” in renormalization group parlance). It is this particular perturbation that opens a gap in the bulk of the 2D array and drives the system into the Laughlin state. Unfortunately, there are other perturbations that compete with the “Laughlin interaction” and, if relevant, drive the system into other phases that we are not interested in. Using bosonization (a method to parametrize fermionic or bosonic quantum fields by bosonic phase- and density fields) in combination with first-order

renormalization group arguments, we show that there are parameter regimes where the “Laughlin interaction” dominates over its competitors and drives the system into the fractional quantum Hall regime.

- Section 5.3 is a spin-off from Chapter 3 where we utilized the symmetry-protected Su–Schrieffer–Heeger chain in its topological phase for the robust transfer of quantum information. We compared this approach with a “non-topological” competing arrangement that allows for quantum state transfer as well. This comparison prompts questions about the comparability of such setups: How can we, formally and objectively, quantify the performance of setups with respect to a given task?

To this end, we conceptualize a (still unpolished) framework to formalize the notions of *tasks*, *solutions* thereof, and the *performance* of the latter with respect to the former. We elaborate on classical mechanics and systems described by Hamiltonian functions to work out the details of our rather abstract concept. The basic idea is inspired by LEGO® Mindstorms: Assume two contestants are given a copy of the same base plate. The plates are empty except for a brick in one corner and a box in the opposite corner; this is the initial state. The target state is the same plate with the brick in the box. The state transformation between initial and target state formalizes the notion of a *task*. In a next step, each contestant is given a collection of LEGO® bricks (possibly including actuators, sensors and the like). Both contestants construct setups (*solutions*), using only the provided parts, with the goal to solve the given task. The winner of this contest solves the task with as few parts as possible. In this scenario, it is evident that a fair and sensible comparison of the solutions is only possible if both contestants are given the same parts. In Section 5.3 we formalize this insight, which eventually sheds light on the claims of Chapter 3 regarding the superiority of the topological SSH chain for quantum state transfer.

- Section 5.4 is the prequel to Chapter 4 where we studied the performance of a strictly local cellular automaton as decoder (or stabilizer) of the topological quantum code that arises as degenerate ground state space of the famous Majorana chain.

This project was preceded by a similar approach based on artificial neural networks (ANN) as decoders (instead of a cellular automaton): After a brief introduction to ANNs, specifically *convolutional* neural networks, we present and discuss the construction of such a network to decode the Majorana chain quantum code. The proposed network is rather unconventional as it does without long-range connections between neurons (known as “dense layers” in the ANN community). The motivation for this restriction stems from scalability issues that typically arise when *physical* systems host infinite-dimensional subsystems (entities that interact instantaneously with

arbitrarily remote counterparts). It is exactly this demand for locality that eventually led to the replacement of neural networks by cellular automata (which are the natural framework to describe the local dynamics of scalable systems). Nevertheless, we demonstrate in Section 5.4 that our ANN performs reasonably well as quantum decoder. We even skim *two* dimensions and train another ANN to mimic the (classical) self-correction of the Ising model (known in physics as spontaneous breaking of the \mathbb{Z}_2 spin-flip symmetry).

- Section 5.5 is the product of pure curiosity and essentially unrelated to the main part of this thesis: We start with a brief survey of quantum stabilizer codes, a particularly well-understood class of quantum codes that can be described in terms of abelian subgroups of the group generated by Pauli matrices. We then motivate the concept of “self-correcting quantum memories” which do not require active control to prevent the accumulation of errors (just like hard drives store *classical* information even when powered down). Recent results suggest that *if* there are (topological) stabilizer codes with these properties, they break translational invariance.

Motivated by this insight, we present a scheme to design two-dimensional stabilizer codes (defined on a square lattice) that are *aperiodic* by construction. We derive them from *Wang tiles*, a mathematical concept that allows for provably aperiodic tessellations of the Euclidean plane by square tiles with colored edges. The placement of these tiles is restricted by their edge colors (similar to dominoes where numbers of adjacent pieces must match up). By means of a particular set of Wang tiles (named *Culik tiles*), we demonstrate the construction of the corresponding stabilizer group which is generated by 13 types of local operators. Note that we make *no* claims about the structure of the codespace that comes with these “Wang stabilizers,” nor do we study the geometry of its logical operators.

- Section 5.6 is, in some sense, a sequel to Section 5.5. The reason is that geometry and size of logical operators that act on a codespace determine the robustness of the encoded qubits in the presence of uncorrelated, local noise. For stabilizer groups with an *extensive* codespace dimension—and the aperiodic “Wang stabilizers” of Section 5.5 are of this type—the evaluation of these geometric properties is a computationally non-trivial task. This makes it hard to decide whether such codes host qubits that are delocalized and potentially protected against local decoherence.

In Section 5.6, we discuss this problem first for the quantum case, which, in turn, motivates a *classical* counterpart that inherits the key complexity of the problem but lacks the intricacies of the quantum version. The problem reads as follows: Consider a classical Hamiltonian on a regular lattice with discrete degrees of freedom on the sites (think of an Ising-like Hamiltonian).

IN A NUTSHELL

Assume that this Hamiltonian has a symmetry group that is extensive, i.e., grows with the system size (a feature of gauge theories, for instance). The question is whether this symmetry group can be generated by *local* generators only. We formalize this problem and discuss possible approaches to assess its computational complexity.

5.1 Symmetry-Protected Topological Phase of Interacting Bosons with Rydberg Atoms

This is a brief survey of the theoretical basement that Ref. [4] is built upon. To draw profit from this section, it is advisable to be familiar with the message of this paper. Then, the following subsections can be read as an extended supplement on the theory with pedagogical emphasis:

In Subsection 5.1.1 we discuss the symmetries of the fermionic Su–Schrieffer–Heeger (SSH) model first in a many-body picture and then on the single-particle level. In Subsection 5.1.2 we use a Jordan-Wigner transformation to translate both the SSH Hamiltonian and its many-body symmetries into the bosonic spin language; we discuss consequences of the non-local nature of this transformation. In Subsection 5.1.3 we review the classification of interacting, symmetry-protected topological phases of one-dimensional spin systems with focus on its application to an SSH chain filled with hard-core bosons. Finally, in Subsection 5.1.4 we explore the environment of this model in “theory space”; in particular, we show how it smoothly connects to the Haldane phase.

5.1.1 Symmetries of the SSH Model

Here we discuss relevant symmetries of the SSH Hamiltonian [126]. We start with their many-body representation on the fermionic Fock space and subsequently derive their action on the first-quantized single-particle Hamiltonian to establish a connection with the Altland-Zirnbauer classification of random matrices [90–93] and the related classification of symmetry-protected topological phases of free fermions [21, 22, 95, 97].

Fermionic Many-Body Theory

The SSH Hamiltonian (Subsection 1.2.1) with fermions a_i and b_i , $i = 1, \dots, L$, is given by

$$H = J_1 \sum_{i=1}^L (a_i^\dagger b_i + b_i^\dagger a_i) + J_2 \sum_{i=1}^{L'} (b_i^\dagger a_{i+1} + a_{i+1}^\dagger b_i), \quad 5.1$$

where $L' = L - 1$ for open (OBC) and $L' = L$ for periodic boundary conditions (PBC). At $|J_1| = |J_2|$ the spectrum of (5.1) is gapless whereas for $|J_1| \geq |J_2|$ the ground state of H is in a gapped phase. For OBC, $|J_1| < |J_2|$ is a topological

phase with exponentially degenerate fermionic edge modes near the boundaries (for $J_1 = 0$, these are just $\tilde{c}_l = a_1$ and $\tilde{c}_r = b_L$). For PBC, the distinction between topological and trivial phase becomes arbitrary as it depends on the definition of the elementary cell, namely (a_i, b_i) or (b_i, a_{i+1}) . The transition from PBC to OBC requires a definite choice since cutting is only allowed between elementary cells. The Hamiltonian (5.1) acts naturally on the (many-body) fermionic Fock space \mathcal{H}_{2L}^f spanned by states $|n_1^a, n_1^b, \dots\rangle \equiv (a_1^\dagger)^{n_1^a} (b_1^\dagger)^{n_1^b} \dots |0\rangle$. Then, \mathcal{H}_{2L}^f forms a finite-dimensional representation of the fermion algebra $\{x_i, y_i^\dagger\} = \delta_{ij} \delta_{xy}$ for $x = a, b$.

The SSH Hamiltonian features several symmetries which, according to Wigner's theorem, are represented as *unitary* or *antiunitary* operators on \mathcal{H}_{2L}^f that commute with the Hamiltonian. These are...

- **Particle number conservation:** The abstract symmetry group is $U(1)$, a Lie group with one-dimensional Lie algebra $\mathfrak{u}(1) = \mathbb{R}$. The representation of the latter is defined by its generator on \mathcal{H}_{2L}^f , namely the particle number operator $N = \sum_{i,x} x_i^\dagger x_i$ which commutes with H . Exponentiation then yields the representation of $U(1)$ on \mathcal{H}_{2L}^f :

$$R_\phi \equiv e^{i\phi N} \quad \text{with} \quad [R_\phi, H] = 0 \quad \text{for all} \quad \phi \in [0, 2\pi). \quad 5.2$$

- **Time-reversal symmetry:** The abstract symmetry group is $\mathbb{Z}_2 = \{1, T\}$ with $T^2 = 1$, sometimes¹⁴⁷ written as \mathbb{Z}_2^T . Its generator T is represented *antiunitarily* on \mathcal{H}_{2L}^f , in our case as complex conjugation K , with $T x_i T^{-1} = x_i$ for $x = a, b$ and $T i T^{-1} = -i$. Then, H commutes with T as both couplings J_1 and J_2 are real. As an operator on \mathcal{H}_{2L}^f , we have

$$T = K \quad \text{with} \quad [T, H] = 0. \quad 5.3$$

- **Particle-hole symmetry:** The abstract symmetry group is again $\mathbb{Z}_2 = \{1, C\}$ with $C^2 = 1$. It is represented *unitarily* on \mathcal{H}_{2L}^f , in our case by $C a_i C^{-1} = a_i^\dagger$ and $C b_i C^{-1} = -b_i^\dagger$ and $C i C^{-1} = i$. It is easy to check that $C H C^{-1} = H$ since there are only couplings between the two sublattices a and b . As an operator on \mathcal{H}_{2L}^f , we have

$$C = \prod_i (a_i^\dagger - a_i)(b_i^\dagger + b_i) \quad \text{with} \quad [C, H] = 0. \quad 5.4$$

Note: It is $(x_i^\dagger \pm x_i)x_i(x_i \pm x_i^\dagger) = \pm x_i^\dagger$ and $(x_i^\dagger \pm x_i)(x_i \pm x_i^\dagger) = 1$. As the total number of sites is even, there is an additional minus coming from the exchange of x_i with the other $2L - 1$ factors in C .

¹⁴⁷See the notes on twisted group cohomology in Subsection 5.1.3.

→ **Sublattice- or chiral symmetry:** The abstract symmetry group is $\mathbb{Z}_2 = \{1, S\}$ with $S^2 = 1$. Its generator S is represented *antiunitarily* on \mathcal{H}_{2L}^f , in our case by $Sa_i S^{-1} = a_i^\dagger$ and $Sb_i S^{-1} = -b_i^\dagger$ and $Si S^{-1} = -i$. The sublattice symmetry is the product of time-reversal and particle-hole symmetry, $S = T \cdot C$; since H already features both of them, it inherits S automatically. As an operator on \mathcal{H}_{2L}^f , we have

$$S = \prod_i (a_i^\dagger - a_i)(b_i^\dagger + b_i) \circ K \quad \text{with} \quad [S, H] = 0. \quad 5.5$$

Note: From the perspective of H , the symmetries C and S seem to be equivalent. This is not true once the hopping amplitudes become complex. Indeed, if we define

$$\tilde{H} = \sum_{i=1}^L (J_1 a_i^\dagger b_i + J_1^* b_i^\dagger a_i) + \sum_{i=1}^{L'} (J_2 b_i^\dagger a_{i+1} + J_2^* a_{i+1}^\dagger b_i), \quad 5.6$$

it is straightforward to show that $[T, \tilde{H}] \neq 0$ and $[C, \tilde{H}] \neq 0$ but still $[S, \tilde{H}] = 0$. This demonstrates two points: First, as complex hopping amplitudes are “natural” perturbations of H , sublattice symmetry is the “natural” symmetry of the SSH chain (C becomes a symmetry only with the aid of time-reversal symmetry T). Second, we see that although $S = T \cdot C$ is the “combination” of two symmetries, it is possible that both of them are broken whereas their product is still conserved because their violations “cancel” each other.

Fermionic Single-Particle Theory

As (5.1) is quadratic in fermion modes, we can write

$$H = J_1 \sum_{i=1}^L (a_i^\dagger b_i + b_i^\dagger a_i) + J_2 \sum_{i=1}^{L'} (b_i^\dagger a_{i+1} + a_{i+1}^\dagger b_i) \quad 5.7a$$

$$= \sum_{i,j=1}^L \sum_{x,y \in \{a,b\}} x_i^\dagger \hat{H}_{(i,x),(j,y)} y_j \quad 5.7b$$

$$= \Psi^\dagger \hat{H} \Psi \quad 5.7c$$

with pseudo-spinor $\Psi = (a_1, b_1, \dots, a_L, b_L)^T$ and $2L \times 2L$ matrix \hat{H} . Since $H^\dagger = H$, we have $\hat{H}^\dagger = \hat{H}$ and there is a unitary U such that $U \hat{H} U^\dagger$ is diagonal. Then $\tilde{\Psi} \equiv U \Psi$ still satisfies the fermionic algebra and one can easily diagonalize the many-body Hamiltonian H in terms of its fermionic eigenmodes $\tilde{\Psi}$; this property makes H a *free* theory. Its many-body ground state $|\Omega\rangle$ is then given by the state

in \mathcal{H}_{2L}^f where all eigenmodes in $\tilde{\Psi}$ with negative eigenenergy are occupied, i.e., $|\Omega\rangle$ describes the Fermi sea of the filled lower band. In the case of OBC, there is always a *unique* ground state in finite systems (for $J_1 \neq 0$)—but there are *four* degenerate ground states in the thermodynamic limit $L \rightarrow \infty$ if $|J_1| < |J_2|$ because the eigenenergies of the two fermionic edge modes become exponentially degenerate with growing chain length.

The matrix \hat{H} is commonly called *single-particle Hamiltonian* for the following reason: Since H is particle number conserving, we can restrict the operator H to the $2L$ -dimensional subspace

$$\mathcal{H}_{2L}^{(1)} = \text{span} \left\{ x_i^\dagger |0\rangle \mid i = 1, \dots, L; x = a, b \right\} \subseteq \mathcal{H}_{2L}^f, \quad 5.8$$

i.e., the subspace with a single particle. If we choose the basis $x_i^\dagger |0\rangle$, the action of H is described by the matrix

$$\hat{H}_{(i,x),(j,y)}^{(1)} \equiv \langle 0 | x_i H y_j^\dagger | 0 \rangle \quad 5.9a$$

$$= \sum_{k,l;u,v} \langle 0 | x_i u_k^\dagger \hat{H}_{(k,u),(l,v)} v_l y_j^\dagger | 0 \rangle \quad 5.9b$$

$$= \hat{H}_{(i,x),(j,y)}. \quad 5.9c$$

Thus the matrix \hat{H} —which encodes the complete structure of the *many-body* Hamiltonian H —is identical to its representation in the *single-particle* subspace if the basis is chosen appropriately.

We can now ask how the symmetries T , C , and S , defined on \mathcal{H}_{2L}^f , act on \hat{H} . This is a non-trivial question as their action is defined on the Fock space operators x_i and \hat{H} encodes H via these operators. Note that the same question for H is trivial: all three operators *commute* with H . The calculations are straightforward:

→ **Time-reversal symmetry:**

We find

$$THT^{-1} = \sum_{i,j;x,y} x_i^\dagger \hat{H}_{(i,x),(j,y)}^* y_j \stackrel{!}{=} H \quad 5.10a$$

$$\Leftrightarrow T\hat{H}T^{-1} = \hat{H}^* = \hat{H}, \quad 5.10b$$

where $T = K$ is the representation of T acting on the single-particle Hamiltonian \hat{H} . In our case, the reality of \hat{H} is equivalent to time-reversal symmetry. More generally, time-reversal can be represented as $T = U_T K$ with an arbitrary unitary U_T ; then the condition reads $U_T \hat{H}^* U_T^\dagger = \hat{H}$ (in our case $U_T = 1$).

→ **Particle-hole symmetry:**

We find

$$CHC^{-1} = \sum_{i,j;x,y} x_i (-1)^{\delta_{xb}} \hat{H}_{(i,x),(j,y)} (-1)^{\delta_{yb}} y_j^\dagger \quad 5.11a$$

$$= \sum_{i,j;x,y} y_j^\dagger [-(-1)^{\delta_{xb}} \hat{H}_{(i,x),(j,y)} (-1)^{\delta_{yb}}] x_i \quad 5.11b$$

$$+ \sum_{i,j;x,y} (-1)^{\delta_{xb}} \hat{H}_{(i,x),(j,y)} (-1)^{\delta_{yb}} \delta_{ij} \delta_{xy}$$

$$= \sum_{i,j;x,y} x_i^\dagger \overbrace{[-(-1)^{\delta_{yb}} \hat{H}_{(j,y),(i,x)} (-1)^{\delta_{xb}}]}^{\stackrel{!}{=} \hat{H}_{(i,x),(j,y)}} y_j \quad 5.11c$$

$$+ \underbrace{\text{Tr}[\hat{H}]}_{\stackrel{!}{=} 0}$$

$$\stackrel{!}{=} H. \quad 5.11d$$

The first condition reads

$$-(-1)^{\delta_{yb}} \hat{H}_{(j,y),(i,x)} (-1)^{\delta_{xb}} = \hat{H}_{(i,x),(j,y)} \quad 5.12a$$

$$\Leftrightarrow U_C \hat{H}^T U_C^\dagger = -\hat{H}, \quad 5.12b$$

with unitary

$$U_C = \mathbb{1}_{L \times L} \otimes \begin{bmatrix} 1 & 0 \\ 0 & -1 \end{bmatrix}. \quad 5.13$$

Because $\hat{H}^\dagger = \hat{H} \Leftrightarrow \hat{H}^T = \hat{H}^*$, we can write

$$C \hat{H} C^{-1} = U_C \hat{H}^* U_C^\dagger = -\hat{H}, \quad 5.14$$

in analogy with time-reversal T . Note that C is a *unitary* operator on the Fock space but C is realized as *antiunitary* operation on the single-particle Hamiltonian \hat{H} . Furthermore, C is not an ordinary symmetry of \hat{H} as it *anticommutes* with the matrix \hat{H} .

The second constraint $\text{Tr}[\hat{H}] = 0$ is not independent but follows from (5.14): The spectrum of $U_C \hat{H}^T U_C^\dagger$ and \hat{H} is the same if U_C is unitary (and thus invertible); then (5.14) requires the spectra of \hat{H} and $-\hat{H}$ to be the same. But this implies that the sum of all eigenvalues vanishes, i.e., $\text{Tr}[\hat{H}] = 0$. Physically, $\text{Tr}[\hat{H}] = 0$ excludes chemical potentials—which is to be expected for a symmetry which maps particles to holes and vice versa.

Again, the form of U_C is special to our representation of particle-hole symmetry. More generally, particle-hole symmetry can be represented as $C = U_C K$ with an *arbitrary* unitary U_C ; the condition still reads $U_C \hat{H}^* U_C^\dagger = -\hat{H}$.

→ **Sublattice- or chiral symmetry:**

We find

$$SHS^{-1} = \sum_{i,j;x,y} x_i (-1)^{\delta_{xb}} \hat{H}_{(i,x),(j,y)}^* (-1)^{\delta_{yb}} y_j^\dagger \quad 5.15a$$

$$= \sum_{i,j;x,y} y_j^\dagger [-(-1)^{\delta_{xb}} \hat{H}_{(i,x),(j,y)}^* (-1)^{\delta_{yb}}] x_i \quad 5.15b$$

$$+ \sum_{i,j;x,y} (-1)^{\delta_{xb}} \hat{H}_{(i,x),(j,y)}^* (-1)^{\delta_{yb}} \delta_{ij} \delta_{xy}$$

$$= \sum_{i,j;x,y} x_i^\dagger \overbrace{[-(-1)^{\delta_{yb}} \hat{H}_{(j,y),(i,x)}^* (-1)^{\delta_{xb}}]}^{\stackrel{!}{=} \hat{H}_{(i,x),(j,y)}} y_j \quad 5.15c$$

$$+ \underbrace{\text{Tr}[\hat{H}^*]}_{\stackrel{!}{=} 0}$$

$$\stackrel{!}{=} H. \quad 5.15d$$

The first condition reads

$$-(-1)^{\delta_{yb}} \hat{H}_{(j,y),(i,x)}^* (-1)^{\delta_{xb}} = \hat{H}_{(i,x),(j,y)} \quad 5.16a$$

$$\Leftrightarrow U_S \hat{H}^\dagger U_S^\dagger = -\hat{H}, \quad 5.16b$$

with the same unitary as before, $U_S = U_C$. Because $\hat{H}^\dagger = \hat{H}$, we can write

$$\mathbf{S} \hat{H} \mathbf{S}^{-1} = U_S \hat{H} U_S^\dagger = -\hat{H}, \quad 5.17$$

in analogy with time-reversal T and particle-hole symmetry C . Note that S is an *antiunitary* operator on the Fock space but \mathbf{S} is realized as *unitary* operation on the single-particle Hamiltonian \hat{H} . Just as C , \mathbf{S} is not an ordinary symmetry of \hat{H} as it *anticommutes* with the matrix \hat{H} . As before, the second constraint $\text{Tr}[\hat{H}^*] = 0$ follows from (5.17) and forbids chemical potentials.

In general, \mathbf{S} follows from $S = T \cdot C$ directly: $\mathbf{S} = T \cdot C = U_T K \cdot U_C K = U_T U_C^* = U_S$. In our case $U_C^* = U_C$ and $U_T = \mathbb{1}$ such that $U_S = U_C$.

In conclusion, we found three *properties of the matrix \hat{H}* that relate to true many-body symmetries on the Fock space. In prosaic form, these properties read as follows:

→ The matrix \hat{H} is called *time-reversal symmetric* if it is unitarily equivalent to its complex conjugate: $U_T \hat{H}^* U_T^\dagger = \hat{H}$.

→ The matrix \hat{H} is called *particle-hole symmetric* if it is unitarily equivalent to its negative complex conjugate: $U_C \hat{H}^* U_C^\dagger = -\hat{H}$.

→ The matrix \hat{H} is called *sublattice symmetric* if it is unitarily equivalent to its negative: $U_S \hat{H} U_S^\dagger = -\hat{H}$.

The unitary matrices U_X for $X = T, C, S$ define the representation of the corresponding symmetries on the single-particle level and are therefore system dependent. For example, on spinful fermions, time-reversal is usually represented by $\mathbf{T} = i\sigma^y K$, i.e., with $U_T = i\sigma^y$.

Remarks

- 1 The three properties (“symmetries”) listed above should be interpreted as abstract features of classes of (Hermitian) matrices \hat{H} [90–93]. If a given combination of these properties is realized by specified unitaries U_X , this allows for the definition of topological invariants (in translationally invariant systems) and thereby *symmetry-protected topological phases of free fermions* [21, 22, 95, 97].
- 2 On this level, all statements are essentially statements about a class of matrices \hat{H} . Therefore all consequences (such as protected edge modes) are inherited by any physical system that makes use of these matrices to encode its dynamics. In our case, we use \hat{H} to encode a fermionic many-body Hamiltonian H which then features protected (fermionic) edge modes. But we could also use the same \hat{H} to describe the classical Hamiltonian of a network of spring-coupled harmonic oscillators [204], radio-frequency circuits [214], photonic waveguides [213], etc. All these systems can host topological features inherited by \hat{H} ; there is nothing quantum about it [199].
- 3 Above we mentioned the alternative time-reversal representation $\mathbf{T} = i\sigma^y K$. It has the characteristic feature that $\mathbf{T}^2 = -\mathbb{1}$. By contrast, for the SSH chain we have $\mathbf{T} = \mathbb{1}K$ with $\mathbf{T}^2 = \mathbb{1}$. This list is exhaustive in the sense that one can show $\mathbf{T}^2 = U_T U_T^* = \pm\mathbb{1}$. The same is true for particle-hole symmetry: $\mathbf{C}^2 = U_C U_C^* = \pm\mathbb{1}$. By contrast, sublattice symmetry always squares to one: $\mathbf{S}^2 = +\mathbb{1}$. In conclusion, there are three possibilities for time-reversal: (1) it is not present, (2) it is present and squares to +1, (3) it is present and squares to −1; one writes $T = 0, \pm 1$ for short. Particle-hole symmetry comes with the same three possibilities ($C = 0, \pm 1$). In total, this makes 9 different symmetry classes that a matrix \hat{H} can belong to. Because $\mathbf{S} = \mathbf{T} \cdot \mathbf{C}$, the presence/absence of sublattice symmetry is determined whenever either T or C (or both) are present. But there is the special case when both T and C are *not* present. Then, as demonstrated above, their product can still be a symmetry and \hat{H} can feature the sublattice property; this gives one additional class ($S = 1$). Thus, in total there are 10 different symmetry classes of *random matrices* \hat{H} [90] which correspond to the exhaustive list

of 10 symmetry classes of free fermion Hamiltonians H described by \hat{H} . This is known as the *tenfold way* [97]. We refer the reader to Ref. [85] for a pedagogical introduction.

- 4 For our specific case of the SSH chain, we find

$$\mathbf{T}^2 = U_T U_T^* = +\mathbb{1} \quad \Rightarrow \quad T = +1, \quad 5.18a$$

$$\mathbf{C}^2 = U_C U_C^* = +\mathbb{1} \quad \Rightarrow \quad C = +1, \quad 5.18b$$

and sublattice symmetry is present, $S = 1$. Thus the SSH chain, as given in (5.1), belongs to the class $(T, C, S) = (+1, +1, 1)$ which is labeled **BDI** (the label has mathematical origin but is not important to us). This is true but actually too restrictive (and not necessary to protect the topological phase of the SSH chain). Above we already demonstrated that complex hopping amplitudes immediately destroy both particle-hole and time-reversal symmetry but keep the sublattice symmetry intact. Such a perturbed Hamiltonian no longer belongs to **BDI** but to **AIII** characterized by $(T, C, S) = (0, 0, 1)$ (which features topological phases in one dimension, see [97]). This can easily be verified numerically: Adding complex hopping does not gap out the edge modes.

- 5 The matrix property $U_S \hat{H} U_S^\dagger = -\hat{H}$ for a Hermitian matrix \hat{H} and a unitary U_S has the following algebraic consequences: We already argued that this implies a symmetric spectrum of \hat{H} around zero. For simplicity, assume that the dimension of \hat{H} is even (in our case this is true since \hat{H} is a $2L \times 2L$ -matrix). Then, the symmetry of the spectrum implies that there is a unitary matrix U such that

$$U \hat{H} U^\dagger = \begin{bmatrix} D & 0 \\ 0 & -D \end{bmatrix} \quad 5.19$$

with diagonal $L \times L$ -matrix D . Now apply the following (unitary) Hadamard transform M :

$$\begin{aligned} M U \hat{H} U^\dagger M^\dagger &= \frac{1}{\sqrt{2}} \begin{bmatrix} \mathbb{1} & \mathbb{1} \\ \mathbb{1} & -\mathbb{1} \end{bmatrix} \cdot \begin{bmatrix} D & 0 \\ 0 & -D \end{bmatrix} \cdot \frac{1}{\sqrt{2}} \begin{bmatrix} \mathbb{1} & \mathbb{1} \\ \mathbb{1} & -\mathbb{1} \end{bmatrix} \\ &= \begin{bmatrix} 0 & D \\ D & 0 \end{bmatrix}. \end{aligned} \quad 5.20$$

If we interpret \hat{H} as quadratic fermion theory, this argument tells us that if there is a unitary U_S such that $U_S \hat{H} U_S^\dagger = -\hat{H}$, there exists a basis of fermionic modes (not necessarily the “physical” modes) in which the couplings/hoppings are described by an off-diagonal block-matrix. But this is the defining property of *bipartite hopping*: There is a subset/sublattice of modes that does not couple within itself but only to a complementary

subset/sublattice of modes. This explains why the property $U_S \hat{H} U_S^\dagger = -\hat{H}$ always implies a *sublattice structure* of couplings and motivates the term *sublattice symmetry*. In the case of the SSH Hamiltonian (5.1), this sublattice structure is already revealed on the level of physical modes a_i and b_i . Note that the decisive feature of the sublattice property is the symmetry of the spectrum and not whether in a *particular* basis the coupling structure is bipartite. The symmetry of the spectrum only guarantees that there *exists* a basis in which the couplings are bipartite.

- 6 We started our discussion with *four* many-body symmetries, namely T , C , S , and particle number conservation R_ϕ . When deriving the action on the single-particle Hamiltonian, we silently dropped the latter. Why? The answer is simple: A *quadratic* Hamiltonian like (5.7) without superconductivity (i.e., pairing) is *always* number-conserving. For such Hamiltonians, $R_\phi H R_\phi^{-1} = H$ does not impose any constraint on the matrix \hat{H} . To put it differently: \hat{H} parametrizes the family of number-conserving, non-interacting many-body Hamiltonians H . The symmetry R_ϕ is “built into” this parametrization and cannot be violated without altering the family of Hamiltonians. Since the tenfold way is only concerned with the classification of *matrices* \hat{H} , many-body symmetries that do not impose restrictions on these matrices are of no interest¹⁴⁸.

5.1.2 Jordan-Wigner Transformation

We are now interested in the bosonic counterpart of the SSH Hamiltonian (5.1). To this end, we apply the Jordan-Wigner transformation ρ [358]. The latter can be seen as a representation of the (abstract) fermion algebra $\{x_i, y_j^\dagger\} = \delta_{ij} \delta_{xy}$ on the 2^{2L} -dimensional space $\mathcal{H}_{2L}^{\rho b} \equiv \bigotimes_{i=1}^{2L} \mathbb{C}_i^2$. Recall that the fermionic Fock space \mathcal{H}_{2L}^f (generated from the vacuum $|0\rangle$) is a different 2^{2L} -dimensional representation of the same algebra [359]. From a mathematical perspective, both representations are isomorphic and therefore equivalent. The difference is an interpretational one: The operator algebra on the Fock space is naturally generated by the fermion modes a_i and b_i . By contrast, the operator algebra on $\mathcal{H}_{2L}^{\rho b}$ is conveniently given by Pauli matrices σ_i^α with $\alpha = x, y, z$ acting on the i th tensor factor \mathbb{C}_i^2 . The subsystem \mathbb{C}_i^2 can either be interpreted as a spin- $\frac{1}{2}$ degree of freedom (d.o.f.) or a hard-core boson (for which one would relabel the Pauli algebra as $b_i = \sigma_i^-$ and $b_i^\dagger = \sigma_i^+$ etc.). In the following, we adopt the “spin picture” as operations with/on spins are more intuitive (see the side note on hard-core bosons below).

¹⁴⁸The tenfold way actually includes superconductivity via an extended parametrization in an artificially doubled mode space (called *Nambu space*); then, fermion *parity* takes the role of R_ϕ as symmetry that is tacitly assumed.

We define the Jordan-Wigner transformation as follows:

$$\rho(a_j - a_j^\dagger) = \prod_{k=1}^{2j-2} \sigma_k^z \cdot (i\sigma_{2j-1}^y), \quad \rho(b_j - b_j^\dagger) = \prod_{k=1}^{2j-1} \sigma_k^z \cdot (i\sigma_{2j}^y), \quad 5.21a$$

$$\rho(a_j + a_j^\dagger) = \prod_{k=1}^{2j-2} \sigma_k^z \cdot (\sigma_{2j-1}^x), \quad \rho(b_j + b_j^\dagger) = \prod_{k=1}^{2j-1} \sigma_k^z \cdot (\sigma_{2j}^x). \quad 5.21b$$

Note that we got rid of the a/b sublattice labels in favor of indices $i = 1, \dots, 2L$. The above definition is equivalent to

$$\rho(a_j) = \prod_{k=1}^{2j-2} \sigma_k^z \cdot \sigma_{2j-1}^+, \quad \rho(b_j) = \prod_{k=1}^{2j-1} \sigma_k^z \cdot \sigma_{2j}^+, \quad 5.22a$$

$$\rho(a_j^\dagger) = \prod_{k=1}^{2j-2} \sigma_k^z \cdot \sigma_{2j-1}^-, \quad \rho(b_j^\dagger) = \prod_{k=1}^{2j-1} \sigma_k^z \cdot \sigma_{2j}^-. \quad 5.22b$$

It is now easy to check that

$$\left\{ \rho(x_i), \rho(y_j^\dagger) \right\} = \delta_{ij} \delta_{xy} \quad \text{and} \quad \left\{ \rho(x_i^{(\dagger)}), \rho(y_j^{(\dagger)}) \right\} = 0, \quad 5.23$$

so that ρ indeed serves as a representation of the fermion algebra on \mathcal{H}_{2L}^b . We stress that ρ is a *non-local* mapping in the sense that a “local” fermion a_i is mapped to an operator with extensive support on \mathcal{H}_{2L}^b in terms of Pauli matrices (depending on the site i). This is due to the string operators $\prod_k \sigma_k^z$ which are necessary to implement the anticommutation of fermions that are “far apart.”

Transformation of the SSH Hamiltonian

If we apply ρ to the SSH Hamiltonian (5.1), $\rho(H)$, we find

$$J_1 \sum_{i=1}^L [\rho(a_i^\dagger)\rho(b_i) + \rho(b_i^\dagger)\rho(a_i)] \quad 5.24a$$

$$+ J_2 \sum_{i=1}^{L-1} [\rho(b_i^\dagger)\rho(a_{i+1}) + \rho(a_{i+1}^\dagger)\rho(b_i)]$$

$$= J_1 \sum_{i=1}^L (\sigma_{2i-1}^- \sigma_{2i}^+ + \sigma_{2i}^- \sigma_{2i-1}^+) + J_2 \sum_{i=1}^{L-1} (\sigma_{2i}^- \sigma_{2i+1}^+ + \sigma_{2i+1}^- \sigma_{2i}^+) \quad 5.24b$$

$$= \frac{J_1}{2} \sum_{i=1}^L (\sigma_{2i-1}^x \sigma_{2i}^x + \sigma_{2i-1}^y \sigma_{2i}^y) + \frac{J_2}{2} \sum_{i=1}^{L-1} (\sigma_{2i}^x \sigma_{2i+1}^x + \sigma_{2i}^y \sigma_{2i+1}^y) \quad 5.24c$$

which is a dimerized spin-exchange model (also known as XY model). How this connects to the commonly studied *isotropic* spin chains is explained in Subsection 5.1.4. Note that here we allow only OBC ($L' = L - 1$) because the non-local Jordan-Wigner string makes $\rho(H)$ a non-local spin Hamiltonian for PBC. The Hamiltonian (5.24b) is the idealization of what is realized experimentally in Ref. [4] if the two Rydberg levels are identified with the two spin states $|\uparrow\rangle$ (and if long-range hopping is ignored).

Transformation of the Symmetries

Just like the Hamiltonian, we can translate its (many-body) symmetries with ρ into the bosonic spin world of \mathcal{H}_{2L}^b . Since ρ is an algebra isomorphism, the commutation relations will survive and the Jordan-Wigner transformed operators will again be symmetries of the Hamiltonian $\rho(H)$. Indeed:

→ **Particle number conservation:** We find the representation

$$\rho(R_\phi) = e^{i\phi\rho(N)} = \exp\left[i\phi \sum_i \frac{\mathbb{1} - \sigma_i^z}{2}\right] \quad 5.25$$

of U(1) on \mathcal{H}_{2L}^b with $[\rho(R_\phi), \rho(H)] = 0$ for all $\phi \in [0, 2\pi)$. In particular, for $\phi = \pi$ we find the *parity symmetry*

$$\rho(R_\pi) = \exp\left[i\pi \sum_i \frac{\mathbb{1} - \sigma_i^z}{2}\right] \propto \prod_i \sigma_i^z \equiv Z \quad 5.26$$

where we used $e^{-i\frac{\pi}{2}\sigma^z} = -i\sigma^z$.

→ **Particle-hole symmetry:** We can directly apply (5.21) and find

$$\rho(C) = \prod_{j=1}^L \rho(a_j^\dagger - a_j)\rho(b_j^\dagger + b_j) \quad 5.27a$$

$$\propto \prod_{j=1}^L \left[\prod_{k=1}^{2j-2} \sigma_k^z \cdot (i\sigma_{2j-1}^y) \prod_{k=1}^{2j-1} \sigma_k^z \cdot (\sigma_{2j}^x) \right] \quad 5.27b$$

$$= \prod_{j=1}^L \left[(i\sigma_{2j-1}^y)\sigma_{2j-1}^z \cdot (\sigma_{2j}^x) \right] \quad 5.27c$$

$$= \prod_{j=1}^L \left[(-\sigma_{2j-1}^x) \cdot (\sigma_{2j}^x) \right] \quad 5.27d$$

$$\propto \prod_{j=1}^{2L} \sigma_j^x \equiv X \quad 5.27e$$

with $[\rho(C), \rho(H)] = 0$. Note that we ignore global phase factors and in the third line the Jordan-Wigner strings canceled up to a single term σ_{2j-1}^z .

The effect of X is nothing but a global spin-flip $|\uparrow\rangle \leftrightarrow |\downarrow\rangle$. Since we can interpret the spin states $|\uparrow\rangle/|\downarrow\rangle$ as empty/occupied by a hard-core boson, the operator X converts particles into holes and vice versa. This makes sense as we started from an operator which describes a particle-hole transformation.

→ **Time-reversal symmetry:** We note that the matrices $\rho(x_i)$ and $\rho(x_i^\dagger)$ are real (because σ^z and σ^\pm are) so that $K\rho(x_i)K = \rho(x_i)$ for $x = a, b$. Therefore

$$\rho(T) = K \quad \text{with} \quad [\rho(T), \rho(H)] = 0. \quad 5.28$$

→ **Sublattice- or chiral symmetry:** The sublattice symmetry is given as $S = T \cdot C$ so that

$$\rho(S) = \rho(T) \cdot \rho(C) = K \circ X = X \circ K \quad 5.29$$

and $[\rho(S), \rho(H)] = 0$ follows immediately.

The transformation of both the Hamiltonian and its symmetries is completely rigorous and, from the perspective of a mathematician, “trivial” as the Jordan-Wigner transformation is an isomorphism between two representations of the same algebra. For every operator \mathcal{O} that acts on the Fock space \mathcal{H}_{2L}^f , there is a bosonic counterpart $\rho(\mathcal{O})$ that acts on the Hilbert space \mathcal{H}_{2L}^b . Since the commutation relations are preserved by ρ , a local perturbation \mathcal{O} that violates/preserves a symmetry \mathcal{S} has a bosonic counterpart $\rho(\mathcal{O})$ that violates/preserves the symmetry $\rho(\mathcal{S})$.

Example

To understand why “the sublattice symmetry is no longer needed” for the bosonic version of the SSH chain implemented in Ref. [4], it is important to realize that there is no *mathematical* difference between the two pictures (ρ is an isomorphism!). What changes is our *interpretation* of operators as description of real-world processes. Let us illustrate this with an example:

The hopping of a fermion between sites a_1 and a_2 is described on the Fock space \mathcal{H}_{2L}^f simply by

$$\text{Fermion hopping} = a_1^\dagger a_2 + a_2^\dagger a_1 \equiv \mathcal{O}^f, \quad 5.30$$

whereas the hopping of a spin excitation/hard-core boson is described on \mathcal{H}_{2L}^b by

$$\text{Spin-exchange} = \sigma_1^- \sigma_3^+ + \sigma_3^- \sigma_1^+ \equiv \mathcal{O}^b. \quad 5.31$$

Since the Jordan-Wigner transformation is nothing but a dictionary between two representations of the same thing, we can translate both operations into their respective counterparts using (5.22):

$$\begin{aligned}\rho(\mathcal{O}^f) &= \rho(a_1^\dagger a_2 + a_2^\dagger a_1) \\ &= \sigma_2^z (\sigma_1^- \sigma_3^+ + \sigma_3^- \sigma_1^+) \neq \mathcal{O}^b, \end{aligned} \quad 5.32a$$

$$\begin{aligned}\rho^{-1}(\mathcal{O}^b) &= \rho^{-1}(\sigma_1^- \sigma_3^+ + \sigma_3^- \sigma_1^+) \\ &= (1 - 2b_1^\dagger b_1) (a_1^\dagger a_2 + a_2^\dagger a_1) \neq \mathcal{O}^f. \end{aligned} \quad 5.32b$$

[The last equation follows from $\rho(1 - 2b_1^\dagger b_1) = \sigma_2^z$.] Thus $\rho(\mathcal{O}^f)$ describes the hopping of a fermion in the mathematical framework of spins on \mathcal{H}_{2L}^b whereas $\rho^{-1}(\mathcal{O}^b)$ describes the spin-exchange in the mathematical framework of fermions on \mathcal{H}_{2L}^f . Most importantly, \mathcal{O}^f and \mathcal{O}^b are not mapped onto each other by the isomorphism ρ : $\rho(\mathcal{O}^f) \neq \mathcal{O}^b$.

Let us now compare these two perturbations with respect to the sublattice symmetry S and its bosonic counterpart $\rho(S) = XK$. Again, since ρ is an isomorphism, we can immediately conclude $[\mathcal{O}, S] = 0 \Leftrightarrow [\rho(\mathcal{O}), \rho(S)] = 0$. This allows us to reduce the computations for the four operators $\mathcal{O}^f, \mathcal{O}^b, \rho(\mathcal{O}^f), \rho^{-1}(\mathcal{O}^b)$ to two cases. We find:

$$[\mathcal{O}^b, \rho(S)] = 0 \quad \Leftrightarrow \quad [\rho^{-1}(\mathcal{O}^b), S] = 0, \quad 5.33a$$

$$[\mathcal{O}^f, S] \neq 0 \quad \Leftrightarrow \quad [\rho(\mathcal{O}^f), \rho(S)] \neq 0. \quad 5.33b$$

The first line follows because $\rho(S) = \prod_i \sigma_i^x \circ K$ clearly commutes with the spin-exchange interaction $\mathcal{O}^b \propto (\sigma_1^x \sigma_3^x + \sigma_1^y \sigma_3^y)$. The second line follows because \mathcal{O}^f clearly violates the fermionic sublattice symmetry S , namely $S\mathcal{O}^f S^{-1} = -\mathcal{O}^f$. Let us comment on the conclusions that we *can* and *cannot* draw from this example at this point:

- 1 The fermionic perturbation $\mathcal{O}^f = a_1^\dagger a_2 + a_2^\dagger a_1$ has two important properties: First, it violates the many-body sublattice symmetry S , and second, it is quadratic. The latter property allows us to treat it in the single-particle picture discussed in Subsection 5.1.1. If we add this perturbation to the Hamiltonian, $H_{\text{pert}} = H + \mathcal{O}^f$ can still be described by a perturbed single-particle matrix \hat{H}_{pert} . This matrix violates the sublattice property, $U_S \hat{H}_{\text{pert}} U_S^\dagger \neq -\hat{H}_{\text{pert}}$, and allows us to gap out the fermionic edge modes of the SSH chain. We know that this really happens as it can be easily checked numerically. This is not too surprising. However, a non-trivial conclusion is that perturbing the *bosonic* Hamiltonian (5.24b) with the rather complicated and interacting spin-exchange $\rho(\mathcal{O}^f) = \sigma_2^z (\sigma_1^- \sigma_3^+ + \sigma_3^- \sigma_1^+)$ must lift the degeneracy of the bosonic edge modes, too!

- 2 The bosonic perturbation $\mathcal{O}^b = \sigma_1^- \sigma_3^+ + \sigma_3^- \sigma_1^+$ satisfies the symmetry $\rho(S) = XK$. But at this point we cannot conclude that this protects anything because we do not yet have a native concept of symmetry-protected topological phases for interacting spins/bosons (all we know is the tenfold way for free fermions). However, we *could* hope that its fermionic counterpart can be exploited to derive the protection from the tenfold way. As shown above, it reads

$$\rho^{-1}(\mathcal{O}^b) = (1 - 2b_1^\dagger b_1) (a_1^\dagger a_2 + a_2^\dagger a_1) \quad 5.34$$

and we can again think of a perturbed many-body Hamiltonian $H'_{\text{pert}} = H + \rho^{-1}(\mathcal{O}^b)$ which satisfies the many-body sublattice symmetry, $[S, H'_{\text{pert}}] = 0$. But here we have reached an impasse: Since H'_{pert} is no longer a *quadratic* fermionic Hamiltonian, there is no single-particle matrix \hat{H}'_{pert} associated with it. This implies that the tenfold way is not applicable and it might be possible to deform $H \rightarrow H(\lambda)$ from $H(0) = H$ to $H(1) = H_{\text{trivial}}$ (with a trivial ground state) without closing the gap and without violating the sublattice symmetry S . The tenfold way only guarantees that this is impossible as long as $H(\lambda)$ remains quadratic along this path; interactions can change this picture completely (and it is known that this happens [107]).

Note: The fermionic operator $\rho^{-1}(\mathcal{O}^b)$ satisfies the sublattice/chiral symmetry S although it couples sites of the same sublattice. This demonstrates that the nature of symmetries changes when interactions are included. Recall that the picture of sublattices and bipartite hopping enters the stage via *matrices* that satisfy a particular property. But this characterization is (just like the tenfold way) only applicable to non-interacting theories.

We conclude: In order to understand why the symmetry $\rho(S) = XK$ [in combination with particle number conservation $\rho(R_\phi)$] protects the edge modes of (5.24b) against bosonic perturbations such as \mathcal{O}^b , we cannot resort to the framework of free fermion theories (the tenfold way) because the latter does not cover interacting perturbations (which is what the simple hopping of hard-core bosons \mathcal{O}^b looks like in the fermionic picture). Now we have two choices:

- 1 We can work in the *fermionic picture* and ask for the effects of interactions on the classification of the tenfold way.
- 2 We can work in the *spin picture* and ask for the classification of symmetry-protected topological phases in one-dimensional spin systems.

Here we choose the second approach because it is the natural framework for the system in Ref. [4]. With this we proceed in Subsection 5.1.3.

Aside: Why Hard-Core Bosons Are Hard

As mentioned above, hard-core boson and spin- $\frac{1}{2}$ picture are mathematically completely equivalent; this is just about names, labels and intuition. But intuition is important when doing calculations, and the hard-core boson picture can provide the wrong one. Here is an example why:

Consider two modes a and b which are (1) fermions, (2) bosons, (3) hard-core bosons, formally¹⁴⁹:

$$\text{Fermions: } \{x, x^\dagger\} = 1 \quad \text{and} \quad \{a^{(\dagger)}, b^{(\dagger)}\} = 0 \quad 5.35a$$

$$\text{Bosons: } [x, x^\dagger] = 1 \quad \text{and} \quad [a^{(\dagger)}, b^{(\dagger)}] = 0 \quad 5.35b$$

$$\text{Hard-core bosons: } \{x, x^\dagger\} = 1 \quad \text{and} \quad [a^{(\dagger)}, b^{(\dagger)}] = 0 \quad 5.35c$$

where $x = a, b$. Now assume that we unitarily transform the old modes a and b into new ones. For instance:

$$\begin{bmatrix} c \\ d \end{bmatrix} = \underbrace{\frac{1}{\sqrt{2}} \begin{bmatrix} 1 & 1 \\ 1 & -1 \end{bmatrix}}_{=U} \begin{bmatrix} a \\ b \end{bmatrix}. \quad 5.36$$

As U is unitary, it is straightforward to show that both fermions and bosons survive this transformation (i.e., the transformation is canonical):

$$\text{Fermions: } \{x, x^\dagger\} = 1 \quad \text{and} \quad \{c^{(\dagger)}, d^{(\dagger)}\} = 0 \quad 5.37a$$

$$\text{Bosons: } [x, x^\dagger] = 1 \quad \text{and} \quad [c^{(\dagger)}, d^{(\dagger)}] = 0 \quad 5.37b$$

where now $x = c, d$. So for fermionic/bosonic a and b , the new modes c and d are again fermionic/bosonic. This property lies at the heart of the solvability of non-interacting theories. More precisely, this is the reason why “quadratic” \Leftrightarrow “non-interacting” for fermionic and bosonic theories.

However, for hard-core bosons we find

$$\{c, c^\dagger\} = \frac{1}{2} \{a + b, a^\dagger + b^\dagger\} = 1 + (a^\dagger b + b^\dagger a) \neq 1 \quad 5.38$$

where we used $[a, b^\dagger] = 0$. Notice that c and d are no longer hard-core bosons but satisfy a more complicated algebra. This makes *quadratic* theories of hard-core bosons *interacting* in general and prevents their exact diagonalization in many cases. Thus hard-core bosons differ on a fundamental level from fermions and bosons, and

¹⁴⁹The careful reader might wonder whether the missing fourth possibility in the suggestive list (5.35) has any physical significance. Indeed it has: Particles that are on-site bosons but off-site fermions are known as *pseudofermions* and play a role in 1D interacting systems [360].

it is dangerous to think of the former as slight modifications of the latter. This is also evident if one thinks of hard-core bosons as true bosons with an on-site repulsive interaction that goes to infinity.

Why is the spin- $\frac{1}{2}$ picture more intuitive? From the “spin perspective,” we write $a = \sigma_a^-$ and $b = \sigma_b^-$ (and similarly for a^\dagger and b^\dagger), where $\sigma^\pm = \frac{1}{2}(\sigma^x \pm i\sigma^y)$ and σ^α are Pauli matrices. But now the new mode c reads

$$c = \frac{1}{\sqrt{2}}(a + b) = \frac{1}{\sqrt{2}}(\sigma_a^- + \sigma_b^-) \propto \Sigma_c^- \quad 5.39$$

where $\Sigma_c \equiv \sigma_a + \sigma_b$ is the angular momentum operator of two coupled spin- $\frac{1}{2}$. However, we know that

$$\frac{1}{2} \otimes \frac{1}{2} = 0 \oplus 1, \quad 5.40$$

i.e., coupling two spins yields the irreducible representations of a singlet (0) and a triplet (1). But these are one- and three-dimensional, respectively. It is intuitively clear that Σ_c^- cannot act irreducibly on a two-dimensional subspace—but this is necessary to describe a hard-core constraint.

Thus the intrinsic complexity of hard-core bosons is much less obscure in spin language than in an abstract, algebraic language. This is why I prefer the former over the latter in this section.

5.1.3 Symmetry-Protected Topological Phases of One-Dimensional Spin Systems

REMARK 5.1:

Here we switch to the spin picture for good. As there are no fermions in this subsection, we omit the Jordan-Wigner transformation ρ from all expressions.

We begin this subsection with a compilation of possible symmetry groups of the bosonic SSH Hamiltonian (5.24b). Then we discuss the classification of symmetry-protected topological phases of one-dimensional spin systems and apply its machinery to the symmetry group generated by particle number conservation and the sublattice/chiral symmetry. After a brief account on the emergence of edge modes, we close with a note on twisted group cohomology—the formal framework needed for the classification of *antiunitary* projective symmetry representations.

Symmetry Groups of the Bosonic Theory

Since the unperturbed Hamiltonian (5.24b) features a variety of symmetries, we can combine them to construct new symmetry groups. Let us first summarize the symmetry groups from above:

$$\text{Particle number: } R_\phi = \exp \left[i\phi \sum_i \frac{1-\sigma_i^z}{2} \right] \rightarrow \text{U}(1) \quad 5.41a$$

$$\text{Parity: } Z = \prod_i \sigma_i^z \rightarrow \mathbb{Z}_2 \quad 5.41b$$

$$\text{Time-reversal: } T = K \rightarrow \mathbb{Z}_2^T \quad 5.41c$$

$$\text{Particle-hole: } X = \prod_i \sigma_i^x \rightarrow \mathbb{Z}_2 \quad 5.41d$$

$$\text{Sublattice/Chiral: } XK = \prod_i \sigma_i^x \circ K \rightarrow \mathbb{Z}_2^T \quad 5.41e$$

In the right column we list the abstract groups represented by these operators. Note that $\mathbb{Z}_2^T \cong \mathbb{Z}_2$; the superscript T only indicates that the group is represented antiunitarily (see the side note on twisted group cohomology below).

We can combine these symmetries to construct new subgroups of the total symmetry group of the SSH Hamiltonian (5.24b). Here we list only three important ones:

- We can combine parity and particle-hole symmetry to generate the symmetry group

$$D_2 = \mathbb{Z}_2 \times \mathbb{Z}_2 = \langle X, Z \rangle \quad 5.42$$

with $X^2 = 1 = Z^2$ and $XZ = ZX$ (because the number of sites is even). More precisely: X and Z constitute a linear representation of D_2 on \mathcal{H}_{2L}^b . D_2 is a *dihedral group* which is well-known to protect the degeneracy of the spin-1 Haldane phase [65, 243]. D_2 protects also the degeneracy of our bosonic SSH model (5.24b). To get an intuition *why* D_2 protects the edge modes in our case (which for $J_1 = 0$ are just two dangling spin- $\frac{1}{2}$ at the ends of the chain) it is instructive to ask whether a magnetic field σ_i^α for $i \in \{1, 2L\}$ and $\alpha = x, y, z$ can be switched on without violating the symmetry. For D_2 the answer is clearly negative as either X or Z (or both) anticommute with σ_i^α for any α . This shows that the most trivial way to gap out the edge modes is prohibited by D_2 (we did not show that this is true for more complicated perturbations, though). The perturbations that are allowed by this symmetry are products of Pauli matrices with an even or odd number of all three types $\alpha = x, y, z$. For instance, $\sigma_1^x \sigma_2^y \sigma_3^z$ is allowed but $\sigma_1^x \sigma_3^z$ is forbidden.

- We can multiply parity and the chiral symmetry to get the simple group

$$\mathbb{Z}_2^T = \langle ZX \circ K \rangle \quad \text{with} \quad ZX \circ K = \prod_j (i\sigma_j^y) \circ K \propto YK \quad 5.43$$

that is antiunitarily represented on \mathcal{H}_{2L}^b . Note that indeed $(YK)^2 = 1$ (as the number of sites is even) whereas on a single site $(i\sigma_j^y K)^2 = -1$. Since $i\sigma_j^y K$ anticommutes with all three Pauli matrices σ_j^α , it is immediately clear that this symmetry protects the edge modes against magnetic fields; as before, the protection against generic perturbations is not evident. On spins, $i\sigma_j^y K$ is interpreted as time-reversal symmetry which is well-known to protect the Haldane phase (as an alternative to D_2 , see [65, 243]). The perturbations that are allowed by this symmetry are products of an *even* number of Pauli matrices (since $i\sigma_j^y K$ anticommutes with all Pauli matrices). For instance, $\sigma_1^x \sigma_3^z$ is allowed but $\sigma_1^x \sigma_2^y \sigma_3^z$ is forbidden.

- We can abandon time-reversal and particle-hole symmetry and require only particle number conservation (which is a natural symmetry of the setup in [4]) and the chiral symmetry (which is the natural symmetry of the SSH chain in the fermionic picture):

$$U(1) \times \mathbb{Z}_2^T = \langle R_\phi, XK \rangle \geq \langle Z, XK \rangle \geq \langle YK \rangle. \quad 5.44$$

Note that this symmetry group includes YK and therefore protects the edge modes *if* YK alone protects the edge modes (which it does due to the connection between our model and the Haldane phase, see Subsection 5.1.4).

To argue why it is sensible to preserve XK but abandon time-reversal K and particle-hole X , imagine that we perturb the hopping in (5.24b) with complex amplitudes:

$$\sigma_i^+ \sigma_j^- + \sigma_j^+ \sigma_i^- \rightarrow e^{i\varphi} \sigma_i^+ \sigma_j^- + e^{-i\varphi} \sigma_j^+ \sigma_i^- \quad 5.45a$$

$$\begin{aligned} &\propto \cos(\varphi) (\sigma_i^x \sigma_j^x + \sigma_i^y \sigma_j^y) \quad 5.45b \\ &\quad + \sin(\varphi) (\sigma_i^x \sigma_j^y - \sigma_i^y \sigma_j^x). \end{aligned}$$

It is obvious that such a perturbation commutes with K and X separately *only* for $\varphi \in \{0, \pi\}$ as the second term violates both time-reversal and particle-hole symmetry. The chiral symmetry XK , however, is preserved for arbitrary φ .

Note that a perturbation that violates a symmetry does not necessarily lift the edge mode degeneracy as there can be other symmetries that protect it. For instance, $\sigma_1^x \sigma_2^y \sigma_3^z$ violates the symmetry generated by YK but does not destroy the edge modes as it commutes with the generators of D_2 (which protects the edge modes, too). Vice versa, $\sigma_1^x \sigma_2^z$ violates the D_2 symmetry but does not gap out the edge modes either because they are still protected by YK . However, the sum of both perturbations $(\sigma_1^x \sigma_2^y \sigma_3^z + \sigma_1^x \sigma_2^z)$ violates *both* symmetries so that there is no symmetry left to protect the edge modes. Numerics (DMRG¹⁵⁰) supports these claims, see Figure 5.1.

¹⁵⁰Density Matrix Renormalization Group.

SPT PHASE WITH RYDBERG ATOMS

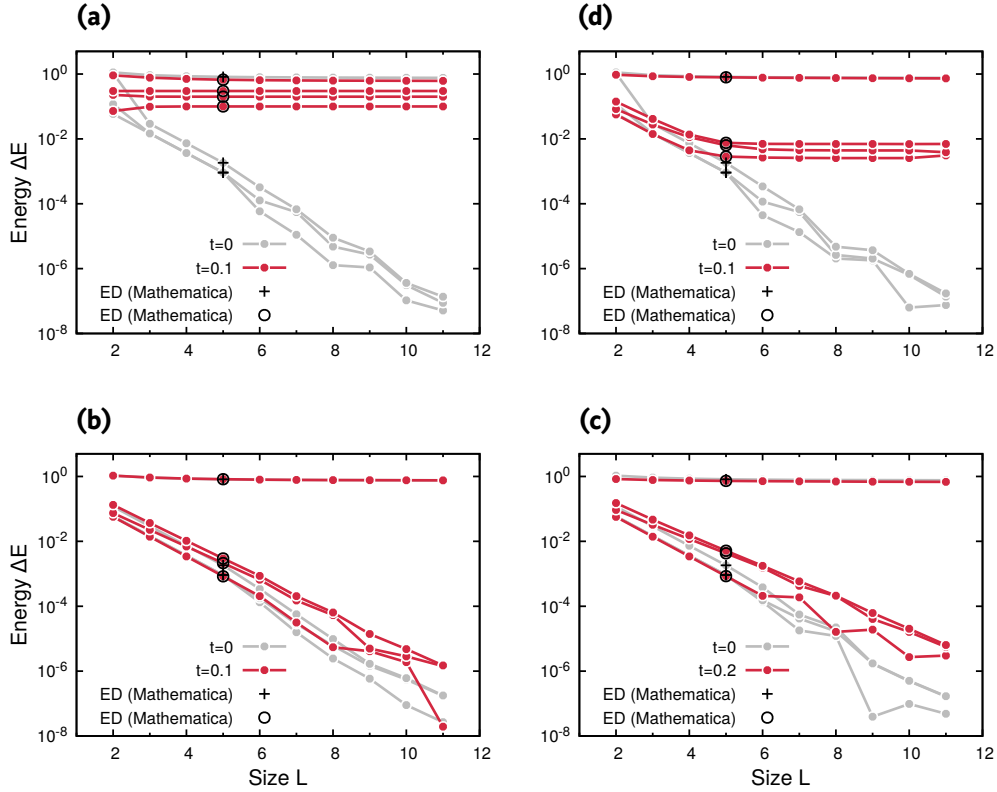


FIGURE 5.1 • Perturbations (DMRG). In each panel we show the five lowest eigenenergies of Hamiltonian (5.24b) with different perturbations $t \times \delta H$ as a function of the number of dimers L ; we set $J_1 = 0.25$ and $J_2 = 1.0$. Bond dimension and number of sweeps used for the DMRG simulations are $D = 200$ and $S = 10$, respectively (we used ALPS for these simulations [251, 361]). The ground state energy is normalized to zero and does not show up in the logarithmic plots. A four-fold ground state degeneracy is therefore indicated by three states with exponentially vanishing energy. The red curves show results with weak perturbations $t = 0.1$; for comparison, the gray curves show results without perturbations ($t = 0$). As consistency check, we performed exact diagonalization (ED) for small systems by means of a completely independent implementation with Mathematica (black crosses and circles). **(a)** $\delta H_1 = \sum_i \sigma_{2i-1}^z + \frac{1}{2} \sigma_{2i}^z$. This is a magnetic field that breaks both D_2 and \mathbb{Z}_2^T and immediately lifts the ground state degeneracy. Note that we explicitly break the (bond-)inversion symmetry of the Hamiltonian by alternating the strength of the perturbation between even and odd sites to exclude potential degeneracies due to inversion symmetry (which we are not interested in as it is a *non-local* symmetry). The perturbation δH_1 lifts the degeneracy already in first-order perturbation theory. **(b)** $\delta H_2 = \sum_i \sigma_{2i-1}^x \sigma_{2i}^y \sigma_{2i+1}^z + \frac{1}{2} \sigma_{2i+2}^x \sigma_{2i+1}^y \sigma_{2i}^z$. This perturbation breaks \mathbb{Z}_2^T (and inversion symmetry) but satisfies D_2 . We clearly see that there is a four-fold ground state degeneracy in the limit $L \rightarrow \infty$. **(c)** $\delta H_3 = \sum_i \sigma_{2i-1}^x \sigma_{2i+1}^z + \frac{1}{2} \sigma_{2i+2}^x \sigma_{2i}^z$. This perturbation breaks D_2 (and inversion symmetry) but satisfies \mathbb{Z}_2^T . Again there is a four-fold ground state degeneracy in the limit $L \rightarrow \infty$. **(d)** $\delta H_4 = \delta H_2 + \delta H_3$. This perturbation breaks *both* D_2 and \mathbb{Z}_2^T . The simulation shows that the degeneracy is indeed lifted for $L \rightarrow \infty$. This splitting is much weaker than for δH_1 as it occurs in second-order perturbation theory.

Classification of One-Dimensional SPT Phases

Here we sketch the idea underlying the classification of symmetry-protected topological phases in one-dimensional interacting spin-systems. Eventually, this leads to a rigorous argument *why* perturbations that respect one of the three symmetry groups discussed above (D_2 , \mathbb{Z}_2^T , $U(1) \times \mathbb{Z}_2^T$) cannot lift the ground state degeneracy and/or connect the topological ground state to the trivial one. The line of arguments is highly non-trivial and asks for advanced mathematical concepts which we will sketch briefly in the following.

Assume that we are given a Hilbert space \mathcal{H} (here \mathcal{H}_{2L}^b) that describes our system, a Hamiltonian H that acts as an operator on this Hilbert space, and an abstract symmetry group G (say $D_2 = \mathbb{Z}_2 \times \mathbb{Z}_2$). The latter is defined by abstract elements (here $D_2 = \{1, x, z, xz\}$) and its multiplication table (here $x^2 = 1$, $z^2 = 1$, $xz = zx$). We say that H features a G -symmetry if there is a (faithful) *linear representation* ρ of G on \mathcal{H} , i.e., an injective map from G to operators on \mathcal{H} with

$$\rho(g_1)\rho(g_2) = \rho(g_1g_2) \quad \text{for } g_1, g_2 \in G \quad 5.46$$

such that $[H, \rho(g)] = 0$ for all $g \in G$. In physics, we are always interested in (anti)unitary representations, i.e., $\rho(g)$ is a (anti)unitary operator on \mathcal{H} (this follows from Wigner's theorem [362]). The representation ρ tells us how the abstract group G is realized in the physical world via its action on states $|\Psi\rangle \in \mathcal{H}$. In our example of D_2 , we define first

$$\rho_i(x) \equiv \sigma_{2i-1}^x \sigma_{2i}^x \quad \text{and} \quad \rho_i(z) \equiv \sigma_{2i-1}^z \sigma_{2i}^z \quad 5.47$$

for each site $i = 1, \dots, L$ (where L is the number of dimers). It is easy to check that these are representations; in particular $\rho_i(xz) = \rho_i(x)\rho_i(z) = \rho_i(z)\rho_i(x) = \rho_i(zx)$ because one anticommutes *two* Pauli matrices. However, the $\rho_i(g)$ are no *symmetries* of H [recall (5.24b)] as they act locally and anticommute with the adjacent coupling terms in H . Thus define a *global* product representation $\rho(g) \equiv \prod_i \rho_i(g)$. In our example, these are

$$\rho(x) = \prod_i \sigma_{2i-1}^x \sigma_{2i}^x = X \quad \text{and} \quad \rho(z) = \prod_i \sigma_{2i-1}^z \sigma_{2i}^z = Z \quad 5.48$$

for which we know that $[H, X] = 0 = [H, Z]$ so that these are true symmetries of the Hamiltonian.

We will return to the concept of representations (5.46) in a minute but first we need a few facts about gapped quantum systems in one dimension. For now, we let go of edge states and consider periodic boundary conditions. This has no impact on the concept of a (topological) phase because the latter is a bulk property; in particular, edge states and a ground state degeneracy for open boundaries are only side-effects of these bulk properties.

So let us consider a one-dimensional, periodic system described by a Hamiltonian H built from local interactions that has a unique ground state $|\Omega\rangle$ and a spectral gap $\Delta > 0$ above the ground state energy E_0 for $L \rightarrow \infty$. Then it can be shown [262, 363–365] that $|\Omega\rangle$ is *short-range entangled* and can be written (or at least approximated) as *matrix-product state (MPS)*,

$$|\Omega\rangle = \sum_{\{i_k\}} \text{Tr} [A^{i_1} A^{i_2} \dots A^{i_{2L}}] |i_1, i_2, \dots, i_{2L}\rangle. \quad 5.49$$

Here, $i_k = 0, 1$ encodes the two spin states at site k , $|i_k\rangle = |0/1\rangle = |\uparrow / \downarrow\rangle$ denotes the local spin state, and the sum is over all 2^{2L} spin configurations. A^i for $i = 0, 1$ are matrices of dimension D (called *bond dimension*) so that the coefficient of the basis state $|i_1, i_2, \dots, i_{2L}\rangle$ in $|\Omega\rangle$ can be encoded as the trace of the matrix product $A^{i_1} A^{i_2} \dots A^{i_{2L}}$ (which motivates the name “matrix-product state”). One can show that if the bond dimension grows exponentially with the system size L , every state in \mathcal{H}_{2L}^b can be written as an MPS. Thus writing states as MPS is only a neat way to encode them (more precisely: their amplitudes) in matrices A^i . The crucial (an non-trivial) point is that for ground states of *gapped* one-dimensional systems $|\Omega\rangle$ this is possible with *constant* bond dimension D , i.e., D does not grow with the system size L . This makes such ground states a rare species in the exponentially large Hilbert space \mathcal{H}_{2L}^b and is directly related to their short-range entanglement. Since MPS are specified by their matrices A^i , we write $|A\rangle$ in the following to emphasize this relation.

In our case, it is beneficial to count the spins σ_{2i-1} and σ_{2i} as *one* site with 4 different states (this is the elementary cell and makes both Hamiltonian and ground state in the fully dimerized limit translational invariant). For $J_1 = 0$ we have a decoupled chain of inter-site Bell pairs $|01\rangle \pm |10\rangle$ as unique ground state (for periodic boundary conditions); the sign depends on the sign of J_2 and I will assume $J_2 < 0$ in the following so that $|01\rangle + |10\rangle$ describes the ground state. Since the Hamiltonian (5.24b) satisfies all of the above criteria, there should be a set of four matrices A^{ij} ($i, j \in \{0, 1\}$) such that

$$|A\rangle = \bigotimes_{i=1}^L (|0\rangle_{2i} |1\rangle_{2i+1} + |1\rangle_{2i} |0\rangle_{2i+1}) \quad 5.50a$$

$$= \sum_{\{i_k\}} \text{Tr} [A^{i_1 i_2} A^{i_3 i_4} \dots A^{i_{2L-1} i_{2L}}] |i_1 i_2, \dots, i_{2L-1} i_{2L}\rangle, \quad 5.50b$$

where the bond dimension of the A^{ij} is independent of L (we ignore normalizing factors throughout this subsection to keep expressions simple). It is easy to check that we can set

$$A_{\alpha\beta}^{ij} \equiv (A^{ij})_{\alpha\beta} = \delta_{i\alpha} \sigma_{j\beta}^x \quad 5.51$$

where σ^x is the Pauli matrix. The indices $\alpha, \beta \in \{0, 1\}$ label the components of the matrix A^{ij} and we see that here $D = 2$ is the bond dimension (for $J_2 > 0$ we had $(A^{ij})_{\alpha\beta} = \delta_{i\alpha} i \sigma_{j\beta}^y$ to account for the negative sign of the Bell states).

In the other phase, for $J_2 = 0$ (and $J_1 < 0$), one finds almost the same ground state—except that the Bell pairs are shifted by one spin,

$$|B\rangle = \bigotimes_{i=1}^L (|0\rangle_{2i-1} |1\rangle_{2i} + |1\rangle_{2i-1} |0\rangle_{2i}) \quad 5.52a$$

$$= \sum_{\{i_k\}} \text{Tr} [B^{i_1 i_2} B^{i_3 i_4} \dots B^{i_{2L-1} i_{2L}}] |i_1 i_2, \dots, i_{2L-1} i_{2L}\rangle. \quad 5.52b$$

Here the structure of the matrices B^{ij} is even simpler, namely

$$B_{\alpha\beta}^{ij} \equiv (B^{ij})_{\alpha\beta} = \sigma_{ij}^x, \quad 5.53$$

where $\alpha, \beta = 0$ are dummy indices, i.e., the matrix product simplifies to a product of numbers and the bond dimension $D = 1$ is sufficient (which characterizes *product states*).

Thus the ground states in both phases can be written as MPS with L -independent bond dimension. Away from the perfectly dimerized points ($J_1 \neq 0$ and $J_2 \neq 0$) and the phase transition ($|J_1| \neq |J_2|$), this remains true with more complicated matrices and larger bond dimensions.

So far, we completely ignored the role played by symmetries in this framework. Let us assume that the Hamiltonian H satisfies all conditions from above and, in addition, features a symmetry G with linear representation ρ . Because of $[H, \rho(g)] = 0$ for $g \in G$ and due to the uniqueness of the ground state $|\Omega\rangle$, it follows that the latter is *invariant* under the action of the symmetry up to a phase,

$$\rho(g)|\Omega\rangle = \alpha(g)|\Omega\rangle \quad \text{with} \quad |\alpha(g)| = 1. \quad 5.54$$

Note that the phase $\alpha(g)$ can be g -dependent and yields a (one-dimensional) representation of G ; for the following discussion, we can ignore this prefactor.

Let us apply $\rho(x)$ for $x \in D_2$ on the ground state $|A\rangle$ from above. Clearly it is invariant,

$$\rho(x)|A\rangle = X|A\rangle \quad 5.55a$$

$$= \bigotimes_{i=1}^L \sigma_{2i}^x \sigma_{2i+1}^x (|0\rangle_{2i} |1\rangle_{2i+1} + |1\rangle_{2i} |0\rangle_{2i+1}) \quad 5.55b$$

$$= \alpha(x)|A\rangle \quad 5.55c$$

with $\alpha(x) = 1$. More interesting is how this invariance is realized in the MPS picture. For simplicity, we check this for one factor of $\rho(x)$, i.e.,

$$\begin{aligned} & \rho_k(x)|A\rangle \\ &= \sum_{\dots} \sum_{i_{2k-1}, i_{2k}} \text{Tr} \left[\dots A^{i_{2k-1} i_{2k}} \dots \right] \sigma_{2k-1}^x \sigma_{2k}^x |\dots i_{2k-1} i_{2k} \dots\rangle \end{aligned} \quad 5.56a$$

$$= \sum_{\dots} \sum_{i, j} \text{Tr} \left[\dots A^{ij} \dots \right] \sigma_{2k-1}^x \sigma_{2k}^x |\dots ij \dots\rangle \quad 5.56b$$

$$= \sum_{\dots} \sum_{i, j} \text{Tr} \left[\dots A^{ij} \dots \right] \sum_{i', j'} (\sigma_{2k-1}^x)_{i', i} (\sigma_{2k}^x)_{j', j} |\dots i' j' \dots\rangle. \quad 5.56c$$

In the second line we replaced $i_{2k-1} \rightarrow i$ and $i_{2k} \rightarrow j$ to clean up the notation. If we write $(\sigma_{2k-1}^x)_{i', i} = \sigma_{i', i}^x$ and $(\sigma_{2k}^x)_{j', j} = \sigma_{j', j}^x$ and exchange the sums over i, j and i', j' , we find

$$\rho_k(x)|A\rangle = \sum_{\dots} \sum_{i', j'} \text{Tr} \left[\dots \sum_{i, j} \sigma_{i', i}^x \sigma_{j', j}^x A^{ij} \dots \right] |\dots i' j' \dots\rangle \quad 5.57a$$

$$= \sum_{\dots} \sum_{i', j'} \text{Tr} \left[\dots \tilde{A}^{i' j'} \dots \right] |\dots i' j' \dots\rangle \quad 5.57b$$

with the transformed matrices

$$\tilde{A}^{i' j'} = \sum_{i, j} \sigma_{i', i}^x \sigma_{j', j}^x A^{ij} \quad 5.58$$

that encode the action of $\rho_k(x)$ on the MPS $|A\rangle$.

In our case, we can evaluate further

$$\tilde{A}_{\alpha\beta}^{i' j'} = \sum_{i, j} \sigma_{i', i}^x \sigma_{j', j}^x A_{\alpha\beta}^{ij} \quad 5.59a$$

$$= \sum_i \sigma_{i', i}^x \delta_{i\alpha} \sum_j \sigma_{j', j}^x \sigma_{j\beta}^x \quad 5.59b$$

$$= \sum_{\alpha'} \sigma_{\alpha', \alpha}^x \delta_{i'\alpha'} \sum_{\beta'} \sigma_{\beta', \beta}^x \sigma_{j'\beta'}^x \quad 5.59c$$

$$= \alpha_k(x) \left[\hat{\sigma}^x A^{i' j'} \hat{\sigma}^x \right]_{\alpha\beta} \quad 5.59d$$

where we reorganized the sums in the third line and introduced $\alpha_k(x) = 1$. In the last line, we write the Pauli matrices with a hat to emphasize that they act on the *virtual* indices α and β whereas the original Pauli matrices of the representation $\rho(x)$ act on the *physical* indices i and j .

Now we know how the matrices transform under the action of $\rho_k(x)$ and can check again the invariance of the ground state under the *global* symmetry $\rho(x)$,

$$\rho(x)|A\rangle = \sum_{\{i_k\}} \text{Tr} \left[\tilde{A}^{i_1 i_2} \tilde{A}^{i_3 i_4} \dots \tilde{A}^{i_{2L-1} i_{2L}} \right] |i_1 i_2, \dots, i_{2L-1} i_{2L}\rangle \quad 5.60a$$

$$= \alpha(x) \sum_{\{i_k\}} \text{Tr} \left[\hat{\sigma}^x A^{i_1 i_2} \hat{\sigma}^x \hat{\sigma}^x A^{i_3 i_4} \hat{\sigma}^x \dots \hat{\sigma}^x A^{i_{2L-1} i_{2L}} \hat{\sigma}^x \right] \times |i_1 i_2, \dots, i_{2L-1} i_{2L}\rangle \quad 5.60b$$

$$= \alpha(x) \sum_{\{i_k\}} \text{Tr} \left[A^{i_1 i_2} A^{i_3 i_4} \dots A^{i_{2L-1} i_{2L}} \right] |i_1 i_2, \dots, i_{2L-1} i_{2L}\rangle \quad 5.60c$$

$$= \alpha(x)|A\rangle, \quad 5.60d$$

where we used the cyclicity of the trace and defined $\alpha(x) \equiv \prod_k \alpha_k(x)$. Along the same lines one can show for the transformation under $\rho_k(z)$ that $\tilde{A}^{i'j'} = \alpha_k(z) \hat{\sigma}^z A^{i'j'} \hat{\sigma}^z$ with $\alpha_k(z) = -1$ so that $\rho(z)|A\rangle = \alpha(z)|A\rangle$ with $\alpha(z) = (-1)^L$.

The results we demonstrated here for a specific example are valid in general [112, 366]: For a symmetry $\rho(g) = \pi(g) \otimes \pi(g) \dots \otimes \pi(g)$ that acts *locally* on each physical site via unitary representations $\pi(g)$, and an MPS $|A\rangle$ that is invariant under the action of $\rho(g)$ up to a phase, $\rho(g)|A\rangle = \alpha(g)|A\rangle$, one can show that the matrices A^i transform as

$$\sum_i [\pi(g)]_{i'i} A^i = \gamma(g) V^{-1}(g) \cdot A^{i'} \cdot V(g) \quad 5.61$$

where the “ \cdot ” denote matrix products and $\gamma(g)$ is a phase (a one-dimensional linear representation of G). We stress that this necessarily requires the invariance of the state under $\rho(g)$! For instance, the reorganization of the sums in (5.59c) was possible because the state encoded by these particular matrices A^{ij} was invariant under this particular representation $\rho(x)$.

If we recall that π satisfies

$$\pi(g_1)\pi(g_2) = \pi(g_1 g_2) \quad \text{for } g_1, g_2 \in G \quad 5.62$$

as a *linear representation* of G , one can show that the matrices V in (5.61) satisfy *almost* the same relation,

$$V(g_1)V(g_2) = \chi(g_1, g_2)V(g_1 g_2) \quad \text{for } g_1, g_2 \in G \quad 5.63$$

where $|\chi(g_1, g_2)| = 1$ is a g_1 - and g_2 -dependent phase. The function $\chi(g_1, g_2)$ is called (*2*-)cocycle or *factor system* of the *projective representation* $V(g)$; it is not arbitrary: Application of associativity, $(g_1 g_2)g_3 = g_1(g_2 g_3)$, yields the *cocycle condition*

$$\chi(g_1, g_2)\chi(g_1 g_2, g_3) = \chi(g_2, g_3)\chi(g_1, g_2 g_3) \quad 5.64$$

which must be satisfied to make (5.63) well-defined on the entire group G .

The reason for this “relaxed” multiplication law is that in (5.61) all phases $\chi(g_1, g_2)$ that violate the multiplication rules of the abstract group cancel because $V(g)$ and $V^{-1}(g)$ always pair up. Matrices that satisfy the relation (5.63) realize a so called *projective representation* of the group G on the virtual bond vector space \mathbb{C}^D ; *linear representations* are then special cases of projective representations with $\chi(g_1, g_2) \equiv 1$.

In our example, we started from the linear representations $\pi(a) = \rho_k(a) = \sigma_{2k-1}^a \sigma_{2k}^a$ ($a = x, z$) that act on the physical sites and showed by straightforward calculations that the action on the bond space is given by

$$V(x) = \hat{\sigma}^x \quad \text{and} \quad V(z) = \hat{\sigma}^z. \quad 5.65$$

However, in D_2 we have $xz = zx$ but clearly $V(x)V(z) = -V(z)V(x)$ so that V cannot satisfy (5.62): we found a projective representation of D_2 . Note that we have two choices to *define* $V(xz) = V(zx)$, namely

$$V_1(xz) = V_1(zx) \equiv \hat{\sigma}^x \hat{\sigma}^z \quad 5.66a$$

$$\text{or} \quad V_2(xz) = V_2(zx) \equiv \hat{\sigma}^z \hat{\sigma}^x. \quad 5.66b$$

Together with $V_i(x) = \hat{\sigma}^x$, $V_i(z) = \hat{\sigma}^z$ and $V_i(1) = \mathbb{1}$, one finds the multiplication rules

$$\begin{aligned} V_1(x)V_1(z) &= \hat{\sigma}^x \hat{\sigma}^z = +1 \cdot V_1(xz), \\ V_1(z)V_1(x) &= \hat{\sigma}^z \hat{\sigma}^x = -1 \cdot V_1(zx) \end{aligned} \quad 5.67a$$

$$\begin{aligned} \text{or} \quad V_2(x)V_2(z) &= \hat{\sigma}^x \hat{\sigma}^z = -1 \cdot V_2(xz), \\ V_2(z)V_2(x) &= \hat{\sigma}^z \hat{\sigma}^x = +1 \cdot V_2(zx). \end{aligned} \quad 5.67b$$

Thus the cocycles for the two projective representations read

$$\chi_1(x, z) = +1, \quad \chi_1(z, x) = -1 \quad 5.68a$$

$$\text{or} \quad \chi_2(x, z) = -1, \quad \chi_2(z, x) = +1, \quad 5.68b$$

so that (5.63) is satisfied for choices. Note that there are also other non-trivial elements, e.g., $\chi_1(xz, x) = -1$ and $\chi_2(xz, z) = -1$. To understand the relation between these two projective representations, let us step back and recall the transformation law of MPS matrices

$$\sum_i [\pi(g)]_{i'i} A^i = \gamma(g) V^{-1}(g) \cdot A^{i'} \cdot V(g) \quad 5.69a$$

$$= \gamma(g) [f(g)V(g)]^{-1} \cdot A^{i'} \cdot [f(g)V(g)] \quad 5.69b$$

$$= \gamma(g) \tilde{V}(g)^{-1} \cdot A^{i'} \cdot \tilde{V}(g) \quad 5.69c$$

where we defined $\tilde{V}(g) \equiv f(g)V(g)$ with an *arbitrary* g -dependent phase $f(g)$, i.e., $|f(g)| = 1$ and $f(g) \in \mathbb{C}$ (note that $[f(g)]^{-1} = f^*(g)$). We conclude that projective representations V and \tilde{V} that are related by a g -dependent phase $f(g)$

are *completely equivalent* on the level of an MPS. Let $\chi(g_1, g_2)$ be the cocycle of the representation V ; then we find for the equivalent representation \tilde{V} :

$$\tilde{V}(g_1)\tilde{V}(g_2) = f(g_1)f(g_2)V(g_1)V(g_2) \quad 5.70a$$

$$= f(g_1)f(g_2)\chi(g_1, g_2)V(g_1g_2) \quad 5.70b$$

$$= f(g_1)f(g_2)[f(g_1g_2)]^{-1}\chi(g_1, g_2)\tilde{V}(g_1g_2) \quad 5.70c$$

$$= \tilde{\chi}(g_1, g_2)\tilde{V}(g_1g_2) \quad 5.70d$$

with the relation between the two cocycles

$$\frac{f(g_1)f(g_2)}{f(g_1g_2)}\chi(g_1, g_2) = \tilde{\chi}(g_1, g_2). \quad 5.71$$

This defines an equivalence relation on the set of all cocycles [i.e., phase-valued functions of two group elements that satisfy the cocycle condition (5.64)]: Two cocycles belong to the same equivalence class, write $\chi \sim \tilde{\chi}$ or $[\chi] = [\tilde{\chi}]$, if and only if there exists a function f such that (5.71) holds. The set of all these equivalence classes of cocycles features an abelian group structure [since the product of two cocycles yields a new cocycle, check (5.64)] and is called *second cohomology group of G in $U(1)$* , write $H^2(G, U(1))$. Here, $U(1)$ signifies that the functions f and the cocycles χ are phases. Equation (5.69) revealed that the action of a linear representation $\rho(g)$ on an invariant MPS is characterized *not* by a *particular* projective representation $V(g)$ on its (virtual) bond space but by the *cohomology class* $[\chi] \in H^2(G, U(1))$ that its cocycle belongs to.

If we return to the example above, it is now clear that the non-uniqueness of the projective representations that can be constructed from the ground state MPS $|A\rangle$ is a consequence of this fact. Indeed, the transformation

$$V_1(1) = \mathbb{1} = +1 \cdot V_2(1) = f(1) \cdot V_2(1) \quad 5.72a$$

$$V_1(x) = \hat{\sigma}^x = +1 \cdot V_2(x) = f(x) \cdot V_2(x) \quad 5.72b$$

$$V_1(z) = \hat{\sigma}^z = +1 \cdot V_2(z) = f(z) \cdot V_2(z) \quad 5.72c$$

$$V_1(xz) = \hat{\sigma}^x \sigma^z = -1 \cdot V_2(xz) = f(xz) \cdot V_2(xz) \quad 5.72d$$

maps the two representations into each other and via (5.71) relates also their cocycles χ_1 and χ_2 , e.g.,

$$\chi_1(z, x) = -1 = \frac{1 \cdot 1}{-1} \cdot 1 = \frac{f(z)f(x)}{f(zx)}\chi_2(z, x). \quad 5.73$$

Thus $[\chi_1] = [\chi_2] \in H^2(D_2, U(1))$ belong to the same cohomology class.

It is important to realize that this concept of equivalence allows for the comparison of projective representations V and \tilde{V} even if they do not have the same dimension D because the equivalence relation (5.71) only relies on their cocycles χ and $\tilde{\chi}$. Then, the equivalence $\chi \sim \tilde{\chi}$ does not imply $\tilde{V}(g) = f(g)V(g)$ [this

equation does not make sense because $V(g)$ and $\tilde{V}(g)$ have different dimensions]. If we keep this in mind, we can now state a crucial (and non-trivial) fact for matrix product states [17, 119]:

Let H_A and H_B be two one-dimensional, gapped Hamiltonians on a common Hilbert space \mathcal{H} with symmetry $\rho(g)$ for $g \in G$ and unique ground states $|A\rangle$ and $|B\rangle$, respectively. The latter are invariant under the action of ρ and can be described by MPS with matrices A^i and B^i of bond dimensions D_A and D_B . The action of the linear representation $\rho(g)$ on these states induces projective representations V_A and V_B on their bond spaces with cocycles χ_A and χ_B and matrix dimensions D_A and D_B . *Then there exists a path $H(\lambda)$ of gapped, ρ -symmetric Hamiltonians on \mathcal{H} with $H(0) = H_A$ and $H(1) = H_B$ if and only if $\chi_A \sim \chi_B$, i.e., iff V_A and V_B are projective representations of the same cohomology class $[\chi_A] = [\chi_B] \in H^2(G, \text{U}(1))$.* This implies that two symmetric states $|A\rangle$ and $|B\rangle$ belong to the same quantum phase if and only if their corresponding cocycles (defined via their MPS representation) are representatives of the same cohomology class. This fact leads to the somewhat cryptic statement that the one-dimensional symmetry-protected topological phases of interacting spin systems (with symmetry group G), are in one-to-one correspondence with elements of the second cohomology group $H^2(G, \text{U}(1))$.

While the proof of the direction “same cohomology class” \Rightarrow “same phase” is rather technical (one has to construct a path between both Hamiltonians), the inverse direction is more intuitive: Assume $H(\lambda)$ parametrizes a manifold of gapped Hamiltonians that do not violate the symmetry $\rho(g)$ for all $g \in G$. For every λ we can follow the above procedure and derive the λ -dependent quantities

$$H(\lambda) \rightarrow |A(\lambda)\rangle \rightarrow A^i(\lambda) \rightarrow V_\lambda \rightarrow \chi_\lambda \rightarrow [\chi_\lambda]. \quad 5.74$$

It is now sensible to assume that none of these steps introduces discontinuities so that the mapping $\lambda \mapsto [\chi_\lambda]$ is continuous in some appropriately defined sense. In all cases relevant for the classification of SPT phases, $H^2(G, \text{U}(1))$ is a discrete group (in many cases even finite). But then the continuous map $\lambda \mapsto [\chi_\lambda]$ must be constant on domains of λ where it is well-defined, i.e., all ground states that can be continuously connected without closing the gap or violating the symmetry belong to the same cohomology class.

If $H(\lambda)$ connects two *different* phases so that $|A\rangle$ and $|B\rangle$ belong to different cohomology classes, then the construction in (5.74) must be ill-defined somewhere on the path from H_A to H_B . There are two possibilities how this can happen:

- 1 $H(\lambda)$ becomes gapless for some λ^* . Then the construction of a well-defined projective representation fails because the bond dimension D_{λ^*} is unbounded in the thermodynamic limit (the ground states of gapless Hamiltonians are weakly long-range entangled in one dimension).

- 2 $H(\lambda)$ violates the symmetry for some λ^* and $|A(\lambda^*)\rangle$ is no longer invariant under $\rho(g)$ such that the construction of a well-defined projective representation fails even though D_{λ^*} remains bounded.

Equipped with this new knowledge, let us return to the example $G = D_2$ with the two ground states $|A\rangle$ and $|B\rangle$. Recall that we still consider periodic boundaries; nevertheless it is clear that cutting the system between physical sites makes $|B\rangle$ the ground state of the trivial phase ($J_1 < 0$ and $J_2 = 0$) whereas $|A\rangle$ becomes the ground state of the topological phase ($J_2 < 0$ and $J_1 = 0$), recall (5.50a) and (5.52a). We can now prove that both cannot be continuously connected without closing the gap or violating the D_2 symmetry $\rho(g)$ if their cohomology classes cannot be related via (5.71). Possible representatives for the cocycles of the topological phase $|A\rangle$ where already given in (5.68). For the trivial phase with $B_{\alpha\beta}^{ij} = \sigma_{ij}^x$, we immediately find

$$\tilde{B}_{\alpha\beta}^{i'j'} = \sum_{i,j} \sigma_{i',i}^x \sigma_{j',j}^x \sigma_{ij}^x = \sigma_{i',j'}^x = \gamma(x) [1 \cdot B^{i'j'} \cdot 1]_{\alpha\beta} \quad 5.75a$$

$$\tilde{B}_{\alpha\beta}^{i'j'} = \sum_{i,j} \sigma_{i',i}^z \sigma_{j',j}^z \sigma_{ij}^x = -\sigma_{i',j'}^x = \gamma(z) [1 \cdot B^{i'j'} \cdot 1]_{\alpha\beta} \quad 5.75b$$

with the one-dimensional representation $\gamma(g)$; thus the projective representation reads

$$V_B(1) = 1, \quad V_B(x) = 1, \quad V_B(z) = 1, \quad V_B(xz) = 1. \quad 5.76$$

This is the trivial representation with trivial cocycle $\chi_B(g_1, g_2) \equiv 1$ that belongs to the cohomology class [1] which is the identity element of $H^2(D_2, U(1))$. Note that this also follows directly from the fact that $|B\rangle$ is a product state and therefore has bond dimension $D = 1$. Consequently, $V_B(g)$ must be a phase (a 1×1 unitary matrix) and the representation (5.76) can always be achieved by appropriate factors $f(g)$.

To show that ($V_A = V_1$)

$$V_A(1) = 1, \quad V_A(x) = \hat{\sigma}^x, \quad V_A(z) = \hat{\sigma}^z, \quad V_A(xz) = \hat{\sigma}^x \hat{\sigma}^z \quad 5.77$$

belongs to a different cohomology class, we have to show that the equation

$$\chi_A(g_1, g_2) = \frac{f(g_1)f(g_2)}{f(g_1g_2)} \chi_B(g_1, g_2) = \frac{f(g_1)f(g_2)}{f(g_1g_2)} \quad 5.78$$

has no solution $f(g)$, i.e., $[\chi_A] \neq [\chi_B] = [1]$. If we assume that there is such a function, we immediately encounter a contradiction:

$$+1 = \chi_A(x, z) = \frac{f(x)f(z)}{f(xz)} = \frac{f(z)f(x)}{f(zx)} = \chi_A(z, x) = -1. \quad 5.79$$

With this we showed that $|A\rangle$ is a non-trivial topological phase protected by D_2 with the on-site representation $\rho_k(a) = \sigma_{2k-1}^a \sigma_{2k}^a$ ($a = x, z$). In addition, we demonstrated that $H^2(D_2, U(1))$ is non-trivial as it contains at least two elements, $[1]$ and $[\chi_A]$. One can show that there are no more inequivalent classes and therefore $H^2(D_2, U(1)) = \mathbb{Z}_2$. Physically this means that there are only two phases possible in one dimension that are protected by D_2 : the trivial $[1]$ (a representative of which is $|B\rangle$) and a topological $[\chi_A]$ (a representative of which is $|A\rangle$). This can be read off the respective classification tables for SPT phases, see e.g. [18, 112].

Application to $U(1) \times \mathbb{Z}_2^T$

Let us now focus on the symmetry group $U(1) \times \mathbb{Z}_2^T$ represented by particle number conservation and the antiunitary ‘‘chiral’’ symmetry,

$$R(\phi) = \exp \left[i\phi \sum_i \frac{\mathbb{1} - \sigma_i^z}{2} \right] \quad \text{and} \quad S = XK = \prod_i \sigma_i^x \circ K. \quad 5.80$$

Note: Here we label the *representation* of the chiral symmetry by $S = XK$ but write $T \in \mathbb{Z}_2^T$ for the abstract group element, i.e., $\rho(T) = S$. This is not to be confused with the $T = K$ in Subsection 5.1.1. Similarly, we write $R(\phi)$ for the (global) *representation* of $U(1)$ and $R_\phi \in U(1)$ for the abstract group element.

On each physical site, the representations are

$$r_k(\phi) = e^{i\phi} e^{-i\frac{\phi}{2}(\sigma_{2k-1}^z + \sigma_{2k}^z)} \quad \text{and} \quad s_k = \sigma_{2k-1}^x \sigma_{2k}^x \circ K. \quad 5.81$$

Note that $s_k^2 = \mathbb{1}$ and $r_k(2\pi) = \mathbb{1}$, but

$$s_k r_k(\phi) = e^{-2i\phi} r_k(\phi) s_k \quad 5.82$$

whereas the abstract elements of $U(1)$ and \mathbb{Z}_2^T *commute* (this is implied by the direct product ‘‘ \times ’’ of groups). Therefore (5.81) defines a *projective* representation on the physical sites (and not a linear one as we assumed in our discussion of D_2). But this is only a pseudo problem as we can multiply each group element by an arbitrary phase $f(g)$ without changing the physical content of the representation. Indeed, since $\rho_k(g)|\Psi\rangle$ and $f(g)\rho_k(g)|\Psi\rangle$ describe the same physical state, there is no physical difference between $\rho_k(g)$ and $f(g)\rho_k(g)$. So let $f(R_\phi) \equiv e^{-i\phi}$ and $f(T) = 1$; this yields the equivalent representation

$$\tilde{r}_k(\phi) = f(R_\phi) r_k(\phi) = e^{-i\frac{\phi}{2}(\sigma_{2k-1}^z + \sigma_{2k}^z)} \quad 5.83a$$

$$\text{and} \quad \tilde{s}_k = f(T) s_k = \sigma_{2k-1}^x \sigma_{2k}^x \circ K \quad 5.83b$$

which now satisfies $\tilde{s}_k \tilde{r}_k(\phi) = \tilde{r}_k(\phi) \tilde{s}_k$ and therefore defines a linear (antiunitary) representation of $U(1) \times \mathbb{Z}_2^T$.

Now we can follow the same procedure as for D_2 and calculate the action of $\tilde{r}_k(\phi)$ and \tilde{s}_k on the matrices A^{ij} and B^{ij} of the MPS $|A\rangle$ and $|B\rangle$. Note that both $|A\rangle$ and $|B\rangle$ are invariant under the action of $\tilde{R}(\phi) = \prod_k \tilde{r}_k(\phi)$ and $\tilde{S} = S$ so that we again expect a projective representation on the virtual bond indices. The question is whether their corresponding cocycles belong to different cohomology classes of $H^2(\text{U}(1) \times \mathbb{Z}_2^T, \text{U}(1))$ which, according to the above continuity argument, would obstruct continuous deformations between the two states without closing the gap or violating the symmetry representation (5.80).

Straightforward calculations yield for the matrices of the ‘‘topological’’ state $|A\rangle$ the action of $\tilde{r}_k(\phi)$

$$\tilde{A}_{\alpha\beta}^{i'j'} = \sum_{ij} \left[e^{-\frac{\phi}{2}\sigma^z} \right]_{i',i} \left[e^{-\frac{\phi}{2}\sigma^z} \right]_{j',j} A_{\alpha\beta}^{ij} \quad 5.84a$$

$$= \sum_{\alpha'\beta'} \left[e^{-\frac{\phi}{2}\sigma^z} \right]_{\alpha,\alpha'} \left[e^{+\frac{\phi}{2}\sigma^z} \right]_{\beta',\beta} \delta_{i'\alpha'} \sigma_{j'\beta'}^x \quad 5.84b$$

$$= \gamma(R_\phi) \left[e^{-\frac{\phi}{2}\hat{\sigma}^z} A^{i'j'} e^{+\frac{\phi}{2}\hat{\sigma}^z} \right]_{\alpha\beta} \quad 5.84c$$

$$= \gamma(R_\phi) \left[e^{\frac{\phi}{2}(\mathbb{1}-\hat{\sigma}^z)} A^{i'j'} e^{-\frac{\phi}{2}(\mathbb{1}-\hat{\sigma}^z)} \right]_{\alpha\beta} \quad 5.84d$$

where the one-dimensional representation $\gamma(R_\phi) = 1$ is trivial. Note that in the last line we inserted the phase $e^{i\frac{\phi}{2}}$ so simplify our discussion of the cocycles below. That this is possible follows from the structure of (5.84c) and illustrates the emergence of *projective* representations in this context. Here we found the projective representation $V_A(R_\phi) = e^{-\frac{\phi}{2}(\mathbb{1}-\hat{\sigma}^z)}$ for $R_\phi \in \text{U}(1)$. Note that $V_A(R_\pi) \cdot V_A(R_\pi) = e^{-\pi(\mathbb{1}-\hat{\sigma}^z)} = \mathbb{1} = V_A(R_0)$ such that $V_A(R_\phi)$ *alone* is a linear representation of $\text{U}(1)$ and the corresponding cocycle is trivial,

$$\chi_A(R_{\phi_1}, R_{\phi_2}) = 1. \quad 5.85$$

(This is false if we do not insert the phase gauge $e^{i\frac{\phi}{2}}$.)

But of course we have to take care of $\mathbb{Z}_2^T = \{1, T\}$ as well. Along the same lines one finds for the action of \tilde{s}_k

$$\tilde{A}_{\alpha\beta}^{i'j'} = \sum_{ij} \sigma_{i',i}^x \sigma_{j',j}^x \left(A_{\alpha\beta}^{ij} \right)^* \quad 5.86a$$

$$= \sum_{\alpha'\beta'} \sigma_{\alpha,\alpha'}^x \sigma_{\beta',\beta}^x \delta_{i'\alpha'} \sigma_{j'\beta'}^x \quad 5.86b$$

$$= \gamma(T) \left[\hat{\sigma}^x A^{i'j'} \hat{\sigma}^x \right]_{\alpha\beta} \quad 5.86c$$

with the trivial 1D representation $\gamma(T) = 1$; thus we have $V_A(T) = \hat{\sigma}^x K$ (the complex conjugation K must be added for the correct evaluation of the projective representation, see [112]). Clearly $V_A(T)V_A(T) = \mathbb{1} = V_A(1) = V_A(T^2)$ so that

again the corresponding cocycle is trivial,

$$\chi_A(T, T) = 1. \quad 5.87$$

But what about $\chi_A(T, R_\phi)$ and $\chi_A(R_\phi, T)$? As for D_2 , we have two choices and we define

$$V_A(TR_\phi) = V_A(R_\phi T) \equiv V_A(R_\phi)V_A(T) = e^{-i\frac{\phi}{2}(\mathbb{1}-\hat{\sigma}^z)}\hat{\sigma}^x K \quad 5.88$$

(one can check that this is a valid choice by concatenating the application of \tilde{s}_k and $\tilde{r}_k(\phi)$). With this choice (that defines a particular representative of the projective representation), we find the multiplication rules

$$\begin{aligned} V_A(R_\phi) V_A(T) &= e^{-i\frac{\phi}{2}(\mathbb{1}-\hat{\sigma}^z)}\hat{\sigma}^x K \\ &= 1 \cdot V_A(R_\phi T) = \chi_A(R_\phi, T) \cdot V_A(R_\phi T) \end{aligned} \quad 5.89a$$

$$\begin{aligned} V_A(T) V_A(R_\phi) &= \hat{\sigma}^x K e^{-i\frac{\phi}{2}(\mathbb{1}-\hat{\sigma}^z)} \\ &= e^{i\phi} \cdot V_A(TR_\phi) = \chi_A(T, R_\phi) \cdot V_A(TR_\phi) \end{aligned} \quad 5.89b$$

so that $\chi_A(T, R_\phi) = e^{i\phi}$ is the only non-trivial value of the cocycle (without the gauge factor $e^{i\frac{\phi}{2}}$, it would be trivial; but then $\chi_A(R_{\phi_1}, R_{\phi_2}) \neq 1$ becomes non-trivial to ensure that the representation is still in the same cohomology class).

If we follow the same procedure for the “trivial” state $|B\rangle$ with matrices $B_{\alpha\beta}^{ij} = \sigma_{ij}^x$, it is clear that (as for D_2) we end up with the trivial representation,

$$\begin{aligned} V_B(1) &= 1, & V_B(R_\phi) &= 1, & V_B(T) &= 1, \\ \text{and } V_B(TR_\phi) &= V_B(R_\phi T) &= 1, \end{aligned} \quad 5.90$$

with the trivial cocycle $\chi_B(g_1, g_2) = 1$ for all $g_1, g_2 \in \text{U}(1) \times \mathbb{Z}_2^T$. Clearly $|B\rangle$ deserves the label “trivial”: it is a product state and its cohomology class is $[\chi_B] = [1] \in H^2(\text{U}(1) \times \mathbb{Z}_2^T, \text{U}(1))$.

The crucial question is now whether $[\chi_A] \neq [\chi_B]$. Since χ_B is trivial, the question is whether χ_A can be trivialized with a phase factor $f(g)$, i.e., whether

$$\chi_A(g_1, g_2) \stackrel{?}{=} \frac{f(g_1)f^{\sigma(g_1)}(g_2)}{f(g_1g_2)} \quad 5.91$$

for all $g_1, g_2 \in \text{U}(1) \times \mathbb{Z}_2^T$. Here, $\sigma(g) = +1(-1)$ if g is represented by a unitary (antiunitary) operator (see the side note on *twisted* group cohomology below); in particular, $\sigma(R_\phi) = +1$ and $\sigma(T) = -1$.

Similar as for D_2 , we can show that this is impossible but the argument is a bit more involved. First, note that $\chi_A(R_{\phi_1}, R_{\phi_2}) = 1 = f(R_{\phi_1})f(R_{\phi_2})/f(R_{\phi_1+\phi_2})$ implies that $f(R_\phi)$ is a linear, one-dimensional representation of $\text{U}(1)$, i.e., it takes the form $f(R_\phi) = e^{ik\phi}$ for $k \in \mathbb{Z}$. If we combine $\chi_A(R_\phi, T) = 1 =$

$f(R_\phi)f(T)/f(R_\phi T)$ and $\chi_A(T, R_\phi) = e^{i\phi} = f(T)f^{-1}(R_\phi)/f(TR_\phi)$ and use that $R_\phi T = TR_\phi$, we find $e^{i\phi} = 1/f^2(R_\phi) = e^{-2ik\phi}$; but this cannot be satisfied for all $\phi \in [0, 2\pi)$ with $k \in \mathbb{Z}$.

We conclude that $[1] \neq [\chi_A] \in H^2(\mathrm{U}(1) \times \mathbb{Z}_2^T, \mathrm{U}(1))$ and therefore $|A\rangle$ indeed is a topological phase, symmetry-protected by $\mathrm{U}(1) \times \mathbb{Z}_2^T$ with physical representation (5.80); in particular, $|A\rangle$ and $|B\rangle$ cannot be connected by a smoothly varying Hamiltonian $H(\lambda)$ that commutes with the symmetry operators and remains gapped in the thermodynamic limit.

As a final remark, we stress that there are in total *four* distinct cohomology classes of $\mathrm{U}(1) \times \mathbb{Z}_2^T$ [18] and

$$H^2(\mathrm{U}(1) \times \mathbb{Z}_2^T, \mathrm{U}(1)) = \mathbb{Z}_2 \times \mathbb{Z}_2. \quad 5.92$$

That is, the symmetry group $\mathrm{U}(1) \times \mathbb{Z}_2^T$ can protect two additional topological phases that smoothly connect neither to $|A\rangle$ nor to $|B\rangle$ (these are related to “chiral” symmetries that square to -1 , i.e., $V(T)^2 = -\mathbb{1}$). This is in contrast to D_2 where $H^2(D_2, \mathrm{U}(1)) = \mathbb{Z}_2$ so that $|A\rangle$ is the only topologically non-trivial phase. There is an important lesson: Whether a given state in some Hilbert space is in a symmetry-protected topological phase is *not* a property of the state alone but rather a feature of the state *with respect to* a representation of a given symmetry group that acts on the Hilbert space. The *same* state can be *trivial* w.r.t. the action of symmetry group G_1 while it is *topological* w.r.t. the action of another symmetry group G_2 . This is the essence of *symmetry protection*.

Edge Modes

So far we considered chains with periodic boundary conditions and a unique, symmetric ground state. The *bulk* properties of short-range correlated states, such as $|A\rangle$ and $|B\rangle$, should not depend on the boundaries. In particular, the MPS description should remain valid—except for the boundaries where we have to modify the matrices since there is no entanglement between the opposite edges of the system¹⁵¹.

For the topological phase, we have the ground state

$$|A(0, 0)\rangle = |0\rangle_0 \otimes \bigotimes_{i=1}^{L-1} (|0\rangle_{2i}|1\rangle_{2i+1} + |1\rangle_{2i}|0\rangle_{2i+1}) \otimes |0\rangle_{2L} \quad 5.93a$$

$$= \sum_{\{i_k\}} A_{[1]}^{i_1 i_2} A_{[2]}^{i_3 i_4} \cdots A_{[L]}^{i_{2L-1} i_{2L}} |i_1 i_2, \dots, i_{2L-1} i_{2L}\rangle, \quad 5.93b$$

¹⁵¹For periodic boundaries, the same correlations are “short-range”; we see that changing from periodic to open boundary conditions only changes our interpretation of mathematical objects, not the mathematical objects themselves.

where the matrices $A_{[k]}^{ij}$ now can depend on the site $k = 1, \dots, L$ as we break translational invariance. The trace is gone because we do not need entanglement between the first and the last site (recall that the trace is nothing but a “long-range” matrix product between the first and the last matrix). Note that the matrices do not have to be square; in particular, the first and last one are row- and column vectors to ensure that the complete matrix product yields numbers as amplitudes of the basis states.

Since the bulk is the same as for periodic boundaries, we find the same matrices

$$A_{[k]\alpha\beta}^{ij} \equiv \left(A_{[k]}^{ij} \right)_{\alpha\beta} = \delta_{i\alpha} \sigma_{j\beta}^x \quad \text{for } k = 2, \dots, L-1, \quad 5.94$$

whereas on the first and last site, we have

$$A_{[1]}^{ij} = \delta_{i0} \sigma_{j\beta}^x \quad \text{and} \quad A_{[L]}^{ij} = \delta_{i\alpha} \delta_{j0} \quad 5.95$$

to account for the fixed boundary spins.

In the trivial phase, the open boundaries do not cut entangled pairs so that the state

$$|B\rangle = \bigotimes_{i=1}^L (|0\rangle_{2i-1} |1\rangle_{2i} + |1\rangle_{2i-1} |0\rangle_{2i}) \quad 5.96a$$

$$= \sum_{\{i_k\}} B_{[1]}^{i_1 i_2} B_{[2]}^{i_3 i_4} \dots B_{[L]}^{i_{2L-1} i_{2L}} |i_1 i_2, \dots, i_{2L-1} i_{2L}\rangle \quad 5.96b$$

is described by the same (site-independent) matrices

$$B_{[k]\alpha\beta}^{ij} \equiv \left(B_{[k]}^{ij} \right)_{\alpha\beta} = \sigma_{ij}^x. \quad 5.97$$

(Note that these are already numbers so that special row/column matrices at the boundaries are not necessary to convert the “matrix product” into an amplitude.)

Let us act with symmetry operators on these states. We demonstrate this for D_2 instead of $U(1) \times \mathbb{Z}_2^T$ because the former is simpler and more suitable for a pedagogical exposition.

First, for the trivial state $|B\rangle$ we find the same transformation rules as for periodic boundaries because the matrices B^{ij} are the same:

$$\sum_{i,j} \sigma_{i',i}^x \sigma_{j',j}^x B_{\alpha\beta}^{ij} = \gamma(x) [1 \cdot B^{i'j'} \cdot 1]_{\alpha\beta}, \quad 5.98a$$

$$\sum_{i,j} \sigma_{i',i}^z \sigma_{j',j}^z B_{\alpha\beta}^{ij} = \gamma(z) [1 \cdot B^{i'j'} \cdot 1]_{\alpha\beta}. \quad 5.98b$$

In particular, the state is still invariant under the global symmetry operators $\rho(g)$ for $g \in D_2$ and there is no ground state degeneracy (more formally, the ground state space forms a one-dimensional representation $\gamma^L(g)$ of the symmetry group D_2).

Similarly, the action on the topological state $|A\rangle$ *in the bulk* (for $k = 2, \dots, L-1$) remains also unchanged,

$$\sum_{i,j} \sigma_{i',i}^x \sigma_{j',j}^x A_{[k]\alpha\beta}^{ij} = \gamma(x) \left[\hat{\sigma}^x \cdot A_{[k]}^{i'j'} \cdot \hat{\sigma}^x \right]_{\alpha\beta}, \quad 5.99a$$

$$\sum_{i,j} \sigma_{i',i}^z \sigma_{j',j}^z A_{[k]\alpha\beta}^{ij} = \gamma(z) \left[\hat{\sigma}^z \cdot A_{[k]}^{i'j'} \cdot \hat{\sigma}^z \right]_{\alpha\beta}, \quad 5.99b$$

whereas on the boundaries we have (here for $k = 1$)

$$\sum_{i,j} \sigma_{i',i}^x \sigma_{j',j}^x A_{[1]\alpha\beta}^{ij} = \sum_i \sigma_{i',i}^x \delta_{i0} \sum_j \sigma_{j',j}^x \sigma_{j\beta}^x \quad 5.100a$$

$$= \sum_i \sigma_{i',i}^x \delta_{i0} \sum_{\beta'} \sigma_{\beta',\beta}^x \sigma_{j'\beta'}^x \quad 5.100b$$

$$= \gamma(x) \sum_i [U_L(x)]_{i',i} \left[1 \cdot A_{[1]}^{i'j'} \cdot \hat{\sigma}^x \right]_{\alpha\beta}. \quad 5.100c$$

Note that the left sum \sum_i cannot be rewritten as a sum $\sum_{\alpha'}$ over bond indices because $i = 0, 1$ whereas the left bond dimension is one, i.e., $\alpha' = 0$. Therefore the unitary action $U_L(x) = \sigma^x$ has to act on the *physical indices* and does not translate to a “gauge transformation” $V_A^{-1}(x)$ on the virtual bonds of $A_{[1]}^{ij}$. The calculation for the action of $\rho_1(z)$ yields an analogous result so that we find

$$\sum_{ij} [\rho_1(g)]_{i',j'} A_{[1]\alpha\beta}^{ij} = \gamma(g) \sum_i [U_L(g)]_{i',i} \left[1 \cdot A_{[1]}^{i'j'} \cdot V_A(g) \right]_{\alpha\beta} \quad 5.101$$

as transformation law for $|A\rangle$ under the linear representation $\rho_1(g)$ of D_2 on the left boundary site. We find a similar relation for the right boundary,

$$\sum_{ij} [\rho_L(g)]_{i',j'} A_{[L]\alpha\beta}^{ij} = \gamma(g) \sum_j [U_R(g)]_{j',j} \left[V_A^{-1}(g) \cdot A_{[L]}^{i'j'} \cdot 1 \right]_{\alpha\beta}, \quad 5.102$$

where now the right bond representation becomes trivial. Here comes a crucial observation: If we apply the transformation (5.101) [or (5.102)] consecutively for two elements $g_1, g_2 \in D_2$, then the left-hand side transforms according to the *linear* representation $\rho_k(g)$ with (5.62) whereas the single bond representation on the right-hand side transforms *projectively* according to (5.63); but the latter violates the multiplication law of linear representations by phases given by the cocycle $\chi_A(g_1, g_2)$ that characterizes the projective class of V_A . There is only one solution: the *physical* representation U_L on the boundary spin must also transform *projectively* to cancel the phases introduced by V_A , i.e.,

$$U_L(g_1)U_L(g_2) = \chi_A^*(g_1, g_2) U_L(g_1 g_2) \quad 5.103$$

so that the combination

$$\begin{aligned} & U_L(g_1)V_A(g_1)U_L(g_2)V_A(g_2) \\ &= \chi_A^*(g_1, g_2)\chi_A(g_1, g_2)U_L(g_1g_2)V_A(g_1g_2) \end{aligned} \quad 5.104a$$

$$= U_L(g_1g_2)V_A(g_1g_2) \quad 5.104b$$

transforms linearly—in accordance with the left-hand side of (5.101). Thus we see that the trivial representation on one bond in (5.101) “lifts” the projective transformation laws of the bond representations in the bulk (V_A) to the physical level (U_L). A similar conclusion holds for the right boundary:

$$U_R(g_1)U_R(g_2) = \chi_A(g_1, g_2)U_R(g_1g_2). \quad 5.105$$

In a nutshell: For periodic boundaries, the emergence of projective representations is “hidden” as it affects only the virtual level of the MPS (where it obstructs the deformation into a trivial product state). However, if one cuts the system open, the projective class of the topological phase is revealed by the—now projective—action of the physical symmetry on the boundaries. This is the mathematical reason for the emergence of degenerate edge states at the boundaries of topological phases.

Indeed, if we combine our findings for the left boundary (5.101), the right boundary (5.102) and the (invariant) bulk (5.99), the action of the *global symmetry* $\rho(g)$ on the ground state $|A\rangle = |A(0, 0)\rangle$ reads

$$\rho(g)|A\rangle = U_L(g)U_R(g)|A\rangle \quad 5.106$$

where $U_L(g)$ ($U_R(g)$) acts only on the left (right) boundary spin. Notice how the product of both boundary representations is again linear,

$$\begin{aligned} & U_L(g_1)U_R(g_1)U_L(g_2)U_R(g_2) \\ &= \chi^*(g_1, g_2)\chi(g_1, g_2)U_L(g_1g_2)U_R(g_1g_2) \end{aligned} \quad 5.107a$$

$$= U_L(g_1g_2)U_R(g_1g_2), \quad 5.107b$$

consistent with $\rho(g)$ being a linear representation of D_2 . This physical “splitting” of a linearly realized symmetry into two projective “parts” is known as *symmetry fractionalization*.

How does this imply a robust ground state degeneracy? To this end, let us write down the explicit form of the boundary representations on the ground state space of our Hamiltonian at the special point with $J_2 < 0$ and $J_1 = 0$:

$$U_L(x) = \sigma_1^x \quad \text{and} \quad U_L(z) = \sigma_1^z \quad \text{and} \quad U_L(xz) = \sigma_1^x \sigma_1^z, \quad 5.108$$

$$U_R(x) = \sigma_{2L}^x \quad \text{and} \quad U_R(z) = \sigma_{2L}^z \quad \text{and} \quad U_R(xz) = \sigma_{2L}^x \sigma_{2L}^z. \quad 5.109$$

It is clear that both belong to the non-trivial projective class $[\chi_L] = [\chi_R] = [\chi_A] \in H^2(D_2, U(1))$ that also classifies the bond representations V_A . It is a feature of the point where $J_1 = 0$ that these boundary representations are *exact symmetries* of the

Hamiltonian H ,

$$[H, U_L(g)] = 0 \quad \text{and} \quad [H, U_R(g)] = 0. \quad 5.110$$

For $J_1 \neq 0$ and finite chain length $L < \infty$, this holds only approximately as long as $|J_1| < |J_2|$, i.e., in the topological phase. Then, the operators U_L and U_R are no longer localized on the left- and rightmost spins but “leak” into the bulk. For $L \rightarrow \infty$ the symmetry (5.110) is restored for $J_1 \neq 0$. This relates to the fact that for $J_1 \neq 0$ the ground state degeneracy is lifted for $L < \infty$ and restored for $L \rightarrow \infty$. Only at $J_1 = 0$ the degeneracy is exact even for finite chains.

That there *must* be a degeneracy is a direct consequence of the non-trivial cohomology class of the boundary operators U_L and U_R . Indeed, recall that their non-trivial cocycle is $\chi_L(z, x) = \chi_R(z, x) = -1$, i.e.,

$$U_L(x)U_L(z) = -U_L(z)U_L(x) \quad 5.111a$$

$$\text{and} \quad U_R(x)U_R(z) = -U_R(z)U_R(x). \quad 5.111b$$

Now recall that the cohomology class of the bond representations V_A does not change for arbitrary perturbations (e.g., $J_1 \neq 0$) as long as the system remains gapped and D_2 -symmetric. Above we argued that the projective class of the boundary representations $U_{L,R}$ must be identical to that of V_A (or its inverse)—so it cannot change either. Thus the relations (5.111) remain valid for perturbed systems even though the specific *form and domain* of the operators $U_{L,R}$ may change. However, they can never act irreducibly on a *one*-dimensional subspace because (complex) numbers *cannot* satisfy (5.111). This implies that the product representation of the two non-trivial projective representations defined in (5.111) requires at least a four-dimensional subspace. Due to (5.110) the ground state space must carry such a representation; i.e., at least a four-fold ground state degeneracy is necessary to realize the projective symmetries U_L and U_R . Since the projective class cannot be changed by (symmetric) perturbations, the ground state degeneracy cannot be lifted by such.

In finite systems, (5.110) is only *approximately* valid for generic parameters in the topological phase. Therefore the conclusion that the ground state space carries a representation of U_L and U_R *separately* is no longer valid; only their product $\rho(g) = U_L(g)U_R(g)$ is a true symmetry of the system. Since this symmetry is represented *linearly*, we cannot exclude the possibility that $\rho(g) \propto 1$ acts with the trivial representation on a one-dimensional ground state space. This is what happens in finite systems where the ground state degeneracy is lifted.

Remarks

- 1 For $U(1) \times \mathbb{Z}_2^T$ the projective representations on the boundary spins are given by

$$U_L(R_\phi) = e^{i\frac{\phi}{2}(1-\sigma_1^z)} \quad \text{and} \quad U_L(T) = \sigma_1^x K, \quad 5.112a$$

$$U_R(R_\phi) = e^{i\frac{\phi}{2}(1-\sigma_{2L}^z)} \quad \text{and} \quad U_R(T) = \sigma_{2L}^x K. \quad 5.112b$$

Again, the fact that the corresponding cocycles $\chi_L(T, R_\phi) = e^{-i\phi} = \chi_R(T, R_\phi)$ cannot be trivialized precludes one-dimensional representations and implies an at least four-fold degenerate ground state space.

Note that the product $U_L(g)U_R(g)$ of the projective representations in (5.112) yields a cocycle with $\chi_L(T, R_\phi)\chi_R(T, R_\phi) = e^{-2i\phi} \neq 1$; this is not a linear representation but a projective one. However, if we retrace our argument to show that $[\chi_A] \neq [1]$ (for the bond representations V_A), it is easy to see that the *even* exponent in $e^{-2i\phi}$ allows for the trivialization of $\chi_L\chi_R$, i.e., $[\chi_L] \cdot [\chi_R] = [\chi_L\chi_R] = [1]$. Thus $U_L(g)U_R(g)$ belongs to the projective class of the linear representation and is therefore physically equivalent to it.

- 2 The line of arguments that led to projective boundary representations (and thereby to edge states and a robust ground state degeneracy) is built upon two crucial assumptions: First, the ground state of the Hamiltonian to be classified is separated by a gap from excited states so that one can describe the ground state as matrix product state with bounded bond dimension even in the thermodynamic limit. And second, the ground state is invariant (up to a phase) under the global symmetry so that its action translates into projective representations on the virtual bonds of the MPS (for periodic boundaries).

When we consider our particular Hamiltonian (5.24b) in a sector of fixed particle number *away* from half-filling, we violate *both* assumptions: First, since one band is no longer completely filled, the ground state of this system is no longer separated by a gap from other states of the many-body spectrum. And second, since $S = XK$ acts like a particle-hole transformation, such a state is no longer invariant under this symmetry. In conclusion, the machinery of symmetry-protected topological phases presented above makes *no claim* about degeneracies in this situation whatsoever (it does not even *require* the degeneracy to be lifted).

A Note on \mathbb{Z}_2^T : Twisted Group Cohomology

Our “chiral” symmetry $S = XK$ is represented *antiunitarily* on the Hilbert space. In the literature (e.g., [18]) this is indicated by $\mathbb{Z}_2^T = \{1, T\}$ although the abstract group structure is clearly that of \mathbb{Z}_2 since $T^2 = 1$ (or $S^2 = \mathbb{1}$ on the representation level). Since the cohomology group $H^2(G, \mathbb{U}(1))$ depends on the *abstract* group G , it is mathematically opaque how we should read the statements [18]

$$H^2(\mathbb{Z}_2, \mathbb{U}(1)) = \mathbb{Z}_1 \quad \text{and} \quad H^2(\mathbb{Z}_2^T, \mathbb{U}(1)) = \mathbb{Z}_2 \quad 5.113$$

if actually $\mathbb{Z}_2^T \cong \mathbb{Z}_2$. The reason for this apparent contradiction is that we are actually interested in the classification of projective representations of a symmetry group G where each element can be represented by either a unitary or antiunitary operator. If one *fixes* this choice by “labeling” the abstract group elements via a map

$$\sigma : G \rightarrow \mathbb{Z}_2, \quad g \mapsto \sigma(g) \in \{1, -1\} \quad 5.114$$

so that we restrict our classification to representations where g is represented by a unitary (antiunitary) operator if $\sigma(g) = +1$ (-1), consistency requires that σ is a group homomorphism (since the product of two antiunitary operators is unitary). Note that this restricts the possibilities for antiunitary representations, e.g., the cyclic group \mathbb{Z}_3 does not allow for any antiunitary representation as it is of odd order.

For $G = \mathbb{Z}_2 = \{1, T\}$, there are exactly two such homomorphisms, namely

$$\sigma_0(1) = 1 \quad \sigma_0(T) = 1 \quad 5.115a$$

$$\text{and} \quad \sigma_1(1) = 1 \quad \sigma_1(T) = -1. \quad 5.115b$$

Here, σ_0 encodes an all-unitary representation and σ_1 a representation where T acts antiunitarily.

We are now interested in a group G *augmented* by such a group homomorphism σ , write (G, σ) . Given this set of data, we can define the set $Z_\sigma^2(G, \mathbb{U}(1))$ of σ -*twisted 2-cocycles* as the set of all maps $\chi : G \times G \rightarrow \mathbb{U}(1)$ that satisfy the “twisted” cocycle condition

$$\chi(g_1, g_2)\chi(g_1g_2, g_3) = \chi^{\sigma(g_1)}(g_2, g_3)\chi(g_1, g_2g_3) \quad 5.116$$

where χ^{-1} here is just the complex conjugate since $|\chi(g_1, g_2)| = 1$.

The motivation for this definition stems from the action of antiunitary operators on the phase factors [367, 368]. Indeed, let ρ be a projective representation of G with $\rho(g_1)$ antiunitary (i.e., $\sigma(g_1) = -1$) and $\rho(g_2), \rho(g_3)$ arbitrary for $g_1, g_2, g_3 \in G$.

Then associativity implies the relation

$$\begin{aligned} & [\rho(g_1)\rho(g_2)]\rho(g_3) \\ &= \chi(g_1, g_2)\rho(g_1g_2)\rho(g_3) \end{aligned} \quad 5.117a$$

$$= \chi(g_1, g_2)\chi(g_1g_2, g_3)\rho(g_1g_2g_3) \quad 5.117b$$

$$\stackrel{!}{=} \rho(g_1)[\rho(g_2)\rho(g_3)]$$

$$= \rho(g_1)\chi(g_2, g_3)\rho(g_2g_3) \quad 5.117c$$

$$= \chi^*(g_2, g_3)\chi(g_1, g_2g_3)\rho(g_1g_2g_3), \quad 5.117d$$

where we used that $\rho(g_1)\chi(g_2, g_3) = \chi^*(g_2, g_3)\rho(g_1)$. Thus the cocycle condition (5.116) is “twisted” whenever g_1 is represented antiunitarily.

A similar “twist” occurs when we multiply the operators by g -dependent phases (remember that we are ultimately interested in projective representations). Let $\tilde{\rho}(g) = f(g)\rho(g)$ with phase factor $f(g)$; then

$$\tilde{\rho}(g_1)\tilde{\rho}(g_2) = f(g_1)\rho(g_1)f(g_2)\rho(g_2) \quad 5.118a$$

$$= f(g_1)f^{\sigma(g_1)}(g_2)\rho_1(g_1)\rho_1(g_2) \quad 5.118b$$

$$= f(g_1)f^{\sigma(g_1)}(g_2)\chi(g_1, g_2)\rho(g_1g_2) \quad 5.118c$$

$$= \frac{f(g_1)f^{\sigma(g_1)}(g_2)}{f(g_1g_2)}\chi(g_1, g_2)\tilde{\rho}(g_1g_2) \quad 5.118d$$

$$\equiv \tilde{\chi}(g_1, g_2)\tilde{\rho}(g_1g_2). \quad 5.118e$$

Therefore we define the σ -twisted equivalence relation R_σ of σ -twisted 2-cocycles

$$\chi_1 \stackrel{R_\sigma}{\sim} \chi_2 \quad :\Leftrightarrow \quad \chi_1(g_1, g_2) = \frac{f(g_1)f^{\sigma(g_1)}(g_2)}{f(g_1g_2)}\chi_2(g_1, g_2) \quad 5.119$$

for some function $f : G \rightarrow \text{U}(1)$, and with this the σ -twisted second cohomology group of G in $\text{U}(1)$ as

$$H_\sigma^2(G, \text{U}(1)) = Z_\sigma^2(G, \text{U}(1)) / R_\sigma, \quad 5.120$$

i.e., the set of equivalence classes in $Z_\sigma^2(G, \text{U}(1))$ with respect to R_σ . With this concept, we can now properly define what we mean by \mathbb{Z}_2^T :

$$H^2(\mathbb{Z}_2, \text{U}(1)) \equiv H_{\sigma_0}^2(\mathbb{Z}_2, \text{U}(1)), \quad 5.121a$$

$$H^2(\mathbb{Z}_2^T, \text{U}(1)) \equiv H_{\sigma_1}^2(\mathbb{Z}_2, \text{U}(1)). \quad 5.121b$$

Let us evaluate both groups:

- 1 For the “untwisted” group $H_{\sigma_0}^2(\mathbb{Z}_2, \text{U}(1))$, the cocycle condition yields the restrictions [we write (g_1, g_2, g_3) in the first column]

$$\begin{aligned} (1, T, T) &\Rightarrow \chi(1, T)\chi(T, T) = \chi(T, T)\chi(1, 1) \\ &\Rightarrow \chi(1, T) = \chi(1, 1), \end{aligned} \quad 5.122a$$

$$\begin{aligned} (T, T, T) &\Rightarrow \chi(T, T)\chi(1, T) = \chi(T, T)\chi(T, 1) \\ &\Rightarrow \chi(1, T) = \chi(T, 1), \end{aligned} \quad 5.122b$$

such that only $\chi(1, 1)$ and $\chi(T, T)$ are independent.

Then the equations

$$\chi(1, 1) = \frac{f(1)f(1)}{f(1)} = f(1) \quad \text{and} \quad \chi(T, T) = \frac{f(T)f(T)}{f(1)} \quad 5.123$$

can easily be solved for $f(1)$ and $f(T)$ for arbitrary cocycles $\chi(g_1, g_2)$ so that all are trivial and $H_{\sigma_0}^2(\mathbb{Z}_2, \text{U}(1)) = \mathbb{Z}_1$; i.e., there are no topological phases protected by a *unitary* \mathbb{Z}_2 -symmetry.

- 2 For the “twisted” group $H_{\sigma_1}^2(\mathbb{Z}_2, \text{U}(1))$ the cocycle condition yields the restriction

$$\begin{aligned} (1, T, T) &\Rightarrow \chi(1, T)\chi(T, T) = \chi(T, T)\chi(1, 1) \\ &\Rightarrow \chi(1, T) = \chi(1, 1) \end{aligned} \quad 5.124$$

(which is the same as above), but also

$$\begin{aligned} (T, T, T) &\Rightarrow \chi(T, T)\chi(1, T) = \chi^{-1}(T, T)\chi(T, 1) \\ &\Rightarrow \chi^2(T, T) = \frac{\chi(T, 1)}{\chi(1, T)}, \end{aligned} \quad 5.125a$$

$$\begin{aligned} (T, 1, 1) &\Rightarrow \chi(T, 1)\chi(T, 1) = \chi^{-1}(1, 1)\chi(T, 1) \\ &\Rightarrow \chi(T, 1) = \frac{1}{\chi(1, 1)}, \end{aligned} \quad 5.125b$$

due to the antiunitarity of $\rho(T)$. So again $\chi(1, 1)$, $\chi(1, T)$ and $\chi(T, 1)$ cannot be chosen independently. However, the relation $\chi^2(T, T) = \chi^{-2}(1, 1)$ allows for two solutions: $\chi(T, T) = \pm\chi^{-1}(1, 1)$.

If we try to trivialize a given cocycle,

$$\chi(1, 1) = \frac{f(1)f(1)}{f(1)} = f(1) \quad 5.126a$$

$$\text{and} \quad \chi(T, T) = \frac{f(T)f^{-1}(T)}{f(1)} = \frac{1}{f(1)} = \frac{1}{\chi(1, 1)}, \quad 5.126b$$

only the possibility $\chi(T, T) = +\chi^{-1}(1, 1)$ can be realized. The cocycles with $\chi(T, T) = -\chi^{-1}(1, 1)$ constitute a non-equivalent class and we find $H_{\sigma_1}^2(\mathbb{Z}_2, \mathbb{U}(1)) = \mathbb{Z}_2$; i.e., there is a single topological phase protected by an *antiunitary* \mathbb{Z}_2 -symmetry.

Our topological ground state $|A\rangle$ is an example of this phase if we choose the symmetry YK with projective representations $U_L(T) = i\sigma_1^y K$ and $U_R(T) = i\sigma_{2L}^y K$ on the boundaries. Note that indeed $U_L(T)U_L(T) = -\mathbb{1} = -U_L(1)$ so that $\chi_L(T, T) = -1 = -\chi_L^{-1}(1, 1)$.

5.1.4 Connection to the Haldane Phase

In this subsection we explore the “neighborhood” of our Hamiltonian (5.24b) and show how it can be smoothly connected to isotropic spin chains that are known to be in the famous Haldane phase. The latter is an iconic, symmetry-protected topological phase, protected by either D_2 or \mathbb{Z}_2^T (which explains why our system can be protected by these symmetries).

We start with the antiferromagnetic Heisenberg model (AFHM)

$$H_{\text{AF}} = J \sum_{i=1}^{L-1} \mathbf{S}_i \mathbf{S}_{i+1} \quad 5.127$$

($J > 0$) for spin-1 representations S_i^α . This is the most prominent model subject to *Haldane’s conjecture* [62, 63], namely that antiferromagnetic Heisenberg chains with integer spin are gapped quantum phases whereas half-integer representations come with a gapless spectrum. The model (5.127) cannot be solved exactly as it is not integrable (at least the author is not aware of any solution); in particular, its ground state cannot be derived exactly although its properties are well understood, see e.g. Ref. [369] and references therein. However, a minor modification yields the AKLT model [370],

$$H_{\text{AKLT}} = J \sum_{i=1}^{L-1} \left[\mathbf{S}_i \mathbf{S}_{i+1} + \frac{1}{3} (\mathbf{S}_i \mathbf{S}_{i+1})^2 \right] \quad 5.128$$

which is in the same phase as (5.127), dubbed the *Haldane phase* (i.e., one can switch on the biquadratic term without closing the gap or violating the $\text{SU}(2)$ -symmetry [371]).

The feature of (5.128) is that its ground state can be derived exactly and takes a particularly simple form known as *valence-bond state* [370]; the latter is the archetype of an (interacting) symmetry-protected topological phase and captures the entanglement structure of the Haldane phase¹⁵². It can be described as follows: Assign each site i *two* (artificial) spin- $\frac{1}{2}$ representations σ_{2i-1} and σ_{2i} . Let \mathcal{P}_{ij}

¹⁵²It is exactly the entanglement structure that characterizes topological phases; recall that their symmetries remain unbroken so that they cannot be characterized by a local order parameter.

denote the projector onto the triplet ($S = 1$) subspace of the two spins σ_i and σ_j . Then, there are four degenerate ground states of (5.128) given by

$$|s_L, s_R\rangle = \left[\prod_{k=1}^L \mathcal{P}_{2k-1, 2k} \right] \times |s_L\rangle_1 \otimes \bigotimes_{i=1}^{L-1} \frac{|\uparrow\rangle_{2i} |\downarrow\rangle_{2i+1} - |\downarrow\rangle_{2i} |\uparrow\rangle_{2i+1}}{\sqrt{2}} \otimes |s_R\rangle_{2L}, \quad 5.129$$

with $s_L, s_R \in \{\uparrow, \downarrow\}$ the states of the unpaired left and right boundary spins. Note that the state in (5.129) essentially consists of spin- $\frac{1}{2}$ dimers/singlets *between* the sites and a subsequent projection onto spin-1 *on* each site. Due to the ‘‘SSH-like’’ pairing of spins, there are dangling boundary spins left on both boundaries which give rise to the four-fold ground state degeneracy. If one ignores the projection onto the triplet sector of the artificial spin- $\frac{1}{2}$ Hilbert space \mathcal{H}_{2L}^b , this describes exactly the ground state of our Hamiltonian (5.24b) for $J_1 = 0$ and $J_2 > 0$ (in our case, \mathcal{H}_{2L}^b is the *physical* Hilbert space).

Sign-(in)dependence and Relation to the Isotropic Point

The relation between dimerized spin- $\frac{1}{2}$ chains (such as ours) and the Haldane phase has been studied before [372–376]. There, commonly an *isotropic* coupling is assumed,

$$H_{\text{iso}} = \frac{J_1}{2} \sum_{i=1}^L \sigma_{2i-1} \sigma_{2i} + \frac{J_2}{2} \sum_{i=1}^{L-1} \sigma_{2i} \sigma_{2i+1}, \quad 5.130$$

which then is deformed to include anisotropies like (5.24c). To relate our model to the isotropic point and to make connections to known results, we introduce the family of Hamiltonians

$$H_\delta = \frac{J_1}{2} \sum_{i=1}^L (\sigma_{2i-1}^x \sigma_{2i}^x + \sigma_{2i-1}^y \sigma_{2i}^y + \delta \sigma_{2i-1}^z \sigma_{2i}^z) + \frac{J_2}{2} \sum_{i=1}^{L-1} (\sigma_{2i}^x \sigma_{2i+1}^x + \sigma_{2i}^y \sigma_{2i+1}^y + \delta \sigma_{2i}^z \sigma_{2i+1}^z) \quad 5.131$$

with arbitrary couplings $J_1, J_2 \in \mathbb{R}$ and isotropy $\delta \geq 0$; then, $\delta = 0$ describes our Hamiltonian (5.24c) and $\delta = 1$ its isotropic counterpart. We discuss 8 cases: The four sign combinations of J_1 and J_2 times the two regimes $|J_1| \gtrless |J_2|$; this is illustrated in Figure 5.2.

We start with the simpler case, namely $\delta = 0$, see Figure 5.2 (a). Without Z -couplings $\sigma_i^z \sigma_j^z$, the Hamiltonian (5.131) maps onto free fermions under Jordan-Wigner transformation. We know that fermions permit for gauge transformations $x_k \rightarrow \tilde{x}_k = e^{i\varphi_k} x_k$ with arbitrary phases φ_k ; i.e., the mapping preserves the

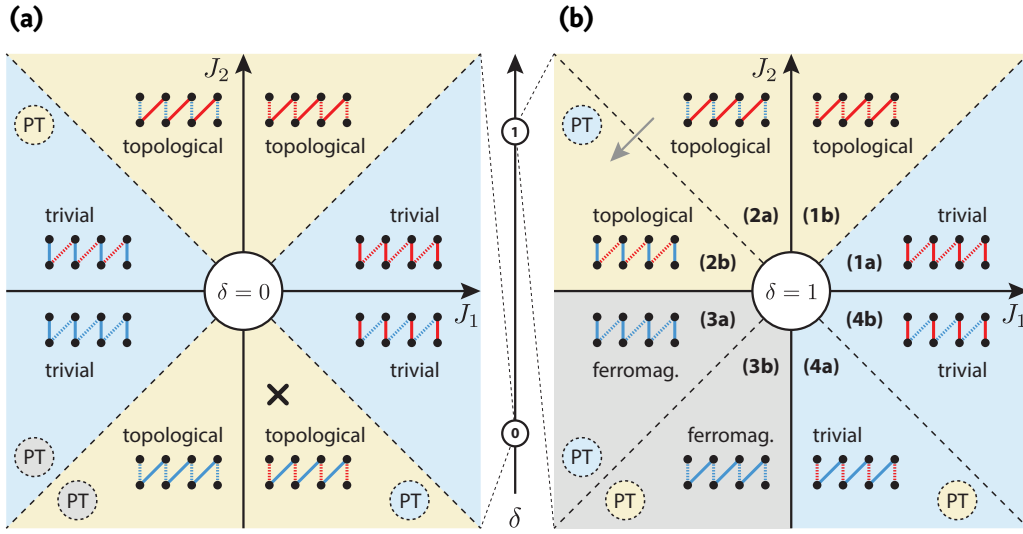


FIGURE 5.2 • Phase diagram. We show the phases of Hamiltonian (5.131) at the non-interacting point $\delta = 0$ in (a) and at the isotropic point $\delta = 1$ in (b) in the J_1 - J_2 -plane. Regions of the same color belong to the same phase. The symbolic chains characterize their sector via the color of couplings (red=positive, blue=negative) and their thickness (dashed=weak, solid=strong). The identification of phases as “topological” and “trivial” is based on the symbolic chains where vertical couplings are “intra-site” and diagonal couplings are “inter-site.” Dashed circles labeled with “PT” indicate phase transitions in the out-of-plane δ -direction that separate the phases for $\delta = 0$ and $\delta = 1$. The cross in (a) locates the experimentally realized phase in [4], the gray arrow in (b) refers to Figure 5.4. Details are discussed in the text.

fermion algebra $\{\tilde{x}_k, \tilde{x}_l^\dagger\} = \delta_{kl}$. It is now straightforward to check that this transformation translates into a unitary mapping between equivalent representations of the Pauli algebra

$$\sigma_\varphi^x \equiv \cos(\varphi) \sigma^x - \sin(\varphi) \sigma^y \quad 5.132a$$

$$\sigma_\varphi^y \equiv \sin(\varphi) \sigma^x + \cos(\varphi) \sigma^y \quad 5.132b$$

$$\sigma_\varphi^z \equiv \sigma^z \quad 5.132c$$

for $\varphi \in [0, 2\pi)$. It is easy to check that $\sigma_\varphi^a \sigma_\varphi^b = \delta^{ab} \mathbb{1} + i \varepsilon^{abc} \sigma_\varphi^c$. Note that the transformation can be compactly written as $\sigma_\varphi^a = e^{i\frac{\varphi}{2}\sigma^z} \sigma^a e^{-i\frac{\varphi}{2}\sigma^z}$. Because of $XK e^{\pm i\frac{\varphi}{2}\sigma^z} XK = e^{\pm i\frac{\varphi}{2}\sigma^z}$, it follows that the commutation relations between the “chiral” symmetry $S = XK$ and the unitarily transformed spins σ_φ^a are independent of φ ; in particular, terms which commute with XK for $\varphi = 0$ do not violate this symmetry for $\varphi > 0$ [the same argument holds for the $U(1)$ symmetry $R(\phi)$].

We now make in (5.131) every other spin φ -dependent, i.e.,

$$\begin{aligned}
 H_\delta(\varphi) = & \frac{J_1}{2} \sum_{i=1}^L (\sigma_{\varphi,2i-1}^x \sigma_{2i}^x + \sigma_{\varphi,2i-1}^y \sigma_{2i}^y + \delta \sigma_{\varphi,2i-1}^z \sigma_{2i}^z) \\
 & + \frac{J_2}{2} \sum_{i=1}^{L-1} (\sigma_{2i}^x \sigma_{\varphi,2i+1}^x + \sigma_{2i}^y \sigma_{\varphi,2i+1}^y + \delta \sigma_{2i}^z \sigma_{\varphi,2i+1}^z).
 \end{aligned} \tag{5.133}$$

This defines a path of smoothly connected Hamiltonians that (1) satisfy both symmetries and (2) do not close the gap for $\varphi \in [0, 2\pi)$ (this follows because their spectrum is independent of φ due to their unitary equivalence). For $\delta = 0$ and $\varphi = 0$ this yields the Hamiltonian (5.24c), $H_0(0) = H$. But for $\varphi = \pi$ we find $H_0(\pi) = -H$ and can conclude that the phases for J_i and $-J_i$ are the same ($i = 1, 2$). This makes the phase diagram in Figure 5.2 (a) inversion symmetric.

A similar argument can be used to show that the phase diagram is mirror-symmetric about the two axes: Replacing *both* spins $\sigma^a \rightarrow \sigma_\varphi^a$ on every other *dimer* (either on-site or between sites) implements the selective sign change of either $J_1 \rightarrow -J_1$ or $J_2 \rightarrow -J_2$.

In conclusion, all regions in Figure 5.2 (a) with the same color can be transformed into each other without breaking the symmetry or closing the gap—they belong to the same phase. This reflects our knowledge about the SSH chain which has only two distinct phases: the trivial and the topological. In particular, the signs of the couplings in Hamiltonian (5.24b) are completely irrelevant.

It is important to stress that in general $H_\delta(\pi) = -H_{-\delta}(0)$ so that for interacting Hamiltonians ($\delta \neq 0$) these arguments do not hold. This explains why at the isotropic point $\delta = 1$ the inversion symmetry of the phase diagram in Figure 5.2 (b) is lost. Let us discuss this case in detail and how it connects to the non-interacting case $\delta = 0$:

1 $J_1 > 0$ and $J_2 > 0$.

- a $|J_1| > |J_2|$. We can consider the limit $J_2 \rightarrow 0$. The isotropic on-site interaction $J_1 \sigma_{2i-1} \sigma_{2i}$ with $J_1 > 0$ leads to on-site singlet pairing. Thus there are no low-energy d.o.f. and switching on J_2 cannot change the non-degeneracy of the ground state manifold. Since these arguments also apply to the non-interacting point $\delta = 0$, we do not expect a phase transition for $\delta = 0 \rightarrow 1$. This is confirmed by DMRG simulations in Figure 5.3 (e) where the gap stays open and the ground state degeneracy does not change.
- b $|J_1| < |J_2|$. Here the same arguments apply for a model shifted by one spin- $\frac{1}{2}$ site. However, now there is a four-fold ground state degeneracy at $J_1 = 0$ due to the dangling edge spins. This degeneracy cannot be lifted for small $0 < |J_1| \ll |J_2|$ due to the lack of low-energy d.o.f. in

the bulk and the $SU(2)$ symmetry of the interaction. This is verified numerically in Figure 5.3 (a) where it is shown that the gap does not close and the four-fold ground state degeneracy is stable for $\delta = 0 \rightarrow 1$. Note that for $J_1 = J_2$ the Hamiltonian describes an antiferromagnetic spin- $\frac{1}{2}$ Heisenberg chain (which is gapless as can be shown by the Bethe ansatz [377]). Hence there is a phase transition between (1a) and (1b).

2 $J_1 < 0$ and $J_2 > 0$.

- a** $|J_1| < |J_2|$. Here a similar argument applies. The only difference is that for $0 < |J_1| \ll |J_2|$ the couplings between the singlets are ferromagnetic and not antiferromagnetic (which does not affect the ground state degeneracy). Since for $\delta = 0$ there is also a four-fold degeneracy, we do not expect a phase transition for $\delta = 0 \rightarrow 1$; this is validated in Figure 5.3 (c). Note that the bulk remains gapped for $J_1 = 0$ so that there is no phase transition between (1b) and (2a).
- b** $|J_1| > |J_2|$. So far, there was no difference between the non-interacting Hamiltonian ($\delta = 0$) and its isotropic counterpart ($\delta = 1$). For $|J_1| > |J_2|$ with $J_1 < 0$ and $J_2 > 0$ this is no longer true. Recall that for $\delta = 0$ the chain is in the trivial phase without ground state degeneracy. For $\delta = 1$, however, the low-energy physics follows from the limit $J_2 \rightarrow 0$ where the negative, isotropic (!) on-site coupling leads to *triplet pairing*. Therefore each on-site pair of spins forms an effective spin-1 d.o.f. that is weakly ($0 < J_2 \ll |J_1|$) coupled by antiferromagnetic, isotropic terms to its neighbors. The effective low-energy description is then given by the antiferromagnetic spin-1 Heisenberg model in (5.127) of which we know that it is in the topological Haldane phase with four-fold ground state degeneracy due to emergent spin- $\frac{1}{2}$ d.o.f. at the boundaries. This line of arguments suggests a phase transition for $\delta = 0 \rightarrow 1$ between gapped phases for $\delta = 0/1$ with one-fold/four-fold ground state degeneracy. This is verified by numerics in Figure 5.3 (g). In particular, we expect no phase transition between (2a) and (2b)—which is not obvious because one has to traverse a point where $|J_1| = |J_2|$ (but $J_1 = -J_2$). Recall that *without* interactions ($\delta = 0$) there *is* a phase transition.

Note: In a sense, the projector used for the AKLT ground state (5.129) to map from the *artificial* Hilbert space \mathcal{H}_{2L}^b of spins onto the physical Hilbert space of spin-1 representations here becomes a projector from the full *physical* Hilbert space \mathcal{H}_{2L}^b onto the low-energy sector of the theory.

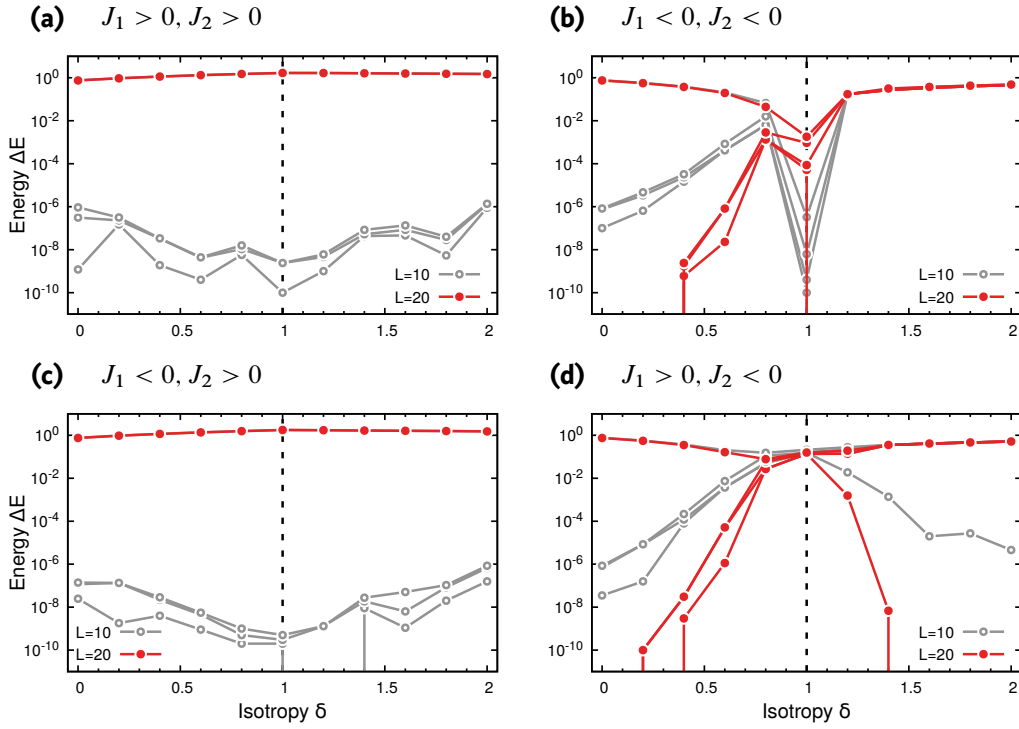


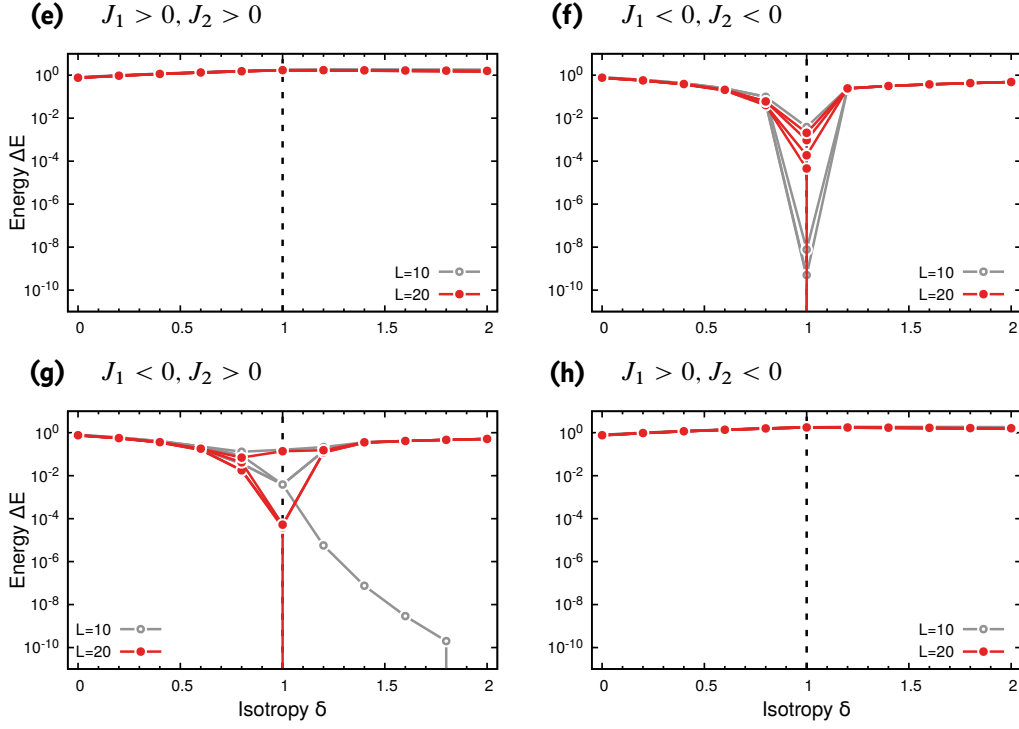
FIGURE 5.3 • Phase transitions (DMRG). Shown are the five lowest eigenenergies of Hamiltonian (5.131) as function of the isotropy δ ; the ground state energy is normalized to zero and does not show up in the logarithmic plots. We show results for two chain lengths $L = 10, 20$ to reveal tendencies for $L \rightarrow \infty$. Bond dimension and number of sweeps used for the DMRG simulations are $D = 300$ and $S = 10$, respectively (we used ALPS [251, 361]). A four-fold ground state degeneracy is often indicated by three energies close to zero for $L = 10$; for $L = 20$ these three energies then vanish from the plots as their energy is essentially zero. For $\delta = 0$ the system maps to free fermions and resembles the XY model. For $\delta = 1$ (dashed vertical line), the system becomes an isotropic Heisenberg model with alternating bonds. In (a-d) we show the four sign combinations for “topological” systems with $|J_1| = 0.25 < 1.0 = |J_2|$. \curvearrowright

3 $J_1 < 0$ and $J_2 < 0$.

- a $|J_1| > |J_2|$. Here the same argument as in (2b) leads to the low-energy effective theory (5.127) but now with a weak *ferromagnetic* coupling between the spin-1 d.o.f. Note that at $J_2 = 0$ the system becomes gapless as it consists of decoupled spins with $S = 1$ in the low-energy sector. Thus we expect a phase transition between (2b) and (3a).

The ground state of ferromagnetic Heisenberg models constructed from L spin- S d.o.f. belongs to the sector of maximum total spin $S_{\max} = LS$ [378, 379] (which contains the stretched state $|S, S, \dots, S\rangle$). Due to the global $SU(2)$ symmetry of (5.127) (which is generated by the total spin algebra $\mathbf{S}_{\text{tot}} = \sum_i \mathbf{S}_i$), this implies an extensive ground state

SPT PHASE WITH RYDBERG ATOMS



↷ In (e-h) we show the four sign combinations for “trivial” systems with $|J_1| = 1.0 > 0.25 = |J_2|$. All panels are discussed in the text.

degeneracy of $2S_{\max} + 1 = 2LS + 1$. These ground states *break* the $SU(2)$ symmetry; in particular, for $S = \frac{1}{2}$ the stretched state $|\uparrow\uparrow \cdots \uparrow\rangle$ breaks the chiral symmetry XK . This ferromagnetic phase therefore differs fundamentally from the topological and the trivial phase [see (1a) and (1b)] which are *XK-symmetric*. The ferromagnetic phase is therefore well-described by Landau’s paradigm of symmetry breaking and there is no need for the machinery developed in Subsection 5.1.3. The numerics for $\delta = 0 \rightarrow 1$ is shown in Figure 5.3 (f) and suggests a vanishing of the five lowest energy states at $\delta = 1$.

- b** $|J_1| < |J_2|$. Here the same arguments as in (3a) apply except for the additional spin- $\frac{1}{2}$ d.o.f. at the chain boundaries. Again, this sector is not interesting from the perspective of SPTs. The numerics for $\delta = 0 \rightarrow 1$ is shown in Figure 5.3 (b) and suggests a vanishing of the five lowest energy states at $\delta = 1$. Note that we do not expect a phase transition between (3a) and (3b) as neither ground state degeneracy nor symmetry change. In particular, for $J_1 = J_2$ the system becomes a spin- $\frac{1}{2}$ ferromagnetic Heisenberg model. But $S_{\max} = 2L \cdot \frac{1}{2} = L$ is the

same as for the effective spin-1 models for $|J_1| \ll |J_2|$ or $|J_2| \ll |J_1|$ (there we count $S_{\max} = L \cdot 1 = L$). Hence the ground state space is the same in the entire region $J_1, J_2 < 0$.

4 $J_1 > 0$ and $J_2 < 0$.

- a** $|J_1| < |J_2|$. We can reduce this setting to (2b) with $J_1 < 0$, $J_2 > 0$, and $|J_1| > |J_2|$ in the bulk. The only difference is that two additional spin- $\frac{1}{2}$ d.o.f. are antiferromagnetically coupled to the boundaries of the effective AFHM (5.127). In (2b) we argued that there are emergent spin- $\frac{1}{2}$ d.o.f. at the boundary of this model; these are here antiferromagnetically coupled to the additional spin- $\frac{1}{2}$ d.o.f. at the boundaries. Then the two spin- $\frac{1}{2}$ d.o.f. at each boundary form a singlet and gap out, lifting the four-fold ground state degeneracy of (2b). We are left with a trivial state that does not break any symmetry. Since for $\delta = 0$ there is a four-fold ground state degeneracy, we expect a phase transition for $\delta = 0 \rightarrow 1$. The change in ground state degeneracy is numerically verified in Figure 5.3 (d).
- b** $|J_1| > |J_2|$. Here the same argument as in (1a) applies: Weakly ($|J_2| \ll |J_1|$) ferromagnetically ($J_2 < 0$) coupled singlets give rise to a unique ground state of unbroken symmetry. It is clear that there is no phase transition between (1a) and (4b); we also expect none between (4b) and (4a), similar to (2b) and (2a). For $\delta = 0$ we also find a chain of singlets so that there is no phase transition for $\delta = 0 \rightarrow 1$. This is shown in Figure 5.3 (h).

In the above discussion it was noted that we do not expect a phase transition between (2a) and (2b). Without interactions $\delta = 0$ there is a phase transition between topological and trivial phase. We argued that this cannot be true for isotropic systems $\delta = 1$ due to the ground state degeneracy of the effective AFHM in (2b). But this is a non-trivial statement which implies that for $|J_1| = |J_2|$ the gap does not close if $J_1 = -J_2$. In Figure 5.4 we checked this numerically by plotting the five lowest eigenenergies for the parametrization $J_1 = -J$ and $J_2 = 1 - J$ along $0 \leq J \leq 1$ [a path following the gray arrow in Figure 5.2 (b)]. We find that the four-fold ground state degeneracy emerges exponentially for $L \rightarrow \infty$ even for $J = -J_1 = J_2 = 0.5$ without closing the gap. This verifies that our arguments are correct and (2a) and (2b) constitute the same phase.

In conclusion, we showed by numerical means and perturbative arguments that all phases in Figure 5.2 of the same color are smoothly connected by deformations of the Hamiltonian (5.131) that do not close the gap or violate the relevant symmetries $[R(\phi)$ and $XK]$. The experiment in Ref. [4] essentially realizes the case $J_1 > 0$ and $J_2 < 0$. This places the system at the black cross in Figure 5.2 (a). From

SPT PHASE WITH RYDBERG ATOMS

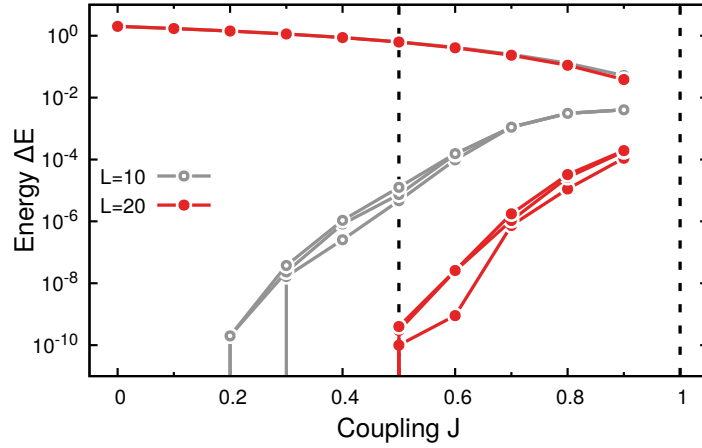


FIGURE 5.4 • Path for $J_2 > 0$ and $J_1 < 0$ (DMRG). Shown are the five lowest energy eigenvalues for systems of length $L = 10, 20$ along a path with $J_1 = -J$ and $J_2 = 1 - J$ for $0 \leq J \leq 1$. The path follows the gray arrow in Figure 5.2 (b). The ground state is normalized to zero energy and does not show up in the plot. Bond dimension and number of sweeps used for the DMRG simulation are $D = 300$ and $S = 10$, respectively (we used ALPS [251, 361]). Clearly there is no phase transition for $J = -J_1 = J_2 = 0.5$. This underpins that the phases in (2a) and (2b) are the same. Note that for $J = 1$ the ground state is a chain of decoupled triplets with extensive ground state degeneracy.

there one can travel smoothly to one of the topological regions with $J_2 > 0$ [using the rotation (5.132)] and subsequently switch on the isotropy $\delta = 0 \rightarrow 1$. One reappears in Figure 5.2 (b) in either (2a) or (1b) and can smoothly cross the border to (2b) which connects to the Haldane phase of the AFHM in the limit $J_1 \rightarrow -\infty$. The upshot is that the SPT phase of Ref. [4] is essentially the Haldane phase.

5.2 Fractional Quantum Hall States from Coupled Luttinger liquids

5.2.1 Introduction

This section is somewhat exotic. While the three main projects in Chapter 2, 3, and 4 fit under the umbrella of symmetry-protected topological phases in one dimension, here we venture into the iridescent realm of two-dimensional intrinsic topological order (long-range entangled phases that neither break nor require any symmetry for their stability). Such *topologically ordered* systems [15] are promising substrates for fault-tolerant (topological) quantum computation—a paradigm that exploits the unusual (anyonic) statistics of quasiparticle excitations above topologically ordered ground states [24, 45], see Ref. [47] for a review of this concept.

To date, the only¹⁵³ candidates for topologically ordered states of matter that can be realized in the laboratory are *fractional quantum Hall states* [27–29]. Their hallmark—quantized Hall resistivities at fractional fillings—sets them apart from the integer quantum Hall effect [69], which can be understood in terms of free fermions that fill smeared Landau levels in the presence of disorder [380]. However, due to the flatness of Landau levels, the Coulomb interaction dominates the physics in the macroscopically degenerate subspace of nearly degenerate fermion modes at fractional fillings (if disorder is not too strong). The fractional quantum Hall effect (FQHE) is therefore an inherently interaction-driven phenomenon that cannot be described by conventional band theory; in particular, ground states and low-lying excitations cannot be constructed from single-particle states.

Due to a constrained set of analytical tools to handle strongly correlated many-body systems, the exact structure of fractional quantum Hall states is unknown. Fortunately, there are structurally simpler trial wave functions that capture the essential features of the true ground states¹⁵⁴. These trial wave functions not only describe the ground states at various fillings, but also reveal the unusual statistics of quasiparticle excitations that can be abelian [37] or non-abelian [38] anyons (see also Chapter 2, especially Subsection 2.5.2).

For a more complete picture of fractional quantum Hall states and their low-energy physics, complementary descriptions are desirable¹⁵⁵. Here we focus on a rather unconventional approach that has recently been put forward by Kane *et al.* [357]:

¹⁵³This statement is not entirely true, see Footnote 11 in Subsection 1.1.1.

¹⁵⁴The trial wave functions are believed to belong to the same phase as the true ground states: Their pattern of long-range entanglement describes (up to quasilocal unitaries) the true ground states.

¹⁵⁵We quote R. P. Feynman: “Therefore psychologically we must keep all the theories in our heads, and every theoretical physicist who is any good knows six or seven different theoretical representations for exactly the same physics.” in *The Character of Physical Law*, p. 168.

In one dimension, it is well-established that gapless phases of (possibly interacting) fermions form a *Luttinger liquid (LL)* [255, 381, 382]. The latter replaces Fermi liquid theory since the paradigm of weakly interacting quasiparticles is not valid in one dimension where all excitations are necessarily collective. As Luttinger liquids are naturally described by quantum field theories within the framework of (abelian) bosonization [255, 383], the renormalization group (RG) can be used to assess their stability in the presence of interacting perturbations. This powerful toolkit makes Luttinger liquid theory an appealing framework to study the effect of strong interactions in electronic systems. The FQHE requires strongly interacting electrons—but in *two* dimensions. However, one of the most striking features of both integer and fractional quantum Hall effect is the existence of chiral (and thereby scattering-free) gapless edge modes; and indeed, these can be described as (chiral) Luttinger liquids [39, 384, 385]. But what about the gapped *bulk* of the fractional quantum Hall state? Can it be understood in terms of Luttinger liquids as well, so that the edge modes emerge naturally?

The answer is affirmative and based on the concept of *coupled Luttinger liquids*. The idea is to start from two-dimensional structures of many parallel quantum wires, each in a gapless Luttinger liquid phase, and couple them by local interactions to construct a truly two-dimensional system. The problem is that there are various relevant (in the RG sense) couplings (generated by, e.g., inter-wire single-particle hopping or density-density interactions) that destabilize the Luttinger liquids and drive the two-dimensional system into—from our perspective—uninteresting phases like Fermi liquids or charge density waves (CDW). However, it has been shown that strong forward scattering¹⁵⁶ between nearest- and next-nearest-neighbor wires can render these couplings irrelevant [386–389]. The resulting gapless phase of the two-dimensional array of wires is highly anisotropic and inherits characteristics of Luttinger liquids along the wires (viz. algebraic correlations) while being short-range correlated in the transverse direction; it has been dubbed *sliding Luttinger liquid (SLL)* (derived from a “sliding symmetry” between the wires). The construction proposed by Kane *et al.* [357] and elaborated by Teo and Kane [390] builds on the sliding Luttinger liquid scenario and adds tailored inter-wire couplings that drive the system into gapped fractional quantum Hall states. To this end, a perpendicular magnetic field is applied that renders the “wanted” couplings relevant and the “unwanted” competing couplings irrelevant. In summary, the combination of magnetic field and strong forward scattering can be used to single out the couplings that drive the system into fractional quantum Hall states as the only relevant operators.

Here we explore this approach in more detail by combining the RG methods of Ref. [388] with the proposal of Teo and Kane [390]. In particular, we aim at a quantification of the inter-wire forward scattering interactions needed to drive the system into the fractional quantum Hall regime. To this end, we focus on

¹⁵⁶Realized by density-density and/or current-current interactions.

the simplest non-trivial (bosonic¹⁵⁷) fractional quantum Hall state: The *Laughlin state* [36] at filling $\nu = 1/2$. The latter allows for abelian anyons as bulk excitations that are known as *semions*¹⁵⁸.

5.2.2 Setup

We consider an array of N one-dimensional quantum wires of length L aligned along the x -axis and stacked in y -direction with distance a , penetrated by a uniform magnetic field B_z in z -direction. The wires are populated with charged ($-e$), interacting hard-core bosons that are described by (complex) bosonic fields $\Psi_j(x)$ (where j denotes the wire index), see Figure 5.5 (a). We work in the Landau gauge $\mathbf{A} = -B_z y_j \mathbf{e}_x$ with $y_j = ja$ and \mathbf{e}_x the unit vector in x -direction. The bosonic fields can be “bosonized,” i.e., expressed in terms of (compact and real) bosonic phase and density fields $\varphi_j(x)$ and $\theta_j(x)$ with canonical commutation relations

$$[\varphi_j(x), \partial_{x'} \theta_{j'}(x')] = i\pi \delta_{jj'} \delta(x - x'). \quad 5.134$$

Then, the fields $\Psi_j(x)$ and densities $\rho_j(x)$ can be written as

$$\Psi_j(x) = \sqrt{\rho_0} e^{-i(\varphi_j(x) + b_j x)} \quad 5.135a$$

$$\rho_j(x) = \rho_0 - \frac{1}{\pi} \partial_x \theta_j(x) + \tilde{c} \cos(2\pi \rho_0 x - 2\theta_j(x)), \quad 5.135b$$

where ρ_0 is the average 1D density on the wires, $b = B_z a e / \hbar$, and \tilde{c} is a parameter that depends non-universally on the microscopic implementation [255, 392]. Note that we take into account density modulations with wave vector $2\pi \rho_0$, in addition to the smooth density profile $\rho_j^{(0)}(x) = -\partial_x \theta_j(x) / \pi$, as those give rise to relevant operators (see below). The filling $\nu = \rho_{2D} / n_\phi$ with the 2D density $\rho_{2D} = \rho_0 / a$ and the density of flux quanta $n_\phi = B_z / (e / \hbar)$ takes the form $\nu = 2\pi \rho_0 / b$; here we will focus on the half-filled lowest Landau level: $\nu = 1/2 \Leftrightarrow b = 4\pi \rho_0$.

The hard-core constraint for the bosons is readily described by the sum of Luttinger Hamiltonians

$$\mathcal{H}_{LL} = \frac{v_0}{2\pi} \int_j \left[K_0 (\partial_x \varphi_j)^2 + \frac{1}{K_0} (\partial_x \theta_j)^2 \right] \quad 5.136$$

with Luttinger parameter $K_0 = 1$ (which also describes free fermions); the sound velocity is v_0 and we introduced the shorthand $\int_j \equiv \sum_j \int dx$. This is schematically illustrated in the leftmost column of Figure 5.5 (a).

¹⁵⁷We focus on fractional quantum Hall states of strongly interacting *bosons* because our context is that of artificial quantum matter that can be realized by ultracold atoms. On these platforms, excitations play the role of particles that are naturally described as *hard-core bosons* (see also Section 5.1).

¹⁵⁸The statistics of semions interpolates between bosons and fermions in that exchanging one semion with another yields a phase of i (and not $+1 / -1$ as for bosons/fermions) [37, 391].

COUPLED LUTTINGER LIQUIDS

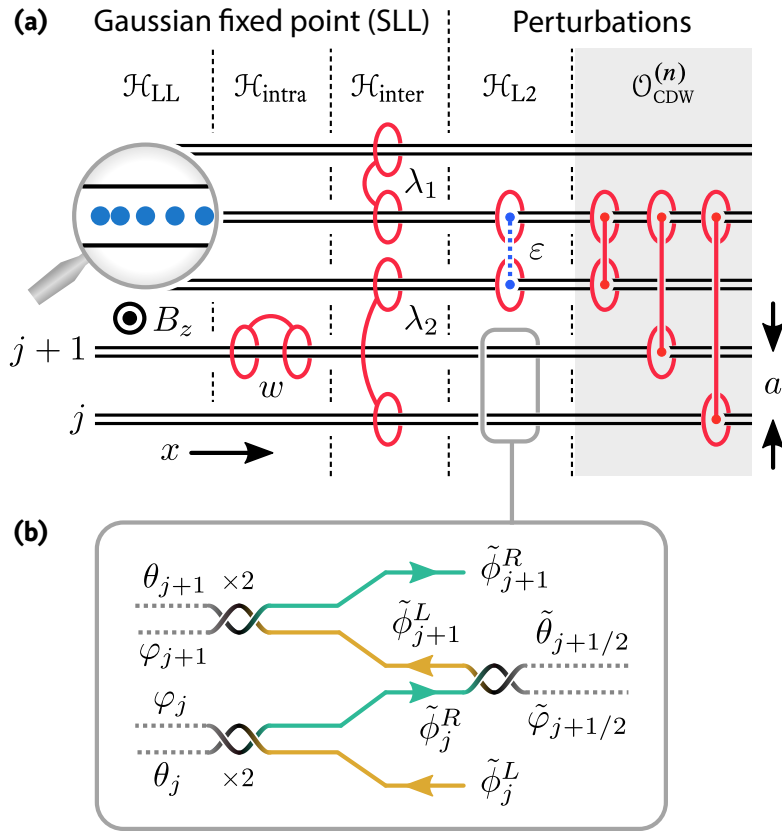


FIGURE 5.5 • Setup. (a) We consider an array of one-dimensional quantum wires populated with hard-core bosons in a perpendicular magnetic field B_z with intra- ($\mathcal{H}_{\text{intra}}$) and inter-wire forward scattering ($\mathcal{H}_{\text{inter}}$). We are interested in parameter regimes where the two-wire Laughlin interaction \mathcal{H}_{L2} becomes relevant and defeats competing charge density wave perturbations $\mathcal{O}_{\text{CDW}}^{(n)}$ to drive the system into the fractional quantum Hall regime at filling $\nu = 1/2$. (b) The action of \mathcal{H}_{L2} is most transparent if the physical fields φ_j and θ_j are combined to chiral bosons $\tilde{\phi}_j^{R,L}$ which, in turn, can be recombined *between* wires to new fields $\tilde{\varphi}_{j+1/2}$ and $\tilde{\theta}_{j+1/2}$. The “twirls” symbolize linear combinations of fields.

Adding repulsive intra-wire density-density interactions,

$$\mathcal{H}_{\text{intra}} = \frac{v_0}{2\pi} \int_j w (\partial_x \theta_j)^2, \quad (w > 0) \quad 5.137$$

allows us to lower the Luttinger parameter $K_0 \rightarrow K = K_0 / \sqrt{1 + K_0 w}$ into the repulsive regime $0 \leq K \leq 1$ [second column in Figure 5.5 (a)]; the sound velocity is rescaled as $v_0 \rightarrow v = v_0 \sqrt{1 + K_0 w}$.

Finally, we couple the wires through density-density interactions described by

$$\mathcal{H}_{\text{inter}} = \frac{v_0}{2\pi} \sum_n \int_j \frac{m_{\theta}(n)}{2} (\partial_x \theta_j) (\partial_x \theta_{j+n}). \quad 5.138$$

Here, m_θ encodes the translationally invariant, symmetric inter-wire couplings of densities (for periodic boundary conditions in y -direction): $m_\theta(n) = m_\theta(n + N)$, $m_\theta(n) = m_\theta(-n)$ and $m_\theta(0) = 0$. Note that one could extend $\mathcal{H}_{\text{inter}}$ by flux-flux couplings [388, 389] (which we do not need in the following). The action of $\mathcal{H}_{\text{inter}}$ is illustrated in the third column of Figure 5.5 (a).

The sum of the three terms (5.136), (5.137), and (5.138) corresponds to a Gaussian fixed point action dubbed *Sliding Luttinger Liquid* (SLL),

$$\mathcal{H}_{\text{SLL}} \equiv \mathcal{H}_{\text{LL}} + \mathcal{H}_{\text{intra}} + \mathcal{H}_{\text{inter}}, \quad 5.139$$

which has been shown to feature islands of stability against generic perturbations. This is an example of a true “non-Fermi liquid” phase in two dimensions, characterized by the *sliding* symmetry $\varphi_j(x) \rightarrow \varphi_j(x) + \bar{\varphi}_j$ and $\theta_j(x) \rightarrow \theta_j(x) + \bar{\theta}_j$ for arbitrary constants $\bar{\varphi}_j, \bar{\theta}_j$ [386–389]. If we define $M_\theta(n) \equiv (1/K) \delta_{n,0} + (v_0/2v) m_\theta(n)$ and $M_\varphi(n) \equiv K \delta_{n,0}$, the SLL Hamiltonian can be compactly written as

$$\mathcal{H}_{\text{SLL}} = \frac{v}{2\pi} \sum_n \int_j [\varphi'_j M_\varphi(n) \varphi'_{j+n} + \theta'_j M_\theta(n) \theta'_{j+n}] \quad 5.140$$

where primes denote derivatives with respect to x .

Following the proposal by Kane *et al.* [357, 390], we additionally couple adjacent wires through the *Laughlin term*

$$\mathcal{O}_{\text{L}_2, j} \equiv \cos[\varphi_j - \varphi_{j+1} - 2(\theta_j + \theta_{j+1})] \quad \Rightarrow \quad \mathcal{H}_{\text{L}_2} = \varepsilon \int_j \mathcal{O}_{\text{L}_2, j} \quad 5.141$$

with small coupling constant ε (compared to the SLL couplings). Then, the complete Hamiltonian reads

$$\mathcal{H} = \mathcal{H}_{\text{SLL}}[M_\varphi, M_\theta] + \mathcal{H}_{\text{L}_2}, \quad 5.142$$

where the second term is treated as a perturbation of the SLL fixed point [fourth column in Figure 5.5 (a)]. Let us briefly sketch the intention behind \mathcal{O}_{L_2} (we omit the wire index j whenever possible); for details we refer the reader to Ref. [390]:

The elementary density and phase fields θ and φ that describe the uncoupled wires can be linearly combined to chiral fields

$$\tilde{\Phi}_j^R \equiv \varphi_j - 2\theta_j \quad \text{and} \quad \tilde{\Phi}_j^L \equiv \varphi_j + 2\theta_j \quad 5.143$$

that live on the wires, see Figure 5.5 (b). In these, the Laughlin term reads $\mathcal{O}_{\text{L}_2} = \cos[\tilde{\Phi}_j^R - \tilde{\Phi}_{j+1}^L]$. Using $[\varphi_j(x), \theta_{j'}(x')] = i\pi/2 \delta_{jj'} \text{sign}(x' - x)$, it is easy to show that right- and left-movers decouple: $[\tilde{\Phi}_j^\alpha(x), \partial_{x'} \tilde{\Phi}_{j'}^{\alpha'}(x')] = \pm 4\pi i \delta_{\alpha\alpha'} \delta_{jj'} \delta(x' - x)$, where $+/-$ corresponds to $\alpha = L/R$.

The Laughlin term can be further simplified by pairing left- and right-moving modes from *adjacent* wires to new density and phase fields $\tilde{\theta}_{j+1/2}$ and $\tilde{\varphi}_{j+1/2}$ that live “between” the wires:

$$\tilde{\varphi}_{j+1/2} \equiv \frac{\tilde{\Phi}_{j+1}^L + \tilde{\Phi}_j^R}{2} \quad \text{and} \quad \tilde{\theta}_{j+1/2} \equiv \frac{\tilde{\Phi}_{j+1}^L - \tilde{\Phi}_j^R}{2}. \quad 5.144$$

In these new variables, the Laughlin term simply becomes a sine-Gordon interaction $\mathcal{O}_{L_2} = \cos(2\tilde{\theta}_{j+1/2})$. It is straightforward to verify that the new fields obey $[\tilde{\varphi}_k(x), \partial_{x'} \tilde{\theta}_{k'}(x')] = 2\pi i \delta_{kk'} \delta(x - x')$ for $k = j + 1/2$ and $k = j' + 1/2$ [cf. Eq. (5.134)].

The crucial observation is that in a system with N parallel wires and boundaries along the x -direction, this procedure leaves the chiral modes $\tilde{\Phi}_N^R$ and $\tilde{\Phi}_1^L$ on the two boundaries unpaired. They remain gapless even when the $N - 1$ couplings \mathcal{O}_{L_2} in the bulk flow to strong coupling and open a gap. Then, the *boundaries* of the gapped bulk host gapless edge modes that are described by a *chiral Luttinger liquid* with topologically pinned Luttinger parameter $K = \nu = 1/2$ —a well-known feature of fractional quantum Hall states [39].

This explains why we are interested in a parameter regime of M_φ and M_θ where \mathcal{H}_{L_2} flows to strong coupling and determines the properties of the gapped bulk (and, by the argument above, the edge mode physics as well).

5.2.3 Allowed Operators

Let us first focus on possible microscopic interactions, in terms of the elementary bosonic fields $\Psi_j(x)$, that give rise to the required Laughlin term \mathcal{O}_{L_2} . Using the bosonized fields (5.135), it is straightforward to show that nearest-neighbor single-particle hopping with additional density interactions gives rise to the Laughlin term \mathcal{O}_{L_2} :

$$\rho_j \Psi_j^\dagger \Psi_{j+1} \rho_{j+1} + \text{h.c.} \sim \mathcal{O}_{L_2} + \mathcal{R}. \quad 5.145$$

Here, \mathcal{R} collects irrelevant and fast oscillating terms that do not enter the renormalization group analysis below, see Subsection 5.2.5 for details. Note that the long-wavelength effective description that derives from the microscopic interaction (5.145) is given by \mathcal{O}_{L_2} *because* of the magnetic field and *only* at the particular filling $\nu = 1/2$.

The perturbation (5.145) is the one needed to drive the SLL into the fractional quantum Hall regime. To this end, \mathcal{O}_{L_2} must be a *relevant* perturbation of the Gaussian fixed point (5.140) in the RG sense. But this is not sufficient if there are competing (symmetry-allowed) perturbations that can be added to the fixed point action. All of these must be *irrelevant* (or less relevant) to ensure that the gapped phase is a $\nu = 1/2$ Laughlin state.

We postpone a comprehensive discussion of allowed perturbations to the future and focus on only one class of competing terms, namely density-density interactions

$$\rho_j \rho_{j+n} \sim \mathcal{O}_{\text{CDW}}^{(n)} + \mathcal{R} \quad 5.146$$

that give rise to the bosonized perturbations $\mathcal{O}_{\text{CDW}}^{(n)} \equiv \cos[2(\theta_j - \theta_{j+n})]$; these are unaffected by the magnetic field and potentially relevant at any filling. When $\mathcal{O}_{\text{CDW}}^{(n)}$ becomes relevant and flows to strong coupling, the density fields θ_j on wires with distance n are locked and the system displays CDW-crystalline order [357, 389].

In the following, we study the competition between the (wanted) Laughlin term \mathcal{O}_{L_2} and the (unwanted) CDW terms $\mathcal{O}_{\text{CDW}}^{(n)}$ with a first-order renormalization group analysis.

5.2.4 Renormalization Group Analysis

The stability of a phase—described by a Gaussian fixed point action—against perturbations is determined by the flow of their coupling constants under first-order RG transformations [256],

$$\frac{d\varepsilon_{\mathcal{O}}}{dl} = (2 - \Delta_{\mathcal{O}}) \varepsilon_{\mathcal{O}}, \quad 5.147$$

where $\varepsilon_{\mathcal{O}} \in \mathbb{R}$ and $\Delta_{\mathcal{O}} \in \mathbb{R}^+$ denotes the coupling constant and scaling dimension of the perturbation $\mathcal{O} \in \{\mathcal{O}_{\text{L}_2}, \mathcal{O}_{\text{CDW}}^{(n)}\}$, respectively. The dimensionless parameter l describes the length scale, where $l \rightarrow \infty$ denotes the infrared limit (“zooming out”). From the RG flow (5.147) it follows that \mathcal{O} is relevant ($|\varepsilon_{\mathcal{O}}| \rightarrow \infty$ for $l \rightarrow \infty$) if $\Delta_{\mathcal{O}} < 2$ and irrelevant ($|\varepsilon_{\mathcal{O}}| \rightarrow 0$ for $l \rightarrow \infty$) if $\Delta_{\mathcal{O}} > 2$.

The scaling dimensions of the operators \mathcal{O}_{L_2} and $\mathcal{O}_{\text{CDW}}^{(n)}$ are straightforwardly evaluated (see Subsection 5.2.5 for details) and read

$$\Delta_{\text{CDW}}^{(n)} = 2K \xi_n^- \quad 5.148a$$

$$\Delta_{\text{L}_2} = \frac{1}{2K} \chi_1^- + 2K \xi_1^+ \quad 5.148b$$

with the K -independent integrals (for wire distance $a = 1$)

$$\xi_n^{\pm} \equiv \int_{-\pi}^{\pi} \frac{dq}{2\pi} \frac{1}{\eta(q)} [1 \pm \cos(qn)] \quad 5.149a$$

$$\chi_n^{\pm} \equiv \int_{-\pi}^{\pi} \frac{dq}{2\pi} \eta(q) [1 \pm \cos(qn)]. \quad 5.149b$$

The marginal inter- and intra-wire couplings of \mathcal{H}_{SLL} are encoded in $\eta(q) = K \sqrt{\tilde{M}_\theta(q)/\tilde{M}_\varphi(q)}$ where $\tilde{M}_{\theta,\varphi}(q)$ is the discrete Fourier transform of $M_{\theta,\varphi}(n)$:

$$\tilde{M}_{\theta,\varphi}(q) \equiv \sum_{n=0}^{N-1} M_{\theta,\varphi}(n) e^{-iqn}. \quad 5.150$$

In the following, we restrict our analysis to nearest- (NN) and next-nearest-neighbor (NNN) density-density interactions as these are sufficient to stabilize the SLL [388]. Thus $m_\theta(n) = m_1 \delta_{n,\pm 1} + m_2 \delta_{n,\pm 2}$ and consequently

$$M_\theta(n) = \frac{1}{K} \delta_{n,0} + \frac{v_0}{2v} (m_1 \delta_{n,\pm 1} + m_2 \delta_{n,\pm 2}). \quad 5.151$$

In combination with $M_\varphi(n) = K \delta_{n,0}$ and the rescaled coupling constants $\lambda_k \equiv m_k K^2/K_0$ ($k = 1, 2$), one finds

$$\eta(q) = \sqrt{1 + \lambda_1 \cos(q) + \lambda_2 \cos(2q)}, \quad 5.152$$

see Subsection 5.2.5 for details. Note that we translated the physically meaningful parameters m_1, m_2 and w into the new parameters λ_1, λ_2 and K as the latter are convenient coordinates for the phase diagram (see below).

Strict Condition

We are now in the position to search the parameter space $(\lambda_1, \lambda_2, K)$ for domains where the system is driven into the fractional quantum Hall regime. To this end, we require $\mathcal{O}_{\text{CDW}}^{(n)}$ to be irrelevant for all $n \geq 1$ and \mathcal{O}_{L_2} to be relevant:

$$\forall_n : \Delta_{\text{CDW}}^{(n)} > 2 \quad \text{and} \quad \Delta_{\text{L}_2} < 2. \quad 5.153$$

Given a pair of couplings λ_1, λ_2 , these conditions translate into intervals for the effective Luttinger parameter K . One finds $K \in \overline{\mathcal{K}}_{\text{CDW}}^{(N)} \equiv \bigcap_{n \leq N} (1/\xi_n^-, \infty]$ for the *irrelevance* of $\mathcal{O}_{\text{CDW}}^{(n)}$ up to distance N , and

$$K \in \mathcal{K}_{\text{L}_2} \equiv ([1 - \Lambda]/2\xi_1^+, [1 + \Lambda]/2\xi_1^+) \quad 5.154$$

with $\Lambda = \text{Re} \sqrt{1 - \xi_1^+ \chi_1^-}$ for the *relevance* of the Laughlin term \mathcal{O}_{L_2} . (Note that this interval is empty for $\xi_1^+ \chi_1^- \geq 1$.) The system is safely driven into the $\nu = 1/2$ Laughlin state if

$$K \in \mathcal{K}^{(N)} \equiv \mathcal{K}_{\text{L}_2} \cap \overline{\mathcal{K}}_{\text{CDW}}^{(N)}. \quad 5.155$$

Thus we are interested in couplings λ_1, λ_2 for which $\mathcal{K}^{(N)} \neq \emptyset$ for $N \rightarrow \infty$.

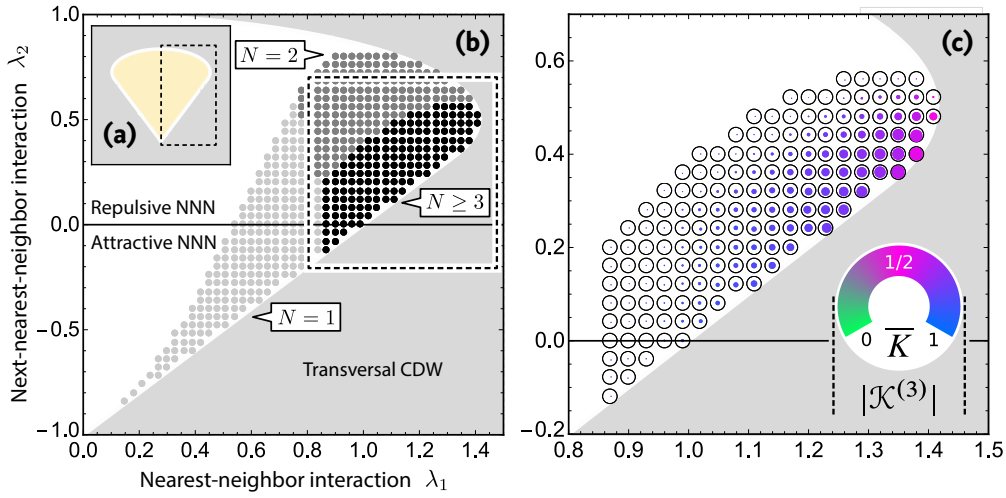


FIGURE 5.6 • Phase diagram. (a) The parameter domain for which the SLL is stable against transversal CDW order is shaded yellow. The marked region (dashed box) with repulsive nearest-neighbor interactions ($\lambda_1 > 0$) is shown in (b): Stability against CDW perturbations $\mathcal{O}_{\text{CDW}}^{(n)}$ with range up to $N = 1, 2, 3$ reduces the domain for which \mathcal{H}_{L2} is the only relevant perturbation considerably. The marked region (dashed box) is shown in the close-up (c): The colored patch is stable against $N \geq 3$ CDW perturbations; color and diameter of the discs encode the center \bar{K} of the K -interval $\mathcal{K}^{(3)}$ and its size $|\mathcal{K}^{(3)}|$, respectively. The maximum diameter corresponds to $|\mathcal{K}^{(3)}| \approx 0.28$ at $\bar{K} \approx 0.55$.

An additional constraint follows from inspection of Eq. (5.149a) in combination with Eq. (5.152): ξ_n^\pm is only well-defined if $\eta(q) > 0$ for all $q \in [-\pi, \pi]$. Physically, this ensures stability against the formation of transversal CDW order [388]. Solving this inequality yields the allowed parameter regime $|\lambda_1| < \sqrt{8\lambda_2(1-\lambda_2)}$ for $1/3 \leq \lambda_2 < 1$ and $|\lambda_1| < \lambda_2 + 1$ for $-1 < \lambda_2 < 1/3$, depicted in Figure 5.6 (a) and derived in Subsection 5.2.5 (see also Figure 5.8). Note that this region covers all four cases: attractive or repulsive nearest-neighbor interactions $\lambda_1 \leq 0$ combined with attractive or repulsive next-nearest-neighbor interactions $\lambda_2 \leq 0$.

Within this admissible parameter regime, the condition $\mathcal{K}^{(1)} \neq \emptyset$ (which guarantees stability against nearest-neighbor CDW order only) restricts the couplings to the marked region in Figure 5.6 (b), which lies completely in the sector of repulsive nearest-neighbor interactions. For $N = 2$ and $N = 3$, this region shrinks gradually to the smallest patch labeled by “ $N \geq 3$ ”—which then remains stable for larger distances $N > 3$. Figure 5.6 (c) shows a close-up of this stable domain and reveals that the center \bar{K} of the interval $\mathcal{K}^{(3)}$ varies from the weakly repulsive regime $\bar{K} \lesssim 1$ to $\bar{K} \sim 1/2$; the interval is rather narrow, with maximum extent close to the transversal CDW instability.

COUPLED LUTTINGER LIQUIDS

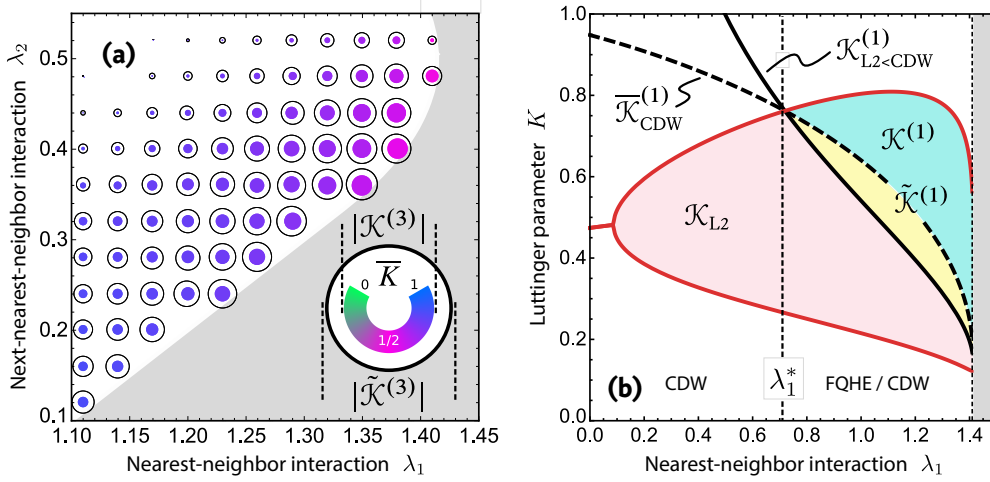


FIGURE 5.7 • Relaxed condition. (a) Comparison of the K -intervals $\mathcal{K}^{(3)}$ and $\tilde{\mathcal{K}}^{(3)}$ in the parameter domain with the largest intervals (see Figure 5.6). The diameter of discs (circles) encodes the size $|\mathcal{K}^{(3)}|$ ($|\tilde{\mathcal{K}}^{(3)}|$) of the intervals; the color encodes the center \bar{K} of $\mathcal{K}^{(3)}$. The maximum diameter of discs and circles corresponds to $|\mathcal{K}^{(3)}| \approx 0.28$ and $|\tilde{\mathcal{K}}^{(3)}| \approx 0.43$, respectively. (b) Interval boundaries for a cut in λ_1 -direction at $\lambda_2 = 0.5$ and $N = 1$ (these parameters were chosen for illustrative reasons); red: \mathcal{K}_{L_2} , green: $\mathcal{K}^{(1)}$, yellow+green: $\tilde{\mathcal{K}}^{(1)}$. Note the interval close to $\lambda_1 \approx 0$ where $\mathcal{K}_{L_2} = \emptyset$. The solid and dashed black curves are the lower boundaries of the intervals $\mathcal{K}_{L_2 < CDW}^{(1)}$ and $\bar{\mathcal{K}}_{CDW}^{(1)}$.

Relaxed Condition

The condition (5.153) is rather strict as it demands that the *only* relevant operator is the Laughlin term. However, depending on the bare values of the coupling constants it may be sufficient for \mathcal{O}_{L_2} to be the *most relevant* operator; this allows for less relevant CDW terms and may relax the constraints on inter-wire couplings and the Luttinger parameter.

Formally, the relaxed condition reads

$$\Delta_{L_2} < \min_{n \geq 1} \{2, \Delta_{CDW}^{(n)}\} \quad 5.156$$

which is equivalent to ($N \rightarrow \infty$)

$$K \in \tilde{\mathcal{K}}^{(N)} \equiv \mathcal{K}_{L_2} \cap \mathcal{K}_{L_2 < CDW}^{(N)}, \quad 5.157$$

where the interval $\mathcal{K}_{L_2 < CDW}^{(N)}$ is a function of λ_1 and λ_2 and reads

$$\mathcal{K}_{L_2 < CDW}^{(N)} \equiv \bigcap_{n \leq N} \left(\sqrt{\chi_1^-} / 2 \operatorname{Re} \sqrt{\xi_n^- - \xi_1^+}, \infty \right]; \quad 5.158$$

see Subsection 5.2.5 for the derivation [starting at Eq. (5.250)].

Numerical results are shown in Figure 5.7: Relaxing the condition of being the *only* relevant operator to being the *most* relevant operator does *not* change the phase boundaries in the λ_1 - λ_2 -plane but expands the interval of allowed Luttinger parameters K instead: $\mathcal{K}^{(N)} \subsetneq \tilde{\mathcal{K}}^{(N)}$, see Figure 5.7 (a). This is explained in Figure 5.7 (b) where we plot the interval boundaries of $\mathcal{K}^{(N)}$ and $\tilde{\mathcal{K}}^{(N)}$ along a cut in λ_1 -direction for fixed λ_2 . The invariant phase boundary for both conditions (strict and relaxed) is rooted in a relation of ξ_n^\pm and χ_n^\pm that is responsible for the threefold intersection of interval boundaries at the critical nearest-neighbor coupling strength $\lambda_1^* = \lambda_1^*(\lambda_2)$.

The upshot is that the relaxation allows for a broader range of Luttinger parameters (determined by the intra-wire interactions), but has no effect on the necessary inter-wire couplings λ_1 and λ_2 .

5.2.5 Technical Details

Here we provide detailed derivations for the results presented above. We start with a careful discussion of the parameters used for the description of the SLL Hamiltonian. Then we construct the allowed perturbations and derive their scaling dimension. Finally, we discuss the intervals for the Luttinger parameter and reproduce the coupling range found in Ref. [388] that is stable against transversal CDW order.

Dictionary of Parameters

The physical parameters relevant for our model are the sound velocity v_0 , the intra-wire repulsion w , and the nearest- and next-nearest-neighbor inter-wire interaction m_1 and m_2 . For these parameters, the SLL Hamiltonian reads

$$\mathcal{H}_{\text{SLL}} = \mathcal{H}_{\text{LL}} + \mathcal{H}_{\text{intra}} + \mathcal{H}_{\text{inter}} \quad 5.159\text{a}$$

$$= \frac{v_0}{2\pi} \int_j \left\{ \begin{aligned} &K_0(\partial_x \varphi_j)^2 + \frac{1}{K_0}(\partial_x \theta_j)^2 + w(\partial_x \theta_j)^2 \\ &+ \frac{1}{2} \sum_{n \neq 0} m_\theta(n) (\partial_x \theta_i)(\partial_x \theta_{i+n}) \end{aligned} \right\} \quad 5.159\text{b}$$

where $K_0 = 1$ for hard-core bosons and $\int_j \equiv \sum_j \int dx$. Combining all intra-wire terms yields the Hamiltonian

$$\mathcal{H}_{\text{SLL}} = \frac{v}{2\pi} \int_j \left\{ \begin{aligned} &K(\partial_x \varphi_j)^2 + \frac{1}{K}(\partial_x \theta_j)^2 \\ &+ \frac{v_0}{2v} \sum_{n \neq 0} m_\theta(n) \int_i (\partial_x \theta_i)(\partial_x \theta_{i+n}) \end{aligned} \right\} \quad 5.160$$

with rescaled Luttinger parameter K and sound velocity v ,

$$K = \frac{K_0}{\sqrt{1 + wK_0}} \quad \text{and} \quad v = v_0 \sqrt{1 + wK_0}. \quad 5.161$$

Collecting intra- and inter-wire interactions yields

$$\mathcal{H}_{\text{SLL}} = \frac{v}{2\pi} \sum_n \int_j \left\{ \frac{K\delta_{n,0}(\partial_x\varphi_j)(\partial_x\varphi_{j+n})}{+ \left(\frac{1}{K}\delta_{n,0} + \frac{v_0}{2v}m_\theta(n) \right) (\partial_x\theta_j)(\partial_x\theta_{j+n})} \right\} \quad 5.162a$$

$$= \frac{v}{2\pi} \sum_n \int_j [M_\varphi(n)(\partial_x\varphi_j)(\partial_x\varphi_{j+n}) + M_\theta(n)(\partial_x\theta_j)(\partial_x\theta_{j+n})] \quad 5.162b$$

with

$$M_\varphi(n) = K\delta_{n,0} \quad \text{and} \quad M_\theta(n) = \frac{1}{K} \left(\delta_{n,0} + \frac{Kv_0}{2v}m_\theta(n) \right). \quad 5.163$$

With $m_\theta(n) = m_1\delta_{n,\pm 1} + m_2\delta_{n,\pm 2}$ and $Kv_0/v = K^2/K_0$ the second term reads

$$M_\theta(n) = \frac{1}{K} \left[\delta_{n,0} + \frac{K^2}{2K_0} (m_1\delta_{n,\pm 1} + m_2\delta_{n,\pm 2}) \right] \quad 5.164a$$

$$= \frac{1}{K} [\delta_{n,0} + \lambda_1 \delta_{n,\pm 1}/2 + \lambda_2 \delta_{n,\pm 2}/2] \quad 5.164b$$

with the rescaled couplings $\lambda_k = m_k K^2/K_0$. The discrete Fourier transform ($2 < N < \infty$) yields

$$\tilde{M}_\theta(q) = \sum_{n=0}^{N-1} M_\theta(n) e^{-iqna} \quad 5.165a$$

$$= \frac{1}{K} [1 + \lambda_1 \cos(qa) + \lambda_2 \cos(2qa)] \quad 5.165b$$

where we used that $M_\theta(n+N) = M_\theta(n)$. Together with $\tilde{M}_\varphi(q) = K$, this leads to

$$\eta(q) = K \sqrt{\tilde{M}_\theta(q)/\tilde{M}_\varphi(q)} \quad 5.166a$$

$$= \sqrt{1 + \lambda_1 \cos(qa) + \lambda_2 \cos(2qa)}. \quad 5.166b$$

In conclusion, we have the following relation between the triple (w, m_1, m_2) of physical parameters and the dimensionless parameters $(K, \lambda_1, \lambda_2)$ used for the RG analysis:

$$\left\{ \begin{array}{l} w = \frac{1}{K_0} \left(\frac{K_0^2}{K^2} - 1 \right) \\ m_1 = \frac{K_0}{K^2} \lambda_1 \\ m_2 = \frac{K_0}{K^2} \lambda_2 \end{array} \right\} \Leftrightarrow \left\{ \begin{array}{l} K = \frac{K_0}{\sqrt{1 + wK_0}} \\ \lambda_1 = \frac{K_0}{1 + wK_0} m_1 \\ \lambda_2 = \frac{K_0}{1 + wK_0} m_2 \end{array} \right\}. \quad 5.167$$

Note that due to the mixing of parameters, the integrals ξ_n^\pm and χ_n^\pm in (5.149) are functions of (λ_1, λ_2) via (5.166b) (but independent of $K!$), while they depend non-trivially on all *three* physical parameters (w, m_1, m_2) . This allows for a straightforward computation of domains for solutions in the dimensionless parameters (as discussed above).

Allowed Perturbations

Here we derive perturbations of the SLL fixed point action that are allowed (i.e., slowly varying) in the presence of the perpendicular magnetic field B_z . We focus on the Laughlin term and the competing CDW coupling. A systematic study of more general perturbations is postponed to the future.

We use the bosonization formulas for bosons with density modulations up to the first harmonic $2k_F = 2\pi\rho_0$ [255]:

$$\Psi_j(x) = \sqrt{\rho_0} e^{-i(\varphi_j(x) + bjx)}, \quad 5.168a$$

$$\rho_j(x) = \rho_0 - \frac{1}{\pi} \partial_x \theta_j(x) + \cos(2\pi\rho_0 x - 2\theta_j(x)). \quad 5.168b$$

The filling is fixed at $\nu = 1/2$ by setting the magnetic field to $b = 4\pi\rho_0$ (i.e., two flux quanta per boson in the lowest Landau level). Note that the absent density field θ in the exponential (5.168a) and the missing Klein factors impose Ψ_j with bosonic commutation relations (single particles manifest as steps of π in the θ -field). As the prefactors of operators are of no relevance for their scaling behavior, we omit them in the following.

As a first observation, we find that *inter-chain single-particle hopping* between chains j and $k \neq j$, described by

$$\Psi_j^\dagger(x) \Psi_k(x) \sim e^{i(\varphi_j(x) + bjx)} e^{-i(\varphi_k(x) + bkx)} \quad 5.169a$$

$$= \underbrace{e^{ib(j-k)x} e^{i(\varphi_j(x) - \varphi_k(x))}}_{\text{fast oscillating}} \sim 0, \quad 5.169b$$

is fast oscillating due to the applied magnetic field and therefore irrelevant for the infrared regime.

To find slowly varying perturbations that may become relevant and affect the low-energy physics, we have to include interactions via the periodic modulation of the density fields. We focus on the two simplest cases:

→ *Inter-chain density-density interactions* between chains j and $k \neq j$ are described by

$$\rho_j(x)\rho_k(x) \sim [1 + \partial_x\theta_j(x) + \cos(2\pi\rho_0x - 2\theta_j(x))] \quad 5.170a$$

$$\begin{aligned} & \times [1 + \partial_x\theta_k(x) + \cos(2\pi\rho_0x - 2\theta_k(x))] \\ & = 1 + \underbrace{\partial_x\theta_k(x) + \partial_x\theta_j(x)}_{\text{chemical potential}} + \underbrace{\partial_x\theta_j(x)\partial_x\theta_k(x)}_{\text{marginal}} \end{aligned} \quad 5.170b$$

$$+ \cos(2\pi\rho_0x - 2\theta_k(x))$$

$$+ \underbrace{\cos(2\pi\rho_0x - 2\theta_j(x))}_{\text{fast oscillating}}$$

$$+ \partial_x\theta_j(x) \cos(2\pi\rho_0x - 2\theta_k(x))$$

$$+ \underbrace{\partial_x\theta_k(x) \cos(2\pi\rho_0x - 2\theta_j(x))}_{\text{fast oscillating}}$$

$$+ \cos(2\pi\rho_0x - 2\theta_k(x)) \cos(2\pi\rho_0x - 2\theta_j(x)) .$$

The last term contains slowly varying components,

$$\rho_j(x)\rho_k(x) \sim \cos(2\theta_j(x) - 2\theta_k(x)) \quad 5.171a$$

$$+ \underbrace{\cos(4\pi\rho_0x - 2\theta_j(x) - 2\theta_k(x))}_{\text{fast oscillating}}$$

$$\sim \cos(2\theta_j(x) - 2\theta_k(x)) , \quad 5.171b$$

which is the CDW term $\mathcal{O}_{\text{CDW}}^{(n)}$ for $|k - j| = n$.

→ *Inter-chain hopping with density-density interactions* between chains j and $k \neq j$ is described by

$$\begin{aligned} & \rho_j(x)\Psi_j^\dagger(x)\Psi_k(x)\rho_k(x) + \text{h.c.} \\ & \sim [\mathcal{O}(0) + \mathcal{O}(2\pi\rho_0) + \mathcal{O}(4\pi\rho_0)] \quad 5.172 \\ & \times \cos[4\pi\rho_0(j - k)x + \varphi_j(x) - \varphi_k(x)] , \end{aligned}$$

where we introduced the notation $\mathcal{O}(k)$ for terms modulated with wavenumber k , see Eq. (5.170). The term can be expanded as a sum of frequency components,

$$\begin{aligned} & \rho_j(x)\Psi_j^\dagger(x)\Psi_k(x)\rho_k(x) + \text{h.c.} \\ & \sim \mathcal{O}(2\pi\rho_0[0 + 2(j - k)]) + \mathcal{O}(2\pi\rho_0[0 - 2(j - k)]) \quad 5.173 \\ & + \mathcal{O}(2\pi\rho_0[1 + 2(j - k)]) + \mathcal{O}(2\pi\rho_0[1 - 2(j - k)]) \\ & + \mathcal{O}(2\pi\rho_0[2 + 2(j - k)]) + \mathcal{O}(2\pi\rho_0[2 - 2(j - k)]) . \end{aligned}$$

It is clear that only the terms in the first and third row can be tuned non-oscillatory with integer i and k . The first row demands $j = k$, which is not an inter-chain interaction; the terms in the third row become slowly varying for

$$|j - k| = 1, \quad 5.174$$

that is, nearest-neighbor interactions.

Without loss of generality, let $k = j + 1$; then the product with slowly varying components is

$$\begin{aligned} & \underbrace{\cos(4\pi\rho_0 x - 2\theta_j(x) - 2\theta_{j+1}(x))}_{\text{fast oscillating from density-density}} \\ & \times \underbrace{\cos[-4\pi\rho_0 x + \varphi_j(x) - \varphi_{j+1}(x)]}_{\text{fast oscillating from hopping}} \end{aligned} \quad 5.175a$$

$$= \cos[\varphi_j(x) - \varphi_{j+1}(x) - 2(\theta_j(x) + \theta_{j+1}(x))] + \mathcal{O}(8\pi\rho_0) \quad 5.175b$$

$$\sim \cos[\varphi_j(x) - \varphi_{j+1}(x) - 2(\theta_j(x) + \theta_{j+1}(x))], \quad 5.175c$$

which is the wanted Laughlin term \mathcal{O}_{L_2} .

Note that this term becomes slowly varying only at filling $\nu = 1/2$ with an applied magnetic field $b = 4\pi\rho_0$.

Renormalization Group Analysis

To derive the scaling dimensions of the operators

$$\mathcal{O}_{\text{CDW}}^{(n)} \sim e^{2i(\theta_j - \theta_{j+n})} \quad 5.176a$$

$$\mathcal{O}_{L_2} \sim e^{i[\varphi_j - \varphi_{j+1} - 2(\theta_j + \theta_{j+1})]} \quad 5.176b$$

we follow the conventional renormalization procedure in momentum space [256]. To this end, we start with a finite system of length L in x -direction, Na in y -direction, and periodic boundary conditions. The classical fields can be expressed as Fourier series

$$\chi_j(\mathbf{r}) = \sum_{\mathbf{Q}} \chi(\mathbf{Q}) e^{i(\mathbf{q}\mathbf{r} + q_y ja)} \quad 5.177a$$

$$\Leftrightarrow \chi(\mathbf{Q}) = \frac{1}{V} \sum_{j=1}^N a \int_0^{\beta v} dz \int_0^L dx \chi_j(\mathbf{r}) e^{-i(\mathbf{q}\mathbf{r} + q_y ja)} \quad 5.177b$$

with $\chi \in \{\varphi, \theta\}$, $\mathbf{Q} = (\mathbf{q}, q_y)$ and volume $V = L_x L_y L_z$ with $L_x = L$, $L_y = Na$ and $L_z = \beta v$. Here $\mathbf{q} = (q_x, q_z) = (q_x, \omega/v)$ is the momentum in Euclidean coordinates $\mathbf{r} = (x, z) = (x, v\tau)$ with sound velocity v and imaginary time $\tau = it$. Periodicity in x -direction demands $q_x \in \frac{2\pi}{L}\mathbb{Z}$ and periodicity in (imaginary) time with period β requires $q_z = \omega/v \in \frac{2\pi}{L_z}\mathbb{Z}$. Finally, $q_y \in \frac{2\pi}{L_y}\mathbb{Z} \cap [-\pi/a, \pi/a]$ is the transversal momentum in y -direction.

We can now split fields into their fast and slow components:

$$\chi_j(\mathbf{r}) = \sum_{\mathbf{Q}}^{\Lambda} \chi(\mathbf{Q}) e^{i(\mathbf{qr} + q_y ja)} \quad 5.178a$$

$$= \sum_{\mathbf{Q}}^{\Lambda'} \chi(\mathbf{Q}) e^{i(\mathbf{qr} + q_y ja)} + \sum_{\mathbf{Q}}^{\Lambda' \dots \Lambda} \chi(\mathbf{Q}) e^{i(\mathbf{qr} + q_y ja)} \quad 5.178b$$

$$\equiv \chi_j^<(\mathbf{r}) + \chi_j^>(\mathbf{r}). \quad 5.178c$$

Here we introduced the circular UV-cutoff Λ in the q_x - q_z -plane to make the integrals that follow convergent; we also introduced the shorthand notation

$$\sum_{\mathbf{Q}}^{\Lambda} \equiv \sum_{\mathbf{Q}, |\mathbf{q}| < \Lambda} \quad \text{and} \quad \sum_{\mathbf{Q}}^{\Lambda' \dots \Lambda} \equiv \sum_{\mathbf{Q}, \Lambda' < |\mathbf{q}| < \Lambda} . \quad 5.179$$

Note that this corresponds to the introduction of a lattice with spacing Λ^{-1} in x - and ($z \propto \tau$)-direction; in y -direction this is not necessary due to the discrete nature of the array of wires.

We are interested in the running of the coupling constants ε_i and $M_\chi(n)$ in the long-wavelength limit of the perturbed action

$$S[\varphi, \theta] = S_{\text{SLL}}[\varphi, \theta] + \varepsilon_1 S_{\text{CDW}}^{(n)}[\varphi, \theta] + \varepsilon_2 S_{\text{L}_2}[\varphi, \theta] \quad 5.180$$

in first order of the perturbations (for $\varepsilon_i \ll 1$). Here, S_{SLL} is the Gaussian fixed point action of the SLL [see Eq. (5.196b) below]. In first order, the perturbations do not couple and we can consider the generic action

$$S[\varphi, \theta] = S_{\text{SLL}}[\varphi, \theta] + \varepsilon S_{\mathcal{O}}[\varphi, \theta] \quad 5.181$$

with

$$S_{\mathcal{O}}[\varphi, \theta] = \int d\tau \int dx \mathcal{O}(\varphi, \theta) \quad 5.182$$

and \mathcal{O} some function of the fields $\varphi = \{\varphi_i\}$ and $\theta = \{\theta_j\}$. In the following, we again write χ for φ and θ to simplify expressions.

Let $\mathcal{D}[\chi^{\lessgtr}]$ denote the functional integration measure for the slow and fast field components, respectively. It is straightforward to show that the quadratic SLL action is additive in the momenta, and thus in the slow-fast decomposition [see Eq. (5.204) below]:

$$S[\chi^< + \chi^>] = S_{\text{SLL}}[\chi^<] + S_{\text{SLL}}[\chi^>] + \varepsilon S_{\mathcal{O}}[\chi^< + \chi^>]. \quad 5.183$$

For an RG step, we integrate out the fast modes in the partition function of the perturbed action,

$$Z_\Lambda \equiv \int \mathcal{D}[\chi] e^{-S[\chi]} \quad 5.184a$$

$$= \int \mathcal{D}[\chi^<] \int \mathcal{D}[\chi^>] e^{-S_{\text{SLL}}[\chi^<] - S_{\text{SLL}}[\chi^>] - \varepsilon S_\theta[\chi^< + \chi^>]} \quad 5.184b$$

$$= \int \mathcal{D}[\chi^<] e^{-S_{\text{SLL}}[\chi^<]} \int \mathcal{D}[\chi^>] e^{-S_{\text{SLL}}[\chi^>]} e^{-\varepsilon S_\theta[\chi^< + \chi^>]} \quad 5.184c$$

$$= Z^> \int \mathcal{D}[\chi^<] e^{-S_{\text{SLL}}[\chi^<]} \left\langle e^{-\varepsilon S_\theta[\chi^< + \chi^>]} \right\rangle_>, \quad 5.184d$$

where $Z^>$ denotes the partition function of the fast components,

$$Z^> \equiv \int \mathcal{D}[\chi^>] e^{-S_{\text{SLL}}[\chi^>]}, \quad 5.185$$

and $\langle \bullet \rangle_>$ is the expectation value with respect to the corresponding SLL fixed point action. With this, we can define the effective action

$$S_{\text{eff}}[\chi^<] \equiv S_{\text{SLL}}[\chi^<] - \ln \left\langle e^{-\varepsilon S_\theta[\chi^< + \chi^>]} \right\rangle_> \quad 5.186$$

which describes the physics of long wavelengths completely. Indeed, if $\theta = \theta(\chi^<)$, one finds

$$\langle \theta(\chi^<) \rangle = Z_\Lambda^{-1} \int \mathcal{D}[\chi] \theta(\chi^<) e^{-S[\chi]} \quad 5.187a$$

$$= Z^> Z_\Lambda^{-1} \int \mathcal{D}[\chi^<] \theta(\chi^<) e^{-S_{\text{eff}}[\chi^<]} \quad 5.187b$$

$$= \frac{Z^> Z_{\text{eff}}}{Z_\Lambda} \langle \theta(\chi^<) \rangle_{\text{eff}}. \quad 5.187c$$

Since $\varepsilon \ll 1$, we can expand the exponent up to first order

$$S_{\text{eff}}[\chi^<] = S_{\text{SLL}}[\chi^<] - \ln \{1 - \varepsilon \langle S_\theta[\chi^< + \chi^>] \rangle_> + \mathcal{O}(\varepsilon^2)\} \quad 5.188a$$

$$= S_{\text{SLL}}[\chi^<] + \varepsilon \langle S_\theta[\chi^< + \chi^>] \rangle_> + \mathcal{O}(\varepsilon^2). \quad 5.188b$$

As our perturbations (5.176) are of the form $\theta(\chi) = e^{i\mathbf{x}(\chi)}$, we can write

$$\langle S_\theta[\chi^< + \chi^>] \rangle_> = \int d\tau \int dx \left\langle e^{i\mathbf{x}(\chi)} \right\rangle_> \quad 5.189a$$

$$= \int d\tau \int dx \left\langle e^{i\mathbf{x}(\chi^>)} \right\rangle_> e^{i\mathbf{x}(\chi^<)}, \quad 5.189b$$

where we used that \mathcal{X} (in our case) is a linear function of the fields, and therefore additive in the slow and fast field components. Using Wick's theorem, we can get rid of the exponential:

$$\left\langle e^{i\mathcal{X}(\chi^>)} \right\rangle_{>} = e^{-\frac{1}{2}\langle \mathcal{X}^2(\chi^>) \rangle_{>}} = 1 - \frac{1}{2}\langle \mathcal{X}^2(\chi^>) \rangle_{>} + \dots \quad 5.190$$

(Recall that $\langle \bullet \rangle$ describes a non-Gaussian expectation value whereas $\langle \bullet \rangle_{>}$ is evaluated at the Gaussian SLL fixed point; then, Wick's theorem applies since \mathcal{X} is linear in the fields [255].) From (5.190) we only keep the first term quadratic in \mathcal{X} since we are interested in infinitesimal momentum shells $\Lambda - \Lambda'$ [see Eq. (5.220b) below].

For the perturbations (5.176) we have

$$\mathcal{X}_{\text{CDW}}^{(n)} = 2(\theta_j - \theta_{j+n}) \quad 5.191a$$

$$\mathcal{X}_{\text{L}_2} = \varphi_j - \varphi_{j+1} - 2(\theta_j + \theta_{j+1}), \quad 5.191b$$

so that we need to evaluate correlators of the form

$$\left\langle (\chi_j^>(\mathbf{r}) \pm \chi_{j+n}^>(\mathbf{r}))^2 \right\rangle_{>} \quad \text{and} \quad \left\langle \chi_j^>(\mathbf{r}) \bar{\chi}_{j+n}^>(\mathbf{r}) \right\rangle_{>} \quad 5.192$$

with the shorthand notation $\bar{\theta} = \varphi$ and $\bar{\varphi} = \theta$. To this end, we refer to the defining path integral formulation ($\hbar = 1$):

$$\langle \mathcal{O}(\chi(x, t)) \rangle \equiv \frac{\int \mathcal{D}[\chi] \mathcal{O}(\chi) e^{i\tilde{S}_{\text{SLL}}[\chi]}}{\int \mathcal{D}[\chi] e^{i\tilde{S}_{\text{SLL}}[\chi]}} \quad 5.193a$$

$$\xrightarrow[\substack{\text{Wick rotation} \\ (t \rightarrow -i\tau)}]{\text{Wick rotation}} \langle \mathcal{O}(\chi(x, \tau)) \rangle = \frac{\int \mathcal{D}[\chi] \mathcal{O}(\chi) e^{-S_{\text{SLL}}[\chi]}}{\int \mathcal{D}[\chi] e^{-S_{\text{SLL}}[\chi]}}. \quad 5.193b$$

To derive the (Minkowski) action \tilde{S}_{SLL} , we use the SLL Hamiltonian

$$\mathcal{H}_{\text{SLL}} = \frac{v}{2\pi} \sum_n \int_j [(\partial_x \theta_j) M_\theta(n) (\partial_x \theta_{j+n}) + (\partial_x \varphi_j) M_\varphi(n) (\partial_x \varphi_{j+n})] \quad 5.194$$

in combination with the canonical commutation relation $[\varphi_j(x), \partial_{x'} \theta_{j'}(x')/\pi] = i \delta_{jj'} \delta(x - x')$. We can write down the action in real time t

$$\begin{aligned} \tilde{S}_{\text{SLL}}[\varphi, \theta] = & \sum_{j=1}^N \int_0^T dt \int_0^L dx \quad 5.195 \\ & \times \left\{ \begin{array}{l} (\partial_x \theta_j / \pi) (\partial_t \varphi_j) \\ - \frac{v}{2\pi} \sum_{n=0}^{N-1} \left[\begin{array}{l} (\partial_x \theta_j) M_\theta(n) (\partial_x \theta_{j+n}) \\ + (\partial_x \varphi_j) M_\varphi(n) (\partial_x \varphi_{j+n}) \end{array} \right] \end{array} \right\} \end{aligned}$$

with the canonical momentum $\Pi_j(x) = \partial_x \theta_j(x)/\pi$. Then, the Wick rotation $t \mapsto -i\tau$ yields the (Euclidean) action S_{SLL} in imaginary time τ ,

$$S_{\text{SLL}}[\varphi, \theta] = - \sum_{j=1}^N \int_0^\beta d\tau \int_0^L dx \left\{ \begin{array}{l} (\partial_x \theta_j / \pi)(i \partial_\tau \varphi_j) \\ - \frac{v}{2\pi} \sum_{n=0}^{N-1} \left[\begin{array}{l} (\partial_x \theta_j) M_\theta(n) (\partial_x \theta_{j+n}) \\ + (\partial_x \varphi_j) M_\varphi(n) (\partial_x \varphi_{j+n}) \end{array} \right] \end{array} \right\} \quad 5.196a$$

$$= \sum_{j=1}^N \int_0^{v\beta} \frac{dz}{v} \int_0^L \frac{dx}{\pi} \left\{ \begin{array}{l} \underbrace{-i v (\partial_x \theta_j) (\partial_z \varphi_j)}_{(A)} \\ + \frac{v}{2} \sum_{n=0}^{N-1} \left[\begin{array}{l} \underbrace{(\partial_x \theta_j) M_\theta(n) (\partial_x \theta_{j+n})}_{(B)} \\ + \underbrace{(\partial_x \varphi_j) M_\varphi(n) (\partial_x \varphi_{j+n})}_{(C)} \end{array} \right] \end{array} \right\} \quad 5.196b$$

with $\varphi = \{\varphi_j\}$, $\theta = \{\theta_j\}$ and $z = v\tau$.

Now we expand the fields in their Fourier coefficients $\chi(\mathbf{Q})$,

$$\chi_j(\mathbf{r}) = \sum_{\mathbf{Q}} \chi(\mathbf{Q}) e^{i(\mathbf{q}\mathbf{r} + q_y j a)}, \quad 5.197$$

to find

$$\partial_x \chi_j(\mathbf{r}) = \sum_{\mathbf{Q}} (i q_x) \chi(\mathbf{Q}) e^{i(\mathbf{q}\mathbf{r} + q_y j a)} \quad 5.198a$$

$$\partial_z \chi_j(\mathbf{r}) = \sum_{\mathbf{Q}} (i \omega / v) \chi(\mathbf{Q}) e^{i(\mathbf{q}\mathbf{r} + q_y j a)}. \quad 5.198b$$

Thus we get for the three terms in the action (5.196b):

(A) The canonical coupling yields

$$\begin{aligned} & -i \sum_{j=1}^N \int_0^{v\beta} dz \int_0^L dx v (\partial_x \theta_j) (\partial_z \varphi_j) \\ &= -i \sum_{\mathbf{Q}, \mathbf{Q}'} \sum_{j=1}^N \int_0^{v\beta} dz \int_0^L dx \begin{array}{l} (i q_x)(i \omega') \theta(\mathbf{Q}) \varphi(\mathbf{Q}') \\ \times e^{i[(\mathbf{q} + \mathbf{q}')\mathbf{r} + (q_y + q'_y) j a]} \end{array} \end{aligned} \quad 5.199a$$

$$= \frac{V}{a} \sum_{\mathbf{Q}} (-i q_x \omega) \theta(\mathbf{Q}) \varphi(-\mathbf{Q}). \quad 5.199b$$

(B) The second term reads

$$\frac{v}{2} \sum_{j=1}^N \sum_{n=0}^{N-1} \int_0^{v\beta} dz \int_0^L dx (\partial_x \theta_j) M_\theta(n) (\partial_x \theta_{j+n}) \quad 5.200a$$

$$= \frac{v}{2} \sum_{\mathbf{Q}, \mathbf{Q}'} \sum_{j=1}^N \int_0^{v\beta} dz \int_0^L dx \begin{aligned} & (iq_x)(iq'_x) \theta(\mathbf{Q})\theta(\mathbf{Q}') \\ & \times e^{i[(\mathbf{q}+\mathbf{q}')\mathbf{r}+(q_y+q'_y)ja]} \end{aligned} \quad 5.200b$$

$$\begin{aligned} & \times \sum_{n=0}^{N-1} M_\theta(n) e^{iq'_y na} \\ & = \frac{vV}{2a} \sum_{\mathbf{Q}} (q_x)^2 \theta(\mathbf{Q})\theta(-\mathbf{Q}) \tilde{M}_\theta(q_y), \end{aligned} \quad 5.200c$$

where we introduced the transverse Fourier transform of $M_\theta(n)$ as

$$\tilde{M}_\theta(q_y) \equiv \sum_{n=0}^{N-1} M_\theta(n) e^{-iq_y na}. \quad 5.201$$

(C) And finally,

$$\frac{v}{2} \sum_{j=1}^N \sum_{n=0}^{N-1} \int_0^{v\beta} dz \int_0^L dx (\partial_x \varphi_j) M_\varphi(n) (\partial_x \varphi_{j+n}) \quad 5.202a$$

$$= \frac{vV}{2a} \sum_{\mathbf{Q}} (q_x)^2 \varphi(\mathbf{Q})\varphi(-\mathbf{Q}) \tilde{M}_\varphi(q_y). \quad 5.202b$$

Note that the reality of $\chi_j(\mathbf{r})$ implies $\chi^*(\mathbf{Q}) = \chi(-\mathbf{Q})$. Similarly, since $M_\chi(n)$ is both real and symmetric, we have $\tilde{M}_\chi(-q_y) = \tilde{M}_\chi^*(q_y) = \tilde{M}_\chi(q_y)$.

Combining our results for the action in Fourier space yields

$$S_{\text{SLL}}[\varphi, \theta] = \frac{V}{\pi a v} \sum_{\mathbf{Q}} \left\{ \begin{aligned} & (-iq_x \omega) \theta(\mathbf{Q})\varphi^*(\mathbf{Q}) \\ & + (vq_x^2/2) \theta(\mathbf{Q})\theta^*(\mathbf{Q}) \tilde{M}_\theta(q_y) \\ & + (vq_x^2/2) \varphi(\mathbf{Q})\varphi^*(\mathbf{Q}) \tilde{M}_\varphi(q_y) \end{aligned} \right\}. \quad 5.203$$

We stress that there are components that drop from the action completely. Namely all \mathbf{Q} -components with $q_x = 0$ and/or $\tilde{M}_\varphi(q_y)\tilde{M}_\theta(q_y) = 0 = \omega$. While the latter condition depends on the chain couplings encoded in $\tilde{M}_\chi(q_y)$ and can be avoided by conditioning the couplings so that $\tilde{M}_\varphi(q_y)\tilde{M}_\theta(q_y) \neq 0$ for all $q_y \in [-\pi/a, \pi/a]$, the first one is generic and a consequence of the *sliding symmetry* that is eponymous for the SLL. Hence we implicitly assume in the following that $q_x \neq 0$ in all expressions (and that the fields θ and φ have no zero-momentum components along the wires in x -direction).

The action (5.203) can be written more compactly as

$$S_{\text{SLL}}[\varphi, \theta] = \frac{V}{\pi a v} \sum_{\mathbf{Q} > 0} [\theta^*(\mathbf{Q}) \quad \varphi^*(\mathbf{Q})] \begin{bmatrix} v q_x^2 \tilde{M}_\theta(q_y) & -i q_x \omega \\ -i q_x \omega & v q_x^2 \tilde{M}_\varphi(q_y) \end{bmatrix} \begin{bmatrix} \theta(\mathbf{Q}) \\ \varphi(\mathbf{Q}) \end{bmatrix} \quad 5.204$$

where $\mathbf{Q} > 0$ indicates a sum over the half 3D Brillouin zone; this is convenient because \mathbf{Q} and $-\mathbf{Q}$ are indices of the same complex field coefficient: $\chi(-\mathbf{Q}) = \chi^*(\mathbf{Q})$. We define the coupling matrix as

$$M \equiv \frac{V}{\pi a v} \bigoplus_{\mathbf{Q} > 0} \begin{bmatrix} v q_x^2 \tilde{M}_\theta(q_y) & -i q_x \omega \\ -i q_x \omega & v q_x^2 \tilde{M}_\varphi(q_y) \end{bmatrix} \quad 5.205$$

with inverse

$$M^{-1} = \frac{\pi a v}{V} \bigoplus_{\mathbf{Q} > 0} \begin{bmatrix} v q_x^2 \tilde{M}_\theta & -i q_x \omega \\ -i q_x \omega & v q_x^2 \tilde{M}_\varphi \end{bmatrix}^{-1} \quad 5.206a$$

$$= \frac{\pi a v}{V q_x^2} \frac{1}{v^2 q_x^2 \tilde{M}_\theta \tilde{M}_\varphi + \omega^2} \bigoplus_{\mathbf{Q} > 0} \begin{bmatrix} v q_x^2 \tilde{M}_\varphi & i q_x \omega \\ i q_x \omega & v q_x^2 \tilde{M}_\theta \end{bmatrix}. \quad 5.206b$$

To evaluate the two-point correlators

$$\langle \chi_1^*(\mathbf{Q}_1) \chi_2(\mathbf{Q}_2) \rangle = \frac{\int \mathcal{D}[\varphi, \theta] \chi_1^*(\mathbf{Q}_1) \chi_2(\mathbf{Q}_2) e^{-S_{\text{SLL}}[\varphi, \theta]}}{\int \mathcal{D}[\varphi, \theta] e^{-S_{\text{SLL}}[\varphi, \theta]}} \quad 5.207a$$

$$= \frac{\int \mathcal{D}[\Phi, \Phi^*] \chi_1^*(\mathbf{Q}_1) \chi_2(\mathbf{Q}_2) e^{-S_{\text{SLL}}[\Phi, \Phi^*]}}{\int \mathcal{D}[\Phi, \Phi^*] e^{-S_{\text{SLL}}[\Phi, \Phi^*]}}, \quad 5.207b$$

we use the Gaussian integral formula [255]

$$\langle \Phi_i^* \Phi_j \rangle_M \equiv \frac{\int \mathcal{D}[\Phi, \Phi^*] \Phi_i^* \Phi_j \exp\left(-\sum_{i,j} \Phi_i^* M_{ij} \Phi_j\right)}{\int \mathcal{D}[\Phi, \Phi^*] \exp\left(-\sum_{i,j} \Phi_i^* M_{ij} \Phi_j\right)} = M_{ij}^{-1} \quad 5.208$$

with the functional integral measure

$$\int \mathcal{D}[\Phi, \Phi^*] \equiv \prod_i \int \frac{d\Phi_i d\Phi_i^*}{2\pi i}. \quad 5.209$$

Note that in momentum space our complex degrees of freedom are $\Phi = \theta(\mathbf{Q})$ and $\Phi = \varphi(\mathbf{Q})$ for $\mathbf{Q} > 0$. Furthermore, it is $S_{\text{SLL}}[\Phi, \Phi^*] = S_{\text{SLL}}[\varphi, \theta]$ since (Φ, Φ^*) and (φ, θ) are just different encodings of the same functions.

We use Eq. (5.208) and Eq. (5.206b) to derive the correlators

$$\langle \theta^*(\mathbf{Q}_1) \theta(\mathbf{Q}_2) \rangle = \frac{\pi av}{V} \frac{\delta_{\mathbf{Q}_1, \mathbf{Q}_2}}{vq_x^2 \tilde{M}_\theta \tilde{M}_\varphi + \omega^2/v} \cdot \tilde{M}_\varphi \quad 5.210a$$

$$\langle \varphi^*(\mathbf{Q}_1) \varphi(\mathbf{Q}_2) \rangle = \frac{\pi av}{V} \frac{\delta_{\mathbf{Q}_1, \mathbf{Q}_2}}{vq_x^2 \tilde{M}_\theta \tilde{M}_\varphi + \omega^2/v} \cdot \tilde{M}_\theta \quad 5.210b$$

$$\langle \varphi^*(\mathbf{Q}_1) \theta(\mathbf{Q}_2) \rangle = \frac{\pi av}{V} \frac{\delta_{\mathbf{Q}_1, \mathbf{Q}_2}}{vq_x^2 \tilde{M}_\theta \tilde{M}_\varphi + \omega^2/v} \cdot \frac{i\omega/v}{q_x} \quad 5.210c$$

(remember that those are only valid for \mathbf{Q} with $q_x \neq 0$). With these results, we can now evaluate the correlators in Eq. (5.192):

$$\frac{1}{2} \left\langle \left(\chi_j^>(\mathbf{r}) \pm \chi_{j+n}^>(\mathbf{r}) \right)^2 \right\rangle \quad 5.211a$$

$$= \frac{1}{2} \sum_{\mathbf{Q}, \mathbf{Q}'}^{\Lambda' \dots \Lambda} \left\langle \chi(\mathbf{Q}) \left[e^{i(\mathbf{q}\mathbf{r} + q_y ja)} \pm e^{i(\mathbf{q}\mathbf{r} + q_y(j+n)a)} \right] \times \chi(\mathbf{Q}') \left[e^{i(\mathbf{q}'\mathbf{r} + q'_y ja)} \pm e^{i(\mathbf{q}'\mathbf{r} + q'_y(j+n)a)} \right] \right\rangle \quad 5.211b$$

$$= \frac{1}{2} \sum_{\mathbf{Q}, \mathbf{Q}'}^{\Lambda' \dots \Lambda} \langle \chi(\mathbf{Q}) \chi(\mathbf{Q}') \rangle \times e^{i[(\mathbf{q} + \mathbf{q}')\mathbf{r} + (q_y + q'_y)ja]} \times \left[1 \pm e^{iq'_y na} \pm e^{iq_y na} + e^{i(q_y + q'_y)na} \right]. \quad 5.211c$$

If we recall the shorthand notation $\bar{\theta} = \varphi$ and $\bar{\varphi} = \theta$ and use $\chi^*(\mathbf{Q}) = \chi(-\mathbf{Q})$, this expression can be evaluated with (5.210a) and (5.210b):

$$\frac{1}{2} \left\langle \left(\chi_j^>(\mathbf{r}) \pm \chi_{j+n}^>(\mathbf{r}) \right)^2 \right\rangle \quad 5.212a$$

$$= \frac{\pi av}{2V} \sum_{\mathbf{Q}, \mathbf{Q}'}^{\Lambda' \dots \Lambda} \frac{\tilde{M}_{\bar{\chi}} \delta_{-\mathbf{Q}_1, \mathbf{Q}_2}}{vq_x^2 \tilde{M}_\theta \tilde{M}_\varphi + \omega^2/v} \times e^{i[(\mathbf{q} + \mathbf{q}')\mathbf{r} + (q_y + q'_y)ja]} \times \left[1 \pm e^{iq'_y na} \pm e^{iq_y na} + e^{i(q_y + q'_y)na} \right] \quad 5.212b$$

$$= \frac{\pi av}{2V} \sum_{\mathbf{Q}}^{\Lambda' \dots \Lambda} \frac{\tilde{M}_{\bar{\chi}}}{vq_x^2 \tilde{M}_\theta \tilde{M}_\varphi + \omega^2/v} \left[1 \pm e^{-iq_y na} \pm e^{iq_y na} + 1 \right] \quad 5.212c$$

$$= \frac{\pi av}{V} \sum_{\mathbf{Q}}^{\Lambda' \dots \Lambda} \frac{\tilde{M}_{\bar{\chi}}}{vq_x^2 \tilde{M}_\theta \tilde{M}_\varphi + \omega^2/v} \left[1 \pm \cos(q_y na) \right]. \quad 5.212d$$

In the thermodynamic limit ($L, \beta, N \rightarrow \infty$) we can approximate this sum by a Riemann integral,

$$\frac{1}{2} \left\langle \left(\chi_j^>(\mathbf{r}) \pm \chi_{j+n}^>(\mathbf{r}) \right)^2 \right\rangle \quad 5.213$$

$$= \pi av \int_{\Lambda'}^{\Lambda} \frac{d^3 \mathbf{Q}}{(2\pi)^3} \frac{\tilde{M}_{\bar{\chi}}}{vq_x^2 \tilde{M}_\theta \tilde{M}_\varphi + \omega^2/v} \left[1 \pm \cos(q_y na) \right]$$

where we used $1/V \rightarrow d^3 Q/(2\pi)^3$. The integration has to be understood in the sense

$$\int_{\Lambda'}^{\Lambda} \frac{d^3 Q}{(2\pi)^3} \equiv \int_{\Lambda' < |\mathbf{q}| < \Lambda} \frac{d^2 q}{(2\pi)^2} \int_{-\pi/a}^{\pi/a} \frac{dq_y}{2\pi} \quad 5.214$$

where the UV-cutoff $\Lambda < \infty$ regularizes the logarithmic divergence of the Green's function. Define now

$$v(q_y) \equiv \sqrt{\tilde{M}_\varphi \cdot \tilde{M}_\theta} \quad \text{and} \quad \kappa(q_y) \equiv \sqrt{\tilde{M}_\theta / \tilde{M}_\varphi}. \quad 5.215$$

Then

$$\begin{aligned} & \frac{1}{2} \left\{ \left\langle \left(\theta_j^>(\mathbf{r}) \pm \theta_{j+n}^>(\mathbf{r}) \right)^2 \right\rangle \right\} \\ & \frac{1}{2} \left\{ \left\langle \left(\varphi_j^>(\mathbf{r}) \pm \varphi_{j+n}^>(\mathbf{r}) \right)^2 \right\rangle \right\} \\ &= \int_{\Lambda'}^{\Lambda} \frac{d^3 Q}{(2\pi)^3} \frac{\pi a v}{v q_x^2 v^2(q_y) + \omega^2/v} \left\{ \frac{v(q_y)/\kappa(q_y)}{v(q_y) \cdot \kappa(q_y)} \right\} [1 \pm \cos(q_y n a)]. \end{aligned} \quad 5.216$$

The \mathbf{q} -integral over the Λ' - Λ -ring reads

$$\int_{\Lambda'}^{\Lambda} \frac{d^2 q}{(2\pi)^2} \frac{\pi a v}{v q_x^2 v^2(q_y) + \omega^2/v} = \int_0^{2\pi} \frac{d\phi}{2\pi} \int_{\Lambda'}^{\Lambda} \frac{d\lambda}{2\pi} \lambda \frac{\pi a v}{v q_x^2 v^2(q_y) + \omega^2/v} \quad 5.217$$

with the momentum coordinates $\mathbf{q} = (q_x, \omega/v) = (\lambda \cos \phi, \lambda \sin \phi)$. We evaluate

$$\int_0^{2\pi} \frac{d\phi}{2\pi} \int_{\Lambda'}^{\Lambda} \frac{d\lambda}{2\pi} \frac{1}{\lambda} \frac{\pi a v}{v v^2(q_y) \cos^2 \phi + v \sin^2 \phi} = \frac{a dl}{2v(q_y)}, \quad 5.218$$

where defined the scale variation $dl \equiv \ln \frac{\Lambda}{\Lambda'}$ and used

$$\int_0^{2\pi} \frac{d\phi}{2\pi} \frac{1}{v^2(q_y) \cos^2 \phi + \sin^2 \phi} = \frac{1}{v(q_y)}. \quad 5.219$$

If we insert this in Eq. (5.216), the expression simplifies to

$$\begin{aligned} & \frac{1}{2} \left\{ \left\langle \left(\theta_j^>(\mathbf{r}) \pm \theta_{j+n}^>(\mathbf{r}) \right)^2 \right\rangle \right\} \\ & \frac{1}{2} \left\{ \left\langle \left(\varphi_j^>(\mathbf{r}) \pm \varphi_{j+n}^>(\mathbf{r}) \right)^2 \right\rangle \right\} \\ &= \frac{a dl}{2} \int_{-\pi/a}^{\pi/a} \frac{dq_y}{2\pi} \left\{ \frac{1/\kappa(q_y)}{\kappa(q_y)} \right\} [1 \pm \cos(q_y n a)] \end{aligned} \quad 5.220a$$

$$= \frac{dl}{2} \int_{-\pi}^{\pi} \frac{dq}{2\pi} \left\{ \frac{1/\kappa(q)}{\kappa(q)} \right\} [1 \pm \cos(qn)] \quad 5.220b$$

where we substituted $q = a q_y$ and implicitly redefined $\kappa(q)$ with $a = 1$.

This result tells us that $\langle e^{i\mathcal{X}(\chi^>)} \rangle_>$ in (5.189b) does not depend on the spatio-temporal coordinate \mathbf{r} and we can write for the effective action

$$S_{\text{eff}}[\chi^<] = S_{\text{SLL}}[\chi^<] + \varepsilon \langle e^{i\mathcal{X}(\chi^>)} \rangle_> \int d\tau \int dx e^{i\mathcal{X}(\chi^<)} \quad 5.221a$$

$$= S_{\text{SLL}}[\chi^<] + \varepsilon \langle e^{i\mathcal{X}(\chi^>)} \rangle_> S_{\mathcal{O}}[\chi^<] \quad 5.221b$$

[combine (5.188b) and (5.189b)]. If we use the expansion (5.190) and write $1/2 \langle \mathcal{X}^2(\chi^>) \rangle_> \equiv d\ell \Delta_{\mathcal{X}}$, this reads

$$S_{\text{eff}}[\chi^<] = S_{\text{SLL}}[\chi^<] + \varepsilon \left(1 - \frac{1}{2} \langle \mathcal{X}^2(\chi^>) \rangle_> \right) S_{\mathcal{O}}[\chi^<] \quad 5.222a$$

$$= S_{\text{SLL}}[\chi^<] + \varepsilon (1 - d\ell \Delta_{\mathcal{X}}) S_{\mathcal{O}}[\chi^<]. \quad 5.222b$$

We can compare this to the original perturbed action (5.181),

$$S[\chi] = S_{\text{SLL}}[\chi] + \varepsilon S_{\mathcal{O}}[\chi], \quad 5.223$$

only if we rescale the momentum cutoff Λ' in $S_{\text{eff}}[\chi^<]$ back to the original cutoff Λ in $S[\chi]$:

$$\mathbf{q}' \equiv \frac{\Lambda}{\Lambda'} \mathbf{q} \quad \Leftrightarrow \quad \mathbf{r}' \equiv \frac{\Lambda'}{\Lambda} \mathbf{r}. \quad 5.224$$

With this coordinate transformation, the integrals and derivatives in the action transform as

$$d\tau dx = \left(\frac{\Lambda}{\Lambda'} \right)^2 d\tau' dx' \quad \text{and} \quad \partial_{\tau} = \frac{\Lambda'}{\Lambda} \partial_{\tau'}, \quad \partial_x = \frac{\Lambda'}{\Lambda} \partial_{x'}. \quad 5.225$$

If we define the new fields

$$\chi'(\mathbf{r}') \equiv \chi^< \left(\frac{\Lambda}{\Lambda'} \mathbf{r}' \right) = \chi^<(\mathbf{r}), \quad 5.226$$

the Gaussian SLL action remains invariant, $S_{\text{SLL}}[\chi^<] = S_{\text{SLL}}[\chi']$, since

$$\int d\tau \int dx (\partial_x \chi_1^<(\mathbf{r})) (\partial_x \chi_2^<(\mathbf{r})) = \int d\tau' \int dx' (\partial_{x'} \chi_1'(\mathbf{r}')) (\partial_{x'} \chi_2'(\mathbf{r}')), \quad 5.227$$

as it is right and proper for an RG fixed point action (or a conformal field theory). Note that

$$\chi'(\mathbf{r}') = \chi^< \left(\frac{\Lambda}{\Lambda'} \mathbf{r}' \right) \propto \int_0^{\Lambda'} d^2 q \chi(\mathbf{q}) e^{i(\Lambda/\Lambda') \mathbf{q} \cdot \mathbf{r}'} \quad 5.228a$$

$$= \int_0^{\Lambda} d^2 q' \chi'(\mathbf{q}') e^{i \mathbf{q}' \cdot \mathbf{r}'} \quad 5.228b$$

with rescaled momentum components

$$\chi'(\mathbf{q}') \equiv \left(\frac{\Lambda'}{\Lambda}\right)^2 \chi\left(\frac{\Lambda'}{\Lambda} \mathbf{q}'\right). \quad 5.229$$

Therefore, in the new coordinates \mathbf{r}' and \mathbf{q}' , the field χ' includes again momentum components up to the initial UV-cutoff Λ .

In contrast to the Gaussian action, the perturbation is *not* scale-invariant and transforms as

$$S_{\mathcal{O}}[\chi^<] = \left(\frac{\Lambda}{\Lambda'}\right)^2 S_{\mathcal{O}}[\chi'], \quad 5.230$$

which follows immediately from (5.182) with (5.225) and $\mathcal{O}(\varphi, \theta) = e^{i\mathcal{X}(\varphi, \theta)}$.

In summary, the effective action reads

$$S_{\text{eff}}[\chi'] = S_{\text{SLL}}[\chi'] + \varepsilon (1 - d\mathbf{l} \Delta_{\mathcal{X}}) \left(\frac{\Lambda}{\Lambda'}\right)^2 S_{\mathcal{O}}[\chi']. \quad 5.231$$

To be consistent, we have to expand

$$\frac{\Lambda}{\Lambda'} = e^{\ln \Lambda / \Lambda'} = e^{d\mathbf{l}} = 1 + d\mathbf{l} + \mathcal{O}(d\mathbf{l}^2) \quad 5.232$$

and linearize the effective action in $d\mathbf{l}$:

$$S_{\text{eff}}[\chi'] = S_{\text{SLL}}[\chi'] + \varepsilon [1 + (D - \Delta_{\mathcal{X}})d\mathbf{l}] S_{\mathcal{O}}[\chi'] \quad 5.233a$$

$$\equiv S_{\text{SLL}}[\chi'] + \varepsilon' S_{\mathcal{O}}[\chi']. \quad 5.233b$$

Here we introduced the spacetime dimension $D = 1 + 1 = 2$ to highlight its role as critical value for the *scaling dimension* $\Delta_{\mathcal{X}}$.

We conclude that integrating out an infinitesimal momentum shell $\Lambda - \Lambda'$ leaves the perturbed action S invariant up to a rescaling of the perturbative coupling ε :

$$\varepsilon' = \varepsilon [1 + (2 - \Delta_{\mathcal{X}})d\mathbf{l}] \Leftrightarrow \frac{d\varepsilon}{d\mathbf{l}} = \frac{\varepsilon' - \varepsilon}{d\mathbf{l}} = (2 - \Delta_{\mathcal{X}})\varepsilon \quad 5.234a$$

$$\Rightarrow \varepsilon(l) = \varepsilon(0) e^{(2 - \Delta_{\mathcal{X}})l}. \quad 5.234b$$

The perturbation $\mathcal{O}(\varphi, \theta) = e^{i\mathcal{X}(\varphi, \theta)}$ is *relevant* (flows to strong coupling) if $\Delta_{\mathcal{X}} < 2$; it is *marginal* for $\Delta_{\mathcal{X}} = 2$ and *irrelevant* for $\Delta_{\mathcal{X}} > 2$. Note that a marginal or irrelevant perturbation may still renormalize other couplings if the renormalization flow is evaluated in higher order, i.e., if the expansion (5.188b) is not truncated after the linear term. With this, we are now ready to evaluate the scaling dimensions of the two operators in Eq. (5.176):

→ For the CDW couplings $\mathcal{O}_{\text{CDW}}^{(n)}$, we can directly apply Eq. (5.220b) with $\mathcal{X} = 2(\theta_j - \theta_{j+n})$ and $\Delta_{\mathcal{X}} = \frac{1}{2} \langle \mathcal{X}^2(\chi^>) \rangle_{>}/dl$:

$$\Delta_{\text{CDW}}^{(n)} = 4 \cdot \frac{1}{2} \int_{-\pi}^{\pi} \frac{dq}{2\pi} \frac{1}{\kappa(q)} [1 - \cos(qn)] = 2K\xi_n^- \quad 5.235$$

with the definitions

$$\xi_n^{\pm} \equiv \int_{-\pi}^{\pi} \frac{dq}{2\pi} \frac{1}{\eta(q)} [1 \pm \cos(qn)] \quad \text{and} \quad \eta(q) \equiv K\kappa(q). \quad 5.236$$

This matches previous results derived in Refs. [388, 389]. Note that [Eq. (5.166b)]

$$\eta(q) = \sqrt{1 + \lambda_1 \cos(q) + \lambda_2 \cos(2q)}, \quad 5.237$$

so that ξ_n^{\pm} depends parametrically on (λ_1, λ_2) .

→ For the Laughlin term \mathcal{O}_{L_2} we have $\mathcal{X}_{L_2} = \varphi_j - \varphi_{j+1} - 2(\theta_j + \theta_{j+1})$. The scaling dimension is

$$\Delta_{L_2} dl = \frac{1}{2} \langle [\varphi_j - \varphi_{j+1} - 2(\theta_j + \theta_{j+1})]^2 \rangle \quad 5.238a$$

$$= \frac{1}{2} \langle [\varphi_j - \varphi_{j+1}]^2 \rangle + 2 \langle [\theta_j + \theta_{j+1}]^2 \rangle - 2 \langle [(\varphi_j - \varphi_{j+1})(\theta_j + \theta_{j+1})] \rangle \quad 5.238b$$

where we omit the labels “>” to lighten the notation. The first two terms follow directly from Eq. (5.220b):

$$\langle [\varphi_j - \varphi_{j+1}]^2 \rangle = dl \int_{-\pi}^{\pi} \frac{dq}{2\pi} \kappa(q) [1 - \cos(q)] = \frac{dl}{K} \chi_1^- \quad 5.239a$$

$$\langle [\theta_j + \theta_{j+1}]^2 \rangle = dl \int_{-\pi}^{\pi} \frac{dq}{2\pi} \frac{1}{\kappa(q)} [1 + \cos(q)] = dl K \xi_1^+ \quad 5.239b$$

where we defined

$$\chi_n^{\pm} \equiv \int_{-\pi}^{\pi} \frac{dq}{2\pi} \eta(q) [1 \pm \cos(qn)]. \quad 5.240$$

As we will argue below, the last term in (5.238b) can be ignored and one ends up with the scaling dimension

$$\Delta_{L_2} = \frac{1}{2K} \chi_1^- + 2K \xi_1^+. \quad 5.241$$

The expressions for the scaling dimensions $\Delta_{\text{CDW}}^{(n)}$ in (5.235) and Δ_{L_2} in (5.241) are the main results of the RG analysis; they determine the relevance/irrelevance of the perturbations (5.176) via the RG flow (5.234b) (see below).

Cross correlator — We conclude this subsection with a rather technical discussion of the cross correlator

$$\langle (\varphi_j - \varphi_{j+1})(\theta_j + \theta_{j+1}) \rangle = \langle \varphi_j \theta_j \rangle - \langle \varphi_{j+1} \theta_j \rangle + \langle \varphi_j \theta_{j+1} \rangle - \langle \varphi_{j+1} \theta_{j+1} \rangle \quad 5.242$$

that we neglected above. Thus we are interested in correlators of the form

$$\langle \varphi_j(\mathbf{r}) \theta_{j+n}(\mathbf{r}) \rangle = \sum_{\mathbf{Q}, \mathbf{Q}'}^{\Lambda' \dots \Lambda} \langle \varphi(\mathbf{Q}) \theta(\mathbf{Q}') \rangle e^{i[(\mathbf{q} + \mathbf{q}')\mathbf{r} + (q_y + q'_y)ja]} e^{iq'_y na}, \quad 5.243$$

where we recall Eq. (5.210c):

$$\langle \varphi^*(\mathbf{Q}_1) \theta(\mathbf{Q}_2) \rangle = \frac{\pi a v}{V} \frac{\delta_{\mathbf{Q}_1, \mathbf{Q}_2}}{v q_x^2 \tilde{M}_\theta \tilde{M}_\varphi + \omega^2/v} \cdot \frac{i\omega/v}{q_x} \quad 5.244$$

for $q_x \neq 0$. Then a straightforward calculation yields

$$\langle \varphi_j(\mathbf{r}) \theta_{j+n}(\mathbf{r}) \rangle \propto \sum_{\mathbf{Q}, \mathbf{Q}'}^{\Lambda' \dots \Lambda} \frac{\delta_{-\mathbf{Q}, \mathbf{Q}'}}{v q_x^2 \tilde{M}_\theta \tilde{M}_\varphi + \omega^2/v} \frac{i\omega/v}{q_x} \times e^{i[(\mathbf{q} + \mathbf{q}')\mathbf{r} + (q_y + q'_y)ja]} e^{iq'_y na} \quad 5.245a$$

$$= \sum_{\mathbf{Q}}^{\Lambda' \dots \Lambda} \frac{1}{v q_x^2 \tilde{M}_\theta \tilde{M}_\varphi + \omega^2/v} \frac{i\omega/v}{q_x} e^{-iq_y na} \quad 5.245b$$

$$= \sum_{\mathbf{Q}, q_x > 0}^{\Lambda' \dots \Lambda} \frac{1}{v q_x^2 \tilde{M}_\theta \tilde{M}_\varphi + \omega^2/v} \frac{i\omega/v}{q_x} e^{-iq_y na} \quad 5.245c$$

$$+ \sum_{\mathbf{Q}, q_x < 0}^{\Lambda' \dots \Lambda} \frac{1}{v q_x^2 \tilde{M}_\theta \tilde{M}_\varphi + \omega^2/v} \frac{i\omega/v}{q_x} e^{-iq_y na}$$

$$= \sum_{\mathbf{Q}, q_x > 0}^{\Lambda' \dots \Lambda} \frac{1}{v q_x^2 \tilde{M}_\theta \tilde{M}_\varphi + \omega^2/v} \frac{i\omega/v}{q_x} e^{-iq_y na} \quad 5.245d$$

$$- \sum_{\mathbf{Q}, q_x > 0}^{\Lambda' \dots \Lambda} \frac{1}{v q_x^2 \tilde{M}_\theta \tilde{M}_\varphi + \omega^2/v} \frac{i\omega/v}{q_x} e^{-iq_y na}$$

$$= 0 \quad 5.245e$$

so that the cross correlators can be safely ignored.

Conditions on Parameters

Here we discuss the conditions on the Luttinger parameter K to drive the system into the fractional quantum Hall regime in dependence of the nearest- and next-nearest-neighbor couplings λ_1 and λ_2 . In addition, we derive the domain where the SLL is stable against transversal CDW order.

Strict Condition

The system is driven safely into the gapped Laughlin state whenever the Laughlin term \mathcal{O}_{L_2} is the only relevant perturbation. Here we translate the conditions for a relevant Laughlin term and irrelevant CDW terms,

$$\forall_n : \Delta_{\text{CDW}}^{(n)} > 2 \quad \text{and} \quad \Delta_{L_2} < 2, \quad 5.246$$

into intervals for the Luttinger parameter K . Note that there may be other competing perturbations; a systematic treatment of such within RG is an interesting topic for future studies.

With $\Delta_{\text{CDW}}^{(n)} = 2K\xi_n^-$ it follows immediately that

$$K \in \overline{\mathcal{K}}_{\text{CDW}}^{(N)} \equiv \bigcap_{n \leq N} (1/\xi_n^-, \infty] \quad 5.247$$

if we require CDW perturbations $\mathcal{O}_{\text{CDW}}^{(n)}$ to be irrelevant up to N th-nearest-neighbors. Then we use $\Delta_{L_2} = \frac{1}{2K}\chi_1^- + 2K\xi_1^+$ to determine the bounds K^\pm above and below which the Laughlin term becomes irrelevant:

$$\frac{1}{2K}\chi_1^- + 2K\xi_1^+ = 2 \Leftrightarrow 4\xi_1^+K^2 - 4K + \chi_1^- = 0 \quad 5.248a$$

$$\Rightarrow K^\pm = \frac{1}{2\xi_1^+} \left[1 \pm \sqrt{1 - \xi_1^+ \chi_1^-} \right]. \quad 5.248b$$

With the reality condition $K \in \mathbb{R}^+$, this yields the interval

$$\begin{aligned} K \in \mathcal{K}_{L_2} &\equiv (K^-, K^+) & 5.249 \\ &= \left(\frac{1}{2\xi_1^+} \left[1 - \text{Re} \sqrt{1 - \xi_1^+ \chi_1^-} \right], \frac{1}{2\xi_1^+} \left[1 + \text{Re} \sqrt{1 - \xi_1^+ \chi_1^-} \right] \right) \end{aligned}$$

where \mathcal{O}_{L_2} becomes relevant.

Relaxed Condition

Depending on the relative strength of microscopic couplings and the RG flow beyond linear order, it might be sufficient for the Laughlin term to be the *most relevant* perturbation to “defeat” *relevant* competing terms.

Restricted to CDW order as the only competitor, this condition reads

$$\Delta_{L_2} < \min_{n \geq 1} \{2, \Delta_{\text{CDW}}^{(n)}\}. \quad 5.250$$

The required relevance of \mathcal{O}_{L_2} leads to the same interval (5.249) as for the strict condition: $K \in \mathcal{K}_{L_2}$. For the Laughlin term to be *more* relevant than $\mathcal{O}_{\text{CDW}}^{(n)}$ up to distance N , we require

$$\frac{1}{2K} \chi_1^- + 2K \xi_1^+ < 2K \xi_n^- \quad \Leftrightarrow \quad \frac{1}{K^2} < 4 \frac{\xi_n^- - \xi_1^+}{\chi_1^-}. \quad 5.251$$

In the case $\xi_n^- - \xi_1^+ \leq 0$ there are no solutions for $K \in \mathbb{R}^+$ since $\chi_1^- > 0$. In the case $\xi_n^- - \xi_1^+ > 0$ we have

$$K > \frac{1}{2} \sqrt{\frac{\chi_1^-}{\xi_n^- - \xi_1^+}}. \quad 5.252$$

If we define $(\infty, \infty] = \emptyset$ and $1/0 = \infty$, we can combine both cases and define the interval

$$K \in \mathcal{K}_{L_2\text{-CDW}}^{(N)} \equiv \bigcap_{n \leq N} \left(\frac{\sqrt{\chi_1^-}}{2 \operatorname{Re} \sqrt{\xi_n^- - \xi_1^+}}, \infty \right], \quad 5.253$$

where the intersection of sets corresponds to the logical conjunction of conditions up to distance N . Note that if there exists an $n^* \leq N$ with $\xi_{n^*}^- \leq \xi_1^+$, it is $\mathcal{K}_{L_2\text{-CDW}}^{(N)} = \emptyset$.

Transversal CDW Stability

Here we derive the admissible parameter regime of λ_1 and λ_2 where the SLL is stable against transversal CDW order [388]. We are looking for the domain $\Gamma \subset \mathbb{R}^2$ of pairs (λ_1, λ_2) where

$$\eta(q) = \sqrt{1 + \lambda_1 \cos(q) + \lambda_2 \cos(2q)} \neq 0 \quad \forall q \in [-\pi, \pi]. \quad 5.254$$

It is easier to characterize the complement $\Gamma^c \subset \mathbb{R}^2$ where

$$\exists q^* \in [-\pi, \pi] : \quad 1 + \lambda_1 \cos(q^*) + \lambda_2 \cos(2q^*) = 0. \quad 5.255$$

Note that $\eta(q^*) = 0 \Leftrightarrow \tilde{M}_\theta(q^*) = 0$. The Hamiltonian \mathcal{H}_{SLL} (5.194), with a partial Fourier transform of the fields in y -direction, reveals that this corresponds to a transversal mode q^* of the SLL with diverging compressibility (indicating an instability towards transversal CDW order). The condition (5.255) therefore characterizes the parameter domain that is unstable against this competing order.

Using $\cos(2q) = 2 \cos^2(q) - 1$ and the substitution $u = \cos(q)$, we find

$$1 + \lambda_1 u + \lambda_2 (2u^2 - 1) = 0 \quad 5.256a$$

$$\Leftrightarrow \quad 2\lambda_2 u^2 + \lambda_1 u + (1 - \lambda_2) = 0 \quad 5.256b$$

with solutions for $\lambda_2 \neq 0$

$$u^\pm = \frac{1}{4\lambda_2} \left(-\lambda_1 \pm \sqrt{\lambda_1^2 - 8\lambda_2(1 - \lambda_2)} \right) \quad 5.257$$

and $u^0 = -1/\lambda_1$ for $\lambda_2 = 0$ and $\lambda_1 \neq 0$ (for $\lambda_1 = 0 = \lambda_2$ there is clearly no solution and the SLL is stable). Solutions for $q \in \mathbb{R}$ require $u^\pm, u^0 \in \mathbb{R}$ and $|u^\pm|, |u^0| \leq 1$. For $\lambda_2 = 0$, both conditions are satisfied for $|\lambda_1| \geq 1$ and the SLL is stable on the segment $\lambda_1 \in (-1, 1)$ with $\lambda_2 = 0$. For $\lambda_2 \neq 0$, the reality condition demands $\lambda_1^2 - 8\lambda_2(1 - \lambda_2) \geq 0$. This parameter domain is parametrized by its boundary

$$|\lambda_1| = 2\sqrt{2\lambda_2(1 - \lambda_2)} \quad \text{for } 0 < \lambda_2 \leq 1. \quad 5.258$$

Within this region, there is no real solution q^* for which $\eta(q^*) = 0$ and the SLL is stable against formation of transversal CDW order.

In the complement of this region there are real solutions for u that correspond to solutions for q iff $|u^\pm| \leq 1$ for $+$ and/or $-$. Note that we can set $\lambda_1 \geq 0$ w.l.o.g. since $|u^\pm(\lambda_1, \lambda_2)| = |u^\mp(-\lambda_1, \lambda_2)|$: If $\lambda_1 < 0$ allows for a solution $|u^+(\lambda_1, \lambda_2)| \leq 1$, $-\lambda_1 > 0$ allows for a solution $|u^-(-\lambda_1, \lambda_2)| \leq 1$ (and vice versa). The SLL is stable if $|u^+| > 1$ and $|u^-| > 1$, which translates into

$$\left| -\lambda_1 \pm \sqrt{\lambda_1^2 - 8\lambda_2(1 - \lambda_2)} \right| > 4|\lambda_2|. \quad 5.259$$

We have to consider several cases separately:

- 1 Let $\lambda_2 > 1$. We have $|\lambda_2| = \lambda_2$ and $\sqrt{\lambda_1^2 - 8\lambda_2(1 - \lambda_2)} > \lambda_1$; therefore

$$\begin{aligned} & -\lambda_1 + \sqrt{\lambda_1^2 - 8\lambda_2(1 - \lambda_2)} > 4\lambda_2 \\ \Leftrightarrow & \sqrt{\lambda_1^2 - 8\lambda_2(1 - \lambda_2)} > 4\lambda_2 + \lambda_1 \end{aligned} \quad 5.260a$$

$$\begin{aligned} \text{and} \quad & +\lambda_1 + \sqrt{\lambda_1^2 - 8\lambda_2(1 - \lambda_2)} > 4\lambda_2 \\ \Leftrightarrow & \sqrt{\lambda_1^2 - 8\lambda_2(1 - \lambda_2)} > 4\lambda_2 - \lambda_1. \end{aligned} \quad 5.260b$$

Since both terms in the first case are positive, we can square them:

$$\lambda_1^2 + 8\lambda_2^2 - 8\lambda_2 > 16\lambda_2^2 + 8\lambda_1\lambda_2 + \lambda_1^2 \quad 5.261a$$

$$\Leftrightarrow 0 > \lambda_2^2 + \lambda_1\lambda_2 + \lambda_2. \quad 5.261b$$

Under the given assumptions ($\lambda_1 \geq 0$ and $\lambda_2 > 1$), this inequality has no solution. Thus there is always a real solution q^* for $\lambda_2 > 1$ and we find no stable SLL above $\lambda_2 = 1$.

MISCELLANEOUS

2 Let $0 < \lambda_2 \leq 1$. We have $|\lambda_2| = \lambda_2$ and $\sqrt{\lambda_1^2 - 8\lambda_2(1 - \lambda_2)} \leq \lambda_1$; therefore

$$\begin{aligned} & +\lambda_1 - \sqrt{\lambda_1^2 - 8\lambda_2(1 - \lambda_2)} > 4\lambda_2 \\ \Leftrightarrow & \sqrt{\lambda_1^2 - 8\lambda_2(1 - \lambda_2)} < -4\lambda_2 + \lambda_1 \end{aligned} \quad 5.262a$$

and

$$\begin{aligned} & +\lambda_1 + \sqrt{\lambda_1^2 - 8\lambda_2(1 - \lambda_2)} > 4\lambda_2 \\ \Leftrightarrow & \sqrt{\lambda_1^2 - 8\lambda_2(1 - \lambda_2)} > 4\lambda_2 - \lambda_1. \end{aligned} \quad 5.262b$$

Assume $\lambda_1 > 4\lambda_2$. Then the second inequality is trivially satisfied and the first one reads after squaring ($\lambda_2 \neq 0$)

$$\lambda_1^2 + 8\lambda_2^2 - 8\lambda_2 < 16\lambda_2^2 - 8\lambda_1\lambda_2 + \lambda_1^2 \quad 5.263a$$

$$\Leftrightarrow 0 < \lambda_2^2 - \lambda_1\lambda_2 + \lambda_2 \quad 5.263b$$

$$\Leftrightarrow \lambda_1 < \lambda_2 + 1. \quad 5.263c$$

We find therefore stable SLL parameters for $4\lambda_2 < \lambda_1 < \lambda_2 + 1$ in the range $0 < \lambda_2 < 1/3 \leq 1$ (here we used that for $4\lambda_2 = \lambda_2 + 1 \Leftrightarrow \lambda_2 = 1/3$ the lower and upper bound are equal).

Now assume $\lambda_1 \leq 4\lambda_2$. Then the first inequality is trivially violated since $-4\lambda_2 + \lambda_1 \leq 0$. Hence we find no additional stable parameters for $0 < \lambda_2 \leq 1$.

3 Let $\lambda_2 < 0$. We have $|\lambda_2| = -\lambda_2$ and $\sqrt{\lambda_1^2 - 8\lambda_2(1 - \lambda_2)} > \lambda_1$; therefore

$$\begin{aligned} & -\lambda_1 + \sqrt{\lambda_1^2 - 8\lambda_2(1 - \lambda_2)} > -4\lambda_2 \\ \Leftrightarrow & \sqrt{\lambda_1^2 - 8\lambda_2(1 - \lambda_2)} > -4\lambda_2 + \lambda_1 \end{aligned} \quad 5.264a$$

and

$$\begin{aligned} & +\lambda_1 + \sqrt{\lambda_1^2 - 8\lambda_2(1 - \lambda_2)} > -4\lambda_2 \\ \Leftrightarrow & \sqrt{\lambda_1^2 - 8\lambda_2(1 - \lambda_2)} > -4\lambda_2 - \lambda_1. \end{aligned} \quad 5.264b$$

Squaring the first inequality yields ($\lambda_2 \neq 0$)

$$\lambda_1^2 + 8\lambda_2^2 - 8\lambda_2 > 16\lambda_2^2 - 8\lambda_1\lambda_2 + \lambda_1^2 \quad 5.265a$$

$$\Leftrightarrow 0 > \lambda_2^2 - \lambda_1\lambda_2 + \lambda_2 \quad 5.265b$$

$$\Leftrightarrow \lambda_1 < \lambda_2 + 1 \quad 5.265c$$

with solutions for $-1 < \lambda_2 < 0$ since $\lambda_1 \geq 0$. Since $-4\lambda_2 + \lambda_1 \geq -4\lambda_2 - \lambda_1$ for $\lambda_1 \geq 0$, there is no additional constraint from the second inequality. Therefore the SLL is stable in the range $-1 < \lambda_2 < 0$ for $0 \leq \lambda_1 < \lambda_2 + 1$.

COUPLED LUTTINGER LIQUIDS

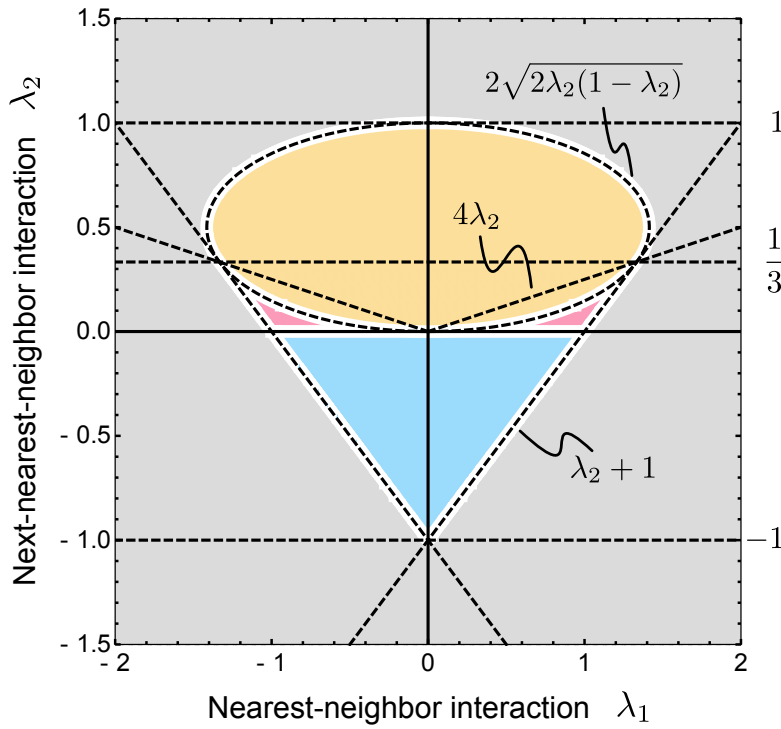


FIGURE 5.8 • Parameter domain for SLL. The union of all colored regions makes up the parameters Γ for which the SLL is stable against the formation of transversal CDW order. In the yellow region there are no real-valued solutions: $u^\pm \notin \mathbb{R}$. In the blue and red regions the solutions are real but $|u^\pm| > 1$ for both $+$ and $-$, precluding solutions for $\eta(q^*) = 0$. The role of the dashed curves/lines is discussed in the text.

If we combine our findings, the domain of stable SLL parameters due to the constraint $|u^\pm|, |u^0| > 1$ is given by

$$0 < \lambda_2 < 1/3 \quad \text{and} \quad 4\lambda_2 < \lambda_1 < \lambda_2 + 1 \quad 5.266a$$

$$\lambda_2 = 0 \quad \text{and} \quad 0 \leq \lambda_1 < 1 \quad 5.266b$$

$$-1 < \lambda_2 < 0 \quad \text{and} \quad 0 \leq \lambda_1 < \lambda_2 + 1. \quad 5.266c$$

This set must be joined with the solutions obtained from the reality condition above:

$$0 < \lambda_2 < 1 \quad \text{and} \quad 0 \leq \lambda_1 < 2\sqrt{2\lambda_2(1-\lambda_2)}. \quad 5.267$$

The combination of (5.266) and (5.267) with the symmetry $\lambda_1 \leftrightarrow -\lambda_1$ yields the complete set of allowed parameters for which $u^\pm \notin \mathbb{R}$ and/or $|u^\pm|, |u^0| > 1$, i.e., for which the SLL is stable against transversal CDW order:

$$\Gamma = \left\{ (\lambda_1, \lambda_2) \in \mathbb{R}^2 \mid |\lambda_1| < 2\sqrt{2\lambda_2(1-\lambda_2)} \wedge 1/3 \leq \lambda_2 < 1 \right\} \cup \left\{ (\lambda_1, \lambda_2) \in \mathbb{R}^2 \mid |\lambda_1| < \lambda_2 + 1 \wedge -1 < \lambda_2 < 1/3 \right\}. \quad 5.268$$

MISCELLANEOUS

This set is illustrated in Figure 5.8 together with all relevant subsets and boundaries. Note that for $\lambda_2 = 1/3$ it is $4\lambda_2 = \lambda_2 + 1 = 2\sqrt{2\lambda_2(1 - \lambda_2)} = 4/3$ and all three boundaries intersect. This domain can also be found graphically in Ref. [388] and in the Figures 5.6 and 5.7 (a) above.

5.3 On Apples and Oranges

This section is a “spin-off” from Ref. [2] on “*Topological networks for quantum communication between distant qubits*” (which is discussed in Chapter 3). What follows is the unpolished¹⁵⁹ product of two to three days pondering the question what it means if a setup is claimed to be better suited for a given task than its competitors. In Ref. [2] we proposed a system with topological band structure for the task of quantum state transfer, and compared its performance with a topologically trivial competitor. In this context, it is a delicate question whether (and if so, in which sense) the comparison is *fair*. On the following pages, I outline the proposal for a framework that formalizes the concept of *fair (and meaningful) comparisons*.

This framework may be of use for future projects that make contact with the rising field of machine learning. For instance, it could be combined with generative models of artificial intelligence (like evolutionary algorithms, or the approach taken in [393]) to challenge the topological setup of Ref. [2] in a well-defined arena of admissible solutions. In any case, developing the framework cleared my mind and satisfied my craving for conceptual rigidity.

Finally, let me point out that the framework draws inspiration from David Deutsch’s *constructor theory* [394]—although the relation of both frameworks is only superficial: Both seek to formalize concepts that commonly elude formalization.

5.3.1 Motivation

Are apples better than oranges? From a personal point of view, there might be an answer to this provocative question, though it seems hopeless if one demands *objectivity* (which usually is a good idea in science). So is there any way of sensibly comparing apples and oranges? Well, of course there is. Think of the function

$$\phi(X) \equiv \text{Water content of } X \quad 5.269$$

and now ask the above question again *with respect to* ϕ . Clearly oranges are ϕ -better than apples if we mean by “ ϕ -better” that

$$\phi(\text{Oranges}) > \phi(\text{Apples}). \quad 5.270$$

A lesson to learn is that this notion of “better” clearly depends on our choice of the *comparison function*. E.g., with

$$\varphi(X) \equiv \text{Skin smoothness of } X \quad 5.271$$

we conclude that now apples are probably a bit φ -better than oranges as $\varphi(\text{Apples}) > \varphi(\text{Oranges})$.

¹⁵⁹Be warned!

MISCELLANEOUS

The bottom line is that one can sensibly compare almost anything as long as there is a shared property among the candidates—and whether this property is useful depends on the context or the *task* given. For instance, if we are interested in storing water most efficiently, ϕ (and not φ) seems to be the means of choice to compare possible candidates (and oranges are clearly better for storing water than apples).

For most real-life applications, however, the degree to which a task is solved (here quantified by ϕ)—despite being a pivotal number of merit—would have to compete with another, “inverse” quantifier: the *costs* γ . Unfortunately (at least where I come from), oranges are much more expensive than apples:

$$\gamma(\text{Oranges}) > \gamma(\text{Apples}) . \quad 5.272$$

The competition between performance ϕ and costs γ complicates the decision about which solution is “better” and depends on the specific choices of ϕ and γ : “better” now refers to the “stored water per costs”-ratio,

$$\frac{\phi(\text{Apples})}{\gamma(\text{Apples})} \quad ? \quad \frac{\phi(\text{Oranges})}{\gamma(\text{Oranges})} , \quad 5.273$$

which cannot be determined unless more is known about ϕ and γ .

One should stress that in a general framework of solving tasks (here: storing water) by given elements (here: oranges and apples), “costs” not necessarily refer to monetary values, contrary to the terms primary meaning, but should be interpreted as a generic quantifier that reflects the bounded availability of resources (e.g., negative environmental hazards). In our economy-based societies though, these “true” costs are then often mapped to monetary costs (as money seems to be the least common denominator for almost everything).

Now comes the big question: Why for all the world are we using oranges (or apples) to store water? Somehow this reminds on a viable solution on Discworld—but certainly not on our spherical one. Well, the reason is that so far the set of available elements (or *building blocks*) is rather sparse, namely

$$\mathcal{A} = \{\text{Apples, Oranges}\} , \quad 5.274$$

such that the set of all contraptions $\langle \mathcal{A} \rangle$ (our *universe*) we can make up to solve the water-storing-task is restricted to whatever one can build from apples and oranges only. If the set of available elements is extended by, say, *water balloons*,

$$\mathcal{A} = \{\text{Apples, Oranges, Balloons}\} , \quad 5.275$$

a whole new world $\langle \mathcal{A} \rangle$ of potential water-storing-solutions unfolds: Since

$$\phi(\text{Balloons}) > \phi(\text{Oranges}) > \phi(\text{Apples}) \quad 5.276$$

(where we think of a filled water balloon), and usually

$$\gamma(\text{Oranges}) > \gamma(\text{Apples}) > \gamma(\text{Balloons}), \quad 5.277$$

we can conclude that

$$\frac{\phi(\text{Balloons})}{\gamma(\text{Balloons})} > \frac{\phi(\text{Apples})}{\gamma(\text{Apples})} \quad ? \quad \frac{\phi(\text{Oranges})}{\gamma(\text{Oranges})}. \quad 5.278$$

This is just a formal way to express the fact that water balloons are way better suited for storing water than apples and oranges. Of course balloons are also much *smoother* than apples and oranges,

$$\varphi(\text{Balloons}) > \varphi(\text{Apples}) > \varphi(\text{Oranges}). \quad 5.279$$

However, we already identified this as an irrelevant property of the available elements for the given task of storing water. It should therefore not enter our assessment of possible solutions (it might be relevant for other tasks, though).

There are a few points to be emphasized:

- Meaningful comparisons of different solutions (or setups) require a common *universe* $\langle \mathcal{A} \rangle$ spanned by all contraptions based on a fixed set of elementary, indivisible elements or *atoms* $a \in \mathcal{A}$ each of which is assigned a fixed cost value $\gamma(a)$.
- Comparing solutions to a given task *quantitatively* requires at least one quantifier ϕ that measures how “good” the proposed solution is—and one inverse quantifier γ that measures the costs of the total setup.
- The possible “best” solution depends on both the costs of available elements and the available elements themselves. A larger set of building blocks \mathcal{A} often allows for much better solutions, although the benefits of new elements might be mitigated by their higher costs.

In what follows, we use these insights for the development of a formal framework to assess and compare physical setups as solutions to specified tasks.

5.3.2 General Concept & Notation

To construct a formal framework for the comparison of physical setups, we take a bottom-up approach and start with the smallest parts of any physical setup. We will call them *atoms* and denote their set as \mathcal{A} . The most prominent property of atoms is their *indivisibility*. We all know that the Greek origin of the word “atom” translates to “indivisible”—and we all know that this is certainly not true for real atoms given the energies involved are high enough. Nevertheless there *are* frameworks, primarily characterized by their energy scale, in which it is perfectly valid to think of real atoms as indivisible entities: chemistry, for instance.

In the more general framework we envision, comparing and gauging setups build from atoms also requires a fixed “periodic table” of available elements which are considered indivisible for the problem at hand. Think of electronic components such as resistors and capacitors as atoms for an electrical engineer defining his universe of possible contraptions (he calls them *circuits*). Clearly a capacitor is not indivisible: it can be decomposed into its electrolyte, metal package etc. But this is not the framework an electrical engineer lives in. The same is true for an experimental physicist working in quantum optics where beam splitters, lasers, oscilloscopes and function generators can be thought of as indivisible atoms of any experimental setup he or she might come up with in the laboratory. In the electrical engineer’s universe, however, the oscilloscope is *not* an atom but a *setup* designed to solve specific tasks most efficiently; it is built from his atoms: resistors, capacitors, etc. Thus it is of fundamental importance to clearly state what the available fundamental building blocks are to solve a given task. This is a necessary preliminary step to allow for well-defined assessments and avoid “comparing apples and oranges” (here used idiomatically).

Formal Framework

In the following, square brackets [...] denote multisets (elements may occur more than once) and curly brackets {...} denote sets (with unique elements). $|A|$ of a (multi-) set A denotes the number of elements.

Generally, a setup is built from a finite multiset of atoms. Here “multiset” is important since the atoms in \mathcal{A} actually denote *types* of elementary building blocks; instances of a type can be used more than once in a setup—just as the periodic table lists *types* of (real) atoms which can occur multiple times in complex molecules. A formal *setup* S is constructed from a finite (multi-) set of *atoms* $[a_1, \dots, a_{M_S}]$ via an *assembler* \mathfrak{S} , we write

$$S = (\mathfrak{S} \rightarrow [a_1, \dots, a_{M_S}]) . \quad 5.280$$

For short, let $[S]$ be the *multiset* of atoms and $\{S\}$ be the derived *set* of atom types that are used in S . The size of a setup is its number of atomic elements, $|[S]|$. A setup is finite if its size is finite.

It is illustrative to think of $[S]$ as a box of electronic elements (resistors, capacitors, etc.) while \mathfrak{S} corresponds to a circuit diagram that tells us how to combine these elements to form a physical circuit S which performs some envisaged task.

We denote the set of all conceivable finite setups over a given atomic set $\mathcal{A} = \{a_1, \dots\}$ as $\langle \mathcal{A} \rangle$ and, paralleling our notion of atoms, call it the *universe* spanned by \mathcal{A} . For the sake of brevity, define $\langle S \rangle \equiv \langle \{S\} \rangle$ as the smallest universe containing the setup S and $\langle S_1, S_2, \dots \rangle \equiv \langle \{S_1\} \cup \{S_2\} \cup \dots \rangle$ as the smallest universe containing the setups S_1, S_2, \dots . The latter becomes important if the setups S_1, S_2, \dots are to be compared with respect to a given task.

A concept that follows naturally is that of a sub-universe, denoted as $\langle \mathcal{B} \rangle \leq \langle \mathcal{A} \rangle$, and spanned by a finite subset of the super-universe $\langle \mathcal{A} \rangle$:

$$\mathcal{B} = \{b_1, \dots\} \subseteq \langle \mathcal{A} \rangle \quad \text{with} \quad |\mathcal{B}| < \infty. \quad 5.281$$

The idea is that the universe $\langle \mathcal{B} \rangle$ is constructed from a selection of setups in $\langle \mathcal{A} \rangle$ which are considered indivisible in $\langle \mathcal{B} \rangle$. For a setup $S \in \langle \mathcal{B} \rangle$:

$$S = (\mathfrak{S}_S \rightarrow [b_1, \dots, b_{M_S}]) . \quad 5.282$$

The same setup as seen from $\langle \mathcal{A} \rangle$ reads

$$S = \left(\mathfrak{S}_S \rightarrow \left[\left(\mathfrak{S}_{b_1} \rightarrow [a_1, \dots] \right), \dots, \left(\mathfrak{S}_{b_{M_S}} \rightarrow [a_1, \dots] \right) \right] \right) \quad 5.283a$$

$$= (\mathfrak{S}'_S \rightarrow [a_1, \dots]) \quad 5.283b$$

where

$$\mathfrak{S}'_S \equiv (\mathfrak{S}_S \rightarrow [\mathfrak{S}_{b_1}, \dots, \mathfrak{S}_{b_{M_S}}]) \quad 5.284$$

is a *modular assembler*.

These concepts can be immediately applied to the previously given universes of an electrical engineer and an experimental physicist: Let S be some experimental setup contrived by the experimentalist according to some theoreticians dreams in form of a proposal given as a description \mathfrak{S}_S . The building blocks are the experimentalist's bread and butter tools:

$b_1 =$ Beam splitter

$b_2 =$ Laser

$b_3 =$ Oscilloscope

\vdots

The electrical engineer, however, sees “into” the devices and perceives them as setups built from *his* atoms, namely

$a_1 =$ Resistor

$a_2 =$ Capacitor

$a_3 =$ Coil

\vdots

and the oscilloscope, for example, is given by

$$\text{Oscilloscope} = (\mathfrak{S}_{b_3} \rightarrow [\text{Resistor, Capacitor, } \dots]) \quad 5.285$$

with a circuit diagram \mathfrak{S}_{b_3} as sub-assembler of the extremely complex modular assembler \mathfrak{S}'_S that describes the experimental setup in terms of its electronic constituents (and not on the functional level of *devices*). \mathfrak{S}'_S may be way to

complicated for a human being to come up with—which is why the electrical engineer is done and satisfied with the construction of an oscilloscope and leaves the design of an optical atomic clock to the experimental physicist, who, in turn, is quite thankful that oscilloscopes can be bought off-the-shelf.

Templates

In physics, tasks and their corresponding solutions/systems often include a parameter that encodes the system size L . That is, both the stated tasks and the proposed solutions are actually given as a family of instances of growing size L . If a setup is part of such a family, we mark the latter by a hat and call it a *template*, defined as mapping

$$\hat{S} : \mathbb{N} \rightarrow \langle \mathcal{A} \rangle, \quad L \mapsto \hat{S}(L) \equiv S_L \quad 5.286$$

with monotonically increasing size, $|\hat{S}(L + 1)| > |\hat{S}(L)|$, but fixed building blocks, $\{\hat{S}(L + 1)\} = \{\hat{S}(L)\}$. Note that this induces a sequence of assemblers

$$\hat{\mathcal{C}} : \mathbb{N} \rightarrow \mathcal{A}^*, \quad L \mapsto \hat{\mathcal{C}}(L) \equiv \mathcal{C}_L \quad 5.287$$

where we introduced the notation S^* to denote the assembler of a setup S and extended this definition to denote the set of all assemblers over an atomic set \mathcal{A} by \mathcal{A}^* . The complexity to compute an assembler \mathcal{C}_L for a given size L (which is best thought of as a *construction plan* or *program*) can impose restrictions on the realizability of the setups S_L .

Payday

We already motivated that the assessment of a proposed setup that performs a given task should not only be based on a quantification of how “good” the task is solved, but also take into account the “costs” of the solution, which, in turn, may reflect both quantity and quality of the elements used. We expect that the combined problem of optimizing the performance and simultaneously minimizing the costs leads to non-trivial “optimal” solutions, a situation faced often in applications.

As an input to a well-posed comparison and optimization problem, one has to assign costs to the indivisible elements of the considered universe, that is, a function

$$\gamma : \mathcal{A} \rightarrow \mathbb{R}_0^+, \quad a \mapsto \gamma(a) \quad 5.288$$

which assigns a price $\gamma(a)$ to all atomic elements $a \in \mathcal{A}$. As the notion of “costs” implies additivity, it is obvious to define the costs of a multiset A of atoms as

$$\gamma(A) \equiv \sum_{a \in A} \gamma(a) \quad 5.289$$

and then the costs of a setup S as $\gamma(S) \equiv \gamma([S])$.

In a nutshell: The costs of a setup are given by the sum of the costs of its elements, neglecting any synergetic effects. This is the most straightforward way of assigning a price tag to a given setup. In some situations it can be necessary to extend the notion of costs to incorporate the assembly procedure described by \mathcal{E} to get a more realistic assessment of the costs. Take again the oscilloscope as an example: If $\gamma(\text{Oscilloscope})$ were the off-the-shelf price of the device (and we take the electrical engineers universe as reference), it is to be expected that the price tag of the oscilloscope is more than the sum of price tags of its electronic components.

A Note on Atoms

So far, we were a bit sloppy with our description of atomic elements. Again in the electrical engineer's universe, we exemplified the notion of atoms by

$$a_1 = \text{Resistor} \qquad 5.290$$

which is, admittedly, not quite correct. So see why, imagine the reaction of an electrical engineer if you ask him to construct a device based on a circuit diagram of your making where all the component-specific symbols (little boxes, zig-zag lines, etc.) are just labeled by "Resistor," "Capacitor," and so on.

To get a notion of what the real atomic elements are (characterized by their properties), it is useful to think of what one can buy in the corresponding field and how these entities are described in a sales catalogue. Then, our resistor-atom would rather be given as

$$a_1 = \text{Carbon composition resistor with ...}$$

resistance of 300Ω
tolerance of 5 %
voltage rating of 150 V ,

and another atomic element in \mathcal{A} might read

$$a_2 = \text{Carbon composition resistor with ...}$$

resistance of 300Ω
tolerance of 1 %
voltage rating of 100 V

which is close to a_1 but still a different indivisible element if one considers tolerance and voltage rating as distinctive features. As one can easily imagine, a_2 -atoms are more expensive than a_1 -atoms,

$$\gamma(a_2) > \gamma(a_1) . \qquad 5.291$$

Given a setup S which uses a_1 -atoms, substituting the latter by a_2 -atoms,

$$S' = S\{a_1 \mapsto a_2\}, \quad 5.292$$

in most cases will not disable the setup to perform a specified task. By contrast, the reverse substitution might severely impact its performance if S is fragile towards perturbations of this particular type of resistors.

To complicate things further (and due to cost additivity), it follows that

$$\gamma(S') > \gamma(S) \quad 5.293$$

which makes the reverse substitution $a_2 \mapsto a_1$ favorable. Depending on the construction of S , this might or might not be detrimental to the performance of the setup. To proceed, a precise and quantitative definition of the performance is therefore essential.

A Note on Physical Theories

To quantify how well a setup solves a task, rigorous descriptions of both the task and its solutions are mandatory. This requires a specification of the physical theory that is used to describe the task (as a desired state transformation) and its solutions (a dynamical evolution of some sort).

A prevalent concept in physics is that of (1) a state space which describes the state of a physical system, augmented by (2) a universally valid dynamical law and (3) a system-specific entity describing the dynamics on the state space by following the dynamical law. In classical mechanics, these are (1) the phase space, (2) the Hamiltonian equations of motion, and (3) the Hamiltonian function. In quantum mechanics, the list reads: (1) the Hilbert space, (2) the Schrödinger equation, and (3) the Hamiltonian operator. Similarly, in electrodynamics we have (1) the space of real vector fields, (2) the Maxwell equations, and (3) external charge- and current distributions.

The specific description of a universe in terms of its atoms and the way they can be combined as well as the definition of a task in general and the assessment of its solutions all crucially depend on the governing field of physics (classical mechanics, quantum mechanics, electrodynamics, etc.). In the following, we focus on models described by *classical mechanics* for pedagogical reasons (despite our quantum mechanical motivation [2]).

Note — The translation to quantum systems is then straightforward due to structural similarities between both theories. For instance, consider a finite collection of systems S_1, \dots, S_N , each described by a state space X_1, \dots, X_N . In both classical and quantum mechanics, the total state space of a combined system

$S = (S_1, \dots, S_N)$ is given by a product of subsystem state spaces:

$$X_S = \begin{cases} \times_{i=1}^N X_i & \text{classical,} \\ \otimes_{i=1}^N X_i & \text{quantum.} \end{cases} \quad 5.294$$

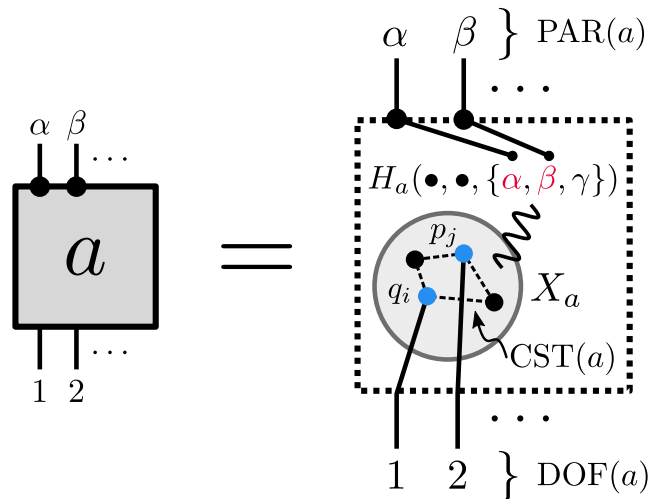
In classical physics, state spaces are combined by Cartesian products whereas quantum mechanics requires the tensor product. Thus it seems reasonable that a framework that describes the composition of classical subsystems can be lifted (with some modifications) to the quantum realm.

5.3.3 Specialization to Classical Mechanics

We start with our more specific treatment of the general concepts from above by fixing the realm to classical mechanics described by the Hamiltonian formalism. This fixes the generic state space for a system with finite number K of real degrees of freedom (d.o.f.) to the phase space \mathbb{R}^{2K} with generalized coordinates q_i and conjugate momenta p_i for $i = 1, \dots, K$.

The concept we propose reads as follows: Each atom $a \in \mathcal{A}$ is a (usually small) Hamiltonian system described by its state space $X_a = \mathbb{R}^{2K_a}$, its Hamiltonian $H_a(\{q_i\}, \{p_i\}, \{\eta_i\})$ with parameter set $\{\eta_i\}$, and featured submultisets $\text{DOF}(a) \subseteq \{q_i, p_i\}$ and $\text{PAR}(a) \subseteq \{\eta_i\}$ that describe the externally available d.o.f. and parameters (with possible multiplicity). The Hamiltonian may be augmented by a set of additional (usually holonomic) constraints $\text{CST}(a) = \{g_1, g_2, \dots\}$ imposed on the generalized coordinates.

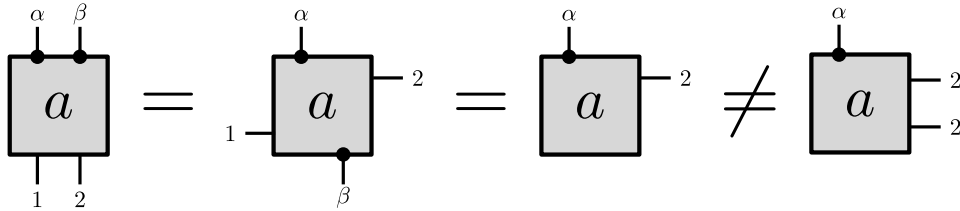
Pictorially, we can illustrate this concept as follows:



Here, the compact left-hand notation hides all (for the construction of setups) unnecessary internal structure and shows only externally available d.o.f. and parameters. The data visible in this notation is termed *external data*; we use lower

MISCELLANEOUS

Greek letters to denote parameters and numbers for d.o.f. Note that only a selection (red) of parameters $\text{PAR}(a)$ and d.o.f. (blue) $\text{DOF}(a)$ are available externally to connect to other atoms. The additional data shown in the right-hand sketch [X_a , H_a and $\text{CST}(a)$] is termed *internal data*. The position where DOF and PAR ports are attached to the square is arbitrary:

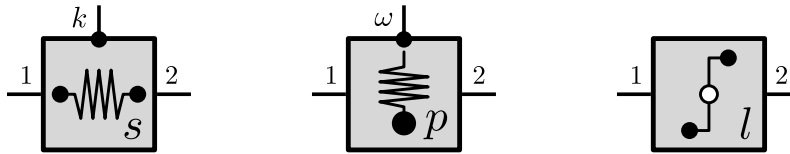


Note that it is also valid to omit available DOF and PAR ports (which corresponds to vanishing coupling and internal fixing of parameters, respectively). *Splicing* an existing DOF port is not allowed per definition; the rightmost atom is therefore distinct from the others.

We illustrate these concepts with an example:

EXAMPLE 5.1: Springs and pendula

As an example, we introduce three atoms that will be of use in the course of our discussion: The spring s , the pendulum p , and the lever arm l . Pictorially:



Formally, the spring s is given by the set of data

$$X_s = \mathbb{R}^2 \times \mathbb{R}^2 \tag{5.295a}$$

$$H_s(q_1, q_2; k) = \frac{f_s(k)}{2} (q_1 - q_2 + l_0)^2 \tag{5.295b}$$

$$\text{DOF}(s) = \{q_1 \mapsto 1, q_2 \mapsto 2\} \tag{5.295c}$$

$$\text{PAR}(s) = \{k\} \tag{5.295d}$$

$$\text{CST}(s) = \{\}, \tag{5.295e}$$

where $q_1 \mapsto 1$ indicates that the generalized coordinate q_1 is accessible via port 1. The spring constant is given as a function of k

$$f_s(k) = [k \geq k_{\max}] k_{\max} + [k_{\max} > k > k_{\min}] k + [k_{\min} \geq k] k_{\min} \tag{5.296}$$

where k_{\min} and k_{\max} denote the minimal and maximal adjustable spring constants. Here, $[x] = 1$ if x is true and $[x] = 0$ otherwise; $[\bullet]$ is known as *Iverson bracket*. The bounding of accessible spring constants ensures that the spring becomes a bit more

realistic. Note that this is already a rather sophisticated mechanical atom as the spring constant *can* be adjusted within certain bounds. A probably much cheaper spring s' with *fixed* spring constant would be characterized by $\text{PAR}(s') = \{\}$.

The pendulum p is specified by

$$X_p = \mathbb{R}^2 \tag{5.297a}$$

$$H_p(q_1, p_1; \omega) = \frac{p_1^2}{2m} + \frac{f_p(\omega)}{2} q_1^2 \tag{5.297b}$$

$$\text{DOF}(p) = \{q_1 \mapsto 1, q_1 \mapsto 2\} \tag{5.297c}$$

$$\text{PAR}(p) = \{\omega\} \tag{5.297d}$$

$$\text{CST}(p) = \{\} \tag{5.297e}$$

with another restricted spring constant $f_p(\omega)$. Note that we exposed the single d.o.f. q_1 twice. Physically, one can imagine a pendulum with two hooks at the mass to attach other equipment.

The lever arm l is given by

$$X_l = \mathbb{R}^2 \times \mathbb{R}^2 \tag{5.298a}$$

$$H_l = 0 \tag{5.298b}$$

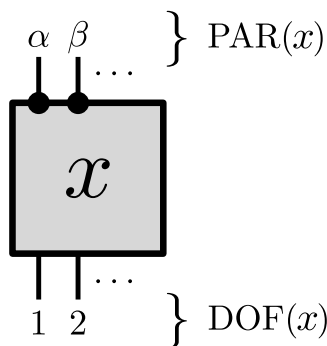
$$\text{DOF}(l) = \{q_1 \mapsto 1, q_2 \mapsto 2\} \tag{5.298c}$$

$$\text{PAR}(l) = \{\} \tag{5.298d}$$

$$\text{CST}(l) = \{q_1 + q_2 = 0\} \tag{5.298e}$$

where the holonomic constraint ensures $q_1 = -q_2$. Here we neglect the mass of the lever arm by setting the Hamiltonian to zero.

We are now ready to put things together. Note that, in principle, there is no difference between *atoms* and *setups* (built from atoms)—except that the former are indivisible. The general term *element* refers to both atoms and setups: Indivisible elements are atoms and divisible elements are setups. Since their outer structure is the same, an element x is depicted as



with adjustable parameters $\text{PAR}(x)$ and d.o.f. $\text{DOF}(x)$.

The formal definition of elements is constructive and given recursively:

DEFINITION 5.1: Syntactic elements

Given an atomic set \mathcal{A} , the universe $\langle \mathcal{A} \rangle$ is the set of all elements constructed as follows:

- 1 Every atom is an element.
- 2 Given two elements x and y and a compliant binary assembler \mathcal{G} (see below), then the setup

$$z = x\mathcal{G}y \equiv (\mathcal{G} \rightarrow [x, y]) \quad 5.299$$

is an element.

Let x and y be two elements, specified by their external data

$$x = (\text{DOF}(x), \text{PAR}(x)) \quad 5.300a$$

$$y = (\text{DOF}(y), \text{PAR}(y)) , \quad 5.300b$$

then a compliant binary assembler \mathcal{G} is a tuple $(\mathcal{C}, \text{DOF}, \text{PAR}, g)$ defined as follows:

→ The connector \mathcal{C} is a subset

$$\mathcal{C} \subseteq [\text{DOF}(x, y) \times \text{DOF}(x, y)] \cup [\text{DOF}(x, y) \times \text{PAR}(x, y)] \quad 5.301$$

connecting DOF with DOF or DOF with PAR ports (connecting parameters among each other is not allowed). Here we introduced the shorthand notation for a generic, set-valued function: $\mathcal{X}(a, b, \dots) \equiv \mathcal{X}(a) \cup \mathcal{X}(b) \cup \dots$

If \mathcal{C} connects only DOF ports,

$$\mathcal{C} \subseteq \text{DOF}(x, y) \times \text{DOF}(x, y) , \quad 5.302$$

we call \mathcal{G} pure assembler.

→ The new sets of d.o.f. $\text{DOF} \subseteq \text{DOF}(x, y) \setminus \mathcal{C}_{\text{DOF}}$ and parameters $\text{PAR} \subseteq \text{PAR}(x, y) \setminus \mathcal{C}_{\text{PAR}}$ are the subsets of the available DOF and PAR ports that are not used by the connector ($\mathcal{C}_{\text{DOF/PAR}}$ denotes the set of DOF/PAR ports that are used by the connector).

→ Whereas DOF that occur neither in the connector nor in the new set of exposed DOF ports can be left floating, parameters that are neither exposed nor connected to a DOF port must be fixed. This is done by the function

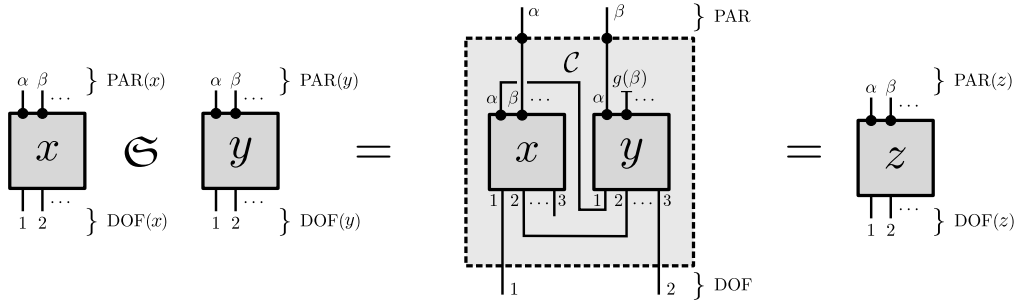
$$g : \text{PAR}(x, y) \setminus [\text{PAR} \cup \mathcal{C}_{\text{PAR}}] \rightarrow \mathbb{R} , \quad \eta \mapsto g(\eta) \quad 5.303$$

which assigns fixed parameters $g(\eta)$ to all floating parameters η of the setup.

The external data of the element $z = x \mathfrak{S} y$ with $\mathfrak{S} = (\mathcal{C}, \text{DOF}, \text{PAR}, g)$ is then given as

$$z = (\text{DOF}, \text{PAR}). \tag{5.304}$$

Although these rules are technical if stated formally, their pictorial representation is much simpler:



Note that all these transformations only determine the *external data* included in the pictorial representation. This already allows for a formally correct construction of setups based on a given set of atoms \mathcal{A} —just as knowledge of German grammar rules allows for the construction of well-formed sentences of the German language. In linguistics and mathematics, such rules are commonly referred to as *syntax*.

The knowledge that a sentence is grammatically (i.e., syntactically) correct German does not imply anything about its *meaning*. Assigning meaning to syntactically correct statements is what *semantics* is about. And we are still missing a bunch of it if we want to interpret our assembled setups in terms of classical mechanics. To this end, we have to define how a given (syntactically valid) setup in combination with the atomic internal data (which we ignored so far) condenses into a complete Hamiltonian description of the total setup (which then has *meaning* as a system of classical mechanics).

In the following, we focus on setups constructed via *pure assemblers* only. (Note that the pictorial example above is *not* pure as there is a connection between a DOF port of y and a PAR port of x .) Pure assemblers construct Hamiltonian systems from Hamiltonian systems, as the following definition of the intended physical semantics shows:

DEFINITION 5.2: Semantic elements from pure assemblers

Let x and y be elements that are combined via the compliant binary pure assembler \mathfrak{S} to $z = x \mathfrak{S} y$. Assume that the physical semantics of x and y is described by their internal data

$$x = (X_x, H_x, \text{CST}(x)) \tag{5.305a}$$

$$y = (X_y, H_y, \text{CST}(y)) \tag{5.305b}$$

which qualifies them as *Hamiltonian systems*.

Then, the setup z is again a Hamiltonian system

$$z = (X_z, H_z, \text{CST}(z)) \quad 5.306$$

with

- the state space $X_z = X_x \times X_y$,
- the Hamiltonian function $H_z = H_x + H_y$,
- and the constraints $\text{CST}(z) = \text{CST}(x, y) \cup \text{CST}(\mathcal{C})$.

Here,

$$\text{CST}(\mathcal{C}) \equiv \{q - q' = 0 \mid (q, q') \in \mathcal{C}\} \quad 5.307$$

is an additional set of holonomic constraints equating d.o.f. connected by \mathcal{C} .

This definition gives rise to a well-defined physical interpretation of any syntactically correct setup together with the internal data of the atoms. The interaction between atoms is encoded by connected d.o.f. that are to be set equal in the sum of atomic Hamiltonians. Note that the set of all constraints of a given setup, $\text{CST}(S)$, singles out a submanifold \bar{X}_S of the state space X_S as valid, physical states. The Hamiltonian equations of motions (EOMs) then describe a flow on this submanifold. If there are no internal constraints on the atoms, the total manifold

$$X_S = \prod_{a \in [S]} X_a \quad 5.308$$

describes the physics of the *free setup* over the atomic elements $[S]$

$$\text{free}([S]) \equiv (\mathbb{1} \rightarrow [S]) \quad 5.309$$

given by the *free assembler* $\mathbb{1}$. Pictorially, this corresponds to drawing all atoms in $[S]$ side by side without any connections between them. Physically, think of a blank sheet as circuit diagram ($\mathbb{1}$), throw a given set of electronic components into a box ($[S]$), and then call the box a “trivial device.”

Before we can finally start to think about what we set out for—defining tasks and quantifying how successful a setup solves them—a short detour on notation is in order. So far we only worked with *binary* assemblers: Given two elements x and y , a binary assembler \mathfrak{C} constructs a new element z by combining them, we write $x \mathfrak{C} y$. Since x and/or y can be setups (divisible elements) themselves, recursion allows for arbitrary complex setups S built from many atoms. Previously we introduced the formal notation

$$S = (\mathfrak{C} \rightarrow [a_1, a_2, \dots]) \quad 5.310$$

to indicate such a complex construction from more than two atoms (where \mathfrak{C} is clearly not a binary assembler). With our new tools, we can now give a formal definition of such assemblers in terms of a recursive, binary construction process:

$$(\mathfrak{C} \rightarrow [a_1, a_2, \dots]) \equiv (a_{M_S} \mathfrak{C}_{M_S} \dots (a_3 \mathfrak{C}_3 (a_2 \mathfrak{C}_2 a_1)) \dots) . \quad 5.311$$

The assemblers \mathfrak{S}_i are binary and attach step by step atomic elements a_i to a growing composite element which finally becomes the desired setup S . If we consider an object of the form $x\mathfrak{S}$ as a partial¹⁶⁰ map

$$x\mathfrak{S} : \langle \mathcal{A} \rangle \rightarrow \langle \mathcal{A} \rangle, \quad y \mapsto x\mathfrak{S}y, \quad 5.312$$

we can omit the parentheses and write

$$(\mathfrak{S} \rightarrow [a_1, a_2, \dots]) = a_{M_S} \mathfrak{S}_{M_S} \dots a_3 \mathfrak{S}_3 a_2 \mathfrak{S}_2 a_1. \quad 5.313$$

This is a kind of *currying* known from functional programming.

This recursive representation with binary elementary construction steps comes actually quite close to what really happens if one follows a construction plan \mathfrak{S} (given as some construction manual in the widest sense): Usually an ordered sequence of simple instructions is given of how to attach elementary building blocks to a growing setup. These correspond to the binary assemblers \mathfrak{S}_i that specify how to attach the i th atom.

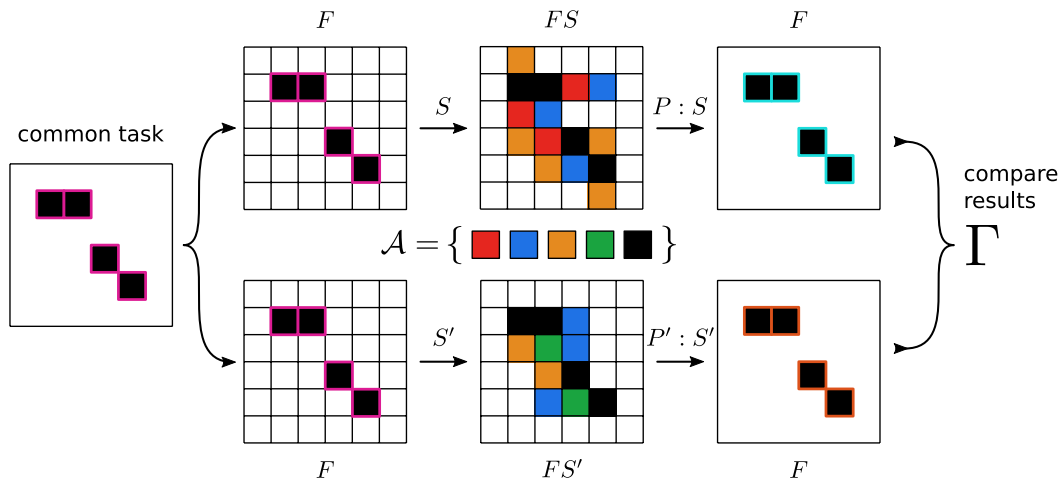
However, if the only statement is that a setup S *can* be constructed from a set of elementary building blocks somehow (but we are not particularly interested in *how* this construction works), it is more convenient to stick to the original notation $S = (\mathfrak{S} \rightarrow [a_1, a_2, \dots])$.

¹⁶⁰A partial map can be *undefined* on some elements of its domain. For $x\mathfrak{S}y$, $y \in \langle \mathcal{A} \rangle$, this occurs whenever \mathfrak{S} is not compliant with y .

Tasks

The ultimate goal and original motivation is an evaluation of the potential of a setup to complete a predefined task and thereby obtain a well-defined method for comparing different setups with respect to a common task.

The crucial point here is “common”: An objective and fair assessment requires some fixed frame which encodes the task in the beginning and the solution afterwards. Competing setups then couple to this common *framing setup* to receive their task and deposit their solution when finished. This can be illustrated as follows:



Squares denote atomic elements where filling color encodes their type and boundary color describes their state. The framing setup F encodes the posed task in its state (red boundary) and is augmented by two competing setups S and S' to form the intermediate setups FS and FS' . Protocols P and P' running on their respective setups lead to an effective transformation of the framing state into a possible solution of the task. These solutions are then compared by a yet undefined weighting function Γ .

This motivates the following definition:

DEFINITION 5.3: Tasks and framing setups

Given an atomic set \mathcal{A} of building blocks and a setup $F \in \langle \mathcal{A} \rangle$ with physical state space \overline{X}_F . Let

$$\Gamma : \text{Ham}(\overline{X}_F) \rightarrow [0, 1], \quad f \mapsto \Gamma[f] \tag{5.314}$$

be a function assigning a real number between 0 and 1 to a given Hamiltonian symplectomorphism (“canonical map”). Here, $\text{Ham}(\overline{X}_F)$ denotes the group of all symplectomorphisms on \overline{X}_F generated by Hamiltonian vector fields (i.e., time evolutions generated by a Hamiltonian flow on phase space). F is termed framing setup with assigned weighting function Γ . The pair $\mathfrak{t} \equiv (F, \Gamma)$ is called a task in the universe $\langle \mathcal{A} \rangle$, write $\mathfrak{t} \in \langle \mathcal{A} \rangle^\times$.

Let us dwell a moment on this rather abstract definition: The essential part of any physical task can be encoded in a desired class of transformations¹⁶¹ on the phase space of a given setup. This motivates both the setup F and the assigned weighting function Γ : As we deal with physical systems (which may be exposed to perturbations), we cannot expect such transformations to be perfect. To allow for a proper assessment of such imperfect transformations, the weighting function Γ is required. It “grades” a proposed canonical transformation f by assigning (discrete or continuous) numbers from 0 (“fail”) to 1 (“success”). This grading is not universal—on the contrary: it *defines* the task to some extent. Often the succeeding transformations with $\Gamma[f] = 1$ are *not* unique because not all properties of the global phase space transformation may be relevant for the given task.

Now that a task has been defined, it begs the question how the transformations f (graded by Γ) enter the stage. The basic idea is to extend the framing setup F by a dedicated setup S (the “solution”) from the same universe $\langle \mathcal{A} \rangle$ to achieve the required transformations as “ Γ -accurate” as possible. This gives rise to an augmented setup

$$FS = (\mathfrak{S}_{FS} \rightarrow [F, a_1, a_2, \dots]) \quad 5.315a$$

$$= (\mathfrak{S}_{F|S} \rightarrow [F, (\mathfrak{S}_S \rightarrow [a_1, a_2, \dots])]) \quad 5.315b$$

which combines a (finite) multiset of atoms $[a_1, a_2, \dots]$ via the assembler \mathfrak{S}_{FS} with the framing setup F . Note that the total assembler $\mathfrak{S}_{FS} = \mathfrak{S}_{F|S}\mathfrak{S}_S$ can be decomposed into \mathfrak{S}_S describing the construction of S which then is connected to F by the binary assembler $\mathfrak{S}_{F|S}$.

Constraints on Phase Space

The physical state space of the total setup FS is $\overline{X}_{FS} = \overline{X_F \times X_S}$ which, in most cases, differs from the free product $\overline{X}_F \times \overline{X}_S$ due to non-trivial connections introduced by $\mathfrak{S}_{F|S}$:

$$\overline{X}_{FS} = \overline{X_F \times X_S} \subset \overline{X}_F \times \overline{X}_S. \quad 5.316$$

In many cases, the task t demands two sets of F -states to be accessible: The initial states $\mathcal{T}_1 \subseteq \overline{X}_F$ and the target states $\mathcal{T}_2 \subseteq \overline{X}_F$. In these cases, the weighting function Γ quantifies how well a given phase space transformation f maps \mathcal{T}_1 onto \mathcal{T}_2 (possibly with additional constraints). This gives rise to a minimum requirement on allowed assemblers $\mathfrak{S}_{F|S}$, namely

$$\forall \Phi_F \in \mathcal{T}_1 \cup \mathcal{T}_2 \exists \Psi_S \in \overline{X}_S : \Phi_F \times \Psi_S \in \overline{X}_{FS}, \quad 5.317$$

¹⁶¹These transformations must be generated by some Hamiltonian time evolution, i.e., they must be Hamiltonian symplectomorphisms.

where we use the notation $\Phi_F \times \Psi_S \equiv (\Phi_F, \Psi_S)$. If this condition is not met, the envisaged task *cannot* be achieved by S as at least one initial or target state of F is not compatible with the augmented setup FS .

We may even be more demanding and require the augmentation to obey

$$\exists \Psi_0 \in \overline{X}_S \quad \forall \Phi_F \in \mathcal{T}_1 \cup \mathcal{T}_2 : \quad \Phi_F \times \Psi_0 \in \overline{X}_{FS}. \quad 5.318$$

Whereas requirement (5.317) allows the compatible state Ψ_S of S to depend on the framing state Φ_F of F , requirement (5.318) demands the existence of a *common* “default” state Ψ_0 of S that is compatible with *all* initial and target states Φ_F . We adopt this condition in the following since it emphasizes the notion of S as being a “substrate” or a “tool” for the completion of a task—just as the same screwdriver can be used to assemble a variety of different furniture. To complete this picture, we will be even more restrictive and demand that the task must be achieved with the boundary condition that S starts in such a “default” state Ψ_0 and *returns* to the very same state after completion of the task,

$$\Phi_F \times \Psi_0 \xrightarrow[\text{with } FS]{\text{Do something}} f(\Phi_F) \times \Psi_0, \quad 5.319$$

where f encodes the transformation performed by FS (see below). Here we borrow vocabulary from *constructor theory* [394] (which, in turn, borrows it from chemistry) and call such transformations *catalytic*: The system S in state Ψ_0 operates as a catalyst—just as the screwdriver operates as a catalyst in the production of furniture¹⁶².

Protocols

The comparison of two solutions (given as setups S and S' with default states Ψ_0 and Ψ'_0) starts with an application of the aspirants to the task,

$$\Phi_F \times \Psi_0 \xrightarrow[\text{with } FS]{\text{Do something}} f(\Phi_F) \times \Psi_0 \quad 5.320a$$

$$\Phi_F \times \Psi'_0 \xrightarrow[\text{with } FS']{\text{Do something else}} f'(\Phi_F) \times \Psi'_0, \quad 5.320b$$

and concludes with a comparison of their transformations,

$$\Gamma[f] \geq \Gamma[f'] \quad \text{or} \quad \Gamma[f'] \geq \Gamma[f], \quad 5.321$$

and costs,

$$\gamma(S) \geq \gamma(S') \quad \text{or} \quad \gamma(S') \geq \gamma(S). \quad 5.322$$

What remains to be discussed is the “do something with FS .”

¹⁶²As in chemistry, going without a screwdriver does not ultimately prohibit the construction of your cupboard, though it definitely slows down the construction process considerably.

DEFINITION 5.4: Protocols

Let $S \in \langle A \rangle$ be an element (composite or atomic) with physical state space \overline{X}_S and parameters $\text{PAR}(S)$, described by a Hamiltonian function H_S .

→ The variability of S is the number of tunable parameters: $\text{Var } S \equiv |\text{PAR}(S)|$.

→ A protocol P is a (sufficiently smooth) function

$$P : [0, 1] \rightarrow \mathbb{R}^{\text{Var } S}, \quad t \mapsto \boldsymbol{\eta}(t) \tag{5.323}$$

describing the driving of the $\text{Var } S$ parameters of S .

→ Let $\Psi_0 = (\{q_i\}, \{p_i\}) \in \overline{X}_S$ be a physical state of S . The Hamiltonian

$$H(\{q_i\}, \{p_i\}, t) \equiv H_S(\{q_i\}, \{p_i\}, \boldsymbol{\eta}(t)) \tag{5.324}$$

defines a Hamiltonian flow on \overline{X}_S and its integral curves $X(t)$ (solutions to the Hamiltonian equations of motion) induce a mapping

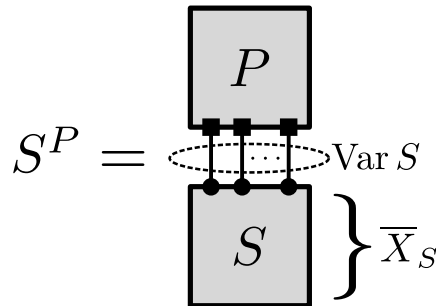
$$S^P : \overline{X}_S \rightarrow \overline{X}_S, \quad \Psi_0 \mapsto \Psi_1 \tag{5.325}$$

with $X(0) = \Psi_0, X(1) = \Psi_1$

which describes the transformation of an initial state Ψ_0 into a final state Ψ_1 under the driving of protocol P on S .

A protocol P allows us to control the unfixed parameters of an element S (usually a composite setup) freely within the normalized time interval $[0, 1]$. For example, think of an experimental setup with coupled pendula, some of which are driven by motors that are controlled by a computer. In this case, the protocol can be identified with the program that controls the driving of these pendula. In other situations, one might control the eigenfrequencies (e.g., spring constants) of mechanical oscillators to some extent. The important point is that the time-dependent parameters of S are *no dynamical d.o.f.* but externally controlled variables with no relevant back action on the controller.

We illustrate the application of a protocol as follows:



Here we omit possible DOF ports if there is no plan to extend the setup further. Note that it is perfectly valid for a protocol to assign constant values to all parameters of a setup. In this case, the state transformation is determined by an undriven Hamiltonian evolution.

Quantifying Success

The various protocols that may be applied to a given setup can vary in complexity — and this might demand for an additional cost function. However, if a computer controls the setup, this seems to be a less important issue and we do not assign protocol-dependent costs in the following: Protocols are “free of charge.”

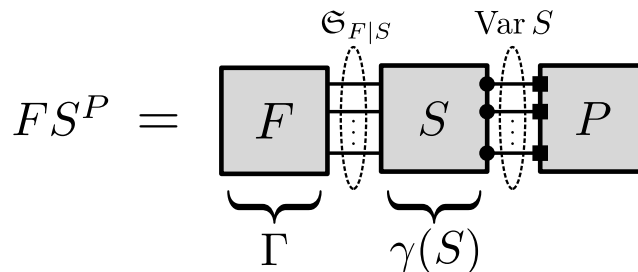
What clearly must be taken into account as an additional cost factor is the variability $\text{Var } S$ of the final setup: The number of required freely controllable parameters often has significant impact on the realizability, complexity, and thereby costs of a setup. For instance, in the framework of circuits a function generator may be employed as controller with a restricted set of applicable protocols (waves of specified period and amplitude). But the available number of independent output channels of such a generator is unfavorably correlated with its (monetary) costs. Thus we arrive at the following quantification of success:

DEFINITION 5.5: Quantification of success

Let $\langle \mathcal{A} \rangle$ be a universe, $t = (F, \Gamma) \in \langle \mathcal{A} \rangle^\times$ a task, $S \in \langle \mathcal{A} \rangle$ a setup to solve t , and P a protocol compatible with S . We call (S, P) an aspirant to solve t . The success of (S, P) with respect to t is quantified by three numbers of merit:

- The costs of the setup, $\gamma(S)$.
- The variability of the setup, $\text{Var } S$.
- The success of the protocol, $\Gamma [FS^P]$.

The total setup for evaluating the success can then be depicted as follows:



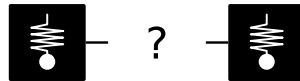
Be aware of the two-step procedure involved in the solution of a task: First, a compatible setup has to be contrived. Second, a protocol for this setup is applied. The protocol depends on the setup and optimizing the success is thus a highly

complex task of choosing the optimal setup equipped with the optimal protocol. The second part (the choice of an efficient protocol for a given, fixed setup) is the subject of *optimal control theory* [395]. The first part (the choice of a promising setup) is usually a product of theoretical proposals and the experience of gifted experimentalists.

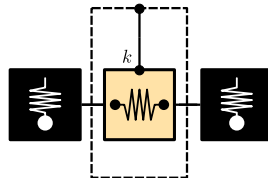
Spatial Embeddings

We need a last concept that extends our notion of setups before we can apply the framework to real-world problems. To see why, consider the following task t :

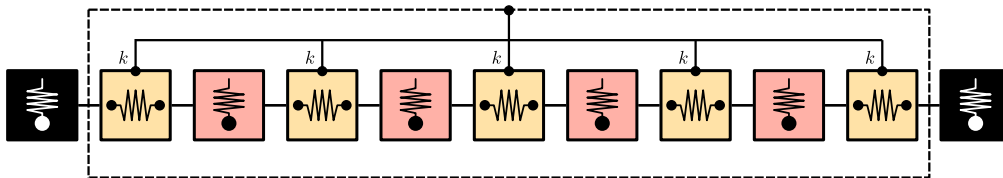
Given are two pendula as framing setup F and the weighting function Γ defines a perfect mode transfer between these two oscillators as success¹⁶³. That is, starting with one of the framing pendula oscillating (and the other one at rest), an aspirant (S, P) is required to transform the state of both pendula such that, after completing the protocol, the states of both pendula are exchanged. This is the described framing setup:



And this is one of the simplest setups S_1 that can complete the task (equipped with an appropriate protocol P_1):



Another, more complex (and more expensive) setup S_2 is the following:



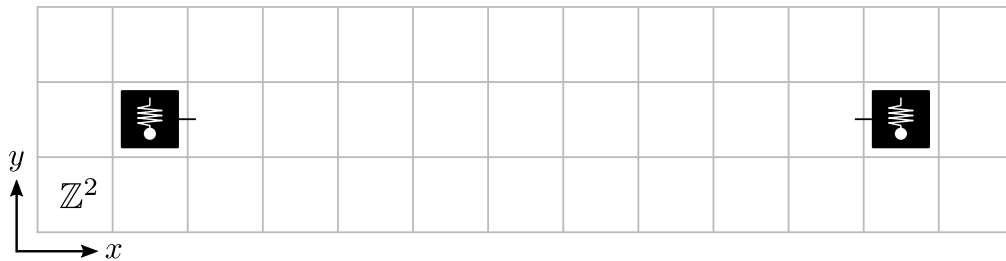
(Again combined with an appropriate protocol P_2 .) It is clear that $\gamma(S_1) \ll \gamma(S_2)$ so that S_1 is presumably better suited for the task than S_2 .

The point is that the given framing setup lacks a property inherent to almost every physical system: a *spatial* configuration. Remember that a generic setup S so far was defined by an assembler \mathfrak{S} which determined the *logical* or *physical*

¹⁶³This is essentially the classical counterpart of the state transfer in Chapter 3 and Ref. [2].

connections between atomic elements. We did not make any statements about the placement of these elements in space, the length of connections etc. This missing aspect of physical setups allows for the very different solutions above. Although spatial constraints may not be necessary for all tasks, the situation encountered in Chapter 3 and Ref. [2] clearly demands for a notion of locality to construct an adequate abstraction of physical reality.

Therefore we require some kind of “breadboard” on which atomic elements are placed and connected. If the connections of DOF ports obey a locality constraint induced by the metric of the breadboard, this gives rise to an embedding of a given setup and, most importantly, prohibits the realization of (sequences of) setups that violate locality. In addition, tasks can be augmented by prescribed embeddings for their framing setups. For example:



Here, one atomic element per site is allowed and DOF connections may only traverse a single edge (to enforce locality). This embedded framing setup realizes the same task t as above but can no longer be solved by the single-spring setup S_1 while respecting the locality of DOF connections. By contrast, the chain-setup S_2 still solves the task. This motivates the following definition:

DEFINITION 5.6: Embeddings

Let S be a setup in the universe $\langle \mathcal{A} \rangle$ with components $[S]$ and pure assembler \mathfrak{C} .

→ Let $\mathbb{E}_{\mathfrak{C}} \subseteq [S]^2$ be the set of edges between atomic elements with connected DOF ports (the interaction graph of the setup).

An injective function

$$\mathcal{E} : [S] \rightarrow \mathbb{Z}^D, \quad x \mapsto \mathcal{E}(x) \tag{5.326}$$

is called D -dimensional embedding of S with radius δ if for all pairs of connected elements $(x_1, x_2) \in \mathbb{E}_{\mathfrak{C}}$ it holds $\|\mathcal{E}(x_1) - \mathcal{E}(x_2)\| \leq \delta$ (where $\|\bullet\|$ denotes the Euclidean norm on \mathbb{Z}^D).

→ We call a setup S equipped with an embedding \mathcal{E} embedded setup (or just setup if it is clear that an embedding is implied) and write $S_{\mathcal{E}}$.

→ A task based on an embedded framing setup $F_{\mathcal{E}}$ is called embedded task, $t_{\mathcal{E}} = (F_{\mathcal{E}}, \Gamma)$. Aspirants are assumed to be embedded in the same dimension and extend the embedding of the framing setup.

ON APPLES AND ORANGES

	Description	Symbol	Cost	
(a)	\mathcal{A}_1	Pendulum, one hook, fixed $\omega = 1$		1
		Pendulum, two hooks, fixed $\omega = 1$		1
		Pendulum, two hooks, variable ω		2
		Spring, fixed $k = 1$		1
		Spring, variable k		2
(b)	\mathcal{A}_2	Pendulum, one hook, fixed $\omega = 1$		1
		Pendulum, two hooks, fixed $\omega = 1$		1
		Pendulum, two hooks, variable ω		2
		Spring, fixed $k = 1$, variance Δk_1		1
		Spring, variable k , variance Δk_2		2

TABLE 5.1 • Example: Two atomic sets. Atomic sets for clean (\mathcal{A}_1) and disordered (\mathcal{A}_2) mode transfer in (a) and (b), respectively. Perfect atoms (without production tolerances) are symbolized by squares; atoms that are drawn from a distribution with finite variance of their parameters (here: spring constants) are symbolized by circles. Atoms with variable parameters are more expensive than comparable elements with fixed parameters; apart from this, the costs are chosen arbitrary.

If not noted otherwise, we assume $\delta = 1$. Getting rid of the somehow arbitrary “interaction radius” δ is only possible if either it is fixed by a specific implementation or if one considers setup *templates* $\hat{S}_\varepsilon(L)$ and demands a finite interaction radius for $L \rightarrow \infty$ (see Appendix E of Ref. [129] for more information on the embedding of templates).

The concept of embedded tasks formalizes the vague notion conveyed by the sketch on page 480: A task is encoded in a spatially distributed (framing) setup and must be solved by a spatially distributed setup arranged around and connected to the former.

Example

A rigorous application of this framework is beyond the scope of this thesis (recall that this is only a *side track* of Chapter 3). However, let us sketch a possible application of the so far abstract concepts to the task of mode transfer between spatially separate oscillators. As already mentioned, this is the classical analogue of the quantum state transfer discussed in Chapter 3 and Ref. [2]. The following connections are easily identified:

- The classical analogue of the bosonic modes in Chapter 3 are pendula with eigenfrequency ω ; the mode couplings are then realized by springs with spring constant k . The parameters of both elements can either be fixed or variable (which affects their costs γ). This set of atoms is denoted by \mathcal{A}_1 and listed in Table 5.1 (a). In Chapter 3, we also consider *disordered* systems that respect the protecting symmetry (see Subsection 3.3.5). A corresponding set of atoms \mathcal{A}_2 is listed in Table 5.1 (b) where the spring constants of coupling springs are drawn from a distribution with finite variance. Note that a comparison of setups makes only sense within either $\langle \mathcal{A}_1 \rangle$ or $\langle \mathcal{A}_2 \rangle$.
- In Chapter 3, we first compare three setups without disorder as aspirants for the task of state transfer. Their classical analogues in $\langle \mathcal{A}_1 \rangle$ are shown in Figure 5.9: (a) the topological “SSH chain” setup S_{SSH} with alternating tunable coupling springs, (b) the trivial “Barrier” setup S_{B} with a tunneling barrier of oscillators with tunable eigenfrequency, and (c) the trivial “Propagation” setup S_{P} with uniformly tunable coupling springs. Note that all three setups have the same variability $\text{Var } S_{\bullet} = 1$. In Chapter 3, the single tunable parameter is controlled by the function $\mathcal{F}(t) = \sin^2(\pi t/\tau)$ which can be used to define all three protocols P_{\bullet} . Combined, this gives three aspirants $(S_{\bullet}, P_{\bullet})$ for the embedded task of mode transfer.
- The common embedded framing setup $F_{\mathcal{E}}$ is given by the two black oscillators (Figure 5.9). Actually we define a *template* of embedded framing setups $\hat{F}_{\mathcal{E}}(L)$ parametrized by their horizontal distance L (since we are interested in the scaling of properties for $L \rightarrow \infty$). In Chapter 3, the performance of an aspirant is measured by, inter alia, the overlap \mathcal{O} . A similar measure allows in the classical case to define the weighting function Γ which then specifies the embedded task (template) $\hat{t}_{\mathcal{E}}(L) = (\hat{F}_{\mathcal{E}}(L), \Gamma)$ for mode transfer completely.
- Finally, we compare the topological “SSH chain” setup with the trivial “Barrier” setup in the presence of symmetric disorder (Subsection 3.3.5). On the classical side, this corresponds to a comparison of the two setups S'_{SSH} and S'_{B} in Figure 5.9 (d) and (e) in the universe $\langle \mathcal{A}_2 \rangle$ where the coupling springs are subject to disorder. Note that the framing setup is contained in

ON APPLES AND ORANGES

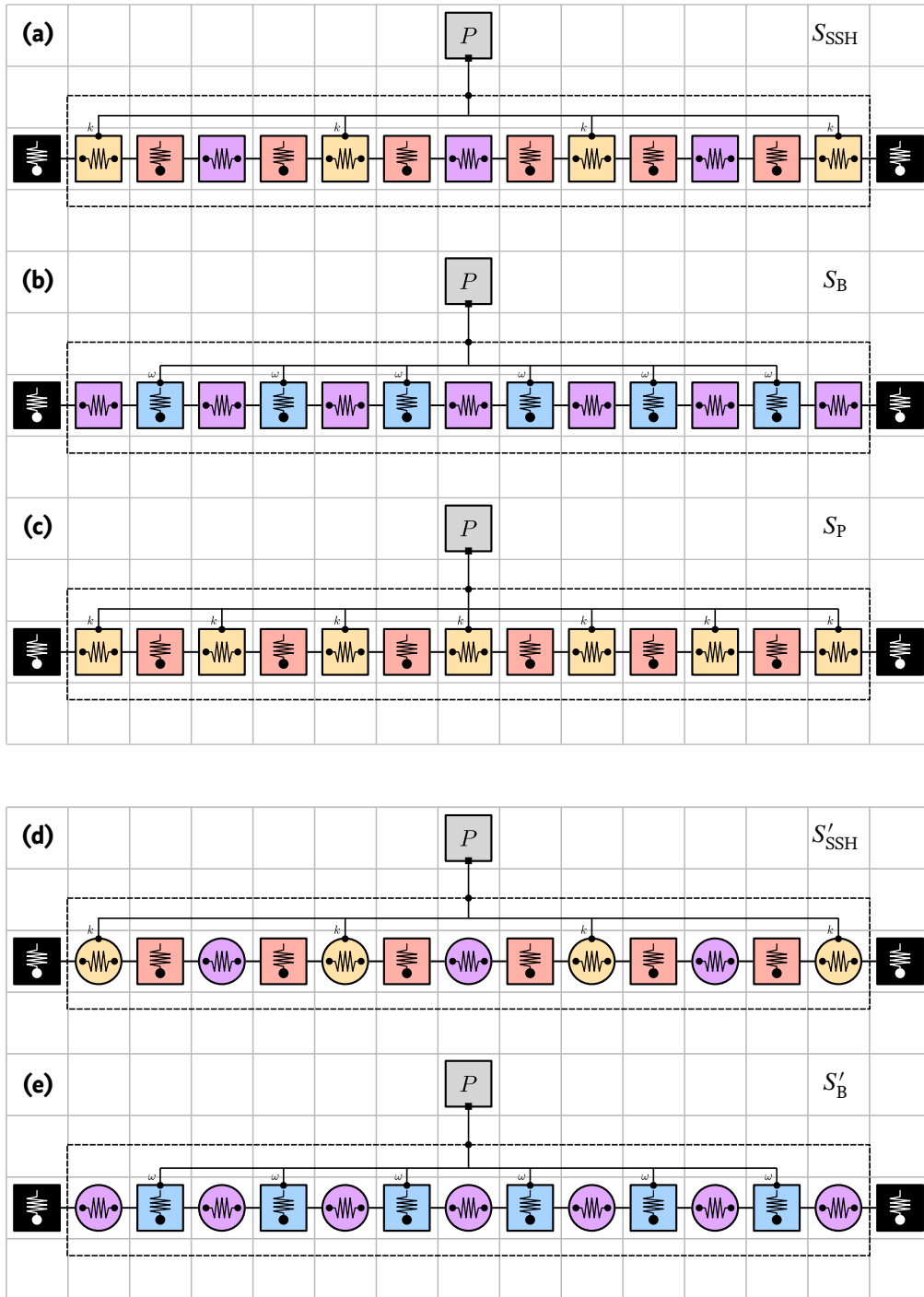


FIGURE 5.9 • Example: Setups for classical mode transfer. Three setups (a,b,c) from the clean universe (\mathcal{A}_1) and two (d,e) from the disordered universe (\mathcal{A}_2) to solve the embedded task of classical mode transfer between the two black oscillators (framing setup). The protocol P of each setup controls a single, time-dependent parameter. The atoms \mathcal{A}_1 and \mathcal{A}_2 are described in Table 5.1; details are given in the text.

both universes, $\langle \mathcal{A}_1 \rangle$ and $\langle \mathcal{A}_2 \rangle$, so that solutions to the same task can be constructed in either of them. However, *fair comparisons* of solutions are only possible within a common universe.

The upshot of this discussion is the following (valid for both classical and quantum setups): If we compare the topological “SSH chain” setup with the trivial “Barrier” setup in the clean universe $\langle \mathcal{A}_1 \rangle$, both allow for nearly perfect mode transfer with appropriate protocols P_\bullet . In that sense, the topological setup does *not* beat the trivial one. However, in the disordered universe $\langle \mathcal{A}_2 \rangle$, the topological setup performs better than the trivial one since the disorder respects the symmetry that protects the topological band structure of S'_{SSH} . Thus, fundamentally it is *symmetry* that is responsible for the superior transfer characteristics of the topological setup. The crucial point is that the trivial setup is constructed from *the same* (symmetric) elements without benefit for mode transfer. In that sense, the topological setup is superior to the trivial one in that the former converts the symmetry into something useful (namely, mode transfer) whereas the latter does not.

We conclude with a suggestion: Fix the framing setup and the universe. Now fire up your favorite generative machine learning algorithm (e.g., a genetic algorithm) to invent setups within this universe and evaluate their performance as solutions of the mode transfer task. Does it eventually come up with the topological one? Are there approaches that are even *better*?

5.4 Deep Convolutional Neural Networks for Topological Quantum Error Correction

In this section, we present the prelude of Chapter 4 and Ref. [3]. Whereas the topic of Chapter 4 is “*Topological quantum error correction with [...] cellular automata*”, here we replace the cellular automaton by a *convolutional neural network* (a particular class of artificial neural networks) to decode the Majorana chain quantum code.

5.4.1 Motivation

Everything starts with the seminal work of Silver *et al.* [396] early in 2016 who shattered the supremacy of mankind in the complex game of Go. Their combination of reinforcement learning, Monte Carlo tree search, and deep convolutional neural networks culminated in a program named *AlphaGo* that defeated, for the first time, a human professional player in the game of Go. At the same time, the paper served as a beacon for the field of machine learning (ML) in general and deep convolutional neural networks (CNN) in particular. This beacon was strong enough to permeate the physics community and spark a wealth of ML-related projects in various fields such as condensed matter physics and quantum information theory (see Ref. [397] and references therein). Let me illustrate what I mean:

Visit the *Web of Science*¹⁶⁴ and query the database with

```
TS=("artificial intelligence" OR "machine learning" OR "neural network*")
AND SU=(PHYSICS)
```

for publications in the research area of physics with a topic related to the keywords given. In a second query, focus on the subclass of publications that address *convolutional neural networks*:

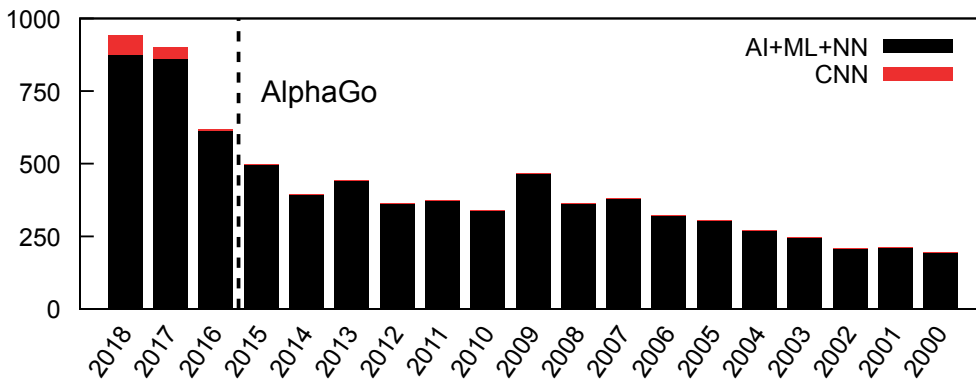
```
TS=("convolutional neural network*") AND SU=(PHYSICS)
```

(This yields a subset of the first query.) If we extract from the results the numbers of publications per year and subtract the data points of the second query from the first query, we obtain the following plot¹⁶⁵:

¹⁶⁴<https://clarivate.com/products/web-of-science/>

¹⁶⁵Data as of 25 September 2018.

MISCELLANEOUS



Separated by a one-year gap from *AlphaGo*, the number of physics papers that somehow relate to “artificial intelligence” (AI), “machine learning” (ML), or “neural networks” (NN) skyrocketed. At the same time, the rather special concept of convolutional neural networks (CNN) appeared for the first time in physics papers. It is standing to reason that the avalanche¹⁶⁶ of papers in 2017 was, at least in part, initiated by *AlphaGo*.

The results in this section are part of this avalanche, although they never directly led to a paper (indirectly they did [3]; but only after I switched gears and replaced the neural networks by cellular automata which are a more comprehensive framework and, for that matter, better suited for rigorous treatment). The idea is to use convolutional neural networks to decode topological quantum memories. Here we use the one-dimensional Majorana chain (see Subsection 1.2.2) as a simple example. The purpose of the CNN is to translate the error syndromes into matching correction operations.

The application of (not necessarily convolutional) neural networks as decoders of topological quantum codes suggests itself if one relates the two-dimensional patterns of Go positions in Ref. [396] with the two-dimensional syndrome patterns of, e.g., the toric code [45]. Hence it is not surprising that this has been discussed in the *AlphaGo*-avalanche as well [398–403].

¹⁶⁶In physics, an avalanche of papers is indicative of lots of low-hanging fruit that are just waiting to drop into the basket of some physicist strolling by.

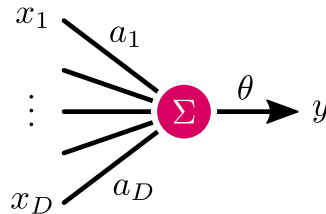
5.4.2 Artificial Neural Networks

To make this section self-contained, we give a very brief introduction to the concept of artificial neural networks. For a more complete and in-depth review, we refer the reader to one of the many primers on the topic (e.g., [404, 405]).

General Concept

Artificial neural networks are a very crude abstraction of the biological tissue of the brain. The latter consists of interconnected neurons that integrate electrical potentials from other neurons via their dendrites. Each dendrite weights the incoming potential differently, and the gradual adjustment of these weights accounts for the plasticity of the brain and plays a fundamental role for *learning*. Once the integrated potential of all dendrites reaches a threshold, the neuron fires a sequence of potential spikes along its axon that, in turn, connects to many dendrites of other neurons.

This elementary process of information integration and transmission is mimicked by *artificial* neurons which are nothing but a special class of mathematical functions that map many inputs $x_i \in \mathbb{R}, i = 1, \dots, D$, (the “dendrite potentials”) to a single output $y \in \mathbb{R}$ (the “axon potential”). The output is given by the weighted sum of the inputs (with weights $a_i \in \mathbb{R}$ and bias $b \in \mathbb{R}$), followed by a nonlinear function $\theta : \mathbb{R} \rightarrow \mathbb{R}$. Pictorially:



Formally, we have

$$y = \theta \left(\sum_{i=1}^D a_i x_i + b \right) = \theta(\mathbf{a}\mathbf{x} + b) \tag{5.327}$$

with *activation function* θ . There are various activation functions possible; prevalent ones are the *rectifier*

$$\theta_1(x) = \max\{0, x\} \tag{5.328}$$

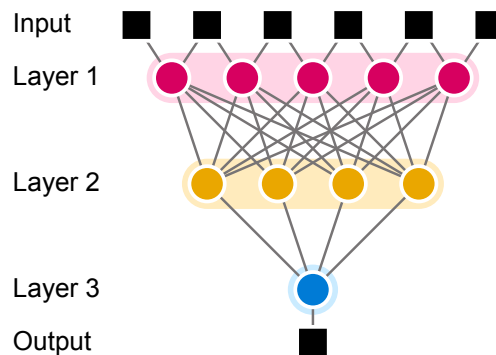
and the Heaviside step function

$$\theta_2(x) = \begin{cases} 1 & \text{if } x > 0, \\ 0 & \text{if } x \leq 0. \end{cases} \tag{5.329}$$

Artificial neurons with $\theta = \theta_1$ are called *rectified linear unit (ReLU)*, neurons with $\theta = \theta_2$ are called *perceptron*. The latter are useful if the neuron's output is to be interpreted as a binary decision. The crucial point is that θ is *nonlinear*; its particular form is often not decisive for the performance of the network.

The classification capabilities of a *single* (artificial) neuron are quite restricted (the perceptron, for instance, is a simple linear classifier). Due to the nonlinearity θ , the connection of multiple neurons to an artificial neural *network* allows for the construction of functions that go beyond that of simple linear classifiers. An artificial neural network is then a *function* that takes many inputs and produces many outputs (for classifiers, the number of outputs is typically much less than the number of inputs; but this is not the case in general, see below). This function is constructed from the elementary function (5.327) by using the output of one neuron as input of other neurons.

An example for a simple (yet common) structure is the following:



This network (or function) maps many input variables (black squares at the top) to a single output variable (black square at the bottom) via three intermediate layers of neurons. As the input of each layer is given by the output of the preceding one, there are no cycles and information flows only in one direction: from top to bottom; this is called a *feedforward network*. Note that the yellow and blue neurons are connected to *all* neurons of the preceding layer; such layers are called *fully connected* or *dense*. This is not necessary: For instance, the red neurons of the first layer connect only to few adjacent inputs.

How does such an artificial neural network operate? What shall we do with it? Recall that the network/function depends on the weights a_i^k and the bias b^k (these parameters can be different for each neuron k). Thus the network sketched above actually represents a *family* of functions with fixed input-output structure, parametrized by many parameters $\{a_i^k, b^k\}$.

A common application of feedforward networks is *image classification*. Assume that we want an automatic procedure to decide whether an image depicts a cat or not. If we interpret the color values of each pixel as an input variable, we ask for a function that takes the image as input and outputs a single (binary) value: 0 for “there is *no* cat” and 1 for “there *is* a cat.” The idea is to use the family of functions

described by the neural network and (numerically) optimize the parameters $\{a_i^k, b^k\}$ to find such a function. This optimization is referred to as (*supervised*) *training* of the artificial neural network and works as follows:

Assume that we are given a set of 50 pictures that depict a cat and another set of 50 pictures that do not. In total, we have a set of 100 pictures each with a label: 0 for “without cat” and 1 for “with cat.” This set will be our *training set*¹⁶⁷. We initialize our network with random values for $\{a_i^k, b^k\}$ and evaluate the function that is described by the network on all 100 pictures. Then we compare the output of this (random) function with the given labels of the pictures. This yields a single figure of merit for the evaluation on the whole training set, namely the percentage of pictures that are correctly classified by the network (recall that we *know* which pictures depict a cat and which do not). Mathematically, this evaluation corresponds to a function that maps a set of parameters $\{a_i^k, b^k\}$ to the interval $[0, 1]$. Our goal is to find values for $\{a_i^k, b^k\}$ such that this function yields 1. The corresponding network/function then classifies all 100 training pictures correctly (although this does not necessarily imply that the network recognizes cats on other, unknown pictures).

The popularity of artificial neural networks nowadays is mainly rooted in the development of efficient algorithms (and the availability of hardware to run them on) that vary the initially random parameters $\{a_i^k, b^k\}$ iteratively to optimize the performance on a given training set. When the performance is good enough¹⁶⁸, the training can be stopped and the resulting parameters $\{a_i^k, b^k\}$ saved for later applications of the network. If the training set is not biased (e.g., includes cats of all fur colors and not just black ones), the training can produce parameters that encode characteristic features of cats such that the network recognizes them even on pictures that were not part of the training set. This ability—to *generalize* beyond the training set—is a crucial feature of neural networks.

Now we can answer our previous question: There are *two* things we can do with an artificial neural network. First, we can *train* it by adjusting its parameters to optimize its performance on a given training set. This is the computationally expensive part. However, training has to be done only once (often on dedicated hardware like graphics cards). The result is an optimized set of parameters that specifies the network. The second step is then to *evaluate* the network with these parameters on data that goes beyond the training set. Since its evaluation reduces basically to linear algebra, it is computationally cheap and can be done on almost any platform (smartphones, surveillance cameras, etc.). The evaluation is where we really *use* the neural network productively. Training is a preliminary step to make it *usable*.

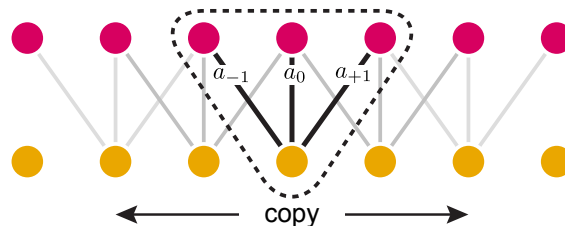
¹⁶⁷Often the labeling of the training set has to be done by hand. Large training sets of high quality are therefore valuable resources for machine learning.

¹⁶⁸It is not guaranteed that the training set can be classified perfectly—this depends on the network topology and the used optimization algorithm.

Convolutional Neural Networks

Since training is computationally expensive, optimization is important. It is clear that the time needed to optimize the parameters $\{a_i^k, b^k\}$ depends on how many there are: Less parameters lead to faster optimization and thereby allow for the evaluation of larger training sets. However, less parameters also make the family of functions that can be encoded by the network less diverse which can have negative effects on the performance of the network.

Fortunately, there are many applications where the number of parameters can be cut to a fraction without detrimental effects. Recall the “cat-classifier” from above: We asked for a classifier that recognizes cats in pictures. Whether the cat is located in the center of the picture or in the upper right corner is not relevant. In an abstract sense, the problem is *translational invariant* and we can expect the network to be translationally invariant as well. The idea is to replace the low-lying dense layers (the layers that are close to the inputs) by sparse layers with only local connections and the same weights all over the layer. Pictorially:

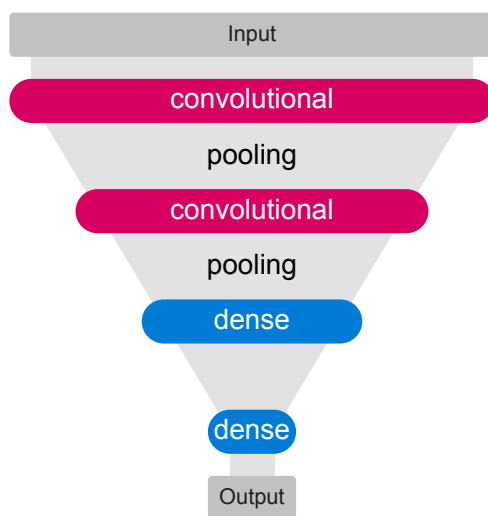


Networks with this structure are called *convolutional neural networks (CNN)* because their mathematical description as a map from one layer to the next is given by the (discrete) convolution of the input layer with a kernel function that encodes the weights. Networks that stack multiple convolutional layers are sometimes referred to as *deep convolutional neural networks*. CNNs are translationally invariant by construction and each layer is specified by a (small) set of weights that describe the local connections (the kernel, a_{-1}, a_0, a_{+1} above). Due to this reduced number of weights, they can be optimized efficiently. Furthermore, their translational invariance makes them scalable: the width of the layers can be changed without adjusting the weights of the kernel.

Convolutional layers are often followed by so called *pooling layers* to reduce the number of parameters further and to get rid of irrelevant information. A typical pooling layer groups the outputs of the previous layer into “pools” and drops all outputs except for the maximum of each pool.

For applications like image classification, one typically stacks several convolutional layers with interjacent pooling layers. The last convolutional layer is followed by few dense layers that condense all information into a fixed number of output neurons. Hence the whole network has a funnel-like structure:

NEURAL NETWORKS FOR QUANTUM ERROR CORRECTION

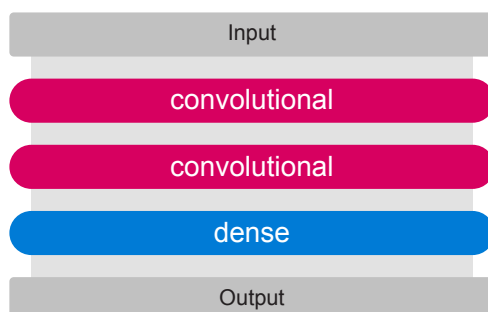


The convolutional layers typically use ReLU neurons whereas the final layer uses perceptrons (their binary outputs then encode the decision of the network).

Local Neural Networks

The most prominent application of artificial neural networks is image classification (recall the “cat-classifier”). Such networks are characterized by many inputs (the pixels of an image) that are condensed to few outputs (a fixed number of classes). This leads to the funnel-shaped structure above.

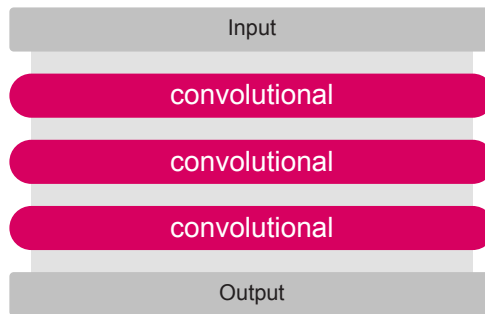
But this is just *one* application of many. Another one is the following: Imagine you want to train your neural network to play a board game like Go [396]. The input would be an “image” of the current state of the board (with three states per “pixel”: empty, white, black); as output we would like the position of the next stone to be placed on the board. Thus we need one (binary) output neuron per site of the board and the network could look like this:



The rectangular shape characterizes a function with as many outputs as inputs. Just as before, we can stack any combination of convolutional, pooling, and dense layers between the input and output layers. Note that whenever the action described by

the output depends on *global* features of the input pattern (as it is to be expected for complex games like Go), it is advisable to include at least one dense layer to enable information flow between remote neurons.

In other situations, this might not be necessary or technically unfeasible. Then we can use only convolutional (and pooling) layers:



We call networks with this structure *local neural networks*. They are scalable in width and do not require communication between neurons that are far apart (as there is no dense layer). This can be an important feature if the network is to be implemented in hardware (for instance, on neuromorphic chips [406, 407]). Below we describe how such local networks can be used—not to play games—but to decode topological quantum memories.

5.4.3 Decoding the Majorana Chain

Here we ask whether local convolutional neural networks (henceforth referred to as CNN) can be used to decode the Majorana chain quantum code (MCQC). For a discussion of the latter, see Subsection 4.2.1.

For the implementation, we use TensorFlow (v0.8) [408] with CUDA on a Nvidia GeForce GTX 1070 graphics card¹⁶⁹. The topology of the CNN is shown in Figure 5.10 and described in the following:

- 1 *Weighted copy (ReLU)*: The first (red) layer is essentially a convolutional layer with ReLU neurons. If the Majorana chain has L sites, there are $L - 1$ syndrome measurements (we use $L = 101$ for training and $L = 31$ for the evaluation). Each syndrome measurement (a single bit) is fed into 100 neurons with weights and biases $\{a_i^k, b^k\}_1$. Thus there are $100 + 100 = 200$ parameters associated with this layer in Figure 5.10.
- 2 *Split, Pad & Recombine*: We need a network topology that takes $L - 1$ binary inputs (the syndromes) and yields L binary outputs (the corrections). Therefore we have to pad the network at some point by one site. To this

¹⁶⁹Now I can justify my purchase with science (gaming is just a nice side-effect).

NEURAL NETWORKS FOR QUANTUM ERROR CORRECTION

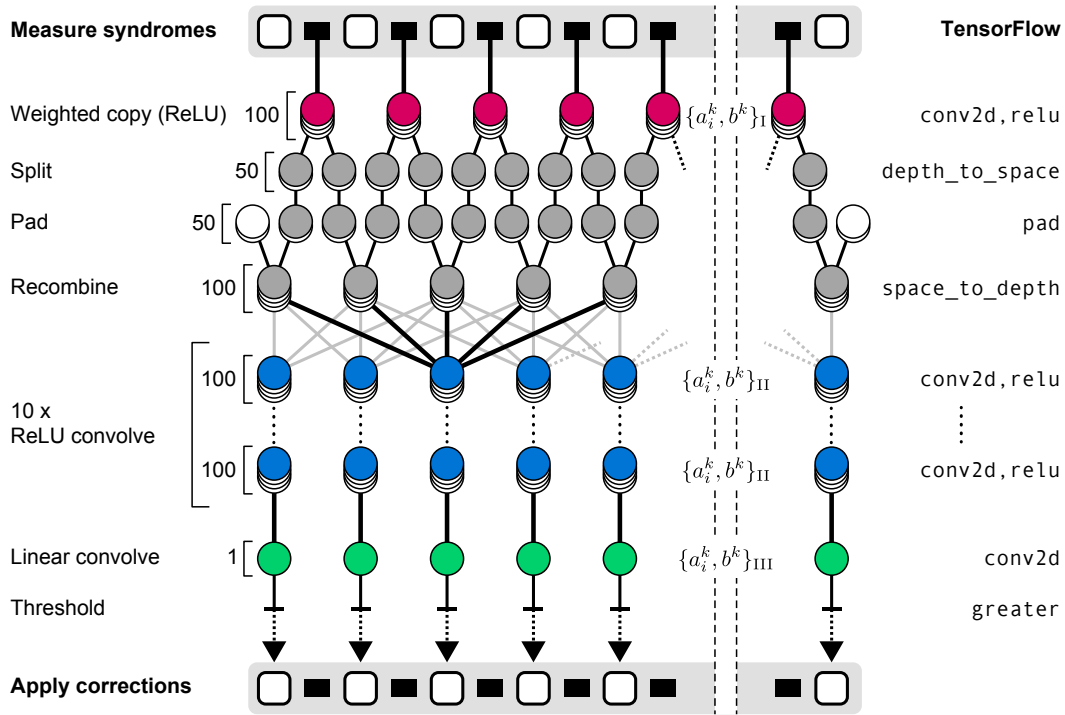


FIGURE 5.10 • MCQC decoding with a CNN—Setup. Structure of the convolutional neural network used to decode the Majorana chain quantum code. The functional role of each layer is described on the left-hand side, the key function(s) to realize this layer with TensorFlow on the right-hand side. The colored neurons are convolutional layers with weights $\{a_i^k, b^k\}_I$ (red), $\{a_i^k, b^k\}_{II}$ (blue), and $\{a_i^k, b^k\}_{III}$ (green). Except for the last (green) layer, all convolutions are realized by ReLU neurons. Gray discs denote copied values of preceding layers. Stacks of disks denote multiple neurons. Details are discussed in the text.

end, we first split the $L - 1$ stacks of 100 neurons (more precisely: their outputs) into $2(L - 1)$ stacks of 50 neurons each. Then we pad the network symmetrically by two stacks of 50 neurons on the boundaries (their output is set to zero) and subsequently recombine pairs of stacks into L stacks of 100 neurons each. Note that the output values of the neurons in the first (red) layer remain unchanged—they are just rearranged and augmented by additional zero outputs.

- 3 *ReLU convolve:* The layer of L sites with 100 neurons per site is followed by a convolutional layer of the same size (blue). Each of the 100 neurons per site of the convolutional layer takes inputs from all neurons of the 5 nearest sites of the preceding layer (bold black edges in Figure 5.10). Thus there are $100 \times (5 \times 100) + 100 = 50100$ (weight and bias) parameters $\{a_i^k, b^k\}_{II}$ associated with this layer. This convolution is applied D times in total (we set

$D = 10$). Importantly, the *same* parameters $\{a_i^k, b^k\}_{\text{II}}$ are reused for each of these layers so that the number of parameters is independent of D . The idea is to adapt the *depth* D of the CNN to its width L to allow for corrections of large error clusters. Note that due to the locality of the CNN, there is a “light cone constraint” in that corrections of sites that are far apart cannot be correlated if the depth the network is too shallow (see Section 4.2).

- 4 *Linear convolve*: The last of the D convolutional layers outputs 100 values per site. In the end, we are interested in a single, binary output per site which determines the application of corrections. Therefore we apply a last convolutional layer (green) with *one* (linear) neuron per site. Each of these neurons takes inputs from all 100 neurons of the preceding convolutional layer (blue). Thus there are $100 + 1 = 101$ parameters $\{a_i^k, b^k\}_{\text{III}}$ associated with this layer. It outputs a single real number per site which we call the *output potential* (sometimes referred to as *logits*).
- 5 *Threshold*: To decide where corrections must be applied, the CNN is completed by a threshold layer that sets output potentials below (above) some threshold r to zero (one). In our simulations, we set $r = 0$. The result is a string of L bits that we want to encode the most likely error pattern compatible with the syndromes.

The performance of decoders for quantum codes depends on the noise model that afflicts the physical qubits, and decoders that exploit characteristic correlations of a particular noise model outperform generic decoders. However, if the noise model that describes an environment is not known (or changes uncontrollably over time), it may be impossible to tailor appropriate decoders. Using neural networks has the advantage that their plasticity allows for adaptive decoding algorithms by training the network in the presence of a given environment. Detailed knowledge of the noise model is not necessary because the only quantity of relevance is the coherence time of the quantum memory (which can be measured without knowledge of the environment). Even if the environment changes over time, the network can be adjusted by additional training iterations.

Here we use a simple, uncorrelated noise model where errors are applied with probability p to all sites independently. For fixed length $L = 101$ and probability $p = 0.2$ we sample from this distribution $N = 10^5$ error patterns as training set. We then use the Adam optimization algorithm [409] (AdamOptimizer in TensorFlow) to train the network. To this end, we compute a *loss function* that quantifies for each application of the network the number of deviations from the true error pattern (recall that a perfect decoder reconstructs the error pattern that gives rise to the measured syndrome). The optimization algorithm tries to minimize this loss function on the training set by iterative variations of the $200 + 50100 + 101 = 50401$ parameters that specify the network. Note that we

NEURAL NETWORKS FOR QUANTUM ERROR CORRECTION

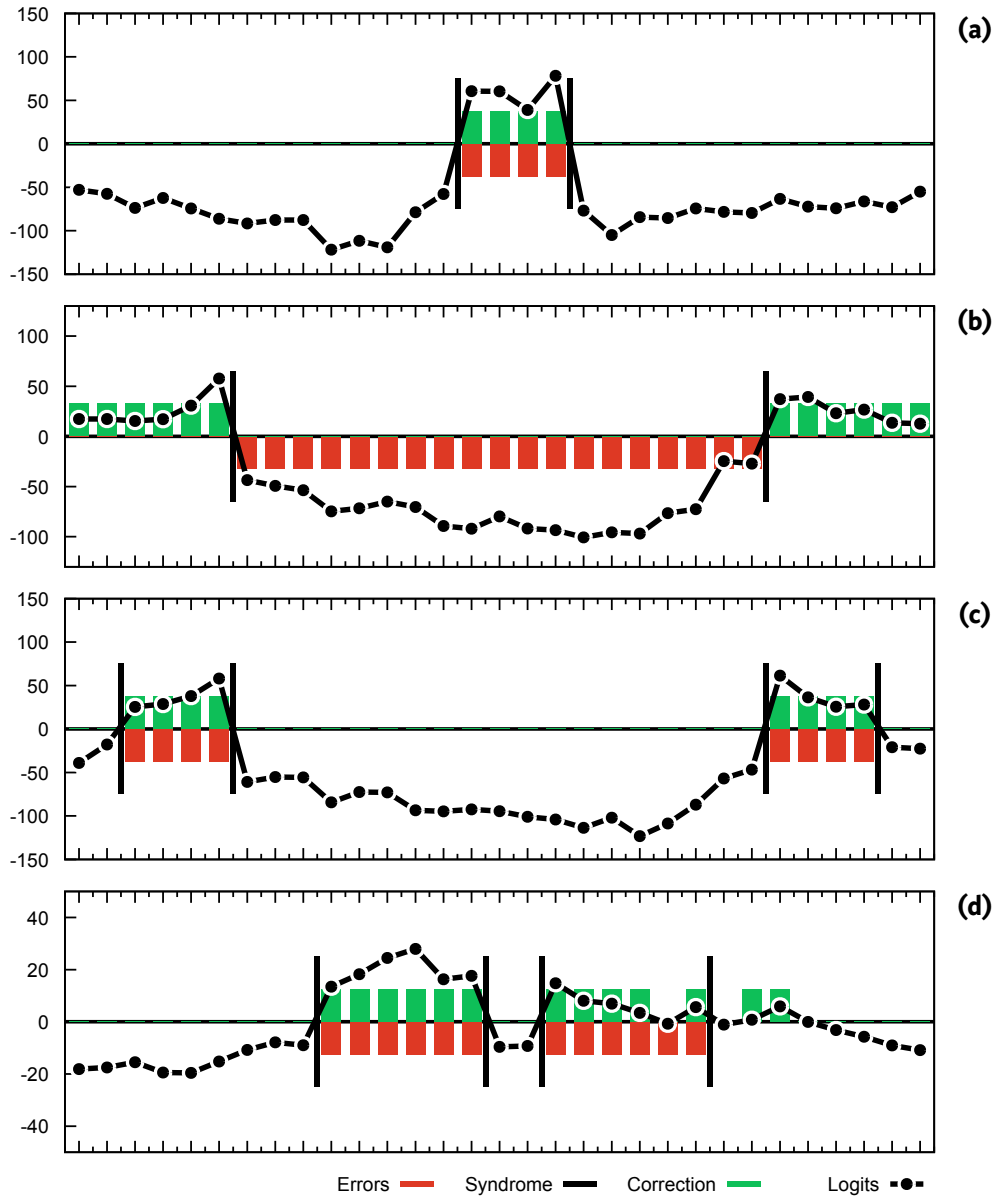


FIGURE 5.11 • MCQC decoding with a CNN—Results. We show four error patterns (red bars) on a chain of length $L = 31$ with measured syndromes (black bars), the output potential (black bullets), and the suggested correction operations (green bars). **(a)** Single minority island of errors; all errors are successfully corrected. **(b)** Single majority island of errors; the majority vote is performed correctly such that a logical error is introduced. **(c)** Two minority islands at opposite ends of the chain; the majority vote is performed correctly and the errors are canceled successfully. **(d)** Two close-by minority islands. The majority vote is performed *almost* correctly, but the right-hand cluster is not completely eliminated due to three erroneous correction operations.

train a network of width $L = 101$ and use the resulting weights for a network of width $L = 31$ to illustrate its performance (see below). This scalability is a feature of the convolutional structure of the network.

We do not provide quantitative results for the performance of the CNN as decoder of the MCQC; instead we show exemplary evaluations for some error patterns in Figure 5.11. They demonstrate that the training was successful in that the CNN applies essentially (an approximate version of) majority voting—at least for small error clusters as in Figure 5.11 (a). Even multiple clusters can be erased successfully if they are well-separated, Figure 5.11 (c). However, adjacent clusters tend to confuse the network and lead to correction errors, Figure 5.11 (d). Note that due to the error probability $p = 0.2 < 0.5$ used for the construction of the training set, the CNN learned to expect a *minority* of error-afflicted sites that match the syndrome; its decision in Figure 5.11 (b) is therefore correct in that it removes all syndromes but introduces a logical error. We checked that the CNN operates in the same fashion for arbitrary code sizes $L \leq 101$ (it even performs reasonably well for $L > 101$ if L is not too large).

In conclusion, the CNN seems to implement the following two rules: First, the output potential changes sign at the position of syndromes. And second, small intervals between syndromes favor *positive* output potentials. In many cases (and for small error rates), this leads to a successful decoding of the MCQC.

5.4.4 Majority Voting in Two Dimensions

If the one-dimensional CNN in Figure 5.10 can perform majority voting, is this also possible in a two-dimensional setup? Note that a two-dimensional square lattice of binary sites with syndromes on the edges (given by the sum modulo-2 of the two adjacent sites) and the two syndrome-free states in which all sites are either 0 or 1, does not map to a *quantum* code but to the *classical* (repetition) code that can be identified with the two ground states of the 2D Ising model. Accordingly, syndromes are identified with “domain walls” that separate clusters of opposite “spins.”

The implementation of this two-dimensional setup was originally intended as preliminary step towards a neural decoder for the toric code (where syndromes are not string- but point-like [45]). Since the focus then shifted to Chapter 4 and Ref. [3], such a decoder was never realized. As the toric code is most conveniently realized on a square lattice with periodic boundary conditions (a *torus*), we came up with a periodic CNN for the classical repetition code above. Periodic network topologies seem to be uncommon¹⁷⁰ and their realization with TensorFlow is cumbersome (but possible). However, once the system of binary sites is placed on a lattice without boundaries, the rather technical padding in Figure 5.10 is no longer necessary.

¹⁷⁰This is reasonable as most images are *not* periodic.

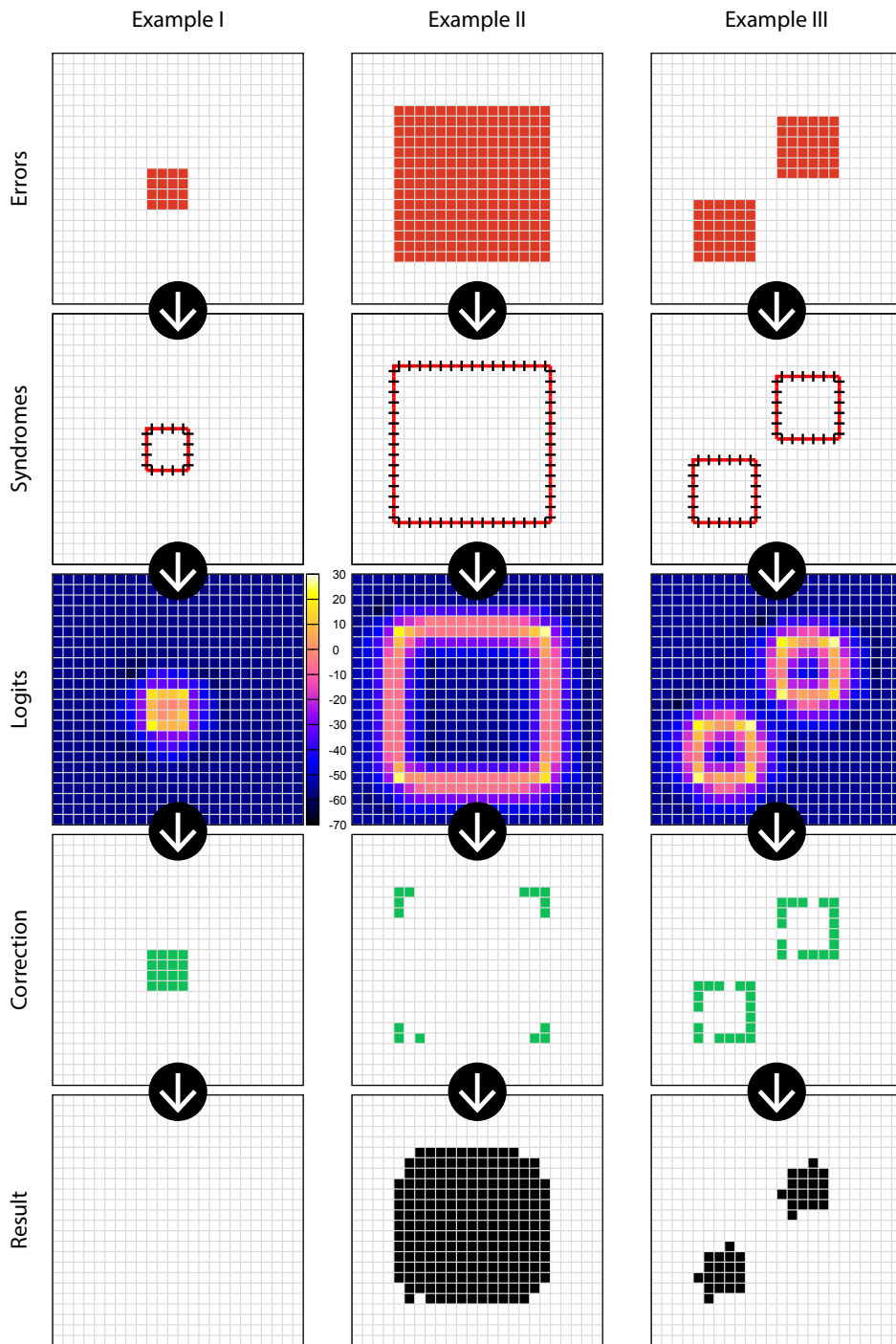


FIGURE 5.12 • 2D majority voting with a CNN—Examples. Three examples (columns) of two-dimensional error patterns: (I) a single small cluster, (II) a single large cluster, and (III) two small clusters. From top to bottom are shown: the errors (red fields), the syndrome pattern (red lines), the output potential (logits), the corrective actions (green fields), and the result of the correction (black fields).

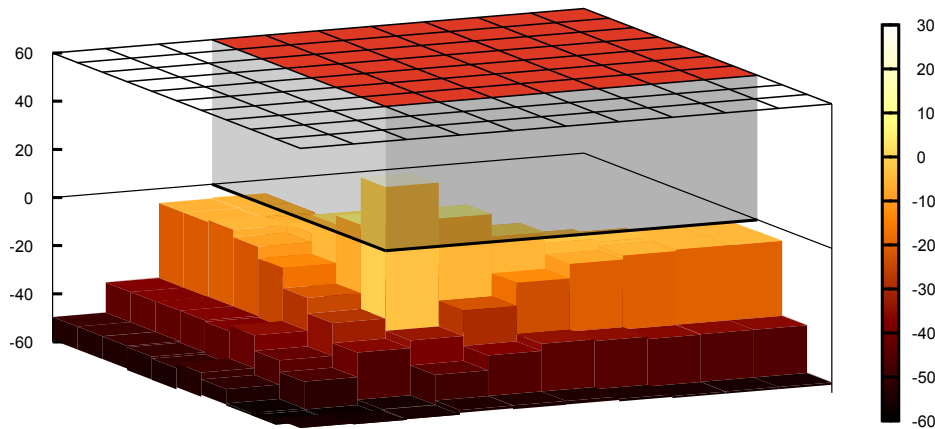


FIGURE 5.13 • 2D majority voting with a CNN—Corner erosion. Shown is the output potential (logits) color-coded at the corner of a rectangular domain of errors (red area). The domain wall is projected onto the bar graph (black line). The CNN applies corrections when the output potential becomes positive. The CNN learned to perform corner erosion and applies corrective actions on the convex side of the corner; on the concave side, the output potential is strongly suppressed. Note how the CNN becomes critical close to straight domain walls where the output potential approaches zero from below.

Indeed, whereas before we had to map $L - 1$ inputs to L outputs, now we have to map $2L^2$ inputs to L^2 outputs (for a lattice of $L \times L$ sites) because there are exactly two edges per site (the ones coming from north and east, for instance).

The input of the new CNN is therefore a $L \times L$ array of *two* binary variables per site. The topology of the network is then essentially a two-dimensional version of Figure 5.10: First, we spread these two values per site onto 100 ReLU neurons with a convolutional layer. Then we apply D ReLU convolutions with the same structure of connections as before. Finally, we condense the 100 neurons per site with a linear convolution to a single real number, the output potential. The decision of the network for each site is then determined by comparison of this potential with the threshold $r = 0$.

We train the network again with a training set of $N = 10^5$ error patterns drawn from an uncorrelated Bernoulli distribution with $p = 0.2$ on a 25×25 square lattice. Here we focus on a shallow network with only $D = 2$ convolutional layers. Since $p = 0.2 < 0.5$, we expect the network to suggest error patterns that satisfy the syndrome and use a minimum number of errors. However, due to the shallow structure of the network with only local connections, this must fail for large clusters (because true majority voting is a *global* operation).

Figure 5.12 shows three exemplary evaluations of the CNN. For each example, the panels show (1) the error pattern, (2) the input of the network (the syndrome), (3) the output potential (the logits), (4) the correction produced by the threshold, and (5) the error pattern after the application of the correction. As expected, the

small cluster in Example I is completely erased, in accordance with majority voting. The larger clusters of Examples II and III reveal the locality of the network, though: Deep within the error clusters the network does not apply corrections because it cannot be aware of the domain walls that are too far away. Nevertheless, the suggested corrections *reduce* the numbers of errors in both examples by eroding the error clusters at the corners. Although the CNN is not capable of “single-shot” corrections of large clusters, applying the network repeatedly erodes the clusters and cleans the system eventually.

The rule found by the CNN that makes this possible is simple: The *curvature* of domain walls is used locally to clean *convex* clusters of errors by eroding corners; iterative application of this local rule implements a global majority vote. In Figure 5.13 we plot the output potential in the vicinity of the corner of an extended error cluster. We notice that the potential is strongly suppressed everywhere except close to domain walls where it approaches the threshold from below. If the domain wall is straight, the potential stays there and no corrections are applied as the network cannot decide which side represents the minority. When the domain wall is curved, the potential *decreases* on the *concave* side and *increases* (above the threshold) on the *convex* side. The applied corrections then reduce the curvature of the domain wall by eroding the corner.

5.5 Aperiodic Stabilizers

This section is unrelated to the main part of this thesis and originates from the author’s interest in topological quantum codes. Its primary result is the construction of an aperiodic stabilizer code derived from *Wang tilings*—aperiodic tilings of Euclidean space that preceded the discovery of quasicrystals such as, for instance, the iconic Penrose tiling. The approach taken may also serve as a recipe for the construction of systems that break translational invariance in a systematic way.

In addition, the complexity of these “Wang stabilizers” serves as entry point of Section 5.6. In the current section, familiarity with the stabilizer formalism for quantum codes is recommended, see Chapter 10.5 of Ref. [264] for a thorough introduction.

5.5.1 Motivation

The stabilizer framework is a powerful algebraic tool to describe a restricted but interesting class of quantum codes [410–412], see also Ref. [264] for an introduction. Here, a quantum code that encodes k *logical* qubits into n *physical* qubits is simply a 2^k -dimensional linear subspace \mathcal{C} of the n -qubit Hilbert space $\mathcal{H} = \bigotimes_{i=1}^n \mathbb{C}^2$. The general idea of quantum codes is to tailor the states in \mathcal{C} so that (sparse) errors on the physical qubits can be detected and corrected by a specific set of projective measurements and unitary gates, see Section 4.2 in Chapter 4 for an example. An intensively studied class of codes/subspaces can be described by *stabilizer groups*: Let \mathcal{P} denote the Pauli group on n qubits, i.e., the group generated by arbitrary products of Pauli matrices σ_i^α for $\alpha \in \{x, y, z\}$ and $i = 1, \dots, n$. A stabilizer (group) \mathcal{S} is an abelian subgroup of \mathcal{P} that does not contain $-\mathbb{1}$. Its corresponding quantum (stabilizer) code is defined as the linear subspace

$$\mathcal{P}\mathcal{S} = \{ |\Psi\rangle \in \mathcal{H} \mid \forall S \in \mathcal{S} : S|\Psi\rangle = |\Psi\rangle \}, \quad 5.330$$

i.e., the subspace of all states that are invariant under the action of all operators in the stabilizer group \mathcal{S} . The idea is to describe the *states* in $\mathcal{P}\mathcal{S}$ (which can be highly non-trivial and strongly entangled) indirectly by their stabilizing *operators* in \mathcal{S} .

A particularly interesting and pedagogically useful example of a stabilizer code is the famous *toric code* [45]. For its construction, one envisages physical qubits placed on the edges of a two-dimensional square lattice that is embedded into a torus. The stabilizer \mathcal{S} of the toric code is then generated by star operators $A_s = \prod_{e \in s} \sigma_e^x$ on sites s and plaquette operators $B_p = \prod_{e \in p} \sigma_e^z$ on faces p [where $e \in s$ ($e \in p$) denotes the four edges that emanate from site s (border face p)]. The stabilizer formalism reveals that the corresponding codespace $\mathcal{P}\mathcal{S}$ is four-dimensional and encodes two logical qubits.

To bridge the gap between quantum information theory and condensed matter physics, one can consider the Hamiltonian

$$H_{\text{TC}} = - \sum_{\text{all sites } s} A_s - \sum_{\text{all faces } p} B_p \quad 5.331$$

and its ground states on the mentioned lattice of qubits (or spins). It is easy to see that the ground state space of H_{TC} is identical to the codespace $\mathcal{P}\mathcal{S}$. Thus the abstract concept of a quantum code is realized as ground state space of a Hamiltonian: *one can encode quantum information into the ground states of H_{TC}* . Following this line of thought, one finds that the abstract *errors* on the quantum code translate into local *excitations* of the Hamiltonian H_{TC} . This leads to an intriguing idea: If one implements H_{TC} and stores quantum information in its ground state space, the energy necessary to create errors might be enough to prevent them from accumulating even at finite temperature. This would render the *active* measurement and correction of errors obsolete: the implementation with H_{TC} is *self-correcting*.

Unfortunately it can be shown that this approach fails for the toric code in two dimensions [311, 413, 414] (see also Ref. [50] and references therein). This thermal fragility is due to the existence of deconfined point-like excitations (or, equivalently, string-like logical operators) that can be used to implement gates on the encoded qubits with finite energy penalty¹⁷¹. Ever since, the quest for a truly self-correcting quantum memory in three dimensions or less became an active area of research, see Refs. [50, 174, 303] for a review.

By now, several no-go theorems in two [415] and three [416–418] dimensions are known which preclude the existence of self-correcting quantum memories under various assumptions (see Ref. [50] for a review). While in *two* dimensions the existence of self-correcting stabilizer codes is essentially precluded [311, 415], in *three* dimensions there are practicable loop holes to sidestep all (known) no-go theorems: In Ref. [416] it is shown that translationally invariant codes with a size-independent number of logical qubits have constant energy barriers. In Ref. [417] the energy barrier is proven to be at most logarithmically divergent for translationally invariant systems (without restrictions on the codespace dimension), and the results of Ref. [418] show that codes with locality-preserving non-Clifford gates cannot have diverging energy barriers.

If we focus exclusively on the *storage* of quantum information, Ref. [417] suggests that truly self-correcting stabilizer codes in three dimensions—if they exist—break translational invariance. Indeed, several codes are known that sidestep these no-go theorems and exhibit diverging energy barriers. Haah’s *cubic code* [307, 419] is translational invariant with a growing number of logical qubits; consistent with Refs. [416, 417], it features a logarithmically divergent energy barrier. The *welded code* proposed by Michnicki [308] and the *fractal code* of Brell [309] break translational invariance and feature polynomially growing energy barriers (which shows that

¹⁷¹The energy barrier that needs to be overcome for gates on logical qubits that are implemented by a sequence of local operations does not increase with the system size.

translational invariance is a crucial ingredient for the no-go theorem of Ref. [417]). For various reasons, none of these codes is proven to be self-correcting in the strict sense (which means that the lifetime of the encoded qubits grows exponentially with the system size $L \rightarrow \infty$).

The fact that aperiodic stabilizers differ fundamentally from their periodic cousins makes the former interesting to study. In this section, we present a method to derive such stabilizers from aperiodic tilings known as *Wang tilings* [420, 421]. Although we are ultimately interested in three-dimensional codes, here we demonstrate the approach in two dimensions for the sake of simplicity. A generalization to three dimensions is possible but cumbersome.

Note — We want to emphasize that the concept of self-correcting quantum memories is not only interesting for their potential application as “quantum hard drives.” The very existence of a truly self-correcting Hamiltonian in three dimensions had profound implications for the quantum-to-classical transition in that it blurs the border between the realms of quantum mechanics and classical physics to an extent that goes beyond any “quantum weirdness” witnessed so far. Figuratively speaking, the existence of such systems entails the possibility that when you go hiking and pick up a chunk of rock, this piece of thermalized matter could host—despite its classical appearance—a bunch of qubits that hid coherently in delocalized degrees of freedom for the last ten thousand years. (It is amusing that on the *classical* level, this situation is realized in nature: There are minerals that can store a single bit—the direction of earth’s magnetic field—for geologic timescales.) Finally, we point out that it has been argued that the existence of self-correcting quantum memories might conflict with the laws of thermodynamics [422].

5.5.2 General Setup

Let us first describe the general setup and fix the notation. We consider infinite, D -dimensional cubic lattices $\mathcal{L} = \mathbb{Z}^D$ (in Subsection 5.5.3 we focus on $D = 2$) and associate a local Hilbert space $\mathcal{H}_x = \bigotimes_{i=1}^K \mathcal{H}_{xi} = (\mathbb{C}^2)^{\otimes K}$ of K qubits with each site $\mathbf{x} = (x_1, \dots, x_D) \in \mathcal{L}$. Thus we have $\mathcal{H} = \bigotimes_{\mathbf{x} \in \mathcal{L}} \mathcal{H}_x$ for the total state space of the systems under consideration. The local standard basis is written as $|q_{x1}, \dots, q_{xK}\rangle$ for $\mathbf{x} \in \mathcal{L}$ and $q_{xi} \in \{0, 1\}$. Let \mathcal{P} , \mathcal{P}_x , and \mathcal{P}_{xi} denote the Pauli groups acting on the global state space $\mathcal{H} = \bigotimes_{\mathbf{x}} \mathcal{H}_x$, the site-local state spaces $\mathcal{H}_x = \bigotimes_i \mathcal{H}_{xi}$, and the single-qubit state spaces $\mathcal{H}_{xi} = \mathbb{C}^2$, respectively.

We are interested in locally generated stabilizer groups $\mathcal{S} < \mathcal{P}$, i.e., abelian subgroups of \mathcal{P} that do not contain $-\mathbb{1}$ and are generated by a (possibly finite) set of \mathcal{L} -local operators $A_n \in \mathcal{P}$, write $\mathcal{S} = \langle A_1, A_2, \dots \rangle$. The \mathcal{S} -invariant subspace $\mathcal{P}\mathcal{S} < \mathcal{H}$, with $|\Psi\rangle \in \mathcal{P}\mathcal{S} \Leftrightarrow S|\Psi\rangle = |\Psi\rangle$ for all $S \in \mathcal{S}$, is called *protected subspace* and completely described by \mathcal{S} .

To describe the structure of the generators A_n , we need additional notation. Let $\mathbf{p} = (p_1, \dots, p_D) \in (\mathbb{Z} + \frac{1}{2})^D \equiv \mathcal{L}'$ describe the center of a D -hypercube in \mathcal{L} (squares for $D = 2$, cubes for $D = 3$). We write $\mathbf{p}[\alpha_1, \dots, \alpha_D]$ for arbitrary $d \leq D$ -dimensional hypercubic faces of \mathbf{p} where $\alpha_i \in \{\bullet, +, -\}$ defines the constraints on points in the i th direction: \bullet = no constraint, \pm = in or against the orientation of the i -axis. For instance, in $D = 2$, $\mathbf{p} = (p_1, p_2)$ denotes a square and $\mathbf{p}[+, \bullet]$ denotes its right-hand edge. The entire square is $\mathbf{p}[\bullet, \bullet]$ and the upper right corner can be addressed by $\mathbf{p}[+, +]$. In general, the 2^D corners \mathbf{x} of \mathbf{p} , write $\mathbf{x} \in \mathbf{p}$ for short, can be addressed by $\mathbf{x} = \mathbf{p}[\pm, \dots, \pm]$.

The stabilizers we are interested in are generated by two distinct types of generators, denoted as T and G . The former are called (*stabilizer*) *tiles* and are associated with a specific D -dimensional hypercube \mathbf{p} , acting non-trivially on its corner Hilbert space $\bigotimes_{\mathbf{x} \in \mathbf{p}} \mathcal{H}_{\mathbf{x}}$ only:

$$T_{\mathbf{p}}^{(k)} = \prod_{\alpha} \prod_{i=1}^K \sigma_{\mathbf{p}[\alpha]i}^{t_{\mathbf{p}}^{(k)}(\alpha;i)}. \quad 5.332$$

Here, $t_{\mathbf{p}}^{(k)}(\alpha;i) \in \{0, x, y, z\}$ encodes the tile with Pauli matrices $\sigma_{\mathbf{x}i}^{x,y,z}$ and $\sigma_{\mathbf{x}i}^0 \equiv \mathbb{1}_{\mathbf{x}i}$. The first product \prod_{α} is shorthand for $\prod_{\alpha_1=\pm} \cdots \prod_{\alpha_D=\pm}$ and the index k labels different tiles that can be placed on the same hypercube \mathbf{p} .

The other generators (G) are called *gauge constraints* and are of technical importance only (but not crucial for the construction that follows): Their job is to “freeze out” site-local excess degrees of freedom. Therefore they act on sites \mathbf{x} and are of the form

$$G_{\mathbf{x}}^{(k)} = \prod_{i=1}^K \sigma_{\mathbf{x}i}^{g_{\mathbf{x}}^{(k)}(i)}, \quad 5.333$$

where k indicates the possibility of more than one gauge constraint per site. Again, $g_{\mathbf{x}}^{(k)}(i) \in \{0, x, y, z\}$ encodes the action of $G_{\mathbf{x}}^{(k)}$ in terms of Pauli matrices.

The generic structure of stabilizers \mathcal{S} that will be of interest in the following is that of a tiling of a (possibly finite) patch $\mathcal{M} \subseteq \mathcal{L}$ by stabilizer tiles $T_{\mathbf{p}}^{(k)}$, in addition with a site-local completion by gauge constraints $G_{\mathbf{x}}^{(k)}$ that depends on the tiling $T_{\mathbf{p}}^{(k)}$. If $k = 1, \dots, M$, we refer to the tiling as M -layered. To describe such structures more conveniently, we need a bit more notational fine-tuning: If \mathbf{e}_i denotes the unit vector in the i th direction, the $2D$ adjacent D -hypercubes of \mathbf{p} can be described by $\mathbf{p}' = \mathbf{p} \pm \mathbf{e}_i$. The common boundary $(D - 1)$ -hypercube is given by $\mathbf{p}[\dots, \bullet, \alpha_i, \bullet, \dots]$ with $\alpha_i = \pm$, we write $\mathbf{p}[\alpha_i] = \mathbf{p}[\pm_i]$ for short. Then we can address the $(D - 1)$ -dimensional boundary components of the stabilizer tiles as

$$T_{\mathbf{p}[\beta_d]}^{(k)} = \prod_{\substack{\alpha \\ \alpha_d = \beta_d}} \prod_{i=1}^K \sigma_{\mathbf{p}[\alpha]i}^{t_{\mathbf{p}}^{(k)}(\alpha;i)}. \quad 5.334$$

If we ignore the gauge constraints for the time being, for \mathcal{S} to be a stabilizer, it is necessary (but not sufficient) that for all \mathbf{p} and $\pm e_i$ adjacent tiles commute: $[T_{\mathbf{p}}^{(k)}, T_{\mathbf{p} \pm e_i}^{(l)}] = 0$ for $i = 1, \dots, D$ and $k, l \in \{1, \dots, M\}$. With the notation above, this condition can be written as $[T_{\mathbf{p}[\pm i]}^{(k)}, T_{\mathbf{p} \pm e_i[\mp i]}^{(l)}] = 0$ since the commutativity of adjacent tiles imposes only restrictions on their contiguous boundary components. In general, there are similar restrictive conditions on all pairs of stabilizer tiles that touch at d -dimensional hypercubes for all $d = 0, \dots, D - 1$. If the tiling is multi-layered ($M > 1$), one has an additional constraint $[T_{\mathbf{p}}^{(k)}, T_{\mathbf{p}}^{(l)}] = 0$ for $d = D$.

Conventional, translationally invariant stabilizers are given by generators that do not depend on position, i.e., $t_{\mathbf{p}}^{(k)}(\boldsymbol{\alpha}; i) \equiv t^{(k)}(\boldsymbol{\alpha}; i)$ for all $\mathbf{p} \in \mathcal{L}'$ (the same for gauge constraints). A non-trivial example in $D = 2$ is the toric code [45] for which $K = 1$, $t(\pm_1, \pm_2; i = 1) = x$ and $t(\pm_1, \mp_2; i = 1) = z$ (without gauge constraints)¹⁷². Since this stabilizer is single-layered ($M = 1$), we can drop the index k . Another example in $D = 3$ is the cubic code [419] with $K = 2$ qubits per site and $M = 2$ layers of tiles $T_{\mathbf{p}}^{(1)}$ and $T_{\mathbf{p}}^{(2)}$ (again without gauge constraints).

In this section, we are interested in tilings of \mathcal{L} that systematically *break* translational invariance, i.e., $t_{\mathbf{p}}^{(k)}(\boldsymbol{\alpha}; i)$ depends explicitly on \mathbf{p} but nevertheless is chosen from a small set $\mathfrak{T} = \{t_1, \dots, t_N\}$ of $N \ll 4^{K2^D}$ (*stabilizer*) *templates*¹⁷³ t_n . For simplicity, we focus on single-layered tilings in the following ($M = 1$). Then, a (*stabilizer*) *tiling* is a function $\lambda : \mathcal{L}' \rightarrow \{1, \dots, N\}$ that assigns one of N templates to each D -hypercube of \mathcal{L} via $t_{\mathbf{p}} \equiv t_{\lambda(\mathbf{p})}$ such that the corresponding tiles $T_{\mathbf{p}}$ commute pairwise. λ is translationally invariant in the i th direction if there is an integer a_i such that $\lambda(\mathbf{p}) = \lambda(\mathbf{p} + a_i e_i)$ for all \mathbf{p} . Here we are interested in template sets \mathfrak{T} and stabilizer tilings λ that break translational invariance in all D directions while still being deterministic (i.e., we do not consider random ensembles of tilings).

In addition, we demand that there is an efficient algorithm to “grow” the tiling λ successively if one starts from an arbitrary “seed hypercube” \mathbf{p}_0 . I.e., given $\lambda(\mathbf{p})$, there is an efficient algorithm to compute $\lambda(\mathbf{p} \pm e_i)$ for all i and \mathbf{p} . This ensures that the construction of the stabilizer (or Hamiltonian) is not rendered impossible by computational complexity (we stress that the evaluation of its *properties* can be intractable nevertheless).

¹⁷²We use a representation of the toric code with a single type of generators and qubits on sites (instead of edges); it is unitarily equivalent to the conventional representation with two types of generators (viz., plaquette and star operators).

¹⁷³Note the difference between templates and stabilizer tiles: The latter are *operators* that act on a specified subset of qubits on the lattice. Templates are mere “construction plans” for such operators without any reference to a particular hypercube \mathbf{p} .

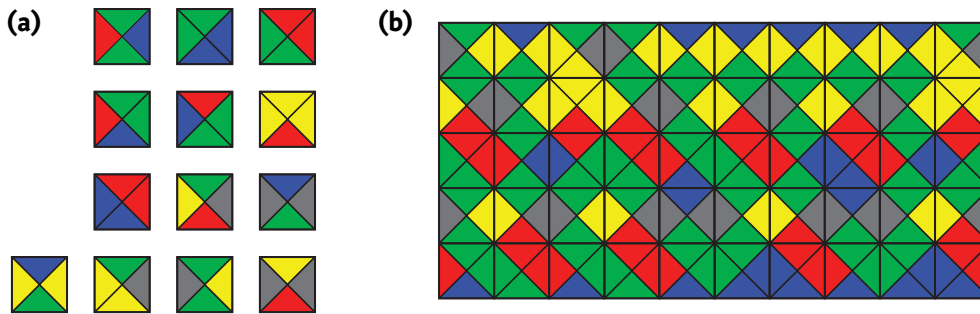


FIGURE 5.14 • Culik tiles. The instance of aperiodic Wang tiles used for the construction of stabilizers in this section. **(a)** Tile set $\mathcal{T}_{\text{Culik}}$ of 13 tiles with 5 colors from Ref. [423] dubbed *Culik tiles*. The orientation of the tiles is fixed. **(b)** Exemplary patch of a valid tiling. The patch can be extended to infinity in all directions without periodicity.

Note — The latter constraint actually leads to a more general, conceptual question: Which properties qualify a Hamiltonian¹⁷⁴ as “physically realistic”? If we focus on Hamiltonians defined on a lattice in $D \leq 3$ dimensions, a common answer is *locality*, i.e., the Hamiltonian is required to be a sum of terms that act non-trivially only on bounded regions of space. For translational invariant Hamiltonians, this seems to be sufficient. But once translational invariance is dropped, one might encounter local Hamiltonians the mere *construction* of which is computationally intractable. This prevents not only the numerical simulation of such systems—even their *implementation* in nature is impossible if we assume that “intractable” refers to arbitrary physical systems as computational frameworks. Such Hamiltonians describe systems that are unphysical from an operational point of view: We can neither simulate nor experimentally study them.

5.5.3 Wang Stabilizers

Wang Tiles

Wang tiles are (abstract) square tiles with colored edges that can be placed on the two-dimensional, infinite square lattice \mathbb{Z}^2 , see Figure 5.14 for an example. A (possibly finite) tiling of this kind is called *valid* if contiguous edges have the same color, Figure 5.14 (b). The set of Wang tiles $\mathcal{T} = \{t_1, \dots, t_N\}$ is fixed and each tile t_i can be used infinitely often to tile the plane \mathbb{Z}^2 . Rotating the tiles in \mathcal{T} is not allowed (this is not a fundamental restriction as one can extend \mathcal{T} by rotated versions of tiles if desired).

¹⁷⁴With “Hamiltonian” we actually refer to a *sequence* $(H_L)_{L \in \mathbb{N}}$ of Hamiltonians which is necessary for the concept of a thermodynamic limit $L \rightarrow \infty$.

This construction was proposed by Hao Wang [420]. The tile set \mathcal{T} determines whether a tiling of the entire plane \mathbb{Z}^2 is possible. For example, if \mathcal{T} contains a single tile with all edges the same color, such a tiling is clearly possible. However, if this single tile is *blue* on the left and top but *red* on the right and bottom, one cannot even place two of them side by side without violating the rule that colors must match up. Wang conjectured [420] that a given tile set \mathcal{T} can tile the entire plane if and only if there exists a *periodic* tiling. This conjecture was disproved by Berger [421] with an ingenious application of results from computability theory (namely, the undecidability of the halting problem). It follows that there exist tile sets which allow for tilings of the plane none of which is periodic (such tile sets are called *aperiodic*). This remarkable result kick-started the research that eventually led to the discovery of quasicrystals, first in theory and later in real materials.

Over the years, aperiodic tile sets with fewer and fewer tiles (and colors) were constructed. Here we use the tile set $\mathcal{T}_{\text{Culik}}$ with 13 tiles and 5 colors introduced by Culik [423] and shown in Figure 5.14 (a). We refer to this particular set of Wang tiles as *Culik tiles*. Culik proved that it allows for tilings that are necessarily aperiodic; a small patch is shown in Figure 5.14 (b). In the following, we demonstrate how to construct a stabilizer group that is generated by 13 templates, and that realizes this aperiodic tiling in a sense to be defined next.

Colorability of Stabilizer Templates

The idea is simple: We aim at a set $\mathfrak{T} = \{t_1, \dots, t_{13}\}$ of stabilizer templates that act on a $D = 2$ -dimensional square lattice with K qubits per site, such that there is a one-to-one correspondence between templates t_i and Culik tiles t_i : Placing tile t_i adjacent to tile t_j is allowed if and only if the operators t_i and t_j commute for the same placement. If we can find a template set \mathfrak{T} with this property for all combinations and placements of tiles, aperiodic tilings of the Culik tiles can be read as construction plans for aperiodic stabilizer groups. Most importantly, these stabilizers can be grown deterministically in all directions to cover the entire two-dimensional lattice without any periodicity (thus the limit $L \rightarrow \infty$ is well-defined).

To achieve this, we have to construct stabilizer templates t_i that can be labeled by colors on their four edges so that stabilizer tiles of equal (different) colors on contiguous edges commute (anticommute). Since we are not allowed to rotate tiles, the problem decomposes into two subproblems, namely the placement in x - and y -direction, respectively. In Figure 5.15 we illustrate both cases by drawing schematic tiles in two columns/rows to form the vertices of a bipartite graph. For a given template set \mathfrak{T} , we can now probe the commutativity of all operators in the first column (row) with the operators in the second column (row) for the shown orientation of tiles. Whenever two operators commute, we connect their corresponding boxes in the graph by an edge. This yields, for each direction, a bipartite graph that is typically not connected (i.e., decomposes into disconnected subgraphs).

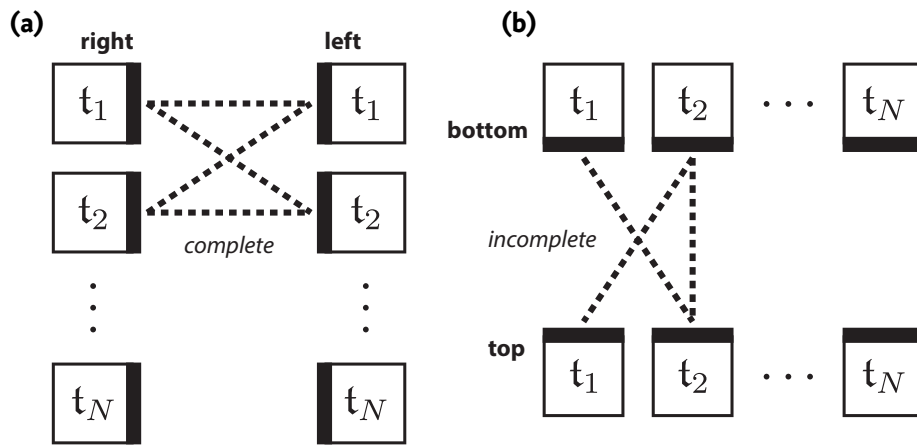


FIGURE 5.15 • Requirements for colorability. Edges connecting templates t_i with t_j indicate commutativity with respect to the shown placement of tiles. For placements in x - (a) and y -direction (b), this gives rise to separate, bipartite commutativity-graphs (which are not necessarily connected). If and only if *all* connected components are *complete* bipartite graphs, the tile set \mathfrak{T} is colorable and each connected component corresponds to a distinct color.

Is there a way to label the edges of stabilizer templates by colors such that they commute if and only if the colors are equal on contiguous edges? The generic answer is “No” for a simple reason: “Having the same color” is clearly an equivalence relation; in particular, it is *transitive*. For instance [see Figure 5.15 (b)], if the bottom-color of t_1 equals the top-color of t_2 which equals the bottom-color of t_2 which equals the top-color of t_1 , we can conclude that top- and bottom-color of t_1 are identical. However, if we have four operators A, B, C, D with a chain of commutation relations

$$[A, B] = 0 \quad \text{and} \quad [B, C] = 0 \quad \text{and} \quad [C, D] = 0, \quad 5.335$$

we *cannot* conclude that $[A, D] = 0$ since commutativity is not a transitive relation (e.g., set $A = \sigma^z, B = C = \mathbb{1}$ and $D = \sigma^x$). In Figure 5.15 (b) this is illustrated by a missing link between the bottom of t_1 and the top of t_1 .

We conclude that coloring is only consistent when the commutation relations of top/bottom- and left/right-pairs of operators are transitive. In the graph-theoretic description of Figure 5.15, this condition is met whenever all connected components of the commutativity-graphs are *complete* bipartite¹⁷⁵ subgraphs [as in Figure 5.15 (a)]. A set of stabilizer templates \mathfrak{T} that satisfies this condition is called *colorable*, and each connected component of the commutativity-graphs is identified with a distinct color (where colors used for top/bottom edges can be reused for left/right edges as

¹⁷⁵A *complete bipartite graph* has vertices of two colors such that all pairs with different colors are connected by an edge and there is no edge connecting vertices of the same color.

rotation of tiles is forbidden). Here we are interested in colorable sets \mathfrak{T} that can be assigned the color scheme of Culik tiles in Figure 5.14 (a). The question is whether this is possible and, if so, how many qubits K per site are necessary.

Solving for Stabilizer Templates

Here we describe a method to construct a set of stabilizer templates \mathfrak{T} from a given tile set \mathcal{T} . We do not claim that this method is the only and/or most efficient one. However, we demonstrate its viability by constructing a colorable set of $N = 13$ stabilizer templates that realize the Culik tiles with $K = 9$ qubits per site. We show that, for this particular tile set and the applied constructive procedure, there are no solutions with fewer qubits.

We start with a convenient notation for the stabilizer templates $\mathfrak{T} = \{t_1, \dots, t_N\}$ on a square lattice. Their elementary factors are on-site corner templates $t_i^{\text{TL}}, t_i^{\text{TR}}, t_i^{\text{BL}}, t_i^{\text{BR}}$ (acting on K qubits each) that can be combined to edge templates $t_i^{\text{L}}, t_i^{\text{R}}, t_i^{\text{T}}, t_i^{\text{B}}$; schematically we can write

$$t_i = \begin{bmatrix} t_i^{\text{L}} & t_i^{\text{R}} \end{bmatrix} = \begin{bmatrix} t_i^{\text{T}} \\ t_i^{\text{B}} \end{bmatrix} = \begin{bmatrix} t_i^{\text{TL}} & t_i^{\text{TR}} \\ t_i^{\text{BL}} & t_i^{\text{BR}} \end{bmatrix}, \quad 5.336$$

where formally

$$t_i = \underbrace{t_i^{\text{TL}} \cdot t_i^{\text{TR}}}_{t_i^{\text{T}}} \cdot \underbrace{t_i^{\text{BL}} \cdot t_i^{\text{BR}}}_{t_i^{\text{B}}} = \underbrace{t_i^{\text{TL}} \cdot t_i^{\text{BL}}}_{t_i^{\text{L}}} \cdot \underbrace{t_i^{\text{TR}} \cdot t_i^{\text{BR}}}_{t_i^{\text{R}}}. \quad 5.337$$

In total, there are $\tilde{N} = 4N$ corner templates t_i^x , $x \in \{\text{TL}, \text{TR}, \text{BL}, \text{BR}\}$, and our first step is to derive (anti)commutation relations between all \tilde{N}^2 pairs of corner templates (t_i^x, t_j^y) from the given tile set \mathcal{T} . The result will be a symmetric $\tilde{N} \times \tilde{N}$ matrix \mathcal{R} over \mathbb{F}_2 with $\mathcal{R}_{ix,jy} = 0 \Leftrightarrow [t_i^x, t_j^y] = 0$ and $\mathcal{R}_{ix,jy} = 1 \Leftrightarrow \{t_i^x, t_j^y\} = 0$. We construct \mathcal{R} in three steps:

- 1 Wang tilings restrict the placement of tiles only by their edge colors. Thus the *diagonal* placement of tiles with a single common corner is never restricted. To ensure this on the level of stabilizer templates, we demand that all pairs of templates commute when placed on faces with a single common corner. This is equivalent to the two relations

$$[t_i^{\text{TL}}, t_j^{\text{BR}}] \stackrel{!}{=} 0 \quad \Leftrightarrow \quad \mathcal{R}_{i\text{TL}|j\text{BR}} = 0 \quad 5.338a$$

$$[t_i^{\text{TR}}, t_j^{\text{BL}}] \stackrel{!}{=} 0 \quad \Leftrightarrow \quad \mathcal{R}_{i\text{TR}|j\text{BL}} = 0 \quad 5.338b$$

for all $i, j = 1, \dots, N$. Here, we introduced the shorthand notation $\mathcal{R}_{i\text{TR}|j\text{BL}} = 0$ for $\mathcal{R}_{i\text{TR},j\text{BL}} = 0 \wedge \mathcal{R}_{j\text{BL},i\text{TR}} = 0$. This fixes 2 of the $10 = (4 \times 3)/2 + 4$ unordered pairs of corner labels.

- 2** The colored tiles in \mathcal{T} determine which stabilizer templates in \mathfrak{T} can be placed side by side. If we identify t_i with \mathfrak{t}_i , this determines the (anti)commutation relations of all pairs of edge templates $(\mathfrak{t}_i^L, \mathfrak{t}_j^R)$ and $(\mathfrak{t}_i^T, \mathfrak{t}_j^B)$, namely

$$\mathfrak{t}_i^R = \mathfrak{t}_j^L \quad \Leftrightarrow \quad [\mathfrak{t}_i^R, \mathfrak{t}_j^L] \stackrel{!}{=} 0 \quad 5.339a$$

$$\mathfrak{t}_i^T = \mathfrak{t}_j^B \quad \Leftrightarrow \quad [\mathfrak{t}_i^T, \mathfrak{t}_j^B] \stackrel{!}{=} 0 \quad 5.339b$$

where t_i^x denotes the color of tile i on the edge $x \in \{T, B, L, R\}$.

These relations do not determine the relations of involved corner operators uniquely. For instance, $[\mathfrak{t}_i^R, \mathfrak{t}_j^L] = 0$ can be realized either by $[\mathfrak{t}_i^{TR}, \mathfrak{t}_j^{TL}] = 0$ and $[\mathfrak{t}_i^{BR}, \mathfrak{t}_j^{BL}] = 0$, or by $\{\mathfrak{t}_i^{TR}, \mathfrak{t}_j^{TL}\} = 0$ and $\{\mathfrak{t}_i^{BR}, \mathfrak{t}_j^{BL}\} = 0$.

Here, for example, we fix

$$\{\mathfrak{t}_i^{BR}, \mathfrak{t}_j^{BL}\} \stackrel{!}{=} 0 \quad \Leftrightarrow \quad \mathcal{R}_{iBR|jBL} = 1 \quad 5.340a$$

$$\{\mathfrak{t}_i^{TR}, \mathfrak{t}_j^{BR}\} \stackrel{!}{=} 0 \quad \Leftrightarrow \quad \mathcal{R}_{iTR|jBR} = 1, \quad 5.340b$$

and then implement the edge relations via

$$\mathfrak{t}_i^R = \mathfrak{t}_j^L \quad \Leftrightarrow \quad \{\mathfrak{t}_i^{TR}, \mathfrak{t}_j^{TL}\} \stackrel{!}{=} 0 \quad \Leftrightarrow \quad \mathcal{R}_{iTR|jTL} = 1 \quad 5.341a$$

$$\mathfrak{t}_i^T = \mathfrak{t}_j^B \quad \Leftrightarrow \quad \{\mathfrak{t}_i^{TL}, \mathfrak{t}_j^{BL}\} \stackrel{!}{=} 0 \quad \Leftrightarrow \quad \mathcal{R}_{iTL|jBL} = 1 \quad 5.341b$$

for all $i, j = 1, \dots, N$.

Note that this construction automatically leads to colorable sets of templates as their (anti)commutation relations derive from an equivalence relation. This step fixes 4 of the 10 combinations of corner labels.

- 3** To determine \mathcal{R} completely, we have to fix the (anti)commutation relations for pairs of templates that are placed on the same face. It is natural (but not necessary) to impose commutativity. This is only crucial for multi-layered ($M > 1$) stabilizer tilings; for single-layered stabilizers, arbitrary relations are valid. (For the construction of Culik stabilizers, we require commutativity for the sake of simplicity.) There are many possibilities to enforce face-commutativity via relations between corner templates.

Here we choose the simplest one, namely commutativity of the corner templates themselves:

$$[\mathfrak{t}_i^x, \mathfrak{t}_j^x] \stackrel{!}{=} 0 \quad \Leftrightarrow \quad \mathcal{R}_{ix|jx} = 0 \quad 5.342$$

for all $i, j = 1, \dots, N$ and $x \in \{TL, TR, BL, BR\}$. (Note that for $i = j$, $\mathcal{R}_{ix,ix} = 0$ is strictly implied.) This step fixes the last 4 combinations of corner labels.

We stress that the construction of \mathcal{R} is not unique due to the freedom in corner relations for the realization of edge relations and face relations. For Wang stabilizers, the prescribed edge relations leave one corner relation per edge undetermined. Furthermore, single-layered stabilizers with undetermined face relations leave four corner relations per face undetermined (even for prescribed face relations, only one of the four corner relations is fixed). Exploiting this “gauge freedom” of \mathcal{R} might be useful to reduce the number K of qubits per site (see below).

The construction of N stabilizer templates t_i that match the coloring of tiles t_i is now reduced to the construction of \tilde{N} corner templates t_i^x with the (anti)commutation relations encoded in \mathcal{R} . To cast this problem into algebraic terms, we encode each corner template t_i^x as a binary row vector $\mathbf{t}_i^x = (x_i^x, z_i^x)$ with $x_i^x, z_i^x \in \mathbb{F}_2^K$. Then,

$$\mathbf{t}_i^x = \prod_{k=1}^K (\sigma_k^x)^{(x_i^x)_k} \cdot \prod_{k=1}^K (\sigma_k^z)^{(z_i^x)_k} . \quad 5.343$$

This allows for an efficient encoding of arbitrary operators in the Pauli group on K qubits (modulo phases ± 1 and $\pm i$, which are irrelevant for commutation relations) [264]. If we define the matrix

$$\mathbb{S} = \begin{bmatrix} \mathbb{0} & \mathbb{1} \\ \mathbb{1} & \mathbb{0} \end{bmatrix} \quad 5.344$$

with $\mathbb{0}$ the $K \times K$ zero matrix and $\mathbb{1}$ the $K \times K$ identity matrix, it is easy to see that two templates commute (anticommute) if and only if the *symplectic* product

$$\langle\langle \mathbf{t}_i^x | \mathbf{t}_j^y \rangle\rangle \equiv \mathbf{t}_i^x \cdot \mathbb{S} \cdot (\mathbf{t}_j^y)^T \quad 5.345$$

equals 0 (1) in \mathbb{F}_2 .

With this notation, our problem reduces to the set of \tilde{N}^2 equations $\langle\langle \mathbf{t}_i^x | \mathbf{t}_j^y \rangle\rangle = \mathcal{R}_{ix,jy}$. If we introduce the $\tilde{N} \times 2K$ -matrix

$$X \equiv \begin{bmatrix} \mathbf{t}_1^{\text{TL}} \\ \mathbf{t}_1^{\text{TR}} \\ \vdots \\ \mathbf{t}_N^{\text{BR}} \end{bmatrix} , \quad 5.346$$

these equations are equivalent to the nonlinear matrix equation

$$X \mathbb{S} X^T = \mathcal{R} \quad 5.347$$

over the binary field \mathbb{F}_2 . Since $\text{rank}(\mathcal{R}) = \text{rank}(X \mathbb{S} X^T) \leq \text{rank}(\mathbb{S}) = 2K$, we can conclude that $K \geq \text{rank}(\mathcal{R})/2$ is a necessary condition for the solvability of Eq. (5.347). Remarkably, the number of solutions of Eq. (5.347) can be *counted* [424]. To apply the (quite complicated) result of Ref. [424], one has to use that both \mathbb{S} and

\mathcal{R} are symmetric with only zeros on their diagonal, and that \mathbb{S} has full rank. Then, Theorem 4.2 in Ref. [424] gives an explicit expression for the number of solutions in dependence of K and the rank of \mathcal{B} .

Construction of Culik templates — If we construct \mathcal{B} for the Culik tiles $\mathcal{T}_{\text{Culik}}$ according to the above procedure, we find $\text{rank}(\mathcal{B}_{\text{Culik}}) = 18$ and thereby $K \geq 9$. The result of Ref. [424] shows that this inequality is sharp, i.e., the minimal number of qubits to solve Eq. (5.347) is $K = 9$. We note that lowering the rank of $\mathcal{B}_{\text{Culik}}$ (and thereby K) might be possible by using the “gauge freedom” discussed above. What remains to be done is to find an explicit solution X of Eq. (5.347) (which need not be unique).

To this end, we restrict the class of solutions to templates with $z_i^{\text{TL}} = \mathbf{0} = z_i^{\text{BR}}$ and $x_i^{\text{TR}} = \mathbf{0} = x_i^{\text{BL}}$. This structure derives from the toric code and satisfies the imposed corner- and face-commutativity per construction while still being flexible enough to realize arbitrary (anti)commutation relations on the edges. As a first step, we shrink $\mathcal{R} \rightarrow \mathcal{R}'$ by removing duplicate columns and their corresponding rows since corner templates that share the same relations to all other templates can be identified. For the particular case of $\mathcal{R}_{\text{Culik}}$ with size $(\tilde{N} = 52) \times 52$ we find the reduced 20×20 -matrix $\mathcal{R}'_{\text{Culik}}$. This symmetric matrix encodes an undirected graph with corner templates as vertices where edges symbolize anticommutation relations. In addition, we construct the adjacency matrix \mathcal{A}_K of a graph with 2×2^K vertices that encode all possible templates with either $x = 0$ or $z = 0$ and edges that connect anticommuting templates. Solutions of Eq. (5.347) can then be found by searching for subgraphs of \mathcal{A}_K that are isomorphic to $\mathcal{R}'_{\text{Culik}}$ (for which there are optimized algorithms available in, e.g., Mathematica).

Our implementation yields solutions only for $K \geq 9$, consistent with the analytical arguments above. In particular, we find the optimal solution $\mathfrak{T}_{\text{Culik}}$ with $K = 9$ qubits depicted in Figure 5.16 (a). In Figure 5.16 (b-c), we show an exemplary 4×4 patch of an aperiodic stabilizer tiling that can be constructed from these templates. It is straightforward to check that all stabilizer tiles commute if their edge colors match up (and anticommute if not). The proven aperiodicity of Culik tiles now carries over to the constructed set of 13 stabilizer templates $\mathfrak{T}_{\text{Culik}}$: they can be used to construct a stabilizer with one generator per face that covers the entire plane—but this stabilizer is necessarily aperiodic.

5.5.4 What to Do Next?

The purpose of this section was to introduce the general concept of Wang stabilizers and present the construction of Culik stabilizers as an example. These results provide several starting points for further studies:

- The proposed construction of Culik stabilizers $\mathfrak{S}_{\text{Culik}}$ assigns a single (independent) generator to each face of the square lattice. However, there are $K = 9$ qubits per face ($9 \times 4 \times \frac{1}{4}$) and we expect ~ 8 degrees of freedom

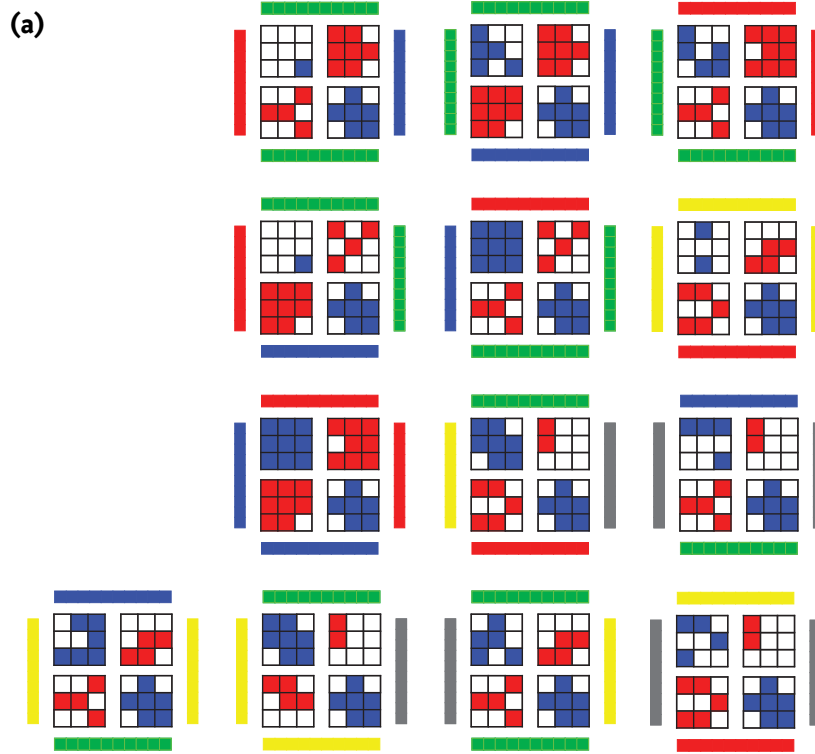
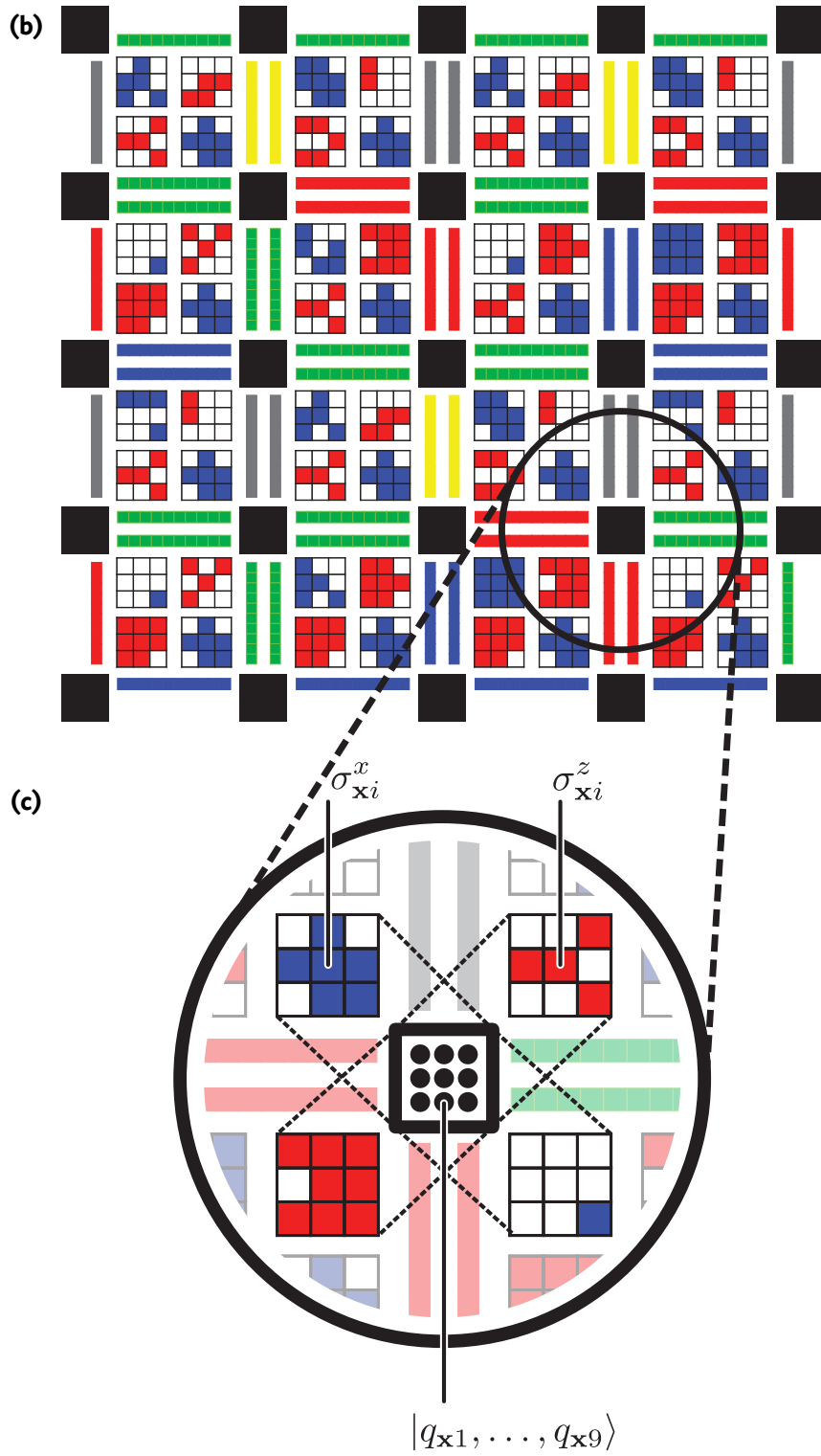


FIGURE 5.16 • Culik templates & Stabilizer. (a) Colorable set $\mathfrak{T}_{\text{Culik}}$ of $N = 13$ stabilizer templates t_i with $K = 9$ qubits per site and 5 edge colors in total (red, blue, green, yellow, gray). The templates realize the abstract Culik tiles in Figure 5.14 (a). The four squares in each template specify the operators σ_i^x (blue squares) and σ_i^z (red squares) that act on the corresponding 9 corner qubits. Adjacent templates commute if and only if the edges that touch carry the same color (and anticommute otherwise). Note that templates that touch at a corner (or occupy the same face) commute per construction. (b) Finite patch of the aperiodic stabilizer that can be constructed from the 13 templates. Only operators with matching edge colors can be placed side by side to ensure commutativity. Since Culik tiles can cover the entire plane only aperiodically, this construction gives rise to an aperiodic stabilizer group with well-defined thermodynamic limit. (c) The $K = 9$ qubits $|q_{x_1}, \dots, q_{x_9}\rangle$ (black bullets) are placed on the sites x of the square lattice \mathcal{L} (black squares). Four adjacent stabilizer tiles act on the same qubits with $\sigma_{x_i}^x$ (blue) or $\sigma_{x_i}^z$ (red).

to remain unfixed by the stabilizer group such that $\dim \mathcal{P} \mathcal{S}_{\text{Culik}} \sim 2^{(K-1)F}$ grows extensively with the number of faces F [264]. If we view the stabilizer $\mathcal{S}_{\text{Culik}}$ (generated by a finite patch of Culik tiles) as description of a quantum code, the Pauli operators that are not in $\mathcal{S}_{\text{Culik}}$ but commute with all stabilizer generators describe logical operations on the codespace $\mathcal{P} \mathcal{S}_{\text{Culik}}$. To reduce the size of $\dim \mathcal{P} \mathcal{S}_{\text{Culik}}$, one can add, in a first step, site-local logical operators as gauge constraints $G_x^{(k)}$ to the stabilizer. This “freezes out” logical qubits that are localized on single sites x . Since potential gauge constraints $G_x^{(k)}$

APERIODIC STABILIZERS



must commute with all four Culik tiles that are adjacent to x , in general there are less than $K - 1 = 8$ independent, commuting gauge constraints on a single site; hence there are logical qubits that cannot be fixed on-site but delocalize between sites. Then, the crucial (and non-trivial) question is whether an augmentation $\mathcal{S}'_{\text{Culik}}$ by quasilocal generators¹⁷⁶ exists that “freezes out” all logical qubits, $\dim \mathcal{P} \mathcal{S}'_{\text{Culik}} = 1$. Only if this is *not* possible, subspaces in $\mathcal{P} \mathcal{S}_{\text{Culik}}$ may exist that are robust against local errors. The intricate structure of $\mathcal{S}_{\text{Culik}}$ makes it hard to answer this question right away, which, in turn, is the starting point of Section 5.6 (where we formalize but do not answer this question).

- Our original motivation was the construction of aperiodic stabilizer codes to sidestep no-go theorems for self-correcting quantum memories. As discussed in Subsection 5.5.1, in two dimensions even aperiodic stabilizers cannot be self-correcting due to string-like logical operators. Thus the two-dimensional Culik stabilizer is not a promising candidate and we have to generalize the concept of Wang stabilizers to three dimensions. For Wang tilings, this generalization is known as *Wang cubes* [425] (cubes with colored faces that can be used to tile \mathbb{Z}^3 aperiodically with matching colors on contiguous faces). The basic structure in Subsection 5.5.2 was described for arbitrary dimensions D so that a generalization of Wang stabilizers to three dimensions is straightforward. The construction given in Subsection 5.5.3 can be generalized accordingly: face relations of stabilizer templates are determined by the tile colorings of the chosen set of Wang cubes, corner- and edge relations enforce commutativity, and volume relations are undetermined for single-layer stabilizers.

Aside: A Hidden Fractal Uncovered

We conclude this section with a construction that gives rise to the presumably fractal set depicted in Figure 5.17. The fractal can be found as follows:

Recall that to find templates that satisfy all imposed corner relations, we constructed the adjacency matrix \mathcal{A}_K of a graph with 2×2^K vertices that encodes the (anti)commutation relations of all K -qubit Pauli operators with either σ^x - or σ^z -matrices. We find

$$\mathcal{A}_K = \begin{bmatrix} \mathbb{0} & A_K \\ A_K^T & \mathbb{0} \end{bmatrix} \tag{5.348}$$

where $\mathbb{0}$ denotes the $2^K \times 2^K$ zero matrix. Let $n_k \in \mathbb{F}_2$ denote the k th digit of $n \in \mathbb{N}$ in base-2, i.e., $n = \sum_{k=0}^{\infty} n_k 2^k$. Then, the off-diagonal block A_K is given

¹⁷⁶Pauli operators that act non-trivially within discs of bounded radius.

APERIODIC STABILIZERS

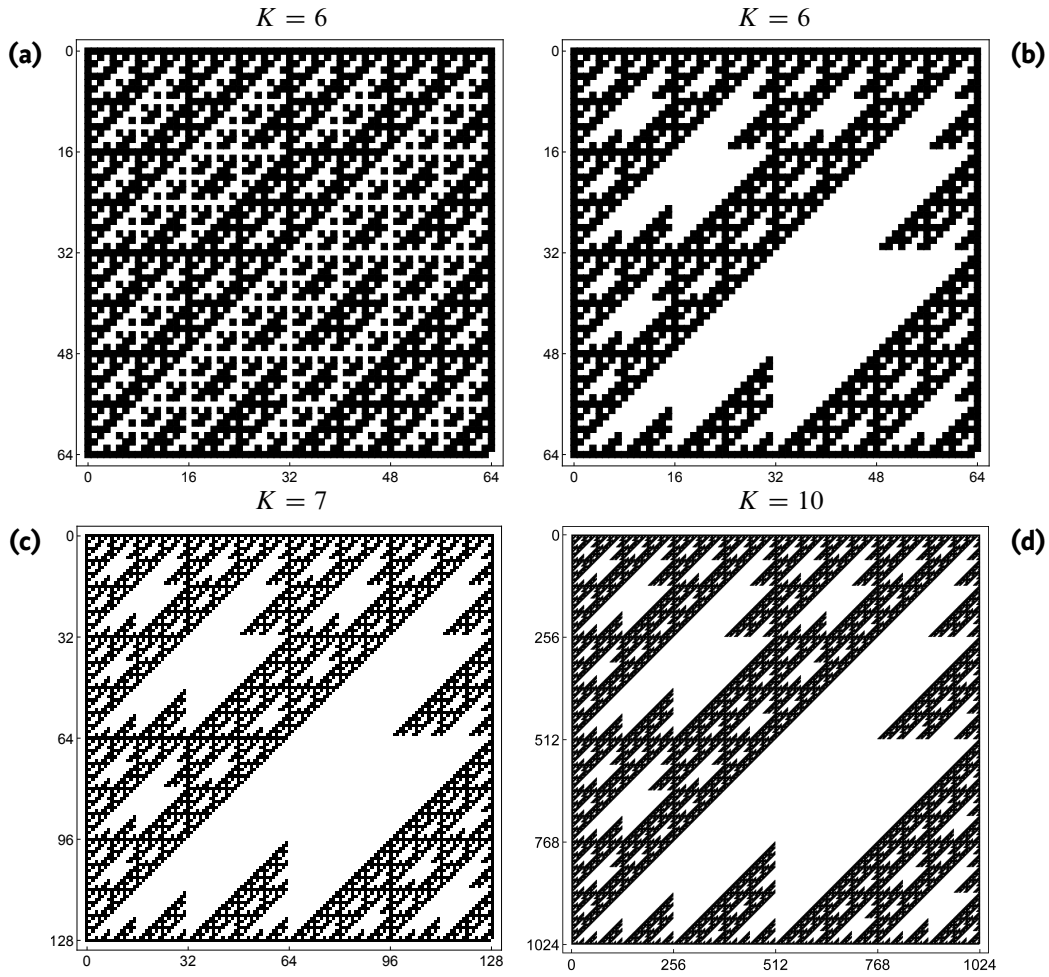


FIGURE 5.17 • A hidden fractal uncovered. (a) The complete commutator matrix A_K for $K = 6$. Black/white fields denote commuting/anticommuting operators. (b) The largest connected cluster of the commutator matrix features wing-like structures on various length scales. Clusters are defined in the sense of site percolation on the square lattice, i.e., each cell has four neighbors. (c) The same (rescaled) cluster for $K = 7$. (d) The same (rescaled) cluster for $K = 10$. The emerging pattern is self-similar, i.e., the set of black sites contains numerous copies of itself on various length scales—the hallmark of a fractal set for $K \rightarrow \infty$.

by the $Q \times Q$ -matrix

$$(\tilde{A}_Q)_{nm} = \bigoplus_{k=0}^{\infty} n_k m_k \quad \text{for} \quad 0 \leq n, m < Q \quad 5.349$$

with $A_K = \tilde{A}_Q$ for $Q = 2^K$.

Here we are interested in the matrix \tilde{A}_Q for $Q = 2^K + 1$. In Figure 5.17 (a) we plot this matrix for $K = 6$ as $Q \times Q$ -array with black cells for $(\tilde{A}_Q)_{nm} = 0$ and white cells for $(\tilde{A}_Q)_{nm} = 1$. The structure of the plot is complex but not very

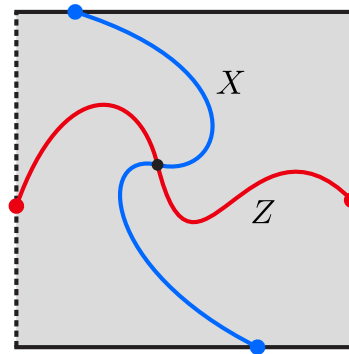
aesthetic. This changes when we view the plot as assemblage of connected clusters (where black cells are adjacent if they share a common edge). If we keep only the largest cluster and erase all disconnected islands, we find the appealing structure in Figure 5.17 (b) with self-similar features akin to the Sierpinski triangle. Rescaling the array to the same size (e.g., the unit square) yields an increasingly porous subset of the square $[0, 1]^2$ for $K \rightarrow \infty$, see Figure 5.17 (c-d). This set comprises multiple copies of itself on various length scales, which is a characteristic feature of fractal sets. We leave it as an open problem to determine the Hausdorff dimension of this limiting set to check whether it is noninteger.

5.6 Localization of Symmetries

This section can be seen as a follow-up on Section 5.5 where we present a two-dimensional stabilizer that realizes aperiodic Wang tilings. The pertinent question whether this complex stabilizer features extensive logical operators sparked the train of thoughts that led to the following concepts and results. We assume that the reader is familiar with the *stabilizer formalism*, see Section 5.5 for a brief review and Ref. [264] (Chapter 10.5) for a thorough introduction.

5.6.1 Motivation

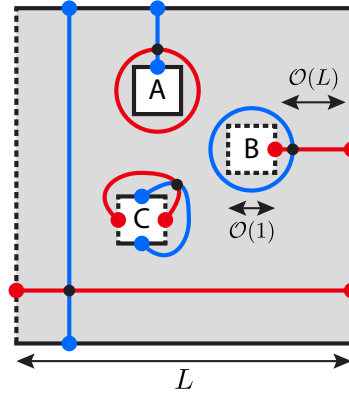
Prime examples of stabilizer codes with extensive code distance are topological surface codes [49], the paradigmatic representative being the toric code [45] which encodes two logical qubits. Here we use a plain patch of stabilizers \mathcal{S} instead with *smooth* (solid) and *rough* (dashed) boundaries [52]; the stabilized subspace $\mathcal{P}\mathcal{S}$ of this code is two-dimensional and encodes a single qubit via the following logical string operators that realize the Pauli group on $\mathcal{P}\mathcal{S}$:



For our purposes, it is sufficient to know that the logical operators in the centralizer of the stabilizer \mathcal{S} are described by X -strings (blue) and Z -strings (red) that either are closed loops or attached to the boundaries [where Z -(X -)strings can be attached to rough (smooth) boundaries only]. X - and Z -strings with an odd number of crossing points anticommute, and all strings square to the identity.

We can perforate this code by removing local clusters of stabilizer generators from $\mathcal{S} \rightarrow \mathcal{S}'$ to form holes with various combinations of boundaries. Since \mathcal{S}' is smaller than \mathcal{S} , its codespace $\mathcal{P}\mathcal{S}'$ is larger than the two-dimensional $\mathcal{P}\mathcal{S}$, and the removed stabilizer generators give rise to additional logical operators in the centralizer of \mathcal{S}' .

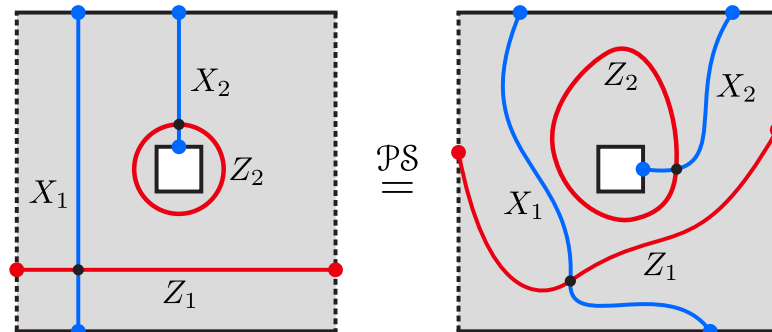
For example:



Such a perforated surface code describes, for instance, an imperfect implementation with faulty stabilizers. Here we are interested in holes of bounded diameter $\mathcal{O}(1)$ that are placed on a patch of linear size $L \rightarrow \infty$. The above example encodes *at least* four qubits in $\mathcal{P}\mathcal{S}'$ which can be identified with the four pairs of independent Pauli generators X_i, Z_i drawn as blue and red strings with a single crossing point (black bullets).

Whether a (logical) qubit is topologically protected depends on the support of its logical operators X and Z : Local (non-extensive) operators couple to local environments and thereby decohere the qubit. In the example above, qubit A is described by a local Z - and a non-local X -operator so that we expect it to dephase quickly. Conversely, qubit B features a local X - and a non-local Z -operator—which removes topological protection against depolarizing noise. Finally, qubit C is controlled by local X - and Z -operators, and is therefore completely unprotected. Note that the qubit defined by the outer boundaries is topologically protected because *both* X - and Z -strings are extensive.

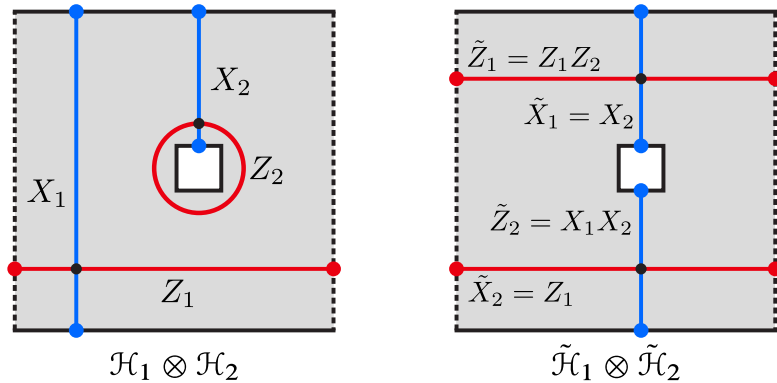
This is not the complete story, though. What complicates the assessment of the locality of logical operators is the *gauge structure* of the codespace:



(Henceforth \mathcal{S} and $\mathcal{P}\mathcal{S}$ denote stabilizer and codespace of this geometry.) Whereas for the *environment* the operators in the left-hand and right-hand panel are distinct, on the *codespace* their action is indistinguishable as they differ only by elements of

\mathcal{S} (which act as the identity on $\mathcal{P}\mathcal{S}$). For surface codes, this “dressing” of logical operators with stabilizers allows for arbitrary deformations of the strings as well as sliding of their endpoints along boundaries of the respective type. Since the environment couples at *representatives* of the gauge equivalence classes that describe logical operators, it is the representative with the smallest support that decides whether a logical operator is local or non-local. This is illustrated above: Whereas the support of Z_1 scales inevitably with $\mathcal{O}(L)$, the loop Z_2 can be contracted to the circumference of the hole with constant size $\mathcal{O}(1)$. Thus Z_1 is non-local and Z_2 is local (despite the existence of non-local representatives).

We conclude that for the assessment of the localization of logical operators, the gauge structure on $\mathcal{P}\mathcal{S}$ can be a severe obstacle¹⁷⁷. Unfortunately, the problem is even worse. Consider again the patch with a single hole:



The strings in both panels provide valid representations of a two-qubit Pauli group—and there is no reason to prefer one over the other. (Note that the operators on the right-hand side can be expressed as products of their left-hand counterparts and vice versa.) This is a graphic representation of two different *factorizations* of the same codespace,

$$\mathcal{H}_1 \otimes \mathcal{H}_2 \cong \mathcal{P}\mathcal{S} \cong \tilde{\mathcal{H}}_1 \otimes \tilde{\mathcal{H}}_2 . \tag{5.350}$$

In contrast to the gauge structure, this feature is not limited to stabilizer codes $\mathcal{P}\mathcal{S}$ but comes in general with Hilbert spaces of nonprime dimension [302].

The important point is that there are different ways to factorize a given Hilbert space into (qubit) subsystems, and there is no distinguished one from the mathematical perspective a priori. However, once a local environment couples to the quantum code, this may change. In our example above, there *is* a relevant difference between the two factorizations: Whereas the second qubit of the left-hand factorization $\mathcal{H}_1 \otimes \mathcal{H}_2$ is *local* (due to the locality of Z_2), there is no local qubit in the right-hand factorization $\tilde{\mathcal{H}}_1 \otimes \tilde{\mathcal{H}}_2$ because none of the operators $\tilde{Z}_1, \tilde{X}_1, \tilde{Z}_2, \tilde{X}_2$ can be made L -independent by gauge transformations.

But this is awkward: Had we chosen the right-hand factorization without thinking about the left-hand alternative, we might have concluded that there are *two* topologically protected qubits—in contradiction to the left-hand factorization.

¹⁷⁷The structure of stabilizers is rarely as intuitive (i.e., *graphic*) as for surface codes.

The hitch is that for two qubits to be topologically protected, *all* operators of the two-qubit Pauli group must be non-local, extensive *generators* are not enough. But this is not true for the factorization $\tilde{\mathcal{H}}_1 \otimes \tilde{\mathcal{H}}_2$ where, e.g., $\tilde{Z}_1 \tilde{X}_2 = Z_2$ is a local operator that acts non-trivially on the codespace. The difference between the two factorizations is that for $\mathcal{H}_1 \otimes \mathcal{H}_2$ decoherence is limited to a particular subsystem (the second qubit) whereas for $\tilde{\mathcal{H}}_1 \otimes \tilde{\mathcal{H}}_2$ coherences *between* the subsystems are susceptible to local perturbations. Thus the two factorizations provide different perspectives on the same physical process.

We conclude that whether a given stabilizer code harbors delocalized (i.e., *topological*) qubits not only requires an exhaustive search over gauge classes but over Hilbert space factorizations as well: If there exists a factorization with logical operators such that the Pauli group of each qubit features at least one operator with bounded support, then a local noise process can decohere the complete codespace.

The search for local representations of a (gauged) multi-qubit Pauli group (or the proof that there is none) is a complex combinatorial optimization problem that becomes particularly daunting for stabilizers where the number of logical operators grows with the system size. Stabilizers like the perforated surface code with a finite density of holes can “hide” potential topological qubits by mixing them with local “garbage” qubits¹⁷⁸. The interesting question is whether there is an efficient algorithm to strip a given stabilizer from these localized “garbage” qubits to probe for the existence of protected, delocalized qubits. Such an algorithm would be particularly useful for the automated generation of useful stabilizer codes [415, 419].

Here we will *not* provide an answer to this question. Instead, we focus on a simpler, *classical* analogue of the problem (which we dub “symmetry localization”) and discuss several interesting aspects thereof.

Example: Hilbert Space Factorization

We conclude this subsection with an explicit example to illustrate the concept of Hilbert space factorization. To this end, consider a two-qubit Hilbert space $\mathcal{H} = \mathcal{H}_1 \otimes \mathcal{H}_2$ with $\mathcal{H}_{1,2} \cong \mathbb{C}^2$ and basis $B = \{|00\rangle, |01\rangle, |10\rangle, |11\rangle\}$. Unitaries on \mathcal{H} are generated by (tensor products of) Pauli matrices, the two-dimensional representations of the angular momentum algebra $[\sigma_k^a, \sigma_l^b] = 2i \delta_{kl} \sum_c \varepsilon_{abc} \sigma_k^c$.

Now define a new algebra

$$\tilde{\sigma}_1^z \equiv \sigma_1^z \sigma_2^z, \quad \tilde{\sigma}_2^z \equiv \sigma_1^x \sigma_2^x, \quad 5.351a$$

$$\tilde{\sigma}_1^x \equiv \sigma_2^x, \quad \tilde{\sigma}_2^x \equiv \sigma_1^z, \quad 5.351b$$

$$\tilde{\sigma}_1^y \equiv \sigma_1^z \sigma_2^y, \quad \tilde{\sigma}_2^y \equiv -\sigma_1^y \sigma_2^x, \quad 5.351c$$

which is easily verified to realize the *same* algebra, namely $[\tilde{\sigma}_k^a, \tilde{\sigma}_l^b] = 2i \delta_{kl} \sum_c \varepsilon_{abc} \tilde{\sigma}_k^c$.

¹⁷⁸The partition of logical qubits into useful topological and useless “garbage” qubits relates to the concept of *subsystem codes* [174, 426].

On \mathcal{H} , it acts naturally on the (unnormalized) Bell basis

$$|\tilde{00}\rangle \equiv |00\rangle + |11\rangle \quad 5.352a$$

$$|\tilde{01}\rangle \equiv |00\rangle - |11\rangle \quad 5.352b$$

$$|\tilde{10}\rangle \equiv |01\rangle + |10\rangle \quad 5.352c$$

$$|\tilde{11}\rangle \equiv |01\rangle - |10\rangle \quad 5.352d$$

with $\tilde{\sigma}_1^z|\tilde{x}\tilde{y}\rangle = (-1)^x|\tilde{x}\tilde{y}\rangle$, $\tilde{\sigma}_2^z|\tilde{x}\tilde{y}\rangle = (-1)^y|\tilde{x}\tilde{y}\rangle$, etc. This defines an alternative factorization of the Hilbert space $\mathcal{H} \cong \tilde{\mathcal{H}}_1 \otimes \tilde{\mathcal{H}}_2$ with $\tilde{\mathcal{H}}_{1,2} \cong \mathbb{C}^2$ and basis $\tilde{\mathcal{B}} = \{|\tilde{00}\rangle, |\tilde{01}\rangle, |\tilde{10}\rangle, |\tilde{11}\rangle\}$.

Note that the concept of *entanglement* crucially depends on the decomposition of a Hilbert space into subsystems. Whether a state is entangled or not is therefore only defined with respect to a given Hilbert space factorization [302]. This fact is often ignored when there is a distinguished factorization given by the physical constituents of the system.

5.6.2 The Classical Problem

The problem to decide whether a logical multi-qubit Pauli group can be completely localized is complicated by the presence of anticommuting operators. The encoding of a stabilizer \mathcal{S} on a binary vector space (which is the appropriate framework for combinatorics) demands for a symplectic structure to keep track of the (anti-)commutation relations [264]. This adds additional clutter to an already non-trivial problem.

To get rid of these complications, we restrict the allowed stabilizer generators to products of σ^z -matrices. As a consequence, $\mathcal{P}\mathcal{S}$ is no longer a *quantum* code as dephasing errors cannot be detected (note that arbitrary products of σ^z belong to the centralizer of \mathcal{S}). The only non-trivial logical operators are products of σ^x -matrices in the centralizer of \mathcal{S} (these can then be “dressed” with arbitrary products of σ^z -matrices to construct other logical operators). Due to the unprotected phases, the codespace $\mathcal{P}\mathcal{S}$ reduces to a *classical* linear (binary) code; if the generators in \mathcal{S} are operators with bounded support (possibly local with respect to some lattice \mathcal{L}), this construction gives rise to *low-density parity-check (LDPC) codes* [427]. The non-trivial logical X -operators perform classical flips of the encoded bits as they map code words to code words.

Let us translate this setting into a language that is more closely related to physics. Consider a D -dimensional lattice \mathcal{L} with one spin $x_s \in \{\uparrow, \downarrow\}$ per site $s \in \mathcal{L}$. We are interested in the ground state(s) of local Hamiltonians of the form

$$H = - \sum_i P_i \quad 5.353$$

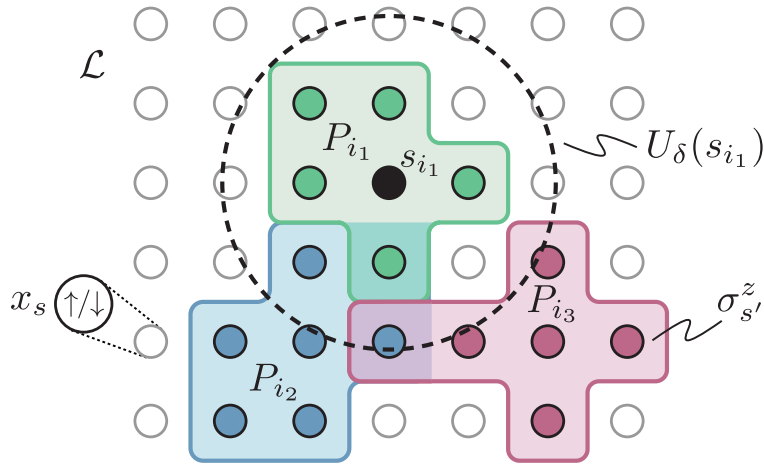


FIGURE 5.18 • Local parity-check Hamiltonian. Schematic structure of a (two-dimensional) local parity-check Hamiltonian. Spins are denoted by circles placed on a regular lattice \mathcal{L} . The Hamiltonian H is a sum of quasilocal parity-check operators P_i with support on a bounded region $U_\delta(s_i)$ around their center site s_i . Note that adjacent parity-check operators can overlap.

with local “parity-check” operators

$$P_i = P(\mathbf{p}_i) = \prod_{s \in \mathcal{L}} (\sigma_s^z)^{p_i^s} \tag{5.354}$$

that are described by binary vectors $\mathbf{p}_i \in \mathbb{F}_2^{|\mathcal{L}|}$. Locality of H demands that \mathbf{p}_i is zero on all sites outside of a ball $U_\delta(s_i)$ of radius $\delta > 0$ centered on some lattice site $s_i \in \mathcal{L}$, see Figure 5.18. This locality constraint is physically motivated and might be relevant for a more specialized treatment of the problem discussed below. For the sake of simplicity, we ignore it so that the conclusions that follow do not exploit the local structure of H .

The ground states of H are given by spin configurations that satisfy all local parity-checks: $P_i|x\rangle = |x\rangle$ for all i . The set of all ground states can be identified with a classical LDPC code as described above; the abelian group $\mathcal{P} = \langle\langle P_i \rangle\rangle$ generated by the parity-check operators corresponds to the stabilizer. [For convenience, we still use the quantum formalism although the Hamiltonian (5.353) is clearly classical.]

Given a Hamiltonian, one of the first things to do is a classification of its symmetries. For Hamiltonians of the form (5.353), the symmetry group $\mathcal{G} = \langle\langle G_k \rangle\rangle$ with $[H, G_k] = 0$ is generated by operators

$$G_k = G(\mathbf{g}_k) = \prod_{s \in \mathcal{L}} (\sigma_s^x)^{g_k^s} \tag{5.355}$$

that are again described by binary vectors $\mathbf{g}_k \in \mathbb{F}_2^{|\mathcal{X}|}$. The elements of \mathcal{G} describe correlated spin-flips that do not violate the parity-checks P_i (they map ground states to ground states). The symmetry group \mathcal{G} can be identified with the logical X -operators of the restricted stabilizer introduced above.

Each element of the groups \mathcal{P} and \mathcal{G} can be identified with a binary vector in the linear \mathbb{F}_2 -subspaces $V_P \equiv \langle \{\mathbf{p}_i\} \rangle$ and $V_G \equiv \langle \{\mathbf{g}_k\} \rangle$, respectively. This follows since $P(\mathbf{p}_1)P(\mathbf{p}_2) = P(\mathbf{p}_1 \oplus \mathbf{p}_2)$ and $G(\mathbf{g}_1)G(\mathbf{g}_2) = G(\mathbf{g}_1 \oplus \mathbf{g}_2)$, i.e., the multiplicative (abelian) groups \mathcal{P} and \mathcal{G} are isomorphic to the additive (abelian) groups V_P and V_G . Here, \oplus denotes the binary addition in $\mathbb{F}_2^{|\mathcal{X}|}$. It is now easy to see that a vanishing commutator of a parity-check operator with a symmetry operator translates into orthogonality of their respective vectors:

$$[P(\mathbf{p}), G(\mathbf{g})] = 0 \quad \Leftrightarrow \quad \mathbf{p} \cdot \mathbf{g} = 0 \quad \text{for} \quad \mathbf{p}, \mathbf{g} \in \mathbb{F}_2^{|\mathcal{X}|}. \quad 5.356$$

(This is where a *symplectic* inner product enters the stage for P and G that contain mixtures of σ^x - and σ^z -matrices; the simple relation $\mathbf{p} \cdot \mathbf{g} = \bigoplus_s p^s g^s$ is a feature of classical setups.)

Since the symmetry generators G_k are *defined* such that $[P_i, G_k] = 0$ for all i (this follows from $[H, G_k] = 0$), the vectors \mathbf{g}_k must be orthogonal to all vectors \mathbf{p}_i ¹⁷⁹. Hence, the symmetry group is described by the orthogonal complement¹⁸⁰

$$V_G = V_P^\perp = \left\{ \mathbf{x} \in \mathbb{F}_2^{|\mathcal{X}|} \mid \forall_i : \mathbf{x} \cdot \mathbf{p}_i = 0 \right\}. \quad 5.357$$

For a given Hamiltonian H , the derivation of its symmetry group \mathcal{G} is then equivalent to the construction of V_P^\perp which is a matter of straightforward linear algebra (Gaussian elimination).

In the parlance of coding theory, the Hamiltonian vectors \mathbf{p}_i define the rows of the *check matrix* of the linear code V_G and are, at the same time, the generators of the *dual code* $V_P = V_G^\perp$. Conversely, the symmetry vectors \mathbf{g}_k are the generators of the linear code V_G and define the check matrix of the dual code V_P . (For an introduction, we refer the reader to one of the many primers on coding theory, e.g. [428].)

Let us focus on the “symmetry code” V_G and define the *Hamming weight* of a vector $\mathbf{x} \in \mathbb{F}_2^{|\mathcal{X}|}$ as the number of non-zero entries, $\|\mathbf{x}\| = \sum_{i=1}^{|\mathcal{X}|} x_i$. A characteristic quantity of the code V_G is its *distance*:

$$d = \min_{\mathbf{x} \neq \mathbf{x}' \in V_G} \|\mathbf{x} - \mathbf{x}'\| = \min_{\mathbf{0} \neq \mathbf{x} \in V_G} \|\mathbf{x}\|. \quad 5.358$$

¹⁷⁹We stress that $[P_i, P_j] = 0$ or $[G_k, G_l] = 0$ does *not* imply $\mathbf{p}_i \cdot \mathbf{p}_j = 0$ or $\mathbf{g}_k \cdot \mathbf{g}_l = 0$! A description of both Z - and X -operators in the same framework is only possible on a doubled vector space $\mathbb{F}_2^{|\mathcal{X}|} \oplus \mathbb{F}_2^{|\mathcal{X}|}$ with symplectic inner product [264].

¹⁸⁰On finite fields, the orthogonal “complement” V^\perp is not a true complement in that $V \cap V^\perp \supsetneq \{\mathbf{0}\}$ in general. For instance, non-zero vectors can be self-orthogonal: $\mathbf{x} \cdot \mathbf{x} = 0$.

The distance d is the minimum number of bit-flips needed to change one valid code word into another; due to the linearity of the code, it equals the minimum Hamming weight of all (non-zero) code words in V_G . It is known that finding the code distance of a binary linear code is NP-hard [429]; thus there exists (presumably) no efficient algorithm to compute the code distance without exploiting specific structures of the code.

The question is whether this should bother us in the context where the code V_G describes the symmetry of a local Hamiltonian H . The answer is “no” for two reasons¹⁸¹: First, the code distance is not a useful quantity for our scenario because it measures the size of the support of the smallest (non-trivial) symmetry operator of H . This seems not like a relevant quantity if we are interested in robust properties of H and its ground state phase. (Note that d can be made artificially small by adding a single uncoupled spin with local symmetries—which should not affect the properties of a phase.) The second reason is that for *quantum* stabilizer codes with extensive codespace, d corresponds to the weight of the smallest logical operator—which might just describes a local “garbage” qubit. The original question was rather whether there is anything left if we get rid of all these local logical operators.

The analogous question in the context of (classical) Hamiltonians is whether its symmetry group is generated by local operators or whether additional global generators are required. Given the fundamentally different roles played by *local* and *global* symmetries in the context of spontaneous symmetry breaking [430], this is a question that merits consideration.

In Figure 5.19 we show three examples to illustrate the concept. The local parity-check operators are denoted by gray edges (two spins) and triangular faces (three spins). Symmetry generators are indicated by colored loops encircling the flipped spins; local (non-local) generators are drawn blue (red) and generate the groups $\mathcal{E}_{\text{local}}$ ($\mathcal{E}_{\text{global}}$). Figure 5.19 (a) shows the Ising chain as prototypical example for systems with finite (L -independent) symmetry group; the only non-trivial symmetry is a global spin-flip. Figure 5.19 (b) shows a rather artificial \mathbb{Z}_2 gauge theory of separate spin pairs coupled by Ising interactions; the symmetry group is extensive and generated by local flips of spin pairs. To be sure, the symmetry group contains *global* operators—but these can be constructed from local generators. The most interesting example is shown in Figure 5.19 (c): A strip of spins with parity-checks of three spins on each gray triangle. There is an extensive number of local symmetry generators given by simultaneous spin-flips along the blue squares. The non-local spin-flip along one edge (red) is an additional symmetry that cannot be constructed from the local generators. This leads to a partition of the total symmetry group $\mathcal{E} = \mathcal{E}_{\text{local}} \times \mathcal{E}_{\text{global}}$ into the subgroups $\mathcal{E}_{\text{local}}$ (which is locally generated) and $\mathcal{E}_{\text{global}}$ (which is not). Notice that the non-local spin-flip along *both* edges *can* be generated from the local symmetries.

¹⁸¹The complete answer is “not at this point,” see below.

LOCALIZATION OF SYMMETRIES

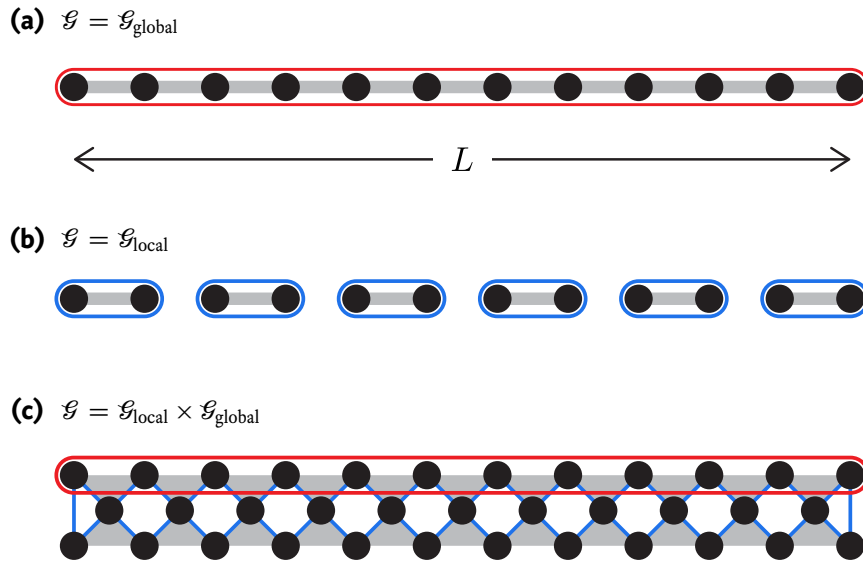


FIGURE 5.19 • Global and local symmetry generators (Examples). Three examples of local, one-dimensional parity-check Hamiltonians. Gray edges/faces denote parity-check operators P_i defined as product of the adjacent spins (two for edges, three for triangular faces). Global (local) symmetry generators G_k are highlighted by red (blue) loops encircling the flipped spins. **(a)** Ising chain with a global spin-flip symmetry (red). **(b)** \mathbb{Z}_2 gauge theory with local spin-flip symmetries (blue). **(c)** Stripe with three-spin parity-checks (gray triangles). There are local (four-spin) symmetry generators (blue); in addition, the global spin-flip along one side (red) is an independent generator that cannot be constructed from the local symmetries.

In the light of these examples, the problem we are interested in can be stated as follows:

DEFINITION 5.7: Symmetry localization

Assume we are given a symmetry group \mathcal{G} in terms of $\mathcal{O}(L)$ generators $\{G_k\}$. Find an equivalent set of generators that minimizes the maximum size of its elements. If the support of the largest generator in this set grows with L (is constant), the symmetry group is non-locally (locally) generated.

We call this the problem of *symmetry localization* and seek either for an efficient algorithm to solve it or a proof that such an algorithm cannot (or is unlikely) to exist.

For an abstract description of symmetry localization, we need the following quantities that seem to be rarely considered in coding theory:

DEFINITION 5.8: Minimum-weight and minimum–maximum-weight bases

Given an M -dimensional linear subspace $V \leq \mathbb{F}_2^L$ and a basis $B = \{\mathbf{b}_1, \dots, \mathbf{b}_M\}$ with $V = \text{span}\{B\}$. For $\mathbf{x} \in V$, let $\|\mathbf{x}\| = \sum_i x_i$ denote the Hamming weight. Define the following two quantities:

$$\text{Weight of } B : \quad \Sigma(B) \equiv \sum_{\mathbf{b} \in B} \|\mathbf{b}\| \quad 5.359a$$

$$\text{Maximum weight of } B : \quad \sigma(B) \equiv \max_{\mathbf{b} \in B} \|\mathbf{b}\| \quad 5.359b$$

- We call B a minimum-weight basis (MWB) if it minimizes the weight $\Sigma(B)$, i.e., $\Sigma(B) \leq \Sigma(\tilde{B})$ for all bases \tilde{B} that span V . The minimum-weight $\Sigma(V)$ of V is the weight of an MWB that spans V .
- We call B a minimum–maximum-weight basis (MMWB) if it minimizes the maximum weight $\sigma(B)$, i.e., $\sigma(B) \leq \sigma(\tilde{B})$ for all bases \tilde{B} that span V . The minimum–maximum-weight $\sigma(V)$ of V is the maximum weight of an MMWB that spans V .

The idea behind the definition of a minimum–maximum-weight basis is clear: Via the isomorphism between \mathcal{G} and V_G it formalizes the problem of symmetry localization since non-locally/locally generated symmetry groups are characterized by $\sigma(V_G) = \mathcal{O}(L)$ and $\sigma(V_G) = \mathcal{O}(1)$, respectively. The concept of a minimum-weight basis is not directly related to a meaningful physical concept (at least it is not obvious why the accumulated size of all symmetry generators should be an interesting quantity). However, relations between MW- and MMW-bases have been studied before; in particular, an MWB is also an MMWB (but not vice versa) [431].

To illustrate the two concepts and highlight their differences, we show two examples in Figure 5.20: In (a) the defining basis B of 6-dimensional vectors spans the entire space $V = \mathbb{F}_2^6$. An MWB (and therefore an MMWB) is the standard basis \tilde{B} with minimum-weight $\Sigma(\tilde{B}) = 6$ and minimum–maximum-weight $\sigma(\tilde{B}) = 1$. The second example in (b) defines a 6-dimensional subspace V of \mathbb{F}_2^8 with minimum-weight $\Sigma(\tilde{B}) = 8$ and minimum–maximum-weight $\sigma(\tilde{B}) = 3$. In the last column of Figure 5.20 (b) we demonstrate that an MMWB is not necessarily an MWB (whereas the converse is true).

As a final step in this subsection, we formalize the problem of symmetry localization as the problem of finding an MMWB for a given binary subspace. It is customary to cast such a problem into three slightly different versions:

LOCALIZATION OF SYMMETRIES

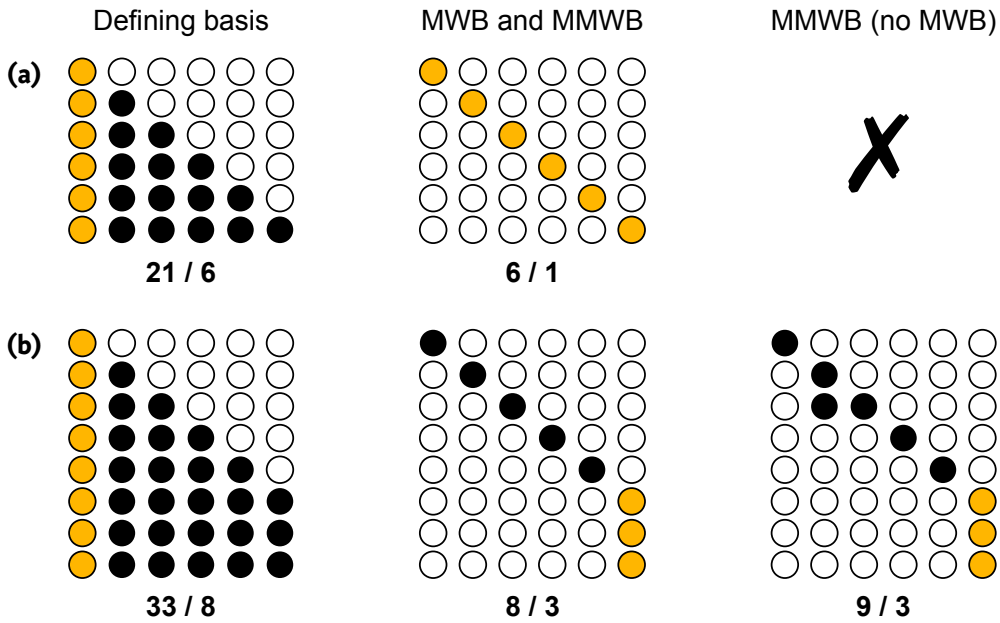


FIGURE 5.20 • MW- and MMW-bases (Examples). Bases $B = \{b_1, \dots, b_M\}$ as lists of binary column vectors where filled circles denote components $b_k^i = 1$. Basis vectors with maximum Hamming weight $\|b_k\|$ are highlighted yellow. Below the bases we list $\Sigma(\bullet)/\sigma(\bullet)$. **(a)** Set $V = \mathbb{F}_2^6$ (the complete space). The chosen defining basis has weight $\Sigma(B) = 21$ and maximum weight $\sigma(B) = 6$. A possible MWB (which is also an MMWB, see Ref. [431]) is the standard basis with minimum-weight $\Sigma(\tilde{B}) = 6 = \dim(V)$ and minimum-maximum-weight $\sigma(\tilde{B}) = 1$. **(b)** Set $V < \mathbb{F}_2^8$ with $\dim(V) = 6$. A possible MWB/MMWB has minimum-weight $\Sigma(\tilde{B}) = 8$ and minimum-maximum-weight $\sigma(\tilde{B}) = 3$. The last column shows an MMWB B' that is *not* an MWB since $\Sigma(B') = 9 > 8 = \Sigma(\tilde{B})$ is not minimal.

DEFINITION 5.9: The problem MMWB

Given a binary basis $B = \{b_1, \dots, b_M\} \subseteq \mathbb{F}_2^L$.

- Decision version: MMWB-DEC
 Given a positive integer $C \in \mathbb{N}$.
 Is there a basis \tilde{B} with $\langle \tilde{B} \rangle = \langle B \rangle$ such that $\sigma(\tilde{B}) \leq C$? (Answer: YES/NO)
- Search version: MMWB-SEARCH
 Given a positive integer $C \in \mathbb{N}$.
 Find a basis \tilde{B} with $\langle \tilde{B} \rangle = \langle B \rangle$ such that $\sigma(\tilde{B}) \leq C$ if it exists. (Answer: \tilde{B} /NO)
- Optimization version: MMWB-OPT
 Find a basis \tilde{B} with $\langle \tilde{B} \rangle = \langle B \rangle$ such that $\sigma(\tilde{B})$ is the minimum of all bases.
 (Answer: \tilde{B})

It is clear that an efficient algorithm for the optimization version implies one for the search- and the decision version. Conversely, an efficient algorithm for the *search* version yields one for the optimization version by lowering C until the minimum is reached. However, an efficient algorithm for the *decision* version can only be used to construct an efficient algorithm that computes $\sigma(\langle B \rangle)$ (by lowering C successively). Note that such an algorithm does *not* output an MMWB \tilde{B} with $\sigma(\tilde{B}) = \sigma(\langle B \rangle)$. Therefore the optimization version MMWB-OPT is at least as hard as the decision version MMWB-DEC¹⁸².

As our original motivation was to find non-local logical operators of a quantum stabilizer code, we are interested the *optimization* version MMWB-OPT. This also makes sense in the context of symmetry localization: We are not only interested in whether or not a symmetry group is non-locally generated but also in the generators themselves.

5.6.3 Directions to Proceed

The results presented so far were conceptualized during a few days of brainstorming and literature research. For a lack of time (cf. Chapter 2, 3 and 4), there are no presentable (or even publishable) results that complete the story. However, there are several interesting questions and links to earlier results in the literature that deserve a closer look:

- The most pressing question is clearly whether there are efficient algorithms to solve any of the MMWB-versions defined above. If we focus on MMWB-OPT, there are two possibilities: Either there *is* an algorithm that generates an MMWB with a runtime polynomial in the subspace dimension, or there is *not*. Betting on the latter, one could try to prove that MMWB-OPT is NP-hard by finding a reduction from a known NP-hard problem to MMWB-OPT. One approach may be the following chain of arguments:
 - 1 It is known that finding the code distance of a binary linear code is NP-hard [429]. This implies that finding a minimum-weight vector \mathbf{x}^* of a linear subspace, $\|\mathbf{x}^*\| = \min_{\mathbf{0} \neq \mathbf{x} \in V} \|\mathbf{x}\|$, is NP-hard.
 - 2 Each MWB includes a minimum-weight vector [431]. Therefore finding an MWB of a linear subspace (MWB-OPT) is NP-hard.
 - 3 A (Turing) reduction from MWB-OPT to MMWB-OPT would prove the NP-hardness of MMWB-OPT. To this end, one could try to construct an algorithm that produces an MWB using only a polynomial number of calls to a given subroutine that returns an MMWB.

¹⁸²If an efficient algorithm for MMWB-DEC can be used to construct one for MMWB-OPT, the problem is called *self-reducible*. Here we make no claims about this property.

Note that it may very well be that the construction of an MWB is strictly more complex than that of an MMWB such that the third step is bound to fail. This possibility is underpinned by the fact that every MWB is an MMWB whereas there are many MMW-bases that are not MW-bases, recall Figure 5.20.

- It seems that the problem MMWB for generic bases/subspaces has not been studied before (at least the author is not aware of any results). However, Ref. [431] studied MMWB for a restricted family of subspaces called *cycle spaces*.

Cycle spaces \mathcal{C} are linear subspaces of $\mathbb{F}_2^{|E|}$ that can be constructed from graphs G with edge set E by encoding all Eulerian¹⁸³ subgraphs G' of G as binary vectors x with $x_e = 1$ if edge e belongs to G' . The set \mathcal{C} of such subgraphs is closed under vector addition in $\mathbb{F}_2^{|E|}$ because the symmetric difference of two Eulerian subgraphs yields another Eulerian subgraph. (For an introduction to graph theory, we refer the reader to one of the many primers on the topic, e.g. [432].)

The results of Ref. [431] were later extended in Ref. [433] where also the NP-hardness of the problem has been shown if one imposes additional, graph-theoretic constraints on the bases. In both references, it has been noted that Horton's algorithm [434] can be used to construct MMW-bases efficiently for cycle spaces by constructing MW-bases instead¹⁸⁴. Thus there *are* efficient algorithms to solve MMWB-OPT if the subspaces are restricted to cycle spaces. Interestingly, for several physically motivated models with gauge structures this condition is met naturally:

For example, if we consider the toric code [45] on the eponymous toroidal square lattice and forget about the star operators $A_s = \prod_{e \in s} \sigma_e^x$, we end up with a classical \mathbb{Z}_2 lattice gauge theory [436, 437]. Its symmetry group is generated by said star operators (except for one) and two additional, homologically non-trivial and inequivalent loops around the torus (the logical X -operators of the code). But this is a cycle basis of the graph defined by the dual (square) lattice; hence Horton's algorithm can be used to solve this MMWB-OPT instance efficiently (which is not very useful as we know the answer already).

Finally, we note that one can decide efficiently whether a given linear subspace is the cycle space of some graph by means of Tutte's algorithm [438] (which hints at possibly fruitful connections to *matroid theory*).

- An instance of MMWB-OPT is given by an arbitrary basis of binary vectors. In the context of symmetry localization, however, we start from a *local* Hamiltonian defined on a lattice of specified dimension. Can one exploit the locality of

¹⁸³A graph is called *Eulerian* if all vertices have even degree.

¹⁸⁴The construction of MW-bases for cycle spaces has received much more attention due to various applications in electrical engineering (circuit design), chemistry and surface reconstruction, see Ref. [435] and references therein.

MISCELLANEOUS

the Hamiltonian for the solution of the corresponding MMWB-OPT-instance? More precisely: are instances of MMWB-OPT that derive as symmetries from local Hamiltonians simpler than generic ones? If so, does this depend on the dimensionality of the lattice?

- Essentially, MMWB-OPT asks whether a given binary subspace allows for a basis that is completely localized. Is there any relation to the localizability of Wannier bases which is known to be obstructed by topological invariants [117, 118]? Are there similar (combinatorial?) invariants that herald obstructions to completely localize a given basis in $\mathbb{F}_2^{|\mathcal{X}|}$?
- Irrespective of the worst-case complexity of MMWB-OPT, the question whether there are useful heuristic approaches to find an MMWB (or bases that are close to an MMWB) is certainly interesting. Note that to discard quantum codes as local, it is enough to find bases with *bounded* maximum weight—it has not to be minimal.
- And finally, how do results for the classical problem (MMWB-OPT) fare in the quantum realm where the symplectic structure and the gauge structure of stabilizer codes must be taken into account? Can the full quantum version of MMWB-OPT be reduced to MMWB-OPT, or are there fundamental differences?

List of Figures

2.1	In a nutshell—Setup & ground states	47
2.2	In a nutshell—Ground state properties	49
2.3	In a nutshell—Braiding	51
2.4	Setup	56
2.5	Ground states—Degeneracy	57
2.6	Ground states—Fermion gauge	58
2.7	Ground state properties—Edge states	64
2.8	Green’s function—Derivation	66
2.9	Ground state properties—Symmetry protection	68
2.10	Symmetry protection—Derivation	70
2.11	Ground state entanglement	73
2.12	Ground states & Gap scaling	84
2.13	DMRG results	87
2.14	Wire networks	94
2.15	Braiding—Setup	98
2.16	Braiding—Results	100
2.17	Braiding—Theory	104
2.18	Braiding—Derivation	106
2.19	Matrix product state representation	117
2.20	Local structure of G	120
2.21	Schematic potential	130
2.22	Temperature dependence of the local density	134
2.23	Low-energy phase slip	142
2.24	Characterization of class-A Bethe wave functions	161
2.25	Detailed analysis of type-A solutions for $\theta \neq \pi$	162
2.26	Typical two-particle wave functions	164
2.27	Even-Odd effect for class-A2 solutions	167
2.28	Spectrum of the even-subchain-parity two-particle sector	173
3.1	In a nutshell—Setup	198
3.2	In a nutshell—Results	200

LIST OF FIGURES

3.3	Basic setup	205
3.4	Setups	208
3.5	State transfer (qualitative results)	216
3.6	State transfer (quantitative results)	218
3.7	Time evolution of a minimal model	220
3.8	Accumulation of transfer phases	221
3.9	Universal scaling	223
3.10	Scaling of the transfer time (numerics)	225
3.11	Edge mode localization	228
3.12	Effects of disorder (numerics)	229
3.13	CP gate—Pulse sequence & Results	231
3.14	Coupling many qubits	234
3.15	The Majorana chain model	244
3.16	Generic network	248
3.17	Effects of disorder—Transfer	251
3.18	Effects of disorder—Phases	253
3.19	Asymptotic vs. numerical results	259
3.20	Analytic spectrum—Bulk modes	263
3.21	Analytic spectrum—Edge modes	264
3.22	Scaling away from the critical point—Lower band edge	269
3.23	Scaling away from the critical point—System size	270
3.24	Universal scaling	275
3.25	Adiabatic bulk-edge decoupling—Pulses	277
3.26	Adiabatic bulk-edge decoupling—Numerics	285
4.1	In a nutshell—The Majorana chain quantum code	292
4.2	In a nutshell—The Two-Line Voting automaton	294
4.3	Topological quantum memories.	301
4.4	Global majority voting	308
4.5	Locality constraints	310
4.6	Two classical density classifiers	318
4.7	Exemplary time evolution	319
4.8	Boundary conditions—Definition.	321
4.9	Boundary conditions—Effects.	322
4.10	Properties of $\overline{\text{TLV}}$ —Fixed points	325
4.11	Properties of $\overline{\text{TLV}}$ —Cycles	326
4.12	Properties of $\overline{\text{TLV}}$ —Attractor landscape	327
4.13	Properties of $\overline{\text{TLV}}$ —Numerics	328
4.14	Independent clusters	331
4.15	Constrained $\overline{\text{TLV}}$ -decoding	335
4.16	Noise-induced deconfinement—Numerics	337
4.17	Noise-induced deconfinement—Example	338
4.18	2D-evolved $\overline{\text{TLV}}$ —Setup	340
4.19	2D-evolved $\overline{\text{TLV}}$ —Details	342

LIST OF FIGURES

4.20	Majority gate	342
4.21	Exemplary evolution of 2D-evolved $\overline{\text{TLV}}$	344
4.22	Failure probability for 2D-evolved $\overline{\text{TLV}}$	345
4.23	Eroders on finite chains	359
4.24	Fixed points	361
4.25	Explanation trees	366
4.26	Eroder parameter	375
5.1	Perturbations (DMRG)	401
5.2	Phase diagram	425
5.3	Phase transitions (DMRG)	428
5.4	Path for $J_2 > 0$ and $J_1 < 0$ (DMRG).	431
5.5	Setup	435
5.6	Phase diagram	440
5.7	Relaxed condition	441
5.8	Parameter domain for SLL	463
5.9	Example: Setups for classical mode transfer	489
5.10	MCQC decoding with a CNN—Setup	499
5.11	MCQC decoding with a CNN—Results	501
5.12	2D majority voting with a CNN—Examples	503
5.13	2D majority voting with a CNN—Corner erosion	504
5.14	Culik tiles	511
5.15	Requirements for colorability	513
5.16	Culik templates & Stabilizer	518
5.17	A hidden fractal uncovered	521
5.18	Local parity-check Hamiltonian	528
5.19	Global and local symmetry generators (Examples)	531
5.20	MW- and MMW-bases (Examples)	533

Bibliography

- [1] N. Lang and H. P. Büchler, *Topological states in a microscopic model of interacting fermions*, Physical Review B **92**, 041118 (2015), doi:[10.1103/physrevb.92.041118](https://doi.org/10.1103/physrevb.92.041118). (Cited on pages [iv](#) and [43](#).)
- [2] N. Lang and H. P. Büchler, *Topological networks for quantum communication between distant qubits*, npj Quantum Information **3**(1), 47 (2017), doi:[10.1038/s41534-017-0047-x](https://doi.org/10.1038/s41534-017-0047-x). (Cited on pages [iv](#), [195](#), [465](#), [472](#), [485](#), [486](#), and [488](#).)
- [3] N. Lang and H. P. Büchler, *Strictly local one-dimensional topological quantum error correction with symmetry-constrained cellular automata*, SciPost Physics **4**, 007 (2018), doi:[10.21468/scipostphys.4.1.007](https://doi.org/10.21468/scipostphys.4.1.007). (Cited on pages [iv](#), [289](#), [491](#), [492](#), and [502](#).)
- [4] S. de Léséleuc, V. Lienhard, P. Scholl, D. Barredo, S. Weber, N. Lang, H. P. Büchler, T. Lahaye and A. Browaeys, *Experimental realization of a symmetry protected topological phase of interacting bosons with Rydberg atoms*, arXiv e-prints arXiv:1810.13286 (2018), arXiv:[1810.13286](https://arxiv.org/abs/1810.13286). (Cited on pages [iv](#), [379](#), [383](#), [393](#), [394](#), [396](#), [400](#), [425](#), [430](#), and [431](#).)
- [5] L. D. Landau, *Zur Theorie der Phasenumwandlungen I*, Physikalische Zeitschrift der Sowjetunion **11**, 26 (1937). (Cited on pages [4](#), [5](#), and [6](#).)
- [6] L. D. Landau, *Zur Theorie der Phasenumwandlungen II*, Physikalische Zeitschrift der Sowjetunion **11**, 545 (1937). (Cited on pages [4](#), [5](#), and [6](#).)
- [7] V. L. Ginzburg and L. D. Landau, *On the theory of superconductivity*, Journal of Experimental and Theoretical Physics (JETP) **20**, 1064 (1950). (Cited on pages [4](#), [5](#), and [6](#).)
- [8] J. M. Kosterlitz and D. J. Thouless, *Ordering, metastability and phase transitions in two-dimensional systems*, Journal of Physics C: Solid State Physics **6**(7), 1181 (1973), doi:[10.1088/0022-3719/6/7/010](https://doi.org/10.1088/0022-3719/6/7/010). (Cited on page [5](#).)
- [9] J. M. Kosterlitz, *The critical properties of the two-dimensional XY model*, Journal of Physics C: Solid State Physics **7**(6), 1046 (1974), doi:[10.1088/0022-3719/7/6/005](https://doi.org/10.1088/0022-3719/7/6/005). (Cited on page [5](#).)
- [10] N. D. Mermin and H. Wagner, *Absence of ferromagnetism or antiferromagnetism in one- or two-dimensional isotropic Heisenberg models*, Physical Review Letters **17**, 1133 (1966), doi:[10.1103/physrevlett.17.1133](https://doi.org/10.1103/physrevlett.17.1133). (Cited on page [5](#).)
- [11] P. C. Hohenberg, *Existence of long-range order in one and two dimensions*, Physical Review **158**, 383 (1967), doi:[10.1103/physrev.158.383](https://doi.org/10.1103/physrev.158.383). (Cited on page [5](#).)
- [12] N. D. Mermin, *Crystalline order in two dimensions*, Physical Review **176**, 250 (1968), doi:[10.1103/physrev.176.250](https://doi.org/10.1103/physrev.176.250). (Cited on page [5](#).)
- [13] S. Sachdev, *Quantum Phase Transitions*, Cambridge University Press, ISBN 0521514681 (2011). (Cited on page [5](#).)

BIBLIOGRAPHY

- [14] E. Witten, *Topological quantum field theory*, Communications in Mathematical Physics **117**(3), 353 (1988), doi:[10.1007/bf01223371](https://doi.org/10.1007/bf01223371). (Cited on pages 6, 8, and 101.)
- [15] X.-G. Wen, *Topological orders in rigid states*, International Journal of Modern Physics B **04**(02), 239 (1990), doi:[10.1142/s0217979290000139](https://doi.org/10.1142/s0217979290000139). (Cited on pages 6 and 432.)
- [16] X. Chen, Z.-C. Gu and X.-G. Wen, *Local unitary transformation, long-range quantum entanglement, wave function renormalization, and topological order*, Physical Review B **82**, 155138 (2010), doi:[10.1103/physrevb.82.155138](https://doi.org/10.1103/physrevb.82.155138). (Cited on pages 6, 7, and 9.)
- [17] X. Chen, Z.-C. Gu and X.-G. Wen, *Classification of gapped symmetric phases in one-dimensional spin systems*, Physical Review B **83**, 035107 (2011), doi:[10.1103/physrevb.83.035107](https://doi.org/10.1103/physrevb.83.035107). (Cited on pages 6, 9, 18, 53, and 409.)
- [18] X. Chen, Z.-C. Gu, Z.-X. Liu and X.-G. Wen, *Symmetry protected topological orders and the group cohomology of their symmetry group*, Physical Review B **87**, 155114 (2013), doi:[10.1103/physrevb.87.155114](https://doi.org/10.1103/physrevb.87.155114). (Cited on pages 6, 18, 411, 414, and 420.)
- [19] Z.-C. Gu and X.-G. Wen, *Symmetry-protected topological orders for interacting fermions: Fermionic topological nonlinear σ models and a special group supercohomology theory*, Physical Review B **90**, 115141 (2014), doi:[10.1103/physrevb.90.115141](https://doi.org/10.1103/physrevb.90.115141). (Cited on pages 6 and 17.)
- [20] A. Kapustin, R. Thorngren, A. Turzillo and Z. Wang, *Fermionic symmetry protected topological phases and cobordisms*, Journal of High Energy Physics **2015**(12), 1 (2015), doi:[10.1007/jhep12\(2015\)052](https://doi.org/10.1007/jhep12(2015)052). (Cited on pages 6 and 17.)
- [21] A. P. Schnyder, S. Ryu, A. Furusaki and A. W. W. Ludwig, *Classification of topological insulators and superconductors in three spatial dimensions*, Physical Review B **78**, 195125 (2008), doi:[10.1103/physrevb.78.195125](https://doi.org/10.1103/physrevb.78.195125). (Cited on pages 6, 15, 16, 203, 209, 229, 242, 247, 383, and 389.)
- [22] A. Kitaev, *Periodic table for topological insulators and superconductors*, AIP Conference Proceedings **1134**(1), 22 (2009), doi:[10.1063/1.3149495](https://doi.org/10.1063/1.3149495). (Cited on pages 6, 15, 16, 25, 27, 34, 53, 69, 203, 209, 242, 247, 383, and 389.)
- [23] P. Anderson, *Resonating valence bonds: A new kind of insulator?*, Materials Research Bulletin **8**(2), 153 (1973), doi:[10.1016/0025-5408\(73\)90167-0](https://doi.org/10.1016/0025-5408(73)90167-0). (Cited on page 5.)
- [24] A. Kitaev, *Anyons in an exactly solved model and beyond*, Annals of Physics **321**(1), 2 (2006), doi:[10.1016/j.aop.2005.10.005](https://doi.org/10.1016/j.aop.2005.10.005). (Cited on pages 5, 8, 38, 39, 97, 103, 185, 297, 305, and 432.)
- [25] S. Sachdev, *Quantum magnetism and criticality*, Nature Physics **4**, 173 (2008), doi:[10.1038/nphys894](https://doi.org/10.1038/nphys894). (Cited on page 5.)
- [26] L. Balents, *Spin liquids in frustrated magnets*, Nature **464**, 199 (2010), doi:[10.1038/nature08917](https://doi.org/10.1038/nature08917). (Cited on pages 5 and 39.)
- [27] D. C. Tsui, H. L. Stormer and A. C. Gossard, *Two-dimensional magnetotransport in the extreme quantum limit*, Physical Review Letters **48**, 1559 (1982), doi:[10.1103/physrevlett.48.1559](https://doi.org/10.1103/physrevlett.48.1559). (Cited on pages 5, 7, 13, 37, 203, and 432.)
- [28] H. L. Stormer, A. Chang, D. C. Tsui, J. C. M. Hwang, A. C. Gossard and W. Wiegmann, *Fractional quantization of the Hall effect*, Physical Review Letters **50**, 1953 (1983), doi:[10.1103/physrevlett.50.1953](https://doi.org/10.1103/physrevlett.50.1953). (Cited on pages 5, 37, 203, and 432.)
- [29] R. Willett, J. P. Eisenstein, H. L. Störmer, D. C. Tsui, A. C. Gossard and J. H. English, *Observation of an even-denominator quantum number in the fractional quantum Hall effect*, Physical Review Letters **59**, 1776 (1987), doi:[10.1103/physrevlett.59.1776](https://doi.org/10.1103/physrevlett.59.1776). (Cited on pages 5, 37, 203, and 432.)

BIBLIOGRAPHY

- [30] G. Giuliani and G. Vignale, *Quantum Theory of the Electron Liquid*, Masters Series in Physics and Astronomy. Cambridge University Press, ISBN 0521821126 (2005). (Cited on page 5.)
- [31] A. Kitaev and J. Preskill, *Topological entanglement entropy*, Physical Review Letters **96**, 110404 (2006), doi:[10.1103/physrevlett.96.110404](https://doi.org/10.1103/physrevlett.96.110404). (Cited on page 7.)
- [32] M. Levin and X.-G. Wen, *Detecting topological order in a ground state wave function*, Physical Review Letters **96**, 110405 (2006), doi:[10.1103/physrevlett.96.110405](https://doi.org/10.1103/physrevlett.96.110405). (Cited on page 7.)
- [33] I. D. Rodríguez and G. Sierra, *Entanglement entropy of integer quantum Hall states*, Physical Review B **80**, 153303 (2009), doi:[10.1103/physrevb.80.153303](https://doi.org/10.1103/physrevb.80.153303). (Cited on page 7.)
- [34] X.-G. Wen, *Colloquium: Zoo of quantum-topological phases of matter*, Reviews of Modern Physics **89**, 041004 (2017), doi:[10.1103/revmodphys.89.041004](https://doi.org/10.1103/revmodphys.89.041004). (Cited on pages 7, 9, 12, 13, 18, 29, and 34.)
- [35] X.-G. Wen and Q. Niu, *Ground-state degeneracy of the fractional quantum Hall states in the presence of a random potential and on high-genus Riemann surfaces*, Physical Review B **41**, 9377 (1990), doi:[10.1103/physrevb.41.9377](https://doi.org/10.1103/physrevb.41.9377). (Cited on page 8.)
- [36] R. B. Laughlin, *Anomalous quantum Hall effect: An incompressible quantum fluid with fractionally charged excitations*, Physical Review Letters **50**, 1395 (1983), doi:[10.1103/physrevlett.50.1395](https://doi.org/10.1103/physrevlett.50.1395). (Cited on pages 8, 13, 37, and 434.)
- [37] D. Arovas, J. R. Schrieffer and F. Wilczek, *Fractional statistics and the quantum Hall effect*, Physical Review Letters **53**, 722 (1984), doi:[10.1103/physrevlett.53.722](https://doi.org/10.1103/physrevlett.53.722). (Cited on pages 8, 53, 432, and 434.)
- [38] G. Moore and N. Read, *Nonabelions in the fractional quantum Hall effect*, Nuclear Physics B **360**(2), 362 (1991), doi:[10.1016/0550-3213\(91\)90407-o](https://doi.org/10.1016/0550-3213(91)90407-o). (Cited on pages 8, 37, and 432.)
- [39] X.-G. Wen, *Chiral Luttinger liquid and the edge excitations in the fractional quantum Hall states*, Physical Review B **41**, 12838 (1990), doi:[10.1103/physrevb.41.12838](https://doi.org/10.1103/physrevb.41.12838). (Cited on pages 8, 433, and 437.)
- [40] A. Zee, *Quantum Hall fluids*, In *Field Theory, Topology and Condensed Matter Physics*, pp. 99–153. Springer Berlin Heidelberg, doi:[10.1007/bfb0113369](https://doi.org/10.1007/bfb0113369) (1995). (Cited on pages 8 and 154.)
- [41] E. Witten, *Quantum field theory and the Jones polynomial*, Communications in Mathematical Physics **121**(3), 351 (1989), doi:[10.1007/bf01217730](https://doi.org/10.1007/bf01217730). (Cited on page 8.)
- [42] X.-G. Wen, *Topological orders and edge excitations in fractional quantum Hall states*, Advances in Physics **44**(5), 405 (1995), doi:[10.1080/00018739500101566](https://doi.org/10.1080/00018739500101566). (Cited on pages 8 and 154.)
- [43] M. Blau and G. Thompson, *Topological gauge theories of antisymmetric tensor fields*, Annals of Physics **205**(1), 130 (1991), doi:[10.1016/0003-4916\(91\)90240-9](https://doi.org/10.1016/0003-4916(91)90240-9). (Cited on page 8.)
- [44] T. Hansson, V. Oganesyan and S. Sondhi, *Superconductors are topologically ordered*, Annals of Physics **313**(2), 497 (2004), doi:[10.1016/j.aop.2004.05.006](https://doi.org/10.1016/j.aop.2004.05.006). (Cited on pages 8 and 9.)
- [45] A. Kitaev, *Fault-tolerant quantum computation by anyons*, Annals of Physics **303**(1), 2 (2003), doi:[10.1016/s0003-4916\(02\)00018-0](https://doi.org/10.1016/s0003-4916(02)00018-0). (Cited on pages 8, 9, 37, 39, 53, 102, 305, 432, 492, 502, 506, 510, 523, and 535.)

BIBLIOGRAPHY

- [46] M. A. Levin and X.-G. Wen, *String-net condensation: A physical mechanism for topological phases*, Physical Review B **71**, 045110 (2005), doi:[10.1103/physrevb.71.045110](https://doi.org/10.1103/physrevb.71.045110). (Cited on page 8.)
- [47] C. Nayak, S. H. Simon, A. Stern, M. Freedman and S. Das Sarma, *Non-abelian anyons and topological quantum computation*, Reviews of Modern Physics **80**, 1083 (2008), doi:[10.1103/revmodphys.80.1083](https://doi.org/10.1103/revmodphys.80.1083). (Cited on pages 8, 37, 53, 203, and 432.)
- [48] Z. Wang, *Topological Quantum Computation*, No. 112 in Regional Conference Series in Mathematics / Conference Board of the Mathematical Sciences. American Mathematical Society, ISBN 9780821849309 (2010). (Cited on pages 8, 9, 101, 105, and 186.)
- [49] E. Dennis, A. Kitaev, A. Landahl and J. Preskill, *Topological quantum memory*, Journal of Mathematical Physics **43**(9), 4452 (2002), doi:[10.1063/1.1499754](https://doi.org/10.1063/1.1499754). (Cited on pages 8, 297, 305, and 523.)
- [50] B. J. Brown, D. Loss, J. K. Pachos, C. N. Self and J. R. Wootton, *Quantum memories at finite temperature*, Reviews of Modern Physics **88**, 045005 (2016), doi:[10.1103/revmodphys.88.045005](https://doi.org/10.1103/revmodphys.88.045005). (Cited on pages 8, 39, 297, and 507.)
- [51] L. Kong and X.-G. Wen, *Braided fusion categories, gravitational anomalies, and the mathematical framework for topological orders in any dimensions*, arXiv e-prints arXiv:1405.5858 (2014), arXiv:[1405.5858](https://arxiv.org/abs/1405.5858). (Cited on page 9.)
- [52] S. B. Bravyi and A. Y. Kitaev, *Quantum codes on a lattice with boundary*, arXiv e-prints quant-ph/9811052 (1998), arXiv:[quant-ph/9811052](https://arxiv.org/abs/quant-ph/9811052). (Cited on pages 9, 305, and 523.)
- [53] X.-G. Wen, *Topological orders and Chern-Simons theory in strongly correlated quantum liquid*, International Journal of Modern Physics B **05**(10), 1641 (1991), doi:[10.1142/s0217979291001541](https://doi.org/10.1142/s0217979291001541). (Cited on page 9.)
- [54] X.-G. Wen, *Quantum orders and symmetric spin liquids*, Physical Review B **65**, 165113 (2002), doi:[10.1103/physrevb.65.165113](https://doi.org/10.1103/physrevb.65.165113). (Cited on page 9.)
- [55] H. Simmons, *An Introduction to Category Theory*, Cambridge University Press, ISBN 0521283043 (2011). (Cited on pages 9 and 101.)
- [56] B. Coecke and É. Paquette, *Categories for the Practising Physicist*, pp. 173–286, Springer Berlin Heidelberg, ISBN 978-3-642-12821-9, doi:[10.1007/978-3-642-12821-9_3](https://doi.org/10.1007/978-3-642-12821-9_3) (2011). (Cited on pages 9 and 101.)
- [57] P. Panangaden and É. Paquette, *A Categorical Presentation of Quantum Computation with Anyons*, pp. 983–1025, Springer Berlin Heidelberg, ISBN 978-3-642-12821-9, doi:[10.1007/978-3-642-12821-9_15](https://doi.org/10.1007/978-3-642-12821-9_15) (2011). (Cited on pages 9, 101, and 105.)
- [58] X.-G. Wen, *A theory of 2+1D bosonic topological orders*, National Science Review **3**(1), 68 (2016), doi:[10.1093/nsr/nwv077](https://doi.org/10.1093/nsr/nwv077). (Cited on page 9.)
- [59] V. Kalmeyer and R. B. Laughlin, *Equivalence of the resonating-valence-bond and fractional quantum Hall states*, Physical Review Letters **59**, 2095 (1987), doi:[10.1103/physrevlett.59.2095](https://doi.org/10.1103/physrevlett.59.2095). (Cited on page 10.)
- [60] X.-G. Wen, F. Wilczek and A. Zee, *Chiral spin states and superconductivity*, Physical Review B **39**, 11413 (1989), doi:[10.1103/physrevb.39.11413](https://doi.org/10.1103/physrevb.39.11413). (Cited on page 10.)
- [61] X.-G. Wen, *Vacuum degeneracy of chiral spin states in compactified space*, Physical Review B **40**, 7387 (1989), doi:[10.1103/physrevb.40.7387](https://doi.org/10.1103/physrevb.40.7387). (Cited on page 10.)
- [62] F. Haldane, *Continuum dynamics of the 1-D Heisenberg antiferromagnet: Identification with the O(3) nonlinear sigma model*, Physics Letters A **93**(9), 464 (1983), doi:[10.1016/0375-9601\(83\)90631-x](https://doi.org/10.1016/0375-9601(83)90631-x). (Cited on pages 12 and 423.)

BIBLIOGRAPHY

- [63] F. D. M. Haldane, *Nonlinear field theory of large-spin Heisenberg antiferromagnets: Semiclassically quantized solitons of the one-dimensional easy-axis Néel state*, Physical Review Letters **50**, 1153 (1983), doi:[10.1103/physrevlett.50.1153](https://doi.org/10.1103/physrevlett.50.1153). (Cited on pages 12 and 423.)
- [64] Z.-C. Gu and X.-G. Wen, *Tensor-entanglement-filtering renormalization approach and symmetry-protected topological order*, Physical Review B **80**, 155131 (2009), doi:[10.1103/physrevb.80.155131](https://doi.org/10.1103/physrevb.80.155131). (Cited on pages 12 and 18.)
- [65] F. Pollmann, E. Berg, A. M. Turner and M. Oshikawa, *Symmetry protection of topological phases in one-dimensional quantum spin systems*, Physical Review B **85**, 075125 (2012), doi:[10.1103/physrevb.85.075125](https://doi.org/10.1103/physrevb.85.075125). (Cited on pages 12, 399, and 400.)
- [66] A. Mesaros and Y. Ran, *Classification of symmetry enriched topological phases with exactly solvable models*, Physical Review B **87**, 155115 (2013), doi:[10.1103/physrevb.87.155115](https://doi.org/10.1103/physrevb.87.155115). (Cited on page 13.)
- [67] M. Barkeshli, P. Bonderson, M. Cheng and Z. Wang, *Symmetry, defects, and gauging of topological phases*, arXiv e-prints arXiv:1410.4540 (2014), arXiv:[1410.4540](https://arxiv.org/abs/1410.4540). (Cited on page 13.)
- [68] C.-K. Chiu, J. C. Y. Teo, A. P. Schnyder and S. Ryu, *Classification of topological quantum matter with symmetries*, Reviews of Modern Physics **88**, 035005 (2016), doi:[10.1103/revmodphys.88.035005](https://doi.org/10.1103/revmodphys.88.035005). (Cited on page 13.)
- [69] K. v. Klitzing, G. Dorda and M. Pepper, *New method for high-accuracy determination of the fine-structure constant based on quantized Hall resistance*, Physical Review Letters **45**, 494 (1980), doi:[10.1103/physrevlett.45.494](https://doi.org/10.1103/physrevlett.45.494). (Cited on pages 14, 203, and 432.)
- [70] D. J. Thouless, M. Kohmoto, M. P. Nightingale and M. den Nijs, *Quantized Hall conductance in a two-dimensional periodic potential*, Physical Review Letters **49**, 405 (1982), doi:[10.1103/physrevlett.49.405](https://doi.org/10.1103/physrevlett.49.405). (Cited on pages 14, 15, and 18.)
- [71] F. D. M. Haldane, *Model for a quantum Hall effect without Landau levels: Condensed-matter realization of the “parity anomaly”*, Physical Review Letters **61**, 2015 (1988), doi:[10.1103/physrevlett.61.2015](https://doi.org/10.1103/physrevlett.61.2015). (Cited on page 14.)
- [72] C. L. Kane and E. J. Mele, *Quantum spin Hall effect in graphene*, Physical Review Letters **95**, 226801 (2005), doi:[10.1103/physrevlett.95.226801](https://doi.org/10.1103/physrevlett.95.226801). (Cited on page 14.)
- [73] C. L. Kane and E. J. Mele, *Z_2 topological order and the quantum spin Hall effect*, Physical Review Letters **95**, 146802 (2005), doi:[10.1103/physrevlett.95.146802](https://doi.org/10.1103/physrevlett.95.146802). (Cited on pages 14, 15, and 18.)
- [74] B. A. Bernevig, T. L. Hughes and S.-C. Zhang, *Quantum spin Hall effect and topological phase transition in HgTe quantum wells*, Science **314**(5806), 1757 (2006), doi:[10.1126/science.1133734](https://doi.org/10.1126/science.1133734). (Cited on page 14.)
- [75] M. König, S. Wiedmann, C. Brüne, A. Roth, H. Buhmann, L. W. Molenkamp, X.-L. Qi and S.-C. Zhang, *Quantum spin Hall insulator state in HgTe quantum wells*, Science **318**(5851), 766 (2007), doi:[10.1126/science.1148047](https://doi.org/10.1126/science.1148047). (Cited on pages 14 and 203.)
- [76] L. Fu, C. L. Kane and E. J. Mele, *Topological insulators in three dimensions*, Physical Review Letters **98**, 106803 (2007), doi:[10.1103/physrevlett.98.106803](https://doi.org/10.1103/physrevlett.98.106803). (Cited on page 14.)
- [77] J. E. Moore and L. Balents, *Topological invariants of time-reversal-invariant band structures*, Physical Review B **75**, 121306 (2007), doi:[10.1103/physrevb.75.121306](https://doi.org/10.1103/physrevb.75.121306). (Cited on page 14.)
- [78] D. Hsieh, D. Qian, L. Wray, Y. Xia, Y. S. Hor, R. J. Cava and M. Z. Hasan, *A topological Dirac insulator in a quantum spin Hall phase*, Nature **452**, 970 (2008), doi:[10.1038/nature06843](https://doi.org/10.1038/nature06843). (Cited on pages 14 and 203.)

BIBLIOGRAPHY

- [79] N. Read and D. Green, *Paired states of fermions in two dimensions with breaking of parity and time-reversal symmetries and the fractional quantum Hall effect*, Physical Review B **61**, 10267 (2000), doi:[10.1103/physrevb.61.10267](https://doi.org/10.1103/physrevb.61.10267). (Cited on pages 14 and 38.)
- [80] R. Roy, *Topological superfluids with time reversal symmetry*, arXiv e-prints arXiv:0803.2868 (2008), arXiv:[0803.2868](https://arxiv.org/abs/0803.2868). (Cited on page 14.)
- [81] X.-L. Qi, T. L. Hughes, S. Raghu and S.-C. Zhang, *Time-reversal-invariant topological superconductors and superfluids in two and three dimensions*, Physical Review Letters **102**, 187001 (2009), doi:[10.1103/physrevlett.102.187001](https://doi.org/10.1103/physrevlett.102.187001). (Cited on page 14.)
- [82] A. Y. Kitaev, *Unpaired Majorana fermions in quantum wires*, Physics-Uspekhi **44**(10S), 131 (2001), doi:[10.1070/1063-7869/44/10s/s29](https://doi.org/10.1070/1063-7869/44/10s/s29). (Cited on pages 15, 27, 28, 38, 53, 58, 183, 203, 207, 211, 241, 297, 298, and 301.)
- [83] D. A. Ivanov, *Non-abelian statistics of half-quantum vortices in p-wave superconductors*, Physical Review Letters **86**, 268 (2001), doi:[10.1103/PhysRevLett.86.268](https://doi.org/10.1103/PhysRevLett.86.268). (Cited on pages 15, 38, 53, and 183.)
- [84] P. Heinzner, A. Huckleberry and M. Zirnbauer, *Symmetry classes of disordered fermions*, Communications in Mathematical Physics **257**(3), 725 (2005), doi:[10.1007/s00220-005-1330-9](https://doi.org/10.1007/s00220-005-1330-9). (Cited on page 15.)
- [85] A. W. W. Ludwig, *Topological phases: Classification of topological insulators and superconductors of non-interacting fermions, and beyond*, Physica Scripta **2016**(T168), 014001 (2016), doi:[10.1088/0031-8949/2015/t168/014001](https://doi.org/10.1088/0031-8949/2015/t168/014001). (Cited on pages 15, 16, 22, 23, 30, and 390.)
- [86] L. Fu, *Topological crystalline insulators*, Physical Review Letters **106**, 106802 (2011), doi:[10.1103/physrevlett.106.106802](https://doi.org/10.1103/physrevlett.106.106802). (Cited on page 15.)
- [87] C.-K. Chiu, H. Yao and S. Ryu, *Classification of topological insulators and superconductors in the presence of reflection symmetry*, Physical Review B **88**, 075142 (2013), doi:[10.1103/physrevb.88.075142](https://doi.org/10.1103/physrevb.88.075142). (Cited on page 15.)
- [88] T. Morimoto and A. Furusaki, *Topological classification with additional symmetries from Clifford algebras*, Physical Review B **88**, 125129 (2013), doi:[10.1103/physrevb.88.125129](https://doi.org/10.1103/physrevb.88.125129). (Cited on page 15.)
- [89] K. Shiozaki and M. Sato, *Topology of crystalline insulators and superconductors*, Physical Review B **90**, 165114 (2014), doi:[10.1103/physrevb.90.165114](https://doi.org/10.1103/physrevb.90.165114). (Cited on page 15.)
- [90] A. Altland and M. R. Zirnbauer, *Nonstandard symmetry classes in mesoscopic normal-superconducting hybrid structures*, Physical Review B **55**, 1142 (1997), doi:[10.1103/physrevb.55.1142](https://doi.org/10.1103/physrevb.55.1142). (Cited on pages 15, 203, 209, 242, 247, 383, and 389.)
- [91] E. P. Wigner, *On the statistical distribution of the widths and spacings of nuclear resonance levels*, Mathematical Proceedings of the Cambridge Philosophical Society **47**(4), 790 (1951), doi:[10.1017/s0305004100027237](https://doi.org/10.1017/s0305004100027237). (Cited on pages 15, 203, 209, 242, 247, 383, and 389.)
- [92] E. P. Wigner, *On the distribution of the roots of certain symmetric matrices*, Annals of Mathematics **67**(2), 325 (1958), doi:[10.2307/1970008](https://doi.org/10.2307/1970008). (Cited on pages 15, 203, 209, 242, 247, 383, and 389.)
- [93] F. J. Dyson, *The threefold way. Algebraic structure of symmetry groups and ensembles in quantum mechanics*, Journal of Mathematical Physics **3**(6), 1199 (1962), doi:[10.1063/1.1703863](https://doi.org/10.1063/1.1703863). (Cited on pages 15, 203, 209, 242, 247, 383, and 389.)

BIBLIOGRAPHY

- [94] J. Zak, *Berry's phase for energy bands in solids*, Physical Review Letters **62**, 2747 (1989), doi:[10.1103/physrevlett.62.2747](https://doi.org/10.1103/physrevlett.62.2747). (Cited on pages 15 and 203.)
- [95] A. P. Schnyder, S. Ryu, A. Furusaki and A. W. W. Ludwig, *Classification of topological insulators and superconductors*, AIP Conference Proceedings **1134**(1), 10 (2009), doi:[10.1063/1.3149481](https://doi.org/10.1063/1.3149481). (Cited on pages 15, 16, 25, 27, 203, 209, 229, 242, 247, 383, and 389.)
- [96] P. W. Anderson, *Absence of diffusion in certain random lattices*, Physical Review **109**, 1492 (1958), doi:[10.1103/physrev.109.1492](https://doi.org/10.1103/physrev.109.1492). (Cited on pages 15 and 229.)
- [97] S. Ryu, A. P. Schnyder, A. Furusaki and A. W. W. Ludwig, *Topological insulators and superconductors: Tenfold way and dimensional hierarchy*, New Journal of Physics **12**(6), 065010 (2010), doi:[10.1088/1367-2630/12/6/065010](https://doi.org/10.1088/1367-2630/12/6/065010). (Cited on pages 15, 16, 53, 56, 69, 203, 209, 229, 242, 247, 383, 389, and 390.)
- [98] Y. Hatsugai, *Chern number and edge states in the integer quantum Hall effect*, Physical Review Letters **71**, 3697 (1993), doi:[10.1103/physrevlett.71.3697](https://doi.org/10.1103/physrevlett.71.3697). (Cited on page 16.)
- [99] A. M. Essin and V. Gurarie, *Bulk-boundary correspondence of topological insulators from their respective Green's functions*, Physical Review B **84**, 125132 (2011), doi:[10.1103/physrevb.84.125132](https://doi.org/10.1103/physrevb.84.125132). (Cited on page 16.)
- [100] T. Fukui, K. Shiozaki, T. Fujiwara and S. Fujimoto, *Bulk-edge correspondence for Chern topological phases: A viewpoint from a generalized index theorem*, Journal of the Physical Society of Japan **81**(11), 114602 (2012), doi:[10.1143/jpsj.81.114602](https://doi.org/10.1143/jpsj.81.114602). (Cited on page 16.)
- [101] J. C. Budich and B. Trauzettel, *From the adiabatic theorem of quantum mechanics to topological states of matter*, physica status solidi (RRL) – Rapid Research Letters **7**(12), 109 (2013), doi:[10.1002/pssr.201206416](https://doi.org/10.1002/pssr.201206416). (Cited on pages 16 and 36.)
- [102] M. Z. Hasan and C. L. Kane, *Colloquium: Topological insulators*, Reviews of Modern Physics **82**, 3045 (2010), doi:[10.1103/revmodphys.82.3045](https://doi.org/10.1103/revmodphys.82.3045). (Cited on pages 16 and 203.)
- [103] X.-L. Qi and S.-C. Zhang, *Topological insulators and superconductors*, Reviews of Modern Physics **83**, 1057 (2011), doi:[10.1103/revmodphys.83.1057](https://doi.org/10.1103/revmodphys.83.1057). (Cited on pages 16 and 203.)
- [104] W. A. Benalcazar, B. A. Bernevig and T. L. Hughes, *Quantized electric multipole insulators*, Science **357**(6346), 61 (2017), doi:[10.1126/science.aah6442](https://doi.org/10.1126/science.aah6442). (Cited on page 16.)
- [105] F. Schindler, A. M. Cook, M. G. Vergniory, Z. Wang, S. S. P. Parkin, B. A. Bernevig and T. Neupert, *Higher-order topological insulators*, Science Advances **4**(6), eaat0346 (2018), doi:[10.1126/sciadv.aat0346](https://doi.org/10.1126/sciadv.aat0346). (Cited on page 16.)
- [106] F. Schindler, Z. Wang, M. G. Vergniory, A. M. Cook, A. Murani, S. Sengupta, A. Y. Kasumov, R. Deblock, S. Jeon, I. Drozdov, H. Bouchiat, S. Guéron *et al.*, *Higher-order topology in bismuth*, Nature Physics **14**(9), 918 (2018), doi:[10.1038/s41567-018-0224-7](https://doi.org/10.1038/s41567-018-0224-7). (Cited on page 16.)
- [107] L. Fidkowski and A. Kitaev, *Effects of interactions on the topological classification of free fermion systems*, Physical Review B **81**, 134509 (2010), doi:[10.1103/physrevb.81.134509](https://doi.org/10.1103/physrevb.81.134509). (Cited on pages 17 and 396.)
- [108] H. Yao and S. Ryu, *Interaction effect on topological classification of superconductors in two dimensions*, Physical Review B **88**, 064507 (2013), doi:[10.1103/physrevb.88.064507](https://doi.org/10.1103/physrevb.88.064507). (Cited on page 17.)
- [109] C. Wang, C.-H. Lin and Z.-C. Gu, *Interacting fermionic symmetry-protected topological phases in two dimensions*, Physical Review B **95**, 195147 (2017), doi:[10.1103/physrevb.95.195147](https://doi.org/10.1103/physrevb.95.195147). (Cited on page 17.)

BIBLIOGRAPHY

- [110] L. Fidkowski and A. Kitaev, *Topological phases of fermions in one dimension*, Physical Review B **83**, 075103 (2011), doi:[10.1103/physrevb.83.075103](https://doi.org/10.1103/physrevb.83.075103). (Cited on pages 17 and 53.)
- [111] A. M. Turner, F. Pollmann and E. Berg, *Topological phases of one-dimensional fermions: An entanglement point of view*, Physical Review B **83**, 075102 (2011), doi:[10.1103/physrevb.83.075102](https://doi.org/10.1103/physrevb.83.075102). (Cited on pages 17 and 72.)
- [112] X. Chen, Z.-C. Gu and X.-G. Wen, *Complete classification of one-dimensional gapped quantum phases in interacting spin systems*, Physical Review B **84**, 235128 (2011), doi:[10.1103/physrevb.84.235128](https://doi.org/10.1103/physrevb.84.235128). (Cited on pages 17, 18, 406, 411, and 412.)
- [113] M. Cheng, Z. Bi, Y.-Z. You and Z.-C. Gu, *Classification of symmetry-protected phases for interacting fermions in two dimensions*, Physical Review B **97**, 205109 (2018), doi:[10.1103/physrevb.97.205109](https://doi.org/10.1103/physrevb.97.205109). (Cited on page 17.)
- [114] A. Kapustin and R. Thorngren, *Fermionic SPT phases in higher dimensions and bosonization*, Journal of High Energy Physics **2017**(10), 80 (2017), doi:[10.1007/jhep10\(2017\)080](https://doi.org/10.1007/jhep10(2017)080). (Cited on page 17.)
- [115] Q.-R. Wang and Z.-C. Gu, *Towards a complete classification of symmetry-protected topological phases for interacting fermions in three dimensions and a general group supercohomology theory*, Physical Review X **8**, 011055 (2018), doi:[10.1103/physrevx.8.011055](https://doi.org/10.1103/physrevx.8.011055). (Cited on page 17.)
- [116] S. Rachel, *Interacting topological insulators: a review*, Reports on Progress in Physics **81**(11), 116501 (2018), doi:[10.1088/1361-6633/aad6a6](https://doi.org/10.1088/1361-6633/aad6a6). (Cited on page 17.)
- [117] C. Brouder, G. Panati, M. Calandra, C. Mourougane and N. Marzari, *Exponential localization of Wannier functions in insulators*, Physical Review Letters **98**, 046402 (2007), doi:[10.1103/physrevlett.98.046402](https://doi.org/10.1103/physrevlett.98.046402). (Cited on pages 18 and 536.)
- [118] M. B. Hastings and T. A. Loring, *Almost commuting matrices, localized Wannier functions, and the quantum Hall effect*, Journal of Mathematical Physics **51**(1), 015214 (2010), doi:[10.1063/1.3274817](https://doi.org/10.1063/1.3274817). (Cited on pages 18 and 536.)
- [119] N. Schuch, D. Pérez-García and I. Cirac, *Classifying quantum phases using matrix product states and projected entangled pair states*, Physical Review B **84**, 165139 (2011), doi:[10.1103/physrevb.84.165139](https://doi.org/10.1103/physrevb.84.165139). (Cited on pages 18, 53, and 409.)
- [120] X. Chen, Z.-C. Gu, Z.-X. Liu and X.-G. Wen, *Symmetry-protected topological orders in interacting bosonic systems*, Science **338**(6114), 1604 (2012), doi:[10.1126/science.1227224](https://doi.org/10.1126/science.1227224). (Cited on page 18.)
- [121] A. Vishwanath and T. Senthil, *Physics of three-dimensional bosonic topological insulators: Surface-deconfined criticality and quantized magnetoelectric effect*, Physical Review X **3**, 011016 (2013), doi:[10.1103/physrevx.3.011016](https://doi.org/10.1103/physrevx.3.011016). (Cited on page 18.)
- [122] C. Wang and T. Senthil, *Boson topological insulators: A window into highly entangled quantum phases*, Physical Review B **87**, 235122 (2013), doi:[10.1103/physrevb.87.235122](https://doi.org/10.1103/physrevb.87.235122). (Cited on page 18.)
- [123] F. J. Burnell, X. Chen, L. Fidkowski and A. Vishwanath, *Exactly soluble model of a three-dimensional symmetry-protected topological phase of bosons with surface topological order*, Physical Review B **90**, 245122 (2014), doi:[10.1103/physrevb.90.245122](https://doi.org/10.1103/physrevb.90.245122). (Cited on page 18.)
- [124] A. Kapustin, *Symmetry protected topological phases, anomalies, and cobordisms: Beyond group cohomology*, arXiv e-prints arXiv:1403.1467 (2014), arXiv:[1403.1467](https://arxiv.org/abs/1403.1467). (Cited on page 18.)
- [125] A. Kapustin, *Bosonic topological insulators and paramagnets: a view from cobordisms*, arXiv e-prints arXiv:1404.6659 (2014), arXiv:[1404.6659](https://arxiv.org/abs/1404.6659). (Cited on page 18.)

BIBLIOGRAPHY

- [126] W. P. Su, J. R. Schrieffer and A. J. Heeger, *Solitons in polyacetylene*, Physical Review Letters **42**, 1698 (1979), doi:[10.1103/physrevlett.42.1698](https://doi.org/10.1103/physrevlett.42.1698). (Cited on pages 19, 203, 207, and 383.)
- [127] J. K. Asbóth, L. Oroszlány and A. P. Pályi, *A Short Course on Topological Insulators: Band Structure and Edge States in One and Two Dimensions*, Lecture Notes in Physics. Springer International Publishing, ISBN 3319256076 (2016). (Cited on page 19.)
- [128] A. Bernevig and T. Neupert, *Topological superconductors and category theory*, Topological Aspects of Condensed Matter Physics: Lecture Notes of the Les Houches Summer School: Volume 103, August 2014 **103**, 63 (2017), doi:[10.1093/acprof:oso/9780198785781.003.0002](https://doi.org/10.1093/acprof:oso/9780198785781.003.0002). (Cited on pages 27, 101, and 105.)
- [129] N. Lang, *Phase transitions and topological phases by driven dissipation*, Master's thesis, University of Stuttgart (2013). (Cited on pages 28 and 487.)
- [130] J. Alicea, Y. Oreg, G. Refael, F. von Oppen and M. P. A. Fisher, *Non-abelian statistics and topological quantum information processing in 1D wire networks*, Nature Physics **7**, 412 (2011), doi:[10.1038/nphys1915](https://doi.org/10.1038/nphys1915). (Cited on pages 34, 38, 92, 97, and 102.)
- [131] M. H. Freedman, *P/NP, and the quantum field computer*, Proceedings of the National Academy of Sciences **95**(1), 98 (1998), doi:[10.1073/pnas.95.1.98](https://doi.org/10.1073/pnas.95.1.98). (Cited on page 37.)
- [132] M. H. Freedman, A. Kitaev, M. J. Larsen and Z. Wang, *Topological quantum computation*, Bulletin of the American Mathematical Society **40**(1), 31 (2002), doi:[10.1090/s0273-0979-02-00964-3](https://doi.org/10.1090/s0273-0979-02-00964-3). (Cited on page 37.)
- [133] S. Das Sarma, M. Freedman and C. Nayak, *Topologically protected qubits from a possible non-abelian fractional quantum Hall state*, Physical Review Letters **94**, 166802 (2005), doi:[10.1103/physrevlett.94.166802](https://doi.org/10.1103/physrevlett.94.166802). (Cited on page 37.)
- [134] M. Freedman, C. Nayak and K. Walker, *Towards universal topological quantum computation in the $\nu = 5/2$ fractional quantum Hall state*, Physical Review B **73**, 245307 (2006), doi:[10.1103/physrevb.73.245307](https://doi.org/10.1103/physrevb.73.245307). (Cited on page 37.)
- [135] J. S. Xia, W. Pan, C. L. Vicente, E. D. Adams, N. S. Sullivan, H. L. Stormer, D. C. Tsui, L. N. Pfeiffer, K. W. Baldwin and K. W. West, *Electron correlation in the second Landau level: A competition between many nearly degenerate quantum phases*, Physical Review Letters **93**, 176809 (2004), doi:[10.1103/physrevlett.93.176809](https://doi.org/10.1103/physrevlett.93.176809). (Cited on page 38.)
- [136] N. Read and E. Rezayi, *Beyond paired quantum Hall states: Parafermions and incompressible states in the first excited Landau level*, Physical Review B **59**, 8084 (1999), doi:[10.1103/physrevb.59.8084](https://doi.org/10.1103/physrevb.59.8084). (Cited on page 38.)
- [137] V. J. Goldman and B. Su, *Resonant tunneling in the quantum Hall regime: Measurement of fractional charge*, Science **267**(5200), 1010 (1995), doi:[10.1126/science.267.5200.1010](https://doi.org/10.1126/science.267.5200.1010). (Cited on page 38.)
- [138] L. Saminadayar, D. C. Glattli, Y. Jin and B. Etienne, *Observation of the $e/3$ fractionally charged Laughlin quasiparticle*, Physical Review Letters **79**, 2526 (1997), doi:[10.1103/physrevlett.79.2526](https://doi.org/10.1103/physrevlett.79.2526). (Cited on page 38.)
- [139] J. Martin, S. Ilani, B. Verdene, J. Smet, V. Umansky, D. Mahalu, D. Schuh, G. Abstreiter and A. Yacoby, *Localization of fractionally charged quasi-particles*, Science **305**(5686), 980 (2004), doi:[10.1126/science.1099950](https://doi.org/10.1126/science.1099950). (Cited on page 38.)
- [140] M. Dolev, M. Heiblum, V. Umansky, A. Stern and D. Mahalu, *Observation of a quarter of an electron charge at the $\nu = 5/2$ quantum Hall state*, Nature **452**, 829 (2008), doi:[10.1038/nature06855](https://doi.org/10.1038/nature06855). (Cited on page 38.)

BIBLIOGRAPHY

- [141] I. P. Radu, J. B. Miller, C. M. Marcus, M. A. Kastner, L. N. Pfeiffer and K. W. West, *Quasi-particle properties from tunneling in the $\nu = 5/2$ fractional quantum Hall state*, *Science* **320**(5878), 899 (2008), doi:[10.1126/science.1157560](https://doi.org/10.1126/science.1157560). (Cited on page 38.)
- [142] V. Venkatachalam, A. Yacoby, L. Pfeiffer and K. West, *Local charge of the $\nu = 5/2$ fractional quantum Hall state*, *Nature* **469**, 185 (2011), doi:[10.1038/nature09680](https://doi.org/10.1038/nature09680). (Cited on page 38.)
- [143] A. Stern and B. I. Halperin, *Proposed experiments to probe the non-abelian $\nu = 5/2$ quantum Hall state*, *Physical Review Letters* **96**, 016802 (2006), doi:[10.1103/physrevlett.96.016802](https://doi.org/10.1103/physrevlett.96.016802). (Cited on page 38.)
- [144] P. Bonderson, A. Kitaev and K. Shtengel, *Detecting non-abelian statistics in the $\nu = 5/2$ fractional quantum Hall state*, *Physical Review Letters* **96**, 016803 (2006), doi:[10.1103/physrevlett.96.016803](https://doi.org/10.1103/physrevlett.96.016803). (Cited on page 38.)
- [145] V. Gurarie, L. Radzihovsky and A. V. Andreev, *Quantum phase transitions across a p -wave Feshbach resonance*, *Physical Review Letters* **94**, 230403 (2005), doi:[10.1103/physrevlett.94.230403](https://doi.org/10.1103/physrevlett.94.230403). (Cited on page 38.)
- [146] S. Das Sarma, C. Nayak and S. Tewari, *Proposal to stabilize and detect half-quantum vortices in strontium ruthenate thin films: Non-abelian braiding statistics of vortices in a $p_x + i p_y$ superconductor*, *Physical Review B* **73**, 220502 (2006), doi:[10.1103/physrevb.73.220502](https://doi.org/10.1103/physrevb.73.220502). (Cited on page 38.)
- [147] S. Tewari, S. Das Sarma, C. Nayak, C. Zhang and P. Zoller, *Quantum computation using vortices and Majorana zero modes of a $p_x + i p_y$ superfluid of fermionic cold atoms*, *Physical Review Letters* **98**, 010506 (2007), doi:[10.1103/physrevlett.98.010506](https://doi.org/10.1103/physrevlett.98.010506). (Cited on page 38.)
- [148] A. Bühler, N. Lang, C. Kraus, G. Möller, S. Huber and H. Büchler, *Majorana modes and p -wave superfluids for fermionic atoms in optical lattices*, *Nature Communications* **5**, 4504 (2014), doi:[10.1038/ncomms5504](https://doi.org/10.1038/ncomms5504). (Cited on pages 38 and 103.)
- [149] L. Fu and C. L. Kane, *Superconducting proximity effect and Majorana fermions at the surface of a topological insulator*, *Physical Review Letters* **100**, 096407 (2008), doi:[10.1103/physrevlett.100.096407](https://doi.org/10.1103/physrevlett.100.096407). (Cited on page 38.)
- [150] J. D. Sau, R. M. Lutchyn, S. Tewari and S. Das Sarma, *Generic new platform for topological quantum computation using semiconductor heterostructures*, *Physical Review Letters* **104**, 040502 (2010), doi:[10.1103/physrevlett.104.040502](https://doi.org/10.1103/physrevlett.104.040502). (Cited on page 38.)
- [151] J. Alicea, *Majorana fermions in a tunable semiconductor device*, *Physical Review B* **81**, 125318 (2010), doi:[10.1103/physrevb.81.125318](https://doi.org/10.1103/physrevb.81.125318). (Cited on page 38.)
- [152] J.-P. Xu, M.-X. Wang, Z. L. Liu, J.-F. Ge, X. Yang, C. Liu, Z. A. Xu, D. Guan, C. L. Gao, D. Qian, Y. Liu, Q.-H. Wang *et al.*, *Experimental detection of a Majorana mode in the core of a magnetic vortex inside a topological insulator-superconductor $\text{Bi}_2\text{Te}_3/\text{NbSe}_2$ heterostructure*, *Physical Review Letters* **114**, 017001 (2015), doi:[10.1103/PhysRevLett.114.017001](https://doi.org/10.1103/PhysRevLett.114.017001). (Cited on pages 38 and 53.)
- [153] H.-H. Sun, K.-W. Zhang, L.-H. Hu, C. Li, G.-Y. Wang, H.-Y. Ma, Z.-A. Xu, C.-L. Gao, D.-D. Guan, Y.-Y. Li, C. Liu, D. Qian *et al.*, *Majorana zero mode detected with spin selective Andreev reflection in the vortex of a topological superconductor*, *Physical Review Letters* **116**, 257003 (2016), doi:[10.1103/physrevlett.116.257003](https://doi.org/10.1103/physrevlett.116.257003). (Cited on page 38.)
- [154] D. Wang, L. Kong, P. Fan, H. Chen, S. Zhu, W. Liu, L. Cao, Y. Sun, S. Du, J. Schneeloch, R. Zhong, G. Gu *et al.*, *Evidence for Majorana bound states in an iron-based superconductor*, *Science* **362**(6412), 333 (2018), doi:[10.1126/science.aao1797](https://doi.org/10.1126/science.aao1797). (Cited on page 38.)

BIBLIOGRAPHY

- [155] M. Barkeshli, C.-M. Jian and X.-L. Qi, *Twist defects and projective non-abelian braiding statistics*, Physical Review B **87**, 045130 (2013), doi:[10.1103/physrevb.87.045130](https://doi.org/10.1103/physrevb.87.045130). (Cited on page 38.)
- [156] S. D. Sarma, M. Freedman and C. Nayak, *Majorana zero modes and topological quantum computation*, Npj Quantum Information **1**, 15001 (2015), doi:[10.1038/npjqi.2015.1](https://doi.org/10.1038/npjqi.2015.1). (Cited on pages 38 and 185.)
- [157] L. Jiang, T. Kitagawa, J. Alicea, A. R. Akhmerov, D. Pekker, G. Refael, J. I. Cirac, E. Demler, M. D. Lukin and P. Zoller, *Majorana fermions in equilibrium and in driven cold-atom quantum wires*, Physical Review Letters **106**, 220402 (2011), doi:[10.1103/physrevlett.106.220402](https://doi.org/10.1103/physrevlett.106.220402). (Cited on page 38.)
- [158] B. Bauer, T. Pereg-Barnea, T. Karzig, M.-T. Rieder, G. Refael, E. Berg and Y. Oreg, *Topologically protected braiding in a single wire using Floquet Majorana modes*, arXiv e-prints arXiv:1808.07066 (2018), arXiv:[1808.07066](https://arxiv.org/abs/1808.07066). (Cited on page 38.)
- [159] R. M. Lutchyn, J. D. Sau and S. Das Sarma, *Majorana fermions and a topological phase transition in semiconductor-superconductor heterostructures*, Physical Review Letters **105**, 077001 (2010), doi:[10.1103/PhysRevLett.105.077001](https://doi.org/10.1103/PhysRevLett.105.077001). (Cited on pages 38 and 53.)
- [160] Y. Oreg, G. Refael and F. von Oppen, *Helical liquids and Majorana bound states in quantum wires*, Physical Review Letters **105**, 177002 (2010), doi:[10.1103/PhysRevLett.105.177002](https://doi.org/10.1103/PhysRevLett.105.177002). (Cited on pages 38 and 53.)
- [161] V. Mourik, K. Zuo, S. M. Frolov, S. R. Plissard, E. P. A. M. Bakkers and L. P. Kouwenhoven, *Signatures of Majorana fermions in hybrid superconductor-semiconductor nanowire devices*, Science **336**(6084), 1003 (2012), doi:[10.1126/science.1222360](https://doi.org/10.1126/science.1222360). (Cited on pages 38 and 53.)
- [162] H. Zhang, C.-X. Liu, S. Gazibegovic, D. Xu, J. A. Logan, G. Wang, N. van Loo, J. D. S. Bommer, M. W. A. de Moor, D. Car, R. L. M. Op het Veld, P. J. van Veldhoven *et al.*, *Quantized Majorana conductance*, Nature **556**, 74 (2018), doi:[10.1038/nature26142](https://doi.org/10.1038/nature26142). (Cited on page 38.)
- [163] G. Jackeli and G. Khaliullin, *Mott insulators in the strong spin-orbit coupling limit: From Heisenberg to a quantum compass and Kitaev models*, Physical Review Letters **102**, 017205 (2009), doi:[10.1103/physrevlett.102.017205](https://doi.org/10.1103/physrevlett.102.017205). (Cited on page 39.)
- [164] J. c. v. Chaloupka, G. Jackeli and G. Khaliullin, *Kitaev-Heisenberg model on a honeycomb lattice: Possible exotic phases in iridium oxides $A_2\text{IrO}_3$* , Physical Review Letters **105**, 027204 (2010), doi:[10.1103/physrevlett.105.027204](https://doi.org/10.1103/physrevlett.105.027204). (Cited on page 39.)
- [165] S. Hwan Chun, J.-W. Kim, J. Kim, H. Zheng, C. C. Stoumpos, C. D. Malliakas, J. F. Mitchell, K. Mehlawat, Y. Singh, Y. Choi, T. Gog, A. Al-Zein *et al.*, *Direct evidence for dominant bond-directional interactions in a honeycomb lattice iridate Na_2IrO_3* , Nature Physics **11**, 462 (2015), doi:[10.1038/nphys3322](https://doi.org/10.1038/nphys3322). (Cited on page 39.)
- [166] G. Cao and P. Schlottmann, *The challenge of spin-orbit-tuned ground states in iridates: A key issues review*, Reports on Progress in Physics **81**(4), 042502 (2018), doi:[10.1088/1361-6633/aaa979](https://doi.org/10.1088/1361-6633/aaa979). (Cited on page 39.)
- [167] A. Banerjee, C. A. Bridges, J.-Q. Yan, A. A. Aczel, L. Li, M. B. Stone, G. E. Granroth, M. D. Lumsden, Y. Yiu, J. Knolle, S. Bhattacharjee, D. L. Kovrizhin *et al.*, *Proximate Kitaev quantum spin liquid behaviour in a honeycomb magnet*, Nature Materials **15**, 733 (2016), doi:[10.1038/nmat4604](https://doi.org/10.1038/nmat4604). (Cited on page 39.)
- [168] A. Banerjee, J. Yan, J. Knolle, C. A. Bridges, M. B. Stone, M. D. Lumsden, D. G. Mandrus, D. A. Tennant, R. Moessner and S. E. Nagler, *Neutron scattering in the proximate quantum spin liquid -RuCl_3* , Science **356**(6342), 1055 (2017), doi:[10.1126/science.aah6015](https://doi.org/10.1126/science.aah6015). (Cited on page 39.)

BIBLIOGRAPHY

- [169] L. Savary and L. Balents, *Quantum spin liquids: a review*, Reports on Progress in Physics **80**(1), 016502 (2017), doi:[10.1088/0034-4885/80/1/016502](https://doi.org/10.1088/0034-4885/80/1/016502). (Cited on page 39.)
- [170] Y. Zhou, K. Kanoda and T.-K. Ng, *Quantum spin liquid states*, Reviews of Modern Physics **89**, 025003 (2017), doi:[10.1103/revmodphys.89.025003](https://doi.org/10.1103/revmodphys.89.025003). (Cited on page 39.)
- [171] S. M. Winter, A. A. Tsirlin, M. Daghofer, J. van den Brink, Y. Singh, P. Gegenwart and R. Valentí, *Models and materials for generalized Kitaev magnetism*, Journal of Physics: Condensed Matter **29**(49), 493002 (2017), doi:[10.1088/1361-648x/aa8cf5](https://doi.org/10.1088/1361-648x/aa8cf5). (Cited on page 39.)
- [172] H. Bombin and M. A. Martin-Delgado, *Topological quantum distillation*, Physical Review Letters **97**, 180501 (2006), doi:[10.1103/physrevlett.97.180501](https://doi.org/10.1103/physrevlett.97.180501). (Cited on page 39.)
- [173] S. Bravyi, B. M. Terhal and B. Leemhuis, *Majorana fermion codes*, New Journal of Physics **12**(8), 083039 (2010), doi:[10.1088/1367-2630/12/8/083039](https://doi.org/10.1088/1367-2630/12/8/083039). (Cited on pages 39, 297, and 302.)
- [174] B. M. Terhal, *Quantum error correction for quantum memories*, Reviews of Modern Physics **87**, 307 (2015), doi:[10.1103/revmodphys.87.307](https://doi.org/10.1103/revmodphys.87.307). (Cited on pages 39, 297, 507, and 526.)
- [175] J. K. Pachos, W. Wieczorek, C. Schmid, N. Kiesel, R. Pohlner and H. Weinfurter, *Revealing anyonic features in a toric code quantum simulation*, New Journal of Physics **11**(8), 083010 (2009), doi:[10.1088/1367-2630/11/8/083010](https://doi.org/10.1088/1367-2630/11/8/083010). (Cited on page 40.)
- [176] C.-Y. Lu, W.-B. Gao, O. Gühne, X.-Q. Zhou, Z.-B. Chen and J.-W. Pan, *Demonstrating anyonic fractional statistics with a six-qubit quantum simulator*, Physical Review Letters **102**, 030502 (2009), doi:[10.1103/physrevlett.102.030502](https://doi.org/10.1103/physrevlett.102.030502). (Cited on page 40.)
- [177] J. M. Chow, J. M. Gambetta, E. Magesan, D. W. Abraham, A. W. Cross, B. R. Johnson, N. A. Masluk, C. A. Ryan, J. A. Smolin, S. J. Srinivasan and M. Steffen, *Implementing a strand of a scalable fault-tolerant quantum computing fabric*, Nature Communications **5**, 4015 (2014), doi:[10.1038/ncomms5015](https://doi.org/10.1038/ncomms5015). (Cited on page 40.)
- [178] J. Kelly, R. Barends, A. G. Fowler, A. Megrant, E. Jeffrey, T. C. White, D. Sank, J. Y. Mutus, B. Campbell, Y. Chen, Z. Chen, B. Chiaro *et al.*, *State preservation by repetitive error detection in a superconducting quantum circuit*, Nature **519**, 66 (2015), doi:[10.1038/nature14270](https://doi.org/10.1038/nature14270). (Cited on pages 40, 297, and 306.)
- [179] A. Córcoles, E. Magesan, S. J. Srinivasan, A. W. Cross, M. Steffen, J. M. Gambetta and J. M. Chow, *Demonstration of a quantum error detection code using a square lattice of four superconducting qubits*, Nature Communications **6**, 6979 (2015), doi:[10.1038/ncomms7979](https://doi.org/10.1038/ncomms7979). (Cited on page 40.)
- [180] M. Takita, A. D. Córcoles, E. Magesan, B. Abdo, M. Brink, A. Cross, J. M. Chow and J. M. Gambetta, *Demonstration of weight-four parity measurements in the surface code architecture*, Physical Review Letters **117**, 210505 (2016), doi:[10.1103/physrevlett.117.210505](https://doi.org/10.1103/physrevlett.117.210505). (Cited on page 40.)
- [181] M. Takita, A. W. Cross, A. D. Córcoles, J. M. Chow and J. M. Gambetta, *Experimental demonstration of fault-tolerant state preparation with superconducting qubits*, Physical Review Letters **119**, 180501 (2017), doi:[10.1103/physrevlett.119.180501](https://doi.org/10.1103/physrevlett.119.180501). (Cited on page 40.)
- [182] G. Wendin, *Quantum information processing with superconducting circuits: a review*, Reports on Progress in Physics **80**(10), 106001 (2017), doi:[10.1088/1361-6633/aa7e1a](https://doi.org/10.1088/1361-6633/aa7e1a). (Cited on page 40.)
- [183] C. D. Hill, E. Peretz, S. J. Hile, M. G. House, M. Fuechsle, S. Rogge, M. Y. Simmons and L. C. L. Hollenberg, *A surface code quantum computer in silicon*, Science Advances **1**(9), e1500707 (2015), doi:[10.1126/sciadv.1500707](https://doi.org/10.1126/sciadv.1500707). (Cited on page 40.)

BIBLIOGRAPHY

- [184] L. A. Landau, S. Plugge, E. Sela, A. Altland, S. M. Albrecht and R. Egger, *Towards realistic implementations of a Majorana surface code*, Physical Review Letters **116**, 050501 (2016), doi:[10.1103/physrevlett.116.050501](https://doi.org/10.1103/physrevlett.116.050501). (Cited on page 40.)
- [185] S. Vijay and L. Fu, *Physical implementation of a Majorana fermion surface code for fault-tolerant quantum computation*, Physica Scripta **2016**(T168), 014002 (2016), doi:[10.1088/0031-8949/t168/1/014002](https://doi.org/10.1088/0031-8949/t168/1/014002). (Cited on page 40.)
- [186] R. Versluis, S. Poletto, N. Khammassi, B. Tarasinski, N. Haider, D. J. Michalak, A. Bruno, K. Bertels and L. DiCarlo, *Scalable quantum circuit and control for a superconducting surface code*, Physical Review A **8**, 034021 (2017), doi:[10.1103/physrevapplied.8.034021](https://doi.org/10.1103/physrevapplied.8.034021). (Cited on page 40.)
- [187] D. Litinski, M. S. Kesselring, J. Eisert and F. von Oppen, *Combining topological hardware and topological software: Color-code quantum computing with topological superconductor networks*, Physical Review X **7**, 031048 (2017), doi:[10.1103/physrevx.7.031048](https://doi.org/10.1103/physrevx.7.031048). (Cited on page 40.)
- [188] L. Jiang, G. K. Brennen, A. V. Gorshkov, K. Hammerer, M. Hafezi, E. Demler, M. D. Lukin and P. Zoller, *Anyonic interferometry and protected memories in atomic spin lattices*, Nature Physics **4**, 482 (2008), doi:[10.1038/nphys943](https://doi.org/10.1038/nphys943). (Cited on page 40.)
- [189] H. Weimer, M. Müller, I. Lesanovsky, P. Zoller and H. P. Büchler, *A Rydberg quantum simulator*, Nature Physics **6**, 382 (2010), doi:[10.1038/nphys1614](https://doi.org/10.1038/nphys1614). (Cited on page 40.)
- [190] J. T. Barreiro, M. Müller, P. Schindler, D. Nigg, T. Monz, M. Chwalla, M. Hennrich, C. F. Roos, P. Zoller and R. Blatt, *An open-system quantum simulator with trapped ions*, Nature **470**, 486 (2011), doi:[10.1038/nature09801](https://doi.org/10.1038/nature09801). (Cited on page 40.)
- [191] N. Yao, C. Laumann, A. Gorshkov, H. Weimer, L. Jiang, J. Cirac, P. Zoller and M. Lukin, *Topologically protected quantum state transfer in a chiral spin liquid*, Nature Communications **4**, 1585 (2013), doi:[10.1038/ncomms2531](https://doi.org/10.1038/ncomms2531). (Cited on pages 40 and 203.)
- [192] C. Dłaska, B. Vermersch and P. Zoller, *Robust quantum state transfer via topologically protected edge channels in dipolar arrays*, Quantum Science and Technology **2**(1), 015001 (2017), doi:[10.1088/2058-9565/2/1/015001](https://doi.org/10.1088/2058-9565/2/1/015001). (Cited on pages 40 and 203.)
- [193] N. Goldman, J. C. Budich and P. Zoller, *Topological quantum matter with ultracold gases in optical lattices*, Nature Physics **12**, 639 (2016), doi:[10.1038/nphys3803](https://doi.org/10.1038/nphys3803). (Cited on page 40.)
- [194] M. Hafezi, E. A. Demler, M. D. Lukin and J. M. Taylor, *Robust optical delay lines with topological protection*, Nature Physics **7**, 907 (2011), doi:[10.1038/nphys2063](https://doi.org/10.1038/nphys2063). (Cited on pages 40 and 203.)
- [195] L. Lu, J. D. Joannopoulos and M. Soljačić, *Topological photonics*, Nature Photonics **8**, 821 (2014), doi:[10.1038/nphoton.2014.248](https://doi.org/10.1038/nphoton.2014.248). (Cited on pages 40, 41, 42, and 203.)
- [196] M. Mancini, G. Pagano, G. Cappellini, L. Livi, M. Rider, J. Catani, C. Sias, P. Zoller, M. Inguscio, M. Dalmonte and L. Fallani, *Observation of chiral edge states with neutral fermions in synthetic Hall ribbons*, Science **349**(6255), 1510 (2015), doi:[10.1126/science.aaa8736](https://doi.org/10.1126/science.aaa8736). (Cited on pages 40 and 203.)
- [197] B. K. Stuhl, H.-I. Lu, L. M. Ayccock, D. Genkina and I. B. Spielman, *Visualizing edge states with an atomic Bose gas in the quantum Hall regime*, Science **349**(6255), 1514 (2015), doi:[10.1126/science.aaa8515](https://doi.org/10.1126/science.aaa8515). (Cited on pages 40 and 203.)
- [198] G. Jotzu, M. Messer, R. Desbuquois, M. Lebrat, T. Uehlinger, D. Greif and T. Esslinger, *Experimental realization of the topological Haldane model with ultracold fermions*, Nature **515**, 237 (2014), doi:[10.1038/nature13915](https://doi.org/10.1038/nature13915). (Cited on pages 40 and 203.)
- [199] S. D. Huber, *Topological mechanics*, Nature Physics **12**, 621 (2016), doi:[10.1038/nphys3801](https://doi.org/10.1038/nphys3801). (Cited on pages 41 and 389.)

BIBLIOGRAPHY

- [200] C. L. Kane and T. C. Lubensky, *Topological boundary modes in isostatic lattices*, Nature Physics **10**, 39 (2013), doi:[10.1038/nphys2835](https://doi.org/10.1038/nphys2835). (Cited on pages 41 and 203.)
- [201] B. G.-g. Chen, B. Liu, A. A. Evans, J. Paulose, I. Cohen, V. Vitelli and C. D. Santangelo, *Topological mechanics of origami and kirigami*, Physical Review Letters **116**, 135501 (2016), doi:[10.1103/physrevlett.116.135501](https://doi.org/10.1103/physrevlett.116.135501). (Cited on page 41.)
- [202] L. M. Nash, D. Kleckner, A. Read, V. Vitelli, A. M. Turner and W. T. M. Irvine, *Topological mechanics of gyroscopic metamaterials*, Proceedings of the National Academy of Sciences **112**(47), 14495 (2015), doi:[10.1073/pnas.1507413112](https://doi.org/10.1073/pnas.1507413112). (Cited on pages 41 and 203.)
- [203] P. Wang, L. Lu and K. Bertoldi, *Topological phononic crystals with one-way elastic edge waves*, Physical Review Letters **115**, 104302 (2015), doi:[10.1103/physrevlett.115.104302](https://doi.org/10.1103/physrevlett.115.104302). (Cited on pages 41 and 203.)
- [204] R. Süsstrunk and S. D. Huber, *Observation of phononic helical edge states in a mechanical topological insulator*, Science **349**(6243), 47 (2015), doi:[10.1126/science.aab0239](https://doi.org/10.1126/science.aab0239). (Cited on pages 41, 203, 204, and 389.)
- [205] R. Süsstrunk, P. Zimmermann and S. D. Huber, *Switchable topological phonon channels*, New Journal of Physics **19**(1), 015013 (2017), doi:[10.1088/1367-2630/aa591c](https://doi.org/10.1088/1367-2630/aa591c). (Cited on pages 41, 203, and 204.)
- [206] M. Serra-Garcia, V. Peri, R. Süsstrunk, O. R. Bilal, T. Larsen, L. G. Villanueva and S. D. Huber, *Observation of a phononic quadrupole topological insulator*, Nature **555**, 342 (2018), doi:[10.1038/nature25156](https://doi.org/10.1038/nature25156). (Cited on page 41.)
- [207] Z. Yang, F. Gao, X. Shi, X. Lin, Z. Gao, Y. Chong and B. Zhang, *Topological acoustics*, Physical Review Letters **114**, 114301 (2015), doi:[10.1103/physrevlett.114.114301](https://doi.org/10.1103/physrevlett.114.114301). (Cited on page 41.)
- [208] Y. Ding, Y. Peng, Y. Zhu, X. Fan, J. Yang, B. Liang, X. Zhu, X. Wan and J. Cheng, *Experimental demonstration of acoustic Chern insulators*, Physical Review Letters **122**, 014302 (2019), doi:[10.1103/physrevlett.122.014302](https://doi.org/10.1103/physrevlett.122.014302). (Cited on page 41.)
- [209] F. D. M. Haldane and S. Raghu, *Possible realization of directional optical waveguides in photonic crystals with broken time-reversal symmetry*, Physical Review Letters **100**, 013904 (2008), doi:[10.1103/physrevlett.100.013904](https://doi.org/10.1103/physrevlett.100.013904). (Cited on pages 41 and 203.)
- [210] S. Raghu and F. D. M. Haldane, *Analogs of quantum-Hall-effect edge states in photonic crystals*, Physical Review A **78**, 033834 (2008), doi:[10.1103/physreva.78.033834](https://doi.org/10.1103/physreva.78.033834). (Cited on page 41.)
- [211] Z. Wang, Y. Chong, J. D. Joannopoulos and M. Soljačić, *Observation of unidirectional backscattering-immune topological electromagnetic states*, Nature **461**, 772 (2009), doi:[10.1038/nature08293](https://doi.org/10.1038/nature08293). (Cited on page 42.)
- [212] M. C. Rechtsman, J. M. Zeuner, Y. Plotnik, Y. Lumer, D. Podolsky, F. Dreisow, S. Nolte, M. Segev and A. Szameit, *Photonic Floquet topological insulators*, Nature **496**, 196 (2013), doi:[10.1038/nature12066](https://doi.org/10.1038/nature12066). (Cited on pages 42 and 203.)
- [213] M. Hafezi, S. Mittal, J. Fan, A. Migdall and J. M. Taylor, *Imaging topological edge states in silicon photonics*, Nature Photonics **7**, 1001 (2013), doi:[10.1038/nphoton.2013.274](https://doi.org/10.1038/nphoton.2013.274). (Cited on pages 42, 203, 204, 206, and 389.)
- [214] J. Ningyuan, C. Owens, A. Sommer, D. Schuster and J. Simon, *Time- and site-resolved dynamics in a topological circuit*, Physical Review X **5**, 021031 (2015), doi:[10.1103/physrevx.5.021031](https://doi.org/10.1103/physrevx.5.021031). (Cited on pages 42, 203, 204, and 389.)

BIBLIOGRAPHY

- [215] C. H. Lee, S. Imhof, C. Berger, F. Bayer, J. Brehm, L. W. Molenkamp, T. Kiessling and R. Thomale, *Topoelectrical circuits*, Communications Physics **1**(1), 39 (2018), doi:[10.1038/s42005-018-0035-2](https://doi.org/10.1038/s42005-018-0035-2). (Cited on page 42.)
- [216] L. Lu, *Topology on a breadboard*, Nature Physics **14**(9), 875 (2018), doi:[10.1038/s41567-018-0235-4](https://doi.org/10.1038/s41567-018-0235-4). (Cited on page 42.)
- [217] C. W. Peterson, W. A. Benalcazar, T. L. Hughes and G. Bahl, *A quantized microwave quadrupole insulator with topologically protected corner states*, Nature **555**, 346 (2018), doi:[10.1038/nature25777](https://doi.org/10.1038/nature25777). (Cited on page 42.)
- [218] S. Imhof, C. Berger, F. Bayer, J. Brehm, L. W. Molenkamp, T. Kiessling, F. Schindler, C. H. Lee, M. Greiter, T. Neupert and R. Thomale, *Topoelectrical-circuit realization of topological corner modes*, Nature Physics **14**(9), 925 (2018), doi:[10.1038/s41567-018-0246-1](https://doi.org/10.1038/s41567-018-0246-1). (Cited on page 42.)
- [219] G. Harari, M. A. Bandres, Y. Lumer, M. C. Rechtsman, Y. D. Chong, M. Khajavikhan, D. N. Christodoulides and M. Segev, *Topological insulator laser: Theory*, Science **359**, eaar4003 (2018), doi:[10.1126/science.aar4003](https://doi.org/10.1126/science.aar4003). (Cited on page 42.)
- [220] B. Bahari, A. Ndao, F. Vallini, A. El Amili, Y. Fainman and B. Kanté, *Nonreciprocal lasing in topological cavities of arbitrary geometries*, Science **358**(6363), 636 (2017), doi:[10.1126/science.aao4551](https://doi.org/10.1126/science.aao4551). (Cited on page 42.)
- [221] M. A. Bandres, S. Wittek, G. Harari, M. Parto, J. Ren, M. Segev, D. N. Christodoulides and M. Khajavikhan, *Topological insulator laser: Experiments*, Science **359**, eaar4005 (2018), doi:[10.1126/science.aar4005](https://doi.org/10.1126/science.aar4005). (Cited on page 42.)
- [222] P. Delplace, J. B. Marston and A. Venaille, *Topological origin of equatorial waves*, Science **358**(6366), 1075 (2017), doi:[10.1126/science.aan8819](https://doi.org/10.1126/science.aan8819). (Cited on page 42.)
- [223] M. Levin and X.-G. Wen, *Fermions, strings, and gauge fields in lattice spin models*, Physical Review B **67**, 245316 (2003), doi:[10.1103/PhysRevB.67.245316](https://doi.org/10.1103/PhysRevB.67.245316). (Cited on page 53.)
- [224] C. W. J. Beenakker, *Random-matrix theory of Majorana fermions and topological superconductors*, Reviews of Modern Physics **87**, 1037 (2015), doi:[10.1103/revmodphys.87.1037](https://doi.org/10.1103/revmodphys.87.1037). (Cited on page 53.)
- [225] X.-G. Wen, *Symmetry-protected topological invariants of symmetry-protected topological phases of interacting bosons and fermions*, Physical Review B **89**, 035147 (2014), doi:[10.1103/physrevb.89.035147](https://doi.org/10.1103/physrevb.89.035147). (Cited on page 53.)
- [226] P. Bonderson and C. Nayak, *Quasi-topological phases of matter and topological protection*, Physical Review B **87**, 195451 (2013), doi:[10.1103/PhysRevB.87.195451](https://doi.org/10.1103/PhysRevB.87.195451). (Cited on pages 53, 67, and 98.)
- [227] J. Alicea, *New directions in the pursuit of Majorana fermions in solid state systems*, Reports on Progress in Physics **75**(7), 076501 (2012), doi:[10.1088/0034-4885/75/7/076501](https://doi.org/10.1088/0034-4885/75/7/076501). (Cited on page 53.)
- [228] A. Das, Y. Ronen, Y. Most, Y. Oreg, M. Heiblum and H. Shtrikman, *Zero-bias peaks and splitting in an Al-InAs nanowire topological superconductor as a signature of Majorana fermions*, Nature Physics **8**, 887 (2012), doi:[10.1038/nphys2479](https://doi.org/10.1038/nphys2479). (Cited on page 53.)
- [229] S. Nadj-Perge, I. K. Drozdov, J. Li, H. Chen, S. Jeon, J. Seo, A. H. MacDonald, B. A. Bernevig and A. Yazdani, *Observation of Majorana fermions in ferromagnetic atomic chains on a superconductor*, Science **346**(6209), 602 (2014), doi:[10.1126/science.1259327](https://doi.org/10.1126/science.1259327). (Cited on page 53.)

BIBLIOGRAPHY

- [230] M. Cheng and H.-H. Tu, *Majorana edge states in interacting two-chain ladders of fermions*, Physical Review B **84**, 094503 (2011), doi:[10.1103/PhysRevB.84.094503](https://doi.org/10.1103/PhysRevB.84.094503). (Cited on pages 53 and 109.)
- [231] L. Fidkowski, R. M. Lutchyn, C. Nayak and M. P. A. Fisher, *Majorana zero modes in one-dimensional quantum wires without long-ranged superconducting order*, Physical Review B **84**, 195436 (2011), doi:[10.1103/PhysRevB.84.195436](https://doi.org/10.1103/PhysRevB.84.195436). (Cited on pages 53 and 109.)
- [232] J. D. Sau, B. I. Halperin, K. Flensberg and S. Das Sarma, *Number conserving theory for topologically protected degeneracy in one-dimensional fermions*, Physical Review B **84**, 144509 (2011), doi:[10.1103/PhysRevB.84.144509](https://doi.org/10.1103/PhysRevB.84.144509). (Cited on pages 53 and 109.)
- [233] J. Ruhman, E. Berg and E. Altman, *Topological states in a one-dimensional Fermi gas with attractive interaction*, Physical Review Letters **114**, 100401 (2015), doi:[10.1103/PhysRevLett.114.100401](https://doi.org/10.1103/PhysRevLett.114.100401). (Cited on pages 53 and 109.)
- [234] A. Keselman and E. Berg, *A gapless symmetry-protected topological phase of fermions in one dimension*, Physical Review B **91**, 235309 (2015), doi:[10.1103/physrevb.91.235309](https://doi.org/10.1103/physrevb.91.235309). (Cited on pages 53 and 109.)
- [235] C. V. Kraus, M. Dalmonte, M. A. Baranov, A. M. Läuchli and P. Zoller, *Majorana edge states in atomic wires coupled by pair hopping*, Physical Review Letters **111**, 173004 (2013), doi:[10.1103/PhysRevLett.111.173004](https://doi.org/10.1103/PhysRevLett.111.173004). (Cited on pages 53, 57, and 109.)
- [236] G. Ortiz, J. Dukelsky, E. Cobanera, C. Eсеbbag and C. Beenakker, *Many-body characterization of particle-conserving topological superfluids*, Physical Review Letters **113**, 267002 (2014), doi:[10.1103/PhysRevLett.113.267002](https://doi.org/10.1103/PhysRevLett.113.267002). (Cited on page 53.)
- [237] T. Wenzel, *Stability of Majorana modes under symmetry breaking terms*, Bachelor's thesis, University of Stuttgart (2016). (Cited on pages 56, 108, and 179.)
- [238] D. Rainis and D. Loss, *Majorana qubit decoherence by quasiparticle poisoning*, Physical Review B **85**, 174533 (2012), doi:[10.1103/physrevb.85.174533](https://doi.org/10.1103/physrevb.85.174533). (Cited on pages 57, 298, and 303.)
- [239] T. Karzig, C. Knapp, R. M. Lutchyn, P. Bonderson, M. B. Hastings, C. Nayak, J. Alicea, K. Flensberg, S. Plugge, Y. Oreg, C. M. Marcus and M. H. Freedman, *Scalable designs for quasiparticle-poisoning-protected topological quantum computation with Majorana zero modes*, Physical Review B **95**, 235305 (2017), doi:[10.1103/physrevb.95.235305](https://doi.org/10.1103/physrevb.95.235305). (Cited on pages 57, 298, and 303.)
- [240] C. N. Yang, *Concept of off-diagonal long-range order and the quantum phases of liquid He and of superconductors*, Reviews of Modern Physics **34**, 694 (1962), doi:[10.1103/revmodphys.34.694](https://doi.org/10.1103/revmodphys.34.694). (Cited on page 63.)
- [241] Z. Nussinov and G. Ortiz, *A symmetry principle for topological quantum order*, Annals of Physics **324**(5), 977 (2009), doi:[10.1016/j.aop.2008.11.002](https://doi.org/10.1016/j.aop.2008.11.002). (Cited on page 67.)
- [242] H. Li and F. D. M. Haldane, *Entanglement spectrum as a generalization of entanglement entropy: Identification of topological order in non-abelian fractional quantum Hall effect states*, Physical Review Letters **101**, 010504 (2008), doi:[10.1103/PhysRevLett.101.010504](https://doi.org/10.1103/PhysRevLett.101.010504). (Cited on pages 72 and 74.)
- [243] F. Pollmann, A. M. Turner, E. Berg and M. Oshikawa, *Entanglement spectrum of a topological phase in one dimension*, Physical Review B **81**, 064439 (2010), doi:[10.1103/physrevb.81.064439](https://doi.org/10.1103/physrevb.81.064439). (Cited on pages 72, 399, and 400.)
- [244] J. Eisert, M. Cramer and M. B. Plenio, *Colloquium: Area laws for the entanglement entropy*, Reviews of Modern Physics **82**, 277 (2010), doi:[10.1103/revmodphys.82.277](https://doi.org/10.1103/revmodphys.82.277). (Cited on page 74.)

BIBLIOGRAPHY

- [245] H. Bethe, *Zur Theorie der Metalle*, Zeitschrift für Physik **71**(3), 205 (1931), doi:[10.1007/BF01341708](https://doi.org/10.1007/BF01341708). (Cited on pages 75, 78, 79, and 146.)
- [246] H. Nielsen and S. Chadha, *On how to count Goldstone bosons*, Nuclear Physics B **105**(3), 445 (1976), doi:[10.1016/0550-3213\(76\)90025-0](https://doi.org/10.1016/0550-3213(76)90025-0). (Cited on page 76.)
- [247] H. Watanabe and H. Murayama, *Unified description of Nambu-Goldstone bosons without Lorentz invariance*, Physical Review Letters **108**, 251602 (2012), doi:[10.1103/physrevlett.108.251602](https://doi.org/10.1103/physrevlett.108.251602). (Cited on page 76.)
- [248] K. Guther, N. Lang and H. P. Büchler, *Ising anyonic topological phase of interacting fermions in one dimension*, Physical Review B **96**, 121109 (2017), doi:[10.1103/physrevb.96.121109](https://doi.org/10.1103/physrevb.96.121109). (Cited on pages 76, 92, and 109.)
- [249] T. Koma and B. Nachtergaele, *The spectral gap of the ferromagnetic XYZ-chain*, Letters in Mathematical Physics **40**(1), 1 (1997), doi:[10.1023/A:1007351803403](https://doi.org/10.1023/A:1007351803403). (Cited on page 85.)
- [250] M. Dolfi, B. Bauer, S. Keller, A. Kosenkov, T. Ewart, A. Kantian, T. Giamarchi and M. Troyer, *Matrix product state applications for the ALPS project*, Computer Physics Communications **185**(12), 3430 (2014), doi:[10.1016/j.cpc.2014.08.019](https://doi.org/10.1016/j.cpc.2014.08.019). (Cited on pages 86 and 87.)
- [251] B. Bauer, L. D. Carr, H. G. Evertz, A. Feiguin, J. Freire, S. Fuchs, L. Gamper, J. Gukelberger, E. Gull, S. Guertler, A. Hehn, R. Igarashi *et al.*, *The ALPS project release 2.0: Open source software for strongly correlated systems*, Journal of Statistical Mechanics: Theory and Experiment **2011**(05), P05001 (2011), doi:[10.1088/1742-5468/2011/05/p05001](https://doi.org/10.1088/1742-5468/2011/05/p05001). (Cited on pages 86, 87, 401, 428, and 431.)
- [252] B. S. Shastry and B. Sutherland, *Twisted boundary conditions and effective mass in Heisenberg-Ising and Hubbard rings*, Physical Review Letters **65**, 243 (1990), doi:[10.1103/PhysRevLett.65.243](https://doi.org/10.1103/PhysRevLett.65.243). (Cited on pages 91 and 126.)
- [253] B. Sutherland and B. S. Shastry, *Adiabatic transport properties of an exactly soluble one-dimensional quantum many-body problem*, Physical Review Letters **65**, 1833 (1990), doi:[10.1103/physrevlett.65.1833](https://doi.org/10.1103/physrevlett.65.1833). (Cited on pages 91 and 126.)
- [254] C. J. Hamer, G. R. W. Quispel and M. T. Batchelor, *Conformal anomaly and surface energy for Potts and Ashkin-Teller quantum chains*, Journal of Physics A: Mathematical and General **20**(16), 5677 (1987), doi:[10.1088/0305-4470/20/16/040](https://doi.org/10.1088/0305-4470/20/16/040). (Cited on pages 91 and 126.)
- [255] T. Giamarchi, *Quantum Physics in One Dimension*, International Series of Monographs on Physics. Clarendon Press, ISBN 0198525001 (2004). (Cited on pages 92, 433, 434, 444, 449, and 452.)
- [256] A. O. Gogolin, A. A. Nersesyan and A. M. Tsvelik, *Bosonization and Strongly Correlated Systems*, Cambridge University Press, ISBN 0521617197 (2004). (Cited on pages 92, 438, and 446.)
- [257] B. Simon, *Holonomy, the quantum adiabatic theorem, and Berry's phase*, Physical Review Letters **51**, 2167 (1983), doi:[10.1103/physrevlett.51.2167](https://doi.org/10.1103/physrevlett.51.2167). (Cited on page 102.)
- [258] F. Iemini, L. Mazza, D. Rossini, R. Fazio and S. Diehl, *Localized Majorana-like modes in a number-conserving setting: An exactly solvable model*, Physical Review Letters **115**, 156402 (2015), doi:[10.1103/physrevlett.115.156402](https://doi.org/10.1103/physrevlett.115.156402). (Cited on page 109.)
- [259] S. Diehl, E. Rico, M. A. Baranov and P. Zoller, *Topology by dissipation in atomic quantum wires*, Nature Physics **7**, 971 (2011), doi:[10.1038/nphys2106](https://doi.org/10.1038/nphys2106). (Cited on page 109.)
- [260] K.-S. Guther, *Topological edge states in a one-dimensional ladder system*, Master's thesis, University of Stuttgart (2016). (Cited on page 109.)

BIBLIOGRAPHY

- [261] R. Orús, *A practical introduction to tensor networks: Matrix product states and projected entangled pair states*, *Annals of Physics* **349**, 117 (2014), doi:[10.1016/j.aop.2014.06.013](https://doi.org/10.1016/j.aop.2014.06.013). (Cited on page 111.)
- [262] F. Verstraete and J. I. Cirac, *Matrix product states represent ground states faithfully*, *Physical Review B* **73**, 094423 (2006), doi:[10.1103/physrevb.73.094423](https://doi.org/10.1103/physrevb.73.094423). (Cited on pages 111, 116, and 403.)
- [263] U. Schollwöck, *The density-matrix renormalization group in the age of matrix product states*, *Annals of Physics* **326**(1), 96 (2011), doi:[10.1016/j.aop.2010.09.012](https://doi.org/10.1016/j.aop.2010.09.012). (Cited on page 111.)
- [264] M. A. Nielsen and I. L. Chuang, *Quantum Computation and Quantum Information: 10th Anniversary Edition*, Cambridge University Press, ISBN 9781107002173 (2010). (Cited on pages 112, 302, 506, 516, 518, 523, 527, and 529.)
- [265] F. Bloch, *Zur Theorie des Ferromagnetismus*, *Zeitschrift für Physik* **61**(3), 206 (1930), doi:[10.1007/bf01339661](https://doi.org/10.1007/bf01339661). (Cited on page 151.)
- [266] C. Kittel, *Introduction to solid state physics*, Wiley, 8th edn., ISBN 047141526X (2004). (Cited on page 151.)
- [267] L. H. Kauffman, *Majorana fermions and representations of the braid group*, *International Journal of Modern Physics A* **33**(23), 1830023 (2018), doi:[10.1142/S0217751X18300235](https://doi.org/10.1142/S0217751X18300235). (Cited on page 185.)
- [268] P. Fendley, *Parafermionic edge zero modes in Z_n -invariant spin chains*, *Journal of Statistical Mechanics: Theory and Experiment* **2012**(11), P11020 (2012), doi:[10.1088/1742-5468/2012/11/p11020](https://doi.org/10.1088/1742-5468/2012/11/p11020). (Cited on page 194.)
- [269] J. Alicea and P. Fendley, *Topological phases with parafermions: Theory and blueprints*, *Annual Review of Condensed Matter Physics* **7**(1), 119 (2016), doi:[10.1146/annurev-conmatphys-031115-011336](https://doi.org/10.1146/annurev-conmatphys-031115-011336). (Cited on page 194.)
- [270] T. Ando, Y. Matsumoto and Y. Uemura, *Theory of Hall effect in a two-dimensional electron system*, *Journal of the Physical Society of Japan* **39**(2), 279 (1975), doi:[10.1143/jpsj.39.279](https://doi.org/10.1143/jpsj.39.279). (Cited on page 203.)
- [271] R. B. Laughlin, *Quantized Hall conductivity in two dimensions*, *Physical Review B* **23**, 5632 (1981), doi:[10.1103/physrevb.23.5632](https://doi.org/10.1103/physrevb.23.5632). (Cited on page 203.)
- [272] Y. Xu, I. Miotkowski, C. Liu, J. Tian, H. Nam, N. Alidoust, J. Hu, C.-K. Shih, M. Z. Hasan and Y. P. Chen, *Observation of topological surface state quantum Hall effect in an intrinsic three-dimensional topological insulator*, *Nature Physics* **10**, 956 (2014), doi:[10.1038/nphys3140](https://doi.org/10.1038/nphys3140). (Cited on page 203.)
- [273] C. W. Ling, M. Xiao, C. T. Chan, S. F. Yu and K. H. Fung, *Topological edge plasmon modes between diatomic chains of plasmonic nanoparticles*, *Optics Express* **23**(3), 2021 (2015), doi:[10.1364/oe.23.002021](https://doi.org/10.1364/oe.23.002021). (Cited on page 203.)
- [274] M. Atala, M. Aidelsburger, J. T. Barreiro, D. Abanin, T. Kitagawa, E. Demler and I. Bloch, *Direct measurement of the Zak phase in topological Bloch bands*, *Nature Physics* **9**, 795 (2013), doi:[10.1038/nphys2790](https://doi.org/10.1038/nphys2790). (Cited on page 203.)
- [275] M. Aidelsburger, M. Lohse, C. Schweizer, M. Atala, J. T. Barreiro, S. Nascimbène, N. R. Cooper, I. Bloch and N. Goldman, *Measuring the Chern number of Hofstadter bands with ultracold bosonic atoms*, *Nature Physics* **11**, 162 (2014), doi:[10.1038/nphys3171](https://doi.org/10.1038/nphys3171). (Cited on page 203.)
- [276] L. Duca, T. Li, M. Reitter, I. Bloch, M. Schleier-Smith and U. Schneider, *An Aharonov-Bohm interferometer for determining Bloch band topology*, *Science* **347**(6219), 288 (2015), doi:[10.1126/science.1259052](https://doi.org/10.1126/science.1259052). (Cited on page 203.)

BIBLIOGRAPHY

- [277] M. Lohse, C. Schweizer, O. Zilberberg, M. Aidelsburger and I. Bloch, *A Thouless quantum pump with ultracold bosonic atoms in an optical superlattice*, Nature Physics **12**, 350 (2015), doi:[10.1038/nphys3584](https://doi.org/10.1038/nphys3584). (Cited on page 203.)
- [278] J. Koch, A. A. Houck, K. L. Hur and S. M. Girvin, *Time-reversal-symmetry breaking in circuit-QED-based photon lattices*, Physical Review A **82**, 043811 (2010), doi:[10.1103/physreva.82.043811](https://doi.org/10.1103/physreva.82.043811). (Cited on page 203.)
- [279] N. Berg, K. Joel, M. Koolyk and E. Prodan, *Topological phonon modes in filamentary structures*, Physical Review E **83**, 021913 (2011), doi:[10.1103/physreve.83.021913](https://doi.org/10.1103/physreve.83.021913). (Cited on page 203.)
- [280] V. Yannopoulos, *Topological photonic bands in two-dimensional networks of metamaterial elements*, New Journal of Physics **14**(11), 113017 (2012), doi:[10.1088/1367-2630/14/11/113017](https://doi.org/10.1088/1367-2630/14/11/113017). (Cited on page 203.)
- [281] T. Kariyado and Y. Hatsugai, *Manipulation of Dirac cones in mechanical graphene*, Scientific Reports **5**, 18107 (2015), doi:[10.1038/srep18107](https://doi.org/10.1038/srep18107). (Cited on page 203.)
- [282] Y.-T. Wang, P.-G. Luan and S. Zhang, *Coriolis force induced topological order for classical mechanical vibrations*, New Journal of Physics **17**(7), 073031 (2015), doi:[10.1088/1367-2630/17/7/073031](https://doi.org/10.1088/1367-2630/17/7/073031). (Cited on page 203.)
- [283] D. Peter, N. Y. Yao, N. Lang, S. D. Huber, M. D. Lukin and H. P. Büchler, *Topological bands with a Chern number $c = 2$ by dipolar exchange interactions*, Physical Review A **91**, 053617 (2015), doi:[10.1103/physreva.91.053617](https://doi.org/10.1103/physreva.91.053617). (Cited on pages 203 and 206.)
- [284] A. A. Houck, H. E. Türeci and J. Koch, *On-chip quantum simulation with superconducting circuits*, Nature Physics **8**, 292 (2012), doi:[10.1038/nphys2251](https://doi.org/10.1038/nphys2251). (Cited on page 206.)
- [285] I. Carusotto and C. Ciuti, *Quantum fluids of light*, Reviews of Modern Physics **85**, 299 (2013), doi:[10.1103/revmodphys.85.299](https://doi.org/10.1103/revmodphys.85.299). (Cited on page 206.)
- [286] M. D. Lukin, M. Fleischhauer, R. Cote, L. M. Duan, D. Jaksch, J. I. Cirac and P. Zoller, *Dipole blockade and quantum information processing in mesoscopic atomic ensembles*, Physical Review Letters **87**, 037901 (2001), doi:[10.1103/physrevlett.87.037901](https://doi.org/10.1103/physrevlett.87.037901). (Cited on page 206.)
- [287] M. W. Doherty, N. B. Manson, P. Delaney, F. Jelezko, J. Wrachtrup and L. C. Hollenberg, *The nitrogen-vacancy colour centre in diamond*, Physics Reports **528**(1), 1 (2013), doi:[10.1016/j.physrep.2013.02.001](https://doi.org/10.1016/j.physrep.2013.02.001). (Cited on page 206.)
- [288] L.-M. Duan and C. Monroe, *Colloquium: Quantum networks with trapped ions*, Reviews of Modern Physics **82**, 1209 (2010), doi:[10.1103/revmodphys.82.1209](https://doi.org/10.1103/revmodphys.82.1209). (Cited on page 206.)
- [289] R. Kubo, *Generalized cumulant expansion method*, Journal of the Physical Society of Japan **17**(7), 1100 (1962), doi:[10.1143/jpsj.17.1100](https://doi.org/10.1143/jpsj.17.1100). (Cited on page 217.)
- [290] M. Suzuki, *General decomposition theory of ordered exponentials*, Proceedings of the Japan Academy, Series B **69**(7), 161 (1993), doi:[10.2183/pjab.69.161](https://doi.org/10.2183/pjab.69.161). (Cited on page 217.)
- [291] E. H. Lieb and D. W. Robinson, *The finite group velocity of quantum spin systems*, Communications in Mathematical Physics **28**(3), 251 (1972), doi:[10.1007/BF01645779](https://doi.org/10.1007/BF01645779). (Cited on pages 223 and 278.)
- [292] S. Jansen, M.-B. Ruskai and R. Seiler, *Bounds for the adiabatic approximation with applications to quantum computation*, Journal of Mathematical Physics **48**(10), 102111 (2007), doi:[10.1063/1.2798382](https://doi.org/10.1063/1.2798382). (Cited on pages 224, 276, and 277.)
- [293] J. Werschnik and E. K. U. Gross, *Quantum optimal control theory*, Journal of Physics B: Atomic, Molecular and Optical Physics **40**(18), R175 (2007), doi:[10.1088/0953-4075/40/18/r01](https://doi.org/10.1088/0953-4075/40/18/r01). (Cited on pages 226 and 239.)

BIBLIOGRAPHY

- [294] C. Brif, R. Chakrabarti and H. Rabitz, *Control of quantum phenomena: past, present and future*, New Journal of Physics **12**(7), 075008 (2010), doi:[10.1088/1367-2630/12/7/075008](https://doi.org/10.1088/1367-2630/12/7/075008). (Cited on pages [226](#) and [239](#).)
- [295] G. Haack, F. Helmer, M. Mariantoni, F. Marquardt and E. Solano, *Resonant quantum gates in circuit quantum electrodynamics*, Physical Review B **82**, 024514 (2010), doi:[10.1103/physrevb.82.024514](https://doi.org/10.1103/physrevb.82.024514). (Cited on page [230](#).)
- [296] L. Valiant, *The complexity of computing the permanent*, Theoretical Computer Science **8**(2), 189 (1979), doi:[10.1016/0304-3975\(79\)90044-6](https://doi.org/10.1016/0304-3975(79)90044-6). (Cited on pages [238](#), [287](#), and [288](#).)
- [297] S. Scheel, *Permanents in linear optical networks*, arXiv e-prints quant-ph/0406127 (2004), arXiv:[quant-ph/0406127](https://arxiv.org/abs/quant-ph/0406127). (Cited on pages [238](#), [287](#), and [288](#).)
- [298] S. Aaronson and A. Arkhipov, *The computational complexity of linear optics*, In *Proceedings of the Forty-third Annual ACM Symposium on Theory of Computing*, pp. 333–342. ACM, doi:[10.1145/1993636.1993682](https://doi.org/10.1145/1993636.1993682) (2011). (Cited on pages [238](#), [287](#), and [288](#).)
- [299] J. B. Spring, B. J. Metcalf, P. C. Humphreys, W. S. Kolthammer, X.-M. Jin, M. Barbieri, A. Datta, N. Thomas-Peter, N. K. Langford, D. Kundys, J. C. Gates, B. J. Smith *et al.*, *Boson sampling on a photonic chip*, Science **339**(6121), 798 (2013), doi:[10.1126/science.1231692](https://doi.org/10.1126/science.1231692). (Cited on pages [238](#) and [287](#).)
- [300] D. P. DiVincenzo, *The physical implementation of quantum computation*, Fortschritte der Physik **48**(911), 771 (2000), doi:[10.1002/1521-3978\(200009\)48:9/11<771::AID-PROP771>3.0.CO;2-E](https://doi.org/10.1002/1521-3978(200009)48:9/11<771::AID-PROP771>3.0.CO;2-E). (Cited on page [297](#).)
- [301] P. W. Shor, *Scheme for reducing decoherence in quantum computer memory*, Physical Review A **52**, R2493 (1995), doi:[10.1103/physreva.52.r2493](https://doi.org/10.1103/physreva.52.r2493). (Cited on page [297](#).)
- [302] P. Zanardi, *Virtual quantum subsystems*, Physical Review Letters **87**, 077901 (2001), doi:[10.1103/physrevlett.87.077901](https://doi.org/10.1103/physrevlett.87.077901). (Cited on pages [297](#), [525](#), and [527](#).)
- [303] J. R. Wootton, *Quantum memories and error correction*, Journal of Modern Optics **59**(20), 1717 (2012), doi:[10.1080/09500340.2012.737937](https://doi.org/10.1080/09500340.2012.737937). (Cited on pages [297](#) and [507](#).)
- [304] X.-C. Yao, T.-X. Wang, H.-Z. Chen, W.-B. Gao, A. G. Fowler, R. Raussendorf, Z.-B. Chen, N.-L. Liu, C.-Y. Lu, Y.-J. Deng, Y.-A. Chen and J.-W. Pan, *Experimental demonstration of topological error correction*, Nature **482**, 489 (2012), doi:[10.1038/nature10770](https://doi.org/10.1038/nature10770). (Cited on page [297](#).)
- [305] R. Barends, J. Kelly, A. Megrant, A. Veitia, D. Sank, E. Jeffrey, T. C. White, J. Mutus, A. G. Fowler, B. Campbell, Y. Chen, Z. Chen *et al.*, *Superconducting quantum circuits at the surface code threshold for fault tolerance*, Nature **508**, 500 (2014), doi:[10.1038/nature13171](https://doi.org/10.1038/nature13171). (Cited on pages [297](#) and [306](#).)
- [306] S. M. Albrecht, A. P. Higginbotham, M. Madsen, F. Kuemmeth, T. S. Jespersen, J. Nygård, P. Krogstrup and C. M. Marcus, *Exponential protection of zero modes in Majorana islands*, Nature **531**, 206 (2016), doi:[10.1038/nature17162](https://doi.org/10.1038/nature17162). (Cited on page [297](#).)
- [307] S. Bravyi and J. Haah, *Quantum self-correction in the 3D cubic code model*, Physical Review Letters **111**, 200501 (2013), doi:[10.1103/physrevlett.111.200501](https://doi.org/10.1103/physrevlett.111.200501). (Cited on pages [297](#) and [507](#).)
- [308] K. P. Michnicki, *3D topological quantum memory with a power-law energy barrier*, Physical Review Letters **113**, 130501 (2014), doi:[10.1103/physrevlett.113.130501](https://doi.org/10.1103/physrevlett.113.130501). (Cited on pages [297](#) and [507](#).)
- [309] C. G. Brell, *A proposal for self-correcting stabilizer quantum memories in 3 dimensions (or slightly less)*, New Journal of Physics **18**(1), 013050 (2016), doi:[10.1088/1367-2630/18/1/013050](https://doi.org/10.1088/1367-2630/18/1/013050). (Cited on pages [297](#) and [507](#).)

BIBLIOGRAPHY

- [310] C. Castelnovo and C. Chamon, *Entanglement and topological entropy of the toric code at finite temperature*, Physical Review B **76**, 184442 (2007), doi:[10.1103/physrevb.76.184442](https://doi.org/10.1103/physrevb.76.184442). (Cited on page 297.)
- [311] M. B. Hastings, *Topological order at nonzero temperature*, Physical Review Letters **107**, 210501 (2011), doi:[10.1103/physrevlett.107.210501](https://doi.org/10.1103/physrevlett.107.210501). (Cited on pages 297 and 507.)
- [312] F. L. Pedrocchi and D. P. DiVincenzo, *Majorana braiding with thermal noise*, Physical Review Letters **115**, 120402 (2015), doi:[10.1103/physrevlett.115.120402](https://doi.org/10.1103/physrevlett.115.120402). (Cited on page 297.)
- [313] R. Raussendorf and J. Harrington, *Fault-tolerant quantum computation with high threshold in two dimensions*, Physical Review Letters **98**, 190504 (2007), doi:[10.1103/physrevlett.98.190504](https://doi.org/10.1103/physrevlett.98.190504). (Cited on page 297.)
- [314] H. G. Katzgraber, H. Bombin and M. A. Martin-Delgado, *Error threshold for color codes and random three-body Ising models*, Physical Review Letters **103**, 090501 (2009), doi:[10.1103/physrevlett.103.090501](https://doi.org/10.1103/physrevlett.103.090501). (Cited on page 297.)
- [315] G. Duclos-Cianci and D. Poulin, *Fast decoders for topological quantum codes*, Physical Review Letters **104**, 050504 (2010), doi:[10.1103/physrevlett.104.050504](https://doi.org/10.1103/physrevlett.104.050504). (Cited on page 297.)
- [316] T. D. Ladd, F. Jelezko, R. Laflamme, Y. Nakamura, C. Monroe and J. L. O'Brien, *Quantum computers*, Nature **464**, 45 (2010), doi:[10.1038/nature08812](https://doi.org/10.1038/nature08812). (Cited on page 297.)
- [317] J. W. Harrington, *Analysis of quantum error-correcting codes: symplectic lattice codes and toric codes*, Ph.D. thesis, California Institute of Technology (2004). (Cited on page 297.)
- [318] P. Gács, *Reliable cellular automata with self-organization*, Journal of Statistical Physics **103**(1), 45 (2001), doi:[10.1023/a:1004823720305](https://doi.org/10.1023/a:1004823720305). (Cited on pages 297, 300, 329, and 337.)
- [319] M. Herold, E. T. Campbell, J. Eisert and M. J. Kastoryano, *Cellular-automaton decoders for topological quantum memories*, Npj Quantum Information **1**, 15010 (2015), doi:[10.1038/npjqi.2015.10](https://doi.org/10.1038/npjqi.2015.10). (Cited on page 298.)
- [320] M. Herold, M. J. Kastoryano, E. T. Campbell and J. Eisert, *Cellular automaton decoders of topological quantum memories in the fault tolerant setting*, New Journal of Physics **19**(6), 063012 (2017), doi:[10.1088/1367-2630/aa7099](https://doi.org/10.1088/1367-2630/aa7099). (Cited on page 298.)
- [321] N. H. Nickerson, Y. Li and S. C. Benjamin, *Topological quantum computing with a very noisy network and local error rates approaching one percent*, Nature Communications **4**, 1756 (2013), doi:[10.1038/ncomms2773](https://doi.org/10.1038/ncomms2773). (Cited on page 298.)
- [322] A. G. Fowler, A. C. Whiteside and L. C. L. Hollenberg, *Towards practical classical processing for the surface code*, Physical Review Letters **108**, 180501 (2012), doi:[10.1103/physrevlett.108.180501](https://doi.org/10.1103/physrevlett.108.180501). (Cited on page 298.)
- [323] A. G. Fowler, A. C. Whiteside and L. C. L. Hollenberg, *Towards practical classical processing for the surface code: Timing analysis*, Physical Review A **86**, 042313 (2012), doi:[10.1103/physreva.86.042313](https://doi.org/10.1103/physreva.86.042313). (Cited on page 298.)
- [324] A. G. Fowler, A. C. Whiteside, A. L. McInnes and A. Rabbani, *Topological code autotune*, Physical Review X **2**, 041003 (2012), doi:[10.1103/physrevx.2.041003](https://doi.org/10.1103/physrevx.2.041003). (Cited on page 298.)
- [325] A. G. Fowler, *Minimum weight perfect matching of fault-tolerant topological quantum error correction in average $O(1)$ parallel time*, Quantum Information and Computation **15**(1-2), 145 (2015). (Cited on page 298.)
- [326] C. D. Freeman, C. M. Herdman and K. B. Whaley, *Engineering autonomous error correction in stabilizer codes at finite temperature*, Physical Review A **96**, 012311 (2017), doi:[10.1103/physreva.96.012311](https://doi.org/10.1103/physreva.96.012311). (Cited on page 298.)

BIBLIOGRAPHY

- [327] A. Toom, *Cellular automata with errors: Problems for students of probability*, pp. 117–157, CRC Press, ISBN 0849380731 (1995). (Cited on pages 298, 317, 324, and 360.)
- [328] K. Park, *Ergodicity and mixing rate of one-dimensional cellular automata*, Ph.D. thesis, Boston University (1996). (Cited on pages 298, 320, and 337.)
- [329] J. Edmonds, *Paths, trees, and flowers*, Canadian Journal of Mathematics **17**, 449 (1965), doi:10.4153/cjm-1965-045-4. (Cited on page 298.)
- [330] C. Wang, J. Harrington and J. Preskill, *Confinement-Higgs transition in a disordered gauge theory and the accuracy threshold for quantum memory*, Annals of Physics **303**(1), 31 (2003), doi:10.1016/s0003-4916(02)00019-2. (Cited on page 298.)
- [331] N. H. Packard, *Adaptation toward the edge of chaos*, In *Dynamic Patterns in Complex Systems*, vol. 212, pp. 293–301. World Scientific, doi:10.1142/9789814542043 (1988). (Cited on pages 299 and 316.)
- [332] P. P. B. de Oliveira, *Conceptual connections around density determination in cellular automata*, In *Cellular Automata and Discrete Complex Systems*, pp. 1–14. Springer Berlin Heidelberg, doi:10.1007/978-3-642-40867-0_1 (2013). (Cited on pages 299, 316, and 317.)
- [333] M. Land and R. K. Belew, *No perfect two-state cellular automata for density classification exists*, Physical Review Letters **74**, 5148 (1995), doi:10.1103/physrevlett.74.5148. (Cited on pages 299 and 316.)
- [334] J. Fritz, *Interacting particle systems (Grundlehren der mathematischen Wissenschaften, 276)*, Bulletin of the London Mathematical Society **18**(2), 223 (1986), doi:10.1112/blms/18.2.223. (Cited on pages 300 and 337.)
- [335] P. Gács, *Reliable computation with cellular automata*, Journal of Computer and System Sciences **32**(1), 15 (1986), doi:10.1016/0022-0000(86)90002-4. (Cited on pages 300, 329, and 337.)
- [336] L. F. Gray, *A reader's guide to Gacs's "Positive Rates" paper*, Journal of Statistical Physics **103**(1), 1 (2001), doi:10.1023/a:1004824203467. (Cited on pages 300, 329, and 337.)
- [337] G. P. Wadsworth and J. G. Bryan, *Introduction to probability and random variables*, McGraw Hill, New York, ISBN 007067650X (1960). (Cited on pages 307 and 349.)
- [338] S. Wolfram, *Statistical mechanics of cellular automata*, Reviews of Modern Physics **55**, 601 (1983), doi:10.1103/revmodphys.55.601. (Cited on page 313.)
- [339] S. Wolfram, *A New Kind of Science*, Wolfram Media, ISBN 1579550088 (2002). (Cited on page 313.)
- [340] P. Gács, G. Kurdyumov and L. Levin, *One-dimensional homogeneous media dissolving finite islands*, Problems of Information Transmission **14**(3), 92 (1978). (Cited on page 317.)
- [341] H. Fukś, *Nondeterministic density classification with diffusive probabilistic cellular automata*, Physical Review E **66**, 066106 (2002), doi:10.1103/physreve.66.066106. (Cited on page 317.)
- [342] M. Schüle, T. Ott and R. Stoop, *Computing with probabilistic cellular automata*, In *Artificial Neural Networks - ICANN 2009*, pp. 525–533. Springer Berlin Heidelberg, doi:10.1007/978-3-642-04277-5_53 (2009). (Cited on page 317.)
- [343] N. Fatès, *Stochastic cellular automata solutions to the density classification problem*, Theory of Computing Systems **53**(2), 223 (2013), doi:10.1007/s00224-012-9386-3. (Cited on page 317.)

BIBLIOGRAPHY

- [344] M. S. Capcarrere, M. Sipper and M. Tomassini, *Two-state, $r = 1$ cellular automaton that classifies density*, Physical Review Letters **77**, 4969 (1996), doi:[10.1103/physrevlett.77.4969](https://doi.org/10.1103/physrevlett.77.4969). (Cited on page 317.)
- [345] H. Fuks-acute, *Solution of the density classification problem with two cellular automata rules*, Physical Review E **55**, R2081 (1997), doi:[10.1103/physreve.55.r2081](https://doi.org/10.1103/physreve.55.r2081). (Cited on page 317.)
- [346] H. F. Chau, L. W. Siu and K. K. Yan, *One dimensional nary density classification using two cellular automaton rules*, International Journal of Modern Physics C **10**(05), 883 (1999), doi:[10.1142/s0129183199000681](https://doi.org/10.1142/s0129183199000681). (Cited on page 317.)
- [347] M. S. Capcarrère and M. Sipper, *Necessary conditions for density classification by cellular automata*, Physical Review E **64**, 036113 (2001), doi:[10.1103/physreve.64.036113](https://doi.org/10.1103/physreve.64.036113). (Cited on page 317.)
- [348] P. G. de Sá and C. Maes, *The Gacs-Kurdyumov-Levin automaton revisited*, Journal of Statistical Physics **67**(3), 507 (1992), doi:[10.1007/bf01049718](https://doi.org/10.1007/bf01049718). (Cited on page 317.)
- [349] S. Wolfram, *Theory and applications of cellular automata*, World Scientific, ISBN 9971501236 (1986). (Cited on page 317.)
- [350] M. Sipper, M. S. Capcarrere and E. Ronald, *A simple cellular automaton that solves the density and ordering problems*, International Journal of Modern Physics C **09**(07), 899 (1998), doi:[10.1142/s0129183198000868](https://doi.org/10.1142/s0129183198000868). (Cited on page 317.)
- [351] S. Taati, *Restricted density classification in one dimension*, In *Cellular Automata and Discrete Complex Systems*, pp. 238–250. Springer Berlin Heidelberg, doi:[10.1007/978-3-662-47221-7_18](https://doi.org/10.1007/978-3-662-47221-7_18) (2015). (Cited on pages 329, 330, and 362.)
- [352] B. Durand, A. Romashchenko and A. Shen, *Fixed-point tile sets and their applications*, Journal of Computer and System Sciences **78**(3), 731 (2012), doi:[10.1016/j.jcss.2011.11.001](https://doi.org/10.1016/j.jcss.2011.11.001). (Cited on pages 329 and 365.)
- [353] S. R. Chowdhury, A. Banerjee, A. Roy and H. Saha, *A high speed 8 transistor full adder design using novel 3 transistor XOR gates*, International Journal of Electronics, Circuits and Systems **2**(4), 217 (2008). (Cited on page 342.)
- [354] S. S. Mishra, A. K. Agrawal and R. Nagaria, *A comparative performance analysis of various CMOS design techniques for XOR and XNOR circuits*, International Journal on Emerging Technologies **1**(1), 1 (2010). (Cited on page 342.)
- [355] S. Vemuru, P. Wang and M. Niamat, *Majority logic gate synthesis approaches for post-CMOS logic circuits: A review*, In *IEEE International Conference on Electro/Information Technology*, pp. 284–289, doi:[10.1109/eit.2014.6871778](https://doi.org/10.1109/eit.2014.6871778) (2014). (Cited on page 342.)
- [356] K. Walus, G. Schulhof, G. A. Jullien, R. Zhang and W. Wang, *Circuit design based on majority gates for applications with quantum-dot cellular automata*, In *Conference Record of the Thirty-Eighth Asilomar Conference on Signals, Systems and Computers, 2004.*, vol. 2, pp. 1354–1357, doi:[10.1109/acssc.2004.1399374](https://doi.org/10.1109/acssc.2004.1399374) (2004). (Cited on page 342.)
- [357] C. L. Kane, R. Mukhopadhyay and T. C. Lubensky, *Fractional quantum Hall effect in an array of quantum wires*, Physical Review Letters **88**, 036401 (2002), doi:[10.1103/physrevlett.88.036401](https://doi.org/10.1103/physrevlett.88.036401). (Cited on pages 379, 432, 433, 436, and 438.)
- [358] P. Jordan and E. P. Wigner, *Über das Paulische Äquivalenzverbot*, pp. 109–129, Springer Berlin Heidelberg, ISBN 978-3-662-02781-3, doi:[10.1007/978-3-662-02781-3_9](https://doi.org/10.1007/978-3-662-02781-3_9) (1993). (Cited on page 391.)

BIBLIOGRAPHY

- [359] J. Dereziński and C. Gérard, *Mathematics of Quantization and Quantum Fields*, Cambridge Monographs on Mathematical Physics. Cambridge University Press, ISBN 9781107011113 (2013). (Cited on page 391.)
- [360] T. Keilmann, S. Lanzmich, I. McCulloch and M. Roncaglia, *Statistically induced phase transitions and anyons in 1D optical lattices*, *Nature Communications* **2**, 361 (2011), doi:[10.1038/ncomms1353](https://doi.org/10.1038/ncomms1353). (Cited on page 397.)
- [361] A. Albuquerque, F. Alet, P. Corboz, P. Dayal, A. Feiguin, S. Fuchs, L. Gamper, E. Gull, S. Gürtler, A. Honecker, R. Igarashi, M. Körner *et al.*, *The ALPS project release 1.3: Open-source software for strongly correlated systems*, *Journal of Magnetism and Magnetic Materials* **310**(2, Part 2), 1187 (2007), doi:[10.1016/j.jmmm.2006.10.304](https://doi.org/10.1016/j.jmmm.2006.10.304). (Cited on pages 401, 428, and 431.)
- [362] E. P. Wigner, *Gruppentheorie und ihre Anwendung auf die Quantenmechanik der Atomspektren*, Vieweg+Teubner Verlag, Wiesbaden, ISBN 978-3-663-00642-8, doi:[10.1007/978-3-663-02555-9](https://doi.org/10.1007/978-3-663-02555-9) (1931). (Cited on page 402.)
- [363] M. B. Hastings, *Entropy and entanglement in quantum ground states*, *Physical Review B* **76**, 035114 (2007), doi:[10.1103/physrevb.76.035114](https://doi.org/10.1103/physrevb.76.035114). (Cited on page 403.)
- [364] M. B. Hastings, *An area law for one-dimensional quantum systems*, *Journal of Statistical Mechanics: Theory and Experiment* **2007**(08), P08024 (2007), doi:[10.1088/1742-5468/2007/08/p08024](https://doi.org/10.1088/1742-5468/2007/08/p08024). (Cited on page 403.)
- [365] N. Schuch, M. M. Wolf, F. Verstraete and J. I. Cirac, *Entropy scaling and simulability by matrix product states*, *Physical Review Letters* **100**, 030504 (2008), doi:[10.1103/physrevlett.100.030504](https://doi.org/10.1103/physrevlett.100.030504). (Cited on page 403.)
- [366] D. Pérez-García, M. M. Wolf, M. Sanz, F. Verstraete and J. I. Cirac, *String order and symmetries in quantum spin lattices*, *Physical Review Letters* **100**, 167202 (2008), doi:[10.1103/physrevlett.100.167202](https://doi.org/10.1103/physrevlett.100.167202). (Cited on page 406.)
- [367] J. Yang and Z.-X. Liu, *Irreducible projective representations and their physical applications*, *Journal of Physics A: Mathematical and Theoretical* **51**(2), 025207 (2018), doi:[10.1088/1751-8121/aa971a](https://doi.org/10.1088/1751-8121/aa971a). (Cited on page 420.)
- [368] A. Kapustin and A. Turzillo, *Equivariant topological quantum field theory and symmetry protected topological phases*, *Journal of High Energy Physics* **2017**(3), 6 (2017), doi:[10.1007/jhep03\(2017\)006](https://doi.org/10.1007/jhep03(2017)006). (Cited on page 420.)
- [369] S. R. Manmana, A. M. Läuchli, F. H. L. Essler and F. Mila, *Phase diagram and continuous pair-unbinding transition of the bilinear-biquadratic $S = 1$ Heisenberg chain in a magnetic field*, *Physical Review B* **83**, 184433 (2011), doi:[10.1103/physrevb.83.184433](https://doi.org/10.1103/physrevb.83.184433). (Cited on page 423.)
- [370] I. Affleck, T. Kennedy, E. H. Lieb and H. Tasaki, *Rigorous results on valence-bond ground states in antiferromagnets*, *Physical Review Letters* **59**, 799 (1987), doi:[10.1103/physrevlett.59.799](https://doi.org/10.1103/physrevlett.59.799). (Cited on page 423.)
- [371] A. Läuchli, G. Schmid and S. Trebst, *Spin nematics correlations in bilinear-biquadratic $S = 1$ spin chains*, *Physical Review B* **74**, 144426 (2006), doi:[10.1103/physrevb.74.144426](https://doi.org/10.1103/physrevb.74.144426). (Cited on page 423.)
- [372] S. Yoshida and K. Okamoto, *Phase diagram of spin-1/2 alternating ferromagnetic chain with XY-like anisotropy*, *Journal of the Physical Society of Japan* **58**(12), 4367 (1989), doi:[10.1143/jpsj.58.4367](https://doi.org/10.1143/jpsj.58.4367). (Cited on page 424.)
- [373] K. Hida, *Ground-state phase diagram of the spin-1/2 ferromagnetic-antiferromagnetic alternating Heisenberg chain with anisotropy*, *Physical Review B* **46**, 8268 (1992), doi:[10.1103/physrevb.46.8268](https://doi.org/10.1103/physrevb.46.8268). (Cited on page 424.)

BIBLIOGRAPHY

- [374] K. Hida, *Crossover between the Haldane-gap phase and the dimer phase in the spin-1/2 alternating Heisenberg chain*, Physical Review B **45**, 2207 (1992), doi:[10.1103/physrevb.45.2207](https://doi.org/10.1103/physrevb.45.2207). (Cited on page 424.)
- [375] M. Yamanaka, Y. Hatsugai and M. Kohmoto, *Phase diagram of the $S = 1/2$ quantum spin chain with bond alternation*, Physical Review B **48**, 9555 (1993), doi:[10.1103/physrevb.48.9555](https://doi.org/10.1103/physrevb.48.9555). (Cited on page 424.)
- [376] R. Haghshenas, A. Langari and A. T. Rezakhani, *Symmetry fractionalization: Symmetry-protected topological phases of the bond-alternating spin-1/2 Heisenberg chain*, Journal of Physics: Condensed Matter **26**(45), 456001 (2014), doi:[10.1088/0953-8984/26/45/456001](https://doi.org/10.1088/0953-8984/26/45/456001). (Cited on page 424.)
- [377] J. des Cloizeaux and J. J. Pearson, *Spin-wave spectrum of the antiferromagnetic linear chain*, Physical Review **128**, 2131 (1962), doi:[10.1103/physrev.128.2131](https://doi.org/10.1103/physrev.128.2131). (Cited on page 427.)
- [378] B. Nachtergaele, W. Spitzer and S. Starr, *Ferromagnetic ordering of energy levels*, Journal of Statistical Physics **116**(1), 719 (2004), doi:[10.1023/b:joss.0000037227.24460.e5](https://doi.org/10.1023/b:joss.0000037227.24460.e5). (Cited on page 428.)
- [379] B. Nachtergaele and S. Starr, *Ferromagnetic Lieb-Mattis theorem*, Physical Review Letters **94**, 057206 (2005), doi:[10.1103/physrevlett.94.057206](https://doi.org/10.1103/physrevlett.94.057206). (Cited on page 428.)
- [380] R. Prange, M. Cage, K. Klitzing, S. Girvin, A. Chang, F. Haldane, R. Laughlin, A. Pruisken and D. Thouless, *The Quantum Hall Effect*, Graduate Texts in Contemporary Physics. Springer New York, ISBN 9781461233503 (2012). (Cited on page 432.)
- [381] F. Haldane, *Demonstration of the “Luttinger liquid” character of Bethe-ansatz-soluble models of 1-D quantum fluids*, Physics Letters A **81**(2), 153 (1981), doi:[10.1016/0375-9601\(81\)90049-9](https://doi.org/10.1016/0375-9601(81)90049-9). (Cited on page 433.)
- [382] F. D. M. Haldane, *‘Luttinger liquid theory’ of one-dimensional quantum fluids. I. Properties of the Luttinger model and their extension to the general 1D interacting spinless Fermi gas*, Journal of Physics C: Solid State Physics **14**(19), 2585 (1981), doi:[10.1088/0022-3719/14/19/010](https://doi.org/10.1088/0022-3719/14/19/010). (Cited on page 433.)
- [383] J. von Delft and H. Schoeller, *Bosonization for beginners — Refermionization for experts*, Annalen der Physik **7**(4), 225 (1998), doi:[10.1002/\(sici\)1521-3889\(199811\)7:4<225::aid-andp225>3.0.co;2-1](https://doi.org/10.1002/(sici)1521-3889(199811)7:4<225::aid-andp225>3.0.co;2-1). (Cited on page 433.)
- [384] X.-G. Wen, *Electrodynamical properties of gapless edge excitations in the fractional quantum Hall states*, Physical Review Letters **64**, 2206 (1990), doi:[10.1103/physrevlett.64.2206](https://doi.org/10.1103/physrevlett.64.2206). (Cited on page 433.)
- [385] X.-G. Wen, *Theory of the edge states in fractional quantum Hall effects*, International Journal of Modern Physics B **06**(10), 1711 (1992), doi:[10.1142/s0217979292000840](https://doi.org/10.1142/s0217979292000840). (Cited on page 433.)
- [386] V. J. Emery, E. Fradkin, S. A. Kivelson and T. C. Lubensky, *Quantum theory of the smectic metal state in stripe phases*, Physical Review Letters **85**, 2160 (2000), doi:[10.1103/physrevlett.85.2160](https://doi.org/10.1103/physrevlett.85.2160). (Cited on pages 433 and 436.)
- [387] S. L. Sondhi and K. Yang, *Sliding phases via magnetic fields*, Physical Review B **63**, 054430 (2001), doi:[10.1103/physrevb.63.054430](https://doi.org/10.1103/physrevb.63.054430). (Cited on pages 433 and 436.)
- [388] A. Vishwanath and D. Carpentier, *Two-dimensional anisotropic non-Fermi-liquid phase of coupled Luttinger liquids*, Physical Review Letters **86**, 676 (2001), doi:[10.1103/physrevlett.86.676](https://doi.org/10.1103/physrevlett.86.676). (Cited on pages 433, 436, 439, 440, 442, 457, 460, and 464.)

BIBLIOGRAPHY

- [389] R. Mukhopadhyay, C. L. Kane and T. C. Lubensky, *Sliding Luttinger liquid phases*, Physical Review B **64**, 045120 (2001), doi:[10.1103/physrevb.64.045120](https://doi.org/10.1103/physrevb.64.045120). (Cited on pages [433](#), [436](#), [438](#), and [457](#).)
- [390] J. C. Y. Teo and C. L. Kane, *From Luttinger liquid to non-abelian quantum Hall states*, Physical Review B **89**, 085101 (2014), doi:[10.1103/physrevb.89.085101](https://doi.org/10.1103/physrevb.89.085101). (Cited on pages [433](#) and [436](#).)
- [391] A. Zee, *Semionics: A theory of superconductivity based on fractional quantum statistics*, In *25th International Conference on High-Energy Physics*, vol. 900802, pp. 206–212 (1990). (Cited on page [434](#).)
- [392] M. A. Cazalilla, R. Citro, T. Giamarchi, E. Orignac and M. Rigol, *One dimensional bosons: From condensed matter systems to ultracold gases*, Reviews of Modern Physics **83**, 1405 (2011), doi:[10.1103/revmodphys.83.1405](https://doi.org/10.1103/revmodphys.83.1405). (Cited on page [434](#).)
- [393] M. Krenn, M. Malik, R. Fickler, R. Lapkiewicz and A. Zeilinger, *Automated search for new quantum experiments*, Physical Review Letters **116**, 090405 (2016), doi:[10.1103/physrevlett.116.090405](https://doi.org/10.1103/physrevlett.116.090405). (Cited on page [465](#).)
- [394] D. Deutsch, *Constructor theory*, Synthese **190**(18), 4331 (2013), doi:[10.1007/s11229-013-0279-z](https://doi.org/10.1007/s11229-013-0279-z). (Cited on pages [465](#) and [482](#).)
- [395] D. E. Kirk, *Optimal Control Theory: An Introduction*, Dover Publications, ISBN 9780486135076 (2012). (Cited on page [485](#).)
- [396] D. Silver, A. Huang, C. J. Maddison, A. Guez, L. Sifre, G. van den Driessche, J. Schrittwieser, I. Antonoglou, V. Panneershelvam, M. Lanctot, S. Dieleman, D. Grewe *et al.*, *Mastering the game of Go with deep neural networks and tree search*, Nature **529**, 484 (2016), doi:[10.1038/nature16961](https://doi.org/10.1038/nature16961). (Cited on pages [491](#), [492](#), and [497](#).)
- [397] V. Dunjko and H. J. Briegel, *Machine learning & artificial intelligence in the quantum domain: A review of recent progress*, Reports on Progress in Physics **81**(7), 074001 (2018), doi:[10.1088/1361-6633/aab406](https://doi.org/10.1088/1361-6633/aab406). (Cited on page [491](#).)
- [398] G. Torlai and R. G. Melko, *Neural decoder for topological codes*, Physical Review Letters **119**, 030501 (2017), doi:[10.1103/physrevlett.119.030501](https://doi.org/10.1103/physrevlett.119.030501). (Cited on page [492](#).)
- [399] S. Krastanov and L. Jiang, *Deep neural network probabilistic decoder for stabilizer codes*, Scientific Reports **7**(1), 11003 (2017), doi:[10.1038/s41598-017-11266-1](https://doi.org/10.1038/s41598-017-11266-1). (Cited on page [492](#).)
- [400] S. Varsamopoulos, B. Criger and K. Bertels, *Decoding small surface codes with feedforward neural networks*, Quantum Science and Technology **3**(1), 015004 (2018), doi:[10.1088/2058-9565/aa955a](https://doi.org/10.1088/2058-9565/aa955a). (Cited on page [492](#).)
- [401] P. Baireuther, T. E. O'Brien, B. Tarasinski and C. W. J. Beenakker, *Machine-learning-assisted correction of correlated qubit errors in a topological code*, Quantum **2**, 48 (2018), doi:[10.22331/q-2018-01-29-48](https://doi.org/10.22331/q-2018-01-29-48). (Cited on page [492](#).)
- [402] N. P. Breuckmann and X. Ni, *Scalable neural network decoders for higher dimensional quantum codes*, Quantum **2**, 68 (2018), doi:[10.22331/q-2018-05-24-68](https://doi.org/10.22331/q-2018-05-24-68). (Cited on page [492](#).)
- [403] C. Chamberland and P. Ronagh, *Deep neural decoders for near term fault-tolerant experiments*, Quantum Science and Technology **3**(4), 044002 (2018), doi:[10.1088/2058-9565/aad1f7](https://doi.org/10.1088/2058-9565/aad1f7). (Cited on page [492](#).)
- [404] R. Lippmann, *An introduction to computing with neural nets*, IEEE ASSP Magazine **4**(2), 4 (1987), doi:[10.1109/massp.1987.1165576](https://doi.org/10.1109/massp.1987.1165576). (Cited on page [493](#).)
- [405] I. Goodfellow, Y. Bengio and A. Courville, *Deep Learning*, Adaptive Computation and Machine Learning series. MIT Press, ISBN 0262035618 (2016). (Cited on page [493](#).)

BIBLIOGRAPHY

- [406] G. Indiveri, B. Linares-Barranco, T. Hamilton, A. van Schaik, R. Etienne-Cummings, T. Delbruck, S.-C. Liu, P. Dudek, P. Häfliger, S. Renaud, J. Schemmel, G. Cauwenberghs *et al.*, *Neuromorphic silicon neuron circuits*, *Frontiers in Neuroscience* **5**, 73 (2011), doi:[10.3389/fnins.2011.00073](https://doi.org/10.3389/fnins.2011.00073). (Cited on page 498.)
- [407] M. Prezioso, F. Merrih-Bayat, B. D. Hoskins, G. C. Adam, K. K. Likharev and D. B. Strukov, *Training and operation of an integrated neuromorphic network based on metal-oxide memristors*, *Nature* **521**, 61 (2015), doi:[10.1038/nature14441](https://doi.org/10.1038/nature14441). (Cited on page 498.)
- [408] M. Abadi, A. Agarwal, P. Barham, E. Brevdo, Z. Chen, C. Citro, G. S. Corrado, A. Davis, J. Dean, M. Devin, S. Ghemawat, I. Goodfellow *et al.*, *TensorFlow: Large-scale machine learning on heterogeneous systems*, Software available from tensorflow.org (2015). (Cited on page 498.)
- [409] D. P. Kingma and J. Ba, *Adam: A method for stochastic optimization*, arXiv e-prints arXiv:1412.6980 (2014), arXiv:[1412.6980](https://arxiv.org/abs/1412.6980). (Cited on page 500.)
- [410] D. Gottesman, *Class of quantum error-correcting codes saturating the quantum hamming bound*, *Physical Review A* **54**, 1862 (1996), doi:[10.1103/physreva.54.1862](https://doi.org/10.1103/physreva.54.1862). (Cited on page 506.)
- [411] D. Gottesman, *Stabilizer Codes and Quantum Error Correction*, Ph.D. thesis, California Institute of Technology (1997), arXiv:[quant-ph/9705052](https://arxiv.org/abs/quant-ph/9705052). (Cited on page 506.)
- [412] D. Gottesman, *Theory of fault-tolerant quantum computation*, *Physical Review A* **57**, 127 (1998), doi:[10.1103/physreva.57.127](https://doi.org/10.1103/physreva.57.127). (Cited on page 506.)
- [413] R. Alicki, M. Fannes and M. Horodecki, *A statistical mechanics view on Kitaev's proposal for quantum memories*, *Journal of Physics A: Mathematical and Theoretical* **40**(24), 6451 (2007), doi:[10.1088/1751-8113/40/24/012](https://doi.org/10.1088/1751-8113/40/24/012). (Cited on page 507.)
- [414] Z. Nussinov and G. Ortiz, *Autocorrelations and thermal fragility of anyonic loops in topologically quantum ordered systems*, *Physical Review B* **77**, 064302 (2008), doi:[10.1103/physrevb.77.064302](https://doi.org/10.1103/physrevb.77.064302). (Cited on page 507.)
- [415] S. Bravyi and B. Terhal, *A no-go theorem for a two-dimensional self-correcting quantum memory based on stabilizer codes*, *New Journal of Physics* **11**(4), 043029 (2009), doi:[10.1088/1367-2630/11/4/043029](https://doi.org/10.1088/1367-2630/11/4/043029). (Cited on pages 507 and 526.)
- [416] B. Yoshida, *Feasibility of self-correcting quantum memory and thermal stability of topological order*, *Annals of Physics* **326**(10), 2566 (2011), doi:[10.1016/j.aop.2011.06.001](https://doi.org/10.1016/j.aop.2011.06.001). (Cited on page 507.)
- [417] J. Haah, *Commuting Pauli Hamiltonians as maps between free modules*, *Communications in Mathematical Physics* **324**(2), 351 (2013), doi:[10.1007/s00220-013-1810-2](https://doi.org/10.1007/s00220-013-1810-2). (Cited on pages 507 and 508.)
- [418] F. Pastawski and B. Yoshida, *Fault-tolerant logical gates in quantum error-correcting codes*, *Physical Review A* **91**, 012305 (2015), doi:[10.1103/physreva.91.012305](https://doi.org/10.1103/physreva.91.012305). (Cited on page 507.)
- [419] J. Haah, *Local stabilizer codes in three dimensions without string logical operators*, *Physical Review A* **83**, 042330 (2011), doi:[10.1103/physreva.83.042330](https://doi.org/10.1103/physreva.83.042330). (Cited on pages 507, 510, and 526.)
- [420] H. Wang, *Proving theorems by pattern recognition - II*, *The Bell System Technical Journal* **40**(1), 1 (1961), doi:[10.1002/j.1538-7305.1961.tb03975.x](https://doi.org/10.1002/j.1538-7305.1961.tb03975.x). (Cited on pages 508 and 512.)
- [421] R. Berger, *The undecidability of the domino problem*, 66. *Memoirs of the American Mathematical Society*, doi:[10.1090/memo/0066](https://doi.org/10.1090/memo/0066) (1966). (Cited on pages 508 and 512.)

BIBLIOGRAPHY

- [422] R. Alicki, *Quantum memory as a perpetuum mobile? Stability vs. reversibility of information processing*, *Open Systems & Information Dynamics* **19**(03), 1250016 (2012), doi:[10.1142/s1230161212500163](https://doi.org/10.1142/s1230161212500163). (Cited on page 508.)
- [423] K. Culik, *An aperiodic set of 13 Wang tiles*, *Discrete Mathematics* **160**(1), 245 (1996), doi:[10.1016/s0012-365x\(96\)00118-5](https://doi.org/10.1016/s0012-365x(96)00118-5). (Cited on pages 511 and 512.)
- [424] P. G. Buckhiester, *Rank r solutions to the matrix equation $XAX^T = C$, A alternate, over $\text{GF}(2^y)$* , *Transactions of the American Mathematical Society* **189**, 201 (1974), doi:[10.1090/s0002-9947-1974-0330196-0](https://doi.org/10.1090/s0002-9947-1974-0330196-0). (Cited on pages 516 and 517.)
- [425] K. Culik and J. Kari, *An aperiodic set of Wang cubes*, pp. 675–686, Springer Berlin Heidelberg, ISBN 978-3-642-80350-5, doi:[10.1007/978-3-642-80350-5_57](https://doi.org/10.1007/978-3-642-80350-5_57) (1996). (Cited on page 520.)
- [426] D. Poulin, *Stabilizer formalism for operator quantum error correction*, *Physical Review Letters* **95**, 230504 (2005), doi:[10.1103/physrevlett.95.230504](https://doi.org/10.1103/physrevlett.95.230504). (Cited on page 526.)
- [427] A. Shokrollahi, *LDPC codes: An introduction*, In *Coding, Cryptography and Combinatorics*, pp. 85–110. Birkhäuser Basel, doi:[10.1007/978-3-0348-7865-4_5](https://doi.org/10.1007/978-3-0348-7865-4_5) (2004). (Cited on page 527.)
- [428] J. van Lint, *Introduction to Coding Theory*, Graduate Texts in Mathematics. Springer Berlin Heidelberg, ISBN 9783540641339 (1998). (Cited on page 529.)
- [429] A. Vardy, *The intractability of computing the minimum distance of a code*, *IEEE Transactions on Information Theory* **43**(6), 1757 (1997), doi:[10.1109/18.641542](https://doi.org/10.1109/18.641542). (Cited on pages 530 and 534.)
- [430] S. Elitzur, *Impossibility of spontaneously breaking local symmetries*, *Physical Review D* **12**, 3978 (1975), doi:[10.1103/physrevd.12.3978](https://doi.org/10.1103/physrevd.12.3978). (Cited on page 530.)
- [431] D. M. Chickering, D. Geiger and D. Heckerman, *On finding a cycle basis with a shortest maximal cycle*, *Information Processing Letters* **54**(1), 55 (1995), doi:[10.1016/0020-0190\(94\)00231-m](https://doi.org/10.1016/0020-0190(94)00231-m). (Cited on pages 532, 533, 534, and 535.)
- [432] R. Diestel, *Graph Theory*, Springer Graduate Texts in Mathematics. Springer, ISBN 9783961340057 (2017). (Cited on page 535.)
- [433] G. Galbiati, *On finding cycle bases and fundamental cycle bases with a shortest maximal cycle*, *Information Processing Letters* **88**(4), 155 (2003), doi:[10.1016/j.ipl.2003.07.003](https://doi.org/10.1016/j.ipl.2003.07.003). (Cited on page 535.)
- [434] J. Horton, *A polynomial-time algorithm to find the shortest cycle basis of a graph*, *SIAM Journal on Computing* **16**(2), 358 (1987), doi:[10.1137/0216026](https://doi.org/10.1137/0216026). (Cited on page 535.)
- [435] K. Mehlhorn and D. Michail, *Minimum cycle bases: Faster and simpler*, *ACM Transactions on Algorithms* **6**(1), 8:1 (2009), doi:[10.1145/1644015.1644023](https://doi.org/10.1145/1644015.1644023). (Cited on page 535.)
- [436] F. J. Wegner, *Duality in generalized Ising models and phase transitions without local order parameters*, *Journal of Mathematical Physics* **12**(10), 2259 (1971), doi:[10.1063/1.1665530](https://doi.org/10.1063/1.1665530). (Cited on page 535.)
- [437] J. B. Kogut, *An introduction to lattice gauge theory and spin systems*, *Reviews of Modern Physics* **51**, 659 (1979), doi:[10.1103/revmodphys.51.659](https://doi.org/10.1103/revmodphys.51.659). (Cited on page 535.)
- [438] W. T. Tutte, *An algorithm for determining whether a given binary matroid is graphic*, *Proceedings of the American Mathematical Society* **11**(6), 905 (1960), doi:[10.1090/s0002-9939-1960-0117173-5](https://doi.org/10.1090/s0002-9939-1960-0117173-5). (Cited on page 535.)